

SAUPEC

Southern African Universities Power Engineering Conference



VUT

Vaal University of Technology



Proceedings of the 24th Southern African Universities Power Engineering Conference

SAUPEC 2016

**Vaal University of Technology and South African
Institute of Electrical Engineers, Vereeniging, South
Africa**

26-28 January 2016

Review:

Authors were invited to submit full papers to the broad subject “Electrical Engineering”.

Each paper was peer reviewed by a specialist reviewer. In the case where the reviewer rejected the paper, a second review was done to decide the outcome. Final acceptance was based on the contribution, scientific and technical merit of the paper.

Disclaimer:

Authors are responsible for the contents of their papers.

Published by the Southern African Universities Power Engineering Conference (SAUPEC) and the South African Institute of Electrical Engineers (SAIEE)

ISBN 978-1-77012-386

List of Reviewers

AO Akumu
AJ Grobler
AJL Joannou
AG Swanson
A Marks
AK Raji
BS Paul
CG Richards
C Nyamupangedengu
D Pentz
E Boje
G van Schoor
HJ Vermeulen
IE Davidson
J Naude
J Braid
J van Coller
J de Kock
K Awodele
KJ Nixon
KA Folly

KR Uren
MJ Kamper
M Adonis
M Ntshani
M Grobler
N Gumede
N Gule
N Smit
P Bokoro
R Wolhuter
R Loubser
S Chan-Wing
S Gerber
S Chowdhury
W Doorsamy
W Cronje
H van Rensburg
J Walker
AK. Saha
R Gouws

PROGRAM

Tuesday 26 January 2016

07h30 - 08h30	Registration
08h45 - 09h00	Opening - TESP
09h00 - 10h15	Breakaway Reportback
10h15 - 10h30	Tea/Coffee
10h30 - 12h30	Breakaway Reportback
12h30 - 13h00	Lunch
13h00 - 14h15	General Report-Back
14h15 - 14h30	Close
14h30 - 15h00	Coffee Break
15H00 - 15H30	Opening SAUPEC
15h30 - 16h30	Plenary Session
	Cocktail Function

Wednesday 27 January 2016

7h30 - 08h30	Registration			
08h30 - 10h00	Session 1 - A	Session 1 - B	Session 1 -C	Session 1 - D
10h00 - 10h30	COFFEE			
10h30 - 12h00	Session 2 - A	Session 2 - B	Session 2 - C	Session 2 - D
12h00 - 13h00	LUNCH			
13h00 - 14h30	Session 3 - A	Session 3 - B	Session 3 - C	Session 3 - D
14h30 - 15h00	COFFEE			
15h00 - 16h30	Session 4 - A	Session 4 - B	Session 4 - C	Session 4 - D
18h00 for 18h30	Gala Dinner			

Thursday 28 January 2016

7h30 - 08h30	Registration			
08h30 - 10h00	Session 5 - A	Session 5 - B	Session 5 -C	Session 5 - D
10h00 - 10h30	COFFEE			
10h30 - 12h00	Session 6 - A	Session 6 - B	Session 6 - C	Session 6 - D
12h00 - 13h00	LUNCH			
13h00 - 14h30	Session 7 - A	Session 7 - B		
14h30 - 15h00	COFFEE			
15h00 - 15h30	Closing			

PAPER PRESENTATION PROGRAM

<u>26 January 2016 - Plenary Session</u>	
P1	Clustering Potential Wind Farm Locations based on Simulated Time-of-Day Power Profiles <i>C.J. Joubert and H.J. Vermeulen</i>
P2	Investigation Into Role of Arcing Horns on 132 kV Sub-transmission Infrastructure <i>BA Smith and AG Swanson</i>
P3	A Proposal for Techno-Economic Analysis Framework for Wave Energy to Electricity Conversion Schemes under South African Conditions <i>S.S. Biyela, W.A. Cronje</i>
<u>27 January - Session 1A – High Voltage</u>	
1A-1	Performance Evaluation of an Entropy-based Image Analysis Algorithm for Insulator Hydrophobicity Classification for Different Image Acquisition Lighting Conditions <i>M.M. Ndamira and H.J. Vermeulen and J.M. Strauss</i>
1A-2	An Investigation into Surge Arresters Failures in the KZN 88 kV Traction System <i>M. Mzulwini and K. Awodele</i>
1A-3	Investigation into the Flashover Mechanism on Mounting Arms of 22 kV Surge Arresters <i>B. Singh, M.F. Khan and A.G. Swanson</i>
1A-4	A Study of the Distribution of Voltage and Electric Field on Glass Insulators using Charge Simulation Method <i>G. Ininahazwe and I.E. Davidson</i>
<u>Session 1B – Renewables</u>	
1B-1	Design and Comparison of Renewable Energy Storage Systems for Emergency use on Farms in South Africa <i>J.C. Campher and R. Gouws</i>
1B-2	Modelling and Simulation of Grid-Connected Photovoltaic Systems <i>M. Mazibuko, A.K. Saha</i>
1B-3	Performance Comparison of Perturb & Observe and Incremental Conductance MPPT Schemes for Solar PV Plants <i>J. Bamukunde, M. Nthontho, S.K. Kibaara and S. Chowdhury</i>
1B-4	Design and development of a remote solar power control, battery monitoring system and internet logging capability <i>J.Bothma, N de Lange and F. Adlam</i>
<u>Session 1C – Machines</u>	
1C-1	Analytical Model Development for the Determination of the Open-Circuit Magnetic Field Distribution in a Moving Coil Tubular Permanent Magnet <i>D.K. Chembe, J.M. Strauss and P.J.Randewijk</i>
1C-2	Designing a 750 W Ironless Stator for an Axial Flux Permanent Magnet Wind Generator <i>N.J. Baker and A.J. Grobler</i>
1C-3	Method for Assessing the Thermal Performance of a Synchronous Generator Rotor <i>A. Narain Singh, W. Doorsamy and W. A. Cronje</i>
1C-4	Evaluation of Hand Carved Timber Blade Performance for a Rutland 910 Wind Turbine <i>P.Ghimire, P. Freere, R. Sinha, L. Mishnaevsky Jr., K. Silwal, M. Freere</i>
<u>Session 1D – Distribution / Transmission</u>	
1D-1	Instability Problems in the SAPP Network <i>H. du Plessis and J.A. de Kock</i>
1D-2	Applying the Herman-Beta probabilistic method to Medium Voltage distribution feeders <i>M.J. Chihota, C.T. Gaunt and R.Herman</i>
1D-3	Drivers and Application of Small Scale DG on Municipal Distribution Networks in South Africa <i>S. Sewchurran and I E Davidson</i>
1D-4	Analytical Approach for Optimal DG Allocation in Primary Distribution Networks <i>O.O. Osaloni and K.O. Awodele</i>
<u>Session 2 A – High Voltage</u>	
2A-1	Evaluation of the Design and Functionality of a Laboratory Corona Cage <i>JS. Djeumen, JJ.Walker and IK. Kyere</i>
2A-2	Natural and Synthetic Ester Based Transformer Insulation Fluid <i>Leeshen Pather and Andrew Swanson</i>
2A-3	The Measurement of HVDC Insulator Leakage Current Using Magnetic Field Sensors <i>M Roman, RR van Zyl, N Parus, N Mahatho and B Nalomo</i>
2A-4	Towards an Explanation of the Abnormal Attenuation of the Power Line Carrier Signals on an HVDC Monopolar Transmission Line <i>J. Schutte, A.C. Britten, J. van Coller and R. Hubbard</i>
2A-5	Electric Field and Ion Current Interactions Between Hybrid High Voltage AC and DC Circuits with a focus on Altitude Effects <i>N Parus and I.R Jandrell</i>
<u>Session 2 B – Renewables</u>	
2B-1	Pvsyst Model Improvement Using Field Data From a 75 MWp Solar Power Plant in South Africa <i>T. Mahachi and A.J. Rix</i>
2B-2	Renewable Energy Technology for Saving and Generating Pollution Free Energy in South Africa <i>ZP Khumalo and Bakhe B. Nleya</i>
2B-3	Comparison of Impacts of Integration of Solar PV Farms and Wind Farms in a Utility Grid <i>K. Ramoreboli, T. Matlokotsi and S. Chowdhury</i>
2B-4	The Impact of Large Penetration of Grid Connected Photovoltaic (PV) Generation on the Utility Grid: a Case for South Africa <i>N. Dhlamini, S.P. Chowdhury, And A. Sendegeya</i>
2B-5	Microgrid and Active Management of Distribution Networks with Renewable Energy sources <i>K.T. Akindeji and I.E. Davidson</i>

<u>Session 2 C – Energy Management</u>	
2C-1	Reliability Centred Maintenance (RCM) Model Implemented to Ethekweni Electricity Network <i>M.P. Lokothwayo and G. Frederick d Almaine</i>
2C-2	Energy Management Efficiency on Traction Network Through Regenerative Braking <i>A. Bani, K. Awodele</i>
2C-3	Performance Study of Locomotive Systems for a Reliable Cost Effective Maintenance Solution <i>T.N. Miyambo and S.P. Chowdary</i>
2C-4	Contrasting three different academic assessments of a compulsory capstone module in power engineering indicates reliability <i>A.J. Swart and P.E. Hertzog</i>
2C-5	Development of an Efficient Longitudinal Rail Impact Test Control System <i>M.J. Lencwe & S.P. Chowdhury</i>
<u>Session 2 D - Distribution / Transmission</u>	
2D-1	A Methodology for Optimal Placement of Distributed Generation on Meshed Networks to Reduce Power Losses for Time Variant Loads <i>S. Malapermal, M. Bello and Dr I.E. Davidson</i>
2D-2	Assessment of Power System Stabilizers for Small Signal Stability using the Population-Based Incremental Learning Algorithm <i>D Dombo and Prof K.A. Folly</i>
2D-3	Guiding Principles for Grid Code Compliance of Medium-High Voltage Renewable Power Plant Distributed Generation Integration onto South Africa's Transmission and Distribution Networks <i>S. Sewchurran and I E Davidson</i>
2D-4	Optimisation of an Experimental Perturbation and Estimation Technique used to Autonomise Nodes on DC Microgrids <i>W. Doorsamy, W.A. Cronje, M. Montaz Ali</i>
2D-5	Modelling of Moving Loads Using Stationary Dynamic Current Sources <i>L. Lategan, P.J. Randewijk and C.J. Fourie</i>
<u>Session 3 A – Power Electronics</u>	
3A-1	Integration of Inverter Constraints in Geometrical Quantification of the Optimal Solution to a MPC Controller <i>J. Raath, H. du Toit and T. Geyer</i>
3A-2	Design and Implementation of a Bidirectional Current-Controlled Voltage-Regulated DC-DC Switched-Mode Converter <i>A. Coetzer, G.R. Turner and H.D.T mouton</i>
3A-3	Design and Simulation of a Charging Algorithm for Lithium Ion Batteries <i>H. Tayob, I. Chotia and S. Chowdhury</i>
3A-4	Designing a Gas Sniffer Monitoring System for a Quadcopter <i>E. Bateman, O. Dobzhanskyi and R Gouws</i>
<u>Session 3 B – Electrical Protection</u>	
3B-1	Analysing and modelling the MV protection scheme of the Aberdare Cables PE factory and investigating the possibility of implementing embedded generation using waste heat <i>Jeshurun William Haigh, Anthony Marks</i>
3B-2	The Importance of Circuit Breaker Testing <i>A. Munhutu, J. Van Coller and Igor Djurdjevic</i>
3B-3	Improving the Overcurrent and Earth Fault Protection in the NMMU's Multiple Ring Distribution Network <i>Timothy de Vos, Anthony Marks</i>
3B-4	Protection Over current Curve plotter with Fault locator application <i>Y Sithole and B Kotze</i>
<u>Session 3 C – Machines</u>	
3C-1	Design of a Controlled Cooling System for a Three-Phase Power Transformer With Support of Renewable Energy <i>I.Coetzee and R. Gouws</i>
3C-2	Starting of Cylindrical Wound-Rotor Synchronous Motor for Fan Loads <i>H.J.S.Roux and M.J.Kamper</i>
3C-3	Simulation Study of Generator Under-excitation Operation and Under-excitation Limiters <i>D.N. Ngema and A.K. Saha</i>
3C-4	Induction Motor Efficiency Test Methods: A Comparison of Standards <i>S. Deda and JA de Kock</i>
<u>Session 3 D – Control</u>	
3D-1	Electromagnetic design of active magnetic bearings for a 30000 r/min PMSM <i>K. Swanepoel and A.J. Grobler</i>
3D-2	Design of a PLC-Based Variable Load, Speed Control System for a Three-Phase Induction Motor <i>B. Coetzer and R. Gouws</i>
3D-3	Inner Loop Current Controller Design for a Solar Array Simulator <i>T.B. Tapfunane, H du T Mouton & A.J. Rix</i>
3D-4	A Torque and Temperature Telemetry System for Rotating Magnet <i>P.J. Friend and A.J. Grobler</i>
<u>Session 4 A – High Voltage</u>	
4A-1	An Investigation into Partial Discharges of XLPE Cable Insulation Defects <i>I.K. Kyere, J.J. Walker</i>
4A-2	Investigation of Breakdown Voltage of Different Transformer Oils <i>K.P. Zondi, L Pather and AG Swanson</i>
4A-3	Partial Discharge Analysis of Failed ZnO Surge Arrester Elements at eThekweni Electricity <i>M. Gumede and F.D Almaine</i>
4A-4	Understanding Altitude in the Study of Air Gap Breakdown under High Voltage <i>P. Naidoo</i>

Session 4 B - Renewables	
4B-1	Dynamic Analysis of Photovoltaic Plant Using Custom Modelled PV System <i>N. Mazibuko, A.K. Saha</i>
4B-2	Optimised Model of a Solar/Wind/Diesel Hybrid Generation System for Rural Application <i>E. Hamatwi and I E Davidson</i>
4B-3	A Study of Synchronization of Single-Phase Inverters in South African Grid with High Degree of Penetration of Renewable Energy <i>M.M. Sibanyoni and S.P. Chowdhury</i>
4B-4	Potential in utilising ferrochrome furnace off-gas in South Africa: A Techno-economic study <i>R.Murray and J.A. de Kock</i>
Session 4 C – Electrical Protection	
4C-1	NMMU South Campus Ring Feeder Protection Design and Analysis <i>Llewelyn Grobler, Anthony Marks</i>
4C-2	Coordination between Overexcitation and Generator Over-voltage Protection with respect to Overexcitation Limiters <i>D.N. Ngema and A.K. Saha</i>
4C-3	Analysis and Solutions of Overcurrent Protection Issues for Distribution Networks with Distributed Generation Integrated <i>S.S. Mahendula and A.K. Saha</i>
4C-4	Implementation of Steam Turbine and Governing System using Programmable Logic Controller for Power Systems Studies <i>A.K. Saha</i>
Session 4 D – Distribution / Transmission	
4D-1	A simulated energy monitoring system to enable undergraduate engineering students to grasp fundamental energy generation principles <i>P.E. Hertzog and A.J. Swart</i>
4D-2	Analysis for Improving Redundancy and Reliability of the Graaff-Reinet Network <i>Anthony Marks, Asekho Mbambiso, A-J Phillips</i>
4D-3	Designing and Integrating a Solar Grid-Tie and Off-Grid System into One System <i>D. Diedericks, O. Dobzhanskyi and R Gouws</i>
4D-4	Measurements and Multipath Characterization of Power Line Communication Channel <i>Steven O. Awino and Thomas J.O.</i>
28 January 2016 - Session 5 A - Power Electronics	
5A-1	Improved Dynamic Response of Flying Capacitor Converter Using Finite Set-Model Predictive Current Control <i>A.M. Almaktoof, A.K. Raji and M.T.E. Kahm</i>
5A-2	Battery Monitoring and Temperature Controller System for the 15E Ore-Line Electric Locomotives <i>S. Krishnamurthy and K.C Gabashane</i>
5A-3	Single phase to three phase variable frequency drive <i>D.E. van Rooyen, W. Kukard, A.J. Grobler</i>
5A-4	Design and Simulation of a Digitally Controlled Class-D Amplifier <i>C.A. van der Merwe, H.D.T. Mouton and B.Putzeys</i>
Session 5 B - Distribution / Transmission	
5B-1	The Impact of HVDC Schemes on Network Transient Rotor Angle Stability <i>K.N.I Mbangula, O.E. Oni and I.E. Davidson</i>
5B-2	Stability Enhancement of HVAC Networks using Supplementary Controllers with HVDC Links <i>S M'bulu Ives and AG Swanson</i>
5B-3	Finite Element Analysis of Mechanical Oscillation of Power Line Conductors <i>E.E. Ojo and M.N. Ijumba</i>
5B-4	Study of Photovoltaic Integration Impact on Eskom Power Station Distribution System using Custom Modelled PV System <i>N. Mazibuko, A.K. Saha</i>
Session 5 C - Smart Grid	
5C-1	Secured Smart Grid Network for Advanced Metering Infrastructure (AMI) <i>Philani Khumalo & Bakhe Nleya</i>
5C-2	DC Optimal Power Flow through the Linear Programming - in Context of Smart Grid <i>A. Goudarzi, M. Kazemi and A.G. Swanson</i>
5C-3	Smart Grid Penetration at the eThekweni Municipality <i>V. Rampirith and I.E. Davidson</i>
5C-4	Smart Grid Applications using ETSI M2M: Domestic Electric Water Heaters <i>A.H. Cloete, J.W.K. Brown, M.J. Booysen R. Steinke and T. Magedanz</i>
Session 5 D - Control	
5D-1	Mitigation of Electromagnetic Interference Generated By GPIB Control-Network In Ac-Dc Transfer Measurement System <i>M.M. Hlakola, E. Golovins and D.V. Nicolae</i>
5D-2	Android Based Vehicle Tracking System with Collision Detection <i>T. Mvindi and F. Adlam</i>
5D-3	Design and development of a remote solar power control, battery monitoring system and internet logging capability <i>J. Bothma, N de Lange and F. Adlam</i>
5D-4	A Review of DSTATCOM for Power Quality Improvement <i>O. Ajayi and R.Tiako</i>
Session 6 A - High Voltage	
6A-1	Validation of the Breakdown Mechanism Between Rotated Arcing Horns <i>BA Smith and AG Swanson</i>
6A-2	Impulse Breakdown of SF ₆ -N ₂ Gas Mixtures <i>C. Babunandan, M.D. Brown and A.G. Swanson</i>
6A-3	Mean Energy, Electron drift and Effective Ionisation Coefficients in SF ₆ -N ₂ Mixtures from Bolsig+ <i>M.D. Brown, A.G. Swanson and L. Jarvis</i>
6A-4	Lightning Overvoltage Protection and Network Performance of Distribution Transformers – Case Study: Swaziland Electricity Company <i>M.T. Maziya and K.O. Awodele</i>
6A-5	A Simulation Study of the Inrush Current Performance of Amorphous Core and C.R.G.O Transformers <i>Naidoo and AG. Swanson</i>

Session 6 B - Smart Grid / Renewables	
6B-1	Economic Advantages of Stirling-Dish Concentrated Solar Power over the Molten Salt Power Tower Type Concentrated Solar Power Using System Advisor Model <i>C. Chukwuka and K.A Folly</i>
6B-2	Evaluation of an empirical model for a flat plate solar collector <i>Nothando Ndlovu, Michael Simon and Stephan Tangwe</i>
6B-3	Impact of Solar Power Generation on Economic Growth - The Role of 3DPV Structure <i>O.A. Mafimidiwo, A.K. Saha</i>
6B-4	The Extraction of Power and Fresh Water from the Ocean off the Coast of KZN utilizing Ocean Thermal Energy Conversion (OTEC) Techniques <i>M. Gumede and F.D. Almaine</i>
6B-5	Aquifer Underground Pumped Hydroelectric Energy Storage in South Africa <i>S.Y. Khan and I.E. Davidson</i>
Session 6 C - Machines	
6C-1	Design Aspects of a Magnetically Geared Permanent Magnet Machine with an Outer Stator <i>PM Tlali, JDG van der Merwe, R-J Wang, S Gerber</i>
6C-2	Design and Optimisation of a Line-Start Synchronous Reluctance Motor <i>Q. Smit, A.J. Sorgdrager and R-J Wang</i>
6C-3	Design of Permanent Synchronous Generator for Geared Direct-Connected Wind Generator Drive Train <i>P.J.J. van Wyk, G. Dawood, and M.J. Kamper</i>
6C-4	Development of an Analytical Model for a Moving Coil Tubular Permanent Magnet Linear Oscillatory Machine <i>D.K. Chembe, J.M. Strauss and P.J. Randewijk</i>
6C-5	Design and Optimisation of an Ironless Double-Rotor Radial Flux Permanent Magnet Machine. <i>A. Joss and P.J. Randewijk</i>
Session 6 D - Distribution / Transmission	
6D-1	Assessment of the Vibration Level at the Catenary value of 2100m for an OPGW using Endurance Limit Approach <i>M. Gizaw, R. Loubser, I.E. Davidson, G. Bright and R. Stephan</i>
6D-2	Power Distribution System Reliability Improvement Through the Application of Smart Technology <i>GC Dumakude, AG Swanson and IE Davidson</i>
6D-3	The Southern African Power Pool (SAPP) steady state security assessment using contingency analysis <i>Stacey J. T Mwale, Innocent E. Davidson</i>
6D-4	A Method for Measuring and Recording Changes in Wood Pole Impedance over Time <i>N.E. Khoza, A. Beutel, J. Van Coller</i>
Session 7 A - Power Electronics	
7A-1	Current Control of a Grid-Tied Inverter With LCL-Filter Through Model predictive Control <i>J.M.C. Geldenhuys, T. Mouton and A. Rix</i>
7A-2	Design and Development of a Laboratory Model for Distribution Static Synchronous Compensator <i>T.E. Mabotja & S.P. Chowdhury</i>
7A-3	Maximum Power Point Tracking Controller for a Wind Energy Conversion System <i>C.P. Brand and A.J. Grobler</i>
7A-4	Design and Implementation of a Power Line Carrier Communication System using Home Plug green PHY for Demand Side Management (DSM) <i>A. Ogunleye, P.J Randewijk , R. Wolhuter</i>
Session 7 B - Machines	
7B-1	Synchronisation Criteria of Line-Start Permanent Magnet Synchronous Motor: A Revisit <i>A. Chama A.J. Sorgdrager and R-J Wang</i>
7B-2	Comparison of Operating Modes for the Rotor-Tied Doubly Induction Generator <i>O.I. Olubamiwa, N.L Zietsman and N. Gule</i>
7B-3	Rotor Position Measurement with Magnetic Stray Fields <i>A. Treurnicht and P.J. Randewijk</i>
7B-4	Enhancing the Dynamic Performance of a Direct-Drive PMSG Wind Turbine Using Damping Controllers <i>A.N. Legesse, A.K. Saha and R. Pillay Carpanen</i>

Clustering Potential Wind Farm Locations based on Simulated Time-of-Day Power Profiles

C.J. JOUBERT* AND H.J. VERMEULEN*

**Stellenbosch University, Department Electrical and Electronic Engineering, 7602 Stellenbosch, South Africa.*

Abstract. The power generation profiles of wind farms are highly dependent on weather conditions and shows cyclic behaviour along diurnal and seasonal timelines. The stochastic nature of wind resources means that wind power cannot always be dispatched when needed. The geographical locations of wind farms can in principle be optimised to improve the variability of the wind resource or maximise grid support at given times of day or seasons of the year. Clustering analysis is a valuable tool to reduce the high number of locations typically associated with a wind resource map to a manageable number of clusters, each representing a particular temporal characteristic, for further analysis. This paper presents the results of a study aimed at evaluating the performance of various clustering methodologies and similarity measures for application to wind data. Results are presented for a South African case study. It is shown that the Ward minimum variance method performs well for time-series clustering aimed at grouping wind locations into clusters with similar time of day and time of year signatures.

Key Words. Renewable Energy, Wind Energy; Clustering.

1 INTRODUCTION

Factors such as climate change due to greenhouse gas emissions, high atmospheric pollution levels and threats to energy security represent major challenges to the modern world. This has given rise global efforts to convert to cleaner and more sustainable energy sources. For the electricity industry, this implies reducing the reliance on fossil fuels such as coal, oil and natural gas, and large scale phasing in of renewable energy sources. Renewable energy sources such as wind and solar energy, unlike traditional fossil fuel power plants, cannot necessarily be dispatched when needed. The availability and generation capacities of these energy sources are stochastic rather than deterministic, due to the influence of location-dependent weather conditions. The available power output profiles, furthermore, exhibit pronounced diurnal and seasonal cyclic behaviour. In view of the above, it is now generally accepted that appropriate optimisation studies, using the load profile of the grid as departure point, are required in demining both the optimum mix of renewable energy sources as well as the optimum locations of individual plants.

In the local context, grid integration studies for both wind and solar sources currently focus mainly on the potential capacity factors and grid connection infrastructure requirements of the individual plants. Financial considerations such as Return on Investment (ROI) are driven by a flat feed-in tariffs that do not take cognisance of the Time of Use (TOU) realities associated with the load profile serviced by the grid. In the medium to long term, power system operational aspects such as economic dispatch, reserve margin at peak consumption periods, the utilisation of installed storage capacities and opportunities for demand response need to be introduced in the process of determining the optimum mix and generation profiles of the renewable energy generation fleet. This requires analysis of the

potential performance of potential renewable energy sources in a temporal context, as represented by the diurnal and seasonal properties of the load profile experienced by the grid.

The analysis of the diurnal and seasonal properties of individual wind farm locations in the context of grid integration optimisation can be assisted by grouping geographical areas with similar signatures into clusters. These clusters can then serve as inputs to optimisation studies involving the geographical positioning of wind farms.

A number of investigations involving the clustering of wind and solar power profiles have been reported in literature. Zagouras et al [1] performed cluster analysis on daily global horizontal irradiance profiles using k-means with the view to aid solar power expansion planning. Duarte et al [2] applied different clustering algorithms to the power output data from a real wind farm to group days of the year that had similar daily power output profiles. Vallée et al [3] clustered wind farms into groups with similar statistical behaviour using a fast incremental algorithm as part of an adequacy evaluation with Monte Carlo simulation.

The research discussed in this paper attempts to cluster potential wind locations with a focus on similarity of hourly wind power output.

2 OVERVIEW OF TIME SERIES CLUSTERING

Time series clustering is an established field of data mining [4]. It is an unsupervised classification which attempts order unlabelled time-series into groups of time-series data which share common behaviours or features. Traditionally the main challenges with time series clustering have been the high dimensionality, the presence of noise and the high feature correlation. There are also different approaches to time series clustering. The approaches to time series clustering have been separated into three groups, namely raw-data-based, feature-based and model-based clustering

[5]. As the focus of this investigation is on the correlation of the hourly power output profiles of different geographical locations, the raw-data-based approach is applied. Feature-based and model-based approaches may hold value in wind power time series clustering, but this is left as options for future research.

Time series clustering involves two important considerations, namely the type of similarity measure to be used and the type of clustering algorithm to be used. Both of these aspects are active research fields and many novel similarity measures and clustering algorithms have been proposed in recent years.

The similarity measure is chosen based on the characteristics of the input data and the intended application of the cluster results. The similarity measure determines whether similarity in time, similarity in shape or similarity in change will be targeted. Typical similarity measures used in time series clustering include Lp-norm distance (also known as the Mikowski distance), Dynamic Time Warping distance (DTW), Longest Common Subsequence (LCSS) distance and the Pearson's correlation factor. As the main focus of this study relates to similarity in time, the Euclidian distance, which is a type of Lp-norm distance (with $p=2$), has been chosen.

In determining the type of clustering algorithm to use, it is generally suggested to apply several algorithms and then determine the best algorithm for the given case using validation methods. Several complex clustering algorithms have been proposed, but the basic clustering algorithms can be classified as either hierarchical or partitional. Partitional clustering divides the datasets into a user-specified number of subsets, whereas hierarchical clustering results in nested clusters organized as a hierarchical tree that can be easily visualized using a dendrogram. This paper focuses on several hierarchical methods and one popular type of partitional method. Other types of clustering algorithms that have been suggested for time series data include fuzzy c-means clustering and density-based clustering.

Cluster validation measures are used to determine the quality of a clustering result. Many cluster validation measures have been proposed and reviewed in the literature [6]. In order to validate the clustering methods in this paper, the average silhouette width, the Caliński-Harabasz method and mean centroid error has been inspected.

3 METHODOLOGY

3.1 Introduction

The clustering methodology is described below in terms of time series, instead of data points as usual. After calculating the distance matrix between different time series datasets using the chosen similarity measure, however, time series datasets can be equated to data points.

3.2 Similarity Measures

The Euclidian distance similarity measure is used in this investigation to calculate the distance matrix between the time series datasets. The Euclidian distance is defined by the relationship

$$D_E = \sqrt{\sum_{i=1}^n (x_{1i} - x_{2i})^2} \quad (1)$$

where x_1 and x_2 are n-dimensional vectors for the two time series datasets in this case.

3.3 Clustering methods

3.3.1 Hierarchical Methods

Several agglomerative hierarchical clustering methods have considered in the investigation. In agglomerative clustering, the bottom-up approach is used to merge the data series into a number of small clusters. These small clusters are then merged into larger clusters by clustering the two data series/clusters with the minimum of the chosen distance criteria.

3.3.1.1 Complete-linkage

The complete-linkage clustering method attempts to find similar clusters. The two elements that represent the maximum distance between two clusters are used as the distance metric.

3.3.1.2 Average-linkage

The average-linkage clustering method attempts to find clusters with similar variances. The average distance between the objects in different clusters is used as the distance metric.

3.3.1.3 Ward's Method

Ward's method, which is also known as the minimum variance method, attempts to minimize information loss when clustering. At each step, it groups the two elements whose grouping would induce the least increase in their sums of squared difference from the mean least. There are different implementations of the ward method. The Ward 2 implementation described by Murtagh *et al* [7] is used in this investigation. The Ward distance metric is given by

$$d(C_k, C_l) = \frac{|C_k||C_l|}{|C_k| + |C_l|} \|\bar{x}_k - \bar{x}_l\|^2 \quad (2)$$

where $|C_k|$ and $|C_l|$ represent the number of elements in cluster C_k and C_l respectively, and \bar{x}_k and \bar{x}_l represent the centers of the respective clusters.

3.3.2 Partitional Methods

There are many different types of partitional clustering methods, of which the k-means algorithm is the most widely used. The partition around medoids (PAM) method, which is generally viewed

as a more robust version of the k-means algorithm, is used in this investigation. The PAM clustering methodology involves the following steps:

- Initialization is performed randomly assign k of the n time series as the medoids.
- Assign each time series to the medoid closest to it.
- Perform an update swap for each medoid k and each time series associated with k . The cost of the configuration, represented by the average dissimilarity of the time series to all the other time series associated to k , is calculated. A new medoid time series, with the lowest cost, is selected.
- Repeat the assignment and update steps, i.e. step 2 and step 3 above, until no new assignments are made.

3.4 Cluster Validation

3.4.1 Overview

Three validation metrics have been applied in validating the performance of the clustering algorithms for the case study. These include the Average Silhouette Widths (ASW), Caliński-Harabasz (CH) index and Average Centroid Error (ACE) metrics.

3.4.2 Average Silhouette Widths

The silhouette width of a time series is a measure of the membership strength of that time series to its assigned cluster. It is based on the average distance a_{x_t} between each time series x_t of a cluster C_k to every other time series in that cluster, and b_{x_t} , the minimum value of the average distance between that time series and the time series belonging to all other clusters. The average silhouette width is defined as

$$ASW(K) = \frac{1}{T} \sum_{k=1}^K \sum_{x_t \in C_k} \frac{b_{x_t} - a_{x_t}}{\max(b_{x_t}, a_{x_t})} \quad (3)$$

where T denotes the number of time series datasets, K denotes the number of clusters. Note that the difference between b_{x_t} and a_{x_t} is normalized by their maximum value. The ASW results in a score between -1 and 1, where -1 one indicates a very poor clustering and 1 represents a very good clustering.

3.4.3 Caliński-Harabasz Method

The Caliński-Harabasz index (CH) calculates the ratio between the cluster scatter matrix and the within-cluster scatter matrix. It is defined by the relationship

$$CH(K) = \frac{Tr(S_B)/(K-1)}{Tr(S_W)/(T-K)} \quad (4)$$

with

$$Tr(S_B) = \sum_{k=1}^K T_k \|\bar{x}_k - \bar{x}\|^2 \quad (5)$$

and

$$Tr(S_W) = \sum_{k=1}^K \sum_{x_t \in C_k} \|x_t - \bar{x}_k\|^2 \quad (6)$$

where T denotes the number of time series datasets, K denotes the number of clusters and S_B and S_W denote the traces of the between-class and the within-class scatter matrices respectively, T_k denotes the number of number of time series datasets in cluster k , x_t denotes a time series in cluster k , \bar{x}_k denotes the center of cluster k and \bar{x} denotes the center of all the time series data points. These centers are calculated using the similarity measure described in section 3.1. The CH index is normalized to account for the increasing number of clusters. The objective of the CH method is to determine a number of clusters K that maximises the CH index. This implies maximising the ratio of $Tr(S_B)$ and $Tr(S_W)$, i.e. the ratio of between cluster scatter and within cluster scatter.

3.4.4 Average Centroid Error

A centroid time series is calculated for each cluster and the total error at each time period i and for every time series x_t is summed and averaged to calculate the average centroid error (ACE). The ACE is defined by the relationship

$$ACE(K) = \frac{1}{nT} \sum_{k=1}^K \sum_{x_t \in C_k} \sum_{i=1}^n \sqrt{(\text{centroid}_i - x_{ti})^2} \quad (7)$$

where n denotes the number of records in the time series, T denotes the number of time series datasets and K denotes the number of clusters.

3.5 Number of Clusters

There is no specific way to determine exactly how many clusters are necessary. In this investigation the L-method was applied for each of the 3 validation measures with the view to get a sense of how many clusters are appropriate.

3.5.1 L-Method

The L-Method [8] attempts to find the K best number of clusters by fitting 2 linear models to the left hand side and right hand side of a validation method dataset and determining a point c such that the total root mean square of the linear models is minimized. The validation method's values, each corresponding to a number of clusters, is split into two groups such that the left hand group L_c has values $2, \dots, c$ and right hand group R_c has values $c+1, \dots, b$, where b represents the maximum number of clusters. After a linear model is fitted to each group using linear regression, the total root-mean-square error (RMSE) is given by the relationship

$$RMSE_T = \frac{c-1}{b-1} RMSE_L + \frac{b-c}{b-1} RMSE_R. \quad (8)$$

The RMSE of the left and right hand groups are weighted proportional to the lengths of L_c and R_c .

The crucial point is found by finding the value c that minimizes $RMSE_r$.

4 CASE STUDY

4.1 Overview

The above clustering methodologies are applied to wind power data sets for a South African case study. All simulations and data handling was done using Excel, R and the “fpc” and “cluster” R packages on a personal computer with an Intel i5-4570 3.2GHz processor and 4GB RAM.

4.2 Wind Data

Wind speed data obtained from the WASA project, which provides 23 years of hourly wind speed and wind direction data for 527 9x9 km sites in the Eastern Cape, Northern Cape and Western Cape provinces of South Africa, is used in the investigation. This translates to 201624 records for every site.

Wind farm sites that are too far away from the existing grid are not economically viable due to the cost of the additional grid infrastructure required. Therefore, the study only includes sites that are within 50 km from existing high voltage power lines and power lines that are already planned for construction. GIS data of the South African power grid show that 367 sites out of the 527 possible sites are eligible. The available sites, as well as the sites included in this investigation, are shown Fig. 1.

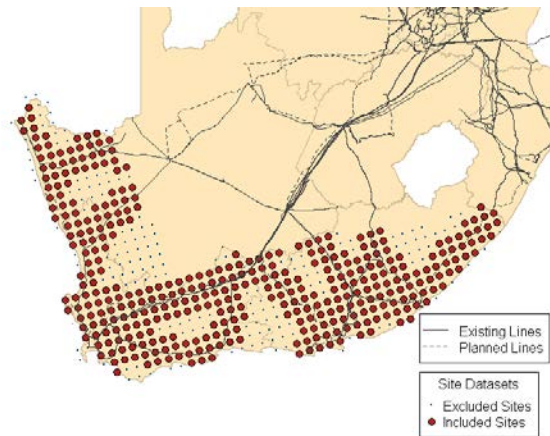


Fig. 1: WASA wind site for sites included and excluded in the investigation.

4.3 Wind Speed to Wind Power Conversion

The wind speed data from the WASA data set was converted to wind power using the power curve of a 2MW Vestas V100 wind turbine shown in Fig. 2.

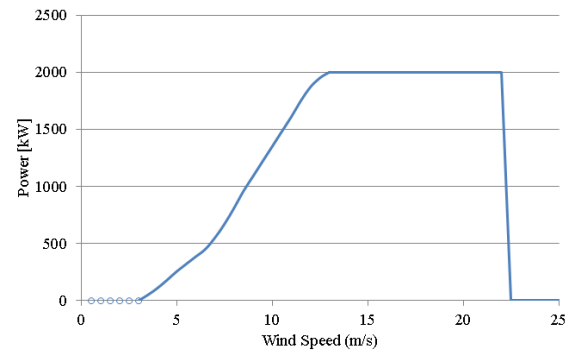


Fig. 2: Power curve for the Vestas V100 2MW.

4.4 Results

The 367 time series datasets of 23-year simulated hourly power was clustered into different numbers of clusters $k \in [5, 200]$ and validated using the methods discussed. The results for the ASW validation measure are shown in Fig. 3. It can be seen that the clustering by Ward's method achieved the best ASW (a value closer to one indicates a better clustering), but that gain in ASW diminishes after using more than around 85 clusters.

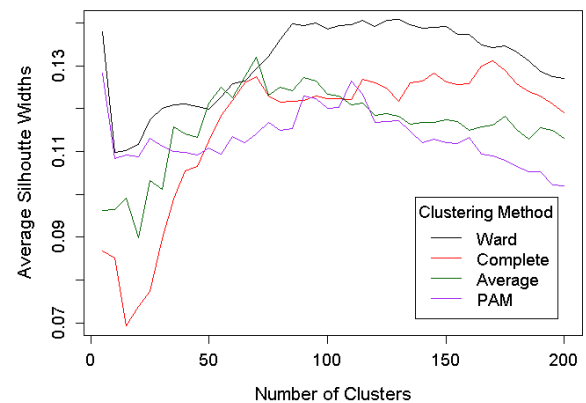


Fig. 3: Average silhouette width versus the number of clusters for different clustering methods.

The results for CH validation measure are shown in Fig. 4. The CH validation measure converges for all the clustering methods as the number of clusters increase. The CH validation measure indicates that fewer clusters would be better. As in the case of the ASW metric, the Ward method has a slightly better performance compared to the complete-linkage and average-linkage methods, and is on par with the PAM method.

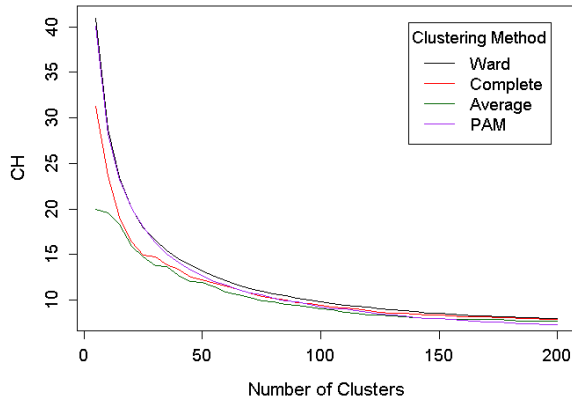


Fig. 4: Calinski-Harabasz index versus the number of clusters for different clustering methods.

The results for the ACE validation measure are shown in Fig. 5. Again the validation measure is quite similar for the different methods and converges for a high number of clusters. The Ward and PAM methods fare slightly better compared to the complete-linkage and average-linkage methods. The results are expected insofar as the average centroid error decreases with increasing number of clusters. The rate of decrease in the ACE value with increasing number of clusters falls from around 50 clusters onwards.

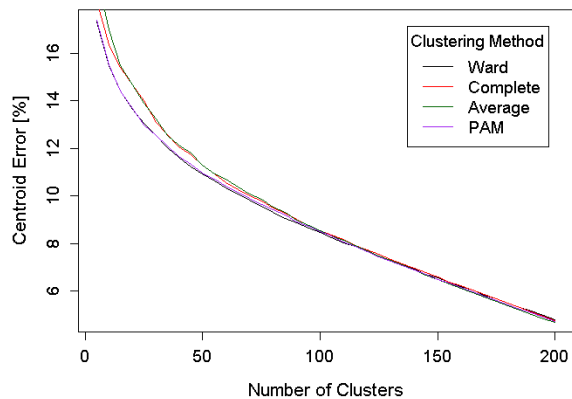


Fig. 5: Average centroid error [%] versus the number of clusters for different clustering methods.

The Ward method of agglomerative hierarchical clustering performed better for the ASW validation measure and the other validation measures were similar for different methods. The Ward method is therefore investigated further. The L-method was used on the Ward Method's ASW, CH and ACE validation measures to determine how many clusters are appropriate. The results of the L-method on the ACE measure are shown as an example in Fig. 6 where c was found to be 45. The value of c found with the L-method in the ASW and CH validation measures were 75 and 25 respectively. A cluster number of 50, i.e. a rounded up value of the average L-method c value of the three validation measures, is selected for the rest of the investigation.

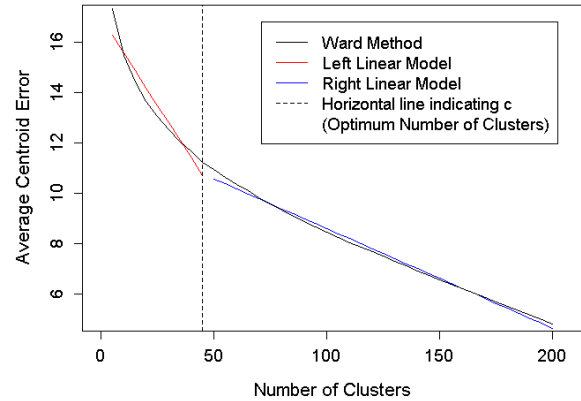


Fig. 6: The L-Method applied to the average centroid error of the Ward Method.

The clustering results using the Ward Method, with $k=50$, are shown in Fig. 7 where sites belonging to the same cluster is shown in the same colour.

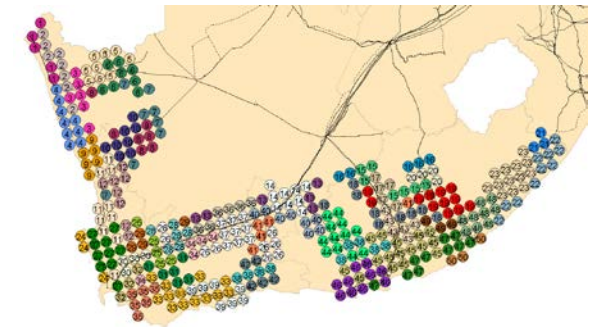


Fig. 7: Wind sites clusters obtained using the Ward method for 50 clusters.

The sites in clusters 38 and 42 will now be examined with the view to determine what type of behaviour can be identified by the clustering approach. The wind profiles of these two clusters differ widely, which is interesting because some of the sites in cluster 38 and cluster 42 are geographically very near to each other. Cluster 38 contains sites that are widely dispersed as can be seen in Fig. 8.

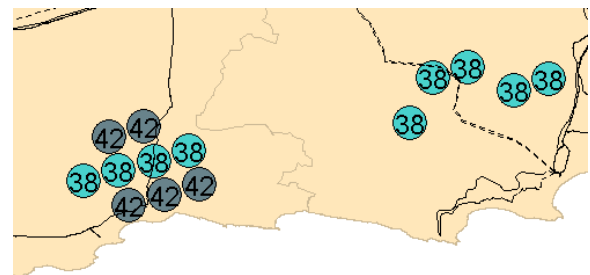


Fig. 8: Sites grouped into clusters 38 and 42.

The difference between these two wind clusters is illustrated by a simple seasonal analysis, where summer is defined as December to February, autumn as March to May, winter as June to August and spring as September to November. The average daily power output profiles are calculated for each site and each season. The difference in the power output profiles of the two clusters is clear from Fig. 9 and Fig. 10. The figures are scaled so that an indication

of capacity factor is evident (the y axis is effectively scaled from 0 to 100% capacity factor).

Cluster 38 is characterized by high wind power output in the evening peak time during summer, autumn and spring with relatively weak performance during the rest of the day and during the whole of winter.

Cluster 42 is characterized by strong wind power output early in the morning and during the late evening in winter, and generally poor performance in the other seasons.

This is the type of behaviour that might be of interest to wind power planners in markets where power generation in peak periods is important due to generation capacity constraints, high peaking generation costs, etc. and where seasonality plays a big role in operational aspects such as reverse margin, etc.

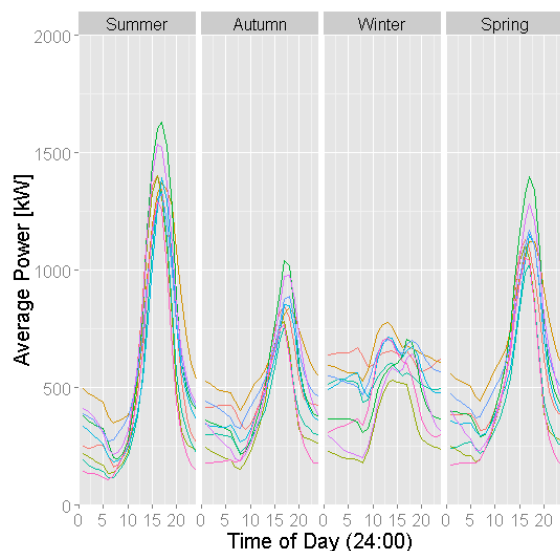


Fig. 9: Seasonal average daily power output for sites in cluster 38.

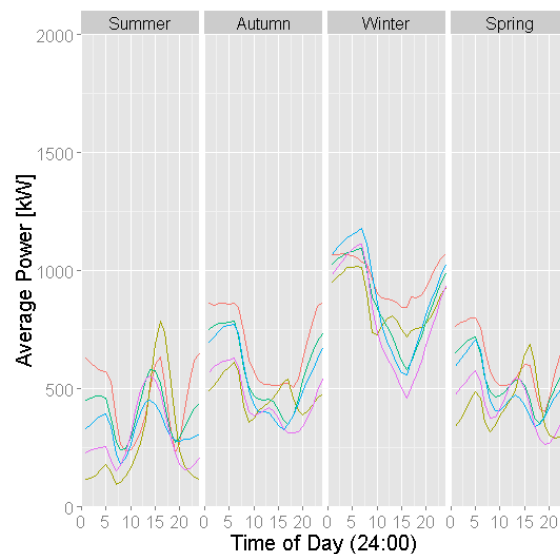


Fig. 10: Seasonal average daily power output for sites in cluster 42.

5 CONCLUSION

Several clustering methods and cluster validation measures have been inspected to facilitate the time-series clustering of the simulated power output profiles of potential wind farm sites. In the South African case study, the Ward method has performed slightly better than the other methods in the various validation measures. The L-method was performed on the validation measures, and indicates that, for the 367 sites, between 25 and 75 clusters are appropriate. In practice, the number of clusters will depend on the intended application of the clustered profiles. Some examples were given of the type of power output profiles that can be clustered and how this might aid in wind power expansion planning.

The methods used in this paper are well known, and it is suggested that in future work more novel clustering methods, along with different similarity measures and clustering validation measures can be inspected.

ACKNOWLEDGEMENTS

This work has been made possible by support from the Centre for Renewable and Sustainable Energy Studies (CRSES) at Stellenbosch University.

REFERENCES

- [1] A. Zagouras, R. H. Inman and C. F. M. Coimbra, "On the determination of coherent solar microclimates for utility planning and operations," *Solar Energy*, vol. 102, pp. 173-188, 2014.
- [2] F. J. Duarte, J. M. M. Duarte, S. Ramos and A. Fred, "Daily wind power profiles determination using clustering algorithms," in *Power System Technology*, Auckland, 2012.
- [3] F. Valleé, G. Brunieau, M. Pirlot, O. Deblecker and J. Lobry, "Optimal Wind Clustering Methodology for Adequacy Evaluation in System Generation Studies Using Nonsequential Monte Carlo Simulation," *IEEE Transactions on Power Systems*, vol. 26, no. 4, pp. 2173-2184, 2011.
- [4] S. Aghabozorgi, A. S. Shirkhorshidi and T. Y. Wah, "Time-series clustering – A decade review," *Information Systems*, vol. 53, pp. 16-38, 2015.
- [5] T. W. Liao, "Clustering of time series data—a survey," *Pattern Recognition*, vol. 38, p. 1857-1874, 2005.
- [6] O. Arbelaiz, I. Gurrutxaga, J. Muguerza, J. M. Perez and I. Perona, "An extensive comparative study of cluster validity indices," *Pattern Recognition*, vol. 46, pp. 243-256, 2013.
- [7] F. Murtagh and P. Legendre, "Ward's Hierarchical Agglomerative Clustering Method: Which Algorithms Implement Ward's Criterion?," *Journal of Classification*, vol. 31, pp. 274-295, 2014.
- [8] S. Salvador and P. Chan, "Determining the number of clusters/segments in hierarchical clustering/segmentation algorithms," in *Tools with Artificial Intelligence*, 2004.

INVESTIGATION INTO ROLE OF ARCING HORNS ON 132 KV SUBTRANSMISSION INFRASTRUCTURE

BA Smith* and AG Swanson

* Discipline of Electrical, Electronic & Computer Engineering, School of Engineering, University of KwaZulu Natal, Durban, KwaZulu-Natal E-mail: basmith1991@gmail.com

Abstract: Insulators perform a vital role in the functioning of a high voltage transmission system as they are expected to withstand external overvoltages such as those caused by lightning. eThekweni municipality maintains the practise of installing arcing horns on both the live and earth side on their polymeric line insulators within a range of 1.5km of a substation. These arcing horns protect the insulator from arc damage in the event of flashover and also perform a role in the insulation co-ordination of the sub-transmission system. Arcing horns which are allowed to undergo a horizontal rotation as a result of adverse weather conditions necessitate an investigation into the effects that this rotation will have on both the insulator unit and the sub-transmission system. In this paper, a model was constructed in ATP/EMTP to conduct an insulation co-ordination study in combination with an earth resistance sensitivity study, to ascertain the probability of a lightning strike causing backflashover for each point of rotation in the case where a tower or shield wire intercept a lightning strike. The ATP/EMTP model was dependant on a leader progression model which was used to simulate flashover across the rotated spark gap. The results of the study suggest that the rotation of arcing horns on the insulators do not require immediate maintenance or replacement of the unit. Rather, the rotated arrangement allows for greater system protection by increasing the CFO voltage of the spark gap. This in turn increases the protection of the sub-transmission system against lightning strikes by decreasing the occurrence of backflashover and the associated earth fault.

Key words: arcing horn, insulation co-ordination, CFO, backflashover

1. INTRODUCTION

Arcing horns are placed in a system to protect insulators against flashover by providing an overvoltage spark gap protection. eThekweni Municipality specify that arcing horns are required to be fitted on the earth side of insulator in addition to the already assembled live side for the section of line for a distance of up to 1.5 km from a substation.

Lightning strokes to transmission structures, phase conductors, or shield wires can cause a flashover across the insulator string which ultimately result in a breaker trip also known as an earth fault. Arcing horns are installed to act as protective device for the line insulation, however the initial spark gap which is formed across the insulator can be observed as part of the co-ordination of the system insulation.

The flashover performance of a rotated arcing horn arrangement is important to understand when dealing with external overvoltages in power systems as it could have an impact on the CFO of the insulator unit.

Unforeseen rotation of these installed arcing horns could pose a risk to the sub-transmission system insulation co-ordination; especially when combined with poor earthing of tower structures as similar studies have shown [6], [10], [13].



Figure 1: 132kV arcing horn arrangement

2. BACKFLASHOVER

Backflashover (BFO) occurs when an electrical discharge is completed from a grounded support to an energised conductor and predominate over those flashovers caused by a shielding failure as cited in [15] and [5].

The Figure illustrates the waveforms present in the case where a tower intercepts a lightning strike. It can be observed that waveforms split and propagate in equal amplitudes down the shield wire while a portion of the strike propagates down the tower structure. The tower bound waveform interacts with the surge impedances of the tower structure and the cross arms carrying the insulators thereby raising its potential.

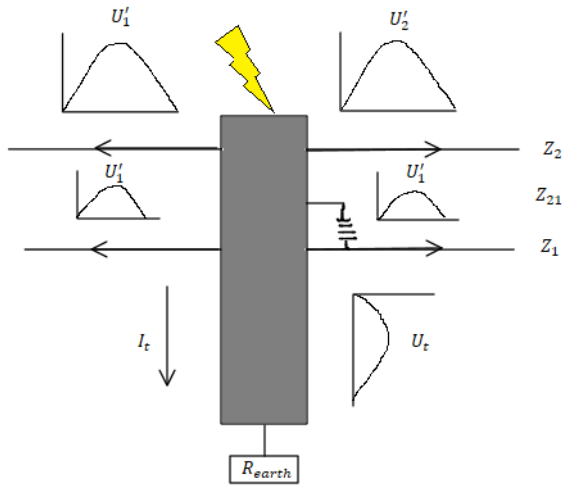


Figure 2: Waveforms present when lightning strikes a tower [18]

The voltage that can be observed at the tower top as described by [11] is governed by the Z_T the surge impedance of the tower, Z_g the surge impedance of the ground wire and the amplitude of the lightning stroke, I_{stroke} :

$$V_{top} = \frac{Z_T \times Z_g}{Z_g + 2Z_T} \times I_{stroke} \quad (1)$$

The frequency of BFO can be calculated by knowing the flash density for a given area, N_g and the probability distribution of lightning current amplitude:

$$BFO_{rate} = 0.6 \times N \times p(I) \quad (2)$$

where N depends on the height of the conductor h , and earth wire separation b and $p(I)$ on the mean lightning current amplitude, $I_c = 31\text{kA}$, as found in [14], [11].

$$N = N_g \times \frac{28h^{0.6} + b}{10} \quad (3)$$

$$p(I > I_c) = \frac{1}{1 + (\frac{I}{I_c})^{2.6}} \quad (4)$$

2.1 What effects backflashover?

There are a number of aspects which influence BFO on high voltage transmission lines. [5] [4] [22]

- Poor grounding of transmission towers: Grounding of transmission line towers performs a pivotal role in their protection. Grounding resistances in excess of 100Ω may require the installation of transmission line surge arresters (TLISA).
- Ineffective shielding: Perfect shielding of phase conductors only permits lightning currents of low

amplitude to strike them thus deferring most strikes onto shielding wires or transmission towers

- Positioning of TLISA: Should they be required, the positioning of TLISA can greatly inhibit the effect of backflashover.

3. ROTATION OF ARCING HORNS

Figure 1 illustrates a typical arcing horn arrangement found on a 132kV sub-transmission line. Arcing horns are installed on insulators in order to primarily protect against insulator flashover damage and puncturing. The initial gap setting however also performs a role in the co-ordination of the system as it represents a volt-time curve set to protect expensive insulated electrical equipment such as transformers.

Rotation of these arcing horns, due mainly to adverse weather conditions, can affect both of these protection functionalities and can result in the replacement of the entire arrangement; this process is costly as well as time consuming to any electrical utility.



Figure 3: Longrod polymer insulator end fitting damage



Figure 4: Burnt grading ring

3.1 Determining Rotation

In the insulation co-ordination study, arcing horns were rotated in order to assimilate the movement under adverse weather conditions. It can be shown that the gap distance produced by a single arcing horn rotating through an angle θ the the other with an initial distance of ,x, and a vertical radius ,r can be governed by: [2]

$$L_{gap}(x, r, \theta) = \sqrt{(x^2) + (r - r\cos\theta)^2 + (r\sin\theta)^2} \quad (5)$$

3.2 Leader progression model

The insulation co-ordination study was supplemented with a modified leader progression model(LPM) implemented as an integration model to simulate backflashover across the insulator. This method for simulating flashover is common in several studies [16], [21] [3]. The rod-rod equation found in [17] is valid for both polarities of impulse for gaps ranging from 1-3m and was utilised in this study. The velocity of a leader

$$\frac{dl}{dt} = k \times d \times \left(\frac{U(t)}{d-l} - E_o \right) \quad (m/s) \quad (6)$$

and the distance travelled can then be found

$$\int \frac{dl}{dt} = x_{leader} \quad (7)$$

and the point of backflashover occurs when equation (8) is satisfied.

$$x_{leader} > d \quad (8)$$

4. INSULATION CO-ORDINATION

Insulation co-ordination is vitally important to correlate the insulation levels of various pieces of electrical equipment to those of the protective devices.

4.1 Volt-time curves

Insulators on high voltage transmission lines can often be represented by a volt-time curve which clearly indicate the breakdown voltage of a piece of equipment relative to the time over which the voltage is applied. An insulator fitted with arcing horns set at an initial distance, L , will have a corresponding volt-time characteristic [21]

$$V_{v-t} = a \times L + \frac{b \times L}{t^{0.75}} \quad (9)$$

Where a and b are arbitrary constants. Therefore, if the arcing horns undergo a rotational shift there will be a corresponding shift in the V-t curve for the insulator arcing-horn arrangement.

In order to assimilate the V-t curve for the different rotated arrangement the LPM was utilised. The points for each rotation curve were obtained by adjusting the crest value

of the lightning impulse and recording the respective times to breakdown. [6]

The CFO for each rotation can be attained by observing the point at which the curve reaches an asymptote. The values can be found in the table below.

Rotation (degrees)	CFO (kV)
0	528
30	539
60	567
90	604

Table 1: CFO Voltage vs. arcing horn rotation

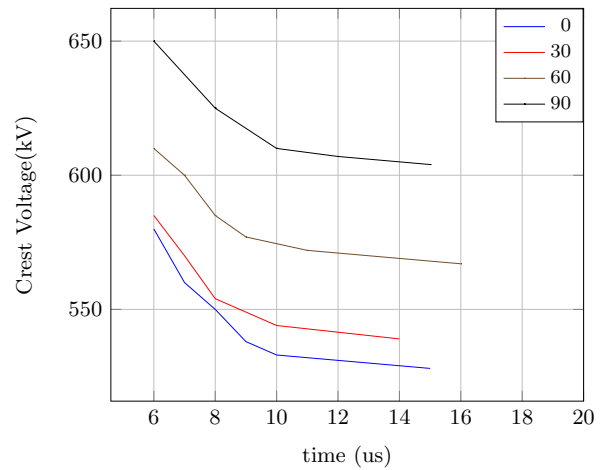


Figure 5: 132kV rotated arcing horn V-t curves

5. SYSTEM MODELLING

5.1 System overview

The insulation co-ordination study consisted of a 132kV feeding 3 single circuit transmission towers separated by spans of 500m and terminating in a substation yard containing surge arrestors for protection of transformers and extinguishing of fault current. The model overview is illustrated in the Figure below.

5.2 Transmission Line

The transmission lines are modelled using the frequency dependant (FD) J-Marti model [12]. The frequency dependant model is suggested in [13] evaluates multiconductor line propagation in the modal domain and taking into account effects due to frequency dependence of the line parameters. Zebra and rabbit conductor bundles were used for the conductor and shield wires respectively.

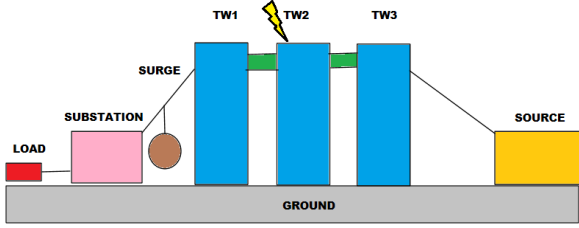


Figure 6: Modelled 132kV sub-transmission system [15]

5.3 Transmission Tower

The three transmission towers are modelled using surge impedances for various sections. The tower model should be divided into four sections and the respective surge impedances calculated for the tower structure itself, the bracings and the cross arms using the following formula as found in [14], [9]

For the central tower structure:

$$Z_{Tk} = 30 \ln \left(\frac{2\sqrt{2}h_k}{r_{ek}} - 2 \right) \quad (10)$$

For the cross arms:

$$Z_{Ak} = 60 \ln \left(\frac{2h_k}{r_{Ak}} \right) \quad (11)$$

Where:

h_k = relative height of section of tower above the ground
 r_k = relative distance of tower section from the central axis of the structure k = tower section numbering $k = 1, 2, 3, 4, \dots$

5.4 Earth Resistance

The earthing of the transmission tower was varied between values 10Ω to 30Ω in order to ascertain the effect on BFO probability. DC resistance is an accepted method of earth resistance as mentioned by [14] and therefore it was deemed acceptable for the purposes of the study.

5.5 Insulator Characteristics

Relevant polymeric longrod 132kV insulators dimensions as specified by the eThekweni Municipality fitted with arcing horns were utilised in the LPM.

5.6 Substation

The substation was modelled in accordance with [18] as shown in the Figure. The typical values of capacitance for current transformers (CT), post insulator (PI) and circuit breaker (CB) were used. The apparatus connections (AC) were modelled using a lumped equivalence of $1\mu\text{H/m}$

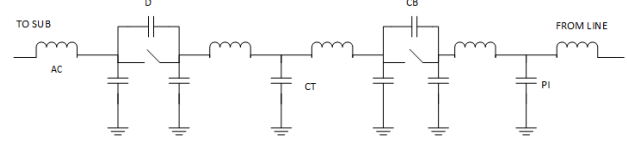


Figure 7: Substation model

5.7 Surge Arrestor

Surge arresters perform a vital role in insulation co-ordination as they provide a path to divert current to ground at high voltage levels. They are prominently utilised and many studies exist demonstrating their importance such as those found in [8] and [7].

The surge arresters were modelled from IEEE standards found in the IEEE WG [19]. The characteristics of the MO surge arresters were specified in accordance to ABB standards. A surge arrester with U_r of 144kV was utilised to simulate protection of the transformer. The Figure below illustrates the IEEE WG equivalent circuit of a surge arrester.

As specified in [1] the initial values of capacitance, resistance and inductance were calculated as follows where:

n = number of parallel MO disks in the surge arrester = 4
 d = height of arrester in $m = 1.584m$

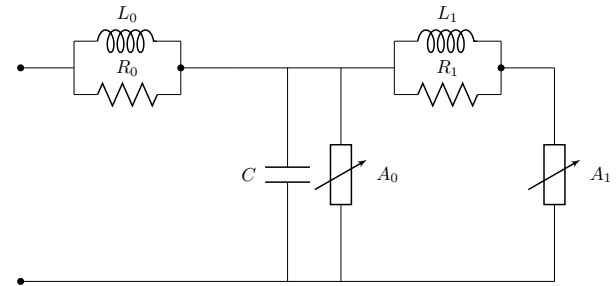


Figure 8: IEEE arrester model

Subsequently, the non-linear components of A_0 and A_1 were used from a table found in [1] in order to replicate the operating characteristics of the surge arrester under varying current surges.

Transformer: The transformer utilised in the model as a hybrid 132/11kV transformer with typical values of capacitance, resistance and inductance obtained from [20].

6. RESULTS

The ATP/EMTP model was run in order to determine the first point of backflashover which would occur if the arcing horns were rotated. Thus, for a certain lightning current amplitude and grounding resistance a plot of current amplitude vs. degree of rotation was plotted and followed by a graph describing probability of flashover vs. ground resistance.

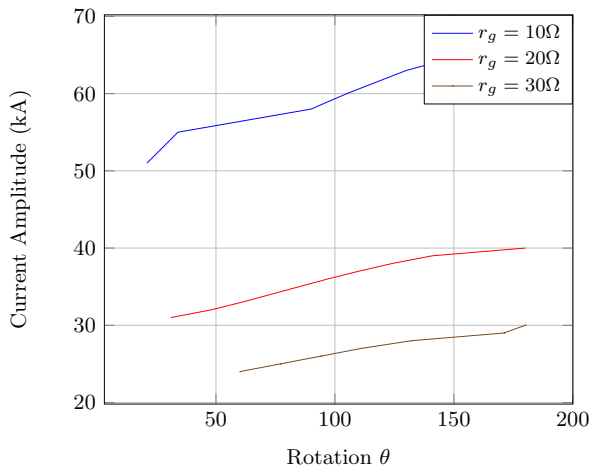


Figure 9: Arcing horn rotation vs. lightning current amplitude

The probability of backflashover was then found using equation (4) and also plotted against the degree of arcing horn rotation.

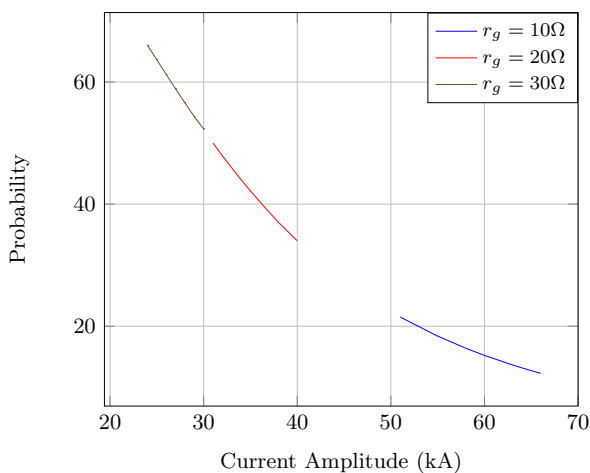


Figure 10: Current amplitude vs. Probability

7. DISCUSSION

Figure 9 illustrates the comparison between two pivotal criteria namely gap-coordination and grounding resistance. As expected, a rotational shift of either arcing horn

relative to one another results in a larger gap in which backflashover takes place. This coupled with the effect of grounding resistance can greatly influence the theoretical protection of a system against backflashover and subsequent earth faults.

Figure 10 details the probability of a flashover occurring given rotation of the arcing horn and constant grounding resistance. It can be observed that system protection against lightning currents as great as 60kA can be greater than 80%. The effect on voltages arriving at the transformer were therefore not in direct danger of causing damage as the BIL of the transformer is 650kV. Even in the worst case scenario of ground resistance 30Ω and $I = 66\text{kA}$ the maximum overvoltage reaching the terminals of the transformer was less than 300kV.

The surge arresters did play a large role in suppressing the overvoltages reaching the transformer by diverting the current to ground, despite the induced overvoltages on the phase conductors being far less than those in the event of a shielding failure.

8. CONCLUSION AND RECOMMENDATIONS

Should a transmission system be equipped with the specified footing resistance of 10 Ohms; then it could be stated that should the arcing horns shift to the full 180 degrees the probability of any strike producing a backflashover would be scaled to just over 10%.

A recommendation for the insulation co-ordination study would be that it could benefit from supplementary laboratory testing of the breakdown mechanism as found in [2] which exists between rotated arcing horns. As equation (5) suggests the shortest distance from live to earth occurs at a rotation of about 60 degrees; therefore, should the arc follow the shortest distance between live and ground the arcing horn arrangement would function similarly to that of a single arcing horn which is rotated through any number of degrees. It could then be argued that a single arcing horn arrangement could be the optimum arrangement.

Arcing horn rotation does not call for immediate replacement or inspection for that matter. The rotated arrangement allows for a greater system protection by increasing the CFO of the spark gap through its own volt-time curve shift and thereby plays a role in decreasing of the BFO rate of the system and the occurrence of the consequential earth faults.

9. ACKNOWLEDGEMENTS

The authors would like to thank Eskom for the funding of the university through the Electrical Power Plant Engineering Institute programme. The authors would like to thank eThekweni Municipality for the use of the equipment.

REFERENCES

- [1] IEEE WORKING GROUP 3.4.11. Modeling of metal oxide surge arresters. *Power Delivery, IEEE Transactions on*, 7(1):302–309, Jan 1992.
- [2] AG Swanson B.A Smith. Validation of the breakdown mechanism between rotated arcing horns. 2015.
- [3] D. Caulker, H. Ahmad, Z. Abdul-Malek, and S. Yusof. Lightning overvoltages on an overhead transmission line during backflashover and shielding failure. In *Universities Power Engineering Conference (UPEC), 2010 45th International*, pages 1–6, Aug 2010.
- [4] W. Diesendorf. *Insulation Co-ordination in High Voltage Electric Power Systems*. Butterworth and Co Ltd., 1974.
- [5] EPRI. *Chapter 6- Improving the Lightning Performance of Transmission Lines, Overhead Transmission Line Lightning and Grounding Reference Book*. Palo Alto, 2013.
- [6] D. Filipovic-Grcic, B. Filipovic-Grcic, D. Brezak, I. Uglesic, and A. Tokic. Leader progression model application for calculation of lightning critical flashover voltage of overhead transmission line insulators. In *Lightning Protection (ICLP), 2012 International Conference on*, pages 1–8, Sept 2012.
- [7] F.M. Gatta, A. Geri, S. Lauria, M. Maccioni, and F. Palone. Tower grounding improvement vs. line surge arresters: Comparison of remedial measures for high-bfor subtransmission lines. *Industry Applications, IEEE Transactions on*, PP(99):1–1, 2015.
- [8] A. Haddad, D.M. German, R.T. Waters, and Z. Abdul-Malek. Co-ordination of spark-gap protection with zinc-oxide surge arresters. *Generation, Transmission and Distribution, IEE Proceedings-*, 148(1):21–28, Jan 2001.
- [9] T. Hara and O. Yamamoto. Modelling of a transmission tower for lightning-surge analysis. *Generation, Transmission and Distribution, IEE Proceedings-*, 143(3):283–289, May 1996.
- [10] T. Hayashi, Y. Mizuno, and K. Naito. Study on transmission-line arresters for tower with high footing resistance. *Power Delivery, IEEE Transactions on*, 23(4):2456–2460, Oct 2008.
- [11] A.R. Hileman. *Insulation coordination for power systems*, volume 19. Sept 1999.
- [12] J.R. Marti. Accurate modelling of frequency-dependent transmission lines in electromagnetic transient simulations. *Power Apparatus and Systems, IEEE Transactions on*, PAS-101(1):147–157, Jan 1982.
- [13] J.A. Martinez and F. Castro-Aranda. Lightning performance analysis of transmission lines using the emtp. In *Power Engineering Society General Meeting, 2003, IEEE*, volume 1, pages 295–300 Vol. 1, July 2003.
- [14] P. Sarma Maruvada. *Chapter 8 - Corona and Gap Discharge Phenomena, EPRI AC Transmission Line Reference Book - 200 kV and Above*. EPRI, 2005.
- [15] I. Cotton b M.Z.A. Ab Kadir a. Application of the insulator coordination gap models and effect of line design to backflashover studies. In *Electrical Power and Energy Systems 32*, 443449, 2010.
- [16] T. Pham and S. Boggs. Flashover model of arcing horn in transient simulation. In *Electrical Insulation (ISEI), Conference Record of the 2010 IEEE International Symposium on*, pages 1–4, June 2010.
- [17] A. Pigini, G. Rizzi, E. Garbagnati, A. Porrino, G. Baldo, and G. Pesavento. Performance of large air gaps under lightning overvoltages: experimental study and analysis of accuracy predetermination methods. *Power Delivery, IEEE Transactions on*, 4(2):1379–1392, Apr 1989.
- [18] W. Nowak R. Tarko. *Chapter10 : Lightning Protection of Substations and the Effects of the Frequency-Dependent Surge*. 2013.
- [19] H. L. Rorden. Insulation levels governed by lightning arresters. *Electrical Engineering*, 69(5):438–438, May 1950.
- [20] IEEE Power & Energy Society. Ieee guide for the application of transient recovery voltage for ac high voltage circuit breakers, 2011. ANNEX B.
- [21] T. Thanasaksiri. Lightning flashover rates of overhead distribution lines applying volt time curve from testing and ieee std.1410-2004. In *Electrical Engineering/Electronics, Computer, Telecommunications and Information Technology (ECTI-CON), 2011 8th International Conference on*, pages 661–664, May 2011.
- [22] J.Anderson W.Chisholm. *Chapter 6- Lightning and grounding, EPRI AC Transmission Line Reference Book - 200 kVInsulation*. EPRI, 2005.

A PROPOSAL FOR TECHNO-ECONOMIC ANALAYSIS FRAMEWORK FOR WAVE ENERGY TO ELECTRICITY CONVERSION SCHEMS UNDER SOUTH AFRICAN CONDITIONS

S.S. Biyela*, W.A. Cronje*

** School of Electrical & Information Engineering, University of the Witwatersrand, Private Bag 3, 2050, Johannesburg, South Africa*

Abstract: This paper presents a project for comparing different wave energy to electricity technologies using a techno-economic approach. The techno-economic approach will form the basis of a framework for rapid comparison of current and future technologies, to assist investment and strategic decision making. Particularly, expediting future deployment of wave energy harvesting in South Africa.

Key words: Wave Energy Converter (WEC), WEC-Sim, Cost of Energy (COE) Calculation Tool

1. INTRODUCTION

The purpose of this paper is to introduce the approach in addressing the techno-economic analysis comparison for WECs. There are some techno-economic analyses that have been done before for European countries and will be discussed in section 2. According to the authors knowledge it has never been done in South Africa. In one of the case studies for a techno-analysis by O'Connor et al: [1] it was concluded that the techno-economic performance of any wave energy converter (WEC) is location specific, i.e. it is dependent on site. This comparison work will include the WEC device in concept phase and developed at the University of Witwatersrand (Wits). A summary of operation and construction of this WEC will be given in Section 3.

1.1 Background

Ocean energy is one of the largest untapped renewable energy sources available on planet, it is said that over 70% of earth's surface is covered with ocean water [2]. Ocean energy includes several conversion principles, and wave energy is one of them. The global wave energy was estimated to be between 1-10TW, which can provide 25-200% of the world's electricity demand by 2005 [2].

In South Africa, Eskom is the largest power producer that generates electricity primarily from coal, approx. 92.8% [3]. Power generation from coal results in high level of greenhouse gases (the largest global warming contributor) and high water usage. With the national demand expected to double in approximately next 15 years Eskom is under considerable pressure to rapidly increase generation capacity and address the aforementioned concerns. For this reason Eskom embarked on an investigation if utility-scale, renewable energy, including wave power, is a viable supply-side option for Eskom and South Africa. The overall program known as the South African Bulk Renewable Energy Program (SABREP) was initiated in 1998 [4]. The conclusion from that study was that the resource available is sufficient, with wave power levels well in excess of

30kW/m [5]. Furthermore, an investigation of the wave energy resource on the South African coast, focusing on spatial distribution of the South West coast study was done by J.R Joubert for an MSc thesis at the University of Stellenbosch [6]. The study confirmed a 3000km exposed coastline along Indian Ocean and it also shown that there is potential for electricity generation but there is no specific regulations in place for wave energy demonstration projects.

2. LITERATURE REVIEWS

Pelamis P1 and the Wavestar WEC devices have been compared for techno-economic performance in six different locations, namely: Ireland, Scotland, Spain, Denmark and Greece [1]. The overall results of the case study conducted were similar in outcome to those of Waveplam study "Wave Energy Planning and Marketing, a European organisation aimed at creating tools, establish methods and standards, and create conditions to speed up introduction of ocean energy onto the European renewable energy market", although they cannot be directly compared due to the significant variations in input criteria and factors including the impact of device access and technology reliability level on availability. The Pelamis P1 WEC produced high energy output at all high resource sites of the case study (Ireland and Scotland), but produced poor results at low resource sites (Denmark and Greece). Wavestar had less variation over the six locations and produced high energy outputs at lower resource sites. At high resource locations Pelamis P1 produced better economic performance when compared to Wavestar but at all other locations Wavestar resulted in better economic performance. Case study results indicate that Wavestar is a more universal WEC, performing well in most case study locations, except for

extremes. The Pelamis P1 is more location specific but performs well in high resource sites.

3. WAVE ENERGY CONVERTER

WEC devices can be categorised depending on how they design to capture the mechanical energy of ocean waves. Three industry accepted categories are Attenuators, Point Absorber and Terminators.

3.1 Attenuator

Attenuator devices consist of multiple buoyant segment positioned parallel to the predominant wave propagation direction. Mechanical energy is extracted from the relative motion of each segment, usually through the compression of fluid in hydraulic pistons. Pelamis wave device discussed in Section 2 is one of the examples of attenuators. Other examples are:

- Oyster (Aquamarine Power)
- bioWave (Bio Power Systems) Ocean Treader (Green Ocean Energy Ltd.)

3.2 Point Absorber

Point absorbers are characterised by one degree of freedom, very small surface area in comparison to the wavelength of ocean waves [7]. They consist of a moving buoyant section that moves up and down reacting with a relative stationary component. This movement translate kinetic energy of a vertical movement by pressurising seawater or hydraulic fluid. Energy is then extracted from pressurised fluid using a variety of power take-off (PTO). Reference model used in WEC-Sim discussed in Section 4.2 is a point absorber concept. Some examples of Point Absorbers are:

- Powerbuoy (Ocean Power Technology)
- AquaBuoy (Finavera Renewables)
- OE Buoy (Ocean Energy Ltd)
- Archimedes Waveswing (AWS Ocean Energy Ltd.)
- Wavebob (Wavebob Ltd.)

3.3 Terminator

Terminator devices have their principal axis parallel to the wave front (perpendicular to the predominant wave direction) and physically intercept waves. These devices are design to absorb the entire, or a large portion of energy content of incident waves. Wave energy is converted to useful energy in one of two ways, Overtopping or through the use of an oscillating water column (OWC).

Overtopping WEC is characterised by elevated basin above water surface. As wave crests approach, water travels up inclined troughs into the raised basin, and then returns through the centre of the WEC, on its way passing through a low-head turbine that extracts the potential

energy of the elevated water [7]. Example is a WaveDragon (WaveDragon ApS).

OWC devices are located at the surface of the water and consist of an air filled chamber with an opening submerged under water. As waves pass under the submerged opening, the water height inside the chamber rises and lowers with the associated crests and troughs. The fluctuating volume of air inside the chamber creates alternating positive and negative pressure gradients with the external atmosphere powering a pneumatic turbine to produce readily accessible mechanical energy [7]. Notable OWC devices are:

- Oceanlinx (Oceanlinx, formerly known as Energetech)
- Limpet (Wave Gen)

Power Take-off (PTO): PTO is an important component in the wave energy conversion to electricity, it usually make use of mechanical energy or any readily available energy from ocean wave (depending on PTO design) to drive the electricity generation. The overall efficiency of a WEC device is greatly influenced by the PTO. All the aforementioned WEC devices employ different kinds of PTO. For the purpose of this paper, the following paragraph focuses on linear generator type, another form of PTO that Wits is interested in and working on its prototype. The advantage of this type is the elimination of intermediate mechanical devices such as turbines and hydraulic systems for power conversion, this, in theory, should have lesser losses thus improving efficiency.

Linear Generator type: The basic concept of this type consist of translator (rotor) on which magnets are mounted with alternating polarity directly coupled to a heaving buoy, with the stator containing windings, mounted in a relatively stationary structure. This is illustrated in Figure 1.

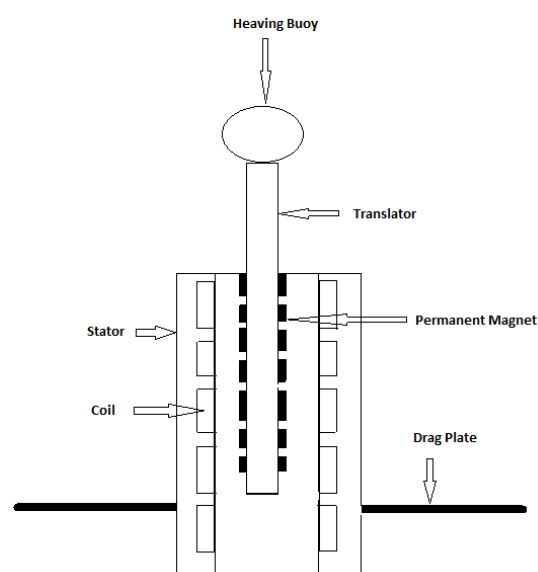


Figure 1: Linear electrical permanent magnet generator, direct drive

As the heaving buoy oscillates, an electric current will be induced in the stator, this type is conceived to have minimal conversion losses from wave energy to electricity. Having less moving parts allows a generator to capture power directly from WEC movement.

4. METHODOLOGY

This section elaborates the proposed approach to techno-economic analysis and framework for South African sea states. This is shown in terms of block diagram in Figure 2.

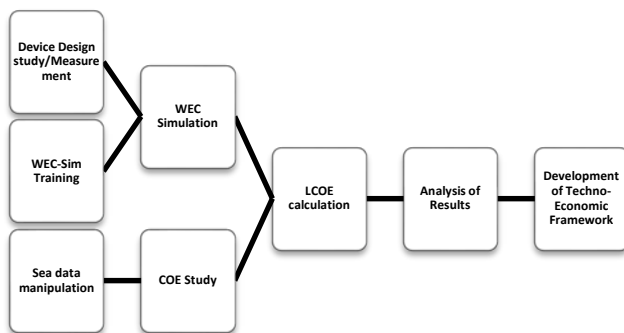


Figure 2: Project methodology block diagram

4.1 Site Chosen

The wave power analysis of measured wave data done in the study by [6] showed that the Slangkop and Cape Point wave recording stations have the highest wave power resource with a mean annual average wave of approximately 40kW/m for Cape Point. The Slangkop wave recording station indicated a dominant wave period of 12s. The wave height and power analysis indicated that Slangkop station is exposed to high level of wave power. This implies that Slangkop station has a favourable wave power resource for power generation with its average wave power of 39kW/m. It was also deduced that the multi-directional wave exposure makes it suitable for power generation by direction independent WEC technologies, i.e. Point Absorber and Linear Generators. Hence, the Slangkop site is chosen for this MSc research and the site data was requested and obtained from CSIR (Council for Scientific and Industrial Research).

4.2 Computer Models

The open-source reference models for marine energy conversions has been developed by the Reference Model Project team, made up of Sandia National Laboratory, National Renewable Energy Laboratory, Pacific

Northwest National Laboratory and Oak Ridge National Laboratory with two consulting firms, Re-Vision Consulting and LLC & Cardinal Engineering, also with the University of Washington and Pennsylvania State University [9]. The aforementioned project is funded by the USA Department of Energy with the objective of collaborative research community that can play a role in speeding up the technology development and meet the rapidly evolving modelling needs. These reference models are used to develop a tool based on MATLAB/Simulink called WEC-Sim, an open-source simulation tool provided to WEC design and research community. It has the ability to model devices that comprise of rigid bodies, power take-off systems and mooring systems.

WEC-Sim: WEC-Sim models the system dynamic of WEC devices using multi-body dynamic methods and simulates hydrodynamic forces using coefficients predicted from potential flow models [9]. Modelling a WEC device involves simulating the interaction between waves, the WEC device motion, and the power take-off (PTO) mechanism. A new feature has recently been added in 2015 to WEC-Sim known as Power Take-Off Simulator (PTO-Sim). It is responsible for accurately modelling a WECs conversion of mechanical power to electrical power through its PTO system. PTO systems can be modeled by linking PTO components from its embedded library, applicable to hydraulic power take-off systems and direct drive power take-off. Wits WEC will be modeled using the direct drive power take-off. The direct drive model can be constructed to deliver single or multiple-phase power by arrangement of generator magnets and coils.

The WEC-Sim tool is developed on MATLAB and its embedded tools as the following modules:

- WaveSim - code developed in MATLAB to generate simulated wave states using measured wave data and standard wave spectra
- BEM-developed to determine hydrodynamic coefficients using boundary element simulation methods
- HydroForce – developed in MATLAB to calculate time dependent hydrodynamic forces using inviscid hydrodynamic coefficient (from BEM module), viscous drag coefficients, relative device motions, and the current sea state
- Multi-Body Solver – developed in SimMechanics a MATLAB toolbox, models WEC device from connected appropriate number of bodies, joint and connections, according to their physical layout. The multi-body multi(six)-degree-of-freedom system, is then solved in the time domain by SimMechanics
- PTO-Sim – developed in SIMULINK to enable time dependant electrical power predictions from the calculated mechanical power. PTO-Sim is broken into modules that allow for different PTO configurations

A WEC-Sim reference model will be adopted for SA conditions using site information from Slangkop in Western Cape Province. Different WEC technologies will be modelled to obtain power output performance and power matrix for a specific site. Thereafter, the WEC device being developed at Wits will be modeled, and the model setup will be populated with parameters from the actual device datasheet. Therefore, the technical analysis obtained from modelling will be used for an economic analysis discussed in Section 4.2.

Figure 3 shows a hierarchy of the techno-economic analysis proposed to be performed on each WEC device.

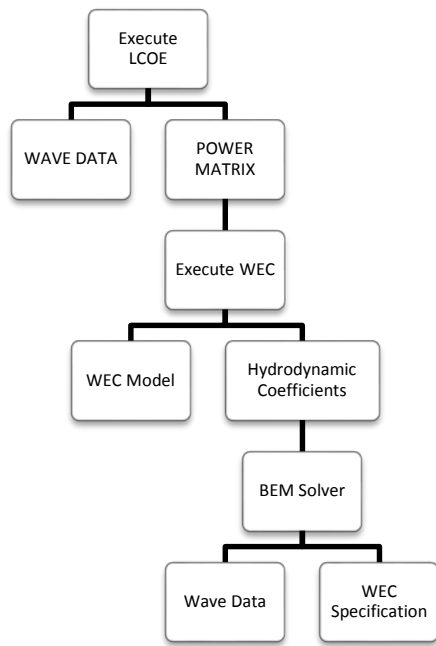


Figure 3: Hierarchy to execution of levelised cost of electricity

The top block is an economic analysis, it is populated with the device power matrix from simulations and also wave data from sea site. The WEC-Sim is executed by drawing a model on SIMULINK and gathering the hydrodynamic coefficients calculated by a BEM solver using the sum of incident, radiation and diffraction wave components method. These hydrodynamic forces are modelled using linear coefficients ideally obtained by solving the Laplace equation for velocity potential, which assumes the flow is inviscid, incompressible and not rotational [9]. The user input wave data such as wave period and height or wave spectrum, and also device geometry properties, such as mass, moment of inertia, centre of gravity. The computer model discussed in this section is based on the mathematical model discussed in Section 4.3.

4.3 Numerical Models

The device system dynamic response calculation is discussed in [10]; Cummins equation is used to represent the equation of motion for marine systems. The equation of motion for floating-body system around the centre of gravity is given by [10] as:

$$m\ddot{X} = F_{ex} + F_{rad} + F_{PTO} + F_v + F_B + F_m \quad (1)$$

Where:

\ddot{X} = translational and rotational acceleration

m = mass matrix

F_{ex} = wave excitation force

F_{rad} = force vector due to radiation

F_{PTO} = PTO force

F_v = viscous damping force

F_B = net buoyancy restoring force

F_m = force due to mooring connection

Each of the terms in Equation 1 is briefly discussed below:

$$F_{ex}(t) = Re(\int_0^\infty \sqrt{2S(\omega)} FX(\omega) e^{i(\omega t + \phi)} d\omega) \quad (2)$$

Equation 2 represents the irregular wave excitation force as the real part of the integral term in frequency, where:

Re = denotes real part of the function

S = wave spectrum

ϕ = random phase

Based on Cummins equation, the irregular radiation term can be calculated by Equation 3:

$$F_{rad}(t) = -A_\infty \ddot{X} - \int_0^t K(t - \tau) \dot{X}(\tau) d\tau \quad (3)$$

Where:

A_∞ = added mass matrix at infinite frequency

\dot{X} = velocity of the body

K = impulse response function

The PTO mechanism is represented as a linear spring-damper system, where the generated power is proportional to the relative motion and velocity as shown in Equation 4:

$$F_{PTO} = -K_{PTO} X_{rel} - C_{PTO} \dot{X}_{rel} \quad (4)$$

Where:

K_{PTO} = stiffness of the system

X_{rel} = relative motion

C_{PTO} = damping coefficient

\dot{X}_{rel} = velocity between two bodies

This tool was verified and validated using experimental data, and against the commercially available tools that renewable energy (i.e. wind energy) industry heavily relies on, such as OrcaFlex, WaveDyn, NAVITAS (economic), and AQWA [11-13].

4.4 Economic Calculations

The dynamic analysis (power output performance) obtained from the simulations on WEC-Sim will be used to populate the COE Calculation Tool for Wave Energy converters [14] as illustrated in Figure 3. This is an open-source spreadsheet tool developed by the consulting engineer Julia F. Chozas together with Aalborg University and Energinet.dk. It provides the following assessments:

- Capital factor
- Annual electricity production (AEP)
- Average annual production
- Average wave-to-wire efficiency
- WEC development stage and uncertainty to the data
- Capital Expenditure (CapEx) and Operational Expense (OpEx)
- Payback period
- Levelized Cost of Electricity (LCOE) (for three different rates)
- Net Present Value, NPV (for three different rates)

The LCOE is calculated from COE by taking into account the variation in time of money value, which is represented by the discount rate. Figure 4 illustrates the flow and connection of each component contributing to COE.

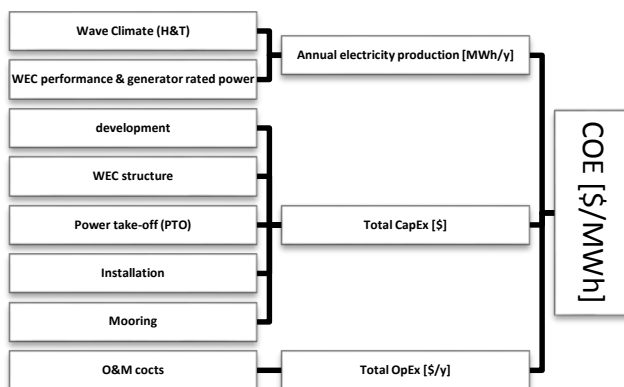


Figure 4: Components of cost of electricity analysis

The COE tool is based on a reference device and gives the opportunity to calculate the scaled equipment and the costs associated with to the reference and the scaled devices. All input data such as dimension, weight, minimum and maximum operative wave conditions, WEC rated power, conversion system efficiency, power production and prices, must be based on the same reference device [14].

The economic calculations will also be done on Reference Model 3 spreadsheet tool that is part WEC-Sim discussed in Section 4.2 the comparison will be made to get a certain level of confidence on the results.

5. CONCLUSION

The techno-economic analysis will be performed for all chosen devices to compare with Wits direct drive WEC, and also their array configurations, it will also form basis for the comparison framework that will be developed. The highlighted methodology will be followed where the models of each device in consideration will be built on Simulink/SimMechanics/Simcape in MATLAB R2014b and simulated using real sea state conditions of Slangkop site. The Wits WEC will be verified against other devices and the simulation results from these devices will be fed into COE Calculation Tool to economic analysis using the same sea conditions. The economic analysis will also be performed using the WEC-Sim spreadsheet to have more confidence in the results. On completion of this project a fast comparison framework should be produced and Wits WEC would have been modeled and design improvement where need will be recommended.

6. REFERENCES

- [1] M. O'Connor, T. Lewis and G. Dalton, "Techno-Economic Performance of Pelamis P1 and Wavestar at Different rating and Various Locations in Europe", *Hydraulics and Maritime Research Centre (HMRC), University College Cork, Ireland*
- [2] J. Fernandez-Chozas, M.A. Stefanovich and H.C. Sorensen, "Towards Best Practice for Public Acceptability in Wave Energy: Whom, When and How to Address", *3rd International Conference on Ocean*, Bilbao, pp.1, October 2010.
- [3] A. Williams, M. Nthonto, S. Chowdhury and S.P. Chowdhury, "Modelling South African Agulhas Marine Current Profile Data for Electricity Generation", *IEEE*, pp.1, 2012.
- [4] B. Teillant, R. Costello, J. Weber and J. Ringwood, "Techno-Economic Optimisation for Wave Energy Converters", *4th International Conference on Ocean Energy*, Dublin 17 October
- [5] John Brooke, "Wave Energy Conversion" Elsevier Ocean Engineering Book Series, Volume 6
- [6] J.R. Joubert and D.E. Bosman, "An Investigation of the Wave Energy Resource on the South African Coast, Focusing on the Spatial Distribution of the South Western Coast", *School of Civil Engineering, University of Stellenbosch*.

- [7] D. Jarocki, "Wave Energy Converter Performance Modeling and Cost of Electricity Assessment" *The faculty California Polytechnic State University*, Master's degree, April 2010
- [8] B. Drew, A.R. Plummer and M.N. Sahinkaya, "A review of wave energy converter technology", Review Paper, Department of Mechanical Engineering, University of Bath, UK, June 2009.
- [9] WEC-Sim, *User Manual*, version 1, June 2014.
- [10] W.E. Cummins, "The Impulse Response Function and Ship Motions", *Schiffstechnik*, vol.47, no.9, pp. 101-109, 1962
- [11] Y. Yu, M. Lawson, K. Ruehl and C. Michelen, "Development and Demonstration of the WEC-Sim Wave Energy Converter Simulator Tool", *2nd Marine Energy Technology Symposium*, USA, pp.1-5, April 2014.
- [12] K. Ruehl, C. Michelen, S. Kanner, M. Lawson and Y. Yu, "Preliminary Verification and Validation of WEC-Sim, an Open-source Wave Energy Conversion Design Tool", *33th International Conference on Ocean, Offshore and Arctic Engineering*, San Fransisco, USA, June 2014.
- [13] K. Ruehl, R. So, A. Simmons, T. Brekken and C. Michelen, "Development of PTO-Sim: A Power Performance Module for the Open-Source Wave Energy Converter Code WEC-Sim", *34th International Conference on Ocean, Offshore and Arctic Engineering*, Canada, May/June 2015.
- [14] J. Fernandez-Chozas, K. Peter, N.E. Helstrup, *User guide-COE Calculation Tool for Wave Energy converter*, Aalborg University, Denamark, 2014.

Performance Evaluation of an Entropy-based Image Analysis Algorithm for Insulator Hydrophobicity Classification for Different Image Acquisition Lighting Conditions

M.M. Ndamira* and H. J. Vermeulen** and J.M. Strauss***

* Dept. of Electrical and Electronic Engineering, Stellenbosch University, Private Bag X1, Matieland, 7602, South Africa
Email: 15499154@sun.ac.za

** Dept. of Electrical and Electronic Engineering, Stellenbosch University, Private Bag X1, Matieland, 7602, South Africa
Email: vermeuln@sun.ac.za

*** Dept. of Electrical and Electronic Engineering, Stellenbosch University, Private Bag X1, Matieland, 7602, South Africa
Email: jstrauss@sun.ac.za

Abstract: Surface hydrophobicity represents a key indicator of the condition of polymeric insulators, especially as metric of ageing and flashover performance under wet and polluted conditions. Hydrophobicity is typically determined using laboratory tests where the average contact angle of water droplets and the wetted surface area are measured. The STRI methodology involves comparing digital images of water droplet distributions on the insulator surface with a set of reference images representing different hydrophobicity classes. This paper describes the results of an investigation to evaluate the performance of a digital image processing methodology for computer-based classification of hydrophobicity for different lighting conditions, including normal indoor lighting, spotlight illumination and flash photography. The methodology uses the Average Normalised Entropy (ANE) of the images as hydrophobicity feature. Results are presented for raw images as well as images subjected to contrast enhancement using the Contrast Limited Adaptive Histogram Equalisation (CLAHE) algorithm as an image enhancement technique. It is shown that the CLAHE algorithm improves the robustness of the relationship between ANE and hydrophobicity, especially for images acquired with spotlight illumination.

Keywords: Hydrophobicity, Insulator, Image analysis, Normalised entropy, Contrast limited adaptive Histogram equalisation.

1. INTRODUCTION

High voltage insulators represent a key component of modern high voltage transmission systems. Factors such as insulator pollution and ageing give rise to flashovers that result in disruptive and costly power outages [1]. The use of polymeric insulators has increased dramatically in recent years due to advantages such as hydrophobic surface properties, light weight, weather resistance, easy installation and ease of transportation [2].

Polymeric insulators deployed under outdoor conditions are, however, susceptible to aging effects caused by ultraviolet radiation, surface abrasion due to wind-borne particles, high temperatures, humidity, pollution deposits such as salt, corona discharges, etc. [3]. Ageing gives rise to a loss of surface hydrophobicity that decreases the flashover performance under wet and polluted conditions [4]. It follows that the hydrophobicity class of an insulator represents a key indicator of insulator condition, especially with reference to the degree of degradation due to ageing.

Extensive research has been conducted on methodologies to measure the hydrophobicity of insulator surfaces. The classical methodology involves measurement of the contact angles of water droplets on the insulator surface

[5]. This methodology, however, requires laboratory conditions, specialised equipment and a high degree of technical training and experience. In an alternative methodology, proposed by the Swedish Transmission Research Institute (STRI), the hydrophobicity class of an insulator is determined by comparing digital images of water droplet distributions on the insulator surface with a set of seven reference images, each representing a hydrophobicity class in the range HC₁ to HC₇ [6]. This methodology, however, has the disadvantage that it is subjective due to human evaluation. This has given rise to the development of number computer-based hydrophobicity classification methodologies using digital image processing techniques [1], [3], [4], [7].

Research on methods for hydrophobicity classification using image analysis focuses strongly on feature definition, feature enhancement and feature extraction. This investigation employs a classification algorithm using the Average of Normalised Entropies (ANE) of a gray scale difference image as main feature, with preprocessing using Contrast Limited Adaptive Histogram Equalisation (CLAHE). The performance of this methodology for images acquired with normal indoor lighting, spotlight illumination and flash photography are compared.

2. EXPERIMENTAL ARRANGEMENT AND TEST PROCEDURES

Digital images representing hydrophobicity classes obtained in a previous investigation were used in the investigation [7]. The images represent water dispersion patterns on flat Silicon Rubber (SIR) samples with dimensions of 12 cm x 14.5 cm. The images cover the full range of hydrophobicity classes, i.e. HC₁ to HC₇, proposed in the STRI hydrophobicity classification guide [5].

In obtaining the images, loss of hydrophobicity was simulated by using a wetting agent consisting of a mixture of ethanol and distilled water using incremental increases of ethanol, ranging from 0% to 100% in steps of 20% [7]. Instead of the standardized wetting method [6], a modified wetting method was applied in order to achieve repeatable and consistent results [7]. The insulator was orientated at a 25° inclination angle to the horizontal plane. Using a household spray bottle, the surface was misted from left to right while spraying 1-2 times per second from a distance of approximately 20 cm. Spraying ceased as the first drop started to run. The image was taken within 10 seconds of water application.

The photographic equipment used to obtain the images consisted of a Nikon D60 digital camera, Nikon 18200mm 1:3.5-56 Lens, Thule tripod and a mounted tungsten spotlight [7]. Different lighting configurations and photography settings were implemented with the view to investigate how these parameters can highlight different features. Image sets obtained with normal indoor lighting, spotlight illumination and flash photography are used in the investigation.

All images were cropped to the same size to ensure consistency. Figure 1 shows a sample image of an insulator surface sprayed with 40% ethanol wetting agent after cropping. The image processing for this investigation was performed using Python, along with various image-processing toolboxes, including the OpenCV toolbox. The Python environment is intuitive to use and provides for easy modification of the available functions to suit users requirements.

3. IMAGE PROCESSING METHODOLOGY

1. Overview

The key steps involved in performing image analysis for hydrophobicity classification, shown in Figure 2, can be summarised as follows:

- *Sample preparation:* Insulator samples representing different hydrophobicity classes as result of natural ageing or accelerated ageing are wetted with distilled water. Alternatively, hydrophobicity can be simulated using virgin insulator samples with a wetting agent consisting of a mixture of distilled water and ethanol. In both cases, a suitable spraying methodology, using

a sample inclination angle determined by run-off considerations, is applied.

- *Image acquisition:* The images are acquired using a high resolution digital camera with appropriate camera settings, shooting distance and shooting angle. A lighting scheme is implemented, using options such as natural inside lighting conditions, a spotlight illumination, flash photography or a combination of these.
- *Feature enhancement:* Morphological operations are performed on the images with view to enhance the success of the feature extraction process. These include operations such as cropping, the conversion of color images to gray scale images, contrast enhancing, thresholding, etc. The feature enhancement methodology depends on the characteristics of the feature and the properties of the original images.
- *Feature extraction:* The desired feature vector, representing hydrophobicity, is extracted. The extraction methodology depends on the nature of the feature.
- *Performance evaluation:* The image processing operation and the results are evaluated with reference to criteria such as processing time, robustness of the classification accuracy, etc. A monotonic and unambiguous relationship between the feature and hydrophobicity is typically required for successful classification.



Figure 1: Cropped sample image with 40% ethanol wetting agent.

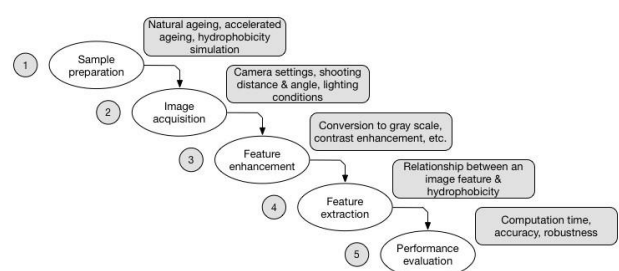


Figure 2: Image analysis for hydrophobicity classification process hierarchy.

The complex background information of the water dispersion images can give rise to difficulties in segmentation of the water droplets because of the water transparency, which may lead to a smaller gray level difference in some parts of a sample image. This is evident from the image shown in Figure 1.

Light reflection also leads to fuzzy boundaries [1]. Gray level image enhancement reduces the noise level as well as enhances certain parts of the image to improve on the results achieved by hydrophobicity classification using the ANE feature.

The methodology applied in this investigation can be summarised as follows:

- The original color images are converted to gray scale in order to reduce storage size and processing time.
- Image enhancement is applied, using one of the following options:
 - No enhancement is applied.
 - A Contrast Limited Adaptive Histogram Equalization (CLAHE) is applied.
- The image is converted to a difference image by subtracting the pixel intensity of each pixel from that of the nearest horizontal neighbour.
- The Average of Normalized Entropies (ANE) of the gray level difference image is calculated to use as feature vector.

2. Adaptive Histogram Equalization

The ANE as a feature of an image should ideally be independent of varying illumination, inconsistencies in insulator surface and other environmental factors that may affect the quality of the image. This is, however, not the case with images acquired under field conditions where inconsistencies result in images with poor contrast. Contrast enhancement can be applied through direct methods where the contrast is measured and manipulated and indirect methods aimed at utilizing the whole dynamic range of an image [8].

The most popular methods used to improve the definition of such images are histogram equalization and contrast stretching, where each pixel is transformed based on the level of segmentation needed. For the purposes of this investigation adaptive histogram equalization and the transform-based technique of histogram stretching are investigated.

Histogram equalization involves spreading the histogram of gray levels of an image across the whole spectrum of image intensities. This removes some noise as well as segments the objects of the image by enhancing the brightness of an image, which assists in feature extraction. In some cases the output maybe too heavily enhanced,

leading to large peaks in unwanted areas and increased noise in other areas of the image [8], [9].

Adaptive histogram equalization mimics human image analysis by taking cognisance of localised effects. This is achieved by focusing the histogram equalisation on rectangular regions or kernels [9] in the image. In areas with small gray level differences, however, this causes undesired amplification of pixel intensities. This effect can be mitigated by using the CLAHE algorithm [9], which clips the histogram at a predefined level, thereby limiting the amplification. The algorithm takes the kernel size and clip limit as parameters.

Figure 3 shows the contrast enhancement effect of applying the CLAHE algorithm for a gray scale image with 60% ethanol wetting agent.

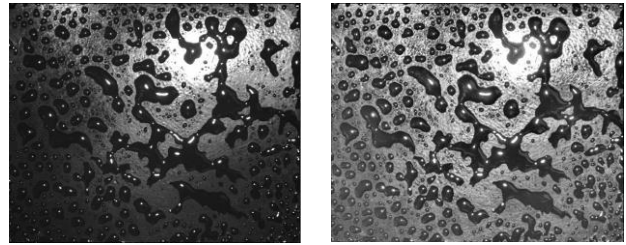


Figure 3: Gray scale image with 60% ethanol wetting agent; (a) Original image (b) After application of CLAHE algorithm.

3. Average of Normalised Entropies

The entropy E of an image represents a statistical measure of the amount of information contained in an image. The entropy is determined from the relative frequency of occurrence each of gray level difference using the relationship

$$E = -\sum_{d=-255, f \neq 0}^{255} f(d) \log_2(f(d)) \quad (1)$$

where $f(d)$ denotes the relative frequency of gray level difference of level d . The normalized entropy E_n and the compliment of normalized entropy E_{cn} are given by the relationships

$$E_n = -\sum_{d=-255, f \neq 0}^{255} f(d) \log_2\left(\frac{f(d)}{\Phi}\right) \quad (2)$$

$$E_{cn} = -\Phi \sum_{d=-255, f \neq 0}^{255} [\sigma f(d)] \log_2(\sigma f(d)) \quad (3)$$

where σ and Φ denote the standard deviation of the gray level differences and the fraction of small differences respectively. The ANE is given by the relationship

$$ANE = \frac{1}{2}(E_n + E_{cn}) \quad (4)$$

4. RESULTS

The ANE analysis using gray scale images was conducted for three sets of images representing three different lighting conditions, i.e. with normal inside lighting conditions, spotlight illumination and a camera flash. Each set consisted of six different water/ethanol mixtures, ranging from 0% ethanol to 100% ethanol. The analysis was conducted for the original gray scale images and after the CLAHE algorithm was applied using a kernel size of 8x8 pixels and a clip limit size of 2. The effect of CLAHE algorithm on image contrast is shown in Figures 3a and 3b.

Figure 4, 5 and 6 show the ANE as a function of hydrophobicity for the different lighting conditions. Two sets of results are plotted in each case, namely ANE values derived for the original gray scale images and the ANE calculated for the images subjected to the CLAHE algorithm. As expected, the lower ethanol percentage mixtures generally exhibit a higher entropy value compared to the higher ethanol percentage mixture. The results can be summarised as follows:

- *Original images:* The relationship between ANE and hydrophobicity only show a monotonically decreasing trend for the images acquired with spotlight illumination, Spotlight illumination, however, also shows the smallest range of ANE values for the hydrophobicity range.
- *Images subjected to the CLAHE algorithm:* The relationship between ANE and hydrophobicity show a monotonically decreasing trend for the images acquired with spotlight illumination and with flash photography. The relationship obtained with the spotlight has a more linear relationship between ANE and hydrophobicity compared to results obtained with flash photography, but also exhibits a lower range of ANE values. In the case of image acquired with normal inside lighting, the relationship between ANE and hydrophobicity is not monotone.

Where monotonic relationships between ANE and hydrophobicity were obtained, the relationships obtained for the original images are less linear compared to the relationships obtained with application of the CLAHE algorithm.

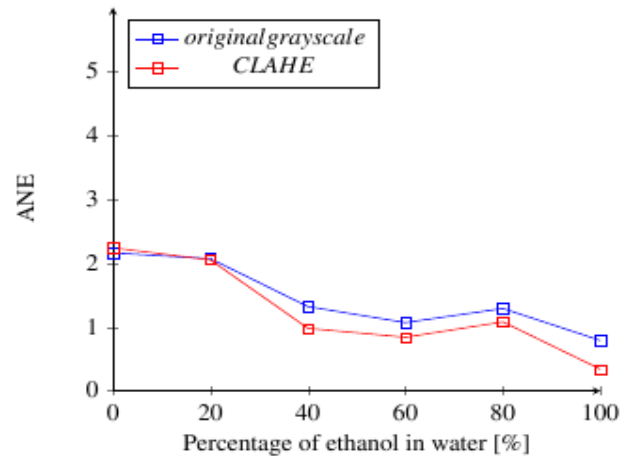


Figure 4: ANE results for images acquired with normal indoor lighting.

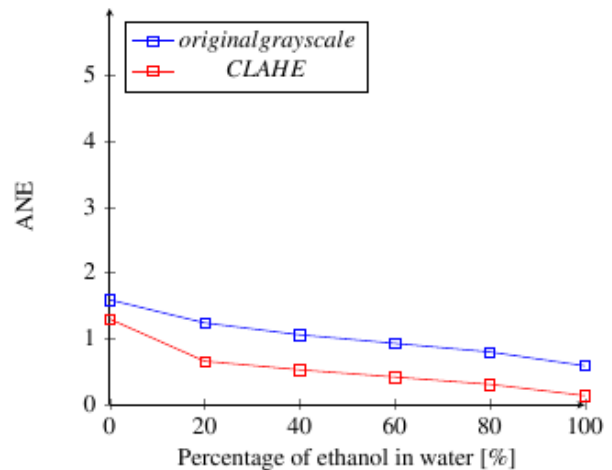


Figure 5: ANE results for images acquired with spotlight illumination.

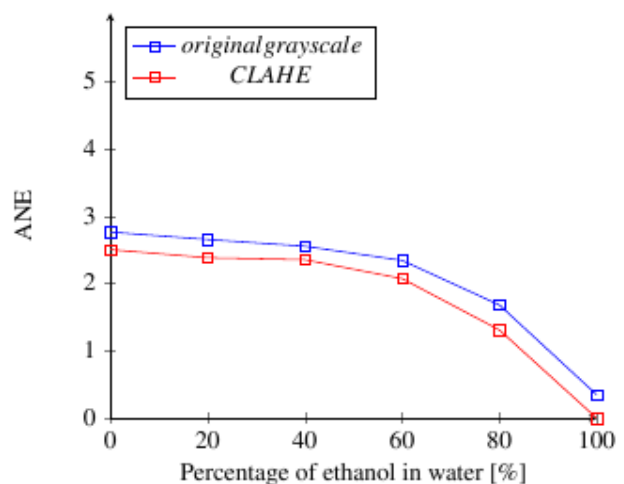


Figure 6: ANE results for images acquired with flash photography.

5. CONCLUSIONS

The ANE method can be used as a hydrophobicity indicator function with fairly good results. The CLAHE algorithm improves robustness of the relationship between ANE and hydrophobicity for hydrophobicity classification. Images acquired with spotlight illumination also yield better results compared to natural room lighting and flash photography.

Further research is required on segmentation of the binary images, as only fairly good results were obtained when analysing images taken with other lighting conditions. The algorithms should be able to work with more accuracy under various illumination conditions and should remain computationally inexpensive. The images used had a very high resolution, which results in increased processing time. The use of images with lower resolutions to reduce the processing time should be investigated.

REFERENCES

- [1] Z. Dong, Y. Fang, X. Wang, Y. Zhao and Q. Wang, "Hydrophobicity Classification of Polymeric Insulators Based on Embedded Methods 2, Experimental Procedure," *Materials Research*, vol. 18, no. 1, pp. 127-137, 2015.
- [2] B. Venkatesulu and M. J. Thomas, "Long-term Accelerated Multistress Aging of Composite Outdoor Polymeric Insulators," *2007 IEEE International Conference on Solid Dielectrics*, pp. 188-191, Winchester, UK, July 2007.
- [3] M. Berg, R. Thottappillil and V. Scuka, "Hydrophobicity Estimation of HV Polymeric Insulating Materials. Development of a Digital Image Processing Method," *IEEE Transactions on Dielectrics and Electrical Insulation*, vol. 8, no. 6, pp. 1098-1107, 2001.
- [4] D. Thomazini, M. V. Gelfuso, R. A. C. Altafim, "Classification of Polymers Insulators Hydrophobicity based on Digital Image Processing," *Materials Research*, vol. 15, no. 3, pp. 365-371, 2012.
- [5] Guidance on the Measurement of Wettability of Insulator Surfaces, IEC Tech. Spec. TS 620722003, June 2003.
- [6] Hydrophobicity Classification Guide, STRI Guide 92/1, Swedish Transmission Research Institute, 1992.
- [7] G. W. Blignault and H. J. Vermeulen, "An Image Processing Methodology for Insulator Hydrophobicity Classification Using Flash Photography," *Southern African Universities Power Engineering Conference (SAUPEC 2014)*, Durban, South Africa, 30 – 31 January 2014.
- [8] T. Arici, S. Dikbas and Y. Altunbasak, "A Histogram Modification Framework and Its Application for Image Contrast Enhancement," *IEEE Transactions on Image Processing*, vol. 18, no. 9, pp. 1921-1935, September 2009.
- [9] B. S. Min, D. K. Lim, S. J. Kim and J. H. Lee, "A Novel Method of Determining Parameters of CLAHE Based on Image Entropy," *International Journal of Software Engineering and its Applications*, vol. 7, no. 5, pp. 113-120, 2013.
- [10] L. G. Moré and M. A. Brizuela, "PSO Applied to Parameter Tuning of CLAHE Based on Entropy and Structural Similarity Index," Available at: http://www.cc.pol.una.py/wpfg2014/pdf/lmore_mbrizu
- [11] A. Mordvintsev, "OpenCV-Python Tutorials Documentation," 2013. Available at: <http://ieeexplore.ieee.org/lpdocs/epic03/wrapper.htm?arnumber=4290784>

AN INVESTIGATION INTO SURGE ARRESTERS FAILURES IN THE KZN 88KV TRACTION SYSTEM

M. Mzulwini* and K. Awodele**

* 1 Langford Road, Westville, KwaZulu-Natal, Republic of South Africa. E-mail: MzulwiniM@eskom.co.za,

** Department of Electrical Engineering, University of Cape Town., Cape Town, South Africa E-mail: Kehinde.Awodele@uct.ac.za

Abstract: Surge arresters are installed in the power system to divert overvoltages to ground under faulty conditions and the system returns to steady state after fault(s) have cleared, therefore these devices form a critical part of the power system as their failures often results in the interruptions of supplies with consequences on the utilities reputation, loss of revenue and cost of replacements. Surge arresters protect against direct lightning strikes on the power system's components and switching surges. This paper outlines design, selection and energy absorption requirements of metal oxide surge arresters in the traction networks. A brief description of MOSA's design, operation and selection is given. A KZN case study is also modelled and simulated in Matlab Simulink power system block (PSB) and results are discussed. The performance impact of MOSAs failures in radial feeders is evaluated and conclusions and recommendations are made.

Keywords: Metal oxide surge arrester (MOSA), switching surges, energy handling capabilities and traction networks

1. INTRODUCTION

A power system comprises of components such as transformers, insulators, surge arresters, connection clamps etc which are subjected to overvoltages or transient voltages. These surges have adverse effects on the performance of protective devices such as surge arresters and therefore are a concern to power system engineers.

The interconnectivity of the power system and its complexity coupled with effects of small signal instability in a large and sparse power network compounds the effects of switching surges and may result in surge arrester failures as a single failure event on one component may result in other cascading failures with serious consequences on the power system performance. These consequences may be the loss of supplies to customers, penalties from the Electricity regulator, high cost of replacement, loss of revenue and reputation damage of the utility. The radial feeds are also vulnerable under N-1 contingencies and therefore any failures of surge arresters on these networks should be contained.

The voltage surge or transient voltage is a sudden rise in the power system's voltage magnitude for a very short duration of time. These temporal overvoltages are detrimental to the power system if uncontrolled and therefore the utility must ensure that protective devices are installed to guard adequately against them. The behaviour of the voltage surge or transient voltage takes a very steep curve in a very short space of time and it is the most dangerous period as its peak can exceed the protective level of surge arresters. It then decays

slowly again this is also dangerous because if left unchecked it may overstress the protective device's insulation and lead to energy storage exceedances which eventually result in the failure. The typical behaviour of a voltage surge is shown in figure 1.

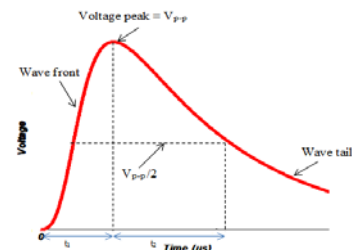


Figure 1: Typical voltage surge characteristic

When surge arresters are selected for any application it is important they can withstand the dynamic nature of these surges as exhibited by that network. t_1 and t_2 are rise time and fall/decay times. The characteristic of a transient or surge is usually described as a t_1/t_2 μ s current or voltage surge for example a 1/50 μ s means the surge reaches its peak voltage in 1 micro seconds and decays in 50 micro-seconds.

The standard surge waveform that is stipulated in the IEC 60099-4 is a 8/20 μ s waveform and manufacturers design their products to meet this requirement. The causes of overvoltages in the power system are due to internal and external factors. The internal surges arise due to switching surges, arcing ground, resonance and insulation failure whereas external overvoltages are due to lightning, moisture ingress into protective devices, pollution, interaction

of the devices with the environment (plants and animals) etc [1].

2. DESIGN, OPERATION AND SELECTION OF METAL OXIDE SURGE ARRESTERS

2.1 Surge arrester design

There are two fundamental principles that must be taken into consideration in the design of a surge arrester, firstly when the surge has dissipated the arc in the surge arrester gap (whatever material it may be) should cease otherwise if the arc is not extinguished the current will continue to follow through the resistive path and the surge arrester may be destroyed, secondly, IR (where I is the surge current and R is the resistance of the arrester) when carrying a surge current should not exceed the breakdown strength of the insulation of the equipment to be protected.

The basic design of any surge arrester is based on the principle depicted in figure 2 below.

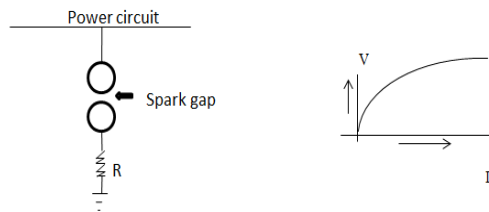


Figure 2.1.1: The basic design of a surge arrester and its V-I characteristic [2].

A surge arrester consists of a spark gap in series with a non-linear resistor. The length of the gap is set such that the normal line voltage is not enough to cause an arc across the gap but a dangerously high voltage may stress the insulation and result in an arc and destroy the surge arrester [2].

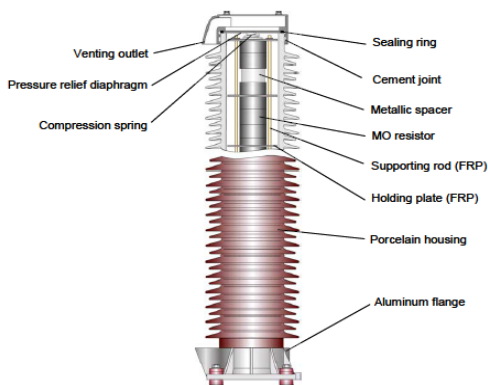


Figure 2.1.2: Polymer gapless MOSA [1]

An example of a MOSA is shown in figure 2.1.2. The V-I characteristic of a MOSA is described by the following expression:

$$I = kU^\alpha \quad (2.1.1)$$

where:

I = conducting current as the arrester operates,

U = lightning impulse voltage level

α and k are parameters of each segment in Figure 2.1.3.

k and α parameters fit the V-I characteristics provided by the manufacturer and are specified by the manufacturer and these do not change with the protection level [6].

The protection level is obtained by adding metal oxide discs of zinc in series in each column. These discs form stacks which are normally connected in parallel depending on the voltage level. The voltage characteristic of MOSA is shown in figure 2.1.3. The points in the characteristic curve are a: capacitive linear area where current is less than 1mA, b: knee point which is a transition from insulating to conducting, c: strongly non-linear area, d: ohmic linear current area, A: area of continuous operating voltage, U_c and B: residual voltage U_{res} , protection area.

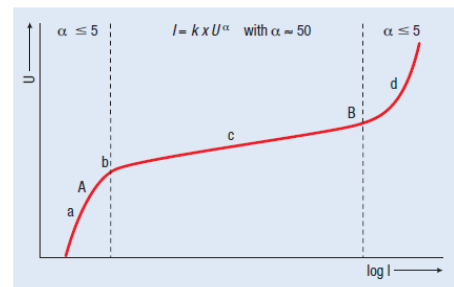


Figure 2.1.3: V-I characteristics of a MOSA [2]

2.2 Basic operation of a surge arrester (MOSA)

The surge arrester must meet the following requirements before, during and after the fault [2]:

- Under normal operating conditions i.e. no surge on the line or any part of the network the surge arrester is 'OFF' there is no conduction of current to earth through the gap and the resistor.
- On occurrence of overvoltage the air insulation across the gap breaks down and an arc develops providing a low resistance path for the surge to ground. In this way the excess charge on the line due to the surge is harmlessly conducted through the surge arrester to the ground instead of being sent back over the line.
- In the event that the surge is extinguished the resistor (through its non-linearity property) provides a high resistance to make the gap non-conducting.

2.3 Selection of a surge arrester

The IEC 60099-4 provides minimum guidelines to be met by manufacturers, these are summarized as:

- Operating conditions: ambient temperature, altitude above sea level, humidity, solar radiation etc.
- Voltage and energy handling ratings: maximum system voltage (U_m), nominal voltage (U_n), basic insulation level (BIL), MCOV and U_{res}
- Arrester housing : materials that form the housing of the arrester
- Creepage distance: 25 mm/kV (for inland installations) and 31 mmkV (for coastal installations).
- Mounting and terminations

The IEC classify surge arresters into two categories i.e. distribution class surge arresters and station class surge arresters. These have different discharge currents at 10 kA and 20 kA respectively. However caution must be exercised in the selection process as the class of the surge arrester is equally important, for example a class 2 , 10 kA distribution surge arrester has a greater energy absorption than a class 1 distribution of the same discharge current level. The requirements in the IEC 60099-4 specifications are a guideline therefore a detailed selection process must be undertaken depending on the specific applications. The parameters that are listed in the IEC (i) continuous operating voltage (U_c), maximum continuous operating voltage (MCOV), (ii) rated voltage (U_r), (iii) discharge current, (iv) residual voltage (U_{res}), (v) discharge current (kA) and (vi) energy absorption capability, E. The energy stored in the surge arrester is the power stored in the arrester integrated over a specific time t , normally this energy is stored in the arrester until the voltage surge dissipates and the time taken for the surge arrester to cool down. Energy absorbed by the arrester is calculated by the following expression:

$$E = \int_{t_0}^t u(t) i(t) dt = \quad (2.3.1)$$

where:

$u(t)$ = is a time varying residual voltage of an arrester,
 $i(t)$ = is the discharge current through the arrester in kA.

This energy is measured in kJ/kV (U_c) and is specified by the manufacturer. The duration of the switching impulse can be estimated as the time for a surge to travel twice the length of the line, L such that the time duration is expressed by:

$$t = \frac{2L}{c} \quad (2.3.2)$$

where:

c = is the speed of light which is 3×10^8 km/s

L = line length covered by the surge as it propagates

Suppose the line is charged to a switching surge level of V_{ss} . The surge is thus discharged through the line surge impedance into the arrester. If the arrester voltage is denoted by V_{arr} , and the line surge impedance by Z_0 , then the equation relating these parameters can be expressed as:

$$V_{ss} = I Z_0 + V_{arr} \quad (2.3.3)$$

where:

I = is the surge current in Amperes (A) and re-arranging equation (4) yields:

$$V_{ss} - I Z_0 = V_{arr} \quad (2.3.4)$$

Noting that equation (2.3.4) is a straight line with a negative slope and that there exists a point in the straight line and the surge arrester voltage-current characteristic we can show this relationship graphically as shown in figure 2.3.1

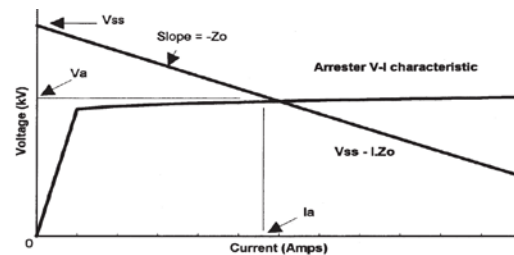


Figure 2.3.1: A graphical representation of surge arrester V-I characteristic with the surge impedance loading of a network [4].

The following example is an illustration of how equations (2.3.2), (2.3.3) and (2.3.4) can be used to select the surge arrester graphically.

Example:

Calculate the energy absorbed by a surge arrester with 84 kV MCOV that is installed to protect a 138 kV line which is 322 km long with a surge impedance of 400 ohms.

Solution to the Example: From a 115 kV line surge arresters characteristics (shown in Figure 2.3.1.2) the intersection of the curves occurs at the point (I_a , V_a), therefore $I_a = 137.5$ A and $V_a = 190$ kV

Using the characteristic curves these points are indicated in figure 2.3..2.

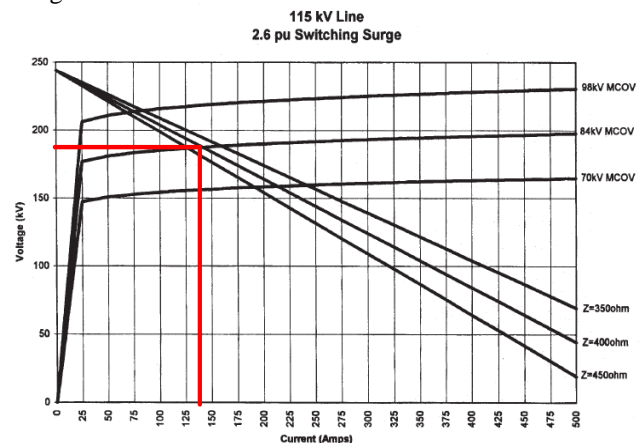


Figure 2.3. 2: The intersection of the (I_a , V_a) point and the line surge impedance is shown below.

Using equation (2.3.2) above the surge duration is,

$$t = \frac{2L}{c} = \frac{2 \times 322 \times 1000}{300,000 \times 1000} \dots\dots = 2.15 \text{ milliseconds}$$

Substituting into equation (2.3.1) we get energy,

$$E = V_a I_{at} = 190 \times 137.5 \times 2.5 \times 10^{-3} \dots\dots = 65.31 \text{ kJ}$$

Therefore the energy absorbed by the 84 kV MCOV arrester is $65.31/84 = 0.78 \text{ kJ/kV}$

Similarly, using the 138kV curve we get the intersection point (250,190), such that:

$E = 250 \times 190 \times 2.5 \times 10^{-3} = 102.13 \text{ kJ}$, therefore the energy absorbed by the 84 kV MCOV arrester is $102.13/84 = 1.22 \text{ kJ/kV}$

This example has shown that the energy absorbed by the surge arrester depends on its terminal voltage and the surge arrester discharge current. Furthermore, the MCOV is required to assess if the surge arrester will withstand a particular surge voltage. It also illustrates how the selection of the surge arrester can be achieved for increased energy storage requirements.

3. CHARACTERISTICS OF A TRACTION NETWORK

3.1 Traction load features and quality of supply

A traction system involves an AC transmission line), a station transformer, a converter (which forms part of the locomotive design), a catenary and the load (train) as shown in figure 3.1.1.

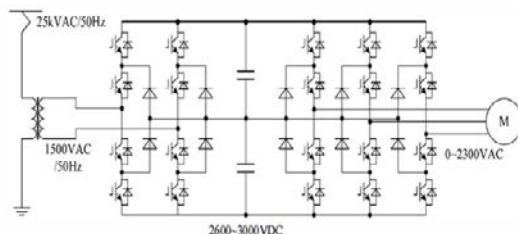


Figure 3.1.1: Typical layout of a traction network [5]

The traction network has the following effects on the quality of the supply [5]:

- Negative sequence currents – which generate heat and lead to protection device maloperations.
- Harmonic currents – which also generate heat in electrical devices such as transformers and also leads to partial discharges especially on FACTS devices.
- Reactive currents – which suppresses the power capability of traction's substation transformers.

The first two effects are relevant in our quest for the understanding of the impact of traction load on the surge arrester performance.

3.1 Modelling the traction network

The KZN 88 kV traction network (figure 3.1.2) was used as a case study in this research.

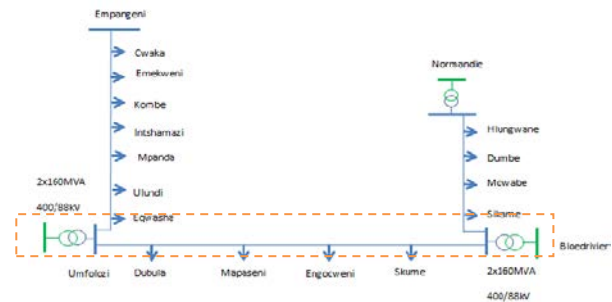


Figure 3.1.2: The KZN 88 kV traction network layout
The electrical data that was collected from drawings and site investigations is shown in table 3.1.1.

Table 3.1.1: Model parameters

Traction 88kV lines	Traction line lengths (km)	Traction loads	All section strung in Wolf ACSR conductor, 370A at 75° deg	
Umfolozi – Empangeni	158.98		R/km	X/km
Umfolozi- Bloedrivier	92.82		0.1932	0.3065
Bloedrivier- Normandie	113.15			

A section of the network (Umfolozi – Bloedrivier substations) was modelled in Matlab Simulink PSB (2009) as shown in figure 3.1.3. The following assumptions were made in the simulations:

- The fault occurs at 0.06 seconds and clears after 0.08 seconds.
- The closing of the breaker occurs when the voltage is at the zero crossing at 0.08 seconds.
- The voltage maximum peak occurs at 0.085 seconds whilst the minimum is at 0.095 seconds.
- The switching surge closely resembles the test signal as defined by the 8/20 μs waveform in the IEC 60099-4.

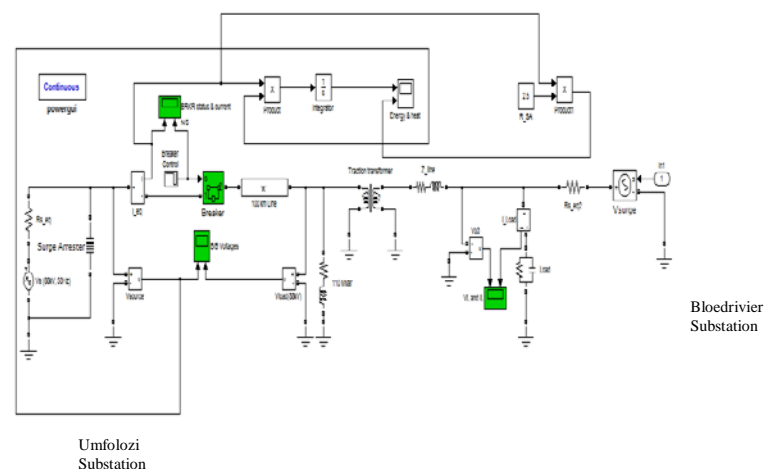


Figure 3.1.3: The KZN traction network as modelled in Matlab PSB.

3.2 Simulation methodology

The 88kV Transmission network is simulated as time varying sinusoidal voltage source with a 88 kV_{p-p}, simulated as time varying voltage source connected in series with a 2 Ω internal impedance.

A two stack 88kV surge arrester is then connected in parallel to the source. The current through the line and source voltage are then measured. A fault is created at 0.06 seconds and clears at 0.08 seconds. The breaker status is controlled by a switch that toggles between zero (fault occurs) and one (fault is cleared). The energy absorption of the MOSA is simulated by multiplying voltage and current output and feeding this through an integrator.

The heat (I^2R) build-up in the MOSA is simulated by squaring the discharge current through the MOSA and multiplying the quantity by the MOSA resistance (60xmetal oxide discs that form two stacks). The resistivity value of $9.71 \times 10^{-8} \Omega\text{m}$ and 37.5 mm zinc disc radius are then used to calculate the resistance of 2.5 Ω . The heat and energy are then plotted. The traction transformer is then simulated as a 2 winding, 88/25 kV, 2.5 MVA transformer. The surge or transient is then initiated from Bloedrivier substation as a controlled voltage source with the input block In1 defined by parameters x and y, where $x = (0:0.00001\text{e}-3:0.002\text{e}-3)$ and $y = 13.2 \times 5 \times 55 \times \exp(-2000 \times 3 \times \text{pix}) \sin(2 \times \text{pix})$.

4. SIMULATION RESULTS AND ANALYSIS

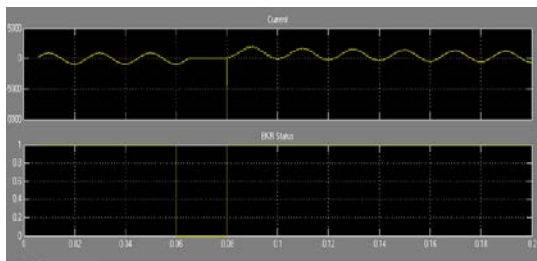


Figure 4.1: The breaker status under pre-fault, during the fault and post-fault conditions.

The operation of the MOSA at the fault occurs is shown in figure 4.2. The 88kV MOSA clamps the surge voltage at 0.06 seconds to about 92 kV.

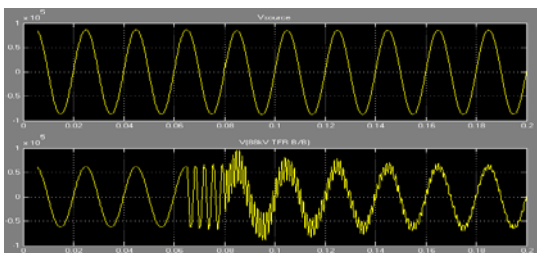


Figure 4.2: The clamping of the surge voltage as the fault occurs.

The load (traction) voltage fluctuates depending on the locomotive's motion while the load current is distorted resulting in harmonic currents [5]. These observations are evident in figure 4.3.

The energy absorbed by the MOSA during and after the fault increases drastically and does not settle after the fault has cleared as the metal elements have a constant heat as shown in figure 4.3. The kJ/kV value if not properly selected results in the implosion of the surge arrester.

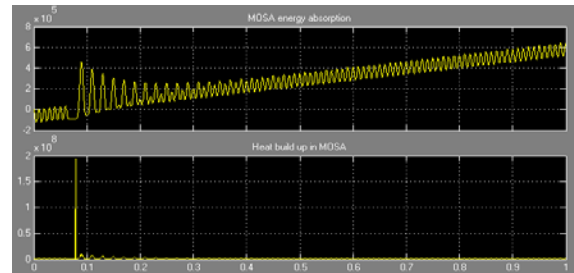


Figure 4.3: The energy absorption in the surge arrester

5. EVALUATION OF RADIAL FEEDERS PERFORMANCE

The failure of MOSAs in radial feeds has a direct impact on the Transmission grid's performance. The impact of the failure is assessed by calculating systems minutes (SM) lost after failure has occurred. This measure is calculated below as:

$$SM = \frac{\text{Load interrupted (MW)} \times \text{Minutes}}{\text{Eskom's annual peak (MW)}} \quad (4.1)$$

The system annual peak is obtained from System's Operator measurements. The 2014 Eskom's system peak is 33722 MW. The duration of the outage is measured in minutes and runs until the network is normalized. The 88kV and 132kV radial feeders in KZN 88 kV and 132 kV are with their associated loads are shown in figure 4.4. Although the distribution network has back feeding capabilities through the use of normal open points and sectionalizers, however some of these networks cannot be backed and therefore any surge arrester (SA) failure poses a load of risk.

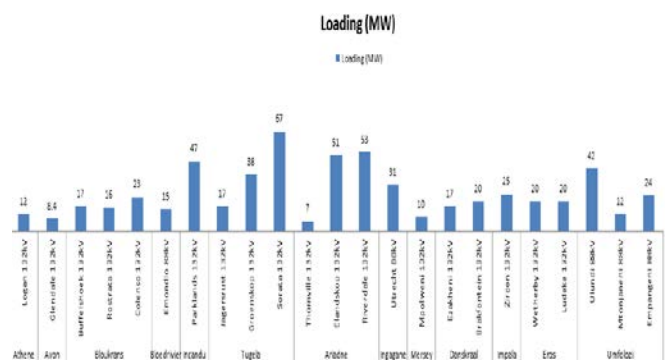


Figure 4.4: Different 88 kV MOSAs makes in KZN traction network

Figure 4.4 shows radial feeders where there is no back feeding capability in the KZN network. The associated loads at risk are also indicated. The ageing of surge arresters at Umfolozi and Bloedrivier substations are shown in figure 4.5.

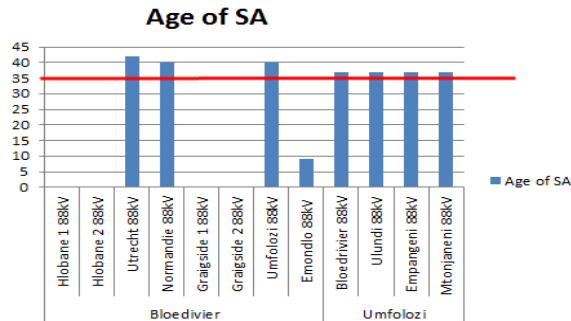


Figure 4.5: Shows the ages of surge arresters installed at these traction stations

The MOSA life expectancy is 35 years. Figure 4.5 shows the MOSA ageing profile for each traction substation feeder. The impact on systems minutes is shown in Figure 4.6 for each main transmission substation.

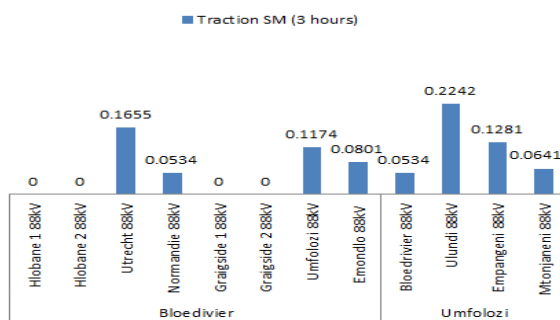


Figure 4.6: The SMs for each main transmission substation

6. CONCLUSIONS AND RECOMMENDATIONS

Based on the above traction simulations and radial feeder performance assessments the following conclusions can be drawn:

- The 88kV surge arrester starts operating at well above the network rated voltage. The surge is always large than the rated voltage and continuous voltage.
- The discharge current is very small as the surge arrester operates.
- The energy absorbed by the surge arrester increases drastically during and after the fault and if the arrester is not properly selected these limits can be exceeded.
- The traction loads are dynamic and generate current harmonics which can result into SA partial discharges and can cause the surge arrester to fail.
- The selection process must be balanced between the operating requirements and the nature of the

network i.e. for traction networks the surge arrester capability must be high.

- The ageing MOSAs installed in radial feeders pose a poor performance risk in the transmission's system performance under N-1 contingencies.

Based on these conclusions the following recommendations are made for traction networks.

- Devise a clear selection guide by ensuring the switching and system overvoltages do not exceed the clamping capabilities of the MOSAs.
- The energy handling capability must be higher for traction load applications.
- The current and voltage harmonics must be monitored as they generate more heat and can lead to surge arrester implosion in particular during the switching of the network after a fault.
- The distribution class 2 up to 4 class arresters must be used for traction load applications.
- It is recommended that 20kA station class surge arresters be used for traction networks.
- It is further recommended that surge arrester care plan be devised with more emphasis on PD tests, tan delta testing, detailed inspection and regular maintenance of the surge arrester housing especially in areas where there is industrial activities and coastal areas. Radial feeders must be give high priority as any failure results in system minutes lost.

7. ACKNOWLEDGEMENTS

Many thanks to Chris Van der Merwe, Eskom corporate specialist for gladly answering my many questions, Siemens, ABB and Cooper personnel for providing manuals and reading materials. The KZN Transmission management team for financial support during this research. My gratitude also goes to my friend Dovhani Mudau for his assistance with the simulation packages.

8. REFERENCES

- [1] Siemens, ABB and Cooper public manuals.
- [2] VK Mehta, R Mehta, "principles of power systems", 2004.
- [3] Kai Steinfeld, "Design of Metal-Oxide Surge Arresters with Polymeric Housings" Siemens AG, Berlin, Germany, 2001.
- [4] Hobbel power systems brochure, "Graphical representation in the selection of surge arresters".
- [5] Li et al, "Study on power systems transient stability considering traction power supply system measurement-based load model", International Conference on Advanced Power System Automation and Protection, 2011.
- [6] Simulink surge arrester demo, Mathworks, Inc, 2009.

INVESTIGATION INTO THE FLASHOVER MECHANISM ON MOUNTING ARMS OF 22 kV SURGE ARRESTERS

B. Singh*, M.F. Khan* and A.G. Swanson**

* Eskom Holdings (Pty) Ltd, 25 Valley View Road, New Germany, 3610, South Africa

** Discipline of Electrical, Electronic and Computer Engineering, University of KwaZulu-Natal, King George V Ave, Durban, 4041, South Africa

Abstract: Distribution class surge arresters are used to protect 11 kV and 22 kV pole mounted transformers and re-closers against lightning surges and switching over-voltages. This study is based on the failure of fibre reinforced plastic mounting arms on surge arresters following concerns raised by field staff. The associated impact of the mounting arm failures are related to network performance and to the equipment the SA's are used to protect (transformers and reclosers). This paper serves to evaluate the possible causes of the failures on the mounting arms. Presented, herewith, are the technical findings from visual inspections and tests conducted which show that the failures are related to over voltage exposure which is dependent on the mode of failure of the surge arrester.

Key words: Surge Arrester (SA), Ground Lead Disconnect (GLD), Basic Insulation Level (BIL), Maximum Continuous Operating Voltage (MCOV), Metal Oxide Varistor (MOV).

1. INTRODUCTION

Surge arresters are semiconductor devices, which are used in electrical power systems in order to protect them against lightning and switching over-voltages. Arresters are installed between phase and earth and act as bypass for the overvoltage impulse, since they are designed to be insulators for nominal operating voltage, conducting at mill amperes of current and good conductors when the voltage of the line exceeds design specifications to pass the energy of the overvoltage wave to the ground. [1]

Constructively, Metal Oxide surge arresters have a simple structure, comprising one or more columns of cylindrical block varistors. An MOV arrester will let through only the current impulse caused by the overvoltage and does not have power-frequency follow current. [2]

The majority of Eskom's medium voltage distribution networks operate at 11 kV and 22 kV and comprise bare overhead lines in harsh environmental conditions. The protection devices available for minimizing risk of damage to transformers are surge arresters which are mounted directly onto the transformer tanks by means of a mounting arm.

A Ground Lead Disconnect (GLD) is applied from the base of the SA, across the mounting arm to the transformer tank providing a path to earth. The GLD is designed to disconnect from the base of the SA (via the operation of an explosion mechanism) when the SA MOV blocks fail. The GLD tail then falls into an open position thus providing a visual indication of the failure for field staff.

The mounting arms of the SA are made of various types of Fiberglass Reinforced Plastic (FRP), depending on the manufacturing process. These mounting arms exhibit a mode of failure whereby the FRP material on the brackets exhibit high temperature burning and resultant damage to

the FRP material. The aim of the investigation was to confirm the root causes leading to the flashover across the mounting arms.



Figure 1: Example of a mounting arm flashover

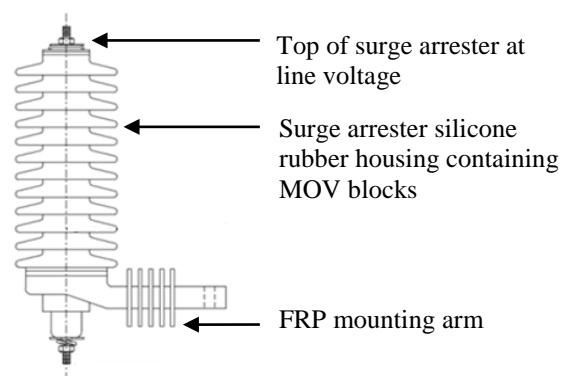


Figure 2: Dimensions of SA

2. POTENTIAL IMPACT

The associated impact of the mounting arm failures are related to network performance and to the equipment the SA's are used to protect. There lies the possibility that the sustained arcing across the mounting arm bracket could lead to the re-closer or network breaker to LOCKOUT; this is dependent on the location of the fault. Potential

lockouts could have a significant impact on SAIDI/SAIFI indicators. The flashover across the surge arrester's mounting arm bracket could terminate on the earthed tank of the recloser or transformer and result in premature failure of the recloser or transformer.

3. SURGE ARRESTER MOUNTING ARM

The mounting arm used on the SA's on Eskom's infrastructure is specified by Eskom with type tests & routine tests conducted by the SA manufacturers. The Eskom Specification of MV SA's indicates the following with regards to the mounting arm:

- I. Arresters shall be supplied with an insulated mounting arm for direct attachment onto the arrester mounting bracket provided on auxiliary equipment.
- II. The insulated mounting arm shall have a mounting hole of 14 mm diameter and a minimum length of 130 mm, but less than 200mm.
- III. The mounting arm shall be supplied with a M12 mounting bolt, nut, serrated washer and three flat washers. The M12 mounting bolt shall have a minimum length of 50 mm.
- IV. The mounting arm shall be insulated to ensure that the arrester shall pass a wet power frequency withstand test as specified in IEC60099-4. [3]

The mounting arm is not specified electrically in terms of following:

- i) Dry arcing distance
- ii) Specific creepage
- iii) Insulating material

This has led to a variety of mounting arm designs across the three approved manufacturers. The table below shows the lengths of the mounting arms for each manufacturer.

Table 1: Varying lengths of mounting arms

Manufacturer	Bracket Length
A	138 mm
B	145 mm
C	195 mm

4. METHODOLOGY

The methodology used to undertake the investigation into the mounting arm failures was:

- Identify possible common modes via visual inspections of the SA's and associated mounting arms, noting for design variable across the various manufacturers that could possibly play a role.
- Evaluate the adherence to International Standards for the mounting arm design and operation.

- Identify and execute further testing to identify possible modes of failure.
- Determine root cause of failures
- Identify possible mitigation measures that can be implemented to prevent future occurrences.

5. VISUAL INSPECTIONS

Visual inspections were performed on a sample of surge arresters which depicted the flashover process across the mounting arm. The results of the inspection showed the following:

- All units were found to have SA's that were failed (i.e. the MOV blocks were no longer able to provide an open circuit condition).
- All units showed housings of the MOV blocks which had been catastrophically blown open.

Two out of the three approved manufacturers showed more visible signs of the damage on the mounting arms. This led to a suspicion that the varying design considerations by the three manufacturers may play a role in the failure mechanism.

6. SPECIFICATION EVALUATION

The damage on the surge arrester mounting arm was found only on devices that have failed. Samples of the failed devices were obtained and tested for a wet power frequency withstand test as per IEC60099-4. The figure below illustrates the test setup used to test the mounting arms.

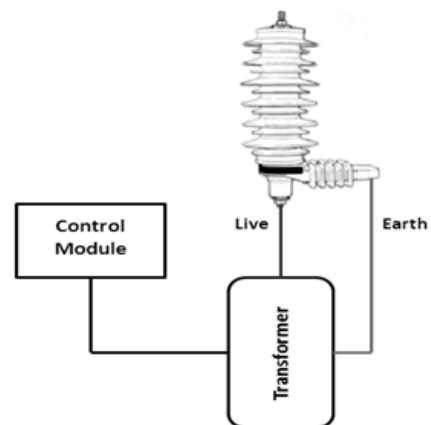


Figure 3: Test set up for wet power frequency withstand

The specification for the surge arrester states the following:

- The insulated mounting arm bracket must "Pass a wet power frequency withstand test"
- According to IEC 60060-1 (which is referenced by IEC 60099-4), the device must be subjected to a 10s power frequency wet withstand of $1.5 \times \text{MCOV}$; applied between the earth terminal and the mounting bolt.

The mounting arm bracket was tested at 1.5xMCOV for both dry and wet conditions for a duration 10s, in accordance with the specification. A total of 20 mounting arm brackets were tested under the conditions stated and all devices passed the tests.

7. FURTHER TEST PROCEDURES

Further tests were conducted to determine the voltage exposure of the mounting arm when the SA fails as well as the effect of this exposure in terms of leakage current across the mounting arm. Two tests were done on the surge arresters which included the mounting arm voltage exposure test & the exposed voltage vs. leakage current test. The tests were conducted on failed surge arresters for all three manufacturer samples.

1. Voltage Exposure of the mounting arm

This test was done to determine the voltage that the mounting arm is subjected to when the SA fails. Samples of failed surge arresters were tested for each manufacturer. The test was used to determine the voltage drop on the MOV's of the failed surge arrester when exposed to full line voltage.

Test Procedure:

- Apply full line voltage at point A on the figure below.
- The exposed voltage of the mounting arm shall be measured at point C.

The measured voltage at point C was applied on the mounting arm of the surge arresters for the next test to determine the leakage current for varying environmental conditions.

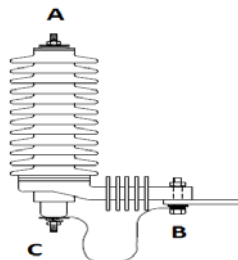


Figure 4: Test set-up

2. Exposed voltage vs. leakage current test

The purpose of the test was to determine the voltage withstand capabilities of the surge arrester mounting arms, by measuring the leakage current across the mounting arm. The test was done on the same sample of failed surge arresters as the previous test.

Test Procedure:

- Apply the voltage obtained from test 1 on the surge arrester bracket at point C of the surge arrester in the figure above.
- Measure the maximum leakage current between point C and B.

8. TEST RESULTS

Table 2: Results for the voltage exposure test

Manufacturer	Applied Voltage	Measured Voltage	Condition of SA housing
C	22	7.50	No visual signs of failure
B	22	21.70	Housing punctured
C	22	7.50	No visual signs of failure
A	22	21.20	Housing punctured
C	22	6.80	No visual signs of failure
B	22	6.40	No visual signs of failure
B	22	21.40	Housing punctured
C	22	6.8	No visual signs of failure
A	22	19.9	Housing punctured
A	22	21.7	Housing punctured
C	22	21.7	Housing punctured
B	22	21.8	Housing punctured
A	22	21.9	Housing punctured

Table 3: Results for the voltage vs. leakage current test

Manufacturer A		Manufacturer B		Manufacturer C	
Voltage (kV)	Current (μ A)	Voltage (kV)	Current (μ A)	Voltage (kV)	Current (μ A)
5	6.8	5	5.8	5	5.8
10	14.3	10	13.5	10	11.2
15	21	15	20.5	15	15.3
20	28.7	20	28.1	20	20.1
22	31.6	22	31.2	22	21.8

Analysis of Tables 2 and 3 as well as Figure 5 shows the following:

When the SA housing completely blows out, the mounting arm is exposed to full line voltage (approximately 22 kV as opposed to the 5 to 10 kV if the housing is not severely damaged). All the mounting arm designs show a similar performance in terms of leakage current when exposed to 5 – 10 kV.

The major difference between the mounting arms is when they are exposed to >10kV. The results show that, at

>10kV, manufacturer C (which supplies a longer arm than the other two) performs better.

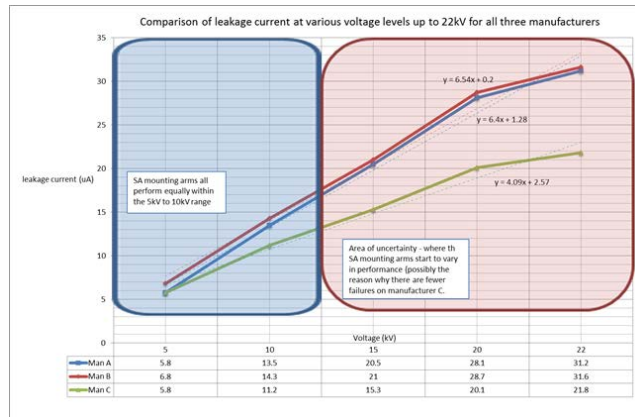


Figure 5: Graph of voltage exposure vs. leakage current

These results lead one to then question why the SA housings blow out in some instances but not in others. It also leads one to question how dependant the rate of tracking and resultant flashover is on pollution exposure.



Figure 6a: SA where the housing has been punctured



Figure 6b: SA where the housing is intact

Hypotheses to housing damage:

1. Water ingress – there has been previous acknowledgement by certain SA manufacturers to flaws within the construction process of SA's that has led to the inability of GLD's to operate. Therefore water ingress could be considered a

potential catalyst to the catastrophic failure of SA housing.

An exercise was undertaken at the University of KwaZulu- Natal HV laboratory to confirm if a failure mechanism could be detected that explained why some arrestors failed by merely discharging the GLD whereas others resulted in a sustained arc that damaged the silicone housing.

A sample of failed devices (for all three manufacturers) which depicted the housing damage was stripped and inspected. The results showed that none of the SA's inspected indicated signs of water ingress which could have resulted in the housing damage.

2. High lightning peak current values – a SA is required a lightning surge that is far above its 10kA rating, resulting in massive damage to the MOV blocks & the SA housing.

The sensitivity of the mounting arm flashovers to discrepancies in lightning peak surge current requires further investigation.

3. Poor earthing profiles on the network – SA's are being stressed at varied rates due to the varied earth profiles at the different transformers could be sinking more lightning peak currents thereby leading to the damage on the SA housing.

Earth resistance tests were conducted on networks from Paulpietersburg and Vryheid depots only at transformer installations where previous failures had occurred. Table 4 is a summary of the results obtained from the tests conducted on both networks.

Table 4: Earth resistance test results

Earth Resistance	Installations
$20\Omega \leq R_e \leq 30\Omega$	0
$10\Omega \leq R_e < 20\Omega$	3
$R_e < 10\Omega$	7

The results show that earth resistance of the transformer installations on these networks are less than 30Ω (as per DST 34-185 for separate MV and LV earthing systems). This limit ensures that for a MV line to transformer tank fault:

- a) No dangerous voltages are experienced on the LV neutral
- b) The LV neutral surge arrester energy absorption limits are not exceeded
- c) Sufficient fault current flows to operate the MV earth fault protection.[4]

Transformer installations around the locations of previous failures were not tested to determine if there was a major discrepancy in earth resistance values across the transformers installed. The sensitivity of the mounting

arm flashovers to discrepancies in earth resistance requires further investigation.

9. FURTHER WORK TO BE UNDERTAKEN

1. Salt fog testing to determine the dependency on the mounting arm flashovers to pollution exposure.
2. Lightning simulations to determine the dependency of housing damage to the exposure of varying lightning peak currents.
3. Lightning simulations to determine the dependency of housing damage to the varying resistances of transformer earthing systems.

10. CONCLUSION

Recent field verification has revealed that the potential impact of the mounting arm flashovers is correct. Mounting arm flashovers have recently begun to cause breaker LOCKOUTS along with evidence that has shown arc roots terminating on the tank of protected transformers.

The research is ongoing and the further work to be undertaken will ensure that the root cause of the flashovers as well as the factors that serve as catalysts to the phenomenon is identified. These findings will be used to make revisions to either the existing specification of 11

kV and 22 kV SA's or the current maintenance practices in Eskom Distribution.

11. REFERENCES

- [1] C.A. Spanias, C.A. Christodoulou, I.F. Gonos and I.A. Stathopoulos: "Electric Field Measurements around a Metal Oxide Surge Arrester", *IEEE Conference Publications - High Voltage Engineering and Application (ICHVE)*, 2010 *International Conference*, pp. 278 - 281, October 2010.
- [2] C. A. Christodoulou, F. A. Assimakopoulou, I. F. Gonos and I. A. Stathopoulos: "Simulation of Metal Oxide Surge Arresters Behavior", *IEEE Conference Publications - Power Electronics Specialists Conference*, 2008. *PESC 2008*, pp. 1862 - 1866, October 2010.
- [3] F. Witbooi, K. Kleinhans, R. Cormack: "Distribution Class Metal Oxide Surge Arresters without Spark Gaps Specification", *Eskom Engineering Specification*, pp. 4, May 2014.
- [4] T. Nkwambule, B. McLaren, V. Singh and M.N. Bailey: "Distribution Standard: Part 2: Earthing. Section 1: MV and LV Distribution System Earthing", *Eskom Engineering Standard*, pp. 9, June 2010.

A Study of the Distribution of Voltage and Electric Field on Glass Insulators using Charge Simulation Method

G. Ininahazwe*, and I. E. Davidson¹

Eskom Centre of Excellence in HVDC Engineering, University of KwaZulu-Natal, 4000 Durban, South Africa

*Email: 214584545@stu.ukzn.ac.za

Abstract: Outdoor insulators are required and expected to be in good operating state at all times to maintain the integrity of the power network despite the numerous stresses they are exposed to. Different environmental conditions such as wind, pollution, ice, hail, temperature and humidity put a lot of stress on insulators. Amongst the other types of stresses are electrical stress. In this paper, electric field and voltage distributions on a pin-and-cap insulator are measured and calculated numerically using charge simulation method. Results obtained are analysed, compared and discussed.

1 INTRODUCTION

High voltages between two electrodes can be insulated by placing insulating materials between them. The insulation material should have a breakdown strength that is high enough than the electric stress exerted by the voltage between the two electrodes; high voltage pin-and-cap glass insulators are commonly used for high voltage transmission [1]. The mean electric field between the electrodes can be calculated using equation 1.

$$E_{mean} = \frac{V}{d} \quad (1)$$

Where: E_{mean} is the average electric field in V/cm, V is the voltage between the electrodes, and d is the distance in cm between the electrodes. In practical cases, the electric fields are not uniform and this increases the likelihood of corona issues in the system [2]. It is important to study electric field to increase the reliability of a transmission line. The study of electric fields yield poison or Laplace's equations, these are difficult, if not impossible to solve analytically due to the complexity of physical systems. Two main numerical methods are used to calculate electric fields in high voltage systems[3]. These methods are based on difference or integral concepts[4]. The first method is based on difference technique employing Laplace's equation and Poison's equations in the space where the field is to be determined. This is done by dividing the whole space into small meshes[5].

The second approach is to integrate Laplace's or Poison's equation either by employing discrete charges, or by dividing the electrode surface into subsection with

charges. This method is known as charge simulation method [6]. In employing this method, fictitious point, line or ring charges are positioned outside the dielectric. Charge Simulation Method (CSM) is based on the understanding that as a voltage is applied on a conductor, charges appear on the surface of the conductor. These charges produce an electric field outside the conductor and keep the conductor at equipotential [6]. In the dielectric, the charged particles of the molecules get shifted from their neutral state to produce a volume of dipoles, in essence, it is possible to replace this volume of polarization by the charged surface. The magnitudes and positions of these fictitious charges are such that their collective effect satisfy the boundary conditions [4].

2 BASIC PRINCIPLES

Poison's equation gives the electric field in a homogeneous medium.

$$\nabla^2 \phi = -\frac{\rho}{\epsilon} \quad (2)$$

Where ϕ is potential, ρ is space charge and ϵ is permittivity of the medium.

Under normal circumstances in the atmosphere, there is zero charge density since negatively and positively charged particles are equal. Equation (2) reduces to the Laplace equation

$$\nabla^2 \phi = 0 \quad (3)$$

A function is said to be a solution to these equations if it satisfies them and the boundary conditions. The potential function for any charge satisfies Laplace's equation outside their volumes [4]. This implies that by placing fictitious charges outside the space in which the field is to be determined, the overall potential function due to these and the real space charges satisfy the Laplace or Poison equation inside the space.

3 CHARGE SIMULATION METHOD

The first step in applying the Charge Simulation Method (CSM), involves replacing the surface charges on the conductor by n fictitious charges inside the conductor.

Fig. 1 shows a charged conductor at U volts above ground potential. The field is to be determined in the space between the conductor and ground, the space consists of air. Let Q_1, Q_2, \dots, Q_n be fictitious charges within the conductor. Since the ground is at Zero potential, imaginary charges of the opposite polarity are placed below the ground surface. Contour points are placed on the conductor boundary corresponding to each fictitious charge in the conductor. The potential at any given contour point i -th is given by equation 4.

$$U_i = \sum_{j=1}^n p_{ij} Q_j \quad (4)$$

Where P_{ij} is the potential coefficient at the i -th contour point due to a unit point charge at the of Q_j , and can be expressed as

$$P_{ij} = \frac{1}{4\pi\epsilon_0} \left(\frac{1}{r_{ij}^-} - \frac{1}{r_{ij}^+} \right) \quad (5)$$

Where x_i, y_i, z_i are coordinates of the i -th contour point; a_j, b_j, c_j are coordinates of the j -th charge.

$$r_{ij}^- = \sqrt{(x_i - a_j)^2 + (y_i - b_j)^2 + (z_i - c_j)^2} \quad (6)$$

$$r_{ij}^+ = \sqrt{(x_i - a_j)^2 + (y_i - b_j)^2 + (z_i - c_j)^2} \quad (7)$$

ϵ_0 is the dielectric constant of air

The application of equation (4) to the n contour points leads to a system of linear equation for n charges which can be expressed in matrix form as

$$U = [P] \times [Q] \quad (8)$$

Solution of equation (8) gives the fictitious charges. The potential at any point is the aggregated effect of these charges and their image charges. The

potential U and field components E_x, E_y, E_z at any point $P(x,y,z)$ can be obtained by:

$$U = \frac{1}{4\pi\epsilon_0} \sum_{j=1}^n Q_j \left[\frac{1}{r_j^-} - \frac{1}{r_j^+} \right] \quad (9)$$

$$E_x = \frac{1}{4\pi\epsilon_0} \sum_{j=1}^n Q_j \left[\frac{x - a_j}{(r_j^-)^3} - \frac{x - a_j}{(r_j^+)^3} \right] \quad (10)$$

$$E_y = \frac{1}{4\pi\epsilon_0} \sum_{j=1}^n Q_j \left[\frac{y - b_j}{(r_j^-)^3} - \frac{y - b_j}{(r_j^+)^3} \right] \quad (11)$$

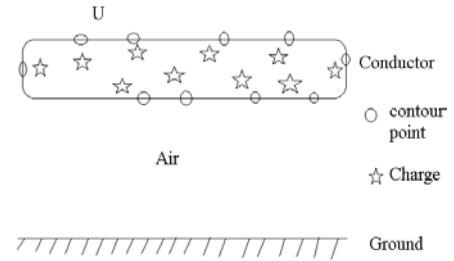


Fig. 1: illustration of CSM

$$E_z = \frac{1}{4\pi\epsilon_0} \sum_{j=1}^n Q_j \left[\frac{z - c_j}{(r_j^-)^3} - \frac{z - c_j}{(r_j^+)^3} \right] \quad (12)$$

4 FIELD ANALYSIS ALONG A GLASS INSULATOR

The method of CSM as described above is applied to a pin – and – cap glass insulator illustrated in fig. 1. The system consists of glass between two electrodes. The cap is connected to ground potential and the pin is connected to 70kV DC voltage. The dielectrics consist of glass and air. The conductor connected to the pin of the insulator is assumed to be of infinite length as compared to the diameter of the insulator. As shown in Fig. 3, most of the voltage appears on the dielectric closest to the pin. The middle part of the glass shares almost levelled voltage.

5 CONCLUSION

As show from the results, CSM can be applied to three dimensional systems to calculate electric stress and voltage at any given point. The method is simple and is developed from basic electrostatic equations. Since the fictitious charges and contour points determine the accuracy of the results obtained, there is a work needed to develop guidelines on their placements.

6 REFERENCES

- [1] Z. Zhijin, J. Xinliang, C. Yafeng, C. Ling, S. Caixin, and H. Jianlin, "Study on DC Pollution Flashover Performance of Various Types of Long String Insulators Under Low Atmospheric Pressure Conditions," *Power Delivery, IEEE Transactions on*, vol. 25, pp. 2132-2142, 2010.
- [2] T. Zhao and M. G. Comber, "Calculation of electric field and potential distribution along nonceramic insulators considering the effects of conductors and transmission towers," *Power Delivery, IEEE Transactions on*, vol. 15, pp. 313-318, 2000.
- [3] A. Ahmed, H. Singer, and P. K. Mukherjee, "A numerical model using surface charges for the calculation of electric fields and leakage currents on polluted insulator surfaces," in *Electrical Insulation and Dielectric Phenomena, 1998. Annual Report. Conference on*, 1998, pp. 116-119 vol. 1.
- [4] P. K. Mukherjee and C. K. Roy, "Computation of Fields in and Around Insulators by Fictitious Point Charges," *Electrical Insulation, IEEE Transactions on*, vol. EI-13, pp. 24-31, 1978.
- [5] K. Yamazawa and H. Yamashita, "Calculation of the electric field distribution under the point-plane gap configurations using the FEM," in *Electrical Insulation and Dielectric Phenomena, 1997. IEEE 1997 Annual Report., Conference on*, 1997, pp. 648-651 vol.2.
- [6] H. Singer, H. Steinbigler, and P. Weiss, "A Charge Simulation Method for the Calculation of High Voltage Fields," *Power Apparatus and Systems, IEEE Transactions on*, vol. PAS-93, pp. 1660-1668, 1974.

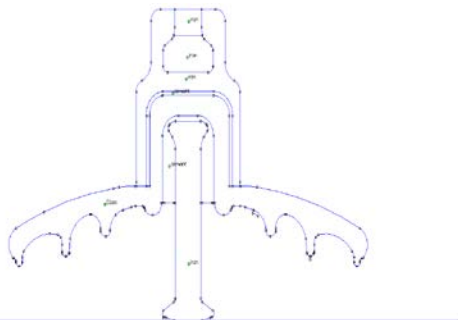


Fig. 2: pin-and-cap glass insulator

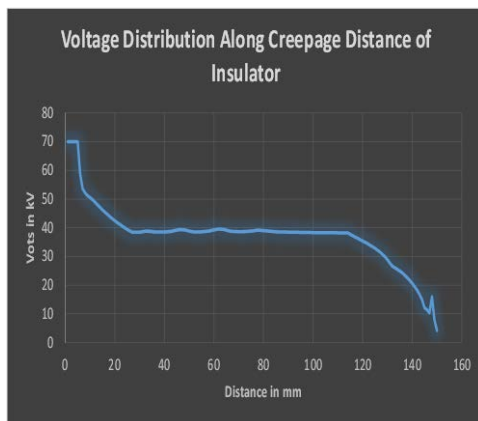


Fig. 3: Voltage distribution

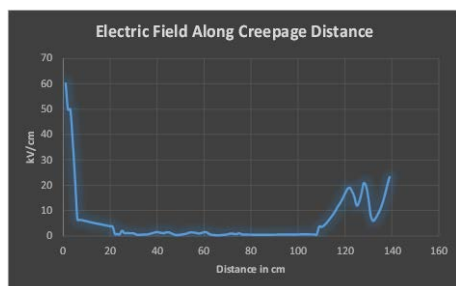


Fig. 4: Electric field distribution

Fig. 4 shows the electric field distribution. The field intensity is very high at the live and dead ends. From the fig. 4, breakdown of the insulation is mostly likely to start at the end fittings and less likely in the middle of the insulator.

DESIGN AND COMPARISON OF RENEWABLE ENERGY STORAGE SYSTEMS FOR EMERGENCY USE ON FARMS IN SOUTH AFRICA

J.C. Campher* and R. Gouws*

* North-West University, School of Electrical, Electronic and Computer Engineering, Potchefstroom, Email: campher93@gmail.com

Abstract: Farmers are experiencing unexpected electrical outages in the Northern provinces of South Africa which can happen for up to six hours. The national electricity utility of South Africa, Eskom, reports that there are irregularities visible on the supply side. Making use of renewable energy storage systems during such an outage would resolve this problem. This project focusses on renewable energy storage systems and illustrates storage systems which can be used in an emergency outage by comparing cost effectiveness between several renewable storage systems. These storage systems use energy from a renewable energy source and store the energy for emergency use. A small-scale model of the proposed system was designed and built for testing and simulation verification; this system is a solar-hydro energy storage system. The prices and effectiveness of a variety of systems are compared to determine the most cost effective system. Simulink® Matlab® was used to simulate the systems and determine effectiveness. PVSyst® was used to simulate some of the solar power designs. Specific systems that were designed were: Solar-Hydro energy storage, Hydro-pumped storage, Solar-battery storage, Hydro-battery storage and Grid-battery storage.

Keywords: renewable energy; energy efficiency; cost effective energy; energy storage system; micro-hydro power design; solar power design.

1. INTRODUCTION

Agriculture is the largest industry in the world, every country have forms of agriculture which contributes to the economy [1]. In modern day farming, the demand for electricity has increased significantly as the use of electricity in the agriculture world grew [2], [3]. South Africa has little renewable energy projects which contribute to primary energy however it struggles to promote renewable energy, because of its high initial capital cost [4]. Renewable energy is suggested because of its enormous potential in South Africa [4]. South Africa also has to look to other forms of energy if it to meet the ever increasing demand [5]. Most renewable energies are suited for off-grid applications and can help make the grid more flexible.

This study focuses on the proposal of introducing renewable energy storage systems to the farming community for emergency use during power outages, which can propose a future development in renewable energy to help make the grid more flexible and help with environmental energy policies. The livelihood of farmers is influenced when they experience an outage. Increasing electricity and fuel cost can threaten the agricultural sector as farmers struggle to keep up with these increased costs. Proposing a cost effective solution to providing renewable electricity to farmers during an emergency would encourage development renewable energies in the agricultural sector of South Africa.

There are several types of renewable energies already available and used in the agricultural world [6]. South Africa still has to evolve its strategy implementing renewable energy projects in the agricultural sector. The most common types of renewable energies found in the agricultural sector are: wind energy, solar energy, hydro energy and biomass [6], [7], however wind energy cannot be used everywhere as in some places wind energy may

be only available momentarily and not continuously as can be seen in the WASA project [8]. Past research has been done on the feasibility of hydro-systems in South Africa [6] but it was not compared to other systems to trade-off which system is more feasible.

2. LITERATURE REVIEW

2.1 Renewable Energy Sources

Solar- and hydro energy is the most feasible for farms in the inland of South Africa. Wind energy is feasible when farms near the coast of South Africa are considered, but only farms in the Northern Central parts of South Africa are experiencing outage problems. Biomass is a high maintenance process and is not available for every farm, making it not suitable for emergency use.

2.1.1 Hydro-Energy System

Hydro-energy is the conversion of potential energy into kinetic energy that turns a turbine which is then mechanical energy and when the turbine turns a generator it is converted to electrical energy [9].

Because of the mechanical energy a hydro system delivers, it has been used for thousands of years in milling, mining, carpentry, etc. [9]. Figure 1 shows a common representation of a pumped hydro energy storage system where water is used to turn a turbine which turns a generator, generating electricity [10].

Some control can be applied by a governor or valve which controls the flow of the water which controls the mechanical power delivered to the turbine. Different hydro energy system sizes are available and are shown in Table 1. In most standalone systems on a farm either a Pico- or a Micro hydro system is used.

Choosing a turbine is important as it affects the price and efficiency of the system. Table 2 shows a trade-off between a typical turbine and a pump-as-turbine as it is important when designing a pumped storage system.

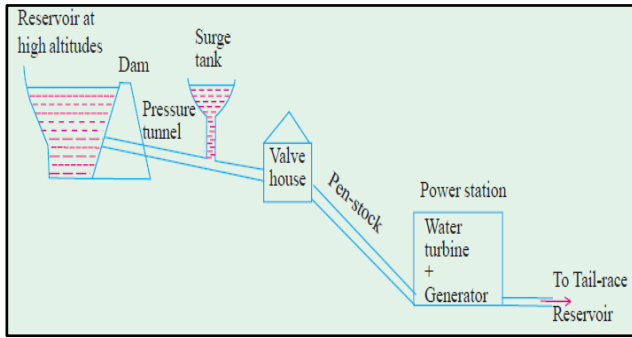


Figure 1: Common Hydro Energy System [10]

Table 1: Hydro System Size [9]

Type	Power Output Capacity (kW)
Pico Hydro	< 5
Micro Hydro	6 to 100
Mini Hydro	101 to 2000
Small Hydro	2001 to 25000
Large Hydro	> 25000

Table 2: Comparison between Turbine and PAT [11]

	Turbine	Pump-as-Turbine
Cost	Expensive	Fairly Priced and cost efficient
Efficiency	Good efficiency	Not as good as turbine
Availability	Not widely available	Widely available
Maintenance	Expensive to maintain	Easy to maintain
Available technology	Documentation available for flow rate as turbine	Flow rate has to be calculated as pump flow rate and turbine flow rate differ.

The mechanical power of the turbine to the shaft of the generator can be calculated with the following equation:

$$P = Q \times H \times \rho \times g \times \eta \quad [9], [12] \quad (1)$$

Where P is the mechanical power in W, Q the flow rate in l/s, H the head in m, ρ the fluid density in kg/m³, g the gravity $g = 9.81 \text{ m/s}^2$ and η the efficiency of the turbine. To calculate the flow rate of a pump as turbine equation (2) is used:

$$Q_T = \frac{Q_{bep}}{\eta_{max}} \quad [12] \quad (2)$$

$$Q_{bep} = 0.75 Q_{max} \quad [12] \quad (3)$$

Where Q_T is the turbines flow rate, Q_{max} the pumps rated flow rate and η_{max} the pumps efficiency, which is also equal to the turbines efficiency.

2.1.2. Solar Energy System

According to the, Basic Research Needs for Solar Energy Utilization [13], the sun is an abundant clean source of energy. The radiation of the sun deposits 120000 TW of energy on the surface of the earth which is more than the basic need for electricity on the earth even in a scenario where the demand is the highest ever [7], [13].

The global horizontal irradiation is the most important parameter for evaluating solar energy potential and the most basic value for solar simulation according to the GeoModel Solar website [14].

South Africa has a high average of horizontal irradiation especially in the northern central part of South Africa where the annual sum can be as much as 2360 kWh/m^2 . For this project the horizontal irradiation of the Limpopo Province is of importance which ranges from 1640 kWh/m^2 up until 2180 kWh/m^2 . Solar cells are the fundamental building blocks of solar-energy [15]. Photovoltaic Panels consists of solar cells connected in series or parallel depending on the wanted power output of the panel [15]. Solar cells are made of semiconductors which convert the energy from the sun to electrical energy they normally have a small output power that is why they are connected together in a larger panel [15]. Photovoltaic panels deliver a DC power output which means if an AC power is needed the system needs an inverter to invert the DC power to AC power [15]. When a DC appliance needs to be powered from the photovoltaic panel it can be connected directly if the specifications of the appliance is satisfied by the specifications of the panel. When the voltage of the panel is greater than the directly coupled DC appliance a regulator is needed to regulate the voltage to the appliance which has extra costs associated. There are three main types of photovoltaic (PV) technologies [16]. Photovoltaic panels, as discussed above, consists out of Monocrystalline panels, Polycrystalline panels and amorphous panels also called thin film panels [16]. Monocrystalline panels are the first PV panels to exist [16]. These panels are reliable and seem to never wear out [16]. Polycrystalline panel's cells are made from the same crystals as monocrystalline cells [16]. The only difference is where monocrystalline cells where cut from the natural form of the grown crystal, in polycrystalline cells the crystals are melted and casted in a mould to minimize losses of cut-away [16]. For this reason the crystals in the polycrystalline cells has imperfections thus having a lower efficiency and performance [16].

2.2 Control System

The controller and the sensors form the control system which keeps the system running at its optimum. In this specific system, the controller receives inputs such as the water level of the reservoir from the float switches, the temperature of the motor from the temperature sensor attached to the motor, the flow rate of the water to the motor from the flow rate sensor, and power information from voltage sensors and current sensors. There are a variety of controllers available to use with such sensors but a PLC, Arduino or PIC is the most commonly used in such applications [17]. The controller should be able to switch between sources as when an outage is experienced the renewable systems energy needs to be used to deliver power to the farm. It is important that the sensors that are selected should also be compatible with the controller chosen. Figure 2 shows the flow Diagram of how the control system in works.

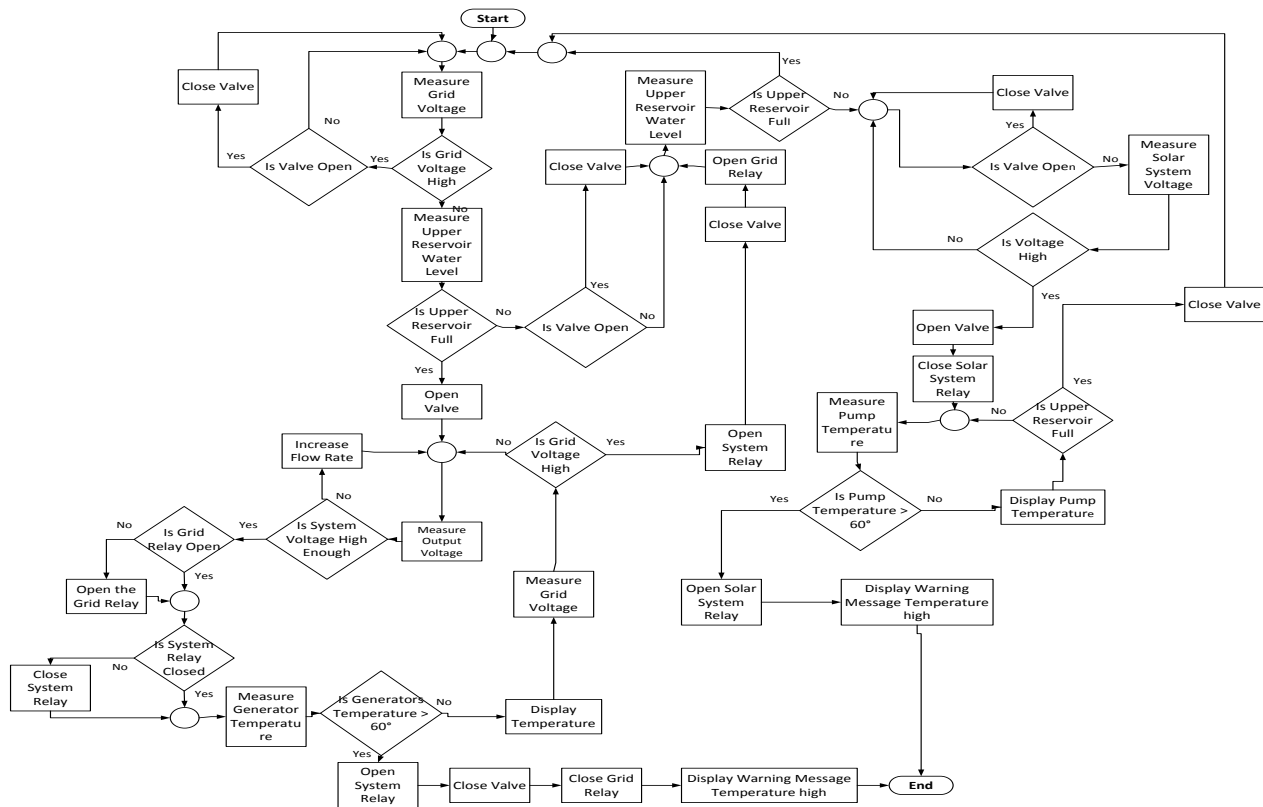


Figure 2: Controller Flow Diagram

2.3 Storage System

The power generated or that needs to be generated has to be stored somewhere. Hydro storage systems and solar-storage systems already exist and can be used to store the energy from energy sources.

2.3.1 Hydro-Power Storage System

Hydro-power is generated by water thus a storage system for hydro-power is a system which is water proof and can hold water for long periods of time. These systems can be dams or reservoirs where high quantities of water can be stored in

2.3.2 Solar-Power Storage System

There are two ways of storing solar power, either in a battery bank or with a Grid Inter-Tie. It is important that storage component has a good life cycle and reliability. The most common way of storing solar-energy is in a battery bank. Depending on the solar system the bank size has to be sufficient enough to store enough energy to satisfy the energy demand [18].

3. DESIGN

There are five design considerations which are simulated to compare the results of each of the designs. These designs are a combination of hydro- and solar energy designs and most of them are on a Pico to Micro level of size. Table 3 shows the power usage of a common household, with the maximum time of six hours as the system is designed to deliver emergency power for a maximum of six hours.

3.1 Micro-Solar-Hydro Energy Storage System

In the micro-solar-hydro energy storage system a pumped hydro storage system is used combined with a solar PV system.

When the farm experience an outage the hydro system is used to generate power for the farm by letting water flow from a upper reservoir to a lower reservoir through a pump which acts as a turbine and generates electricity and when the outage is over and the solar system has power, the power of the solar system is used to pump the upper reservoir full again. For this system either two machines can be used or just one. In the case that two machines are used, the one machine can be used to generate power and the other machine can be used to pump the water back to the upper reservoir, where the machine used to pump the water back can be much smaller than the machine used to generate power, which causes the solar system also to be smaller. In the case of just one machine used, it acts as a pump and a generator. In this case the machine may be large which means a larger solar system is needed. Two designs are done for the hydro system and solar system, one for a system with one machine and one for a system with two machines. Simulink[®] is used to do simulations for the solar-hydro energy storage system and the pumped-hydro energy storage system.

3.1.1. Hydro Storage System Design

A 6 kW system should be used as seen from Table 3. To calculate the needed flow rate of the system to generate the wanted power a few parameters are needed so that equation 1 can be used to calculate the power.

A table with varying head and flow rate are set up with the power of 6 kW, the efficiency of a pump as turbine at 80% and the water density at 1000 kg/m³ using equation (1).

$$6000 = 0.8 \times 1000 \times 9.81 \times H \times Q \quad (4)$$

Table 3: Common Household Energy Needs

Home Applications	#	Approx. Starting Wattage	Approx. Running Wattage	Running Time (Hours)	Total Watt hours
Refrigerator or freezer	1	1200	192	6	1152
Microwave oven: 1000 watts	1	1500	1500	1	1500
Incandescent lights: 100 watts	6	600	600	6	3600
Television Flat screen 46"	1	190	190	6	1140
Coffee maker (4 cup)	1	600	600	1	600
Desktop Computer	1	800	800	6	4800
Computer Monitor	1	30	30	6	180
Printer	1	600	600	1	600
Total		5520	4512	33	13572
Highest Wattage		1500	1500		

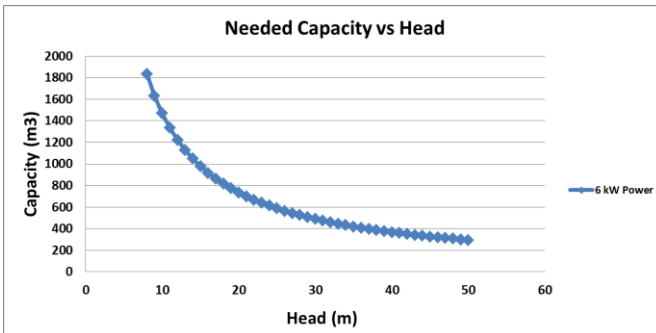


Figure 3: Graph of Head vs. Flow Rate for 6 kW Power Delivered

Figure 3 shows the graph of head vs. flow rate for a 6 kW system. The graph acts as a guide to what flow rate is needed for a certain head to achieve a power of 6 kW. Figure 4 acts as a guide to how much water is needed to run the system at a certain head for 6 hours. With a pump with 0.8 efficiency the motor rating should be at least 7.5 kW. The volume of the reservoir has to be more than 1500 m³ with the head for the scenario at 10 m according to Figure 3 and Figure 4. The flow rate of the 7.5 kW pump with a pump efficiency of 0.8 is 229.18 m³/h which takes 6.81 hours to pump 1500 m³, 51.12 kWh. If the motor is to run at 75% of its rated value, thus 5.63 kW it will be at a rate of 165.14 m³/h and will pump 1500 m³ in 9.08 hours, 51.12 kWh. If autonomy of 4 days is taken with maximum irradiation for 4.5 hours estimated, the maximum pump power needed will be 2.84 kW at a flow rate of 83.33 m³/h, 51.12 kWh. Thus for a two motor system one motor only needs to be 3 kW and the other 7.5 kW.

3.1.2. Solar Energy System Design

Designing a solar system for pumping requires a few parameters. These parameters are estimated for the worst case scenario. Only a pump controller needs to be bought extra when running a dc pump directly from the solar system. For the single machine system an inverter also

has to be bought to switch the dc power of the solar system to ac power the pump needs. The solar array will be rated as if the power loss through the inverter or controller to the pump is 28% thus for a 7.5 kW pump the solar array should be rated at 10 500 W, for a 5.63 kW pump the solar array should be rated at 7 880 W and for a 3 kW pump the solar array should be rated at 4 200 W.

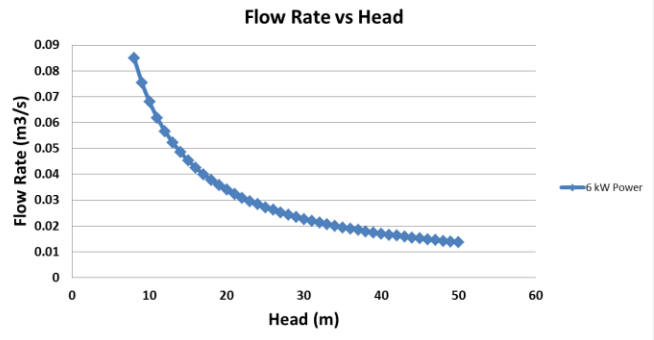


Figure 4: Tank Size for Needed Flow Rate

3.2 Hydro-Pumped Energy Storage System

The hydro-pumped storage system works on exactly the same principle as the solar-hydro-energy storage system, the only difference is that grid power is used to pump back the water to the upper reservoir instead of a solar PV system. The hydro system design is the same as in section 3.1.1., and the power needed for pumping is also the same which is 51.12 kWh.

3.3 Solar-Battery Energy Storage System

In the solar-battery storage system, a solar PV system is used to charge batteries in a battery bank which then delivers energy to the farm during an outage by means of an inverter which inverts the dc power of the batteries to ac power for common household appliances. For this system the following has to be sized: inverter, solar PV array, battery ratings and the charge controller ratings.

3.3.1. Inverter

The inverter should be rated to the most power needed to be delivered which is 5520 W as seen in Table 3. Thus an 6 kW inverter will work, as not all the appliances would be used at the same time.

3.3.2. Solar PV Array

The effective charging hours per day is between 4.5 and 6 hours. The power usage as in Table 3 is 13572 Wh. Thus a safe value would be chosen as 15000 Wh.

By taking the worst case charging hours which are 4.5 hours we can calculate the needed power as follow:

$$\frac{15000}{4.5} = 3333.33 \text{ W} \quad (6)$$

Thus a 4 kW solar array can be used to deliver power.

Figure 5 shows the simulation results done in PVSyst to determine the size of the array needed. Figure 6 and Figure 7 shows the response of a solar array to the change in irradiation and temperature respectively by looking at the change in the solar arrays maximum power point and current.

3.3.3. Battery Bank

For a 48 V system the battery bank rating should be:

$$\frac{15000}{48} = 312.5 \text{ Ah} \quad (7)$$

For a 24 V system the battery bank rating should be:

$$\frac{15000}{24} = 625 \text{ Ah} \quad (8)$$

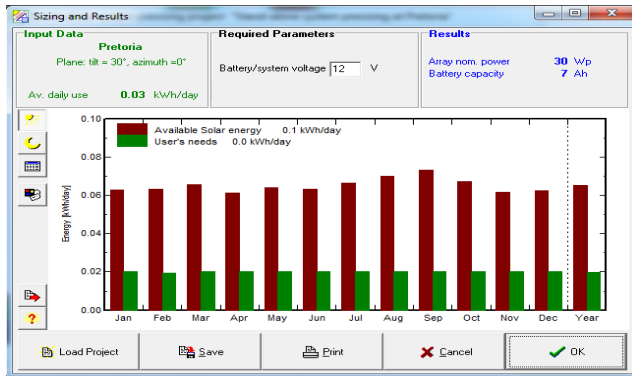


Figure 5: PVSyst Simulation Results

3.3.4. Charge Controller

For a 48 V system the charge controller rating should be:

$$\frac{4000}{48} = 83.3333 \text{ A} \quad (9)$$

For a 24 V system the charge controller rating should be:

$$\frac{4000}{24} = 166.6667 \text{ A} \quad (10)$$

3.4 Hydro-Battery Energy Storage System

The hydro-battery storage system uses a small hydro system which can be in the form of a stream or river, where a turbine and motor can be built in line with the flow of the water. The flow of the water then turns the turbine and motor which generates energy that can be stored in a battery bank for use when an outage occurs. This system can be designed on the same basis as in section 2.3., with a dc motor rating of 4 kW, a battery bank of either 312.5 Ah for a 48 V system or a battery bank of 625 Ah for a 24 V system. In the case that a ac motor is used to generate the power a rectifier can be used to invert the ac power to dc power to charge the batteries.

3.5 Grid-Battery Energy Storage System

The grid-battery storage system is a non-renewable system as it does not include any renewable sources but can be an alternative to fuel combustion generators used for emergency power. The grid-battery storage system is where the energy that the grid delivers, charges a battery bank which stores the energy for emergency use during an outage. The battery bank can be charged at off-peak times when electricity is cheaper and the demand for electricity is low. These system ratings are also calculated on the same basis as in section 2.3., and section 2.4., with a grid power consumption of 15 kWh, a battery bank of either 312.5 Ah for a 48 V system or a battery bank of 625 Ah for a 24 V system.

4. EXPERIMENTAL SYSTEM

A small-scale dc model of the solar-hydro energy storage system was built and tested. This system resulted to have great losses because of its small size. The losses were a result of the low pressure and thermal-dynamic losses caused by mechanical implementations like the piping. This system only used one machine, a 12 V 8 W DC pump. The tests that were done were to show how the system reacts to an increase in head, flow rate and load.

It was found that the power increases linearly with the flow rate and head. The system also has a point where it reaches a maximum power for a certain load. For future reference it will be good to design, build and test a micro-system which can be implemented on a farm.

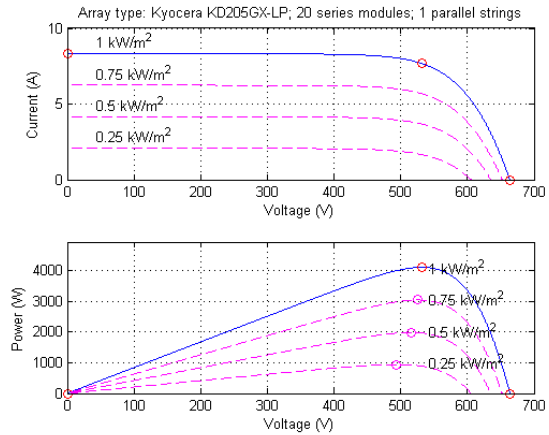


Figure 6: Irradiation Change Response of a 4 kW Solar Array

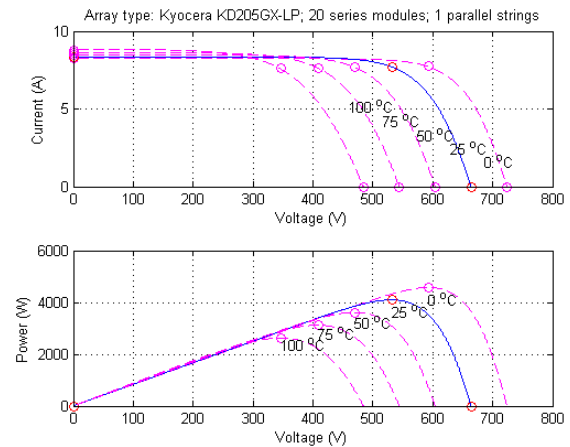


Figure 7: Temperature Change Response of a 4 kW Solar Array

5. DISCUSSION

The price of each system needs to be compared to each other to find the most affordable prices for the system. Table 4 shows the comparison of the initial cost, efficiency, maintenance, upkeep cost and installation cost of each system with reference to each system. In some cases the installation cost may be lower than expected as for instance if a pipeline already exists between two dams and it is sufficient that a motor can be installed in line with the already installed pipeline. The solar-hydro energy storage systems cost can be high if only one motor is used because of the price of solar panels which is needed to power the motor. It is found that the pumped-hydro energy storage systems are more cost efficient but has a monthly electricity cost which has to be paid each month and this can make this system more costly over the years. The solar-battery energy storage systems are found to be the second most cost efficient but the batteries may need to be replaced as batteries only have a certain life span and can make this system also more costly over a few years, as the battery bank is one of the expensive components in the system.

Table 4: Comparison of Different Systems

	Solar-Hydro Energy Storage System	Hydro-Pumped Energy Storage System	Solar-Battery Energy Storage System	Hydro-Battery Energy Storage System	Grid-Battery Energy Storage System
Initial Cost	Mode-rate	Low	Mode-rate	Mode-rate	Low
Efficiency	Mode-rate	Mode-rate	High	Mode-rate	Mode-rate
Maintenance	Mode-rate	Mode-rate	Low	Mode-rate	Low
Upkeep Cost	Low	High	Mode-rate	Low	High
Installation Cost	High	High	Mode-rate	Mode-rate	Low

The efficiency of the hydro systems on a micro scale is between 60% and 90% when using a pump as turbine this efficiency is mainly dependent on the efficiency of the pump. The efficiency of solar panels differ from the solar technology as monocrystalline panels are more efficient than polycrystalline but their efficiency can already range from 79% to 98%. The choice of inverters used for a dc to ac system is very important as low end inverters have efficiencies of 45% to 50% and high end inverters can have efficiencies up to 98%. When giving up price for efficiency the solar-battery energy storage system may have the best efficiency with a high end inverter but its initial price would then be high. A battery is highly efficient with a charge efficiency which is close to a 100% and only very small discharge losses [20]. The solar hydro-energy storage system with two motors can have a very good efficiency as one motor can have a highly efficient turbine connected to it which increases the efficiency, but also increases the initial cost. This can lead to another advantage that when the power is out during daylight time the pump motor can keep pumping as power is generated although it is at a much slower rate it can give somewhat more energy capacity.

6. CONCLUSION

The pumped-hydro energy storage system is found to be the lower cost system with the advantage of having efficiencies of over 70%. One drawback is that it has a monthly cost which may make the system costly over a number of years, depending on the electricity price. An alternative to the pumped-hydro energy storage system, for when a farm does not have two reservoirs but still has a constantly flowing stream or river, can be the hydro-battery storage system. If a farmer has no hydro energy sources available and the solar systems initial cost is too high to afford the grid-battery storage system can make a good alternative to gas generators as the electricity cost per month for generating power can be less than the fuel cost. Every design will differ as not every situation on a farm will be the same. Thus the costs and efficiencies may differ and this should only be a guideline to help focus on the systems which can be implemented but the final system choice relies upon the user, but the same design strategies can be followed to design any system. Some costs can also be cut if the farmer already has some resources which can be used, like a pump or a solar system and the design can be done from the resources available.

7. REFERENCES

- [1] R. B. Matthews, "Electro-Farming, or the Applications of Electricity To Agriculture. Matthews: Electro-Farming, or the Applications of," *I.E.E.J.*, vol. 60, no. 311, pp. 725–741, 1922.
- [2] G. Ordish and G. W. Crawford, "Encyclopædia Britannica," *Encyclopædia Britannica*, 2014. [Online]. Available: <http://global.britannica.com/EBchecked/topic/9647/origins-of-agriculture/10707/Electricity-in-agriculture>. [Accessed: 06-Feb-2015].
- [3] G. Riva, "AGRICULTURE AND AUTONOMOUS POWER SUPPLY," *Agric. Mech. Autom.*, vol. I, pp. 232–250, 2009.
- [4] H. Winkler, "Renewable energy policy in South Africa: policy options for renewable electricity," vol. 33, pp. 27–38, 2005.
- [5] Aurecon South Africa, "Solving South Africa's energy crisis: renewable energy projects offer new hope," *Aurecon*, 2013. [Online]. Available: <http://www.aurecongroup.co.za/en/about/latest-news/2013/jan/solving-south-africa-energy-crisis-renewable-energy-projects-offer-new-hope.aspx>. [Accessed: 14-Sep-2015].
- [6] S. J. van Vuuren, C. L. Blerch, and M. van Dijk, "Modelling the feasibility of retrofitting hydropower to existing South African dams," *Water SA*, vol. 37, no. 5, pp. 679–692, 2011.
- [7] A. Chel and G. Kaushik, "Renewable energy for sustainable agriculture," *Agron. Sustain. Dev.*, vol. 31, no. 1, pp. 91–118, 2011.
- [8] N. G. Mortensen, J. C. Hansen, M. C. Kelly, S. Szewczuk, E. Mabile, and E. Prinsloo, "Wind Atlas for South Africa (WASA) Observational wind atlas for 10 met. stations in Northern, Western and Eastern Cape provinces," *Wind Atlas South Africa*, p. 5, 2012.
- [9] M. T. Gatte and R. A. Kadhim, "Hydro Power," pp. 95–124, 2012.
- [10] Energy Systems, "Introduction to Electrical Energy Generation," *Electr. Technol.*, pp. 855–864, 1914.
- [11] B. H. Teuteberg, "Design of a Pump-As-Turbine Microhydro System for an Abalone Farm," *M. Engineering*, pp. 1–56, 2010.
- [12] A. Williams, *Pumps As Turbines - a Users Guide*. London: Intermediate Technology Publications, 1995.
- [13] N. S. Lewis, G. Crabtree, A. J. Nozik, M. R. Wasielewski, and P. Alivisatos, "Basic Research Needs for Solar Energy Utilization," *Basic Energy Sci. Work. Sol. Energy Util.*, p. 276, 2005.
- [14] 2015 GeoModel Solar, "Solar radiation maps: Global Horizontal Irradiation (GHI)," *SolarGIS © 2015 GeoModel Solar*, 2011. [Online]. Available: <http://solargis.info/doc/71>. [Accessed: 13-Mar-2015].
- [15] R. F. Pantelimon, M. Adam, M. Andrusca, and C. Pancu, "Aspects Regarding Solar Battery Charge Controllers," *8th Int. Symp. Adv. Top. Electr. Eng.*, 2013.
- [16] dako power GO SOLAR, "Three Photovoltaic Technologies: Monocrystalline, Polycrystalline and Thin Film," *dakopower*, 2008. [Online]. Available: http://www.dako.co.za/photovoltaic_types.html. [Accessed: 13-Mar-2015].
- [17] R. N. Deshmukh, P. H. Zope, and S. R. Suralkar, "Generation of Electricity by Renewable Energy Sources & Transmission of Energy Production Units using PLC & SCADA," vol. 1, no. 9, pp. 19–27, 2012.
- [18] T. R. Cook, D. K. Dogutan, S. Y. Reece, Y. Surendranath, T. S. Teets, and D. G. Nocera, "Solar energy supply and storage for the legacy and nonlegacy worlds," *Chem. Rev.*, vol. 110, no. 11, pp. 6474–6502, 2010.
- [19] Energy Matter, "Solar Water Pumping Calculator," *SunEdison Company*. [Online]. Available: <http://www.energymatters.com.au/climate-data/solar-water-pumping-calculator.php>. [Accessed: 01-Sep-2015].
- [20] Cadex Electronics, "BU-104a: Comparing the Battery with other Power Sources," *Battery University*, 2015. [Online]. Available: http://batteryuniversity.com/learn/article/comparing_the_battery_with_other_power_sources. [Accessed: 01-Sep-2015].

MODELLING AND SIMULATION OF GRID-CONNECTED PHOTOVOLTAIC SYSTEMS

N. Mazibuko^{1*}, A.K. Saha²

¹Group Technology & Commercial Engineering, Power, Eskom, 2157 Sunninghill, South Africa.

²School of Electrical, Electronic & Computer Engineering, UKZN, 4041 Durban, South Africa.

*Email: MazibuNu@eskom.co.za

Abstract: This paper presents a comparative study of four methods for extracting solar cell parameters of the 5-p single diode model. The five-parameter model is capable of characterising the electrical behaviors of a photovoltaic module for outdoor operating condition of temperature and solar irradiance. The method to be implemented in PowerFactory DigSilent (PFD) is chosen based on good compromise between simplicity and accuracy. The established model is compared with the generic model (four-parameter model) which replicates the electrical behaviors of PV modules based on some assumptions. Various tests and evaluations will be observed to measure the established PV system accuracy and reliability of results. The developed model is expected to improve the simple generic DigSilent PV model

1 INTRODUCTION

The growing interests in photovoltaic generation systems, prompts studies to develop precise solar cell simulators hence the importance to accurately understand the physical properties of solar cells. However, solar cell models have a non-linear form with numerous parameters [1]. To obtain accurate parameter values, assumptions that differ from real operating conditions must be made to avoid computational complexity. In this paper, methods for extracting parameter values are discussed. Customarily manufacturers typically provide limited operational data for photovoltaic under laboratory conditions (STC) consisting of 1000 W/m² with spectral distribution conforming to 1.5 AM and cell temperature of 25 °C [2]. Thus, PV system studies need a reliable and accurate mathematical model to predict energy production from the PV generation under various irradiance and temperature conditions [3].

2 PV OPERATING PRINCIPLE

The solar cell operating principle is based on the photovoltaic effect [4]. When light is absorbed by matter, photons are given up to excite electrons to higher energy states within the material thus, energy is superior to the bandgap generating electricity, but only the energy corresponding to the bandgap is used. Energies lower than the bandgap of the solar cell are useless and generate no voltage or electric current. The extra energy of the excited electrons generates a potential difference or electron motive force (EMF). This force drives the electrons through a load in the external circuit to do electrical work [4-5].

3 PV ELECTRICAL CHARACTERISTIC

Photovoltaic models can be classified into various types as shown in Fig. 1 & 2 the simplest one being the single diode model shown in Fig. 1 (a). It is described with a single diode which the modified Shockley diode equation is incorporating n-ideality factor to account for the recombination mechanism that occurs in the P-N junction, represented as anti-parallel diode to the current source [4]. The simplicity of this model compromises the accuracy of PV cell especially at maximum point of operation [7]. The evolved model with the added series resistor improves the model accuracy as shown in Fig. 1 (b) but the model accuracy is not adequate for the intended study [8]. Thus, further evolution of the single diode model to a (5-p) model is shown on Fig. 2 (a) described by equation (1), as it is fairly accurate in comparison to experimental data [9].

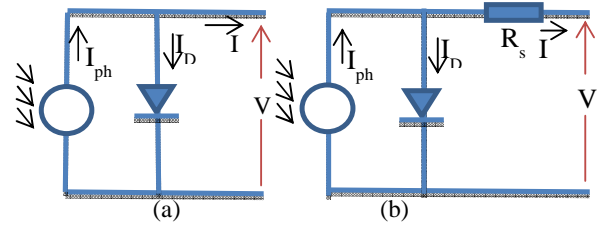


Figure 1: Solar cell: (a) ideal model and (b) 4-p model

$$I = I_{ph} - I_0 \left(e^{\left(\frac{V + IR_s}{nV_t} \right)} - 1 \right) - \frac{V + IR_s}{R_p} \quad (1)$$

3.1 5-p model

The five parameters from which it gets the name are: I_{ph} , I_0 , n , R_s & R_p . From Fig. 2, applying Kirchhoff law yield equation (1) [3-5]. The 5-p model accuracy is fairly precise to measured features with only a small percentage error [12]. It has been noted that the series and parallel resistance influence the characteristics of a PV cell, where the parallel resistance reduces the output current and the series resistance reduces the output voltage of PV cell [4].

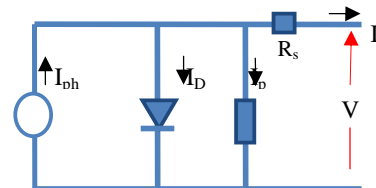


Figure 2: Solar cell: single diode 5-p model

In comparison the single diode model of Fig. 2 exhibit precise results demonstrated by experiments [13] with only one exception where at low voltages and lower irradiance the model tends to be less accurate [11-12]. In this paper the model will be evaluated as a solar module for power source and implemented at large voltages. Thus, 5-p model is adequate for use in this paper.

4 AVAILABLE EXTRACTING METHODS

Many studies have been conducted attempting to solve equation (1). Basically, to calculate the model parameters, analytical and numerical methods can be used. A few methods employed by several authors are discussed as follows:

Numerical methods use powerful mathematical tools and iterative methods to solve the non-linear equations such as of PV cell model. These methods are widely used in engineering as they offer good accuracy [7-8] for the extracting of PV cell parameters. But numerical methods require powerful and dedicated software tool to achieve a solution and most cannot be implement in conventional power system engineering tools. In order to simplify the process, the parameters are extracted by means of analytical methods discussed below implementing systematic solution method to obtain the five parameter model [6] [13-15].

4.1 Car11 extracting method

The proposed method uses a simplified procedure that allows the estimate of the ideality factor and the loss resistances of any PV cell. The method uses the five parameter model and information from the manufacture as input namely the three points on the I-V curve as input (open circuit voltage, short circuit current, maximum power point) which greatly simplifies the data acquisition process. To ensure the convergence of the iterative process the derived equations do not containing exponential terms and, the values that the ideality factor can take is limited in order for the values of the loss resistances to overlap with those presented by the actual PV cell generator, which is not always guaranteed by other methods. The initial conditions are obtain through the developed equations which make the iteration process efficient, at most four iterations give an accuracy at the maximum point that differs by 0.03% from experimental results therefore fast convergence and quite a good accuracy [15].

4.2 Pha84 extracting method

This method derives the analytical expressions to extract solar cell single diode from experimental data or good initial guess. The method evaluates and derives equations from equation (1) to give explicit non-linear equations. The derivations of the analytical expressions include many assumptions therefore neglecting some significant equation terms which influence the accuracy of the model. The validation of the method was done using PV cell

characteristic obtained by developed analytical expressions and compared with the actual values used in generating the characteristic. The differences were expressed in terms of percentage errors and plotted in a grid of R_s and R_{sh} values. The results presented where the 1% and 5% error contours for parameters n , I_s , R_s and R_{sh} are drawn in an R_s - R_{sh} grid. The results showed that the analytical expressions for all four parameters are accurate to within 1% provided R_s is in the range of 1 m Ω to 150 m Ω and R_{sh} is in the range of 30 Ω to 3000 Ω . For 5% errors, the range of validity is even wider, and would include most solar cells. The assumptions incorporated in the derivations of the analytical expressions introduced errors in the final results. But a plus for this method is it does not involve iteration processes therefore rapid convergence [14].

4.3 MAd02 extracting method

The method evaluates a simple analytical method that extracts parameters involved in the photovoltaic module behaviour equation. Based on a series of experimental voltage-intensity curves obtained under various temperature and irradiance conditions, R_{so} and R_{sho} values are obtained to extract the model parameters. The values at data point's short circuit current, open circuit voltage and voltage at maximum power point and in the entire I-V curve yield errors that are less than 1%. The values for series and parallel resistance are initially assumed, which are not given by manufacture specifications. The challenge involved with this method is obtaining a sufficient number of data points that are near the points of intersection with the axes, to obtain the slope, as required for the analytical calculation of the parameters, but this can be overcome by assigning fixed values for series and parallel resistance. If the fixed assigned values are properly selected, the adjustment errors between experimental curves under different temperature and irradiance conditions and the theoretical model become less than 1%. The sensibility of the model to the value of parallel resistance is minor but is particularly sensitive to thermal voltage n value [6].

4.4 Cub13 extracting method

This method presents an analytical method that easily calculates the equivalent circuit parameters from the data that manufacturers usually provide. The analytical approximation is based on a new methodology which uses four boundaries at open circuit voltage, short circuit current and maximum power point at (I_m , V_m) but only four equations can be derived from four boundaries and these are not enough for five unknowns therefore the fifth parameter has to be estimated and in this method the ideality factor is estimated according to [13] ranging from 1-1.5 for a single junction solar cell. The method is simple, non-iterative and straightforward. The accuracy of the results compared with experimental results is less than 1% in terms of current around the maximum power point. However the *RMSE* (root-mean-square difference) to the experimental results is computed to improving the fitting of the I-V curve and accuracy [13].

5 VALIDATION OF MODEL RESULTS

The data of solar panel from a typical manufacture datasheet is shown on Table 1 [9] and the results obtained after implementing the different methods are shown on Table 2. All the methods have agreed closely with each other. The different is the computation time, degree of complexity and assumptions to create boundaries. From the chosen methods used in the paper one has the advantage of not having to assume any initial values, thus, it is fast and simple to implement and also has good accuracy. The other methods have the shortfall that they require an initial value to be assumed indicated by asterisk “*” on Table 2 which leads to further iterations to improve the assumed value.

Table 1: KC200GT solar array at 25°C, 1.5 AM, 1000W/m²

Characteristics	Value
Open-Circuit Voltage (V_{oc})	32.9 V
Voltage at maximum power point (V_m)	26.3 V
Short-Circuit Current (I_{sc})	8.21 A
Current at maximum power point (I_m)	7.61 A
Maximum Power at STC (P_m)	200.1 W
Number of cells connected in series	54
Temperature coefficient of I_{sc} (alpha)	3.2 mA/C
Temperature coefficient of V_{oc} (beta)	-123 mV/C

Table 2: Extracted parameters using different methods

Method	I_{ph}	I_0	n	R_s	R_{sh}
[Car11]	8.25	1.65E-14	0.702	0.454	90.88
[Cub13]	8.23	3.22E-09	1.1*	0.126	44.29
[MA02]	8.25	2.97E-13	0.767	0.414*	90*
[Pha84]	8.26	9.95E-20	0.662	0.459	90

The simulation results of the different models were compared under different solar radiation levels. Fig. 3 presents the I-V curves and the P-V curves respectively for solar radiation of 600W/m² & 1000W/m² when the cell temperature is 25 °C. It can be seen that only a slight difference between the models is in the knee of the curves, which may result from the ideality factor being less than one for Car11 and greater than one for Cub13. Other curves agree well. The results illustrate the methods agree well and validates the model to be used for PV simulation performance prediction.

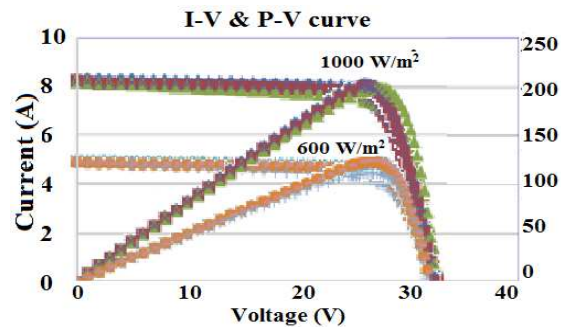


Figure 3: I-V & P-V [used],[1],[2]&[3]: 600 & 1000 W/m²

6 PFD PHOTOVOLTAIC MODELLING

The modelling method [Car11] is implemented in PFD aided by the DigSilent Simulation Language (DSL) function available to perform dynamic modelling. The DSL functions allow creation, initialization and testing of dynamic models for use in time-domain power systems simulations [18, 19]. The PV model in PFD can be represented in two configurations either in static generator or PWM converter. The static generator configuration is the generic model in PFD as shown in Fig. 4 (a) and for the PWM converter interfacing it is shown in Fig. 4 (b). The PV array is represented with a constant current source connected to a DC busbar in parallel with DC link capacitor and the PV system as a whole is represented in the control frame modelled using DSL codes.

The developed PV system (PWM converter) rules out some assumptions of the PFD model (static generator) by improving the modelling using referenced scientific modelling equations thereby, improving prediction accuracy of the PV cell power output behavior due to (Temperature & irradiance). The developed model will incorporate two MPPT methods Perturb & Observation and Incremental Conductance not discussed here.

The developed PV frame: The control schematic for the developed PV system is shown in Fig. 6. Calculation and measurement block is showing the PV array block with temperature, radiation and voltage as inputs modelled using DSL function and the measuring blocks. Controller block is fed by PV array block and processes the inputs to the inverter block as shown.

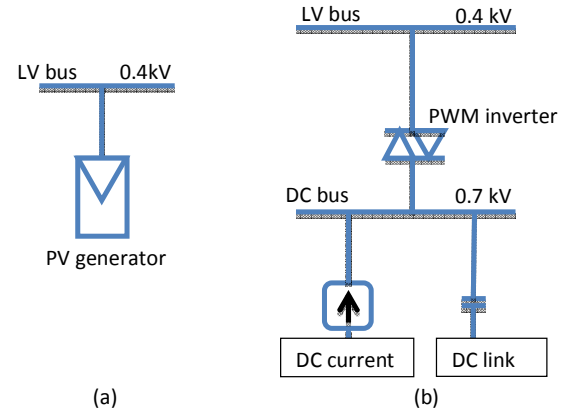


Figure 4: PV model (a) static generator, (b) PWM converter

6.1 Developed model

The calculation & measurements measures the DC voltage from the dc bus, irradiance and temperature, grid side voltage & frequency. After processing output array current I_{pv} and voltage V_{pv} are fed to the MPPT to generate the dc-voltage V_{mp} used for tracking the mpp. The phase locked-loop (PLL) generates a signal synchronized in phase to the grid-side voltage to provide the reference phase angle θ used for the abc to dq transformation. [16] [17].

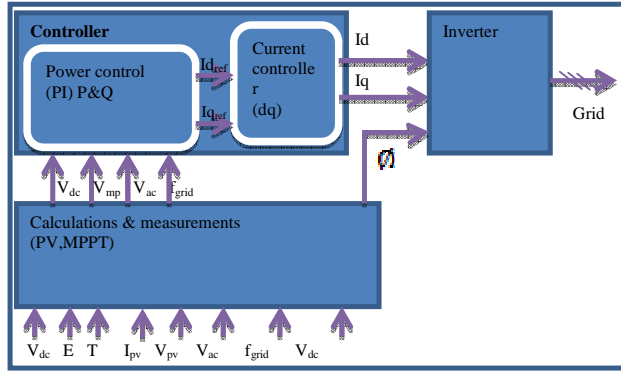


Figure 5: Overview of PV control

The generated V_{mp} is compared to the actual value V_{dc} and the error between the two values is processed as I_d through a PI controller. The measured and set point grid voltage at the POC is also compared and similarly the error is processed into I_q and passed through a droop to obtain the relative required reactive power. The d-axis current reference is limited to the range between [0:1] to protect the inverter from excessive heating and reverse current flow through the PV array. The q-axis have reference limits [-1:1] to allow absorption and producing reactive power and the limits may be set by considering the q-axis current ability range and the inverter thermal rating [17] shown in Fig. 6.

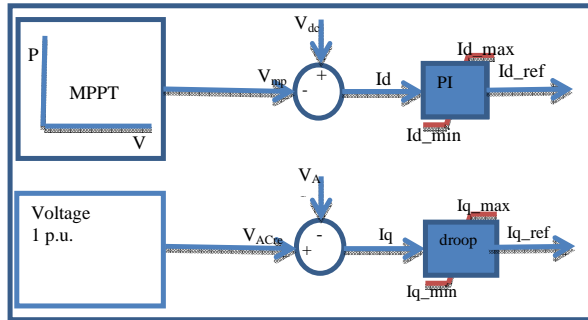


Figure 6: Power control block

6.2 Model analysis and case studies

Since the generic model in PFD gives basic understanding of the working principle of the PV, a comparison between the generic and the developed model through case studies will validate the developed model. Fig. 7 shows the PV (0.5 MVA) connected to the LV bus (0.4 kV), transformer (0.4/22 kV) rated 0.5 MVA with the inverter rating (0.9pf 0.5 MVA). The transmission lines with distance 5 km.

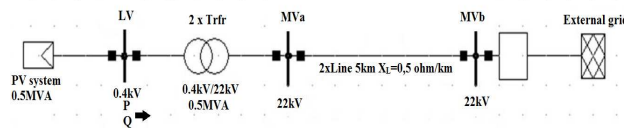


Figure 7: single line diagram of power system

Table 3: Comparison of PV system functions

Developed PV model in PF	Generic PV model in PF
Referenced scientific equations used for modelling	Undefined equations of the model
five parameter model	four parameter model (no shunt resistance)
MPPT block	No MPPT control

Table 4: PV system parameters at STC

PV module Parameters	
Short circuit current	5 A
Open circuit voltage	43.8 V
Current at MPP	4.58 A
Voltage at MPP	35 V
K_i	0.0004
K_v	-0.0039
No. of series modules	20
No. of parallel modules	140

PV response due to weather conditions (Irradiance change): The irradiance input is changed from 1000W/m² to 500W/m² and back to 1000W/m². The graph results are shown below for: DC voltage (U_{array}), DC current (i_{0dc}), Active power and AC voltage at LV bus and explained.

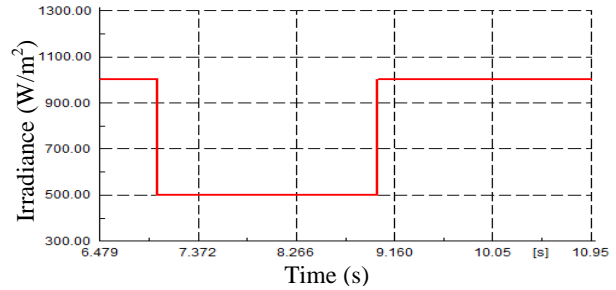
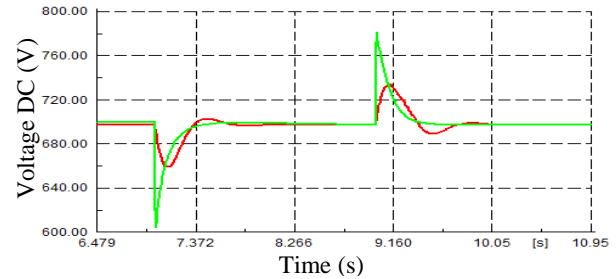

Figure 8: Input irradiance change (W/m²)


Figure 9: DC voltage (V)

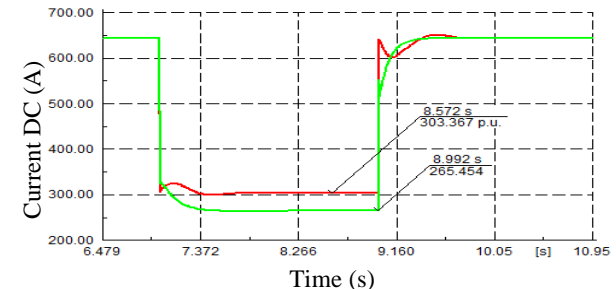


Figure 10: DC current (A)

Fig. 9 shows the DC voltage change due to change in irradiance from Fig. 8. The response in comparison show similar results from both models the green graph being a model from PFD and the red is the developed PV.

Fig. 10 shows the DC current response of the two models and in comparison a slight different is seen in the dynamic behavior due to the different in modelling method and mathematical equations used. From [4] & [7] indicated through equation (1) that the current output is directly proportional with irradiance hence at 500 W/m^2 DC current is expected to be half and the developed model gives a prediction close to expected $140 \times 4.58 \text{ A} / 2 = 320.6 \text{ A}$, the losses can be accounted by the leakage losses in the solar cell.

Fig. 11 shows the active power response is similar with a slight different in the dynamic behavior for the developed model having an overshoot at the changes. The prediction of the power generated once irradiance change is different by a margin of about $\Delta P_{pv} = 0.026 \text{ MW}$. This can be accounted for the extra control of MPPT included for the developed model to track mpp. The PV array response noted above is very instant at point of 1000 to 500 W/m^2 the PV array vertically moves down, whereas the inverter reaction is delayed by its controller delay. Thus, generic controller is faster than developed controller concluding the overshoot response of developed model also seen from author [17] & [20].

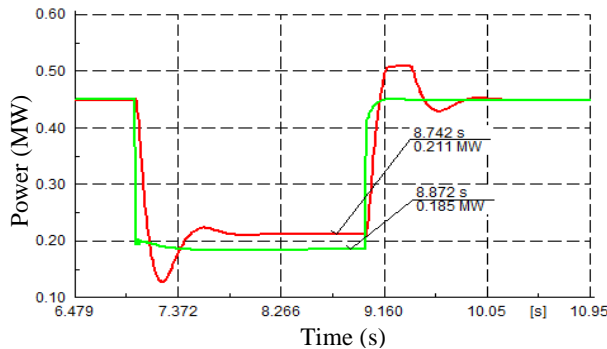


Figure 11: AC power of PV in (MW)

PV response due three phase fault (Fault applied at the grid connection): A three phase short circuit is applied to the point of connection (MVA busbar). Under abnormal conditions both models will be observed to see similarities in behavior. The fault will last for 1s which is extreme as the typical maximum fault duration is around 150ms [21].

Fig. 12 shows the DC voltage response for both models and the behavior is similar but for the developed model the voltage during a fault reaches the rated open circuit voltage $43.8 \text{ V} \times 20 = 876 \text{ V}$ of the array and it transients just after the fault is cleared and settles on the new higher value [22]. The rise in voltage is due to the active power from PV array being dumped in the capacitor. Fig. 13 the DC current decreases for both models but the generic model decreases sharply than developed model and the

delay is assumed to be caused by PV inverter controller and some transients can be seen after fault is cleared. Fig. 14 shows the active power and both models decrease to zero and as soon as the fault is cleared returns to the initial values.. Even though the AC side faults current increases (not shown) but the drop on the voltage at the point of connection side outweighs resulting to the output power drop [22].

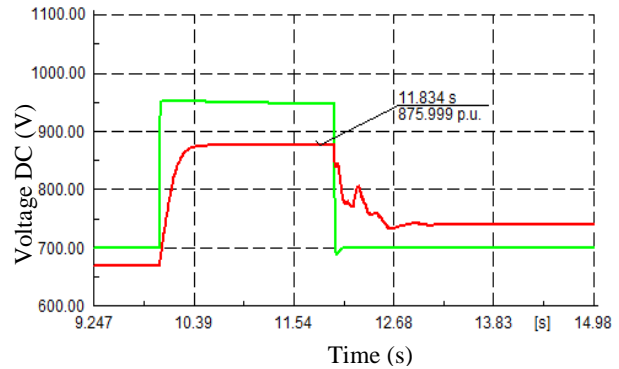


Figure 12: DC voltage (V)

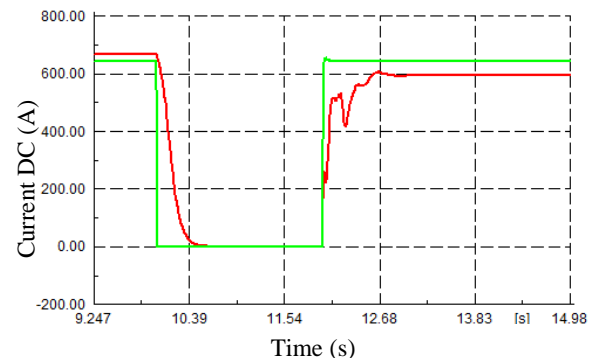


Figure 13: DC current (A)

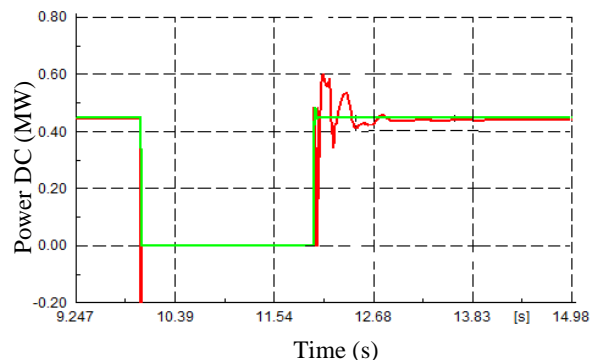


Figure 14: Active power (MW)

Fig. 15 show reactive power and the response is similar for both models and some transients are seen for the developed model, the reactive control reacts to keep up the oscillating voltage and to help the system network to stabilize by the reactive power injection during a fault.

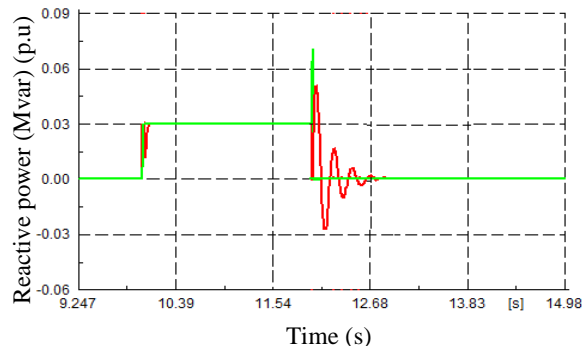


Figure 15 : Reactive power (MVar)

PV simulation results of developed and PF model are consistent with each other. The observed fluctuations can be due to reactive power injected algorithm and inverter control characteristics

7 DISCUSSION AND CONCLUSION

The employed five-parameter model solved using analytical method in simple and rapid manner. The validation of the model was done by comparing results produced by other methods Cub13, MAd02, Pha84. The results showed that the chosen model Car11 can accurately simulate the entire I-V characteristic curves. The detailed mathematical model was then implemented in simulation tool PFD incorporated with control scheme for the grid-connected PV system. Since the proposed model of the PV array uses theoretical and empirical equations together with data provided by the manufacturer and atmospheric data enhances the accuracy of predicting the PV cell characteristic curve. The controls established for dynamic active power and reactive power also included the MPPT algorithm. The results demonstrate the validation of the proposed model and the effectiveness of the model control. Therefore, from the results obtained it can be concluded that the developed model in comparison with PFD model is similar and the observed differences are due to the differences in PV modelling method. These similarities verify the developed model.

8 REFERENCE

- [1] W. D. Soto, S. Klein and W. Beckman, "Improvement and validation of a model for photovoltaic array performance," *Solar energy*, vol. 80, pp. 78-88, 2006.
- [2] G. M. Masters, *Renewable and Efficient electric power systems*, New Jersey: John Wiley & Sons, 2004.
- [3] R. A. Messenger and J. Ventre, *Photovoltaic Systems engineering*, Florida: CRC Press LLC, 2003.
- [4] V. Quaschnig, *Understanding Renewable Energy Systems*, UK and USA: Earthscan, 2005.
- [5] K. Ishaque, Z. Salam and H. Taheri, "Simple, fast and accurate two diode model for photovoltaic modules," *Solar energy materials & solar cells*, vol. 95, pp. 586-594, 2011.
- [6] M. d. Blas, J. Torres, E. Prieto and A. Garcia, "Selecting a suitable model for characterizing photovoltaic devices," *Renewable energy*, vol. 25, pp. 371-380, 2002.
- [7] J. Hernandez, G. Gordillo and W. Vallejo, "Predicting the

behaviour of a grid-connected photovoltaic system from measurements of solar radiation and ambient temperature," *Applied energy*, vol. 104, pp. 627-537, 2013.

- [8] T. Ma, H. Yang and L. Lu, "Solar photovoltaic system modeling and performance prediction," *Renewable and sustainable energy reviews*, vol. 36, pp. 304-315, 2014.
- [9] *KC200GT high efficiency multicrystal photovoltaic*.
- [10] S. Kim, J. Jeon, C. Cho, E. Kim and J. Ahn, "Modelling and simulation of a grid-connected PV generation system for electromagnetic transient analysis," *Solar energy*, vol. 83, pp. 664-678, 2009.
- [11] K. Manohar and P. Rani, "Mppt and simulation for a grid-connected photovoltaic system and fault analysis," *The international journal of engineering and science*, vol. 1, no. 2, pp. 158-166, 2012.
- [12] A. Yazdani and P. Dash, "A control methodology and characterization of dynamics for a photovoltaic (PV) system interfaced with a distribution network," *power delivery*, vol. 24, no. 3, pp. 1538-1551, 2009.
- [13] Y. Xu, X. Kong, Y. Zeng and X. Xiao, "A modeling method for photovoltaic cells using explicit equations and optimization algorithm," *Electrical power and energy systems*, vol. 59, pp. 23-28, 2014.
- [14] J. Phang, D. Chan and J. Philips, "Accurate analytical method for the extraction of solar cell model parameters," *Electronics letters*, vol. 20, no. 10, pp. 406-408, 1984.
- [15] C. Carrero, D. Ramirez, J. Rodriguez and C. Platero, "Accurate and fast convergence method for parameter estimation of PV generators based on three points of the I-V curve," *renewable energy*, vol. 36, pp. 2972-2977, 2011.
- [16] A. Yahya, H. Fadil, F. Giri and H. Erguig, "Advanced control of three-phase grid connected," *IEEE*, pp. 753 - 758, 2014.
- [17] C. Meza, D. Biel and J. Negroni, "Considerations on the control design of DC-link based inverters in grid-connected photovoltaic systems," *IEEE*, vol. 6, no. 2, pp. 5067-5070, 2006.
- [18] D. GmnH, "DigSilent PowerFactory 15 user manual," DigSILENT GmbH, Gomaringen, 2013.
- [19] D. GmbH, "DigSilent PowerFactory Application Guide," DigSILENT GmbH, Gomaringen, 2013.
- [20] S. Kim, J. Jeon, C. Cho, E. Kim and J. Ahn, "Modeling and simulation of a grid-connected PV generation system for electromagnetic transient analysis," *Solar Energy*, vol. 83, pp. 664-678, 2009.
- [21] T. Neumann and I. Erlich, "Short circuit contribution of a Photovoltaic power plant," *Institute of electrical power systems*.
- [22] I. Banu and M. Istrate, "Study on three-phase photovoltaic systems under grid faults," *electrical and power engineering*, vol. 8, pp. 1132-1137, 2014.

PERFORMANCE COMPARISON OF PERTURB & OBSERVE AND INCREMENTAL CONDUCTANCE MPPT SCHEMES FOR SOLAR PV PLANTS

J. Bamukunde*, M. Nthontho*, S.K. Kibaara* and S. Chowdhury*

**Electrical Engineering Dept., University of Cape Town, Rondebosch, Cape Town, South Africa*

Abstract: Electric power generated from solar PV arrays continuously varies with weather conditions such as varying insolation, varying temperature and partial shading conditions. A Maximum power point tracking (MPPT) feature is implemented in the PV system to ensure that the maximum power is tracked and delivered with these varying weather conditions. The paper compares the performance of Perturb and Observe (P&O) and the Incremental Conductance MPPT schemes implemented in a solar PV system under varying solar insolation and varying atmospheric temperature. It is seen from results that Under varying solar insolation the P&O algorithm is able to track the varying levels of insolation but with oscillations which leads to significant loss of power in the PV output while the Incremental Conductance algorithm is able to track the gradual and rapid changes in insolation without oscillations in the steady state conditions and hence no power losses at the output of the PV module. In the case of temperature variations, incremental conductance is able to track variation in atmospheric temperature without major power losses unlike the P&O.

Keywords: Solar PV, MPPT scheme, Perturb and Observe algorithm, Incremental Conductance algorithm, solar insolation, atmospheric temperature

1. INTRODUCTION

Generation of electricity from solar energy has become increasingly popular because of the shortage of non-renewable resources, environmental pollution and climate change caused by fossil fuels [1]. Furthermore, solar PV plants are simple in design, require very little maintenance and are capable of providing outputs in the range of megawatts [2]. The PV generation system is made up of PV arrays, power conditioner, battery storage and inverter [3, 4, 5]. The PV array consists of a series and parallel combination of PV cells which capture the solar energy and converts it to DC power. The amount of DC power generated depends on the weather conditions (amount of insolation and atmospheric temperature). A blocking diode is included in the PV system to ensure that the power that is generated by the PV array flows only towards the power conditioner and also ensures that the battery does not discharge through the solar array during periods of low insolation [5]. The power conditioner consists of a maximum power point tracker and a battery charge /discharge controller. The battery charge and discharge controller ensures that there is no overcharging or over discharging of the battery storage during periods of low insolation levels. The maximum power point tracker ensures that at all times maximum power is extracted from the PV array [6].

1.1 Maximum Power Point Tracking with Boost Converter

In order to obtain maximum power at all times during varying solar insolation, temperature, and shading conditions a maximum power point tracking (MPPT) feature needs to be implemented. Maximum power point tracking is an electronic system which captures maximum power from the PV modules and transfers this power to the load [6]. The maximum power is obtained by coinciding the converter's operating voltage and current

to the MPP [7]. A basic MPPT configuration with a converter is shown in Figure 1.

The MPPT system functions as follows. The voltage and current of the PV arrays are sensed by current and voltage sensors of the MPPT Controller. The sensed current and voltage values are then utilized in an MPPT algorithm to calculate the maximum power point of that particular cycle [7]. The output of the MPPT block is a duty cycle or voltage which is used as the input to the DC-DC Converter [6]. By varying the duty cycle of the DC-DC converter the operating voltage is maintained at the maximum power point [6].

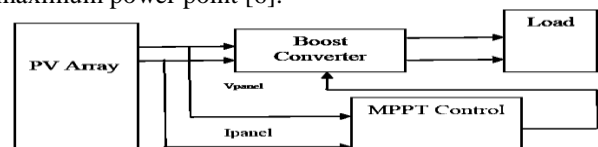


Figure 1: Basic MPPT system with converter [8]

The DC-DC converter between the PV array and the load is usually a boost converter because of its simple topology and high efficiency [6]. The MPPT algorithm controls the duty cycle of the converter which allows the PV module to provide maximum power [9]. When the duty cycle is varied, the load impedance seen by the source is varied. This allows the source impedance to be matched with the load impedance so that the load receives maximum power [6]. Furthermore the boost converter steps up the output voltage of the module so that the load is provided with a somewhat constant voltage [11]. The boost converter can be modelled as shown in Figure 2. The boost converter consists of an inductor, diode, capacitor, MOSFET and a resistor which acts as a load [9]. The output duty cycle of the MPPT is fed into the MOSFET of the boost converter which acts like a switch and regulates the load voltage V_o .

The paper models two MPPT schemes in Matlab Simulink, which are Perturb and Observe (P&O) and Incremental Conductance (IC). The performance of the two schemes is investigated and compared under varying insolation levels and varying ambient temperature.

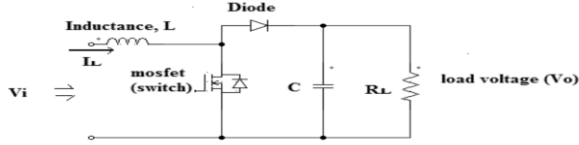


Figure 2: DC-DC boost converter [9]

2. MPPT SCHEMES

There are several MPPT schemes, such as Perturb and Observe (P&O), Incremental Conductance (IC), Hill Climbing (HC) and the Fuzzy Logic (FLC) techniques. This paper however focusses on P&O and IC schemes only.

2.1 Perturb and Observe (P&O) Scheme

The P&O scheme is simple in implementation and structure [4]. It can be implemented by using digital or analogue circuitry [5]. It is the most frequently used MPPT scheme [3, 9]. Also the cost of implementation is less when compared with other MPPT algorithms as it requires one voltage and current sensor to sense the PV array voltage and current [10].

This MPPT scheme operates as follows: The PV array's voltage and current is sensed by the MPPT algorithm and these values are used to compute the power from the PV array. The output power of the PV array, $P(k)$, is periodically compared with the previous measured output power, $P(k-1)$. If $P(k)$ is equal to $P(k-1)$, then the MPP is found and no perturbation of voltage occurs. Depending on whether $P(k)$ is less or more than $P(k-1)$ and whether $V(k)$ is less or more than $V(k-1)$, the present measured voltage is incremented or decremented by the perturbation voltage [5]. Perturbing the voltage implies modifying the duty cycle between the DC link of the PV module and the DC-DC converter [10]. If the perturbation in terminal voltage leads to an increase in power, the perturbation is kept in the same direction but if not then it is moved in the opposite direction. The perturbation is repeated until the maximum power is reached [3]. The flowchart of this MPPT algorithm is shown in Figure 3.

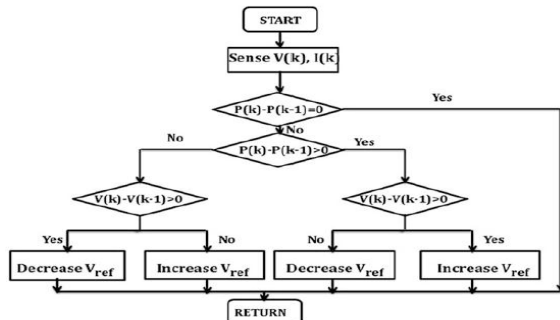


Figure 3: Flowchart of P&O MPPT algorithm [10]

The problems associated with the P&O scheme is that it does not stop perturbing when the MPP is found and it oscillates around the MPP [3]. This leads to unnecessary power loss [1]. The amplitude of the oscillations is directly proportional to the amplitude of the perturbation voltage that is added or subtracted from the system [1]. The perturbation voltage also determines the convergence rate of the output power [1]. Therefore the larger the perturbation the larger the oscillation voltage and the faster the maximum power point (MPP) is found. Therefore with the P&O technique, a compromise needs to be reached between convergence time and oscillation amplitude. To avoid this problem, there is a modified P&O technique [5]. The modified P&O utilizes a variable perturbation size, where large perturbations are applied when the output power is far from the MPP and smaller perturbations are applied when the MPP is found and the output power oscillates around it, therefore minimizing power loss [1]. The variable perturbation size is found from the slope of the Power vs. Current curve [4].

2.2 Incremental Conductance (IC) Scheme

The IC scheme is often used because it tracks the MPP excellently during steady state conditions and also adapts efficiently to changes in atmospheric conditions [3]. It is implemented by using digital circuitry. The Incremental Conductance scheme (IC) is based on the fact that the derivative of the PV array's power with respect to the voltage, i.e., $\left(\frac{dP}{dV}\right)$, is zero at maximum power point [11]. With this reference in mind, the slope of the Power vs. Voltage curve will be positive for voltage values smaller than the voltage at MPP and the slope will be negative for voltage values larger than the output voltage at the MPP [11]. Therefore by computing the derivative it can be determined whether the PV generator is functioning at the MPP, near the MPP or far from the MPP [4] as shown in equations (1) and equations (2). Mathematically, at MPP:

$$\frac{dP}{dV} = \frac{d(VI)}{dV} = I + V \frac{dI}{dV} = 0 \quad \text{Equation (1)}$$

$$-\frac{I}{V} = \frac{dI}{dV} = \frac{\Delta I}{\Delta V} \quad \text{Equation (2)}$$

with the left hand side of the above equations equal to the PV array's negative instantaneous conductance and the right hand side being the incremental conductance, ΔI and ΔV being the PV incremental current and voltage. Therefore, at MPP, the negative instantaneous conductance is equal to the incremental conductance [1]. Therefore, the IC scheme rules are as shown in equations (3)-(5) and as depicted in Figure 4:

$$\frac{dI}{dV} = -\frac{I}{V}; \left(\frac{dP}{dV} = 0\right), \quad \text{Equation (3), at MPP}$$

$$\frac{dI}{dV} > -\frac{I}{V}; \left(\frac{dP}{dV} > 0\right) \quad \text{Equation (4), left of MPP}$$

$$\frac{dI}{dV} < -\frac{I}{V}; \left(\frac{dP}{dV} < 0\right) \quad \text{Equation (5) right of MPP}$$

The MPP is determined by comparing the instantaneous conductance with the incremental conductance. In the flow chart V_{ref} is the reference voltage which the PV array is forced to operate at. When the MPP is reached V_{ref} is equal to the V_{MPP} (voltage at MPP). At MPP the changes in current and voltage i.e. the difference between the present and previous values of current and voltage will be zero ($\Delta I = 0$ and $\Delta V = 0$). The PV array will continue to operate at the MPP until changes in current are detected as a result of changes in atmospheric conditions [5].

When the levels of solar insolation increases ($\Delta I > 0$) and $\Delta V = 0$, the MPP voltage is increased and the MPPT must increase the PV array's voltage to capture the MPP [5]. On the other hand when levels of sunlight decreases ($\Delta I < 0$) and $\Delta V = 0$, the MPP voltage will be decreased and will require that the operating voltage of the PV array to be decreased by the MPPT [5]. When both $\Delta V \neq 0$ and $\Delta I \neq 0$ then equations (1-5) are used to determine the direction in which the voltage must be incremented or decremented so that the MPP is tracked [5]. Thus when $\frac{\Delta I}{\Delta V} > -\frac{I}{V}$, the PV operating point will lie in the region left to the MPP on the P-V curve and the PV array voltage will have to be incremented to reach the MPP [5]. When $\frac{\Delta I}{\Delta V} < -\frac{I}{V}$, the PV operating point will lie in the region to the right of the MPP on the P-V curve and the PV array voltage will have to be decremented to reach the MPP [5].

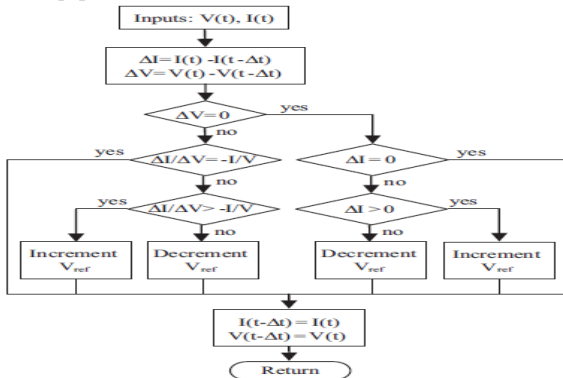


Figure 4: Flowchart of IC MPPT algorithm [4]

It is clear that the main advantage of the IC scheme is that it can calculate the direction to increment and decrement the array's voltage to track the MPP and is also aware of when the MPP has been found. Therefore, it will not track in the wrong direction when atmospheric conditions vary and will not oscillate around the MPP when it is found [2].

The IC scheme also requires a compromise to be reached between the tracking speed and the likelihood of oscillations in the region of the MPP [4]. This is because a large perturbation voltage will result in fast tracking of the MPP but the PV may not operate exactly at the MPP and may result in oscillations in the region of the MPP [5]. However, a small perturbation voltage will result in slow tracking of the MPP and a low likelihood of oscillations around the MPP [5]. Therefore a reasonable

compromise needs to be met between the sizes of the perturbation voltage [5].

3. SIMULATION OF SOLAR PV SYSTEM

In this paper a solar PV system is modelled in MATLAB Simulink for performance comparison of P&O and IC schemes under varying solar insolation levels and atmospheric temperature. The solar PV system comprises a PV module, MPPT algorithm, DC-DC boost converter and a load as shown in Figure 5. The inputs into the PV module are solar insolation in kW/m^2 and atmospheric temperature in $^{\circ}\text{C}$. The solar insolation and temperature values are used to calculate the output current I_{pv} .

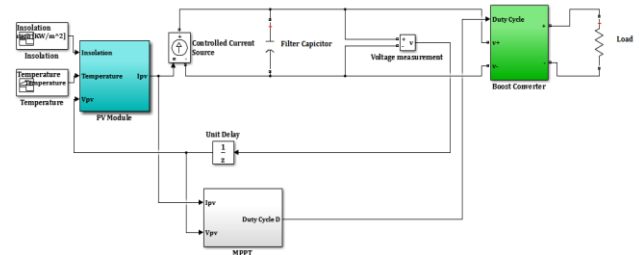


Figure 5: Simulation of solar PV system in Matlab

The output current of the PV module is connected to a controlled current source to allow for it to be connected to the electrical circuit consisting of the filter capacitor, boost converter and load resistor. A voltmeter was used to measure the output voltage of the PV module and is fed back into the PV module to allow for the calculation of I_{pv} . A delay block was implemented at the output of the voltmeter to avoid the algebraic loop that would otherwise be created during the simulations. The electrical characteristics of the PV module are shown in Table 1.

Table 1: Specifications of PV Module

Specification	Value
Maximum Power at STC	245W
Maximum Operating Voltage	30.5V
Maximum Operating Current	8.04A
Open Circuit Voltage	37.3V
Short Circuit Current	8.52A
No of cells in series	60
Temperature Coefficient Of short circuit current	0.067% / $^{\circ}\text{C}$
Module Efficiency	15.1%

The DC-DC boost converter forms the interface between the PV module and the load. The boost converter consists of an inductor, diode, MOSFET and capacitor as previously shown in Fig 5 above. A filtering capacitor is included at the input of the converter and a load resistor is attached to the output of the converter. In Table 2 the design specifications for a voltage of 50V at the load and at standard operating conditions of 1000W/m^2 and atmospheric temperatures of 25°C are shown. By employing equation 1 and design specifications of Table 2, the duty cycle D is calculated from the desired output voltage V_o and input voltage V_i as shown in equation (6).

$$\frac{V_o}{V_i} = \frac{1}{1-D} \quad \text{Equation (6)}$$

$$D = 1 - \frac{V_i}{V_o} = 1 - \frac{30.5}{50} = 0.39$$

Depending on the atmospheric conditions, the duty cycle of the converter is to be adjusted by the MPPT algorithm to maintain a constant voltage at the load.

Table 2: Design specifications of boost converter

Specification	Value
Input voltage	30.5V
Input Current	8.04A
Switching Frequency	20kHz
Voltage Ripples	5%
Current Ripples	10%
Output Voltage	50V

Based on the design specifications of the boost converter and equations (2)-(3), the calculated values of the boost converter in continuous mode are shown in Table 3.

Table 3: Calculated values of boost converter

Calculated Parameter	Value
Duty Cycle	0.39
Load Resistance	10.19Ω
Inductance, L	739.74μH
Capacitor, C	38.25μF
Filter Capacitor	19μF

3. SCENARIOS DEVELOPED FOR PERFORMANCE COMPARISON

The performance of the P&O and IC schemes are simulated under similarly varying solar insolation and temperature to determine which one performs most efficiently during varying atmospheric conditions. The performance of each MPPT under the above mentioned varying levels of insolation and temperature is assessed by plotting the output current vs. time graph, output voltage versus time graph and output power versus time graph of the PV module. The scenarios are discussed below.

3.1 Scenario 1: Varying Solar Insolation

The performances of the above mentioned MPPT algorithms were each tested under the same varying levels of solar insolation. For this case the atmospheric temperature is held constant at 25°C while rapidly and gradually varying solar insolation is given as input to the PV module. The Figure 6 shows the varying insolation pattern applied to the PV module for Scenario 1.

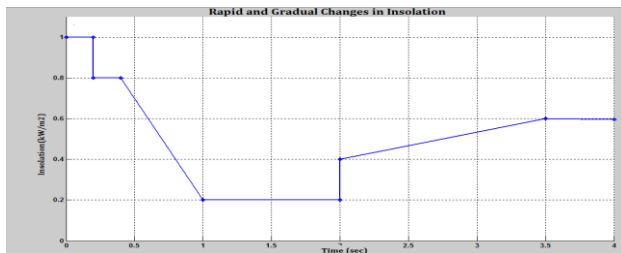


Figure 6: Varying solar insolation levels

The solar insolation is initially at 1.0 kW/m². At time t=0.2s of the simulation, the solar insolation decreases rapidly to 0.8 kW/m². The solar insolation is maintained at 0.8kW/m² for a further 0.2s after which there is a gradual decrease in solar insolation for about 0.6s. The solar insolation eventually reaches a steady value of 0.2kW/m² and is maintained at that value for 1s. The insolation then increases rapidly to 0.4kW/m² at time t=2s from the start of the simulation. From then on there is a gradual increase in insolation to 0.6kW/m², after which the insolation is maintained at that value for the rest of the simulation.

3.2 Scenario 2: Varying Atmospheric Temperature

The performance of the above-mentioned MPPT algorithms are each tested under the same varying levels of atmospheric temperatures. For this case, the solar insolation is held constant at 1000W/m² while rapidly and gradually varying atmospheric temperature value is given as input to the PV module. Figure 7 shows the varying temperature pattern that is applied to the PV module for Scenario 2.

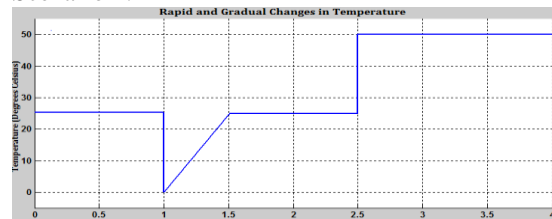


Figure 7: Varying atmospheric temperature levels

The input temperature of the PV module is initially maintained at 25°C. At time t=1s from the start of simulation, the temperature decreases rapidly to 0°C and from then on increases gradually to 25°C over a time duration of 0.5s. The temperature is maintained at 25°C for 1s. After this there is rapid increase to 50°C. The temperature is then maintained at 50°C for the remaining duration of the simulation.

4. RESULTS AND ANALYSIS

4.1 Results for Scenario 1: P&O Algorithm

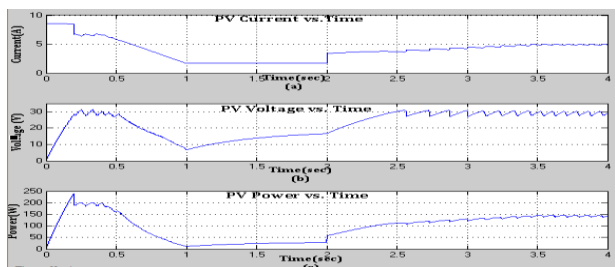


Figure 8: (a) current (b) voltage and (c) power response for PV module with P&O algorithm for Scenario 1

The dynamic response PV module current, voltage and power for the P&O algorithm and varying insolation is shown in Figure 8(a), (b) and (c) respectively. The current, voltage and power curves show that the P&O algorithm tracks the rapidly decreasing and increasing

levels of insolation smoothly at $t=0.2s$ and at $t=2s$. The output current, voltage and power is seen to increase with increasing levels of insolation and to decrease with decreasing levels of insolation. The P&O algorithm also tracks the gradually decreasing and gradually increasing levels of insolation smoothly between $t=0.4s$ and $t=1s$ and between $t=2s$ and $t=3.5s$.

4.2 Results for Scenario 1: IC Algorithm

The dynamic response PV module current, voltage and power for the IC algorithm under varying insolation is shown in Figure 9(a), (b) and (c) respectively. The current, voltage and power curves show that the IC algorithm tracks the rapidly decreasing and increasing levels of insolation smoothly at $t=0.2s$ and at $t=2s$. The output current, voltage and power increases with increasing levels of insolation and decreases with decreasing levels of insolation. The IC algorithm also tracks the gradually decreasing and increasing levels of insolation smoothly and effectively between $t=0.4s$ and $t=1s$ and between $t=2s$ and $t=3.5s$. It is noted that during steady state conditions there are no oscillations.

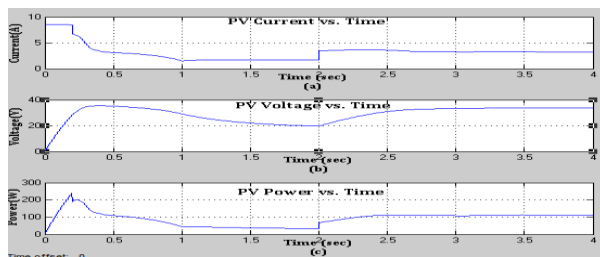


Figure 9: (a) current (b) voltage and (c) power response for PV module with IC algorithm for Scenario 1

4.3 Performance Comparison for Scenario 1

To further assess the MPPT performances, the output powers produced as shown in Figure 8 and Figure 9, at the insolation levels of 1.0, 0.8, 0.6, 0.4 and 0.2kW/m^2 are compared to the expected datasheet output power given in Table 4. P&O algorithm does not capture the maximum power at low insolation levels efficiently. However its performance at high insolation levels is satisfactory. At the highest insolation level of 1.0kW/m^2 the P&O algorithm tracks just above 96% of the expected power while it tracks 62.76% at the lowest insolation level. Incremental Conductance algorithms track 96.84% of the expected power at highest insolation and 77.9% at lowest insolation.

Table 4: Performance comparison for Scenario 1

Solar Insolation [kW/m^2]	Output Power [W]		Datasheet output power (maximum power) [W]
	P&O	INC	
1.0	237	239	246.8
0.8	190	193.1	195.8
0.6	138.1	110.4	144.7
0.4	58.14	66.84	94.46
0.2	28.4	35.25	45.25

4.4 Results for Scenario 2: P&O Algorithm

The dynamic response PV module current, voltage and power for the P&O algorithm under varying atmospheric temperature is shown in Figure 10(a), (b) and (c) respectively. The current, voltage and power curves of Figure 10 show that the P&O algorithm tracks the rapidly decreasing and increasing levels of temperature at $t=1s$ and $t=2.5s$ adequately. At $t=1s$, the output current decreases with decreasing temperature and increases at $t=2.5s$ with the rapid increase in temperature. At $t=1s$ there is an increase in voltage and power when the temperature decreases rapidly. At time $t=2.5s$ there is a decrease in voltage and power when the temperature increases rapidly. The reason for this phenomenon is that as the PV cell temperature rises their respective internal resistance increases and thus decreasing the cell current. The voltage and power are both a function of the cell current and hence they decrease [12].

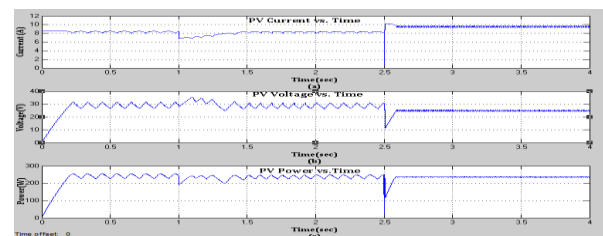


Figure 10: (a) current (b) voltage and (c) power response for PV module with P&O algorithm for Scenario 2

4.5 Results for Scenario 2: IC Algorithm

The dynamic response PV module current, voltage and power for the IC algorithm under varying atmospheric temperature is shown in Figure 11(a), (b) and (c) respectively.

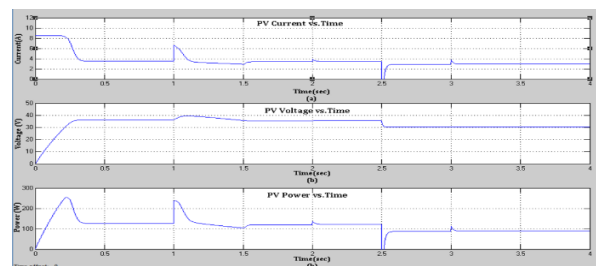


Figure 11: (a) current (b) voltage and (c) power response for PV module with IC algorithm for Scenario 2

It is seen that when the temperature is maintained constant for some time, the power output is also remains constant. On the other hand, when the temperature is maintained at a constant value of 25°C , from period $t=0$ to $t=1s$ the maximum power is captured but reduces and settles at lower new steady state value. The reason behind this is that the IC MPPT checks the output of the PV module then compares it with the voltage of the battery fixing it to what is best power that PV can produce to charge the battery and convert it to the best voltage to get the maximum current into the battery [12]. This new steady state is maintained without any oscillations. During $t=1.5s$ to $t=2.5s$ for a constant temperature of

25°C, power is seen to stay approximately constant, but with a slight overshoot at $t=2s$ because the internal resistances of the cells decreases and hence the current increases, subsequently leading to an increase in power. Finally from $t=2.5s$ to $t=4s$ when the PV module is exposed to a constant temperature of 50°C, power is maintained at a constant value but with a slight overshoot at $t=3s$ because of the resistance drop

4.6 Performance Comparison for Scenario 2

To further assess the MPPT performance under varying levels of temperature the output power produced at the atmospheric temperatures 25°C and 50°C is compared to the expected datasheet output power in Table 5. With the implementation of the P&O algorithm, the PV module produces 97.61% of the expected power at 25°C and 93.30% of the expected power at 50°C. On the other hand, the IC algorithm produces 50.97% of the expected power at 25°C and 37.57% of the expected power at 50°C.

Table 5: Performance comparison for Scenario 2

Temp [°C]	Output Power [W]		Datasheet output power (maximum power, W)
	P&O	INC	
25	240.9	125.8	246.8
50	220	88.66	235.8

5. CONCLUSION

Under rapid and gradual changes in insolation the P&O algorithm is able to track the varying levels of insolation. However, during steady state conditions excessive oscillations are observed which result in power losses at the output of the PV module. Additionally the oscillations imply that the P&O algorithm does not produce stable operating points. The IC on the other hand is able to track the gradual and rapid changes in insolation without oscillations and hence no power losses are expected at the output of the PV module. The P&O algorithm has the slowest response time to varying levels of insolation. Under rapid changes in temperature and the gradual decrease in temperature the P&O algorithm is able to track the varying temperatures but unable to track the gradual increase in temperature. At steady state the power-time graph generated by the P&O algorithm shows significant oscillations. The IC algorithm is able to track the gradual and rapid changes in temperatures without oscillations during steady state conditions but slight overshoot of power is present at each steady state. There is no significant power losses are expected at the output of the PV module. The observations here show that PV panels work best in lower temperatures, and hence installation of MPPTs can help in the extraction of maximum power and at the same time provide a regulated DC supply.

6. ACKNOWLEDGEMENT

The authors gratefully acknowledge the support and infrastructure provided by Electrical Engineering

Department, University of Cape Town, South Africa for carrying out this research.

7. REFERENCES

- [1] M. F. Ansari, S. Chatterji and I. Atif, "Fuzzy logic based MPPT controllers for three-phase grid-connected inverters," *International Journal of Sustainable Energy*, vol. 32, no. 3, pp. 186-195, 2013.
- [2] M. A. Eltawil and Z. Zhao, "MPPT techniques for photovoltaic applications," *Renewable and Sustainable Energy Reviews*, vol. 25, pp. 793-813, 2013.
- [3] H. Rezk and A. M. Eltamaly, "A comprehensive comparison of different MPPT techniques for photovoltaic systems," *Solar Energy*, vol. 112, pp. 1-11, 2014.
- [4] A. R. Reisi, M. H. Moradi and S. Jamasb, "Classification and comparison of maximum power point tracking techniques for photovoltaic system: A review," *Renewable and Sustainable Energy Reviews*, vol. 19, pp. 433-443, 2013.
- [5] G. Singh, "Solar power generation by PV (photovoltaic) technology: A review," *Energy*, vol. 53, pp. 1-13, 2013.
- [6] S. Sholapur, K. R. Mohan and T. R. Narsimhegowda, "Boost Converter Topology for PV System with Perturb And Observe MPPT Algorithm," *IOSR Journal of Electrical and Electronics Engineering (IOSR-JEEE)*, vol. 9, no. 4, pp. 50-56, 2014.
- [7] Z. Salam, J. Ahmed and B. S. Merugu, "The application of soft computing methods for MPPT of PV system: A technological and status review," *Applied Energy*, vol. 107, pp. 135-148, 2013.
- [8] S. Ganesh and L. Muthuvel, "FLC based Maximum Power Point Tracking of Solar," *The International Journal of Computer Science & Applications (TIJCSA)*, vol. 1, no. 6, pp. 59-68, 2012.
- [9] P. K. Ainah, "Design of Dc-Dc Converter with Maximum Power Point Tracker Using Pulse Generating (555 Timers) Circuit for Photovoltaic Module," *International Journal of Scientific & Engineering Research*, vol. 3, no. 6, pp. 1-10, 2012.
- [10] S. Sumathi, L. A. Kumar and P. Surekha, *Solar PV and Wind Energy Conversion Systems: An Introduction to Theory, Modeling with MATLAB/SIMULINK, and the Role of Soft Computing Techniques*, Switzerland: Springer International Publishing, 2015.
- [11] K. Ishaquea and Z. Salam, "A review of maximum power point tracking techniques of PV system for uniform insolation and partial shading condition," *Renewable and Sustainable Energy Reviews*, vol. 19, pp. 475-488, 2013.
- [12] D. Saravana, "Modelling and Simulation of Incremental Conductance MPPT Algorithm for Photovoltaic Applications," *Inter. Journal of Scientific Eng & Tech*, Vol.2, No.7, pp 681-685, 2013.

Design and development of a remote solar power control, battery monitoring system and internet logging capability

J. Bothma¹, N de Lange² and F. Adlam^{1*}

¹Nelson Mandela Metropolitan University (NMMU)
Port Elizabeth, South Africa

²Department of Research and Development Microcare Solar Components
Port Elizabeth, South Africa

*Email: Frank.Adlam@nmmu.ac.za

Abstract

Improper utilization of the battery bank in a solar power system will lead to a reduction in lifespan and increase in maintenance for the battery bank as well as an overall increase in cost in operating the solar power system. By implementing a battery monitoring system (BMS) such problems can be reduced or completely removed. The BMS offers the ability to analyse the solar power system given monitoring for example: battery state of charge (SOC), time remaining in the battery, charge current and discharge current. The BMS also has the ability to control all charge sources and loads connected to the battery bank with the purpose of projecting the battery bank from undesired conditions.

This paper covers all aspects that had been taken into consideration in the design and development of the solar power controller and BMS. This BMS and all related designs of the BMS is property of Microcare solar components.

Keywords: Battery monitoring system (BMS); Microcontroller unit (MCU); State of charge (SOC); Maximum power point tracker (MPPT); Analog to digital converter (ADC)

1. Introduction

This paper covers all aspects that had been taken into consideration in the design and development of the solar power controller and BMS.

Off-grid solar power systems consist of solar panels charging batteries through charge regulators and inverters, converting the battery bank DC voltage into a usable AC voltage for the load. This allows the individual or corporation to reduce or erase their dependence on a power grid. A large, expensive battery bank is needed for this system to operate with reliability and to maintain the load throughout night times.

This chapter covers aspects of the BMS that needs to be taken into consideration in later stages of design. The author states a brief overview of the aspects which is considered in the design and how the interpretation of the information affected the design of the BMS.

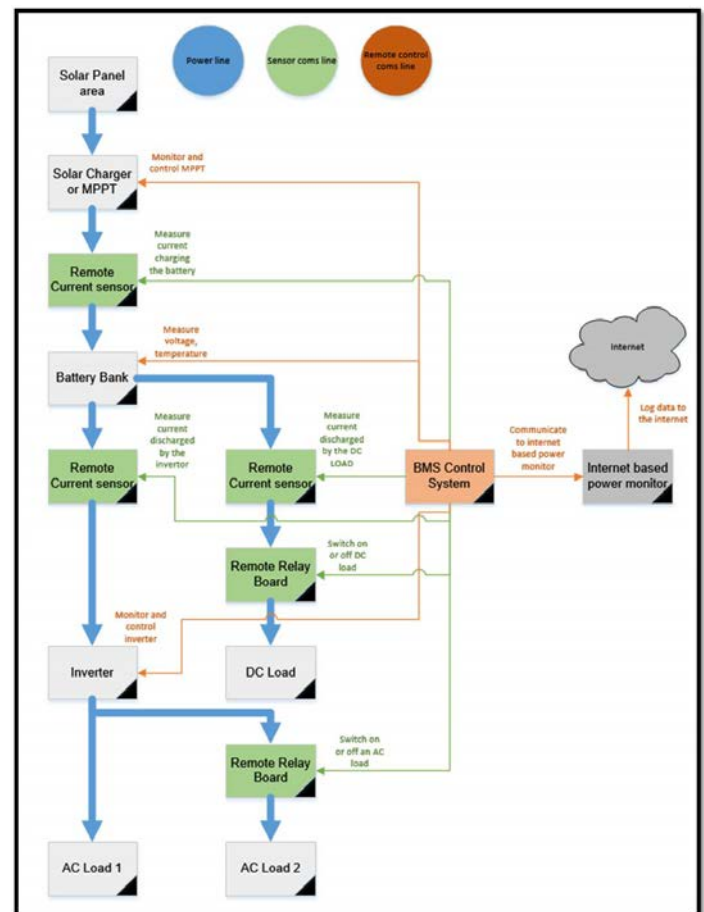
As shown in

Figure 1 a detailed connection diagram of the BMS. The BMS would have current sensors placed in line with all charging or discharging devices connected to the battery bank. The battery bank would provide power to the BMS and the same cables would be used to detect the voltage of the battery bank. The BMS would have control of relay modules that can be signalled to switch specific loads on or off depending on the conditions of the battery bank. The BMS has communication to the Microcare MPPTs and inverters, giving it the ability to monitor the state of those devices and power them on or off as needed. Finally, there should be a communication connection between the BMS and the Microcare Web-logger to allow for internet logging of the BMS's data.

In

Figure 1 the blue lines represents power cables connected to power components. The green lines represents communication cables between the remote sensors and the BMS.

Figure 1: Detailed Connection Diagram



including situations where the load would discharge the battery in less than 20 hours.

Factors that can have a negative influence on the lifespan of a battery include:

- Discharging a battery too deeply.
- Leaving a battery bank at a low state of charge for an extended period.
- Applying a load greater than the rated discharge of the battery.
- Allowing a battery bank to overheat during the charge cycle.
- Allowing a battery bank to become unbalanced, thus undercharging some batteries and overcharging others.

The BMS monitor these factors, and enforce certain actions to prevent or correct these problems. Possible steps that such a monitoring system can implement, include:

- Disconnecting all loads to the battery when it reaches a maximum battery bank discharge point.
- When the BMS finds that the battery bank has not been fully charged for an extended period, it should prevent lower priority loads from running.
- The BMS should warn the user of loads that exceed that of the battery rating and possibly disconnect those loads for a set amount of time.
- The BMS should monitor the temperature of the battery bank while it is being charged and instruct the charge regulator to reduce charge if the battery bank's temperature becomes in excess of its rated operating conditions.
- When a battery bank becomes unbalanced the BMS should inform the operator of the problem and attempt to correct the problem by equalizing the battery bank.

2. Peukert's Exponent

A key feature of a BMS is to accurately measure the state of charge (SOC) of the battery bank, as well as to predict the estimated time remaining in the battery bank when a constant load is applied. The Peukert's Exponent calculation as can be seen in Figure 2, takes into account the size of the battery bank and the relative size of the load applied to the battery bank, for more accurate calculations, including the effect of other factors on the battery. [6]

Battery manufacturers rate their batteries in terms of a 20 hour rate of discharge, for example a 20 Amp hour battery is rated to provide 1 Amp to the load for 20 hours when fully charged. When discharging the same battery at 20 Amps not considering the Peukert's Exponent the battery should be able to provide to the load for 1 hour, but when the Peukert's Exponent with a number of 1.19 (a good modern lead acid average) we find that the battery is only be able to provide power to the load for 34 minutes or less before being completely discharged. [7]

By implementing the Peukert's Exponent into the BMS software, the system was able to accurately predict the SOC and the time remaining in the battery bank in any situation,

Figure 2: Peukert's Exponent Calculation

$$C_{n1} = C_n \left(\frac{I_n}{I_{n1}} \right)^{pc-1}$$

3. Unbalance in a Series Battery Bank

A DC load such as an inverter normally stop discharging when the batteries become too low, but when a battery bank is unbalanced the inverter is not able to detect that one of the batteries has reached a dangerously low point. When a battery is discharged to deeply it can cause irreversible sulfation in the battery, which reduces the capacity of the battery. Sulfation can also cause the battery plates to warp and bend, which can cause internal faults to the battery, this can bring down the whole battery bank and solar power system. [8]

When charging a battery with a device such as an MPPT, the batteries are brought to a voltage at which it should reach 100 % SOC and kept at that voltage for the time it should take for the battery to reach 100 % SOC. When a battery bank is imbalanced, fuller batteries have a higher voltage across them compared to the flatter batteries. The higher voltage battery warms up and the excess heat can cause damage to the battery .The flatter battery would need more time at a set voltage to reach full state.

For the BMS to reduce the problem, it needs to know the voltages of the batteries in the system. When the BMS detects an unbalance in the battery bank, it must indicate to the battery charger that a equalise charge is required. The BMS would monitor the temperature of the battery bank and indicate to the MPPT, to reduce charge when the battery bank gets hot, to avoid damage to the fuller batteries. If the battery equalise is not successful the BMS should notify the user to take further steps to recharge or replace problematic batteries.

4. Web-Logger Device

The Microcare web-logger was used as an internet-of-things connection to the BMS. This is a small Linux based computer that needs to be provided with an internet connection using an Ethernet port. The BMS then sent data packets using the Microcare communication protocol on an RS485 bus. The BMS would then upload the data to the website under a given serial number provided for the BMS. [9]



The user can use the data provided from the BMS on graphs, gauges and dials on the website. As shown in Figure 3.

Figure 3: Screenshot of Internet Based Power Monitor Website

5. Design Considerations of Sensor Module

The main purpose of the sensor module is to accurately measure current flowing in and out of the battery bank, and the voltage the battery bank is operating at.

In general, a 200 Amp sensor was selected as this sensor is the closest match to the most popular solar product sold by Microcare, namely the 5 kW 48 Volt bidirectional inverter. (5000 Watt / 40 Volt = 125 Amp).

The selection of a Hall Effect sensor for current measurement is the Allegro ACS758xCB. [10]

It was selected for having a Nominal Power loss due to the 100 $\mu\Omega$ resistance, galvanic isolation in the Hall Effect sensor of up to 4800 and a much lower cost than the alternatives.

The voltage divider used to measure the voltage of the battery bank consist of the following: two 100 k Ω resistors in series going from the battery voltage sense pin to the MCU's ADC pin and a 10 k Ω resistor going to battery negative. All the resistors are 1% tolerance. There is also a 10 nano ferrite ceramic capacitor connected as a noise filter to the MCU.

A resistor based temperature sensor was added to the sensor module to allow users to monitor the temperature surrounding the battery bank. The sensor should be located as close as possible to the battery bank to allow the temperature sensor to measure the temperature surrounding the battery bank. A battery over-temperature-error is used as an indicator to turn off chargers or loads.

A relay control circuit has also been added to the Sensor module to allow for control of devices such as lights. The relay is located off board to reduce cost when it is not needed.

- The final completed sensor module can be found in Figure 5.

6. Design Considerations of Relay Module

The main purpose of relay module is to allow the BMS to control external conditions, for instance starting a generator, turning on a battery charger and turning lights on and off, or any other combination of these.

A 6 Volt relay was selected because the supply voltage on the MC_COMS bus is 8 Volt. This is not high enough to reliably switch a 12 Volt relay. The 16 Amp double pole relay capability is a good middle-sized relay that can be used for the following. In a 230V AC system (16 * 2 * 230) it can be used to switch resistive loads of up to 7 kW, alternatively it can be used to switch larger contactor of other applications.

The relay circuitry consists of two sets of transistor circuits per relay. The start transistor puts the full 8 Volts of the MC_COMS bus onto the coil of the relay for approximately 20ms. At this point the relay is considered on. The second relay switches the 8 Volts to the coil through a 220 Ω resistor. The first relay turns off for the remainder of the time that the

relay should stay on for. When the relay must turn off, the secondary stay on relay turns off as well. Using this method of relay switching reduces the power consumption of each of the 4 relays on the relay module from (8.2Vx8.2V/90 Ω) 747 milliwatt per relay, down to (8.2Vx8.2V/310 Ω) 216 milliwatt per relay.

- The final completed relay module can be found in Figure 6.

7. Design Considerations of Control Module

The main purpose of the control module is to interpret all information gathered by the sensors, display the information to the user in a sensible way and control the external devices based on the sensor information.

A Graphical LCD display has been selected for the control module because compared to a multiline display (for example A 2 line 16 character or a 4 line 20 character display) that the author has used in the past. The selected 64 by 128 dot display has the ability to display 64 / 8 = 8 lines and 128 / 6 = 21.3 characters. This allows for a greater amount of information to be displayed at once. Using this graphic display has the added advantage of allowing for a graphic user interface and menu systems that is more user friendly.

MC_Com is the communication protocol of all Microcare solar products (1-15KW inverters, 20-10Amp MPPT charge controllers and the Microcare web-logger). For this reason this communication protocol has been selected for this project. The communication protocol can be used in non-bus interfaces such as RS232 or bus interfaces such as RS485. The RS485 interface is used in the control module.

Having an accurate track of time is essential to this project as some logging facilities, for instance measuring kWh and Ah going in and out of the battery and graphing the information onto the display, require accurate timekeeping. This control module also offers a 2 year computed log which would not work if the control module were not able to retain the time when power source is removed from the control module. The selected RTCC is the microchip MCP79400. [13]

The selected flash chip is the Atmel AT25M01. Some of the key features relevant to this project is A 100Year retention and 1,000,000 write cycle capability to ensure that this is not a future point of failure in this control module. Having 1,048,576 bits programmable memory space was an ample amount of space for the control module. [14] See Figure 4.

The design has been changed to surface mounted devices to facility a compact design that can easily be hung on a wall in a house or in a cupboard. The main advantage of using surface mount components besides the obvious reduction in size, is the cost of components, cost of labour and a reduced PCB size.

An audio buzzer has been added to the PCB. This was used on button presses for feedback on button press, and during error condition to indicate to the user that there is a problem with the battery bank or the BMS and that attention need to be given.

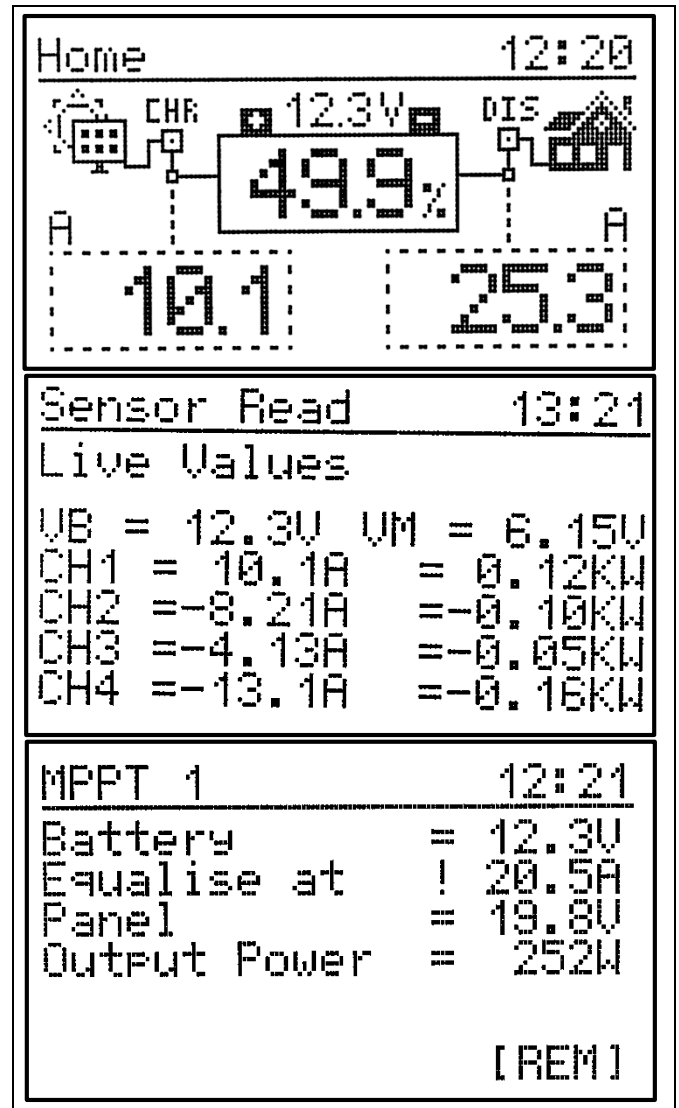
A matrix keypad membrane switch label has been designed by the author. It also houses indication LEDs which indicate simple states of operation to the user from a distance or at a glance.

8. Real-Time Displays

The real-time displays are used to give a current state on how the battery bank and solar system as a whole is functioning. This allows the user to view the following information as it happens:

The battery bank voltage. Current flowing in and out of the battery bank from various sources. Power flowing in and out of the battery bank from various sources. The current time of the day. The estimated time of operation remaining in the battery bank, if the current load remains stable. The estimated percentage that the battery bank is at. The amount of Amp hours, that needs to put back into the battery bank for full charge. The middle-point voltage of the battery bank. Individual current and power through each of the four possible sensor modules. The temperature around the battery bank. The estimated amount of Amp hours remaining in the battery bank. The status of all 8 possible relays, "on" or "off". The panel voltage, battery bank voltage, charge current, charge status and charge power of all 5 possible connected Microcare MPPT charge controllers to the BMS. The output voltage, battery bank voltage, charge or discharge current, output current, output power, operating temperature and operating status of all 5 possible Microcare inverters connected to the BMS. An indication whether or not the Microcare web-logger is connected to the BMS, and if it is functioning correctly.

Figure 8: Real Time Displays Screenshot

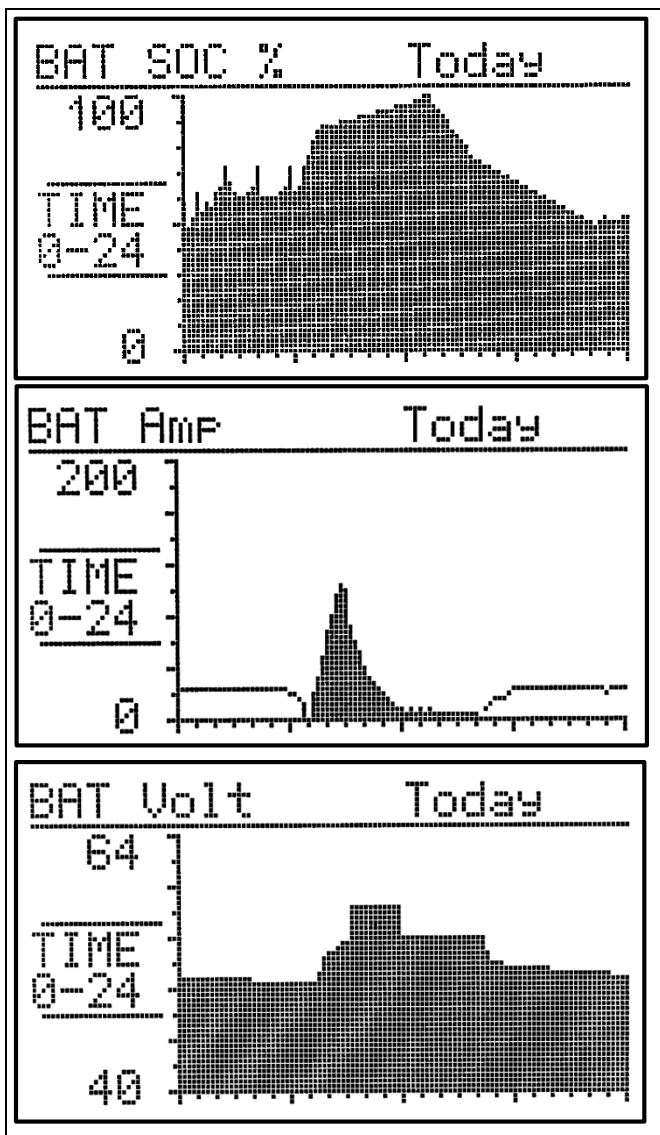


9. Graph Displays

The graph displays are used to give a more complete full day view of the state on how the battery bank and solar system as a whole are functioning. This allows the user to view the following information which happened throughout the day for a duration of 31 days.

The percentage of the battery bank throughout the day, to identify problem areas in over discharge or underutilization. The battery bank voltage throughout the day, to identify correct charging and any possible under voltage conditions. The current being charged into the battery bank throughout the day, to monitor the correct operation of the charge source. The current being discharged out of the battery bank throughout the day, to identify problems with the loads. The temperature near the battery bank throughout the day, to identify if the battery bank is working at accepted temperature levels.

Figure 9: Graph Displays Screenshot



10. Conclusions

This designed BMS has great abilities in data logging and to the trained user it would be a useful tool in ensuring a long life for any large solar battery bank. The remote monitoring and control functionality is useful, but only if the control module is located in a more convenient location than the rest of the solar system. For example, if the inverter and MPPT is located in a garage and the control module is placed in the house. There is the disadvantage that it is only able to operate with other Microcare products, but this is only because of the selected communication protocol being used is Microcare specific.

Using a PIC24 was mainly motivated because of the authors past experience with the manufacturer and software tools, but the MCU proved to be a limiting factor in this project as the available program memory of the MCU forced the author to have to rewrite software in order to fit the newer software. The graphic display did prove to help in visualising larger amounts of data in the form of graphs, but it was only capable of low resolution.

Acknowledgments

- Nelius De Lange - Microcare mentor
- Frank Adlam - University mentor
- Winston Dyson - Enclosure designer

References

- [1] A. a. P. B. Ausswamaykin, "Design of Real Time Battery Management Unit for PVHybrid," in *Design of Real Time Battery Management Unit for PVHybrid*, Rajamangala, SciRes, 2004, pp. 186-193.
- [2] G. Burley, "Microcare - Solar," Microcare, 28 January 2015. [Online]. Available: <http://microcare.co.za/solar/>. [Accessed 20 April 2015].
- [3] Q. Barnard, "powermonitor," QBSOft, 20 January 2015. [Online]. Available: <https://powermonitor.co.za/user/view>. [Accessed 20 April 2015].
- [4] S. A. S. Dennis Doerffel, "A critical review of using the Peukert equation for determining the remaining capacity of lead-acid and lithium-ion batteries," *Journal of Power Sources*, vol. 155, no. 2, pp. 395-400, 2004.
- [5] SmartGauge Electronics, "smartgauge.co.uk," SmartGauge Electronics, 20 January 2008. [Online]. Available: <http://www.smartgauge.co.uk/peukert2.html>. [Accessed 20 April 2015].

- [6] S. C. C. M. Yao Ching Hsieh, "Balance discharge for series-connected batteries," *Power Electronics Specialists Conference*, vol. 4, no. 35, pp. 2697-2702, 2004.
- [7] Allegro Micro Systems LLC, "ACS758," Allegro Micro Systems LLC, 07 04 2015. [Online]. Available:
<http://www.allegromicro.com/~media/Files/Datasheets/ACS758-Datasheet.ashx?la=en>. [Accessed 15 09 2015].
- [8] Riedon Inc, "RS Series," Riedon Inc, 01 08 2014. [Online]. Available:
http://riedon.com/media/pdf/DC_Current_Shunt.pdf. [Accessed 15 09 2015].
- [9] Microchip Technology Inc, "MCP79400," Microchip Technology Inc, 28 10 2013. [Online]. Available:
<http://ww1.microchip.com/downloads/en/DeviceDoc/20005009D.pdf>. [Accessed 15 09 2015].
- [10] Atmel Corporation, "AT25M01," Atmel Corporation, 07 07 2015. [Online]. Available:
<http://www.atmel.com/Images/Atmel-8824-EEPROM-AT25M01-Datasheet.pdf>. [Accessed 19 09 2015].

ANALYTICAL MODEL DEVELOPMENT FOR THE DETERMINATION OF THE OPEN-CIRCUIT MAGNETIC FIELD DISTRIBUTION IN A MOVING COIL TUBULAR PERMANENT MAGNET LINEAR OSCILLATORY MACHINE

D. K. Chembe J. M. Strauss and P. J. Randewijk *

* Department of Electrical and Electronics, Stellenbosch University, Private Bag X1, Matieland 7602, South Africa E-mail: 18336078@sun.ac.za

Abstract: This paper presents a 2-D analytical model for determining predictive values of the open-circuit magnetic field distribution of surface mounted permanent magnet tubular linear short-stroke oscillatory machine. A resolution of Maxwell equations and separation of variables are used to solve two dimensional Laplace and Poisson equations to develop an analytical model. The presented model is for predicting the air-gap magnetic field in slot-less tubular linear permanent magnet machines and validation is carried out through finite element analysis

Key words: Analytical model development, tubular linear machine, free-piston application

1. INTRODUCTION

Moving coil tubular linear surface mounted permanent magnet oscillatory machine is a type of a short stroke (15 mm), single-phase linear oscillatory generator (LOG) which operate at fixed resonant frequency (mechanical eigenfrequency = electrical frequency). While there are three main types of linear oscillatory machines (LOMs) or (LOGs), the moving coil as compared to its counterparts; the permanent magnet (PM) mover and the iron mover, has a reduced mover mass as an advantage. Due to this, high frequency oscillations are achieved. With air-coils, LOGs of moving coil type have smaller inductance which lead to larger power factors [1]. Although these machines have lower thrust density, high efficiency and high force density can be achieved according to Amara *et al* [2]. Fixed frequency and stroke length distinguishes linear oscillatory machines from other linear electromagnet machines which have variable frequency and long strokes [3].

Development of analytical models has been pursued due to demand for accurate and quick machine analysis [4]. Polinder *et al* [5] and Bianchi *et al* [6] have used the magnetic equivalent circuit (MEC) method to analyse to develop an analytical model for permanent magnet machines. Although the method they have used is very fast and accurate, it suffers from inaccuracy if there is any large variation in the geometrical parameters. Xu and Chang have proposed an improved MEC for the purpose of optimisation. Still, the improvements could not solve big challenge of MEC [7]. Although finite element method (FEM) is accurate and fast, it is not suitable for design optimization from premature design stages as it takes too long to converge as highlighted by Gysen *et al* [8], Wang *et al* in [9], [10], and others [11], [12], [13].

This paper develops an analytical model using Maxwell equations solutions, a method widely used for its fastness and accuracy and for early machine designs. Similar models have been developed by Wang *et al* (1999) [14],

(2007) [15], [16], Gysen *et al* [8], [17]. However, the models considered are not only for PM mover topologies but also for iron-cored machines. Yan *et al* proposed a model for a similar topology with halbach arrays but with a short coil length and stroke length is not mentioned [18], [19]. Therefore, this paper proposes an analytical model for tubular machine topologies of double layered magnet structure but with longer coils in relation to magnet pole length and air-cored.

2. ANALYTICAL MODEL DEVELOPMENT FOR FIELD DISTRIBUTION DUE TO PERMANENT MAGNETS

Due to the tubular structure of the permanent magnet linear oscillating machine (LOM), cylindrical coordinate system is adopted in the formulation of Laplace and Poisson equations [15]. The development of the analytical model is concentrated on radial magnetization topologies which are air-cored and slot-less. To accommodate analysis of the permanent magnet field distribution of the machine, the model is sub-divided into regions based on their magnetic characteristics. Magnetic vector potential expressions are formulated for each region such that Laplace and Poisson equations are satisfied. Together with boundary conditions applied to separate regions, coefficient solutions are obtained.

The following assumptions are implemented for simplicity of the analytical model:

1. Axial length of the machine is considered infinite so that the field distribution is axi-symmetric and periodic in the z-direction,
2. The armature is slot-less and the stator cores are assumed to have a permeability of 10000 Henry per meter,

3. The relative differential permeability of the permanent magnet is assumed unity ($\mu_r = 1$).

The figure below shows the sub-divisions in which all the five regions are considered to determine the field distribution in the air gap.

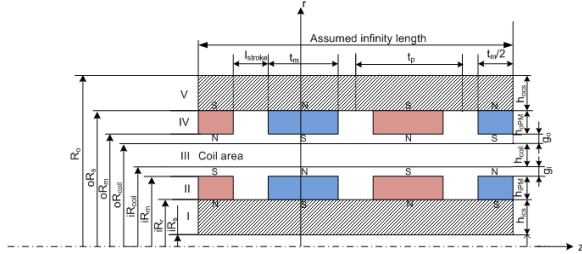


Figure 1: Sub-divisions of LOM

The magnetic field analysis focusses on two main aspects of the machine: the regions consisting of permanent magnets and the regions without them. In this case, regions I, III, and V have the magnetic flux density \mathbf{B} of the form:

$$\mathbf{B} = \mu_0 \mathbf{H} \quad (1)$$

whereas the regions II and IV containing the permanent magnets have \mathbf{B} of the form:

$$\mathbf{B} = \mu_0 \mu_r \mathbf{H} + \mu_0 \mathbf{M} \quad (2)$$

Where \mathbf{H} , \mathbf{M} are the magnetic field strength and magnetisation vector respectively. The magnetisation vector is given by:

$$\mathbf{M} = M_r \mathbf{e}_r + M_z \mathbf{e}_z \quad (3)$$

here M_r, M_z , express the components of r and z coordinates respectively. In this case however, the machine being only radially magnetised will have the magnetisation vector in the radial direction only such that $\mathbf{M} = M_r \mathbf{e}_r$ as shown in the following diagram. In the figure 2 τ_p, τ_m, B_{rem} are

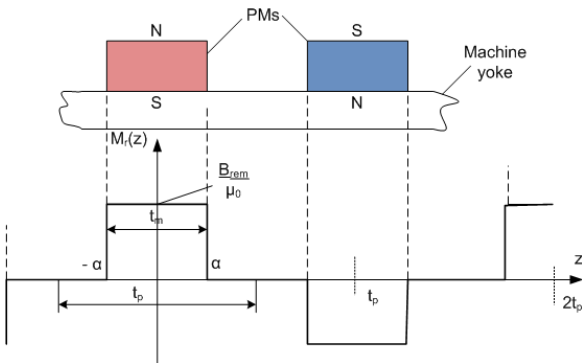


Figure 2: magnetization radial component of the magnetic flux along the axial coordinate

the pole pitch, magnet length and remnant magnetization respectively. M_r can be expressed as a Fourier series expansion by:

$$M_r(z) = \frac{a_0}{2} + \sum_{n=1}^{\infty} a_n \cos(\omega_n z) \quad (4)$$

where $\omega_n = \frac{n\pi}{\tau_p}$ since the period is $2\tau_p$. From the figure displaying the radial component of the field, it is clear that:

$$a_n = \frac{1}{\tau_p} \int_{-\tau_p}^{\tau_p} f(z) \cos(\omega_n z) dz \quad (5a)$$

which is equal to

$$a_n = \frac{2}{\tau_p} \int_0^{\tau_p} f(z) \cos(\omega_n z) dz \quad (5b)$$

after mathematical manipulation and application of trigonometric identities, a_n is obtained as:

$$a_n = \frac{2B_{rem}}{n\pi\mu_0} (1 - (-1)^n) \sin\left(\frac{n\pi\tau_m}{2\tau_p}\right) \quad (6)$$

where $(-1)^n = \cos(n\pi)$ whence,

$$a_{2n-1} = \frac{4B_{rem}}{(2n-1)\pi\mu_0} \sin\left(\frac{(2n-1)\pi\tau_m}{2\tau_p}\right) \quad (7)$$

The value of $M_r(z)$ is therefore equal to:

$$M_r(z) = \frac{a_0}{2} + \frac{4B_{rem}}{\pi\mu_0} \sum_{n=1}^{\infty} \frac{1}{(2n-1)} \sin\left(\frac{(2n-1)\pi\tau_m}{2\tau_p}\right) \cos(m_n z) \quad (8)$$

where $m_n = (2n-1) \frac{\pi}{\tau_p}$

2.1 Governing equations

Governing equations are derived from Maxwell equations. Magnetic vector potential A is used for the development of Laplace and Poisson equations. This is because it may be used in regions where current density J is zero or non-zero. Noting that $\nabla \cdot \mathbf{B} = 0$ and taking into consideration that the divergence of the curl of any vector field is zero.

$$\mathbf{B} = \nabla \times \mathbf{A} \quad (9)$$

As the vector field are related through the permeability μ as displayed in (1) and $\nabla \times \mathbf{H} = \mathbf{J}$ we obtain:

$$\nabla \times \mathbf{B} = \mu \mathbf{J} \quad (10)$$

Inserting (9) into (10) results in:

$$\nabla \times \nabla \times \mathbf{A} = \mu \mathbf{J} \quad (11)$$

This equation represents the axi-symmetric nature of the topology under scrutiny. If the current density $\mathbf{J} = 0$, then the equation (11) becomes a Laplace equation and

represents non-magnet regions of the machine I, III, V ,

$$\nabla \times \nabla \times \mathbf{A} = 0 \quad (12)$$

whereas a Poisson equation is obtained for permanent magnet regions of II, IV of the form:

$$\nabla \times \nabla \times \mathbf{A} = -\mu_0 \nabla \times \mathbf{M} \quad (13)$$

Due to the axi-symmetric nature of the magnetic field distribution of the tubular LOM, the magnetic vector potential A has only the A_ϕ component and therefore, Laplace and Poisson equations with respect to the subdivisions of the machine will appear as follows in cylindrical coordinate system, For the regions I, III, V Laplace equations are:

$$\frac{\partial^2 A_{I\phi}}{\partial z^2} + \frac{\partial^2 A_{I\phi}}{\partial r^2} + \frac{1}{r} \frac{\partial A_{I\phi}}{\partial r} - \frac{1}{r} A_{I\phi} = 0 \quad (14a)$$

$$\frac{\partial^2 A_{III\phi}}{\partial z^2} + \frac{\partial^2 A_{III\phi}}{\partial r^2} + \frac{1}{r} \frac{\partial A_{III\phi}}{\partial r} - \frac{1}{r} A_{III\phi} = 0 \quad (14b)$$

$$\frac{\partial^2 A_{V\phi}}{\partial z^2} + \frac{\partial^2 A_{V\phi}}{\partial r^2} + \frac{1}{r} \frac{\partial A_{V\phi}}{\partial r} - \frac{1}{r} A_{V\phi} = 0 \quad (14c)$$

Poisson equations for permanent magnet regions of II and IV are presented as:

$$\frac{\partial^2 A_{II\phi}}{\partial z^2} + \frac{\partial^2 A_{II\phi}}{\partial r^2} + \frac{1}{r} \frac{\partial A_{II\phi}}{\partial r} - \frac{1}{r} A_{II\phi} = -\mu_0 \nabla \times \mathbf{M} \quad (15a)$$

$$\frac{\partial^2 A_{IV\phi}}{\partial z^2} + \frac{\partial^2 A_{IV\phi}}{\partial r^2} + \frac{1}{r} \frac{\partial A_{IV\phi}}{\partial r} - \frac{1}{r} A_{IV\phi} = -\mu_0 \nabla \times \mathbf{M} \quad (15b)$$

The vector \mathbf{M} being the value described in equation (3) is related to the remnant magnetization by $\mathbf{M} = \frac{B_{rem}}{\mu_0}$. The value of M as determined in equation (8) is key to getting the solution to the Poisson equation as expressed in equation (15) and will be demonstrated later.

2.2 Solution to the Laplace equation

With the application of separation of variables to the Laplace equation of equation (14), the magnetic vector potential is therefore assumed to be $A_{i\phi}(r, z) = R(r)Z(z)$ where i represents the regions I, III , and V . Separation of variables is achieved by replacing A_ϕ into the Laplace equation (14) and dividing by $R(r)Z(z)$. the separated variables must be equivalent to a constant c_k .

$$\frac{1}{Z(z)} \frac{d^2 Z(z)}{dz^2} = - \left[\frac{1}{R(r)} \frac{d^2 R(r)}{dr^2} + \frac{1}{R(r)r} \frac{dR(r)}{dr} - \frac{1}{r^2} \right] = c_k \quad (16)$$

whence,

$$\frac{d^2 Z(z)}{dz^2} - c_k Z(z) = 0 \quad (17a)$$

$$Z'' - c_k Z = 0 \quad (17b)$$

which is a second order linear differential equation and the radial variable is obtained as:

$$r^2 \frac{d^2 R(r)}{dr^2} + r \frac{dR(r)}{dr} + (r^2 c_k - 1)R(r) = 0 \quad (18a)$$

$$r^2 R'' + rR' + (r^2 c_k - 1)R = 0 \quad (18b)$$

The solutions to the separated variables of $R(r)$ and $Z(z)$ depends on the case values of c_k . Three case values are obtained for which solutions are sort for and these are: $c_k = 0, c_k > 0$, and $c_k < 0$. The required solution for A_ϕ from the mentioned cases has to be periodic in z direction. Therefore, the solutions obtained for the case values of $c_k = 0$ and $c_k > 0$ are not periodic in z direction and are thus not considered. The case of $c_k < 0$, taken as $c_k = -k^2$, provides a solution which is periodic in z direction. Replacing c_k with $-k^2$ in equations (17) and (18) gives the general solution as:

$$A_\phi(r, z) = [A_0 I_1(mr) + B_0 K_1(mr)] [C_0 \cos(mz) + D_0 \sin(mz)] \quad (19)$$

which can be rewritten as

$$A_\phi(r, z) = \begin{cases} [E_0 I_1(mr) + F_0 K_1(mr)] \cos(mz) \\ + \\ [G_0 I_1(mr) + H_0 K_1(mr)] \sin(mz). \end{cases} \quad (20)$$

In this solution, m is a real number defined by $k = jm$, whereas I_1, K_1 are Modified Bessel functions of the first and second order respectively.

Due to the fact that the axial component of the magnetic flux density is very minimal on $z = 0$ which means $B_z|_{z=0} = 0$ and also considering that I_1 and K_1 are independent of each other, E_0 and F_0 are taken as zero (0).

Therefore the general solution to Laplace equation is:

$$A_\phi(r, z) = [a_n I_1(mr) + b_n K_1(mr)] \sin(mz). \quad (21)$$

To form a complete series solution, superposition principal is applied while considering that $a_n = G_0$ and $b_n = F_0$ to obtain:

$$A_\phi(r, z) = \sum_{n=1, \dots}^{\infty} [a_n I_1(m_n r) + b_n K_1(m_n r)] \sin(m_n z). \quad (22)$$

This equation is the final equation for the homogeneous solution of Laplace equation.

2.3 Solution to Poisson equation

The Poisson equation (15) has a corresponding homogeneous equation's general solution equivalent to that of Laplace equation shown in equation (22). However the full solution can only be completed when the right side of equation (15) ($\mu_0 \nabla \times \mathbf{M}$) is replaced by the harmonic expansion of the magnetization vector solved in equation

(8). Since

$$\nabla \times M = \frac{\partial M_r}{\partial z} e_\phi \quad (23)$$

The differentiation and multiplication with μ_0 leads to the solution of the whole right side of Poisson equation to be:

$$\nabla^2 A_{\phi j} = \frac{4B_{rem}}{\tau_p} \sum_{n=1}^{\infty} \sin\left(\frac{(2n-1)\pi}{2} \frac{\tau_m}{\tau_p}\right) \sin(m_n z) \quad (24)$$

In this equation j represents the regions *II* and *IV*. The Poisson equation in cylindrical coordinate appears as:

$$\frac{\partial^2 A_\phi}{\partial z^2} + \frac{\partial^2 A_\phi}{\partial r^2} + \frac{1}{r} \frac{\partial A_\phi}{\partial r} - \frac{1}{r} A_\phi = P_n \sin(m_n z) \quad (25)$$

Separation of variables is again applied in a similar way it has been handled for the Laplace equation. With $P_n = \frac{4B_{rem}}{\tau_p} \sin\left[(2n-1)\frac{\pi}{2} \frac{\tau_m}{\tau_p}\right]$, the anticipated result for the Poisson equation is:

$$A_\phi = \sum_{n=1, \dots}^{\infty} [a_n I_1(m_n r) + b_n K_1(m_n r)] \sin(m_n z) + S(r, z) \quad (26)$$

After applying the separation of variables together with mathematical manipulation while taking into consideration that $S(r, z) = R(r)Z(z)$ we obtain the equation for $S(r, z)$ as:

$$S(r, z) = R(r)Z(z) = \frac{\pi L_1(m_n r)}{2m_n^2} P_n \sin(m_n z) \quad (27)$$

where $L_1(x)$ is the solution to the inhomogeneous Bessel's equation and it is a Modified Struve Function according to Bowman [20]. Therefore, the solution to Poisson equation in this case becomes:

$$A_{\phi j} = \sum_{n=1, \dots}^{\infty} [a_n I_1(m_n r) + b_n K_1(m_n r)] \sin(m_n z) + \frac{\pi L_1(m_n r)}{2m_n^2} P_n \sin(m_n z) \quad (28)$$

The magnetic vector potential for all the regions has been obtained following the obtained Laplace and Poisson equations solved and displayed as:

$$A_\phi(r, z) = \begin{cases} \sum_{n=1, \dots}^{\infty} [a_{In} I_1(m_n r) + b_{In} K_1(m_n r)] \sin(m_n z) \\ \sum_{n=1, \dots}^{\infty} [a_{IIIn} I_1(m_n r) + b_{IIIn} K_1(m_n r)] \sin(m_n z) \\ + \frac{\pi L_1(m_n r)}{2m_n^2} P_n \sin(m_n z) \\ \sum_{n=1, \dots}^{\infty} [a_{IIIIn} I_1(m_n r) + b_{IIIIn} K_1(m_n r)] \sin(m_n z) \\ \sum_{n=1, \dots}^{\infty} [a_{IVn} I_1(m_n r) + b_{IVn} K_1(m_n r)] \sin(m_n z) \\ + \frac{\pi L_1(m_n r)}{2m_n^2} P_n \sin(m_n z) \\ \sum_{n=1, \dots}^{\infty} [a_{Vn} I_1(m_n r) + b_{Vn} K_1(m_n r)] \sin(m_n z) \\ + \frac{\pi L_1(m_n r)}{2m_n^2} P_n \sin(m_n z) \end{cases} \quad (29)$$

The coefficients a and b have subscripts *I, II, III, IV, V* which represent the regions of analysis as shown in figure 1.

2.4 Solution to Magnetic Flux Density

The magnetic flux density is calculated from equation (9)

$$B = \nabla \times A = -\frac{1}{r} \frac{\partial r A_\phi}{\partial z} e_r + \frac{1}{r} \frac{\partial r A_\phi}{\partial r} e_z \quad (30)$$

A_ϕ is only a component of ϕ . From the equation (30) it is clear that $B_r = -\frac{\partial r A_\phi}{\partial z}$ and $B_z = \frac{1}{r} \frac{\partial r A_\phi}{\partial r}$. Therefore after differentiating the magnetic vector potential for the r and z results into:

$$B_r = \begin{cases} \sum_{n=1, \dots}^{\infty} -m_n [a_{In} I_1(m_n r) + b_{In} K_1(m_n r)] \cos(m_n z) \\ \sum_{n=1, \dots}^{\infty} -m_n \{ [a_{IIIn} I_1(m_n r) + b_{IIIn} K_1(m_n r)] \cos(m_n z) \\ + \frac{\pi L_1(m_n r)}{2m_n^2} P_n \cos(m_n z) \} \\ \sum_{n=1, \dots}^{\infty} -m_n [a_{IIIIn} I_1(m_n r) + b_{IIIIn} K_1(m_n r)] \cos(m_n z) \\ \sum_{n=1, \dots}^{\infty} -m_n \{ [a_{IVn} I_1(m_n r) + b_{IVn} K_1(m_n r)] \cos(m_n z) \\ + \frac{\pi L_1(m_n r)}{2m_n^2} P_n \cos(m_n z) \} \\ \sum_{n=1, \dots}^{\infty} -m_n [a_{Vn} I_1(m_n r) + b_{Vn} K_1(m_n r)] \cos(m_n z) \end{cases} \quad (31)$$

The values of the magnetic flux density in the radial direction can only be obtained and used after obtaining the coefficients. Boundary equations have to be applied in order to achieve the required results. The equations for the axial direction for the magnetic flux density B_z are obtained after differentiation and results into:

$$B_z = \begin{cases} \sum_{n=1, \dots}^{\infty} m_n [a_{In} I_0(m_n r) - b_{In} K_0(m_n r)] \cos(m_n z) \\ \sum_{n=1, \dots}^{\infty} m_n \{ [a_{IIIn} I_0(m_n r) - b_{IIIn} K_0(m_n r)] \cos(m_n z) \\ + \frac{\pi L_0(m_n r)}{2m_n^2} P_n \cos(m_n z) \} \\ \sum_{n=1, \dots}^{\infty} m_n [a_{IIIIn} I_0(m_n r) - b_{IIIIn} K_0(m_n r)] \cos(m_n z) \\ \sum_{n=1, \dots}^{\infty} m_n \{ [a_{IVn} I_0(m_n r) - b_{IVn} K_0(m_n r)] \cos(m_n z) \\ + \frac{\pi L_0(m_n r)}{2m_n^2} P_n \cos(m_n z) \} \\ \sum_{n=1, \dots}^{\infty} m_n [a_{Vn} I_0(m_n r) + b_{Vn} K_0(m_n r)] \cos(m_n z) \end{cases} \quad (32)$$

Dirichlet and discontinuous Boundary conditions are applied between the boundaries of the the machine displayed in figure 1 so as to obtain the values of the coefficients in equations (29), (31) and (32). The boundary condition applied are:

$$\begin{aligned} A_I|_{r=R_s} &= 0 & A_V|_{r=R_o} &= 0 \\ B_{rI}|_{r=iR_r} &= B_{rII}|_{r=iR_r} & H_{zI}|_{r=iR_r} &= H_{zII}|_{r=iR_r} \\ B_{rII}|_{r=iR_m} &= B_{rIII}|_{r=iR_m} & H_{zII}|_{r=iR_m} &= H_{zIII}|_{r=iR_m} \\ B_{rIII}|_{r=oR_m} &= B_{rIV}|_{r=oR_m} & H_{zIII}|_{r=oR_m} &= H_{zIV}|_{r=oR_m} \\ B_{rIV}|_{r=oR_s} &= B_{rV}|_{r=oR_s} & H_{zIV}|_{r=oR_s} &= H_{zV}|_{r=oR_s} \end{aligned} \quad (33)$$

The magnetic flux density is related with the magnetic field intensity as:

$$\mathbf{H} = \frac{\mathbf{B}}{\mu} \quad (34)$$

Upon application of the boundary equation ten simultaneous equations are formed and the coefficients are solved through a matrix of the form:

$$\begin{bmatrix} I_1(m_n i R_s) & \cdot & \cdot & \cdot & \cdot & \cdot & \cdot & \cdot & \cdot & \cdot \\ I_1(m_n i R_r) & \cdot & \cdot & \cdot & \cdot & \cdot & \cdot & \cdot & \cdot & \cdot \\ I_0(m_n i R_r) & \cdot & \cdot & \cdot & \cdot & \cdot & \cdot & \cdot & \cdot & \cdot \\ \cdot & \cdot & \cdot & \cdot & \cdot & \cdot & \cdot & \cdot & \cdot & \cdot \\ \cdot & \cdot & \cdot & \cdot & \cdot & \cdot & \cdot & \cdot & \cdot & \cdot \\ \cdot & \cdot & \cdot & \cdot & \cdot & \cdot & \cdot & \cdot & \cdot & \cdot \\ \cdot & \cdot & \cdot & \cdot & \cdot & \cdot & \cdot & \cdot & \cdot & \cdot \\ \cdot & \cdot & \cdot & \cdot & \cdot & \cdot & \cdot & \cdot & \cdot & \cdot \\ \cdot & \cdot & \cdot & \cdot & \cdot & \cdot & \cdot & \cdot & \cdot & \cdot \\ \cdot & \cdot & \cdot & \cdot & \cdot & \cdot & \cdot & \cdot & \cdot & \cdot \end{bmatrix} \begin{bmatrix} a_{In} \\ b_{In} \\ a_{IIIn} \\ b_{IIIn} \\ a_{IVIn} \\ b_{IVIn} \\ a_{Vn} \\ b_{Vn} \end{bmatrix} = \begin{bmatrix} 0 \\ \frac{\pi L_1(m_n i R_r)}{2m_n^2} P_n \\ \mu_I \frac{\pi L_0(m_n i R_r)}{2m_n^2} P_n \\ -\frac{\pi L_1(m_n i R_m)}{2m_n^2} P_n \\ -\frac{\pi L_0(m_n i R_m)}{2m_n^2} P_n \\ \frac{\pi L_1(m_n o R_m)}{2m_n^2} P_n \\ \frac{\pi L_0(m_n o R_m)}{2m_n^2} P_n \\ -\frac{\pi L_1(m_n o R_s)}{2m_n^2} P_n \\ -\mu_V \frac{\pi L_0(m_n o R_s)}{2m_n^2} P_n \\ 0 \end{bmatrix} \quad (35)$$

The final solution of the magnetic vector potential and the magnetic flux densities are obtained by replacing the calculated coefficients ($a_{In}, a_{IIIn}, a_{IVIn}, a_{Vn}$) and ($b_{In}, b_{IIIn}, b_{IVIn}, b_{Vn}$) into the equations (29), (31) and (32) to get the particular solution for particular domains or regions of the machine for a number of harmonic order. The magnitude of the magnetic flux density can be obtained from:

$$B(r, z) = \sqrt{B_r^2(r, z) + B_z^2(r, z)} \quad (36)$$

Since this equation provides us with the total flux density, the graph plot of the equation shows the peak value of the total flux density obtained.

3. VALIDATION OF OPEN CIRCUIT MODEL WITH FINITE ELEMENT METHOD(FEM)

The 2-D analytical model developed has been compared with finite element method (FEM) for particular dimensions of the linear double layered permanent magnet oscillating machine topology. Neodymium Iron Boron 48/11 magnets with $B_{rem} = 1.39[T]$ and $\mu_r = 1.04$ were adopted for both the analytical model and FEM. It should be noted that $\mu_r = 1$ was the assumed value for the magnets.

Periodic boundary conditions are used at the axial boundaries of the finite element model as well as continuous boundary conditions have been adopted between the stator and armature for desired solutions. Since the topology under study is a slot-less, coil-mover linear oscillatory machine, with surface mounted radially magnetised permanent magnets, the developed analytical model can only apply to such topologies. The figures below show the comparison of results from analytical model and FEM in the permanent magnets, both lower and upper and in the air-gap. As can be seen from the figures below, the analytical model compares well with finite element results.

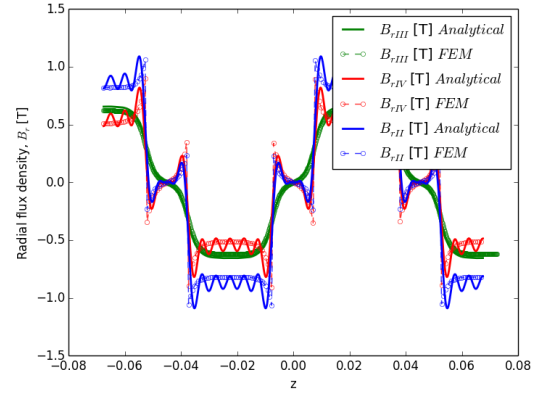


Figure 3: Radial component of flux density comparison as a function of z at $r = (iR_m + oR_m)/2$ is B_{rIII} in green (air-gap), at $r = (iR_r + iR_m)/2$ is B_{rII} in blue (inner PMs) and at $r = (oR_r + oR_m)$ is B_{rIV} in red (outer PMs)

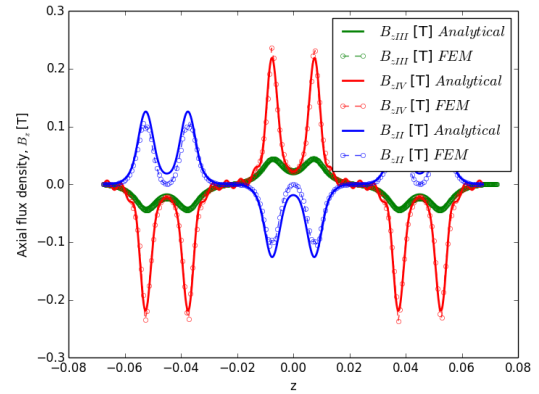


Figure 4: Axial component of flux density comparison as a function of z at $r = (iR_m + oR_m)/2$ is B_{zIII} in green (air-gap), at $r = (iR_r + iR_m)/2$ is B_{zII} in blue (inner PMs) and at $r = (oR_r + oR_m)$ is B_{zIV} in red (outer PMs)

4. DISCUSSION

The figures shown above display the radial (figure 3) and axial (figure 4) flux density distributions in the air-gap and in the both layers of permanent magnets. Considering that the model uses the $(2n - 1)th$ harmonic, it is observed that upto the 17th harmonic, the model operates excellently well. However, over the 17th harmonic the model begins to struggle. Nevertheless, this challenge is very particular to Bessel functions in cylindrical coordinate system on which coefficient (a_n, b_n) scaling techniques cannot be applied [8]. The effects of a finite number of harmonics can be well observed in the radial flux densities especially in the PMs. Therefore, for better results, the 17th harmonic is recommended.

5. CONCLUSION

The analytical model has for the open-circuit magnetic field distribution has been successfully developed for a class of radially magnetised tubular linear permanent magnet oscillating machines. This model is ideal as a design tool for design optimisation and also for comparative studies. The model is further used to determine thrust force, flux-linkages and EMF for performance analysis which has not been shown in this paper. The model is validated with 2-D finite element analysis and results show that the analytical model agrees very well with those of finite element method.

ACKNOWLEDGEMENT

The Author would like to thank the Africa for Innovation, Mobility, Exchange, Globalization and Quality (AFIMEGQ) and the Copperbelt University for sponsorship.

REFERENCES

- [1] I. Boldea, Linear Electric Machines, Drives, and MAGLEVs *Handbook*. CRC Press, Taylor and Francis Group, 2013.
- [2] Y. Amara, G. Barakat, and P. Reghem, "Armature Reaction Magnetic Field of Tubular Linear Surface-Inset Permanent-Magnet Machines", *IEEE Trans. Magn.*, vol. 47, no. 4, pp. 805811, 2011.
- [3] I. Boldea and S. A. Nasar, "Linear electric actuators and generators, *IEEE Trans. Energy Convers.*, vol. 14, pp. 712717, 1999.
- [4] Y. Amara and G. Barakat, "Analytical modeling of magnetic field in surface mounted permanent-magnet tubular linear machines, *IEEE Trans. Magn.*, vol. 46, pp. 38703884, 2010.
- [5] H. Polinder, J. G. Sloopweg, J. . Compter, and M. . Hoeijmakers, "Modelling a linear PM motor including magnetic saturation, *IEEE Power Electronics, Machines and Drives*, 2002.
- [6] N. Bianchi, S. Bolognani, and F. Tonel, "Design Criteria of a Tubular Linear IPM Motor, *IEEE Trans. Ind. Electron.*, vol. 3, pp. 17, 2001.
- [7] Z. Xu and S. Chang, "Improved moving coil electric machine for internal combustion linear generator, *IEEE Trans. Energy Convers.*, vol. 25, no. 2, pp. 281286, 2010.
- [8] B. L. J. Gysen, K. J. Meessen, J. J. H. Paulides, and E. A. Lomonova, "General Formulation of the Electromagnetic Field Distribution in Machines and Devices Using Fourier Analysis, *Magn. IEEE Trans.*, vol. 46, pp. 3952, 2010.
- [9] J. Wang, D. Howe, and G. W. Jewell, "Fringing in Tubular Permanent-Magnet Machines : Part I . Magnetic Field Distribution , Flux Linkage , and Thrust Force, *IEEE Trans. Magn.*, vol. 39, no. 6, pp. 35073516, 2003.
- [10] J. Wang, Z. Lin, and D. Howe, "Analysis of a short-stroke , single-phase , quasi-Halbach magnetised tubular permanent magnet motor for linear compressor applications, *IET Electr. Power Appl.*, vol. 2, no. January, pp. 193200, 2008.
- [11] H. Tiegna, Y. Amara, and G. Barakat, "Overview of analytical models of permanent magnet electrical machines for analysis and design purposes, *Math. Comput. Simul.*, vol. 90, pp. 162177, 2013.
- [12] X. Chen, Z. Q. Zhu, and D. Howe, "Modeling and Analysis of a Tubular Oscillating Permanent-Magnet Actuator, *IEEE Trans. Ind. Appl.*, vol. 45, 2009.
- [13] H. Tiegna, A. Bellara, Y. Amara, and G. Barakat, "Analytical modeling of the open-circuit magnetic field in axial flux permanent-magnet machines with semi-closed slots, *IEEE Trans. Magn.*, vol. 48, no. 3, pp. 12121226, 2012.
- [14] J. Wang, G. W. Jewel, and D. Howe, "A general framework for the analysis and design of tubular linear permanent magnet machines, *IEEE Trans. Magn.*, vol. 35, no. 3, pp. 19862000, May 1999.
- [15] J. Wang, D. Howe, and Z. Lin, "Comparative study of winding configurations of short-stroke , single phase tubular permanent magnet motor for refrigeration applications, *Ind. Appl. Conf. 2007. 42nd IAS Annu. Meet. Conf. Rec. 2007 IEEE*, pp. 311318, 2007.
- [16] J. Wang, D. Howe, and Z. Lin, "Comparative studies on linear motor topologies for reciprocating vapor compressors, in *Proceedings of IEEE International Electric Machines and Drives Conference, IEMDC 2007, 2007*, vol. 1, pp. 364369.
- [17] B. L. J. Gysen, E. A. Lomonova, J. J. H. Paulides and A.J.A Vandenput, "Analytical and Numerical Techniques for Solving Laplace and Poisson Equations in a Tubular Permanent-Magnet Actuator :, *IEEE Trans. Magn.*, vol. 44, no. 7, pp. 17511760, 2008.
- [18] L. Yan, I. Chen, and C. K. Lim, "Magnetic Field Modeling of Linear Machines with, *fluid power mechatronics, IEEE*, pp. 16, 2011.
- [19] L. Yan, L. Zhang, T. Wang, Z. Jiao, C. Chen, and I. Chen, "Magnetic Field of Tubular Linear Machines, *Prog. Electromagn. Res.*, vol. 136, no. November 2012, pp. 283299, 2013.
- [20] F. Bowman, "Introduction to Bessel Functions," *Handbook*. Longmans, Green and Co., 1938.

DESIGNING A 750 W IRONLESS STATOR FOR AN AXIAL FLUX PERMANENT MAGNET WIND GENERATOR

N.J. Baker and A.J. Grobler

Abstract: This paper presents the design and analysis of axial flux permanent magnet machine for small-scale power generation. Stator needs to be designed and manufactured since most of the components for the machine is supplied by the North-West University. Due to unconventional flux distributions in this machine, a 3-D finite element method was employed for the design of the stator. The design of the stator has been validated by experimental results from an experimental AFPM machine prototype.

Key words: Axial Flux Permanent Magnet Machine(AFPM)

1. INTRODUCTION

The increasing demand for electricity has led to more pollution. With the increasing pollution of greenhouse gas emissions, consumers have become more concerned for the environment. The concerns for the environment has led to renewed interest in renewable energy sources. Due to the millions of tons of fossils fuels that is burned every day this results into damaging the environment. Renewable energy source is energy made from a source without polluting the environment and is an unlimited source of energy.

Wind energy well suited for small scale power generation. One of the benefits of using a wind generator, is that it only takes up a small plot of land. Wind generators use the kinetic power of wind to generate electricity. This energy is an unlimited and sustainable energy source. The increasing interest in renewable energy sources increased the use of axial flux and radial flux permanent magnet machines. The AFPM generators flux flow in an axial direction through the air-gap, parallel to the axis and the RFPM generators flux flow in a radial direction through the air-gap, perpendicular to the axis.

The AFPM machine is becoming a more attractive alternative as to the RFPM machine due to its flat shape, compact construction and high power density [1]. AFPM machine is also known as a disc-type machine. These machines are best suited for small to medium power generators and for low speed applications due to a large number of poles that can be constructed on the stator of the machine [1]. Due to the fact that a large number poles can be accommodated on the machine the required frequency in this case 50Hz can be easily generated at low speeds. With this larger number poles there will be no need for a gearbox and this decreases the total cost of the machine [2].

There consist a number topologies for an AFPM generator. Figure 1 illustrate the different typologies available for this machine type:

From Figure 1 it can be seen that there are three catagories that an AFPM machine can be devided in. Since the rotor of the machine is already manufactured. It limited the

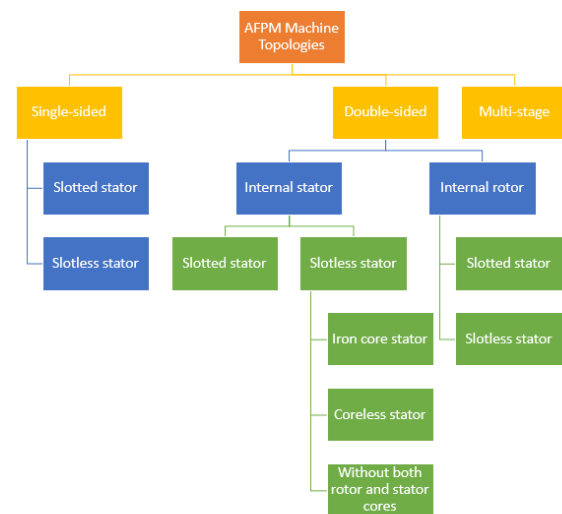


Figure 1: Topologies available for an AFPM generator

topology only to double-sided rotor with a single internal stator. The designing of a new improved stator using the existing stator is the aim of this project.

Sizing equations, 2-D FEMM and 3-D FEMM simulations is used to design the stator. The results of the simulations and experimental results is compared. 3-D FEMM simulation is used to determine the flux leakage and the results is used to do some alterations on the rotor.

In Section 2 the design of the stator is discussed, followed by the simulations presented in Section 3. Section 4 is a summary of implementation and evaluation of the work presented in this article.

2. MACHINE DESIGN

2.1 Topology

From Figure 1 the available stator designs for the generator are:

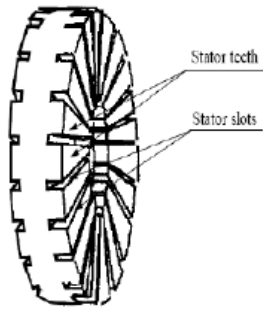


Figure 2: Slotted Core

- Slotted Iron Core
- Slotless Iron Core
- Ironless Stator

Slotted Iron Core:

The slotted stator mechanical airgap is small since the windings are wound between the slots. This allows for higher magnetic loading and the use of thinner magnets. The drawback of the design is that the teeth of the slotted stator have iron losses, can have high cogging torque and saturate at high magnetic densities [3].

Figure 2 shows the iron core of a slotted topology.

Slotless Iron Core:

The drawbacks of the slotted stator can be eliminated by using a slotless stator design. The slotless design uses a toroidal core without stator slots which makes the construction of the stator simpler [3]. But slotless stators require a large magnetic air-gap which will lead to larger magnets. The windings on the slotless stator are directly exposed to the magnets on the rotor which results in higher eddy-current losses in the conductors.

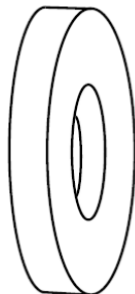


Figure 3: Slotless Core

Coreless Stator:

The slotted and slotless stators make use of an magnetic core where the windings are wound around them. That

makes the losses and the weight of the the AFPM machine higher [4]. The coreless stator can eliminate these disadvantages, because the stator is only made of copper windings which is moulded into a single using fiberglass and epoxy resin. Since an coreless stator is made of non-magnetic materials the magnetic reluctance forces between the rotor and stator can be eliminated [5]. It is difficult to keep the stator cooled to minimize the losses which make it a disadvantage for an coreless stator.

From this research a trade-off study is done and from the matrix it was chosen to design an coreless stator. The criteria used for the decision matrix are cost, simplicity of construction and efficiency.

2.2 Windings

Coreless stator windings is where the stator only consists of windings which is moulded in a structure. These windings usually consist of a number of single layer trapezoidal shaped coils that can be overlapping or non-overlapping [6]. In overlapping stator windings the end windings of the coils overlap each other. Bending of end windings will be required for overlap windings which will require more space between the rotor discs. Non-overlapping windings is placed next to each other on the same plane [5]. No bending of end windings will be required required in non-overlapping windings which makes the constructions of these coils simpler [7]. Figure 4 show examples of overlapping and non-overlapping windings [8].



Figure 4: (a) Overlapping windings and (b) Non-overlapping windings

Non-overlap windings is used in the design of the stator. Since results in smaller end windings.

2.3 Sizing Equations

The sizing equation for coreless stator, given by equation 1 was used to determine the total turns per coil for a desired voltage. The following assumptions are made for using the sizing equations:

- The power rating for the generator are known
- N_1 is the turns per stator phase group.
- e_f is the back EMF of one stator winding.

EMF induced in the stator at no-load:

Table 1: Machine Parameters

Variable	Value
Induced voltage (E_f)	160 V
Rotational speed (n_s)	400 r/min
Number of poles (p)	16
Diameter ratio	0.4
Outer diameter	25
Magnetic flux density (B_{mg})	0.5 T

$$e_f = 2\pi f N_1 k_{w1} \phi_f \cos(\omega t) \quad (1)$$

where:

N_1 is the total turns for stator, f - frequency, k_{w1} - constant, ϕ_f - maximum magnetic flux.

The rms value is expressed by dividing the peak EMF (e_f) by $\sqrt{2}$:

$$E_f = \pi \sqrt{2} f N_1 k_{w1} \phi_f \quad (2)$$

3. SIMULATION

In this section the design for stator is done. The number of turns per coil and magnetic air-gap is determine using the sizing equations that are discussed in Section 2.

3.1 Coil design

Copper wire of 1 mm in diameter is used for the design of the stator. The current capacity of $6A/mm^2$ is used for copper. This gives a rated current of 4.7 A. It was decided a rated power of 750 W need to be generated, which will need a voltage of 160 V.

The rotor of the machine has 16 pole pairs and the permanent magnets are aligned the conventional N-S magnet array. Alternative from the conventional array is the Halbach array. In the Halbach array magnetization vector of permanent magnets should rotate as a function of distance along the array. Implementing the Halbach array the backiron of the rotor can be eliminated and total weight of the machine will be less. The Halbach array wasn't implemented because to implement partailly Halbach will not have a large effect on the output voltage.

Table 1 shows the parameters of the machine. Since the rotor is symmetrical only four of the poles will be used in the 2-D FEMM simulation as seen in Figure 5. Airgap simulation is done to get total flux that is going to move through each coil. This flux is used in the sizing equations to determine the number of coils needed for the desired voltage.

The simulation was repeated for variations in air-gap lengths to determine the number of coils needed to produce

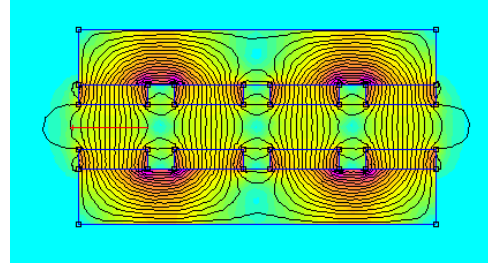


Figure 5: Air-Gap Simulation

a voltage of 160V at a rotation speed of 400 rpm. FEMM simulation is ideal for calculating the magnetic flux densities that will flow through the coil but it difficult to calculate the flux leakages in the machine. From the results of the simulation it was calculated that only 40 turns per coil is needed for the desired output voltage.

3.2 Flux Leakages

Since the rotor of the machine is already constructed certain components of the rotor are investigated and discussed in detail to design the stator for the machine. It is difficult to model the leakage flux in a 2D simulation package. Thus, a 3D model is created and imported in COMSOL[®] to see which changes can be made to the machine to minimize the flux leakage. Figure 6 shows the model used for the 3D simulation.

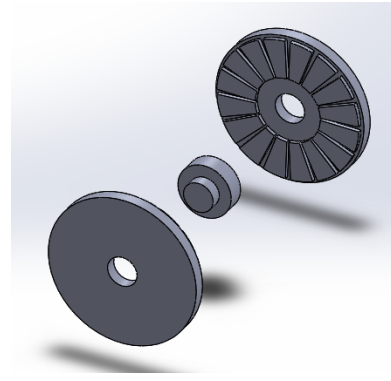


Figure 6: Explosion view of 3-D FEMM model

From the results of the simulations it was seen that the sleeve of the machine create the most of the flux leakages in the machine. The sleeve of the machine is the part that holds the two back-irons together and to keep the mechanical airgap at desired lenth. The following graphs shows amount of flux that flows into the sleeve. Figure 7 is the flux leakage created by the iron sleeve.

Figure 8 is the flux leakage created by sleeve with an non-magnetic material such as aluminium.

From these results, it can be seen using a mild steel sleeve will have a large effect on the flux leakages. Using an aluminum sleeve will result in a 42% decrease in flux

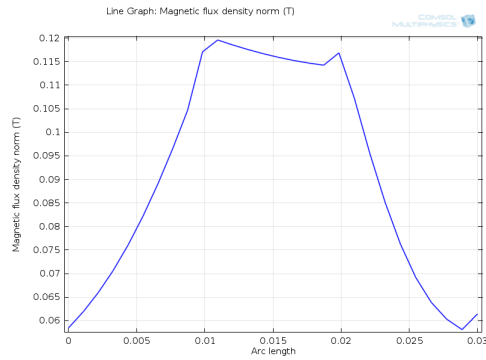


Figure 7: Line graph of flux leakage to the iron sleeve

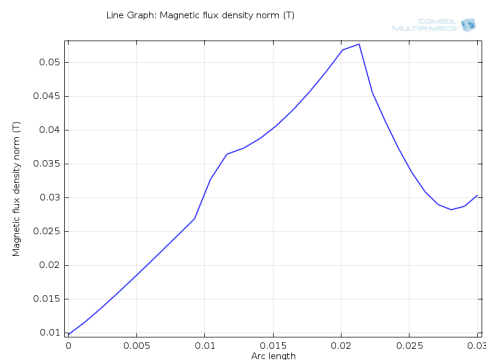


Figure 8: Line graph of flux leakage to the aluminium sleeve

leakages. From this results, it was decided to use a non-magnetic material for the construction of the sleeve.

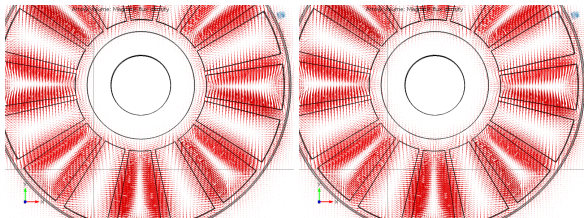


Figure 9: (a) Rotor with iron sleeve and (b) Rotor without iron sleeve

In Figure 9 flux lines can be observed over the sleeve. This result is taken by cutting the sleeve in half. In the first figure, it can be seen that the flux lines is cutting the sleeve. This results in a flux leakage of 0.12T that is seen in Figure 7. Fewer flux lines are cutting the sleeve in the second Figure, which is also seen in the Figure 8.

3.3 Final Simulation

Since a new sleeve needs to made from aluminum, the air-gap will be reduced to 12mm to increase the flux density that will decrease the number of turns. Since most of the flux leakages was created by the sleeve, a 2D simulation will be used to determine the voltage of the different coils. FEMM 4.2 simulation software is used to determine the induced voltage of each coil.

Figure 10 is the output of the simulation. The red line between the magnets is used to determine the magnetic flux at the given point in the simulation. The Lua script is used to move the coil 5 mm increments through the rotor to save the data to a csv file. Then the sizing equations are used the determine the induced voltage of each coil.

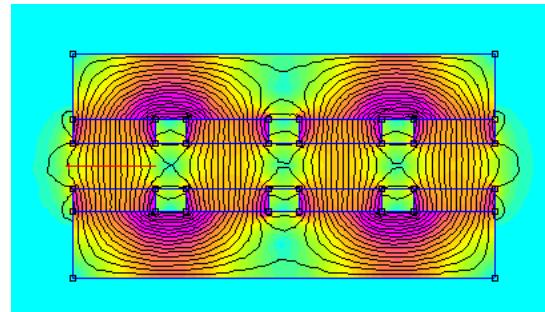


Figure 10: 12mm Air-Gap simulation

30 Turns:

Figure 11 illustrates the induced voltage of a single coil with 30 turns. From these results it can be seen that 9.5 V can be induced with a single coil with 30 Turns.

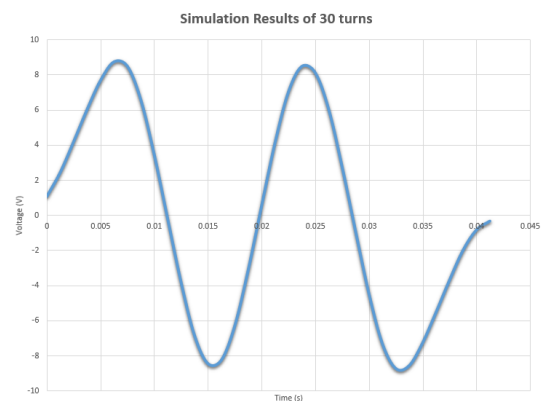


Figure 11: 30 Turns induced voltage

40 Turns:

Figure 12 illustrates the induced voltage of a single coil with 40 turns. From these results it can be seen that 10.5 V can be induced with a single coil with 40 Turns.

4. IMPLEMENTATION AND EVALUATION

4.1 Alteration on rotor

The aluminum sleeve was constructed with the specified air gap of 12mm. Tests were done using the previously iron sleeve and the new sleeve to determine the flux density improvement in the machine.

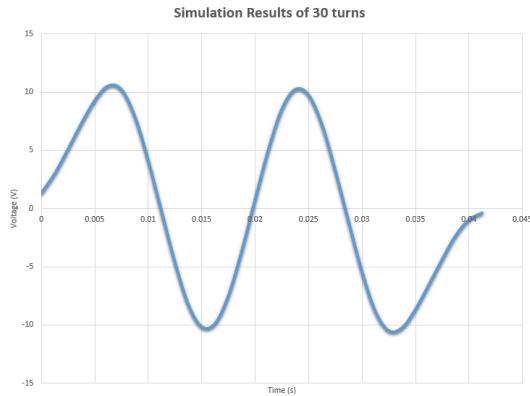


Figure 12: 40 Turns induced voltage



Figure 13: Aluminium sleeve

Figure 14 shows the practical results of the flux measured over the magnet using a fluxmeter Hirst Magnetics GM08. This testing was done to validate the 3D simulation in compiled in COMSOL[®]. The rotor discs are placed over each and the probe of the meter is moved between one of the magnets pair with increments of 0.5 cm.

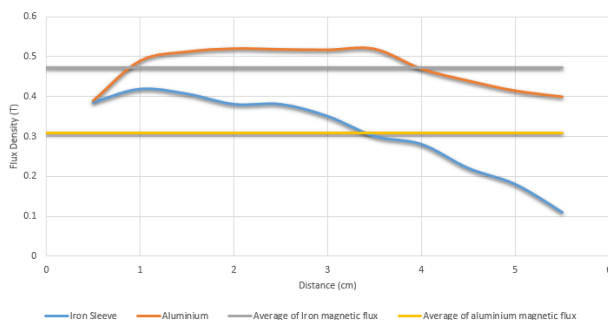


Figure 14: Practical results of flux measurements

The average of the magnetic flux of each graph is plotted and a difference of 0.16 T is achieved that increased the flux density with 40%. Since these results corresponded with the simulation, most of the leakages is eliminated, and the design of the stator in a 2D simulation is sufficient.

4.2 Stator construction

The complete stator is wound with all 16 coils in series; the direction of each coil is alternated to ensure that the

induced voltage of each coil is added to each other. Each coil has 40 turns. The complete stator can be seen in Figure 15.



Figure 15: Complete Stator

The complete stator were placed in a mold where the epoxy resin is added to create a single unit and keeping the coils in position. Three aluminum mounting plates are added to the structure of the mold to prevent movement during operation of the machine. The coils were then compressed in the axial direction using two iron plates and four g-clamps. Figure 16 shows the structure used to achieve a stator with a thickness of 9 mm.

Cable ties are used to prevent the coils from moving when their are pressed in the structure. Fiberglass also added to the epoxy resin to reinforce the stator. The stator is kept in this mold with epoxy resin for three days to ensure the epoxy is set fully. Shoe polish was used to prevent the epoxy from sticking to the mold. From this process, the final stator is manufactured and can now be implemented on the machine for testing. Final stator is shown in Figure 17



Figure 16: Pressed epoxy structure

4.3 Test Setup

The stator is tested using an experimental AFPM machine prototype that is rotated by a DC motor where a fan belt is used as coupling device. This setup was chosen since it is best method where speed control can be applied and eliminate alignment problems.

The speed of the motor or generator is monitored using a tachometer. Tie-Pie scopes are used to evaluate the



Figure 17: Final Stator

induced voltage and current of the generator. Figure 18 show a photo of the setup for testing.



Figure 18: Test-Setup

4.4 Final Results

No-Load Test: Figure 19 shows the output voltage of the generator at a rated speed of 400 r/min which generate a frequency of 53.3 Hz since the machine is a 16 pole machine. The peak induced voltage of the generator is 160V, which corresponded with expectations of the simulation of the single coils. The output of the generator is increased with the increasing the rotational speed of the machine. But the speed of the machine is limited by the mechanical structure of the machine.

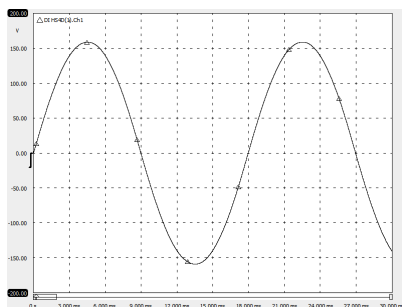


Figure 19: Induced Voltage at no-load

Figure 20 shows the results of the induced voltage at different speeds.

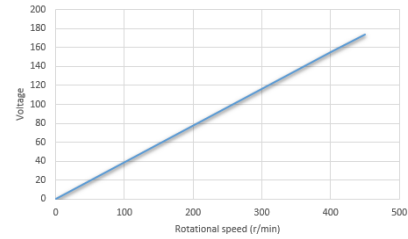


Figure 20: Rotational speed vs. Induced Voltage

Load-Test:

The generator is connected to a load to examine the power output capabilities of the machine. The variable load is used for testing to determine the maximum power output of the generator. The induced voltage decreases as the current increases since the increasing current has an influence on the flux density.

In Figure 21 the effect of the current on the voltage can be seen.

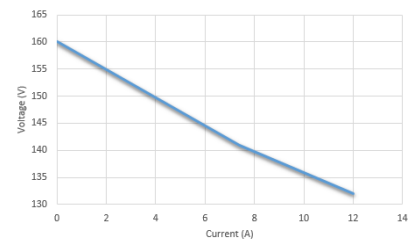


Figure 21: Current vs. Generator Terminal Voltage

The rated power of the machine is easily achieved, and the machine can continuously deliver this power. Figure 22 illustrated voltage and current of the generator at rated load. The output of 795W is achieved at rated conditions.

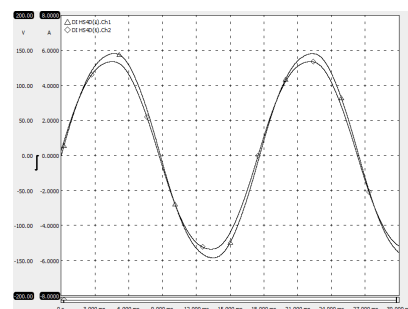


Figure 22: Rated Power of generator

4.5 Performance Evaluation

The performance of the generator is tested by changing the load thus examining the power capabilities of the machine. Figure 23 shows the power and voltage regulation of the generator at various currents.

The maximum power of 1.58kW is achieved at 12A, the voltage regulation at this point is 16.5%.

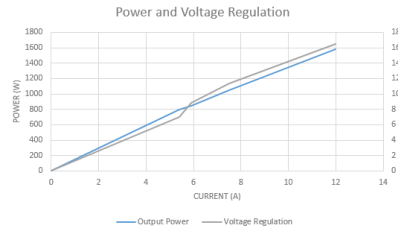


Figure 23: Maximum Power vs Voltage regulation

5. CONCLUSION

The rated power of the machine is achieved by a voltage regulation of 6.4%. The induced voltage of the machine has a close to sinusoidal form. The results of the 3D and 2D simulations corresponded with the practical results of the generator. The single coils help to verify if the simulation and the sizing equations used for the design of the stator are done correctly. From these results the rated power of the generator was easily achieved and the generator is capable of delivering double the power rating of the stator if extra cooling methods is added to the machine. A maximum power of 1.5kW was achieved from the final stator. From these results, it can be seen that the design of the stator was successful.

REFERENCES

- [1] S. O. Ani, H. Polinder, and J. A. Ferreira, "Low cost axial flux PM generator for small wind turbines," in *Energy Conversion Congress and Exposition (ECCE)*, 2012 IEEE, Sep. 2012, pp. 2350–2357.
- [2] S. Ani, H. Polinder, and J. Ferreira, "Energy yield of two generator systems for small wind turbine application," in *Electric Machines Drives Conference (IEMDC)*, 2011 IEEE International, May 2011, pp. 735–740.
- [3] G. S. Liew, "Analysis, design of singled-sided Slotted AMM AFPM," *PhD Disseration*, no. August, 2009.
- [4] J. F. Gieras, R.-J. Wang, and M. J. Kamper, *Axial Flux Permanent Magnet Brushless Machines*, 2004.
- [5] S. Lomheim, "Analysis of a Novel Coil Design for Axial Flux Machines," no. June, pp. 16–21, 2013.
- [6] J. Colton, D. Patterson, and J. Hudgins, "Design of a Low-Cost and Efficient Integrated Starter-Alternator," pp. 357–361.
- [7] M. J. Kamper, R. J. Wang, and F. G. Rossouw, "Analysis and performance of axial flux permanent-magnet machine with air-cored nonoverlapping concentrated stator windings," *IEEE Transactions on Industry Applications*, vol. 44, no. 5, pp. 1495–1504, 2008.
- [8] F. Giulii Capponi, G. De Donato, and F. Caricchi, "Recent advances in axial-flux permanent-magnet machine technology," *IEEE Transactions on Industry Applications*, vol. 48, no. 6, pp. 2190–2205, 2012.

Method for Assessing the Thermal Performance of a Synchronous Generator Rotor

A. Narain Singh^{1*}, W. Doorsamy¹ and W. A. Cronje¹

¹University of the Witwatersrand, 1 Jan Smuts Avenue, Braamfontein 2000, Johannesburg, South Africa

*Email: amesh.singh@eskom.co.za

Abstract: This paper presents a methodology and experimental setup for physically mapping the temperature profile of the surface of a generator rotor. Infrared thermography is used to acquire the profiles of both the rotor body as well as the winding temperature. Heat maps are generated using the measurements obtained under different test conditions. The presented methodology and analysis of the experimental results of this test setup will aid in better understanding the phenomena of generator rotor thermal instability.

1 INTRODUCTION

Thermally induced imbalances of a generator rotor experienced during operation can lead to excessive mechanical vibration that far exceeds the operating limits of the rotor [1]. The result of which is a tripped unit and the loss of generating capacity, and a rather difficult fault finding process to identify and correct the cause of the thermally induced vibration. This condition is commonly referred to as rotor thermal instability.

Throughout the years many utilities world-wide have tried to perform Thermal Instability Testing (TIT) at specially designed balancing facilities to be able to determine the thermal behaviour of the rotor. This testing is generally performed after any major refurbishment work has been conducted on the rotor i.e. rewind, slot liner replacements, major overhaul, retaining ring replacement etc.

Two main testing methods are used world-wide: 1) Direct current injection into the rotor winding and, 2) Windage or friction heating. Different utilities prefer specific tests based on their own propriety experiences. The variations in methodology and lack of published data supporting either of the aforementioned tests creates uncertainty as to which test is able to best detect any latent thermal imbalances within the rotor assembly [2].

This paper presents a method which maps the thermal distribution of a rotor under different test conditions. A direct thermal mapping of the rotor body is presented using a scale model of a 600 MW generator rotor. This physical and practical approach is used as opposed to any simulations. The complex construction of the rotor makes a simulation approach very difficult

as the computer processing power at present is limited. This practical approach of physical measurement is beneficial as a basis to determine exactly what the thermal distribution of the rotor is and how it behaves during different sources that induce a temperature rise in the rotor. This will assist in determining which tests are better suited to detecting rotor thermal instability.

2 BACKGROUND

The generator rotor is a highly stressed component. The rotor is composed of a number of different materials such as copper, diverse insulation materials, steel, aluminium etc. The properties of these materials may vary drastically from each other in material strength; coefficient's of friction; coefficients of expansion and thermal conductivity, just to name a few. This unique composition of materials and properties have to interact harmoniously for the rotor to be able to perform its primary function within design limits [3].

Taking into account the distinctive design of the generator rotor a computer generated model will require a great amount of detail. Once this is achieved the processing power required to simulate the thermal performance of the rotor may not be readily available. More readily available sources of processing power will eventually result in the model needing to be simplified. The simulation will eventually lose accuracy and the results may not be indicative of the true performance of the rotor.

Current practices rely on a calculation to be able to determine the temperature of the rotor [4]. Since the temperature/resistance relationship of copper is linear in nature getting an accurate reading of the rotor resistance during the test is important. Another aspect of calculating the temperature is to be able to get an initial physical reading of the copper temperature. The copper is not easily accessible since it is enclosed within the rotor slots and the coil retaining rings.

To overcome this, a direct approach is required to accurately determine the temperature profile of the generator rotor.

2.1. Thermal Stability of Synchronous Generator Rotor (general – basics)

In essence, thermal instability occurs when a change in field current causes a corresponding change in vibration levels. A rotor that is in both mechanical and electrical balance is stable and fit for service. Conversely - if a rotor is unbalanced - the resulting uneven loading will lead to bowing of the rotor shaft and increased vibrations.

Thermally induced vibrations may be the result of one or a combination of the following:

- *Shorted Turns* - One of the most common failure mechanisms on a generator rotor is inter-turn shorts. Shorted turns occur when there is a breakdown in the insulation between turns. These shorted turns can cause thermal and/or magnetic imbalances. This can be accompanied by mechanical vibration as well.
- *Coil movement* - During the heating cycle coils may move to one side of the rotor creating a ratcheting effect that leads to imbalance.
- *Blocked ventilation slots or inadequate cooling* - Restrictions in cooling can severely affect the thermal balance of the rotor. This results in an uneven temperature distribution along the length of the rotor generating an imbalance.
- *Non-uniform winding* - If the rotor is not wound uniformly from pole to pole with the same insulation thickness and build up materials, differences in frictional forces may result leading to a restriction in expansion of the copper coils.
- *Blocking* - Blocking used within the overhangs of the rotor must be spaced and fitted correctly to ensure uniform expansion of the coils without restriction. Incorrectly fitted blocking can result in coil restriction and the rotor bowing.
- *Body wedges* - Ill-fitting rotor body wedges that may be too loose or too tight create an uneven interference fit throughout the slot length. This can lead to the restriction of movement of copper coils in the axial direction resulting in a thermal bend.
- *Tight Slots* - Rewound rotors may sometimes experience tight slots when the original copper is being reused. The original copper may not be symmetrical and flat after years of usage. Design clearances are then compromised creating an uneven expansion within the slots causing thermal bowing of the rotor.

Continuously operating a generator rotor that exhibits signs of thermal instability and generates high vibrations will lead to breakdown and the unit being taken offline for repairs [2, 5, 6, 7].

2.2. Condition monitoring/Current Techniques that are available

A thermal instability is most often characterised by a rise in vibration levels. These vibrations are easily detected with online condition monitoring tools. The difficulty is that once a refurbished unit is returned to service in the absence of thermal instability testing and high vibrations are exhibited the unit needs to be decommissioned, disassembled and investigated for the cause of the instability. The investigation process normally involves the rotor being returned to the utility's workshop for disassembly and investigation of the rotor. This is a time-consuming exercise and results in lost generating capacity. The ideal situation would be that the rotor is properly tested for thermal instability issues prior to leaving the utility's workshop.

There are further challenges associated with TIT within large purpose built balancing facilities. In general, these facilities monitor both shaft and pedestal vibrations which aid in determining that there is a problem but seldom help pin-point the problem area. The temperature of the rotor winding is usually determined using one of the following equations:

$$T_{HOT} = \left\{ \left(\frac{R_{HOT}}{R_{COLD}} \right) (234.5 + T_{COLD}) \right\} - 234.5 \quad (1)$$

$$\Delta T = \frac{\left(\frac{R_t}{R_0} \right)^{-1}}{\alpha} \quad (2)$$

From equations (1) and (2), it can be seen that the resistance as well as a physical temperature measurement must be known at a specific current and voltage level. Then the subsequent temperature rises can be calculated by utilising the rotor resistance measurement. The resistance measurement needs to be accurate and can be significantly affected by the slipping/brush gear interaction.

On the other hand - when the friction method of TIT is preferred - current injection is still used as a method to determine winding resistance and calculate the temperature.

3 DIRECT THERMAL MAPPING

Through precise numerical calculations the winding temperature may be determined but this would exclude the temperature of the rotor body, wedges, pole faces, shaft, retaining rings and other extremities of the rotor

assembly. The uneven thermal profiles of all of these components can lead to thermal instability. The presented direct method can pin-point areas of concern and reduce guess-work during trouble shooting. The method physically determines and maps the winding and body temperature of the rotor which eliminates the deficiencies in contemporary testing methodology.

3.1. Use of Infrared (IR) Sensors

The widespread use of infrared thermography within the electrical industry has become common place for a number years now [8, 9]. This non-contact method produces reliable and accurate results for fault finding and trouble shooting. Temperature measurements are made possible by detecting the radiant flux of an object and through a calibration algorithm a temperature output is calculated.

Also referred to as a radiation thermometer many varieties are available on the market today, from thermal imaging cameras to singular probes. Devices are able to measure a wide variety of temperature ranges and can operate at high speeds making it ideal for the proposed test setup [10].

3.2. Heat Map

The preferred method for data capture is in the form of a matrix of temperature values corresponding to the physical mapping of the surface of the generator rotor. The presented method transforms these temperature measurements and physical coordinates into a 2-D heat map.

Simply put, the direct thermal mapping method presents the 3-D temperature data (of rotor) as a 2-D heat map. A heat map consists of a number of rectangular rows and columns that represent data values against a colour scale. This has been a widely used method to display large matrices within many different fields such as natural sciences and biological science [11, 12].

The experimental setup required to map the temperature distribution of the rotor must be able to ultimately output data that can lead to the information being displayed as a heatmap for easy interpretation. Each block within the heatmap will represent a measuring pixel of the IR camera. Each pixel of the IR camera will represent a physical portion of the rotor. The distance of the IR camera away from the rotor will

determine the physical size of the area that will be sampled.

3.3. Experimental Setup

The experimental setup constructed is based on the use of a mini-rotor rated at 20 kVA that is designed to mimic a 600 MW generator rotor. The rotor is similar to a 600 MW rotor in the following aspects:

Two-pole 3000 rpm, 50 Hz

Distributed and concentric field windings

Damper bars

Shaft mounted slip rings

Insulated bearings

Mono-block milled shaft with slots

Table 1 sums up the dimensional aspects of both the mini-rotor as well as a common 600 MW generator rotor.

Table 1: Comparison of specifications for mini-gen rotor and turbine-generator rotor

PARAMETER	MINI-ROTOR	600 MW
Rotor slots	32	32
Damper bars	48	48
Rotor diameter	178.5 mm	1165 mm
Shaft length (journal centres)	885 mm	10990 mm
Shaft diameter	180 mm	1165 mm

A 3-D model of the constructed test setup is shown in Figure 1. The rotor will be driven by an induction motor rated to 3000 rpm. The enclosure of the setup will also be scaled to simulate the local utility balancing facility. The scaling is based on the length of the rotors thus the mini-rotor is approximately 12.5 times smaller than a convention 600 MW rotor. The enclosure was designed around this scaling factor as compared to the utility balancing dimensions.

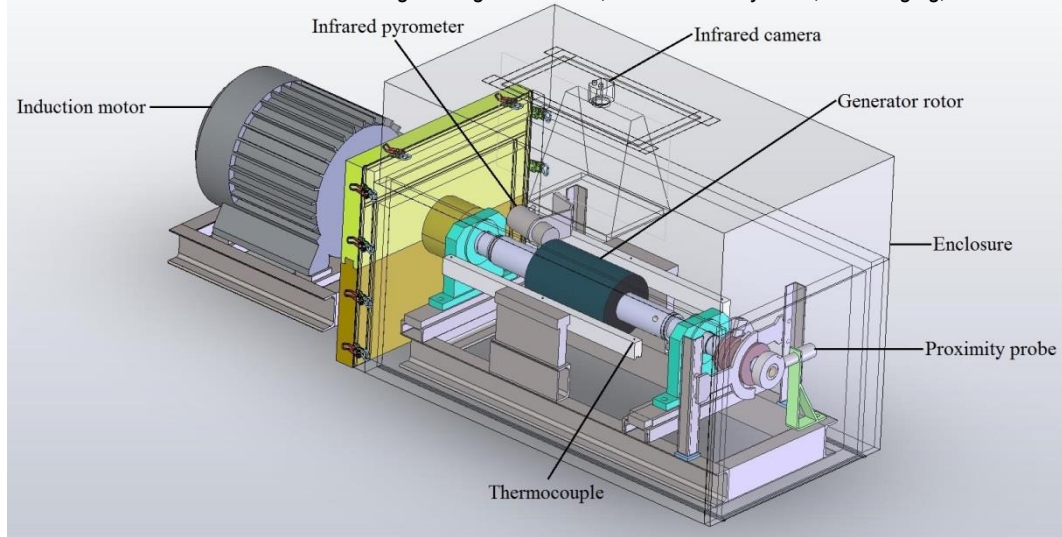


Fig. 1: Experimental configuration used for rotor thermal instability testing and measurement

The enclosure was constructed out of 12 mm fibre board and insulated with a number of layers of Styrofoam to be able to mimic the insulative and dimensional properties of a full-scale balancing facility.

The test setup utilises a high speed high resolution 80 Hz IR Camera that captures the surface data of the rotor through a viewing window. The rotor body is painted black to improve accuracy of the data captured as IR technology responds better to black bodies translating to a higher emissivity [10].

The winding temperature is being captured with a laser guided IR pyrometer. The copper windings have been painted black as well to improve accuracy.

A proximity probe is used to differentiate each revolution of the mini-rotor. This is achieved with the aid of a fixed collar with a machined notch. The output received when the notch passes the proximity probe will indicate when one revolution has passed.

A number of thermocouples are being used to monitor the ambient temperature as well as the temperature within the enclosure. Thermocouples are positioned on either side of the mini-rotor with pairs of thermocouples near the slipring, the centre of the body as well as near the drive end.

A number of test conditions are investigated to prove that the setup is viable for its intended purpose.

3.4. Test Condition 1 - with excitation

The initial investigation entails mapping of the mini-rotor under excitation conditions. The rotor is operated

at 3000 rpm and excited at different levels: 5 A, 10 A, 20 A and 35 A. Each level is maintained for an hour with test data taken every ten minutes. Figure 2 illustrates the results obtained at 35 A, 10 minutes.

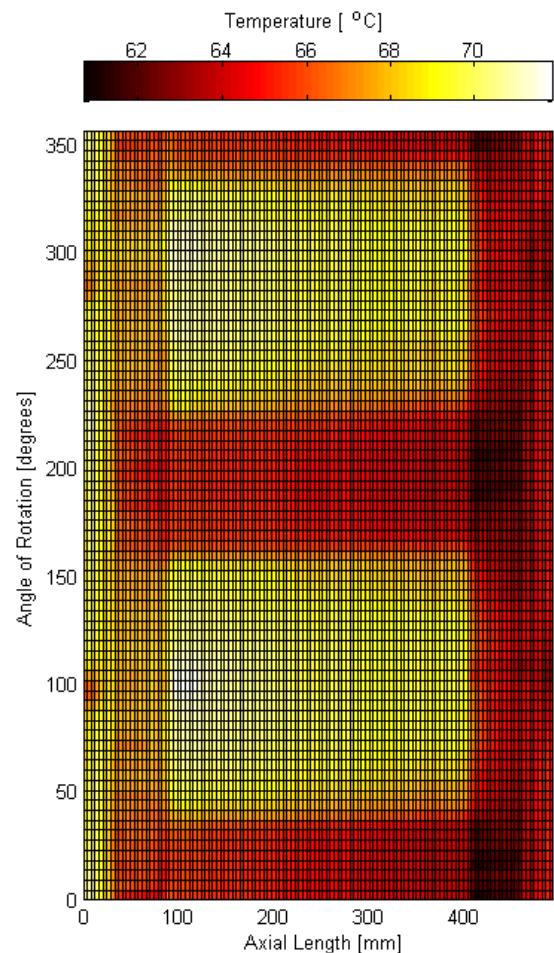


Fig. 2: Heat map of rotor for test-condition 1 i.e. with 35 A current injection

3.5. Test condition 2 – no excitation including brush gear

This test involves heating the rotor by air friction or windage. The brush gear remains connected. The test runs for eight hours and readings are taken every 30 minutes as the heating process is anticipated to be quite slow. Figure 3 shows the results obtained after five hours.

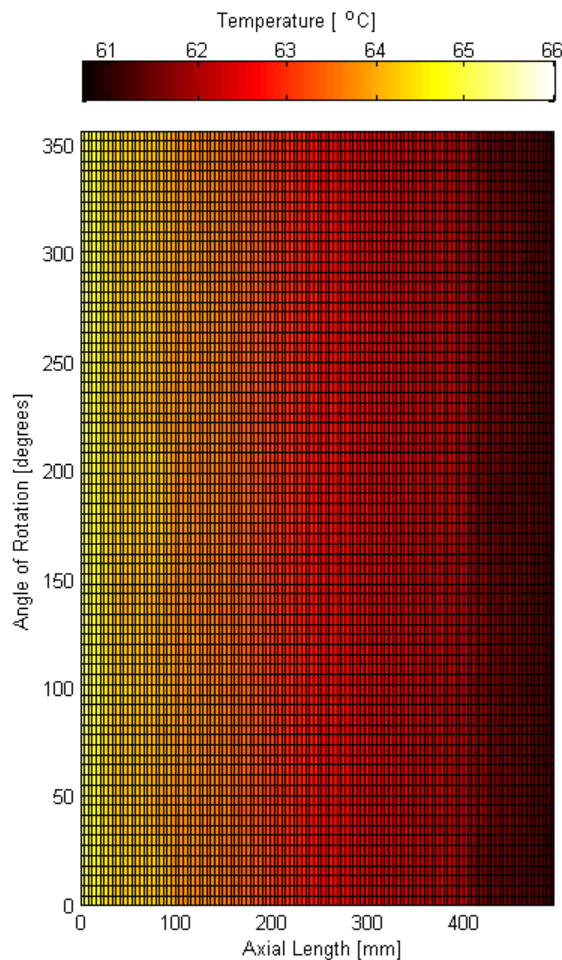


Fig. 3: Heat map of rotor for test-condition 2 i.e. no excitation, with brushgear, after 5 hours

3.6. Test condition 3 – no excitation excluding brushgear

The final test condition is carried out with the brush gear being disassembled allowing the rotor to freely move just on the bearings. The test methodology is the same as in Test condition 2. The results obtained after 5 hours are summarised in Figure 4.

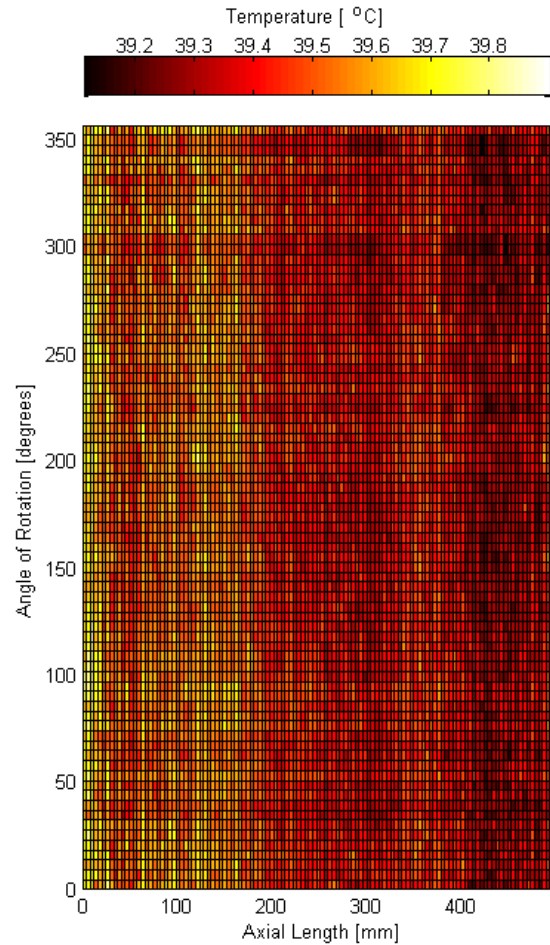


Fig. 4: Heat map of rotor for test-condition 3 i.e. no excitation, excluding brushgear, after 5 hours

3.7. Discussion

The results obtained substantiate that the test setup can produce the required output. The heat maps created had an excellent resolution of 120x77 points. Each point measured is represented by a 4.14 mm x 6.9 mm portion of the rotor body. The result is that 94 % of the rotor body is mapped. The rotor winding temperature was also measured as well as the temperature within different locations of the enclosure.

Figures 2, 3 and 4 show remarkable differences in the rotor thermal signature under the different test conditions. Method 1 showed great detail in regard to how the winding heated and the heat was then conducted to other parts of the rotor. The average surface temperature is found to be 67°C while the winding temperature is 67.1°C.

The heat map for Method 2 showed an even heating of the rotor body. There is also a clear thermal gradient

along the rotor where the slip-ring end of the rotor experienced a higher temperature as compared to that of the drive end. The average body temperature is measured to be 56.2°C while the winding temperature is measured as 47.3°C - with a difference of 8.9°C. Thus the measurement of the winding temperature alone does not translate to the surface temperature being the same.

Finally, results from test-condition 3 prove that the interaction between the brush gear/slip-ring assembly aided in heating of the rotor. The friction created between these components alone are able to heat the rotor in test-condition 2 to a significantly higher temperature. The average temperature of the rotor body measured 37°C and the winding is measured at 33°C. The same applies to this scenario as the winding and body temperatures differ substantially - i.e. by 4°C.

The classical method of calculating the winding temperature and using it as a gauge for the entire rotor temperature has proven to be unreliable. The results obtained from the heat-mapping method produces a detailed picture of the thermal behaviour of the rotor.

4 FUTURE WORK

The test setup has been proven to perform satisfactorily. Improvements can be made to increase the number of samples used to create the heat map, thus developing a higher resolution map. The three test conditions will be studied in greater detail. Testing will be carried out for a longer period of time to develop the heat signatures.

The results obtained will be compared to the existing methods of thermal instability testing to be able to make conclusions on which testing methodology may be better going forward. Furthermore, the suitability of the presented methodology for accurate and speedy fault finding will be tested.

5 CONCLUSION

A methodology for directly mapping the thermal distribution of an experimental generator's rotor was presented in this paper. A test setup was developed and constructed to scale, tested and proven to be able to map the surface of the mini-rotor. The setup was able to directly measure the winding temperature and various temperature points within the model enclosure.

The results showed that there are dissimilarities between the different methods of TIT. The mini-rotor responded differently during the three test conditions. Moreover, the presented methodology enables a detailed mapping of the thermal response of the rotor to be obtained which is otherwise not available. This will

assist in diagnosing rotor thermal instability more effectively than classical methods.

6 ACKNOWLEDGMENT

The first author acknowledges Christian Sagot for his assistance with the 3-D model.

7 REFERENCES

1. Klempner, G., *Optimized Maintenance of Generator Rotors*. 2004, EPRI.
2. Singh, A.N. and W.A. Cronje, *Improved Understanding of Instability Failures Under Thermal Stress Testing of Repaired Generator Rotors*, in *Iris Rotating Machine Conference*. 2015: Nashville, Tennessee.
3. Greg C. Stone, E.A.B., Ian Culbert, Hussein Dhirani, *Electrical Insulation for Rotating Machines*. Power Engineering, ed. M.E. El-Hawary. 2004: John Wiley & Sons, INC. 371.
4. TurboGenServices, *High Speed Balancing Specifications for Generators*. 2013, Eskom: Eskom.
5. Jevtić, M., V. Zeljković, and M. Dapić, *Thermal influences on turbogenerator dynamic behaviour*. *Elektrotehnika i Elektronika*, 2006. **25**: p. 157-161.
6. Juhlin, G.A., *Deformation of Turbo-Alternator Rotor Windings, Due to Temperature Rise*. *Journal of the Institute of Electrical Engineers*, 1939. **85**(514): p. 544-522.
7. Zawaosky, R.J. and W.M. Genovese, *Generator Rotor Thermal Sensitivity – Theory and Experience*. 2001, GE Reference Library.
8. Holliday, A.J. and J. Kay. *The use of infrared viewing systems in electrical control equipment*. in *Pulp and Paper Industry Technical Conference, 2005. Conference Record of 2005 Annual*. 2005. IEEE.
9. Suesut, T., et al. *Emissivity measurements on material and equipment in electrical distribution system*. in *Control, Automation and Systems (ICCAS), 2011 11th International Conference on*. 2011. IEEE.
10. DeWitt, D.P. and G.D. Nutter, *Theory and practice of radiation thermometry*. 1988: Wiley Online Library.
11. Chen, C.-H., *Generalized association plots: Information visualization via iteratively generated correlation matrices*. *Statistica Sinica*, 2002. **12**(1): p. 7-30.
12. Wilkinson, L. and M. Friendly, *The history of the cluster heat map*. *The American Statistician*, 2009. **63**(2).

Evaluation of Hand Carved Timber Blade Performance for a Rutland 910 Wind Turbine

P. Ghimire^{#1}, P. Freere^{#2}, R. Sinha^{#3}, L. Mishnaevsky Jr.^{#4}, K. Silwal^{#5}, M. Freere^{#6},

¹Aalborg University, Denmark

²Nelson Mandela Metropolitan University, South Africa

³Kathmandu University, Nepal

⁴RISO National Laboratory, Technical University of Denmark

⁵Kathmandu Alternative Power and Energy Group (p) Ltd., Kathmandu, Nepal

⁶Monbulk Secondary College, Victoria, Australia

¹p.ghimire@kapeg.com.np

²pfreere@gmail.com

Abstract: In developing countries, access to manufactured parts or materials can be limited and expensive. This paper presents the evaluation of the steady state performance of hand carved Nepalese timber blades compared to the original plastic blades. This has been done for the Windcharger 910, 50W, Rutland wind turbine. The advantages of using wind turbine blades which are locally manufactured, and using locally available resources, are discussed.

Keywords—small wind turbine, timber, blade

1. INTRODUCTION

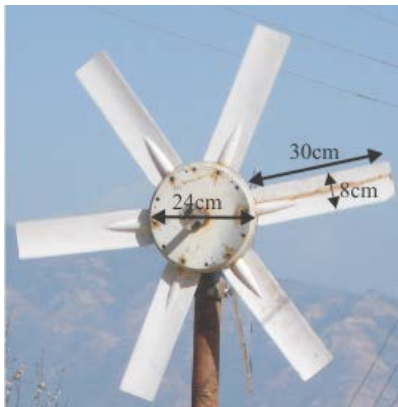


Fig. 1: A 50W Rutland wind turbine with timber blades.

A major barrier to promoting small wind power technology in a developing country is the cost and the lack of skills and material to manufacture wind turbine parts. A small wind turbine generator system consists of wind turbine blades, generator, tail, braking mechanism and tower. In Nepal, except for materials for the generator construction, all other parts can usually be built from locally available sources using simple technology. The use of wood for the blades is expected to assist with recycling of material at the end of life of the turbine [1] and is much simpler to recycle than artificial composites [2]. Timber often has excellent fatigue properties [3] and its anisotropic properties can be utilised by orienting the grain radially in the blades. A further advantage is that short pieces of timber for small wind turbine blades are often quite inexpensive.

There is a wide variety of hard and soft woods available. Timber is a natural fibre-reinforced composite, with a cellular, low mass structure, which gives it very good specific properties. It is cheap, readily available and performs well under fatigue loading [4]. Nepalese timber can have excellent fatigue and strength properties [5].

2. WIND TURBINE DESCRIPTION

The original blades, as provided by the manufacturer, were constructed using plastic. The generator uses six aerodynamically shaped blades as shown in Fig. 1 and Fig. 3. The blades are directly attached to the axial flux permanent magnet generator. The generator was designed to charge a 12V battery.

Including the generator, the total diameter of rotor is 84cm. [6] discusses the issues of accuracy of hand carved wooden blades for a wind turbine with a twist and variable chord length. Hence these rotors which have a fixed chord length and no twist are likely to be more suitable for hand carving. The rotors are aerodynamically shaped but designed at a constant chord length of 8cm wide with a constant pitch angle.

The density of the plastic blade was measured using the water displacement method, whereas, the density for the local Lakuri (*Fraxinus floribunda*) timber used to make the wooden blades was calculated by measuring its dimensions and weight. The density of the plastic blade material was found to be about $1375 \pm 10\%$ Kg/m³ density. The density for selected timber was found about 624 Kg/m³ at moisture content of the timber in between 10% to 18%. The moisture content of timber was measured using a two pin digital moisture meter. Hence the wooden blades will be approximately half the weight of the plastic blades. In principle, this would allow the turbine with the wooden blades to start more easily and rapidly in light winds. The wooden blades are painted white, to reduce ingress of moisture.

3. TIMBER MATERIAL AND SELECTION PROCESS

The local timber, Lakuri, was used to construct the wind turbine blades. The Lakuri timber is readily available at 2000m or higher altitude in Nepal. The

timber is a softwood, but because of long, strong fibres, it has been used to make handles for mechanical tools (e.g. hammers) in Nepal since ancient times.

The requirements for the turbine blades are that they should neither break, nor bend so much that they hit the tower and should be hard enough to keep their shape despite being hit by hail, insects and the occasional birds. Other associated factors such as availability of timbers, their cost and growing time should also be considered during the timber selection process, in order to make the wind turbine cost effective. [7]

4. BLADE CONSTRUCTION

A plywood template, for the wooden blade manufacture, was designed and constructed by measuring the profile of the original plastic blade as shown in Fig. 2. The template was taken to a local, skilled carpenter and he was asked to carve a new set of blades by using the template and observing the original blade.



Fig. 2: Plywood template for Rutland timber blade construction

To construct the wind turbine blades, the timber piece should be dried, free from knots and with a uniform grain structure down the length of the piece. The skilled carpenter was able to carve the 6 blades in two days, using locally available hand tools.

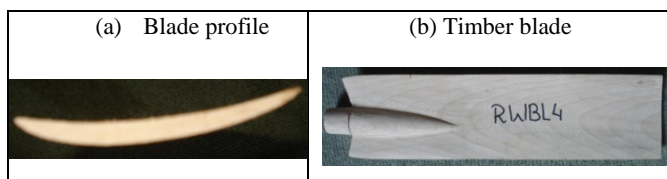


Fig. 3: Wind turbine blade profile and timber blade

The aerodynamic profile and hand carved wind turbine blade for the Rutland turbine are shown in Figs. 3 (a) and (b).

Table 1 shows the physical measurements of the hand carved timber blades. Column 7 shows the weight and length of the plastic blades [8]. The length differences are due to lack of care in the hand preparation. Although the size of the wooden blades makes a difference, as the last row shows, the larger differences in the weight of the blades are likely to be due to differences in wood density. To overcome this would require a more careful choice of wood pieces for the

blades, or the selection of equal blades after manufacture [9]. However, the Rutland 910, being a six bladed turbine means that the blade imbalances will not be expected to cause many issues, but a two or three bladed turbine may have starting and running issues with the unbalanced blade weights. From [10], it can be seen that a multibladed turbine offers increased options for non identical blades, in terms of weight and centre of gravity, without the need to add weights to balance each blade. It can be concluded that multibladed turbines are more appropriate for hand carved wooden blades than 2 or 3 bladed turbines.

TABLE 1

HAND CARVED TIMBER BLADE MEASUREMENTS USED FOR RUTLAND 910 WIND TURBINE GENERATOR

Specifications	Blade						Plastic
	Timber						
	1	2	3	4	5	6	
Weight (gm)	108	134	98	115	101	106	208
Moisture content (%)	15	15	15	16	15	14	
Length from root (mm)	298	310	298	299	298	299	300
Weight for a blade length of 300mm (gm)	109	130	99	115	102	106	208

5. BLADE PERFORMANCE

It was attempted to measure the output performance of the Rutland wind turbine generator at a variety of sites.

However, due to the low wind speeds at the time and the unavailability of wind tunnels, it was not possible to obtain the wind turbine and generator performance at a wide range of wind speeds.

Hence, the wind turbine system was tested on top of a running vehicle (TATA truck), as shown in Fig. 4. Initially, the vehicle was run to check the anemometer at different vehicle speeds. Fig. 5 shows the calibration curve for wind speed with respect to vehicle speed for different vehicle speeds. The wind speed was measured by an anemometer at hub height. The linearity and gradient of the curve supports the view that the wind speed the turbine experienced was not significantly influenced by the aerodynamics of the vehicle.

The wind turbine generator was tested at wind speeds ranging from 3m/s to 15m/s. A lead acid battery at 12.6V was used as the load to test the turbine power performance at different wind speeds. The battery was loaded with adjustable resistive loads in order to keep the voltage constant. The wind turbine output power with respect to the wind speed was obtained as shown in Fig. 6, and is compared with the results obtained for plastic blades from the wind tunnel test done in [11].



Fig. 4: Rutland wind turbine system under test on vehicle

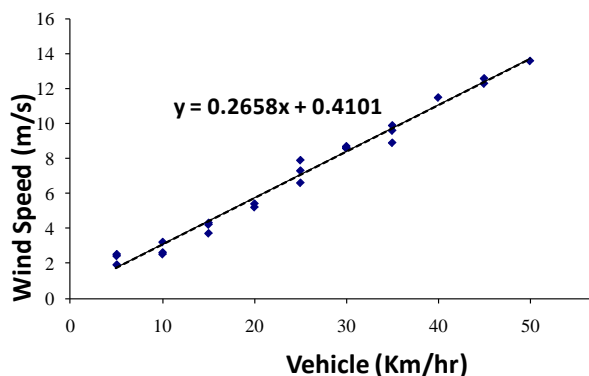


Fig. 5: Wind speed check at different vehicle speeds

In Fig. 6, the square solid markers show the output power for the timber blades, while the crosses show output power for the plastic blades. The output power as a function of the wind speed for the wooden blades is very close to those of the plastic blades. Hence, the timber blade can replace the plastic blades and obtain the same steady state output power performance. This can reduce the cost of the wind turbine generator system and its maintenance. The blade manufacturing process is simple and cheap. A local skilled carpenter can carve these simple blades, hence the maintenance of these wind turbine blades will also be simpler.

6. CONCLUSION AND DISCUSSION

This paper presented the load power performance curve for a Rutland 910 wind turbine with hand carved timber blades, and plastic blades, and found power characteristics to be the same. The advantages of using hand carved, local timber for the construction of small wind turbine blade are principally low cost and availability. The main issue can be that the blades are not identical and due to variations in hand carving and timber density, and so may have different weights and centres of gravity. However, with multibladed turbines, these effects can be minimised.

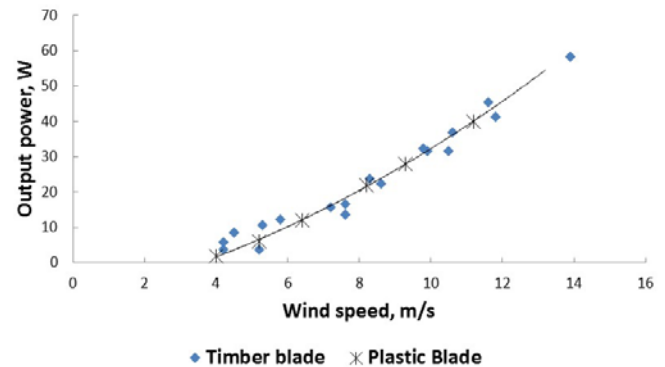


Fig. 6: Measured power from timber and plastic wind turbine blades.

ACKNOWLEDGMENTS

The authors would like to thank truck driver Bijaya for his help and interest to drive the truck continuously from 8pm to until 1am in the morning. The authors also would like to remember the late Michael Freere, who had been a great help and participated actively during the wind turbine tests in the night.

REFERENCES

- [1] K. Ortegon, L. Nies, J. Sutherland, "Preparing for the end of service life of wind turbines", *Journal of Cleaner Production*, 2013, vol. 39, pp 191-199.
- [2] R. Cherrington, V. Goodship, J. Meredith, M. Wood, S. Coles, A. Vuillaume, A. Feito-Boirac, F. Spee, K. Kirwan, "Producer responsibility: defining the incentive for recycling composite wind turbine blades in Europe", *Energy Policy*, 2012, vol. 47, pp 13-21.
- [3] C. Astle, I. Burge, M. Chen, T. Herrler, L. Kwan, N. Zibin, D. Wood, "Timber for small wind turbine blades", *Energy for Sustainable Development*, 2013, vol. 17, pp 671-676.
- [4] I. Bond, M. Ansell, "Fatigue properties of jointed wood composites," *Journal of Material Science*, Speech, Kluwer Academic Publishers., vol. 33, pp. 2751-2762, 1998.
- [5] R. Sharma, R. Sinha, P. Acharya, L. Mishnaevsky Jr., P. Freere, "comparison of test results of various available Nepalese timbers for small wind turbine application", *Proceedings of 3rd international Solar Energy Society Conference – Asia Pacific Region (ISES –AP 08) and 46th ANZSES Conference*, Sydney, 2008.
- [6] P. Clausen, P. Freere, P. Peterson, S. Wilson, D. Wood, "The shape and performance of hand carved small wind turbine blades", *Wind Engineering*, 2009, vol. 33.
- [7] R. Sinha, P. Acharya, P. Freere, R. Sharma, P. Ghimire, L. Mishnaevsky Jr, "Selection of Nepalese Timber for small Wind Turbine Blade Construction", *Wind Engineering*, vol.34(3), pp 263-276, 2010.
- [8] G. Riahy, "Dynamic and predictive dynamic wind turbine control," PhD thesis, Monash University, 1999.
- [9] K. Hitz, D. Wood, "On blade matching after batch production", *Wind Engineering*, 2010, Vol. 34, no. 3, pp 325-334.
- [10] K. Hitz, D. Wood, "On blade arrangement for multiblade rotors", *Wind Engineering*, 2011, vol. 35.
- [11] P. Sykes, P. Freere, "Design of Prototype Wind Turbine" *Proceedings of Solar' 97, Australia and New Zealand Solar Energy*, 1997.

INSTABILITY PROBLEMS IN THE SAPP NETWORK

H. du Plessis* and J.A. de Kock**

* *School of Electrical, Electronic and Computer Engineering, North-West University, Potchefstroom 2520, South Africa E-mail: hduplessis111@gmail.com*

** *School of Electrical, Electronic and Computer Engineering, North-West University, Potchefstroom 2520, South Africa E-mail: jan.dekock@nwu.ac.za*

Abstract: The instability in power systems are not a common occurrence, however parts of the SAPP network do become unstable from time to time. Power outages caused by instability are due to various disturbances in the system. The disturbances in the SAPP network are caused by severe weather conditions, overload, equipment failure, transmission line faults and power oscillations. The SAPP network remained largely unchanged in the last 20 years, while power demands kept rising. This will introduce problems in the future that are currently masked by the limited power generation in many countries within SAPP. The limited interconnection development and improvements reduce system stability. Some of the large power outages are discussed, showing the problem is often related to power transfer of the network. Several solutions are proposed to improve the power flow and increase the SAPP network stability.

Key Words: Instability, interconnections, power outages (blackouts), transmission lines, flexible AC transmission systems (FACTSs), SAPP network.

1. INTRODUCTION

The South African Power Pool (SAPP) network consists of a large area with numerous interconnections. The focus in this article is on the Zimbabwean, Zambian, Botswana and South African network and interconnections with them. This section of the network is also referred to as the Zimbabwe central corridor. The corridor is from Zambia through Zimbabwe and Botswana to South Africa in a single path (see figure 1). This clearly shows the bottleneck effect limiting the amount of power transfer capability, which affects system stability. The SAPP interconnection between Zimbabwe and neighbouring countries and reactive power support are evaluated in this article. Development in the SAPP network is slow versus the increase in power consumption every year. The limitation in development increases instability and the amount of power outages (also known as a blackout). System stability affects the reliable continuous power supply to factories, mines, and business to maintain profitability of the country's economy and to provide residents with the comfort that electricity provide. Although the power outage can cause problems in individual countries/utilities, it may also introduce complications in the entire grid due to interconnections affecting other countries. After a power outage, restarting of the power system requires additional power, which may be difficult to obtain due to limitations of neighbouring countries. SAPP, with the respective utilities, are working on solutions to improve

system stability by increasing the power generation and transmission grid in the network. Some of these solutions such as additional transmission lines and FACTS devices are introduced in the article.

2. SAPP

2.1 Interconnection development

The SAPP network was established in 1995, although interconnections between countries started in the 1950s. The Democratic Republic of the Congo (DRC) and Zambia constructed one 220 kV transmission line, capable of transferring 250 MVA in 1954 [1]. The interconnection was constructed to provide the power for the copper mines in northern Zambia. In the 1960s interconnection between Northern and Southern Rhodesia (now known as Zambia and Zimbabwe) was established after construction of the Kariba dam in 1959. The interconnection consists of two 330 kV lines, allowing a maximum transfer of 1400 MVA. After the completion of the Cahora Bassa dam in 1975, a 500 kV 2000 MW High Voltage Direct Current (HVDC) line was constructed to provide an interconnection between Mozambique and South Africa. In 1996 the 400 kV connection between South Africa and Zimbabwe was established running through Botswana, capable of transferring 750 MVA. Just a year after completing the interconnection to South Africa, Zimbabwe finished another 400 kV line to Mozambique. The connection with the

HVDC is parallel to the connection between Zimbabwe and South Africa. There is also a 220 kV connection between Zimbabwe and Botswana, but this is normally kept open [1]. These interconnections are shown in Figure 1 illustrating the limited connections between Zimbabwe and its neighbouring countries.

2.2 SAPP goals

The Southern African Development Community (SADC), which consists of Southern African Countries, established SAPP, to manage the interconnection between the members of the SADC. SAPP's objectives are to provide a reliable interconnected electrical system in the Southern African power network while measuring and monitoring the system's performance. SAPP is an independent organisation, which provides support to a country and utilities after a problem occurred. SAPP manages the buying and selling of electricity between countries to allow efficient power exchange. The SAPP network regularly experiences disturbances and even blackouts. The common causes of these disturbances are severe weather conditions, overload, equipment malfunction, transmission line faults, and power oscillations. These causes are identified by analysing the SAPP monthly and annual reports. If the causes are known, possible solutions can be investigated to improve the overall system stability.

The SAPP network can be simulated to analyse the system performance. This can help evaluate the suggested improvements to be made to the system. The performance of each improvement on the network must be analysed and its practical implementation and cost considered. The devices that may improve system stability are additional power lines, conventional compensators, flexible AC transmission systems (FACTS) or power system stabilisers (PSSs) or both.

2.3 SAPP network development

This section covers development in the SAPP network's interconnections and reactive power control. The SAPP network development have decreased over the years while the power demand increased. The high demand in power causes constraints in the power system due to inefficient power generation and limited transmission lines. The transmission of power over the network can be improved by building new transmissions and by adding conventional compensator devices or even more complex systems known as FACTS. The SAPP network has remained mostly unchanged over the last couple of years, while the demand keeps on increasing. The annual growth rate of the overall power consumption in the SAPP network is 5%, as

determined in 2014. This will result in limited power generation in the SAPP network over time [2, 1].

Figure 1 shows the transmission lines in the Zimbabwe corridor as well as the interconnections between the countries and the potential transmission lines to improve the system. The transmission lines are colour coded to show the different voltages of each. The 400 kV is shown in brown with the first solution in a brown (400 kV) and orange (330 kV) dashed lines. The second solution is shown with dashed blue and red lines, representing 400 kV and 330 kV lines, respectively. The remaining two are the 330 kV (red) and 220 kV (green).

3. REACTIVE POWER CONTROL

Reactive power can be controlled by installing conventional compensators devices, such as shunt reactors and capacitors, and Static VAR Compensators (SVCs), which are dynamic compensators (FACTS). In Zimbabwe, shunt reactor banks are the most common, but SVCs and shunt capacitors are also installed. These devices were installed between 1960 to 2000. The total reactive power control range varies from -300 Mvar to +600 Mvar. The following few sections discusses the three different devices used in the Zimbabwean network.

3.4 Shunt Reactor Banks

In Zimbabwe most of the reactor banks are rated at 20 Mvar with one or two units per substation. Substations with shunt reactor banks are Harare, Dema, Hwange, Marvel, Norton, Alaska, Insukamini, Sherwood and Bindura substation [4]. The shunt reactors banks are installed to reduce overvoltage during open circuit or light load conditions. The shunt reactors can be disconnected near full-load conditions to ensure the line loadability does not decrease [4].

3.5 Shunt Capacitor Banks

Shunt capacitors banks at substations are limited, with only four substations equipped with shunt capacitor banks. The substations are Kadoma, Mkwazine, Sherwood and Warren. The shunt capacitors are used to deliver reactive power, which may improve the overall power factor. Shunt capacitors are also used if an EHV line is heavily loaded and the voltage drops. By inserting shunt capacitors, the transmission voltage will increase, compensating for the voltage drop caused by the load [4].

3.6 SVCs

SVC, a FACTS device, helps with system damping reducing power oscillations and dynamic voltage control [5]. At

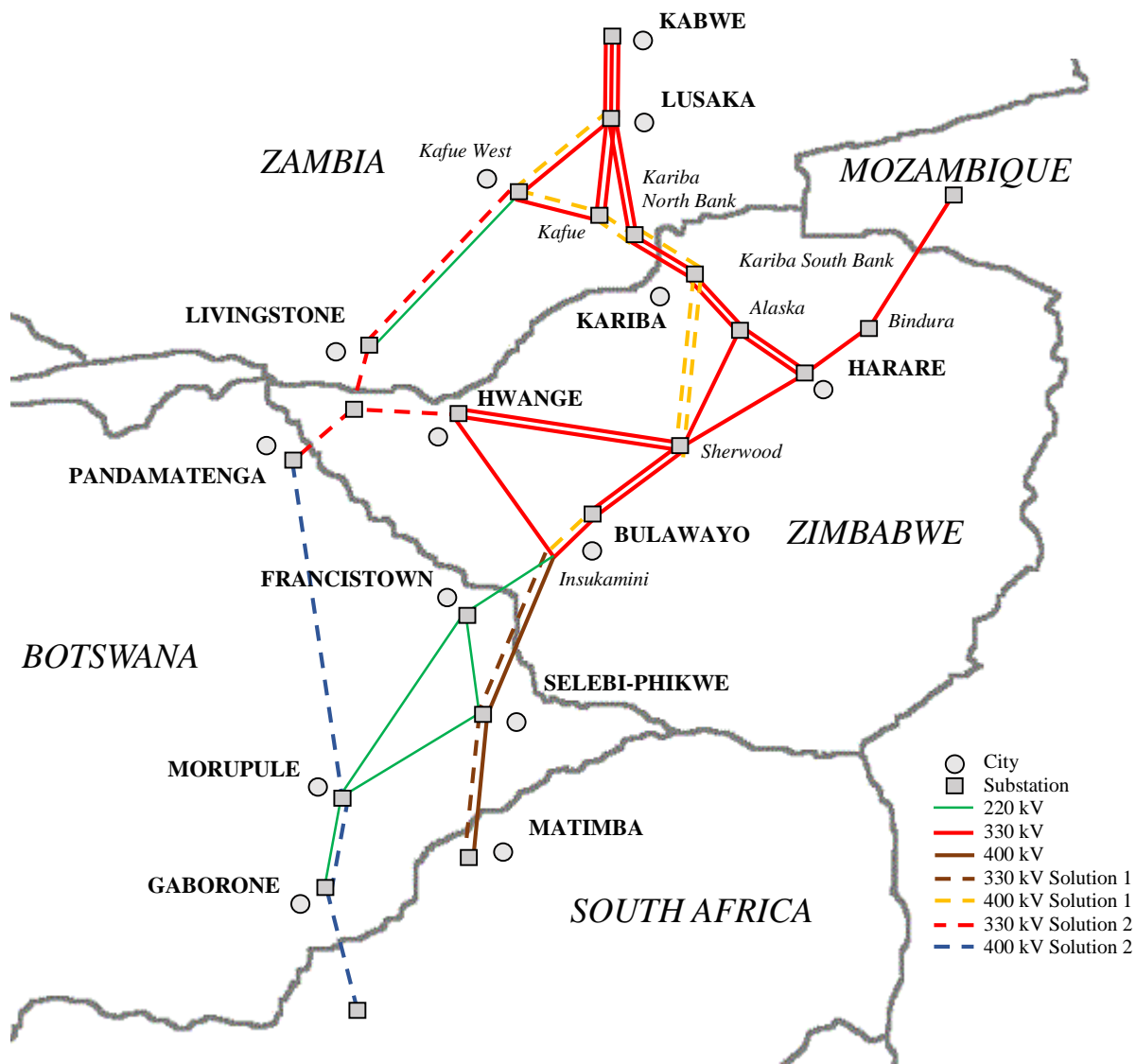


Figure 1: SAPP Network in the Zimbabwe Central Corridor

Insukamini substation a 100 Mvar 420 kV reactor is connected to the line to South Africa. A SVC is also connected on to the 330 kV busbar system in Insukamini. The SVC is a combination of a 150 Mvar Thyristor-Controlled Reactor (TCR), 150 Mvar Thyristor-Switched Capacitor (TSC) and 50 Mvar harmonic filters. The SVC provides high-speed dynamic voltage control of the single 400 kV connection between South Africa and Zimbabwe. Low frequency deviation causes active power oscillations between the countries. The SVC is also equipped with a power oscillation damper (POD). The POD helps to reduce the power oscillations in the system. The SVC was upgraded in 2014 to help extend the life span of the SVC [6, 7]. Two

SVCs are also installed at Sherwood power station. The SVCs each consist of a 66.3 Mvar TCR and 34.6 Mvar filter. Some of the SVCs as well as static compensators are decommissioned due to damaged parts.

The role of reactive power control of the interconnected network was discussed. The main concern is the slow pace of expansion of power transfer corridors in the SAPP network. The decrease in improvements in the network increases system instability. Over the last couple of years, the system has experience various large disturbances.

4. POWER OUTAGES

A power outage happens when a system experiences a failure due to power system instability, which results in a region being left without power. Although interconnections improve power system stability, the distance between utilities and the large load areas cause an increase in risk to external interferences. Power outages can cause the interconnections between power stations to disconnect due to faults, power shortages or constraints on the system, which may isolate the power stations of lines. The SAPP network is not the only power system facing power outages. Other countries have also experienced large power outages [8].

4.1 Power Outages in the SAPP Network

The SAPP network has seen several disturbances, which lead to power outages over the last number of years. On the 4th of June 2006, a fault occurred at the Kariba South power station's 330 kV switchyard in Zimbabwe. The disturbance caused a large blackout in Zambia. The Kariba South power station at caused the Kariba North and Kafue Gorge power stations trip in Zambia. The total system power loss was 1.1 GW. The two tie lines between Zimbabwe and Zambia connects the north and south bank power stations at Kariba. This is the only connection between the two countries, which introduces large power swings if the lines are opened due to a disturbance [9].

The SAPP network experienced several power outages, which occurred between 19 and 22 January 2008, and continued to be fragile up to February 2008. The first national power outage occurred on 19 January 2008 in Zambia. The main causes were the system frequency being too high, cascade tripping of generation at all the main power stations and load loss in the SAPP network. The next blackout was on 21 January 2009 due to a tower failure, tripping the first 330 kV line from Kariba to Lusaka. This resulted in overloading and tripping of the second 330 kV line. At this point, a decision was made to disconnect the interconnection between Zimbabwe and Zambia. After opening the interconnection and without the connection between Kariba and Lusaka the power system was under severe constraints due to the rising load. After removing the connection between Zimbabwe and Zambia, Zimbabwe suffered a further three national blackouts. The increase in system instability in Zimbabwe, due to the Zambian connection, caused the connection between Zimbabwe and South Africa to be opened. The interconnections were opened due to the limited power transfer capability between the countries [10].

More recently on the 28th April 2015, a system failure at Kafue Gorge caused three 330 kV lines at Leopard Hills' 330 kV substation to trip. This resulted in loss of supply to eight of the ten provinces in Zambia. At the same time, a generator tripped at Kariba North Bank power station. On Zimbabwe's side the Kariba South and Hwange power stations tripped, affecting the whole country. Bulawayo power station and a piece of the town was powered by South Africa. Zambia's main power generation is located south in Zambia at Kariba and Kafue Gorge, which accounts for 89% of the total generation in the country. If the connection between the north and south of Zambia fails, most of Zambia is left without any power. This also caused a constraint on the connection between Zambia and Zimbabwe at Kariba, resulting in power failure in Zimbabwe as well [12].

By analysing the power outages in the SAPP network, common problems were identified such as limited power transfer, damping power of oscillations and voltage regulation (see figure 2). The SAPP network can be improved in various ways.

5. SUGGESTIONS

The following section introduces a few options to increase system stability in the network. The system can be improved by adding additional lines or by installing additional compensators in the network or both. An option is to add an additional line between Zimbabwe and South Africa, parallel to the existing 400 kV transmission line, as shown in Figure 1. The additional transmission line and transformer would double the line transfer capability to 1500 MVA. The increase in power transfer is a third of the projected power Zimbabwe maximum demand. The double line would increase the interconnection stability. The solution can be improved by including additional lines from Insukamini substation to Lusaka. The solution improves the corridor from South Africa to Zambia and strengthens the Zimbabwe central corridor.

A better, but more expensive, option is to improve the network in Botswana and connect it with Zimbabwe, Zambia and South Africa. The additional transmission lines allow an alternative path for power flow between Zimbabwe and South Africa. The interconnections provide additional export and expansion potential in Botswana. The proposed transmission line will be built to Pandamatenga in north of Botswana and connected to Hwange in Zimbabwe. The expansion is indicated in Figure 1 as solution two. From figure 1, the additional power flow path is clear.

The transmission line can also be connected to Victoria Falls power station, creating an additional line in parallel to Kariba. This introduces more stability, if any of the transmission lines were taken out of service, because the power flow has an alternative path to connect the system. From Victoria Falls the 220 kV line can be upgrade to a 330 kV line increase power transfer from Victoria Falls to Kafue.

The Zimbabwe central corridor can also be improved by managing the reactive power control in the network. Zimbabwe has a few devices to control the reactive power such as SVC, shunt reactor- and shunt capacitor banks. First, the performance of devices can be analysed to help determine the effect on the system as well as repair and reinstate the decommissioned devices. If the total reactive control is not enough, additional devices can be installed to help power transfer in the country as well as over the borders. Compensators can be added to Hwange, Harare and Kariba to improve interconnection capability and the Zimbabwean network.

6. CONCLUSION

The SAPP network experiences regular disturbances, which in some cases cause power outages in one or more countries. The power system remained mostly unchanged for the last two decades although the demand increased, which resulted in insufficient power transfer capacity. The large power outages were analysed, and show that the system has limited interconnection and power generation. The disturbances recorded in the SAPP network are grouped into the following categories: natural causes (weather conditions & fires), transmission faults (line, busbars and transformers), generation faults, equipment malfunction, insufficient generation, power oscillations and overloaded lines. The number of disturbances in the SAPP network are shown in Figure 2. The data was obtain through analysing the SAPP monthly reports from 2010 to 2015. From the 72 reports 52 reports provided useful data. The data shows that the majority of disturbances are transmission and generation faults. A few suggestions to overcome the shortcoming of the network were discussed. The possible solutions to solve the SAPP instability will be investigated in the next study by simulating the SAPP network. This will determine the feasibility of the solutions.

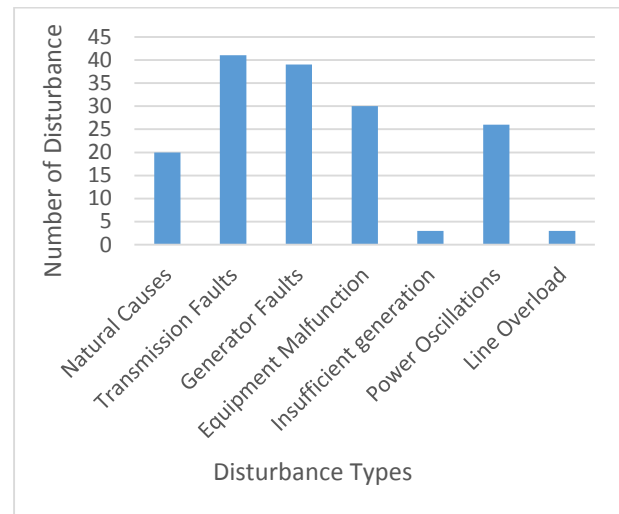


Figure 2: SAPP Disturbances from 2010-2015

7. REFERENCES

- [1] AllAfrica Global Media , "Zambia: CEC - Zambia's Oldest Private Owned Power Company," AllAfrica Global Media , 23 10 2014. [Online]. Available: <http://allafrica.com/stories/201410240361.html>. [Accessed 21 11 2015].
- [2] Economic Consulting Associates Limited, "Southern African Power Pool (SAPP) : Transmission & Trading Case Study," Economic Consulting Associates Limited, London, 2009.
- [3] Zambia Development Agency, "Energy Sector Profile," Zambia Development Agency, Lusaka, 2014.
- [4] High Voltage Construction, "High Voltage Installations," High Voltage Construction (Pvt) Ltd, [Online]. Available: <http://www.hvcafrica.com/projects/high-voltage-installations>. [Accessed 13 11 2015].
- [5] J. Glover, M. Sarma and T. Overbye, Power System Analysis and Design, Stamford: Cengage Learning, 2011.
- [6] S. Bamasak and M. Abido, "Robust Coordinated Design of PSS & STATCOM Controllers for Damping Power System Oscillation," *15th PSCC*, p. 107, 2005.
- [7] ABB, "Increase of Power Transmission Capacity in South Africa-Zimbabwe Interconnection by Means of SVC," ABB, Västerås, 2015.
- [8] R. Gouws, "Analysis of a 405 km Transmission Line with Series Compensation," EE Publishers, 2012.

- [9] A. Atputharajah and T. Saha, "Power System Blackouts - Literature review," in *Fourth International Conference on Industrial and Information Systems*, Sri Lanka, 2009.
- [10] Energy Regulation Board, "Zambia Nation-Wide Power Blackout of June 4, 2006," Energy Regulation Board, Lusaka, 2006.
- [11] G. Nkombo, "Report of the Committee on Energy, Environment and Tourism on the Familiarisation Tour of Kafue Gorge and Kariba North Bank Power Stations," National Assembly of Zambia, Lusaka, 2008.
- [12] Kafue, "Mwebantu," Mwebantu New Media, 2015 April 2015. [Online]. Available: <http://www.mwebantu.com/2015/04/28/zambia-suffers-nationwide-power-outage/>. [Accessed 20 June 2015].
- [13] R. Bacher and U. Näf, Report on the blackout in Italy on 28 September 2003, Berne: Swiss Federal Office of Energy (SFOE), 2003.

8. BIOGRAPHIES



Hermi du Plessis obtained a B Eng. degree in Electrical Engineering at the North-West University Potchefstroom campus in 2014. He is a fulltime post-graduate student investigating the dynamic behaviour of the SAPP network, at the North-West University.



Jan A de Kock holds a B Eng, M Eng and PhD in Electrical Engineering from Stellenbosch University in South Africa. At present, he is Professor in Electrical Engineering at the North-West University, Potchefstroom campus, in South Africa. His academic and consulting interests include power system dynamic performance, power quality, protection performance and optimization studies, improvements of generator dynamic response, induction and synchronous machine transient performance, and high speed bus transfer system. He is the author of a number of papers and the co-author of a book.

Applying the Herman-Beta probabilistic method to Medium Voltage distribution feeders

M.J. Chihota*, C.T Gaunt¹ and R. Herman²

^{1,2}University of Cape Town, Department of Electrical Engineering, Rondebosch, Cape Town, South Africa

*Email: mjchots2@yahoo.co.za

Abstract: This paper presents a probabilistic approach for voltage drop calculations on Medium Voltage (MV) feeders. The approach discussed is based on the Herman-Beta method, an algorithm developed for Low Voltage (LV) feeders characterised by negligible line reactance and nearly unity power factor loads. To extend this method to MV feeders, approximate modifications to the input parameters for feeder impedance and load currents are implemented in order to include the effects of line reactance and load reactive power in voltage drop calculations. Using this modified approach, voltage drop computation for passive and active MV feeders is presented. For validation, a Monte-Carlo Simulation (MCS) with exact feeder parameters is used.

1 INTRODUCTION

Load flow or power flow analysis is the most fundamental tool used by power system engineers to analyse the steady state condition of power systems with regard to bus voltages, real and reactive power flows, line losses and faults. Through load flow analysis, consumer (bus) voltages and angles at steady state can be attained. This is essential as these parameters are meant to be kept within specified limits [1]. Load flow studies are therefore crucial tools in network planning and design in the field of power system engineering. Techniques used to solve the load flow problem can be categorised based on the manner in which the solutions are obtained.

1.1. Deterministic Load Flow – Classic Approach

Deterministic Load Flow (DLF) methodologies use specified (fixed) values of power generation, loads and network parameters to compute system steady-state operating conditions. The use of these traditional methods consequently becomes inaccurate and therefore less reliable amidst uncertainty. This is simply because the DFL methodology disregards uncertainty elements of the power system such as failure rates, intermittent power generation, and the general stochastic customer load variations [2].

In the Medium Voltage (MV) network, the deterministic approach to power flow studies remains prevalent in many countries. This approach is based on a non-statistical load modelling methodology that represents loads with mean values referred to as After Diversity Maximum Demand (ADMD) together with correction factors that attempt to address diversity and

imbalances in loads. South Africa also utilises DLF methods for voltage drop analysis on MV feeders. Though the load represented by MV/LV transformers is modelled statistically, it is converted into a fixed value at the transformer terminals in order to apply DFL tools. The loads from direct MV customers are represented through ADMD values. A deterministic load flow calculation with the consideration of power factor and reactance is then done in the assessment of consumer voltage in the network [3]. Though this was found to be adequate within customer load variability, the uncertainties of DGs are likely to cause inaccuracies in this method [4].

Inaccuracy and inefficiency cannot be freely tolerated in power systems as design parameters are directly linked to the overall system cost, the magnitude of losses in the network and power system reliability. Design uncertainties therefore pose a great impact to network planning and design [5]. Hence, the explicit consideration of uncertainties requires the deployment of probabilistic approaches so as to provide the ability to manage the wide spectrum of all possible values of the input and state variables [6].

1.2. Probabilistic Load Flow – Modern Approach

In order to account for the uncertainty elements in the power system, probabilistic methods are required to cater for the stochastic variance in the generation as well as the load profiles. Probabilistic Load Flow (PLF) methods were first proposed in 1974 by Borkowska [7] and have since been developed over the decades. PLF methods regard both loads and DG sources as random variables due to their stochastic unpredictable natures. These methods have resulted in more reliable and accurate results than the classic deterministic (DLF) methods [2]. PLF's make use of probability or cumulative density functions allowing the analysis of the load flow or feeder voltage drop within risk or confidence intervals. With the use of pdfs, PLF's are able to account for the uncertain power production and load variations through an iterative selection of random input values from the distributions to represent the possible input variables.

The choice of which probability density function to use in the modelling of loads is an area of evolving research presently. According to Neimane [8] the normal, log-normal and beta pdfs adequately fit MV load data as demonstrated through Chi-square fitness tests. It was however found that in cases where the data was not symmetrical, the beta and log-normal pdfs were

more appropriate. Most PLF methods for voltage computation in MV systems are based on a Gaussian model[9]–[11].

The Monte-Carlo method is quite a renowned tool in this class of numeric PLF methods. High computational time as a result of the iterations has however limited the use of these methods. An attempt to address this inadequacy led to the development of analytical methods.

The problem of slow computation speed brought about through the iterative approach to voltage calculation is dealt with using analytical probabilistic techniques. The most renowned methods are based on parameter estimation using the method of moments. Celli and Pilo [9] made use of the mean and variance of normally distributed input random variables to compute similar parameters for voltages on MV distribution feeders. The method proved successful but however restricts the modelling of input data to a Gaussian fit without allowance of skewness. This shortfall can be addressed by PLF methods based on pdfs that allow modelling of input variables with flexibility of skewness such as the beta function.

The implementation of such pdfs was proposed and developed for LV feeders by Herman and Gaunt [12]–[14] in 1994. Their approach referred to as the Herman-Beta (HB) algorithm is an analytical statistical method used for voltage drop computation for LV feeders in South Africa [15]. This method uses the first two statistical moments to represent beta distributed currents drawn by loads and those injected by DGs. Using the parameter estimation method, the resulting voltage pdfs on the feeder are then computed. This method is a non-iterative approach which has proven to be superior to other methods as investigated by Sellick and Gaunt [16]. However, the method was specifically derived for LV feeders as seen with the assumption of zero feeder X/R ratio (negligible reactance) and that of unity power factor loads (negligible Var) at the instant of maximum demand, which is not the case for MV.

Regardless of this specificity, Siebert et al. [2] applied the HB algorithm without modification to MV feeders. A comparison of its performance against a DLF method and the Monte-Carlo simulation indicated that the HB method was computationally faster but however less accurate than the other methods. The conclusion drawn suggested that the HB algorithm could be used for voltage computation on MV feeders.

This paper investigates the possible improvement of the accuracy of the HB PLF method on voltage calculations on MV feeders through compensation of omitted parameters in the approach used on LV feeders.

2 PARAMETER SENSITIVITY ANALYSIS

A comparative analysis of the network models of LV and MV feeders reveals that MV feeders have higher X/R ratios than LV feeders [17]. Actually, in MV feeders, X/R ratios are usually around unity which implies that feeder reactance is as significant as resistance [3], [9], [18]. The assumption of negligible reactance in the HB approach for LV feeders is therefore inconsistent with MV feeders.

With regards to loads, literature reveals that MV loads are usually of lagging power factor [9], [19]–[21]; with the exception of the loads represented at MV/LV transformer terminals [19], [21]. This means that there is a substantial flow of reactive power in MV than LV feeders. Consequently, the assumption of unity power factor loads is inconsistent with the load composition in MV networks.

The extent to which these ignored parameters in the HB algorithm affect voltage calculation on MV feeders was investigated to establish the necessity of compensation for reactance and reactive power in the calculation of voltages on MV feeders.

2.1. Variation of feeder voltages with line reactance

To investigate the necessity of compensation of line reactance in the calculation of feeder voltages, a comparison of voltage outcomes on a loaded passive feeder for different values of line reactance was performed using the Monte-Carlo Simulation (MCS). Fig. 1 shows the voltage pdfs at the end of the feeder for the different cases of feeder reactance.

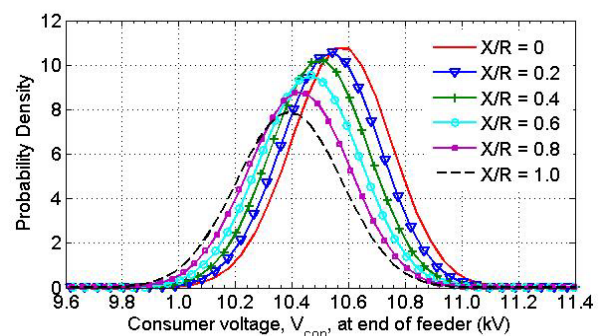


Fig 1: Variation of feeder voltage with line reactance

The results obtained reveal a significant decrease in feeder voltages with increasing line reactance. In this specific application, a relative voltage error of up to 2% would result if reactance was not factored in the calculation of voltages on the feeder. Considering the permissible 5% (in South Africa) voltage drop specification for MV feeder design, the error margin noted with the exclusion of line reactance in voltage calculations is substantial. The result points to the requirement of compensation of line reactance in the HB algorithm.

2.2. Variation of feeder voltages with power factor

An investigation on the sensitivity of feeder voltages to non-unity power factor loads was also conducted for to investigate the effects of reactive power flow on the calculation of feeder voltages. Using a MCS, feeder voltages for varied cases of load power factors were calculated whilst the line reactance was kept constant. Fig. 2 shows the variation of voltages with load power factor.

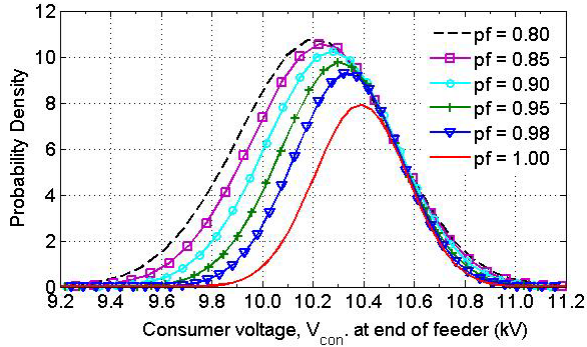


Fig 2: Variation of feeder voltage with load power factor

The output pdfs shown in Fig. 2 reflect an increase in voltages with power factor. In other words, lagging power factors are seen to cause notable increases in voltage drops thereby lowering feeder voltages. In this specific application, relative errors of up to 3% would result if the assumption of unity power factor loads as applied to LV feeders is extended to MV feeders. This find suggests the need to modify the approach to which the HB algorithm is applied to MV feeders. The compensation of load reactive power is essential.

3 THE MODIFIED HB APPROACH

Sensitivity tests established that the effects of reactance in voltage drop calculations in MV networks cannot be ignored. Errors in network power flow analysis would arise leading to uneconomical and incorrect network planning and design decisions. However, the inclusion of these parameters in the voltage drop equations for the HB algorithm requires the reformulation of the entire algorithm since it is dependent on the voltage drop equations.

In this work, an approximation approach is applied to compensate for the effects of reactance and non-unity power factor loads on voltage calculations. Using this approach, only the input parameters for impedance and load current are modified to mimic the respective effects of line reactance and lagging power factor loads on feeder voltages. The methodology implemented is described segmentally in the sections that follow.

3.1. Compensation for line reactance

Mathematically, the line impedance vector, Z_p can be expressed in phasor form as follows:

$$Z_p = R_p + jX_p = |Z_p| \angle \theta \quad (1)$$

In this work, the approximation of feeder impedance by its absolute value without its phasor angle is used. The phasor angle is avoided as it results in new terms in the voltage equations from which the HB algorithm is formulated. Its inclusion would require an entire re-formulation of the algorithm.

Using $|Z_p|$ in place of R_p , the effects of reactance are partly incorporated in the calculation of voltages. This is expected to achieve better and comparable results with the MCS with the exact feeder and load parameters.

3.2. Compensation for load reactive power

Non-unity power factor loads unlike unity power factor loads draw complex currents. The representation of such currents in the HB method is problematic since the formulation was done considering real load currents only. Therefore, in order to be able to utilise the same algorithm for voltage calculations on MV feeders with lagging power factor loads, a compensation technique is considered.

Power factor variation has a direct effect on customer load current. The phase load current, I_L , increases as power factor decreases as expressed in the equation below.

$$I_L = \frac{P_L}{\sqrt{3}V \cos \theta} \quad (2)$$

where $\cos \theta$ is the load power factor and P_L and V are phase quantities denoting real power consumed and bus (or nodal) voltage respectively.

Considering the phase quantities P_L and V to be constant, a low power factor as depicted by $\cos \theta$ would result in a higher current than usual in the network. This causes increased voltage drops along the feeder, hence the falling voltages noted in Fig. 2.

The inflation of nodal currents with load power factor as in (2) is used as an approach to compensate for the effects of lagging power factors on feeder voltages. Therefore, for each load, the load current is inflated by the power factor value. For cases in which only the substation power factor is given, the real power parameters for each load are used with the common power factor.

3.3. Approach for voltage calculations on active feeders

Active feeders with DG are merely the same as passive feeders with additional generator nodes. The approaches discussed in the preceding two sections are used for the load nodes. However, for generator nodes, the HB approach for active feeders in particular to DG nodes is used without modification. This is because the generators considered in this study only inject real power. The compensation approaches discussed earlier would result in over-estimations of volt drops since the

variations of voltages are minimal for the condition of unity power factor power flow on reactive elements.

4 SIMULATION RESULTS

In order to validate the proposed approach and assess the level of improvement it makes in comparison with the HB algorithm without modified input parameters, voltage results from the two HB approaches are compared with those from a Monte-Carlo Simulation (MCS) with 15000 iterations. The MCS used is based on exact network parameters without simplification.

A relative consumer voltage error test index, $\varepsilon_{V_{con}}$, is used to quantify the performance of the algorithm. This index, expressed as a percentage of the nominal voltage is defined as follows:

$$\varepsilon_{V_{con}} = \left| \frac{E(V_C)_{HB\Delta inputs} - E(V_C)_{MCS}}{V_{nom}} \right| \quad (3)$$

where $E(V_C)_{HB\Delta inputs}$, $E(V_C)_{MCS}$ and V_{nom} indicate the expected consumer voltage of the modified approach, that of the MCS and the nominal bus voltage.

The same index is used to determine the error in the calculation of voltages using the unmodified HB approach (HB_{original}). The networks used in the tests conducted are described as follows.

4.1. The MV test feeder

An 11kV, 3-phase 4-wire MV test feeder is used in the study. The one line diagram for the feeder is shown in Fig. 3 below.

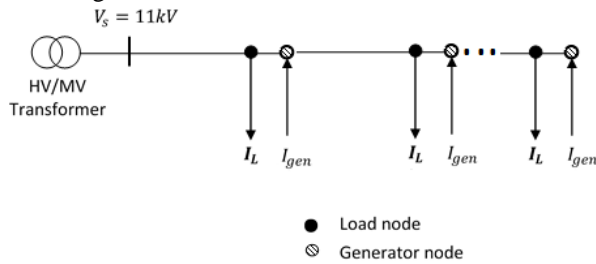


Fig 3: MV test feeder one-line diagram

In the tests conducted, 6 paired nodes (6 for loads, 6 for generators) are used. In the case of passive feeder tests, the generator nodes are ignored. However, for the case of active feeder tests, generator nodes separated by short distances of 0.1metres for the sake of algebraic identity are included.

4.2. Variation of feeder voltages with line X/R ratios

To assess the performance of the proposed approach on realistic MV feeders, the feeder X/R ratio is varied from 0 to 1.5 whilst the load power factor is kept constant at 0.8 lagging. The effects of the modifications applied to cater for reactance on MV feeders can thus be

investigated by comparing the accuracy of the two HB approaches in computing voltages on the test feeder based on outcomes from the MCS.

Fig. 4 shows the variation of consumer voltage with feeder X/R ratios using the three methods.

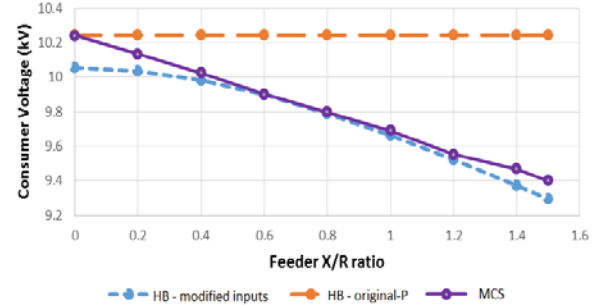


Fig 4: Variation of feeder voltage with load power factor

As depicted by the alignment of the voltage traces in Fig. 4, the proposed method (HB-modified inputs) generally achieves better accuracy than the unmodified approach which gives the same voltage result for all cases. Fig. 5 shows the voltage pdfs for an extract case with loads at a power factor of 0.8 lagging on a loaded feeder with unity X/R ratio.

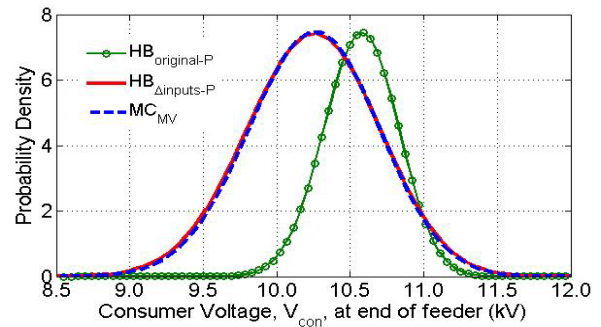


Fig 5: Variation of feeder voltage with load power factor

From Fig. 5, it can be seen that the proposed approach, HB_{Δinputs-P}, attains improved accuracy in the calculation of voltages. The relative error noted with HB_{Δinputs-P} in this specific application is only 0.07% as compared to 3% in the unmodified approach.

4.3. Variation of feeder voltages with power factor

Tests results on the performance of the proposed approach for varied conditions of load power factor on an MV feeder of unity X/R ratio are shown in Fig. 6.

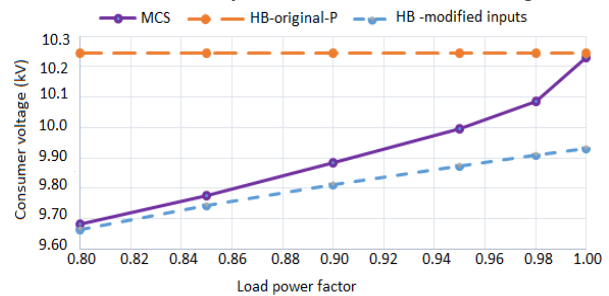


Fig 6: Variation of feeder voltage with load power factor

The results in Fig. 6 generally indicate an improved performance of the HB method using the proposed approach. For power factors below 0.95, $HB_{\Delta inputs-P}$ calculates voltages within relative errors values below 1%. In contrast, the error noted with the unmodified approach ranges between 2 and 5%. However, for cases of power factor equal and higher than 0.98, the modified approach results in parameter overcompensation leading to reduced accuracy.

Fig. 7 shows the comparison of the voltage probability distribution curves for the two HB approaches against the MCS for a loaded feeder of unity X/R ratio with loads of 0.9 lagging power factor. The case shown is an extract of the investigated scenarios presented in Fig. 6.

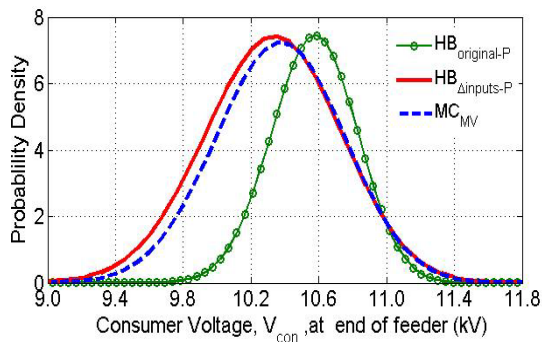


Fig 7: Variation of feeder voltage with load power factor

As can be seen from Fig. 7, the voltage pdf for the unmodified HB approach is misaligned with a voltage error of about 3.3%. The approach results in underestimation of feeder voltage drops in this specific application. On the contrary, $HB_{\Delta inputs-P}$ offers an improvement in the accuracy of voltage calculation as noted with the alignment of its trace with that of the MCS. The relative error noted in this case is only approximately 0.6%.

4.4. Variation of voltage with DG penetration

In order to demonstrate the performance of the modified approach on active MV feeders, tests were conducted on a feeder of unity X/R ratio with loads of 0.9 lagging power factor and unity power factor generators. DG connections were gradually increased on the feeder and voltage results compared with those from the MCS. Fig. 8 below shows the comparison of voltage error between the two HB approaches.

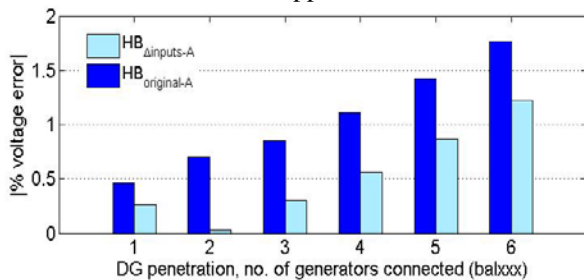


Fig 8: Variation of feeder voltage with load power factor

The bar graphs illustrate the improvement in accuracy of the HB algorithm using the proposed method. The increase in error with DG penetration is common to both methods since voltage calculations at DG nodes are done in the same way.

4.5. Performance consistency tests

In order to fully validate the proposed approach, voltage calculations using the method were performed for diverse load and feeder X/R ratio conditions. Fig. 9 shows a surface plot for voltage relative error, compared to the MCS, attained for the different cases tested.

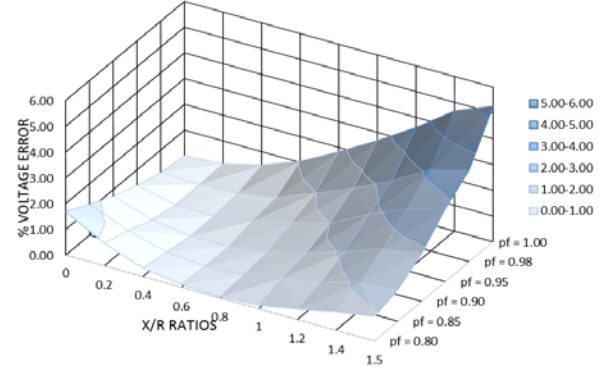


Fig 9: Variation of relative error for diverse feeder conditions

Looking at the distribution of error shown in Fig. 9, it is seen that the majority of the points on the surface plot correlate to errors less than 1% (most faint shade, between 1st and 2nd contour lines). The areas with errors greater than this are mainly as a result of the following combinatory conditions:

- Feeder X/R ratio greater than 1 across power factors greater than 0.85
- Unity power factor loads across X/R ratios greater than 0.8
- Zero X/R ratio with power factors 0.8 and 0.85

The majority of these errors are as a result of the over-estimation done by $HB_{\Delta inputs-P}$. In order to minimise these errors, no compensation is applied for cases involving unity power factor loads and zero X/R ratios.

5 CONCLUSIONS

In this paper, an approach to apply the HB algorithm on MV feeders was presented and validated using the MCS. The results showed that the modification of input parameters to compensate for line reactance and reactive power substantially improves the accuracy of the HB method on MV feeders. However, the accuracy of this modified approach in comparison to the Monte-Carlo simulation cannot be easily quantified as errors are not constant. Nevertheless, the general improvements in accuracy compared to the HB algorithm without adjustments encourage further work on the algorithm for voltage calculations on both passive and active MV feeders.

6 ACKNOWLEDGMENT

We would like to greatly acknowledge financial support from the University of Cape Town and the subsidiary funding through the Dutkiewicz Family Trust Fund. The success of this work is also as a result of the input from research peers in the Power Systems Research Group at the University of Cape Town.

7 REFERENCES

- [1] Eskom, *Electricity supply — quality of supply Part 2: Voltage characteristics, compatibility levels, limits and assessment methods*, NRS Standards NRS048-2:2003.
- [2] L. C. Siebert, L. R. Ferreira, A. Aoki, A. Bonelli, A. R. R. Souza, and F. D. O. Toledo, "Deterministic versus Probabilistic approaches to self-healing in Smart Grid," in *22nd International Conference on Electricity Distribution*, 2013, p. 1413.
- [3] C. G. Carter-Brown, "Effect of conductor size on the total cost of electricity distribution feeders in South African Electrification," Ph.D. dissertation, University of Cape Town, 2006.
- [4] F. Adinolfi, F. Baccino, M. Marinelli, S. Massucco, and F. Silvestro, "Model of a real medium voltage distribution network for analysis of distributed generation penetration in a SmartGrid scenario," *2012 3rd IEEE PES Innov. Smart Grid Technol. Eur. (ISGT Eur.)*, pp. 1–7, 2012.
- [5] R. Herman and C. T. Gaunt, "Electrification: Uncertainties, Models and Design Procedures townhouses," *CIGRE*, vol. 6, no. Coll, pp. 6–7, 2005.
- [6] D. D. Le, A. Berizzi, C. Bovo, E. Ciapessoni, D. Cirio, A. Pitto, and G. Gross, "A probabilistic approach to power system security assessment under uncertainty," in *2013 IREP Symposium Bulk Power System Dynamics and Control - IX Optimization, Security and Control of the Emerging Power Grid*, 2013, pp. 1–7.
- [7] B. Borkowska, "Probabilistic load flow," *IEEE Trans. Power Appar. Syst.*, vol. 93, no. 3, pp. 752–759, 1974.
- [8] V. Neimane, "Distribution network planning based on statistical load modeling applying genetic algorithms and Monte-Carlo simulations," *2001 IEEE Porto Power Tech Proc. (Cat. No.01EX502)*, vol. 3, 2001.
- [9] G. Celli, S. Mocci, F. Pilo, and R. Cicoria, "Probabilistic optimization of MV distribution network in presence of distributed generation," in *Proc. PSCC Conf*, 2002, pp. 24–28.
- [10] S. Repo, H. Laaksonen, and P. Jarventausta, "Statistical Models of Distributed Generation for Distribution Network Planning," in *CIREN 18th International Conference on Electricity Distribution*, 2005, pp. 1–5.
- [11] R. Singh, B. C. Pal, and R. Jabr, "Statistical representation of distribution system loads using Gaussian Mixture Model," *IEEE Trans. Power Syst.*, vol. 25, no. 1, pp. 29–37, 2010.
- [12] R. Herman and C. T. Gaunt, "A Practical Probabilistic Design Procedure for LV Residential Distribution Systems," *IEEE Trans. Power Deliv.*, vol. 23, pp. 2247–2254, 2008.
- [13] C. T. Gaunt, R. Herman, M. Dekenah, R. L. Sellick, and S. W. Heunis, "Data collection, load modelling and probabilistic analysis for LV domestic electrification," in *International Conference on Electricity Distribution (CIREN)*, 1999.
- [14] R. Herman and J. Kritzinger, "The statistical description of grouped domestic electrical load currents," *Electr. Power Syst. Res.*, vol. Volume 27, no. 1, pp. 43–48, 1993.
- [15] Eskom, *Electricity distribution — Guidelines for the provision of electricity distribution networks in residential areas Part 1: Planning and design of distribution networks*, NRS Standards NRS 034-1:2007.
- [16] C. T. Gaunt and R. L. Sellick, "Comparing methods of calculating voltage drop in low voltage feeders," in *Trans SA Institute of Electrical Engineers*, 1995, vol. 86, no. 3.
- [17] C. L. Masters, "Voltage rise the big issue when connecting embedded generation to long 11kV overhead lines," *Power Eng. J.*, vol. 16, no. 1, pp. 5–12, 2002.
- [18] C. T. Gaunt, R. Herman, G. Celli, and S. Mocci, "MV and LV distribution feeder design using probabilistic approaches to load and DG Introduction," presented at *CIREN 21st International Conference on electricity Distribution*, Frankfurt Germany, 2011.
- [19] E. Zio, M. Delfanti, L. Giorgi, V. Olivieri, and G. Sansavini, "Electrical Power and Energy Systems Monte Carlo simulation-based probabilistic assessment of DG penetration in medium voltage distribution networks," *Int. J. Electr. Power Energy Syst.*, vol. 64, pp. 852–860, 2015.
- [20] A. S. Safianni, V. C. Poulous, and G. N. Koutroumpetis, "Penetration of Mixed Distributed Generators in a Medium Voltage Network," in *Universities Power Engineering Conference (UPEC), 2012 47th International*, 2012, pp. 1–6.
- [21] D. P. Stojanović, L. M. Korunović, and J. V. Milanović, "Dynamic load modelling based on measurements in medium voltage distribution network," *Electr. Power Syst. Res.*, vol. 78, no. 2, pp. 228–238, 2008.

Drivers and Application of Small Scale DG on Municipal Distribution Networks in South Africa

S. Sewchurran^{1*} and I E Davidson²

¹*eThekweni Electricity, eThekweni Municipality, Durban 4001, South Africa

² University of KwaZulu-Natal, Eskom Centre of Excellence in HVDC Engineering, Durban 4001, South Africa

*Email: SewchurranSan@elec.durban.gov.za

Abstract: South Africa is experiencing regular power outages due to under-frequency load shedding, rising electricity tariffs, environmental concerns and delays in constructing new power stations. This has led consumers and producers alike to explore various energy generation options to assist the sector to meet the electricity demands whilst reducing their own electricity needs. Electric utilities are faced with various concern in understanding the impact arising from the potential uptake figures that these Small Scale Distribution Generation (SSDG) plants will have on their existing distribution networks. This is due to limited guidance or industry standards and lack of expertise within utilities to ensure the safe, intelligent disbursement and technical integration of these plants into existing low voltage (LV) networks in South Africa. This paper discusses the drivers of SSDG in the local utilities distribution networks using eThekweni Municipality as a case study example to determine the potential of SSDG projects based on these drivers. The feasibility of these SSDG projects is carried out and the current guidelines regarding SSDG is discussed.

1 INTRODUCTION

The Electricity Supply Industry in South Africa has undergone considerable restructuring since 2008 when the National Electricity Supplier (Eskom) had to undergo forced load shedding in order to maintain the stability of the national electricity network. Ever since, the reserve margin between the supply and demand of electricity has been tight and the possibility of rolling blackouts has been high [1]. South Africa was historically the cheapest electricity supplier in the world, but this position has changed over the last 7 years as a result of constraints in building new generation plants within the country. This has led to a doubling of electricity prices in the country over the past 7 years. With the ongoing electricity price increases, connection of SSDG on the local electricity distribution network is becoming an increasingly attractive prospect in South Africa [2]. Distributed Generation (DG) is predicted to play an increasing role in the electric power system of the near future. Various DG technologies are entering a period of rapid

expansion and commercialization [3]. Solar-PV and wind energy have become cheaper over the past few years and their prices are expected to drop even further going forward [2]. Given the recent reduction in the cost of PV, it has become probable that residential and commercial customers, as well as some industrial customers will begin installing PV to meet some or all of their electricity requirements [4]. Studies have shown that Durban is well situated and blessed with good climatic conditions and resources to support these PV projects [5]. Fig.1 shows the world map of Global Horizontal Irradiation which indicates that South Africa has some of the best Global Horizontal Irradiation in the world and is hence well suited for solar PV

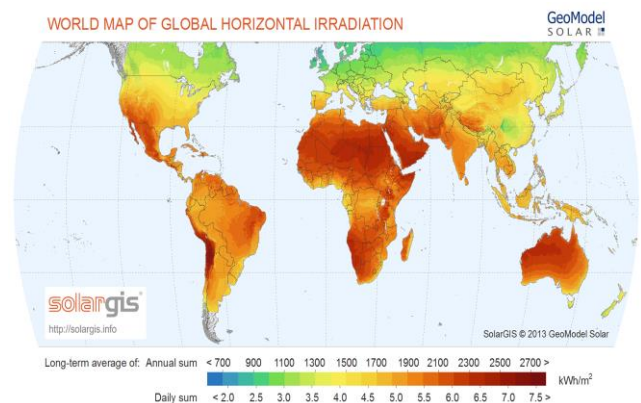


Fig. 1: World map of Global Horizontal Irradiation [6]

The adoption of these SSDG schemes have been driven in part by the impact of environmental, regulatory and economic challenges, as well as changing public perception prevalent in the 1990s [7]. The environmental awareness created by the promotion of green energy and energy sustainability following the Conferences of the Parties 17 Climate Change Conference in Durban has prompted an increasing number of residents to reduce their carbon footprint [8].

Load shedding and the unstable supply of electricity have hampered economic growth and diminished investor confidence in the economy. However, customers are now more aware of the concepts of electricity usage and continuously seeking for

innovative ways to reduce their consumption. Many are turning to energy efficiency projects whilst others are looking into the feasibility of SSDG. With electricity prices rising in the country, the pay back periods and viability of small scale generation projects are becoming even shorter and more feasible [9].

In SSDG projects, there is a reluctance to combine expensive energy storage technologies to these systems but rather synchronize and utilise the municipal grid as a virtual battery. Whilst the advantages make synchronization to the grid a logical choice, the municipal network design and framework is not designed to facilitate this. The municipal mandated core function is to procure electricity from Eskom, transform it and distribute it to the end users. Power flow is from Eskom to the end user and all technical, administrative, regulatory and legal aspects are structured to support this unidirectional flow of electric power [10]. The introduction of DG introduces bi-directional power flow on the distribution network. This has an impact on quality of supply, planning, network losses, protection, metering and control of power flow on the existing distribution network.

2.0 DRIVERS OF SSEG IN SA

The Integrated Resource Plan (IRP) of South Africa estimates that Embedded Generation (EG) of residential and commercial PV could reach 22.5 GW by 2030. Even if these estimates are partially correct, this points to a significant level of installed small-scale PV projects in South Africa by 2030 [11]. Based on the National Energy Regulator of South Africa research and analysis, solar photovoltaic (PV) in higher demand in South Africa at the moment than any other technologies. This is largely in the under 1 MW installation category [12]. There have been several requests to eThekwin Electricity for the installation and connection of small scale rooftop PV projects to the distribution network. This suggests a demand out there for these systems in South Africa.

2.1 Drivers of SSDG in South Africa

There are a number of drivers of DG in South Africa which include but are not limited to the following:

2.1.1 Load Shedding

South Africa is currently facing one of its greatest challenges of all time in the electricity sector, often leading to daily load shedding in order to prevent a collapse of the national grid. Since the commencement of loading shedding in 2008, the country has been struggling to meet its electricity demands. To date there has been numerous delays in the commissioning of units at the two new (4800 MW) coal fired power stations. Only one 800 MW unit from the Medupi Power station was brought online as of the 1 March 2015 and approximately 2000 MW of renewable energy IPP projects have started to contribute to the country's electricity needs. Eskom has also supplemented its energy shortages by running its expensive diesel Open Cycle Gas Turbines to provide electricity generation shortfalls but even this has not averted the constant need for load shedding. Government has hence encouraged the country to explore renewable energy sources.

2.1.2 Rising Electricity Tariffs

Since the start of load shedding in 2008, there have been large increases in the electricity tariff year on year. Fig. 2 shows the annual electricity tariff increase for the eThekwin Municipality who purchases its electricity from the national generator (Eskom) and then pass it onto its consumers. The residential electricity tariffs have increased by an average of 14.5 percentage over the past 7 years. [13]

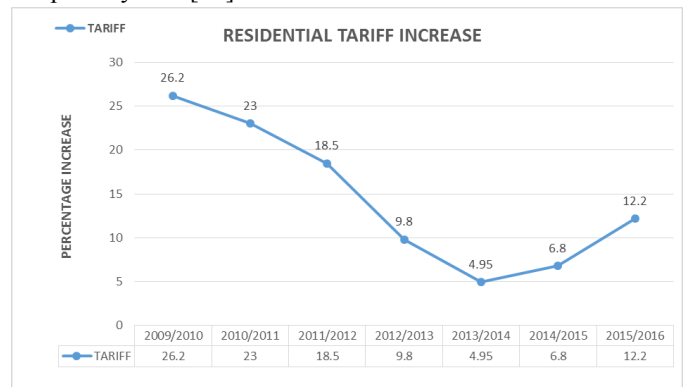


Fig. 2: Rising Municipal electricity tariffs [13]

The currently eThekwin Electricity (EE) residential single and three phase tariffs are R1.475/kWh. There are presently 319 875 (44%) single and three phase credit residential customers that utilize an average of 700 kWh a month. There are also 358 411 (49%) prepaid customers that are made up of rural, RDP and informal dwellings that utilize an average of 200 kWh

on average a month. Based on their consumption figures, dwelling sizes and income levels, credit customers are more likely to install rooftop PV systems.

Tab. 1: Residential Tariff R/kWh [13]

EE Tariff Scales	Descriptions	2015/2016 – Tariff (R/kWh)
3, 4, 8 & 9	Single and three phase residential tariffs	1.4750

2.1.3 Reduction in Carbon Footprints

There are numerous companies in Durban that are installing DG technologies such as PV and gas to electricity in order to reduce their carbon footprints. One such company is Man Truck and Bus Manufacturing situated in Westmead, Durban. They are currently the first Carbon Neutral truck production company in Africa. Fig. 3 shows their roof top PV installation which was installed for the purpose of reducing their carbon footprint. This driver was also used by other companies in Durban such as Standard Bank (45 kW rooftop PV installation) and Dube Tradeport (600 kW roof top PV installation).



Fig. 3: First Carbon neutral truck manufacturing facility

2.1.4 Reduction in the payback period of DG installations

There has been a reduction in the payback period of various DG technologies as prices of technologies such as PV have drastically reduced whilst the price of electricity has been on a constant rise. [4] According to a study by international business consultant, Frost and Sullivan, PV solar power could be the cheapest generation source in South Africa by 2020. At a cost of

between 65c/kWh and R1.36/kWh, solar energy may cost less than half of the R1.69/kWh that Eskom electricity is expected to reach over the same period [2].

2.2 Driver of DG technology around the world

There are a number of drivers of SSEG around the world as shown in Table 2 with the main drivers been Feed-in-tariffs (FIT), Net metering, net billing, self-consumption and generation export tariffs.

Tab. 2: International Drivers of DG [14]

Country	Scheme Type	Comments
Australia	Feed-in-tariff (FIT)	The FIT is lower than the retail electricity price.
Belgium	Net – metering	Brussels and Wallonia also have green certificates.
Brazil	Net – metering	Virtual net-metering is available.
Canada (Ontario)	Net metering and FIT	Also a FIT scheme, with compensation higher than retail electricity price.
China	Feed-in-tariff	FIT is equal to the wholesale electricity price plus a bonus.
Denmark	Feed-in-tariff	The FIT is lower than the retail electricity price.
France	Feed-in-tariff	FIT is above retail electricity price.
Germany	Feed-in-tariff	The FIT is lower than the retail electricity price.
Israel	Net metering	T&D costs are subtracted from the credits.
Italy	Net billing	Quarterly compensation.
Japan	Feed-in-tariff	FIT is above retail electricity price.
Mexico	Net metering	Virtual net-metering is available.
Spain	Self Consumption	PV excess are not compensated but are charged to cover T&D costs.
Switzerland	Feed-in-tariff	The FIT is lower than the retail electricity price.
Netherlands	Net metering	For up to 5 MW/h per year.
United Kingdom	Generation export tariff	A generation tariff remunerates PV generation and export tariff is added to electricity exported to the grid.
USA (California)	Net-metering	Positive balance at the end of each year can be either cashed in or rolled over.

2.3 Feasibility of small scale PV projects

The feasibility of small scale DG projects are largely dependent to two factors, namely: the cost of the DG plant and the electricity tariffs. To evaluate the feasibility, there is a need to estimate the electricity tariffs going into the future. Figure 4 shows the

predicted eThekweni Electricity residential tariff increases projected for 8% (low growth scenario), 11.5% (medium growth scenario) and 14.5% (high increase scenario) increase from 2015 – 2025. The bases for the selection of the 8% tariff increase for the low increase scenario is from the Multi Year Price Determination 3 (MYPD3), which was approved by the National Energy Regulators of South Africa for 8% until 2018. Eskom has, however, applied to the National Energy Regulator to allow for additional increases above the approved 8%. The basis for the high increase selected was derived from the average residential tariff increase over the last 7 years, which was 14.5% at eThekweni Electricity. The medium increase scenario was selected in-between the high and low increase scenario.

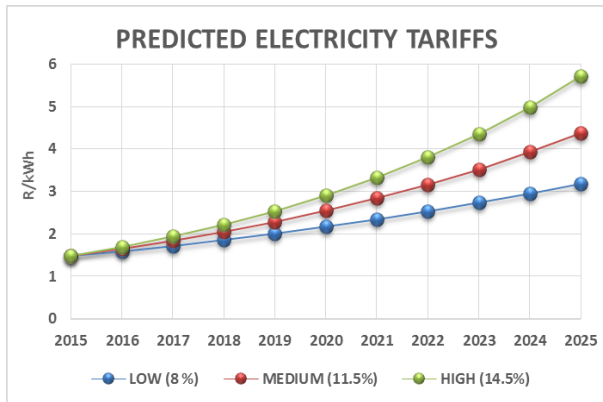


Fig. 4: Projected Electricity residential tariffs

As it can be seen from the above figure, the electricity prices increase in 2020 could vary from 216.72 c/kWh to 290.28 c/kWh and between 318.44 c/kWh to 571.27 c/kWh in 2025. Together with the reducing prices in the PV sector, this makes residential PV a lucrative option and hence it is projected to see an increase in PV installations going forward.

2.3.1 Case Study 1: Payback of a residential 5 kW rooftop PV

The feasibility of a rooftop PV system depends on a number of factors namely:

- Import electricity tariff
- Cost of PV installation
- Positioning of the PV panels
- Shading effects
- Export or Renewable Energy Feed in Tariff (REFIT)
- Life span of the inverter
- Percentage of generated electricity utilised

- Degradation rate of the PV panels (generation output)

The problem with residential PV in comparison with the residential load profile is that during the PV generation peak, which is around noon, the electricity usage by the household is low resulting in electricity being exported to the grid. With the Municipalities currently not offering any payback (export tariff or REFIT tariff), the feasibility of these projects depends largely on the amount of electricity utilized and the savings received from electricity not purchased from the grid. Fig. 5 shows a typical residential load profile and a PV generation profile.

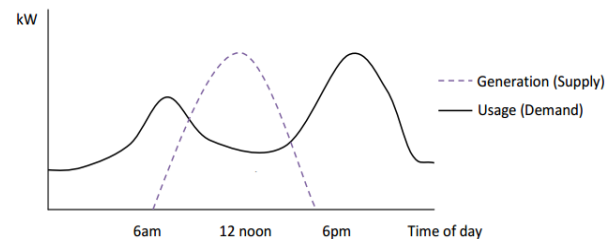


Fig. 5: typical residential load profile vs PV generation profile [15]

We investigate the payback periods of rooftop PV by carrying out a few payback period calculations to look at the payback period of rooftop PV assuming that 50%, 75% and 100% generated electricity from the system was utilised. The actual figures from an existing rooftop PV project in Kloof was utilised. This PV system parameters are shown in Table 3. The calculations utilised the cost of R20/Watt installed rooftop PV obtained from quotations received from PV installers in Durban for the equipment shown in Table 3.

Tab. 3: Five kW rooftop PV details [16]

Location	Kloof, Durban
PV System Power	5 kWp
Annual Production	7420 kWh (1.484kWh/kWp)
CO ₂ Avoided	5.2 Tons
Modules	20×Solar World AGSW 250 Poly
Angle of Inclination	30°
Inverters	SMA Sunny Boy 5000TL - 21

Looking at Fig. 7 – 9, the payback period varies between 8 and greater than 10 years for a PV system which has a lifespan of around 20 to 25 years (according to the PV panel manufacturer the guarantee is 20 – 25 years whilst the PV inverter will require changing during the life of the project). The calculations do not take into account any export tariff paid to the consumer (currently eThekweni Electricity does not pay for

exported energy to the grid) for excess energy exported to the grid. However this is an ideal case where panel degradation and inverter failure/replacement or capital cost of borrowing to finance the system is not taken into account. It is assumed that the resident pays for the system on his own and no panel degradation takes places or inverter replacement occurs for the purpose of these calculations. However we look at the possibility of the Municipality paying a reasonable export tariff and look at how this will improve the payback period since this is what drives these schemes in other countries.

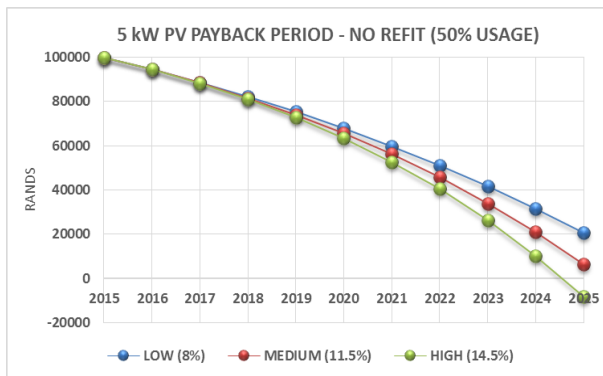


Fig. 6: Roof Top 5 kWp PV payback period with 50% usage

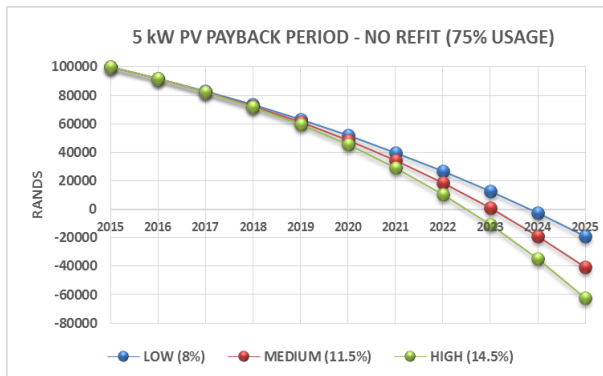


Fig. 7: Rooftop 5 kWp PV payback period with 75% usage

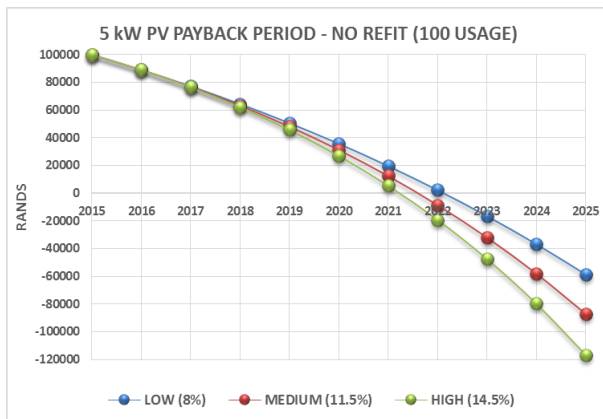


Fig. 8: Rooftop 5 kWp PV payback period with 100% usage

Table 4 provides the payback period for the 5 kW PV system.

Tab. 4 Summary of rooftop PV payback periods

	Payback Period – No REFIT		
	50% Usage	75% Usage	100 % Usage
Low (8%)	> 10 years	9 years	9 years
Medium (11.5%)	> 10 years	9 years	8 years
High (14.5%)	10 years	8 years	8 years

2.3.2 Renewable Energy Feed in Tariff

Most residential and small customer tariffs are not cost-reflective as they do not reflect the fixed costs associated with the management, operations and maintenance of the grid and the retail related costs to serve the customers. If the electricity tariff supplying a customer is not cost reflective and embedded generation is installed, it means that there will be loss of revenue to the utility. This loss will need to be recovered from other customers as there is no commensurate reduction in costs. Most residential tariffs comprise of a variable c/kWh charge only and no fixed charges to recover the fixed costs. This implies that if consumption decreases due to own generation, the utility loses revenue that is not commensurate with a reduction in costs. From the utility perspective, revenue loss is a major concern as DG reduces their sales and revenue. A mechanism needs to be determined to facilitate the development of Small Scale Distribution Generation (SSDG) in South Africa while mitigating a potential negative impact to the utilities revenue. [12]

The municipality is in the business of electricity distribution. The primary aim is to transport electricity from the generation point to the end customer. The generating source is immaterial. Hence, the kWh's generated from embedded generators is welcomed onto the network provided that the kWh's is purchased at the same price that it is available in the open market. In the case of the Municipality, the cost of electricity should be in line with the Eskom Megaflex tariff structure. This is to ensure compliance to the Municipal Financial Management Act which prohibits the Municipality from paying more for a product then what is available on the open market. In order to remain compliant, the Municipality will at best be able to pay avoided costs (equal to the Eskom 275 kV Megaflex Time of Use tariff) for any energy not purchased from Eskom.

However, currently eThekweni Electricity (EE) residential customers pay a flat rate per a kWh

purchased and EE pays Eskom on a TOU tariff. The Eskom 275 kV Megaflex TOU tariff structure is a complicated tariff structure which has different rates for different times of the day, days of the week and different demand season. We need to then work out the average cost per a kWh of electricity from the Megaflex rate to a single flat rate. This could then be the bases for a potential generation/REFIT tariff.

Tab. 5: Eskom 275 kV Megaflex Tariff structure [13]

	Peak (Hours)	Standard (Hours)	Off-Peak (Hours)
Week Days	5	11	8
Saturday	0	7	17
Sunday	0	0	24
Total Hours/Week	25	62	81
Percentage	14.88	36.9	48.21
Season	Duration		Months
Winter	1 June – 31 August		3
Summer	1 Sept – 31 May		9
Eskom Megaflex Time of Use Tariff			
Winter	234.55	71.06	38.58
Summer	76.50	52.66	33.40

Average Winter Cost = Peak + Standard + Off-peak

Where:

$$\text{Peak} = (0.1488 \times 234.55) = 34.90 \text{ c/kWh}$$

$$\text{Standard} = (0.369 \times 71.06) = 26.22 \text{ c/kWh}$$

$$\text{Off-peak} = (0.4821 \times 38.58) = 18.60 \text{ c/kWh}$$

$$\text{Total Winter} = 34.90 + 26.22 + 18.60 = 79.72 \text{ c/kWh}$$

Average Summer Cost = Peak + Standard + Off-peak

Where:

$$\text{Peak} = (0.1488 \times 76.50) = 11.38 \text{ c/kWh}$$

$$\text{Standard} = (0.369 \times 52.66) = 19.43 \text{ c/kWh}$$

$$\text{Off-peak} = (0.4821 \times 33.40) = 16.10 \text{ c/kWh}$$

$$\text{Total Summer} = 11.38 + 19.43 + 16.10 = 46.91 \text{ c/kWh}$$

Overall Average Cost = (0.25 × Average Winter Cost) + (0.75 × Average Summer Cost) + Other Chargers

Other Chargers = Ancillary Service Charge + Electrification and rural subsidy charge

$$\text{Other Charges} = 0.29 + 6.39 = 6.68 \text{ c/kWh}$$

$$\text{Overall Average Cost} = (0.25 \times 79.72) + (0.75 \times 46.91) + 6.68$$

Overall Average Cost = 62 c/kWh

Hence the average flat rate cost per a kWh of electricity from Eskom is 62c. We then look at the possible increases in this flat rate tariff going forward for the low, medium and high tariff increase scenario. The flat rate Eskom tariff will vary between 91.09 c/kWh to 122.01 c/kWh in 2020 whilst it will vary between 133.85 c/kWh to 240.13 c/kWh in 2025 as depicted in Fig. 9

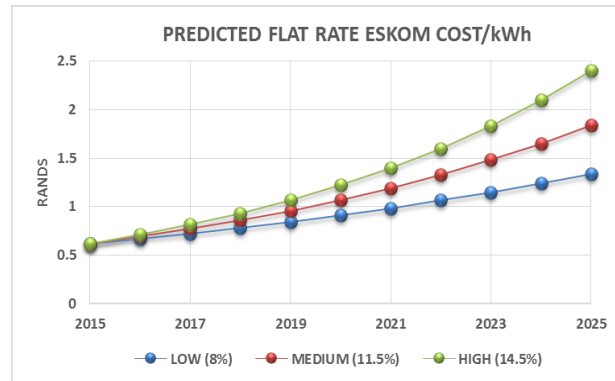


Fig. 9: Predicted flat rate Eskom costs

2.3.3 Case Study 2: Payback of a residential 5 kW rooftop PV with REFIT

We then utilize the potential REFIT and then recalculate the payback period with the introduction of this generation tariff which is equal to the Eskom avoided costs. With REFIT, the payback period of the 5 kW PV system now ranges between 7 and 10 years as shown in Fig. 10, 11 and Table 6. There has clearly been an improvement in the payback period with the introduction of the REFIT tariff as oppose to the case study with no REFIT.

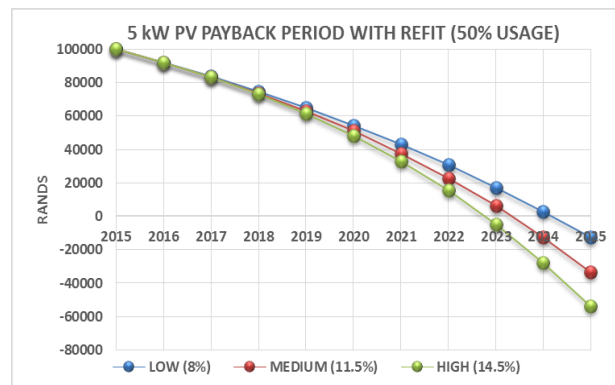


Fig. 10: Payback period (50% usage) with REFIT

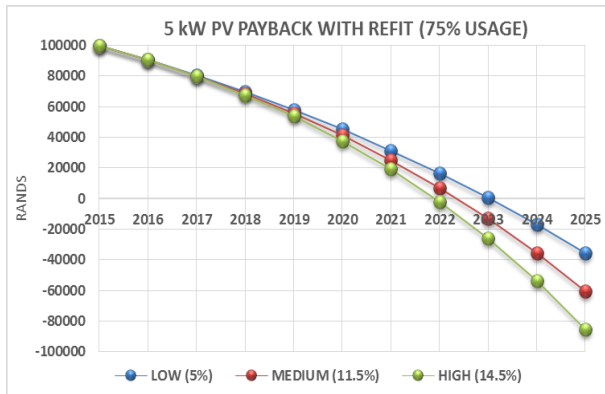


Fig. 11: Payback period (75% usage) with REFIT

Tab. 6: Payback period with REFIT

	Payback Period with REFIT		
	50% Usage	75% Usage	100 % Usage
Low (8%)	10	9	Unchanged
Medium (11.5%)	9	8	Unchanged
High (14.5%)	8	7	Unchanged

3. GUIDELINES AND STANDARDS

To date there has been limited standards and guidelines in South Africa to govern the connection of these small scale generation projects into the local distribution networks. Local utilities require assistance in devising guidelines that will assist them when allowing connection of small scale embedded generation into their existing networks. To facilitate this, a working group was set up. The working group was made up of members from various utilities around South Africa and Eskom was set up to create more detailed guidelines for small scale (LV connected) embedded generation. This was not covered in as fine detail in the South African Renewable Energy Grid Code as the MV/HV plant were. This was to cater for the growing number of existing and proposed SSDG projects which is predicted to increase over the next few years.

This working group created a standard called the National Rationalization Standard 097 (NRS 097) which provided more detail and focus on the minimum requirements for small scale LV connected DG plants from 0 to 1000 kW. The NRS 097 was broken down into Part 1 to Part 4 focusing on different aspects as described Table 7.

Tab. 7: Status and focus area of the NRS 097 guidelines

NRS Documents	Focus Area
Part 1	Utility Interface
	Covers all technical requirements of the embedded generator to connect onto the utility distribution network. First published in 2010, currently under review.
Part 2	Embedded Generator Requirements
	Standard to cover type testing requirements of generation plant and equipment to certify compliance to NRS 097 Part 1. Currently under development
Part 3	Simplified Utility Connection Criteria for low voltage connected generators
	A simplified criteria was developed to safely connect small scale EG plant to LV networks. Developed and approved in May 2014
Part 4	Procedures for implementation and application
	Standard still to be developed

A brief summarized version of the NRS 097 – 2 -3 (Simplified utility connection criteria for LV (230/400V) connected generators) is discussed below outlining the main points of the guideline. The purpose of the guideline was to assist the local South African Utilities, many of whom did not have technical expertise to approve the connection of SSDG plants on their local distribution networks. This criteria was drawn up by the NRS 097 working group after carrying out many case studies which indicates that an individual limit of 25% of the customer Notified Maximum Demand (NMD) will typically safely support a penetration level (percentage of customers that install a generator) of 30 to 50%. This is considered a reasonable and acceptable compromise between restricting individual sizes versus restricting penetration levels. The further assumption is that the design After Diversity Maximum Demand is unknown. [17]

Table 8 shows the simplified connection criteria for LV connected DG.

Tab. 8: Generation connection limits on MV/LV feeders [18]

LV dedicated feeder	LV Shared Feeder	MV Feeder
Maximum EG \leq 75% of NMD.	Maximum EG \leq 25% of NMD.	Total EG \leq 15% of the MV feeder loading.
Multi-phase supplies: $>$ 4.6 kVA shall be balanced.	EG $>$ 4.6 kVA shall be balanced 3 phase.	
Single-phase supplied: maximum generator size is 13.8 kVA.	Total shared EG shall be \leq 25% of the transformer rating.	
	Allowed maximum individual limit is 20 kVA.	

3.1 Simplified Connection Criteria

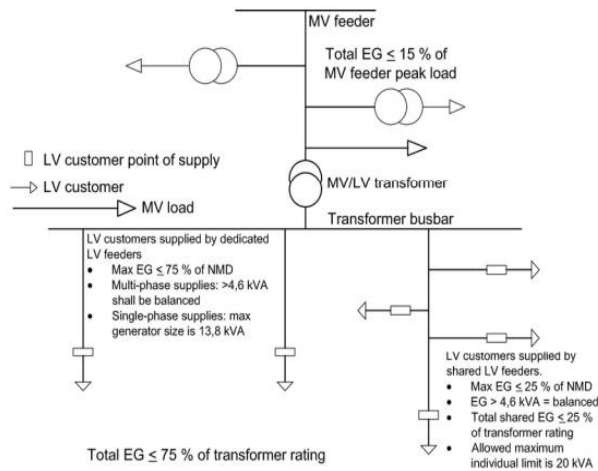


Fig. 12: Summary of the simplified connection criteria [18]

The technical limits that constraint generation are as follows [17]:

1. Thermal ratings of the lines and cables.
2. LV voltage regulations ($\pm 10\%$).
3. The maximum change in LV voltage is limited to 3%.
4. Islanding of the utility network is not allowed.
5. The fault level at the customer point of supply shall be greater than 210 A or the minimum fault level at which the generator is rated.

The application of the limits then gave rise to the following proposed criteria [17]:

1. Voltage rise on the LV feeders should be limited to 1% (to ensure compliance to NRS048 voltage limits, MV voltage control practices and the MV/LV transformer voltage ratio and tap settings).
2. The maximum generation connected across the MV/LV transformer is limited to 75%.
3. The individual customer limit on a dedicated feeder is limited to 75%.
4. The dedicated LV feeder minimum size is based on a maximum voltage rise of 1%.
5. The individual customer limit of 25% of a shared feeder will typically support penetration levels of 30 – 50%.

The total generation connected to an MV feeder is limited to 15% of the MV feeder. (This value of 15% is informed by practices in the United States and Europe

and is based on the ratio of maximum to minimum feeder loading for a typical consumer load profile. A 15% limit also ensures low probability of reverse power flow into the MV source thereby preventing voltage rise on the MV feeder).

The flow chart in Fig. 13 shows the method in which the utility will go about utilizing the simplified connection criteria. This criteria is limited to sizes less than or equal to 350 kVA and LV connected. It utilizes the generation size limit discussed in Fig. 12. If the generator meets all of the criteria in Fig. 13, then the Utility can safely allow the connection of this generator onto the network. However if the criteria is not met, then it offers solutions or suggest that detailed studies be carried out before allowing the connection onto the network.

This criteria is now utilized by most utilities in South Africa when approving DG connections on to the local distribution networks.

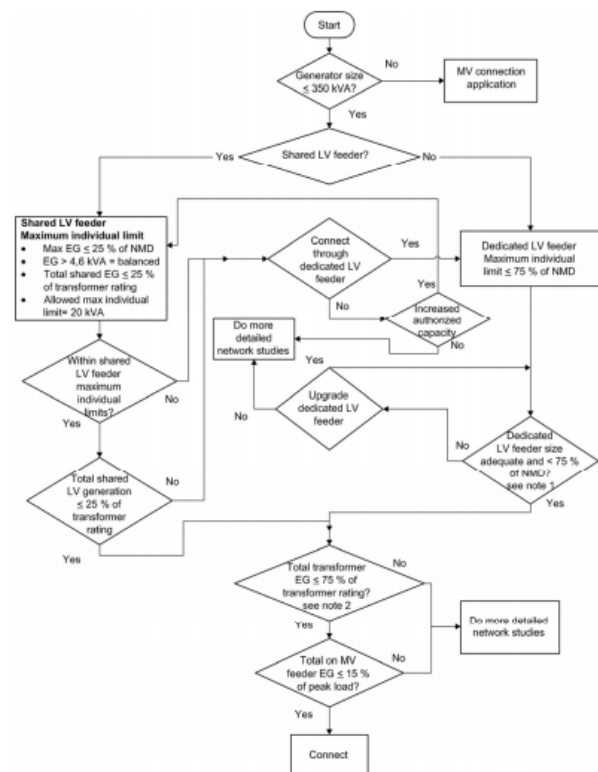


Fig. 13: Flow chart of simplified connection technical evaluation criteria [18]

4.0 CONCLUSION

Case studies investigating the feasibility of small scale residential PV shows that the minimum payback period is currently 8 years and above. This reduces to 7 years and above with the implementation of a REFIT based on Eskom avoided costs. This is unlikely to attract huge patronage of residential solar PV as predicated by many especially with no REFIT tariff for excess energy exported to the grid. The take-off of the residential PV market is expected when the payback period reduces to 5 years and below. This can be achieved by the introduction of subsidies which will assist in reducing the payback period. This was confirmed in a survey done on a number of customers in South Africa who indicated that they will invest in PV when the payback period reduces to 5 years and below. [19] This will make obtaining finance from banks and suppliers more accessible prompting great growth in this sector.

The barriers of residential solar PV include:

- No payment schemes for exported tariffs
- Lack of guidelines and standards
- Revenue loss concerns by the utilities
- Lack of expertise within utilities to deal with generation
- May introduce quality of supply problems to the grid
- Municipal systems and networks were not designed to accommodate DG
- Utilities unable to offer long term Power Purchase Agreements due to Municipal Financial Management Act
- Current meters are not designed to measure bi-directional powerflow
- Lack of policy on SSDG from the National Energy Regulator of South Africa
- Battery technology still very expensive

A catalyst to increase the uptake of rooftop PV will be the implementation of a renewable energy feed in tariff and subsidies that may be offered for the installation of these schemes. In order to allow easier calculations of the payback period of a PV system, an equation was derived to calculate the payback period for solar PV.

$$\text{Solar PV payback period} = \frac{1}{\alpha} \quad (1)$$

Where:

$$\alpha = \sum_{n=0}^{n=i} \frac{A + B}{C - D - E}$$

$$A = [IT(1 + PI)^N \times \left(\frac{PU}{100}\right) \times TKWG]$$

$$B = [ET(1 + PI)^N \times \left\{\frac{(1 - PU)}{100}\right\} \times TKWG]$$

$$C = [TCOI(1 + M)^N]$$

D=Subsidy Value

E= Annual Maintenance and Repair costs

Table 9 defines the symbols used in (1).

Tab. 9: Symbols in (1)

Description	Symbol
Total Capital Cost of Installation	TCOI
Export Tariff	ET
Total kWh generated from system over a period of one year	TKWG
Average Annual Percentage increase in tariff	PI
Percentage electricity utilised by the consumer from the PV system	PU
Number of years	N
Percentage interest rate of loan obtained for installation	M
Number of years	i
Annual percentage degradation in output	PD

From (1), it can be seen that there are a number of factors that can influence the payback period of rooftop PV. The uptake of residential solar PV can however, still be influenced by the following factors:

- Reduction in the cost of a PV installations
- Higher FIT
- The increases in the residential electricity tariff
- Subsidies
- Generation export tariffs
- Net metering schemes
- Easier and cheaper financing for these projects by banks
- Introduction of Carbon taxes
- Third party ownership of rooftop PV installation/renting of roof schemes
- Improvement in the efficiencies of PV systems

Utilities are currently awaiting guidelines from the National Energy Regulator on guidelines to create and approve such tariffs as it has a major impact of revenue. Utilities may have to unbundle their residential tariffs to

a more cost reflective tariff to allow creation of a generation tariff. The utilities has however to date been proactive in the creation of the simplified guideline for the connections of SSEG. This will drastically help the utilities in South Africa to safety and technically limit the amount of small scale PV on their existing networks whilst still ensuring that the network parameters are not violated.

5.0 REFERENCE

[1] S J T Mwale and I E Davidson, "Power deficits and outage planning in South Africa". In proceedings of 2nd International Symposium on Energy Challenges and Mechanics, 19 – 21st August, Scotland, United Kingdom.

[2]<http://www.engineeringnews.co.za/article/how-embedded-electricity-generation-could-shake-up-the-system,2014-01-31>

[3] Víctor H. Méndez Quezada, Juan Rivier Abbad and Tomás Gómez San Román, "Assessment of Energy Distribution Losses for Increasing Penetration of Distributed Generation", *IEEE Transactions on Power Systems*, Vol. 21, No. 2, May 2006

[4] South Africa Department of Energy, "Integrated Resource Plan for Electricity (IRP) 2010 – 2030 Update Report", 21 Nov 2013

[5] E Zawilska and M J Brooks, "An assessment of the solar resource for Durban, South Africa", *Renewable Energy Journal*, 2011

[6] <http://solargis.info/doc/free-solar-radiation-maps-GHI>

[7] J Driesen and R Belmans, "Distribution Generation: Challenges and Possible Solutions", IEEE, 2006

[8] COP 17 Climate Change Conference, Last accessed on the 4 December 2014, at URL <http://www.cop17-cmp7durban.com/en/south-africa-on-climate-change/durban-climate-work.html>

[9] L Moodliar and S Sewchurran, "Creation of a small scale embedded generation framework for eThekweni Municipality", eThekweni Municipality Policy document

[10] J Hunsley and S Sewchurran, "Journey towards a smart utility: an eThekweni Electricity perspective". AMEU Conference 2014

[11] National Energy Regulator of South Africa, "Integrated Resource Plan for electricity, 2010 – 2030", Update report, 21 November 2013

[12] National Energy Regulator of South Africa, "Small-Scale Embedded Generation: Regulatory Rules Consultation Paper", 25 February 2015

[13] eThekweni Electricity Tariff Booklet 2015/2016

[14] European Commission, JRC Science and Policy Reports, "PV Status Report 2014", Italy, November 2014

[15] Actewagl, "Guidelines for embedded generator connection to Actewagl's low voltage (LV) networks", March 2013

[16] <https://www.sunnyportal.com/>

[17] <https://www.eskom.co.za>

[18] S J Van Zyl, B Matjila, P R Groenewald and S Sewchurran "National Rationalisation Standard 097: Code of Practice for the Connection of Embedded Generation to Electricity Distribution Networks" National Standard for South Africa, March 2009

[19] C R Millson, "The potential for rooftop solar photovoltaic installations on commercial sector buildings in the City of Cape Town" MSc Dissertation, University of Cape Town

Analytical Approach for Optimal Distributed Generation Allocation in Primary Distribution Networks

O O Osaloni* and K O Awodele

University of Cape Town, Department of Electrical Engineering, Rondebosch, 7701, Cape Town, South Africa

*Email: wole_osaloni@yahoo.com

Abstract: This paper proposes an analytical expression to calculate the optimal size and an effective methodology to identify the corresponding optimum location for DG placement for minimizing the total power losses in primary distribution systems. The analytical expression and the methodology are based on the exact loss formula. The effect of size and location of DG with respect to loss in the network is also examined in detail. The proposed methodology was tested and validated on a 33-bus radial distribution test system. Results obtained from the proposed methodology are compared with that of the exhaustive load flow and loss sensitivity method. Results show that the proposed approach achieves better placement for loss reduction than the loss sensitivity factor based approach.

Key words: Distributed generation, Exact loss formula, Optimum size, Optimum location, Sensitivity factors.

1 INTRODUCTION

With the increasing demand for clean and renewable energy, the issue of distributed generation (DG) is drawing more attention worldwide. DG stands as one better way of fulfilling the higher demand for electricity. Moreover, it provides voltage support to large scale distribution power systems, which results in reliability improvement and loss reduction in the power system. DG technology is one of the current areas of intense research given the increasing global concerns about environmental protection, energy conservation, and increasing sophistication of wind power, photovoltaic power generation and other renewables energy technologies [1]. The planning of the electric power systems with the presence of DG requires several factors to be taken into considerations, such as; the best technology to use, the number and the capacity of the units, the best location, and the type of network connection etc. [2].

However, there are some integration issues which should be analysed to maximize these technical benefits. From previous studies, it has been seen that different penetration levels and various placement of DG will impact the distribution system differently [3].

Studies have indicated that inappropriate selection of location and size of DG, may lead to greater system losses than the losses without DG [4]. Utilities already facing the problem of high power loss and poor voltage profile, especially in the developing countries cannot

tolerate any increase in losses. By optimum allocation, utilities take advantage of reduction in system losses, improved voltage regulation and improvement in reliability of supply [5]. It will also relieve capacity from transmission and distribution system and hence, defer new investments, which have a long lead-time.

Therefore, a detailed and exact analysis method is required to determine the proper location and size of DG more accurately and precisely [6]. In distribution systems, DG should be allocated in an optimal way such that it will reduce system losses and hence improve the voltage profile. In this paper, an analytical expression to calculate optimum size and an effective methodology to identify the optimum location for DG placement are proposed, its accuracy and superiority over loss sensitivity factor method is investigated.

2 DEFINITION OF DISTRIBUTED GENERATION AND RATING (SIZE) OF DG

Generally, Distributed generation means the electric power generation within a distribution network to fulfil the rapid energy demand of consumers. However, distributed generation can be defined in a variety of ways.

- i. The Electric Power Research Institute (EPRI) defines distributed generation as generation from 'a few kilo-watts up to 50 MW [7].
- ii. International Conference on large High Voltage Electric Systems (CIGRE) defines DG as 'smaller than 50-100 MW [7].
- iii. International Energy Agency (IEA) defines distributed generation as generating plant serving a customer on-site or providing support to a distribution network, connected to the grid at distribution level voltages [8].

3 LOCATION AND SIZING ISSUES

Typical graphs of power loss versus size of DG at each bus in a distribution system are shown in Fig. 1 below. From the figure, it is obvious that for a particular

bus, as the size of DG is increased, the losses are reduced to a minimum value and increased beyond a size of DG (i.e. the optimal DG size at that location). If the size of DG is further increased, the losses start to increase and it is likely that it may overshoot the losses of the base case. Also notice that the location of DG plays an important role in minimizing the losses.

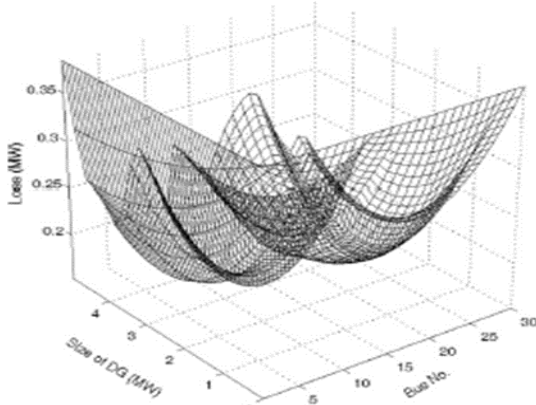


Fig.1: Effect of size and location of DG on system losses [6].

The important conclusion that can be drawn from Fig. 1 is that, given the characteristics of the distribution system, it is not advisable to integrate very high DG capacity in the network. The size at most should be such that it is consumable within the distribution substation boundary.

4 LOSS SENSITIVITY

The real power loss in a system is given by (1). This is popularly known to as the “exact loss” formula

$$P_L = \sum_{i=1}^N \sum_{j=1}^N [\alpha_{ij} (P_i P_j + Q_i Q_j) + \beta_{ij} (Q_i P_j - P_i Q_j)] \quad (1)$$

Where,

$$\alpha_{ij} = \frac{r_{ij}}{V_i V_j} \cos(\delta_i - \delta_j),$$

$$\beta_{ij} = \frac{r_{ij}}{V_i V_j} \sin(\delta_i - \delta_j) \text{ and}$$

$$r_{ij} + jx_{ij} = z_{ij}$$

are the ij th element of $[Z_{bus}]$ matrix with $[Z_{bus}] = [Y_{bus}]^{-1}$

The sensitivity factor of real power loss with respect to real power injection from DG is given by

$$\alpha_i = \frac{\partial P_L}{\partial P_i} = 2 \sum_{j=1}^N (\alpha_{ij} P_j - \beta_{ij} Q_j) \quad (2)$$

Sensitivity factors are evaluated at each bus, firstly using the values obtained from the base case power flow. The buses are ranked in descending order of the values of their sensitivity factors to form a priority list.

The top-ranked buses in the priority list are the first to be studied alternatives location. This is generally done to take into account the effect of nonlinearities in the system. The first order sensitivity factors are based on the linearization of the original nonlinear equation around the initial operating condition and is biased towards a function which has a higher slope at the initial condition that might not identify the global optimum solution. This condition is depicted in Fig. 2. Therefore, a priority list of candidate locations is a prerequisite to get the optimum solution [9]. The curve with a solid line has a higher sensitivity factor at the initial operating condition than the dotted curve, but does not give the lowest loss, as $PL1 > PL2$. It shows why the sensitivity factor may not give the optimum result if a number of alternative locations are not taken into account.

4.1 Priority list

The sensitivity factor will reduce the solution space to few buses, which constitute the top ranked buses in the priority list. The number of buses taken in priority will have an effect on the optimum solution obtained for a system. For each bus in the priority list, the DG is placed and the size is varied from minimum (0 MW) to a higher value until the minimum system losses is found with the DG size.

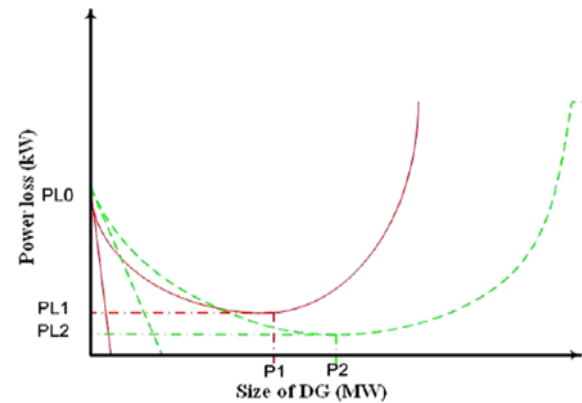


Fig. 2: Nonlinearity in loss curve [6].

In this study, 30% of the total number of buses is considered in preparing the priority list for each case. The process is computationally demanding as one needs a large number of load flow solutions.

4.2 Computational procedure

The computational procedure is given below:

Step 1: Run the base case load flow.

Step 2: Find the sensitivity factor using Eq. (2) and rank the sensitivity in descending order to form the priority list.

Step 3: Select the bus with the highest priority and place DG at that bus.

Step 4: Change the size of DG in “small” steps and calculate the loss for each by running load flow.

Step 5: Store the size of DG that gives the minimum loss.

Step 6: Compare the loss with the previous solution. If the loss is less than the previous solution, store this new solution and discard the previous solution.

Step 7: Repeat Step 4 to Step 6 for all buses in the priority list.

5 PROPOSED METHODOLOGY

In this section, an analytical approach is proposed to find the optimum size and location of DG in the distribution system. This methodology requires load flow to be carried out only two times, one for the base case and another at the end with DG included to obtain the final solution.

5.1 Sizing at various locations

As shown in Section 3, the total power loss against injected power is a parabolic function and at minimum losses the rate of change of losses with respect to injected power becomes zero.

$$\frac{\partial P_L}{\partial P_i} = 2 \sum_{j=1}^N (\alpha_{ij} P_j - \beta_{ij} Q_j) \quad (3)$$

It follows that

$$\alpha_{ii} P_i - \beta_{ii} Q_i + \sum_{j=1, j \neq i}^N (\alpha_{ij} P_j - \beta_{ij} Q_j) = 0 \quad (4)$$

$$P_i = \frac{1}{\alpha_{ii}} [\beta_{ii} Q_i + \sum_{j=1, j \neq i}^N (\alpha_{ij} P_j - \beta_{ij} Q_j)] \quad (4a)$$

Where, P_i is the real power injection at node i , which is the difference between real power generation and the real power demand at that node:

$$P_i = P_{DG_i} - P_{D_i} \quad (5)$$

Where, P_{DG_i} is the real power injection from DG placed at node i and P_{D_i} is the load demand at node i . By combining (4) and (5) equation (6) is obtained.

$$P_{DG_i} = P_{D_i} + \frac{1}{\alpha_{ii}} [\beta_{ii} Q_i + \sum_{j=1, j \neq i}^N (\alpha_{ij} P_j - \beta_{ij} Q_j)] \quad (6)$$

The above equation gives the optimum size of DG for each bus i , for the loss to be minimum. Any size of DG other than P_{DG_i} placed at bus i will lead to higher loss. This loss, however, is a function of loss coefficients α and β .

5.2 Location to minimize losses

The next step is to find the optimum DG location, which will give the lowest possible total losses. Calculation of loss with DG one at a time at each bus again requires several load flow solutions, as many as the number of buses in the system. Therefore a new methodology is proposed to quickly calculate approximate loss, which would be used for the purpose of identifying the best location. Numerical results show that the approximate loss follows the same pattern as that calculated by accurate load flow. It means that, if accurate loss calculation from load flow gives minimum for a particular bus then, loss calculated by approximate loss method will also be minimum at that bus.

5.3 Computational procedure

Step 1: Run the base case load flow.

Step 2: Find the optimum size of DG for each bus using Eq. (6).

Step 3: Compute approximate loss using Eq. (1) for each bus by placing DG of optimum size obtained in step 2 for that bus. Add the injection from DG for that bus and use base case values for state variables.

Step 4: Locate the bus at which the loss is minimum after DG placement. This is the optimum location for DG.

Step 5: Run load flow with DG to get the final result.

6 TEST SYSTEM AND ANALYTICAL TOOLS

The proposed methodology is tested on a 33-bus test system shown in Fig. 3. It is a radial system with a total load of 3.72 MW and 2.3 Mvar [10]. The line and bus data of this test system can be found in the appendix. Also a computer program has been written in MATLAB 7 to calculate the optimum sizes of DG at various buses and approximate total losses with DG at different locations to identify the best location. A Newton–Raphson algorithm based load flow program is used to solve the load flow problem.

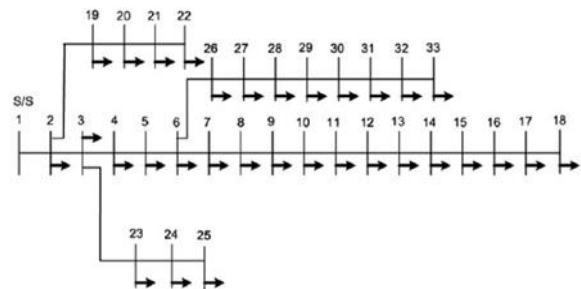


Fig. 3: Single line diagram of the 33-bus distribution test system.

7 SIMULATION RESULTS

7.1 Sizes allocation

Based on the proposed analytical expression, optimum sizes of DGs are calculated at various nodes of the test system. Fig. 4 shows optimum sizes of DG at various nodes for the 33-bus distribution test systems.

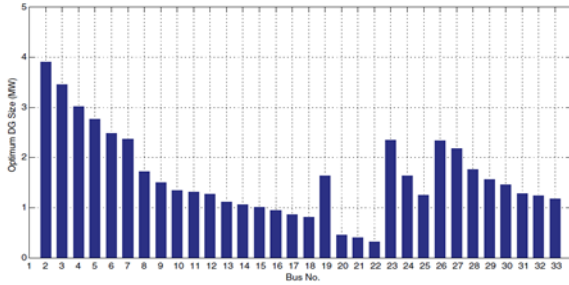


Fig. 4: Optimum size of DG at various locations for the 33-bus distribution system.

As far as one location is concerned, in a distribution test system, the range of DG sizes for the test system at various locations is between 0.1–4.0 MW. However, it is important to identify the location at which the total power loss is minimum. This can be identified with the help of the approximate method described in section 5.2.

7.2 Location selection

The approximate total power losses for the 33-bus distribution system is shown in Fig. 5 with optimum DG sizes obtained at various nodes of the system. The figure also shows the accurate loss. As can be seen from these figures the trend of the losses is captured with the help of approximate solution which is good enough to identify the location that would lead to the least total power losses. Notice that approximate losses pattern of the system with optimum sizes of DG at various nodes follows the accurate losses in all the cases. For the 33-bus distribution test system, the best location is bus 6 with a total power loss of 0.111 MW and the second best location is bus 7 with slightly higher total power losses as shown in Fig. 5 below.

8 SUMMARY

The summary of results, optimum location, corresponding optimum size of DG and total power loss with and without DG, of the test system is shown in Table 1. The reduction in real power loss is 47.3%. As can be seen from the results of various approaches the location and size of DG play an important role in loss reduction of primary distribution systems. From the results obtained for the test system one can conclude that by placing DG of optimum size at optimum location, significant reduction in loss can be achieved.

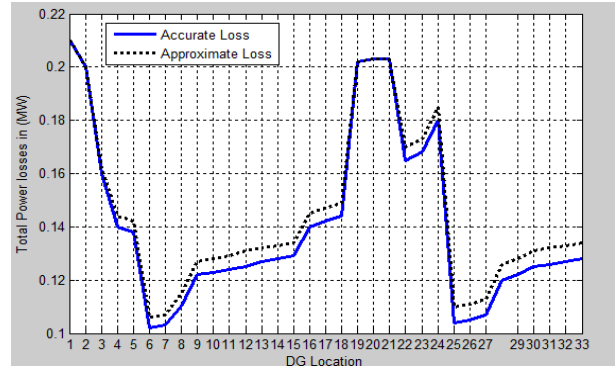


Fig. 5: Approximate and accurate losses of the 33-bus distribution test system.

Voltage profile improvement, reduction in thermal loading of the main feeder and better voltage regulation are some consequent results apart from power quality and reliability improvement.

Tab. 1: Summary of the simulation results

Test system	Optimum location	Optimum Size(MW)	Power loss (kw)	
			Without DG	With DG
33-bus	Bus 6	2.49	211.20	111.24
	Bus 7	2.12	211.20	101.25

8.1 Comparison of results

In this section, the traditional loss sensitivity approach for DG location selection is compared with the proposed approach and repeated load flow or “exhaustive” approach. Table 2 shows the best locations obtained. The loss sensitivity approach is not able to identify the best location, instead it picked up the ninth optimum location as its first choice in the 33-bus distribution test system. Also power losses in this case is higher compare to the analytical approach. This happens due to the linearization and approximation as explained in Section 4. Table 2 also shows the optimum sizes of DG. In calculating the optimum sizes of DG at various locations using Equation (6), it was assumed that the values of variables remain unchanged.

Tab. 2: Comparison of the results of different approaches

Approach	Test System	Optimum Location	Optimum size MW)	Real power loss (kw)
Loss sensitivity	33-bus	Bus 10	3.2	156.28
Proposed approach		Bus 6	2.49	111.24
Repeated Load Flow		Bus 6	2.6	111.1

This is the reason why there is a small difference between the optimum size obtained from the proposed approach and repeated load flow. However, in reality, one would go for the closest size available in the market and these differences are within margin of error.

9 CONCLUSION

Size and location of DG are crucial factors in the application of DG for loss minimization. This paper presents an algorithm to calculate the optimum size of DG at various buses and proposes a fast methodology to identify the best location corresponding to the optimum size for reducing total power losses in primary distribution networks. The benefit of the proposed algorithm for size calculation is that a look up table can be created with only one power flow calculation and the table can be used to restrict the size of DG at different buses, with the view of minimizing total losses. However, if a DG is installed in the system, the look up table needs to be updated with new calculation. The proposed methodology for location selection correctly identifies the best location for single DG placement in order to minimize the total power losses.

In practice, the choice of the best site may not be always possible due to many constraints. However, the analysis here suggests that the losses arising from different placement varies greatly and hence this factor must be taken into consideration while determining appropriate location. The paper also shows that the loss sensitivity factor approach for location selection may not lead to the best choice.

10 APPENDIX

Tab. AI Load data for 33-bus distribution system

Bus No.	P _L (kW)	Q _L (kVAr)	Bus No.	P _L (kW)	Q _L (kVAr)
2	100	60	18	90	40
3	90	40	19	90	40
4	120	80	20	90	40
5	60	30	21	90	40
6	60	20	22	90	40
7	200	100	23	90	50
8	200	100	24	420	200
9	60	20	25	420	200
10	60	20	26	60	25
11	45	30	27	60	25
12	60	35	28	60	20
13	60	35	29	120	70
14	120	80	30	200	100
15	60	10	31	150	70
16	60	20	32	210	100
17	60	20	33	60	40

Tab. AII. Branch data for 33-bus distribution system

Branch Number	Sending end bus	Receiving end bus	R (Ω)	X (Ω)
1	1	2	0.0922	0.0470
2	2	3	0.4930	0.2512
3	3	4	0.3661	0.1864
4	4	5	0.3811	0.1941
5	5	6	0.8190	0.7070
6	6	7	0.1872	0.6188
7	7	8	0.7115	0.2351
8	8	9	1.0299	0.7400
9	9	10	1.0440	0.7400
10	10	11	0.1967	0.0651
11	11	12	0.3744	0.1298
12	12	13	1.4680	1.1549
13	13	14	0.5416	0.7129
14	14	15	0.5909	0.5260
15	15	16	0.7462	0.5449
16	16	17	1.2889	1.7210
17	17	18	0.7320	0.5739
18	2	19	0.1640	0.1565
19	19	20	1.5042	1.3555
20	20	21	0.4095	0.4784
21	21	22	0.7089	0.9373
22	3	23	0.4512	0.3084
23	23	24	0.8980	0.7091
24	24	25	0.8959	0.7071
25	6	26	0.2031	0.1034
26	26	27	0.2842	0.1447
27	27	28	1.0589	0.9338
28	28	29	0.8043	0.7006
29	29	30	0.5074	0.2585
30	30	31	0.9745	0.9629
31	31	32	0.3105	0.3619
32	32	33	0.3411	0.5302
34	8	21	2.0000	2.0000
36	9	15	2.0000	2.0000
35	12	22	2.0000	2.0000
37	18	33	0.5000	0.5000
33	25	29	0.5000	0.5000

11 ACKNOWLEDGEMENT

The authors gratefully acknowledge the provision of financial support and research infrastructure by Eskom Holdings through TESP and the University of Cape Town respectively in carrying out this research.

12 REFERENCES

- [1] D. R. Gavane, C. Mallareddy, J. Patil and S. B. Bhosale, "Optimal placement of Distributed Generation for loss reduction in Distribution System," *International Journal of Innovations in Engineering Research and Technology*, vol. 2, no. 5, may 2015
- [2] M. F. Kotb, K.M. Shebl, M. El Khazaendar and A. El Hussein, "Genetic Algorithm for optimum Siting and Sizing of Distributed Generation," *International Middle East Power System Conference*, Cairo, 2010.

- [3] A. Anwar, and H. R. Pota, "Loss reduction of Power Distribution Network using optimum size and location of Distributed Generation," Australia Universities Power Engineering Conference (AUPEC), 2011 21st Australasian, Brisbane, QLD, 2011.
- [4] T. Griffin, K. Tomosovic, D. Secrest, and A. Law, "Placement of Dispersed Generations Systems for reduced losses." *Proceedings of the 33rd Hawaii international conference on sciences*, Hawaii,, 2000.
- [5] N. Mithulanathan, O.O. Than, and V. Phu Le., "Distributed Generator placement in Power Distribution System using Genetic Algorithm to reduce losses," *Thammasat International Journal of Science And Technology*, vol. 9, no. 3, pp. 55 - 62, 2004.
- [6] N. Acharya, P. Mahat, and N. Mithulanathan, "An analytical approach for DG allocation in primary distribution network," *Elsevier, Electrical Power and Energy Systems*, vol. 28, no. 22, pp. 669-678, 2006.
- [7] T. Ackermann, G. Anderson, and L. Sder, "Distributed Generation: a definition," *Electric Power Systems Research*, vol. 57, no. 3, pp. 195-204, 2001.
- [8] IEA, publication, "Distribution generation in liberalized electricity market" [Online]. Available: <http://www.iea.org/textbase/nppdf/free/2000distributed2002,2002Page19>. [Accessed 31 03 2015].
- [9] K. C. Julius, and N. A. Otero, "A combined sensitivity factor based GA-IPSO approach for system loss reduction and voltage profile enhancement." *International Journal of Research in Engineering & Science*, vol. 2, no. 3, 2013.
- [10] M. A. Kashem, V. Ganapathy, G.B. Jasmon, and G. B. Buhari, "A novel method for loss minimization in Distribution Networks.," in *Proceedings of International Conference on Electric Utility Deregulation and Restructuring and Power Technologies* pp . 251–255., 2000.

Evaluation of the Design and Functionality of a Laboratory Corona Cage

JS. Djeumen¹, JJ. Walker¹⁺ and IK. Kyere¹⁺⁺

¹Vaal University of Technology, Andries Potgieter Blvd, 1900, Vanderbijlpark, South Africa

¹⁺julesd@vut.ac.za; ¹⁺⁺jerrywalker@walmart.co.za; ¹⁺⁺isaack@vut.ac.za

Abstract: Corona discharge is a partial discharge which is a well-known phenomenon that can cause damages and losses in a transmission or power system. Corona discharge is a common phenomenon in power transmission lines external insulation, and it may also cause interference in communication systems. The Corona cage detection technology has been widely used to detect the corona discharge in research laboratories and the evaluation is based on corona detection through Partial Discharge, Acoustic, Radio Interference Voltage and Visual detections. In this paper, the corona inception voltage, as the corona discharge associated with a “tern” conductor which is used for overhead energy transmission and distribution lines is experimentally measured. To simulate the corona discharge process, a smooth surface corona cage is built. Test measurements were carried out to determine whether the corona discharge is more dependent on the different combination of guards or segments. One, two, three or four segments corona cage were under testing by measuring the inception voltage. The Partial Discharge (PD) using the coupling capacitor, Acoustic method with Tettex Ultrasonic Detector and visual detection with CoroCam have been used. The test results reveal that the type of the corona cage can have an impact on the results with a little of difference

1 INTRODUCTION

Corona discharges is a well-known phenomenon occurring in high voltage (HV), extra high voltage (EHV) and ultra-high voltage (UHV) ac and dc transmission line that cause various problems and damage around and in the conductor, including losses, the electromagnetic field in their vicinity, results in radio interference, audible noise, ion flow electrification (IFE) and interference with carrier transmission. These damage and losses in power systems can results also by gas emissions such as ozone gas, transient currents in the conductor and it poses a potential shock hazard [1]-[2], where all of these are both technically and environmentally undesirable [3], [4], [5]. The design of the new equipment must consider the solutions to minimize corona effects.

2 TEST METHODS

Many researchers and institutions around the world undertake corona studies in different experimental ways. Theoretical studies only provide the basic understanding of corona phenomena occurring on transmission line conductors, where the experimental studies are critical to know the corona effects on the insulation or the transmission line conductors. Many methods have been employed for the corona test studies, the small or indoor corona cage [6]-[7], the outdoor or larger corona cage have been used [8]-[9], the mobile corona cage [10] and the outdoor test line technique [11]. Although the test line remains the most efficient and the results approaching the characteristic of practical transmission lines and could directly guide design and construction of lines, this is very costly and dangerous. The corona cage remains the preferable method as the distance becomes small from single-phase conductor to earth electrode, making the conductor reaching the required surface electrical field levels at a lower test voltage, hence showing corona characteristic similar to the high voltage range.

The most popular testing arrangements for corona studies involve a corona cage around a single-phase conductor [1]. The corona cage, either square or circular is an important method to research the effects on corona discharges. Corona cages has been widely used for many experimental work such as he evaluation of the effects of conductor temperature on corona inception [1], transmission line corona noise issues [12], ion current using a small corona cage [13], the onset voltage and power losses in an indoor corona cage [14] and the influence of the high altitude on the corona loss in the corona cage [15].

3 CORONA CAGE EVALUATION DESIGN

The corona cage is a concentric metal cage with large radius, whose section form is circular or square with a test line at its centre to simulate a single/multiple (bundle) conductor(s). At the axial boundary region of the corona cage, the electrode structure results in the distortion of the electrical field in the end region of corona cage. In order to ensure basically identical surface electric field in the measurement segment, corona cage is divided into different electrical insulation

sections. The inner part some time call measurement guard and the outer part call protection guard.

It is advisable that after the design of the cage, different methods of detection, to evaluate the cage after its design should be done. An evaluation based on corona detection through Partial Discharge, acoustic and visual detections is advisable to ensure that the cage is corona free, by eliminating any sharp edges or points.

3.1. Functionality and General Corona Cage

In general corona cage is typically a single-phase test facility, in which conductors or conductor bundles are centred in a grounded mesh cage. In order to make the surface electric field distribution of sub-conductor more consistent in corona cage, the section of corona cage must be symmetrical and this can be circular and square. The main aim of the corona cage configurations and dimensions is to reproduce the electric field distribution in the region under investigation around the conductor with a small scale measurement setup.

Corona cage is an ideal tool to study the corona discharge performance of transmission lines and conductors in a laboratory set-up. Its practicability has been confirmed by [16][17] and this present some advantages, for example, it reduces the test space, low investment, controllable test conditions, convenient structure adjustment and short test period compare to other test methods mentioned above.

Many studies have been done on the circular corona cage having three parts, the middle part for measurement and both sides for protection [18][19]-[20]. Very few studies have been carried out on the four section circular corona cage.

3.2. Particular Corona Cage Design Objectives

Generally the indoor corona cage has three parts, one inner part called measuring part and two outer parts called protective guards. This particular corona cage consists of two middle measuring parts with an equal length and two shielding parts. Figure 1 show the layout of the corona cage consisting of four sections (two inner and two outer), all with the possibility to be electrically connected.

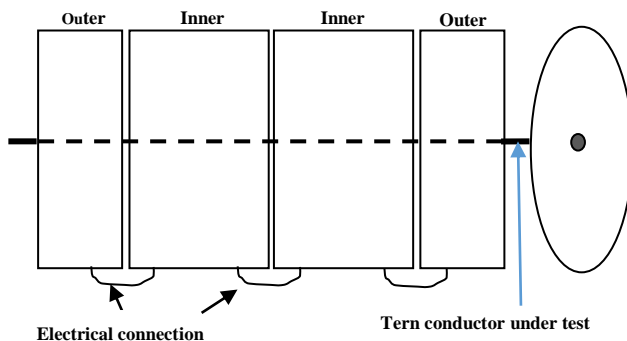


Figure 1: Layout modelling of the corona cage

There are several description about how to design a corona cage [13], with the main reason to optimize the corona loss measurement or radio noise for full-size conductor. This study manipulates the different sections of the corona cage to see the effect on the inception voltage and the magnitude of the corona. Its particularity is the separation of the inner part into two equal half-cylinders. Both half-cylinders (as well as the protective guards) are made of wire mesh. At the two ends the conductor are attached to the frame of the cage through the insulators and corona shielding.

3.3. The Completed Corona Cage

Only single aluminium stranded conductors were used for the tests. Two corona rings, each with a diameter of 30cm, were fitted at both ends of the test conductor to eliminate corona activity at the end-fittings. Figure 2 shows close-up view of the corona rings.



Figure 2: Corona rings at the end of the test conductor

Figure 3 below displays the full cage in the High Voltage laboratory and connected to 300 kV AC transformer



Figure 3: The full corona cage under test

After the completion of the cage, visual and acoustic detection have been used to check if the cage is corona free. For the visual detection the CoroCam III has been

used to visualize the entire cage and the sharp edge, figure 4 shown the CoroCam III used for the visual inspection and has assisted greatly to identify and eliminate many sharp points which are corona sources.



Figure. 4: CoroCam III instrument used for the visual detection

The acoustic Tettex instrument is equipped with the parabolic antenna to focus on the source of the corona and detect the discharge in a very small area. It is equipped with a pair of earphones through which the operator can hear the corona activity as well as an analogue readout. Figure 5 below shows the Tettex Ultrasonic detector.



Figure 5: Tettex Ultrasonic Detector

3.4. Conductor under test and theoretical corona inception voltages

Corona inception voltage is the lowest voltage at which continuous corona of specified pulse amplitude occurs as the applied voltage is gradually increased. Corona inception voltage decreases as the frequency of the applied voltage increases.

The Aluminium Conductor Steel Reinforced (ACSR) with the code word “tern” was used during the evaluation tests. Given the corona cage diameter and the conductor diameter, it is possible to estimate the corona inception voltage. This is often done by using Peek’s empirical constants (E_0 and K) in the formula for the corona inception gradient E_c [14].

$$E_c = m * E_0 * \delta * \left(1 + \frac{K}{\sqrt{\delta * r_c}} \right) \quad (1)$$

m : surface irregularity factor

r_c : conductor radius

δ : relative air density factor, resulting from:

$$\delta = \left(\frac{273 + t_0}{273 + t} \right) + \frac{P}{P_0} \quad (2)$$

t : Temperature of the ambient air

p : Pressure of the ambient air

t_0 : 25° C

P_0 : 101.3 kPa

4 TEST ARRANGEMENT PD MEASUREMENT

Partial discharge (PD) in electrical insulation is a phenomenon that results from localized electrical breakdown, or discharge, which occurs at defect within an insulation system to which electric stress is applied. The physical nature of a defect that may cause PD can include small internal voids within an insulation surface [11]. Different test arrangements were used for testing the insulator with corona rings and the aluminium cable (TERN). Smoothed aluminium tubes with diameter bigger than the tern conductor under the test were used in the test arrangement to connect the test equipment and the conductor to the high voltage source.

5 CORONA DISCHARGE TESTS AND ANALYSIS

An indoor corona cage with a length of 387 cm and a radius of 75 cm is used in the experiments. It was built for such corona discharge measurements and has a cylindrical shape consisting of two shield segments at both ends and a measuring segments in the middle adjustable in one or two shield segments which can be electrically connected or not. Shield segments are electrically isolated from the measuring segment(s) in order to measure the corona discharge on the conductor surface and to eliminate the corona discharge on the cage. The detailed setup schematic diagram of the corona cage is shown in Fig. 6.

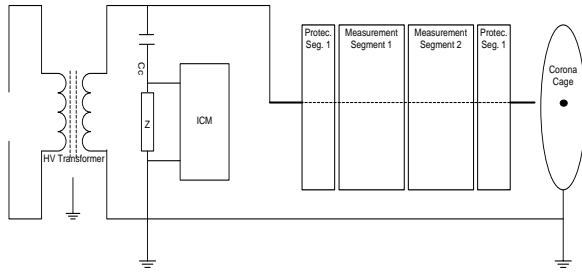


Figure 6: Setup test arrangement for measurement

The HV test circuit used consisted of an object under test, measuring impedance, coupling capacitor and 300 kV power transformer.

5.1. Polarity checking

Before any tests can be performed it must be checked that the polarity of the HV supply is synchronised with that of the partial discharge detection equipment.

Figure 7 displayed a piece of wire connected on the conductor in the cage, this piece of wire simulate a sharp point on the HV electrode and ensure corona activity at a much reduced voltage. With the voltages synchronised, the corona activity will appear on the negative half cycle of the phase resolved pattern observed in the detector. This can be seen on figure 8 below.



Piece of wire

Figure 7: Piece of wire connected on the conductor

Figure 8 below displays the pattern of the corona measurement at 4 kV and as it can be seen that the first corona appeared at a very low voltage range, this is due to the presence of the wire which dramatically decreased the breakdown voltage.

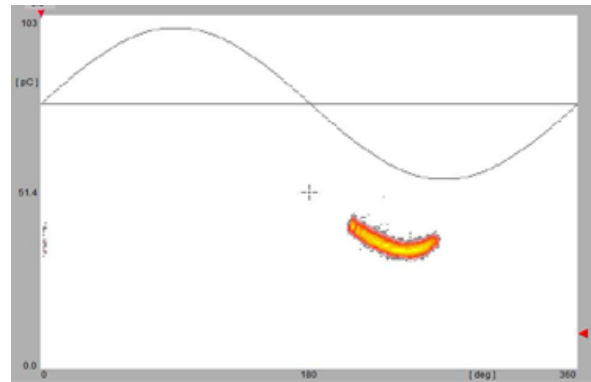


Figure 8: Corona at 4 kV with the wire connected

After removing the piece of wire and continuing with the test, no corona could be observed on the HV side anymore. The next activity observed with an applied voltage of 18 kV but in this case it appeared on the positive half cycle of the applied voltage. This is shown in Figure 9

From Figure 9, it can be seen that at 18 kV, there is no corona discharge in the negative half cycle due to the lower free electrons to start an ionisation process in the negative electrode. The magnitude of the positive corona is much higher than the negative.

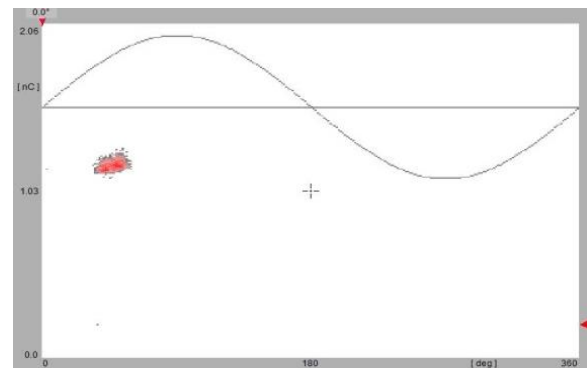


Figure 9: PD at 18 kV

When the applied voltage at the electrode exceeds the breakdown strength of the gas, ionisations of air near the sharp point electrodes occur. The formation of Positive and negative streamers depends on the polarity of the applied voltage [21].

6 EXPERIMENTAL RESULTS AND DISCUSSION

6.1. Results

Using the experimental results given below under different figures, for the corona inception voltage pattern of the different combinations of the corona cage, with a close observation they have different apparition position of the inception voltage at different charge as well. The comparisons of the inception voltage for the different cage setting are shown in figure 10 to 13.

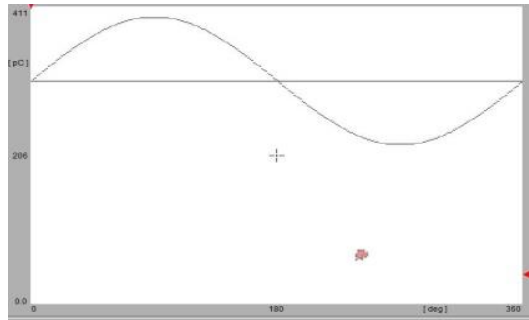


Figure 10: The two inner guard are connected together

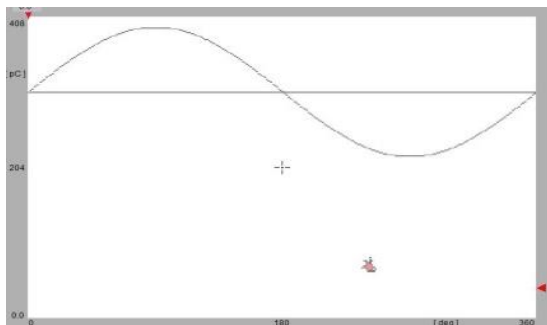


Figure 11: All four guards are electrically together

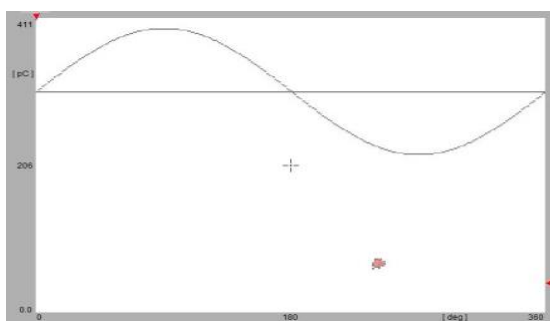


Figure 12: All guards are not electrically connected

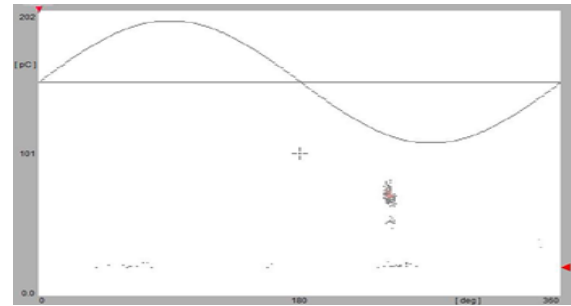


Figure 13: The outer and inner are electrically connected

Table 1: Test summary

Possible combination of the Corona Cage	Corona Inception Voltage Value	Magnitude or Charge & Figure Number
	15 kV	66.08 pC Fig: 12
	16kV	72.6 pC Fig: 10
	15.5 kV	75.40 pC Fig: 13
	15 kV	72.0 pC Fig:11

Table 1 summarized the corona inception voltage value, the magnitude or charge of four possible combinations.

7 CONCLUSION

This study presented the corona test results obtained based on phase-resolved pattern of a corona cage having four sections. The reason for the four sections was for transport purposes during the manufacturing. The results show that the inception voltage and magnitude of the corona discharge change very little with the structure of the cage under the AC voltage supply. During the evaluation an area of discharge was found on the earth side of one of the insulators which can be seen in Figure 9 clearly showing the activity during the positive half cycle.

8 REFERENCES

- [1] G. J. Reid and H. J. Vermeulen, "Effects of conductor temperature on corona inception," in *Power Engineering Conference (UPEC)*, 49th International Universities, 2014, pp. 1-5.
- [2] P. Jefferson-Martin, "Corona and Induced Current Effects," PgandE Delta Distribution Planning Area Capacity Increase Substation Project, August 2005.
- [3] X. B. Bian, D. Y. Yu, L. C. Chen, J. M. K. MacAlpine, W. Liming, G. Zhicheng, and F. C. Chen, "Influence of aged conductor surface conditions on AC corona discharge with a corona cage," *Dielectrics and Electrical Insulation, IEEE Transactions on*, vol. 18, pp. 809-818, 2011.
- [4] P.S. Maruvada, *High voltage engineering-theory and practice*, Marcel Dekker, New York, 2000
- [5] C. Larson, B. Hallberg and S. Israelsson, "Long term audible noise and radio noise performance of American electric power's operating 765 kV lines" *IEEE Tran. Power Appar. Syst.* Vol. 98, pp. 1859-1859, 1979.
- [6] Y. Shaohua, L. Fangcheng, L. Yunpeng, Z. Wenfang, and W. Xiangyuan, "Discussion on problems of single conductor small corona cage's design," in *Electrical and Control Engineering (ICECE)*, 2011 International Conference on, 2011, pp. 2187-2190.
- [7] M. Lekganyane, N. M. Ijumba, and A. C. Britten, "A comparative study of space charge effects on corona current using an indoor corona cage and a monopolar test line," in *Power Engineering Society Conference and Exposition in Africa, 2007. PowerAfrica '07. IEEE*, 2007, pp. 1-6.
- [8] N. G. Trinh, P. S. Maruvada, and B. Poirier, "A Comparative Study of the Corona Performance of Conductor Bundles for 1200 kV Transmission Lines," *Power Apparatus and Systems, IEEE Transactions on*, vol. PAS-93, pp. 940-949, 1974.
- [9] R. D. Dallaire, P. S. Maruvada, and N. Rivest, "HVDC Monopolar and Bipolar Cage Studies on the Corona Performance of Conductor Bundles," *Power Apparatus and Systems, IEEE Transactions on*, vol. PAS-103, pp. 84-91, 1984.
- [10] X. B. Bian, W. Liming, G. Zhicheng, C. Jing, Y. Yingjian, and W. Xiong, "Experimental investigation on altitude correction factor of positive dc corona inception voltages of transmission lines based on the mobile corona cage," in *High Voltage Engineering and Application (ICHVE)*, 2010 International Conference on, 2010, pp. 548-551.
- [11] D. Mengting, Y. Zhanqing, G. Zhiye, L. Shi, Z. Rong, Z. Bo, L. Min, L. Ruihai, L. Lei, and G. Chao, "Corona onset characteristics of grading rings on 800kV UHVDC transmission line," in *Information Science, Electronics and Electrical Engineering (ISEEE)*, 2014 International Conference on, 2014, pp. 800-804.
- [12] R. Urban, H. Reader, and J. P. Holtzhausen, "AC transmission line corona noise issues in a small corona cage," in *Africon Conference in Africa, 2002. IEEE AFRICON. 6th*, 2002, pp. 639-644 vol.2.
- [13] J. Wulff, T. Vogt, and F. Jenau, "Ion current studies using a small corona cage," in *Environment and Electrical Engineering (EEEIC)*, IEEE 15th International Conference on, 2015, pp. 2205-2210.
- [14] C. Eroncel, S. Ilhan, A. Ozdemir, and A. Kaypmaz, "Corona Onset Voltage and Corona Power Losses in an Indoor Corona Cage," in 14th International Middle East Power Systems Conference (MEPCON' 10), Cairo University, Egypt, 2010, pp. 791-794.
- [15] Y.-p. Liu, L.-j. Ren, y. Chen, Q.-f. Wan, S.-h. You, and W. Chen, "Research on High Altitude Corona Loss Measurement System Based on Small Corona Cage," in *High Voltage Engineering and Application, 2008. ICHVE 2008. International Conference on*, 2008, pp. 144-147.
- [16] W. Wei, L. Chengrong, L. Yunpeng, L. Bing, L. Xiaolin, J. Yitao, A. Bing, and W. Yixu, "Study of full scale UHV DC transmission line corona performance in corona cage," in *Electrical Insulation, 2008. ISEI 2008. Conference Record of the 2008 IEEE International Symposium on*, pp. 63-65.
- [17] Y. Nakano, Y. Sunaga, Availability of corona cage for predicting audible noise generated from HVDC transmission line IEEE transaction on power delivery, Vol. 4, No. 2, April 1989.
- [18] Y. Shaohua, L. Fangcheng, L. Yunpeng, Z. Wenfang, and W. Xiangyuan, "Discussion on problems of single conductor small corona cage's design," in *Electrical and Control Engineering (ICECE)*, 2011 International Conference on, 2011, pp. 2187-2190.
- [19] G. Zhi-Cheng, M. Min-hua, H. Jin-liang Discussion on the design and application of corona cage (J). *High Voltage Engineering*, 2006, Vol. 32 No. 11 pp. 74-77.
- [20] L. Fang-Cheng, Y. Shao-Hua, L. Yun-Peng, W. Qi-Fa, and Z. Zhi-Bin, "AC Conductors' Corona-Loss Calculation and Analysis in Corona Cage," *Power Delivery, IEEE Transactions on*, vol. 27, pp. 877-885, 2012.
- [21] H. Illias, T. S. Yuan, AB H. Abu. Bakar, H. Mokhlis, G. Chen, and P. L. Lewin, "Partial Discharge Patterns in High Voltage Insulation," In proceedings of IEEE International Conference on Power and Energy (PECon), Kota Kinabalu Sabah, Malaysia, pp. 751-755, 2-5 December 2012.

Natural and Synthetic Ester Based Transformer Insulation Fluid

Leeshen Pather*Andrew Swanson*

School of Engineering, University of KwaZulu-Natal Durban, South Africa E-mail:
209504460@stu.ukzn.ac.za

Abstract: There is an increasing need for the replacement of petroleum based oils due to non-renewable supply of the raw materials required for their manufacture. Great interest has been placed on substituting mineral oil for ester based transformer oils due to its biodegradability and high flash point. This paper outlines the colour changes and extrapolates the fatty acid composition of ester based and naphthenic transformer oils which have undergone accelerated thermal ageing. The oils are further analyzed using light spectrometry. Ester based oils contain fatty acids which are not common in mineral oils which can affect the performance and fluid flow within distribution and power transformers.

Key words: Transformer, Ester, Naphthenic.

1 INTRODUCTION

Transformers are the key pieces of equipment for large power utilities and serve as the basis for power distribution. A diminishing non-renewable oil supply and methods for improving life span and durability of transformers are some of the driving forces behind this paper [1].

Majority of transformers in service use oil as a medium of insulation. The insulation oil undergoes both mechanical and electrical stresses with its main function being a medium for heat transfer [2]. In addition the oil provides electrical insulation between the internal live parts [3].

Mineral oil is the most commonly used insulation liquid for transformers due to its cheap cost and adequate dielectric properties, however due to a steady decline in raw materials and a greater emphasis being placed on the environment, viable alternatives are being investigated [4]. Ester based transformer oil is one of these alternatives

Esters are alcohols emulsified by an acid, the most commonly used ester oils comprise of glycerol and fatty acids or synthetic esters of pentaerythritol and organic acids [5]. Esters are derived from renewable products making the oil a long term sustainable alternative.

The rheological and dielectric properties of Esters differ from that of naphthenic mineral oil [6]. These differences will impact the transformers electrical and mechanical performance. Differences in insulation fluid viscosity will affect the heat transfer rate of the oil which will impact the transformers performance.

An indication of the level of degradation experienced by transformer oils in service can be understood by a colour

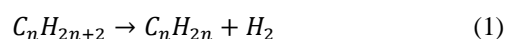
analysis. The results from this analysis can be a trigger for a further detailed investigation. Currently ASTM has a visual scale which can serve as guidance in the analysis of mineral oils in order to decipher the level of degradation. A detailed colour analysis can be accomplished in accordance with ASTM D1500 [7]. This however does not address the colour changes experienced by Ester based transformer oils nor does a visual scale exist to determine the level of oil degradation. Due to certain ester based transformer oils being produced in colours out of the norm, this makes a colour analysis challenging.

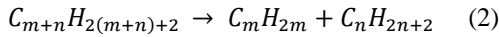
This paper will focus on analyzing ester based and naphthenic transformer insulation oils which have undergone thermal accelerated ageing. The change in oil colour due to degradation has been analyzed through a visual analysis coupled with the use of a light spectrometer. The possible implication of a change in the ester based transformer oils fluid flow is understood by studying the amount of fatty acids in the oils throughout the ageing process by quantifying the saponification number. The results from these tests are then analyzed and the implications that these parameters have on the performance of the transformer are put forward.

2 TRANSFORMER OIL DEGRADATION

Whilst a transformer is in service, the oil and cellulosic paper insulation are subjected to numerous thermal, electrical and environmental stress factors which ultimately degrade the insulation [8].

The most significant reactions that lead to degradation of mineral oil are those that lead to C-C bonding fracture, with the formation of an alkene, alkane [cracking reaction] and dehydrogenation [1]. These reactions are stipulated in equation 1 and 2.





Considering the decomposition of vegetable oil, the main reactions which are the cause of this are oxidation and hydrolysis, with byproducts being produced such as Carbon Monoxide, Carbon Dioxide, water and acids [1].

The cellulosic insulation paper also undergoes degradation due to the temperature stresses involved, chemical reactions take place which result in byproducts such as CO , CO_2 , H_2O , H_2 , CH_4 and furans. The byproducts produced from such reactions dissolve in the oil and therefore alter the oils chemical and electrical properties to an extent [1].

Oxygen is one of the most critical parameters in oil degradation and ageing. The oxygen can be naturally present in the oil or ingresses from the environment. The presence of high temperatures accelerates the ageing of oil, and metals such as aluminium and copper act as catalysts further accelerating the oxidation process [1].

With the case of mineral oil the oxygen present in the oil degrades the hydrocarbons through a process based on free radical reactions. These reactions then generate hydro peroxides which are unstable and ultimately decompose to free radicals which lead to the formation of water, ketones and other various oxidation byproducts [1].

3 SAPONIFICATION NUMBER

The saponification value can influence the heat dissipation characteristics of the insulation fluid due to the effect it has on fluid viscosity. The saponification number is the number of milligrams of potassium hydroxide required to neutralize one gram of sample [9]. The saponification number indicates the average molecular weight of the triacylglycerol in the sample. The saponification value is inversely proportional to the mean molecular weight of fatty acids (or chain length).

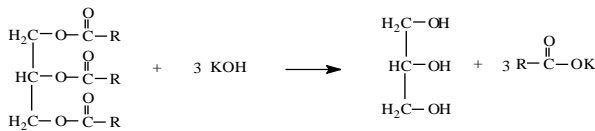


Figure 1: Process of Saponification

4 VISCOSITY AND FLUID FLOW

The insulation fluid in transformers has a critical role to play in electrical insulation as well as fluid flow. The viscosity of the oil has a direct impact on its fluid flow. For cold climatic conditions, oil with a low viscosity is preferred due to its increased fluid flow [10]. Mineral oil typically has viscosity which is the same range for temperatures between 60 & 100 degrees [10]. The viscosity of the natural and synthetic esters are

significantly lower than that of mineral oil and are generally around $33 \text{ mm}^2/\text{S}$.

5 EXPERIMENTAL SETUP AND ANALYSIS

For the experimentation, Ester and mineral based oils were aged for 184 hours in an ageing oven (Figure 2) with a standard paper insulation insert with a mass of 5 grams in a sealed vessel in accordance with IEEE STD 101 1987 [1]. The temperatures had varied between 60°C and 110°C with a virgin sample used as a reference for comparison as stipulated in Table 1. A colour analysis was then performed on the oils together with the use of light spectrometry. The saponification number was determined according to ASTM D 94-2 Method A [9].



Figure 2: Associated Environmental Systems Ageing Oven

Table 1: Accelerated Thermal Ageing of Transformer Oils

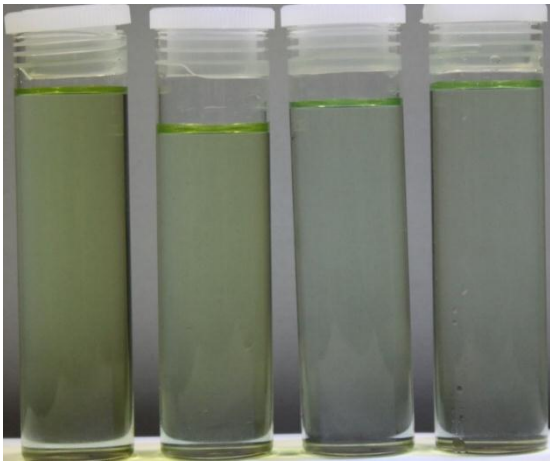
Oil Name	Oil Type	Sample	Temperature
Envirotemp FR3	Natural Ester	A	Virgin (Ambient Temperature)
		B	60°C
		C	90°C
		D	110°C
Nitro Libra Mineral	Mineral	A	Virgin (Ambient Temperature)
		B	60°C
		C	90°C
		D	110°C
Midel 7321	Synthetic ester	A	Virgin (Ambient Temperature)
		B	60°C
		C	90°C
		D	110°C
Shell Diala S4	Mineral	A	Virgin (Ambient Temperature)
		B	60°C
		C	90°C
		D	110°C

5.1 LIGHT SPECTROMETER SETUP

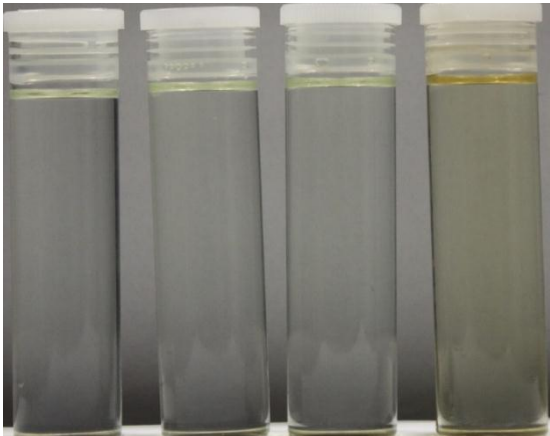
An ocean optics light spectrometer was used to measure the amount of light that passed through each of the various aged samples of transformer oil with an incandescent beam of light being the source. The amount of light being emitted from the source was controlled using a 1mm pin hole.

6 RESULTS AND DISCUSSION

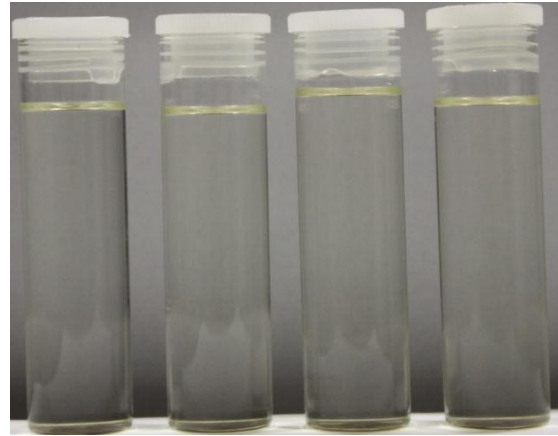
After completion of the ageing process, the oils were stored in glass vials to make a visual inspection possible.



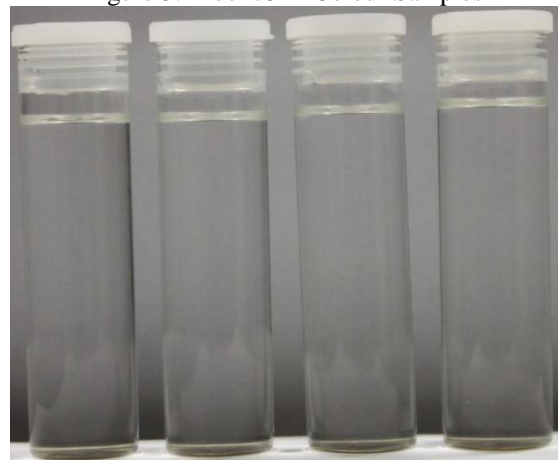
(Sample A) (Sample B) (Sample C) (Sample D)
Figure 3: Envirotemp FR3 Colour Samples



(Sample A) (Sample B) (Sample C) (Sample D)
Figure 4: Nitro Libra Mineral Oil Colour Samples



(Sample A) (Sample B) (Sample C) (Sample D)
Figure 5: Midel 7321 Colour Samples



(Sample A) (Sample B) (Sample C) (Sample D)
Figure 6: Shell Diala D4 Colour Samples

Upon successful undertaking of a visual analysis it can be seen that the Natural Ester based transformer oil starts off being dark green and after accelerated thermal ageing at escalated temperatures it becomes lighter until it is almost clear at an ageing temperature 110 °C. The reasons for this phenomenon are possible due to the breakdown of molecules in the oil (Pyrolysis).

The mineral oil samples showed a similar performance as with the oil degradation chart as outlined in the ASTM standards. The oil had become darker in colour as the ageing temperature had increased.

The Midel 7321 and Shell Diala S4 had experienced very little change in colour throughout the ageing temperature range.

6.1 SAPONIFICATION NUMBER

The saponification number of the aged samples were determined according to ASTM D94-2 Method A.

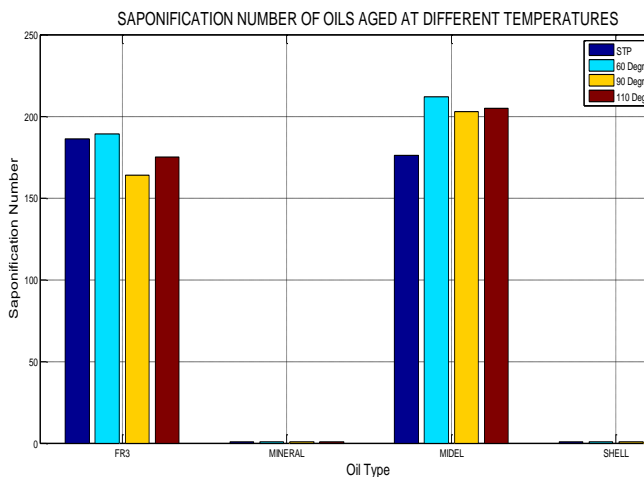


Figure 7: Saponification Number of Tested Oils

From the Figure 7 it can be noted that there is a steady decrease in the saponification number of the Envirotemp FR3 natural ester which signifies that the fatty acids within the oil increase in number or chain length as the ageing temperature escalates. This would lead to an increased fluid viscosity which will negatively influence fluid flow within a transformer decreasing the heat transfer rate. This property will affect fluid flow greatly in cold climatic conditions as the oil will be more viscous during these conditions.

The Midel synthetic ester shows a steady increase in the saponification number which suggests that during the ageing process fatty acids had broken down within the oil to form shorter chains. One of the benefits of this would be an increased fluid flow within the transformer due to the oil decreasing in viscosity during the ageing process.

Mineral oil and Shell oil show a constant saponification number of one which was expected as they are petroleum based.

6.2 LIGHT SPECTROMETRY

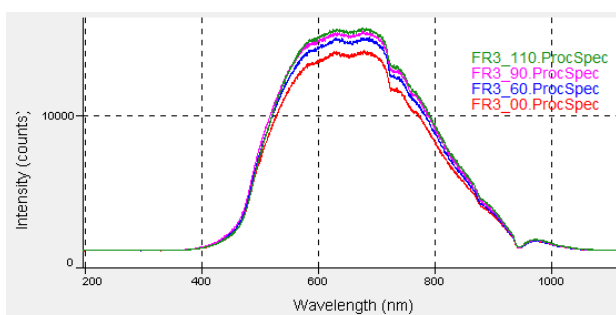


Figure 8: Graph representing Spectrometer Results for Envirotemp FR3

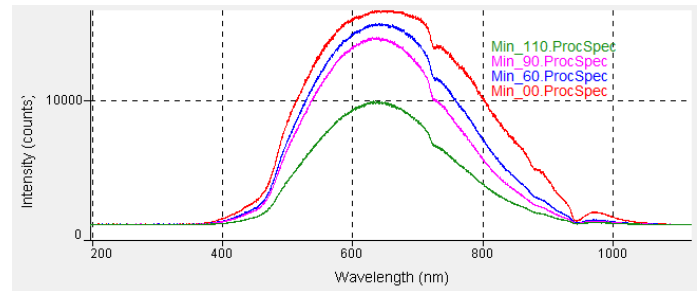


Figure 9: Graph Representing Spectrometer Results for Naphthenic Mineral Oil

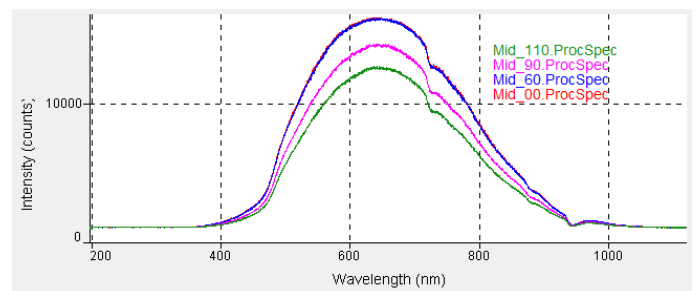


Figure 10: Graph Representing Spectrometer Results for Naphthenic Midel synthetic Ester

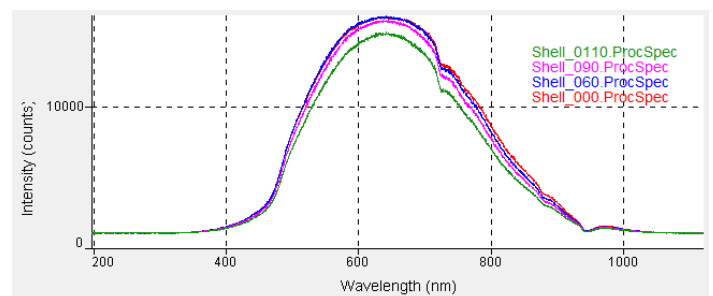


Figure 11: Graph Representing Spectrometer Results for Naphthenic Shell Diala S4

The light spectrometer results for the Envirotemp FR3 indicate that as the samples have aged at higher temperatures they allow more light to pass through it. The reasons for this is possible due to the breakdown of pigments within the oil. The transformer can experience performance due to the minimal amount of contaminants found in the oil. It is possible that the oil breakdowns the cellulosic fibers of the paper at a lower rate as apposed to the mineral and synthetic ester oils.

The mineral oil spectrometer results show that as the oil aged and became darker, more contaminants were being produced in the oil thus making it more difficult for light to pass through the samples. These contaminants could possible be the cellulosic fibers which have been broken down from the insulation paper. The light intensity drop was fairly constant between the virgin sample and the sample aged at 60 degrees Celsius and 90 degrees Celsius however there was a substantial drop between the sample aged at 90 degrees Celsius and the sample aged at 110 degrees Celsius. This large drop is due to the oil having

reached its flash point, rapidly oxidising the oil. The oils dielectric properties would be severely hampered and would possibly have to be discarded if evident in a transformer in service.

The Midel synthetic ester showed a drop in light intensity for the samples aged at 90 degrees Celsius and 110 degrees Celsius. This would suggest that more contaminants were present in the oil from an ageing temperature of 90 degrees Celsius upwards which may have been derived from the paper insulation breaking down and oxidation. The presence of contaminants will negatively affect the dielectric capabilities of the oil.

The light spectrometer results for the Shell Diala mineral oil showed little change between the aged samples. The only significant change was between the sample aged at 90 degrees Celsius and the sample aged at 110 degrees Celsius however this drop in light intensity was marginal. This would suggest that there were little contaminants produced within the oil throughout the ageing temperature range which will therefore result in a sustained long term transformer performance.

7 CONCLUSION

A series of accelerated ageing experiments have been investigated for both ester and mineral based transformer oils. The tests performed on the aged oils included a visual analysis, the determination of saponification number and a detailed light spectrometer analysis.

The natural ester had displayed different results from that of the naphthenic based oils. The samples had become lighter in colour as the ageing temperature had increased. Based on the saponification findings it is probable that the performance of the transformer will be negatively affected with time due to a decreased fluid flow from a mechanical perspective however, the clarity of the oil at escalated temperatures is excellent which is due to the production of fewer contaminants and slower breakdown of the insulation paper which is a beneficial. The behaviour of the natural esters colour throughout the ageing process is different from that of standard mineral oil which will need to be further specified by an official standard as it is not covered in ASTM D1500 [7].

The synthetic ester had showed a decrease in the number of fatty acids as the oil aged. This would suggest a positive impact on transformer performance due to an increased fluid flow. The synthetic ester will be preferred over the natural ester in colder climates due to its lower viscosity.

It was evident from the results that the mineral oils deterioration was greater than that of the Esters and the Shell Diala S4. The Shell Diala and mineral oil do however have no impact by the presence of fatty acid molecules as they are petroleum based.

8 ACKNOWLEDGEMENTS

The authors would like to thank Annalie Lombard and the Eskom oil laboratories for the assistance in the undertaking of the saponification test.

The authors would like to thank Eskom for the support of the research through the TESP programme.

9 REFERENCES

- [1] M. S. V. L. M. D. a. P. V. N. Alexandra Ciuriuc, "Comparative Study of Power Transformers," University Politehnica of Bucharest, Bucharest.
- [2] Vailsala, "The effect of moisture on the breakdown voltage of transformer oil," 2013.
- [3] P. O. R. LTD, "KNnowledge Base: Transformer oil/Insulating Oil," PowerLink Oil Refinery LTD, 2015. [Online]. Available: <http://powerlinkoil.com/knowledge-base-transformer-oil-insulating-oil/>. [Accessed 29 September 2015].
- [4] R. L. C. S. H. S. Lijun Yang, "Study on the Influence of Natural Ester on Thermal Ageing Characteristics of Oil-paper in Power Transformer," China, 2008.
- [5] "IEEE Guide for Interpretation of Gases Generated in Natural Ester and Synthetic Ester-Immersed Transformers," New York, 2014.
- [6] M. Spohner, "Comparison of Mineral Oil with Natural and Synthetic Oils".
- [7] A. International, "Standard Test Method for ASTM colour of Petroleum Products (ASTM Color Scale)," American National Standard.
- [8] A. G. H. R. T. Mohammad Mirzaie, "Insulation Condition Assessment of Power Transformers Using Accelerated Ageing Tests," Tubitak, Iran, 2009.
- [9] A. International, "Standard Test Methods for Saponification Number of Petroleum Products," American National Standard, 2014.
- [10] C. O. Olsson, "Buoyancy driven flow in counter flow heat exchangers," ABB, Sweden.
- [11] M. S. V. L. M. D. a. P. V. N. Alexandra Ciuriuc, "Comparative Study on Power Transformers".
- [12] "IEEE Guide for the Statistical Analysis of Thermal Life Test Data".

THE MEASUREMENT OF HVdc INSULATOR LEAKAGE CURRENT USING MAGNETIC FIELD SENSORS

M Roman*, RR van Zyl*, N Parus**, N Mahatho** and B Nalomo***

*Cape Peninsula University of Technology, Cape Town, South Africa

Email: roman.morne@gmail.com, vanzylr@cput.ac.za

**Eskom Holdings SOC Ltd, Johannesburg, South Africa and the University of the Witwatersrand, Johannesburg

Email: NishanP@eskom.co.za, MahathN@eskom.co.za

***Eskom Holdings SOC Ltd, Johannesburg, South Africa

Email: NalomoGB@eskom.co.za

Abstract: Insulators form a critical component in a high voltage plant. This paper focuses on high voltage direct current (HVdc) schemes, with particular reference to the complexities of measuring direct current leakage current across insulators. The focus of this work is the design and implementation of a clamp-on, non-intrusive leakage current (LC) prototype that will be able to measure LCs from 0 mA to 200 mA. To date, Eskom, the South African power utility, does not have a device with the above-mentioned specifications. Research shows that magnetic field sensors can be used as a possible LC sensor technology. A new prototype was developed by CPUT and is based on the detection of the magnetic field induced by the flow of LC across the glass insulator. Using this new prototype, LC measurements were conducted on glass insulators and the results were compared to the simultaneously measured shunt resistor method. Experimental results show that the prototype can detect and accurately measure leakage current in the specified current range. The expected outcome is to develop a hand-held / clamp-on LC prototype that can be used by live line workers and for future real time insulator performance monitoring.

Key words: HVdc, insulator, leakage current, magnetic fields sensor, monitoring

1 INTRODUCTION

Leakage current (LC) exists on glass insulators primarily because of the accumulation of pollution and subsequent wetting of the polluted glass surface [1]. The magnitude of leakage current can be used as a good indicator of the insulator's performance under voltage stresses. High levels of leakage current are an indication of potential insulator string flashover.

At present, the South African power utility, Eskom, does not have a non-intrusive, in-situ technology solution to measure the LC flowing on their HVdc transmission lines' insulators. A study of the leakage current in real time can be used as a condition based monitoring system for early detection of possible line faults and may also be used to classify safe and unsafe conditions for live line workers. Figure 1, shows live line workers performing maintenance on glass insulators. Before any live work can be carried out it is preferential to have an indication on the level of the leakage current. If there is substantial leakage current flowing across the insulator, there is a risk of drawing a high current arc between the live conductor, the insulator and the line.

LC monitoring can be used as an early warning flashover detection system [2]. In order to use Figure 2 for insulator monitoring applications, an acceptable LC must first be

defined which will act as an alarm to commence maintenance of the insulators.

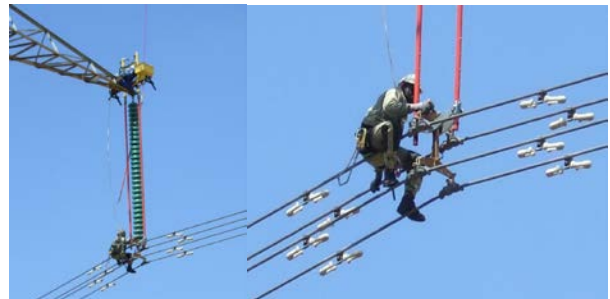


Figure 1: Eskom live line workers performing maintenance on glass insulators

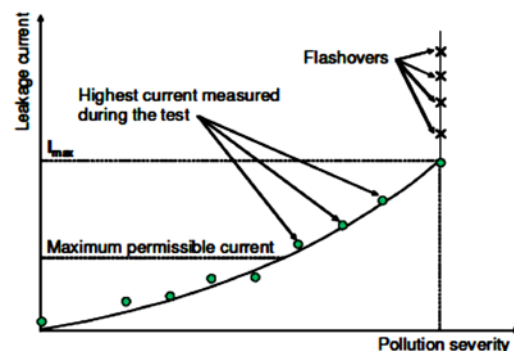


Figure 2: Relationship between LC and the pollution severity as determined through laboratory testing [2]

A device was developed to measure the LC and will be discussed in this paper. Laboratory measurements were conducted with the prototype and two glass discs, and the results were compared to a simultaneous shunt resistor measurement.

2 REVIEW OF LEAKAGE CURRENT SENSORS

Measurement of LC has become important for power utilities due to the damage it can cause to power grids if left unattended. Research indicates that light rain or high humidity together with a thin pollution layer increase the conductivity of insulators. Dry band arcing may occur and may eventually lead to flashover [3]. Accidents involving insulator flashover, especially near the coast, have been a major issue for a long time. Consequently, various LC measurement techniques for insulators have been designed and developed.

One such technique uses fibre optics. The LC modulates an ultra-bright light-emitting diode (LED) that produces a modulated light signal [3]. This signal is transmitted along an optic fibre cable. This technique was successfully implemented for an alternating current (ac) transmission line insulator case.

Current transformers can be used for measuring LC on insulators. For example, a ferrous current transformer can be used with a straight conductor as primary winding [2]. However, current transformers are only suitable for ac current measurements.

Techniques for measuring both ac and dc leakage current include the resistive shunt method [4] and measurement with an online leakage current analyser (OLCA) [5, 6]. A glass stand-off insulator is typically installed in series with the insulator under test – typically at the ground-end. This is not practical for energised transmission lines as the insulator string will have to physically be removed in order to install the stand-off. OLCA and resistive shunt measurements are more applicable to laboratory tests.

A non-intrusive sensor that can measure ac LC over a wide frequency band of several Hz to a few tens of MHz was developed by Chen *et al.* [7]. It is based on the Rogowski coil principle. This technique is not suitable for dc LC measurements since it needs an alternating current to couple into the device.

The selection of appropriate magnetic field sensors has previously been reviewed by the authors [8]. Numerous techniques have been developed for ac, but insulators respond differently under dc conditions, as explained in [8].

3 PRELIMINARY MAGNETIC FIELD CALCULATIONS

In the development stage of the prototype, the magnetic field for the Cahora Bassa needed to be known to select an appropriate magnetic field sensor. For this round of development, the minimum measurable current was specified as 1mA. It is further assumed that the conductor bundle (carrying the main line current of the Cahora Bassa line) is at a position approximately 4 m away from the position of the magnetic field sensor.

The field measured in close proximity of the insulators consists of the field contribution of the LC and the main line current. It is recommended that the sensor is close to the cap of the glass insulator so that repeatable measurements can be conducted. The modelling shows that the magnetic field magnitude decreases with a decrease in distance from the overhead transmission line but magnetic shielding material may have to be implemented, since the magnetic field associated with the main line current is still of the order 10^3 higher than the field at the insulator. Figure 3 shows the approximate magnetic field of the Cahora Bassa line and its insulators with an increase in distance using Ampere's Law for a long straight wire.

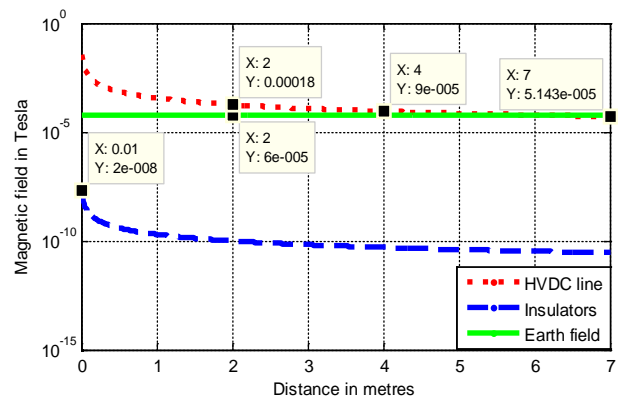


Figure 3: Calculated magnetic field due to a 1800 A main line current ('HVdc line') and a 1 mA LC ('Insulators') based on Ampere's law for long line currents

4 LEAKAGE CURRENT TESTS WITH DEVELOPED PROTOTYPE

The developed prototype detects the magnetic field associated with the current that is flowing on the insulator's surface. The primary components of the prototype are a magneto-resistive (MR) sensor and a high permeability soft magnetic core. The core is cut in half for clamping purposes. A slot has been cut out into which the sensor is positioned. The MR sensor also has additional signal conditioning circuitry.

The developed prototype was tested at Eskom's Corona cage high voltage test facility to determine if it can measure leakage current flowing across an insulator's surface in a non-intrusive manner.

4.1 Calibration of prototype

The calibration of the prototype, together with the shunt resistor, was first conducted on a dc glass insulator (see Figure 5). A 10 Ω , 5 W shunt resistor was used during the measurements. The shunt resistor measurement was based on Ohms law; where for a known current, a constant voltage could be measured across the fixed value shunt resistor. The shunt resistor was used with a clean (unpolluted) stand-off glass insulator to ensure that most of the leakage current will be 'directed' into the shunt resistor.

Figure 4 shows the LC prototype around a test glass insulator. Figure 5 shows the schematic of the setup and Figure 6, the physical test setup at the Corona cage test facility. The first test entailed injecting a known (low voltage) current through the insulator setup as shown in Figure 7. In order to ensure current flow through the prototype, a wire was connected from the cap to the pin of the insulator (viz. a short circuit of the glass area of the insulator disc, through the LC prototype). The prototype was wrapped with aluminium material for shielding purposes. The shunt resistor and the prototype's transfer function was determined after the calibration was performed and the results are presented in Figure 8.

The measurements show that the prototype has good linearity. This curve was then used to determine the actual leakage current being measured by the prototype. It is important to note that the calibration curve was affected by the orientation of the prototype and the background magnetic fields at the time of the tests. The resolution can be adjusted by using the electronic conditioning circuitry. The measured current was compared to the current applied and both the shunt resistor and the prototype had an error of not more than 1 %.

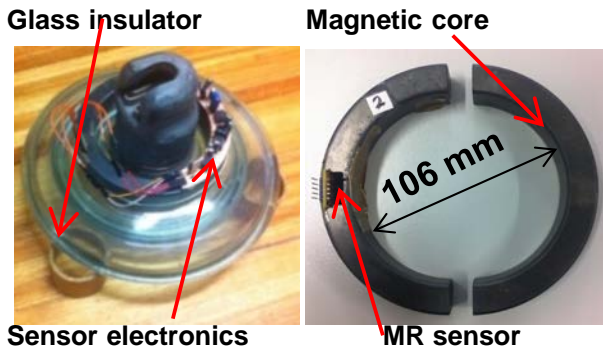


Figure 4: Prototype with its electronics around a test glass insulator

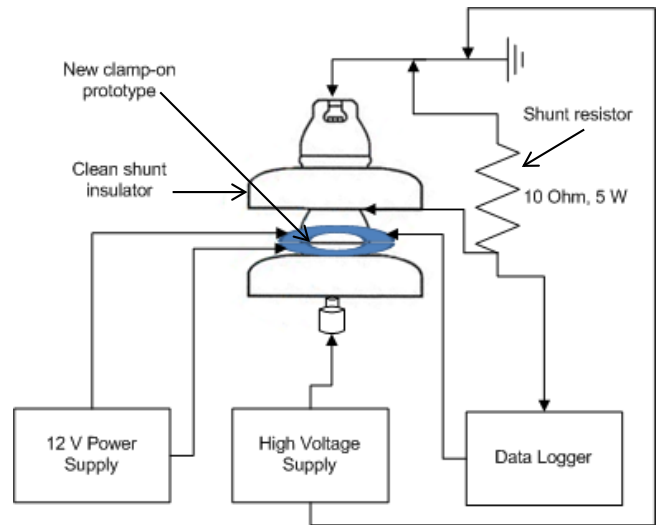


Figure 5: Schematic diagram of leakage current measurement setup



Figure 6: Calibration test setup for the leakage current prototype and the shunt resistor



Figure 7: Position of leakage current prototype and shunt resistor

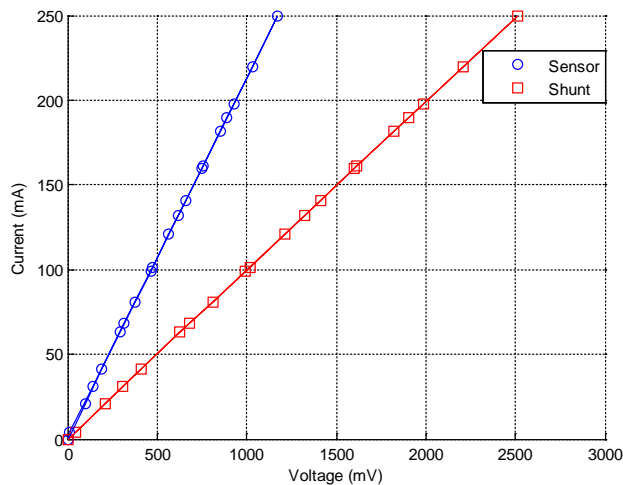


Figure 8: Transfer function of prototype and shunt resistor

5 LEAKAGE CURRENT MEASUREMENTS USING A HIGH VOLTAGE SUPPLY

After calibration was completed, an HVdc power supply was used to generate leakage current on a polluted insulator under test. During the initial calibration tests, a steady known leakage current was injected into the setup. For the second set of tests, a high voltage was applied across the polluted insulator and an unknown transient current flowed across the insulator. The insulator was sprayed with salt water (10 g of NaCl in 500 ml of distilled water) to aid the flow of leakage current on the insulator's surface. Before the measurement process started, the prototype was wrapped with a non-conductive material to prevent leakage current from flowing on the outside of the prototype's aluminium enclosure. A high voltage dc power supply with a 12 mA maximum rating was used during the measurement procedure. Data was logged every 500 ms and the measurements results can be seen in Figure 9.

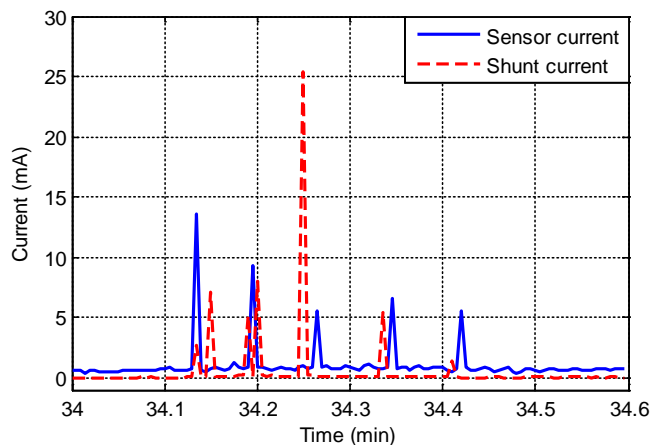


Figure 9: Leakage current comparison between the prototype and the shunt resistor

Another stand-off glass insulator was inserted (as seen in Figure 10) to further increase the impedance to ground and hence observe if there are any changes in the shunt measurement leakage current value. As seen in Figure 11, a shunt leakage current was only observed in the form of an impulse, with the normal being zero. This result was expected as the dry band arcing results in current pulses rather than a steady/constant current (depending on the pollution level and the amount of wetting). The insulators were re-sprayed with salt water and the measurement process repeated. Figure 11 shows the leakage current comparison between the shunt resistor and the prototype for the case of two stand-off insulators. However, no difference was seen in the shunt resistor's results at the low level current amplitudes. A moving average of Figure 11, was also plotted in Figure 12, to observe the trend of the shunt and prototype current. After the measurement, it was also observed that the insulation tape which forms part of the enclosure for the prototype, was covered with the salt pollution (seen in Figure 13). This was not anticipated and may have had an effect on the results.

Two stand-off insulators



Figure 10: Leakage current test setup using two stand-off glass insulators

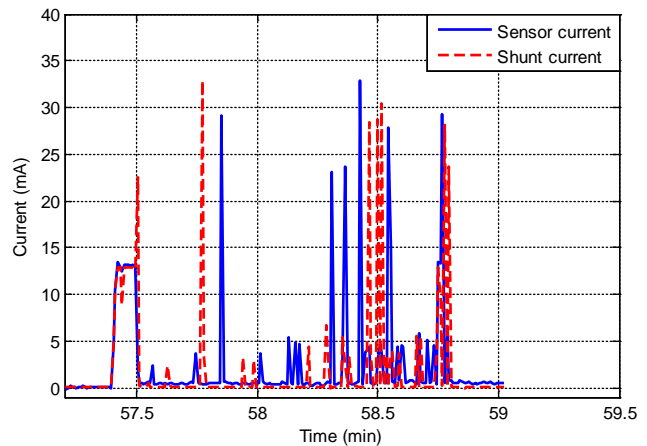


Figure 11: Leakage current comparison between the prototype and the shunt resistor for the case of two stand-off insulators

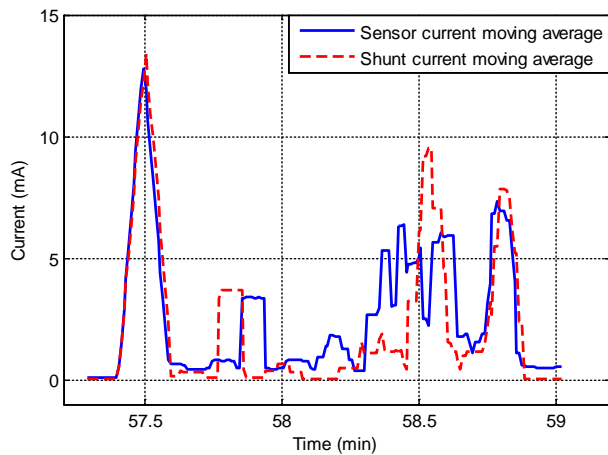


Figure 12: Moving average of prototype and shunt leakage current



Figure 13: Insulator and prototype's enclosure covered with dried saltwater

Another leakage current measurement was conducted but with the salt content doubled (i.e. 20 g of NaCl in 500 ml of distilled water) and with the LC sampled at 100 ms. For this tests a delay in measurement results between the shunt and the prototype (seen in Figures 11 and 12) was observed. Figure 14 shows the leakage current comparison between the shunt resistor and the prototype for the case of two stand-off insulators. Due to the large number of data points, a moving average was also plotted (see Figure 15) to observe the trend of the shunt and prototype current.

6 DISCUSSION OF RESULTS

The tests show that the new magnetic field sensor can detect dc leakage current that is flowing on an insulator's surface. During measurements, the shunt resistor's measurements either lag or precede the prototype's leakage current data. The reason for this is still unknown and will be investigated as part of future work. The data logger has a saving delay time of 10 ms and cannot log data at a rate

faster than 10 ms. The lowest sampling time used during tests is 100 ms.

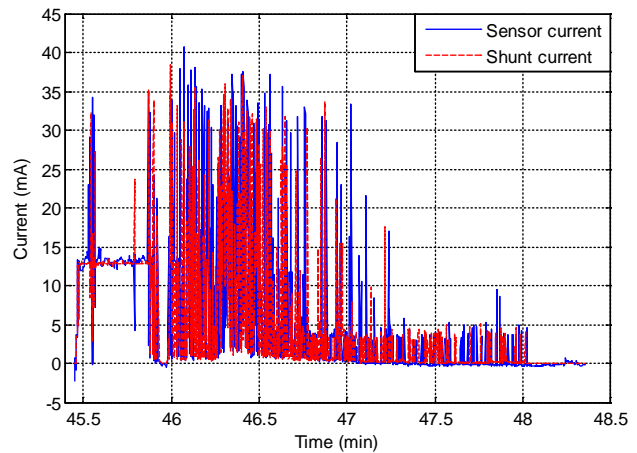


Figure 14: Leakage current comparison between the shunt and the prototype (100 ms sampling rate)

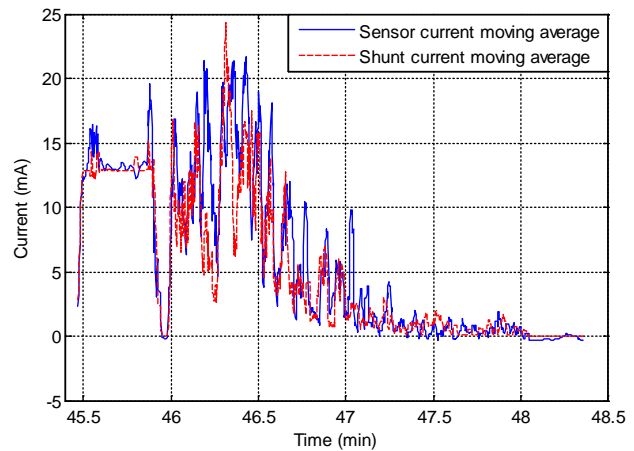


Figure 15: Moving average of prototype and shunt leakage current

The prototype's current is generally higher than that recorded by the shunt resistor. In some instances the prototypes' current measurement increases / decreases while at the same time the shunt's current decreases / increases by a similar magnitude as seen in Figure 11 (time: 57:5) and Figure 14 (time: 45:79). This behavior can also be seen in the moving average (Figures 12 and 15). A possible reason for this might be that the prototype is detecting a change in current polarity (since the MR sensor in the prototype detects the magnitude and direction of current impulses) on the insulator's surface caused by the discharges which is not everywhere on the insulator at the same time. Again, more research is required to fully understand the nature of the impulses.

For the calibration tests, the output of the prototype agreed well with that of the shunt (viz. the both techniques yielded

the same leakage current value). However, for the high voltage pollution tests, differences in the magnitude and phase of the current pulses were noted. Further investigation of the nature of these impulses and the effect on the measurement circuitry is needed.

Currently, another iteration of the prototype is being developed which will comprise of two magnetic field sensors instead of one (which is presented in this paper). The second sensor as depicted in Figure 16 will be used to cancel out the effect of external magnetic field interferences such as the influence of the line current of the Cahora Bassa HVdc overhead transmission (which has much higher current readings than that flowing on an insulator surface) as well as the natural background/ambient fields.



Figure 16: New prototype CAD model

7 CONCLUSION

A new clamp-on non-intrusive dc LC prototype was developed. LC measurements were performed at Eskom's Corona Cage to observe if the prototype can indeed measure leakage current flowing across a glass insulator surface. An HVdc glass insulator was used during these experiments and the leakage current measurement results compared to a shunt resistor that was placed in parallel with the insulator. The results showed that the prototype could detect the leakage current that was flowing on an insulator. The leakage current impulses occurring during dry-band activity need to be given greater consideration; this will be done, possibly using an oscilloscope for characterizing the current in the further planned research. Future iterations of the prototype will incorporate the use of two sensors to allow for differential measurements through which the effect of unwanted external magnetic fields is removed from the leakage current measurements.

8 ACKNOWLEDGEMENTS

The financial support of the French South African Institute of Technology and Eskom towards this research is acknowledged.

9 REFERENCES

- [1] L. Holtzhausen, J. P., Pieterse, P. J., Vermeulen, H. J., Limbo, S. "Insulator aging tests with HVac and HVdc excitation using the tracking wheel tester", *International conference on high voltage engineering and application (ICHVE 2010)*, pp. 445 - 448.
- [2] A. J. Phillips, F. F., Bologna, J. M., Major, C. S., Engelbrecht, "Development and demonstration of low cost robust leakage current sensors for evaluating contaminated insulators". *Proceedings of the 16th international symposium on high voltage engineering*, paper 5-3, 2009, pp. 1-6.
- [3] M. M., Werneck, D. M., Santos, C. C Carvalho, F. V. B. de Nazare, R. C. S., Allil. 2014. "Detection and monitoring of leakage currents in power transmission insulators". *IEEE sensors journal*, 1-9.
- [4] Z., Jia, C., Chen, X., Wang, H., Lu. 2014. "Leakage current analysis on RTV coated porcelain insulators during long term fog experiments". *IEEE transactions on dielectrics and electrical insulation*. Vol 21(4):1547-1553.
- [5] P. J., Pieterse, A. I., Elombo, G. N. J., Mouton, H. J., Vermeulen, J. P., Holtzhausen, W. L., Vosloo, 2011. "A coastal insulator pollution test station for the evaluation of the relative ageing performance of power line insulators under ac and dc voltage". *Proceedings of the 17th international symposium on high voltage engineering*, C-007, 1-5.
- [6] A. I. Elombo, J. P., Haultzhausen, H. J., Vermeulen, P. J., Pieterse, W. L., Vosloo. 2013. "Comparative evaluation of the leakage current and aging performance of HTV SR insulators of different creepage lengths when energised by ac, dc+, dc- in a severe marine environment". *IEEE transactions on dielectrics and electrical insulation*, 20(2):421-428.
- [7] W., Chen, C., Yao, P., Chen, C., Sun, L., Du, R., Liao. 2008. "A new broadband microcurrent transducer for insulator leakage current monitoring system". *IEEE transactions on power delivery*, 23(1):355-360.
- [8] M. Roman, R. R. van Zyl, N. Parus, N. Mahatho, "Insulator leakage current monitoring: challenges for high voltage direct current transmission lines". *Industrial and commercial use of energy (ICUE)*, pp. 1-7, 2014.
- [9] S. A. Macintyre. 1999. *Magnetic field measurement*. [Online]. Available: <http://engineering.dartmouth.edu/dartmag/docs/macintyre.pdf>

Towards an Explanation of the Abnormal Attenuation of the Power Line Carrier Signals on an HVDC Monopolar Transmission Line

J. Schutte^{1*}, A.C. Britten², J. van Coller³, R. Hubbard⁴, I. Davidson⁵

¹Eskom/University of Witwatersrand, Johannesburg, South Africa

²Private Consultant affiliated with UKZN, Johannesburg, South Africa

³University of Witwatersrand, Johannesburg, South Africa

⁴Eskom Research, Testing and Development, Johannesburg, South Africa

⁵UKZN, Eskom Centre of Excellence in HVDC Engineering, Durban, South Africa

*Email: SchuttJ@eskom.co.za

Abstract: This article reports on the Power Line Carrier (PLC) signal attenuation on the shield wire of the Cahora Bassa HVDC scheme. The increased attenuation due to the glass shield wire insulators is explained and quantified by means of an analytical model. Results obtained are presented and discussed.

1 BACKGROUND

The Cahora Bassa HVDC scheme was commissioned in three stages starting in March 1977, with full operation achieved in June 1979 [1]. The bipolar scheme, rated at $\pm 533\text{kV}$, can transfer approximately 1900 MW of power generated by the hydro-electric scheme in Songo (Mozambique) over a distance of approximately 1414 km to the Apollo converter station in Tshwane (South Africa). The distance between the two pole-conductors is 1 to 2km, effectively transforming the scheme into two monopolar transmission lines of positive and negative polarity. The pole conductor consists of a quad-Zambezi bundle, while a single Oden aluminium conductor with steel reinforcing (ACSR) is used as an insulated shield wire [1], [2].

Long distance HVDC lines require dependable communication systems in order to operate reliably. Power Line Carrier (PLC) can be used as a means of communication. In some cases, it is necessary to insulate the shield wire of a long HVDC line so that some of the PLC signals can be propagated along it [3]. The behaviour of the insulated shield wire for PLC applications forms the focus of this study.

2 INTRODUCTION

The Cahora Bassa HVDC scheme uses Power Line Carrier (PLC) as the main form of communication between the two terminal converter stations for speech, control and protection purposes. It is therefore important to ensure the reliable transfer of this carrier signal. The Oden shield wire, situated with an offset above the pole conductor, is an insulated shield wire which is earthed through a line trap only at each end. The transmission line was originally designed with porcelain shield wire insulators which were later replaced with glass shield wire insulators. A section of the line has recently been

reinsulated with polymeric shield wire insulators. The focus of this paper is thus to explain the reasons for the increased attenuation of the PLC signal for when glass shield wire insulators are used.

2.1. Hypothesis

The lumped loading line model was initially used to investigate the influence of pollution on the glass insulators [3]. This model is used to show that the lumped shunt resistance of the shield wire insulator at each tower is the underlying cause of the additional attenuation.

3 THEORY OF THE LUMPED LOADED TRANSMISSION LINE

The theory used treats the system as a loss-free, i.e. quasi-ideal transmission line which has lumped shunt loading at each tower. The shunt loading impedance (Z) takes the form of the shunt capacitance (C) and shunt resistance (R) of the glass shield wire insulator at each tower. This model is an approximation since the precise effect of modal conversion is not taken into account. The basic configuration is shown in Figure 1 below.

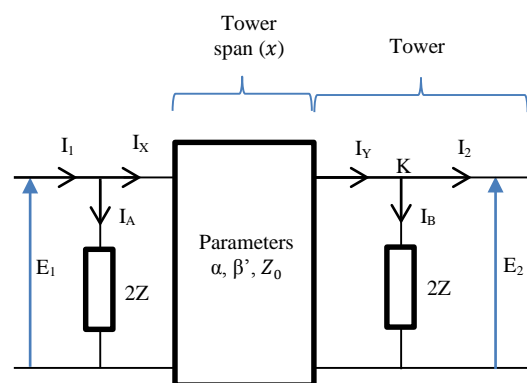


Figure 1: Block diagram showing the position of the lumped loadings.

For ease of analysis the lumped shunt impedance is split into two parallel impedances of $2Z$ each.

By applying the theory of the ABCD parameters to the above linear and bilateral network, it is possible to

find the additional attenuation caused by the quasi regularly- spaced insulator shunt impedance. The relation between the sending end and the receiving end quantities can be written as

$$E_1 = AE_2 + BI_Y \quad (1)$$

$$I_x = CE_2 + DI_Y \quad (2)$$

- where A, B, C, and D are parameters that depend on the transmission-line constants R, L, C and G. The ABCD parameters are, in general, complex numbers. A and D are dimensionless. B has units of ohms and C has units of Siemens. Also

$$A = D = \cosh \theta \quad (3)$$

- where θ denotes the propagation constant/image transfer constant,

$$\theta = \alpha + j\beta \quad (4)$$

- with α and β the attenuation constant and the phase constant respectively, which result from filter action. Equations for parameters B and C are shown in equations (5) and (6), where Z_0 denotes the characteristic impedance of the line.

$$B = Z_0 \sinh \theta \quad (5)$$

$$C = \frac{1}{Z_0} \sinh \theta \quad (6)$$

From Figure 1 at K

$$I_Y = I_B + I_2 = \frac{E_2}{2Z} + I_2 \quad (7)$$

Substituting equations (3), (5) and (7) into equation (1) and replacing θ with equation (4) results in

$$E_1 = E_2 \cosh(\alpha + j\beta) + I_Y Z_0 \sinh(\alpha + j\beta) \quad (8)$$

For a loss-free transmission line approximation α is zero, $\alpha = 0$, therefore,

$$E_1 = E_2 \cosh(j\beta) + \left(\frac{E_2}{2Z} + I_2\right) Z_0 \sinh(j\beta) \quad (9)$$

Expanding the hyperbolic sine and cosine identities gives

$$E_1 = E_2 (\cos(\beta x) + j \frac{Z_0}{2Z} \sin(\beta x)) + j I_2 Z_0 \sin(\beta x) \quad (10)$$

For the case of R in parallel with C,

$$\frac{1}{Z} = \frac{1}{R} + j\omega C \quad (11)$$

Substitution of (11) in (10) gives

$$A = \cos(\beta x) - \frac{\omega C Z_0}{2} \sin(\beta x) + j \frac{Z_0}{2R} \sin(\beta x) \quad (12)$$

Therefore,

$$\cosh a \cos(b) = \cos(\beta x) - \frac{\omega C Z_0}{2} \sin(\beta x) \quad (13)$$

and

$$\sinh a \sin b = \frac{Z_0}{2R} \sin(\beta x) \quad (14)$$

- where x is 425 metres (average tower span) and Z_0 (the characteristic impedance of the line is 534 ohms [4], with β given as,

$$\beta = \frac{2\pi f}{v} \quad (15)$$

- where v is the speed of light (300×10^6 m/s) and f is the specific frequency. The parameter a in nepers/unit length is the additional attenuation per span and is superimposed on the basic line attenuation. The phase shift b equals 90 degrees outside the band where half wavelength effects will not occur [4].

In terms of the basic hypothesis, it was decided to investigate the influence of the shunt resistance of the glass insulators used. Measurements of the glass insulator properties were therefore done where the results are shown in Table 1, and Figures 2 and 3.

The additional attenuation, a dB per span, can now be plotted against the resistance per insulator for a given frequency. Figure 2 depicts the plot for frequencies 250 kHz and 300 kHz.

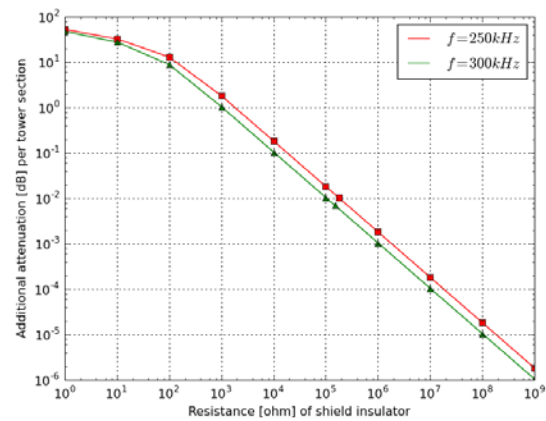


Figure 2: Shunt resistance of glass cap and pin insulator and the resulting additional attenuation per tower section.

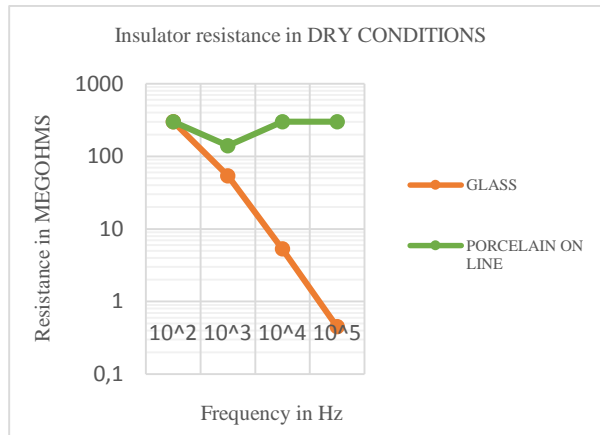


Figure 3: Measured insulator shunt resistance for the case of glass and porcelain pin types and polymeric types

4 VARIATION OF INSULATOR SHUNT RESISTANCE AS A FUNCTION OF FREQUENCY

The results of the measurements of shunt resistance, shunt capacitance and tan delta are given in Table 1.

Comments and observations are:

- 1) The measurements were conducted in clean, dry conditions.
- 2) The measurements have been verified by two independent techniques.

Table 1: Measured electrical parameters of .relevant insulators (The values apply to dry conditions)

	Type	Parameter	Frequency				
			100 Hz	120 Hz	1 kHz	10 kHz	100 kHz
Insulators	36 kV Polymeric type	Resistance (Megohms)	>200	>200	50	>200	>200
		Capacitance (picoFarad)	-	-	7.5	-	7.0
		Loss factor	-	-	-	-	-
	Glass cap and pin Cahora Bassa shield wire	Resistance (Megohms)	>200	>200	56	5.3	0.67
		Capacitance (picoFarad)	62	60	60	57	53
		Loss factor	0.064	0.064	0.047	0.052	0.046
	22 kV porcelain pin type	Resistance (Megohms)	>200	>200	>200	>200	>200
		Capacitance (picoFarad)	23.5	24.8	24.3	24.8	23.7
		Loss factor	0.007	0.007	0.008	0.009	0.007

5 CONCLUSIONS

The main conclusions coming out of this research are:

- 7) A practical and simple method of calculating the additional PLC attenuation has been developed; it is still to be evaluated more rigorously than space allows for in this paper.
- 8) The relatively low shunt resistance of the glass insulator is the main cause of the additional attenuation.
- 9) It appears that the cement surrounding the pin of the glass insulator is the underlying cause of the reduced resistance.
- 10) The polarisation current or aging of the cement appears to be an important cause of the low shunt resistance.
- 11) It will be important for more research to be done on this topic, at least to the point where the choice of suitable shield wire insulator can be confidently made so as to ensure acceptable PLC performance in future regional HVDC schemes.

6 APPENDIX

The additional attenuation per tower span is calculated using (14).

$$\sinh a \sin b = \frac{Z_0}{2R} \sin(\beta x)$$

- where $x = 425$ m, $f = 300$ kHz, $Z_0 = 534$ ohms, $v =$ speed of light (300×10^6 m/s), $b = 90$ degrees and $R = 150$ kilo-ohms.

Now:

$$\sinh a = \frac{534}{2 \times 150 \times 10^3} \sin\left(2\pi \times \frac{300 \times 10^3}{300 \times 10^6} \times 425\right)$$

$$\frac{e^a - e^{-a}}{2} = \frac{534}{2 \times 150 \times 10^3} \sin(2\pi \times 0.425)$$

Let $e^a = k$, then

$$k^2 - 0.001616k - 1 = 0$$

This gives $k = 1.00080843$ ($k > 1$)

Thus,

$$a = \ln(k) = 0.8081 \times 10^{-3} \text{ Np}$$

$$a = 0.8081 \times 10^{-3} \times 8.68588 \text{ dB}$$

$$a = 0.00719 \text{ dB per tower section}$$

7 ACKNOWLEDGEMENTS

The authors are grateful to the Eskom Power Plant Engineering Institute (EPPEI) for financial assistance; also to Rob Allen, Antonio Pereira, Tejin Gosai, and Thomas Tshikalange, for their professional contributions and support for this investigation.

8 REFERENCES

- [1] G.C. Sibilant, A.C. Britten and W. de Villiers, "Determination of the Noise Signatures of Various Sparkover Phenomena on the Insulated Shield Wire of Long Hvd Lines. Inaugural IEEE PES 2005 Conference and Exposition in Africa, 11-15 July, 2005.
- [2] A. J. Otto, "Direct Current Conductor Corona Modelling and Metrology", Doctoral thesis, University of Stellenbosch, 2009.
- [3] P. S. Maruvada, "Corona in transmission systems: Theory, Design and Performance". Crown Publications. Johannesburg. 2011.
- [4] A. C. Britten, "Anomalous carrier frequency propagation on the Cahora Bassa High Voltage DC transmission line", Master thesis, University of the Witwatersrand, 1976.
- [5] R. Arora and W. Mosch, *High voltage and electrical insulation engineering*. IEEE, 2011, pp 286-293.

Electric Field and Ion Current Interactions Between Hybrid High Voltage AC and DC Circuits with a focus on Altitude Effects

N Parus and I.R Jandrell

The University of the Witwatersrand, Johannesburg, South Africa

*Email: nishanth.parus@eskom.co.za

Abstract: In many cases, due to limited servitude near high voltage alternating current (ac) substations and direct current (dc) converter stations, the transmission lines of the ac and dc circuits are more frequently being constructed in close proximity to one another. Having ac and dc circuits in close proximity to each other presents practical design challenges in relation to meeting regulatory limits for ground level electric fields and ion current. Literature indicates that the initial prediction techniques that were developed using test and practical line data were from facilities located at sea level. New information suggests that the relative air density and other weather parameters have a marked impact on the corona performance of dc transmission lines – and it is not the same as that of equivalent ac lines. This paper discusses a research proposal for investigation into the hybrid ac/dc interactions and the impact that altitude has thereon.

1 INTRODUCTION

Today, high voltage direct current (HVdc) schemes provide many techno-economic benefits when compared to similarly power-rated alternating current (ac) schemes [1]. These benefits include a reduced environmental impact due to the usage of smaller servitudes for similar power throughput and lower magnetic fields; and lower capital cost for transmission lines that are greater than approximately 600 km in length. HVdc schemes are ideal for point-to-point bulk power transfer. As such, many HVdc schemes have been built or are being planned, worldwide.

In many cases, due to limited servitude near substations and converter stations, the transmission lines of the ac and direct current (dc) circuits are more frequently being located in close proximity to one another. Transmission lines in such a configuration are known as hybrid corridors. Further, related research has been conducted to include hybrid multi-circuit ac and dc lines - on a single tower. Such solutions are being considered in order to make use of restricted servitudes.

Having ac and dc circuits in close proximity to each other presents practical design challenges in relation to meeting limits for ground level electric fields and ion currents. There are various electrical coupling mechanisms between the circuits that influence the

conductor surface electric field and thus the generation of corona, space charge and ionic current. Historically, the design of ac and dc lines (with respect to the corona performance) was done independently. For cases where ac and dc lines are in close proximity, several assumptions relating to the weather and space charge have to be made with regard to the induced voltages between the circuits. As such, lines that have been designed to be well within the corona inception gradients may - in some specific cases - be forced into corona due to these induced effects. This issue is also of importance with regard to induced effects on the earthed shield wires on HVdc lines.

1.1. A Case Study

Figure 1, is an example of a hybrid corridor. Line inspections have revealed that the outer phase (viz. towards the HVdc line) of the 11 kV line is in corona. There is considerable safety margin between the transmission circuits so no corona induced effects are seen on the other circuits. The effectively-grounded earth electrode line also provides some shielding between the transmission dc and ac circuits.

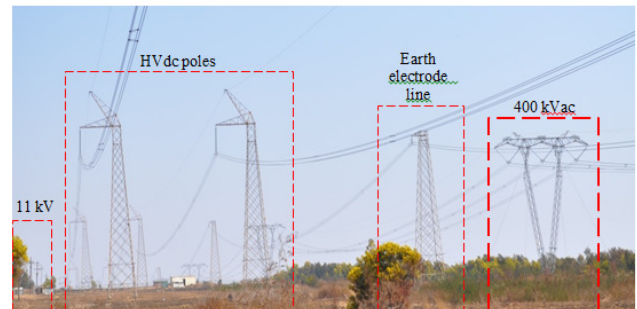


Fig. 1: A hybrid transmission corridor showing (from left to right), an 11 kV distribution line, both poles of the Cahora Bassa transmission lines, the earth electrode line and a 400 kV ac line.

Figure 2, shows corona scans and photography of a perpendicular ac/dc line crossing. Even at the perpendicular crossing the ac circuit is forced into corona. Should this be a parallel line in a hybrid corridor, this unwanted induced effect will be multiplied along the length of the line resulting in excessive audible noise, quality of supply problems on the reticulation network, and potentially other related environmental issues (viz. micro-shocks under the line), etc.

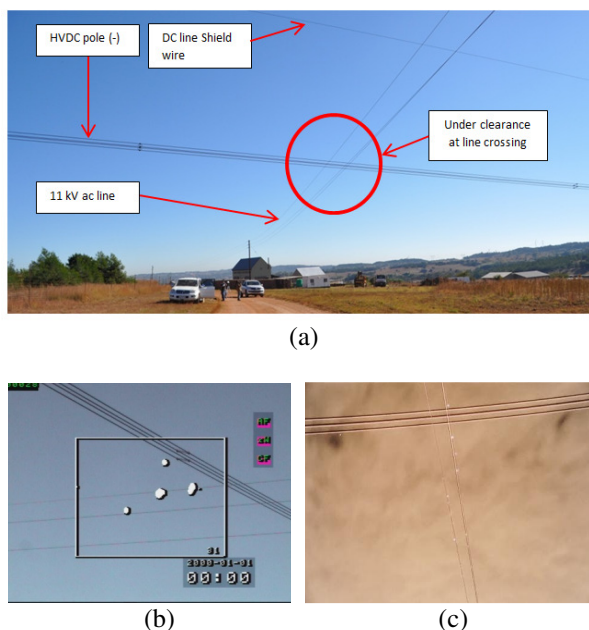


Fig. 2: (a) AC and dc line crossing, (b) CoroCAM ® image of the line crossing, and (c) corona photography of the line crossing.

1.2. Environmental Effects

Electrostatic charge in the vicinity of the transmission lines – due to the generation of space charge - may be responsible for several unwanted environmental aspects [2]. Such environmental issues include static charging of hair; micro-shocks, etc. (see Figure 3). Corona generation therefore needs to be kept as low as possible. Should the ion currents and electric fields be sufficiently large, there could be sense perception issues for animals and humans around the vicinity of the line and these could lead to public complaints, which may be difficult to rectify post commissioning. Figure 3, is an example of the result of static charge in the vicinity of a HVdc line. The electrostatic charge causes hair to stand on-end and some people may experience a ‘tingling’ sensation on their skin



Fig. 3: Static charge in the vicinity of the HVdc transmission line causes hair to stand on end

1.3. A Global and Southern African Perspective

Development of HVdc schemes for transmission backbone and point-to-point connections continue to

gather momentum in China, India, Canada and Brazil. China has recently built the Qinghai-Tibet HVdc interconnection that traverses an average altitude of 4300 m, with the maximum at 5300 m [3]. Although much information has been published relating to the technical accomplishments of the project, little information has been published relating to the corona design and performance of the lines, at such extreme altitudes.

In South Africa, the power utility’s ten-year transmission development plan proposed to implement new ± 600 kV HVdc schemes within the country [4]. The proposed schemes are to be developed with a high availability requirement in order to ensure a reliable and high quality of supply. The Cahora Bassa scheme is a crucial link in the South African Main Transmission System (MTS). The South African power utility, Eskom, currently operates and maintains the South African section of the Cahora Bassa HVdc scheme. The nominal operating voltage of the scheme is ± 533 kV. It provides approximately 1600 MW of renewable power, roughly 5% of South Africa’s supply capacity [5]. There are possibilities of possible upgrade of the scheme to ± 600 kV and to possibly relocate the converter station to a new site.

At the time of writing of this proposal, the Mozambican power company Electricidade de Mozambique (EDM) – the operator of the Mozambique section of the Cahora Bassa lines, is planning the CESUL project [6], which plans to develop the 1500 MW Mphanda Nkuwa and the 1245 MW Cahora Bassa North Bank hydroelectric power projects. The Mozambique transmission backbone plans are to develop ± 500 kV HVdc and 550 kV High voltage alternating current (HVac) power networks and is projected to interlink the Southern African Power Pool (SAPP) member countries. Due to limited access to servitudes, these transmission systems (both ac and dc) may have to share long parallel sections through the power corridors and at high altitudes.

1.4. Altitude Effects

Altitude, and in particular, the relative air density (RAD) has been proven to have an effect on the corona onset and extinction gradients [2]. The effect of altitude on dc voltage is generally similar to that of ac; however, the degree of influence is different. Although there are industry accepted recommendations for altitude correction factors for HVac corona generation (i.e. 1 dB/300 m), these have not been officially standardised. No published work has been found on altitude correction factors for HVdc corona.

2 HYPOTHESIS

The following is hypothesised:

- AC and dc circuits in close proximity to each other will have electrostatic and inductive coupling between the two. The surface gradient of the ac circuit may have a dc offset while the dc circuit may have an ac ripple. The maximum peak value of the surface gradient may therefore be raised on each conductor (See Figure 4).
- The increase of the conductor surface gradient may alter the point at which corona is generated on each circuit. Corona generation may result in space charge generation around the conductor and may in turn lead to a further modification of the local fields.
- The net effect of the change of the surface gradients around the conductors will lead to a change between the expected/calculated and the measured ground level electric fields and ion current.
- This resultant/net effect may be different at different altitudes above sea level (i.e. different relative air densities). This difference may be quantified and used to compensate for the low altitude configuration testing of high altitude application transmission lines.

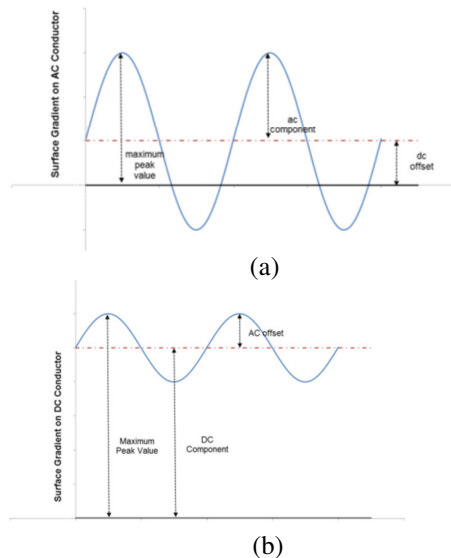


Fig. 4: (a) Induced surface gradient on an ac conductor due to the presence of a dc field, and (b) Induced surface gradient on the dc conductor due to the presence of the ac field [7].

This research will aim to address the following questions:

- What is the intensity of the coupling between the ac and dc circuits?
- Can small-scale tests be used to evaluate full-scale configurations?
- What are the ground level electric fields and ion currents for the various configurations being studied?
- What is the magnitude of the induced gradients on both circuits?
- Does the induced gradient have a pronounced effect on the corona performance of the respective circuits?
- To what extent does altitude (or relative air density) affect the corona performance of the configurations tested?
- To what extent do weather variables (e.g. temperature, wind and humidity) affect the corona performance of the configurations tested?
- To what extent do available mathematical computation techniques agree with practical measured data for the configurations tested?

These offsets as shown in Figure 4, may adjust the maximum conductor surface gradients experienced by both lines and may result in the new operating gradients exceeding the corona inception or extinction gradients. Increased levels of corona results in an increase in the ionic current flowing to the ground or to the opposite polarity pole conductor. This situation may be dynamic in nature and the characteristics thereof need to be studied by practical experimentation. It is difficult to simulate such a situation as the issue of the influence of space charge has not been fully researched and modelling thereof is not standardised.

3 GAPS IN CURRENT LITERATURE

A high level literature review was undertaken in order to determine the current state of research into this topic. Initial research was undertaken by several organisations such as Institut de Recherche d'Hydro-Québec (IREQ) [8-10], the Bonneville Power Administration (BPA) [11-13], the Electric Power Research Institute (EPRI) [14]; in the 1970's and '80 and again by Cigré from 2013.

While several references were found relating to the independent study of corona effects (viz. audible noise (AN), radio interference (RI), corona loss (CL), ion current (IC) and ground level electric fields), for both single and hybrid corridors, little information was found relating to the effect of altitude on these parameters and how they may affect the design of the transmission lines.

Both the BPA and IREQ have published semi-empirical prediction formulae based on theory and results from monopole and bipole test as well as practical lines. These formulae have been developed into software applications and have been extensively used for related studies; however, they provide different results for similar studies. A newly formed Cigré

working group (WG B2.62) is currently evaluating these differences as part of their scope of work.

The issue of the influence of space charge is better understood for mono or bipole cases. When applied to the hybrid case, the effects have not been properly studied, and at this time, no literature has been found on this topic.

Power utilities worldwide have been developing multi-circuit ac power corridors for many years. Parallel ac lines have an advantage in that the cyclical effect of the electric and magnetic fields results in a minimal net generation of space charges around the conductor bundle. The electrical interaction between the different circuits is thus limited to the electromagnetic coupling due to induction. Provided that sufficient phase spacing and appropriate phase angles are maintained between circuits this effect can be managed and the net effect on all parallel circuits can be studied and effectively designed-for. For transmission schemes having ac and dc lines in relatively close proximity to each other there will be electrostatic induction between the circuits.

4 PROPOSED RESEARCH PROGRAM

This research aims to address three issues. The first aim is to determine if the existing computational modelling techniques agree with small and full scale test results. The second aim is to investigate the effect of the interaction between HVac and HVdc circuits in close proximity to one another, and lastly, to determine if altitude has any effects on the coupling mechanism between the circuits.

4.1. Simulation and Modelling

The scientific computation of corona and related phenomenon has been well researched and documented [15]. It is proposed to utilise the Flux Tracing Technique (FTT) as well as the BPA ‘Anypole’ software to calculate the electric field, ion current and conductor surface fields for the various proposed line configurations. These software applications have been developed taking into consideration all the known mathematical models used for the calculation of electric field and ionic current. The FTT has been developed using empirical data for monopole and bipolar HVdc lines, however, it has not been validated against test data from hybrid lines. It is thus intended to compare the results from computation using Anypole and the FTT, with the data obtained from the small scale and full-scale tests. The analysis of the results will determine if the existing modelling and computation techniques are acceptable for the hybrid line case.

4.2. Small Scale Laboratory Tests (Low and High Altitude)

The small scale tests are intended to investigate the second and third aims of the project and will specifically focus on the issues related to the surface gradients on the conductors. The experimental setup will comprise of two conductors strung above a large metallic ground plane with one conductor energized at dc and the other at ac voltage (see Figure 5). The height above the ground plane (h), of the conductors and the spacing between the dc and ac conductors (p) should be of the order of one to two meters. This size is estimated based on the knowledge that the radius of the space charge region around the ac conductor may be in the order of 25 cm [15]. The choice of one to two meters may then be sufficiently large to not be affected by this issue. Simultaneous measurements of the following parameters will be made (as per Figure 5):

- dc and ac conductor voltages;
- corona onset gradients of the ac and dc conductors;
- ac and dc components of corona current on both the conductors;
- lateral profiles of ground-level ac and dc electric fields along a line perpendicular to and at the centre of the conductor span, and finally,
- the dc ion current density in the lateral profile.

Both the height above ground (h) and the phase to phase spacing (p) will be varied in order to obtain statistical data. The tests will be conducted at approximately 1500 m and 50 m altitudes, respectively, in order to investigate the relative air density aspect.

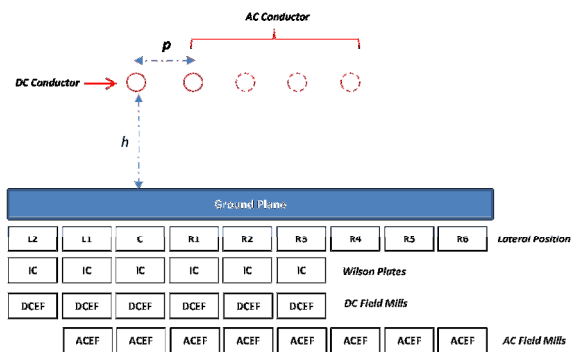


Fig. 5: Schematic representation of the test and ground level measurement requirements.

4.3. Full Scale Laboratory Tests (Low and High Altitude)

The large-scale outdoor test comprises of two aspects. To compare the results of the small scale laboratory tests with the large-scale tests and also to investigate altitude correction aspects. A practical test line setup will be required for this aspect of the research. The test line configuration will comprise of two stranded conductors, with diameters in the range of

2 cm to 3 cm (typical of conductors used on transmission lines), strung approximately 10 m above ground, with one conductor energized at dc and the other at ac voltage. Both horizontal and vertical configurations should be tested (for the twin bundle configuration), with the separation between the dc and ac conductors varying between 5 m and 10 m. In addition to all the measurements described above, the conducted radio interference voltage (RIV) from both dc and ac conductors (see Figure 6) and AN measurements (using a calibrated microphone) could also be made.

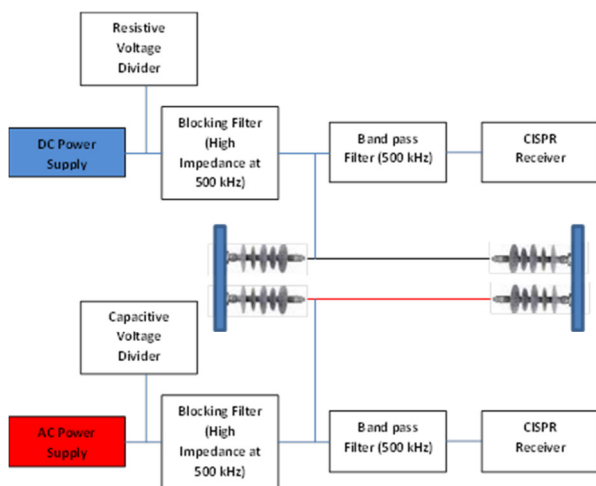


Fig. 6: Schematic representation of the radio interference measurement requirements

5 SUMMARY AND CONCLUSIONS

This proposal documents the potential development of HVdc transmission schemes in Southern Africa. The proposed schemes may be located in close proximity to HVac circuits and it is known that there will be electrostatic and inductive coupling between the two. Further, these schemes may be built at varying altitude.

This research is therefore important in order to properly understand and possibly quantify the hybrid ac/dc interactions in order to further improve and optimise the transmission line design.

The benefit of the research is thus to attempt to quantify the effect of the coupling between high voltage ac and dc circuits in terms of the changes in the surface gradients and to possibly determine an altitude correction factor for corona performance, for different altitudes.

6 REFERENCES

- [1] Eskom Power Series, "HVDC Power Transmission – Basic Principles, Planning and Converter Technology (Part 1)", Crown Publications, ISBN 978-0-9921781-0-9, Johannesburg, 2012.
- [2] "High Voltage Direct Current (HVDC) Transmission reference book", Electric Power Research Institute (EPRI), Report no: 1024318, Palo Alto, CA, 2012.
- [3] Insulator News and Market Report. Website reference: <http://www.inmr.com/worlds-highest-hvdc-line-delivers-power-totibet/>. Last accessed: 20 September 2015.
- [4] Eskom Transmission Ten-year Development Plan. Website reference: http://www.eskom.co.za/Whatweredoing/TransmissionDevelopmentPlan/Documents/TransDevPlan2010_20192.pdf. Last accessed: 20 September 2015.
- [5] E.F. Raynham, "Apollo – Cahora Bassa, Enigma and Diversions", First Edition, EE Publishers (Pty) Ltd, ISBN 0-620-32261-6, Johannesburg, 2004.
- [6] Website reference: "Mozambique invites consultancy bids for CESUL project" <http://www.globaltransmission.info/archive.php?id=14467>, Last accessed January 25, 2014.
- [7] V.L. Chartier, S.H. Sarkinen, R.D. Stearns, and A.L. Burns, "Investigation of corona and field effects of ac/dc hybrid transmission lines", IEEE transactions on Power Apparatus and Systems, Vol. PAS-100, No 1, pp. 72-80, January 1981.
- [8] P.S. Maruvada and S. Drogi, "Field and ion interactions of hybrid ac/dc transmission lines", IEEE transactions on Power Delivery, Vol. 3, No 3, pp. 1165-1172, July 1988.
- [9] P. S. Maruvada and W. Janischewskyj, "Analysis of corona losses on DC transmission lines: Part I—Unipolar lines," IEEE Trans. Power App. Syst., Vol. PAS-88, no. 5, pp. 718–731, May 1969.
- [10] P. S. Maruvada and W. Janischewskyj, "Analysis of corona losses on DC transmission lines. Part II—Bipolar lines," IEEE Trans. Power App. Syst., vol. PAS-88, no. 10, pp. 1476–1491, Oct. 1969.
- [11] V.L. Chartier, R.D. Stearns, and A.L. Burns, "Electrical environment of the uprated pacific NW/SW HVDC intertie", IEEE Transactions on Power Delivery, Vol. 4, No 2, pp. 1305-1317, April 1989.
- [12] V. L. Chartier and R.D. Sterns, "Examination of Grizzly mountain database to determine effects of relative air density and conductor temperature on HVDC corona phenomena", IEEE transactions on Power Delivery, Volume 5, No 3, pp. 1575-1582, July 1990.
- [13] V.L. Chartier, R.D. Stearns, L.D. Dickson and L.Y. Lee, "Performance of a long-term unattended station for measuring dc fields and air ions from an operating HVDC line", IEEE Transactions on Power Delivery, Vol. 4, No 2, pp. 1318-1327, April 1989.
- [14] B.A. Clairmont, G.B. Johnson, L.E. Zaffanella and S. Zelingher, "The effect of HVAC – HVDC line separation in a hybrid corridor", IEEE Transactions on Power Delivery, Vol. 4, No 2., pp. 1338-1350, April 1989.
- [15] P.S. Maruvada, "Flux Tracing Method (FTM) software reference book", Eskom Power Series, Unpublished, 2015.

PVsyst MODEL IMPROVEMENT USING FIELD DATA FROM A 75 MW_p SOLAR PV POWER PLANT IN SOUTH AFRICA

T. Mahachi and A. J. Rix

Department of Electrical and Electronic Engineering, Stellenbosch University, Stellenbosch, South Africa, E-mail: rix@sun.ac.za.

Abstract: The statistical average performance ratio (PR) of new photovoltaic (PV) installations in moderate climates has improved from 65 % to 85 % over the last 20 years. This continuous improvement is as a result of continued operational monitoring and the analysis of the monitored data. To ensure reliable and high performance solar PV systems, understanding the performance drivers and losses within a solar PV system is crucial. In this article an overview of the losses in a solar PV system is given and the findings of the loss analysis of an operational 75 MW_p solar PV plant in South Africa are shown. The calculated losses are then used to improve the PVsyst model for the solar PV plant and finally the PVsyst model and the improved PVsyst model for the solar PV plant are compared to the measured data from the operational 75 MW_p solar PV plant in South Africa. This analysis is essential for accurate forecasting of the available generation capacity, as required by the utility provider.

Keywords: PVsyst modelling, PV system loss analysis, Solar PV grid yield

1. INTRODUCTION

To ensure reliable and high quality solar PV systems, it is important that reliable evaluation methods of PV system losses and performance should be established and verified by quantitative analysis [1]. An essential part of enhancing the performance of an installed solar PV system is to understand the power losses which occur in the system and to develop methods to minimise these losses [2]. Various large solar PV systems use analytical monitoring to avoid economic losses due to operational problems [3, 4]. The power loss of solar PV systems is worth considering since there is rapid growth in the production of electricity from solar PV systems [5]. Therefore this analysis is needed for a better understanding of loss mechanisms in utility scale solar PV systems and for the design of low-loss solar PV systems.

In this article, the losses of a grid connected 75 MW_p solar PV power plant in South Africa are investigated. Firstly, power losses are analysed, then practical methods are used to present and review the losses using quantitative values calculated from the 30-minute averaged field data, whilst preserving high accuracy. The calculated losses are then used to improve the default PVsyst model for the 75 MW_p solar PV power plant. The PVsyst default loss model uses reasonable parameter values in order to execute an initial simulation, whereas the improved model makes use of modified parameter values according to the measured system performance. The improved model enables accurate forecasting of the available generation capacity, as required by the utility provider.

2. SITE AND SYSTEM DESCRIPTION

The 75 MW_p solar PV power plant is situated in the Northern Cape region of South Africa at Latitude 30° South. The solar PV plant is located in a generally high

solar radiation area and the area has abundant sunlight with an average of 11.5 daily sun hours, a daily average solar radiation of 5.8 kWh/m² and an annual global horizontal irradiation (GHI) of 2117 kWh/m².

The solar PV plant makes use of a fixed 30° tilt sub-structure system that supports 312 504 polycrystalline modules. Figure 1 shows a full description of the system, the respective quantified losses and their location within the plant.

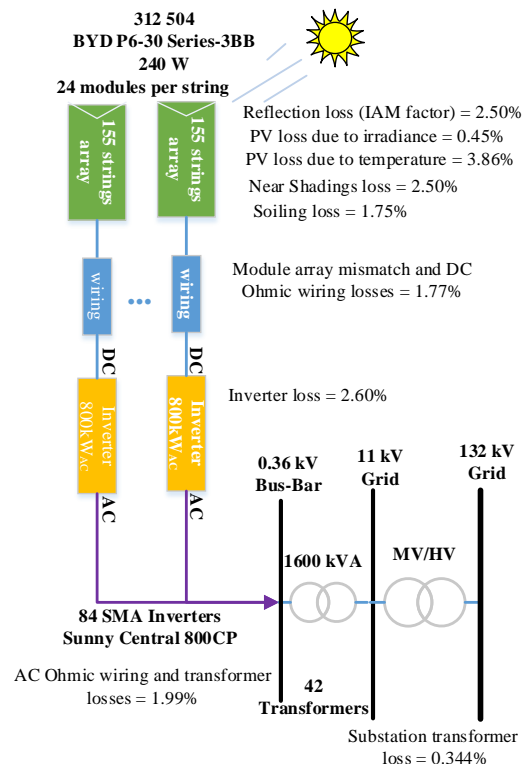


Figure 1: Schematic diagram of the loss analysis of the solar PV system

3. LOSS CALCULATION

3.1 Near shadings loss

Near shading losses are due to the mutual shading of modules that are in the front of each row on the PV field, as well as near objects like buildings and trees. There is a direct correlation between power loss due to partial shading and the distance between the rows of the solar PV modules, therefore in order to minimise the row shading losses it is essential to calculate the appropriate inter-row spacing [6].

The shading losses were calculated in PVsyst using the inter row spacing distance on site and the trajectory of the sun, simulated in hourly step values. This geometric calculation determined the portions of the arrays in shade during each time step, and a resultant near shading loss of 2.5 % was obtained.

3.2 Reflection/Incidence angle loss

Fixed-tilt solar PV modules receive varying amounts of solar radiation throughout the day and this is primarily due to the constant change of the angle of incidence (AOI) [7]. The angle of incidence at which the sun enters the atmosphere and strikes the surface of the solar PV module determines the reflection losses of a PV system. There will be a certain degree of reflectance at angles of incidence which are not normal to the solar panels. The incidence effect relates to the reduction of the irradiance on the PV cell's surface, with respect to normal incidence irradiance [8]. Reflection losses are based on an Incidence Angle Modifier (IAM) which is estimated as follows [9]:

$$IAM = 1 - b_0 \left(\frac{1}{\cos i} - 1 \right) \quad (1)$$

where:

i = incidence angle on the plane

b_0 = ASHRAE parameter

The IAM depends only on one parameter b_0 , and a b_0 value of 0.05 was recommended by BYD for their polycrystalline modules. The resulting reflection loss was calculated as 2.5 %.

3.3 Soiling loss

The accumulation of dirt and its effect on system performance is difficult to predict as it depends on the site rainfall conditions, environment of the system and the frequency at which the modules are cleaned [9]. While average energy losses due to soiling are typically in the range 1-6 % [10], for some locations soiling can account for up to 70 % of all the losses [3]. Researchers, operators and developers of solar power plants are constantly seeking better methods to quantify soiling related losses and several methods do exist [11, 12]. For this analysis,

soiling losses were estimated based on the 30-minute interval measured precipitation for the site, according to the loss scale shown in Table I [9]. The site's average yearly soiling losses were calculated at 1.75 %. Independent soiling measurements permit more accurate determination of soiling losses compared to estimates based on precipitation or plant metrics alone. At utility scale facilities, an ongoing measurement of soiling loss is an important component of performance monitoring that will also inform the cleaning schedule of the modules in order to reduce the soiling losses [8, 10].

Table I: Soiling loss scale

Monthly Precipitation [mm]	Soiling Loss
0-20	3 %
20-50	2 %
>50	1 %

3.4 PV loss due to irradiance level

A PV module's conversion efficiency increases at high light intensities and decreases at low light intensities [13]. In practice there is a gain/loss in the module output with respect to the standard irradiance conditions, 1000 W/m², that the modules are rated at [9]. The module efficiency according to measured incident irradiance on the collector plane was determined from the plot of the module efficiency as a function of the plane of array irradiance at a module temperature of 33.22 °C as shown in Figure 2, and the results are shown in Table II. For the fixed-tilt system under investigation, the PV loss due to irradiance level was extracted from the above-mentioned plot and it is 0.45 % with respect to standard test conditions (STC).

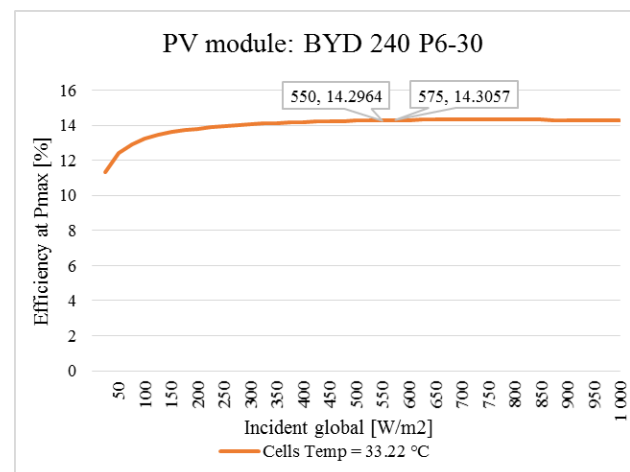


Figure 2: Efficiency vs Irradiance curve

Table II: Relative efficiency loss with respect to STC

Temperature [°C]	POA [W/m ²]	Module Efficiency [%]	Relative efficiency loss [%]
25	1000	14.75	-
33.22	567	14.30	0.45
STC = 1000 W/m ² , 25 °C and AM = 1.5			

3.5 PV loss due to temperature

The thermal characteristics of solar PV modules have a significant impact on the PV system's performance. Increasing temperatures lower the open circuit voltage of PV modules, thereby causing a decrease in cell performance [14]. Literature suggests that direct measurement of module temperatures can improve accuracy when continuously forecasting expected system performance and losses [15].

Figure 3 shows the measured annual distribution of the back of module temperature and the ambient temperature for the solar PV plant under investigation. It can be seen that the distribution of ambient temperature is centred on approximately 25 °C and it ranges from -10 to 40 °C, whereas the back of module temperature is centred on approximately 35 °C and ranges from -5 to 65 °C. This shows that in the case of the solar PV plant, the modules operate at temperatures above 25 °C on average and this in turn results in losses due to module temperature rise with respect to STC [16]. The PV loss due to temperature is based on the power temperature coefficient of the module, and a BYD P6-30 polycrystalline module has a peak power temperature coefficient of - 0.47 %/°C at STC.

The PV loss due to temperature (P_{loss}) is then determined according to the following expression [16]:

$$P_{loss} = P_{actual} - P_{25} \quad (2)$$

where:

P_{actual} = the actual power of the solar PV system
 P_{25} = is the temperature corrected yield of the PV array by compensating measured PV array yield to PV array yield at STC, and can be calculated as follows [2, 16, 17]:

$$P_{25} = P_{actual} (1 - T_{coeff} (T_{module} - 25)) \quad (3)$$

where T_{coeff} is the power temperature coefficient and T_{module} is the measured module temperature.

According to the data recorded at the solar PV power plant, the overall PV loss due to temperature amounted to 3.86 % during production.

In high solar radiation regions, the module temperatures often reach 65 °C or higher in peak operating conditions and at 65 °C the conventional solar modules' power output is reduced by up to 20 % [18]. In the case of the Solar PV power plant under investigation the majority of solar energy production occurred when the ambient temperature was lower than the back of module temperature, and Figure 4 depicts the distribution of energy production at low, (< 25 °C) and high, (≥ 25 °C) module temperatures for the 75 MW_p solar PV power plant. The energy generated at module temperatures of 25 °C or higher, accumulated to 87 % of the total generation.

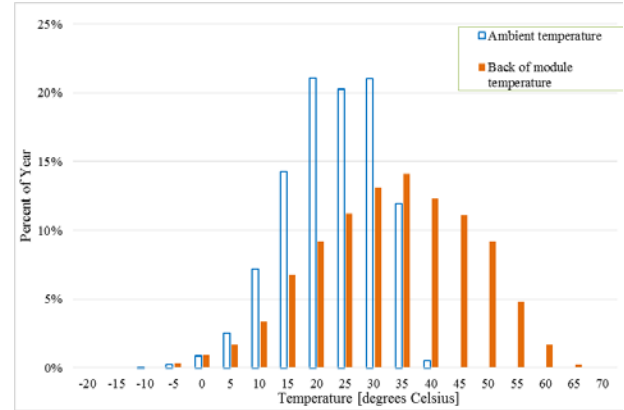


Figure 3: Distribution of ambient temperature and back of module temperature for the solar PV system.

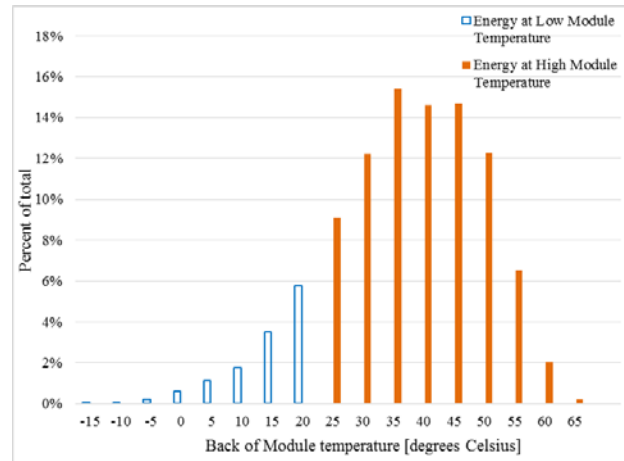


Figure 4: Distribution of power production vs. back of module temperatures for the solar PV system.

3.6 Module array mismatch and Ohmic wiring losses

Due to the lack of specific I-V measurements of the solar PV modules in the field and real array energy, mismatch losses and Ohmic wiring losses were combined and calculated so as to make the calculated energy at the inverter input terminals equal to the measured inverter input energy.

Mismatch loss:

Due to variations in the current-voltage characteristics, the PV modules connected in parallel or series to a PV array do not necessarily operate at their maximum power point [19]. The sum of the maximum output of the individual modules ($\sum P_{max,module}$) is always greater than the maximum power output of the total PV array ($P_{max,array}$), at the same operating irradiance level [3]. The resulting difference is commonly called circuit mismatch (CM) [20]. Reducing mismatch losses improves the global PV array efficiency, and mismatch losses can be calculated as follows:

$$CM = \frac{\sum P_{max,module} - P_{max,array}}{\sum P_{max,module}} \quad (4)$$

DC Ohmic wiring loss:

In utility scale PV systems, the cause of DC Ohmic wiring losses is the resistance of the cabling that interconnects PV modules. The total DC Ohmic wiring loss between the modules and the inverters is related to the type, thickness and length of the cables [9]. In addition to the cable loss, the transition resistances in fuses, terminals and connectors also contribute as DC Ohmic losses. The DC-Ohmic power loss ($P_{DC,ohmic}$) can be accurately calculated by multiplying the square of the 30-minute averaged DC-array current (I) with the resistance of the cables (R) as per Equation (5). The sum of all DC-Ohmic power losses during the year multiplied by time gives the yearly energy DC-Ohmic losses $E_{DC,ohmic}$ as given in Equation (6). In the case of the solar PV system, the combined mismatch and DC-Ohmic wiring losses were calculated from measurements as 1.77 %.

$$P_{DC,ohmic} = I^2 R \quad (5)$$

$$E_{DC,ohmic} = \sum I^2 R t \quad (6)$$

3.7 Inverter loss

In the case of grid connected solar PV systems, the inverter converts DC power from the PV array to AC power for exporting to the utility grid. The AC energy from the inverter depends on the input at the inverter terminal i.e. the output power from the arrays and the inverter losses [21]. Inverter losses are due to Ohmic and switching losses in semiconductors, as well as standby power. The ratio of the power at the inverter output terminals ($P_{inverter,output}$) to the power at the input terminals ($P_{inverter,input}$) gives the inverter efficiency. The inverter losses ($P_{inverter,loss}$) of 2.60 % were determined as follows:

$$P_{inverter,loss}(\%) = 100(1 - \frac{P_{inverter,output}}{P_{inverter,input}}) \quad (7)$$

3.8 AC Ohmic and external transformer losses

AC Ohmic losses occur between the inverters and the utility connection point [9]. In this paper, the AC Ohmic losses were combined with the transformer losses due to insufficient measured field data for the two to be calculated separately. Losses in the transformers are due to hysteresis and eddy-currents in the core, as well as Ohmic losses in the primary and secondary windings [8]. The resulting AC Ohmic and transformer losses ($P_{AC+trans,loss}$) of 1.99 % were calculated from the ratio of the power at the substation transformer input terminals ($P_{subinput}$) to the power at the inverter output terminals ($P_{inverter,output}$) as follows:

$$P_{AC+trans,loss}(\%) = 100(1 - \frac{P_{subinput}}{P_{inverter,output}}) \quad (8)$$

3.9 Substation transformer loss

Electricity is transmitted along power lines at high voltages to reduce the Ohmic losses. In order to achieve this, another transformer installed at the substation is used to step up the voltage. The substation transformer loss, of 0.344 %, was calculated from the ratio of the power supplied to the grid (P_{grid}) to the power at the input terminals of the substation transformer ($P_{subinput}$) as per Equation (9).

$$P_{subloss}(\%) = 100(1 - \frac{P_{grid}}{P_{subinput}}) \quad (9)$$

4. PVsyst MODEL CORRECTION

The starting point for evaluating the losses of a PV system is to calculate the energy which would be produced if the system always worked at STC. The solar PV plant's system losses are listed along with simulated loss values from the PVsyst default loss model and the improved PVsyst model of the 75 MW_p solar PV power plant. The losses explicitly specified by the user in PVsyst, are: soiling loss, mismatch loss, module quality loss, availability loss, reflection loss, light induced degradation (LID) loss, module quality loss and array wiring loss, whereas those calculated using standard models are spectral loss, PV loss due to irradiance level, PV loss due to temperature, inverter loss and external transformer loss [22]. Module quality loss expresses the real behaviour of modules with respect to the manufacturer's specifications and was kept at 0 % for all the models, i.e. the average manufacturer specified inferior tolerance [22] and LID losses were not quantified in this article because this loss mechanism is not proposed as default by PVsyst [8].

Loss analysis (Measured vs PVsyst model losses):

Table 3 shows the loss analysis results. The conversion ratio of the GHI to global irradiance incident in the collector plane (i.e. Global Plane Irradiance - GPI) is 12.3 % for simulations done in PVsyst, whereas the conversion ratio from the field data was calculated as 12.61 %. Soiling losses estimated according to the received precipitation are close to half the respective PVsyst default loss model value. It can be seen that the improved PVsyst model's values for inverter loss, AC Ohmic and external transformer losses are close to the respective calculated losses. The calculated mismatch and DC Ohmic losses are half the respective PVsyst default loss value, and inverter losses calculated from measured values are within 0.3 % of the respective improved PVsyst model value. The PVsyst default loss model value for the PV loss due to temperature is close to double the calculated value whereas the respective improved model value is 2.5 % greater than the calculated value. The results show that the PVsyst software package tends to underestimate the electrical energy generated by the installation due to the overestimation of losses for this solar PV power plant.

The PVsyst simulation accuracy is in the order of 2 to 3 % (MBE–Mean Bias Error) due to the uncertainty with regard to the model used to transpose GHI to the incident irradiation in the collector plane [8].

Table III: Loss analysis results

Parameter	PVsyst default model	Determined from measured data	Improved PVsyst model
GHI [kWh/m ²]	2 117	2 117	2 117
Global incident in coll. plane	12.3 %	12.61 %	12.3 %
POA [kWh/m ²]	2 377.4	2 384	2 377.4
Near shadings irradiance loss	-3.0 %	-2.50 %	-3.0 %
Reflection loss	-2.6 %	-2.50 %	-2.6 %
Soiling loss	-3.0 %	-1.75 %	-1.8 %
Effective coll. plane irradiance [kWh/m ²]	2 179	2 227	2 206
PV loss due to irradiance level	-0.3 %	-0.45 %	-0.3 %
PV loss due to temperature	-8.4 %	-3.86 %	-6.4 %
Mismatch + DC Ohmic loss	-3.2 %	-1.77 %	-1.3 %
Inverter loss during operation	-1.8 %	-2.60 %	-2.3 %
Transformer and AC Ohmic loss	-1.36 %	-1.99 %	-2.07 %
Substation transformer loss		-0.344 %	
Deviation from the Grid yield	6.3 %	0 %	2.07 %

Energy yield comparison:

Figure 5 shows the energy yield from the energy meters at the solar PV plant normalised to the monthly average grid yield, in comparison to the forecasted energy yield from the improved PVsyst model and the PVsyst default loss model. The improved PVsyst model best follows the measured grid yield trend line compared to the PVsyst default loss model. The improved model's trend line follows that of the measured data from January to March and then from October to December. The differences of approximately 4% observed from April to September shows that the arrays are outperforming the improved model simulation, and the cause of this will be investigated further. In literature, a real world-system that also outperformed PVsyst software by an average over performance of 5.4% was reported [23]. A better performance model with all the losses derived from accurately measured data and losses given as monthly values would produce simulation results even closer to the field data.

The differences in expected and measured energy yield are also due to the respective variances in the models used to calculate losses. Loss values are expressed as constant yearly values in PVsyst, whereas in reality the loss values vary from time to time. The PVsyst's simulated energy yield using default loss model is 6.3 % lower than the actual measured grid yield as shown in Figure 5, therefore the PVsyst's default loss model overestimated the solar PV system's losses. The energy yield from the improved model is 4.23 % better than the yield obtained when using the default loss model and this resulted in an energy yield which is 2.07 % lower than the energy meter readings. The main uncertainties regarding the PV production using PVsyst software are: the meteorological data (source and annual variability) as well as the PV model (Hay or Perez model), soiling, and the validity of the manufacturer's specifications [22].

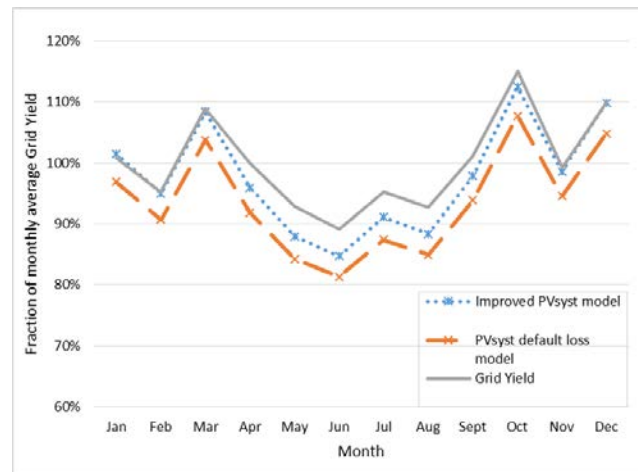


Figure 5: Comparison between forecasted yield and grid yield normalised to the average monthly grid yield

5. CONCLUSION

An essential part of enhancing the performance of installed solar PV systems is understanding the energy losses which occur in the system and developing methods to minimise these losses where possible. From the analysis it can be concluded that it is important to evaluate the losses in each part of the solar PV system and to make specific improvements in order to decrease the major losses. This will help to improve the design of future solar PV systems.

The PVsyst V6.39 (Perez) default loss model overestimated the solar PV plant's actual losses by 6.3 %. The calculation of the losses in the operational system resulted in an improved PVsyst model and when simulated gave a 4.23 % higher yield. The improved model is essential for accurately forecasting PV system generation capacity, as required by the utility providers. According to the analysis, the operational system significantly outperformed the software simulations. The differences in the improved model and the grid yield observed in the winter season will be investigated further. In conclusion, the analysis contributes to the enhancement of the

performance model's accuracy when continuously forecasting expected system performance and losses.

6. REFERENCES

- [1] J. H. So, B. G. Yu, H. M. Hwang, G. J. Yu, J. Y. Choi, I. Choy, "Performance Monitoring and Analysis of Middle Scale Grid-Connected PV System," *The 7th International Conference on Power Electronics*, Daegu, Korea, October 2007.
- [2] J. H. So, H. M. Hwang, B. G. Yu, J. S. Yoo, G. J. Yu, "Loss analysis of grid-connected PV system using yield model," *26th European Photovoltaic Solar Energy Conference and Exhibition*, Hamburg, Germany, September 2011.
- [3] A. Woyte, M. Richter, D. Moser, S. Mau, N. Reich, U. Jahn, "Monitoring of photovoltaic systems," *EU PVSEC*, France, September 2013.
- [4] D. Munro, G. Blaesser, "Guidelines for the assessment of PV system monitoring," *Commission of the European Communities*, Ispara, Italy, EUR 16338 EN, March 1995.
- [5] R. Yuan, H. Ding, J. Qian, Y. Chen, X. Xi, X. Yang, "Loss analysis of 100kW PV Inverter," *International Power, Electronics and Materials Engineering Conference*, China, May 2015.
- [6] S. Elies, T. Reis, B. Müller, U. Kräling, K. Kiefer, "Influence of row shading on the performance of PV systems- simulation and measurement," *5th World Conference on Photovoltaic Energy Conversion*, Valencia, Spain, September 2010.
- [7] M. Bui, C. Voelker, B. Li, D. M. J. Doble, "Oblique angle of incidence measurement of PV modules on a solar simulator," *26th European Photovoltaic Solar Energy Conference and Exhibition*, Fraunhofer, Hamburg, Germany, pp. 3476-3479, September 2011.
- [8] PVsyst help file, <http://files.pvsyst.com/help/> [Accessed 18/09/2015].
- [9] ARUP (Pty) Ltd, "Energy Yield Simulations. Module Performance Comparison for Four Solar PV Module Technologies," 224283-00 Issue 1, Johannesburg, South Africa, May 2015.
- [10] M. Gosteinl, J. R. Caron, B. Littmann, "Measuring Soiling Losses at Utility-scale PV Power Plants," *PVSC - IEEE*, San Francisco, USA, June 2014.
- [11] J. Zorrilla-Casanova, M. Piliougine, J. Carretero, P. Bernaola-Galván, P. Carpena, L. Mora-López, and M. Sidrach-de-Cardona, "Losses produced by soiling in the incoming radiation to photovoltaic modules," *Progress in Photovoltaics: Research and Applications*, pp. 790-796, Feb. 2012.
- [12] J. R. Caron and B. Littmann, "Direct Monitoring of Energy Lost Due to Soiling on First Solar Modules in California," *IEEE Journal of Photovoltaics*, vol. 3, no. 1, pp. 336-340, 2013.
- [13] S. Shaari, K. Sopian, N. Amin, M. N. Kassim, "The temperature dependence coefficients of amorphous silicon and crystalline photovoltaic modules using Malaysian field test investigation", *American Journal of Applied Sciences*, 6 (4): pp. 586-593, 2009.
- [14] J. J. Wysocki, P. Rappaport, "Effect of temperature on photovoltaic solar energy conversion," *Journal of applied physics*, 31 (3): pp. 571-578, 2009.
- [15] J. M. Kuitche, R. Pan, G. TamizhMani, "Statistical Analysis of back surface vs. cell temperatures of c-Si Modules using Measurement Error Models," *38th PVSC*, Arizona, USA, pp. 2953-2956, June 2012.
- [16] C.W. A. Baltus, J.A. Eikelboom, R.J.C. van Zolingen, "Analytical monitoring of losses in PV systems," *14th European Photovoltaic Solar Energy Conference*, Barcelona, pp.1547-1550, September 1997.
- [17] Y. Ueda, K. Kurokawa, K. Kitamura, M. Yokota, K. Akanuma, H. Sugihara, "Performance analysis of various system configurations on grid-connected residential PV systems," *Solar Energy Materials and Solar Cells*, vol 93, pp. 945-949, 2009.
- [18] N. Strevel, L. Trippel, M. Gloeckler, "Performance characterization and superior energy yield of First Solar PV power plants in high-temperature conditions", First Solar, Perrysburg, Ohio, USA, *17th Photovoltaics International journal*, August 2012.
- [19] A. Larsen, P. Lindquist, "Forecasting mismatch losses: An empirical study investigating module level inverter- and string inverter systems," Bachelor of Science Thesis, SE-100 44 STOCKHOLM, 2014.
- [20] S. Silvestre, A. Chouder, "Analysis of power losses in PV systems," *23rd European Photovoltaic Solar Energy Conference and Exhibition*, Valencia, Spain, September 2008.
- [21] F. Vignola, F. Mavromatakis, J. Krumsick, "Performance of Inverters," Greece, July 2007.
- [22] A. Mermoud, "Modelling Systems Losses in PVsyst," Institute of the Environmental Sciences, Université de Genève, 2012.
- [23] Renewable Energy Corporation (REC), "Real world performance exceeds expectations," Sandvika, Norway, June 2012.

Renewable Energy Technology for Saving and Generating Pollution Free Energy in South Africa

ZP Khumalo, Bakhe B. Nleya

20250262@dut4life.ac.za

Philanipk@gmail.com

Abstract – Energy is one of the most important basic needs for everyone. Since energy makes everything possible, almost everyone on planet earth is depended on it. The increase in population and economic growth in South Africa (SA) resulted in power shortage in SA. Eskom (SA power utility) maintenance that was long overdue on the units has also contributed significantly to the power shortage which resulted in load shedding. High consumption of electricity has put Eskom generation plant under severe strain to meet this high energy demand. Due to the fact that Eskom had no capacity to exceed high power demand it had no choice but to implement the power savings techniques. Government and Eskom have run campaigns for people to save and utilize power sparingly in order to avoid load shedding but the attempt was unsuccessful. SA energy power grid is currently under strain and there are no solutions so far except load shedding in order to avoid total blackout. This paper will present the energy crisis and possible solutions in SA. Load shedding has led to a decline in economy and potential new investors. Some companies were closed down which resulted in job losses. Load shedding has resulted in damage of electrical equipment's, food going to waist, loss of life for patients on life support etc. Short term solution will be to engage with consumers to reduce power usage, using solar power, and energy saving bulbs. The primary solution for this will be to build more generation plants and implement technology on the Smart Grid that will enforce utility to view real time consumption of power to save energy and prevent energy theft. This can be achieved by using Secured Power Line Communication (PLC) network for Advanced Metering Infrastructure (AMI). Coal generation plants are not a solution due to air pollution. The best solution is to construct environmental friendly hydroelectric power generation plants. Coal plants pollute air and contribute massively to global warming. Hydroelectric Plants will use water without depleting it. The solar energy, wind energy and other types of renewable technology were implemented in SA but they did not make a remarkable change. Hydroelectric is the hope for the future and beyond.

Index Terms – Power, Load shedding, Energy servings, Generation plant, Hydro-electric, solar energy, PLC, AMI.

I. INTRODUCTION

Electricity has become one of the outmost basic needs for every household due to the modernized way of living. The country's economic growth and sustainability relies on the constant availability of power in order to be productive and continue growing. Health facilities depend on the constant availability of electricity supply in order to be able to save people's lives. Our social and wellbeing as human beings nowadays relies on electricity, hence there is a need to ensure that we have enough electricity to supply the country in order to sustain our country's economy and the citizens life styles.

The purpose of this study is to execute a comprehensive survey and research to derive a solution of energy crisis using a clean energy technology.

The available sources of energy are categorized as follows:

- Renewable sources i.e.: solar, wind, geothermal, wave, tides, ocean thermal, hydroelectric power and ocean currents energy.
- Non-renewable resources i.e.: Fuels (coal, oil) and nuclear

energy. The gradual increase in population has put a strain on the electricity grid due to an increase in power demand. The generation plant cannot

withstand this high demand due to lack of capacity. Eskom has resorted to load shedding as an essential option to safeguard the power generation plant, and to allow the maintenance to be executed in order to assure the reliable supply of energy. A further knock on the electricity grid is due to the shortage of generating capacity as several units are constantly out of service due to maintenance and breakdowns.

Government and Eskom had tried to explore other means of generating electricity to reduce pressure on the power grid by encouraging citizens to utilize solar energy and subsidizing citizens who are purchasing them with a certain percentage as means of motivation. Government also rolled out solar energy geysers on newly built RDP houses which didn't relieve the electricity grid in anyway [1]. Campaigns and advertisements were placed on all social platforms for all citizens and commercials customers to utilize electricity sparingly by switching of all unessential appliances in order to reduce electricity usage [2].

SA is one of the biggest manufacturers of platinum in the world [3]. Some of the mines had to shut down due to the power crisis as they were restricted in the energy usage. Mining companies are being hit by the shortage of electricity and the country's GDP had dropped significantly. Commercial companies had also been affected badly by the energy crisis. Job losses have been suffered due to this problem. The rate of crime had increased due to perpetrators utilizing an opportunity to rob and steal during load shedding [4].

In order to overcome the power crisis the country is facing we need to increase the power generating plants and explore more or revert to renewable energy to solve the energy crisis. We have divulged in diverse methods of renewable energy that we can utilize in order to increase the electricity capacity.

Fig.1 below depicts the block diagram of the power generator system. The generator is indicated in red and it indicates that we need to take action to improve the generating plants in S.A.

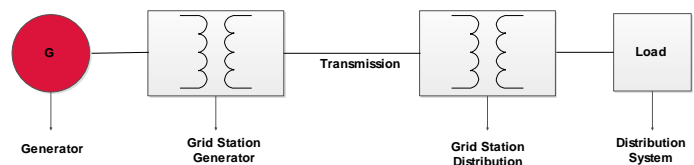


Fig. 1 Power system block diagram

Electricity supply crisis is a major setback on our fast developing economy. The electricity price increases as per the tariff reviews approved by NERSA for Eskom to be able to build more generation stations affected the economy of the country. The poor citizens cannot

afford this new tariffs implemented by Eskom which can result in more illegal connections. Currently there is a rising power demand in SA. Since the inhabitants and new technology is always growing and advancing, the demand for energy is expected to increase even further annually.

The energy sector needs to change in order to keep up with the high demand and make a change that will keep the country running on more than just coal generation plants due to the fact that burning coal pollutes air and it contributes highly to global warming. We need nonconventional energy, this has a big potential for energy security in future [5].

II. SURVEY ON CURRENT POWER ENERGY CRISIS

The demand for energy is steadily rising, but the generation of energy has not risen to meet this high and growing demand. There are various factors affecting the energy sector. 95% of overall country's electricity supply comes from Eskom's electricity grid. The majority of SA's energy is generated through the coal power plants, as coal is abundantly available in S.A. and relatively cheap compared to the other countries, and the infrastructures generating electricity through coal are well established.

The limiting factor is that coal is only found in certain areas of the country which restricts the location of the coal fired power plants. The coal plants contribute significantly to global warming due to the greenhouse gases and other wastes that it emits to the air. Although coal is readily available erecting the coal power plants is lengthy process and it is very expensive which challenges the building of more coal power plants in the country [1].

The nuclear power plant generates 5% of the country's electricity [2]. Nuclear power stations are not prominent in the country as they are perceived to be dangerous and the public is resistant to accept these plants on the local areas. Nuclear is associated with nuclear weapons and their safety is questionable due to the waste that is emerging from them. Although Nuclear power plants are not harmful to the environment as they don't emit the green gases and carbon dioxide, the public has a negative perception about its implementation. Nuclear is unlikely to make a remarkable influence to energy generation in the country for the future due to government rules and regulations [7].

The hydroelectric and pumped storage schemes generate another 5% of the country's electricity. Although the hydroelectric reacts very quickly to electricity demands and has all the advantages that encourages one to utilise it, Eskom resolute on not investing on hydro as it is deemed not feasible for the country due to shortage of rivers. The use of other sources like solar energy is very restricting as it is not available all the time and is reliant to the sunrays. Wind energy also has its restrictions as it is subjected to the availability of the wind [8], [19].

In November 2007 South Africa started experiencing widespread load shedding because it could not meet the power demand from customers. What led SA to this power crisis? The political decisions made by politicians led SA to the crisis that we are in today. [2]

Eskom's has increased the export of electricity. Table 1 below shows us how the supply of electricity declined in some areas from 1996 to 2007 when the problem started. Looking at the below information it is clear to see the decline in supply in most sectors in SA, while there is an increase in supply for international sector [1]

Table 1 Electricity supply decline [1]

Electricity Supply: 1996 vs 2007		
Year	1996	2007
Mining	19%	15%
Agriculture	2%	2%
Transport	2%	1%
International	3%	6%
Municipalities	42%	40%
Households	3%	5%
Commercial clients	0%	4%
Industries	29%	27%

Analysis of the table above interprets clearly on the following factors: The mining sector had a 4% decrease in supply from Eskom. The transport sector was reduced by 1%. The municipalities' power experienced a decrease of 2%. Furthermore the industries also experienced supply reduction of 2%. The only sector that has received an increase is the international sector; commercial clients as well as households that were increased by 3%, 4% and 2% respectively. Analyzing these figures it is clear that SA was heading to darkness. The paper released in 1998 by solidarity alleged that the country will run out of power in 2007 and no one acted upon these predictions. Considering the fact that SA is a newly born democratic country that had a backlog of service deliveries to be fulfilled to better people's lives including electrifying households and developing small businesses. All the distribution of electricity was growing significantly with no growth on the generating grid. Eskom's plan to expand the electricity grid for the future in order to meet the demand was presented to the Department of Energy and Minerals as it is a state owned utility. The plan and budget to build more generation power plants were denied in 1998 by the government. In 2004 South Africa's economy continued developing and growing faster than it was anticipated and the demand for power increased significantly. Approximately additional 1000MW was required to stably run the power grid. It is clear from this analysis that poor planning, inadequate research, investigations and studies made by government led SA to this crisis. [2].

Fig. 2 below confirms that SA's most power is generated from coal. This is a problem since we contribute significantly to air pollution which leads to global warming.

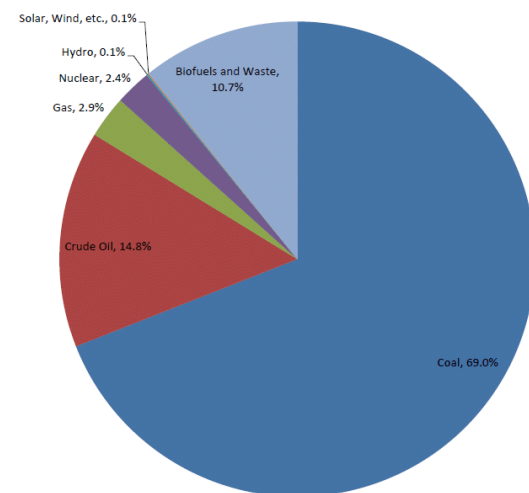


Fig. 2 Energy primary supply in SA statistics 2012 [2]

Looking at Fig. 3 below you can observe that SA is number seven on the list and the biggest coal users in Africa. China is the highest user followed by US [10].

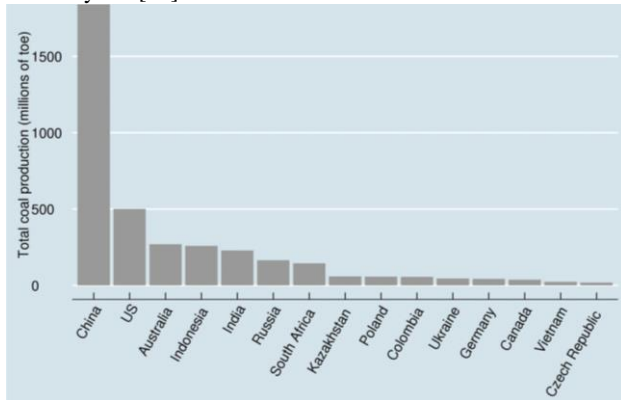


Fig. 3 World Coal usage statistic graph [2]

Seeing SA in the top ten list of the world in using coal shows us that we are big coal user worldwide.

To avoid more power crisis, Government and Eskom need to have the following in place.

- 1) Better planning and management of the national grid and its distribution.
- 2) Maintain the generation plants efficiently by ensuring that maintenance is done timeously.
- 3) Assuring that there is enough power generated to meet demand.
- 4) Keep skilled employees within the utility to ensure the continuous sustainability of the electricity grid.
- 5) Focus attention to training employees to secure resource competency and to keep up with the generation technology.

III. METHODOLOGY

This study will be based on, firstly merely looking at the current situation and why there are failures on energy industry. Secondly executing research and looking on the current utilised energy technologies. Thirdly what technologies were developed based on this theory and why it failed. The analysis will be executed, and propose a better solution to solve energy crisis that also supports green economy like pollution free energy (with less contribution to global warming).

A. Objectives of the Study

- 1) To investigate energy generation crisis on energy in South Africa
- 2) To find out the problems affecting the energy sector.
- 3) To analyse and find the best renewable energy to solve electricity crisis in South Africa.

B. The Aim

The aim of this research is to find the best and pollution free form of generation power energy in SA which will be able to generate enough energy.

IV. PRESENT POWER CRISIS

Looking at the present power crisis that the country is experiencing, Energy Policy of SA and orders issued by the government not to approve Eskom's request to construct new generation plants led load shedding we are experiencing at the present moment [1]. When the government realised the effect of the rejection of the expansion of the electricity grid they then instructed Eskom to construct new generation plants, but it was a little too late [11].

In 2004, minerals and energy sector requested the private sectors to submit their proposals and applications in an attempt to increase energy generation to approximately 1000MW additional energy daily that was needed in 2007.

Private companies were not interested to take part on this exercise, because Eskom wanted to keep 70 percent of energy generation in-house. One of the major challenges Eskom is facing now is the skills scarcity. Professionals said Eskom eventually started preparing to meet the challenge of skills development [1] [2].

Load shedding is categorised in different stages which depends on the status of the national grid, each stage lasts up to 2 hours:

- Stage one requires 1000 MW of load to be shed.
- Stage two requires 2000 MW of load to be shed.
- Stage three requires 3000 MW of load to be shed.
- Stage four requires 4000MW of load to be shed.

Eskom is dependent on the SA's citizens to utilise electricity wisely and for the commercial industries to use electricity sparingly and to stick to the restrictions put in place by government to reduce power usage.

We are likely to experience the load shedding for the coming 5 years due to the delays on the construction of the new power stations. The commissioning dates of the new plants are uncertain due to the challenges on the projects execution. The existing power generating units are under severe strain to produce and meet the energy demands hence the maintenance was never carried out and they are starting to fail and causing a further strain on the electricity grid [12].

Fig. 4 below depicts recently how Eskom's power supply and demand from 24 to 29 March 2015 looked like.

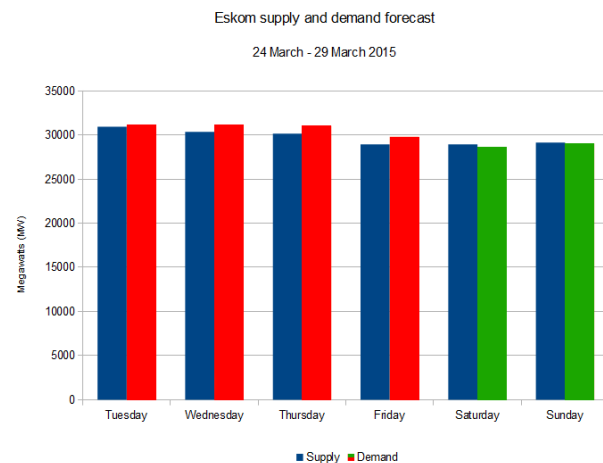
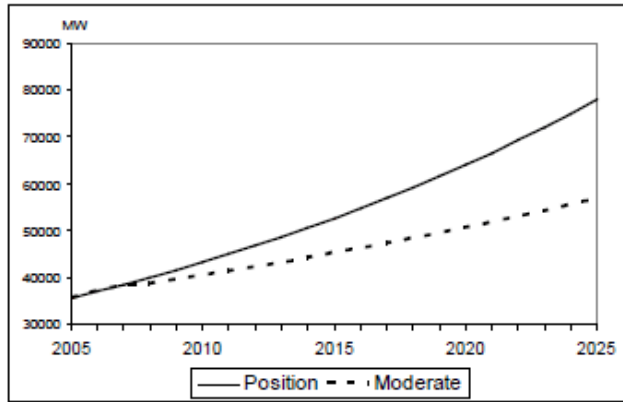


Fig. 4 Eskom supply demand forecast [13]

Looking at Fig. 4 above you can observe that Eskom's supply is below demand, and that is the main reason for load shedding. The only time where Eskom merely meets the demand is mostly on weekends as most companies and factories are closed.

It can also be observed that on the weekend that is the only time when the demand and supply are balanced, there is no substantial supply difference.

Fig. 5 below depicts Eskom's long term forecast considering growth.



Source: Eskom presentation²

Fig. 5 Eskom's long term forecast [15]

The graph Fig. 5 above shows that by 2020 SA energy demanded will be almost doubled. Currently Eskom supplies 40 000 MW by 2020 Eskom needs to supply SA with at least 51 000MW that is an increase of 11000MW in five years from this year of 2015 this is a lot of power energy. If Eskom and government don't act by increasing the generation plant capacity we are heading to dark days in the near future.

V. IMPACT ON ENERGY PROBLEMS

South Africa is losing millions of rands each day when load shedding is executed and potential foreign investors are reluctant to invest in the country as they have lost confidence due to uncertainty on their returns [16]. Economists believe that country's economy will decline even further if load shedding continues. The targeted outputs are not being met by industries on their production as load shedding persists. Various industrial sectors are losing millions. The mining, steel and aluminium industries are the hardest hit by this problem. Steel manufacturing surveyed a few of their businesses which manifested a loss of at least R40- million in productions [2] The mining division also confirmed these findings and projected its losses to be approximately R250 million daily[17]. Therefore the energy problem is disturbing the economic development and employment targets in a negative way. Power cut is affecting everyone from a mere household losing the refrigerated food and electrical appliances to major companies losing millions of rands due to production being affected. The impacts are as follows:

- Companies shut down because of losing profit
- Job losses
- Investors withdrawal
- Decline in GDP
- Undesirable impact on the economy
- Job creation affected
- Tax revenue reduced
- Damaging result on the current accounts deficit and currency.

VI. POWER CRISIS SOLUTION

A. Short Term Solutions

Eskom stated that load shedding is not a resolution but a precaution measure that Eskom executes as a last option whenever the electricity system is under stress to avoid blackouts. The interim solutions include private sector contribution to reduce their power consumption. Sasol for example is already expanding its power generation plant capability

to reduce 10 % of energy on energy usage from the national grid. The SA government and Eskom are enforcing that industries and household's unessential lighting and appliances be switched off. The implementation of load shedding zones should be obligatory in cities. The zones can have their power switched off at scheduled hours as per different load shedding stages [18].

B. Increased Generation Capacity

The Generation plants almost run at a normal plant factor of approximately 50% to 60% this means that only 50% to 60% of generation plant capacity that is commissioned is used. At least 70 to 80 percent must be used but that requires high maintenance. This will improve energy production and availability significantly. If the power factor of the existing generation plant is improved they will run more economical and efficient.

C. Renewable Energy Solution

Wind Energy

Most countries abroad for an example Germany and America etc. have invested a huge amount of capital on research and the development of the wind energy in order to achieve power from the wind. The total worldwide contribution in making of power energy from wind is nearly 30000MW, which is evident that with research and through developments SA can benefit significantly on this technology. Germany is the biggest beneficiary in this aspect with over 12,000 megawatts of wind energy realised at the end of 2002. SA government should consider implementing this technology in deserted areas along the coastal regions. Although it is much more expensive implementing wind energy as opposed to the coal-fired plants it is definitely something to consider as it will ensure stability on the national grid. SA is implementing this technologies but it is not sufficient. Not all is perfect with this technology, since it does not provide base line power. Wind energy provides power during certain times since wind is not always available. Wind power is economical for areas only experiencing satisfactory regular wind. Wind farms have a potential to become a substantial source of energy for the future. It is clear that this is definitely something to consider, there is hope in this form of technology [19].

Solar Energy

South Africa has high potential of renewable energy sources like solar energy. This is implemented mostly in rural areas where there's low energy usage and government has introduced it in newly built RDP houses through solar geyser. The solar energy sources are not restricted; they are also widely distributed in the cities and abundantly available in the country. The public health department has installed water pumps that use solar energy to pump drinking water to minimise usage on the national grid. Both public and private sectors are playing their role in promoting the photovoltaic system in the republic. If this technology is used in huge scale in commercial production of electricity the crisis of energy scarcity can be considerably reduced. Solar energy has its limitations and restrictions as it does not provide baseline energy, it can only supply energy to its full capacity during the day, hence it requires a boost from the battery storages to sustain the supply at an additional cost to the user. The other challenge is that it requires a space of 3000 square meter to give an output of 1MW [9]. There are limits to the collection of solar energy from the sun radiation. It is clear we cannot cover all available land with solar panels.

Tidal Energy

The tidal energy can be produced by mounting turbines at the mouths of estuaries where there are huge tidal waves. Power can be generated when the flow of ocean current moves in and out of the estuary and is converted into electricity. We don't have one of this technology here in SA but there are some available overseas. This is a complicated installation and it is expensive. It is uncertain that it could be

implemented in SA at a reasonable cost. Eskom is currently conducting research on this form of energy production [20].

Ocean Thermal Energy

This is a possible source of energy. The sun rays heats the water's surface of the sea, making them hot and evaporation occurs. The heat engine can be run between the two thermal regions. Ammonia, located in the vacuum, is vaporised by heat taken from the hot ground of water. Evaporated gas swells against the turbine, triggering it to spin and power is generated. The gas is then condensed after passing the turbine by chilling it with deep ocean water. Till today there is no commercial Ocean Thermal Energy Conversion (OTEC) plant that has been constructed due to cost of building one and its maintenance. Eskom has concluded on the assessment on this form of Energy which was deemed to be very positive and have proceeded to conducting laboratory tests which are anticipated to take up to 3 years. [16]

Ocean Waves

The ocean waves can create huge amount of power. The U.S. Department of Energy said, the total power of surfs flouting on the world's seashores are estimated to be up to 2 to 3 billion kW.[16] Due to environmental complications, land use encounters, hazards and risks to navigation and other factors only a small fraction of this power can be taken out and be utilised for human use. Wave power devices extract energy directly from surface waves or from pressure fluctuations below the surface. Eskom is currently conducting resource assessment, it is a matter of time before they conclude on this type of energy source whether it will be positively implemented in the country or not. [17]

Geothermal

This energy arises from the inner heat of the Earth surface. A heated liquid below the earth surface is taken upwards and used to generate electricity. Geothermal power is providing power in many countries worldwide. This type of energy relies on the location. It is to be situated in the natural places that bring up lots of heat within the country. The only place we recall in SA that has this type of heat is warm bath situated in the North West province.

Biomass Power

Biomass energy is generated from renewable organic wastes that are dumped. When these wastes are burned, the power is released as heat. In Biomass energy generation plants, unwanted wastes are burned to yield steam that turns turbines to make electricity. This is type of renewable energy is not clean since there are emissions involved. In Durban, eThekweni Electricity has one plant of this sort. It was constructed in 2007 and it aims to generate 10MW that will be enough to illuminate 9000 households.

Hydro-Electric Power Potential

Water is approximately 71% of the planet earth and has a huge amount of energy in it. Hydroelectric energy in 2005 managed to deliver to the world about 19% of its energy [22]. Hydroelectric power could be a solution to a growing crisis of energy supply. Hydroelectric generation plants usually use the reservoir of water made by a dam or from the river, for a constant high pressure flow rate to pass through a turbine and in that way the power is generated. This technology is very promising, energy is produced without pollution and it is economically feasible if situated in a suitable area where there's sufficient supply of water. [19]

VII. FUTURE SOLUTION

South Africa needs to construct more generation stations to overcome this energy crisis. The resolution is to build more power stations. Eskom has already started to build new power stations which are expected to be online. The ideal situation is that the future power station should not be coal generation plants but renewable energy

plants in order to minimize the emission of green gases. Although we require energy at the same time we need to save the globe by not contributing to air pollution and global warming. The future solution is pollution free energy. Renewable energy is the solution

A. Best Selected Renewable Energy Generation Technology

Hydro-Electric Power Generation Plant

Hydro-electric power is the selected option that we should implement. The only problem is that in SA there is scarcity of rivers and dams. We can engage Africa as whole especially neighbouring countries that have big rivers to construct hydro plants and import the power. Hydro is the clean technology for green economy and it can provide us with base line power. Water can be utilised without being depleted. There are some disadvantages of hydro like all other sources of energy but it has more advantages and it is pollution free.

At the present moment SA is currently running four hydro plants namely: Gariep dam (360MW), Vanderkloof dam (240MW), Drakensberg (1000MW) and Palmiet (400MW) supplying power during peak and emergency periods. The power generated by these stations is supplied to Eskom national grid. South Africa has a potential to produce energy from hydro-electric power plants but currently SA only produces 6 % of energy from hydro technology. If we can increase hydro plant to supply SA with 3000MW to 11000MW we will be out of power crisis or even dominate the generation grid and reduce the coal fired generation plant to save our environment [6]. What this means is that we need to increase energy generation by 12% but this will only be enough to avoid black outs, then an extra 15% is required to run as reserve energy.

Technically Eskom needs to increase its capacity by 27% to be in good standing and increase this amount by 4% every year. Currently SA is pushing the Grand Inga Hydro power project that can be a solution for current and future energy challenges. Hydroelectric power generation plants are used comprehensively all over the world. We can benchmark our targets with countries such as United States which is generating supply to 28 million households through hydroelectric and that is equivalent to almost 500 million barrels of oil per year. The total U.S. hydropower capacity is approximately 95 gigawatts which is mere two times more than what we produce using coal, if they can in USA so can we in SA [5]. The Advantages of hydro-electric are:

- The power generation is continuous
- The generation process is pollution free, it has no emissions
- Low maintenance and less running costs
- The technology last longer and it is robust

Fig. 6 below shows a diagram of a typical hydro generation plant.

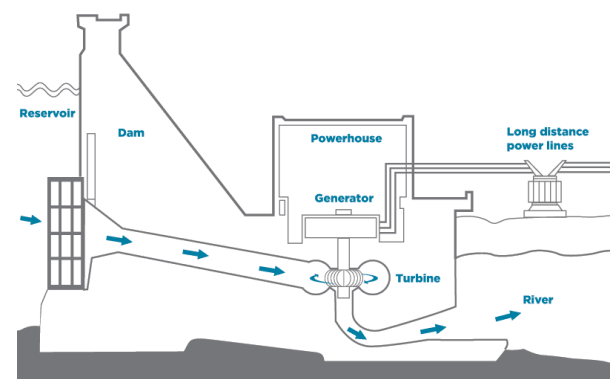


Fig. 6 Hydro-electric generation plant [13]

Hydro-electric generation plant depends on the speed of the water.

Stream flow of water is the fuel of a hydro-power generation plant and without it generation plant ceases. Irrespective of the water path through an open channel, the power generated in a turbine is given as
Turbine power:

$$P_t = \rho * g * H_n * Q * \eta_t (\text{watt}) \quad (1)$$

ρ = water density (1000 Kg/m³).

H_n = net head (m)

Q = rate of flow (m³/s)

g = gravitational constant (9.8m/s²)

η_t = turbine efficiency (80-90%).

P_t = power in watt generated in the turbine shaft.

Energy generated per year (KWH)

$$P_t = \rho * g * H_n * Q * \eta_t * \eta_{\text{turbine}} * \eta_{\text{generator}} * \eta_{\text{gearbox}} * \eta_{\text{transformer}} * n \quad (2)$$

Where g is the gravitational constant (9.8m/s²)

ρ = water density (1000 Kg/m³).

Q = rate of flow (m³/s)

H_n = net head (m)

η_{turbine} = Turbine efficiency

$\eta_{\text{generator}}$ = Generator efficiency

η_{gearbox} = Gearbox efficiency

$\eta_{\text{transformer}}$ = Transformer efficiency

n = no of hours in one year [5]

VIII. CONCLUSION

Electricity is the engine of the country without it its economy will be non-existence so is our modern life. To safe guard the wellbeing of the South Africans the construction of more power stations will help SA to overcome the energy crisis. Although coal fired power plants have their own disadvantages and limitations building more of the power station of its kind will help meet the required supply demand.

The problem is that most power stations in SA use coal and this practice is undesirable. Recently SA has experienced shortage of coal and coal burning pollutes air and that has a big impact in contributing to global warming. With electricity there's no clear cut on what is to be done, but with thorough assessment, planning and research the solution is guaranteed. Renewable energy sources discussed above can definitely help SA produce more clean energy and to meet the energy demand. Therefore, the government and the private sector should work hand in hand to emphasize more on renewable energy source to produce electricity to solve our power crisis problem.

The chosen technology for SA is hydroelectric. Hydroelectric power is the way to go due to its ability to react almost instantaneously to the rising of the consumer energy demand, it has low running cost, minimal maintenance, it is robust and safe to use as it doesn't have any effect in terms of harming the environment. It uses water without depleting it and the capacity it can carry. It is the hope for the country, its restriction can be easily resolved if we don't want to build new dams we can negotiate with the neighboring to utilize their rivers in order to produce electricity. We need not dwell too much on the amounts that will be spent in generating these kinds of plants as the country will benefit on the investment returns in long term and will secure the future and wellbeing of all South Africans.

REFERENCES

- [1] Francois Caldo, 2008 "Eskom's power crisis: Reasons, impact & possible solutions", Solidarity, 15 February 2008.
- [2] Srinivasan Chinnammal "A Study on Energy Crisis and Social Benefit of Solar Energy"
- [3] Sifat Shah, M.K. L. Bhatti, "Crisis of Electrical Energy in Pakistan and Future guideline for Policy makers" COMSATS Institute of Information Technology, Abbottabad Pakistan
- [4] A Von Ketelhodt, A Wöcke "The impact of electricity crises on the consumption behavior of small and medium enterprises" Sasol Limited Gordon Institute of Business Science, University of Pretoria
- [5] B. A. Naisir, June 2013 IJEAT "Design of Micro Hydro Electric Power Station" ISSN:2249-8958 volume 2, issue 5.
- [6] D. Peter, Dr H Wadron, March 2008, "Desert-ocean thermal energy conversion", volume 14
- [7] R McClueney, 2004, "Renewable energy limits" FSEC-GP-216-03, university of Florida USA.
- [8] JC Nkomo, August 2005, "Energy and Economic Development Challenges for SA", Energy research University of Cape Town.
- [9] Hilary Joffe "Challenges for South Africa's Electricity Supply Industry"
- [10] Narayana Swamy. R, Dr. G. Mahadevan "Power Saving Device "International" journal of science and technology research volume 1 issue 7 August 2012
- [11] S B Pasquier, 2011 "Saving Electricity in a Hurry", international energy agency.
- [12] J F Nicoll, TS Chang and H.E. Stanley "A differential generator for the energy and the magazine equation of state" Physics Department, Massachusetts Institute of Technology, Cambridge. Massachusetts 02139, USA
- [13] Khairul Anam, Husnain-Al-Bustam, "Power Crisis & Its Solution through Renewable Energy in Bangladesh" Department of Electrical & Electronic Engineering, Islamic University of Technology.
- [14] Abdeen Mustafa Omer "The Energy Crisis, the Role of Renewable and Global Warming" Energy Research Institute (ERI), Nottingham NG7 4EU, UK
- [15] Eng. Rafat Saikly, Dr. Aeman Aead, Prof. Dr. Samy Abu Naser "The Contribution of Solar Energy to Reduce Electricity Shortage in the Gaza Strip through Using Photovoltaic Panels as a Replacement to Roofing Tiles"
- [16] Ogunlade Davidson, Harald Winkler, Andrew Kenny, Gisela Prasad, Jabavu Nkomo, "Energy policies for sustainable development in South Africa"
- [17] C. P. Kruger and F. Newman, 2012, "A Survey in Energy Related behavior perception in South Africa", Department of energy Pretoria.
- [18] Marcelo S. Sthell, José G. R. Tostes1, Juliana R. Tavares1,2 "Current energy crisis and its economic and environmental consequences" Intense human cooperation
- [19] Mayank Grover, B. Lohith Kumar, Isaac Ramalla December 2014 1 "The Free Energy Generator" International Journal of Scientific and Research Publications, Volume 4, Issue 12, ISSN 2250-3153
- [20] Ameer Nawaz Khan, Toheeda Begum, Mehwish Sher. "Energy Crisis in Pakistan: Causes and Consequences"
- [21] R Kempener, F. Newman, June 2014 "Ocean Thermal Energy Conservation", IRENA



Zephania Philani Khumalo (Pr Tech Eng)

He was born on 06 January 1978 in KZN South Africa. He is currently a Masters of Engineering student at Durban University of Technology. He received his Bachelor of Technology Degree in Electronic Engineering in the year 2013 from Durban University of Technology. His research interests are in the fields of Smart Grids, Data Security, SCADA Systems, Artificial Intelligence, Power Line Communications, and Cryptology.

COMPARISON OF IMPACTS OF INTEGRATION OF SOLAR PV FARMS AND WIND FARMS IN A UTILITY GRID

K. Ramoreboli*, T. Matlokotsi* and S. Chowdhury*

** Electrical Engineering Dept., Upper Campus, Rondebosch, University of Cape Town, South Africa*

Abstract: The interest in deployment of renewable energy sources such as wind and solar PV is motivated by environmental concerns resulting from the use of conventional energy sources for energy generation. Grid-integration of renewable energy sources however pose challenges that may have adverse impacts on the power quality of the utility grid. Based on the voltages and line loadings in the network, this paper investigates the performance of the power system under different grid-integration scenarios of wind and solar PV generators. Modelling and simulation of utility network with wind and solar PV based distributed generation is done in DIgSILENT Powerfactory. The comparison of the impacts of grid-integration of solar PV farms with wind farms is made with reference to the South African codes governing the grid-integration of renewable energy sources. Observations show that high penetration levels of wind and solar PV affect both voltage quality and line loadings of utility network.

Keywords: Solar PV, Doubly-Fed Induction Generator, Bus Voltage, Line Loading, Point of Common Coupling, Grid Strength

1. INTRODUCTION

Renewable energy integration to utility grid has been an increasing trend in power generation in recent years as a result of prevailing energy crisis and environmental pollution brought about by the use conventional energy sources. Electrical power generation using wind and photovoltaic technologies is a key but still evolving technology and the global cumulative installed capacity of these energy sources is increasing annually. South Africa, in particular targeted to introduce about 10 000 GWh of cumulative renewable energy by the year 2013 [1].

Electricity generation using wind and solar PV is assuming increased importance as a renewable energy source application due to technical, environmental and economic benefits offered by their grid-integration. The merits of distributed generation (DG) integration include improved voltage supply, reduction in line losses, enhancement of the power system's security and reliability, etc. [2] [3]. Even though there are myriad benefits associated with integration of DG into utility grids, there are several challenges which system planners should consider for proper planning of DG grid-integration. Understanding the impacts of grid-integration of solar PV farms and wind farms will not only ensure informed network planning decisions but will also ensure that the performance of the network is improved in terms of power quality and stability.

Poor network planning can adversely affect the utility grid operation, resulting in increased network disturbances such as, harmonic injection, increased line loadings, voltage rises and dips, etc. The common problem in networks with DG integration is the reverse power flow which increases line loadings; an effect that can cause maloperation of protection devices such as circuit breakers. This paper investigates through modelling and simulation in DIgSILENT Powerfactory, the impacts of grid-integration of solar farms and wind farms on bus voltages and line loadings at distribution and sub-transmission level of the test network. The grid strength, penetration level of renewable DGs, voltage level and point of integration are explored to observe their impact on both line loadings and bus voltages at the point of

integration of the DGs. A doubly-fed induction generator (DFIG) wind turbine and a simple solar photovoltaic generator are considered for this research due to maturity of these technologies and their promising commercial prospects.

2. MODEL OF ELECTRICITY NETWORK WITH WIND AND SOLAR PV FARMS INTEGRATION

2.1 Test network model

All the modeling and simulation for this research is done in DIgSILENT PowerFactory version 14.1.6. DIgSILENT is an integrated power system analysis tool that incorporates reliable and flexible system modelling with state-of-the-art solution algorithms and unique object-oriented database management [11]. It performs load-flow, short circuit calculations, harmonic calculations, harmonic analysis, protection coordination, stability calculation and modal analysis of networks. Furthermore, it allows for modelling of not only wind energy conversion systems but also solar photovoltaic models. The software has further advantages such as allowing the user to export results files as .txt files for ease of use somewhere [11], for example Microsoft Excel for graph plotting. In a case where one model cannot fit in one window, the user can create a new tab to create the subsystem that could not fit and then later interconnect the two with ease.

The 9-bus, 50Hz test network used for the study and shown in Figure 1 and modeled in DIgSILENT is adopted from [4] and is modified by adding the sub-transmission and distribution levels as shown in Figure 1. The test network is divided into different voltage levels to represent the practical electricity network with generation at 22 kV, transmission at 230 kV, sub-transmission at 66 kV and distribution at 11kV. The network consists of two sources; a synchronous generator rated at 100 MVA and an external grid with short circuit power of 10 000 MVA. Parameter choice for the three 2-winding transformers, 5 loads and 7 feeders is made such that the safe operation of the system is achieved.

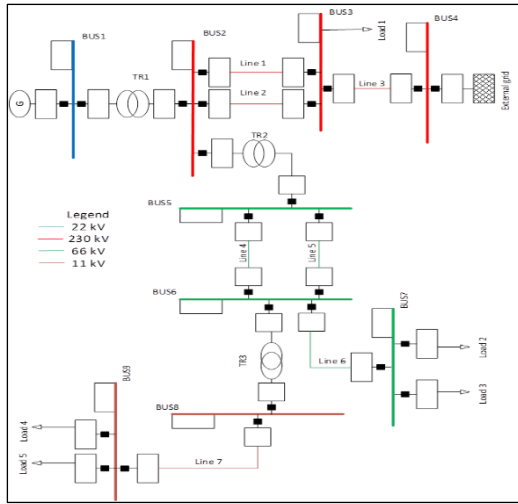


Figure 1: Test network model

2.2 Solar PV model

Energy conversion in Solar PV systems is achieved by means of photovoltaic cell which is basically a p-n semiconductor junction that directly converts solar radiation into electrical energy using the photovoltaic effect [5]. When the semiconductor atom receives photons, the PV array outputs a DC current whose magnitude depends on solar radiation density and cell temperature. PV cells grouped together in units called PV modules are either connected in series or parallel depending on the desired output current and voltage [6]. The equivalent circuit of a solar cell is composed of a light-generated current source, a diode representing the nonlinear impedance of the p-n junction and parallel resistances as shown in Figure 2.

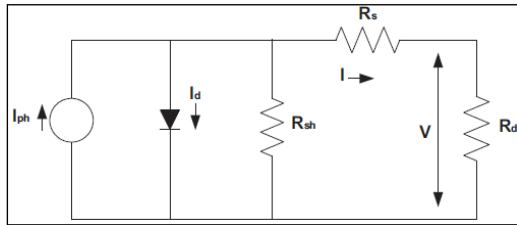


Figure 2: Equivalent circuit of a PV [7]

The mathematical models defining the output current, I and voltage, V of a PV array are given by equation (1) and equation (2), respectively.

$$I = N_p I_{ph} - N_p I_d \left[\exp \left(\frac{qV}{kTAN_s} \right) - 1 \right] \quad (1)$$

$$V = \left(\frac{AkT}{q} \right) \ln \left[(I_{ph} + I_d - I) / I_d \right] - R_s I \quad (2)$$

where N_p and N_s are the number of modules connected in series and parallel, respectively; q is the electron charge, k is the Boltzman's constant, A is the p-n junction ideality factor and T is the solar cell temperature. I_{ph} and I_d are the photo current and diode current, respectively and are dependent on the cell temperature and solar radiation.

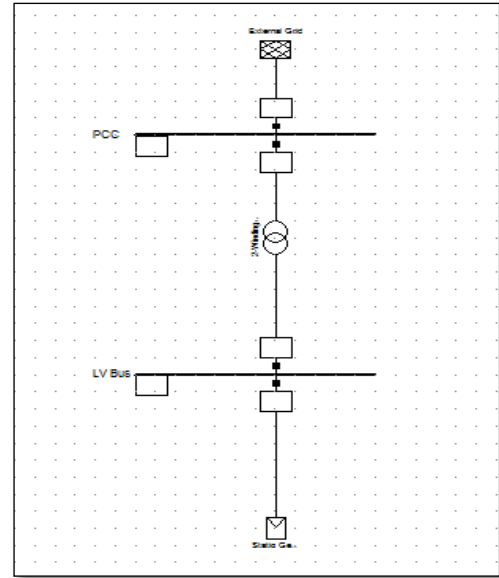


Figure 3: Solar PV model

The PV model in DIgSILENT Power factory is modelled as a static generator due to the absence of any rotating machinery in a PV system. This model is available in DIgSILENT power factory in a form of a template consisting of a PV generator along with its design and control features. The PV generator in DIgSILENT already has a DC-AC converter incorporated in its design, the generic template of a PV is therefore connected directly to the two-winding transformer that steps up the PV generator's output voltage to that of the utility grid. The active power of one PV module is 20MW and is modelled at unity power factor due to PV system's inability to generate reactive power. Figure 3 shows the model of an on-grid solar PV system simulated in DIgSILENT Power factory with a static generator.

2.3 DFIG wind turbine model

The model of the DFIG wind turbine is modelled comprising of the aerodynamics block, mechanical block, electrical block and the control system. The interaction of the wind turbine with wind is simplified by modelling the aerodynamic torque developed on the main shaft of the wind turbine using equation (3) below [8]:

$$T_{rot} = \frac{P_{rot}}{\omega_{rot}} = \frac{1}{2\omega_{rot}} \rho \pi R^3 U^2 C_q(\theta, \lambda) \quad (3)$$

In equation (3), U is the wind speed, R is the rotor radius, ρ is the air density and $C_q = C_q(\theta, \lambda)$ is the torque coefficient that is a function of the pitch angle, θ and the tip speed ratio, λ . P_{rot} and ω_{rot} are the rotational power and speed of the wind turbine, respectively.

The DFIG wind turbine has its stator winding connected to the power grid and its wound rotor connected to the grid through a frequency converter. The two control mechanisms developed in the model of the DFIG wind turbine system are that of the rotor side-controller which is responsible for controlling the rotor current of the induction machine while that of the grid-side controller stabilizes the dc at its nominal voltage [9]. The DFIG model provided by DIgSILENT however extends the traditional induction generator by adding a rotor impedance Z_{rot} connected in series with the PWM rotor side converter as

depicted in an electrical equivalent circuit of Figure 4. The PWM converter is therefore added at the grid-side to convert the output DC power into AC power ready to be fed into the grid.

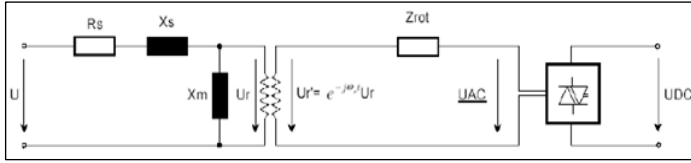


Figure 4: The equivalent circuit diagram of a DFIG [10]

In this paper, the capacity of the DFIG wind turbine system is set at 32.6 MVA which corresponds to 25% of the rated capacity of the utility generator (100MVA at 0.8 pf). The PWM converter used in the DFIG model is rated at 30% of the MVA rating of the DFIG machine and has the rated AC and DC voltages of 2.2 kV and 1.15kV, respectively. The shunt filter, with the nominal voltage equal to that of the DC side of the PWM converter is used for reactive power compensation and harmonic filtering. The 150 MVA, three winding transformer with LV side connected to the output of the grid-side converter, MV side connected to the stator bus and the HV side connected to the point of common coupling (PCC) is rated according to the voltage levels of the respective busbars. The LV and MV windings are equal at 2.2 kV while the HV winding is rated at 11 kV. The complete model of DFIG wind turbine system as modelled in DIgSILENT as shown in Figure 5.

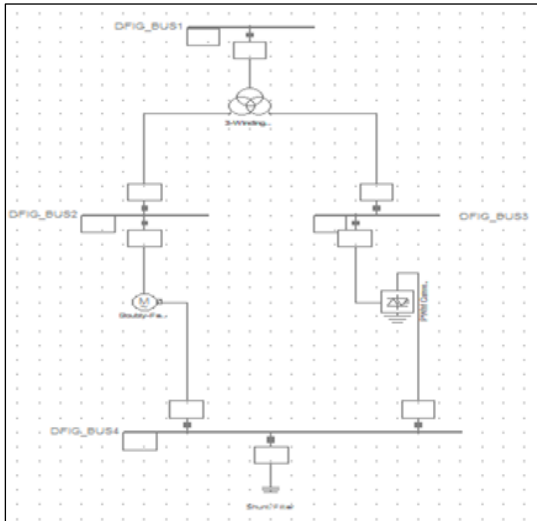


Figure 5: DFIG model for grid integration

3. CASE STUDIES AND RESULTS

This section presents the case studies conducted for comparison of the impacts of grid-integration of solar PV farms and wind farms on bus voltages and line loadings in the utility test network. For better quality of power, the power system is required to comply with the grid codes governing grid-integration of DGs. The South African renewable energy grid code [11] has been developed to allow renewable energy power producers to effectively plan the connection of DG units to the Transmission Systems (TS) or Distribution systems (DS).

In conducted case studies, voltage levels are expected to be within the range specified by the grid code, such that the performance of the power system does not deteriorate in terms

of the power quality and stability. Table 1 below presents the summary of grid code requirements for DG units integrated at the transmission (230 kV), sub-transmission (66 kV) and distribution levels (11 kV) as will be the case in this work. DG systems in Table 1 are classified in categories based on their rated power and voltage level at which they are connected.

Table 1: Summary of grid code requirements for DGs [11]

Output power [kVA]	0 – 1000	>1000 – 20000	> 20 000
Voltage level	HV	MV	MV/HV
Operating voltage range	-15 to +10%	±10%	
Operating power range	20 -100%		

3.1 Case 1: Impact of DG integration for different PCCs and voltage of integration

This case study investigates how the voltage level and point of DG integration impact on bus voltages and line loadings at transmission (230kV), sub-transmission (66kV) and distribution (11kV) levels of the test network. At transmission level, DGs are connected at Bus 3 which is 600 km away from the utility generator. At sub-transmission and distribution levels, the proximity to loads is considered, when deciding the bus at which DGs should be connected. DGs are therefore connected to different busbars, viz., Bus 5 to Bus 9 of the test network.

For each point of integration, the capacity of solar PV and DFIG is increased from 0 to 150% of the utility generator which is rated at 100MVA at 0.8 pf. Line loadings are observed for lines 5 and 6 of the sub-transmission level as well as line 7 of the distribution network as DG penetration level is altered. It may be noted that Line 5 and Line 6 are both rated at 10 kA and are connected to Bus 5 and Bus 6 and Bus 6 and Bus 7, respectively. Line 6 is a feeder to the loads supplied from the sub-transmission network which is at 66 kV. Line 7 is rated at 2 kA and is a feeder to the loads on 11 kV distribution network. Voltage at PCC bus is also plotted for 0% to 150% DG penetration. Comparison is then made between impacts of solar PV integration and DFIG wind turbine integration based on the resulting bus voltage and line loadings in the network. The percentage penetration (%) is calculated from equation (4) below:

$$\% \text{ DG penetration} = \frac{\text{DG power}}{\text{Total power in the test network without DG}} \quad (4)$$

3.1.1 PV integration at transmission (Bus 3), sub-transmission (Bus 5) and distribution (Bus 9) voltage levels

The results for voltage at the PCC bus when solar PV is integrated at different busbars of the network are shown in Figure 6, Figure 7 and Figure 8.

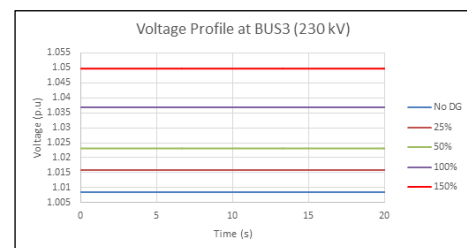


Figure 6: Voltage at Bus 3 PCC for increasing PV penetration

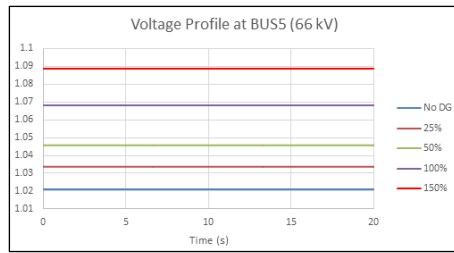


Figure 7: Voltage at Bus 5 PCC for increasing PV penetration

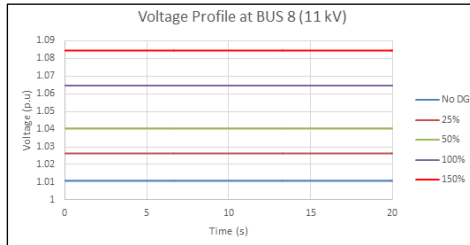


Figure 8: Voltage at Bus 8 PCC for increasing PV penetration

The bus voltages shown in Figure 6, Figure 7 and Figure 8 indicate that voltage magnitude rises as the penetration level of integrated PVs is increased. At 150% PV penetration level, voltage magnitude is highest when PV is integrated at the distribution network. The lowest and highest voltage magnitudes reached for the above PV integration scenarios are 0.99 p.u. and 1.094 p.u., respectively. When level of penetration of solar PV is gradually increased from 0% to 150% at the transmission (Bus 3) and sub-transmission (Bus 5) levels, as shown in Figure 6 and Figure 7 respectively, bus voltages are found to be within the prescribed voltage range specified for MV/HV networks in Table 1. The required voltage range at distribution networks is however exceeded at 150% penetration level of solar PV at Bus 8 of the distribution network (11kV) as shown in Figure 8. This may have detrimental impacts on voltage sensitive equipment connected on the distribution network. If the penetration level of integrated PVs is increased above 150%, reverse power flow may also occur.

The results of the percentage line loadings when solar PV is integrated at the transmission (Bus 3), sub-transmission (Bus 5) and distribution (Bus 8) levels are presented in Table 2, Table 3 and Table 4, respectively. Tables 2 and 3 indicate that when solar PV is integrated at transmission and sub-transmission busbars, line loadings for all lines decrease with increasing penetration level. Table 4 indicates that PV integration at the distribution level Bus 8, where loads are connected, results in an increase in line loadings when the capacity of solar PV exceeds the active power rating of the loads. This is due to increased current flowing through the lines as a result of reverse power flow that occurs when excess power flows away from the loads. The loading on Line 7 of the distribution network rises to an unacceptable value of 189.55% at 100% PV penetration. Excessive loading of the line may cause excessive heating of the conductors and consequently increase the resistance of the wire, resulting in power loss. The power flow calculation with 150% PV penetration could not be performed for Line 7 loading as the DIgSILENT power flow solutions did not converge beyond 100% penetration. This is because Line 7 is connected to Bus 9 and is used to transfer the excess power in reverse power flow from Bus 9 to Bus 8, leading to excessive loading of the line.

Table 2: Line loading with increasing PV penetration at Bus 3

Line loading (%)	% PV Penetration at 230kV Bus 3				
	0%	25%	50%	100%	150%
Line 5	2.29	2.27	2.25	2.22	2.20
Line 6	4.19	4.16	4.13	4.07	4.02
Line 7	13.27	13.17	13.07	12.89	12.72

Table 3: Line loading with increasing PV penetration at Bus 5

Line loading (%)	% PV Penetration at 66kV Bus 5				
	0%	25%	50%	100%	150%
Line 5	2.29	2.26	2.23	2.18	2.14
Line 6	4.19	4.14	4.09	4.00	3.93
Line 7	13.27	13.09	12.93	12.65	12.40

Table 4: Line loading with increasing PV penetration at Bus 8

Line loading (%)	% PV Penetration at 11kV Bus 8				
	0%	25%	50%	100%	150%
Line 5	2.29	1.43	0.87	1.78	-
Line 6	4.19	4.13	4.10	4.11	-
Line 7	13.27	41.16	89.16	189.55	-

3.1.2 DFIG integration at transmission (Bus 3), sub-transmission (Bus 5) and distribution (Bus 8) voltage levels

The results of the voltages at the PCC bus when DFIG wind turbine is integrated at the transmission, sub-transmission and distribution busbars are presented in Figure 9, Figure 10 and Figure 11 respectively.

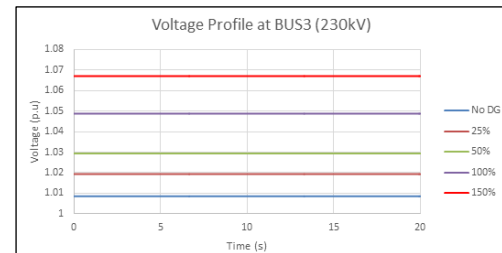


Figure 9: Voltage at Bus 3 PCC for rising DFIG penetration

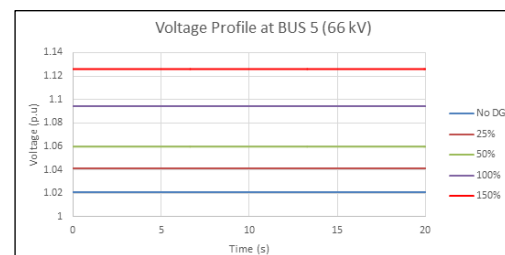


Figure 10: Voltage at Bus 5 PCC for rising DFIG penetration

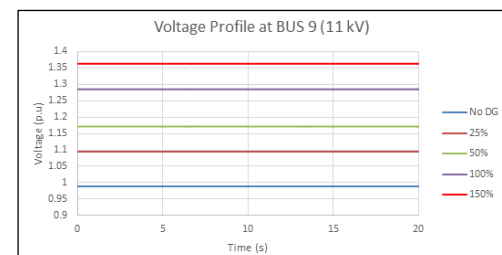


Figure 11: Voltage at Bus 8 PCC for rising DFIG penetration

It can be seen that the voltage magnitude rises with increasing DFIG penetration level for all PCC. Figure 9 shows that voltage rise is maintained within the acceptable range as the

capacity of DFIG, integrated at transmission level (Bus 3) is increased. For DFIG integration at sub-transmission level (Bus 5), it is observed that voltage magnitude rises from 1.02 p.u. to 1.07 p.u. when penetration level is increased from 0% to 100%. However, beyond 100% penetration level, voltage magnitude rises above acceptable limits as depicted in Figure 10. Voltage rise however becomes severe when DFIG is integrated at distribution level Bus 8 as the penetration level is increased. As shown in Figure 11, the voltage rises from 0.99 p.u. at 0% penetration of the DFIG and reaches 1.36 p.u. at the penetration level of 150%. This can also affect the power flows in the network. In comparison with solar PV, grid integration of DFIG results in higher voltage rise for the same capacity and PCC.

The results for the percentage line loadings when DFIG is integrated at the transmission, sub-transmission and distribution levels are presented in Table 5, Table 6 and Table 7 respectively. Table 5 and Table 6 show that line loadings decrease when the capacity of DFIG, integrated at the transmission (Bus 3) and sub-transmission (Bus 5) busbars is increased. The lines are therefore not overloaded as the line loadings are always below 100%. Table 7 shows that when DFIG is integrated at the distribution Bus 8, line loadings for Lines 5 and 6 also decrease with increasing DFIG penetration. However it is seen that loadings for Line 7 connecting the load busbar to the PCC, increase with increasing DFIG penetration. The line starts to be overloaded at just over 50% DFIG penetration level. This is because when the power requirements for Loads 4 and 5 are exceeded, excess power is carried back to the grid through Line 7. It is crucial to consider the acceptable penetration level of DG integrated at close proximity to the loads to avoid excessive loading of the corresponding lines.

In comparison with solar PV, the decrease in line loadings is greater for the same penetration level of DFIGs. Line 7 overloading for distribution level integration at Bus 8 is also less severe than in the case of PV integration for similar penetration level. The loadings for Line 7 are able to be determined at 150% penetration level due to DFIG's capability to absorb reactive power during high penetration levels hence the % loading is relatively lower than that of PV integration for the same busbar.

Table 5: Line loading with rising DFIG penetration at Bus 3

Line loading (%)	% DFIG Penetration at 230kV Bus 3				
	0%	25%	50%	100%	150%
Line 5	2.29	2.26	2.24	2.20	2.16
Line 6	4.19	4.15	4.10	4.03	3.96
Line 7	13.27	13.12	12.99	12.74	12.51

Table 6: Line loading with rising DFIG penetration at Bus 5

Line loading (%)	% DFIG Penetration at 66kV Bus 5				
	0%	25%	50%	100%	150%
Line 5	2.29	2.24	2.20	2.13	2.07
Line 6	4.19	4.11	4.03	3.90	3.79
Line 7	13.27	12.99	12.75	12.33	11.96

Table 7: Line loading with rising DFIG penetration at Bus 8

Line loading (%)	% DFIG Penetration at 11kV Bus 8				
	0%	25%	50%	100%	150%
Line 5	2.29	2.24	2.20	2.13	2.07
Line 6	4.19	4.11	4.03	3.90	3.79
Line 7	13.27	12.99	12.75	12.33	11.96

Line 5	2.29	1.38	0.62	0.88	2.13
Line 6	4.19	4.09	4.02	3.92	3.87
Line 7	13.27	41.98	88.31	169.58	243.47

3.2 Case 2: Impact of DG integration for different grid strength

In this case study, the impact of grid connection of solar PV and DFIG is investigated for different grid strengths. Grid strength may be defined in terms of the Short Circuit Ratio (SCR) or reactance to resistance ratio of the external grid. A grid with an SCR value less than 10 or X/R value less than 0.5 is considered weak and may present serious technical constraints. Grid strength is increased from a very weak (SCR = 1) to a strong grid (SCR = 10) by varying the short circuit power capacity (SCC) of the grid.

The busbars used for DG integration in this case are Bus 5 and Bus 8 located at the sub-transmission and distribution networks, respectively. For this case study, DG capacity is fixed at 50% of utility generator because it proved to be the best capacity for integration at Bus 8 and Bus 5 in case 1. The flow of power does not change at constant DG capacity and network loading hence the change in line loadings becomes insignificant. Line loadings are therefore not considered for this case study. Voltage at the PCC bus is observed for increasing SCR values. The simulation is run by applying a short circuit event on Line 1 at t=4 seconds and clearing it at t=4.08 seconds, where time is measured from the start of the simulation. Figure 12 and Figure 13 show the resulting voltages at 66 kV and 11kV busbars as the SCR of the network with solar PV integration is altered.

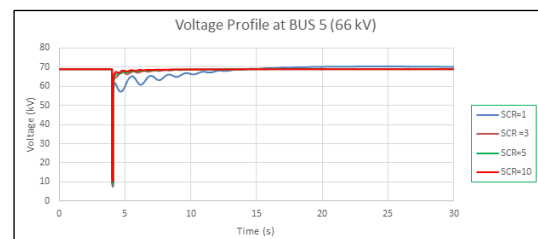


Figure 12: Voltage at Bus 5 with 50% PV penetration for different SCR values

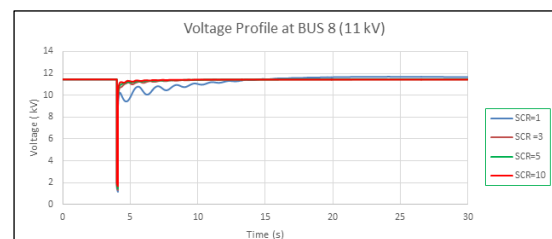


Figure 13: Voltage at Bus 8 with 50% PV penetration for different SCR values

As can be seen, after the fault occurs, voltage recovery time is longest when SCR is 1 and shorter for SCR of 10. The post-fault settling time of the voltage therefore decreases with increasing SCR for PV integration at both the sub-transmission and distribution networks. It is evident that PV integration in weak grid results in prolonged voltage recovery and this may be detrimental to voltage sensitive equipment at customer's side.

The results for DFIG integration at sub-transmission and distribution networks are shown in Figure 14 and Figure 15, respectively. The settling time is shorter and almost the same

at all grid strengths as opposed to PV integration case. However, some decaying oscillations that decrease with the grid strength occur after the fault is cleared. As opposed to PV, DFIG integration at both weak and strong grids have minimum impact on voltage recovery time following fault occurrence.

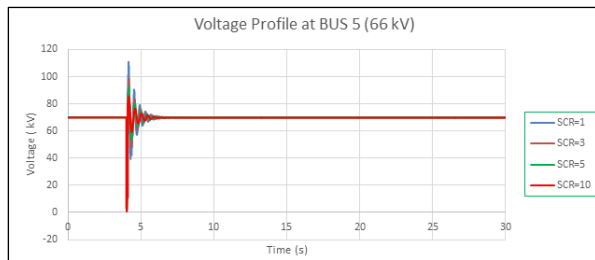


Figure 14: Voltage at Bus 5 with 50% DFIG penetration for different SCR values

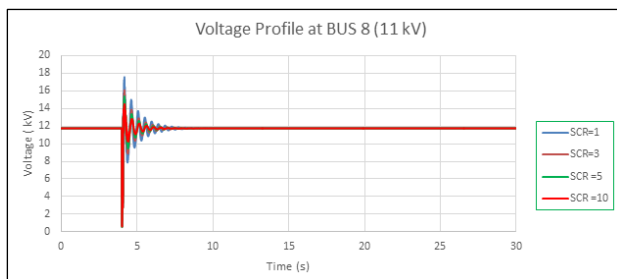


Figure 15: Voltage at Bus 8 with 50% DFIG penetration for different SCR values

4. CONCLUSION

The observations made indicate that the point and voltage of integration of DGs have an impact on network bus voltage and line loadings depending on the point of common coupling (PCC) and grid strength. The network's bus voltages improve more when both solar PV and DFIG are integrated at PCC far away from utility generator. Voltage rise however occurs as the penetration level of both solar PV and DFIG is increased. During high penetration levels of DFIG, voltage magnitude rises above the limits specified by the grid codes. This occurs at penetration levels of 100% and 150%. Solar PV outperforms DFIG at higher penetration levels in terms of the resulting bus voltages. This is attributed to the fact that DFIG exceeds both the active and reactive power requirements of the load as opposed to solar PV which only generates active power. The well planned and acceptable penetration levels of both PV and DFIG will however provide support to the system voltage in the case of high power demands.

Line loadings decrease for both solar PV and DFIG integration as the penetration level of DGs is increased. However, for DGs integrated closer to the loads, an increase in line loadings occurs as DG penetration level is increased. This is attributed to the reverse power flow phenomena. The impact is more severe at distribution level than sub-transmission level as the loads connected to the distribution network are relatively smaller and result in more excess power being sent back through the feeders to the external grid. At high penetration levels, line loadings for PV integration are higher than that of DFIG integration for the same penetration levels. Loadings at Line 5 and Line 6 are found to be within acceptable levels for both PV and DFIG integration at different busbars. For distribution level integration, an

enormous increase in line loadings is observed at Line 7 which carries excess power back to the external grid. Line loadings are therefore observed to be severe for lines connecting the PCC to the rest of the network busbars.

The grid strength also impacts the network bus voltages for both solar PV and DFIG integration. DFIG integration however outperforms solar PV since voltage recovery time is shorter than that of solar PV after the fault is cleared. The relatively better performance of DFIG at different grid strengths is due to DFIGs ability to inject reactive power for voltage support while solar PV only produces active power. It is therefore important for generating utilities and network planners to carefully select right the type DG technology depending on the point of integration, penetration level and grid strength at PCC.

The impacts of solar PV and DFIG integration into utility grids are crucial in DG integration planning scenarios on the weak South African grid. The widespread deployment of DG in South African electricity networks will require network expansion or infrastructure upgrading such that the grid strength is improved. The strategic combination of optimal capacity and placement of these energy sources will also not only provide support to the network voltage profiles, but will also improve the security of supply on the South African electricity network.

5. ACKNOWLEDGEMENT

The authors gratefully acknowledge the support and infrastructure provided by Electrical Engineering Department, University of Cape Town, South Africa for carrying out this research.

6. REFERENCES

- [1] M. Chidi, O. Ipinnimo, S. Chowdhury and S. P. Chowdhury, "Investigation of impact of integrating on-grid home based solar power systems on voltage rise in the utility network," in *IEEE Power and Energy Society General Meeting*, pp. 1-7, 2012.
- [2] P. Paliwal, N.P.Patidar and R.K.Nema, "Planning of grid integrated distributed generators: A review of technology, objectives and techniques," *Renewable and Sustainable Energy Review*, vol. 40, pp. 557-570, Dec. 2014.
- [3] C. Lucia and T. Borges, "An overview of reliability models and methods for distribution systems with renewable energy distributed generation," *Renewable and Sustainable Energy Reviews*, no. 16, pp. 4008-4015, 2012.
- [4] G. Singh, "Solar power generation by PV (photovoltaic) technology: a review," *Energy*, vol. 53, pp. 1-13, 2013.
- [5] M. Molina and E. Espejo, "Modeling and simulation of grid-connected photovoltaic energy conversion systems," *international journal of hydrogen energy*, vol. 39, pp. 8702-8707, 2014.
- [6] B. N. Alajmi, K. Ahmed, S. J. Finney and B. W. Williams, "A maximum power point tracking technique for partially shaded photovoltaic systems in microgrids," *IEEE Trans. Industrial Electronics*, vol. 60, no. 4, pp. 1596-1606, 2013.
- [7] L.Mihet-Popa, F. Blaabjerg and I. Boldea, "Wind turbine generator modeling and simulation where rotational speed is the controlled variable," *IEEE Trans. Industry Applications*, vol. 40, no. 1, pp. 3-10, 2004.
- [8] T. Matlokotsi and S. Chowdhury, "Voltage and Frequency Profile Analysis of Electricity Networks with Wind Energy Integration," in *IEEE AFRICON*, Addis Ababa, 2015.
- [9] A. D. Hansen, C. Jauch, P. E. Sorensen, F. Iov and F. Blaabjerg, "Dynamic wind turbine models in power system simulation tool DiGSILENT", 2004.
- [10] S. Std., "Grid connection code for renewable power plants(RPPs) connected to the electricity transmission and distribution systems in South Africa," 2014.
- [11] O. K. Mokoka and K. Awodele, "Reliability Evaluation of distribution networks using NEPLAN & DiGSILENT power factory," in *AFRICON*, 2013, Pointe-Aux-Piments, 2013.

THE IMPACT OF LARGE PENETRATION OF GRID CONNECTED PHOTOVOLTAIC (PV) GENERATION ON THE UTILITY GRID: A CASE FOR SOUTH AFRICA

N. Dhlamini*, S.P. Chowdhury* and A. Sendegeya**

**N.Dhlamini, Tshwane University of Technology Dept. of Electrical Engineering Faculty of Engineering and the Built Environment, Pretoria 0001 South Africa E-mail: nhamodhlamini@hotmail.com*

** S.P. Chowdhury, Tshwane University of Technology Dept. of Electrical Engineering Faculty of Engineering and the Built Environment, Pretoria 0001 South Africa E-mail: spchowdhury2010@gmail.com*

*** A. Sendegeya, Tshwane University of Technology Dept. of Electrical Engineering Faculty of Engineering and the Built Environment, Pretoria 0001 South Africa E-mail: spchowdhury2010@gmail.com*

Abstract: Photovoltaic (PV) generation systems continue to be built at increasing levels and their impact on the utility grid needs to be investigated more accurately. This includes the impact both on the local grid where they are connected and the impact on the whole electricity grid infrastructure. This research seeks to investigate the impact of a large penetration of grid connected PV generation on the utility grid with particular emphases on the South Africa grid network and in particular its compliance to the South African grid code on embedded generation. The research seeks to highlight the characteristics of PV generation, its control and component parts. A model for the simulation of PV generation will be developed in Matlab/Simulink to investigate the impact of penetration of a large PV generation under steady state, its dynamic response to rapid changes in irradiance and finally its response under faulty environments.

Key Words: Photovoltaic (PV), Global Horizontal Irradiation (GHI), Solar Cell, Inverter, Maximum Power Point Tracking (MPPT).

1. INTRODUCTION

Solar Photovoltaic (PV) generation systems are now one of the fastest growing renewable energy sources being integrated into the utility grid worldwide. The need for sustainable development of electricity, energy efficiency improvement and environmental pollution reduction due to carbon emissions has favoured the introduction of more environmentally friendly methods of electricity generation. Large PV plants in the order of several megawatt amperes (MWs) are now common methods of electricity generation worldwide. The large penetration of PV renewable energy sources are mainly due to declining PV module prices and the strong feed in tariff policies for grid connected PV power systems in different countries. Global cumulative PV capacity reached new record by the end of 2012 with more than 100GW installed capacity [1]. The growth of the PV market has mainly been in Europe, with Germany, Spain and Italy with the biggest share, while other countries like China, Japan and the USA have set ambitious targets for the high penetration of PV systems as part of their energy mix [1]. The growth and high penetration of PV renewable energy systems impose new challenges for System Operators (SO) globally. South Africa embarked on an ambitious renewable energy drive to diversify its energy mix with PV generation being among the targeted generation mix. South Africa is now ranked amongst the top 10 countries in the world in 2014, with PV generation installed capacity of 800MW. According to the integrated resource

plan (IRP) 2010 to 2030, South Africa intends to install a total solar PV generation capacity of 8,400MW by 2030 [2]. The current PV market in South Africa is mainly driven by the Renewable Energy Integrated Power Purchase Procurement Program (REIPPPP), which was introduced in August 2011 by the Department of Energy (DoE). The success of South Africa's utility scale targeted growth in PV generation has made the country an attractive investment destination and an emerging PV market globally.

The growth and penetration of large PV generation in South Africa brings with it integration challenges to the existing transmission and distribution electricity infrastructure. Developers of utility scale PV generation consider areas with good solar resource. Therefore it has become common for utility scale PV developers in South Africa to plan solar generation in the highest solar irradiation areas such as the Northern Cape also known as the "Solar Corridor", as shown in figure 1, which brings with it lower cost of PV generation. However larger penetration of PV generation in such areas as the solar corridor brings with it challenges due to low load centres which then requires upgrading of existing or construction of new transmission lines at high voltage levels. It is evident in figure 1 that South Africa has excellent solar irradiation in most regions with an annual average global horizontal solar irradiation (GHI), which varies approximately between 1,500 kWh/m² and 2,400 kWh/m² which makes PV installation favourable. According to [16], three scenarios have been identified with respect to PV generation integration into the South

Africa utility grid. These integration scenarios were identified as follows:

- Scenario A: As planned

According to existing applications for solar PV farms, 6.4GW will be installed in the solar corridor and 2GW solar PV will be distributed across the country's regions.

- Scenario B: Close to load centers

2.6GW of solar PV will be installed in the solar corridor and 5.8GW solar PV distributed across the country the country's regions.

- Scenario C: According to Renewable Energy Development Zones (REDZ)

2.8GW of solar PV will be installed in the solar corridor and 5.6GW of solar PV will be distributed (predominantly in the REDZ) and more concentrated than scenario B.

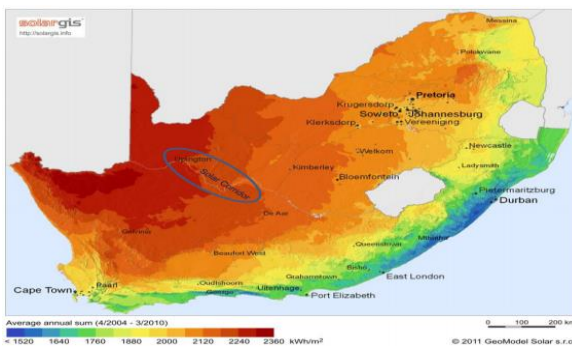


Figure 1: Global Horizontal Irradiation in South Africa Solar Corridor

Table 1 below gives an overview of the solar PV allocation for each province for the three scenarios A, B and C given above.

Table 1: PV allocation per region for scenario A, B and C [16]

Province	Scenario A[MW]	Scenario B[MW]	Scenario C[MW]
Northern Cape	6000	2600	2800
North West	350	750	2100
Free State	500	950	2100
Mpumalanga	250	600	0
Limpopo	500	1050	0
KwaZulu Natal	150	400	0
Gauteng	300	650	0
Eastern Cape	200	750	750
Western Cape	150	650	650
Total	8400	8400	8400

This increasing penetration of large scale PV generation into transmission and distribution network has put tremendous challenge to the power system operators/planners to ensure a reliable and secure grid operation. System operators have to plan for sudden changes in irradiance which can cause rapid disconnection or reduction in PV generation capacity. In South Africa the high penetration of solar PV generation will mainly be concentrated in the Northern Cape as shown in table 1 for all the three integration scenarios given above, in the so called Solar Corridor, therefore the Northern Cape will be used as the benchmark for the this study to analyse the impact of large penetration of PV generation on the utility grid.

2. COMPONENTS OF PV GENERATION

The main components of a PV generation system are the solar cells and the inverter. The size of the PV generator determines the number of solar cells and the number of inverters to be used. PV generation can be divided into two main categories, off grid and grid connected PV systems. Off grid systems are connected as standalone and are connected directly to feed the load. Grid connected PV generation systems are connected to the grid and operate at the same frequency as the grid. The main emphasis of this research is to evaluate the characteristics of grid tied PV generation systems. Figure 2 shows a functional diagram of a grid connected PV system. The dc output current of the PV array I_{pv} is converted to ac and injected into the grid via an inverter. The inverter is built with control and protection functions that includes maximum power point tracking (MPPT), islanding protection as well as protection relays.

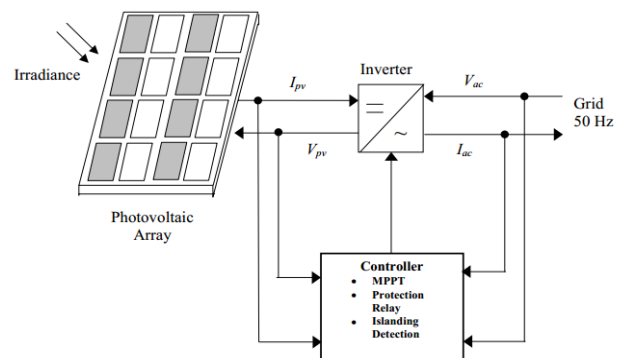


Figure 2: Basic grid tied PV configuration

The equivalent PV cell generator is shown in figure 3 and describe by equation 1 [6, 8].

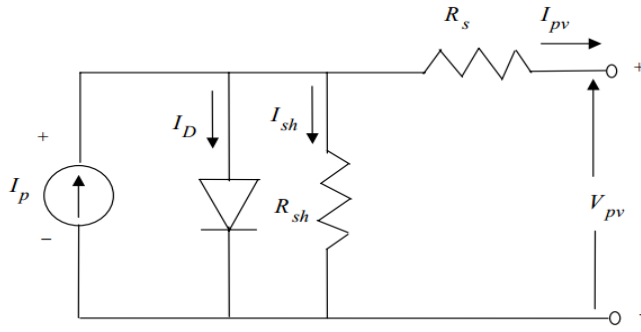


Figure 3: Equivalent Circuit of PV cell

$$I_{PV} = I_P - I_D - I_{sh}$$

$$= I_P - I_0 \left[e^{\frac{q(V_{pv} + R_s I_{pv})}{n k T}} - 1 \right] - \frac{V_{pv} + R_s I_{pv}}{R_{sh}} \quad (1)$$

Where I_P is the photo current, V_{pv} cell terminal voltage, I_D diode current, I_0 saturation current, I_{sh} shunt current, n ideality factor, q electron charge, k Boltzmann's constant, T Junction Temperature, R_s Series Resistance, R_{sh} Shunt Resistance.

The I_{pv} - V_{pv} operating characteristics of a PV solar cell is given in figure 4. In order to get the total output of a PV array, a number of cells are connected in series to obtain a desired voltage and power rating of the PV array. There are 3 operating points of a PV cell that needs to be noted and are given in figure 4. These are the open circuit voltage, the short circuit current and the maximum power point [6, 8].

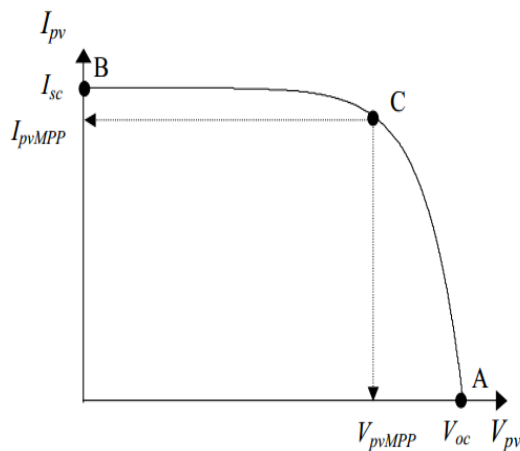


Figure 4: Characteristics of PV cell and operating points

The open circuit voltage (V_{oc}) of the PV cell neglecting the shunt current and the open circuit voltage is represented by equation 2 [7, 8].

$$I_P - I_0 \left[e^{\frac{q(V_{oc})}{n k T}} - 1 \right] = 0$$

$$V_{oc} = \frac{n k T}{q} \ln \left[\frac{I_P + I_0}{I_0} \right] \quad (2)$$

The short circuit condition is given with the series resistance R_s neglected and short circuit condition is represented by equation 3 [8].

$$I_{sc} = I_p \quad (3)$$

When the PV cell is operating at constant irradiance and cell temperature, the operating point of PV array is determined by the intersection of the I_{pv} - V_{pv} characteristic and the load characteristic as shown in figure 5. The load characteristic is represented by a straight line. The operating points move along the I_{pv} - V_{pv} characteristic curve from B to A as the load resistance increases from zero to infinite. Position C is the maximum power operating point. If the load resistance is too high the operating points will be in the CA region and if the load resistance is low the operating region will be in the CB region. Therefore the operating point can be obtained by matching the load resistance to the PV array characteristics.

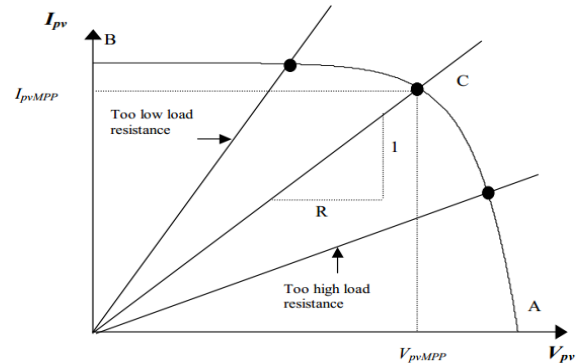


Figure 5: Load Characteristic of a PV Cell

The effect of irradiance and cell temperature on the I_{pv} - V_{pv} characteristic curve is shown in figure 6 and figure 7 respectively. Figure 6 shows that the maximum power output varies almost linearly with the irradiance. Figure 7 shows that the maximum power from the PV array decreases as the temperature increases [8].

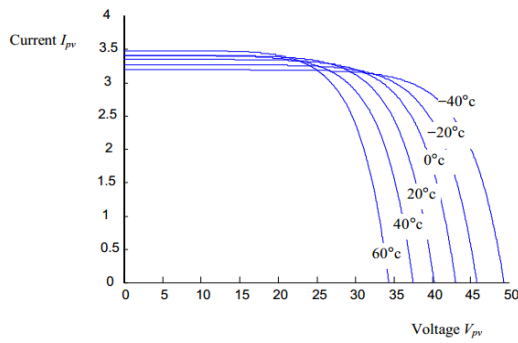


Figure 6: Effect of irradiance on the I-V characteristic at constant temperature

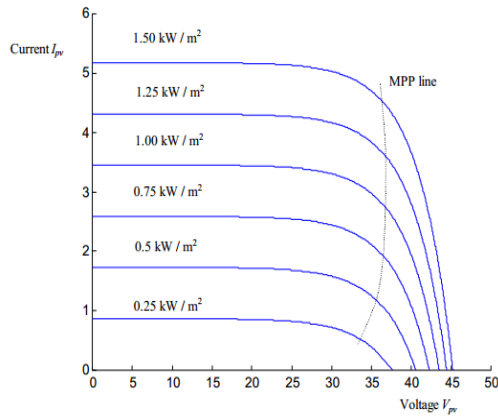


Figure 7: Effective temperature on the I-V characteristic at constant irradiance

The inverter forms part of the grid connected PV system as it converts the dc from the PV array to ac which is connected to the electricity grid. The two most common type of inverters are the thyristor based line commutator inverters (TLCI) and the pulse width modulated (PWM) voltage source inverters. Many existing PV systems use the TLCI type of inverters because of its lower cost. The current can be controlled by varying the firing angle. It is commonly used in grid connected PV systems.

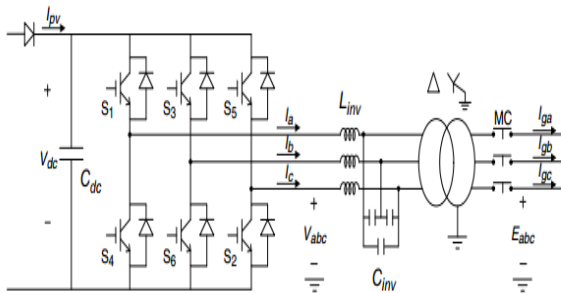


Figure 8: Circuit model of Grid connected inverter

The circuit above include a reverse current blocking diode, dc capacitor, six IGBT switched Voltage Source

Inverters (VSI), LC reduction filter, a step transformer and magnet contact switches for grid interface.

The inverter controller, regulates the real and reactive power of the grid connected PV generator and returns its q- and d- axis current orders, I_q^* and I_d^* , which are inputs to the current controller. The block diagram of the current controller is given in figure 9. The lower level controller generates the desired values of V_q^* and V_d^* , the q- and d-axis components of the inverter terminal voltage. The PWM generator creates the gating signals of $S_1 - S_6$. The protection controller monitors the terminal current magnitude of the inverter, I_{mag} , the grid side voltage magnitude, E_{mag} , and the grid frequency of f_{sys} to determine the grid fault condition and give tripping and closing signals to the MC switches [6].

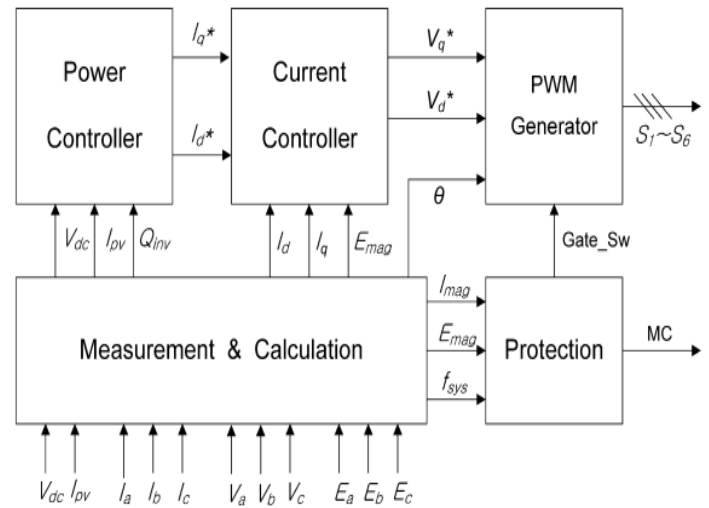


Figure 9: Block diagram of an inverter controller.

The power controller diagram of the inverter is shown in figure 10. In the synchronous reference frame, the real and reactive power of the inverter can be controlled separately by the q-axis current I_q and the d-axis current I_d of the inverter [6]. When I_q is positive, the inverter generates real power and for negative I_q it absorbs real power. When I_d is positive, the inverter absorbs reactive power, when I_d is negative the inverter generates reactive power.

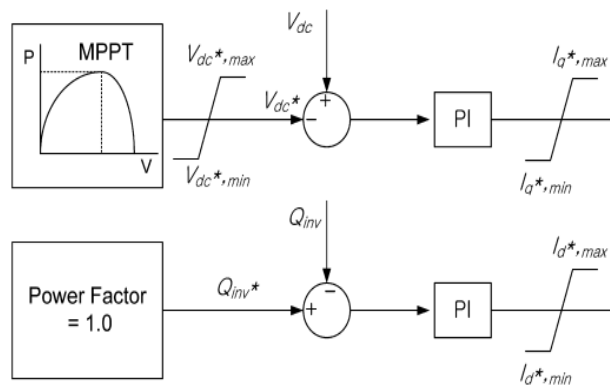


Figure 10: Inverter Power Controller

Real power is controlled by maximum power point tracking (MPPT). The MPPT block generates the desired value of dc-link voltage, V_{dc}^* to be compared to the actual value V_{dc} . The error generated is processed as I_d^* through a proportional integral (PI) controller. Generally, distributed generators are not permitted to regulate the voltage at the point of coupling and control their power generation at or within a specified range of power factor, typically at unity. The error compared between the desired and the actual value of Q_{inv}^* and Q_{inv} , is processed into I_q^* . The q-axis current is limited to the range between $I_{q,min}^*$ and $I_{q,max}^*$ to protect the inverter from excessive heating and reverse current flow through the PV array. The d-axis reference limits of $I_{d,min}^*$ and $I_{d,max}^*$, may be set by considering the q-axis current range and the inverter thermal limit (6).

Islanding of grid connected PV inverters refers to the independent operation of the PV generator when the utility is disconnected. This raises concern because it can be dangerous because of the potential lack of earthing. It therefore places maintenance personnel in danger. As a consequence of this inverters connected to the grid are not permitted to island. Over voltage/undervoltage and frequency protection are essentially incorporated in inverters as anti-islanding protection features. Grid voltage and frequency are constantly checked to detect loss of grid. In the event of loss of grid, the inverter is disconnected within 0.1sec to prevent islanding operation.

The load of grid connected inverters is the utility network. As seen from the inverter, this network looks like an infinity energy sink. The requirements of the grid connected PV system are dictated by the electric utility and each utility imposes unique sets of requirements. These requirements can be divided into protection, power quality operation and safety.

3. CONCLUSION

This research topic will continue to examine the impact of a high level penetration of PV generation on the utility grid which will enable system operators to determine the optimum operation of the utility grid. Varied level of PV penetration will be injected at different percentage to evaluate the changes in system and bus bar voltages. Further studies will examine the impact of high penetration of PV generation under system faulty conditions. These results will then be compared with the requirements of the South African grid code to determine compliancy.

Acknowledgement

The authors would like to acknowledge National Research Foundation, TUT Pretoria and the NUST (PoN), Windhoek for providing necessary research infrastructure to conduct this research project.

5. REFERENCES

- [1] Y. Yang, P.Enjeti, F.Blaabjerg, H. Wang, Suggested Grid Code Modifications to Ensure Wide-Scale Adoption of Photovoltaic Energy in Distributed Power Generation Systems. IEEE, 2013.
- [2] South Africa's Renewable Energy IPP Procurement Program: Success Factors and Lessons, May 2014.
- [3] R. J. V. Overstraeten and R. P. Mertens, "Physics, technology and use of photovoltaic", Adam Hilger, 1986.
- [4] EPIA. Global Market outlook for Photovoltaics 2013-2017.
- [5] EIA. Technology Roadmap: Solar photovoltaic energy, 2010.
- [6] S.K. Kim, J.H.Jeon, C.H.Cho, E.S.Kim, J.B. Ahn. Modeling and simulation of grid-connected PV generation system for electromagnetic transient analysis. Solar Energy 83, 664-678, 2009.
- [7] J. Hernandez, G. Gordillo, W. Vallejo. Predicting the behavior of a grid-connected photovoltaic system from measurements of solar radiation and ambient temperature. Applied Energy 104, 527-537, 2013.
- [8] Planning and installing photovoltaic systems; A guide for installers, architects, and engineers, DGS-2nd edition, 2010.
- [9] M.J. Hosain, T.K.Saha, N.Mathlanathan, H.R.Pota. Robust control strategy for PV system integration in distribution systems. Applied Energy 99, 355-362, 2012.
- [10] S.J.Pinto, G.Panda. Wavelet technique based islanding detection and improved repetitive current control for reliable operation of grid-connected PV systems. Electrical Power Energy Systems 67, 39-51, 2015.
- [11] R. Shah, N.Mithulanathan, R.C. Bansal. Oscillatory stability analysis with penetrations of large scale

- photovoltaic generation. *Energy conversion and management* 65, 420-429, 2013.
- [12] G.Bayrak. A remote islanding detection and control strategy for photovoltaic-based distributed generation. *Applied Energy* 104, 527-537, 2013.
- [13] J.C.Hernandez, J.D.Cruz, B. Ogayar. Electrical protection for grid-interconnection of photovoltaic distributed generation. *Electrical Power Systems Research* 89, 85-99, 2012.
- [14] S.I.Nanou, S.A.Papathanassiou. Modelling of a PV system with grid code compatibility. *Electrical power system research* 116, 301-310, 2014.
- [15] G.Notton,V.Lazarov,L.Stoyanov. Optimal sizing of a grid-connected PV system for various PV module technologies and inclinations, inverter efficiency characteristics and locations. *Renewable energy* 35, 541-554, 2010.
- [16] Analysis of options for the future allocation of PV farms in South Africa, GIZ MPE, 2015

Microgrid and Active Management of Distribution Networks with Renewable Energy Sources

K.T. Akindeji^{1*} and I. E. Davidson²

¹Durban University of Technology, Steve Biko Campus, Durban 4000, South Africa

²Eskom Centre of Excellence in HVDC Engineering, University of KwaZulu-Natal, Durban, 4001, South Africa

*Email: kayodea@dut.ac.za

Abstract: Economic challenges, environmental issues, increased regulation, and changing public perception have contributed to the profound changes or reform been embarked upon by electric utilities. The need to replace the conventional generation of electricity using fossil fuels with renewable energy sources to reduce environmental pollution and global warming has led to changes in the way the electric power distribution network is operated. The distribution network (DN) can no longer be passive but must be active for security, quality and reliability of supply to consumers. Microgrid has evolved over the years as a potential instrument to aggregate these renewable energy sources or distributed generation. Due to the intermittent nature of some renewable energy sources and time-variant loads, smart or intelligent energy management techniques must be employed in a Microgrid. This paper evaluates the role and operation of a Microgrid as a tool for active power management of distribution network with renewable energy sources.

1 INTRODUCTION

The generation of energy through fossil fuel comprising coal, oil and gas is one of the largest sources of CO₂ emissions. More than half of the energy produced using fossil fuel in the vertically integrated system is lost as waste heat into the environment. Also, due to ageing, complexity of most infrastructure and the vertical integration of the three functions of generation, transmission and distribution, the central power generating system is no longer popular [1]. Consequently, there is an ongoing drive for a cleaner, reliable and efficient power grid worldwide [2]. Combining information communication technology with renewable energy (RE) integrated distribution network (DN) can produce new ways of reducing CO₂ emission and also saving energy [3]. Renewable energy sources (RES) such as wind, solar and biomass are gradually taking the place of these traditional energy sources [4]. However, random integration of these RES into the distribution network might cause many problems as it may solve [5]. In recent years, the concept of microgrid has evolved as a technical tool to maximize the potentials of RES. With the integration of RES, the distribution network is no longer passive but now call an active distribution network (ADN) [6]. Microgrid is an old concept having a lot of similarities with the early power systems that generated locally with dedicated

loads [7]. A microgrid can be viewed as an ADN defined as a low voltage network comprising of RES, distributed generator (DG) units and loads connected to the main grid as a single controllable load. In [8], ADN is defined as a distribution network that controls a combination of RES and energy storage system (ESS). Similarly, the authors of [9] defined ADN as a new system that integrates both control and communication technologies to manage and accommodate the new distribution network. ADN could also be seen as an upgrade of the traditional DN that harmonizes or synchronizes RE, ESS and active demands [10]. ADN is described in [8] as DN that has the ability to control a combination of distributed energy resources inform of generator, storage and load. Implementing the microgrid concept to integrate RES eliminates the need to redesign or re-engineer the distribution network [11]. The technical drivers of microgrid include (i) demand for improved reliability, quality and efficiency in power system, (ii) transmission constraints necessitating generation closer to load, (iii) integration RES and (iv) demand for energy security and sustainability as a result of fossil fuels depletion [12]. Hence this paper reviews the role and operation of the microgrid as an active distribution network. The remaining sections of the paper are as follows: Section 2 introduces the microgrid concept and renewable energy sources integration. The need for active management of DN is discussed in section 3 while section 4 highlights methods of active management in microgrid. Conclusions are drawn in section 5.

2 MICROGRID CONCEPT AND RES INTEGRATION

Recently, a lot of factors such as technical, cost and social have fuelled the drive for the implementation of the microgrid concept [13]. Likewise, climate change continues to be a motivation for the global interest in RES to increase the energy and electricity supply capacity worldwide [14]. In South Africa over a period of only three and a half years, 5243 MW was generated from RES with 1827MW supplied to the national grid. It is estimated that this will grow to approximately 7000 GWh per annum by mid-2016 [15]. An estimate of RES contribution to power generation is shown in Table 1 below (Source: Energy in South Africa).

The challenge with RES is the intermittent nature of their energy sources (wind, sun) as such the power

generated is also intermittent or not of a required power quality. As a result, there are stability, reliability and power quality problems when they are connected to the main grid without a technical platform [7], [16].

Table 1: Total Primary Energy Supply in South Africa, 2012

Type of source	Generation capacity (percentage)
Coal	69
Crude Oil	14.8
Gas	2.9
Nuclear	2.4
Hydro	0.1
RES	0.1
Biofuels and Waste	10.7

Voltage and fault current levels are examples of primary network parameters that could change dramatically with high penetration of RES in DN [8]. Also, the consequences of increased penetration of RES inform of distributed generation (DG) as a result of different operating condition in the distribution network include equipment thermal rating, stability issues, voltage rise, protection issues and increased fault levels [9], [11]. Microgrid concept was first introduced by the Consortium for Electric Reliability technology Solutions (CERTS) in USA as a new paradigm shift in distributed generation network with wide range of prospects. CERTS sees generation and associated loads as a subsystem or a “microgrid” [17], [18]. Microgrid operates both in parallel to the main grid and in an island of its own [5]. A transition-to-island mode could occur due to scheduled or unscheduled event, the latter is triggered by fault or loss of grid connection [13]. Examples of the scheduled event includes planned outage or maintenance [12]. In the advent of faults, microgrid must island seamlessly and as fast as possible [19]. Microgrid concept can be applied in various ways, commercial, industrial, residential etc. A residential microgrid is described in [20], where an optimal energy management system for the tertiary control of a household microgrid is presented as shown in figure 1 below.

The output of some RESs could be DC or AC voltages, therefore to interface them with the network power electronics interfaces (PEIs) inform of converters or inverters are used [7]. The developments of these PEIs and other digital controllers have enabled the integration of all types of RES to the DN inform of a self-supported microgrid that operates independently of the main grid in islanded mode [21]. However, a hybrid ac/dc microgrid can be implemented to reduce the number of multiple reverse conversions in an individual ac or dc grid and to enhance the connection of different RES of ac and dc sources and loads to power system [22].

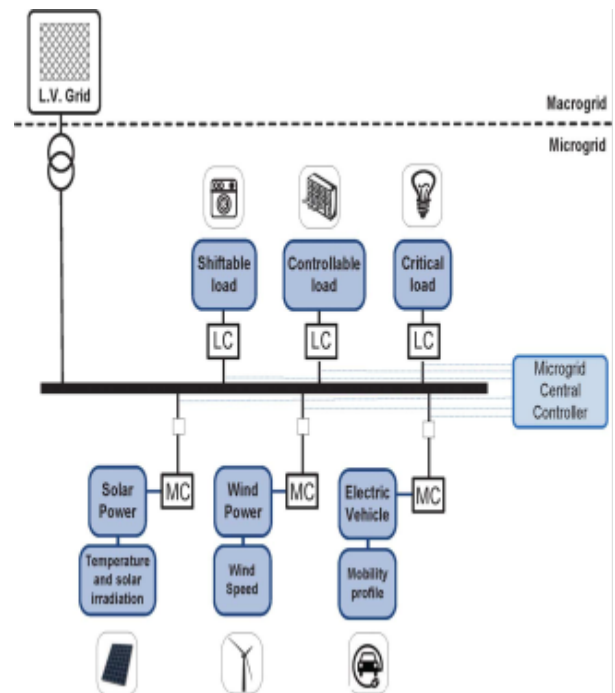


Fig. 1. Residential microgrid representation [20]

As much as there benefits resulting from RES integration, numerous technical, economic and commercial challenges are there to be solved. The current supervisory control and data acquisition (SCADA) system can no longer meet the basic control requirement due to certain limitations for example; lack of communication base in most low voltage sites, poor scalability of technologies, constrained data-rate and limited interoperability due to standard protocol inconsistency [23], [24]. One of the technical problems of high penetration of Res in DN is mismatch between the location of RES and ability of the DN to accommodate new generation without reinforcement [25]. RES integration limitation could also be because of the negative effects on voltage profile and actual voltage regulations as a result of unpredicted power flow [26]. Another prominent short coming of the RES is that the limited energy generated due to climatic conditions of the site cannot be stored for later use. Hence the need for energy storage systems (ESS) they can be of chemical or mechanical type. (Common examples used in Microgrid setup are batteries, fly-wheels, electric vehicles and ultra- capacitors) that stores energy while connected in the grid mode and use it later to supply critical loads in the island mode [7], [27]. ESS also controls the power outputs and provides ancillary services as and when required. The capacitors provide a transient power back up while the batteries are for extended back up [28]. Although not yet researched widely, ESS has been investigated as one of the methods of active network management (ANM). ANM

in this case aims at increasing the amount of energy received from the RES connected to the DN by adapting network or RES parameters without network upgrade [29]. The authors in [23] also indicated that it is possible to make the DN smarter with customer-driven microgrid by giving special consideration to ESS. AM therefore utilizes ESS to alleviate network congestion where there is change in the demand pattern [30]. [31] evaluates the potential of ESS in providing primary voltage control through broadcast signals to control thermal loads. Many ANM pilots, research, trials are already published in literature highlighting voltage control and power control as major reasons for curtailing the integration of RES [32]. The microgrid is connected to the main grid through a point of common coupling (PCC) in form of a static switch for seamless islanding and reconnection as a result of a fault in the main grid [7]. In other words, PCC is the point where the RES DN and loads meet [33]. In most configurations, the RES, ESS and loads are tied together (as a microgrid) on their own feeders, which are linked to the main grid at a single PCC.

3 THE NEED FOR ACTIVE MANAGEMENT

The convectional flow of power in DN was unidirectional until nowadays when more and more Res are being integrated into it. The DN can no longer be seen as a load but also considered as a virtual power plant (VPP) that could supply power to local and even feed the transmission system [10]. In view of the above, the DN should not be treated as a simple PQ-load bus. It is thus obvious that new methods are required to manage and operate the DN as a result of connecting intermittent renewable energy to electricity DN [29]. To utilize effectively the generated renewable energy and for DNOs to allow latent capacity to be used under closely monitored conditions, there is need for active management [34]. Efficient and effective operation of a microgrid depend largely on the strategy used to manage and control the power flows. This strategy relies on the present and forecasted information of the generations, technical constraints, loads and market information on energy trades in order to adjust the net power injected from or to the main , the RES and the controllable loads [9], [35]. Due to the intermittent nature of the RES as a result of climatic variation, there is need for real time interactions between the microgrid and the main grid [2]. Also, in the grid connected mode, there is bidirectional power flows in the entire grid which necessitate redesigning of the power system control and protection [6]. Another major challenge with RES that calls for AM is that the time when the RES produce energy does not often correspond to the period when the energy is needed. For example, in remote or rural areas with photovoltaic (PV) sources, ESS can be used to correct this discrepancy or by

shifting energy consumption period [36]. In view of the above, an intelligent energy management system will be required for a robust and reliable power grid. The microgrid or ADN energy management must not be limited to generation scheduling but taking into consideration the management of the ESS [37]. ADN will help the distribution network operator (DNO) to understand the level of new RES that can be integrated into the network without network upgrade or reinforcement within the operational constraints [38]. As highlighted in [25], AM of DN with high penetration of RES produces better voltage control, power quality enhancement, deferral of DN reinforcement and loss reduction. It must be noted that the inclusion of RES in DN informs the need for a greater level of control (including reactive power control of RES) and protection. The integration of RES is not a “fit and forget” approach, AM must be used to realise the full potential of the network capacity [30].

4 METHODS OF ACTIVE MANAGEMENT IN MICROGRIDS

The rise of renewable generation particularly wind generation in DN has necessitated the development of AM schemes. Generation curtailment is one of such schemes, whereby a generator is instructed to reduce its output under certain conditions [32]. As highlighted in [9], maintaining an acceptable voltage level within the distribution network when there is increased penetration of RES becomes a technical problem that must be solved. Several approaches are recorded in literatures for active management of distribution networks. AM is applied to minimize the use of the existing DN resources by regulating transformer tap positions, generator dispatch, reactive power, voltage regulator in a distributed or centralised manner [8]. In terms of objective, AM principal objective is to reduce the overall system cost through novel control strategies that would make RES or DER to have the same flexibility and controllability similar to the traditional plant [39]. AM makes use of real time control and communication systems to link and utilize the different network assets and participants. In other words, AM focuses on employing control and communication channels for optimal operation of RES [25]. AM schemes as highlighted in [38] include coordinated voltage control, adaptive power factor and energy (generation) curtailment to improve the controllability and reliability of DN. Three AM strategies are described in [25] as follows;

- i. Active power management
- ii. Voltage control using on-load tap-changer (OLTC)
- iii. Reactive power compensation

Several studies reported in [40] focus on active voltage control to address voltage rise issue induced by

RES integration, whereas, the paper itself discusses the cost-benefits of an autonomous regional active network management system (AURA-NMS) that provides both active and flexible control in maintaining voltage and minimize active power loss. Similarly, Zhang et al [24] define AM as controlling and managing RES and DN devices using real time primary system data (i.e. current and voltage). Three active voltage control schemes that aim to increase RES penetration and at the same time maintain DN voltage limits are outlined below;

- i. Power generation curtailment
- ii. On-load-tap-changer voltage control
- iii. Reactive power compensation.

The AM as described is an optimization problem that is solved to minimize the cost of generation curtailment (RES generation) without violating voltage and thermal limits. A demand side management (DSM) is proposed in [36] to actively manage energy generated by RES. The general objective is to shift electric water heater (EWH) load to the time of high Res energy generation using the energy storage capabilities of the EWHs. These include; integrated wide area active network management, active network voltage control, smart metering etc. In [37], a generalized formulation for intelligent energy management system using artificial intelligent techniques combined with linear-programming based multiobjective optimization is proposed for a microgrid. The following methods of AM are described in [8] to mitigate the negative impacts of Res integration; (i) ESS (ii) DSM (iii) dynamic line rating (iv) voltage and power control (v) fault current limiters and (vi) advanced distribution protection.

A structure that is made up of real-time dynamic thermal rating (DTR) and coordinated voltage control (CVC) is proposed in [41] to solve the problems of voltage quality and thermal limit. This scheme makes use of OLTC, active and reactive power control and RPC. [42] describes a centralised voltage control scheme, model predictive control (MPC) to regulate DN voltages in the presence of high RES integration. Three categories of AM framework are discussed in [43]. The centralised framework controls the voltage and power flow by adjusting active and reactive power from RES. The second framework is the decentralised control system whereby control decisions are based on load information of each device. The third is the hybrid hierarchical management that combines that last two and has a multi-layer structure. In terms of AM, application of smart grid technologies to DN will lead to quicker detection and analysis of data as a result of real-time information transmission, the smart DN will be able to take corrective action per time. In other words, smart grid ensures a balance between demand and supply by automatic control of generation and load. Smart DN intelligently control all elements connected to the DN, matching closely supply with demand thereby improving efficiency and reliability [3][44][45].

5 CONCLUSION

This paper summaries the challenges of RES integration and the methods of AM available to solve some of these problems. The microgrid as described in this paper is a technical framework designed to ingrate more RES into the DN in order to maximize the free potential of RES in reducing the impacts of CO₂ emission globally and ultimately reduce the cost of energy. Implementing the microgrid concept with ICT tools to actively manage the emerging power grids will further improve the security, reliability and quality of supply to the end user of DN.

6 REFERENCES

- [1] A. K. Basu, S. P. Chowdhury, S. Chowdhury and S. Paul, "Microgrid: energy management by strategic deployment of DERs-A Comprehensive survey," *Renewable and Sustainable Energy Reviews* 2011; 15:4348-4356.
- [2] Y. A. I. Mohamed, and A. A. Radwan, "Hierarchical Control System for Robust Microgrid Operation and Seamless Mode Transfer in Active distribution systems," *IEEE Trans. Smart Grid*, vol. 2, No.2, pp. 352-362, June 2011.
- [3] Miceli, Rosario, "Energy management and smart grids." *Energies*, vol. 6, no. 4, pp. 2262-2290, 2013.
- [4] G. Bayrak, and M. Cebeci, "Grid connected fuel cell and pv hybrid power generating system design with Matlab Simulink," *International Journal of Hydrogen Energy*, No. 39, pp. 8803-8812, 2014.
- [5] M. S. Mahmoud, S. A. Hussain, and M. A. Abido, "Modeling and control of microgrid: An overview," *Journal of the Franklin Institute*, No. 351, pp. 2822-2859, 2014.
- [6] S. Chowdhury, S. P. Chowdhury, and P. Crossley, "Microgrids and Active Distribution Networks," *The Institution of Engineering and Technology*, London, United Kingdom, 2009.
- [7] F. A. Hina, and K. Palanisamy, "Optimization in microgrids with hybrid energy systems-A review." *Renewable and Sustainable Energy Reviews* 2015; 45:431-446.
- [8] H. Rodrigo, C. Abbey, and G. Joos, "A review of active distribution networks enabling technologies." In *IEEE Power and Energy Society General Meeting*, pp. 1-9, 2010.
- [9] T. J. Hashim, A. Mohamed, and H. Shareef, "A review on voltage control methods for active distribution networks," *Prz. Elektrotech.*, vol. 88, pp. 304-312, Jun. 2012.
- [10] J. Hongjie, W. Qi, Z. Liu, B. Wang, Y. Zeng, and T. Xu, "Hierarchical Risk Assessment of Transmission System Considering the Influence of Active Distribution Network." *IEEE Transactions on Power Systems*, vol. 30, no. 2, pp. 1084-1093, March 2015.
- [11] Y. A. I. Mohamed, and A. A. Radwan, "Hierarchical Control System for Robust Microgrid Operation and Seamless Mode Transfer in Active distribution systems," *IEEE Trans. Smart Grid*, vol. 2, No.2, pp. 352-362, June 2011.
- [12] F. Qiang, A. Nasiri, V. Bhavaraju, A. Solanki, T. Abdallah, and D. C. Yu, "Transition management of microgrids with high penetration of renewable energy." *IEEE Transactions on Smart Grid*, vol. 5, no. 2, pp. 539-549, March 2014.
- [13] Z. Binyan, X. Dong, and J. Bornemann, "Service Restoration for a Renewable-Powered Microgrid in Unscheduled Island Mode." *IEEE Transactions on Smart Grid*, vol 6, no. 3, pp. 1128-1136, May 2015.
- [14] D. Pudjianto, C. Ramsay, and G. Strbac, "Microgrids and virtual power plants: concepts to support the integration of distributed energy resources." *Proceedings of the Institution of Mechanical Engineers, Part A: Journal of Power and Energy*, vol. 222, no. 7, pp. 731-741, 2008.

- [15] Department of Energy, South Africa: Annual Report for 2014/15 Financial Year.
- [16] A. Etxeberria, I. Vechiu, H. Camblong, and J. M. Vinassa, "Hybrid energy storage systems for renewable energy sources integration in microgrids: A review." In IPEC, 2010 Conference Proceedings, pp. 532-537, October 2010.
- [17] S. M. Hakimi, and S. M. Moghaddas-Tafreshi. "Optimal planning of a smart microgrid including demand response and intermittent renewable energy resources." IEEE Transactions on Smart Grid, vol. 5, no. 6, pp. 2889-2900, November 2014.
- [18] A. Eduardo, T. Brown, E. Minear, and R. H. Lasseter. "CERTS microgrid demonstration with large-scale energy storage and renewable generation." IEEE Transactions on Smart Grid, vol. 5, no. 2, pp. 937-943, March 2014.
- [19] C. L. Moreira, and J. A. Lopes. "Microgrids operation and control under emergency conditions." Intelligent Automation & Soft Computing, vol. 16, no. 2, pp. 255-272, 2010.
- [20] I. Lucia, C. Corchero, M. Cruz-Zambrano, and F. Heredia. "Optimal energy management for a residential microgrid including a vehicle-to-grid system." IEEE Transactions on Smart Grid, vol. 5, no. 4, pp. 2163-2172, July 2014.
- [21] S. Dasgupta, S. K. Sahoo, S. K. Panda and G. A. J. Amaratunga, "Single-Phase inverter-Control Techniques for Interfacing Renewable Energy Sources with Microgrid-Part II: series-Connected Inverter Topology to Mitigate Voltage-Related problems Along With Active Power Flow Control," IEEE Trans. Power Electronics, vol. 26, No.3, pp. 732-746, March 2011.
- [22] L. Xiong, P. Wang, and P. C. Loh. "A hybrid AC/DC microgrid and its coordination control." IEEE Transactions on Smart Grid, vol. 2, no. 2, pp. 278-286, June 2011.
- [23] H. S. V. S. Nunna, and S. Doolla. "Multiagent-based distributed-energy-resource management for intelligent microgrids." IEEE Transactions on Industrial Electronics, vol. 60, no. 4, pp. 1678-1687, April 2013.
- [24] Z. Jietan, H. Cheng, and C. Wang. "Technical and economic impacts of active management on distribution network." International Journal of Electrical Power & Energy Systems, vol. 31, no. 2, pp. 130-138, 2009.
- [25] A. Saeed, K. Zare, and B. Mohammadi-Ivatloo. "Evaluation of technical risks in distribution network along with distributed generation based on active management." IET Generation, Transmission & Distribution, vol. 8, no. 4, pp. 609-618, 2014.
- [26] B. Johanna, and R. Majumder. "Integration of distributed generation in the volt/VAR management system for active distribution networks." IEEE Transactions on Smart Grid, vol. 6, no. 2, pp. 576-586, March 2015.
- [27] L. P. Chiang, Y. K. Chai, D. Li, and F. Blaabjerg. "Autonomous operation of distributed storages in microgrids." IET Power Electronics, vol. 7, no. 1, pp. 23-30, 2014.
- [28] S. S. Thale, R. G. Wandhare, and V. Agarwal, "A Novel Reconfigurable Microgrid Architecture With Renewable energy sources and Storage," IEEE Trans. Industry Applications, vol. 51, No.2, pp. 1805-1816, March/April 2015.
- [29] C. Stephen, G. C. Premier, A. J. Guwy, R. M. Dinsdale, and J. Maddy. "Energy storage for active network management on electricity distribution networks with wind power." IET Renewable Power Generation, vol. 8, no. 3, pp. 249-259, 2014.
- [30] M. Jim. "Adaptive intelligent power systems: Active distribution networks." Energy Policy, vol. 36, no. 12, pp. 4346-4351, 2008.
- [31] C. Konstantina, D. C. Tomozei, M. Bahramipanah, J-Y. Le Boudec, and M. Paolone. "Primary voltage control in active distribution networks via broadcast signals: the case of distributed storage." IEEE Transactions on Smart Grid, vol. 5, no. 5, pp. 2314-2325, September 2014.
- [32] K. Laura, and G. W. Ault. "Evaluation of Wind Power Curtailment in Active Network Management Schemes." IEEE Transactions on Power Systems, vol. 30, no. 2, pp. 672-679, March 2015.
- [33] S. Wencong, and J. Wang. "Energy management systems in microgrid operations." The Electricity Journal, vol. 25, no. 8, pp. 45-60, October 2012.
- [34] M. Z. Degefa, M. Humayun, A. Safdarian, M. Koivisto, R. J. Millar, and M. Lehtonen. "Unlocking distribution network capacity through real-time thermal rating for high penetration of DGs." Electric Power Systems Research, vol. 117, pp. 36-46, 2014.
- [35] W. Shi, X. Xie, C. Chu and R. Gadh, "Distributed Optimal Energy Management in microgrids," IEEE Trans. Smart Grid, vol. 6, No.3, pp. 1137-1146, May 2015.
- [36] M. Ondrej, and P. Havel. "Active demand-side management system to facilitate integration of res in low-voltage distribution networks." IEEE Transactions on Sustainable Energy, vol. 5, no. 2, pp. 673-681, April 2014.
- [37] A. Chaouachi, R. M. Kamel, R. Andoulsi and K. Nagasaka, "Multiobjective Intelligent Energy Management for a Microgrids," IEEE Trans. Industrial electronics, vol. 60, No.4, pp. 1688-1699, April 2013.
- [38] L. F. Ochoa, C. J. Dent, and G. P. Harrison. "Distribution network capacity assessment: Variable DG and active networks." IEEE Transactions on Power Systems, vol. 25, no. 1, pp. 87-95, February 2010.
- [39] J. Mutale, "Benefits of active management of distribution networks with distributed generation." In IEEE Power Systems Conference and Exposition, PSCE'06, pp. 601-606, 2006.
- [40] H. Zechun, and F. Li. "Cost-benefit analyses of active distribution network management, part I: Annual benefit analysis." IEEE Transactions on Smart Grid, vol. 3, no. 3, pp. 1067-1074, September 2012.
- [41] M. Z. Degefa, M. Lehtonen, R. J. Millar, A. Alahäivälä, and E. Saarijärvi. "Optimal voltage control strategies for day-ahead active distribution network operation." Electric Power Systems Research, vol. 127, pp. 41-52, 2015.
- [42] V. Gustavo, and T. Van Cutsem. "Model predictive control of voltages in active distribution networks." IEEE Transactions on Smart Grid, vol. 4, no. 4, pp. 2152-2161, December 2013.
- [43] Z. Junhui, C. Wang, B. Zhao, F. L. Q. Zhou, and Y. Wang. "A review of active management for distribution networks: Current status and future development trends." Electric Power Components and Systems, vol. 42, no. 3-4, pp. 280-293, 2014.
- [44] V. E. Nnaemeka, and S. D. Yusuf. "Integrating renewable energy and smart grid technology into the Nigerian electricity grid system." Smart Grid and Renewable Energy, vol. 5, pp. 220-238, 2014.
- [45] P. Oshevire, T. Oladimeji, and S. Onohaebi. "Smart Grid Technology and Its Possible Applications to the Nigeria 330 kV Power System." Smart Grid and Renewable Energy, vol. 4, no. 05, pp. 391-397, 2014.

RELIABILITY CENTERED MAINTENANCE (RCM) MODEL IMPLEMENTATION TO ETHEKWINI ELECTRICITY NETWORK

M.P Lokothwayo^{1*} and G. Frederick d'Almaine²

Durban University of Technology, Power Engineering Dept., Durban 4000, South Africa

Email: *Email: mplokothwayo@gmail.com, dalmaine@dut.ac.za

Abstract: Traditionally power utilities have developed and conducted maintenance activities on their equipment without using a quantitative approach to the system. When maintenance measures are utilised effectively they can impact on reliability by either enhancing the state of equipment or extending the lifetime of equipment at a minimum budget. Presently, maintenance activities are heuristic. This paper presents a model for the implementation of reliability centered maintenance to the eThekweni power network. In selecting a critical component, historical data of failure is thoroughly analysed. Transformer was found to be a critical component for the system under study.

Keywords: Maintenance; Reliability; asset management; transformer; Heuristic; IEEE Std C57.104-1991

1. INTRODUCTION

Power system planning, design, operations and maintenance are significant factors for the financial success and customer satisfaction of a power system [1]. Traditionally, municipalities have conducted equipment maintenance according to predetermined schedules based on manufacturer guidelines [2]. Consequently, it often difficult to determine with a reasonable degree of confidence, what the best frequency of inspection is or even what should be inspected. As a result, some maintenance techniques are far more costly than they should be, and critical equipment is often unnecessarily taken out of service for prolonged periods of time [3].

The implementation of reliability centered maintenance (RCM) in the power system sector can optimise maintenance processes with minimum cost [21]. RCM is condition-based, with maintenance intervals based on actual equipment criticality and historical failure data [4]. The RCM model was first developed in the late 1960s, by the airline industry which concentrates on avoiding failures whose results are almost certain to be serious [5]. On account of the increased size and complicated nature of commercial aeroplanes, airlines were worried that utilising conventional maintenance techniques would make the new aeroplanes uneconomical [5]. After the effective implementation of RCM in the aviation industry, numerous industries commenced applying the RCM concept in their sectors [6]. In this paper, the RCM model is applied to the eThekweni electricity (EE) network.

2. NETWORK DESCRIPTION

EThekweni Electricity is one of the largest power utilities in South Africa (SA) and serves more than 723 593 customers in a region covering about 2,000 kilometers with approximately 1 900 MW system

maximum demand [23]. It has a turnover of over R7 billion and an asset value of R17, 7 billion [23]. EE receives bulk power from Eskom at five intake points at 275 kV which is then transformed to the lower voltages required by residential, business, commercial and industrial customers at 230 V, 400 V and 11 kV via power transformers. The visual representation in figure 1 indicates the EE geographical map and bulk power received from Eskom at the five intake points. At these stations, the voltage is transformed down to 132 kV for onward transmission via eThekweni's transmission network to over 100 major step-down substations.

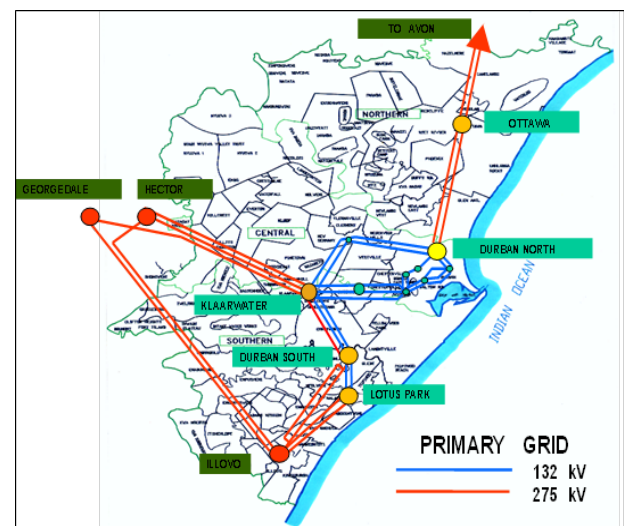


Fig. 1: Shows general lay-out of the Eskom/EThekweni High Voltage Network

The EE Network is complex and highly integrated and, for this reason, is segmented into three regions; (1) Northern, (2) Central and (3) Southern. Within these regions, there are six construction works Depots namely; Central, Western, Northern, North Western, Southern, South Western which are responsible for the construction works and maintenance activities of the entire EE network. North Western construction works

Depot with reference to Phoenix substation, had the feeder with the greatest failure rates for the period considered. Therefore, the study was centered on this region which is made up of a mix of residential, commercial and industrial customers.

Fig. 2 shows a single line diagram indicating a portion of the Northern region network, made up of seven major substations fed from Ottawa Major Substation. These stations are fed by 2x315 MVA, 275/132 kV power transformers. From these seven major stations many 11 kV customer feeds are tapped off. The feeder subjected to most failures was found to be fed from Phoenix substation.

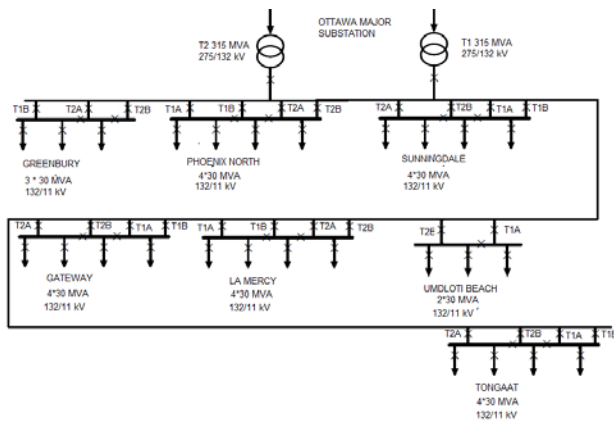


Fig. 2: Line diagram showing major substations in the Northern region

3. RCM MODEL IMPLEMENTATION

3.1. Failure Data Gathering

RCM starts with collecting and examining failure data for the system considered. Maintenance planning constitutes a fundamental part of asset management [2]. In most utilities, this important element of asset management may get no consideration at all or at best very restricted attention. The outputs of this would be frequent power interruptions associated with equipment failures/repairs.

The present power system requires an effective method for determining maintenance activities of critical components. The collection and development of a components database is the foundation of this process. This will assist in deriving the failure sample space. It is the resulting analysis of the sample space that will give valuable knowledge into the failure rate and time to failure of each component. These are the necessary construction blocks for the RCM program [5]. Choosing the type of data to collect and the method of collection

is the initial step for a successful maintenance policy based on records of failure data [14]. EThekweni Electricity uses a system called Ellipse to facilitate business processes within the organisation. All the outages and their causes are captured and recorded on the Ellipse System referred by their order numbers. This system enables the user to extrapolate the outage information as needed at that certain time. To accomplish the objectives of this study, the outage information was exported from the Ellipse System and examined. In identifying the feeder with the higher failure rate for greater attention, five years (2010 to 2014) of outages information was collected and processed from the Ellipse system for the entire EE network. This was then plotted on the histogram presented in figures 3. The feeder with the highest failure rate was then selected for deeper analysis. For the purpose of this work all the irrelevant events such as outages due load shedding and scheduled maintenance were excluded.

3.2. Data Analysis Techniques

The failure sample space must be thoroughly considered in order to produce meaningful results from the collected data. This was achieved by building a histogram over the sample space. This basic histogram instantly gives indication of the leading failure events and similarly the region or customer feeder that is mostly affected. Thereafter, the properties of the total component leading to failure can be considered before going deeper into the statistical analysis of the components. Figures 3 shows the failure histogram built for EE Network failure data consisting of six Depots.

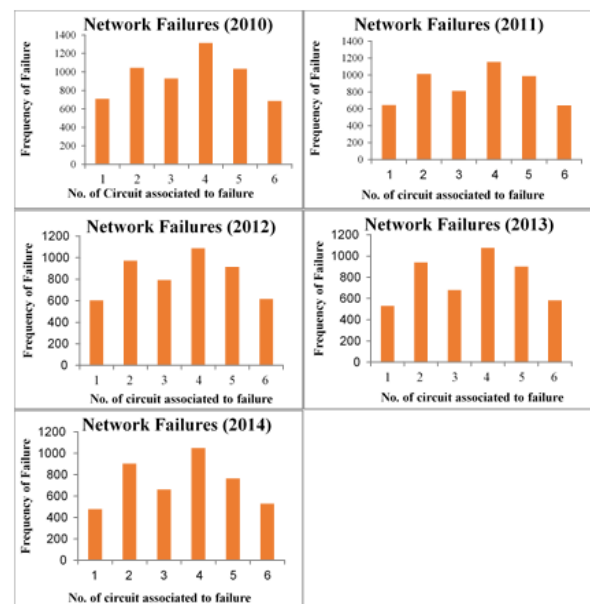


Fig.3: Processed failure data for EE area of supply

The Phoenix substation in the North Western Depot in the Northern region of the EE area of supply was found to have higher than normal failure rates and was selected for deeper analysis. In order to better understand exactly what is going on in North Western Depot, further analysis of the failure data of this particular Depot was conducted. This was graphically illustrated in the histogram shown in figures 4. This information is useful to the asset manager to help focus more attention on this feeder to determine the component/components responsible for the high rate of failure in that feeder.

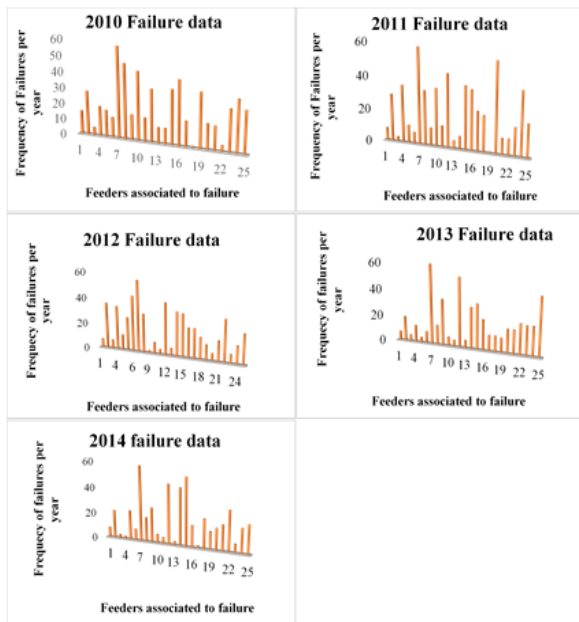


Fig. 4: Processed Outage data for Phoenix station feeders

Further analysis of the data indicates that, Feeder seven (F7) of the Phoenix major substation has the leading failure rate. Using this information the components making up feeder 7 (F7) were probed in greater depth. Six groups of electrical components are found in distribution power system, which includes; (1) overhead lines, (2) underground cables, (3) protective equipment's, (4) power transformers, (5) distribution transformers, and (6) capacitors. In analyzing these components, only those maintenance impact was identified as critical were considered. The analysis of the failure data collected on this critical feeder when plotted on the histogram showed that the components of the distribution system presenting the greatest challenge to uninterrupted operation of power included; overhead line conductors, power transformers and underground cables. This plot is shown in figure 5. From this plot the transformer was identified as the critical item of equipment to customer's electric power interruption.

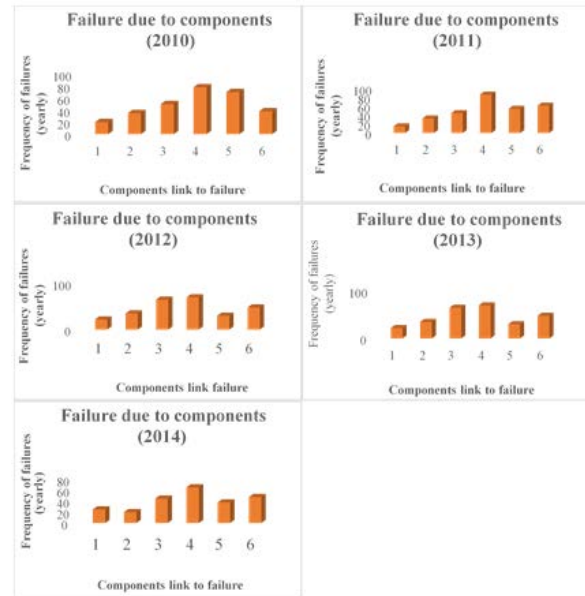


Fig. 5: Processed components data for critical feeder

Transformers are one of the assets that have a critical function in power systems. The failure of a transformer can result in massive financial losses because of unsupplied power to customers, repair expense including labor, and negatively affects supply reliability to customers [7]. It is therefore important to know the condition and performance of power transformer in the system. EE is responsible for the maintenance of more than 10 000 transformers. Of these, roughly 250 function at voltages between 275, 132 and 33 kV to provide the primary network from which the other distribution level transformers and major customers are supplied. The ratings of these transformers, which have an average age of twenty-five years, are from 315 to 15 MVA. The economy is highly dependent on electricity and the maintenance of transformers and discovery of faults in them is an essential factor of infrastructure support for the economy [7]. A typical single line diagram for eThekweni network is presented in figure 6 below.

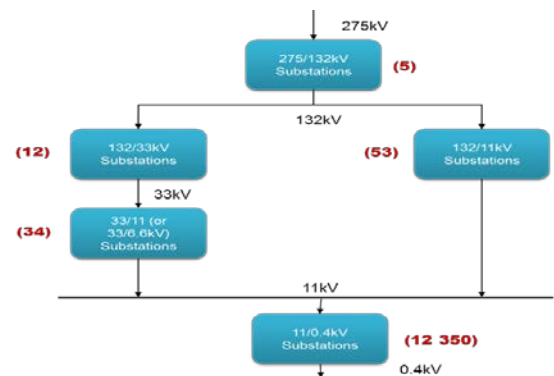


Fig 6: Typical line diagram for eThekweni Network [22]

4. MAINTENANCE TASK SELECTION

Maintenance task selection involves the identification of appropriate tasks to address the cause of critical failure modes identified as a result of the RCM systems evaluation i.e. selecting tasks involves the identification of applicable and cost effective approaches to maintenance that are best suited to maintain system equipment [8]. According to figure 7, the maintenance is classified into corrective maintenance, preventive maintenance and reliability centered maintenance.

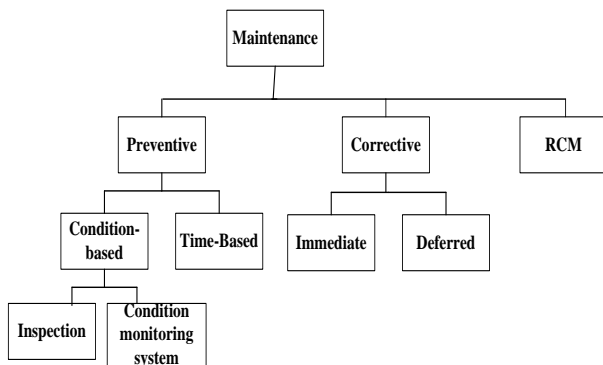


Fig. 7: Classification of maintenance activities [8]

To appropriately select the maintenance tasks necessary to address the causes of critical equipment failure modes, a standardized approach was used.

4.1. Transformer Failure Modes

A failure mode is a way in which a component or machine failure can happen, usually in terms of how the failure is observed (in contrast to how the failure is caused) [3]. For instance, the dielectric breakdown of transformer oil is a failure mode, which may have several reasons, for example, oil pollution, oil oxidization, thermal decomposition, and humidity in oil from cellulose breakdown [9].

4.2. Transformer Failure Causes

Transformers fail for various reasons, which can interrupt electricity supply, cause potential risk to operators, loss in industrial production and to economic losses [13]. Financial outcomes of transformer failure can be substantial, because of the expense of property damage, repair cost, and the production losses due to service interruption [10]. The most frequent causes of failures are presented in figure 8. The leading cause of transformer failure is an insulation failure. The life of a transformer is dependent upon the life of its insulation [11]. Transformer insulation deteriorates as a function

of time and temperature [11]. The lifespan of the transformer is generally achieved by effective maintenance planning, site inspections and appropriate testing during the transformers useful life.

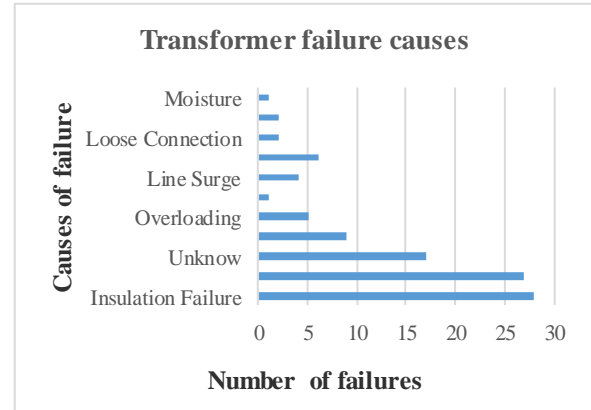


Fig. 8: Failure mode distribution for transformers [12]

5. INSULATION CONDITION EXAMINATION

The oil insulation condition examination is conducted with reference to eThekweni transformer identified as critical. Power transformer's serve as the one of the most critical assets in eThekweni's power network. Transformer procurement comprise about 60 percent of the total substation costs [16]. These transformers need significant attention due to their cost, which extends from R1-million to R14-million for each unit, and the possible consequence of failure [15]. Examining the oil state of the transformer can assist in detecting any premature deterioration [17]. A typical picture of 132/11 kV is illustrated in figure 8 below.



Fig. 9: Picture of 132/11 kV Transformer, 30 MVA

5.1. Dissolved Gas-In-Oil Analysis

According to [20], Dissolved gas analysis (DGA) can be interpreted by various international guidelines. Nevertheless, interpretation of DGA is more of an art than an exact science [20]. DGA test measures various gas ppm levels that are present [17]. Inside the transformer the gasses will dissolve in the oil which indicate different types of thermal and electrical stress developing [16]. "The health of the oil reflects the health of the transformer itself" [19]. The DGA results is very useful to help in diagnosing a fault [17]. DGA is conducted by taking oil samples test from the transformer least once a year depending on the age and state of the transformer [12]. In this work, oil tests are interpreted using the criteria found in [18] for the transformer under consideration.

5.2. Dissolved gas analysis Interpretation

Table 1 provide the oil sample test taken from the eThekweni transformer under consideration. These results are interpreted base on the IEEE standard criteria in [18]. This criteria classify oil condition under four groups as follows:

- (1) **Condition one (C_1) means** - Satisfactory;
- (2) **Condition two (C_2) means** - Should be reconditioned for further use;
- (3) **Condition three (C_3) indicates** - level of decomposition (additional investigation required);
- (4) **Condition three (C_4) means** - Poor condition, dispose and replace (Continued operation could result in failure of the transformer).

Using this criteria, for the transformer under consideration we found the oil condition to be condition two (C_2). So, this mean that the oil can reconditioned for further use. Please refer to appendix A1 for more detail.

Table 1: DGA from 132/11kV eThekweni transformer

Sample Date	CO	H ₂	CH ₄	C ₂ H ₄	C ₂ H ₆	C ₂ H ₂	TDCG
2001/07/25	604	81	16	22	24	26	773
2002/10/23	700	61	14	0	30	29	834
2004/12/20	650	54	11	26	30	20	791
2005/06/15	708	47	0	0	0	0	755
2007/06/22	755	46	11	0	0	0	812
2009/01/07	750	0	27	34	0	16	827
2010/09/15	780	0	1	3	0	2	787
2011/11/23	680	43	27	35	21	16	822
2012/06/19	850	42	8	1	13	6	920
2013/10/23	860	43	28	5	10	4	950

The maintenance activity is chosen based on the condition of oil. In the event that oil condition is C_1 , nothing is done. On the possibility that oil condition is

C_2 , C_3 or C_4 , three alternatives are accessible and are chosen with distinctive probabilities: **oil filtering** or **oil substitution** or **oil replacement**.

6. APPENDIX A

Status	H ₂	CH ₄	C ₂ H ₂	C ₂ H ₄	C ₂ H ₆	CO	CO ₂	TDCG
Condition 1	100	120	35	50	65	350	2500	720
Condition 2	101-700	121-400	36-50	51-100	66-100	351-570	2501-4000	721-1920
Condition 3	701-1800	401-1000	51-80	101-200	101-150	571-1400	4001-10000	1921-4630
Condition 4	>1800	>1000	>80	>200	>150	>1400	>10000	>4630

Appendix A1: Dissolved gas concentrations limits (ppm)

7. CONCLUSION

In conclusion, this paper has presented the implementation of the RCM model to eThekweni electricity network. The RCM model has been discussed in details. The transformer was selected as a critical component for the network under consideration and examined in detail. Transformer outage has risky effects on the system and can be assumed as one of the most catastrophic outages. Accordingly, maintenance of the transformers should be planned carefully to avoid harmful outages. The RCM approach in power system is promising to provide an opportunity to justify one of the most vulnerable economic sectors in developing countries by improving design, operations and maintenance of equipment or system. The adaption of the RCM model to power system equipment's will aids to optimization of resources there by decreasing maintenance expenditures while improving the overall system reliability and improve service delivery to the end users. The RCM model is not only limited to power transformers, it can be applied to any asset in the power system.

8. RECOMMENDATION

It is recommended that EThekweni Electricity give more attention on acquiring and understanding the state of all transformers in the system. Moreover, development of computer models to determine the equipment's average remaining life are needed in today power system.

9. ACKNOWLEDGMENT

The authors wish to acknowledge the Durban University of Technology for funding work. We also acknowledge all the individuals who contributed to the improvement of this work.

10. REFERENCES

- [1] Willis, L.H, "Power distribution planning Reference Book", Marcel Decker INC, NY, 1997.
- [2] IEEE/PES Task Force on Impact of Maintenance Strategy on Reliability, "Impact of maintenance strategy on reliability", Final report, July 1999.
- [3] Allan, R.N, Billinton, R Shaidehpour, S.M and Singh, C., "Bibliography on the Application of Probability methods in power system Reliability Evaluation", 1982-1987, IEEE Transactions on power systems 3 (4), November 1988.
- [4] H. Jae-Haeng et al., "A Reliability-Centered Approach to an Optimal Maintenance Strategy in Transmission Systems Using a Genetic Algorithm", IEEE Transactions on Power Delivery, vol. 26, no. 4, pp. 2171-2179, Oct. 2011.
- [5] "Application of Reliability Centered Maintenance to Optimize Operation and Maintenance in Nuclear Power Plants, Report, May 2007.
- [6] J. Moubray, Reliability-Centered Maintenance, 2nd Ed. New York: Industrial Press, 1997.
- [7] T .Dold, Early Detection of Electrical Transformer Faults by using Sweep Frequency Response Analysis, EThekweni Municipality, 2007.
- [8] Reliability centered maintenance technical reference for substations, EPRI TR-106418, 3882, final report, June 1996.
- [9] M.Wang, A. J. Vandermaar, K. D. Srivastava, "Review of condition assessment of power transformers in service," Electrical Insulation Magazine, IEEE Vol. 18, Issue 6, Nov.-Dec. 2002 pp.12- 25.
- [10] M. Minhas, P. de. Klerk, J. Reynnders, "A study of failure modes of large power transformer," Proc of 10th International Symposium on High Voltage Engineer, Montreal, Canada, Aug 25-29, 1997.
- [11] Milos Hammer, Jakub Ertl, Ondrej Janda "Estimation of reliability characteristics of power oil transformers", March 5, 2012.
- [12] M Hammer, J Ertl, O Janda, "Estimation of reliability characteristics of power oil transformers", Engineering Mechanics, 2012.
- [13] W. R. Blischke, D.N. Prabhakar Murthy "Reliability, modeling, prediction and optimization," John Wiley & Sons, 2000.
- [14] Apelgren R., "Using P – F Intervals to map and avert failures", Applied reliability, Reliability plant magazine, March – April, pp. 5-7, 2008.
- [15] T .Dold, Early Detection of Electrical Transformer Faults by using Sweep Frequency Response Analysis, EThekweni Municipality, 2007.
- [16] Chatterton B G, "Network Reliability Measurement, Reporting, Benchmarking and Alignment with International Practices", Eskom Distribution Technology, 2004.
- [17] L. R. Lewand, "Using dissolved gas analysis to detect active faults in oil-insulated electrical equipment", Sep. 2010.
- [18] IEEE Std C57.104-1991, "IEEE Guide for the Interpretation of Gases Generated in Oil-Immersed Transformers."
- [19] Hydro Plant Risk Assessment Guide, "Transformer Condition Assessment", Appendix E5, September 2006.
- [20] I.A.R. Gray, a guide to transformer oil analysis, transformer chemistry services.
- [21] Cooper, G.R., McGillem, C.D., "Probabilistic methods of Signal and System analysis", 1999.
- [22] "EThekweni electricity smart grid strategy", pg. 16, version 1.0, 2015-2020.

- [23] http://www.durban.gov.za/City_Services/electricity/Documents/2012-2013%20Annual%20Report.pdf.

AUTHORS



Musawenkosi Lokothwayo was born in Durban, South Africa on August 08, 1985. He has National Diploma and BTech degree in electrical from Mangosuthu University of Technology and Durban University of Technology respectively. From 2012, his is pursuing Masters in electrical Engineering at Durban University of Technology. He is registered with ECSA as Candidate Technician. His research interests are on electrical power system planning, design, operation optimization and cost effective maintenance planning.



G. Frederick d'Almaine is a Senior Director in the Department of Power Engineering at the Durban University of Technology. He specializes in power systems both on grid and off grid and is a director of the Real Time Power System Simulator at the university.

Energy Management and Efficiency on a Traction Network through Regenerative Braking

A. Bani^{1,2*}, K. Awodele²

¹ Passenger Rail Agency of South Africa,
OFF Malta Road, Salt River 7925, South Africa

² University of Cape Town,
Department of Electrical Engineering,
Private Bag X3, Rondebosch, 7701, South Africa
*Email: abani662@gmail.com

Abstract: This paper presents an Energy Efficiency Management System for DC Traction Network. Regenerative braking system, Energy Storage and Rearrangement of the incoming Power supplies are considered in the paper. The regenerative braking concept is further used to have a spare motor capable of generating power whenever needed. This generated power will be mostly used during peak hours when the network is congested with traffic. The energy efficiency system will reduce the energy usage tremendously and the saved funds could be used elsewhere to improve the system even further. An extension of the 33 kV AC line would also be considered.

Keywords: Regenerative Braking; Energy Efficiency; Standby Generator; Energy Storage

1 INTRODUCTION

The traction system of Passenger Rail Agency of South Africa (PRASA) is supplied by a 3 kV DC network. Each single line (overhead 3 kV DC) is fed by two adjacent substations using one set of rail as the negative return.

Most PRASA 3 kV DC substations are double units substations with 5 MVA transformers and 4.5 MW rectifiers.

The fleet has two train set classes (10M3 and 8M) with the capability of using regenerative braking. During regenerative braking, the motor acts as a generator and feeds back to the line if there is another train otherwise the regenerated power will then dissipate through resistor banks (wasted power). Once the DC line voltage is above 3.6 kV DC the generated power is then dissipated through resistors.

PRASA gets 33 kV AC supply from Eskom and distributes it to different 3 kV DC substations. It also gets 66 kV AC directly from Eskom at selected points and steps it down to 3 kV DC. The 66 kV AC (direct feed) tariff is cheaper than 33 kV AC since Eskom is charging for stepping down the voltage from 66 kV to 33 kV AC for PRASA. This means that Eskom would have a 66 kV / 33 kV substations dedicated only for PRASA hence the higher tariffs compared to 66 kV AC direct feeds.

Energy savings can be realized by using the regenerated energy or storing it for later usage. The energy bill can also be reduced by extending the 33 kV AC distribution network to be fed from the 66 kV AC (Eskom) through a 66 kV / 33 kV AC transformer. This paper will therefore discuss energy management efficiency through regenerative braking and through the extension of the 33kV AC line.

2 REGENERATIVE BRAKING

During braking, Train sets are capable of regenerating power back to the Overhead line to supply nearby trains, store it (on-board or substation) or feed back to the grid.

The motors used on the traction networks can either work as motors or generators. Regenerative braking is not a new concept; it was done in South Africa with mercury arc rectifiers and inverters between Johannesburg and Durban railway line and also in Japan, using thyristor controlled rectifiers [1]. When the motor is acting as a generator the input is mechanical power and the output would be the electrical power.

2.1. Energy Storage

The regenerative braking energy can be stored at substations and onboard for later use. Energy Storage devices are Batteries, Flywheels, Electric Double Layer Capacitors (EDLC) and Hybrid Energy storage [2], [3].

Battery Energy Storage System (BESS): Batteries are the simplest energy storage systems and have a life cycle of approximately 100th of Electrical Double Layer Capacitors (EDLC) and Flywheel's life cycle [2]. Battery storage devices are high energy density and can store higher energy compared to Flywheel Energy Storage System (FESS) and EDLCs. Batteries are very expensive especially for high voltages like those on 3 kV DC networks. Lithium ion batteries have been used in the late 2003/2005 in Japan for their Catenary-Free system [2].

Flywheel Energy Storage System (FESS): The FESS has the capability of regulating the DC line voltage to a desired or set value. As soon as the DC bus voltage rises above the set value then the FESS absorbs the excess

energy in the DC bus and the Flywheel speed will increase (charging) [1]. The FESS releases the stored energy once the DC bus voltage falls below the predetermined value as depicted in Fig. 1 below [3].

It is also shown in Fig. 1 that the flywheel speed increases during motoring and decreases during regenerative braking.

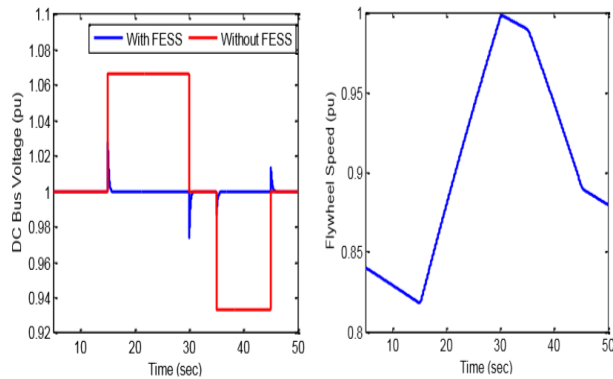


Fig. 1: a) DC bus voltage with and without FESS and b) Flywheel speed [3].

Electric Double Layer Capacitors (EDLC): EDLCs have good performance in terms of power density and charge/discharge time. They have reduced maintenance costs and have lower internal resistance. EDLCs power density is higher than that of batteries. EDLCs are modelled by a resistor and a capacitor as shown in Fig.2, and are widely used for storing regenerative braking energy [2].

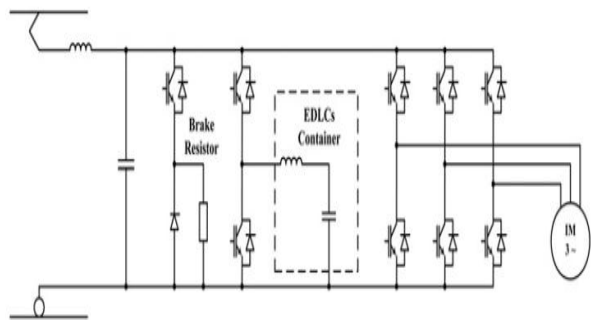


Fig. 2: Electric Double Layer Capacitors [2].

EDLCs were installed in Japan at Agon and Shumaru substations to effectively store and reuse the regenerative braking energy. These were installed in 2007 for 7.146 km spacing between two substations with a gradient of 2.5 % [2]. The regenerated power storage and energy storage capacity for the line is 2.560 MW and 6.875 kWh respectively [2].

Hybrid Energy storage (HESS): Hybrid is a combination of batteries and EDLCs or batteries with

Flywheels [2]. The storage performance can be improved by combining batteries and EDLCs or Flywheels [2]. Lithium – ion and Nickel – Metal Hybrid (Ni – MH) are preferred over Lead – acid because of their energy density. Ni –MH batteries are widely used in transport industries to improve energy efficiency [2].

Most energy storage systems use the DC bus voltage (line voltage) to control the charging/discharging currents. Japanese railway industry has installed these energy storage systems along track side. The track side energy storage systems have the advantage since their storage capacity can be maximized while the on-board system is limited because of size and weight [5].

2.2. Reversible Substation

In reversible substations the regenerated power would be fed back to the incoming supply (Eskom or Municipality). PRASA's DC Traction network is fed from 33 kV AC distribution network. This 33 kV AC network also feeds the 11 kV AC distribution network which is the dedicated supply to the Signal relay rooms.

The reversible substation could be used to supply the 11 kV and 33 kV AC networks before it is fed back to the grid (Eskom or Municipality).

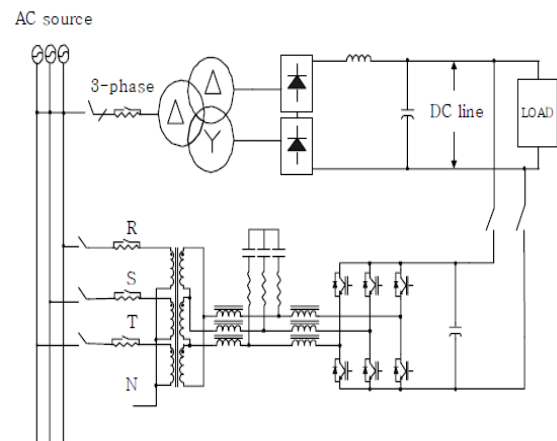


Fig. 3: Reversible/invertible substation [4].

The inverter is not that expensive and it can be easily added to the existing diode rectifier systems [4]. The inverter has an added benefit to the system, it can absorb all the current harmonics generated by the diode rectifier [4].

The system also regulates the DC line voltage to its nominal value.

3 EXTERNAL MOTOR – GENERATOR

This paper presents a study on using an external or abandoned motor as a generator. The motor will be used to generate power during peak times which will be used to drive the other motors of the same train in the system.

The regenerated energy can be stored on an onboard Flywheel Energy Storage System (FESS) and get used later when needed [3].

The maximum allowable regenerated current on the existing PRASA traction motors is 200 A.

The regenerated power could be further used to compensate for the DC line losses, keeping the line voltage constant as shown in Fig. 1a).

This generator could also be used to constantly generate power to supply the 11 kV AC, 33 kV AC network as well as the train station buildings which also contribute to the cost of energy in traction system.

4 ENERGY CONSUMPTION

PRASA Traction DC network is fed from Municipality and Eskom of which Eskom is supplying 78% of the network in the Western Cape region.

Fig. 4 below shows traction power load flow on all substations fed by Eskom. PRASA and Eskom peak hours overlap hence the realized high costs during these peak times.

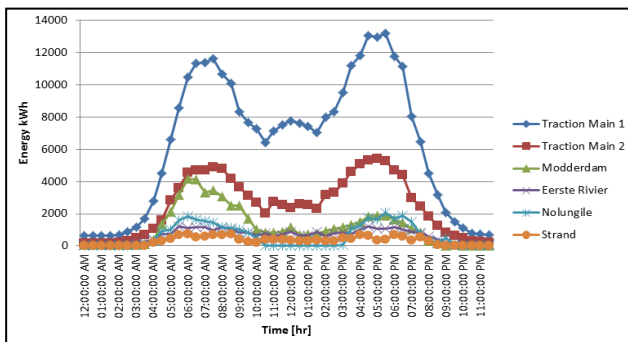


Fig. 4: Daily Energy Usage

Regenerative braking will assist in reducing the morning and afternoon peak demands. The standby or constant generator will reduce the costs even further during these times.

The energy usage has fairly increased by less than 1GWh. The train traffic is the same throughout except in 2010 where a number of train trips were introduced to accommodate passengers (fans) for the soccer world cup as can be seen in Fig. 5.

Eskom tariffs are increasing every year by approximately R 12 000 000 as shown in Fig. 6. The energy cost for the traction network is tremendously increasing while the train traffic will not be reduced but will be increased in the future to accommodate more customers.

Regenerative braking would be very beneficial in reducing the energy costs

The Eskom feeding points to PRASA Traction network are 33 kV AC and 66 kV AC with two 11.66 kV AC (Municipality) feeding points. Eskom 33 kV AC tariffs are more expensive than 66 kV AC

since Eskom has specially built a substation to step down the 66 kV AC to 33 kV AC.

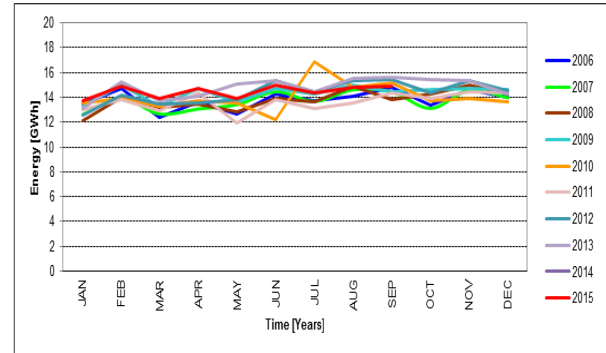


Fig. 5: Yearly Energy Usage

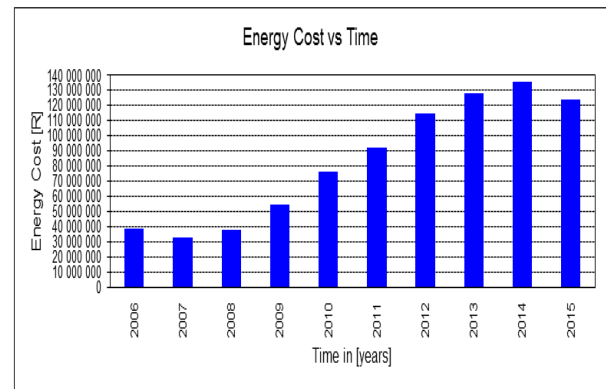


Fig. 6: Yearly Energy Cost 2006 – 2015.

The 8 M class has motors which are rated at 245 kW each and each motor coach consists of 8 motors. The motor coach set has different notching stages/transitions, series and parallel. Parallel notch is when the two sets of series motors are connected in parallel with the other two series motors. Series notch is when all motors are connected in series.

The 10M3 Class Motor coach consists of 4 motors and the rated voltage across each motor is 1 250 V in parallel mode and 725 V in series mode. Total rated current drawn by each motor coach is 165 A.

The exact current drawn by each motor coach depends on a variety of external factors such as the train loading, train speed as well as the track geometry (gradient, curve or straight road). At this stage an assumption is made to use the rated values of the motors to approximate the power drawn by the motors and the regenerated power.

$$P = V * I \quad (1)$$

$$= 725 * 165 \quad \text{rated values}$$

$$= 119.62 \text{ kW (each motor)}$$

PRASA train stations are very close to each other and this makes it difficult to reach higher speeds especially during peak times when there are more trains running in the network. This limits the amount of energy to be regenerated since the trains would take shorter time to stop. The maximum allowable speed in the network is 90km/h but there are future plans to increase the speed limit to 120 km/h on the longer sections.

It is assumed that a train set would run at an average speed of 60 km/h between stations. PRASA stations are approximately 3 km apart in the central line.

$$\text{Speed} = \text{distance} / \text{time} \quad (2)$$

$$\text{Time } t = 3 \text{ (km)} / 60 \text{ (km/h)}$$

$$= 0.05 \text{ h (180 seconds)}$$

Energy drawn by each motor coach can be calculated using equation 3 below. The 10M3 full set consists of 3 motor coaches in the Central line and 2 motor coaches on the Southern line.

$$\text{Energy} = \text{power} * \text{time} \quad (3)$$

$$\text{Energy} = (4 * 119\ 625) * 0.05$$

$$= 23.93 \text{ kWh per motor coach}$$

One set of 10M3 classes has 3 motor coaches meaning that the total energy would be:

$$E_{\text{total}} = 71.78 \text{ kWh or (1.44 MW)}$$

Braking time depends mainly on the driver's experience as to when he/she starts applying brakes, hence the braking time differs. For the 60 km/h speed in 3 km, the train can be stopped within 15 – 25 seconds.

Regenerative braking energy would be calculated using equation 3. The worst case is when the speed is low which limits/reduces the stopping time. 15s would be 0.0042 h

$$E_{\text{regen}} = 3 * (4 * 119.62) * 0.0042 = 6.03 \text{ kWh}$$

This means that in every 180 seconds travelled 6.03kWh of energy would be saved if the regenerative energy is used.

If regenerative energy can be used properly by PRASA, a saving of about 0.299 GWh each month can be realized as shown in Fig. 7. Yearly energy savings would be approximately 3.59 GWh.

The daily energy usage for the 11.66 kV AC Municipality supply to 3 kV DC network is shown in Fig. 8. The Municipality supply is more expensive than the Eskom supply, therefore the power consumed by PRASA can also be reduced by extending the PRASA 33 kV AC distribution network to eliminate the Municipality feeding points.

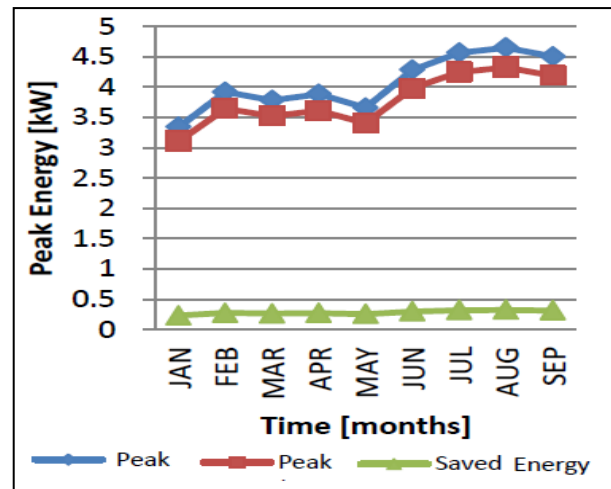


Fig. 7: Energy Usage vs Energy Saved

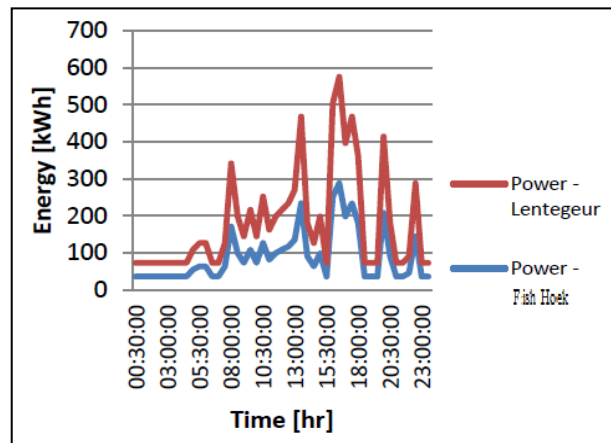


Fig. 8: Daily Energy Usage (Municipality Supply)

The length of the proposed extension is 23.53 km and most of the supporting steel structures are already installed for the 3 kV DC network therefore only 33 kV Vees (cross arm) are required to be installed on the existing steel structures. The cost of the Vees and labour is approximately R 6.5 M. Lentegour substation (Municipality) recorded a usage of 356 951.6 kWh in September 2015. This costs R 743 452.05 from the Municipality supply of which R 534 635 of that is the peak demand charge. This value would be saved monthly since Eskom does not charge PRASA based on demand peaks but its charges are based on fixed tariffs (during peak, off peak and standard) for real and reactive power. Based on monthly savings, the cost of the extension could be recovered within a year.

$$\text{Yearly savings} = \text{R } 534\ 635 \times 12 = \text{R } 6.4 \text{ Million}$$

The extension of the line would eliminate the Municipality supplying points therefore the costs would be reduced.

Once the extension is done reliability of the network will increase since there will be flexibility to supply the whole network from 4 different Eskom sources of supply (Traction Main, Modderdam, Nolungile and Chris Hani).

Fig. 9 below, shows power consumed on a single daily train trip. The power usage of a train set is high at start up to move the train from rest and it then gradually decreases as the train reaches the desired speed and only uses low power to overcome friction while keeping the speed constant.

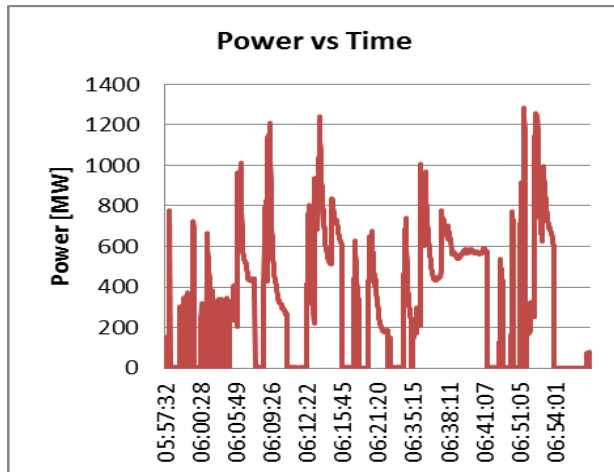


Fig. 9: Train Trip Power Usage vs Time

The power is approaching zero at the stations where the train stops, during the stoppage times the power can be regenerated to supply nearby trains. There are many stopping times and that is an added advantage for regenerative braking.

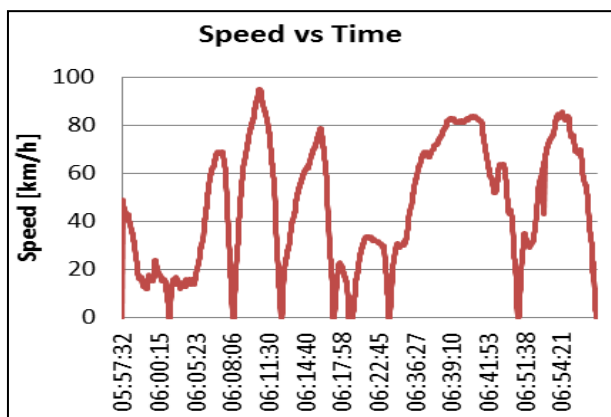


Fig. 10: Train Trip Speed vs Time

The maximum allowable speed in the PRASA network is 90 km / h as can be seen in Fig. 10.

More energy would be regenerated if the speed has reached maximum before applying regenerative braking.

5 FUTURE WORK

A further study regarding the external motor would be conducted to see the impact on the energy usage during peak hours. A Simulation as well as practical measurements would be reported in the future.

6 CONCLUSIONS

The yearly energy cost increase and the recent Eskom load shedding calls for Energy saving methods. The traction motor will be used to constantly generate Energy (when needed) to cut the cost on Eskom tariffs. The excess regenerated energy will be used to supply the 11kV AC and 33 kV AC network if there are no running trains in the section.

During peak hours there is no need for the energy storage devices since there are more trains running in the system/network to absorb the regenerated energy. If regenerative braking is used during standard time then energy storage systems should be installed to absorb the excess energy since there are fewer trains in the system.

On the PRASA network, Energy costs can also be cut by extending the 33 kV AC network to be supplied from the 66 kV AC incomer which is cheaper than 33 kV AC. The extension of the line would improve network reliability since the whole network would be supplied from different points of Eskom supply.

7 ACKNOWLEDGEMENT

The authors gratefully acknowledge the provision of financial support, data and research infrastructure provided by Eskom Holdings through TESP, PRASA and the University of Cape Town in carrying out this research. They also give thanks to the following people who assisted during the research: P.T. Xorile, D Keet, N. Maphuza and Morema.

8 REFERENCES

- [1] P.J. Randewijk and J. R. Enslin: "Inverting DC Traction Substation with Active Power Filtering", presented at the 26th IEEE Power Electronics Specialists Annual Conference, University of Stellenbosch, South Africa, 1995.
- [2] T. Ratniyomchai, S. Hillmanssen, P. Tricoli: "Recent Development and applications of Energy Storage Devices in Electrified Railways", *IET Electr. Syst. Transp.*, 2014, Vol. 4, Iss. 1, pp. 9–20.
- [3] M. I. Daoud, A.S. Abdel-Khalik, and A. Elserougi, S. Ahmed and A.M. Massoud: "DC Bus Control of an Advanced Flywheel Energy Storage Kinetic Traction System for Electrified Railway Industry", presented at the 39th IEEE Industrial Electronics Society (IECON) Annual Conference 2003.
- [4] S. Jang, C. Choi, C. Hwan Bae, S. Song, C. Won: "Study of Regeneration Power Control Inverter for DC Traction with Active Power Filter Ability", Presented at the 31st Industrial Electronics Society (IECON) Annual Conference 2005.

- [5] R. Takagi, T. Amano: "Evaluating On-Board Energy Storage Systems using Mltilevel-Train Simulator RTSS", presented at the Railway Traction Systems IET Conference 2010.

PERFORMANCE STUDY OF LOCOMOTIVE SYSTEMS FOR A RELIABLE COST EFFECTIVE MAINTENANCE SOLUTION

T.N. Miyambo* and S.P. Chowdhury**

* Tshwane University of Technology Dept. of Electrical Engineering, Pretoria 0001, South Africa E-mail: Tekan.Miyambo@Transnet.net

**Tshwane University of Technology Dept. of Electrical Engineering, Pretoria 0001, South Africa E-mail: Spchowdhury2010@gmail.com

Abstract: Transnet Freight Rail is a parastatal organisation within South Africa responsible for transportation of the economy's freight. Its market share currently sits at approximately 14% compared to other modes of transportation. TFR signed a deal with a Japanese Company known as Mitsui to acquire new locomotive fleets, which were eventually deployed in the year 2008 and 2009. The signed Supply Agreement between the two parties included a clause to monitor locomotive fleet reliability and availability. Monitoring the fleet reliability presented challenges for the project team responsible to execute the service level agreement during the 24 months warranty phase of the project life cycle. The lack of proper monitoring of sub-system failures, led to an increase of operational maintenance costs. A need to develop a modern monitoring system which is user friendly for the TFR maintenance environment is necessary in order to enhance effective monitoring of the locomotive systems/ sub-systems. It is essential that the Reliability/availability of the locos during the contractual duration is met, prior to the locomotive been officially handed over to Transnet Freight Rail's Rolling Stock Maintenance Department at the end of the 24 months guarantee period. The Project Manager responsible to administer the project work break down activities has to ensure that the failure statistics are captured and exercise according to the agreed contractual clauses. In order to track and monitor failure statistical data a software program is to be developed to allow failure data to be captured at Transnet Freight Rail maintenance depots as and when locomotives are pre-checked prior to departing for the integrated train plan (ITP) by the Operations Department and data will be stored in a central database. The software program allows data to be extracted from the central database, will allow the data to be interpreted in various ways that will assist the Locomotive Fleet Owner to better monitor the line/locomotive faults or locomotive sub-systems reliability. Accessibility to the consolidated data is processed from a main computer station from the Project Manager's office. TFR is currently on process to acquire 1064 locomotive for the general freight business, in which the development of the proposed capturing system will have a huge benefit for the company.

Key words: Reliability and Availability measurements; monitoring reliability. Microsoft access Database server, Borland Delphi software tool, Graphic user interface.

1. INTRODUCTION

In February 2006 a South African company responsible for freight logistics known as Transnet Freight Rail embarked on a new locomotive acquisition contract for 110 Class 19E and 76 Class 15E electric locomotives, in which the Class 19E fleet was earmarked for the export coal corridor and the Class 15E fleet for export Iron Ore corridor. Both the fleets propulsion system was supplied by a Japanese company known as Toshiba Corporation and the mechanical assembly portion was done by a South African company based in Nigel known as Union Carriage and Wagon through a joint venture partnership. The Locomotive Supply Agreement (LSA) between Transnet Freight Rail and Mitsui included a clause which called for a 24 months guarantee

period, in which reliability of the systems performance had to be closely monitored at the maintenance depots. Monitoring of the locomotive components (sub-systems) failure statistics was thoroughly capturing failure statistical data on a excel spread-sheet, which can be a labour intensive exercise for the project team. Contractually each fleet had a threshold of 10% for each sub-system/component to qualify for declaring an inherent fleet defect, and simultaneously to the requirement, the fleet reliability was not to exceed 14 faults per million kilometres travelled on a service revenue earning train.[4]

A need to develop a modern system which is user friendly for the TFR maintenance environment is

necessary in order to enhance effective monitoring of system reliability during the contractual duration prior to the fleet of locomotives been officially handed over to Transnet Freight Rail's Rolling Stock Maintenance Department after the 24 months guarantee period. The project manager responsible to administer project work break down activities has to ensure that the failure statistics are captured and exercised as per the agreed contractual clauses. In order to track and monitor failure statistical data a software program is to be developed to allow data to be captured at Transnet Freight Rail maintenance depots as an when locomotives are pre-checked prior to departing for integrated train plan (ITP) by operations department and data is stored into a central database. A software program allows data to be extracted from the central database.

Further on the, software program enables data to be interpreted in various ways that will assist in improved monitoring of faults or sub-systems reliability. Accessibility to consolidated data is processed from a main computer station from the project manager's office. [1]

The need to monitor reliability of locomotive sub-systems (or components) performance will be closely discussed with necessary focus on the LSA's initial 24 months guarantee of the project deliverables phase. Monitoring of reliability statistics plays a pivotal role for Transnet Freight Rail project office, in which if the process is not properly administered, it leads to higher maintenance costs whereas the cost must be borne by the Original Equipment Manufacturer or the Main Contractor.

The following points will be discussed in detail:

- Previous method of capturing failure statistics
- How lack of reliable sub-systems affect integrated train service plan
- Software solution to be implemented

In brief locomotive reliability of sub-systems is key to financial yearly growth of freight railed with trains; therefore urgent attention on how to monitor component or system reliability is extremely important [2].

A. Previous method of capturing failure statistics

The project manager administering the procurement contract is the main person who requires foreseeing that project work breakdown structure is executed within the necessary budget, quality requirements and on time. One of the challenges that lead to Transnet Freight Rail spending excessive funds on maintenance was lack of record keeping on failure statistical data by relevant maintenance depots as personnel perceived the exercise for capturing failure statistical data as a tedious exercise. Prior to the software solution been applied for capturing, the used of Microsoft excel was the only suitable way to monitor records of locomotive failures.

TABLE 1: SHOW A SNAPSHOT OF PREVIOUS WAY TO CAPTURE FAULTS.

Item No.	Loco System Description	OSM	Loco No.	Date	No. of failure occurrences (once specific)	Failure Type (Mechanical/Electrical)	Quantity per loco	Percentage estimate (NPS) for fleet defect	Disposition (Open)	Comments / Contractor Report
1	Package Brake Unit	UCM2000 and S400	E10006	09-Mar-12	1	Mechanical	12	3.50%	Open	
			E10006	20-Mar-12						
			Total no. of failures		1					
2	Secondary Brdg Spring	R80	E10005	09-Apr-12	1	Mechanical	20	5.00%	Open	
			Total no. of failures		1					
3	Traction Motor Blower	UCM2000	E10005	09-Oct-12	1	Mechanical	2	3.12%	Open	
			E10005	22-Sep-12	1	Mechanical				
			Total no. of failures		2					
4	ESB	UCM2000	E10006	17-Apr-13	1	Electrical	1	3.12%	Open	Loco went dead 200 km/h and 200 km/h, no power and no power, NPS to get feedback on failure
			Total no. of failures		1					
5	VACUUM CIRCUIT BREAKER		E10006	28-Jun-13	1	Electrical	1	3.12%	Open	
			Total no. of failures		1					
6	T1 SERVICE	TELIMA	E10006	14-Sep-13	1	Electrical	4	3.12%	Open	
			Total no. of failures		1					

B. How lack of reliable sub-systems affect integrated train service plan

The operational department for scheduling trains does not plan for failures in the integrated train plan for the Iron Ore corridor. The plan caters for at least 6 hours in between train slots, however the plan should be as a result of a failure of a locomotive/component, a service technician would have to be dispatched should the fault not be resolved remotely.

If the highly trained technician is not successful in solving the technical fault, this would mean that the locomotive must but uncoupled from the train and returned dead to the maintenance depot. The results of such a fault require a spare locomotive to be dispatched or the removal of loaded wagons at a specific loop. The total time waiting to exchange the locomotive often let to the following disruptions:

Negative train turnaround time

Train slot cancellations, which translates to loss of revenue

C. Software solution to be implemented

A software solution to capture and monitor failure statistical data will provide a necessary and easier solution to execute the LSA and lead to minimized maintenance operational costs. The software solution basically will offer maintenance depots to

enter data on technician computer and data will be stored on a central database. There after the second part of the solution will allow the project office to retrieve data from the central database through an Area Point Network that will be connected via the MTN GPRS cloud and present data in a suitable format that the project team will be enabled to apply the LSA adequately.

2. DESIGN SOLUTION APPROACH

The method that is about to be described offers a Programmable Software Solution that will be divided into two portions. Portion one will require remote data to be inserted from various maintenance depots (i.e. 5 to 7 depots) in which the web IP address would provide APN access to the graphic user interface that will be developed. Portion two will allow one person from the central database to access recorded statistical data through the APN channel remotely and interpret data in various graphical formats through the application of programmable software solution.

Portion no.1

A software program will be developed to enable remote depot technician to insert or captured failure statistical data into a central database. The GUI to be developed via the software tool will require password protection to minimize tampering with system data by unauthorized personnel. The software program will also have a function to prompt the depot technician to double check data to be inserted prior to allowing it to be stored on the database.

Portion no.2

The second part of the software algorithm will be developed to enable the project manager to access the database server via the access point network and retrieve stored data from the database for interpretation in the following various ways:

- All failure statistics for various

components

- Single locomotive failure statistics Filter data by data
- Filter by specific fleet category
- Filter by specific system/sub-system equipment failures
- Graphical representation of specific failures
- Data percentage (%) count for specific component/sub-system

The following block diagram below shows the process to be followed when a software solution is applied.

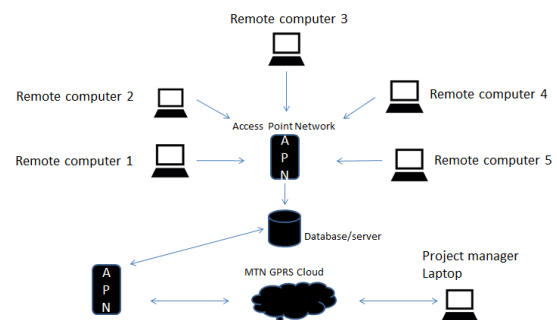


Figure 1: Depicts entire block diagram on how data can be processed for the software solution

The above Figure 1 provides a summarized view for how maintenance depots will capture data and how data is stored into a central database. The portion on how the project team will retrieve data from the central database is also depicted.

3. RELIABILITY AND AVAILABILITY DEFINITION

Reliability and availability according to the Transnet Freight Rail LSA has been simplified defined as follows based on the service level agreement:

“Fleet reliability in relation to a Batch, means the average number of Faults per Locomotive in such Batch in relation to distance travelled expressed as Faults per million kilometres travelled where the target is to achieve on average less than or equal to 14 (fifteen) Faults per million Locomotive kilometres travelled by the Fleet. Reliability shall be measured for each calendar month using the following formula:

$$Z = X \div Y \times 1,000,000$$

where:

Z = Reliability;

X = number of Faults reported and confirmed in relation to the Fleet for the calendar month being measured (on the basis that the Faults reported and confirmed during the relevant calendar month for any Locomotive in such Batch that has not achieved a minimum average monthly travelling distance of 5,000 kilometres as at the end of that calendar month, shall not be counted in the Fault measurement for that calendar month);

Y = total distance travelled by the Fleet for the calendar month being measured (on the basis that the distance travelled during the relevant calendar month by any Locomotive in such Batch that has not achieved a minimum average monthly travelling distance of 5,000 kilometres as at the end of that calendar month, shall not be counted in the distance measurement for that calendar month),

and where average monthly travelling distance of a Locomotive in such Batch for any calendar month which expires after commencement of Phase 2 of the Reliability measurement process shall be determined using the following formula:

$$A = B \div C$$

where:

A = the average monthly travelling distance of that Locomotive for the relevant calendar month;

B = the total distance travelled by that Locomotive during the 6 (six) months immediately preceding the date of calculation (or during such shorter period as may then have expired since the date on which Phase 2 of the Reliability measurement process commenced);

C = the number of calendar months expired in the period referred to in variable B above.

Fleet availability means, on any relevant day and in relation to a Batch, the number of operational Locomotives in such Batch which are available for service on that day expressed as a percentage of the Fleet where the target is to achieve monthly Fleet Availability of more than 90% (ninety five per cent) within 6 (six) months after the Fleet Performance Commencement Date. Monthly Fleet Availability shall be calculated at the end of each calendar month

as the average of the Fleet Availability for each day during that calendar month. Daily Fleet Availability shall be calculated in terms of the following formula:

$$Z = X \div Y \times 100$$

Z = daily Fleet Availability;

X = the number of Locomotives in that Batch that have been in actual operation for at least 1 (one) month at the relevant time, which are available for service on that day;

Y = the total number of Locomotives at the relevant time constituting the Fleet of Locomotives in that Batch (but excluding all Locomotives which became Accepted Locomotives in the relevant month.) "[4]

3. RESULTS FOR DESIGN SOLUTION APPROACH

The figures and tables to be discussed are based on the concept of software solution expectations.

The development of the GUI had to be carefully arranged and focused at ensuring that relevant information is captured.



Figure 2: Shows snapshot of what the depot GUI

The web based software will require the maintenance depot technician to insert data on all the fields to ensure that data is captured accurately. In order to make sure that data is captured accurately an additional prompt screen will pop-up requiring the depot technician to validate the recorded data. Thereafter information will be stored into the central database.

Table 2 below gives a summary of the central database of stored data.. In order to test the functionality of the software solution simulation data had to be created and determine if the expected outcome is measurable.

TABLE 2: SUMMARY OF DEPOT SIMULATION DATA

LocoFleetClass	Locomo	FaultyComponent	Typeoffailure	ComponentOEM	DepotName	LogDateTime
Class 15E [Fleet Size = 76]	E15005	Bre Stack Blower no.1	Electrical	Telesma	SLD Depot	2015/06/04 12:12:12 PM
Class 15E [Fleet Size = 76]	E15016	Cooling Tower	Mechanical	Toshiba	SLD Depot	2015/06/08 08:00:00 PM
Class 15E [Fleet Size = 76]	E15017	TBU no.4	Mechanical	KBSA	SLD Depot	2015/04/08 08:00:00 PM
Class 15E [Fleet Size = 76]	E15044	DDU no.1	Electrical	Toshiba	SLD Depot	2015/02/12 12:24:00 AM
Class 19E [Fleet Size = 110]	E19032	Compressor Motor	Electrical	ABB	Ermenlo Depot	2014/12/15 09:24:00 PM
Class 19E [Fleet Size = 110]	E19048	Master Controller	Electrical	Rollmach	RBay Depot	2014/10/15 09:30:00 PM
Class 19E [Fleet Size = 110]	E19057	HCB	Electrical	Microelectronics Scientifica	Ermenlo Depot	2014/06/15 08:30:00 AM
Class 19E [Fleet Size = 110]	E19078	Surge Arrestor no.1	Electrical	Sachertan	RBay Depot	2014/04/15 10:40:00 AM
Class 19E [Fleet Size = 110]	E19107	Compressor Motor	Electrical	ABB	Ermenlo Depot	2014/09/15 10:00:00 AM
Class 19E [Fleet Size = 110]	E19130	Pantograph	Mechanical	Siemens	Ermenlo Depot	2014/05/10 08:22:00 AM
Class 20E [Fleet Size = 95]	E20011	Main Compressor	Mechanical	Webtec	Beaconsfield Depot	2015/02/12 06:27:55 AM
Class 20E [Fleet Size = 95]	E20009	Mini Compressor	Mechanical	Webtec	PE Depot	2015/07/12 12:08:12 PM
Class 20E [Fleet Size = 95]	E20028	Converter Unit (PPC no.1)	Electrical	CSR	PE Depot	2015/09/22 12:28:29 AM
Class 20E [Fleet Size = 95]	E20027	Wiper Motor (Driver side)	Mechanical	Synlabamba	Beaconsfield Depot	2015/09/10 09:08:30 PM
Class 20E [Fleet Size = 95]	E20078	TBU no.2	Mechanical	Webtec	PE Depot	2015/08/10 09:08:40 AM
Class 21E [Fleet Size = 240]	E21034	TM no.6	Electrical	ABB	Postmasburg Depot	2015/09/22 12:12:12 PM
Class 21E [Fleet Size = 240]	E21034	TM no.6	Electrical	ABB	Postmasburg Depot	2015/09/22 12:12:12 PM
Class 19E [Fleet Size = 110]	E19042	Bre Stack Blower no.2	Electrical	Telesma	SLD Depot	2015/09/20 11:11:00 AM
Class 15E [Fleet Size = 76]	E15013	Pantograph	Mechanical	Siemens	SLD Depot	2015/07/07 10:12:12 PM
Class 21E [Fleet Size = 240]	E21031	Foot Heater	Electrical	Boyoyo Eng	Beaconsfield Depot	2015/08/12 01:30:12 AM
Class 20E [Fleet Size = 95]	E15021	Converter Unit (PPC no.2)	Electrical	Toshiba	SLD Depot	2011/09/12 07:08:03 AM
Class 21E [Fleet Size = 300]	E21002	Air Con (HVAC)	Electrical	Boyoyo Eng	Ermenlo Depot	2015/08/01 10:10:12 AM
Class 21E [Fleet Size = 240]	E21034	Compressor Motor	Mechanical	KBSA	PE Depot	2015/09/21 08:10:12 AM
Class 21E [Fleet Size = 240]	E15009	Converter Unit (PPC no.1)	Mechanical	Toshiba	SLD Depot	2015/09/23 09:22:22 AM
Class 21E [Fleet Size = 300]	E21060	TM no.1	Mechanical	CSR	RBay Depot	2015/09/23 11:12:12 AM

Figure 3 below details a summary of simulation data that was captured by the various depots. The web based software that the project manager used to retrieve data displays data as depicted. It has to be note that data can be represented in any format depending on the checkboxes activated.

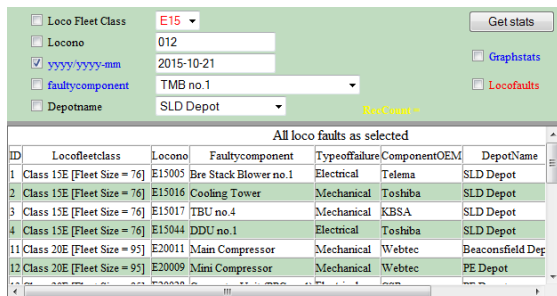


Figure 3: Snapshot of type of faulty component summary

The ultimate purpose of the software solution is to give a holistic view of the fleets affected failure statistical data, in which the below figure 4 denotes the expectation. [3]

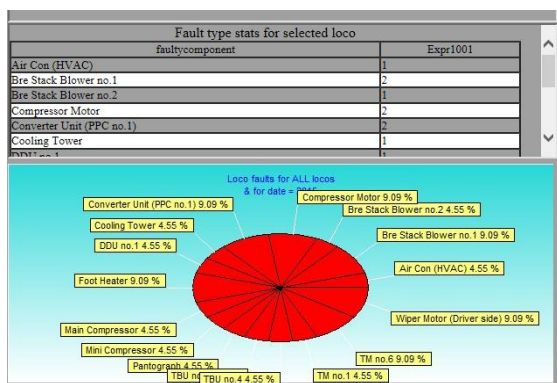


Figure 4: Shows percentage split of the components failures

4. CONCLUSION

It is evident from the illustrated results captured in the implemented web based project solution that the statistical data captured from the remote maintenance depots, the project manager can rely on the system available information without having to travel to various depots located around the country.

The foundation of the software development through the use of Borland Delphi was mainly contributed by an external supervisor. In addition to ensure that the expected project objectives is met, I had to embed the algorithm and design the relevant GUI to best meet/suit the project expectations.

The benefit realizations for embarking on this the project are outlined below.

- Minimized travel costs to maintenance depots
- Reduction on operational maintenance costs
- 24 months contract execution will be efficient/reliable
- Failure data will be permanently available on the central database.
- In future locomotive acquisition project, careful consideration of reliable sub-system or component will lead to minimized teething challenges
- Reduction of train cancellations which leads to loss of revenue

It is evident that the software solution provided a feasible and reliable method of monitoring and capturing locomotive failure statistical data as it was initially envisaged.

5. REFERENCES

- [1] Burke, Rory, 1952-. Project management: planning & control techniques 1 Rory Burke
- [2] Golafshani, N. (2003). Understanding Reliability and Validity in Qualitative Research. The Qualitative Report, 8(4), 597-606. Retrieved from <http://nsuworks.nova.edu/tqr/vol8/iss4/6>
- [3] Delphi Programming © Neil Moffatt 2002 - 2015. All rights reserved.
- [4] Contract supply agreement between Transnet limited and VENUS RAILWAY SOLUTION (PTY) LTD © 2006. All rights reserved.
- [5] Herman Steyn, 2010. Project management: A multi-Disciplinary Approach, second Revised Edition
- [6]. Kazdin A. E. Artifact, bias, and complexity of assessment: The ABCs of reliability. Journal of Applied Behavior Analysis. 1977;10:141–150.
- [7] Bartholomew, D. J. (2002). Measuring intelligence: Facts and fallacies. Cambridge: Cambridge University Press
- [8] Graphical representation for Data links, <http://www.statcan.gc.ca/edu/power-pouvoir/ch9/pie-secteurs/5214826-eng.htm>

- [9] C.R. Kothari, Research Methodology: Methods and Techniques (Wiley Eastern, New Delhi, 1985).
- [10]. St. Peter Pipkin C. C. A laboratory investigation of the effects of treatment integrity failures on differential reinforcement procedures. 2006. Unpublished doctoral dissertation, University of Florida, Gainesville.

Contrasting three different academic assessments of a compulsory capstone module in power engineering indicates reliability!

A.J. Swart and P.E. Hertzog

Dept. of Electrical, Electronic and Computer Engineering, Central University of Technology, Private Bag X20539, Bloemfontein, South Africa, 9300. Email: drjamesswart@gmail.com

Abstract: Industrial Projects IV is a compulsory capstone module for students enrolled for the postgraduate Baccalaureus Technologiae (BTech) in Electrical Engineering (Power) in South Africa. Many graduates from the National Diploma course often struggle to pass this module at their first attempt. This may be due to a number of challenges, such as; struggling to integrate theory with practice; perceiving their postgraduate studies to be overwhelming; feeling anxious as a result of uncertainty about what is expected of them; not knowing how they will be assessed; and finally experiencing a lack of support and understanding from their mentors. The purpose of this paper is to highlight the course structure of a compulsory capstone module offered at a university of technology which has helped students to overcome some of these challenges. The paper further contrasts the assessment results of three different academics that were tasked with mentoring these power engineering students and evaluating their various submissions. Results show that the use of a variety of pedagogies enables postgraduate power engineering students to successfully attain academic success, while predefined rubrics are essential in achieving reliability and validity of assessments among different academics.

Keywords: Industrial Projects IV, capstone, UoT, theory, practice

1. INTRODUCTION

“In order to arrive at knowledge of the motions of birds in the air, it is first necessary to acquire knowledge of the winds, which we will prove by the motions of water in itself, and this knowledge will be a step enabling us to arrive at the knowledge of beings that fly between the air and the wind” [1]. These words, by Leonardo Da Vinci, well illustrate that man needed to gain knowledge of birds in air, knowledge of winds and knowledge of water motions to *enable* man to successfully fly! Conversely, students need to acquire knowledge of specific graduate attributes, which, if used effectively, can become the *enabler* in helping them to successfully achieve academic success. This is especially true with regard to capstone modules.

The purpose of a capstone module is to provide students with the opportunity of earning credits by integrating and applying knowledge and skills acquired from other modules so as to extract the best possible benefit from the programme in a particular career [2]. The integration of knowledge and skills in an electrical engineering capstone module often involves the design and development of an engineering project [3]. Large research projects within capstone modules have also been used for postgraduate Master’s degrees [4] while many of these modules lend themselves readily to problem-based learning [5] where a number of graduate attributes may be assessed. Ten graduate attributes have been adopted by the Central University of Technology (CUT) and must collectively feature within a given qualification or curriculum [6]. These include sustainable development, problem solving, entrepreneurship, community engagement, numeracy, technological literacy, teamwork, communication,

leadership and technical competence. Many of these graduate attributes exist in capstone modules, including the module Industrial Projects IV (IP4).

However, the assessment procedures for capstone modules pose challenges and need careful structuring [7] while the ever growing number of students registering for these modules provide logistical challenges. The purpose of this paper is twofold. Firstly, it aims to present the course structure for a compulsory capstone module offered to power engineering students at a university of technology, termed IP4. Secondly, it aims to contrast the assessment results of three different academics that were tasked with mentoring some 85 power engineering students and assessing their various submissions.

The importance of predefined graduate attributes is firstly established. The power engineering module (IP4) is then introduced and contextualized. The research methodology follows with the results which are presented in a series of graphs and tables conveying quantitative data.

2. GRADUATE ATTRIBUTES

The fundamental purpose of engineering education is to build a knowledge base and attributes to enable the graduate to continue learning and to proceed to formative development that will develop the competencies required for independent practice [8]. This highlights the need for academics to regularly review their course material and assessments to ascertain if they are assessing the right graduate attributes. These attributes must currently be required by Industry so that the graduate may successfully engage in independent

practice. Graduate attributes form a set of individually assessable outcomes that are the components indicative of the graduate's potential to acquire competence to practice at the appropriate level (IEA, 2013). The sum of these individually assessable outcomes must exist across an entire curriculum, and must not be confined to a singular module. These graduate attributes are exemplars of the attributes expected of graduated from an accredited programme (IEA, 2013). An accredited engineering programme often incorporates a capstone module, where students are required to draw on their knowledge and skills acquired in other modules to complete the desired learning outcomes. The 12 graduate attributes stipulated by the International Engineering Alliance are intended to assist signatories and provisional members to develop outcomes-based accreditation criteria for use by their respective jurisdictions (IEA, 2013). These 12 attributes may be linked to the 10 attributes adopted by CUT (see Table 1) which need to be demonstrated by all students.

Engineering knowledge refers to the ability of students to apply mathematics, science, and engineering fundamentals to engineering problems and is equated to the numerate attribute of CUT (see Table 2 for a definition). Problem analysis not only refers to the ability of the student to analyse complex engineering problems but also the ability to identify relevant literature to reach a viable solution (equated to the innovation and problem solving attribute of CUT). Engineering students must furthermore be able to design solutions for broadly defined engineering problems that often require the use of the right technical equipment (similar to the technical and conceptual competence attribute of CUT). The fourth attribute indicates that students must be able to conduct investigations into complex problems, using relevant research methods and experiments to provide valid conclusions (also linked to innovation and problem solving using the iUSE model). Students must further be able to create, select and apply modern engineering and information technology tools with an understanding of their limitations. This is equated to technological literacy at CUT, where students need to use computer hardware and software in many of their practical assignments.

The Engineer and Society refers to knowledge of the societal, health, safety, legal and cultural issues which may be equated to the CUT attribute of community engagement. Engineering students must understand the impact of engineering solutions on the environment and must have the knowledge needed for sustainable development. They must commit to and understand professional ethics and responsibilities which may be linked to the citizenship and global leadership attribute of CUT. Students must furthermore be able to function effectively as individuals or as members of a team. Communication, in the engineering context, refers to the ability of the student to effectively communicate with

society, to give clear instructions and to compile effective reports.

Project management and finance indicates that students must demonstrate knowledge and understanding of engineering management principles, being able to manage projects in multidisciplinary environments (this is similar to the citizenship and global leadership attribute of CUT). The last attribute refers to the student's ability to engage in independent lifelong learning, which is a key requisite of entrepreneurship. Many, if not all, of these graduate attributes may be assessed in capstone modules, such as IP4.

Table 1: Linking the graduate attributes prescribed by the IEA and by CUT along with succinct definitions

International Engineering Alliance	Central University of Technology	Definitions of the CUT graduate attributes
Engineering Knowledge	Numerate	Performing correct calculations and equation manipulations
Problem Analysis	Innovation and problem solving	Promoting the iUSE model as described by Swart and Toolo [9]
Design / development of solutions	Technical and conceptual competence	Operating specific equipment or apparatus effectively in a laboratory
Investigation	Innovation and problem solving	Promoting the iUSE model as described by Swart and Toolo [9]
Modern Tool Usage	Technologically literate	Efficiently using computer hardware and software to complete assignments
The Engineer and Society	Community engagement	Encouraging students to benefit their communities
Environment and Sustainability	Sustainable development	Incorporating aspects of sustainability into a module
Ethics	Citizenship and global leadership	Including aspects relating to citizenship, leadership or management in a module
Individual and Team work	Teamwork	Nurturing group work of two or more students in a module
Communication	Communication	Promoting good written and oral communication in a module
Project Management and Finance	Citizenship and global leadership Nurate	Including aspects relating to citizenship, leadership or management in a module
Lifelong learning	Entrepreneurship	Featuring aspects relating to entrepreneurship in a module

3. COURSE STRUCTURE OF IP4

IP4 is a compulsory module in the Baccalaureus Technologiae: Engineering: Electrical qualification, more commonly referred to by students as the BTech in Power Engineering. The course structure (highlighting six different submission requirements) used at CUT for this module is shown in Table 2, which needs to be completed over a 1 year period (registration takes place in January with the final assessment in October). No formal electrical or electronic based project or operational circuit is required from these students who often work with power systems up to 132 kV. Their final summative report or dissertation is usually based on a real life case study which exists in Industry.

The structure and purpose of the project proposal along with the research methodology course and project plan is presented over the first 9 weeks. This usually comprises a singular 4 hour session per week arranged for a late afternoon / early evening in order to grant full time working students the opportunity to attend. Theory relating to the title, problem statement and proof of the problem is emphasized! The project proposal is assessed formatively, giving students the opportunity to rectify any deficiencies. This is important as the project proposal usually forms the core of the first chapter in the final summative report or dissertation.

Table 2: Course structure of IP4

Requirement	Month	Weighting
Project proposal	April	10%
Progress formative report	July	10%
Article	August	5%
Poster	August	5%
Oral presentation	September	10%
Final summative report	October	60%
	TOTAL	100%

The formative progress report covers the first three chapters of the dissertation, along with the front matter (declaration, expression of thanks, abstract and table of contents), references (a minimum of 12 references are required of which at least 50% must be journal references). In-text references are emphasised as well as the importance of plagiarism. The first chapter basically comprises the updated project proposal, while Chapter 2 should cover relevant literature that supports the problem and the proposed solutions. Students are requested to include specific references to previous practical Industry examples where their proposed solutions to their problem have been used before. This lends credence to their proposed solution, establishing its validity in the student's research project. Reasons must be given with regard to WHY the solution was required, HOW it was implemented and WHAT the results were. Chapter 3 of the progress report should introduce at least three proposed solutions to the problem, presenting proposed electrical diagrams,

possible installation sites, geographical topologies and the advantages and disadvantages of each solution.

The article requires students to compile a two page article based on the official IEEE template. This helps students to understand the importance of structuring a research publication as well as what important sections or topics need to be covered. Limiting the number of pages helps negate the so called "cut and paste" syndrome so often encountered with student reports or dissertations. Students cannot simply copy a huge amount of data from the Internet or from another study, but need to evaluate the information and select only that which is relevant, phrasing it in such a way that it makes sense to the reader. All figures and tables need to be edited by the student to include 3 specific highlighted sections / blocks which need to be explained in the text. This helps students to reason on the figures and tables, interpreting their significance in the context of their study.

An A3 poster is required where the student must provide at least 4 sketches or figures relating to the current geographical layout, proof of problem and results. Each figure must be briefly explained with two brief sentences below or above the figure. In addition, each figure must have three key aspects highlighted. This discourages students from simply cutting and pasting images from the Internet or software packages, with no substantial interpretation or explanation. A brief problem statement and conclusion section is required, while no references must be given on the poster. The inclusion of excessive amounts of text is discouraged.

The oral presentation requires students to complete a 14 slide PPT where their details, problem statement, proof of the problem, three possible solutions and results must be shown. Excessive amounts of text are discouraged, while the results must feature some type of simulation in order to make an informed decision about the preferred solution. All possible solutions must be visually presented, with as little text as possible. The conclusion must state the preferred solution and provide substantive reasons for this decision.

The final summative report comprises the largest weighting towards the student's final mark which is based on academic feedback given to the student with regard to the progress report (Chapter 1 – 3), article and presentation. The final dissertation must include chapter 4 (results section comparing the alternative solutions by means of simulation software and cost analysis) and chapter 5 (conclusion of the project substantiating the use of the preferred solution along with pertinent recommendations). 40% of the final dissertation is awarded to the structure of the portfolio, the front matter (declaration, expression of thanks, abstract and table of contents) and the back matter (references and annexures). 60% of the final dissertation is awarded to the actual content of the five chapters.

Table 3 correlates the 10 graduate attributes of CUT to the six requirements of the IP4 module. This capstone module, requiring knowledge from previous modules, features seven of the ten graduate attributes adopted by CUT, with the most dominant ones being problem solving, technological and technical literacy!

Table 3: Graduate attributes required in IP4

Requirement	Problem solving	Community engagement	Technological literacy	Numeracy	Teamwork	Communication	Technical literacy
Project proposal	√	√	√	√	√	√	√
Progress report	√		√	√	√	√	√
Article	√		√				√
Poster	√		√				√
Oral presentation	√		√	√	√	√	√
Final report	√		√	√	√	√	√

4. ASSESSMENT RUBRICS

Rubrics are tools for assessing learning outcomes and evaluating critical thinking skills and are currently of interest given a changed emphasis in education [10]. The learning outcomes were defined for each submission, where after the rubrics were designed. Assessment rubrics are written to guarantee proper understanding of the expectations among various assessors, resulting in fair assessments [11]. This leads to the transparency, reliability and validity of the final results. Rubrics can also be used to provide a mapping of learning outcomes and graduate attributes within minimum standards to allow students to evidence their skills beyond the assignment criteria [12]. This provides a scale from not the criterion NOT being present to the criterion being EXCELLENTLY mastered (see Table 4). This gives rise to an analytical rubric. Analytical rubrics are scored by assigning individual scores to each criterion which are added together to create a total score, while a holistic rubric takes all of the criterion into consideration to develop a composite score without assigning sub-scores [13].

An assessment rubric was developed for each of the six requirements and is included in the study guide which is electronically made available to all registered students at the start of the module. Students are thus well informed of how and where marks will be allocated for their different submissions. This lessens, to some degree, the anxiety that some students experience in compulsory capstone modules in not knowing how they will be assessed [14]. Space does not allow for the presentation of all six rubrics.

However, the fundamental structure of the rubrics is shown in Table 5. 15% is generally awarded to the layout of the submission, which assists students to understand the individual requirements for each

submission. The introduction and explanation of figures and tables is awarded the largest weighting (35%), as this is usually equated to the content of the dissertation. Chapter 4 of many engineering dissertations primarily contains figures and tables showing the results of the project [15], and forms the basis for the conclusion chapter where the original problem is finally addressed with a suitable validated solution.

Table 4: Generic summarised rubric used by all three academics in assessing the six required submissions

Requirement	Criterion not present (0)	Criterion NOT mastered (1-4)	Criterion PARTIALLY mastered (5-6)	Criterion SUFFICIENTLY mastered (6-7)	Criterion mastered BEYOND expectations (8-9)	Criterion EXCELLENTLY mastered (10)
Layout according to the given template with all student details		Usual average weighting of 15% Consistency in font size, spacing, structure and term usage required				
Introduction includes general background, problem statement, proof of problem and time line		Usual average weighting of 20% The proof of the problem must support the problem statement by means of a figure or table				
Figures and tables are introduced and explained in the text and are relevant to the work		Usual average weighting of 35% A minimum of three figures / tables are required for each chapter with 3 relevant aspects highlighted by means of a block				
At least 12 correctly formatted references are given with 50% from journals		Usual average weighting of 15% At least 1 correctly formatted in-text reference per page for Chapters 1 – 3 must be correlated to the full reference				
Annexures are provided and relevant to the work		Usual average weighting of 5% At least 1 relevant annexure				
Grammar and language quality		Usual average weighting of 10% Acceptable language and grammar usage required which can be checked by peers				

5. RESEARCH METHODOLOGY

A case study using quantitative data is used. A case study intends to explore a bounded system in-depth [16]. A system could refer to a programme, event or activity (in this research it is the grades awarded to IP4 students for the various submission as outlined in Table 2), while the word bounded implies that the research is conducted within the boundaries of a specific place (in this research it is CUT). A singular case study was used by Lajoie et al. [17] to describe in detail an online international problem-based learning approach. Quantitative data is used to highlight the grades awarded by three different academics to a group of 85 power engineering students during 2014, which form

the target population for this study. The three academics include an Associate Professor (A/P), a Senior Lecturer (S/L) and a Lecturer (L). All three academics have more than 20 years of academic experience. This quantitative data is given in the form of tables and figures, with a histogram contrasting the three academics assessment of the final summative dissertation. Students are required to achieve an overall grade of more than 50% to successfully complete this module. The assessment of all the power engineering students' submission for 2014 followed the same process as that outlined under the course structure in the previous section.

6. RESULTS

Table 5 shows the profile of the three academics that were tasked with mentoring and assessing the IP4 students during 2014. All three academics have 20 years or more academic experience, having lectured more than seven different modules over this time period. Professors and Associate Professors usually constitute the most highly qualified and experienced academics [18], and would be more productive in terms of publications [19]. This suggests that the AP would be more experienced in academic writing, having a well-grounded understanding of what research really entails and how an article or poster should be structured. This further suggests that the A/P would more critically assess the six required submissions than would the other two academics.

Table 5: Academic profile

	A/P	S/L	L
Highest qualification	DTech	DTech	BTech
Year joined academia	1995	1992	1993
Number of modules lectured	14	13	7
Number of journal articles	22	10	0
Number of completed M's and D's	3	9	0

Figure 1 through 3 highlights the distribution of final grades awarded to the IP4 students by the three academics. Figure 1 presents the grades awarded by the A/P, where the majority of students received between 50 and 60%. Figure 2 illustrates that the S/L awarded more grades between 60 and 70% than the A/P did. This trend is also observed for the L, but to a lesser degree.

Figure 4 presents some of the descriptive statistics of the final grades awarded by the three academics. The maximum grade awarded varies between 65% (for the S/L) and 69% (for the L). The mode (value that occurs most often), median (value with half the grades above and below it) and mean are very close together for both the L and S/L, suggesting a normal distribution which is symmetrical or bell-shaped. The A/P values are also relatively close together (52% for the mean and 55% for the mode). The Kurtosis values in Figure 5 suggest a platykurtic distribution (kurtosis less than 3) rather than a leptokurtic distribution (kurtosis more than 3).

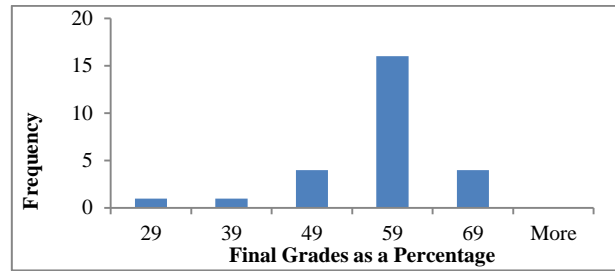


Figure 1: Histogram showing the distribution of final grades as a percentage awarded by the Associate Professor (A/P) – (n = 26 and throughput = 77%)

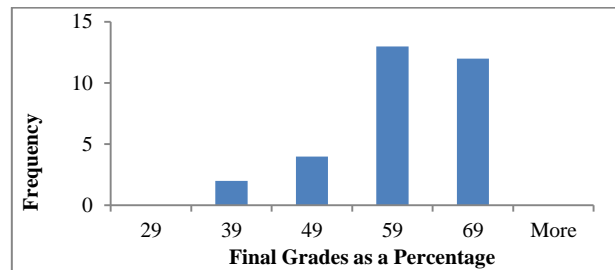


Figure 2: Histogram showing the distribution of final grades as a percentage awarded by the Senior Lecturer (S/L) – (n = 31 and throughput = 81%)

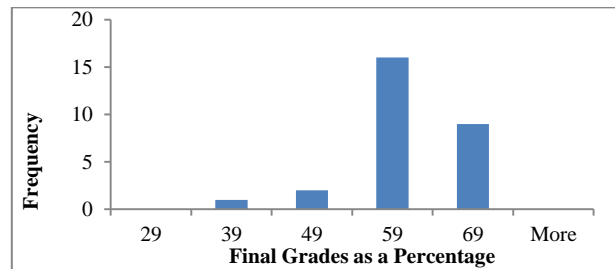


Figure 3: Histogram showing the distribution of final grades as a percentage awarded by the Lecturer (L) – (n = 28 and throughput = 89%)

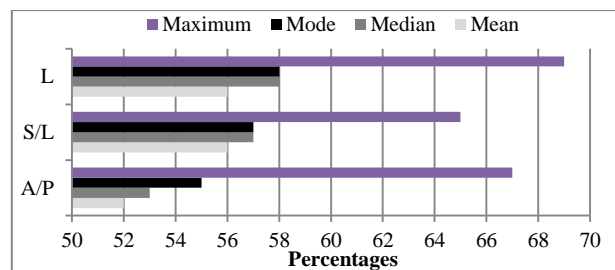


Figure 4: Descriptive statistics of the final grades awarded by the three academics

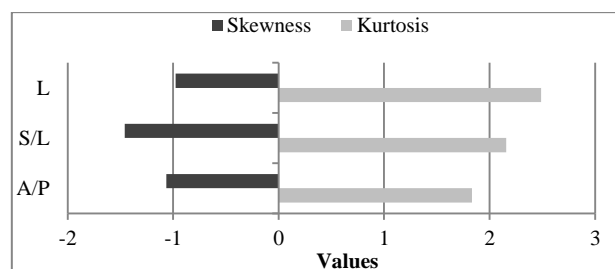


Figure 5: Skewness and Kurtosis values of the final grades awarded to IP4 students by the three academics

Figure 5 indicates a low degree of clustering of values. This suggests that all three academics strove to apply the rubrics to each individual student, not grading each submission in a nonchalant manner.

7. CONCLUSIONS

The purpose of this paper was to present the course structure for a compulsory capstone module offered to power engineering students at a university of technology and to contrast the assessment results of these students by three different academics. The A/P mentored 26 students, of which 77% successfully passed the module. The S/L mentored 31 students, of which 81% were successful. The L mentored 28 students, where 89% achieved a final grade of 50% or more. This may suggest that the A/P was a little more critical in the assessment, drawing on his previous experience in academic writing for publication. All three academics used the same predefined analytical rubrics to assess six different submissions, including a proposal, a progress report, an article, a poster, an oral presentation and a final report. The low negative Skewness results indicate that no extreme grades were awarded by any of the academics, while their maximum grade varied by only 4%. The Kurtosis values (lower than 3 indicating a flatter distribution) also bear testimony to this. These results tend to suggest that the rubrics were applied consistently by the three academics, resulting in the reliability and validity of the assessments in this compulsory capstone module.

8. REFERENCES

- [1] Brainy Quote. (2015, 9 January 2015). *Homepage*. Available: <http://www.brainyquote.com/quotes/>
- [2] A. Burger, "Research support for masters students," *Administratio Publica*, vol. 17, pp. 94 - 115, 2009.
- [3] A. J. Swart, *et al.*, "Exploring the relationship between time management skills and the academic achievement of African engineering students - A case study," *EJEE, European Journal of Engineering Education*, vol. 35, pp. 79 - 89, 2010.
- [4] I. Horrocks, "Developing a Capstone Research Module for Multiple Masters Qualifications at the Open University (UK): The Case of T847," in *Proceedings of the 13th European Conference on Research Methodology for Business and Management Studies: ECRM 2014*, 2014, p. 177.
- [5] S. Kilcommmins, Ed., *Capstone courses as a vehicle for integrative learning* (Integrative Learning: International research and practice. New York: Routledge, 2014, p.^pp. Pages.
- [6] N. Luwes and A. J. Swart, "Student Perspectives of Practical Work done in a Laboratory – a Case Study from Logic Design III " presented at the ICEE 2015, Zagreb, Croatia, 2015.
- [7] E. Farisani, "Impact of new policy developments in higher education on theological education," *Studia Historiae Ecclesiasticae*, vol. 36, pp. 287-303, 2010.
- [8] International Engineering Alliance. (2014, 12 December 2014). *Homepage*. Available: <http://www.ieagrements.org/GradProfiles.cfm>
- [9] A. J. Swart and L. E. Toolo, "Fundamental problem-solving skills are found across the board in education: Are our power engineering students on-board?," presented at the ICEE 2015, Zagreb, Croatia, 2015.
- [10] A. Hebble and M. Richards, "Assessing student critical thinking skills for online quantitative courses," in *Fifth Annual General Business Conference*, 2013, p. 214.
- [11] P. Desai, *et al.*, "A novel approach to carrying out mini project in Computer Science & Engineering," in *Engineering Education: Innovative Practices and Future Trends (AICERA), 2012 IEEE International Conference on*, 2012, pp. 1-4.
- [12] S. McKenzie and G. Wood-Bradley, "Using rubrics in IT: Experiences of assessment and feedback at Deakin University," in *Teaching, Assessment and Learning (TALE), 2014 International Conference on*, 2014, pp. 474-479.
- [13] K. D. McConnell, "Rubrics as catalysts for collaboration: a modest proposal," *European Journal of Higher Education*, vol. 3, pp. 74-88, 2013.
- [14] B. Mavis, "Assessing Student Performance," in *An Introduction to Medical Teaching*, ed: Springer, 2014, pp. 209-241.
- [15] M. Đ. Carić, *et al.*, "Construction and techniques of writing a scientific paper in natural and engineering sciences," *Zbornik Matice srpske za prirodne nauke*, pp. 119-128, 2013.
- [16] J. Creswell and V. Plano Clark, *Understanding research: A consumer's guide*. Upper Saddle River, NJ: Pearson Education, Inc, 2010.
- [17] S. P. Lajoie, *et al.*, "Using online digital tools and video to support international problem-based learning," *Interdisciplinary Journal of Problem-Based Learning*, vol. 8, p. 6, 2014.
- [18] S. Badat, "Producing, transforming the social composition of, and retaining a new generation of academics: The Rhodes University programme of accelerated development," in *University Leaders Forum: Developing and retaining the next generation of academics*, Accra, Ghana, 2008.
- [19] M. Bravidor, "What Determines Time Spent in Peer Reviews?—Evidence from The Accounting Review," *Evidence from The Accounting Review (November 30, 2013)*, 2013.

DEVELOPMENT OF AN EFFICIENT LONGITUDINAL RAIL IMPACT TEST CONTROL SYSTEM

M.J. Lencwe* and S.P. Chowdhury**

* M.J. Lencwe, Transnet Freight Rail, Railway and Technology Development Centre, 1000 Bluegum Street, Koedoespoort, Pretoria 0039, South Africa E-mail: mpholencwe@gmail.com or Mpho.Lencwe@transnet.net

** S.P. Chowdhury, Tshwane University of Technology Dept. of Electrical Engineering Faculty of Engineering and the Built Environment, Pretoria 0001 South Africa E-mail: spchowdhury2010@gmail.com

Abstract: A longitudinal Rail Impact Test is a very important test conducted by Railway and Technology Development Centre (RTDC) on new or upgraded railway vehicles, which are Wagons, Locomotives and Tank Containers. These railway vehicles are subjected to this test in order to evaluate their structural compliance in accordance to Transnet Freight Rail specifications BBD6022. The test Wagon, Locomotive or Tank Container is pulled up an inclined ramp of 30° at different levels from the horizontal ground level. It is then released down the ramp, allowing it to run freely and impact on the stationary loaded wagon and the three loaded DZ wagon. The loaded wagon and the three DZ wagons are used as buffer cars to create a secondary breaking system for the test wagon, locomotive or tank container. The breaks of the three DZ buffer cars are set and the slack is removed. The pulling system consists of a three phase slip ring induction motor, winch, control circuit and a wagon. The system is required to pull a maximum of 100 tons per wagon and a maximum 400 tons per train. The current control system used to pull the train utilizes a push-to-make switches for forward and reverse (up or down) control of the induction machine and with the use of contactors. This research paper present the development of a user friendly, safe, energy efficient, reliable and cost effective Longitudinal Rail Impact Test Control System as well as steady-state analysis of the induction motor. The control system will include an AC 3-phase induction motor, AC motor drive, Programmable logic controller, toggle switches, siren (alarm) and safety light indicator. The emergency switch will also be included for safety purposes. By introducing the PLC, Limit Switches and VFD, the accuracies and energy consumption of the control system is improved.

Key Words: Locomotives, Tank Containers, Wagons, Programmable Logic Controller (PLC), Longitudinal Rail Impact Test Control System (LRITCS), Variable Frequency Drives (VFDs)

1. INTRODUCTION

Transnet Freight Rail (TFR) a division of Transnet is a highly dynamic freight company. It is the largest freight company in the African continent and wishes to be one of the top five freight company in the world by 2020 [1]. TFR is constantly pursuing the development and implementation of services offered to clients. One way in which these is achieved, is by designing new or upgrading existing wagons and tank containers. Before a new or upgraded wagon or tank container can be taken to service, it has to undergo multiple testing to ensure its structural compliance and safe working of all systems according to TFR's specifications BBD6022 Revision 3 [2]. One such test is the longitudinal rail impact test, whereby a wagon, locomotive or a tank container is instrumented with accelerometers to measure vibration, and the wagon, locomotive and tank container is pulled up an inclined ramp to a specified level. Once the specified level is reached, the wagon is released down the ramp and allowed to run freely and impact into stationary wagon and DZ wagons in the test track. These tests are conducted at Railway and Technology Development Centre (RTDC) Koedoespoort, Pretoria. The centre was built in the 1970's. The longitudinal rail impact test system is equipped with a large winch (Winder-House), 3-phase AC slip ring induction motor, gears for speed reduction and the control circuit. The control circuit is

equipped with obsolete mechanical contactor and relays for direct-online-start (D.O.L) of the machine. The cost of electricity has increased significantly over the last few years. Many researchers and manufacturers of electrical goods have sought to minimize the use of electrical consumptions while maintaining the efficiency of electrical equipment's. One such approach is through the use of single minded technology for on time solution by replacing control contactors with more an efficient system. It has come to reality that AC motor drives integrated with PLCs provide a very efficient solution to many industrial applications; however it has been used in many control and automation systems. Many industries are using AC motor drives and PLCs to drive their motors, like at mines where V-belts or crushers machines are driven by motors integrated with PLCs and motor drives [3]. The current control system of the longitudinal rail impact test utilizes push-to-make switches for forward or reverse (up or down) control. The control consists of contactors, mechanical relays as well as mechanical breaks. The system cannot stop the test wagon, locomotive or tank container at a specified level; hence after releasing the control switch, the test wagon continues to move for period of approximately two minutes and therefore the accuracy of the wagon at the specified level is not precise.

The new control system that is being developed includes the in-house 3-phase AC slip ring induction motor, toggle switches, limit switches, siren (alarm), safety light indicators and emergency switch button for safety purposes. The control circuit of the system is integrated with PLCs and VFD. When simulating the behaviour of the system, the voltage, current, speed, torque and energy consumption during no mechanical load and maximum mechanical load of the motor are of major concern at this stage while the major concern of the system may be ignored. Modelling and simulating of the system behaviour under different load conditions shows the energy consumption as well as the steady-state response of the system. By using software models such as Matlab/Simulink that have been developed increases the computational speed of the model and enabling the collective systems response of the longitudinal rail impact control system with the AC motor being easily simulated.

By integrating the control system with the PLC, limit switches and the VFD in the control system, the stopping accuracies of the motor and the energy consumption of the longitudinal rail impact test control system are improved. The old control system accuracy and energy consumption was a major concern.

This paper reviews the behaviour of the longitudinal rail impact test control system as follows; section 2 reviews the design information of the system as well as its components, the model of the machine under different load case. The main mathematical equations that describes the relationship between voltage, current, ohmics, torque, speed and weight are briefly explained. Section 3 gives detail review of the longitudinal rail impact test control system comprising with VFD system. Section 4 shows the analyses of the system of the LRITCS and conclusions derived are provided in this section.

2. MODELING AND DEVELOPMENT

The development strategy of the longitudinal rail impact test control system is implemented as shown in fig 1. As shown in figure, the most prominent load to be pulled by the system is major concern and need to be determined taking into consideration of future railway vehicles and locomotive. This information helps in the determination of the control circuit components to be considered.

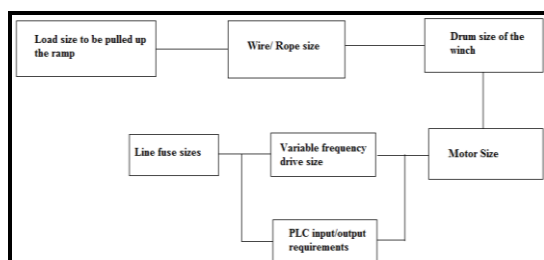


Figure 1 shows the information of the longitudinal rail impact test control system.

Table 1 shows the relevant weight of different locomotives, wagons and tank container's. These weights are demonstrated on design specifications (M-1001, issued 2011) [4]. The load required to be pulled is determined based on the load sizes of the wagon, locomotive or tank container during the longitudinal rail impact test. The load stated on the table is verified by the wagon, locomotive or tank container by using load cells placed in four distinct jacking pads of the wagon, locomotive or tank container. The locomotive is lifted in four jacking pads until the wheels are off the rail and weight measured is recorded.

Table 1 illustrate the relevant weight of different wagons, locomotives and tank containers.

Type	Description	Tare mass (kg)	Load mass (kg)	Total test mass (kg)
CHR-1	Wagon	15 150	62 400	77 550
21E	Locomotive	21 000	83 000	104 000
30 000l	Tank Container	2 269.5	33 695.5	35 965
AR-5	Wagon	22 400	57 600	80 000
CR-1	Wagon	15 150	No Load	15 150
DZ/NZ	Wagon	19 450	39 000	58 450
Greyhop	Wagon	23 600	50 000	73 600

Figure 2, give the complete model of the motor that is built using the software package known as Matlab/Simulink. The motor is connected directly to the VFD and its operating at synchronous speed when the frequency of the VFD is set at 50Hz. The supply voltage to the motor is 380V AC, and has the illustrated parameters in table 2. The motor is simulated at no-load and full load because the steady state analyses at full load can demonstrated the operational efficiency of the motor at that specified load.

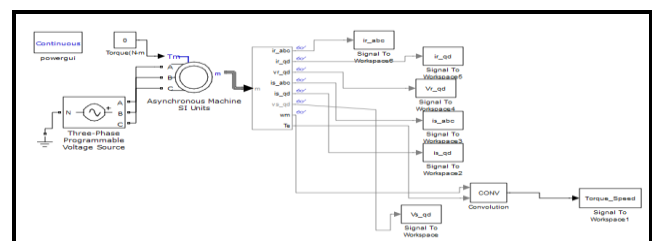


Figure 2 model designed for the motor simulation.

The parameters of the motor are calculated based on the information illustrated in table 2. The maximum load required for the simulation is also calculated as mechanical to required to pull the maximum critical weight.

Table 2 Motor description and ratings.

Description	Rating
Serial number	SMT1771311
Frame	CW315 5
Power	110kW
Voltage	380Vac
Current	216A
Speed	975 rpm
Insulation	F
Connection	Δ
Duty	CMR
Rotor Voltage	420V
Rotor Current	167A
Grade	CM 58
Bearing Type	N320

The motor parameters are calculated and were used in the simulation model to obtain the results, however they are calculated as follows:

i_{sd}, i_{sd}	d-and-q axis stator current components respectively expressed in a stationary reference frame
L_m	Mutual magnetizing inductance
L_s, L_r	Stator and rotor inductance respectively
R_s, R_r	Stator and rotor resistance respectively
S	Slip
T_e, T_l	Electromechanical torque and load torque reflected to motor shaft respectively
v_{sd}, v_{sq}	d-and-q axis stator voltage components and expressed stationary reference frame
X_s, X_r	Leakage reactance of the stator and rotor respectively
ω_m, ω_r	Mechanical and electrical angular rotor speed respectively
σ	$1 - \frac{L_m^2}{L_s L_r}$

$$P_o = V_l \times I_l \times \sqrt{3} \quad (1)$$

Where P_o is the output power of the motor, V_l the operating line voltage of the motor and I_l is the line current of the motor.

$$P_o = P_{in} \cdot \cos\theta \quad (2)$$

P_{in} = Input power of the motor.

$\cos\theta$ = the motors' power factor.

$$P_{in} = V_l \cdot I_{in} \cdot \cos\theta \cdot \sqrt{3} \quad (3)$$

$$I_{in} = I_{ph} \cdot \sqrt{3} \quad (4)$$

I_{ph} = phase current of the motor.

$$V_{ph} = Z_{eq} \cdot I_{ph} \quad (5)$$

Z_{eq} = equivalent impedance of the motor.

V_{ph} = motors phase voltage

$$R_{eq} = Z_{eq} \cdot \cos\theta \quad (6)$$

R_{eq} = equivalent resistance of the motor.

$$X_{eq} = Z_{eq} \cdot \sin\theta \quad (7)$$

X_{eq} = equivalent reactance of the motor.

$$\sigma = \frac{1 - \cos\theta}{1 + \cos\theta} \quad (9)$$

$$L_m = \frac{V_{ph}}{2\pi \cdot f \cdot I_{in} \cdot \sqrt{\sigma}} \quad (10)$$

$$\%S = \frac{N_s - N_r}{N_s} \quad (11)$$

$$R_r = \frac{V_r}{I_r} \quad (12)$$

R_r = rotor resistance.

$$L_s = 0.3\sigma L_m \quad (13)$$

$$\omega_r = \frac{2\pi f(1-s)}{p} \quad (14)$$

ω_r = rotor speed in rad/s

$$T_m = \frac{P_o}{\omega_r} \quad (15)$$

$$X_m = 2\pi f L_m \quad (16)$$

$$X_2 = 2\pi f L_s \quad (17)$$

$$R_1 = Z_{eq} - \frac{\frac{R_2 \times j(X_2 + X_m)}{S}}{j(X_2 + X_m) + \frac{R_2}{S}} \quad (18)$$

The maximum critical load is calculated based on the created formulae as follows:

$$M_T = M_{CR} + M_{Test}$$

$$= 15\,150 + 104\,000$$

$$M_{CTL} = M_{CR} + M_{Test} + M_{GH} + 3M_{DZ}$$

$$M_T = M_{CR} + M_{Test}$$

$$M_{CTL} = M_{CR} + M_{Test} + M_{GH} + 3M_{DZ}$$

$$= 15\,150 + 104\,000 + 73\,000 + 175\,350$$

The above shown formulas are created in order to understand how the maximum critical mechanical load required for the simulation is obtained.

3. LONGITUDINAL RAIL IMPACT TEST

The longitudinal rail impact test control system is powered from a 3-phase 380V AC power supply. Currently the system is designed to the motor using the direct-on-line (D.O.L) method with old mechanical contactor's and relays. This method has an influence in operation failure of the longitudinal rail impact test control system. During the operation of the system, the control mechanical contactor's and relay's induced arc flashes on the contacts of the contactor's, which sometimes leads to system's operations failure.

Due to the high electricity cost and technology advancement in industrial environment, the old control system pose a negative impact on operation of the system during the locomotive, wagon or tank container tests. Because the control components are very old, spares are very difficult to find, frequent operational failure and using the direct-on-lone method is no longer viable for such systems. For this reasons, an alternative method to start and control the motor was realized, which is much cost effective, safe, reliable, efficient and easier to control. This method is deemed necessary to replace the current longitudinal rail impact test control system.

The cost of electricity for the facility were compared during the during the normal operation of the business without the operation of the longitudinal rail impact test, the old control of the system and the recent control of the system. Due to the business policies, only the results of the electricity consumption of the new control system with VFD are captured and analysed.

Figure 3 and 4; demonstrate the longitudinal rail impact test track and the longitudinal rail impact test control system (circuit) that is built in-house. Figure 5, shows the integration of the Siemens PLC with the new control system of the longitudinal rail impact test.



Figure 3 Longitudinal rail impact test track.

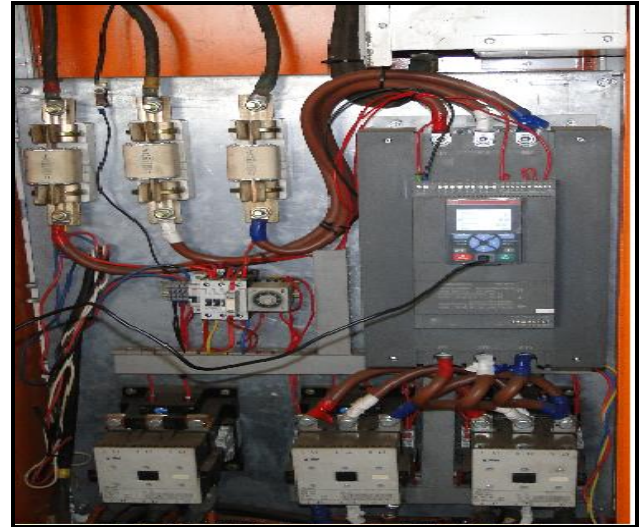


Figure 4 New longitudinal rail impact test control system



Figure 5 Siemens PLC integrated with the control system

4. SIMULATED RESULTS AND ANALYSIS

The steady state analysis of the results obtained from using the simulation of the motor are analysed and displayed in figures below. The results of the energy consumption for the control system are analysed and displayed in table 3. Due to company policies of not displaying the figures on public without proper authorizations, the results of the electricity consumption were compared with the old control system and the new control system. The new control system shows that the electricity consumption of the system can be improved by changing the operational frequency of the VFD as presented in table 3.

The motor used for the longitudinal impact test control system is analysed based on its characteristic parameters. The torque-speed characteristic curve shows that, during operation at full load. The machine operates in the first quadrant of the Cartesian plane. Hence the machine shows that during the inverting mode, 65-80% of the total cost of the electricity can be saved. The motor steady state characteristics shows that the motor's current stabilizes at approximately 20 Amperes, whereas it's starting current is very high at four times the stabilizing current. Due to these facts, the VFD is used to co-ordinate between the supply and the motor, as the exercise will improve the efficiency and the lifespan of the motor.

It can be seen in Table 3 that when frequencies of the supply are reduced, the energy consumption is also reduced. Therefore the motor used is a 110kW and if the operating frequency is reduced from 50 Hz to 35 Hz while operating, the energy consumed by the motor will be at 34%, hence 66% of the total electricity will be saved.

The D.O.L method is proven not to be suitably viable for the longitudinal rail impact test control system, because of the high starting current experienced by the motor. Therefore the rotor bars and conductors can be damaged easily and cause the malfunctioning of the system.

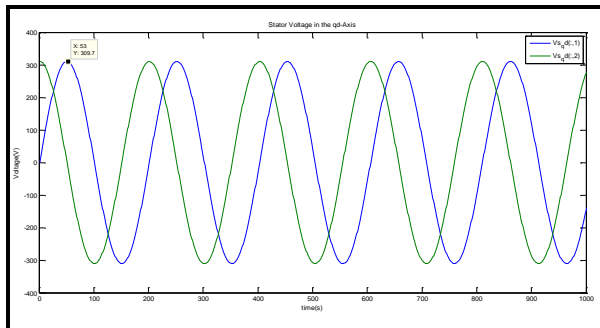


Figure 6 The stator voltage in the dq-axis during no-load

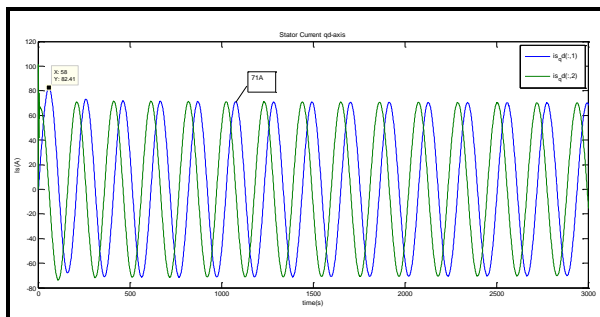


Figure 7 The stator current in the dq-axis at no-load

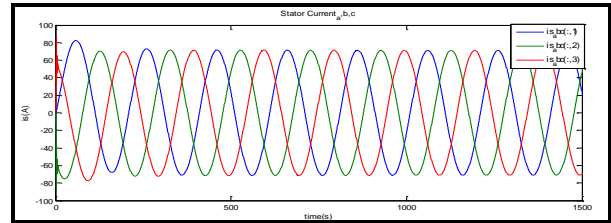


Figure 8 The stator current on the a,b,c lines at no-load

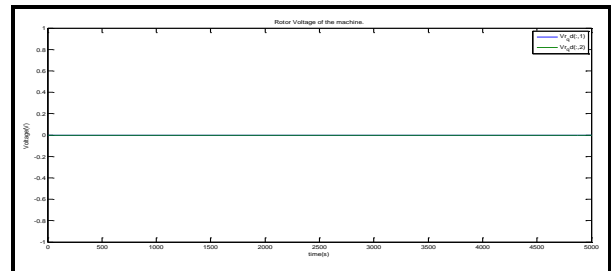


Figure 9 The rotor voltage of the machine at no-load

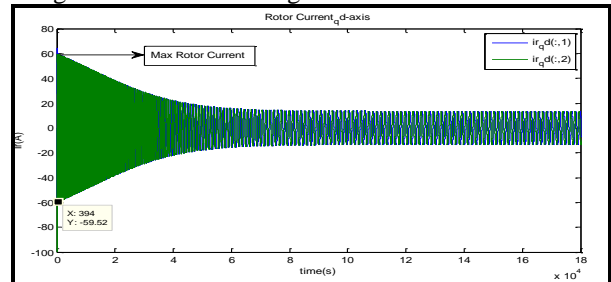


Figure 10 Steady state of the rotor current at no-load in the dq-axis.

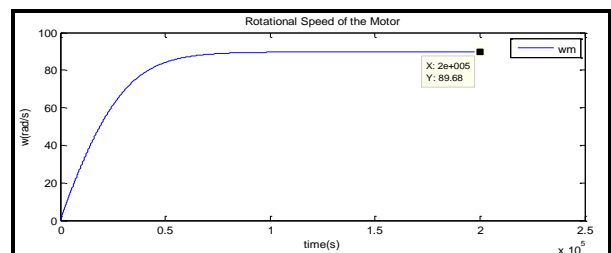


Figure 11 Motor speed at no-load.

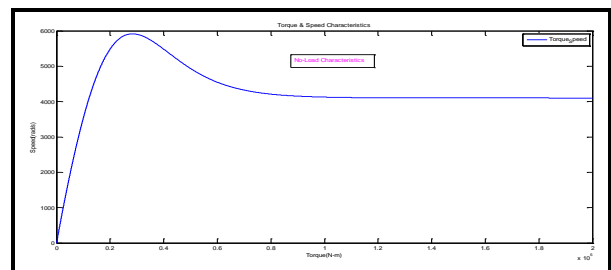


Figure 12 Torque-Speed characteristics at no-load.

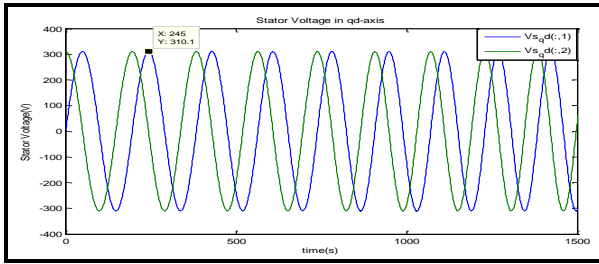


Figure 13. Stator voltage at full-load torque.

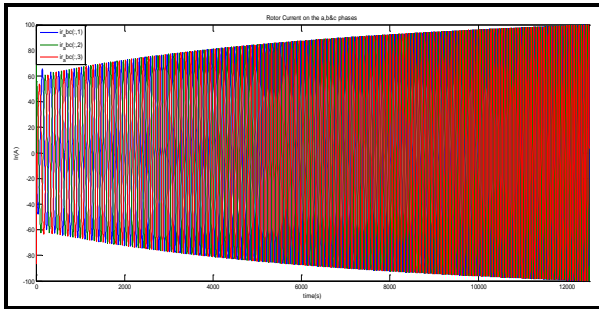


Figure 14. Rotor current at full-load torque.

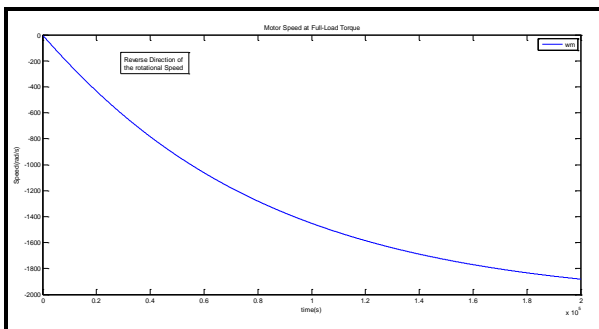


Figure 15. Speed of the motor at full-load torque

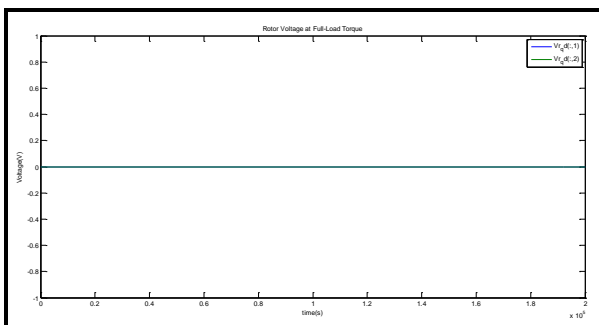


Figure 16 Rotor voltage at full-load torque.

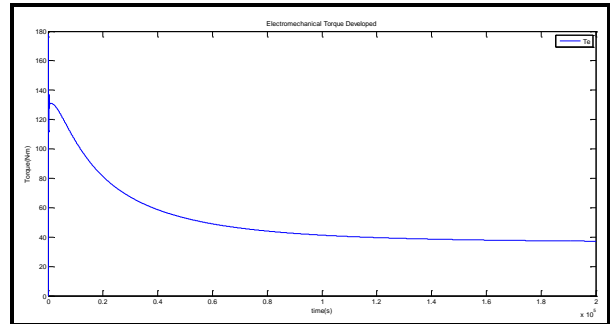


Figure 17. Torque-Speed characteristic at full-load torque.

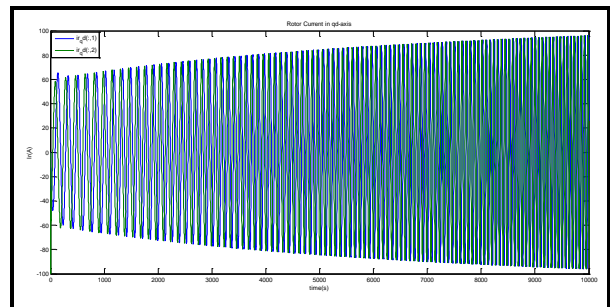


Figure 18 Rotor current at full-load torque in the dq-axis.

Table 3 Analysed VFD results during operation at different frequency ranges.

Frequency (Hz)	% Reduction	Energy Consumption (%)	Energy Consumption Saving (%)
25	50	13	88
30	40	22	78
35	30	34	66
40	20	51	49
45	10	73	27
50	0	100	0

Table 4 Analysed data results between the no-load and full-load torque

Description	SC at NL	SV at NL	SC at FL	SV at FL	% Difference
1	71A	310V	160A	310V	I= 55.62%, V= 0%
2	78A	-	161A	-	I= 51.55%

Acknowledgement

The authors would like to acknowledge the Transnet Freight Rail, Railway and Technology Development Centre Koedoespoort, Pretoria as well as TUT Pretoria campus for providing necessary research infrastructure to conduct this research project.

5. REFERENCES

- [1] Transnet Freight Rail weekly news bulletin (287th_Publication), 01 September 2014.
- [2] Robert Fröhling, Sheraton Sigh, Eduard Rietmann, "Structural Requirements for Transnet Freight Wagon Bodies", Specification BBD6022 Rev3, 23 August 2013.
- [3] Nasir Khalid, "Is Variable Frequency Drives the Solution", Research Journal ICGSM, 2014.
- [4] TD. Madileng, RS. Hartley, "Drawgear Impact (Ramp) Testing Procedure", Specification BBC6405 Rev01, 27 May 2009.
- [5] R. Saidur, S. Mekhilef, MB. Ali, A. Safari, H.A. Mohammad, "Applications of Variable Speed Drives (VSDs) in Electrical Motors Energy Savings", Research Journal, 2011.
- [6] J. Borges. "PC vs PLC for machine and process control, Real-time magazine", 1997, Vol. pp 4, 71-72.
- [7] Yunhai Li, Mingsheng Liu, Josephine Lau, Bei Zhang. "A novel method to determine the Motor Efficiency under Variable Speed Operations and Partial Load Conditions, Research Journal, October 2014.
- [8] A. Caggiano, R. Teti. "Modelling, Analysis and Improvement of mass and small batch production through advanced simulation tools", Research Journal, September 2013.
- [9] Siemens PLC. "The Control method and Applications of PLC S7-200 or LOGO", Manual, June 2014.
- [10] Qing-Chang Zhong. "AC Ward Leonard Drive Systems: Revisiting the forth quadrant operation of AC machine", Research Journal, October 2013.
- [11] Association of American Railroads, Manual of Standards and Recommended Practices, Section C-Part II, "Design, Fabrication and Construction of Freight Cars", [M-1001], issued 2011, accessed 26 September 2015.

A Methodology for Optimal Placement of Distributed Generation on Meshed Networks to Reduce Power Losses for Time Variant Loads

S. Malapermal^{1*}, M. Bello² and Dr I.E. Davidson³

¹Eskom Holdings SOC Limited, South Africa

²Electric Power Research Institute (EPRI), USA

³ Eskom Centre of Excellence in HVDC Engineering, University of KwaZulu-Natal, Durban, South Africa

*Email: sanjian.malapermal@eskom.co.za

Abstract: Distributed or embedded generation usually connected to distribution networks, are located close to load centres. Distributed generation integrated into power systems have many advantages over classic power systems when connected optimally. This paper focuses on the optimal placement of distributed generation on a meshed utility network to reduce power losses. An ideal loss optimization power flow method has been developed. This paper highlights the importance of reactive power support when integrating solar PV onto the grid. The impact of solar PV penetration on system losses will also be discussed. Power flow simulation results will confirm that distributed generation is optimally placed when at or closer to the load centre.

1 INTRODUCTION

This paper proposes a method for optimal placement of distributed generation (DG) on a typical utility network. A 56 bus meshed network is used to reduce power loss for time variant loads. The methodology needs to be pragmatic, repeatable and logical. Assessment of tactical planning decision is required with respect to sizing and placement of distributed generation. Characteristic load profiles drive power system losses [1]. These losses are dependent on renewable energy (RE) generation patterns that vary as climatic conditions and network topology vary. Modelling these parameters to analyse ideal placement of DG are important in the utility connection process.

Various methodologies to optimize the placement and sizing problem have been cited by [2]. The objective is to provide utility engineers with a methodology for assessing, optimizing, placing and sizing DG connections to the grid. The functional objective is to minimize power loss while respecting technical power systems criteria such as voltage limits, thermal and fault level management [3].

Utility engineers must have an oversight of the impact and constraints resulting from planned DG connection to the power system. Application of non-standard assessments will result in poor power loss management. For multi-generation placements, initial placement changes network limits and further placements require re-assessment. Large-scale integration of DG is predominantly determined by resource availability. Unfortunately, the cost of losses is

not a key factor in determining optimal placement of DG.

Technical constraints of steady state voltage at each bus shall remain within a permissible range as defined by [3]. Thermal limits for line equipment shall not exceed 100% of line ampacity under normal operating conditions. Transformer loading shall not exceed 100% under normal operating limits. Voltage variation resulting from loss of generation for solar PV is limited to 3% at point of connection as stipulated in [4].

2 ASSESSMENT METHODOLOGY

The methodology enables utility planners to work across all voltages on the power system. These voltages included medium voltage (MV) to high voltage (HV) and extra high voltage (EHV). While the applicability of this method applies to all voltage ranges, only category B [4] and C [4] are demonstrated in the test utility network. Category B represents generation with maximum export capacity of less than 20 MVA and category C, greater than or equal to 20MVA.

The following requisites and assumptions were made in formulating a method for optimal placement and sizing of DG on the network:

All power system analysis was performed in DigSILENT Power Factory version 15.1.4 (DPF). The test grid is representative of a typical meshed EHV, HV and MV utility network. DG was only applied to the HV and MV busbars. Utility generation supplied through two constant power and voltage (P, V) busbars. An active and reactive (P, Q) slack bus completes the external grid. No new load was added nor removed from the utility network over the study period and no network changes were applied. No MV feeders were assessed for solar PV connection. A twenty-four hour load profile was assigned to each load bus based on the nature of the downstream customer base. Typical load profiles for bulk, municipality and rural customer loads were used. Constant power load types were assumed on all busbars. Neither network contingencies nor maintenance outages were modelled during the assessment. Due to the non-predictable nature of wind power and data on climatic wind models, wind sources of DG were not considered.

The following conditions were assumed for solar PV DG connection. Climatic conditions were assumed to be for a cloudless day. Sunrise to sunset was assuming to be from 6am to 6pm following a normal distribution pattern of solar irradiance shown in the solid line in

Figure 2. Only one solar PV connection per busbar was tested. Only unity power solar PV DG was connected. Solar PV plants have complete reactive power capability curves as specified by [4], generators are not obliged to supply ancillary services such as reactive power.

Dynamic studies in the milliseconds time range were excluded.

2.1 Optimal placement methodology

The development of the methodology employed critical network factors that contribute to optimal DG placement. The methodology ensures an overview of the 3 ϕ fault levels; existing per unit p.u. voltage levels and real and reactive power flow at each bus. Preventing voltage and thermal violation of equipment is constantly managed throughout the selection process. The final selections of candidate busbars are derived by assessing the optimum system wide loss reduction.

The following flow chart depicts the process followed in the optimal placement methodology.

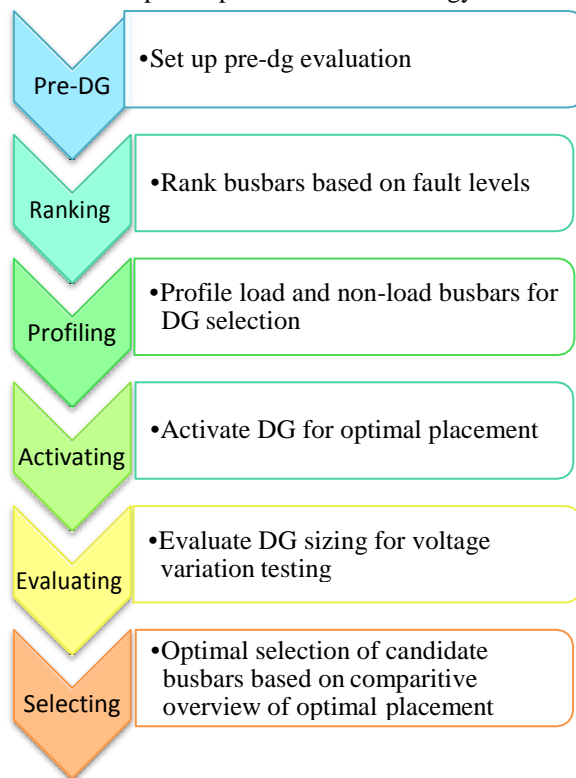


Figure 1 Optimal Placement Methodology

Pre-DG evaluation and analysis commenced with a convergent DIgSILENT Power Factory version 15.1.4 utility network project file. Each load type is configured as a constant power load. Assigning a daily load profile to each load based on the dominant downstream load

characteristics, completes the pre-DG initial configuration setup.

A 24-hour Quasi-Dynamic Simulation (QDS) recorded changes in high and low load and real and reactive power flow was executed. A time based load flow at both high load and low load based on QDS profile was executed. Using the load profile to assess high and low load is more superior than scaling the peak based on assumption. Busbar voltages together with real and reactive power flow results were recorded.

System wide losses were recorded using the grid summary report.

Ranking of busbars for DG sizing was obtained through a 3 phase fault simulation using the IEC 60909 [5] calculation method. Ranking the busbars based on fault level provides an indication of robustness to system disturbance. The ratio of rated DG to system fault level was used as a proxy for percentage disturbance in voltage. Fault level was a useful predictor for DG sizing. DG sizes based on 3-4 percent of fault level did not violate voltage variation.

Profiling load and non-load (network) busbars based on the nature of the load was critical for busbar selection. A good match between the DG profile and load profiles yielded placement with optimum loss reduction results. When real power from the DG source exceeded real power load demand, the surplus power flowed upstream to balance supply and demand. The reverse power flow [6] incurred system losses through transformer and line impedances and should be avoided. Profiling load and non-load busbars supported this process.

Activation of DG on targeted busbars enabled recording of individually study results. DG activation was based on voltage level groupings. DPF scripting was used for multiple DG connections, controlled by variations. Activation required configuration of connections by voltage group. Each variation and expansion stage was assigned a calendar day. Configuration of DG size was based on the percentage of the fault level at the point of connection. Configuration of generator transformers (number of parallel units) to match the generation output was ensured to avoid internal farm losses that contributed to system losses. Configuration of the station controller at unity power factor assured delivery of real power.

Evaluation of voltage variation, through loss of generation, at time of solar peak provided an indication of DG connection suitability. Evaluation of post-DG load flows and grid summary report concluded the evaluation process.

The selection process compared pre- and post-DG results aimed at optimum placement to reduce grid losses.

3 GRID ANALYSIS

The 56 bus sub-transmission grid is characterized by 28 load centred busbars. Load varies as the load profile changes over the course of the day. Network busbars carry aggregated loads and are not deemed to be load centre busbars. Both network and load busbars contribute to the supply of losses as X/R ratios [7] vary of the interconnected power system.

3.1 Reactive power control

Generation of reactive power reduces the maximum export capacity of a solar PV generator. Therefore they operate at unity power factor where they do not have reactive power agreements with utilities. Technically these plants have the capability of supplying and absorbing reactive power. Economically and contractually they may not, unless called upon by the utility's control centre.

Solar power DG reduces the real power requirement on the grid. Alternative reactive power compensation methods must be employed to compensate for the reactive power. Networks with high X/R ratios are more sensitive to changes in reactive power flow and larger compensation may be required.

Utilities must take advantage of solar PV power plants during ramps up and ramp down cycles. This can supplement the supply of reactive power without jeopardizing the maximum export capacity of the plant. A complimentary reactive power curve shown in a dashed line in Figure 2 should be considered. This maintains full apparent power during ramp-up and ramp-down cycles by generating reactive power based on real power requirements. This very important criterion for operation seeks to optimize the reactive power flow through solar DG without additional reactive power compensation. Classical installation of shunt capacitors may still be employed where size exceeds the natural limitation of the solar DG.

Pre-DG phase angles were recorded at all busbars excluding the load busbars. The cosine of the phase angle is the power factor. The power factor of the 11kV Earth bus reflected through the transformer impedance onto the 66kV Earth bus as shown in Table 1. The 66kV Earth bus is supplied via two lines and the impedance of these supply lines affect the phase angle and power flow.

Comparison of pre-and post-DG shows the widening of phase angle and consequently the worsening of the power factor on the HV busbars. As active power is reduced by the supply of DG, reactive power remains unchanged and the power factor at the HV busbar reduces. Utilities can take advantage of the untapped reactive power as explained above to mitigate the need for separate reactive power compensation.

3.2 Impact of penetration and concentration of DG on power losses

The optimal placement methodology can broadly be applied to any form of renewable energy DG. Both wind and solar PV constitute non-dispatchable sources of RE. In this paper, a more predictable solar PV generation pattern was used to confirm the methodology. A solar PV irradiance curve without any cloud disturbance was modelled in DPF shown in Figure 2.

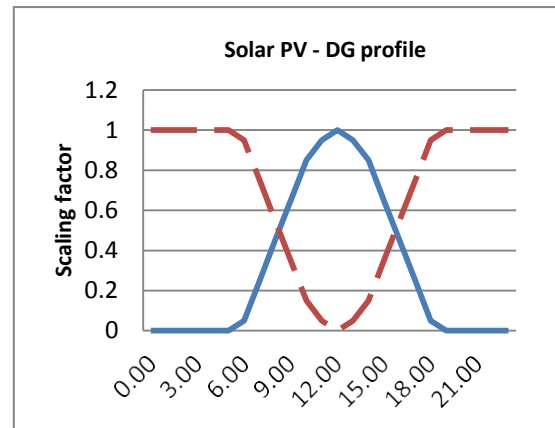


Figure 2 Solar PV Power Output

Subtracting the DG profile from the load profile, results in the “duck” shaped resultant profile visualized in Figure 3. Negative real power represents surplus DG that will flow upstream, from the point of connection, to supply neighbouring load centres through the network. Reverse power flow will incur losses, when the mismatch between the load profile and DG profile is large.

Networks with large penetration and concentration levels of DG will experience increased reverse power flow, thereby leading to an increase in losses. Optimal placement of DG aims to optimize the penetration and concentration levels.

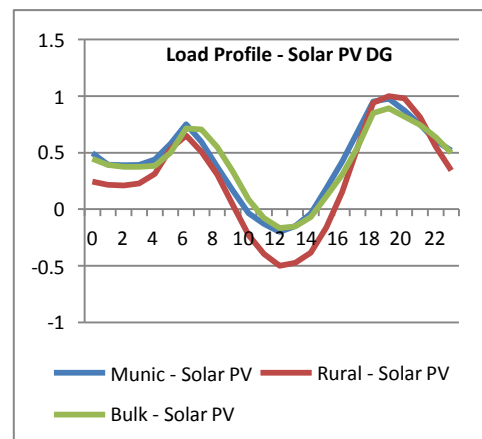


Figure 3: Resultant differential load VS Solar PV profile**3.3 Optimal placement of dg for loss reduction**

The ideal placement methodology was employed on the 56 bar utility network. Results confirmed that varying grid losses were experienced for various DG connections. Critical network factors, such as fault level; load and DG profiles contribute to the loss reduction methodology. Table 2 and Table 3 tabulate the summary of the post-DG connections. The tables list the busbar name at the point of connection busbar and the maximum allowable DG at the point of connection. The pre-DG load at time of solar peak is provided for comparative purposes. The real and reactive power losses calculated as a result of the methodology. The pre- to post-DG percentage change in real and reactive power losses.

Post-DG results for the grouped 11kV busbars revealed the largest impact of reduce losses, since DG was applied at the load centre. The application of solar PV at the 11kV Earth busbar yields the most optimum location for DG. The 11kV Earth busbar carries a characteristic municipality load profile. This profile is suited for solar PV reduction as there is sufficient mid-day load to reduce active power without creating reverse power flow. Application of solar PV to typical rural “twin peak” profiles has not yielded optimum results.

Post-DG results for the grouped 22kV busbar reveal the 22V Sapphire and Mercury busbars are close contenders for optimal DG placement. Sapphire and Mercury carry a municipality and bulk load profiles respectively. Ranking the fault levels of these locations reveal the following. The fault level at the 11kV Earth busbar is 200MVA, followed by Sapphire with 175MVA and Mercury with a fault level of 100MVA.

All 33kV busbars feed 11kV busbars and 11kV load. Comparison of losses studied showed a higher loss reduction at 33kV compared with the 11kV busbars. Higher 33kV fault levels imply larger sources of DG. Injection of DG at 33kV reduced the power required from the upstream network, thereby reducing the losses. Table 2 confirms support of the 33kV voltage grouping of at least twice the DG capacity at 11kV. The 33kV busbars also show approximately two-thirds loss reduction.

Increased power losses for larger sizing of DG at 66kV busbar voltages were observed. Earth and Mercury 66kV busbars display optimized loss reduction compared to pre-DG.

Even higher power losses for larger sizing of DG at the 88kV busbar groupings were observed. The pre-DG load flow at 12pm shows 57MW flowing through the 88kV Sub busbar. This bus has 45 MW solar PV connected, but since it is not a load bus, the injected DG needs to flow to the closest load centre. This results in an increase in real and reactive power losses as shown in the “Delta Grid Loss MW and MVar” columns of

Table 2. The reason for the reduced reactive power losses compared with Sub 88kV lies in the impedance of the 33kV network

The 132kV busbar grouping of voltages experienced the largest increase in losses. In cases where local load exists, these loads are serviced first and surplus power flows to adjacent load centres. 132kV Pearl and White busbar fits this description and have relatively smaller losses. The 132kV busbar grouping experienced large amounts of DG being injected into the busbars. These busbars serve only to redirect the flow of power to other parts of the network, thereby incurring losses. Diamond and ST1 SUB 132kV experienced a doubling of the losses when compared to the base case, prior to DG.

Small amounts of DG applied at the load centre busbar are more effective than large amounts of DG further from the load centre. A good profile match between the type of DG and load is also required.

4 CONCLUSION

The optimal methodology for DG placement was presented in this paper. The process of ranking, profiling, activating, evaluating and selecting busbars for DG connection to reduce losses was defined. This methodology enabled a consistent approach to be followed DG connection. Future scholars and utility engineers can apply this logical approach to study the impact of DG connections.

Integration of DG highlighted the critical nature of reactive power compensation. When real power is supplied by DG, power factor and subsequently reactive power needs to be compensated. High X/R ratios at higher voltage levels are more sensitive to changes in reactive power. Compensation from DGs at load level can be used to reduce the compensation of reactive power. The absence thereof will require independent costly solution. [8] Provides a technique for optimum placement of reactive power compensation to reduce reactive power flows.

Table 1 confirmed the change in power factor from pre- to post-DG at the 66kV Earth busbar. Similar comparisons were made for each pre- and post-DG connection to validate the changes in the phase angle and resulting reactive power flow. Losses based on penetration of DG follows a “U-Shaped” trajectory [9], initially decreasing, followed by an increase as a result of increased penetration and concentration.

The most favourable response observed for DG injection, whilst reducing losses was on municipality and bulk load profiles. High load factor profiles present ideal characteristics for complete absorption of solar DG. Reduced surplus injected power reduces reverse power flow and ultimately losses.

Generator characteristics are equally important as the renewable energy sources of wind and solar PV are neither continuous nor constant throughout the day. The net power flow (P_{Net}) from a DG injected busbar is the

algebraic difference between active (P_{Load}) and distributed generated power (P_{Gen}). By convention power flowing into a busbar is represented as negative. When (P_{Net}) is negative, surplus DG power flows upstream to supply load at neighbouring load centres. Where (P_{Net}) is positive, all DG power has been consumed by the load.

Storage of solar power beyond daylight hours enables an extended solar profile. Broadening the shape of the solar power pattern will enable the supply of solar power to impact the evening peak. This will have a significant impact on loss reduction. Technologies such as concentrated solar power (CSP) are preferred if cost effective. Alternative storage via battery power may also be considered to alter the solar PV daily profile.

This research supports the theory that these technologies will positively impact on ideal placing of DG on meshed network to reduce power loss.

5 ACKNOWLEDGMENT

The author would like to acknowledge the Smart Grid centre (UKZN) and Eskom Holdings Limited SOC for their financial support.

6 REFERENCES

- [1] L. L. Grigsby, *Electric Power Generation, Transmission, and Distribution, Third Edition*, vol. 20124365. CRC Press, 2012.
- [2] W. Tan, M. Y. Hassan, M. S. Majid, and H. A. Rahman, "Optimal distributed renewable generation planning: A review of different approaches," *Renewable and Sustainable Energy Reviews*, vol. 18, pp. 626–645, Feb. 2013.
- [3] "Electricity Supply - Quality of Supply - PART 2," National Rationalized Specification Ed. 3, Dec. 2007.
- [4] "South African Grid Code Requirements for Renewable Power Plants," Eskom Transmission Division, South Africa, Version 2.8, Jul. 2014.
- [5] T. N. Boutsika and S. A. Papathanassiou, "Short-circuit calculations in networks with distributed generation," *Electric Power Systems Research*, vol. 78, no. 7, pp. 1181–1191, Jul. 2008.
- [6] A. Gabash and P. Li, "Variable reverse power flow-Part I: A-R-OPF with reactive power of wind stations," in *2015 IEEE 15th International Conference on Environment and Electrical Engineering (EEEIC)*, 2015, pp. 21–26.
- [7] RaoS Thallam and Géza Joós, "Reactive Power Compensation," in *Electric Power Generation, Transmission, and Distribution, Third Edition*, 5 vols., CRC Press, 2012, pp. 1–20.
- [8] M. Ntusi, "Optimal placement of shunt capacitor banks on a sub-transmission network," Dissertation, 2009.
- [9] V.H.M. Quezada, J.R. Abbad, and T.G.S. Román, "Assessment of energy distribution losses for increasing penetration of distributed generation," *IEEE Transactions on Power Systems*, vol. 21, no. 2, pp. 533–540, May 2006.

7 APPENDIX

Table 1, Table 2 and Table 3 are presented as the table of results.

Table 1 Phase angle comparison pre and post DG

DG Status	Terminal i	Terminal j	Angle between Voltage and Current Terminal i in deg.	Angle between Voltage and Current Terminal j in deg.
Pre-DG	Earth 66kV	Mercury 66kV	-135.1113	42.9492
Pre-DG	Sapphire 66kV	Earth 66kV	9.3246	-171.0584
Post-DG	Earth 66kV	Mercury 66kV	-113.6103	62.93881
Post-DG	Sapphire 66kV	Earth 66kV	18.65493	-160.8706

Table 2: Medium voltage table of results

Bus Name Voltage	Max RE (MVA)	Pre DG load MW @ 12PM	Pre DG load MVA @ 12PM	Sub Tx Grid Loss MW	Sub Tx Grid Loss MVA	Delta Grid Loss MW	Delta Grid Loss MVA
Earth 11kV	8	19.6490	5.3359	7.03	16.24	-9.5%	-13.3%
Nandos 11kV	7	18.2617	-5.2482	7.56	16.82	-2.7%	-10.2%
Yellow 11kV	6	13.7973	2.9603	7.56	16.41	-2.7%	-12.4%
Blou 11kV	6	7.6028	2.5667	7.58	16.73	-2.4%	-10.7%
Pink1 11kV	6	3.8021	0.7822	7.6	16.82	-2.2%	-10.2%
Pink2 11kV	6	5.3897	1.1892	7.6	16.94	-2.2%	-9.6%
Orange 11kV	6	6.5435	2.1442	7.63	17.03	-1.8%	-9.1%
Basket 11kV	7	4.6455	1.0742	7.64	16.87	-1.7%	-9.9%
Green 11kV	6	4.8667	1.4457	7.65	17.16	-1.5%	-8.4%
Black 11kV	4	6.0242	1.1620	7.66	17.45	-1.4%	-6.8%
Ruby 11kV	4	2.5650	1.5333	7.82	18.31	0.6%	-2.2%
LinkedIn 11kV	9	18.5820	-7.0437	7.87	17.42	1.3%	-7.0%
Sapphire 22kV	7	10.3217	1.8484	7.34	16.97	-5.5%	-9.4%
Mercury 22kV	4	3.4761	0.6682	7.45	17.72	-4.1%	-5.4%
Saturn 22kV	4	4.3228	1.1534	7.59	17.91	-2.3%	-4.4%
Emerald 22kV	6	5.1609	0.9708	7.59	17.61	-2.3%	-6.0%
Jupiter 22kV	5	2.6357	0.7419	7.62	17.88	-1.9%	-4.5%
Uranus1 22kV	4	3.9600	0.7314	7.63	17.94	-1.8%	-4.2%
Uranus2 22kV	4	2.9700	0.5679	7.64	17.99	-1.7%	-4.0%
Pluto 22kV	4	2.8350	-1.7034	7.66	18.28	-1.4%	-2.4%
Topaz 22kV	3	2.3520	0.9373	7.66	18.16	-1.4%	-3.0%
Pearl 22kV	6	6.2208	1.7326	7.7	17.7	-0.9%	-5.5%
Jade 22kV	3	2.9400	0.7462	7.75	18.19	-0.3%	-2.9%
Ruby 22kV	4	3.0240	1.1291	7.8	18.28	0.4%	-2.4%
Mars 22kV	10	4.7700	-2.6984	8.05	18.06	3.6%	-3.6%
Blou 33kV	12	7.6447	2.8427	7.53	15.66	-3.1%	-16.4%
Yellow 33kV	12	20.1666	7.0702	7.53	15.68	-3.1%	-16.3%
Red 33kV	5	5.1815	1.8465	7.54	17.03	-3.0%	-9.1%
Pink 33kV	12	7.6447	1.8237	7.57	15.87	-2.6%	-15.3%
Orange 33kV	13	6.5795	2.3599	7.58	15.73	-2.4%	-16.0%
Green 33kV	14	8.1242	0.0022	7.6	15.64	-2.2%	-16.5%
Basket 33kV	16	19.4249	9.8507	7.6	15.26	-2.2%	-18.5%
Black 33kV	14	9.0460	0.4092	7.61	15.69	-2.1%	-16.2%
White 33kV	15	17.1908	0.4541	7.62	15.57	-1.9%	-16.9%

Table 3: High voltage table of results

Bus Name Voltage	Max RE (MVA)	Pre DG load MW @ 12PM	Pre DG load MVA _r @ 12PM	Sub Tx Grid Loss MW	Sub Tx Grid Loss MVA _r	Delta Grid Loss MW	Delta Grid Loss MVA _r
Earth 66kV	13	19.7955	6.2409	7.52	16.88	-3.2%	-9.9%
Mercury 66kV	11	7.2681	4.2762	7.69	17.28	-1.0%	-7.7%
Saturn 66kV	6	4.3491	1.2512	7.88	18	1.4%	-3.9%
Sapphire 66kV	16	26.6554	4.8990	7.96	17.3	2.4%	-7.6%
Topaz 66kV	7	2.3664	0.9944	8	18.1	3.0%	-3.4%
Uranus 66kV	13	6.9671	1.4930	8.15	17.77	4.9%	-5.1%
Emerald 66kV	13	5.1798	1.1598	8.17	17.8	5.1%	-5.0%
Jade 66kV	5	2.9563	0.8204	8.25	18.71	6.2%	-0.1%
Jupiter 66kV	16	10.2016	4.7614	8.28	17.76	6.6%	-5.2%
Pluto 66kV	16	29.1642	8.7594	8.28	17.77	6.6%	-5.1%
Ruby 66kV	9	5.6245	2.8332	8.5	18.74	9.4%	0.1%
Diamond 66kV	41	77.4664	17.3212	10.93	20.13	40.7%	7.5%
Sub 88kV	45	57.7221	0.9387	11.26	21.75	44.9%	16.1%
Basket 88kV	20	19.5157	11.0402	8.67	18	11.6%	-3.9%
Nandos 88kV	10	18.2781	-4.4193	8.01	17.67	3.1%	-5.7%
LinkedIn 88kV	17	18.5985	-6.1468	8.86	18.97	14.0%	1.3%
Pearl 132kV	25	43.7958	10.6134	8.25	18.71	6.2%	-0.1%
Yellow132kV	20	20.1839	8.2596	8.55	17.62	10.0%	-5.9%
Pluto 132kV	23	32.1047	8.4864	8.73	19.18	12.4%	2.4%
White 132kV	24	37.4567	8.7442	8.83	17.9	13.6%	-4.4%
Diamond 132kV	89	77.7192	21.2553	15.43	30.17	98.6%	61.1%
ST1 Sub 132kV	98	78.1757	17.4836	16.61	31.44	113.8%	67.9%

Assessment of Power System Stabilizers for Small Signal Stability using the Population-Based Incremental Learning algorithm

D Dombo* and Prof K A Folly*

* University of Cape Town, Department of Electrical Engineering, South Africa

Abstract – In this paper, the performance of power system stabilizers (PSSs) designed using adaptive Population-Based Incremental Learning (APBIL) algorithm is assessed by comparing it to the standard PBIL. The main difference between PBIL and APBIL is that APBIL has a varying learning rate while the standard PBIL has a fixed learning rate. After converting the problem of tuning of PSS parameters into an optimization problem, the above mentioned algorithms are applied to solve the small signal improvement problem. In this case, the main objective of the design is to achieve adequate damping over a wide range of operating conditions of the power system. The simulation results show that the APBIL based PSSs are more effective than the standard PBIL based PSSs at damping low frequency oscillations.

Key Words –PBIL, Learning Rate, Damping ratio, Power System Stabilizer

1. INTRODUCTION

Over the years there has been an increase in the application of Evolutionary Algorithms (EAs) to solve various optimization problems in engineering. Some of the EAs which have been developed to solve some of the optimization problems are Genetic Algorithms [1], Breeder Genetic Algorithms (GA) [2], Particle Swarm Optimization (PSO) [3], Population-Based Incremental Learning (PBIL) [4], [5], [6], [7], [8], Differential Evolution (DE) [9], [10], etc. Among the above listed algorithms, the most commonly applied EA for solving optimization problems is GAs [11]. These algorithms are motivated by natural selection and natural genetics [1]. The GAs incorporate the concept of survival of the fittest which ensures better approximations to a solution are produced [4], [12]. During the optimization process, genetic diversity has to be maintained so as to perform thorough search of the search space [4]. In the cases where diversity is not maintained, premature convergence may result [6]. This is one main limitation faced by GAs. Some of the other drawbacks of GAs are related to the difficulties in selecting optimal genetic operators and high computational cost in solving complex problems. To overcome some of the shortcomings of GAs, PBIL has been proposed by Baluja [4]. It is evident that PBIL has been receiving increasing attention in recent years [6], [7], [8], [13], [14].

In the study being reported in this paper, adaptive PBIL (APBIL) and standard PBIL are used to tune Power System Stabilizer parameters so as to improve the damping on the system. The performances of the designed controllers are evaluated by analyzing the time domain and frequency domain simulation results. The results show that both the APBIL based controllers and PBIL based controllers are successful in providing sufficient damping to the system. However, the APBIL based PSSs provide better damping.

2. THEORETICAL BACKGROUND

2.1 Background to PBIL

PBIL is a technique which combines mechanisms of a general genetic algorithm with simple competitive learning [4]. This algorithm belongs to the family of Estimation of Distribution Algorithms. PBIL just like all other EDAs adapts most of the GA operators although the crossover operator is abstracted away by the estimation and sampling of the joint probability vector of the chosen individuals [15], [16]. This algorithm makes use of the probability vector (PV) to generate sample solutions. The main purpose of the PV is to guide the search during the learning process and from it, sample solutions are drawn to produce the sample solutions of the next generation [17].

The following is the summary of the PBIL used in this paper [17], [18]- [19], [20]:

- Step 1: Initialization of the probability vector (PV) so as to ensure uniformly-random bit strings.
- Step 2: Generation of a population of uniformly-random bit strings and comparing them element by element with the PV. Wherever an element of the PV is greater than the corresponding random element, a '1' is generated, otherwise a '0' is generated.
- Step 3: Interpretation of each bit string as a solution to the problem and evaluation of its merit in order to identify the "Best".
- Step 4: Adjusting the PV by slightly increasing $PV(i)$ to favor the generation of bit strings which resemble "Best", if $Best(i) = 1$ and decrease $PV(i)$ if $Best(i) = 0$.
- Step 5: Generation of a new population reflecting the modified distribution. Terminate if a satisfactory solution is found or else go to step 3.

In the next section, the PBIL with adaptive learning rate is discussed.

2.2 APBIL

The proposal of this variant of PBIL attempts to overcome challenges faced when a fixed learning rate (LR) is used. Unlike on the standard PBIL where the learning rate is fixed, on this algorithm the learning rate is allowed to vary as the optimization process is being carried out, from generation to generation. Some of the challenges faced by using a fixed learning rate are that it limits the algorithm's capability and more time has to be spent on selecting the most suitable LR. There is also no guarantee that after spending large amounts of time choosing the most suitable LR that it will be best value to use. In the cases where the search space environment is dynamic and ever changing, which is the case in power systems a fixed LR may not be adequate for obtaining optimal control parameters [19].

In developing the APBIL, a trade-off between exploration and exploitation has to be established and it is directly affected by the LR [21]. These terms have been defined differently in literature [21], [22], [23]. Where exploitation can be defined as the generation of new individuals through thoroughly searching in as yet untested regions of the function space and exploitation can be defined as the concentration of the search in the vicinity of good solutions based on the information that the algorithm has gained about the search space [22]. During the optimization process it is assumed that diversity is needed at the early stages of the run and this is referred to as the exploration phase [24]. If diversity is not maintained during the run, premature convergence may result [23]. In PBIL, the issue of premature convergence results if the LR value is too high which could lead to the algorithm converging to a local optimal solution. On the other hand, in the case of a LR which is too small, the algorithm may require more time to converge to an optimal solution, which may be time consuming and it is computationally costly [19]. Taking this into consideration the LR value is chosen to be very small ($LR \approx 0$) at the beginning of the run. Consequently for the first generations, the emphasis is more on the exploration than exploitation. With the increase in the number of generations, the emphasis is then gradually shifted from exploration to exploitation. In this paper, during optimization process the LR is varied linearly according to the following equation:

$$LR(i) = LR \frac{G(i)}{G_{max}} \quad (1)$$

where

$LR(i)$ is the learning rate at the i th generation

LR is the final learning rate

$G(i)$ is the i th generation

G_{max} is the maximum generation

3. SYSTEM MODEL AND OPERATING CONDITIONS

The power system model considered in this paper is the two-area four machine system as shown in Fig. 1 [25]. For small signal stability analysis purposes all the machines are sixth order models, also known as the sub-transient models. Each machine is equipped with a simple exciter which is modelled by a first order differential equation [10], [19], [26]. Several operating conditions which involve power transfer from area 1 to area 2 were considered in the design but for simplicity, only 3 operating conditions are discussed here. The operating conditions used in the design of controllers are listed in Table I. The double transmission line between bus 3 and 13 is in service for case 1 and 2. For Case 3 of the operating conditions, one transmission line between bus 3 and 13 is out of service thus the power is transferred to area 2 using the remaining single line.

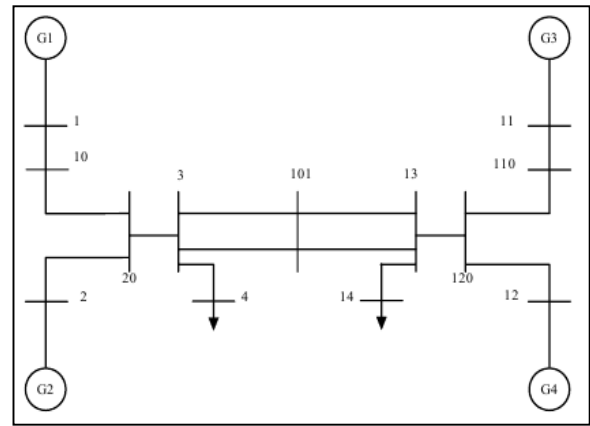


Fig. 1 Two area multi-machine system [25]

Table I: Selected Operating Conditions

Case	Real Power Flow[MW]
1	400
2	500
3 (One line out of service)	300

4. OBJECTIVE FUNCTION

In this paper, PSS parameters are optimized using PBIL and APBIL such that the controllers provide sufficient damping to the power system over a wide range of operating conditions.

The objective function is formulated as follows:

$$J = \max(\min(\zeta_{i,j})) \quad (2)$$

where:

$i = 1, 2, 3 \dots n$ and $j = 1, 2, 3 \dots m$

$$\zeta_{i,j} = \frac{-\sigma_{i,j}}{\sqrt{\sigma_{i,j}^2 + \omega_{i,j}^2}}$$

where, $\zeta_{i,j}$ is the damping ratio of the i -th eigenvalue corresponding to the j -th operating condition. The eigenvalues are made up of $\sigma_{i,j}$ and $\omega_{i,j}$ which represent the real part and the imaginary part (frequency of oscillation) respectively.

The power system controller parameters for both PBIL and APBIL are designed to maximize the objective function J subject to the following constraints:

$$\begin{aligned} 0 &\leq K_p \leq 30 \\ 0 &\leq T_1, T_3 \leq 1 \\ 0.01 &\leq T_2, T_4 \leq 0.3 \end{aligned}$$

5. PARAMETER SETTINGS OF PBIL AND PBIL

5.1 PSS Design using PBIL

Parameter settings that were used for PBIL-PSS are as follows:

Length of Chromosome: 15 bits

Population: 100

Generation: 400

Learning rate: 0.2

Forgetting Factor: 0.005

5.2 PSS Design using APBIL

Parameter settings that were used for APBIL-PSS are as follows:

Length of Chromosome: 15 bits

Population: 100

Generation: 400

Learning rate: minimum: 0.0005 and maximum 0.2

Forgetting Factor: 0.005

6. RESULTS

6.1 Frequency domain results

Table presents the open loop and closed-loop eigenvalues for the inter-area mode. It can be seen that the open-loop inter-area mode is unstable for all the three cases considered, as can be seen by the negative values of the damping ratios. Considering the closed-loop modes, it can be seen that the damping ratio has been improved significantly by both PSSs. However, APBIL-PSS provides better damping ratios of 0.2435, 0.2616 and 0.2506 for cases 1, 2, and 3 respectively compared to damping ratios of 0.1644, 0.1811 and 0.1733 for case 1, 2 and 3, respectively for PBIL-PSS. The closed-loop inter-area mode is stable for all cases.

Table II: Open and closed loop Inter-area modes

Case Study	No-PSS	PBIL	APBIL
1	$0.063 \pm 3.393i$ (-0.0186)	$-0.73 \pm 4.38i$ 0.1644	$-1.05 \pm 4.19i$ 0.2435
2	$0.025 \pm 3.477i$ (-0.00719)	$-0.81 \pm 4.41i$ 0.1811	$-1.15 \pm 4.24i$ 0.2616
3	$0.012 \pm 2.641i$ (-0.00454)	$-0.66 \pm 3.77i$ 0.1733	$-0.91 \pm 3.52i$ 0.2506

Note: damping ratios are in brackets

6.2 Time domain results under small disturbance

A small disturbance of 5 % is applied to the reference voltages of the generators. The following figures show the change in generator active power for the cases considered for G1 and G4 only. Fig. 2 - Fig. 4 show the responses for G1, while Fig. 5 - Fig. 7 show the responses for G4. From the Fig. 2 - Fig. 4 shown, it can be seen that APBIL-PSS has better settling times of about 3 sec while PBIL-PSS has about 5 sec. Both controllers are able to damp the oscillations and improve the stability of the system. It should be noted that in all the cases, APBIL-PSS has slightly higher overshoots and undershoots than PBIL-PSS for the first swing. This still needs to be investigated.

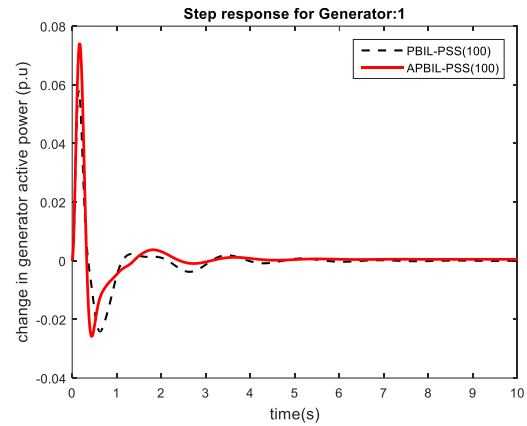


Fig. 2 Change in active power of G1 for case 1

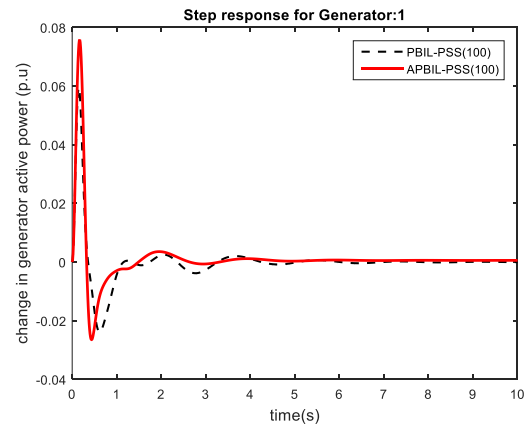


Fig. 3 Change in active power of G1 for case 2

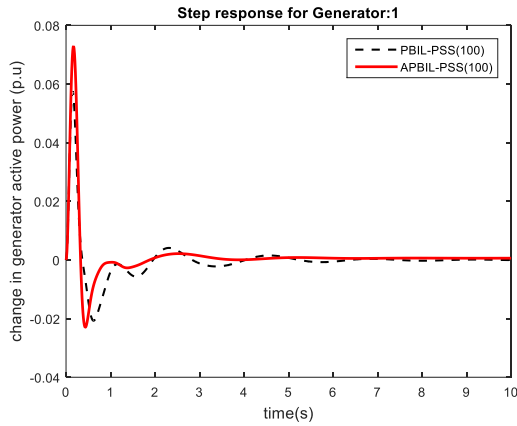


Fig. 4 Change in active power of G1 for case 3

From Fig. 5 - Fig. 7 it can be seen that APBIL-PSS has settling times of about 5 sec whereas PBIL-PSS has settles at about 7 sec. Again APBIL-PSS has slightly higher overshoots and undershoots than PBIL-PSS for the first swing, however, the oscillations damped out very quickly in the subsequent swings. .

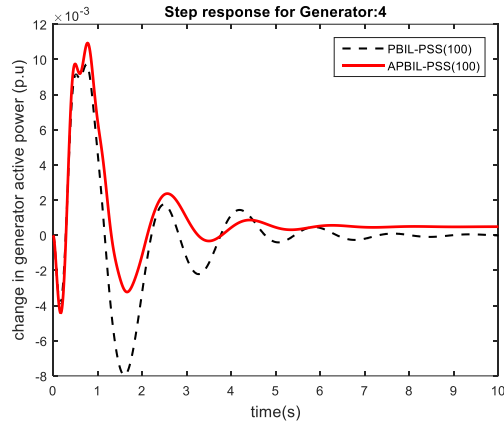


Fig. 5 Change in active power of G4 for case 1

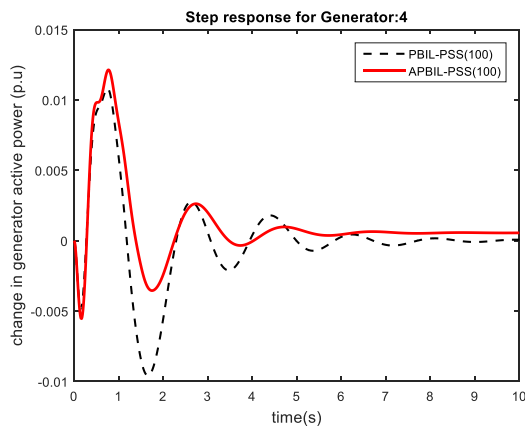


Fig. 6 Change in active power of G4 for case 2

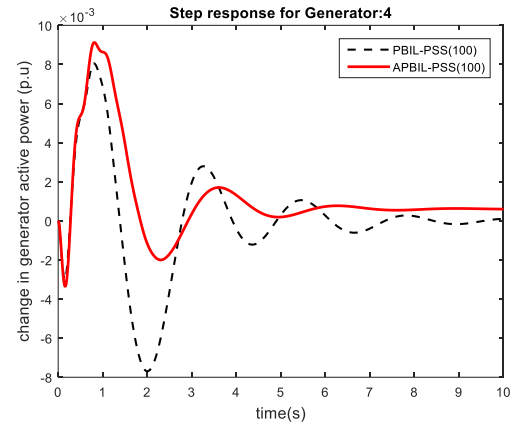


Fig. 7 Change in active power of G4 for case 3

6.3 Time domain results under large disturbance

A three phase fault was applied at bus 3 at 0.5 sec for a duration of 3 cycles. For these simulations only the electrical power output responses of G3 are considered here for the 3 cases. It can be seen that the PSSs perform adequately with very similar settling time. However, APBIL-PSS performing slightly better than PBIL with slightly lower overshoots and undershoots than PBIL-PSS.

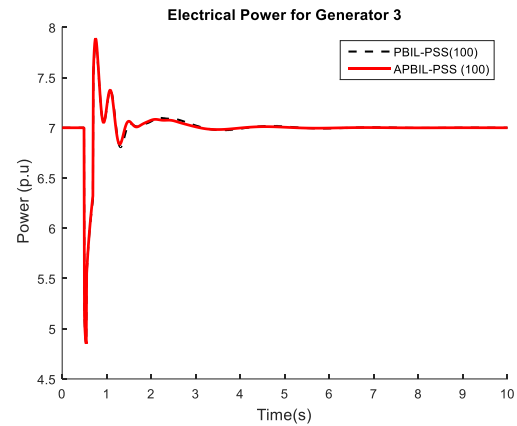


Fig. 8 Electrical Power for G3 case 1

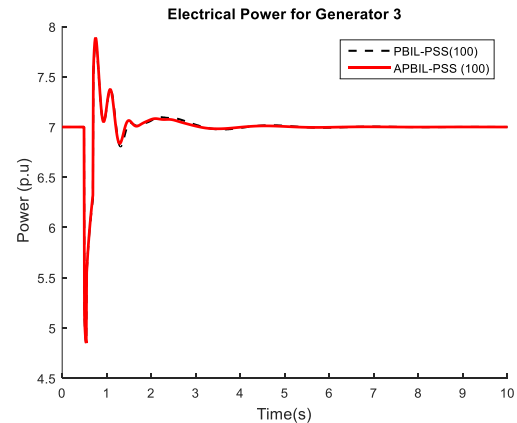


Fig. 9 Electrical Power for G3 case 2

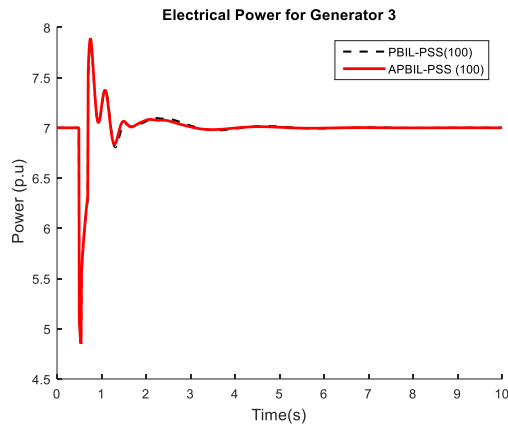


Fig. 10 Electrical Power for G3 case 3

7. CONCLUSIONS

APBIL and PBIL algorithms have been successfully applied to the problem of improving the small-signal stability. Frequency and Time domain results show that all the PSSs are able to provide adequate damping thus improving the overall dynamic stability of the system. Generally, APBIL based PSSs performs much better than the PBIL based PSSs as observed from the damping ratios. Time domain simulations under large disturbance are presented to validate the results. The issue on the overshoots and undershoots of APBIL is still under investigation.

REFERENCES

- [1] R. Shivakumar, M. Panneerselvam and R. Lakshminpathi, "Robust Optimal Controller Design for Multimachine Systems using Genetic Algorithms," *International Journal of Engineering and Technology*, vol. 2, no. 2, pp. 97-101, 2010.
- [2] H. Mühlenbein and D. Schlierkamp-Voosen, "The Science of Breeding and Its Application to the Breeder Genetic Algorithm (BGA)," *Evolutionary Computation*, vol. 1, no. 4, pp. 335-360, Dec 1993.
- [3] L. Changhe, Y. Shengxiang and T. N. Trung, "A Self-Learning Particle Swarm Optimizer for Global Optimization Problems," *Systems, Man, and Cybernetics, Part B: Cybernetics, IEEE Transactions on*, vol. 42, no. 3, pp. 627-646, June 2012.
- [4] S. Baluja, "Population-Based Incremental Learning: A Method for Integrating Genetic Based Search Function Optimization and Competitive Learning," Carnegie-Mellon University Pittsburgh Pa Dept Of Computer Science, 1994.
- [5] K. Folly and G. K. Venayagamoorthy, "Effects of learning rate on the performance of the population based incremental learning algorithm," in *Neural Networks, 2009. IJCNN 2009. International Joint Conference on*, 2009.
- [6] S. P. Sheetekela and K. A. Folly, "Power system controller design: A comparison between breeder genetic algorithm and Population Based Incremental Learning," in *Neural Networks (IJCNN), The 2010 International Joint Conference on*, 2010, pp. 1-8.
- [7] K. Folly and G. K. Venayagamoorthy, "A Real-Time Implementation of a PBIL Based Stabilizing Controller for Synchronous Generator," in *Industry Applications Society Annual Meeting, 2009. IAS 2009. IEEE*, 2009, pp. 1-8.
- [8] K. Folly, "An Improved Population-Based Incremental Learning Algorithm," *International Journal of Swarm Intelligence Research (IJSIR)*, vol. 4, no. 1, pp. 35-61, 2013.
- [9] T. Mulumba, K. A. Folly and O. P. Malik, "Tuning of PSS parameters using Differential Evolution," in *Proc. of the 20th Southern African Universities' Power Engineering Conference-SAUPEC 2011*, 2011.
- [10] K. A. Folly and T. Mulumba, "Self-Adaptive DE Applied to Controller Design," *Journal of Computer and Communications*, vol. 2, no. 9, pp. 46-53, 2014.
- [11] A. H. Ahmad and A. Abdelqader, "Power system stabilizer design using real-coded genetic algorithm," in *Control, Instrumentation and Automation (ICCIA), 2011 2nd International Conference on*, 2011.
- [12] H. Guo-qiang, X. Dong-jie and H. Ren-mu, "Genetic algorithm based design of power system stabilizers," in *Electric Utility Deregulation, Restructuring and Power Technologies, 2004.(DRPT 2004). Proceedings of the 2004 IEEE International Conference on*, 2004.
- [13] K. A. Folly, "Robust controller design based on a combination of genetic algorithms and competitive learning," in *Neural Networks, 2007. IJCNN 2007. International Joint Conference on*, 2007.
- [14] K. A. Folly, "Design of power system stabilizer: a comparison between genetic algorithms (GAs) and population-based incremental learning (PBIL)," in *Power Engineering Society General Meeting, 2006. IEEE*, 2006.
- [15] C. Gonzalez, J. A. Lozano and P. Larranaga, "Analyzing the Population Based Incremental Learning Algorithm by Means of Discrete Dynamical Systems," *Complex Systems*, vol. 12, pp. 465-479, 2000.

- [16] K. A. Folly and S. P. Sheetekela, "Application of a simple Estimation of Distribution Algorithm to power system controller design," in *Universities Power Engineering Conference (UPEC), 2010 45th International*, 2010, pp. 1-6.
- [17] K. Folly, "Parallel PBIL Applied To Power System Controller Design," *Journal of Artificial Intelligence and Soft Computing Research*, vol. 3, no. 3, pp. 215-223, 2013.
- [18] S. P. Sheetekela and K. A. Folly, "Power system controller design: A comparison between breeder genetic algorithm and Population Based Incremental Learning," *The 2010 International Joint Conference on Neural Networks (IJCNN)*, pp. 1-8, 2010.
- [19] K. A. Folly, "Population-Based Incremental Learning with Adaptive Learning Rate Strategy," in *Advances in Swarm Intelligence*, Springer Berlin Heidelberg, 2012, pp. 11-20.
- [20] K. A. Folly and G. K. Venayagamoorthy, "Performance Evaluation of a PBIL-Based Power System Damping Controller," *IEEE Congress on Evolutionary Computation (CEC)*, pp. 1-7, 2010.
- [21] K. A. Folly and G. K. Venayagamoorthy, "Optimal tuning of System Stabilizer parameters using PBIL with adaptive learning rate," in *Power and Energy Society General Meeting, 2010 IEEE*, 2010, pp. 1-6.
- [22] A. E. Eiben and J. E. Smith, *Introduction to Evolutionary Computing*, Springer Science & Business Media, 2003.
- [23] A. E. Eiben and J. E. Smith, *Introduction to Evolutionary Computing*, Springer Science & Business Media, 2015.
- [24] Y. Tenne and C.-K. Goh, *Computational intelligence in expensive optimization problems*, vol. 2, Springer Science & Business Media, 2010.
- [25] J. Chow and G. Rogers, "Power System Toolbox Version 3.0 manual".
- [26] P. Kundur, *Power system stability and control*, McGraw-hill New York, 1994.

Guiding Principles for Grid Code Compliance of Medium-High Voltage Renewable Power Plant Distributed Generation Integration onto South Africa's Transmission and Distribution Networks

S. Sewchurran^{1*} and I E Davidson²

¹eThekweni Electricity, eThekweni Municipality, Durban 4001, South Africa

² University of KwaZulu-Natal, Eskom Centre of Excellence in HVDC Engineering, Durban 4001, South Africa

*Email: SewchurranSan@elec.durban.gov.za

Abstract: Electricity shortages, rising electricity prices, carbon taxes and delays in constructing new power stations have plunged South Africa into blackouts and frequent power outages due to a need for load shedding. This has led the South African Government calling on Independent Power Producers and the stakeholders to explore renewable energy generation options to meet its electricity demands. There has been interest shown in the distributed generation sector by Independent Power Producers and consumers. Electric power utilities are now faced with various challenges in understanding the impact these DG plants will have on their existing networks in view of limited technical expertise and industry standards to ensure the safe, and technical integration of these plants into existing medium and high voltage networks in South Africa. The paper discusses the current South African Renewable Energy Grid Code and testing methods for Renewable Power Plants to ensure compliance to the Grid Code.

1 INTRODUCTION

Energy security, economic and environmental benefits have produced an increased interest in the widespread usage of Distributed Generation (DG) worldwide [1]. In South Africa there has been an increasing number of requests to connect DG onto Eskom and local municipal distribution networks. This is driven in part by the prevailing energy shortages, load shedding, rising electricity prices, lower DG technology costs, proposed carbon taxes, reduction in greenhouse gas emissions (GHG) and carbon footprint, the Department of Energy (DOE) Renewable Energy Independent Power Producer Procurement Programme (REIPPPP) and DG ability to alleviate network congestion and to improve overall electricity security in South Africa [2].

Hitherto, South Africa's renewable energy (RE) policy (2003) has been largely driven by the target of 10000 GWh by 2013 and RE project subsidies offered through the Renewable Energy Finance and Subsidy Office. From 2009 to 2011, a renewable energy feed-in tariff (REFIT) was considered and published, which resulted in great interest by Independent Power

Producers (IPP) to develop RE projects in South Africa. However due to legislation in 2001 the REIPPPP was launched by the DOE as a competitive procurement program in its place. In terms of section 34 of the South African Electricity Regulation Act (Act No. 4 of 2006), the Minister has determined that 3725 Megawatts (MW) is to be generated from RE sources to ensure uninterrupted supply of electricity. This 3725 MW is broadly defined in accordance with the capacity allocated to RE generation in the Integrated Resource Plan (IRP) 2010 - 2030. This procurement program has been designed to contribute towards: the 3725MW target; enhance social-economic and environmentally sustainable growth, and to stimulate the RE industry in South Africa. [3]

The IRP 2010, approved and published in May 2011 by the DOE, outlines the proposed power mix for South Africa. The IRP 2010 seeks to increase the overall contribution of new RE generation to 17800MW by 2030. This is 42% of all new-build generation. Based on the approved IRP 2010, on the 2nd July 2011, the Minister of Energy issued a determination for the IPP procurement programme in accordance with section 34(1) of the Electricity Regulation Act, 2006. The Energy Regulator concurred with the Ministerial determination on the 7th July 2011. On the 19th December 2012, the Minister of Energy made a new determination for the procurement of an additional 3200 MW capacity to the previous determination of 3750 MW. The total capacity to be procured is currently 6925 MW [3].

It accordance to the Electricity Regulation Act (Act 4, 2006), it is mandatory for all Renewable Power Plants (RPP) connecting on the transmission or distribution grid to comply with the requirements of the South African Renewable Energy Grid Code (SAREGC). The SAREGC was first published in 2010 and has evolved into the current version 2.8 of the code released. In the SAREGC, the minimum technical

requirements for an RPP is specified and determined based on size of the plant and connection voltage level. The Grid Code is applicable to all RE technologies, namely: photovoltaic plants, concentrated solar power plants, small hydro power plants, landfill gas power plants, biomass power plants, biogas power plants and wind power plants.

To date, the SAREGC has been used to certify compliance of all medium and large scale REIPPPP projects connecting onto the local South African grid. Fig. 1 shows the allocation of REIPPPP RPP locations in each province from round 1 to round 3.5 with a cumulative power output of 4131 MW.

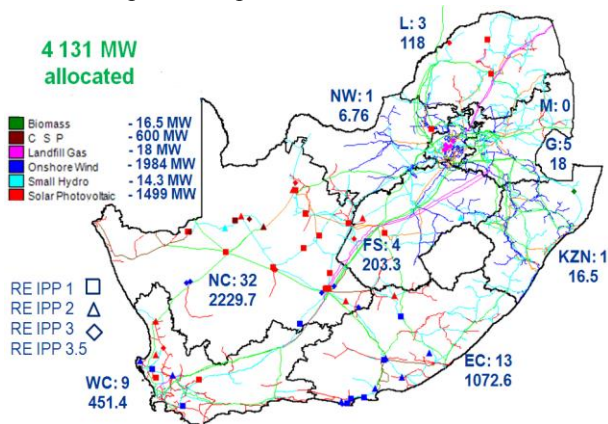


Fig. 1: REIPPPP projects in South Africa [4]

Size and connection voltage level of an RPP is then assigned to a category ranging from Category A to Category C as defined in Table 1.

The paper focusses on the requirements for the connection of medium and large scale (Category B and C) MV/HV connected RPP DG plants. The SAREGC requires all testing of RPP compliance to be done at the Point of Connection (POC) and not at the generator terminals as required by some international grid codes.

Tab. 1: SA Renewable Energy Grid Code Categories [5]

Category	Minimum Size (kVA)	Maximum Size (kVA)	Type
A1	0	13.8	LV connected
A2	13.8	100	LV connected
A3	100	1000	LV connected
B	0	20000	MV connected
C	>20000		MV/HV connected

2. SAREGC RPP PLANT DESIGN REQUIREMENTS

The SAREGC has many design and operation requirements from Category B and C RPPs

2.1 Tolerance to Voltage Deviations

The SAREGC requires Category B and C RPPs to be designed in order to operate continuously within the POC voltage range specified by U_{min} and U_{max} in Table 2.

Tab. 2 RPP continuous operating voltage limits [5]

Nominal (U_n) [kV]	U_{min} (PU)	U_{max} (PU)
132	0.90	1.0985
88	0.90	1.0985
66	0.90	1.0985
44	0.90	1.08
33	0.90	1.08
22	0.90	1.08
11	0.90	1.08

2.2 Voltage Ride through Capability

The capability of an RPP to be able to ride through voltage disturbances often caused by faults on the network is very important on the local network to ensure that stability of the grid is maintained at all times. Voltage Ride Through Capability (VRTC) assists with preventing loss of generation on the network when a voltage disturbance is experienced on the network. Hence the code requires the RPP to be designed to withstand voltage drops to zero measured at the POC for a minimum period of 0.15 seconds. Category C RPP plants are required to withstand voltage peaks up to 120% measured at the POC for a minimum period of 2 seconds. The required voltage operating capability of the RPP is shown in Fig. 2 whilst Fig. 3 shows the reactive power requirements from the RPP based on a function of the voltage.

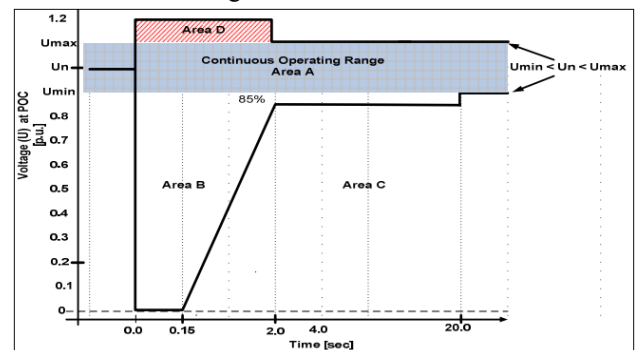


Fig. 2: VRTC for Category B and C RPP [5]

Both Low Voltage Ride Through (LVRT) and High Voltage Ride Through (HVRT) are tested using power systems simulation package (e.g. DigSilent Powerfactory) to simulate the appropriate low and high voltage durations and scenarios to ensure that the plant remains connected to the grid in the event of a disturbance on the network. To check compliance, the IPP is required to provide the Network Service Provider (NSP with a type tested, manufacturer specific RMS model of their plant which can then be used to check how the plant behaves for different under and over voltage conditions on the network. Checks need to be done to ensure that no disconnection of the plant occurs as long as the POC voltage remains within the lower and upper limit curve in Fig. 3. The SAREGC requires the RPP to either supply or absorb reactive current based on the function of the POC voltage (LVRT or HVRT) level following a network incident. Two cases are considered: first, a case of over voltage; second, the case of under voltage at the POC. Figure 3 shows the Area A which is normal operating area ($0.9 \leq V \leq 1.1$), Area B ($0.9 < V \leq 0.2$), and Area E ($V < 0.2$), where reactive current support is required to help in stabilizing the voltage whilst Area D ($V > 1.1$) requires reactive current absorption to assist in reducing the voltage. [5]

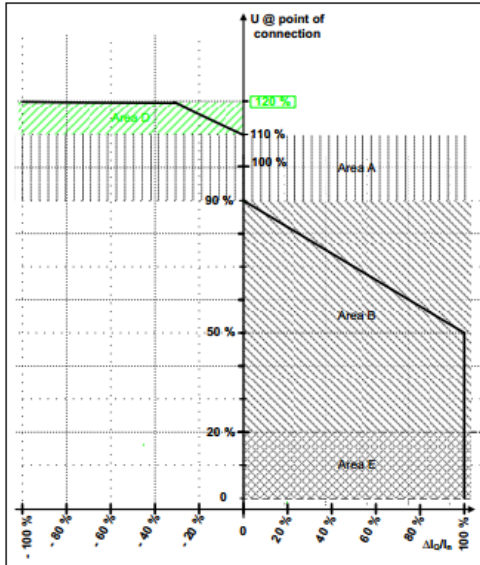


Fig. 3: Reactive power requirements during voltage drops or peaks from Category B and C RPP [5]

2.3 Tolerance to Frequency Deviations

The RPP is required to be designed to operate continuously from 49 – 51 Hz and the plant must be able to withstand phase jumps of up to 20° . However if the frequency is higher the 51.5 Hz for more than 4

seconds or less than 47 Hz for greater than 200 milliseconds, the plant is allowed to disconnect from the network as shown in Fig. 4. This simulates an over frequency and under frequency event on the grid.

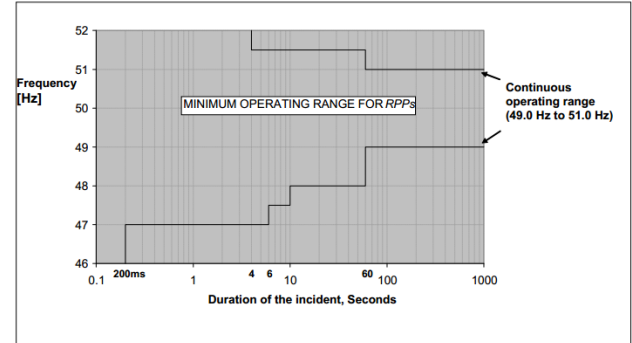


Fig. 4: Minimum RPP plant frequency operating range [5]

2.4 Frequency Response Requirements

In Fig. 5, frequency F2 to F3 forms a dead band where no-action is required from the plant whilst F1 and F4 forms a Control Band. Once the frequency exceed F2, indicating an under frequency event (the load exceeds the network generation) and the plant is required to injected P_{Δ} into the network to assist in stabilizing the frequency. The plant is required to follow the Droop 1 setting on the network. Where droop is defined as a percentage of the frequency change required for an RPP to move from no-load to rated power or from rated power to no-load. All RPPs shall be equipped with frequency controlled droop settings which shall be adjustable between 0% and 10%. During an over frequency event, the network frequency will exceed F3 (there is more generation than load on the network), the plant is required to follow the Droop 2 setting. This dictates the reduction in power required from the RPP for a change (increase) in frequency. Fig. 5 and Table 3 show the required default plant frequency settings.

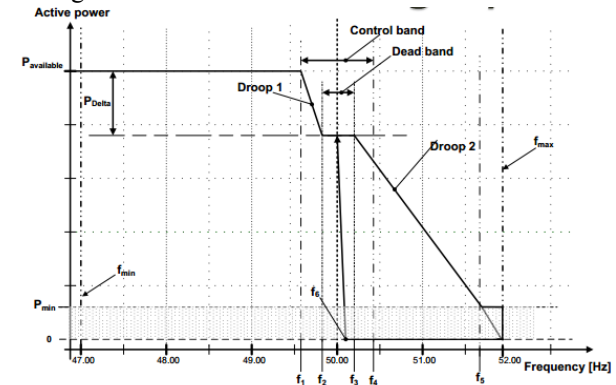


Fig. 5: Frequency response requirement for Category C plant

Frequencies f_1 , f_2 and f_3 shown in Fig. 5 and Table 3 will be set and agreed upon by the IPP and the System Operator (SO).

Tab 3: Required frequency default settings [5]

Parameter	Magnitude (Hz)
f_{min}	47
f_1	As agreed with the SO
f_2	As agreed with the SO
f_3	As agreed with the SO
f_4	50.5
f_5	51.5
f_6	50.2
f_{max}	52

To prove grid code compliance to the frequency response curve in Fig. 5, a frequency generator is required to inject the frequencies shown in table 3. This is carried out by simulating an under frequency event on the grid to check if the RPP responds in accordance to the requirements of Fig. 5 in an under frequency situation. To begin, select a value for P_{Delta} (P_{Delta} shall be minimum 3% of $P_{Available}$) which is a percentage of $P_{Available}$ and a suitable Droop 1 and Droop 2 (value range from 0 to 10% although Droop 1 is usually selected at 4% and Droop 2 at 8% for testing purposes). Calculation of the Droop settings are shown in Fig. 6. Five tests are carried out as shown in Table 4 and the results are recorded. Compliance of the tests is determined if the recorded results after 10 seconds is within $\pm 2\%$ of the set point value or $\pm 5\%$ of the rated power, depending on which yields the highest tolerance.

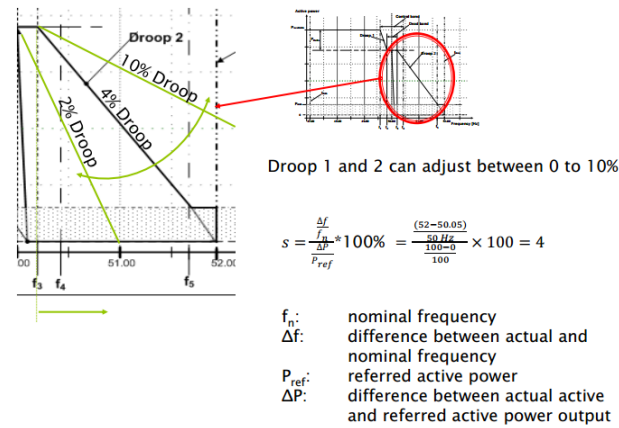


Fig. 6: Calculation of the droop [6]

Tab. 4: Test for under frequency response [7]

Set value of P_{delta} :	_____ % of $P_{available}$
Set value of Droop 1:	4%
1 st test: Frequency from 50 Hz to 49.85 Hz	
2 nd test: Frequency from 49.85 Hz to 49.5 Hz	
3 rd Test: Frequency from 49.5 Hz to 49.0 Hz	
4 th Test: Frequency from 49.0 Hz to 48.0 Hz	
5 th Test: Frequency from 48.0 Hz to 50 Hz	

The next step is to simulate an over frequency event on the grid to check if the RPP behaves according to the requirements of Fig. 5 in an over frequency situation. Select a suitable Droop 2 and use a frequency generator to simulate the frequencies in Table 3. Five tests are carried out as shown in Table 5 and results recorded to ensure that the RPP response within the required time and accuracy to check compliance.

Tab. 5: Test for over frequency response [7]

Set value of Droop 2:	_____ MW/Hz
1 st test: Frequency from 50 Hz to 50.50 - 50.55 Hz	
2 nd test: Frequency to 51.00 - 51.05 Hz	
3 rd Test: Frequency to 51.10 - 51.20 Hz	
4 th Test : Frequency to 51.35 to 51.45 Hz	
5 th Test : Frequency to Back to 50 Hz	

2.5 Control Functions Required for the RPP

The RPP is required to have the following control functions as shown in Table 6.

Tab. 6: Control functions required for RPPs [5]

Control Function	Category B	Category C
Frequency Control	-	x
Absolute Production Constraint	x	x
Delta Production Constraint	-	x
Power Gradient Constraint	x	x
Reactive Power (Q) Control	x	x
Power Factor Control	x	x
Voltage Control	x	x

2.6 Reactive Power Capability

The grid code specifies the reactive power requirements from:

Category B plant $[-0.228 \leq (Q/P_{Max}) \leq 0.228]$; and
 Category C plant $[-0.33 \leq (Q/P_{Max}) \leq 0.33]$

This is measured at the POC, and shown in Fig. 7.

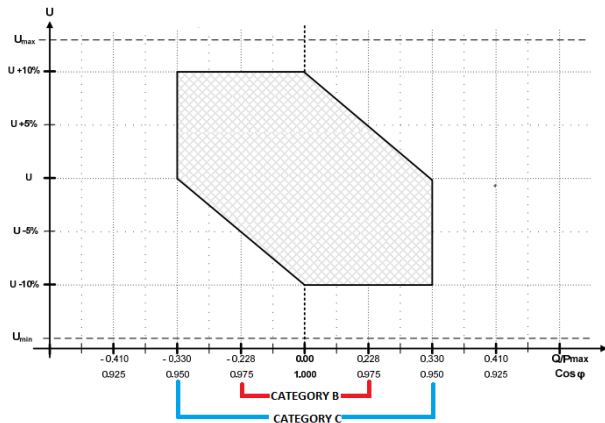


Fig. 7: Reactive power requirements [5]

To check grid code compliance of RPPs with regards to reactive power requirements, tests and measurements shall be carried out in accordance with Tables 7 and 8 which is for the case of $U = 1$ PU. If U is not equal to 1 PU then the plant shall operate in accordance to Fig. 7. The measured values are recorded after 30 seconds upon receipt of the set point to a measured accuracy to the higher value of either $\pm 2\%$ of the set-point value or $\pm 5\%$ of maximum reactive power.

Tab. 7: Reactive Power Q Control Test at $P_{Available}$ [7]

$P = P_{Available}$
$Q = 0$ Mvar
$Q_{max} = 0.228 P_{max}$ (overexcited) Category B only
$Q_{max} = 0.33 P_{max}$ (overexcited) Category C only
$Q = 0$ Mvar
$Q_{max} = 0.228 P_{max}$ (underexcited) Category B only
$Q_{max} = 0.33 P_{max}$ (underexcited) Category C only
$Q = 0$ Mvar

Tab. 8: Reactive Power Q Control test at $20\% P_{MAX}$ [7]

Reactive power control – fixed Q (at a fixed power of $20\% P_{max}$)
$Q = 0$ Mvar
Q_{max} over excited
$Q = 0$ Mvar
Q_{max} under excited
$Q = 0$ Mvar

2.7 Power Factor Control Function

Category B: Shall be designed to operate from 0.975 lagging to 0.975 leading, measured at the POC from 20% and above of the rated power.

Category C: Shall be designed to operate from 0.95 lagging to 0.95 leading, measured at the POC from 20% and above of the rated power.

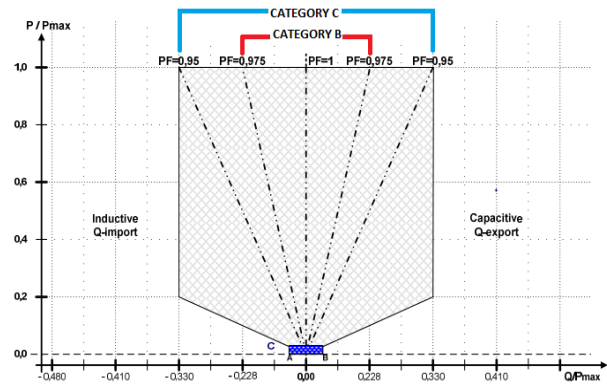


Fig. 8: Power Factor requirements from RPP [5]

The RPP is required to respond within 30 seconds of receipt of the set point to a measured accuracy of ± 0.02 in order to pass the test. The tests that needs to be carried out is shown in Table 9 below which tests the plants ability to meet the required Power Factor values in Fig. 8. The plant must be able to provide the required Power Factor from $P > 20\% P_{Max}$.

Tab. 9: Power Factor Control function test [7]

Reactive power control – fixed cos (ϕ)
Pf Set point
PF= 1
0.975 overexcited (Category B only)
0.95 overexcited (Category C only)
PF= 1
0.975 under excited (Category B only)
0.95 under excited (Category C only)
PF= 1

2.8 Voltage Control Functions

The voltage control function for RPPS is shown in Figure 9. If the RPP voltage set point is to be changed, a set point is issued and the change needs to be implemented within 30 seconds with the accuracy of $\pm 0.5\%$ of V_{Normal} whilst the accuracy of $\pm 2\%$ of the required injection or absorption of reactive power according to the droop characteristic defined.

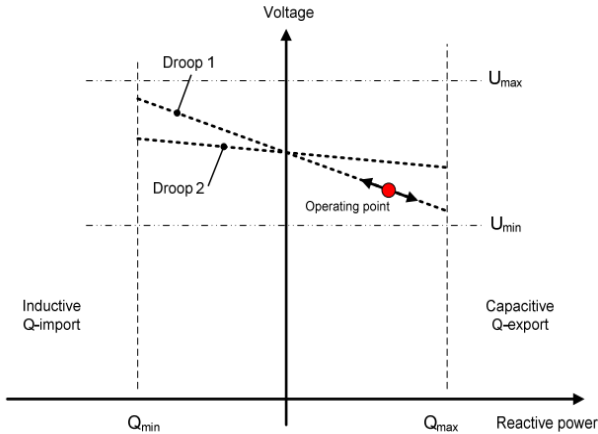


Fig. 9: Voltage Control for RPPs [5]

The tests to be carried out are shown in tables 10 and 11 using 4% and 8% droop.

Tab. 10: Voltage Control Function Test with 4% droop [7]

Reactive power control – Q(U) characteristic
Test 1: Set the Droop to 4%: $(Q_{max})/4\% U_n$
Reactive power testing at different values of active power
Nominal voltage
1.02 of U_n
0.98 of U_n
Nominal Voltage

Tab. 11: Voltage Control Function Test with 8% droop [7]

Reactive power control – Q(U) characteristic
Test 2: Set the Droop to 8%: $(Q_{max})/8\% U_n$
Reactive power testing at different values of active power
Nominal voltage
1.04 of U_n
0.96 of U_n
Nominal voltage

2.9 Power Quality

Power Quality is required to be monitored at the POC and the following parameters shall be monitored:

- Rapid Voltage Change
- Flicker
- Harmonics
- Unbalance voltage and current

These power quality parameters can be checked utilizing the type tested, manufacturer specific model in a Power Systems simulation package prior to the construction of the RPP. After construction of the RPP, on site Power Quality meters can be installed to gather the data which can then be utilized to check compliance against values given to the IPP by the NSP. The PQ limits given by the NSP to the IPP are apportioned values which takes the PQ limits given in NRS 048 and

apportioned to the upstream contribution together with current and future customer's contribution limits. If the plants violates the PQ limits, then the IPP will need to design filters to be installed to ensure compliance.

2.10 Active Power Constraint Function

For reasons of system security, the RPP may be requested to curtail active power output when requested by the SO. Hence the RPP shall have the following Active Power Constraint functions shown in Figure 10.

- Absolute Production constraint
- Delta Production constraint
- Power Gradient constraint

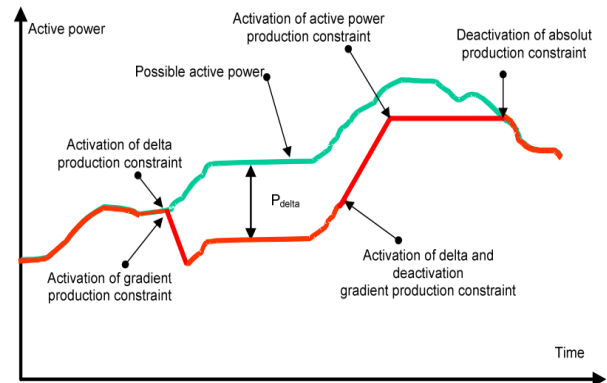


Fig. 10: Required RPP active power control functions [5]

2.10.1 Absolute Power Gradient Function

An Absolute Production Constraint (APC) is used to constrain the output active power from the RPP to a predefined power MW limit at the POC. This is typically used to protect the network against overloading. In order to check compliance of the RPP to the APC function, the plant shall be tested as per Table 12. The measured values shall be recorded after 30 seconds after receipt of the set point to a measured accuracy to the higher value of either $\pm 2\%$ of the set-point value or $\pm 5\%$ of the rated power for each set-point. If the plant meets the required set-point within the time period and accuracy limit, then the plant passes [5].

Tab. 12: Tests to check operation of constraint function [7]

Select a $P_{reference}$ value in MW
1 st test: $P_{reference}$ to $80\% P_{reference}$
2 nd test $80\% P_{reference}$ to $40\% P_{reference}$
3 rd test $40\% P_{reference}$ to $20\% P_{reference}$
4 th test $20\% P_{reference}$ to $10\% P_{reference}$

5 th test Increasing limit to 30% $P_{reference}$
6 th test 30% $P_{reference}$ to 50% $P_{reference}$
7 th test 50% $P_{reference}$ to 80% $P_{reference}$
8 th test only for responds time: $P_{reference}$ to $\leq 0\%$
After the 8 th test the RPP shall go back to normal operation

2.10.2 Delta Production Constraint Function

A Delta Production Constraint (DPC) function is used to constrain the active power from the RPP to a required constant value in proportion to the possible active power is typically used to establish a control reserve for control purposes in connection with frequency control. To check compliance of the RPP to the DPC function, the plant shall be tested as per Table 13. The measured values shall be recorded after 30 seconds after receipt of the set point to a measured accuracy to the higher value of either $\pm 2\%$ of the set-point value or $\pm 5\%$ of the rated power for each set-point. If the plant meets the required set-point within the time period and accuracy limit, then the plant passes [5].

Tab. 13: Tests for of delta production constraint function [7]

DELTA CONTROL – ($P_{available} > 20\%$ of P_{max}) Time for Test: 10 Minutes	
Ref No	Description
SETUP	
1.	Check Pavailable at least 20% P_{max}
2.	Check PPC control ready
TEST	
3.	Check P_{delta} control enabled
4.	Send e.g. 10% of $P_{available}$ (> 1 MW)
5.	Check if power reduces to set point value on Park controller, SCADA or better measurement system.
6.	Hold for at least 10 min
7.	Further tests as optional. For e.g. longer period if the primary energy do not change during the 10 min test period or other setting like P_{delta} of 3% would be tested
8.	Disable Pdelta control

2.10.3 Power Gradient Constraint Function

A Power Gradient Constraint Function is used to limit the RPP maximum ramp rates by which the active power can be changed in the event of changes in primary renewable energy supply or the set-points for the RPP. A Power Gradient Constraint is typically used for reasons of system operation to prevent changes in active power from impacting the stability of the network. The test to check compliance is shown in Table 14. The measured values shall be recorded after

30 seconds after receipt of the set point to a measured accuracy to the higher value of either $\pm 2\%$ of the set-point value or $\pm 5\%$ of the rated power for each set-point. If the plant meets the required set-point within the time period and accuracy limit, then the plant passes [5].

Tab. 14: Test to check operation of constraint function [7]

1 st Test: down Ramp rate has to be set to : $(0.4 \times P_{reference})/\text{min}$ The active power has to set to $P_{reference}$ before the start of 1 st test.
1 st test from $P_{reference}$ to 20% $P_{reference}$
2 nd test: up ramp rate has to be set to : $(0.4 \times P_{reference})/\text{min}$
2 nd test from 20% $P_{reference}$ to $P_{reference}$
3 rd test: down ramp rate has to be set to : $(0.2 \times P_{reference})/\text{min}$
3 rd Test from $P_{reference}$ to 20% $P_{reference}$
4 th test: up ramp rate has to be set to : $(0.2 \times P_{reference})/\text{min}$
4 th Test from 20% $P_{reference}$ to $P_{reference}$
After the last test the RPP is allowed to go back to normal operation

2.11 Signal, Communication and Control Requirements

Table 15 shows the signals that are required from the RPP plant. This will then assist the Network Controller to manage the DG connection together with the network more effectively. Each signal list made up of a number of signals.

Tab. 15: Signal required from the RPP plant [5]

Signals List	Description
List 1	General plant data and set points
List 2	RPP available estimate
List 3	RPP MW curtailment data
List 4	Frequency response system settings
List 5	RPP Meteorological data

Fig. 11 shows a typical screen of signals brought back to the network control room via SCADA from an RPP.

2.11.1 Testing of SCADA Compliance

The following tests shall be performed from the Network Service Providers Control Room to the RPP Power Park Controller on the day of the grid code compliance tests [5].

- [1] Check capability to remotely open the breaker at the POC from the respective NSP SCADA. Capability to change the mode of operation at the RPP.
- [2] Check capability to change the set-point in any mode of operation such that the RPP adjusts accordingly.

- [3] Anti-islanding test: The facility shall be subjected to a self-islanding condition to determine the response of the anti-islanding protection function. Following this test, the RPP's automated response to the synchronisation function to the network at the POC shall be evaluated.

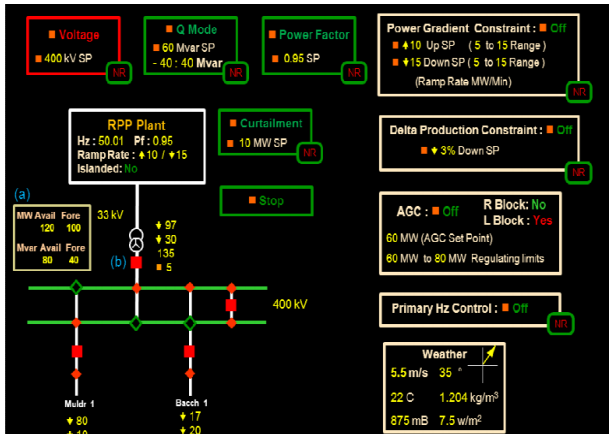


Fig. 11: Example of signals brought back via SCADA [5]

3.0 CONCLUSION AND RECOMMENDATIONS

Hitherto, there is on-going work being done on the medium and large scale (MV and HV) connected RPP, which has been captured in the SAREGC Version 2.8. This code is currently undergoing further changes to include other internal standards used to cover detailed protection requirements and power quality requirements. The SAREGC has been used to certify grid code compliance of all REIPPP projects. However certain plants such as CSP have encountered problems meeting grid code requirements due to the slow response of the plant. Most technologies easily complies to the SAREGC however there has been requests for exemptions from plants which do not meet the harmonic emission limits and some which could not meet the reactive power capability limits.

This required power quality meters to be installed on site to gather data to correctly design harmonic filters and installation of suitability sized capacitor banks to provide the required reactive power. If all connected RPP to the grid are Grid Code compliant, it will make operating and managing the network easier for the SO at Eskom National Control or at the NSP Control Room. With all plants complying with the SAREGC, the SO will have both control and visibility of these RPP plants

making it displayable and controllable. To date there is around 2000 MW of RPP connecting onto the National Grid in South Africa with a number of RPPs still in design, implementation or commissioning stages. This paper has provided fundamental information to stakeholders and investing utilities regarding the SAREGC requirements and testing methods, which can be utilized to achieve compliance with the grid code.

4.0 REFERENCE

- [1] D. Q. Hung, N. Mithulananthan and R.C. Bansal, "An Optimal Investment Planning Framework for Multiple Distributed Generation Units in Industrial Distribution Systems", *Applied Energy*, Vol. 124 (2014), pp. 62–72
- [2] M M Bello, R Smit, C Carter-Brown and I E Davidson, "Power Planning in a Smart Grid Environment - A Case Study of South Africa". In *Proceedings of the IEEE Power Engineering Society (PES) 2013 Meeting*, Vancouver, BC, Canada, 21-25 July 2013. IEEE Explore Digital Object Identifier: 978-1-4799-1303-9/2013.
- [3] National Energy Regulator of South Africa, "Small-Scale Embedded Generation: Regulatory Rules Consultation Paper", 25 February 2015
- [4] R. Smit, "Current IPP Status Quo", Renewable Energy Conference, Midrand, February 2015
- [5] Grid Connection Code for Renewable Power Plants (RPPs) connected to the Electricity Transmission System (TS) or Distribution System (DS) in South Africa, Version 2.8, National Energy Regulator of South Africa, July 2014
- [6] J. Möller, Presentation to Renewable Energy Technical Evaluation Committee on "Grid Integration of Renewable Energies", 2014
- [7] Renewable Energy Technical Evaluation Committee, "Renewable Power Plant Grid Code Compliance Standard Test Procedure Rev 2.2" 2014

Optimisation of an Experimental Perturbation and Estimation Technique used to Autonomise Nodes on DC Microgrids

W. Doorsamy*, W. A. Cronje, M. Montaz Ali
University of the Witwatersrand, 1 Jan Smuts Avenue, Braamfontein 2000,
Johannesburg, South Africa
*Email: wesley.doorsamy@wits.ac.za

Abstract: The concept of autonomy is becoming more popular in power systems with modern microgrids being designed with the power and ability for self-control. This paper presents the optimisation of an experimental estimation technique used to enable autonomy at the nodal/subsystem level of a microgrid. This online technique uses Recursive Least Squares Estimation together with a passive perturbation method to determine an aggregation of the system's state at any node of the microgrid requiring autonomy. The state aggregate provides the autonomous node with sufficient information about the operating conditions of the rest of the system without the need for communications infrastructure and a central controller. An analysis of the constraints on the accuracy of the technique is carried out to determine the optimal perturbation requirements. The efficacy of the estimation system is also experimentally tested and validated during quasi-static and transient conditions.

1 INTRODUCTION

The paradigm shift in power generation from central to distributed brings about new technical challenges with the management, control and integration of distributed resources [1]. Microgrids are becoming more popular as a means of integrating distributed generation into a central grid [2] and providing electricity when a grid connection is not feasible e.g. islanded [3], remote [4], rural [5] and other specialised applications [6, 7]. Autonomous microgrids, in both grid-connected and stand-alone applications, can offer improved reliability and power quality through Distributed Energy Resource (DER) scheduling and intelligent load control. Although there have been recent advancements in microgrid development with AC-DC hybridisation [8], self-healing networks [9], and coordination via wireless networks [10], there are still major challenges with scalability, integrity and flexibility. The control system of an autonomous microgrid comprising intelligent sources, storage and loads requires accurate and reliable information regarding the state of the entire system. Therefore the scale and architecture of the system is limited and changes in this regard usually require redesign or additional infrastructure [11]. Furthermore, the integrity of the microgrid is critically dependent on the health of the communications network and central controller [11, 12].

In order to assist with these challenges, a multi-agent microgrid (shown in Fig. 1) is proposed. Each agent is autonomous with local goals collectively achieving the intended operation of the overall system [13]. The nodes of the microgrid are equipped with independent estimation and control which eliminates the need for communication with other nodes or a central controller. This paper focuses on the estimation component required to autonomise these nodes. A passive perturbation and estimation technique intended for application in low-voltage DC microgrids is presented. The DC-type microgrid is growing in popularity as it facilitates integration of distributed generation systems due to inherent compliance with modern DC input-type electronic loads, DC output-type renewable energy sources and storage devices [12, 14].

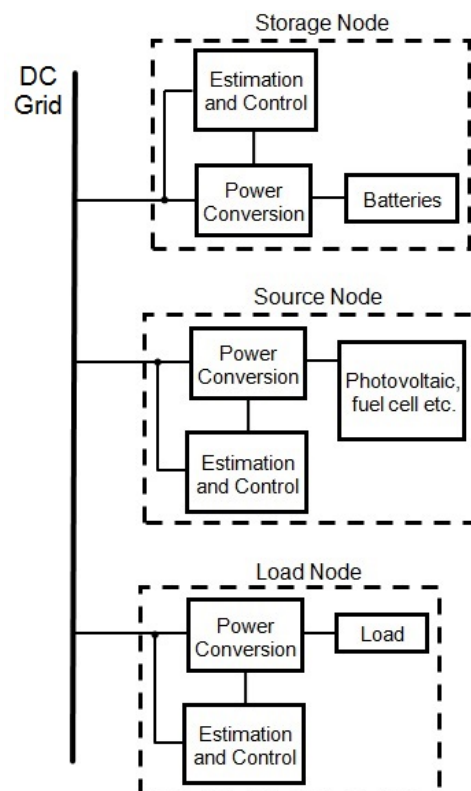


Fig. 1: Low-voltage DC microgrid with autonomous nodes, each consisting of independent measurement, estimation and control

This paper is organized as follows. The motivation and background for the perturbation and estimation technique is given in the subsequent section. Section 3 describes the system parameters, cost function design and optimisation methodology. Numerical results and experimental validation of the optimisation are then presented in Section 4. Some future work is described in Section 5, followed by a final summary of the research.

2 PERTURBATION AND ESTIMATION TECHNIQUE

The intelligence of each node of the microgrid can be separated into two major components – the ability to estimate reliable references from the available information and the ability to act accordingly to these references in fulfilment of specific goals. The first component, or the estimation system, is the main focus of this paper. The fundamental nodes of the system shown in Fig. 1 – i.e. source, storage and load nodes – are categorized in terms of operation. The control of the behaviour of each node type is specific to the goals of that node. However, the presented estimation system may be applied to any node i.e. only specific nodes may be autonomised (made intelligent) according to design choices relevant to the microgrid application. A general overview of the microgrid's system interfaces and hierarchy is shown in Fig. 2 to illustrate this point.

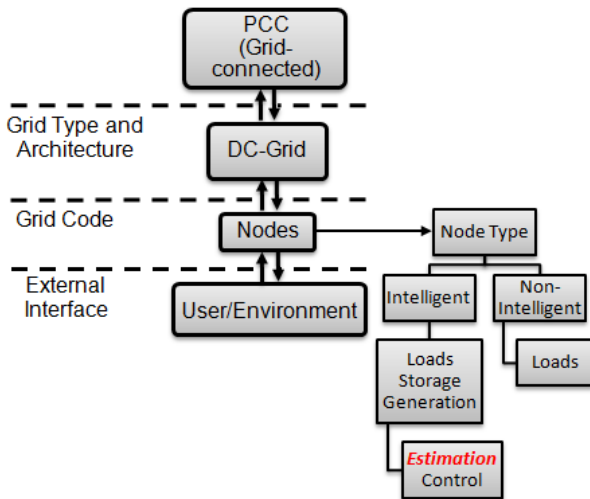


Fig. 2: Overview of microgrid's system interfaces and hierarchy

2.1. Recursive Least Squares Estimation (RLSE)

The control components of most power systems with distributed intelligence require Thevenin equivalent parameters for decision-making purposes [15, 16]. These parameters represent an aggregation of the system's operating conditions and provide the node with sufficient information about the rest of the system so it

can respond accordingly e.g. unexpected system undervoltage will initiate disconnection of a load node (pre-assigned priority level) with the intention of stabilising the overall system [16]. Some examples of control and protection methods used for energy storage and sources which utilize Thevenin equivalent parameters are presented in [17], [18] and [19].

On-line estimation is the estimation of the present state using all the measurements that are available [20]. In this case, the state variables required for suitable control of the autonomous nodes are the Thevenin equivalent voltage and resistance. The presented on-line estimation algorithm uses the RLSE method which is one of the most commonly used algorithms in adaptive filtering applications [21]. The RLSE algorithm is selected here as it provides fast updating and convergence in on-line applications with relatively diminutive memory requirement [22]. The Thevenin equivalent – as seen by a node of the microgrid – is shown in Fig. 3. This represents an equivalent model of the microgrid system seen from the node terminals constituted by a voltage source and a series resistance. Voltage and current measurements obtained at these node terminals are used to determine the Thevenin equivalent of the system as seen by the node. The resistance of the node can be used as a substitute for the current measurement however this may be unreliable in practice.

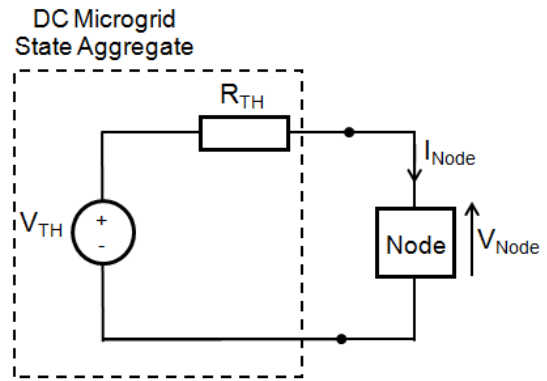


Fig. 3: Thevenin equivalent model - as seen by a node - representing the microgrid's state aggregate

Equation (1) is obtained by applying Kirchoff's Voltage Law (KVL) to the equivalent circuit shown in Fig. 2.

$$V_{TH} = I_{Node} R_{TH} + V_{Node} \quad (1)$$

In order to solve for the unknown Thevenin parameter, (1) is parameterised to the form given in (2). The unknowns are contained in matrix X and the i_{th} sample represents a specific instance of a node measurement:

$$Y_i = H_i \times X_i \quad (2)$$

where

$$X_i = \begin{pmatrix} V_{TH,i} \\ R_{TH,i} \end{pmatrix}; Y_i = V_{Node,i}; H_i = \begin{pmatrix} 1 & -I_{Node,i} \end{pmatrix} \quad (3)$$

The RLSE method is used to assess the best estimates of the unknowns taking into account new measurements, given the initialisation parameters (*a priori*). The following equations are applied:

$$K_i = P_{i-1} H_i^T (\lambda I + H_i^T P_{i-1} H_i)^{-1} \quad (4)$$

$$P_i = \frac{1}{\lambda} (I - K_i H_i^T) P_{i-1} \quad (5)$$

$$X_i = X_{i-1} + K_i (Y_i - H_i^T X_{i-1}) \quad (6)$$

Where I is the identity matrix, λ is the forgetting factor, P is the covariance matrix, and K is the gain [23]. The standard RLSE routine is intended for estimation when the target parameters remain constant and it therefore has poor tracking performance. Additionally, if the new measurements are constant, accurate convergence to the target estimate is not achieved. There are a number of different extensions of the standard RLSE used to overcome these issues in practice. The presented algorithm extends on the standard RLSE method by providing covariance resetting and controlled excitation. Resetting the covariance limits the memory of the routine and allows it to react to more rapid variations in the environment including sudden appearance of an interferer [22]. State estimation on the microgrid requires that all past input information be removed when significant changes in the target parameters occur and confidence in the current estimate is lost. A controlled excitation or perturbation of the input parameters is used to obtain a suitable variation in the node measurements thus ensuring convergence and improving accuracy.

2.2. Perturbation Requirements

The controlled-excitation extension of the RLSE algorithm ensures that there is convergence when there is a change in the targeted Thevenin parameters. Physical excitation can be achieved in two ways: actively and passively. Active perturbation uses an additional source of energy to obtain a suitable variation in the node measurement. More commonly, estimation systems of components of renewable energy sources (such as inverters) utilising active current-injection methods have been proposed [24, 25]. The technique presented here is passive and uses a perturbation resistor (shown in Fig. 4) to achieve the same variation at the node of interest. Figure 4 also shows the timing used for the covariance resetting and estimate storing in relation to the switching method.

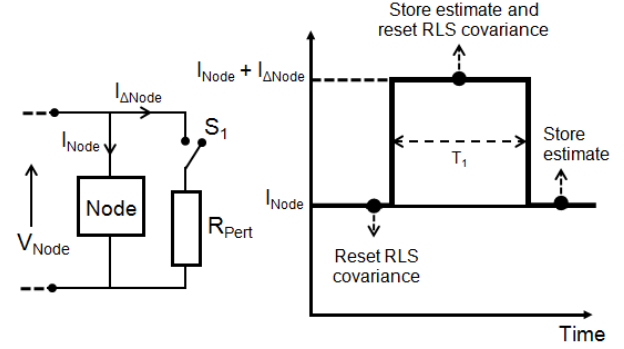


Fig. 4: Passive perturbation technique used for controlled excitation and dynamic tracking of Thevenin parameters

There are two types of triggers which initiate these controlled perturbations i.e. Type 1 and 2. In the first instance, a perturbation is triggered periodically for regular updating of the estimate and accounts for any relatively slow drift in the target parameters (quasi-static state). The second type of trigger is a rapid change in the node measurements which indicates a change in the targeted parameters (transient state).

3 OPTIMISATION

The standard method for obtaining a Thevenin equivalent model (Thevenin voltage and resistance) requires that the node be open-circuited and short-circuited. This is not feasible for online application as it is intrusive, unsafe and potentially catastrophic to the microgrid. The proposed estimation system can determine the Thevenin parameters of the microgrid, as seen by a specific node, while the microgrid is in operation. However, as previously mentioned, controlled excitation is required to intentionally vary node measurements. It is therefore critical to obtain a suitable level of perturbation that is non-intrusive to the system, sustainable and parsimonious in its energy consumption. Optimisation of the technique is carried out here to determine the properties of the perturbation and its effects on the accuracy of the state estimate.

3.1. System Parameters and Cost Function

The error of the estimation system is defined as the difference between estimates (V_{TH} and R_{TH}) and the actual Thevenin equivalent parameters. The controlled perturbation is effected on the actual system by varying the total current flowing in or out (depending on node type) by switching in a resistance (R_{Pert}), as show in Fig. 4. For the purpose of generalisation, the perturbation parameter (x_i) is defined here as a the ratio of the change in the node current ($I_{\Delta Node}$) and the node current (I_{Node}). Similarly, the perturbation parameter for voltage is x_v . The objective of optimising the estimation accuracy is to minimise the error function, which is

dependent on the perturbation parameter (x) and measurement error (σ) as given by (7),

$$\min E(x, \sigma) \quad (7)$$

where the error function is the sum of the squares of the difference between the estimated parameters and the target parameters as follows:

$$E(x, \sigma) = \left(\tilde{V}_{TH}(x, \sigma) - V_{TH} \right)^2 + \left(\tilde{R}_{TH}(x, \sigma) - R_{TH} \right)^2 \quad (8)$$

3.2. Optimisation Procedure

Although the presented problem has a large number of interdependencies, the objective function captures the system in its entirety by resolving the accuracy of the estimate by focusing on inputs x and σ . Simply put, the accuracy of the estimation ultimately depends on these parameters, namely, the intentional perturbation and the measurement (node voltage and current) uncertainty. Generalisation is also necessary because in practice the range of components found on different LVDC microgrids is unquantifiable. Hence, a contrived set of internal system parameters are used with the aim of understanding the conditions for perturbation optimality. While the error function, given by (8), may have a quantifiable minimum - the physical constraints of the microgrid excludes a variety of possible minimums. Hence, the optimisation procedure here requires a more physical interpretation rather than seeking a mathematical minimum. A simulation model of the circuit shown in Fig. 3 is constructed in Simulink with V_{TH} , R_{TH} and R_{Node} fixed at 15V, 50Ω, and 50Ω respectively. The parameter R_{Pert} is varied to obtain different levels of perturbation x , and σ is the noise added to the measurements V_{Node} and I_{Node} . Figure 5 gives an example of the node measurements (without measurement error) during a single perturbation.

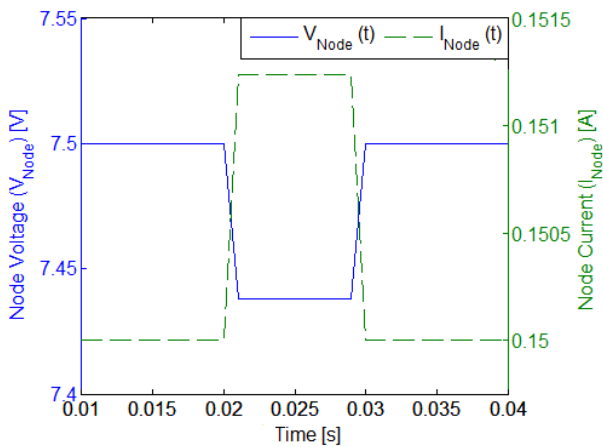


Fig. 5: Example of simulated node measurements during perturbation (without additive noise)

4 ANALYSIS OF RESULTS

4.1. Effects of Perturbation Parameter (x)

Figure 6 shows the simulations results for the effects of the perturbation parameter on the accuracy of estimation system, for a fixed level of measurement noise. This result shows that a mathematical minimum exists, but physically, this corresponds to a short circuit across the node terminals which is highly intrusive and potentially catastrophic. Therefore, selection of the optimal perturbation parameter is based on the operational criteria of the microgrid system or specific 'grid code' e.g. voltage perturbation parameter must be less than 10%.

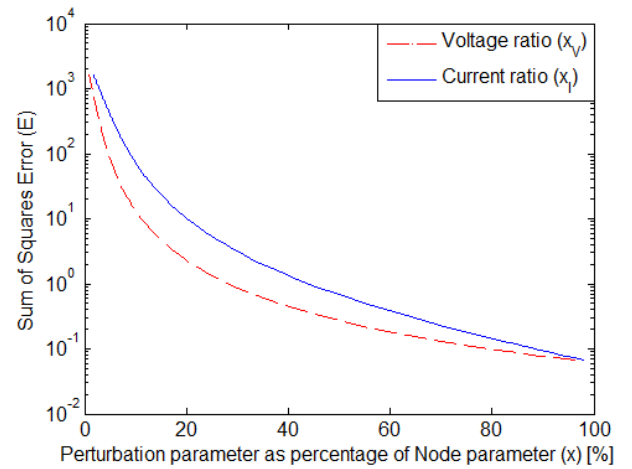


Fig. 6: Simulated performance of estimator for varying perturbation levels (with fixed additive measurement noise $\sigma_{PSD} = 1e-9$ W)

4.2. Effects of Measurement Noise (σ)

The measurement uncertainty is the other significant parameter which affects the estimation accuracy. In practice, there will be a limitation on accuracy of the supply and the measurement instruments on the microgrid. For test purposes, noise is added to the simulated measurements and represents a compounded effect of the total uncertainty.

The graphs of different levels of measurement noise, corresponding to different levels of uncertainty, is given in Fig. 7. In each instance, the accuracy of the estimation system is simulated for a range of perturbation levels (only the voltage perturbation parameter is presented). These graphs indicate that higher levels of uncertainty require relative increases in the voltage perturbation parameter to maintain a specific level of estimation accuracy.

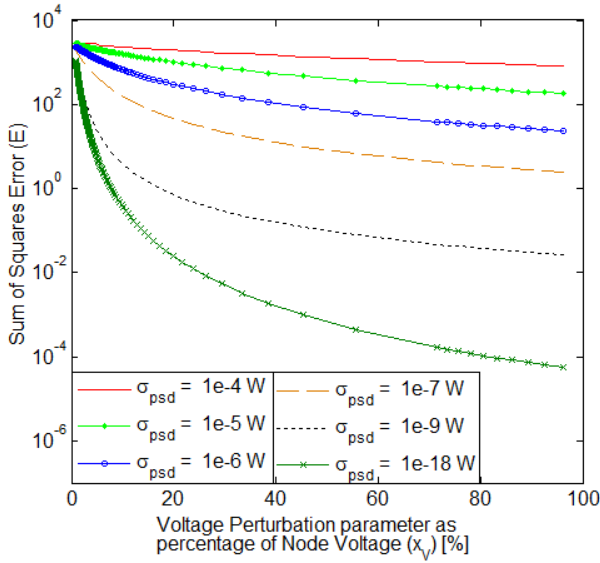


Fig. 7: Simulated estimator performance with varying voltage perturbation parameter for different levels of uncertainty

4.3. Experimental Testing and Validation

The estimation algorithm is experimentally tested using the setup shown in Fig. 8. A controllable voltage source is used together with known resistances (preset to aforementioned simulation model values). The estimation algorithm is implemented in Matlab Real-Time Interface (RTI) with dSPACE. Node measurements are read via the dSPACE analogue inputs. The digital output of the dSPACE controller board outputs the perturbation signal to a switching circuit consisting of a DC high-speed switching power MOSFET with driver, photocoupler and DC/DC converter. Results from two experimental performance tests are given in figures 9 and 10. These results show that the estimator closely tracks the intentionally varied Thevenin parameters. Perturbations in the node current is also shown in Fig. 10. Relatively large perturbations are required to achieve accuracy due to inherent supply fluctuations and measurement error (no noise filtering).

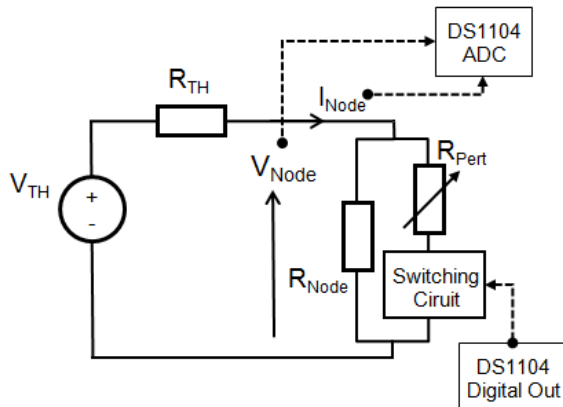


Fig. 8: Overview of experimental configuration used for testing the performance of the estimation system

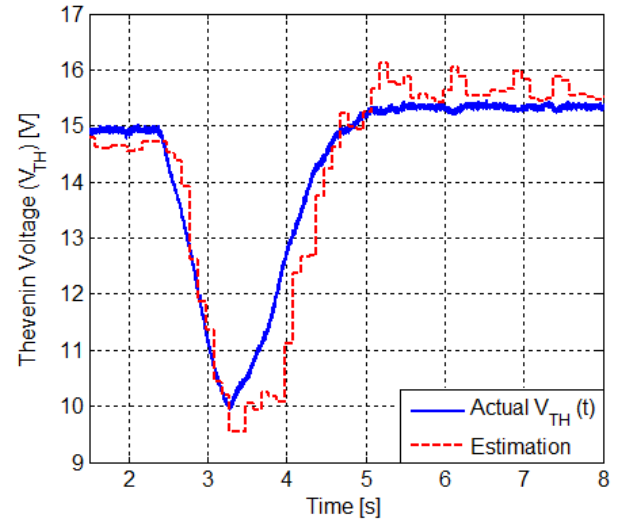


Fig. 9: Experimental performance of on-line estimator in dynamically tracking Thevenin voltage during transient state

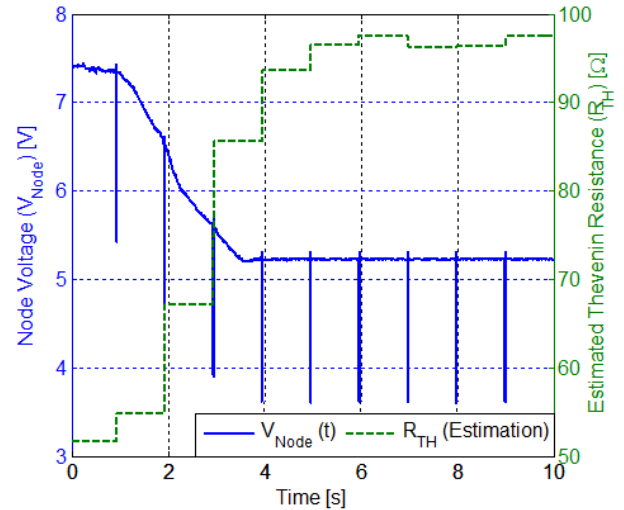


Fig. 10: Experimental performance of on-line estimator in dynamically tracking Thevenin resistance during slow-transient and steady-state (quasi-static), and node voltage measurement consisting of perturbations

5 FUTURE RESEARCH

Although the perturbation and estimation technique has been shown to be effective, complexity arises when multiple nodes are involved. Currently, a method for communication-less collaboration of multiple nodes is being developed. The limitations and requirements for this method will be further investigated. An extensive study of the response times of typical node components and microgrid events in practice is required to optimise the timing of perturbations. Additionally, testing of the estimation algorithm using active perturbation - e.g. current injection - is envisaged.

6 CONCLUSION

Microgrids are becoming increasingly popular for the integration and utilisation of DERs. Although much research and development has already been done in this area - there are still major challenges with scalability, robustness and operational flexibility. The work presented in this paper aims to assist with these challenges through adopting a decentralised approach to control and estimation. A novel on-line estimation system, based on an extended RLSE algorithm, is proposed for autonomising nodes of an LVDC microgrid. The estimation system uses a passive perturbation technique with RLSE to determine the state of the microgrid using local node-measurements only. The effects of the perturbation level and measurement uncertainty were investigated in order to optimise estimation accuracy. Results from experimental tests indicate that the estimation system accurately tracks the transient and quasi-static states of the microgrid.

7 ACKNOWLEDGMENT

The first author acknowledges the financial support of the University of the Witwatersrand's Research Committee (URC) in the form of the prestigious Postdoctoral Research Fellowship.

8 REFERENCES

- [1] J. M. Guerrero, F. Blaabjerg, T. Zhelev, K. Hemmes, E. Monmasson, S. Jemei, M. P. Comech, R. Granadino, and J. I. Frau, "Distributed generation: Toward a new energy paradigm," *IEEE Industrial Electronics Magazine*, vol. 4, no. 1, pp. 52-64, Mar. 2010.
- [2] D. B. Chiesa, and S. K. Zirkelbach, "Microgrids help more than they hurt," *IEEE Electrification Magazine*, vol. 2, no. 1, pp. 95-102, 2014.
- [3] L. A. S. Ribeiro, O. R. Saavedra, S. L. De Lima, and J. G. De Matos, "Isolated micro-grids with renewable hybrid generation: The case of lençois island," *IEEE Trans. Sustain. Energy*, vol. 2, no. 1, pp. 1-11, Jan. 2011.
- [4] R. Paleta, A. Pina, and C. A. S. Silva, "Polygeneration energy container: Designing and testing energy services for remote developing countries," *IEEE Trans. Sustain. Energy*, vol. 5, no. 4, pp. 1348-1355, Oct. 2014.
- [5] K. Ubilla, G. A. Jiménez-Estévez, R. Hernández, L. Reyes-Chamorro, C. H. Irigoyen, B. Severino, and R. Palma-Behnke, "Smart microgrid as a solution for rural electrification: Ensuring long-term sustainability through cadastre and business models," *IEEE Trans. Sustain. Energy*, vol. 5, no. 4, pp. 1310-1317, Oct. 2014.
- [6] J. Van Roy, N. Leemput, F. Geth, J. Büscher, R. Salenbien, and J. Driesen, "Electrical vehicle charging in an office building microgrid with distributed energy resources," *IEEE Trans. Sustain. Energy*, vol. 5, no. 4, pp. 1389-1396, Oct. 2014.
- [7] T. Dragičević, H. Pandžić, D. Škrlec, I. Kuzle, J. M. Guerrero, and D. S. Kirschen, "Capacity optimisation of renewable energy sources and battery storage in an autonomous telecommunications facility," *IEEE Trans. Sustain. Energy*, vol. 5, no. 4, pp. 1367-1378, Oct. 2014.
- [8] F. Nejbatkhah, and Y. Wei Li, "Overview of power management strategies of hybrid AC/DC microgrid," *IEEE Trans. Power Elec.*, vol. 30, no. 12, pp. 7072-7089, Dec. 2015.
- [9] Z. Wang, and J. Wang, "Self-healing resilient distribution systems based on sectionalization into microgrids," *IEEE Trans. Power Sys.*, vol. 30, no. 6, pp. 3139-3149, Nov. 2015.
- [10] H. Liang, B. Jun Choi, W. Zhuang, X. Shen, A. S. A. Awad, and A. Abdrabou, "Multi-agent coordination in microgrids via wireless networks," *IEEE Recent Advances in Wireless Tech. for Smart Grid*, vol. 19, no. 3, pp. 14-22, June 2012.
- [11] G. Chen, and E. Feng, "Distributed secondary control and optimal power sharing in microgrids," *IEEE/CAA Journal of Automatica Sinica*, vol. 2, no. 3, pp. 304-312, July 2015.
- [12] A. Khorsandi, M. Ashourloo, and H. Mokhtari, "A decentralized control method for a low-voltage DC microgrid," *IEEE Trans. Energy Conv.*, vol. 29, no. 4, pp. 793-801, Dec. 2014.
- [13] S. D. J. McArthur, E. M. Davidson, V. M. Catterson, A. L. Dimeas, N. D. Hatziaargyriou, F. Ponci, and T. Funabashi, "Multi-agent systems for power engineering applications - Part I: Concepts, approaches, and technical challenges," *IEEE Transactions on Power Systems*, vol. 22, no. 4, pp. 1743-1752, November 2007.
- [14] C. Jin, P. Wang, J. Xiao, Y. Tang, and F. H. Choo, "Implementation of hierarchical control in a DC microgrids," *IEEE Trans. Ind. Elec.*, vol. 61, no. 8, pp. 4032-4042, Aug. 2014.
- [15] B. Brusilowicz, W. Rebizant, and J. Szafran, "Influence of the voltage regulation local stability margin of the receiving node", *IEEE International Conference on Development in Power Systems Protection*, Birmingham, pp. 1-6, April 2012.
- [16] M. Xiaoming, L. Weixing, and W. Li, "A preliminary study on the Thevenin equivalent impedance for power systems monitoring", *IEEE International Conference on Electric Utility Deregulation and Restructuring and Power Technologies*, Shandong, pp. 730-733, July 2011.
- [17] S. J. S. Tsai, and K. H. Wong, "On-line estimation of thevenin equivalent with varying system states," *IEEE Power and Energy Society General Meeting - Conversion and Delivery of Electrical Energy in the 21st Century*, Pittsburgh, pp. 1-7, 2008.
- [18] D. Shi, and R. K. Sharma, "Adaptive control of energy storage for voltage regulation in distribution system" *IEEE International Conference on Smart Energy Grid Engineering*, Oshawa, pp. 1-7, August 2013.
- [19] M. Malengret, and T. C. Gaunt, "Using Thevenin equivalents to improve electricity delivery efficiency in AC and DC systems", *IEEE Proceedings of the Conference on Domestic Use of Energy*, Cape Town, pp. 1-4, April 2014.
- [20] Y. Wang, P. Zhang, W. Li, W. Xiao, and A. Abdollahi, "Online overvoltage prevention control of photovoltaic generators in microgrids", *IEEE Trans. on Smart Grid*, vol. 3, no. 4, pp. 2071-2078, December 2012.
- [21] S. Haykin, A. Sayed, J. Zeidler, P. Yee, and P. Wei, "Adaptive tracking of linear time-variant systems by extended RLS algorithms," *IEEE Trans. on Signal Proc.*, vol. 45, pp. 1118-1128, May 1997.
- [22] G. W. K. Colman, and J. W. Wells, "On the use of RLS with covariance reset in tracking scenarios with discontinuities," *IEEE Canadian Conference on Electrical and Computer Engineering*, Ottawa, pp. 693-696, May 2006.
- [23] J. Mikles, M. Fikar, *Process modelling, identification and control*, Springer, 2007.
- [24] M. Ciobotaru, R. Teodorescu, P. Rodriguez, A. Timbus, and F. Blaabjerg, "Online grid impedance estimation for single-phase grid-connected systems using PQ variations," *IEEE Power Electronics Specialists Conference*, Ottawa, pp. 2306-2312, June 2007.
- [25] S. Gab-Su, C. Bo-Hyung, L. Kyu-Chan, "DC islanding detection algorithm using injection current perturbation technique for photovoltaic converters in DC distribution," *IEEE Energy Conversion Congress and Exposition*, Raleigh, pp. 3722-3726, September 2012.

MODELLING OF MOVING LOADS USING STATIONARY DYNAMIC CURRENT SOURCES

L. Lategan*, P.J. Randewijk[†] and C.J. Fourie[‡]

* Dept. of Electrical & Electronic Engineering, Banghoek Avenue, University of Stellenbosch, 7600, South Africa E-mail: sun@luca.la

[†] Dept. of Electrical & Electronic Engineering, Banghoek Avenue, University of Stellenbosch, 7600, South Africa E-mail: pjrandew@sun.ac.za

[‡] PRASA Chair for Maintenance and Engineering Management, Dept. of Industrial Engineering, Banghoek Avenue, University of Stellenbosch, 7600, South Africa E-mail: cjf@sun.ac.za

Abstract: Determining the best arrangement for an electrical traction network is difficult without the use of computer simulations. DIgSILENT PowerFactory is widely used for power system analysis of AC and DC networks, but lacks the functionality to simulate moving loads along DC lines. A solution is proposed that utilises a relative displacement function to allocate current values to two stationary current sources to mimic moving loads. By using circuit analysis it is shown that this method almost perfectly simulate the amount of power that each substation contributes whilst the load is moving along the line. The method is used to simulate the electrical traction network for a full day. The simulation results are benchmarked against measurements taken with power data loggers and shows excellent correlation. This gives the confidence to run simulations with altered network configuration and rolling stock to predict the future state of the electrical network.

Key words: trains, railway, modelling, load flow, energy saving, climate change, capacity study, regenerative braking

1. INTRODUCTION

In the very competitive transport market, operators are constantly looking for ways to drive down operational expenses and act on social sentiment to promote their service. Energy recovery through regenerative braking provides an answer to both these issues by reducing energy expenditure and acting on the call for “greenness” by reducing the carbon-footprint of the operation.

Many railways that utilise DC traction power have difficulty in optimally exploiting regenerated energy, since the energy cannot be easily stored on the vehicle itself and the low voltage and high resistance of the traction supply limits the distance that it can travel to be utilised elsewhere. Fortunately, various techniques exist to increase the utilisation of regenerated energy. Unfortunately, determining the solution, or combination of solutions, that will be best suited, is not a trivial process. Even networks that appear similar often have vastly different optimal solutions [1].

Computer simulations offer the advantage that the effect of any combination of solutions can be investigated before a single change is made to the physical infrastructure. Various simulation suites have been developed to assist in this regard. Unfortunately many are (of a proprietary nature)/(only for internal use) and employed as part consulting work. Railways that can't or don't want to utilise them usually have to undertake the tedious process of developing their own software from scratch or utilise numerical computing environments, such as Matlab, to build models from first principles.

DIgSILENT's PowerFactory offers a stand-alone solution that is widely used by electrical network designers and power utilities around the world for power system analysis. It features support for simultaneous load flow analysis of both the AC and DC networks, but lacks the functionality to simulate moving loads along DC lines.

In this paper, we propose a method that mimics moving loads by allocating a load's current to two stationary dynamic current sources. Our model is evaluated both theoretically, by using electrical circuit analysis, and through comparing the simulation results with real measured data. Theoretically, it is shown that the proposed method perfectly mimics the loading that a moving train places on the substations that feed the relevant, uninterrupted, section. The power dissipated in or generated by the load is also very close to that of the moving load. On sections where a substation is located between a departure and arrival station, the proposed method does not load the substations perfectly. It is shown that the error is in fact small, so that the method can still be successfully used. The model is then benchmarked by comparing simulation results of a full weekday with energy measurements recorded with power data loggers. This creates confidence that the model is able to accurately model a railway traction system to simulate any time table and rolling stock.

A few simulations will be completed to investigate various solutions to reduce the prevalence reduced train performance due to low pantograph voltages caused by high loading.

2. THE SYSTEM ANALYSIS TOOL

Since our main focus is not the detailed working of trains, but rather the capacity of the electrical network, it is not considered necessary to model the rolling stock in detail. Trains are instead modelled as moving, time-dependant current sinks.* PowerFactory lacks the functionality to dynamically simulate a moving load along a DC line. An alternative method had to be sought that would be able to realistically simulate the amount of power that each substation contributes whilst the load is moving along the line.

By using two stationary current sources and varying the amount of current that is allocated to each source, it is hoped that the system response to moving loads can be mimicked accurately.

The resultant model is a dynamic (time varying) system that can simulate any rolling stock and timetable. Note that for this network, it was not deemed necessary to make provision for track gradient or speed variations, but this can be modelled by using different current profiles for the relevant sections.

Figure 1 shows a flow-diagram of the system analysis tool. A Python algorithm was developed to read the timetable, rolling stock current profiles and network characteristics. It calculates the current value that must be allocated to each current source for every second of the day and creates a single CSV-file that PowerFactory use as input. A number of simulation output variables are defined for each element type in PowerFactory, such as node voltage, loading and power consumption. These variables are written to a csv file and post-processed to create summaries in table and graph form.

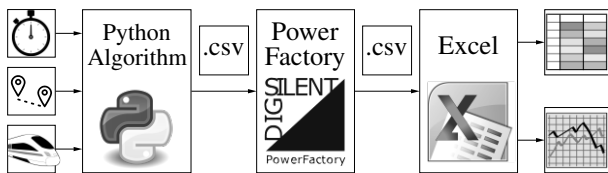


Figure 1: Flow-diagram of system analysis tool

3. SIMULATING MOVING LOADS

A method has to be found that allocates current to the stationary current sources in order to mimic the movement of trains along the DC transmission lines. One possibility is to place a single current source mid-way between stations. This model will only represent the real power

*The terms current source and current sink are used interchangeably and both refer to the "DC - Current Source" element in PowerFactory (ElmDci). This element, by definition, sinks (draws) current for positive setpoint values (dissipates power). For negative setpoint values it is a source and injects current into the node to which it is connected (generates power).

division at a single point in time, i.e. when the train passes the location of the current source.

Another possibility is to use two stationary current sources and vary the amount of current that is allocated to each source in a way that would produce the same system response as a single, moving load. Typically a source will be placed at every departure and arrival point (station platform).

By making use of superposition, the system response of all trains operating together will equal the sum of the responses caused by each train acting alone, where all the other independent sources are replaced by their internal impedances. Since we model the trains as ideal current sources, their internal impedances are infinite and they have no influence whenever their current is zero. If we can therefore prove that the system response to a single train modelled as two stationary dynamic loads will be the same as a single train modelled as a single, moving load, then the amount of trains that will eventually be operating in the system should have no effect on the validity of the model.

3.1 Defining the Relative Displacement Function

We will first introduce the concept of a relative displacement function, $m(t)$. Irrespective of the load representation, the location of the load along the line at a certain time instance will play a significant role in the amount of power that each substation will contribute.

The typical form of this function is shown in Figure 2. It represents three stages of the journey between two stations: acceleration (quadratic change in displacement), constant speed (linear change in displacement) and braking (quadratic change in displacement). Note that $m(0) = 1$ indicate that the train is "100%" at its departure station and "0%" at the destination. Similarly, $m(t_f) = 0$ indicate that the train is "0%" at the departure station but "100%" at its destination.

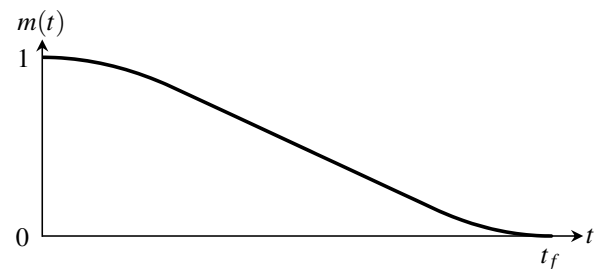


Figure 2: Typical form of the displacement function $m(t)$

By using simple equations of motion and the average acceleration and deceleration rate of the specific class of rolling stock, an idealised displacement function can be calculated. For this idealised model, a train will accelerate at a constant rate up to the velocity which is needed to cover the distance between stations in the amount of time allowed in the timetable. It will then travel at that velocity until commencing a constant deceleration, so that the train arrives the destination station at exactly the timetabled

time. Allowance can be made to cover the distance in less time, say 5 %, to cover delays.

Note that the maximum train speed is based purely on the amount of time allocated to the station-to-station journey in the official time table and the distance between the substations. It can therefore not take individual speed restrictions, nor the associated deceleration and acceleration, into consideration.

Figure 3 illustrates the acceleration $a(t)$, speed $v(t)$ and displacement $x(t)$ of a typical station-to-station journey. The train departs and continues to accelerate at a_v m/s² until reaching a speed of v_{max} m/s after t_v seconds. It then maintains this speed until $t_f - t_s$ seconds after departure. From this time it accelerates at a_s m/s² (deceleration) and continues to do so (for t_s seconds) until reaching the destination. The journey is x_f metres long and takes t_f seconds to complete.

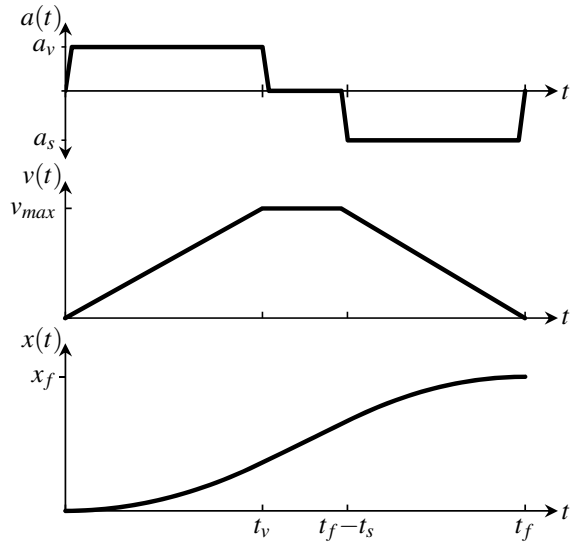


Figure 3: Idealised acceleration, speed and displacement curve of a single station-to-station journey

Substituting these variables into the standard motion equation

$$x(t) = x_0 + v_0 t + \frac{1}{2} a t^2 \quad (1)$$

yields the following piecewise continuous function for the displacement $x(t)$

$$x(t) = \begin{cases} \frac{1}{2} a_v t^2 & \forall 0 \leq t \leq t_v, \\ \frac{1}{2} a_v t_v^2 + v_{max} (t - t_v) & \forall t_v \leq t \leq t_f - t_s, \\ \frac{1}{2} a_v t_v^2 + v_{max} (t - t_v) + \frac{1}{2} a_s (t - t_f + t_s)^2 & \forall t_f - t_s \leq t \leq t_f \end{cases} \quad (2)$$

where

$$t_v = \frac{v_{max}}{a_v}, a_v > 0 \quad \text{and} \quad t_s = -\frac{v_{max}}{a_s}, a_s < 0 \quad (3)$$

Substituting (3) into (2), one can solve the maximum

speed:

$$v_{max} = \frac{-t_f + \sqrt{t_f^2 + 2 \left(\frac{1}{a_s} - \frac{1}{a_v} \right) x_f}}{\frac{1}{a_s} - \frac{1}{a_v}} \quad (4)$$

Note that the function for $x(t)$ in (2) and its graphical representation in Figure 3 does not conform to the definition for $m(t)$ stated at the start of this section and shown in Figure 2. In order for $m(0) = 1$ and $m(t_f) = 0$ to hold true, we can define $m(t)$ in terms of $x(t)$ as follow:

$$m(t) = 1 - \frac{x(t)}{x_f} \quad (5)$$

3.2 Moving train on an open section

Consider a load moving along an uninterrupted section of line, illustrated by Figure 4. It represents the load moving between points 1 and 2 along an overhead line of length d , fed by two substations. Each substation's transformers and rectifiers are replaced by a Thévenin equivalent circuit, indicated by a voltage source. Between each substation and the extremes of movement is a piece of overhead line, of length x_1 and x_2 respectively. Using the superposition theorem again, the system response of the moving current sink can be calculated by solving the accompanying circuit. The relative displacement of the train is represented by the function $m(t)$.

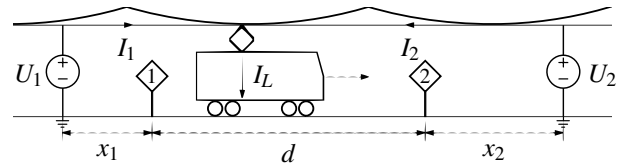


Figure 4: Diagram of a train moving between two points, supplied by two substations

Single moving load: First examine the case where the load is represented by a single, moving load I_L . Load movement is represented by changing the resistance of the overhead wire with a function, $m(t)$, that represents the position of the train in time. By solving the circuit of Figure 5, we can solve I_{U1} , the amount of current that is contributed by substation 1 at time instance t to feed the moving load.

Node voltage equation:

$$I_L = I_{U1} + I_{U2} \quad (6)$$

Mesh current equations:

$$-U_1 + I_{U1} [R_{thU1} + \rho x_1 + \rho d (1 - m(t))] + U_{IL} = 0 \quad (7a)$$

$$-U_2 + I_{U2} (R_{thU2} + \rho x_2 + \rho d m(t)) + U_{IL} = 0 \quad (7b)$$

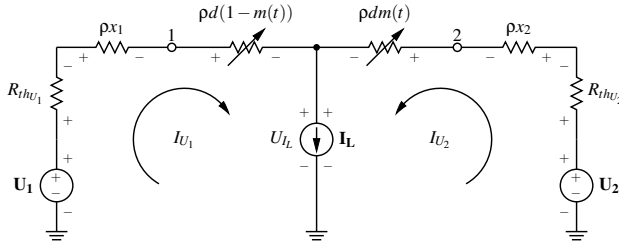


Figure 5: Circuit of a single, moving load fed by two substations

Writing (7a) in terms of U_{IL} and substituting in (7b) gives

$$-U_2 + I_{U_2} (R_{thU_2} + \rho x_2 + \rho d m(t)) + U_1 - I_{U_1} [R_{thU_1} + \rho x_1 + \rho d (1 - m(t))] = 0 \quad (8)$$

From (6) we know that $I_{U_2} = I_L - I_{U_1}$ and let $\Delta U = U_1 - U_2$, then it follows:

$$I_{U_1} [R_{thU_1} + \rho x_1 + \rho d (1 - m(t)) + \rho d m(t) + R_{thU_2} + \rho x_2] = I_L (R_{thU_2} + \rho x_2 + \rho d m(t)) + \Delta U \quad (9)$$

To give the current contribution of substation 1 as:

$$I_{U_1} = \frac{I_L (R_{thU_2} + \rho x_2 + \rho d m(t)) + \Delta U}{R_{thU_1} + R_{thU_2} + \rho (x_1 + x_2 + d)} \quad (10)$$

The power that will be dissipated by the moving load can be calculated from (7a) and (10).

$$P_{IL} = U_{IL} I_L \quad (11)$$

$$= I_L \left\{ U_1 - I_{U_1} [R_{thU_1} + \rho (x_1 + d - dm(t))] \right\} \quad (12)$$

Two stationary dynamic loads: Now consider Figure 6, where there is two current loads and load movement is represented by changing the amount of current allocated to each source using the same relative displacement function, $m(t)$. By setting $I_1 = I_L m(t)$ and $I_2 = I_L (1 - m(t))$, we forecast that the full load current will initially be allocated to I_1 and gradually transferred until it is fully allocated to I_2 at $t = t_f = m^{-1}(0)$. I_{U_1} , the amount of current that is contributed by substation 1 at time instance t to feed the stationary loads I_1 and I_2 can then be calculated using circuit analysis.

Let

$$I_1 = I_L m(t) \quad \text{and} \quad I_2(t) = I_L (1 - m(t)) \quad (13)$$

and

$$I_L = I_{U_1} + I_{U_2}. \quad (14)$$

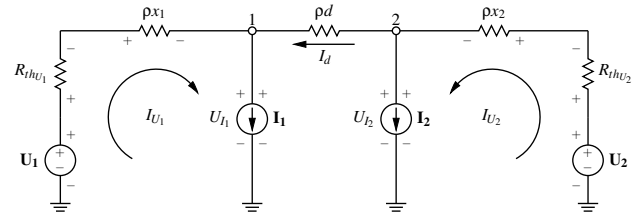


Figure 6: Circuit of two stationary dynamic loads fed by two substations

Mesh current equations:

$$-U_1 + I_{U_1} (R_{thU_1} + \rho x_1) + U_{I_1} = 0 \quad (15a)$$

$$-U_2 + I_{U_2} (R_{thU_2} + \rho x_2) + U_{I_2} = 0 \quad (15b)$$

$$-U_{I_2} + \rho d I_d + U_{I_1} = 0 \quad (15c)$$

Substituting (15a) and (15b) in (15c):

$$I_{U_1} (R_{thU_1} + \rho x_1) - U_1 - \rho d (I_{U_2} - I_2) + U_2 - I_{U_2} (R_{thU_2} + \rho x_2) = 0 \quad (16)$$

From (14) and (13) let

$$I_{U_2} = I_L - I_{U_1}, \quad (17)$$

$$I_{U_2} - I_2 = -I_{U_1} + I_L m(t) \quad \text{and} \quad (18)$$

$$\Delta U = U_1 - U_2 \quad (\text{the diff. in supply voltage}). \quad (19)$$

Then

$$I_{U_1} (R_{thU_1} + \rho x_1) - \Delta U - \rho d (I_L m(t) - I_{U_1}) - (I_L - I_{U_1}) (R_{thU_2} + \rho x_2) = 0. \quad (20)$$

To give the current contribution of substation 1 as:

$$I_{U_1} = \frac{I_L (R_{thU_2} + \rho x_2 + \rho d m(t)) + \Delta U}{R_{thU_1} + R_{thU_2} + \rho (x_1 + x_2 + d)} \quad (21)$$

The power that will be dissipated by the moving load itself can be calculated as the sum of the power dissipated in both stationary loads. The power dissipated in I_1 can be calculated using (15a) and (21):

$$P_{I_1} = U_{I_1} I_1 \quad (22)$$

$$= U_{I_1} I_L m(t) \quad (23)$$

$$= I_L m(t) [U_1 - I_{U_1} (R_{thU_1} + \rho x_1)] \quad (24)$$

Similarly, the power dissipated in I_2 can be calculated

using (15b), (17) and (21):

$$P_{I_2} = U_{I_2} I_2 \quad (25)$$

$$= U_{I_2} I_L (1 - m(t)) \quad (26)$$

$$= I_L (1 - m(t)) \left[U_2 - I_{U_2} (R_{thU_2} + \rho x_2) \right] \quad (27)$$

P_{I_L} , the total power that will be dissipated by the train, is the sum of (24) and (27).

Comparison of two methods: Note that the current supplied by substation 1 to the two stationary loads (21) is exactly the same as the current that will be delivered to the moving load (10). From (6) and (17), the current supplied by substation 2 will also be the same. Since the power delivered by each substation is directly proportional to the current flowing through it, the power that each substation contribute will also be identical. This proves that the response of substations due to moving trains along an open section can be mimicked by manipulating the current profiles with an external script. These profiles can then be used as input for the stationary current loads in PowerFactory.

Due to space constraints, the full equation will not be written out, but by looking at (24) and (27), one can already deduce that it will not be equal to (12). Consequently, the power dissipated in the load itself will be different for the two methods. The extent to which they differ was evaluated using Microsoft Excel with sample values of $m(t)$ and I_L .

Even on a very long section (large d) and a faraway substation (large x_1 , but small x_2), the largest error in instantaneous power for two stationary dynamic sources is only 4,059 %. The total power dissipated in the two stationary dynamic sources is 1,757 % higher than the moving load.

For a more realistic section ($d = 1,87\text{km}$, $x_1 = 2,399\text{km}$ and $x_2 = 3,088\text{km}$) the maximum error in instantaneous power is 0,827 %. The total energy dissipated in the two sources is 0,434 % higher than in the moving load.

The results are encouraging and the total power dissipated by two stationary dynamic sources is deemed close enough to that of a moving load. The recorded values of minimum and maximum voltage also compares very well.

3.3 Moving train on an interrupted section

Another scenario exists where the train will depart from a point between substation 1 and 2, but arrive at a point between substation 2 and 3, graphically portrayed by Figure 7. The circuit of Figure 5 is not applicable any more, since a third substation now divides our previously uninterrupted line of length d .

For the case of the single moving load, the current contribution of each substation will now need a piece-wise

continuous function to explain the time period $0 \leq t \leq m^{-1}(0)$.

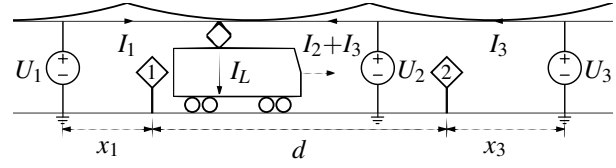


Figure 7: Diagram of a train moving between two points, supplied by three substations

By solving the circuits that describe this scenario, it can be shown that the current contribution of each substation is not the same. This also implies that the power contribution of each substation will not be the same. For an interrupted section, the response of substations due to moving trains along it can thus not be perfectly mimicked by manipulating the current profiles using the relative displacement function and an external script.

From mere observation of the equations for current contribution and power dissipation that result from the circuit analysis, it is not immediately clear to which extent the two methods will vary for the network under review. This was again evaluated using Microsoft Excel with sample values of $m(t)$ and I_L .

The results are encouraging and the total power dissipated by two stationary dynamic sources is deemed close enough to that of a moving load. The recorded values of minimum and maximum voltage also compares very well.

Even on a very long section ($d = 10,21\text{km}$) and a faraway substation (large x_1 , but small x_3 and substation 2 located close to point 1), the largest error in instantaneous power for two stationary dynamic sources is only 1,189 %. The total power dissipated in the two stationary dynamic sources is 1,189 % higher than the moving load.

For a shorter section ($d = 1,91\text{km}$, $x_1 = 7,259\text{km}$ and $x_3 = 6,9\text{km}$) and substation 2 located a bit further from point 1, the maximum error in instantaneous power is 0,286 %. The total energy dissipated in the two sources is 0,108 % higher than in the moving load.

For a short section ($d = 0,85\text{km}$, $x_1 = 6,199\text{km}$ and $x_3 = 5,691\text{km}$) and substation 2 located almost in the middle between point 1 and 2, the maximum error in instantaneous power is 0,092 %. The total energy dissipated in the two sources is 0,042 % higher than in the moving load.

This proves that the movement of the trains on open and interrupted sections can be sufficiently mimicked by manipulating the current profiles with an external script. These profiles can then be used as input for the stationary current sources in PowerFactory.

4. REALISATION

Figure 8 gives an example of the current demand for a station-to-station journey, as calculated by the processing algorithm and using $m(t)$. These graphs are for the new trains, with regeneration. Figure 8(a) shows the total calculated current demand of a train travelling between two stations. The train will first accelerate (increase in current), then travel at a constant velocity (constant current) and then brake regeneratively (negative current). The algorithm divided the current between the two sources, based on the displacement of the train. Figure 8(b) gives the current that will be allocated to the source at the departure platform and Figure 8(c) the source at the arrival platform. Initially, the full load current will be allocated to the source at the departure. It will decrease until eventually all the current is allocated to the source at the arrival point, at t_f .

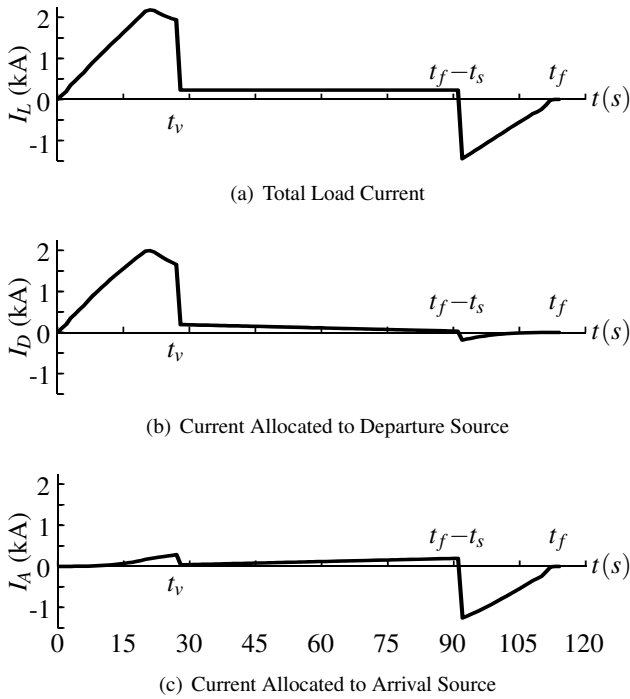


Figure 8: Divided current profile

5. MODEL BENCHMARKING

Before using the model to do any predictions, it was validated by benchmarking simulation results of the present network layout and rolling stock model against power data logger measurements. The measurements were done as part of a study by Royal Haskoning DHV in 2013 [2]. The present rolling stock's model was based on a current profile that was recorded by one of the motor coaches' on board trip logger. Figure 9 shows the current profile for a single motor coach at 3 kV line voltage.

The graph of Figure 10 shows the total averaged power at the most important feeding point to the ring network. The solid line is the simulated value, while the dashed line gives

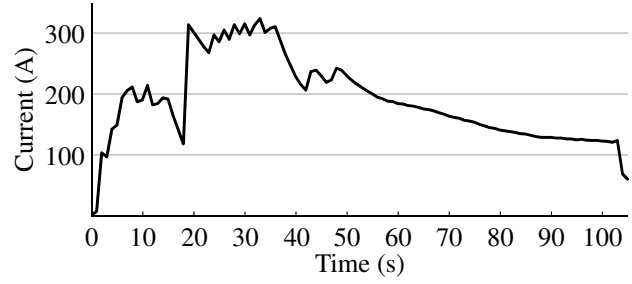


Figure 9: Traction current for a single motor coach of the present rolling stock

the measured values. The dotted line gives the simulated averaged power flow at the secondary feeding point, with measured values in dash-dot. The plots correlate very well, both in terms of form and magnitude. The largest error, of about 1 MW, is less than the energy demand of a single train and can be attributed to operational factors, such as delays. The graph for the secondary feeding point shows excellent overall correlation.

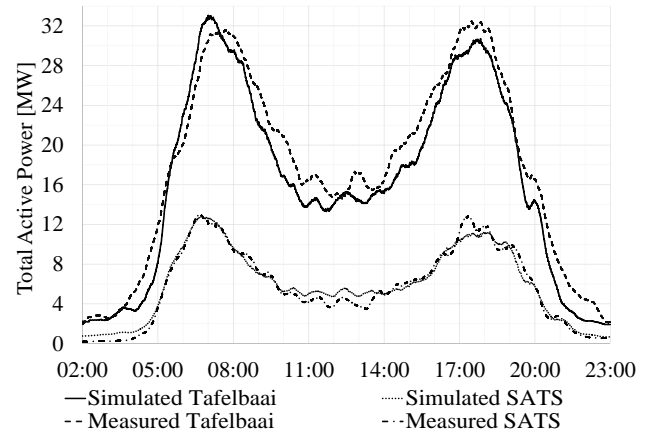


Figure 10: 30 min Average Power Feed-in for Current Rolling Stock

Due to the good correlation between the simulation results and the measured data, we are confident that the simulation results of the network with altered configuration and the new rolling stock should also prove to be equally accurate.

6. CONCLUSION

A few simulations have been completed to investigate various solutions to reduce the prevalence reduced train performance.

PowerFactory was successfully used to build a virtual model of an electrical traction network and conduct dynamic simulations. An excellent correlation between the simulation results of the present network and measured data was achieved. Consequently, various scenarios could be investigated to determine the projected future state of the network.

PowerFactory was successfully used to build a virtual

model of an electrical traction network and conduct dynamic simulations. An excellent correlation between the simulation results of the present network and measured data was achieved. Consequently, various scenarios could be investigated to determine the projected future state of the network.

REFERENCES

- [1] R. Barrero: *Energy Recovery Technologies in Public Transport*, PhD Thesis, Electrical Engineering and Energy Technology, Vrije Universiteit Brussel, November 2012.
- [2] Royal Haskoning DHV: *Brief Report :- Metering Study Outcomes, Revision 0*, Unpublished, October 2013.

INTEGRATION OF INVERTER CONSTRAINTS IN GEOMETRICAL QUANTIFICATION OF THE OPTIMAL SOLUTION TO A MPC CONTROLLER

J. Raath^{*} and H. du Toit Mouton[†] and T. Geyer[‡]

^{*} Department of Electrical, Electronic and Computer Engineering, Central University of Technology, Bloemfontein, South Africa, E-mail: jraath@cut.ac.za

[†] Department of Electrical and Electronic Engineering, University of Stellenbosch, Cape Town, South Africa, E-mail: dtmouton@sun.ac.za

[‡] ABB Corporate Research, ABB Switzerland Ltd, Power Electronic Systems, Switzerland, E-mail: t.geyer@ieee.org

Abstract: This paper considers a model predictive controller with reference tracking that manipulates the integer switch positions of a power converter. It can be shown that the optimal switch position can be computed without solving an optimization problem. Specifically, in a new coordinate system, the optimization problem can be solved offline, leading to a polyhedral partition of the solution space. The optimal switch position can then be found using a binary search tree. This concept is exemplified for a three-level single-phase converter with an RL load.

Key words: Model Predictive Control, Vector Quantization, Delaunay triangulation, Voronoi diagram, Binary Search Tree.

1. INTRODUCTION

Model predictive control (MPC), also referred to as receding horizon control is a type of predictive control which in general uses a model of the system to predict the future behavior of the controlled parameters. The predictions are then used to obtain the optimal control decision by following a specific optimization criterion. Traditional MPC demanded a great amount of online computation, since an optimization problem (often a constrained quadratic program) is solved at each sampling instant. This has limited the use of these controllers to processes with relatively slow dynamics but because of advances in the fields of mathematical optimization and computational power of the controller hardware it became possible to consider MPC in power electronic systems with short sampling intervals [1]. MPC using larger horizons also has the potential to give significant performance benefits, but requires more computations at each sampling instant to solve the associated optimization problem [2, 3]. The online computational burden of MPC can be lessened by obtaining an solution to the MPC problem offline by means of multi-parametric quadratic programming (mpQP) [4, 5]. The offline solution is a state-feedback control over a polyhedral partition of the state-space. The control law can be stored in a look-up table, avoiding the need for solving an optimization problem online [6].

The main purpose of our research is to reduce the online computational burden so as to practically implement MPC for a multilevel inverter. To achieve this goal it is necessary in the offline solution to construct a binary search tree with minimum depth, which can only be achieved if the partitioned state-space is of lowest complexity. This paper presents an algorithm for reducing the complexity of the partitioned state-space by utilizing the Delaunay

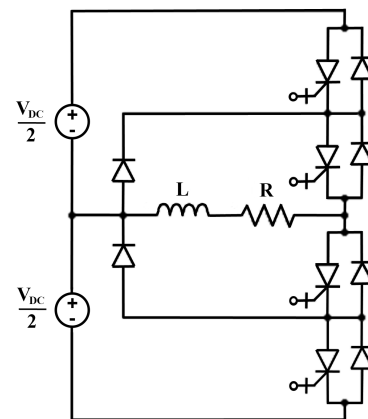


Figure 1: Single-phase Neutral Point Clamped inverter.

triangulation. The paper is organized as follows: Section 2 introduces the model of a multilevel inverter with RL load. The mathematical background to the MPC problem is laid out in section 3. In section 4 the partitioned state-space is geometrically presented. The approach to complexity reduction along with the proposed algorithm are presented in section 5. Section 6 concludes the paper.

2. MODELING

We consider a single-phase multilevel inverter as one leg of a Neutral Point Clamped (NPC) inverter with neutral point assumed to be constant. The topology is shown in figure 1. The inverter leg can deliver three voltage levels of $-0.5V_{DC}$, $0V_{DC}$ and $+0.5V_{DC}$ across the load. These output levels can be represented by the integer values $u \in \{-1, 0, +1\}$ that define the state of the switch positions

in the inverter leg. The voltage applied to the RL load can thus be stated as $v(t) = 0.5V_{DC} \cdot u(t)$. A possible destructive situation that can occur in this inverter topology is switching directly from state $+1$ to state -1 and vice versa. It is called shoot-through and can lead to high currents in the inverter leg. This transition is undesirable. For detailed operation and switching sequence of a NPC inverter refer to [7].

3. MODEL PREDICTIVE CONTROL

Model predictive control is a method in which the control action is determined by solving a finite horizon open-loop optimal control problem at each sampling instant, using the current state of the system as initial state, searching for an optimal control sequence over the set horizon and then applying the first control in this sequence to the system. With reference tracking the general aim is to control the inverter switches in such a manner so as to generate an output current i in the RL load that tracks a reference current i_r as close as possible. The closer the output tracks the reference, the lower the harmonic distortion will be. With the switching frequency being inversely proportional to harmonic distortion in the output current and directly proportional to internal switching losses of the inverter, a trade-off between current distortions and switching losses arises.

An MPC controller operates in the discrete time domain with the sampling interval T_s . During every sample period the load current is sampled and from its value all the possible future load currents are determined which may arise from applying the different switching states also called control options, $u \in \{-1, 0, +1\}$ to the inverter. The effect of the possible voltages, $v(t) = 0.5V_{DC} \cdot u(t)$ applied to the mathematical model of the load results in a number of possible load currents equal to the number of control options. These predicted currents are subjected to a cost function as one of the control objectives that define the control system. The switching state u that result in a predicted current of minimal cost is selected as the optimal control input for application to the inverter. The cost function for our application includes the two contradictory objectives, optimal reference-current tracking and minimal switching cost.

3.1 Load model

In order for the MPC controller to predict the possible currents in the load, a mathematical model for the system needs to be derived. The RL load equation in the continuous time domain,

$$v(t) = Ri(t) + L \frac{di}{dt}$$

can be rewritten as,

$$\frac{di(t)}{dt} = -\frac{Ri(t)}{L} + \frac{0.5V_{DC}(t) \cdot u(t)}{L} \quad (1)$$

With the controller operating at discrete time instants $t = kT_s$ and $k \in \mathbb{N}$ the load model can be redefined in the discrete-time domain with $u(k)$ as input vector and $i(k)$ as state vector. The predicted load current at the discrete time step $(k+1)$ originating from the present output current value $i(k)$ for an applied control option $u(k)$, can be stated as,

$$i(k+1) = Ai(k) + Bu(k) \quad (2)$$

with,

$$A = e^{-T_s/\tau}, \quad B = \frac{V_{DC}}{2R} (1 - e^{-T_s/\tau}),$$

$$\tau = \frac{L}{R}.$$

3.2 Cost function

To find the optimal control input to the inverter, all the predicted load currents $i(k+1)$ and the respective switching states $u(k) \in \{-1, 0, +1\}$ are subjected to a cost function (J),

$$J = \|i_r(k+1) - i(k+1)\|_2^2 + \lambda_u \|\Delta_u(k)\|_2^2 \quad (3)$$

with,

$$\|\Delta_u(k)\|_2^2 = \|u(k) - u(k-1)\|_2^2 \quad (4)$$

This quadratic cost function J , consist of two terms. The first one determine the tracking error of the predicted load current $i(k+1)$ with respect to the reference current $i_r(k+1)$, and the second term determines the switching cost from the previous switching state $u(k-1)$ to $u(k)$. A tuning factor $\lambda_u > 0$ adjusts the balance between tracking error cost and switching cost. To avoid shoot through, the switching constraint $\|\Delta_u(k)\|_2^2 \leq 1$ must be adhered to. The switching state that satisfies this constraint and results in minimum cost is deemed the optimal control option $u_{opt}(k)$ for application to the inverter.

3.3 Extended horizons

Solving the problem stated above results in a control action after evaluating the predicted currents at *one* discrete time-step into the future, a horizon (N) of one. This horizon can be extended by determining the predicted currents over a finite number of time-steps into the future. The cost of the possible switching sequences are determined and result in an improved optimal control decision while still adhering to the the switching constraint. Equation (3) can be written as a finite horizon quadratic cost function,

$$J = \sum_{l=k}^{k+N-1} \|i_r(l+1) - i(l+1)\|_2^2 + \lambda_u \|\Delta_u(l)\|_2^2 \quad (5)$$

J is now a function of the switching sequence $U(k) =$

$[u(k), u(k+1), \dots, u(k+N-1)]$ over the prediction horizon N . The number of possible switching sequences that needs to be evaluated thus increases exponentially with an extension of the prediction horizon. With $U(k)$ the optimization problem for N -horizon can be formulated as,

$$U_{opt}(k) = \arg \min_{U(k)} J \quad (6)$$

subject to

$$i(l+1) = Ai(l) + Bu(l) \quad (7)$$

$$u(l) \in \{-1, 0, +1\}$$

$$\|\Delta_u(l)\|_2^2 \leq 1$$

$$\forall l = k, \dots, k+N-1$$

3.4 Vectorization of cost function

In order to obtain a solution for the optimization problem (6) it is useful to vectorize the cost function (5). Iterating (7) for all l and rewriting in matrix notation gives,

$$I(k) = \Gamma i(k) + \Upsilon U(k) \quad (8)$$

with,

$$I(k) = \begin{bmatrix} i(k+1) \\ i(k+2) \\ i(k+3) \\ \vdots \\ i(k+N) \end{bmatrix}, \Gamma = \begin{bmatrix} A \\ A^2 \\ A^3 \\ \vdots \\ A^N \end{bmatrix},$$

and

$$\Upsilon = \begin{bmatrix} B & 0 & \dots & 0 \\ AB & B & \dots & 0 \\ A^2B & AB & B & 0 \\ \vdots & \vdots & \vdots & \vdots \\ A^{N-1}B & A^{N-2}B & \dots & B \end{bmatrix}.$$

$I(k)$ then represents the predicted output currents over the finite horizon from time step $k+1$ to $k+N$. Substituting (8) into the cost function (5) results in,

$$J = \|\Gamma i(k) + \Upsilon U(k) - I_R(k)\|_2^2 + \lambda_u \|SU(k) - Eu(k-1)\|_2^2 \quad (9)$$

I_R is the reference current values over the prediction horizon. S and E are introduced to extract the switching cost over the extended horizon.

$$S = \begin{bmatrix} 1 & 0 & \dots & 0 \\ -1 & 1 & \dots & 0 \\ 0 & -1 & 1 & 0 \\ \vdots & \vdots & \vdots & \vdots \\ 0 & 0 & \dots & 1 \end{bmatrix} E = \begin{bmatrix} 1 \\ 0 \\ 0 \\ \vdots \\ 0 \end{bmatrix}$$

Minimization of (9) and omitting all constraints, results in the well known expression for the unconstrained optimum [2] or unconstrained minimizer [6].

$$U_{unc}(k) = -Q^{-1}\Theta(k) \quad (10)$$

with,

$$Q = \Upsilon^T \Upsilon + \lambda_u S^T S$$

$$\Theta(k) = ((\Gamma x(k) - I_R(k))^T \Upsilon - \lambda_u (Eu(k-1))^T S)^T$$

and resulting cost function,

$$J = [U(k) - U_{unc}(k)]^T Q [U(k) - U_{unc}(k)] + const(k) \quad (11)$$

The Cholesky decomposition of Q produces a lower triangular matrix H so that $H^T H = Q$. Substituting in (11) gives,

$$J = \|HU(k) - HU_{unc}(k)\|_2^2 + const(k) \quad (12)$$

The constant term in (12) is independent from $U(k)$ and can be excluded with the resulting optimization problem,

$$U_{opt}(k) = \arg \min_{U(k)} \|HU(k) - HU_{unc}(k)\|_2^2 \quad (13)$$

subject to the switching constraint,

$$\|\Delta_u(l)\|_2^2 \leq 1, \forall l = k, \dots, k+Np-1$$

3.5 Nearest Neighbor Quantization

In summary, the optimization problem (13) states that the optimum switching sequence for the finite horizon N , can be found as the minimum Euclidean distance from the optimal unconstrained vector $HU_{unc}(k)$ to any of the switching-sequence vectors $HU(k)$ in the coordinate system set by the H -transformation matrix with $H \in \mathbb{R}$. This translates into the nearest neighbor search of the multi-dimensional vector $HU_{unc}(k)$ to the finite set of output vectors $HU(k)$ in N -dimensional Euclidean space.

A general technique for solving the optimization problem (13) is the exhaustive search method. This method enumerates all possibilities and verifies if the switching constraint is satisfied. For example, consider an MPC current controller with reference tracking and horizon $N = 2$ for the single-phase three-level NPC inverter with an RL load as in figure 1. Steady state conditions with the following parameters are assumed. A sampling interval of $T_s = 25\mu s$, load- resistance of $R = 2\Omega$, and inductance $L = 2mH$. The rated rms output voltage of the inverter is $V_{AC} = 3.3kV$ with an input dc-link voltage of $V_{DC} = 5.2kV$. Base quantities are used to establish a per unit system and the current reference is assumed to be 0.8pu amplitude at 50Hz. Applying a tuning factor of $\lambda_u = 0.02$ and the above

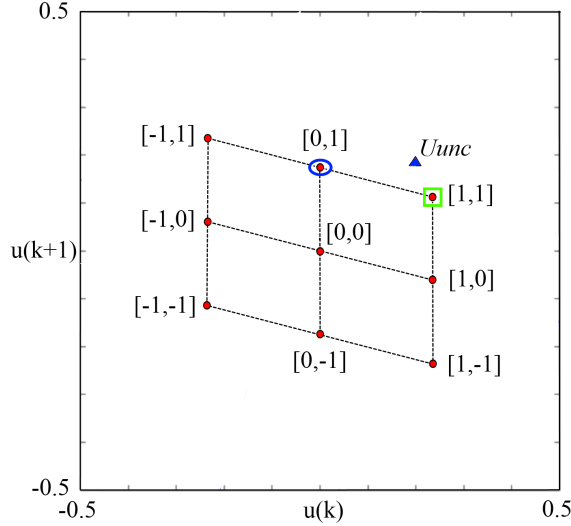


Figure 2: Transformed H-coordinate system

stated parameters generates an H -transformation matrix of,

$$H = \begin{bmatrix} 0.2286 & 0 \\ -0.0679 & 0.1711 \end{bmatrix}.$$

A horizon $N = 2$ results in a transformed H -coordinate system in the two-dimensional Euclidean space. Figure 2 shows the transformed H -coordinate system with possible switching sequences $U(k)$ indicated as dots. For explanation sake consider the unconstrained optimum $U_{unc}(k)$ indicated by the triangle. Assuming a previous switching state of $u(k-1) = -1$ and investigating the spatial arrangement of the vectors it is evident that the switching sequence $U(k) = [+1, +1]$ (enclosed by the rectangle) has the smallest Euclidean norm $\|HU(k) - HU_{unc}(k)\|_2^2$ and seems to be the optimum solution but the first control action in this switching sequence is $u(k) = +1$. This value does not satisfy the switching constraint $\|u(k) - u(k-1)\|_2^2 \leq 1$ since $u(k-1) = -1$. Further investigation leads to the second nearest neighbor $U(k) = [0, +1]$ (enclosed by the ellipse) with $u(k) = 0$ which do satisfy the switching constraint. This sequence is then considered the optimal solution with $u(k) = 0 = u_{opt}(k)$ which is applied as control input to the inverter. This process of finding the optimal control input to the inverter repeats at every sampling interval, generating an inverter output voltage for application to the RL load which results in subsequent current flow. Figure 3 shows the simulated result of one cycle of the sinusoidal reference current i_r , switched inverter output voltage v and tracking load current i displayed in per unit values.

4. VECTOR QUANTIZATION

Although the exhaustive search technique suggested above is simple to implement, its computational cost is proportional to the number of possible solutions which increases exponentially as the horizon is extended.

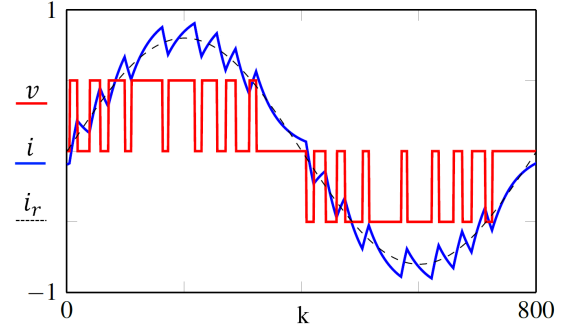


Figure 3: Inverter output voltage and reference tracking load current.

Therefore, it is only used for short horizon solutions [8]. Various solution algorithms for (13) have been developed but only a recent initiative by [2] incorporated the switching constraint $\|u(k) - u(k-1)\|_2^2 \leq 1$ into an very effective adaptation of the Sphere decoding algorithm. In contrast, this research is aimed at exploring the H -space and attempting to compute a geometrical solution in the format of a binary search tree (BST) to solve the MPC problem.

4.1 Voronoi partitioning

A Voronoi diagram of a set of points also called sites or seeds, is the partition of \mathbb{R} Euclidean space into convex polyhedra of points nearest to each of the sites [9]. Each of these polytopes is called a Voronoi- or Dirichlet cell. The nearest neighbor search or quantification of the vector HU_{unc} can be done by partitioning the N -dimensional H -space ($H \in \mathbb{R}$) into a finite subset of Voronoi cells from the HU -sites and then determine in which of these cells HU_{unc} resides. In our case, the Voronoi diagram for 3^N number of HU -sites can be defined as the following set of polytopes,

$$V_i = \{x : \|x - HU_i\| < \|x - HU_j\|\} \quad (14)$$

for

$$i = 1, 2, \dots, 3^N, \forall j \neq i$$

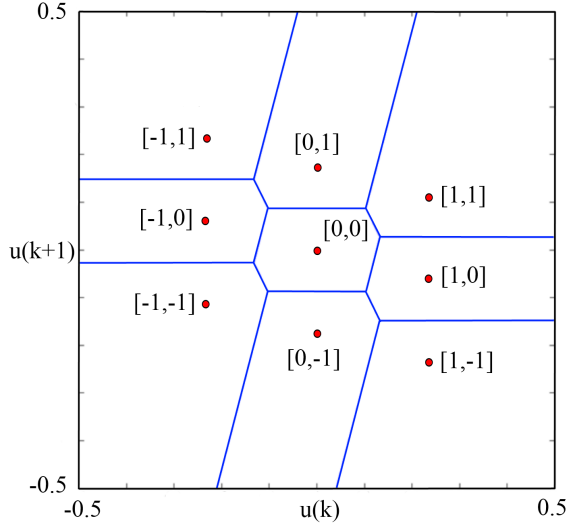
The vector HU_{unc} thus resides in a Voronoi cell V_i corresponding to a site HU_i if,

$$\|HU_{unc} - HU_i\| < \|HU_{unc} - HU_j\| \quad (15)$$

for

$$i = 1, 2, \dots, 3^N, \forall j \neq i$$

Figure 4 graphically illustrates the partitioned H -coordinate space into nearest-neighbor Voronoi cells for the respective HU -sites. The most immediate way of determining in which polyhedral region HU_{unc} resides is to do a sequential search through all the regions but this is computationally expensive and not viable for application in higher dimensions [10]. By example, to determine the location of HU_{unc} as stated in (15), requires

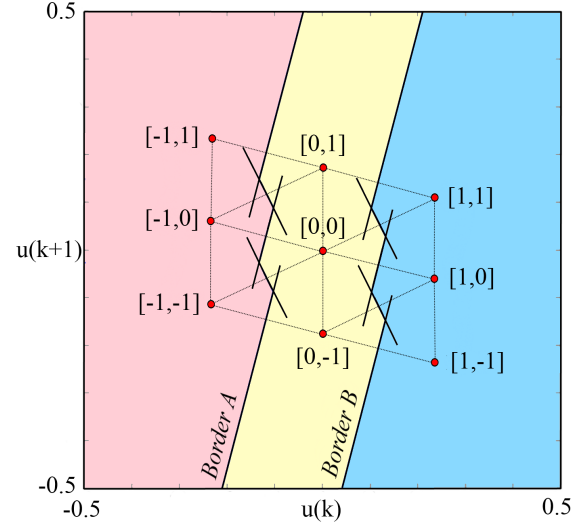

 Figure 4: Voronoi partitions for HU -sites in the transformed H -coordinate space.

the linear investigation ($A^T x - b$) of 16 hyperplanes that defines the 9 polyhedral regions (figure 4), $N = 3$ results in 27 polyhedra with 98 hyperplanes and $N = 4$ results in 81 polyhedra with 544 hyperplanes. Thus finding the region wherein HU_{unc} resides will result optimal control sequence $U(k)$ and hence $u(k)$, the optimal control action for application to the inverter.

5. COMPLEXITY REDUCTION

From the example above it is evident that the complexity rapidly increases with an extension of the horizon resulting in higher dimensionality of the H -space. The standard approach to complexity reduction is to unify adjacent polyhedral partitions with similar control laws $u(k)$. From figure 4 it can be noticed that some of the $HU(k)$ -sites have the same first term value and thus represent the same control law. Unification of the 9 polyhedral regions into subsets, each representing one of the control laws $u \in \{-1, 0, +1\}$ reduces the number of hyperplanes to be investigated in the point location of HU_{unc} from 16 to 10 for the horizon $N = 2$ case. Horizon $N = 3$ reduce from 98 to 50 and $N = 4$ from 544 to 250. Figure 5 shows the three sets of unified polyhedral regions representing the different control laws for the $N = 2$ case. It can be observed that the control regions are separated by two decision borders, made up of five hyperplanes each. Investigation of border A will result in a decision between control laws -1 and 0 and border B will distinguish between laws 0 and $+1$. The investigation of the border hyperplanes in solving the point location problem can further be optimized by constructing a binary search as proposed by [10]. Further discussion on binary search trees are omitted since the major concern of this paper is obtaining the border hyperplanes to a partitioned state-space of minimal complexity.

The unified polyhedral regions are made up of convex polyhedral sets but the combined regions them self are


 Figure 5: Unified Voronoi partitions in the transformed H -coordinate space.

non-convex in nature which complicate the process of defining the border hyperplanes. This paper proposes an algorithm with a more direct approach in finding *only* the hyperplanes defining the decision-borders. Other than following the traditional approach of determining Voronoi regions, applying complexity reduction and extracting common facets, we utilize the Delaunay triangulation and unique spatial arrangement of the $U(k)$ sites to extract only the border defining hyperplanes.

The Delaunay triangulation have various structural properties, see [11]. One in specific, being that the Voronoi diagram is the dual graph of the Delaunay triangulation and vice versa [9]. This duality translates into a Delaunay edge (line-segment connecting two sites) being orthogonal to, and bisected by the Voronoi plane shared by the respective sites. It can be observed in figure 5 where the Delaunay triangulation edges are shown in dotted lines. The principle is used in many algorithms for obtaining the Voronoi diagram from its dual. We apply the same principle but only determine the exact border defining hyperplanes, hence eliminating unnecessary computations. We achieve complexity reduction by removing certain edges from the Delaunay triangulation before calculating the respective Voronoi planes. Delaunay edges that connect sites with the same control law values $u(k)$ are removed since their dual (Voronoi plane) would be of no significance in solving the point location problem. Various algorithms exist for determining the Delaunay triangulation of which the *Bowyer-Watson* algorithm is a good option since it is effective in any number of dimensions. Our proposed procedure for the complexity reduction and extraction of the border defining hyperplanes is described in Algorithm 1.

The border hyperplanes obtained from algorithm 1 have been used in the generation of a binary search tree adapted from [10]. The binary search tree was then implemented

Algorithm 1 Border selection algorithm

Step 1 Find the Delaunay triangulation of $HU(k)$ -sites.

Step 2 For all Delaunay edges(line segments),
Index edges connecting sites with non-similar control laws $u(k)$, realizing border-spanning edges.

Step 3 For each border-spanning edge,
Assign the site with $u(k) \neq 0$ as the normal vector to a hyperplane,
Assign the mid-point of the edge as a point in the hyperplane,
Define the hyperplane in point-normal format.

Step 4 Index the hyperplanes in border defining sets (Border A and B).

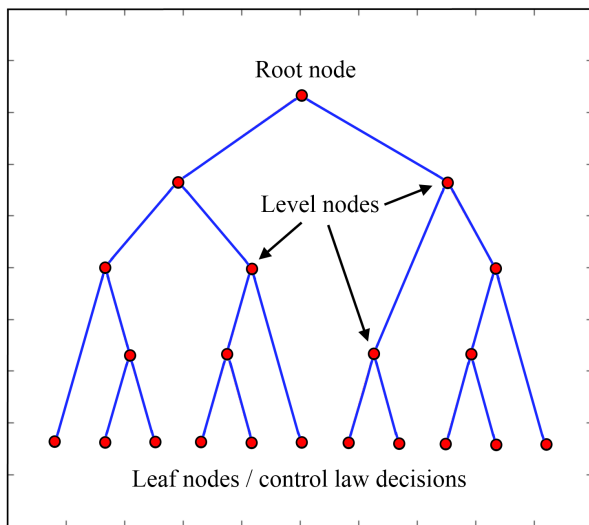


Figure 6: Binary Search Tree structure utilizing 10 border hyperplanes

in a MPC controller for the mentioned inverter. For the horizon $N = 2$ case with 10 border defining hyperplanes a tree structure of 4 levels and 20 nodes as shown in figure 6 was obtained. This translated into a maximum of 4 linear ($A^T x - b$) calculations that is required during online operation to traverse the tree in finding a solution to the point location problem and hence the control action $u_{opt}(k)$. Simulations utilizing algorithm 1 up to horizon $N = 4$ has produced identical inverter outputs (voltage and current waveforms) as found from simulations using the benchmark exhaustive search method.

6. CONCLUSION

We have presented an algorithm for extracting the border hyperplanes defining the control regions in the partitioned state-space of an MPC controller for a single phase multi-level NPC inverter. The algorithm is simple, efficient and extend into higher dimensions. The simulation results to date are encouraging in terms of system output parameters. Currently more work is being done on reducing the complexity of the partitioned state-space to an even lower level. Ensuring a minimum hyperplane count

equates to an optimal binary search tree which will be necessary if we are to be successful in implementing the MPC controller in a practical real-time application.

REFERENCES

- [1] J. Rodriguez, M. P. Kazmierkowski, J. R. Espinoza, P. Zanchetta, H. Abu-Rub, H. Young, et al., "State of the art of finite control set model predictive control in power electronics", *Industrial Informatics, IEEE Transactions on*, vol. 9, pp. 1003-1016, 2013.
- [2] T. Geyer and D. E. Quevedo, "Multistep finite control set model predictive control for power electronics", *Power Electronics, IEEE Transactions on*, vol. 29, pp. 6836-6846, 2014.
- [3] D. Quevedo, R. Aguilera, and T. Geyer, "Predictive Control in Power Electronics and Drives: Basic Concepts, Theory, and Methods", in *Advanced and Intelligent Control in Power Electronics and Drives*, Vol. 531, T. Orowska-Kowalska, F. Blaabjerg, and J. Rodriguez, Eds., ed: Springer International Publishing, pp. 181-226, 2014.
- [4] Bemporad, A., Morari, M., Dua, V., and Pistikopoulos, E. N., "The explicit linear quadratic regulator for constrained systems", *Automatica*, Vol. 38, No. 1, pp. 320, 2002.
- [5] P. Tondel, T.A. Johansen, and A. Bemporad, "An algorithm for multi-parametric quadratic programming and explicit MPC solutions", *Automatica*, Vol. 39, No. 3, pp. 489-497, 2003.
- [6] D. E. Quevedo, G. C. Goodwin, and J. A. De Dona, "Finite constraint set receding horizon quadratic control," *International journal of robust and nonlinear control*, vol. 14, pp. 355-377, 2004.
- [7] A. Nabae, I. Takahashi, and H. Akagi, *A new neutral-point-clamped PWM inverter*, *Industry Applications, IEEE Transactions on*, pp. 518-523, 1981.
- [8] Y. Wang and S. Boyd, "Fast model predictive control using online optimization", *Control Systems Technology, IEEE Transactions on*, vol. 18, pp. 267-278, 2010.
- [9] G. M. Voronoi, "Nouvelles applications des parametres continus a la theorie des formes quadratiques. deuxieme Memoire: Recherches sur les paralleloedres primitifs", *J. Reine Angew. Math.*, 134:198-287, 1908.
- [10] P. Tondel, T. A. Johansen, and A. Bemporad, "Evaluation of piecewise affine control via binary search tree", *Automatica*, Vol. 39, pp. 945-950, 2003.
- [11] B. Delaunay, "Sur la sphere vide. A la memoire de Georges Voronoi", *Izv. Akad. Nauk SSSR, Otdelenie Matematicheskikh i Estestvennykh Nauk*, 7:793-800, 1934.

DESIGN AND IMPLEMENTATION OF A BIDIRECTIONAL CURRENT-CONTROLLED VOLTAGE-REGULATED DC-DC SWITCHED-MODE CONVERTER

A. Coetzer*, G.R. Turner[†] and H.D.T. Mouton[‡]

* Dept. of Electrical & Electronic Engineering, University of Stellenbosch, Stellenbosch 7600, South Africa E-mail: 16462920@sun.ac.za

[†] Council for Scientific and Industrial Research, PO Box 395, Pretoria, South Africa E-mail: gturner@csir.co.za

[‡] Dept. of Electrical & Electronic Engineering, University of Stellenbosch, Stellenbosch 7600, South Africa E-mail: dtmouton@sun.ac.za

Abstract: The design and implementation of a bidirectional current-controlled voltage-regulated DC-DC converter is presented. The converter is required to connect a battery of electrochemical cells (the battery) to an asynchronous motor-drive unit via a regulated DC bus. A two-stage soft-start circuit is included to limit the peak current drawn from the battery during start-up. During normal operation the converter controls the battery current as a function of the DC bus voltage in order to regulate the DC bus. The focus of the presented work is upon the design and implementation of the current and voltage control loops, where the voltage control loop encloses the current control loop. Circuit stability is ascertained by means of both frequency and time domain analysis. It is shown that both control loops are stable and provide good transient response. The presented circuit is manufactured and tested. Test results are compared to the results of the simulation. The converter efficiency is determined by comparing the power drawn from the DC bus (with a load in place) to that drawn from the battery.

Key words: Bidirectional converter, current control, voltage control, soft-start, stability analysis.

1. INTRODUCTION

The design and implementation of a non-isolated bidirectional current-controlled voltage-regulated DC-DC converter is presented. The converter is required to transfer up to 1 kW of electrical power between a battery of electrochemical cells (the battery) and an asynchronous motor-drive unit via a regulated DC bus. The converter is bidirectional to facilitate extended periods of regenerative braking (during which energy is returned to the battery). The bus voltage is required to be regulated in the range of 170 V to 180 V DC (175 V nominal), regardless of the direction of current flow through the battery. A relatively high bus voltage of 175 V was chosen to reduce the rated current of the circuit, thus reducing self-heating while improving the efficiency of the converter.

To facilitate the regulation of the DC bus voltage, two control loops (an inner and an outer) are employed. The inner loop measures and compares the mean battery current to a set-point current generated by the outer control loop, where the outer control loop measures and compares the DC bus voltage to a fixed set-point (corresponding to a bus voltage of 175 V DC). The current set-point, generated by the outer control loop, is limited such that the mean battery current is retained in the range of -10 A to +10 A. During start-up a two-stage soft-start circuit limits the inrush current from the battery to the DC bus.

2. BASIC CIRCUIT OPERATION

Fig. 1 outlines the plant portion of the converter circuit. While in essence a half-bridge, the circuit may be viewed

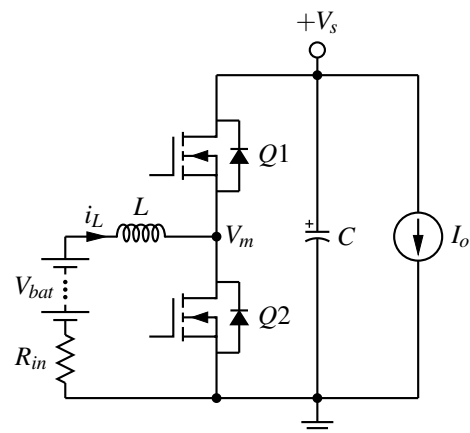


Figure 1: Bidirectional DC-DC converter circuit.

as a simple boost converter with synchronous rectifier when functioning in the forward direction ($\bar{i}_L > 0$), and as a simple buck converter with synchronous rectifier when functioning in the reverse direction ($\bar{i}_L < 0$).

The battery comprises ten 12 V, 40 Ah rated deep-cycle lead-acid batteries. The internal battery resistance is denoted by R_{in} . MOSFET's are used as the switches and the switching frequency is set to 40 kHz. Inductor L comprises 55 turns of Litz wire of 3.8 mm² total cross-sectional area (120 strands of 0.2 mm diameter enamelled copper wire) wound over an Arnold A-866142-2 powdered-iron toroidal core with $A_l = 140$ nH/turn², to achieve a final inductance of 420 μ H.

At a mean current of 10 A the current density through the inductor windings is 2.65 A/mm². The value of the inductor was chosen to achieve a peak to peak current ripple of approximately 20 % of the absolute maximum value of the mean current. That is to say, 2 A.

2.1 Soft Start Circuit

The two-stage soft-start circuit comprises pre- and post-charge mechanisms [1]. The pre-charge circuit limits the peak battery in-rush current to 5 A by means of four parallel connected 100 Ω resistors. At such time as the bus capacitor C is charged to the battery potential (through the anti-parallel diode of switch Q_1) the resistors are short-circuited by a relay (effectively removing the resistors from circuit). A resistor divider (connected across the DC bus), a reference voltage source, and a comparator control the action of the relay.

The post-charge circuit continues to limit the battery in-rush current by initially setting the switching signal dead-time to maximum. This limits the on-time of the switches, thus slowing the rate at which charge is delivered to the bus (as the bus charges the remaining 120 V to 175 V), during which time the dead-time is progressively ramped down to its minimum value (where the minimum value was chosen to eliminate MOSFET shoot-through currents).

2.2 Current Limiting Circuit

An active clamp circuit [2] is used to limit the absolute maximum of the mean current demanded from the battery. This action is realised by clamping the range of the set-point current dictated by the voltage control loop.

2.3 Isolated Gate Driver Circuit

An isolated gate-drive circuit is employed to communicate the switching signals generated by the converter control circuit to the gate of each MOSFET. Galvanic isolation between the switches and the control circuit is essential to prevent damage to the control circuit (due to the large voltage excursions encountered by the MOSFET's).

Each isolated drive circuit comprises an optocoupler [3], a simple push-pull oscillator circuit (oscillating at approximately 300 kHz), a small toroidal transformer (with split primary and secondary windings), and two fast rectifier diodes. The oscillator supplies power to the output section of the optocoupler via the transformer and fast rectifier diodes, while the optocoupler communicates the switching signals.

3. PWM CONTROL CIRCUIT DESIGN

A linear model of the modulator circuit is assumed, where the duty-cycle of the PWM signal is calculated as the ratio of the error voltage V_e to the amplitude of the ramp wave V_R . The mean voltage \bar{V}_m measured at the mid-point

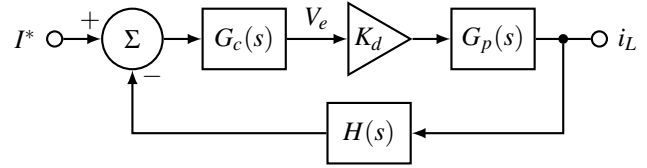


Figure 2: Current control loop.

between switches Q_1 and Q_2 , is thus the product of the duty-cycle and the mean bus voltage \bar{V}_s .

The forward transfer function G_p describing the mean battery and inductor current \bar{i}_L as a function of the duty cycle δ , is given by

$$G_p(s) = \frac{1}{sL + R_{in}}. \quad (1)$$

3.1 Current Control Loop

The current control loop, shown in Fig. 2, functions to regulate the mean inductor current flowing to and from the battery. An error voltage V_e is generated as a function of the difference between the set-point current I^* and the mean battery current \bar{i}_L . This error voltage is compared (by means of high-speed comparator) to a triangular waveform in order to generate the required PWM switching signals.

In the initial design of the current controller the bus voltage was assumed constant, which is reasonable given that the current control loop is designed to respond significantly faster than the voltage control loop. Once, however, the voltage and current control loops were combined, the bus voltage was considered variable.

Ten parallel connected 0.68 Ω metal film resistors were used for current sensing. The feedback voltage provided to the inverting input of the summation in Fig. 2 is thus the product of the inductor current i_L and the feedback transfer function $H(s)$, where $H(s)$ is simply the combined resistance of the current sense resistors, 0.068 Ω .

With reference to Fig. 2, the open loop transfer function is

$$G_{ol}(s) = G_c(s)K_dG_p(s)H(s), \quad (2)$$

and the closed loop transfer function is thus

$$G_{cl}(s) = \frac{G_c(s)K_dG_p(s)}{1 + G_c(s)K_dG_p(s)H(s)}. \quad (3)$$

In adherence with the Nyquist stability criterion, the open loop transfer function is required to have both positive phase and gain margin in order for the closed loop transfer function to be stable (not oscillate). The phase margin should, preferably, be at least 30° [4]. Furthermore, the unity gain crossover frequency of the open-loop transfer function should be chosen according to the desired

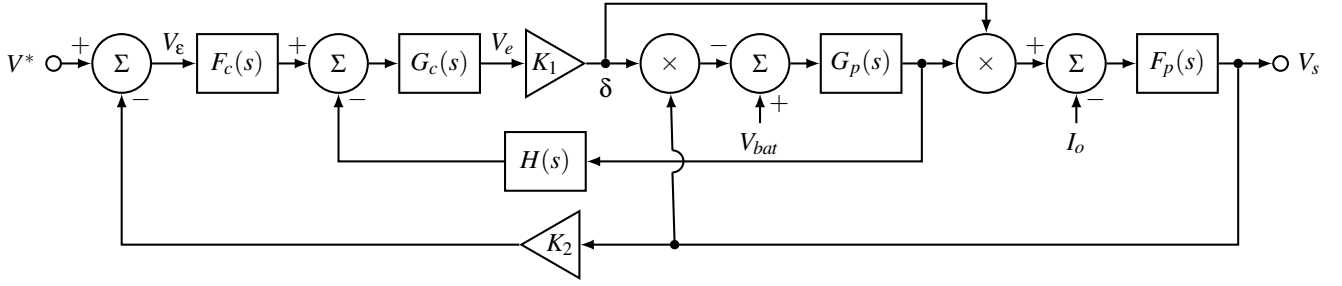


Figure 3: Voltage control loop.

performance of the system, but is generally designed to be at around one-fifth of the systems' switching frequency [5]. In accordance with the above requirements, a pole-zero compensator, also known as a type 2 amplifier, was selected as the current controller $G_c(s)$. As the name suggests, this compensator consists of a pole-zero pair, where the pole and zero are placed to achieve the required closed-loop stability of the system. This compensation method was chosen due to the good transient response and load regulation that it provides [6].

3.2 Voltage Control Loop

The combined voltage and current control loops are shown in Fig. 3. The set-point voltage V^* is indicated on the left, while the bus voltage (the object of the voltage control loop) V_s is on the right. The current control loop, described earlier, is enclosed by the voltage control loop. The bus voltage applied to the modulator circuit within the current control loop is derived from the output of the voltage control loop. The gain block K_1 represents the pulse-width modulator and outputs the switch's duty cycle δ . The bus capacitor C shown in Fig. 1, is denoted $F_p(s)$. Hence:

$$F_p(s) = \frac{1}{sC}. \quad (4)$$

Feedback provided to the inverting input of the summation on the left of the voltage control loop is a scaled version of the bus voltage, where K_2 is the scaling factor. The difference between the set-point voltage V^* and the scaled bus voltage $K_2 \times V_s$, is V_e , which is the input to the voltage controller $F_c(s)$.

The open-loop transfer function of the voltage control loop (of which the current controller is an element) is given by

$$F_{ol}(s) = K_2 \left(\frac{(G_p(s)F_p(s)V_{bat} - 2\delta G_p(s)F_p(s)V_s)}{1 + \delta^2 G_p(s)F_p(s)} \right) \times \left(\frac{K_1 F_c(s) G_c(s)}{1 + K_1 G_c(s) G_p(s) H(s) V_s} \right), \quad (5)$$

where

$$\delta = K_1 \left(\frac{F_c(s) G_c(s) V_e + G_c(s) G_p(s) H(s) V_{bat}}{1 + K_1 G_c(s) G_p(s) H(s) V_s} \right). \quad (6)$$

With reference to (5) and (6), it is apparent that the open-loop transfer function is non-linear. Thus, in order to undertake a Bode plot of (5), it is necessary to assume that V_s is constant, which is assuredly not the case depending upon the magnitude of the current sink or current source attached to the bus. We thus undertook multiple Bode plots of the open-loop transfer function for values of V_s in the range of 170 V to 180 V in order to ascertain stability throughout. Below or above these values we are assured that the battery current will be current-limited, where the current loop is inherently stable, regardless of the value of V_s . Furthermore, the changing bus voltage during start-up is not considered relevant for frequency domain stability analysis since the start-up voltage is controlled by the two-stage soft-start circuit. Thus, to maintain stability in the prescribed voltage range, a pole-zero compensator was also selected for $F_c(s)$. The output of $F_c(s)$ provides the current set point I^* input to the current control loop shown in Fig. 2.

3.3 Triangular Wave Generator

A 4 MHz crystal-controlled square-wave oscillator is divided down to 40 kHz using multiple D-latches, and then integrated to generate a triangular wave. The DC component is removed from the square-wave (to prevent the integration of a constant) by capacitively coupling the output of the final D-latch to the input of the integrator. The output of the integrator is buffered.

4. SIMULATION RESULTS

Frequency and time domain simulations were undertaken to ensure the stability and accuracy of the DC-DC converter design.

4.1 Frequency Domain Simulation

Bode plots of the current control open-loop and closed-loop transfer functions, (2) and (3), are shown in Fig. 4. A DC gain of 6.04 dB is indicated, corresponding to a static loop sensitivity of 2.0 A of battery current per volt of excitation applied to the set-point input. Thus, at an absolute maximum set-point voltage of 5 V, the battery current will rise to 10 A. An infinite gain margin, and a 50.6 degree phase margin are further indicated. Since an infinite gain margin cannot be realised in practice, a

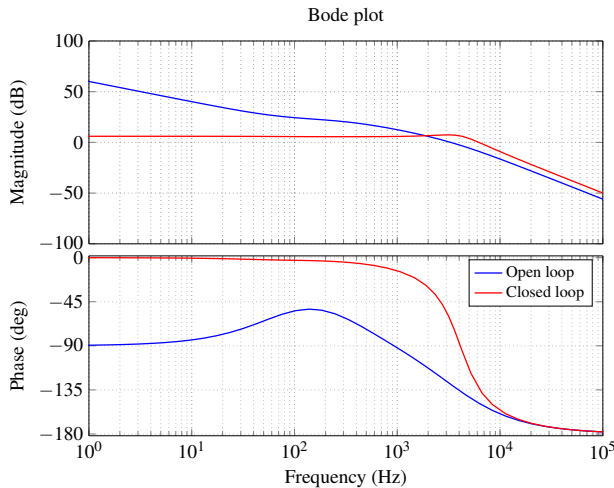


Figure 4: Current regulator bode plot.

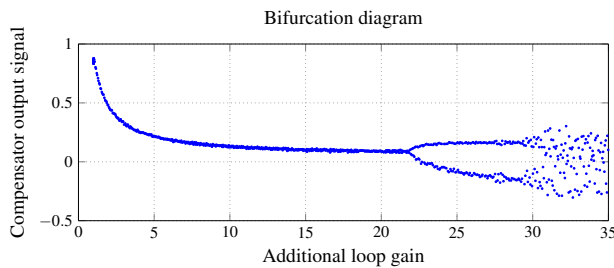


Figure 5: Bifurcation diagram used for stability analysis.

bifurcation test [7] was undertaken to determine a more realistic prediction of the gain margin. The result of the bifurcation test is shown in Fig. 5. An additional gain of 22 was added to the open-loop before the output of the compensator was observed to bifurcate, thus indicating a more realistic gain margin of 26.8 dB. Fig. 4 further indicates a unity-gain crossover frequency of 3.5 kHz, which is well below the 40 kHz switching frequency. Thus, all values within the loop may be considered to be time-averaged, as opposed to instantaneous. A positive gain and phase margin suggests that the current control loop is stable.

Bode plots of the complete control open-loop and closed-loop transfer functions (5) and (6) at the nominal bus voltage of 175 V are shown in Fig. 6. A DC gain of 30.9 dB is indicated, corresponding to a static loop sensitivity of 35 V of bus voltage per volt of excitation applied to the set-point input. Thus, at a set-point value of 5 V, the bus voltage will rise to 175 V. A phase-margin, gain-margin and unity gain crossover frequency of 79.2 degrees, 18.1 dB and 310 Hz are further indicated, suggesting that the voltage control loop is stable.

4.2 Time Domain Simulation

To confirm the stability of the system during start-up, as well as to examine the step response of the control loop (such as when a load is applied or removed from

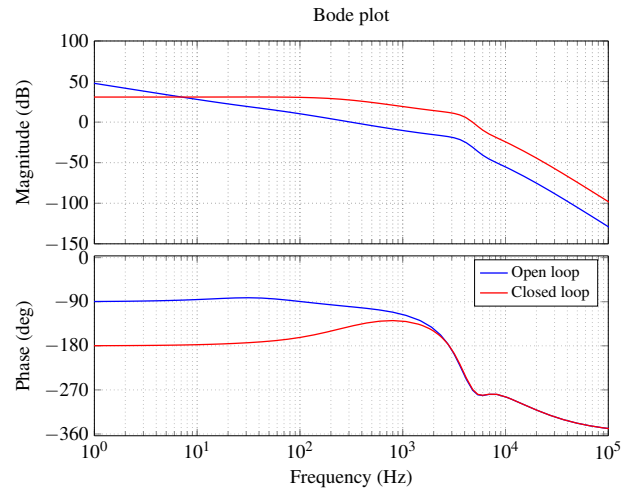


Figure 6: Voltage regulator bode plot.

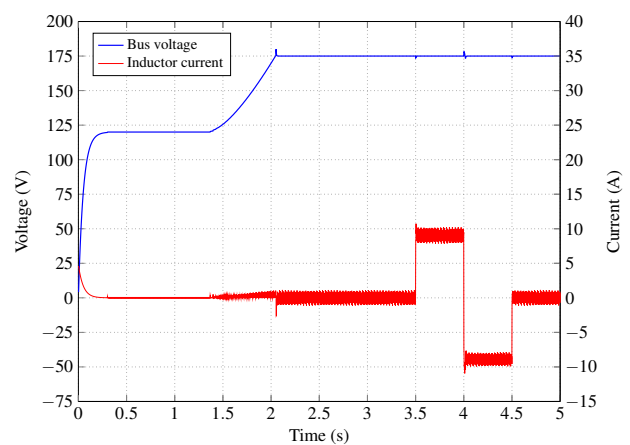


Figure 7: Time domain simulation of DC-DC converter from start-up.

the DC bus) a time domain simulation of the complete DC-DC converter, with current and voltage control loops, was implemented. The simulation was implemented in MATLABTM and corresponds to a simple iterative Euler solution of the relevant differential equations that describe the behaviour of the circuit. Switching and conduction losses were accounted for in the model, thus enabling a basic prediction of the converter's efficiency.

Fig. 7 shows the simulated bus voltage and battery current from the application of the battery to the converter circuit at time $t = 0$. The first stage of the soft-start circuit, the pre-charge circuit, is active for the first 200 ms after start-up, during which time the bus voltage rises from zero to the battery voltage, 120 V. At approximately 1.2 s the second stage of the soft-start circuit is activated, causing the bus voltage to rise from 120 V to 175 V over the next half-second. When the bus voltage reaches 175 V there is a small voltage overshoot of 2 V, which is within the allowed range of 170 V to 180 V. It is thus not necessary to implement any additional anti-windup scheme [8] to prevent the DC bus voltage from overshooting after

reaching its nominal value of 175 V.

Fig. 7 indicates that the predicted bus voltage dips briefly to 173.9 V at 3.5 s, settling back to 175 V, when a 5.7 A current-sink (drawing 1 kW of power) is attached to the DC bus. In response to the connected load the battery current is predicted to rise to a mean value of 9.1 A. Fig. 7 further indicates that the bus voltage peaks briefly at 178.2 V at 4.0 s, settling back to 175 V, when the 5.7 A current-sink is replaced with a 5.7 A current source (supplying 1 kW of power). This latter test was implemented to examine the bidirectional capability of the converter, in response to which the battery current was predicted to fall to a mean current of -9.1 A, indicating that the battery is being charged. At 4.5 s the current source is removed from the DC bus and the battery current observed to return to a mean value of 0 A.

In accordance with that presented above, the overall system is considered to provide good transient response at the extremes (sink or source) of its functional requirements.

Finally, the simulation predicts a current ripple of magnitude 2.2 A peak, which is approximately 20 % of absolute maximum mean current that the inductor is intended to conduct at full power (sink or source). The magnitude of the current ripple is independant of the mean current provided the bus voltage, battery voltage and inductance of the inductor remain constant. The current ripple is of saw-tooth form due to the response of the inductor to the voltage V_m at the mid-point between the two MOSFET switches, which is at either zero or bus potential depending upon the state of switches $Q1$ and $Q2$ at any given moment.

5. TEST RESULTS

The DC-DC converter and control circuit, as described above, were built and tested. Fig. 8 shows the measured DC bus voltage and time averaged battery current at start-up. We note that the magnitude and rate of change of the bus voltage is similar to the result of the time domain simulation shown in Fig. 7. The battery current is time averaged over the period of a single oscillation of the PWM oscillator in order to display the mean, as opposed to instantaneous, current.

As predicted, the bus voltage is observed to rise to the battery potential within 200 ms of connecting the battery to the converter. The bus voltage is subsequently observed to rise to and regulate at 177 V as the dead-time is progressively reduced over a period of approximately 0.5 s. We note that the bus voltage is observed to regulate 2 V higher than the nominally required value of 175 V (due to an inaccuracy in the set-point value). The battery current is observed to peak at 5 A during start-up, after which an audible click is heard as the relay short-circuits the soft-start resistors.

A 28 Ω water cooled dummy-load was employed to load the converter to approximately 1.1 kW. A converter efficiency of

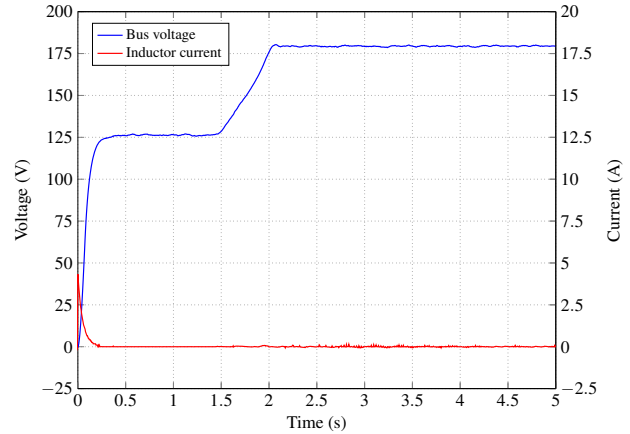


Figure 8: Experimental results: DC bus voltage and battery current during start-up.

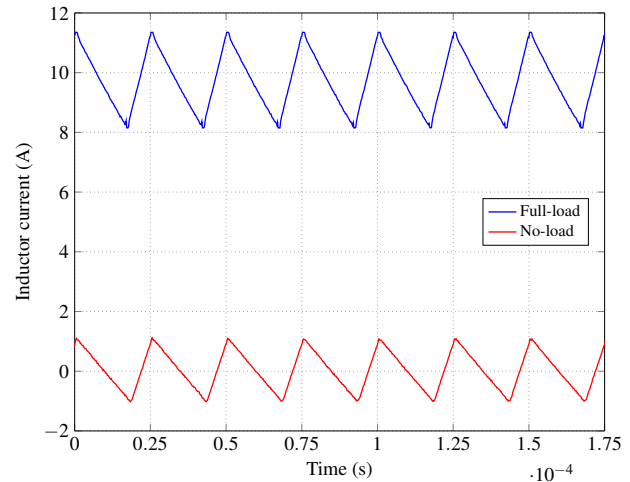


Figure 9: Experimental results: Measured inductor current.

$$\eta = \frac{P_{out}}{P_{in}} = 94.4\% \quad (7)$$

was determined by comparing the power delivered to the load to that drawn from the battery.

The instantaneous battery current at full and zero load are shown in Fig. 9. We note that the peak to peak current increases to 3A at full load, compared to 2.2 A at zero load. This is due to a marginal decline in the inductance of the inductor, due to the decreased instantaneous permeability of the inductor core material at greater magnetisation. In both cases, the current is of saw-tooth form with a duty cycle of approximately 70 %, during which time switch $Q1$ is turned on and the inductor current is observed to decrease linearly.

Unfortunately, no current source (with compliance voltage as high as 175 V) was available to test the bi-directional capability of the manufactured converter. It was, however, possible to disconnect the voltage control loop in order to directly control (from an external bi-polar voltage

reference source) the current control loop set-point. With the voltage regulation thus removed, a second battery of electrochemical cells (totalling 168 V) was connected to the DC bus and the external voltage reference source employed to control both the magnitude and direction of the current between the two batteries. In this way one battery could be made to charge the other, and vice versa. A galvanometer was employed to monitor the mean current flowing to or from the 120 V battery.

6. CONCLUSION

The design and implementation of a bidirectional current-controlled voltage regulated DC-DC converter has been presented. The converter is required to interface a battery of electrochemical cells to an asynchronous motor-drive unit via a DC bus. A two-stage soft-start circuit was successfully implemented to limit the in-rush current during start-up. The converter employs both a current control and voltage control loop, where the current control loop is encircled by the voltage control loop. That is to say, the converter controls the battery current in order to regulate the bus voltage. Both control loops were shown to be stable using frequency and time domain analysis. Test results showed that the current control loop was able to regulate the mean battery current accurately. The outer voltage control loop was shown to servo the current set point in order to regulate the bus voltage to well within specification. A momentary deviation (typically lasting no more than 100 ms) from the mean of up to 2 V was observed when a 1.1 kW load was applied or removed from the bus. Simulated and test results compared well. The DC-DC converter demonstrated an efficiency of 94.4 % with the 1.1 kW load connected.

In the next stage of this project, a bidirectional asynchronous motor-drive unit will be designed and implemented in order to interface the DC bus to an asynchronous motor. The motor will ultimately sink or source power to a bi-directional mechanical load.

ACKNOWLEDGEMENT

The authors would like to thank the CSIR, in particular Adrian Adams, for allocating funding in support of the presented work.

REFERENCES

- [1] W.-R. Liou, P.-H. Chen, and J.-C. Tzeng, "A synchronous boost regulator with pwm/pfm mode operation," in *ASIC, 2009. ASICON '09. IEEE 8th International Conference*, October 2009, pp. 1066–1069.
- [2] P. Horowitz and W. Hill, *The Art of Electronics*, 2nd ed. Cambridge University Press, 1995, p. 221.
- [3] N. Mohan, T. M. Undeland, and W. P. Robbins, *Power Electronics. Converters, Applications and Design*, 3rd ed. John Wiley and Sons, Inc, 2003, pp. 703–707.
- [4] F. Golnaraghi and B. C. Kuo, *Automatic Control Systems*, 9th ed. John Wiley and Sons, Inc, 2009, pp. 426–459.
- [5] G. C. Chryssis, *High-Frequency Switching Power Supplies: Theory and Design*, 2nd ed. McGraw-Hill, 1989, pp. 237–241.
- [6] M. Brown, *Power Supply Cookbook*, 2nd ed., ser. EDN Series for Design Engineers. Newnes, 2001, pp. 212–216.
- [7] T. Mouton, A. de Beer, B. Putzeys, and B. McGrath, "Modelling and design of single-edge oversampled pwm current regulators using z-domain methods," in *ECCE Asia Downunder (ECCE Asia), 2013 IEEE*, June 2013, pp. 31–37.
- [8] X. Li, J. G. Park, and H. B. Shin, "Comparison and evaluation of anti-windup pi controllers," *Journal of Power Electronics*, vol. 11, no. 1, pp. 45–50, 2011.

DESIGN AND SIMULATION OF A CHARGING ALGORITHM FOR LITHIUM ION BATTERIES

H.Tayob*, I. Chotia* and S. Chowdhury*

* Electrical Engineering Dept., Upper Campus, Rondebosch, University of Cape Town, South Africa

Abstract: Lithium-ion battery research has undergone major growth in recent years due to its application in cell phone, tablet and laptop devices. This paper compares battery models and various charging protocols in terms of time responses of terminal voltage, battery temperature and state of charge (SOC) at different C Rates. Based on this comparison proposes a charging algorithm with temperature and time of charge monitoring features. The 1500Ah, SONY US18650, Lithium-ion battery is selected for this research. Various battery charging strategies are simulated using the Virtual Test Bed software and so is the charging algorithm. From the comparison it is observed that the Constant Current Constant Voltage (CC-CV) charging protocol performs best and hence this is selected as the basis for developing the proposed charging algorithm. The performance of the proposed algorithm is evaluated for different C Rates in terms of time responses of terminal voltage, battery temperature and SOC as done for the CC-CV charging protocol comparison. The results show that the algorithm produced the similar results as the CC-CV protocol while successfully restricting the battery temperature.

Keywords: Charging Protocol, Charging Algorithm, Constant Current, Constant Voltage, Lithium Ion Battery, Temperature, State of Charge

1. INTRODUCTION

The 21st century has sparked an increase in the demand for less costly but more efficient ways to store energy. This is due to the technological improvements made in the fields of electronics such as portable devices and electric vehicles. These advances have forced battery experts and manufacturers to further their research and ultimately improve battery technologies and storage management. Lithium-ion (Li-ion) batteries have rapidly become the most suitable battery chemistry for portable applications. This ranges from mobile devices (tablets and mobile phones) all the way to electric vehicles. They provide better energy densities and very good weight-to-energy ratio when compared to all other chemistries [1]. Along with improvement in battery technology and broadening their application areas, development of quicker and more reliable charging methods is continuously being researched. This paper compares different charging protocols for Li-ion batteries and develops a complete algorithm for the efficient and reliable charge of these batteries.

2. BATTERY DYNAMICS AND THEORY

In order to understand the charging strategies and its significance in Li-ion batteries, battery dynamics and factors affecting them need to be considered. The most important issues which contribute to the condition of a battery are voltage level, state of charge/discharge and the internal resistance of the battery.

2.1 Rates and State of Charge

Unlike theoretical voltage sources or power supplies a battery does not discharge linearly. The charge rates of a battery are dependent on its capacity at that time of charging or discharging. The battery state of charge (SOC) represents the residual capacity of the battery as a percentage of fully entirely charged capacity. State of discharge (SOD) represents the discharge percentage of

the entire capacity. The SOC and SOD relationship is shown in equation (1).

$$SOD + SOC = 1 \quad (1)$$

This relationship is essential to the quality of storage. During operation outside of the rated SOC interval a significant strain is applied on the battery. This strain leads to lifespan degradation of the cell [2].

2.2 Temperature affects during charging

An internal resistance (IR) exists within every battery and is strongly dependent on battery temperature. It varies during charging and discharging. This factor impacts the battery performance by affecting its efficiency and temperature. As a result, the temperature strongly affects the voltage characteristics, battery capacity and therefore its lifespan. Internal chemical reactions react strongly to temperature and voltage. Lower temperatures reduce electrochemical activity and increase IR while higher temperatures increase electrochemical activity and therefore accelerate the rate of reaction [3, 11]. Despite this the lifespan of the battery will remain relatively unaffected by temperature which serves as a key strength in Li-ion batteries. However, the capacity of the storage device will be affected as the case in all batteries [3, 4].

Table 1: OCV of Li-ion Battery at Various Temperatures

Temperature	Voltage at 0% SOC	Voltage at 100% SOC
-15°C	2.191 V	3.8190
0°C	2.453 V	4.083
15°C	2.5395	4.1675
30°C	2.662	4.29
45°C	2.8285	4.4565

Table 1 lists the Open Circuit Voltage (OCV) of an unloaded Li-ion battery. The temperature is varied from 15°C to 45°C and its effect on the battery at 0% SOC (fully discharged state) and 100% SOC (fully charged state) is monitored in terms of Voltage. The empty and full SOC voltages increase with a temperature increase. This means the entire operational voltage range understood is changing with temperature. Monitoring the

temperature is essential when considering battery charging tests.

3. ELECTRICAL MODELLING OF BATTERIES

Electrical models present an accurate and simple battery representation useful for simulations required at system level design and performance analysis. A comparison of electrical models is conducted under dynamic performance criteria. The criteria are then considered for the model designed and used in the Virtual Test Bed software.

3.1 Thevenin Model

The basic general battery Thevenin model consists of a series resistor and a parallel resistor-capacitor (RC) branch. This branch allows the modelling of transient behaviour but it does so by assuming a constant OCV; hence the basic Thevenin model cannot capture battery runtime information. Improved Thevenin models are proposed in [2] and [11] with additional components allowing runtime prediction and DC response. But these models still have disadvantages, for instance the model reported in [5] uses a capacitor rather than V_{OC} . This complicates parameters and further increases the runtime error by approximately 5%. The Thevenin model can be modified to represent transient behaviour; however, the parameters are assumed to remain constant despite being directly related to the state of charge, temperature and charge characteristics [4, 6].

3.2 Impedance-based Model

The impedance-based model consists of a resistor and an inductor in series. The resistor accounts for internal resistance whereas the inductor models the electrochemical aspect of the battery. The SOC of the battery is represented by the voltage source. Impedance models use a method called electrochemical impedance spectroscopy. This is done to obtain a model in the frequency domain representing the AC-equivalent impedance. Thereafter, a complicated equivalent network Z_{ac} is used for the spectra. This model does not allow runtime prediction or DC response [5].

Table 2: Comparison of Electrical Models

Criteria	Thevenin	Impedance	Runtime	Combined
DC prediction	No	No	Yes	Yes
AC prediction	Restricted	Yes	No	Restricted
Transient behaviour	Yes	Restricted	Restricted	Yes
Battery runtime	No	No	Yes	Yes

3.3 Runtime-based model

The runtime model uses of a complex network of circuits shown on the right hand side in Figure 1. This network of circuits model the SOC, transient response through a parallel RC network and the rate of Voltage lost in the model. Considering all of these factors allows for simulation of battery runtime and DC response but is done for a constant discharge current. Reference [7] presents a discrete-time implementation of this model whereas [5] shows the more common continuous-time based model.

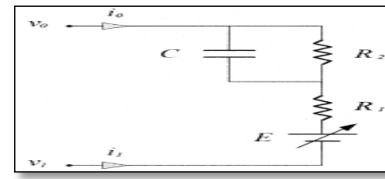


Figure 1: Runtime-based Battery Model [5][7]

3.4 Combined Battery Model

A comprehensive circuit-orientated model is proposed in [8]. The runtime and the Thevenin circuit models are combined in Figure 1. The left hand side scheme of Figure 1 is developed from the runtime model. The current controlled source as well as $C_{capacity}$, allows for SOC, capacity and runtime modelling. The Thevenin network at the right hand side represents transient behaviour. Thus, the combination of the Thevenin, impedance and runtime models enable all dynamic electrical characteristics to be simulated [11].

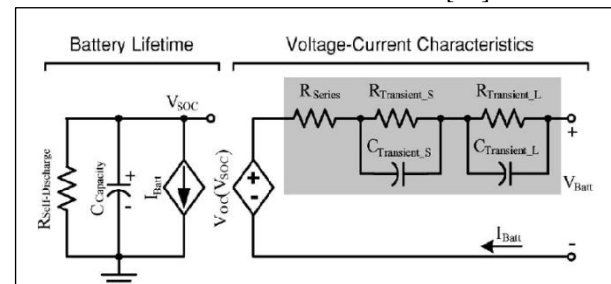


Figure 2: Combined Electric Circuit Model [8]

3.5 Model Comparison

Various criteria of the electrical models are listed and compared in Table 2. None of the individual models can accurately predict the I-V curve properties and runtime characteristics simultaneously. Using the Table 2 the required characteristics per application can be considered. If transient behaviour, runtime operation and current prediction are essential then the combined electric circuit model can be used. The comprehensive combined model does come at the cost of system complexity and longer computation times. In addition, the theoretical controlled current and voltage source can be problematic in simulation software when combined.

3.6 Proposed Battery Model for Design of Charging Algorithm

In an attempt to find a battery model detailed enough to capture accurate electrical and thermal characteristics yet simple enough to neglect in-depth electrochemical calculations, the Equivalent Circuit Li-ion model is proposed in [9]. The simple proposed design consists of a parallel RC bridge, series resistor and varying voltage source as seen in Figure 2. The difference between this model and the others listed in Table 1 is that its primary objective is simulation of battery dynamics in the real world with emphasis on its charging curve characteristics. This means that chemical properties of the active materials available need to be considered in the electric circuit design. In addition to active material availability the SOC and temperature significantly influence the

charging curve and terminal voltage observed. The proposed design considers their influences through the discrete and continuous equations used as well as the reference curves selected in the procedure shown below. The equilibrium potential is influenced by temperature and availability of active materials. The amount of active materials can be demonstrated in terms of the SOD where the discharge capacity is affected by temperature and discharge rate. The system is modelled as follows:

- A reference curve representing the battery voltage versus depth of discharge is chosen; thereafter an nth-order polynomial is fitted to the curve selected.
- The reference rate is chosen as the discharge rate (current) and the factor $\alpha(i)$ is used to account for the SOD dependence on rate.
- A reference temperature is now chosen for the curve and the factor $\beta(T)$ is used to account for the SOD dependence on temperature.
- Finally, a correction term, $\Delta E(T)$ is selected to compensate for the variation of the OCV due to temperature.

The procedure above along with Equations (2 - 4) is used to obtain the terminal voltage, equilibrium potential and SOD.

$$E[i(t), T(t), t] = v[i(t), T(t), t] - Rint^i(t) \quad (2)$$

$$v[i(t), T(t), t] = \sum_{k=0}^n c_k (SOD^k[i(t), T(t), t]) + \Delta E(T) \quad (3)$$

$$SOD[i(t), T(t), t] = \frac{1}{Q_r} \int_0^t \alpha[i(t)] * \beta[T(t)] * i(t) dt \quad (4)$$

The procedure explained is used to model the Lithium Ion US18650 Sony battery. The model manages to capture all relevant battery dynamics and is already embedded in Virtual Test Bed software. A more in-depth analysis of this model is available in [9].

4. CHARGE PROTOCOL AND SIMULATION

A summary of the Sony US18650 datasheet specifications is shown in Table 3. The battery performance is then modelled under different charge protocol strategies. The performance of each strategy in terms of terminal voltage, SOC and charging time are compared through simulation in various case studies.

4.1 Constant Current (CC) Charging

Table 3: US18650 Sony Battery Parameters [10]

Parameter	Magnitude	Unit
Minimum Capacity	1500	mAh
Nominal Capacity	1600	mAh
Maximum Voltage	4.2	Volts
Nominal Voltage	3.7	Volts
Minimum Voltage	2.75	Volts
Charge Time - Default	3	Hours
Charge Time - Fast	2.5	Hours
Charge Current – Normal	0.75	Amps at (0.5C)
Charge Current – Fast	1.5	Amps at (1C)
Max Charge Current	3	Amps
Temperature range	273 – 313	Kelvin

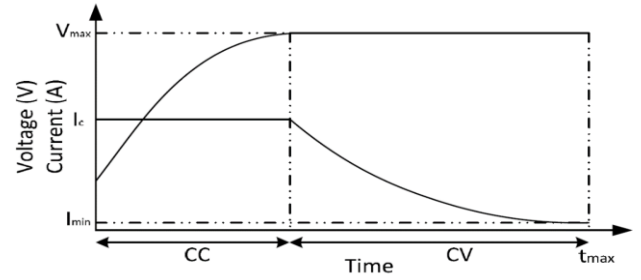


Figure 3: Typical Charging Profile of CC and CV Protocols [9]

This simulation monitored the battery responses to a constant current charge at various C rates. Looking at Figure 4, a constant 'MaxSOC' is set to 100. The model uses a 'GreaterOrEqual' block to check if the current SOC has reached 100%. The block outputs a 0 (false) when current SOC has not reached 100%. A 'NoCharge' block supplies no current and the 'Charge' block supplies a positive current. When the input to the condition block is false, the positive magnitude is supplied and when the input is true, no current is supplied to the battery terminals. Therefore, as long as the current SOC is below 100%, a 0 (false) enters the condition block and allows the battery to charge until it reaches 100% SOC.

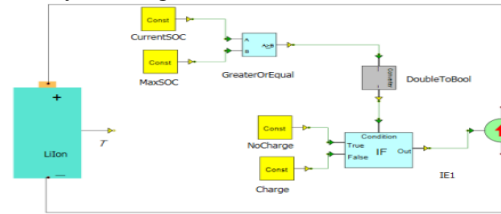


Figure 4: Simulation Model for CC Charging

When considering Figure 3 the initial voltage is seen to be quite low. The voltage gradually increases from this low value in the CC region. Charging in this region is quite slow when compared to the CV region. With that being said, Li-ion batteries are notoriously known for requiring additional current protection circuits. Using a CV protocol will not regulate this current and therefore result in temperature rises and battery damages. This study therefore only considers charging strategies which begin with a current monitoring phase.

4.2 Constant Current – Constant Voltage (CC/CV)

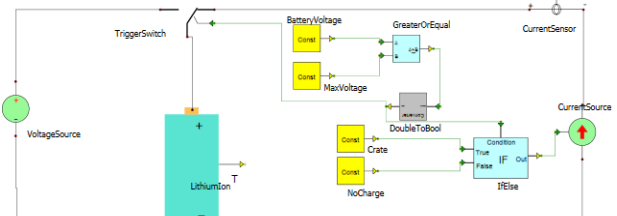


Figure 5: Simulation Model for CC-CV Charging

The Constant Current – Constant Voltage protocol is the most popular charging method used in Li-ion batteries. The method allows for two charging stages by combining the CC and CV regions of Figure 3. Firstly, a constant current is applied to the battery until it the terminal

voltage reaches the maximum voltage. Thereafter, the voltage is kept constant allowing the current to decay exponentially until it reaches a pre-set minimum current. The battery is then deemed fully charged.

The combination of the CC and CV blocks is shown in Figure 5. The circuit in Figure 5 initially begins as a CC system since the battery terminals will begin charging at a relatively low voltage and will gradually increase. Time spent in the CC region causes slower and less efficient battery charging. It is however necessary as beginning in the CV region is problematic for Li-ion batteries. This method therefore exploits the fast operation of CV and the protection benefits of CC charging.

4.3 Constant Current Pulse-Constant Voltage

In an attempt to reduce the time spent in the slow CC region, the alternative Constant Current Pulse Constant Voltage (CCP-CV). Figure 6 shows a green PWM input signal is sent to the current decision input terminals creating a current pulse. The pulse current allows the battery to stabilise during off time.

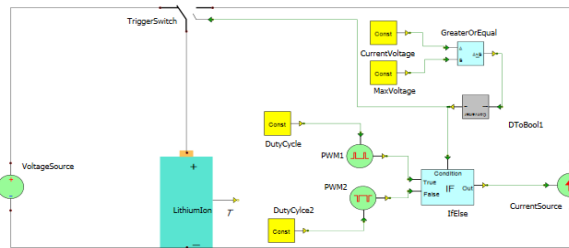


Figure 6: Simulation Model for CCP-CV Charging

Since a PWM waveform that is half on and half off (50% duty cycle) is used, the average output current is affected. Therefore, to obtain an average of 0.5C (0.75A), a current pulse of 1.5A is used. This is the case with all the pulses for this simulation. A larger current pulse means that, parameters such as temperature and voltage need to be especially monitored when using this method.

5. COMPARISON OF CHARGING PROTOCOL

The charging protocol strategies of CC, CC-CV and CCP-CV results are now compared and shown in Figures 7-11. The main comparison criteria are speed of charge, state of charge, terminal voltage, battery protection and temperature. Once the charge protocol is selected it will then be optimised using the proposed charging algorithm.

5.1 Constant Current (CC)

In Figure 4 a large constant current is applied onto the battery terminals allowing it to reach a larger voltage at 100% SOC. Looking at the 2C rate curve in Figure 7, the battery reaches 4.9V whereas a 1C rate reaches 4.5V and a 0.5C rate reaches 4.3V. Although higher voltages may be reached by higher C rates, the voltage eventually falls to the maximum OCV of 4.2V for all C rate curves, when the constant current magnitude is reduced to zero. This is due to the natural response (transient response) as voltage is not limited in this protocol. The non-constant voltage does result in a faster charge but comes at the expense of

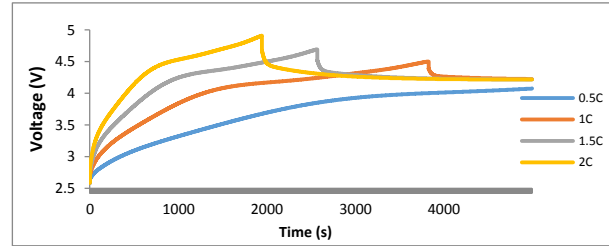


Figure 7: Terminal Voltage for CC Charging

high temperature and low percentage of SOC as seen in the charge comparisons shown in Figures 10 and 11.

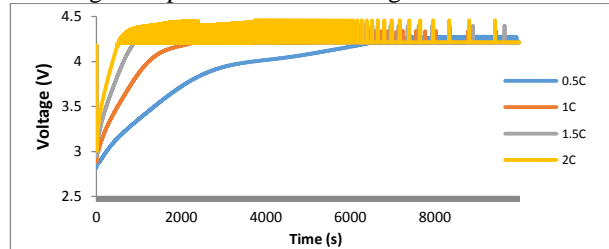


Figure 8: Terminal Voltage for CC-CV Charging

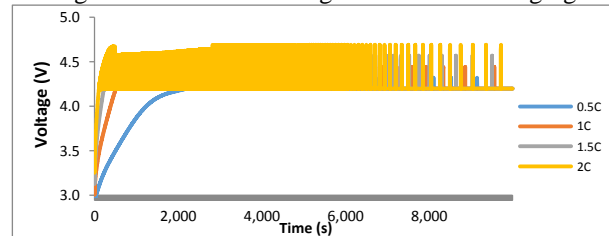


Figure 9: Terminal Voltage for CCP-CV Charging

5.2 Constant Current Constant Voltage (CC-CV)

The CC-CV protocol begins with a constant current until the maximum voltage is reached. Thus, all C rate curves in Figure 8 that occur before the CV stage are similar to the CC protocol. This can be confirmed by observing the first 2000 seconds for all curves in Figures 7 to 9. Unlike previous protocols, the terminal voltage does not exceed the maximum 4.2V during the CC-CV charge in Figure 8. This is established by the constant voltage stage. The oscillations noticed in Figures 8 and 9 are due to the switching mechanism in place. These oscillations do not correspond to an ideal CC-CV or CCP-CV charging curve. When the battery falls anything below 4.2V it switches back to the constant current phase for a brief moment. Higher charge rates have a greater effect on the ability of the battery to stay at a constant 4.2V. Therefore, larger oscillations are noticed at higher C rates. However, the oscillations decrease with time and the curve smoothens out.

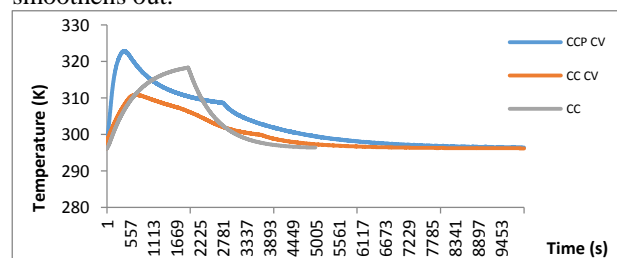


Figure 10: Battery Temperature for CC, CC-CV and CCP-CV Charging

Figure 10 compares three charging protocol temperatures all at the rate of 2C in order to obtain the clearest observation at high rated conditions. The CC-CV regulates the temperature best when compared to all other charging procedures. It follows the same protocol as the CC region but then when entering the CV region the temperature steadily declines allowing for more reliable charging and component protection. In addition to this steady decline the maximum temperature recorded for the CC-CV region is lower than all other protocols for all C rates actually tested.

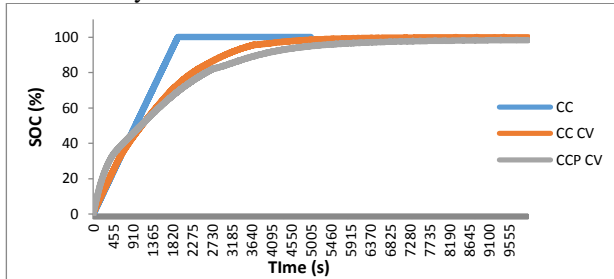


Figure 11: SOC for CC, CC-CV and CCP-CV Charging

Figure 11 shows the difference the additional CV region makes in terms of SOC when comparing CC to CC-CV because the curve saturates as it reaches 100% SOC. The saturation is due to the reduction of current as the battery approaches 100% SOC. However, this slightly lengthens the charge time.

5.3 Constant Current Pulse Constant Voltage (CCP-CV)

Comparing Figures 8 and 9 shows that the CCP-CV strategy reaches its maximum voltage before the CC-CV protocol does. The higher current pulse is used to apply an equal average current to the CC-CV protocol. Therefore, CCP-CV spends more time in the constant voltage phase. Due to the higher magnitude of currents explained in section 4.3 the temperature of the CCP-CV is higher than the CC-CV, as illustrated in Figure 10. When comparing both strategies in terms of Voltage, Temperature and SOC in Figures 7 to 11 it is confirmed that only the initial CC region distinguishes this protocol from the CC-CV.

6. DESIGN OF CHARGING ALGORITHM

Section 5 clearly shows that the CC-CV protocol works best overall for Li-ion batteries. The CCP-CV method does provide less time in the slow CC region due to the initial current pulse seen in Figure 9 but this does come at the expense of high temperatures which are confirmed in Figure 10. Due to its superior protection and reliability the CC-CV method was selected as a basis for implementation of the Algorithm monitoring strategy.

Using the CC-CV basis the timer and temperature monitoring circuits were attached to the circuit as seen in the final circuit diagram of Figure 13. These blocks were monitored by a limiting algorithm which maintained the temperature and the time of charging. The timer was used to protect the battery from being overcharged (SOC) as this is a major weakness in Li-ion batteries specifically.

The flow chart for the algorithm is shown in Figure 12. The algorithm begins in the CC region and monitors the temperature and voltage. When 4.2V is reached the system moves to the CV region and continues whilst monitoring the temperature, time and SOC as well.

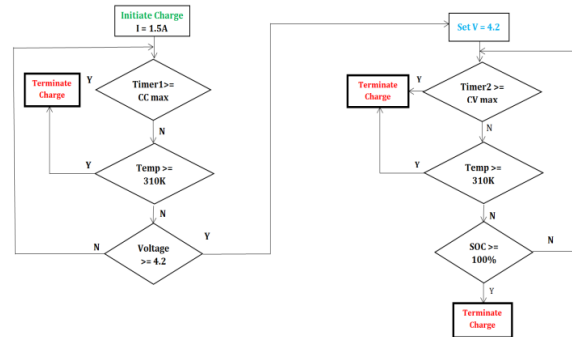


Figure 12: Flow Chart for Proposed Charging Algorithm

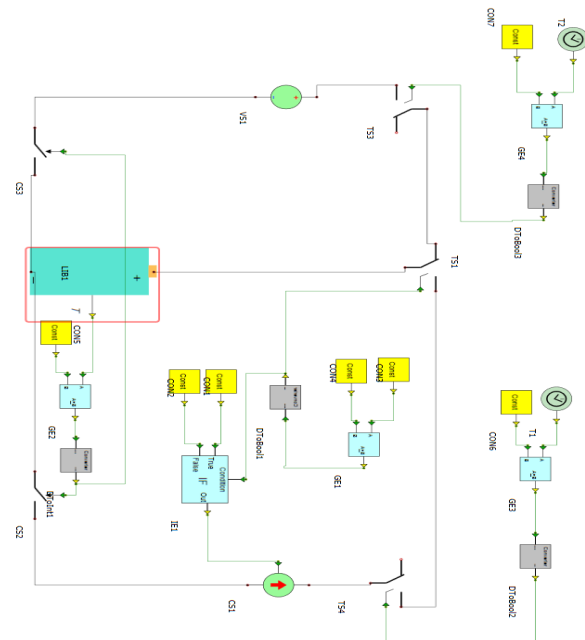


Figure 13: Simulated Circuit for Proposed Charging Algorithm

Considering Figures 7 to 11 the effect of temperature and SOC is substantial for all charging strategies. Table 3 states that the US18650 has a maximum temperature of 313K, hence the simulated temperature limit was set at 310K for safe operation.

7. EVALUATION OF CHARGING ALGORITHM

Using the baseline CC-CV Charging protocol the Algorithm Monitoring design system is evaluated in terms of temperature, SOC and terminal voltage at various C rates in Figures 14 to 15.

7.1 Temperature

Considering the temperature peak at 2C in Figure 14 it is clear that the proposed algorithm successfully limits the temperature at 310K. This can be compared at the varying C rates. Once again all temperature curves that

occur before the CV region are similar to the CC protocol constantly monitoring the battery temperature.

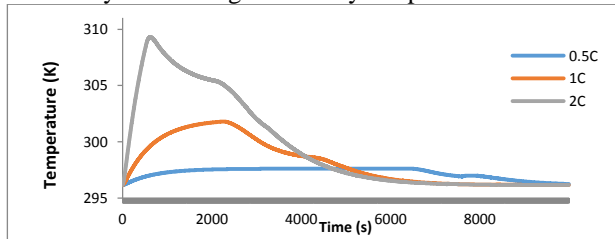


Figure 14: Battery Temperature at Different C Rates for Proposed Charging Algorithm

7.2 State of Charge

This algorithm follows the standard CC-CV protocol SOC and its results are identical for the C rates of 0.5C and 1C seen when comparing Figure 11 to Figure 15. The 2C curve shows a slight bend at approximately 400 seconds in Figure 15. This differs from the CC-CV SOC result as the temperature monitoring circuit terminated the charge for a brief moment due to the temperature exceeding the 310 Kelvin limit. When terminated the curve operated under the CC protocol briefly and then back into the CV region.

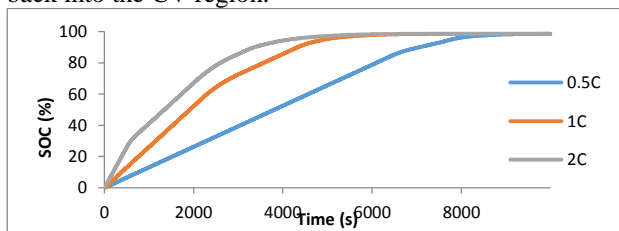


Figure 15: SOC at Different C Rates for Proposed Charging Algorithm

7.3 Terminal Voltage

The only difference found in Figure 16 above when compared to the CC-CV protocol voltage in Figure 8 is the 2C curve. In this case, the voltage fluctuation begins earlier due to the temperature limit being exceeded before the 4.2V limit is reached. The charging algorithm spends a slightly longer time in the CC phase with the charge being terminated in small intervals causing the voltage oscillation. Thereafter, at 2000 seconds, the constant voltage phase is reached and the graph follows the previous result of the CC-CV protocol of Figure 8.

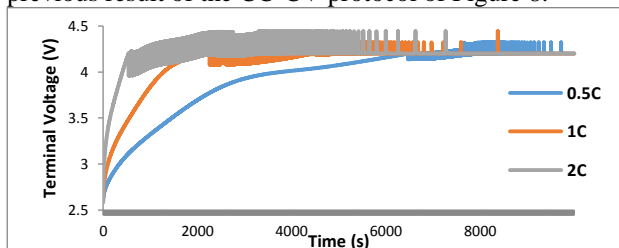


Figure 16: Terminal Voltage of Algorithm for different C rates

8. CONCLUSIONS AND RECOMMENDATIONS

Lithium Ion batteries are among the emerging technologies in industry. Attempts to improve the charging accuracy of models will assist with the storage device penetration in market and industry. When

considering the CC-CV protocol the condition that terminates the CC is the maximum OCV and not the SOC. This stops the battery from exceeding the 4.2V. In addition, the charge rate can be increased to decrease the charging time. The CCP-CV protocol does use the initial current pulse to reduce time spent in the charge time in the CC region. Consequently, a decreased total charge time is observed. However, this does come at the expense of temperature rises due to higher average currents. It is therefore concluded that the CC-CV protocol is the best suitable protocol for adaption of Li-Ion battery management techniques. From this conclusion the monitoring algorithm was implemented and observed and successfully limited the charge time and temperature while adequately maintaining the Voltage levels observed in the CC-CV protocol. An alternative software other than the Virtual Test Bed is recommended due to the time consuming bugs found during design in addition to the lack of graphing tools available is proposed. The Algorithm should be designed such that the switch may not return to the CC phase once entering the CV phase. This will eliminate the oscillations observed when operating at 2C or higher C rates.

9. ACKNOWLEDGEMENT

The authors gratefully acknowledge the support and infrastructure provided by Electrical Engineering Department, University of Cape Town, South Africa for carrying out this research.

10. REFERENCES

- [1] C. Spataru, Y. C. Kok, and M. Barrett, "Physical Energy Storage Employed Worldwide," *Energy Procedia*, vol. 62, pp. 452–461, 2014.
- [2] A. A. H. Hussein and I. Batarseh, "An overview of generic battery models," *Proc. of IEEE Power Energy Soc. Gen. Meet.*, no. 4, pp. 4–9, 2011.
- [3] S. B. Peterson, J. Apt, and J. F. Whitacre, "Lithium-Ion battery cell degradation resulting from realistic vehicle and vehicle-to-grid utilization," *J. Power Sources*, vol. 195, no. 8, pp. 2385–2392, 2010.
- [4] I. Hadjipaschalis, A. Poullikkas, and V. Efthimiou, "Overview of current and future energy storage technologies for electric power applications," *Renew. Sustain. Energy Rev.*, vol. 13, no. 6–7, pp. 1513–1522, 2009.
- [5] M. Dürr, A. Cruden, S. Gair, and J. R. McDonald, "Dynamic model of a lead acid battery for use in a domestic fuel cell system," *J. Power Sources*, vol. 161, no. 2, pp. 1400–1411, 2006.
- [6] O. Tremblay and L. a. Dessaint, "Experimental validation of a battery dynamic model for EV applications," *World Electr. Veh. J.*, vol. 3, no. 1, pp. 289–298, 2009.
- [7] L. Benini, G. Castelli, A. Macii, E. Macii, M. Poncino, and R. Scarsi, "Discrete-time battery models for system-level low-power design," *IEEE Trans. Very Large Scale Integr. Syst.*, vol. 9, no. 5, pp. 630–640, 2001.
- [8] M. Valvo, F. E. E. Wicks, D. Robertson, and S. Rudin, "Development and Application of an Improved Equivalent Circuit Model of a Lead Acid Battery," *Proc. of 31st Intersoc. Energy Convers. Eng. Conf. IEEEC 96*, vol. 2, pp. 1159–1163, 1996.
- [9] L. Gao, S. Liu, and R. A. Dougal, "Dynamic Lithium-Ion Battery Model for System Simulation," *IEEE Trans. Comp. Packag. Technol.*, vol. 25, no. 3, pp. 495–505, 2002.
- [10] M. Number, C. Type, C. Name, S. Code, and C. Us, "Lithium Ion Sony US18650 Datasheet," 2012.
- [11] K. C. Divya and J. Østergaard, "Battery Energy Storage Technology for Power Systems—an Overview," *Electr. Power Syst. Res.*, vol. 79, no. 4, pp. 511–520, 2009.

DESIGNING A GAS SNIFFER MONITORING SYSTEM FOR A QUADCOPTER

E. Baterman*, O. Dobzhanskyi* and R Gouws*

*North West University, School of Electrical, Electronic and Computer Engineering, Potchefstroom Campus, odobzhanskyi@gmail.com

Abstract. Eskom is the leading power supplier in South Africa and safety is one of their biggest concerns. One of these safety concerns are gas leakage in and around power plants. Current systems implemented to detect these gas leakages work very well but there are still some areas where it cannot detect gas leakage. This is where the gas sniffer monitoring system for a quadcopter comes into play. This system is capable of detecting variety of gasses and provides photos, temperatures and GPS readings from where these gasses were detected. The whole system is attached to a quadcopter so that any area of concern can be tested where the current implemented systems cannot. This paper therefore focuses on designing and testing such a system in real conditions.

Key words. Monitoring system, gas detection, quadcopter.

1. INTRODUCTION

Eskom is the largest producer of electricity in Africa and produces 92% of the electricity used in South Africa being of the top 11 utilities in the world [1]. Safety is one of their biggest concerns and they are always looking for new ways to improve safety in the work place [2]. In the context of this project Eskom aims to reduce the risk involving gas inhalation. Existing current gas detection systems cannot cover all the areas of a power plant. Eskom reduces their safety risks each year, and they reduced the number of employees affected from gas inhalations from two personnel in 2011 to zero in 2012 [3]. This project will therefore assist Eskom by providing information about possible unsafe areas due to high volumes of gas. In the remainder of the paper the following topics are discussed: a background of the current solutions used with proposed solution, then system analysis, functional analysis, system design, system operation, results, and a conclusion.

2. BACKGROUND

The following section provides a brief background on the current solutions used for gas detection by Eskom around South Africa and the proposed solution for gas detection.

2.1 Existing solutions to problem

Eskom uses many detection systems to monitor hazardous gasses and air quality in and outside power plants since the 1980's. All sites are equipped with SO₂, NO, Ozone (O₃) and Fine Particulate Matter (FPM) monitor systems. This is to ensure a safe working environment and the annual concentrations at all sites within the guidelines set by the DEAT [4].

There are different types of hazardous gasses found in the industry [2], mainly three categories - Asphyxiant, Flammable and Toxic. Each of these gasses reacts differently and has different effects on people.

There are mainly two types of gas monitoring systems in place at Eskom today. These systems are: gas monitors outside the power plants at certain areas, and gas monitors inside the power plants. Both of these systems come with their advantages and disadvantages.

2.1.1 Outdoor Monitoring

At Eskom, emission controls need to be done inside and outside the power stations. The current monitoring system installed works effectively but still has its disadvantages and advantages. Table 1 highlights some of these advantages and disadvantages.

Table 1: Outdoor monitoring, advantages and disadvantages.

Advantages	Disadvantages
Personnel are notified when hazardous gas is detected in the area.	Weather conditions can disrupt the data readings.
These sites can be accessed from the control room.	Only covers the area where the monitors are installed.

2.1.2 Indoor Monitoring

An indoor gas monitoring system should be able to monitor emissions continuously without interrupt [5]. The indoor monitoring system used by Eskom is manufactured by a company called SICK. This company specializes in sensor development for big industrial companies [4]. Table 2 shows some of the

advantages and disadvantages of the indoor monitoring system used by Eskom.

Table 2: Indoor monitoring: advantages and disadvantages.

Advantages	Disadvantages
Personnel are notified when hazardous gas is detected in the area.	Main circuitry of the system can only be accessed at a specific point.
These sites can be accessed from the control room.	Only covers the area where the monitors are installed.
Extra sensors can easily be added and integrated into the whole monitoring system.	The system can easily be damaged.
Online 24/7.	System is dependent on a constant power supply.

2.2 Proposed Solution

To create a system that can monitor gas emissions in a more effective way than the existing solutions cannot, all the shortcomings of existing solutions should be taken into consideration.

After all the research done on the gas monitoring system required by Eskom it is clear that there are three main gasses that take place on the factory. These gasses are Sulphur oxide, Nitrogen oxide and Carbon dioxide. Other gas detectors can also be installed but for now these are the gasses to be focusing on [6].

Gas sensors are integrated with a microcontroller mounted onto an existing quadcopter. The remote access of the quadcopter makes it easy to control these gases from a distance and monitor areas with difficult access which makes it to be a perfect solution for the problem. The data from the gas sensors is recorded and the processed data is available to a remote user.

What makes this project unique is that it could be used indoors and outdoors, and at different power stations where there are areas of concern. Table 3 represents all the advantages and disadvantages of this proposed solution.

Table 2 : Quadcopter monitoring system: advantages and disadvantages.

Advantages	Disadvantages
Covers any area of concern.	Weather can affect the readings of the gas detection outdoors.
Remote access is available.	The quadcopter has a limited power source and will only last a few minutes.
Extra sensors can easily	The wind thrust produced

be added and integrated into the whole monitoring system.	by the quadcopters propellers will have an effect on the gas detection.
This project can be modified to satisfy a wide verity of concerns.	Weather can affect the handling of the quadcopter.
The user is able to see exactly what the quadcopter does via video.	
If gas is detected it is recorded and processed according to Eskom's needs.	
The exact position is available where gas is detected via GPS readings.	

3. SYSTEM ANALYSIS

In this section an overview of the whole system analysis is presented as well as the requirement analysis of the proposed solution.

3.1 Requirements Analysis

The proposed design solution was done with the following specifications in mind:

- Access remote areas for monitoring.
- The system should be able to detect the following gasses: Methane, Butane, LPG, smoke, Natural gas, Carbon Monoxide and Ozone.
- The monitoring system is able to take pictures of the area where gas is detected as well as GPS can coordinate the temperature for extra safety measurements.
- The whole system should not be too heavy and should not affect the control of the quadcopter.
- The system should be able to run for a long time on its power source to collect reliable data.
- The system should be designed in a way so that future improvements are possible.

3.2 Operational Analysis

Figure 1 shows the operational analysis of the whole system. The user will control the software from a PC (I/F 1.0), the control terminal will then collect the data from the monitoring system (I/F 2.0). From there the monitoring system will fit onto the quadcopter where the areas of concern can be monitored and the external interferences will have to be taken into consideration (I/F 4.0).

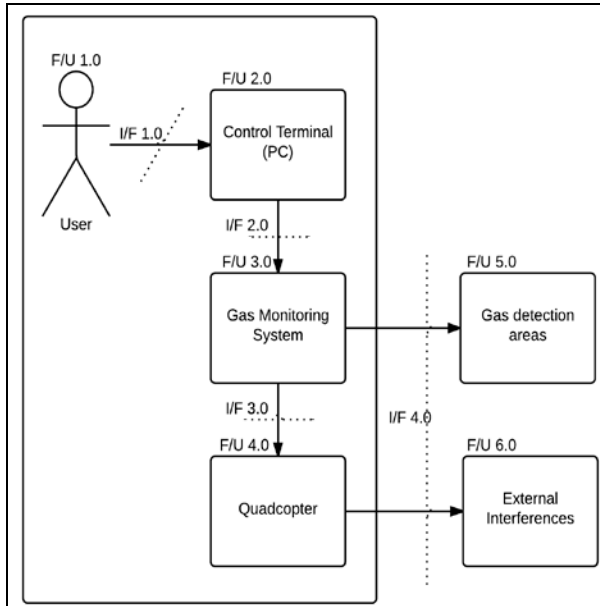


Figure 1 : Operational architecture.

4. MONITORING SYSTEM FUNCTIONAL ANALYSIS

In this section all the separate parts of the monitoring system is looked in detail and described how all the technologies interact with each other.

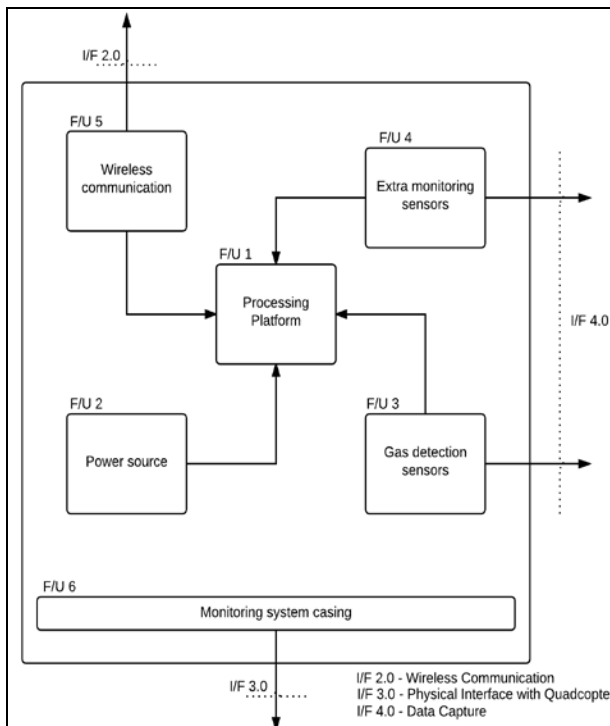


Figure 2 : Monitoring system functional architecture.

Figure 2 gives a brief overview of how all the technologies interact with each other. The main part of

the integrated system is the processing platform (F/U 1), from here all the sensors and communication medium are controlled. The power source will provide constant power to the whole system (F/U 2). There are many sensors used in the system and can be categorized: the gas detection sensors (F/U 3), and all the extra monitoring sensors (F/U 4). This whole system is enclosed in a casing to protect and keep the monitoring system stable.

Figure 3 describes all the sub systems in much more detail and it covers its main sections.

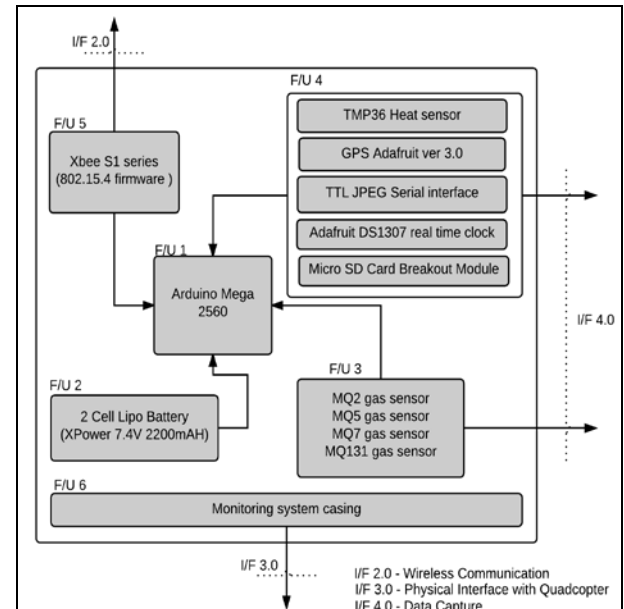


Figure 3 : Monitoring system design.

5. MONITORING SYSTEM DESIGN

In this section all the separate sub systems are described in detail as shown in figure 3. All the components from each sub system will also be discussed.

5.1 Processing Platform

The processing platform (F/U 1) used for this system is an Arduino Mega 2560. It is very small and its processing speed is fast enough (16 MHz) to control all the sensors and communication medium. The Mega has 54 I/O pins making it ideal for the monitoring system which consists of many sensors.

5.2 Power Source

The power source (F/U 2) used for this system is a 2 Cell LiPo battery (XPower 7.4V 2200 mAh). This power source is able to provide enough power to power all the components on the system and for the significant time needed. The advantage of using this battery is that after every monitoring session the battery can be recharged.

5.3 Gas Detection Sensors

The following gas sensors are used to detect the necessary gas. These gas sensors can also be calibrated with a resistor so that the sensitivity of the sensors can be controlled. The higher the value of the resistors the less accurate it becomes; and the lower the value the less sensitivity is achieved. The resistor value used for all the gas sensors is a 12 k Ω making it reliable and very sensitive to all gasses.

The four gas sensors combined will give a very variety of gasses that can be detected as seen from the following:

- MQ2 - Methane, Butane, LPG, smoke
- MQ5 - Natural gas, LPG
- MQ7 - Carbon Monoxide
- MQ131 - Ozone

5.4 Extra Monitoring Sensors

These extra monitoring sensors (F/U 4) make the system much more accurate and reliable for gas detection. Each of these sensors is described to show how they interact with each other and how they make the system more reliable.

5.4.1 TMP36 Heat sensor

With a heat sensor on the monitoring system the temperature of the gas detected can also be given, this will also contribute to making it safer in the workplace.

5.4.2 GPS Adafruit ver 3.0

Using a GPS it is easy to get the exact coordinates from where the gas is detected.

5.4.3 TTL JPEG serial interface

Using a camera on-board the user can see exactly where and how the gas is detected; each photo captured is stored on the SD card reader on-board of the system.

5.4.4 Adafruit DS1307 real time clock

The real time clock on-board of the system is used to give the exact time and date for when gas is detected, making the system very accurate.

5.4.5 Micro SD Card Breakout module

As stated earlier the SD card is used to store the necessary data that the user cannot access while the system is in use on the quadcopter.

5.5 Xbee Series one

The Xbee S1 is used for communication between the user and the monitoring system. These Xbee modules operate at 2.4 GHz and its RF data rate is 250 Kbps and can cover a range of approximately 100 m [7]. These Xbee modules are more than sufficient for the system.

5.6 Software

The software used for this project has two sides, the software that is used by the user and the software programmed to control the whole monitoring system

on the microcontroller. The software on the user side is a C# application done in Visual Studio and is discussed in detail in the following section. As for the microcontroller a sketch was programmed in C/C++ to control all the sensors and to process all the data before sending it to the user.

6. MONITORING SYSTEM OPERATION

In the following section the monitoring software is described, showing all the different options and how the data is presented to the user.

From figure 4 it is clear to see that the user has three choices to choose from how the system should monitor the areas around the quadcopter. The three choices are:

- **Monitoring only** - The system will continuously collect data from all the sensors, but will not take any photos.
- **Stop Monitoring** - Close the connection between user and monitoring system.
- **Photos and monitoring** - The system will monitor the area with the gas sensors and when gas is detected the system will take a photo and it will continue in this loop.
- **Photos only** - The system will only take photos continuously without stop and without any data from the sensors.

It is also clear from figure one how all the data is presented in the program.

Figure 4 : User software layout.

Figure 5 shows the layout where the gas sensor data will be displayed. The data is represented in two different graphs: one for representing gas and one for

the temperature. Each gas can also be shown separately as seen from the figure in the different tabs available. All the data coming from the monitoring system is stored in a database and from there the program displays it in a graph. All the charts data can also be erased when new data wants to be recorded with the "RESET Charts" button. The exact time and date of data to be displayed (shown in figure 4) can also be chosen by the user. When levels of concern are detected the program also let the user know indicating levels from LOW to VERY HIGH.

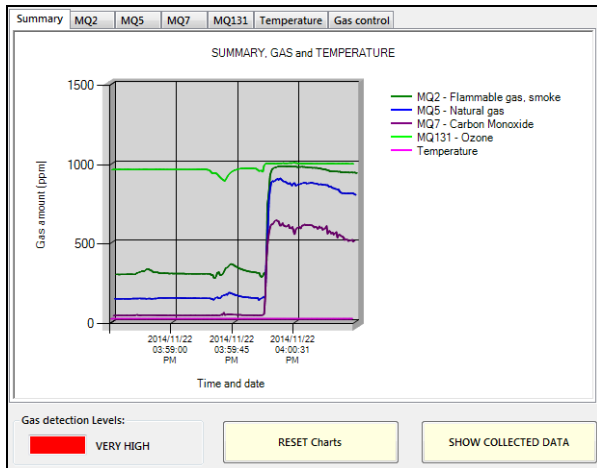


Figure 5 : Gas and temperature representation via graphs.

Each time a gas is detected with a spike in the data readings the program stores all the data from that instance in a text file. The data stored in the text file is the time and date, the name of the image taken, the exact GPS coordinates and the temperature. The format of the text file saved is shown in figure 6.

```
Gas detected ( IMAGE00.JPG ), Time: DATE 2014/9/9 TIME 18:22:17 GPS Latitude, Longitude: 2641.56,2705.42 Temperature: 19.0
Gas detected ( IMAGE28.JPG ), Time: DATE 2014/9/9 TIME 18:40:13 GPS Latitude, Longitude: 2641.56,2705.42 Temperature: 17.0
Gas detected ( IMAGE29.JPG ), Time: DATE 2014/9/9 TIME 18:40:21 GPS Latitude, Longitude: 2641.56,2705.42 Temperature: 17.9
Gas detected ( IMAGE30.JPG ), Time: DATE 2014/9/9 TIME 18:40:29 GPS Latitude, Longitude: 2641.56,2705.42 Temperature: 16.9
Gas detected ( IMAGE31.JPG ), Time: DATE 2014/9/9 TIME 18:40:46 GPS Latitude, Longitude: 2641.56,2705.41 Temperature: 16.3
Gas detected ( IMAGE32.JPG ), Time: DATE 2014/9/9 TIME 18:41:11 GPS Latitude, Longitude: 2641.56,2705.42 Temperature: 17.2
```

Figure 6 : Text data stored.

7. RESULTS

The results of the testing of all the components are given in the following section. Figure 7 shows the integrated system with quadcopter.

7.1 Gas detection

Each gas sensor was tested in a short period of time just to show that each sensor reacts to a certain gas being applied to them. All the gas sensors are very sensitive and the spikes shown in figure 8 indicate that each sensor is working effectively.

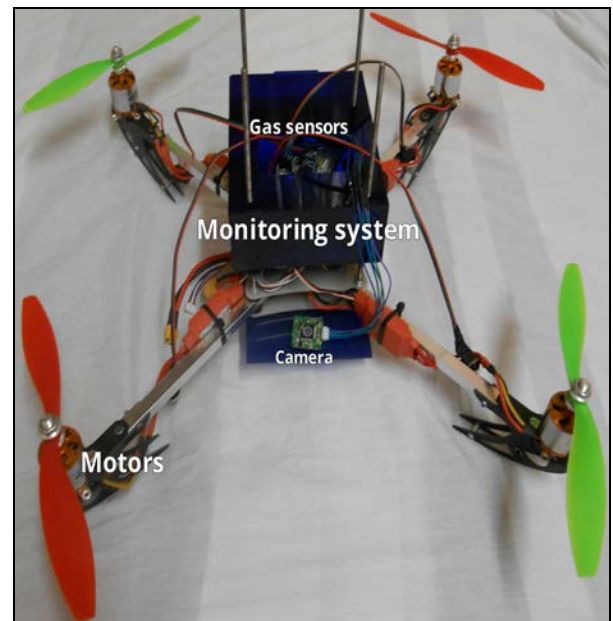


Figure 7 : Integrated system with quadcopter.

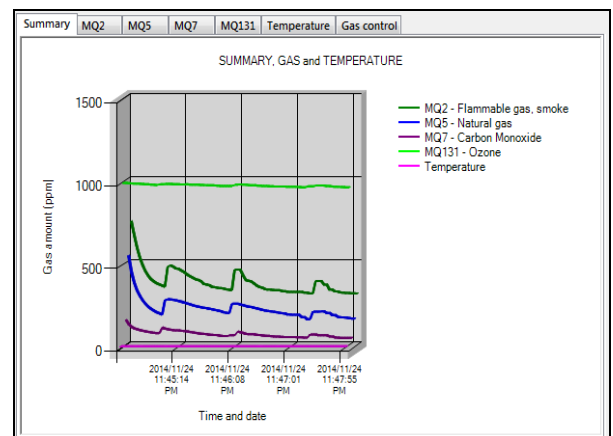
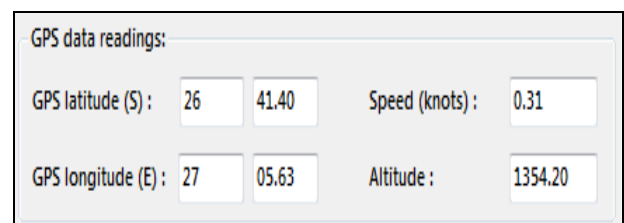


Figure 8 : Sensor affected by gas detection.

7.2 GPS accuracy

The GPS used by Adafruit® is very accurate and reliable, the only drawback is that the GPS will not function 100% in a closed area inside a building. The GPS also gives the speed in knots and the altitude making it perfect for the use with the quadcopter. Figure 9 shows the accuracy of the GPS with the latitude and longitude compared with a Garmin GPS.



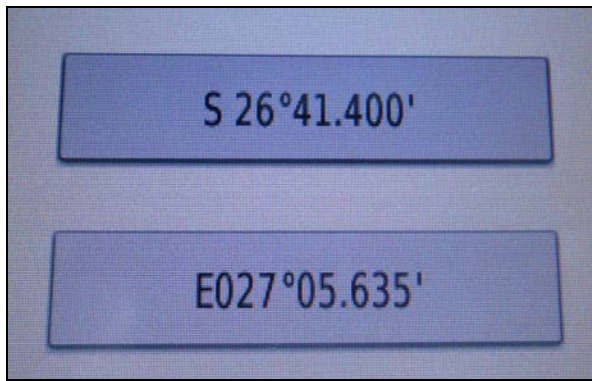


Fig. 9: GPS data reading.

7.4 Power usage

The power usage of the whole system can be seen by the following graph shown in Figure 10. It is clear that the four gas sensors draw the most current when in use. The operating time is also given in figure 12, showing that the system with all the sensors can run a maximum time of 2.6 hours.

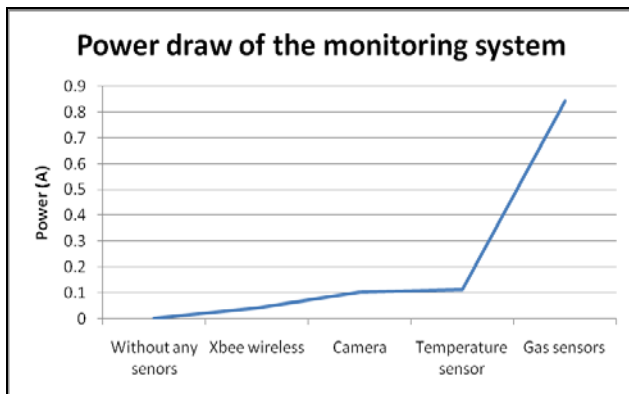


Figure 10 : Power draw of the monitoring system.

7.3 Camera

The Serial camera can take pictures in sizes:

- 640x480
- 320x240

8. CONCLUSION

In this paper the design of a gas sniffer monitoring system for a quadcopter was discussed. This system fits onto the quadcopter making the system portable and easy in use. The monitoring system as a whole consists out of a microcontroller, four gas sensors, a camera, SD card reader, real time clock and a heat sensor. It detects a wide variety of different gasses and gives a good graphical representation for the user. The software designed for this system is user friendly. The

GPS coordinates, the temperature of the detected area. It is available for the user to make the whole monitoring system very accurate.

9. REFERENCES

- [1] Michael R. Carrell, Norbert F. ELbert, Robert C. Hatfield. *Human Resource Management in South Africa 3rd edition*. London: Thomson, 2006, pp 329
- [2] Clitheroe, Moys, Lawrence, Awerbuck. *FCS Workshop practice L2*. South Africa: Pearson, 2009, pp. 40-42.
- [3] Fact sheet, Eskom, [online] 2010, http://www.eskom.co.za/AboutElectricity/FactsFigures/Documents/ES_0003EskCommitEnviroRev71.pdf (Accessed : 6 of May 2014).
- [4] Monitoring and controlling, Sickinsightonline, [online] 2012, <http://www.sickinsight-online.com/south-africas-largest-electricity-producer-eskom-measures-its-mass-emissions-rate-with-sick/> (Accessed : 15 May 2015).
- [5] Stephen DeFriend, Mark Dejmek, Leisa Porter, Bob Deshotels, Bernt Natvig. "A risk-based approach to flammable gas detector spacing". *Journal of Hazardous Materials*, vol. 159, pp. 142-151, October 2007
- [6] Emanuel T. Voeltz, Kamini Shah. "Virtual continuous emission monitoring system". *Emission monitoring*, vol. 5, pp. 1-2, Jan. 1995
- [7] JIANG Xiao-ling, ZHENG Yu-zheng, ZHANG Xian-chao, MA Yao-yao (School of Communication Engineering, CUIT, Chengdu 610225, China); Program Design of ZigBee Wireless Pressure Gauge [J]; *Journal of Chengdu University of Information Technology*; 2010

jesh.haigh@gmail.com

Anthony Marks

Department of Electrical Engineering
Nelson Mandela Metropolitan University

Port Elizabeth, South Africa

Anthony.Marks@nmmu.ac.za

Abstract— Today the world faces inevitable consequences because of what has become a well-known threat to the survival of the human race and other species on our planet Earth [1]. Global warming has resulted in many manufacturing organisations in industry resorting to make their use of energy more efficient and finding “greener” ways to do things [1]. Embedded generation is one of the ways in which manufacturing companies can increase the efficiency of their energy usage and also reduce their carbon foot print [2]. Aberdare Cables is the leading cable manufacturer in South Africa with three manufacturing plants operating in South Africa. The work that this paper aims to achieve will be focused on the Aberdare Cables Port Elizabeth Factory. The Port Elizabeth (PE) Factory has an After Diversity Maximum Demand of 5MVA and a maximum fault level of 25kA. The MV ring operates at a voltage level of 6.6kV and the LV radial network operates at a voltage level of 400V. This paper shall discuss how Organic Rankine Cycle (ORC) technology can be used to solve the problem of industrial waste heat as it is applied to the Aberdare Cables PE factory. The paper will also deal with the simulation of the current network and the network containing the ORC solution, showing the relay time overcurrent plots with cable damage curves that prove that the relays protect the feeders assigned to their respective protection zones.

Keywords- *Organic Rankine Cycle; Electrical Engineering; overcurrent relays; damage curves; cables; generator; fault current, fault voltage; grading margin, relay; circuit breaker.*

I. INTRODUCTION

The Aberdare Cables Port Elizabeth Factory uses a boiler to generate steam that is used in the impregnation process for paper insulated lead covered cables. The waste heat energy from this process is pumped out of the heat stacks into the atmosphere. There is currently no means of capturing the wasted heat energy to improve the efficiency of this process and to harvest this excess heat to generate electricity. This is a case of industrial waste heat and this problem could be solved by implementing ORC technology to capture the waste heat and use it for generating electricity. In 2012 the Port Elizabeth Factory had to add another substation to deal with the

increasing capacity required by the factory due to expansions that were taking place on site (from 3MVA to 5MVA). This expansion and other upgrades were not yet analysed and modelled by Aberdare engineering personnel on a software package that could be used in the future to easily facilitate further expansions, upgrades and investigations. A software package called DigSilent Power Factory was used to model the abovementioned shortfalls. The internal MV infrastructure also had to be converted from a 6.6kV radial system to a 6.6kV ring mains system and the Municipality Fault level requirement was increased from 20kA to 25kA. This resulted in a need to replace the existing MV cabling to the transformers. None of these improvements had yet been modelled on a software package. If Aberdare Cables chooses to implement idea put forward in this paper, a section of the factory may be disconnected from the Municipality supply. Decisions needed to be made as to what section of the factory this would be. Based on this information and the available waste heat, the capacity of the Organic Rankine Cycle generator needed to be determined. Fault analysis was conducted on the current network so that relay settings could be calculated and be available to qualified personnel. The current network and the selected solution were also simulated on DigSilent and will be dealt with further in this paper. The following is a network diagram of the current Aberdare Cables Factory MV network:

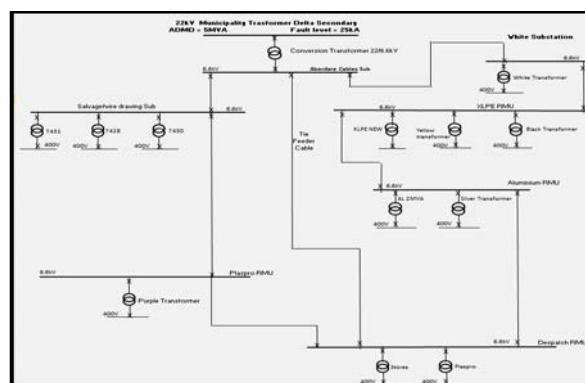


Figure 1.1 Aberdare Cables Port Elizabeth Operations

II. THE ORGANIC RANKINE CYCLE

The Rankine Cycle is a thermodynamic process in which heat energy is converted into electrical energy and it is the cycle that is implemented in conventional power stations today [2]. The Organic Rankine Cycle (ORC) is the Rankine Cycle where instead of using water/steam, organic liquids such as refrigerants and hydrocarbons are used as working liquids [3]. ORCs make use of clean energy resources. Examples of these are geothermal fluids, solar irradiation, ocean thermal gradient, heat from biomass combustion and waste heat from industrial thermal processes [3]. For the purpose of this project the focus has been on harnessing the waste heat from industrial thermal processes seeing that the heat source that will be used at the Aberdare Cables PE factory will be the heat that is expelled from the boiler heat stacks. The manufacturers of ORCs design these units to convert medium and low temperature heat into power by using refrigerants or hydrocarbons with lower boiling temperatures instead of water [3]. The Port Elizabeth factory has two heat stacks from which the flue gas is emitted. The expected temperature range of the flue gas in one of the exhausts at Aberdare is 190°C - 270° and the other one is 135°C - 190°C. Making use of ORC technology is an attractive concept because of the following features:

- The ability of the technology to adapt to various heat sources. [4]
- The technology is proven. [4]
- There is less complexity and less maintenance. [4]
- The investment and maintenance costs are low. [4]
- The technology is available on the market and the suppliers are well known. [4]
- The commissioning time is short and the technology is generally accepted in industry. [4]
- The Technology also has a short payback period. [4]

Figure 2.1 below shows the different components of an ORC unit manufactured by Turboden, one of the leading ORC unit manufacturing companies:

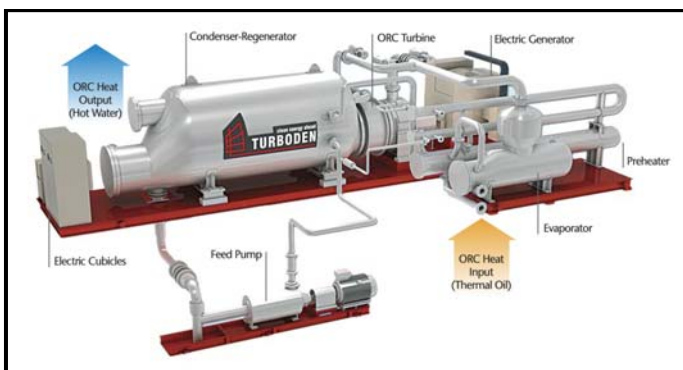


Figure 2.1 [5]

As seen in figure 2.1, the ORC has a compact design which makes it convenient in terms of space.

Figure 2.2 below shows a schematic of the four main components of the ORC system:

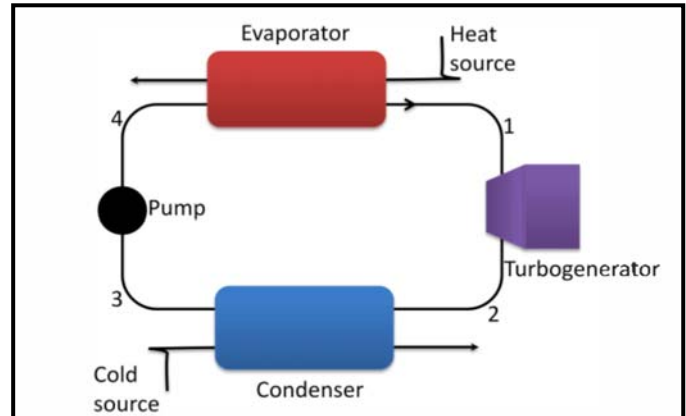


Figure 2.2 [3]

The heat source depicted in figure 2.1.2 shall be the hot flue gas that exits the heat stacks. The heat shall be harvested using heat exchangers in which the heat shall be transferred to the working fluid to preheat it before it is evaporated; this increases the efficiency of the Evaporator [4]. The working liquid will be expanded in a turbine that is directly connected to the generator [6] that will supply two substations in the Aberdare Cables Port Elizabeth factory

III. GENERATOR CAPACITY, VOLTAGE AND CURRENT LEVELS

The proposed substations in the Port Elizabeth factory that are going to be supplied by the ORC generator are Salvage substation and Plaspro RMU. There are four transformers connected to these substations in total. The Aberdare Cables PE factory has an After Diversity Maximum Demand (ADMD) of 5MVA and a total of 12 transformers in the ring mains network that supply loads at the moment. Bearing this in mind, it is safe to assume that a generating capacity around 2MVA can be chosen to supply the loads that are connected to these two substations via the four transformers.

The typical range of operation and performances supplied by Turboden, one of the leading ORC manufacturing companies, shows a unit available with a net active electric power output of 2040 kW with a generator that generates a voltage of 6kV 50Hz [5]. The power factor of the generator is not supplied, so assuming a typical generator power factor of 0.8, [7] the kVA rating of the generator shall be:

$$\text{kVA} = \text{kW}/\text{p.f} = 2040\text{kW}/0.8 = 2550\text{kVA} = 2.55\text{MVA} \quad [8]$$

2.55MVA would be more than enough to supply the needs of the loads connected to the White and Salvage substations.

The following shows a table that shows the above information. Highlighted in yellow is the net active electric power output and the generator voltage and frequency output of a heat recovery unit that, would suit the needs of this Project:

DigSILENT Power Factory is a software package that allows the user to model generation, transmission, distribution and industrial grids [12]. It is within the many capabilities of this powerful software to do Power flow analysis, Fault analysis, Distribution network functions etc. [12]. As related to this project, the DigSilent software package has been used to model the existing network with its protection settings. Load flow analysis as well as fault analysis has and will also be simulated for the existing network and the proposed solutions using this Software Package.

VI. PROTECTION RELAYS AND CIRCUIT BREAKERS

Faults in power systems are unavoidable [13]. When faults occur in the system, the faulty part of the electrical system needs to be detected and disconnected as soon as possible to prevent interruption of supply to customers and to limit the amount of damage the fault energy can inflict on healthy equipment [13]. For the purpose of this project, fault energy needs to be disconnected as soon as possible in order to prevent damage to plant. The detection and disconnection of fault current is achieved by using relays and circuit breakers where the relay detects the fault current and the circuit breaker interrupts the circuit [13]. The Port Elizabeth factory employs ABB PR512 microprocessor based protection units that do the detection and interruption functions all in one unit. These units are used only in the MV infrastructure. When simulating the directional fault current detection functionality, the generic directional relay model, Rel-Loc-Toc-Dirext, was used. For the simulation of the normal overcurrent relays, the Siemens 7SJ50 IT relay model was used. A deviation from the norm worth noting with these relays is that Definite Minimum Time (DMT) occurs at 20 times the effective setting instead of 30 times the effective setting. This is shown below:

The most downstream relay characteristic is one of the directional relay models used in the project simulation, and it has an effective setting of 120 A. Therefore, DMT occurs at $20 \times 120 = 2400\text{A}$.

The most upstream relay characteristic is a Siemens 7SJ50 IT overcurrent relay with an effective setting of 186A. Therefore, DMT occurs at $20 \times 186 = 3720\text{A}$.

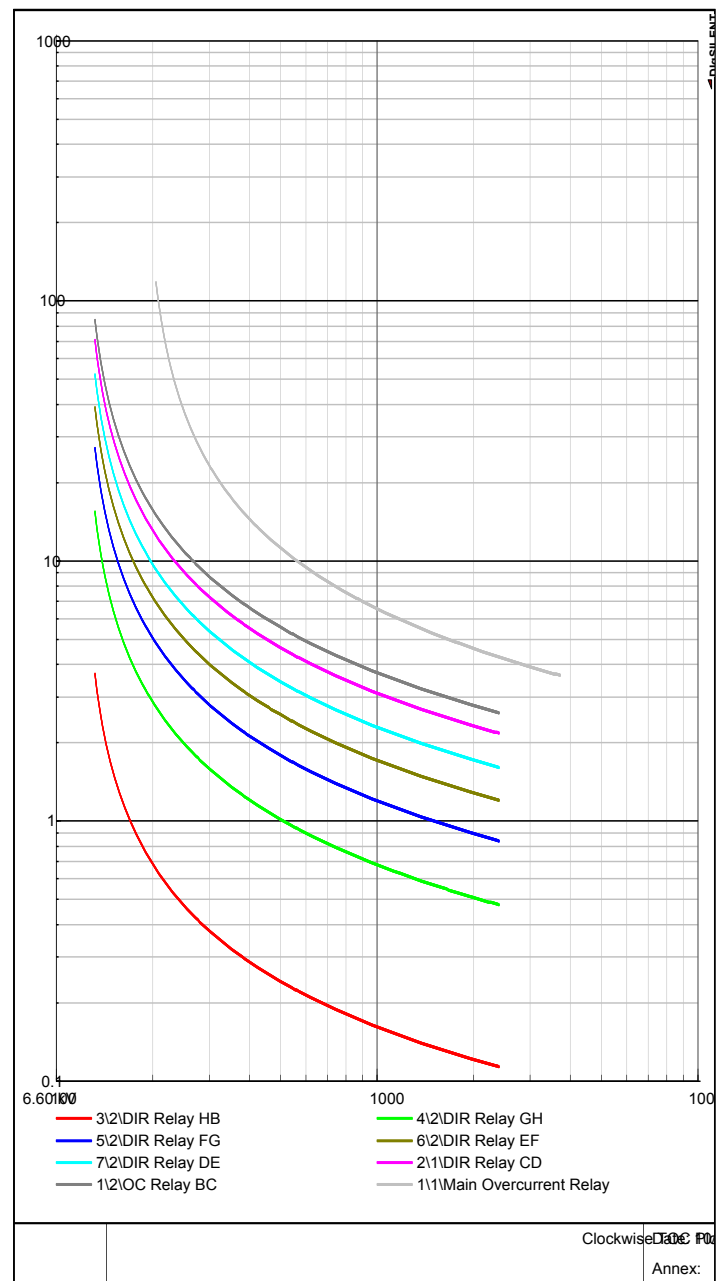


Figure 6.1- DMT @ 20 times ES instead of 30 times ES.

VII. FEEDER PROTECTION IN DISTRIBUTED GENERATION AND RING FEED SITUATIONS

Distributed generation or embedded generation introduces special challenges to the traditional protection schemes [14]. One of these challenges are that during a fault condition, the embedded generator contributes to the fault current in addition to the fault current coming from the existing power grid [14]. If the embedded generator in this project is going to be connected in parallel with the municipality supply, it may add to fault currents and this will have to be considered when setting sensitivity and selectivity of the protection relays. Another problem that is faced is the bi-directional nature of fault current in these situations [14]. If the relays that are to detect this fault

are not direction sensitive, problems will be encountered [14]. Relays that were previously coordinated may be upset by the addition of an embedded generator because the addition of the embedded generator may affect the fault level [14]. In ring connected networks where it is possible for fault current to flow in two directions, it also becomes necessary for relays to be direction sensitive [15]. The existing MV infrastructure of the PE factory is a ring connected network and employs directional relays for the protection of the feeders in the ring mains network. In the project solution proposed, the substations that are not connected to the embedded ORC generator are connected in a ring and therefore require directional protection.

VIII. FAULT CALCULATIONS

The following equations were used to calculate the Symmetrical fault currents, symmetrical fault voltages, Phase to Earth fault currents and voltages and the phase to phase fault currents and voltages. The formulae were obtained from the Network Protection & Automation Guide [16].

$$S_b = 100 \text{ MVA}$$

$$I_b (6.6kV \text{ OR } 22kV) = \frac{S_b}{\sqrt{3} \times V_L}$$

$$Z_b (6.6kV) = \frac{V_L^2}{S_b}$$

$$Z_{pu} (\text{Transformers}) = Z_{pu} (\text{rated}) \times \frac{S_b}{S_{rated}}$$

$$Z_{pu} (\text{Cables}) = \frac{\text{Actual}}{\text{Base}}$$

$$I_{fpu} = \frac{1}{Z_{pu} (\text{Fault})}$$

For a Symmetrical Fault:

$$I_{fault} = I_{fpu} \times I_b (6.6kV \text{ OR } 22kV)$$

$$V_{fault} = 0V$$

The following diagram represents the zero sequence equivalent circuit of the current MV infrastructure at the Aberdare Cables PE factory:

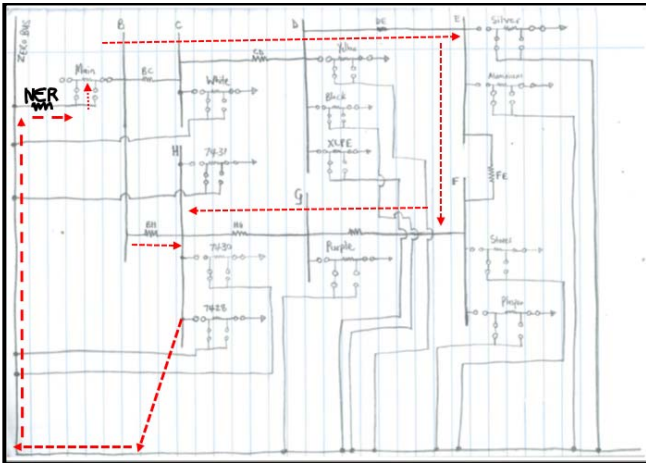


Figure 8.1

The Red dashed arrows show the path that the earth fault current will flow if an earth fault originated at the Salvage/wire drawers Substation. The delta connected primaries of all the smaller factory transformers ensure that the only path for the earth fault current to get back to where it originated from is through the main 5MVA transformer. The aforementioned will hold true for an earth fault on any of the MV substations and RMUs. The factory is resistively earthed through a 1.8 Ω Neutral Earthing Resistor that is connected on the secondary star point of the main 5 MVA transformer.

For phase to earth faults:

$$I_{a1} = I_{a2} = I_{a0} = \frac{E_1}{\Sigma Z}$$

$$I_a \text{ pu} = 3 \times I_{a1}$$

$$I_a = I_a \text{ pu} \times I_b (6.6kV)$$

$$V_{a1} \text{ pu} = E - Z_1 \times I_{a1}$$

$$V_{a2} \text{ pu} = -Z_2 \times I_{a2}$$

$$V_{a0} \text{ pu} = -Z_0 \times I_{a0}$$

$$V_a \text{ pu} = V_{a1} \text{ pu} + V_{a2} \text{ pu} + V_{a0} \text{ pu}$$

$$V_b \text{ pu} = a^2 V_{a1} \text{ pu} + a V_{a2} \text{ pu} + V_{a0} \text{ pu}$$

$$V_c \text{ pu} = a V_{a1} \text{ pu} + a^2 V_{a2} \text{ pu} + V_{a0} \text{ pu}$$

$$V_a = V_a \text{ pu} \times V_{base}$$

$$V_b = V_b \text{ pu} \times V_{base}$$

$$V_c = V_c \text{ pu} \times V_{base}$$

The Sequence impedance diagram for a phase to earth fault looks as follows:

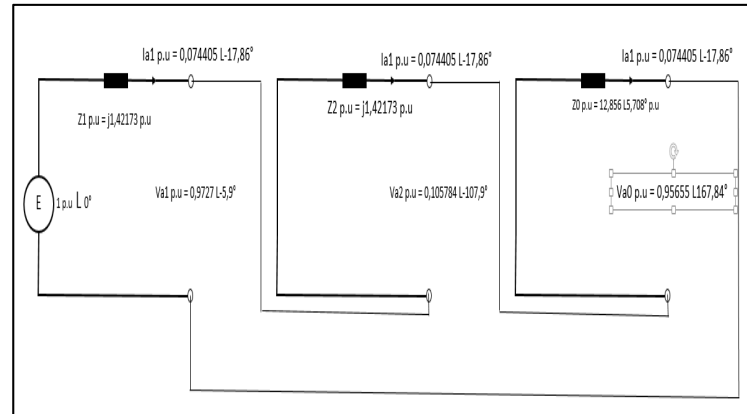


Figure 8.2

For phase to phase faults:

$$I_{a1} = \frac{E_1}{\Sigma Z_1, Z_2}$$

$$V_{a1} = V_{a2} = E - Z_1 \times I_{a1}$$

$$V_{a0} = 0 \text{ pu}$$

$$I_{a2} = -\left(\frac{V_{a2}}{Z_2}\right)$$

$$\begin{aligned}
 I_{a0} &= 0 \text{ pu} \\
 I_{a \text{ pu}} &= I_{a1} + I_{a2} + I_{a0} \\
 I_{b \text{ pu}} &= a^2 I_{a1} + a I_{a2} + I_{a0} \\
 I_{c \text{ pu}} &= a I_{a1} + a^2 I_{a2} + I_{a0} \\
 V_{a \text{ pu}} &= V_{a1} + V_{a2} + V_{a0} \\
 V_{b \text{ pu}} &= a^2 V_{a1} + a V_{a2} + V_{a0} \\
 V_{c \text{ pu}} &= a V_{a1} + a^2 V_{a2} + V_{a0} \\
 I_a &= I_{a \text{ pu}} \times I_b(6.6 \text{ kV}) \\
 I_b &= I_{b \text{ pu}} \times I_b(6.6 \text{ kV}) \\
 I_c &= I_{c \text{ pu}} \times I_b(6.6 \text{ kV}) \\
 V_a &= V_{a \text{ pu}} \times \frac{V_{\text{base}}}{\sqrt{3}} \\
 V_b &= V_{b \text{ pu}} \times \frac{V_{\text{base}}}{\sqrt{3}} \\
 V_c &= V_{c \text{ pu}} \times \frac{V_{\text{base}}}{\sqrt{3}}
 \end{aligned}$$

IX. RELAY SETTINGS CALCULATIONS

The following equations were used to calculate the relay settings for plain overcurrent relays, clockwise directional relays and anti-clockwise directional relays.

$$\begin{aligned}
 PBS &= \frac{I_{\text{max}}}{CT \text{ primary}} \\
 PBS \text{ (used)} &= X \text{ pu} \rightarrow \text{Depending on available steps} \\
 ES &= PBS \times CT \text{ primary} \\
 PSM \text{ (min)} &= \frac{I_f \text{ (min)}}{ES} \\
 t_{(TSM=1 \text{ pu})} &= \frac{0.14}{PSM \text{ (min)}^{0.015397} - 1} \\
 TSM_{\text{Approx}} &= \frac{t_{(TSM=1 \text{ pu})}}{\text{Required Time}} \\
 TSM_{\text{Used}} &= X \text{ pu} \rightarrow \text{Depending on available steps} \\
 PSM \text{ (max)} &= \frac{I_f \text{ (max)}}{ES} \\
 t_{(TSM=1 \text{ pu})} &= \frac{0.14}{PSM \text{ (max)}^{0.015397} - 1} \\
 t_{(\text{Fastest})} &= TSM_{\text{Used}} \times t_{(TSM=1 \text{ pu})} \\
 t_{(\text{upstream relay})} &= G.M + t_{(\text{fastest})}
 \end{aligned}$$

A grading margin on 0.35s was used.

X. SIMULATION OF CURRENT NETWORK AND SOLUTION NETWORK

The following figure shows the current MV ring mains network at Aberdare Cables simulated on the DigSilent software package. The black arrows point to the locations of all the non-directional plain overcurrent relays. All the other relays installed in the network are either clock-wise directional or anti-clock-wise directional relays.

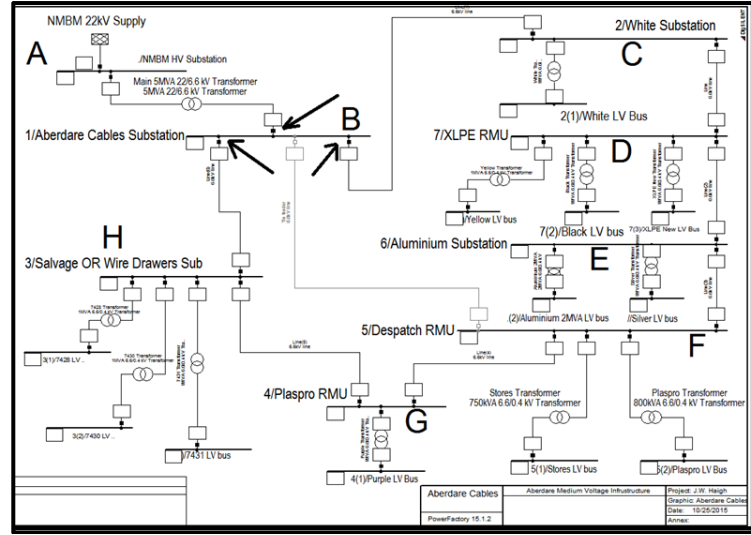


Figure 10.1

The following figure depicts the simulation of what the MV network would look like with the ORC generator included. As seen below, the two substations connected to the ORC generator are Salvage/Wire drawers Substation and Plaspro RMU. The rest of the substations form a new ring that is isolated from the two substations connected to the ORC generator.

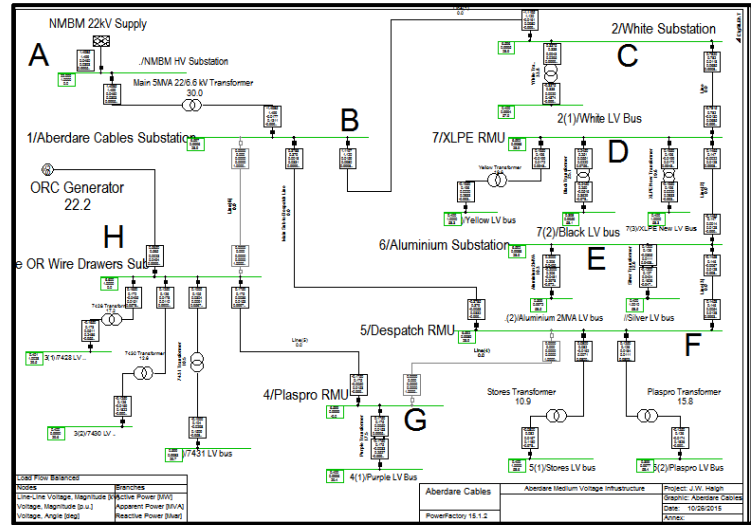


Figure 10.2

The directional relays were set up separately according to the direction of energy flow they experience. For example; the clock-wise directional relays were set up by disconnecting the circuit breaker at the Aberdare Cables Substation that connects the Substation to the feeder B-H. Then minimum and maximum faults were simulated from the most downstream zone to the most upstream zone to ensure that all the clockwise relays were set up for the worst case scenario with regards to fault currents and load currents. The figure below is an example of one of the relay overcurrent plots for a clockwise maximum fault at the most downstream feeder.

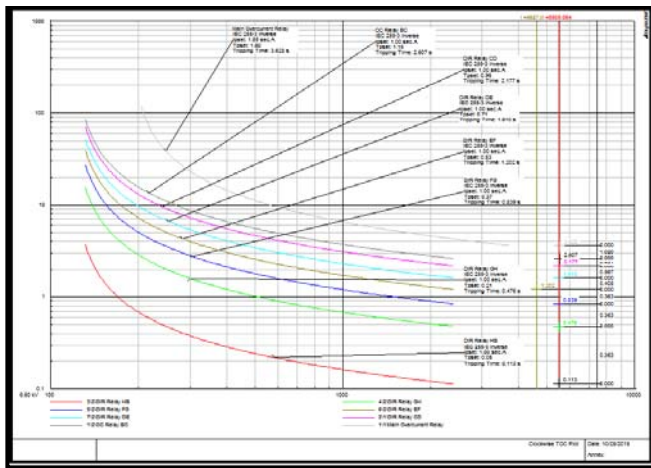


Figure 10.3

As seen in figure 10.3, the most downstream relay rightfully responds first to the downstream fault. The upstream relays respond afterwards while observing the grading margin of 3.5 seconds.

XI. CONCLUSIONS

In conclusion, this project has simulated the current MV ring mains network solving the problem of the current network not being simulated. If any expansions or changes are to be made in the future, these expansions or changes can now first be made on DigSilent Power Factory to see how those expansions of changes will affect the system.

Two Excel spreadsheets have been developed to aid with the calculations. One of the spreadsheets deals with the calculation of the positive, negative and zero sequence impedances for the Aberdare Cables MV Ring Mains system. The second spreadsheet takes the positive, negative and zero sequence impedances obtained from the first spreadsheet and calculates Symmetrical and asymmetrical fault currents and voltages for the specific sequence impedances entered in as inputs.

The solution proposed in this project results in there being two sets of relay settings (one set of settings for when the generator is operational and one set of settings for when the boiler room is undergoing maintenance and the generator is NOT operational). It is recommended that the engineering

personnel responsible for changing the settings to accommodate these two conditions are qualified personnel who are in possession of the necessary qualifications.

XII. REFERENCES

- [1] B. K. Bose, "Global Warming: Energy, Environmental Pollution, and the Impact of Power Electronics," *Industrial Electronics Magazine, IEEE*, vol. 4, pp. 6-17, 2010.
- [2] P. Nag, *Power Plant Engineering*. New Delhi: Tata McGraw Hill Education Private Ltd, 2012.
- [3] B. F. Tchance, P. Loonis, M. Petrisans, and H. Ramenah, "Organic Rankine cycle systems Principles, opportunities and challenges," in *Microelectronics (ICM), 2013 25th International Conference on*, 2013, pp. 1-4.
- [4] D. Pintacsi and P. Bihari, "Investigation of a low-grade industrial waste heat recovery system," in *Energy (IYCE), 2013 4th International Youth Conference on*, 2013, pp. 1-7.
- [5] P. P. Systems, "Organic Rankine Cycle Technology," *Combined Cycle Journal*, 2015.
- [6] I. Obernberger, P. Thonhofer, and E. Reisenhofer, "Description and evaluation of the new 1000kW Organic Rankine Cycle process integrated in the biomass CHP plant in Lienz, Austria," *Euro Heat and Power*, vol. 10, p. 17, 2002.
- [7] (2013, 22/03/15). *Industrial Generator Frequently Asked Questions*. Available: http://www.dieselserviceandsupply.com/generator_faq.aspx
- [8] M. V.K., *Principles of power system*, 4th ed. New Delhi, India: S. Chand & Company LTD, 2012.
- [9] S. D. Umans, *Fitzgerald & Kingsley's Electric Machinery*, 7th ed. Singapore: McGraw-Hill Education, 2014.
- [10] S. J. Chapman, *Electric Machinery Fundamentals*, 5th edition ed. Asia: Mc Graw Hill, 2012.
- [11] E. M. Software. (2014, 23/04/15). *Power Studio Scada Deluxe*. Available: <http://circuitur.com/en/products/measurement-and-control/energy-management-software/powerstudio-scada-deluxe-detail>
- [12] (2015, 29/04/15). *DigSilent PowerFactory*. Available: <http://www.digsilent.de/index.php/products-powerfactory.html>
- [13] D. S. Nair and S. Reshma, "Optimal coordination of protective relays," in *Power, Energy and Control (ICPEC), 2013 International Conference on*, 2013, pp. 239-244.
- [14] P. Yan, I. Voloh, and R. Wei, "Protection issues and solutions for protecting feeder with distributed generation," in *Protective Relay Engineers, 2013 66th Annual Conference for*, 2013, pp. 92-111.
- [15] H. M. Sharaf, H. H. Zeineldin, D. K. Ibrahim, and E. E. D. Abo El Zahab, "Protection coordination of directional overcurrent relays considering fault current direction," in *Innovative Smart Grid Technologies Conference Europe (ISGT-Europe), 2014 IEEE PES*, 2014, pp. 1-5.

THE IMPORTANCE OF CIRCUIT BREAKER TESTING

A. Munhutu*, J. Van Coller† Igor Djurdjevic‡

*†School of Electrical & Information Engineering, University of the Witwatersrand, Private Bag 3, 2050, Johannesburg South Africa

*‡South African Bureau of Standards, National Electrical Test Facility, 1 Apollo Road, Olifantsfontein Johannesburg South Africa

E-mail: *auxilia.munhutu1@students.wits.ac.za †john.vancoller@wits.ac.za ‡igor.djurdjevic@sabs.co.za

Abstract: It is proposed that an in-depth study be done to explore the ways in which the test capabilities for switchgear and transformers can be improved in South Africa. The research will focus on tests done on LV, MV and HV Switchgear and Transformers, and those that manufacturers and would-be manufacturers in industry need but are currently not being done. The study will cover aspects of the layout, design and operation of the Short Circuit Laboratory at the National Electrical Test Facility (NETFA) in South Africa in an attempt to provide guidelines for expansion or process improvements in order to satisfy current and future demands in industry based on NETFA's existing equipment and test capability. It will involve a detailed look at existing IEC, SABS and other standards; assess to what extent NETFA is testing to those specifications and explore the reasons why some tests are not being conducted. Circuit breakers serve a very important role in the transmission and distribution network. Their reliability is crucial for the smooth and efficient supply of electrical energy. To ensure this, they need to be tested to make sure that they are able to do the work that they are designed for, and later to check that they are still in good operational mode. This paper seeks to highlight the importance of putting circuit breakers through type testing, routine testing and in field maintenance; as well as to explain ways in which this may be improved in South Africa.

Keywords: Circuit Breakers, Testing, Circuit Breaker Maintenance

1. INTRODUCTION

Circuit breakers are placed at key points of the electrical energy transmission and distribution system and therefore need to be reliable. Circuit breaker failure can expose people to serious harm. It is therefore imperative that all circuit breakers that go out into the market be tested by an impartial, independent test facility to check their compliance to compulsory specifications and other national as well as international standards.

Testing can be done at various stages in the life of a Circuit Breaker, including:

- Development
- Production
- Commissioning
- Maintenance/fault tracing
- After service (re-commissioning)

2. TYPE TESTS

Circuit breakers provide the last line of defence for the entire electrical system, and hence having great confidence in their performance is crucial. This assurance in their performance can only be achieved from years of experience or from rigorous testing that simulates the conditions that the circuit breakers face in the field. Previously most of this testing was done directly in the field using the power line itself to supply the required current. Although this is still being practiced, for the most part, tests are done in dedicated laboratories, using generators specially designed for short circuit testing.

When a circuit breaker is type tested by an independent test facility, it gives the manufacturer confidence in their product, and their clients also get the quality assurance they need that the circuit breakers they are purchasing are not going to fail to perform under the conditions specified by the manufacturer. Under the type test programs, they need to be tested again after a certain period to ensure that they are still complying with the relevant specifications. At times, for instance, the insulation material or other parts of the breaker used in the manufacturing process may have been changed due to unavailability or to save costs. Testing this product again is very important, as these changes may affect the electrical and/or mechanical performance of the circuit breakers.

Type tests are conducted to prove a circuit breaker's capabilities and to confirm its assigned ratings. Representatives from a manufactured lot are used for type tests. Type tests include [5]:

- Mechanical operation test
- Temperature rise tests
- Dielectric tests
 - Power frequency voltage test
 - Impulse voltage test
- Measurement of resistance of the main circuits
- Short Circuit tests
 - Short-time withstand current and peak withstand current test
 - Short circuit current making and breaking test

2.1 Short-Circuit Tests

Short Circuit tests include breaking capacity tests, making capacity tests, duty cycle tests and short time and peak current withstand tests. Short circuit testing, is one of the most crucial and intricate activities that have to be done at the development stage. It is also significant from a technical engineering design perspective because, in spite of all that is known today about circuit interruption and the ability to model the process, modelling itself is based, in large part, on experimental findings. This makes testing the essential tool in the development of circuit breakers [1].

A typical circuit for this test is shown below:

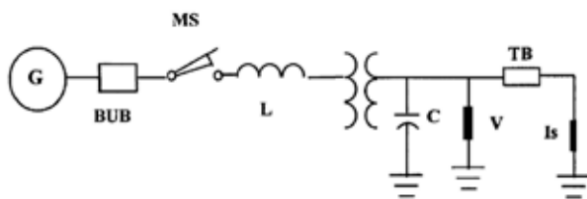


Figure 1

G – Power source (utility supply/ short circuit generators)
 BUB – Back Up Breaker
 MS – Make Switch
 L – Current limiting reactors
 C – TRV Capacitors
 V – Voltage dividers
 TB – CB under test
 Is – Shunts

Due to the necessary levels of power, the difficulty of the tests and the very high costs involved, a lot of leeway is given as far as short circuit current design testing of a circuit breaker is concerned. Even at the biggest test stations, the total power needed to test circuit breakers may be unachievable; therefore alternate approaches that give the same results but involve less power had to be developed [1].

3. ROUTINE TESTS

Once the design features and quality of a circuit breaker have been proven, further tests are required on individual circuit breakers of that design, called routine tests. Routine tests are performed by the manufacturer on each circuit breaker to check for defects in materials and confirm correct construction. Routine tests include [5]:

- Dielectric test on main circuit
- Measurement of resistance of main circuits
- Mechanical Operating tests
- Design and visual checks

- Tests on auxiliary and control circuits

Through participation in such programmes the quality of standards can also be improved through suggestions from participants that may include indicating where there may be standard gaps.

4. FIELD TESTING AND MAINTENANCE

Type testing and routine tests alone are not enough. Circuit breakers tend to require regular maintenance because they consist of several moving parts. Planned maintenance and testing of circuit breakers in the field reduce downtime due to unscheduled maintenance and enhance circuit breaker reliability. If a problem is picked up during scheduled maintenance and testing, this will alert the maintenance department to check for more faulty circuit breakers. This will improve the life expectancy of the circuit breakers. Circuit breakers have to function within very small tolerances when a fault is sensed in the network. Even if a circuit breaker has not operated for several years, it still needs to interrupt fault currents efficiently when the situation calls for it; therefore regular testing is important to check that it can still perform its intended function.

According to Omicron [3], a provider of products and services for testing, diagnostics and monitoring of assets, “typical faults that occur in circuit breakers are short circuits in the coils, damage/wear to the mechanical connections and incorrect behaviour, for example due to worn contacts.” Therefore, circuit breakers need to be regularly and carefully tested. Timing tests, resistance tests across the closed contacts and also motion tests on individual components within the circuit breaker are important in this regard.

Wierman, Rasmuson and Stockton [2] conducted a study looking at the trends and characteristics of circuit breaker common-cause failures (CCF) based on information from the U.S. Nuclear Regulatory Commission's (NRC) CCF Database. When they looked at the method of discovering these faults, they found that, testing discovered 71 events (60 percent), demand led to the discovery of 25 events (21 percent), maintenance 11 events (9 percent), and Inspection 12 events (10 percent). This shows that having a testing program is a successful method of detecting faults.

Although it may seem obvious that testing is crucial in monitoring circuit breakers, in reality companies do not always have a proper maintenance and testing plan. The assumption that new parts are functional and meet the specification requirements they say they do has proven detrimental, due to the presence of fraudulent individuals and organisations in the industry. An example is a 1992 case where the Nuclear Regulatory Commission in the United States, working with the Inspector General was issuing an alert on suspect circuit breakers. The suspected dealer refurbished the exteriors of used circuit breakers from different manufacturers, fabricated circuit breaker

data and sold them as new. "These breakers had experienced premature tripping, failure to trip (some breakers were not of proper amperage, i.e., mislabelled), and some had exploded." [6] Fortunately the Kennedy Space Centre (KSC), a client who purchased these circuit breakers intending to use them in supporting the Space Shuttle program, had in place a maintenance and test plan for circuit breakers, that enabled them to detect the circuit breaker faults. Maintenance programs that include the testing of circuit breakers before and during installation will save the end user a lot of money.

5. STANDARD SPECIFICATIONS

Circuit breaker design and operation as well as type and routine tests are defined by international standards such as:

IEC 62271-100:2013 - High-voltage switchgear and controlgear. Part 100: Alternating-current circuit breakers
IEC 60947-1: 2015 Low-voltage switchgear and controlgear Part 1: General rules

IEC 60947-2: 2014 Low-voltage switchgear and controlgear Part 2: Circuit-breakers

IEC 60898-1 2015 Electrical accessories – Circuit-breakers for overcurrent protection for household and similar installations – Part 1: Circuit-breakers for a.c. operation

ANSI/IEEE C37 - Guides and Standards for Circuit Breakers, Switchgear, Relays, Substations, and Fuses

IEC/TR 62063 ed1.0 (1999-08) TC/SC 17A - High-voltage switchgear and controlgear - The use of electronic and associated technologies in auxiliary equipment of switchgear and controlgear

Compulsory specifications in particular countries, such as VC8036:2006 Circuit-breakers for South Africa are made available on a non-commercial basis in order to promote public education and public safety, and a better informed citizenry.

6. CONCLUSION

The utility is there to generate power, transmit it and distribute it with maximum availability, while maintaining acceptable levels of power quality and safety and keeping losses at a minimum. Circuit Breakers play an important role in ensuring this; and are very important for the function of electric power supply systems. Circuit breakers often need to perform their duties within some tens of milliseconds, after months, perhaps years of idly being in circuit. It is very important to test them to ensure that they can do this, because the cost of damage caused by a malfunctioning circuit breaker can be astronomical, often reaching millions of rands.

REFERENCES

- [1] Garzon, Rueben D. High Voltage Circuit Breakers: Design and Applications. CRC Press 2002.

- [2] Wierman T. E., Rasmuson D. M., Stockton N. B. "Common-Cause Failure Event Insights: Circuit Breakers" U.S. Nuclear Regulatory Commission Office of Nuclear Regulatory Research May 2003
- [3] Omicron. "Circuit Breaker/Switchgear Testing." 25 August 2015 < <https://www.omicron.at/en/products/switchgear-circuit-breaker/>>
- [4] "Routine Test of Circuit Breakers" Online Electrical Engineering pages 1-7. 17 August 2015 < <http://www.electrical4u.com/routine-test-of-circuit-breakers/>>
- [5] IEC 62271-100:2013 - High-voltage switchgear and controlgear. Part 100: Alternating-current circuit breakers
- [6] NASA. "Maintenance & Test Criteria for Circuit Breakers." AT33-AT37
- [7] Megger. "Circuit Breaker Testing Guide." Pages 6-9
- [8] Renaudin Thomas, Circuit breaker testing – New Approach. SEEI conference Sustainable Energy Africa. (n.d.). Retrieved June 26, 2014, from Sustainable Energy Africa: <http://www.sustainable.org.za/>.
- [9] Cousins T, Valentim L, Design and manufacture of testing equipment for switchgear. Vector April 2008 pages 42-46.

Improving the Overcurrent and Earth Fault Protection in the NMMU's Multiple Ring Distribution Network

Timothy de Vos

Electrical Department, Nelson Mandela Metropolitan University
Port Elizabeth, South Africa
s208002171@live.nmmu.ac.za

Anthony Marks

Electrical Department, NMMU
Port Elizabeth, South Africa
Anthony.Marks@nmmu.ac.za

Abstract— This paper analyses a protection network with multiple rings. Overcurrent, Earth Fault and Differential Protection techniques are used and methods of improving these protection techniques are investigated and analysed. When a fault occurs, the protection scheme is required to trip as quickly as possible while still being accurately selective. Should too many relays have to trip in a sequence before the supply authority's protection scheme takes over, the TMS of the slowest relay may be slower than the supply authority's TMS and this results in an ineffective protection design. The analysis shall look at methods of ensuring that requirement is met.

Keywords— Overcurrent Protection, Earth Fault, Earth Fault Protection, Inverse Definite Minimum Time, IDMT, Differential Protection, Zero Sequence Impedance, Yyn0 Transformer

I. INTRODUCTION

The Nelson Mandela Metropolitan University's (NMMU) South Campus was built in 1974 [1, 2] and the majority of the Medium Voltage (MV) infrastructure, belonging to the university, was installed at the same time and has not been upgraded since. This has resulted in unacceptable reliability and safety of the equipment based on tests done in 2014 by a private consulting firm [2]. This was verified during a site visit in 2015, where it was confirmed that many of the switchgear and differential protection relays were decommissioned [2].

Three alternative solutions to this problem were investigated. These solutions were calculated by hand and simulated on DIGSILENT PowerFactory with correct transformer information, loads and cables. The analysis on the results of these simulated solutions is discussed.

II. FAULT LEVELS

The short circuit fault current, or fault level, at each substation was calculated using the Per Unit System of fault current analysis due to the familiarity with the process and its widespread implementation [2-5].

The fault level at the 132 kV busbars, in the supplying 132/11 kV Substation, is 1.86kA with a capacity of 426 MVA in winter and 1.84 kA with a capacity of 420 MVA in summer, from the external grid feeding in [2][6].

The two 132kV/11kV parallel supply transformers, within the Summerstrand Substation, are of the Yyn0 vector group [2, 6]. The 11kV/0.4kV distribution transformers, within the university, are of the Dyn11 vector group [2]. Owing to the

university having harmonics due to non-linear loads, e.g. computer centres for students etc., the 30° shift nullifies the 3rd harmonic and prevents it from being reflected on the delta side of the transformer [2, 7].

The earthed star point of the Dyn11 transformers provides an earth point for the LV network. The earth for the 11kV network is provided by the supply Yyn0 transformers in the Summerstrand Substation. The Yyn0 transformers are earthed via a NER [2]. The fault current is therefore limited through this NER. The value of the NER is 3.175Ω [2, 6].

Cable resistance was not ignored in paper based fault calculations as the reactance of the cable was not at least three times greater than the resistance [2, 4].

When calculating symmetrical three phase short circuit faults, only the positive sequence impedance was used in calculations [2, 3].

Unbalanced single phase to earth faults have positive sequence, negative sequence and zero sequence impedance components [2, 3]. When the paper based fault calculations were performed, negative sequence impedance calculations were assumed to be equal in magnitude, but opposite in phase rotation, to the positive sequence impedance [2, 3]. The zero sequence impedance was calculated with a zero sequence impedance diagram. When drawing the zero sequence diagrams, magnetising impedance is generally ignored. This is an exception in the case where the transformer is star/star and either or both of the neutrals are earthed [2, 3, 8, 9]. This was the case with the Yyn0 Summerstrand Substation Transformers.

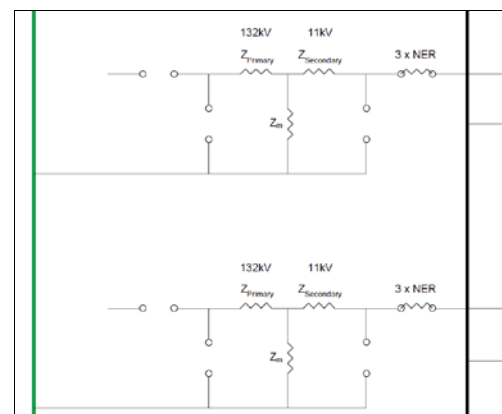


Fig. 1 Zero Sequence Diagram: Yyn0 Transformers showing the inclusion of the magnetising impedance. [2]

Due to the absence of ampere turns, the earth fault current flows through the air, tank and other conductive parts of the transformer [2, 3, 8, 9]. This is the reason the magnetising impedance was factored into the calculations [2, 3, 8, 9]. The transformer is of 3 limb construction and therefore the magnetising impedance is 100 times the transformer's zero sequence impedance [2, 9]. The zero sequence impedance of the transformer is 80% of the transformer positive sequence impedance [2, 3, 8, 9]. The magnetising impedance, zero sequence impedance and NER values are added together when doing zero sequence impedance calculations.

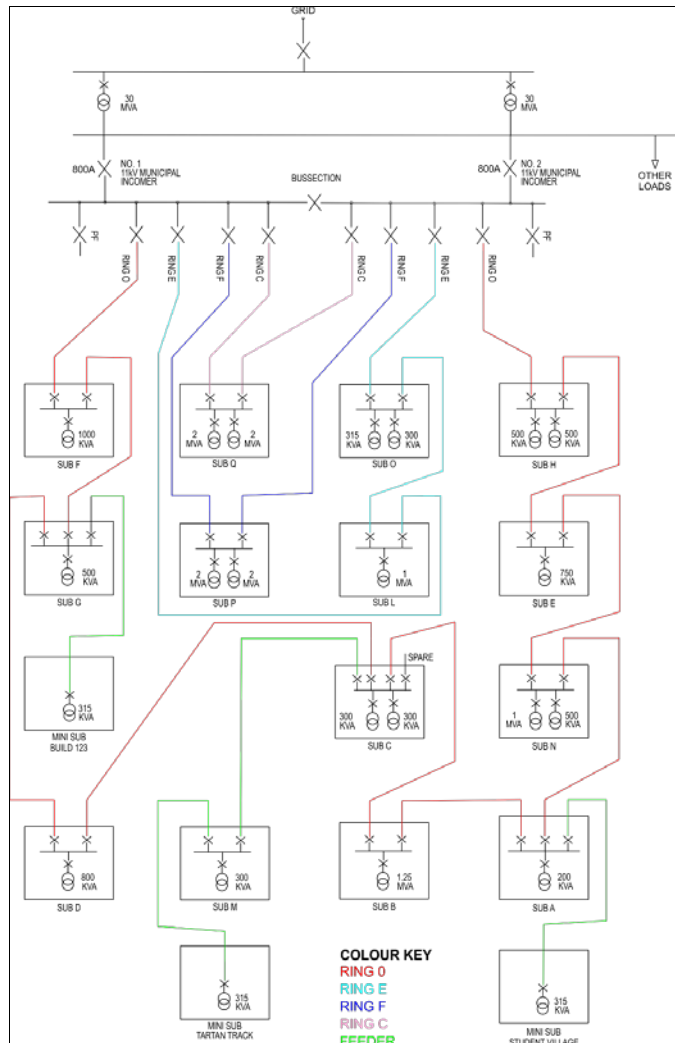


Fig. 2 The current NMMU South Campus 11kV Reticulation Layout (Solution 1). [2]

III. OVERCURRENT AND EARTH FAULT (IDMT) PROTECTION

Grading Protection or Inverse Definite Minimum Time (IDMT) protection isn't always effective in complex networks. For this reason, Unit or Differential Protection is used [3]. Differential protection measures the difference in currents between the outgoing and incoming terminals of the feeder or transformer being protected [3]. Backup protection is required in an effective protection scheme. Overcurrent and Earth Fault (IDMT) Protection acts as backup protection to the primary

Differential Protection [2]. Differential Protection is not discussed, but only briefly mentioned, in this paper.

The grading margin between relays determines the time of operation between two adjacent relays. The grading margin depends on these factors [3, 4] [2]:

- relay timing errors
- relay disk momentum or overshoot
- CT errors
- circuit breaker arc clearing time
- a safety margin.

A grading margin of 0.3 seconds is employed between the digital IDMT relays used in this study [2, 3, 14]. There were applications where a high set relay element was employed to clear faults quicker than usual [2, 3].

For earth fault protection, on transformers and feeders, the grading margin remained as 0.3 seconds, as discussed above, but the minimum operating current for the earth fault protection was calculated from 30% of the rated current [2, 3].

At times, a fault current can flow in both directions [3]. This occurs in rings and with parallel feeders. In this case, directional relays were employed [2]. While normal IDMT relays require CTs, directional IDMT relays require a CT and VT [3].

IV. MODELLING OF THE SYSTEM

A. Solution 1

Maintain the current MV network infrastructure design (four ring distribution) but install new fibre pilot wires for differential protection. In addition, new switchgear, panels and differential, over current and earth fault protection settings were designed [2].

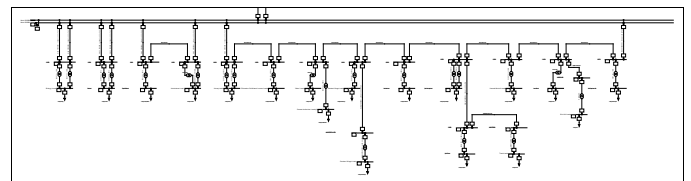


Fig. 3 Solution 1—Four Ring Layout

B. Solution 2

Redesign of the MV network infrastructure design entirely with a new six ring main layout. The installation shall utilise fibre pilot wires for differential protection. In addition, new switchgear, panels and differential, over current and earth fault protection settings were designed.

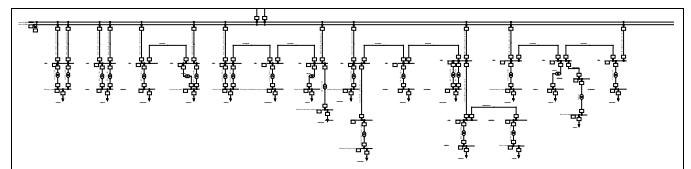


Fig. 4 Solution 2—Six Ring Layout

C. Solution 3

Redesign of the MV network infrastructure design entirely with a new nine ring main layout. The installation shall utilise fibre pilot wires for differential protection. In addition, new switchgear, panels and differential, over current and earth fault protection settings were designed.

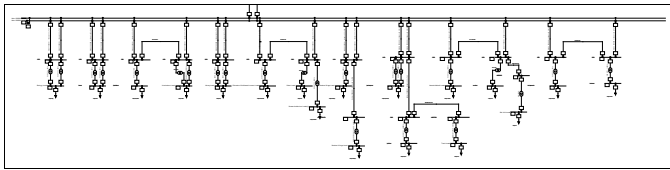


Fig. 5 Solution 3— Nine Ring Layout

V. VALIDATION RESULTS

The results from DigSILENT PowerFactory for normal load flows and short circuit faults are analysed below to show that the protection scheme proposed operates correctly and as designed. Not all feeders, relays, fuses and sections shall be documented here but there will be enough to establish the trustworthiness of the design and these results shall act as a model for the rest of the protection scheme.

A. Solution 1: Overcurrent IDMT Relay Settings: Data Collection, Analysis and Interpretation

1) Fault Simulated at 50% of Radial Feeder 3

Current will flow from the supply to the fault simulated at 50% of Radial Feeder 3.

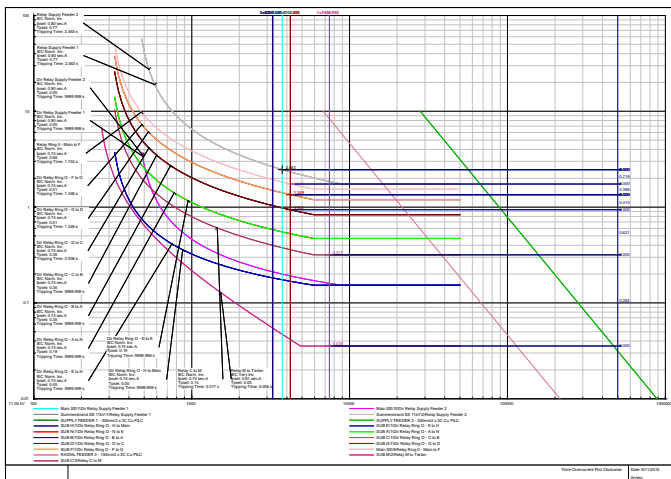


Fig. 6 Solution 1 Overcurrent Radial Feeder 3 Clockwise Fault Time Overcurrent Plot [2]

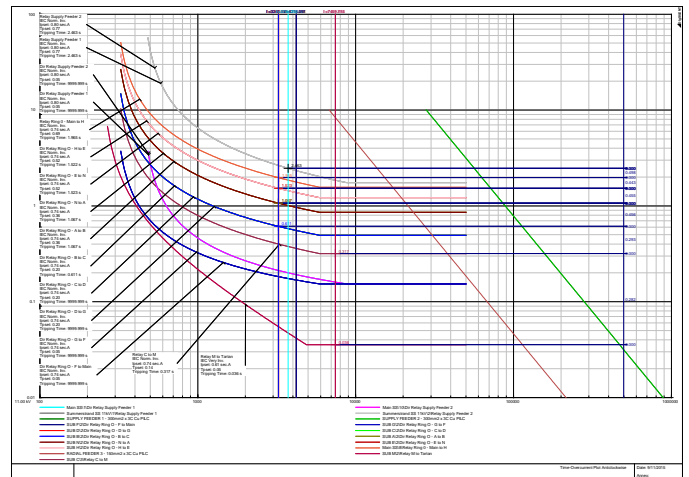


Fig. 7 Solution 1 Overcurrent Radial Feeder 3 Anticlockwise Fault Time Overcurrent Plot [2]

TABLE I. RELAY TRIP TIMES AND ANALYSIS

Relay	Trip Time (Seconds)	Analysis
Relay M to Tartan	0.036	Relay should trip first.
Relay C to M	0.317	Relay acts as backup protection to Relay M to Tartan tripping 0.282 seconds later.
Anticlockwise Group 2: Dir Relay Ring O – B to C	0.611	Relay acts as backup protection to Relay C to M tripping 0.294 seconds later.
Clockwise Group 2: Dir Relay Ring O – D to C	0.938	Relay acts as backup protection to Anticlockwise Group 2 Relays tripping 0.327 seconds later.
Anticlockwise Group 3: Dir Relay Ring O – A to B	1.067	Relay acts as backup protection to Clockwise Group 2 Relays tripping 0.127 seconds later.
Anticlockwise Group 3: Dir Relay Ring O – N to A	1.067	Relay acts as backup protection to Clockwise Group 2 Relays tripping 0.127 seconds later.
Clockwise Group 1: Dir Relay Ring O – G to D	1.349	Relay acts as backup protection to Anticlockwise Group 3 Relays tripping 0.282 seconds later.
Clockwise Group 1: Dir Relay Ring O – F to G	1.348	Relay acts as backup protection to Anticlockwise Group 3 Relays tripping 0.281 seconds later.
Anticlockwise Group 4: Dir Relay Ring O – E to N	1.523	Relay acts as backup protection to Clockwise Group 1 Relays tripping 0.175 seconds later.
Anticlockwise Group 4: Dir Relay Ring O – H to E	1.522	Relay acts as backup protection to Clockwise Group 1 Relays tripping 0.174 seconds later.
Clockwise Group 0: Relay Ring O – Main to F	1.744	Relay acts as backup protection to Anticlockwise Group 4 Relays tripping 0.222 seconds later.
Anticlockwise Group 5: Relay Ring O – Main to H	1.965	Relay acts as backup protection to Clockwise Group 0 Relays tripping 0.221 seconds later.
Relay Supply Feeder 1	2.463	Relay acts as backup protection to Anticlockwise Group 5 Relays tripping 0.498 seconds later.
Relay Supply Feeder 2	2.463	Relay acts as backup protection to Anticlockwise Group 5 Relays tripping 0.498 seconds later.

The slow final feeder tripping time of 2.463 isn't within the supply authority's requirements.

The following applies to all subsequent solution analysis:

- The correct tripping sequence is taking place. The relays are selective and discriminate with each other. The plot indicates that the cables will not be damaged before the relays trip.
- The relays, looking for a fault in the opposite direction, should not detect the fault and do not trip.
- Dir Relay Supply Feeder 1 and 2 are only for the protection of the supply feeders, hence the crossing of the IDMT curve with other relay curves. They are shown on time overcurrent plots to indicate that they will not trip for faults except for faults in the main supply ring.
- The minimum grading margin requirement of 0.3 seconds is met in the majority of the cases. Where it has not been met, in order to grade the large number of relays, this is acceptable as an exception.
- There are rare cases where relays trip in just over 0.1 seconds, which is much lower than the desired grading margin. This is not ideal but the protection scheme will still trip in the correct sequence. In order for these relays to be required to trip, the primary differential protection and at least four downstream IMDT relays would have to fail, which is an unlikely scenario.

B. Solution 1: Earth Fault IDMT Relay Settings: Data Collection, Analysis and Interpretation

Current will flow from the supply to the fault simulated at 50% of Radial Feeder 3.

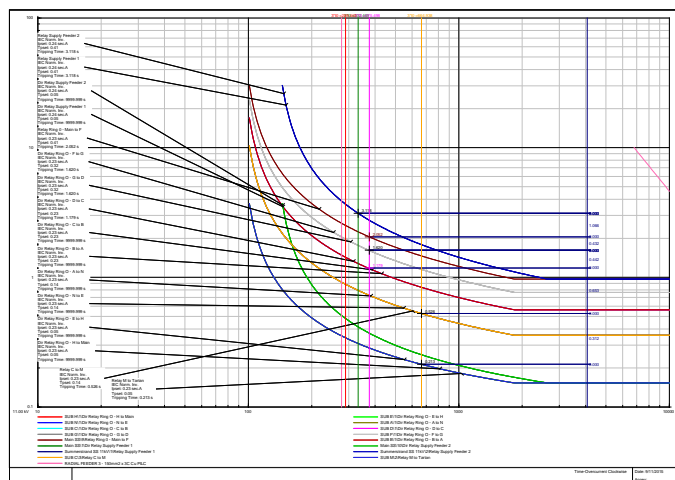


Fig. 8 Solution 1 Earth Fault Radial Feeder 3 Clockwise Fault Time Overcurrent Plot [2]

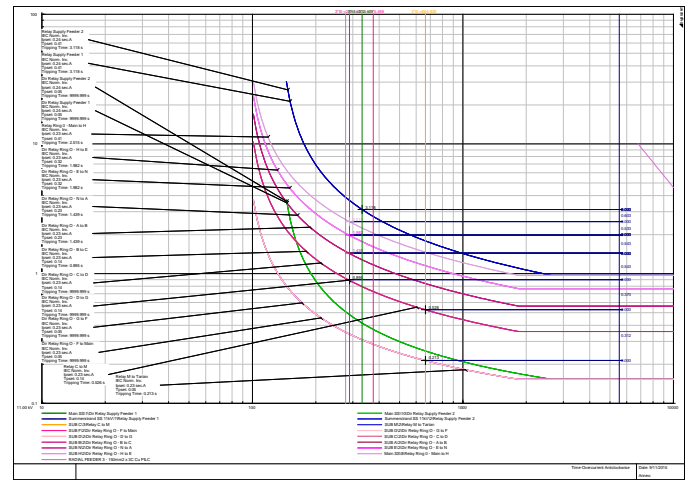


Fig. 9 Solution 1 Earth Fault Radial Feeder 3 Anticlockwise Fault Time Overcurrent Plot [2]

TABLE II. RELAY TRIP TIMES AND ANALYSIS

Relay	Trip Time (Seconds)	Analysis
Relay M to Tartan	0.213	Relay should trip first.
Relay C to M	0.526	Relay acts as backup protection to Relay M to Tartan tripping 0.313 seconds later.
Anticlockwise Group 2: Dir Relay Ring O – B to C	0.895	Relay acts as backup protection to Relay C to M tripping 0.369 seconds later.
Clockwise Group 2: Dir Relay Ring O – D to C	1.179	Relay acts as backup protection to Anticlockwise Group 2 Relays tripping 0.284 seconds later.
Anticlockwise Group 3: Dir Relay Ring O – A to B	1.439	Relay acts as backup protection to Clockwise Group 2 Relays tripping 0.260 seconds later.
Anticlockwise Group 3: Dir Relay Ring O – N to A	1.439	Relay acts as backup protection to Clockwise Group 2 Relays tripping 0.260 seconds later.
Clockwise Group 1: Dir Relay Ring O – G to D	1.620	Relay acts as backup protection to Anticlockwise Group 3 Relays tripping 0.181 seconds later.
Clockwise Group 1: Dir Relay Ring O – F to G	1.620	Relay acts as backup protection to Anticlockwise Group 3 Relays tripping 0.181 seconds later.
Anticlockwise Group 4: Dir Relay Ring O – E to N	1.982	Relay acts as backup protection to Clockwise Group 1 Relays tripping 0.362 seconds later.
Anticlockwise Group 4: Dir Relay Ring O – H to E	1.982	Relay acts as backup protection to Clockwise Group 1 Relays tripping 0.362 seconds later.
Clockwise Group 0: Relay Ring O – Main to F	2.052	Relay acts as backup protection to Anticlockwise Group 4 Relays tripping 0.070 seconds later.
Anticlockwise Group 5: Relay Ring O – Main to H	2.515	Relay acts as backup protection to Clockwise Group 0 Relays tripping 0.463 seconds later.
Relay Supply Feeder 1	3.118	Relay acts as backup protection to Anticlockwise Group 5 Relays tripping 0.603 seconds later.
Relay Supply Feeder 2	3.118	Relay acts as backup protection to Anticlockwise Group 5 Relays tripping 0.603 seconds later.

The slow final feeder tripping time of 3.118 isn't within the supply authority's requirements.

C. Solution 2: Overcurrent IDMT Relay Settings: Data Collection, Analysis and Interpretation

1) Fault Simulated at 50% of Radial Feeder 3

Current will flow from the supply to the fault simulated at 50% of Radial Feeder 3.

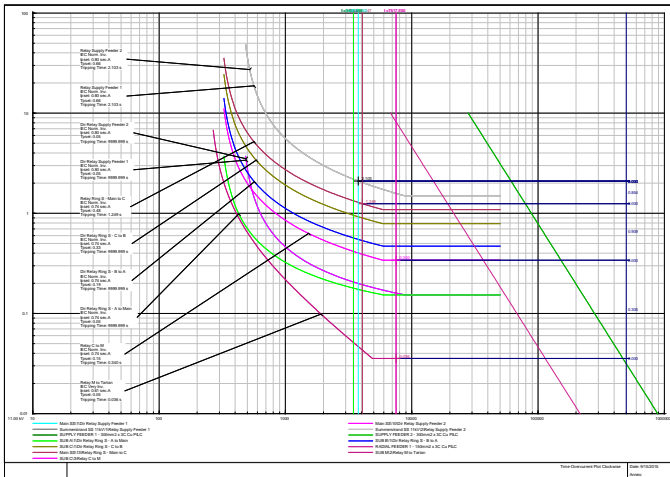


Fig. 10 Solution 2 Overcurrent Radial Feeder 3 Clockwise Fault Time Overcurrent Plot [2]

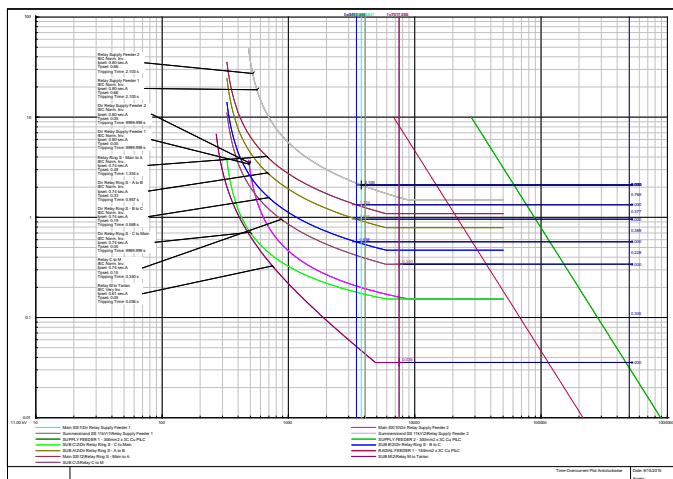


Fig. 11 Solution 2 Overcurrent Radial Feeder 3 Anticlockwise Fault Time Overcurrent Plot [2]

TABLE III. RELAY TRIP TIMES AND ANALYSIS

Relay	Trip Time (Seconds)	Analysis
Relay M to Tartan	0.036	Relay should trip first.
Relay C to M	0.340	Relay acts as backup protection to Relay M to Tartan tripping 0.305 seconds later.
Anticlockwise Dir Relay Ring S – B to C	0.568	Relay acts as backup protection to Relay C to M tripping 0.228 seconds later.
Anticlockwise Dir Relay Ring S – A to B	0.957	Relay acts as backup protection to Clockwise Dir Relay Ring S – B tripping 0.389 seconds later.
Clockwise Relay Ring S – Main to C	1.249	Relay acts as backup protection to Anticlockwise Dir Relay Ring S – A to B tripping 0.292 seconds later.

Relay	Trip Time (Seconds)	Analysis
Anticlockwise Relay Ring S – Main to A	1.334	Relay acts as backup protection to Clockwise Relay Ring S – Main to C tripping 0.085 seconds later.
Relay Supply Feeder 1	2.103	Relay acts as backup protection to Anticlockwise Relay Ring S – Main to A tripping 0.769 seconds later.
Relay Supply Feeder 2	2.103	Relay acts as backup protection to Anticlockwise Relay Ring S – Main to A later 0.769 seconds later.

The slow final feeder tripping time of 2.103 isn't within the supply authority's requirements.

D. Solution 2: Earth Fault IDMT Relay Settings: Data Collection, Analysis and Interpretation

1) Fault Simulated at 50% of Radial Feeder 3

Current will flow from the supply to the fault simulated at 50% of Radial Feeder 3.

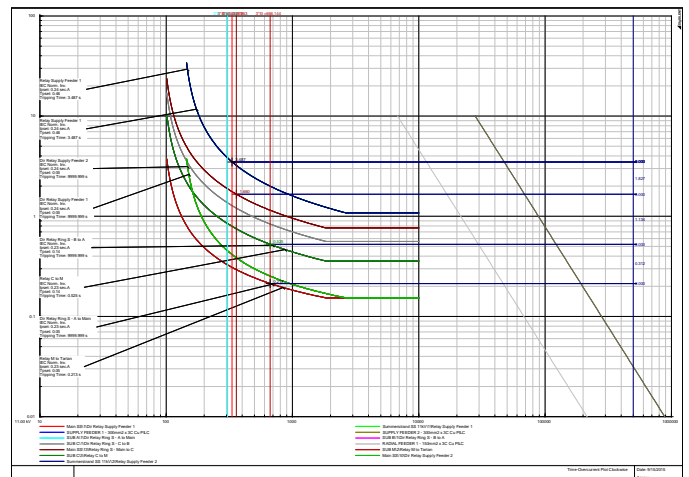


Fig. 12 Solution 2 Earth Fault Radial Feeder 3 Clockwise Fault Time Overcurrent Plot [2]

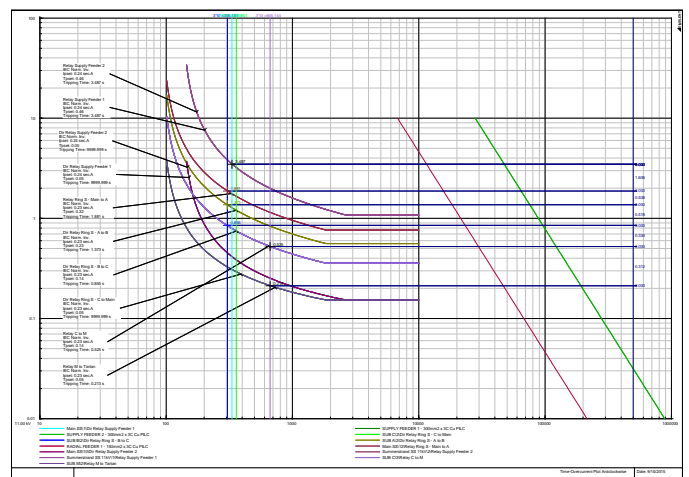


Fig. 13 Solution 2 Earth Fault Radial Feeder 3 Anticlockwise Fault Time Overcurrent Plot [2]

TABLE IV. RELAY TRIP TIMES AND ANALYSIS

Relay	Trip Time (Seconds)	Analysis
Relay M to Tartan	0.213	Relay should trip first.
Relay C to M	0.525	Relay acts as backup protection to Relay M to Tartan tripping 0.312 seconds later.
Anticlockwise Dir Relay Ring S – B to C	0.855	Relay acts as backup protection to Relay C to M tripping 0.330 seconds later.
Clockwise Relay Ring S – Main to C	1.249	Relay acts as backup protection to Anticlockwise Dir Relay Ring S – B to C tripping 0.394 seconds later.
Anticlockwise Dir Relay Ring S – A to B	1.373	Relay acts as backup protection to Clockwise Relay Ring S – Main to C tripping 0.124 seconds later.
Anticlockwise Relay Ring S – Main to A	1.881	Relay acts as backup protection to Anticlockwise Dir Relay Ring S – A to B tripping 0.508 seconds later.
Relay Supply Feeder 1	3.487	Relay acts as backup protection to Anticlockwise Relay Ring S – Main to A tripping 1.606 seconds later.
Relay Supply Feeder 2	3.487	Relay acts as backup protection to Anticlockwise Relay Ring S – Main to A tripping 1.606 seconds later.

The slow final feeder tripping time of 3.487 isn't within the supply authority's requirements.

E. Solution 3: Overcurrent IDMT Relay Settings: Data Collection, Analysis and Interpretation

1) Fault Simulated at 50% of Radial Feeder 3

Current will flow from the supply to the fault simulated at 50% of Radial Feeder 3.

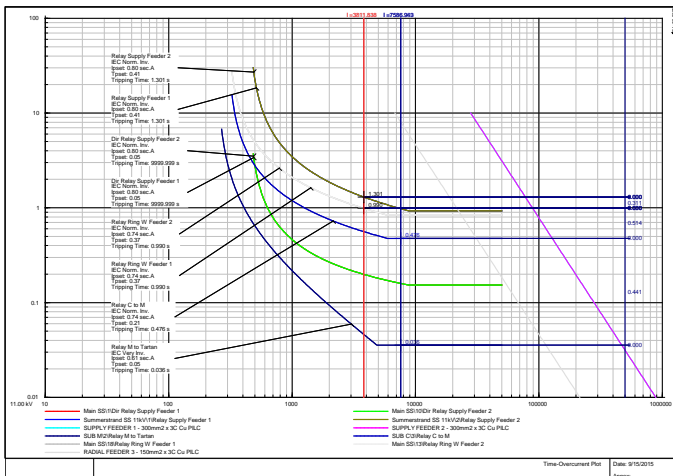


Fig. 14 Solution 3 Overcurrent Radial Feeder 3 Fault Time Overcurrent Plot [2]

TABLE V. RELAY TRIP TIMES AND ANALYSIS

Relay	Trip Time (Seconds)	Analysis
Relay M to Tartan	0.036	Relay should trip first.

Relay	Trip Time (Seconds)	Analysis
Relay C to M	0.476	Relay acts as backup protection to Relay M to Tartan tripping 0.441 seconds later.
Relay Ring W Feeder 1	0.990	Relay acts as backup protection to Relay C to M tripping 0.514 seconds later.
Relay Ring W Feeder 2	0.990	Relay acts as backup protection to Relay C to M tripping 0.514 seconds later.
Relay Supply Feeder 1	1.301	Relay acts as backup protection to Relay Ring W Feeder 2 tripping 0.311 seconds later. This is an improvement over Solution 1 and Solution 2.
Relay Supply Feeder 2	1.301	Relay acts as backup protection to Relay Ring W Feeder 2 tripping 0.311 seconds later. This is an improvement over Solution 1 and Solution 2.

The final feeder tripping time of 1.301 is drastic improvement on Solution 1 and 2 and is acceptable.

F. Solution 3: Earth Fault IDMT Relay Settings: Data Collection, Analysis and Interpretation

1) Fault Simulated at 50% of Radial Feeder 3

Current will flow from the supply to the fault simulated at 50% of Radial Feeder 3.

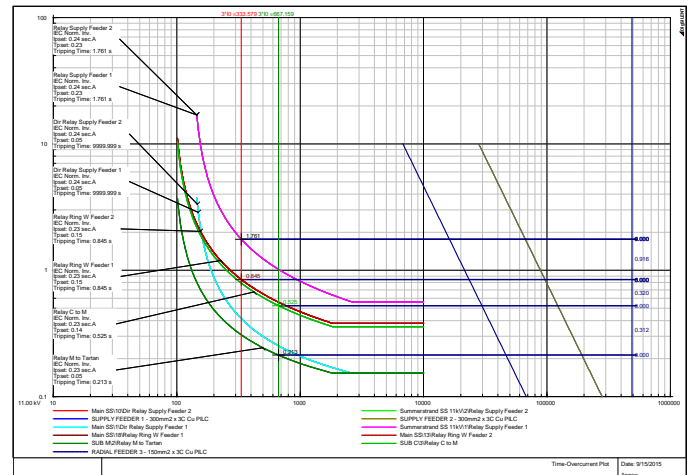


Fig. 15 Solution 3 Earth Fault Radial Feeder 3 Fault Time Overcurrent Plot [2]

TABLE VI. RELAY TRIP TIMES AND ANALYSIS

Relay	Trip Time (Seconds)	Analysis
Relay M to Tartan	0.213	Relay should trip first.
Relay C to M	0.525	Relay acts as backup protection to Relay M to Tartan tripping 0.312 seconds later.
Relay Ring W Feeder 1	0.845	Relay acts as backup protection to Relay C to M tripping 0.320 seconds later.
Relay Ring W Feeder 2	0.845	Relay acts as backup protection to Relay C to M tripping 0.320 seconds later.

Relay	Trip Time (Seconds)	Analysis
Relay Supply Feeder 1	1.761	Relay acts as backup protection to Relay Ring W Feeder 2 tripping 0.916 seconds later. This is an improvement over Solution 1 and Solution 2.
Relay Supply Feeder 2	1.761	Relay acts as backup protection to Relay Ring W Feeder 2 tripping 0.916 seconds later. This is an improvement over Solution 1 and Solution 2.

The final feeder tripping time of 1.301 is a drastic improvement on Solution 1 and 2 and is acceptable.

VI. CONCLUSION AND RECOMMENDATIONS

In the study, paper based overcurrent and earth fault settings were within 10% of overcurrent and earth fault values on the DIGSILENT simulation, with the majority of the settings within a 5% difference. Paper based calculations were only done for Solution 1 and compared with a simulation on DIGSILENT. Once the simulation could be trusted, Solution 2 and 3 could be designed purely on DIGSILENT.

The supply transformers in the NMBM Summerstrand Substation are Yyn0 vector grouping. Due to the absence of ampere turns, the earth fault current flows through the air, tank and other conductive parts of the transformer [3, 8, 9], therefore, magnetising impedance is factored into the earth fault calculations. This is a vague subject with various sources not providing a definitive method for this calculation. Additional expertise or information regarding calculating Yyn0 earth faults would be a welcomed addition to this research. The paper based results correlate with DIGSILENT results for these earth faults using the settings discussed.

IDMT relays trip in the correct sequence from downstream relays to upstream relays. All the relays, in all three solutions, do not trip for normal load currents.

When grading relays in Ring O in Solution 1, the relays had to be grouped in order to lower the tripping times. If this had not been done, upstream relays would have had a very long tripping time. This is anticipated to be about 6 seconds and is unacceptable as a protection model. The downside of tripping relays in groups is that multiple substations shall trip at the same time. This, however, does not mean that one is unable to isolate the fault by a process of elimination.

In the NMBM Summerstrand Substation, the TMS settings on the upstream overcurrent and earth fault relays are 0.44 seconds and 0.24 seconds respectively, which are set by the supply authority. The protection scheme on the current ring layout (Solution 1), and a proposed ring layout (Solution 2), don't have TMS settings of the same or lower value. Only Solution 3 will trip with a TMS very similar to what has been set by the supply authority. This is the preferred solution and is a strong indication that when using IDMT protection in a distribution network with a large number of substations, many smaller rings are preferable to fewer large rings. This solution also avoids the use of grouping relay times together, as was

done in Ring O of Solution 1, which, although it works, is not an idea protection method. The negative side of Solution 3 is that it is costly to move and rearrange ring layouts. Another alternative, not investigated in this research study, is to feed the radial feeders off the smaller rings instead of the Ring O, which will improve the grading times of the relays, while not incurring the large costs of restructuring the ring layouts.

In order to improve on earth fault IDMT settings, it is recommended that a Neutral Earth Compensator (NEC) is installed at NMMU Main Substation. This would enable NMMU infrastructure to use the created earth instead of the earth in the Yyn0 transformers in the NMBM Summerstrand Substation.

When analysing the IDMT relay settings for both overcurrent and earth faults, one can see that IDMT is not the best form of protection when large rings are in the network. It leads to long relay time settings which weakens the strength of the protection scheme. This is why differential protection is recommended as the primary protection method and IDMT protection as the backup protection. Differential protection has a minimum trip time of 50 ms, which is significantly lower than the trip time settings for IDMT. Differential protection was included in the research study but has not been included in this paper as only the improvement of IDMT protection was analysed in this paper.

REFERENCES

- [1] (2015, 2015-03-17). NMMU - History. Available: <http://www.nmmu.ac.za/About-NMMU/Management---Identity/History>
- [2] T. de Vos, "The Redesign of the NMMU South Campus MV Protection Infrastructure and Ring Main Layout with Backup Power Generation," Nelson Mandela Metropolitan University 2015.
- [3] Network protection & automation guide : protective relays, measurement & control, [New ed.]. ed. [Great Britain]: Alstom Grid, 2011.
- [4] A. Marks, "Protection 3 Lecture Notes," ed. Port Elizabeth: Nelson Mandela Metropolitan University, 2013.
- [5] D. Beeman, Industrial power systems handbook: McGraw-Hill, 1955.
- [6] D. Frost, "PR Eng BSc (Eng) GovtCert MSAIEE MIEEEE," ed.
- [7] J. Parmar. (2012, 25 March). Vector Group of Transformer. Available: <http://electricalnotes.wordpress.com/2012/05/23/vector-group-of-transformer/>
- [8] R. Roeper, F. Mitlehner, B. Ehmcke, and A. Webs, Short-circuit currents in three-phase systems: Siemens Aktiengesellschaft, 1985.
- [9] M. J. Heathcote and D. P. Franklin, The J & P Transformer Book: A Practical Technology of the Power Transformer, 12 ed. Linacre House, Jordan Hill, Oxford: Newnes, 1998.
- [10] S. C. Sun and R. E. Ray, "A Current Differential Relay System Using Fiber Optics Communications," Power Apparatus and Systems, IEEE Transactions on, vol. PAS-102, pp. 410-419, 1983.
- [11] O. Bagleybter and S. Subramanian, "Enhancing differential protection stability during CT saturation with Transient Bias," in Developments in Power Systems Protection, 2012. DPSP 2012. 11th International Conference on, 2012, pp. 1-4.
- [12] "615 series," in Technical Manual, K ed: ABB Group, 2014.
- [13] "Line Differential Protection and Control RED615 " in Product Guide, ed: ABB Group, 2014.
- [14] J. Parmar. (2013, 25 March). overcurrent relay | Search Results | Electrical Notes & Articles. Available: <http://electricalnotes.wordpress.com/?s=overcurrent+relay>

Protection Over current Curve plotter with Fault locator application

Y Sithole and B Kotze

Department of Electrical, Electronic and Computer Engineering, Central University of Technology-Free State, Private Bag X20539, Bloemfontein, South Africa, 9300.

Emails: ysitholey@gmail.com and bkotze@cut.ac.za

Abstract: The development of a software application to plot protection coordination curves and provide a distance to fault locator is presented in this paper. The purpose of the application is to aid fault location in power systems. Incorrect tripping of protection relay and fault location on power lines have a significant impact on power system performance. Often protection engineers and technicians need to verify grading of protection relays and to locate faults on power lines. The application developed will allow drawing of protection relay curves to observe coordination of relays. It also has a fault locator for non-homogenous medium voltage networks in distribution which estimates distance to fault given the network topology and measured fault current. The application was developed on Microsoft Excel® using the Visual Basic programming language. This will allow the application to be run on any device supporting Excel, originally planned to run on a smart phone, thus making the software easily accessible. The application allows up to four relay curves to be drawn with a variety of curve types to choose from. The fault locator allows up to four conductor types to be used in the network topology to accurately model the fault path. The fault locator was tested with data obtained from two medium voltage overhead lines and gave satisfactory results.

Keywords: Protection, over current, curve plotter, fault locator, Excel, Visual Basic, medium voltage

1. INTRODUCTION

Any power system is susceptible to short circuit faults that may be induced by natural elements such as lightning or maintenance issues, even human error. These short circuit currents cause thermal stresses which may damage power system equipment. Circuit breakers and their associated relays are deployed across the power system to detect and isolate sections with faults. In a distribution network the isolated section may contain a significantly large customer base which makes it paramount that the fault is located, remedied and supply restored. At times incorrect coordination of protection relays can delay the fault location process, which is undesirable. Distribution networks have long power lines which need to be patrolled when searching for a permanent fault. These long drives also delay the restoration of supply and are also costly.

A software application is proposed to be used on distribution power lines by protection engineers and technicians to plot relay protection curves to aid in coordination (grading). By plotting these curves an assessment can be made as to the correct coordination and allow quick corrections to be made where needed. The application will also be able to afford the user to model a basic distribution power line allowing the selection of up to 4 different conductor types. Using the relay measured fault current the distance to fault will be provided by the application.

2. AIM OF THE PROJECT

The aim of this project is to develop a software application for drawing of protection relay curves to be used in relay coordination assessment and

implementation as well as to provide distance to fault functionality for distribution non-homogeneous medium voltage power lines.

3. BACKGROUND TO THE PROBLEM

3.1 Distribution Power Line Topology

A typical distribution power line is supplied from a single bus bar from the source substation. Figure 1 shows a radial type of network. A variety of conductors can be used on a single line which is the reason why distribution networks are labelled as non-homogenous. pole mounted breaker (PMB) which are a combination of a breaker and relay are installed strategically on the back bone (along conductor 1, 2 and 4) and on major T-off's (conductor 3 and 5) to ensure that only a small portion of the network is removed if a short circuit is detected.

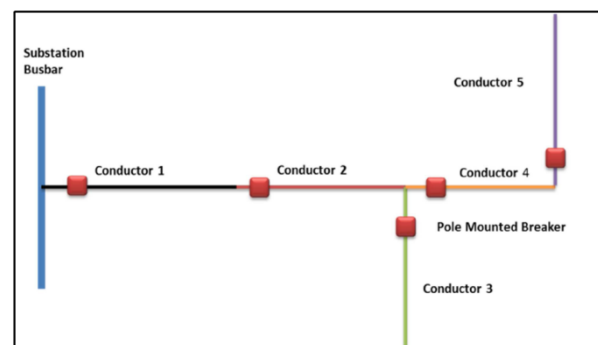


Figure 1: Distribution Power line Topology

3.2 Relay Coordination

Relay coordination is important to ensure that only the section of the power system affected by the short circuit is isolated. Relays can be coordinated using time, current magnitude or a combination of both. The Inverse Definite Minimum Time (IDMT) group of curves is used for this purpose as they provide both current and time coordination. The short circuit current is related to the relay operating time (t_{trip}) indicated by Equation 1 where TM is the time multiplier used to coordinate by time, I_T is the starting or pick-up current used to coordinate by current. I_f represent the fault current as an independent variable. The gradient of the IDMT can be varied by changing the parameters as given in Table 1 [1].

$$t_{trip} = \frac{\beta}{\left(\frac{I_T}{I_f}\right)^\alpha} \times TM \quad (1)$$

Table 1: IEC IDMT Curves

Relay Characteristic	IEC 60255	
	α	β
Standard Inverse	0.02	0.14
Very Inverse	1	13.5
Extremely Inverse	2	80
Long Time Standby Earth Fault	1	120

3.3 Fault Location

Successful fault location in a power system requires good coordination between protection devices coupled with human intervention. Opening of a PMB is the first indication of a short circuit or fault and their strategic positioning indicate the possible location of the fault. Human intervention is then required to patrol the line to locate the fault. This may take a long time as well as long drives due to the complex topology of distribution power lines. Some major T-off on a distribution line may have minor T-off's which do not have PMBs installed. Such T-off's are at times the cause of longer fault location times as they also need to be patrolled. Sectionalisers as well as fault path indicators are sometimes used on the minor T-off's to indicate to the field engineers and technicians where the short circuit flowed [2] [3].

Advanced relays used at the substation incorporate a distance to fault locator that uses the measured current and voltage at the relay point to predict the fault location thus aiding in fault finding. The short coming with these relays is that they do not cater for the non-homogeneous topology of distribution power lines.

4. METHODOLOGY OF THE PROJECT

4.1 Curve Plotter

A software tool was developed in Microsoft Excel® to aid in the protection curve coordination. It allows up to four relays to be coordinated. ANSI/IEEE and IEC IDMT curves as well as the definite time curve are implemented as per Equation 1 and Table 1 respectively. Inputs to be entered by the user to alter the result are the pick-up (I_T) and time multiplier (TM) setting. The other choices are electable.

4.2 Fault Locator

The fault locator function in the application uses a predefined network short circuit versus distance profile to estimate the distance to fault. The basic principle used is ohms law as show in Equation 2. The total impedance in the equation is dependent on the source impedance Z_s , conductor characteristics and its length. The impedance thus determines how much short circuit current can flow in the circuit [4].

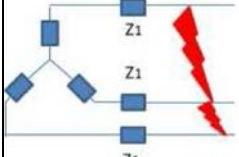
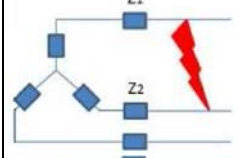
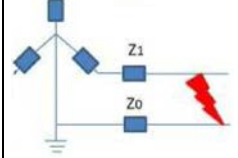
$$V = I_{sc} \times [Z_s + Z(R, X/km \times l)] \quad (2)$$

Re-arranging the equation the distance to fault can be represented as a function of the short circuit current with the conductor kept as constant.

$$l = \frac{V}{[Z(R, X) \times I_{sc}]} - Z_s(km) \quad (3)$$

In a power system sequence impedances of conductors are used to calculate short circuit current based on symmetrical component methods [5]. Table 2 show the equations that are used to calculate the short circuit (SC) current for a 3 Phase, 2-Phase and Single Phase short circuit in the network. Z_1 , Z_2 .

Table 2: Sequence impedance calculation of a SC

Fault Type	Diagram	Equation
Three Phase		$I_{sc} = \frac{U}{\sqrt{3} Z_1 }$
Phase-Phase		$I_{sc} = \frac{U}{ Z_1 + Z_2 } = \frac{U}{ 2Z_1 }$
Phase-Earth		$I_{sc} = \frac{U}{\sqrt{3} Z_1 + Z_2 + Z_0 }$

4.3 Software development in Excel

The software was programmed using the Visual Basic for Applications (VBA) programming language in Microsoft Excel® 2010. VBA was chosen as it provides handling of large data stored in tables and provides in-built functions such as "VLOOKUP" to access data in multi-column multi-row tables. Excel also provides the UserForm functionality to create user interfaces which can be interfaced with the VBA code. The application has three main layers i.e. Data, Application and User Interface. Figure 2 illustrates these layers and the basic functions of each [6].

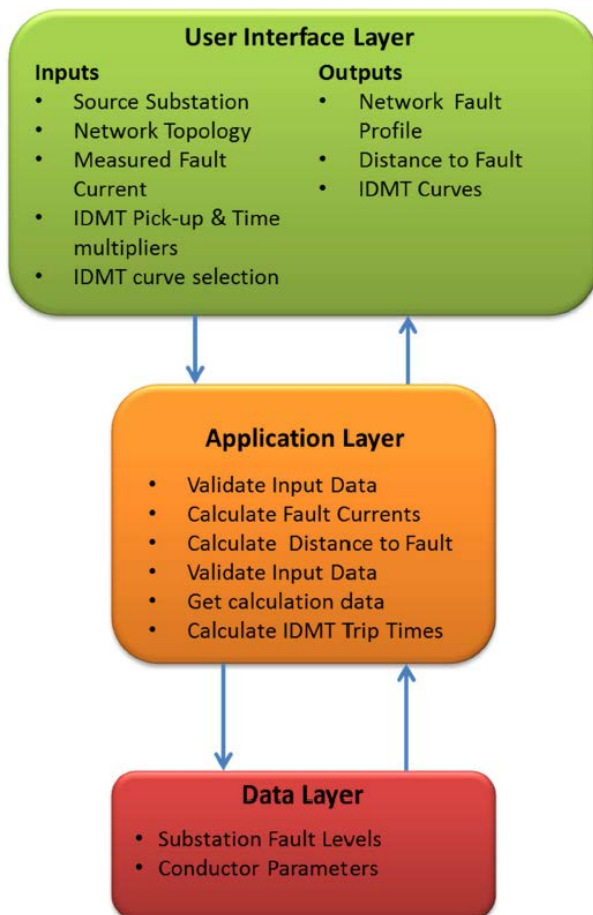


Figure 2: Application design levels

The user Interface allows the user to choose up to four conductor types from a range of conductor types used on distribution lines. The length of each conductor is also required. The user also needs to select the PMB position and the measured fault current for the fault being investigated. The feeder substation 3-phase and single faults are also required as inputs to calculate the source impedance. The application will then draw fault current versus distance curves for 3 phase, phase-phase and single phase faults. From these plots an estimate of the distance to fault is given as an output.

The application then uses this information to plot a fault current versus distance curve for the particular topology selected.

4.4 Data Used

Typical conductor types used on distribution power lines are Hare, Mink, and Fox etc. Measured parameters for these conductors were obtained from Eskom to accurately model the power lines. They were provided in table form with positive (Z1 to Z2) and zero (Z0) sequence impedances per kilometer.

Four different power line topology layouts were also sourced from Eskom to be used for testing. The topology layouts were obtained in two forms. The first is the geographical layout which illustrates the power line distribution as well as conductor types and lengths. These are obtained from the geographical modeling software called Smallworld [7]. The second format was Reni diagrams which are normally used by field staff during fault finding.

The Reni diagram provides details on power line conductors, pole numbers and PMB positions. The Reni diagrams do not have information on conductor lengths, however an assumption is made on span lengths between consecutive line poles of 100m. Thus if there are 10 poles from the substation to the point of interest or where the PMB is located one can estimate a total length of 1000m = 1km.

Fault data was sourced in the form of event logs downloaded from a number of PMB on the power lines. An example of event log is shown in Figure 3.

2015/03/06	03:48:01.23	PM	Lockout
2015/03/06	03:48:01.17	PM	Prot Trip 4
2015/03/06	03:48:01.17	PM	Phase Prot Trip
2015/03/06	03:48:01.17	PM	Prot Group A Active
2015/03/06	03:48:00.40	PM	Pickup
2015/03/06	03:47:58.68	PM	Automatic Reclose
2015/03/06	03:47:28.74	PM	E Max 128 Amp
2015/03/06	03:47:28.74	PM	C Max 447 Amp
2015/03/06	03:47:28.74	PM	B Max 425 Amp
2015/03/06	03:47:28.68	PM	Prot Trip 3
2015/03/06	03:47:28.68	PM	Earth Prot Trip
2015/03/06	03:47:28.68	PM	Prot Group A Active
2015/03/06	03:47:27.78	PM	Pickup
2015/03/06	03:47:25.77	PM	Automatic Reclose
2015/03/06	03:47:14.92	PM	Load Supply OFF
2015/03/06	03:47:10.88	PM	E Max 137 Amp
2015/03/06	03:47:10.88	PM	C Max 448 Amp
2015/03/06	03:47:10.88	PM	B Max 425 Amp
2015/03/06	03:47:10.77	PM	Prot Trip 2
2015/03/06	03:47:10.77	PM	Earth Prot Trip
2015/03/06	03:47:10.77	PM	Prot Group A Active
2015/03/06	03:47:10.70	PM	Pickup
2015/03/06	03:46:58.23	PM	Load Supply ON
2015/03/06	03:46:54.14	PM	Automatic Reclose
2015/03/06	03:46:53.29	PM	Load Supply OFF
2015/03/06	03:46:49.20	PM	E Max 115 Amp
2015/03/06	03:46:49.20	PM	B Max 558 Amp
2015/03/06	03:46:49.20	PM	A Max 532 Amp
2015/03/06	03:46:49.14	PM	Prot Trip 1
2015/03/06	03:46:49.14	PM	Earth Prot Trip

Figure 3: PMB event log example

The PMB, Nulec CAPM4 series, was used for the project and is manufactured by Schnieder Electric. Following analysis of the fault log, information about where on the network the fault was found was sourced. This was obtained from the Eskom in a list of Work Orders including detail of the time, date as well as feedback from the field staff that performed the fault finding. PMB protection settings were also sourced from the Eskom Protection Coordination & Configuration department. These were used to evaluate and validate the protection curve plotter function.

5. EVALUATION OF THE APPLICATION

The application's use is best illustrated using examples. Case studies will be presented to cover usage of the curve plotter as well as the fault locator functions.

5.1 Curve Plotter Case Study

A technician is on site to do maintenance on 4 PMB's connected in series as shown in Figure 4.

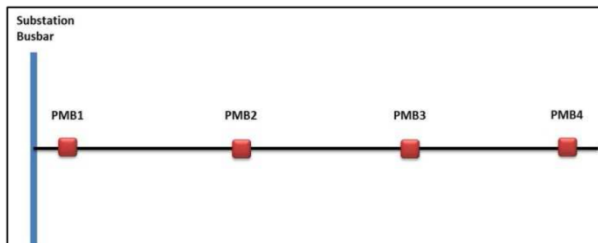


Figure 4: Curve Plotter Example network

Part of the maintenance schedule is to check that the settings on the PMB are the same as that on the database in the office. On inspection of the settings sheets for all the breakers it becomes clear that the time settings may not be coordinating as indicated in Table 3.

Table 3: Curve Plotter Example Relay Settings

PMB	Pick-Up Setting	Time Setting	Curve Type	Fault level
1	200A	0.3	IEC NI	3000
2	150A	0.25	IEC NI	2600
3	100A	0.23	IEC NI	1500
4	70A	0.25	IEC NI	1000

The technician then inputs the settings into the curve plotter application which was loaded onto a portable device to be used in the field to confirm the suspicion. The result is indicated by a screen capture in Figure 5 and enlarged plots in Figure 6.

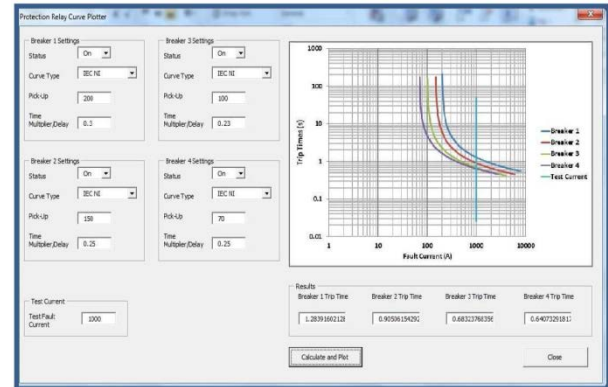


Figure 5: Screen capture of Curve plotter user interface

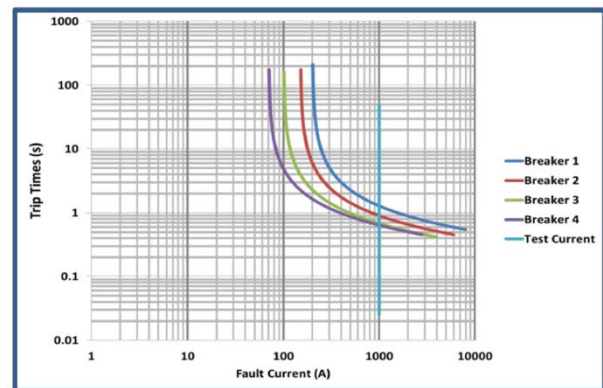


Figure 6: Poorly coordinated relay curves

To correct the possible mistake and investigate a more proper setting the technician then changes PMB3's time setting to 0.2 and PMB4 to 0.15. The result is as shown in Figure 7.

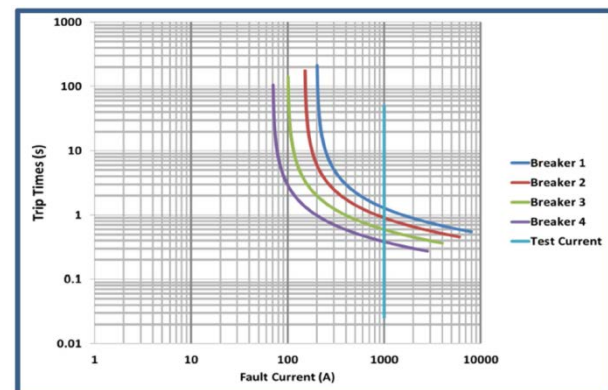


Figure 7: Coordinated relay curves

5.2 Fault Locator Case Study

This case study is based on an actual fault that occurred on the Reddersburg Munic-Sydenham line denoted RESY.

The network layouts are shown in Figure 8. The PMB at RESY351 tripped at 4:15 PM on 22/01/2014, see event log, Figure 9. The measured current was about 270A on each phase.

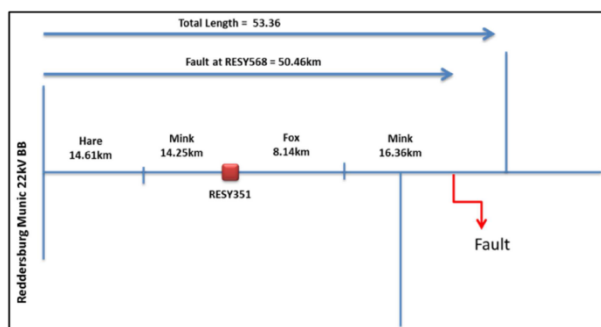


Figure 8: Reddersburg Munic – Sydenham line topology

2014/01/22	04:15:18.88	PM	E Max	37	Amp
2014/01/22	04:15:18.88	PM	C Max	266	Amp
2014/01/22	04:15:18.88	PM	B Max	275	Amp
2014/01/22	04:15:18.88	PM	A Max	257	Amp
2014/01/22	04:15:18.82	PM	Prot Trip	1	

Figure 9: RESY351 Trip Event Log

Using the fault locator tool the conductor types and lengths were entered into the application. The substation was selected from a list and the measured fault current entered. The screen capture is shown in Figure 10.

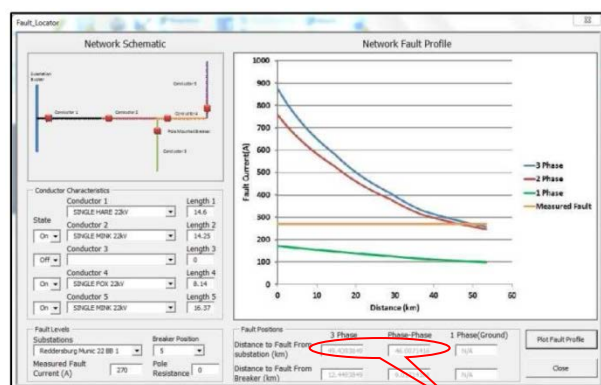


Figure 10: Fault Locator Screen capture

The fault locator estimates that the fault is either a 3 phase fault at 49.43km from the substation bus bar or a Phase-Phase fault at 46km (point 1, Figure 10).

Looking at the event log one can see that all three phases produced about the same fault current meaning the fault must have been a 3 phase fault at 49.43km and 12.44km from the RESY351 PMB that tripped.

Work order data shows that the fault was found RESY568 which is 50.46km from the substation, Figure 8. The fault was caused by a failed pole mounted transformer. This example illustrates how the fault locator can be used to aid in fault finding. Similar tests were done with earth faults and the results were proven to be satisfactory.

6. CONCLUSIONS

An application tool has been developed to aid in fault finding on distribution power lines which could be used

remotely. The software was developed in Microsoft Excel® VBA. A protection curve plotter was implemented to help in coordinating protection relays. An example was given of how this can be done and to evaluate the applications operation. A fault locator component was also implemented with and tested with 3 phase and earth fault. The results were satisfactory evaluated and tested.

Although the end product was not implemented on a smart phone as originally planned it proofed the concept to be implemented as a future research project.

7. REFERENCES

- [1] “Relay Coordination,” in *Distribution Automation Handbook*, ABB in Southern Africa, 2015, pp. 4-20.
- [2] J. H. Teng, W. H. Huang and S. W. Luan, “Automatic and Fast Faulted Line-Section Location Method for Distribution Systems Based on Fault Indicators,” *IEEE Transactions on Power Systems*, vol. 29, no. 4, pp. 1653-1662, 2014.
- [3] M. Mirzaei, M. Z. A. Ab Kadir, E. Moazami and H. Hizam, “Review of Fault Location Methods for Distribution Power Systems,” *Australian Journal of Basic Applied Sciences*, vol. 3, no. 3, pp. 2670-2676, 2009.
- [4] *Network Protection & Automation Guide-Protective Relays, Measurement & Control*, ALSTOM, 2011.
- [5] B. de Metz-Noblat, F. Dumas and C. Poulain, “Calculation of short-circuit currents,” in *Cahier Technique no. 158*, Schneider Electric, September 2005, pp. 7-16.
- [6] Walkenbach, *Microsoft Excel® 2010, Power Programming with VBA*, Hoboken, NJ: Wiley, 2010.
- [7] S. Shekhar and H. Xiong, *Encyclopedia of GIS*, Minneapolis, MN: Springer Reference, 2008.

8. ACKNOWLEDGEMENTS

The authors acknowledge Eskom for provided PMB event downloads, conductor ratings as well as fault data for testing purposes.

DESIGN OF A CONTROLLED COOLING SYSTEM FOR A THREE-PHASE POWER TRANSFORMER WITH SUPPORT OF RENEWABLE ENERGY

I. Coetzee* and R. Gouws*

* North-West University, School of Electrical, Electronic and Computer Engineering, Potchefstroom,
Email: iwan.coetzee@gmail.com

Abstract: The national electricity supplier in South Africa (Eskom) struggles more and more each year in supplying sufficient amount of power. This is partially due to residential consumers that use appliances that require more power. This results in transformers that overheat which decrease the efficiency of the transformer. A possible solution to this problem is to cool the transformer in a controlled manner. This paper therefore provides the design of a controlled cooling system for a three-phase power transformer that is energy efficient and also makes use of renewable energy. The cooling of the transformer make use of a thermoelectric cooling module (TECM) which is controlled by an programmable logic controller (PLC) which receives its data from a PT 100 thin sensors which is placed between the windings and core of the transformer. A prototype model of the actual transformer was used to perform the tests to indicate the cooling results. Solidworks® where used for the transformer simulation which were then implemented based on the results. Solar energy was used as renewable energy which was simulated by PVSyst®.

Keywords: TECM; PLC; transformer; cooling system; solar energy, PT 100.

1. INTRODUCTION

South Africa electricity supplier Eskom, struggle to supply sufficient amount of power each year, resulting in transformers that overheat due to the power required of residential consumers [1-3]. Implementing a controlled cooling system which is powered by renewable energy can support Eskom in easing the power demand by the consumers [4].

This study focuses on making cooling systems more energy effective, and it was decided to demonstrate such a system by making use of a 5 kVA, 400 V three-phase power transformer. Transformers lifetime and efficiency decrease due to overheat [3]. This results in power outages since insufficient power can be distributed [4]. A controlled cooling system for a transformer can improve the efficiency as well as the lifetime of transformers. This solution can relieve the strain on Eskom and provide the consumers with the required power without power outages.

There are already several cooling methods available for power transformers which work very sufficiently, but not necessarily energy efficiently. They are commonly known as: ONAN, ONAF, OFAN and OFAF. It was thus decided to make use of TECMs as the cooling mechanism and testing it as the cooling device combined with the cooling liquid and a pump for a prototype of the actual transformer. TECMs have also been used as part of an air-conditioning system in a previous project in [5], a TECM holder for vaccines in [6] and for a bulk tank on a dairy farm in [7]. The research for the support of renewable energy was done on solar energy. The cooling system consist of a TECM, PLC, pump and PT100 sensors which forms the controlled cooling system which must be powered by solar energy.

With this background the main problem with this solution lies in the placement of the PT100 sensors between the core and windings of the transformer. This means that the transformer design must be done and re-winded with the sensor placed between the two parts. The design was simulated using Solidworks® and the results obtained were implemented. As mentioned the transformer serves as a prototype for the real transformer used for residential consumers. As most residential consumers are home during peak hours, the solar energy consists of a grid tied interactive topology. This means that it was simulated for when the transformer is operated during the day where there are irradiation as well as for a part into the night to cover the peak time where there is no irradiation available. The cooled down transformer was compared to a non-cooled down transformer to see the effect of the efficiency. It is also important to determine whether the use of the cooling system is cost effective.

The remainder of this paper consist of a literature review for the components used in the system. Thereafter a methodology that describes the finding of the solution to the problem. The results obtained from testing the transformer is displayed and a conclusion on the findings of this study.

2. LITERATURE REVIEW

This literature review describes the components used in designing the system. These components are the TECM, renewable energy, PLC controller and PT 100 thin sensor. Other components not described in this paper are the pump, tube, cooling liquid, and batteries. The literature review focussed only on the components for this solution and not the alternative solutions as mentioned in the introduction.

2.1 Thermoelectric Cooling Module

The TECMs were suggested by the client as cooling devices and have been used in previous final year projects [5-7] - in 2012 as part of a “TECM holder” for vaccines, in 2013 as part of a “Mini TECM Solar Air Conditioning System” and, in 2014 as an “Energy efficient bulk tank.” Thus the investigation was not done in depth as the component has already been supported by other articles. The TECM that was used are a liquid-to-air TECM.

The TECM is a device based on the “Peltier effect”. Peltier is a scientist who discovered that when a DC supply is applied the thermocouples, a temperature difference is found between the n- and p-junctions. In figure 1 the liquid-to-air TECM can be seen with the hot and cold side. This means that the liquid get hot and the heat of the liquid was dissipated by the use of the fan attached to the TECM. There are a variety of TECM available that can be chosen from [8].

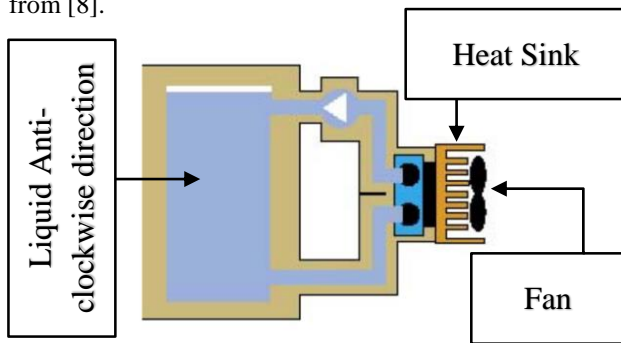


Figure 1: Working of a liquid-to-air TECM [8]

2.2 Renewable Energy

South Africa has a very large area which can be used for solar energy. The solar energy is formed by absorbing the irradiation of the sun. Approximately 10-20% of the irradiation is converted to electrical energy [9]. Solar energy was not decided on based on the cost effectiveness but also due to the availability of irradiation as can be seen in figure 2.

Figure 2 shows the global horizontal irradiation of South Africa [10]. This map is considered the most important to evaluate the irradiation in certain regions of South Africa. From the figure it can be seen that approximately 80% of the map the average irradiation is expected to be above 2000 kW/m² per annum. This means that South Africa is an ideal place for solar energy due to the high irradiation availability.

In the North-West province, Potchefstroom have an approximately 2100 kW/m². This means that Potchefstroom have more than sufficient amount of irradiation for the project. There are a variety of different ways in generating electricity by means of solar energy.

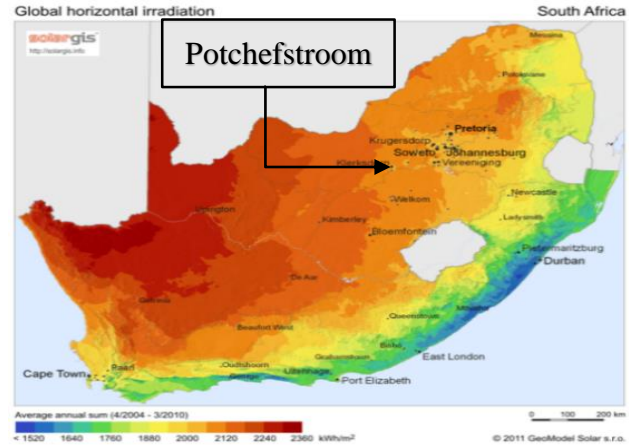


Figure 2: Global horizontal irradiation in South Africa [9]

Examples of photovoltaic panels include: poly-crystalline, mono-crystalline and CIR silicon panels. It was decided to use poly-crystalline panels.

2.3 Controller

For this system five PT100 thin sensors are placed between the windings and core of the transformer as indicated in figure 3. The controller received the data from the sensors and based on the temperature, the controller determine whether the TECM and pump must be switched on or off.

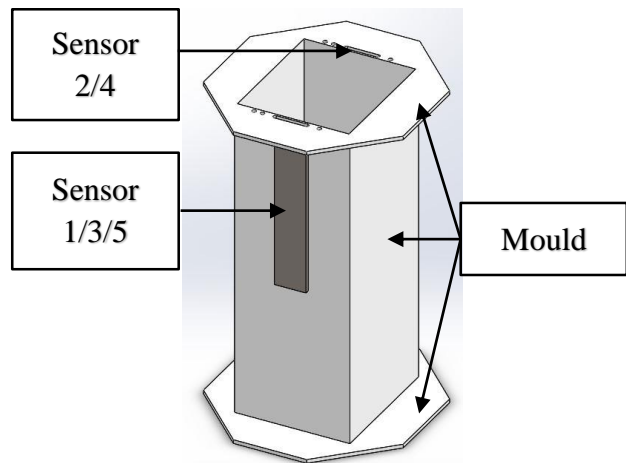


Figure 3: PT100 thin sensor placements

The controller depends on sensors 1, 2, 4 and 5. Sensors 1, 2, 4 and 5 working together respectively. Both of them are used to verify on another by setting a difference value between them. This is to determine whether one of the sensors is broken and show an error message if the results is bigger than the difference. Sensor 4 and 5 are used to determine the upper and lower limits of the cooling for example. If the sensor reaches 100 °C the TECM and pump switch on and the cooling system is active. Once the transformer is cooled to 90 °C the cooling system is deactivated by the controller

The controller must also be able to switch between solar energy and backup batteries. This is for the time when no irradiation is absorbed by the solar panels. From the controllers that were considered: Arduino, PLC, PIC and Panda board. It was decided to use the PLC based on its implementation difficulty and its amazing capability with the PT 100 sensor as well as solar energy [11].

The PLC that was chosen was the “Siemens LOGO! 0BA6” with two RTD expansion modules which are specifically designed to work with the PT100/1000 sensors. Its operation is based on logic controlling the system using only a high or low operator. It can also be connected to a PC where an online test can be conducted showing the results on the PC screen.

2.4 PT100 thin sensor

As mentioned in the controller section PT100 thin sensors are used to determine the temperature between the core and windings or the transformer. These sensors are specifically designed for this purpose. The “thin” refers to the fact that the sensor is approximately 1.5 mm thick which makes it ideal to slide between the two parts. The sensor operates between -50 °C and 250 °C which is ideal for the prototype design [12] but for the actual transformer the PT1000 thin sensors must be used. The PT100 thin sensor is shown in figure 4a and figure 4b is the round PT 100 sensor.

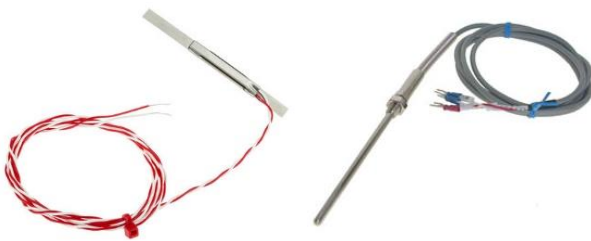


Figure 4: PT 100 sensor a) Thin b) Round [12]

2.5 Remaining components

The remaining components for the project are given in table 1 as well as the components listed in the literature review.

Table 1: Component Choices

Component	Chosen product
Pump	Facet Cube Electronic Fuel Pump
Cooling Liquid	Ethylene Glycol (Antifreeze)
Tube	Silicon Rubber plated for thermal conduction
Batteries	Lead-acid battery
Cooling Device	TECM
Renewable Energy	300 W Solar power panels
Controller	PLC 0BA6 with AM2 RTD expansion modules
Sensor	PT 100 thin sensor

3. METHODOLOGY

The engineering process was followed to achieve completion of this project. The process include identifying the problem, confirming specifications with the client, research the current solutions and decide on the knowledge obtained if the current solution can be improved for the required specifications or must a complete new design be constructed with new technology. Then designing and simulating the suggested solution. Test and evaluate the solution of the system. Process the results obtained and then verify if the results comply with the specifications of the client. This paper only contains the design, implementation and results of the system.

After conducting the literature review and deciding on the components listed in table 1, the design process needed to be initiated. Thus the transformer which serves as the prototype of the actual transformer used for residential consumers are a 5 kVA 400 V three-phase power transformer which was connected in a Y||Y configuration with a Y load. The cooling device was selected as a liquid-to-air TECM is LA-115-24-02-0710 from Laird Technologies [8]. The tubes of the TECM are connected with the silicon rubber tube and the electronic fuel pump with the ethylene glycol inserted into the tube. The silicon rubber tube is coiled around phase C.

As mentioned the transformer represents a residential use, thus in practice to demonstrate that the system works. Phase A was operated at half the load as well as phase B and phase C was operated at full load. Thus meaning that for example phase A have a radio connected to it, phase B have a kettle connected and phase C have an oven connected to it. Conducting the tests all appliances was replaced with resistors to represent the load. Figure 5 shows how the transformer looks in simulation with the tube coiled around phase C.

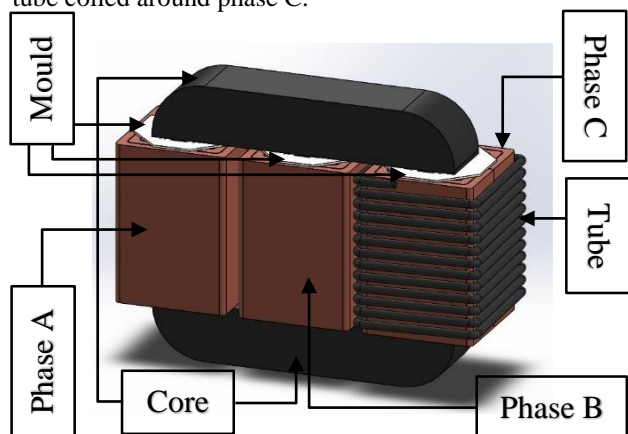


Figure 5: Transformer with silicone rubber tube

The PT100 thin sensors place between the windings and core of the transformer and are connected to the PLC which makes the decisions on whether to switch the system on or off. Figure 6 show the operation of the PLC.

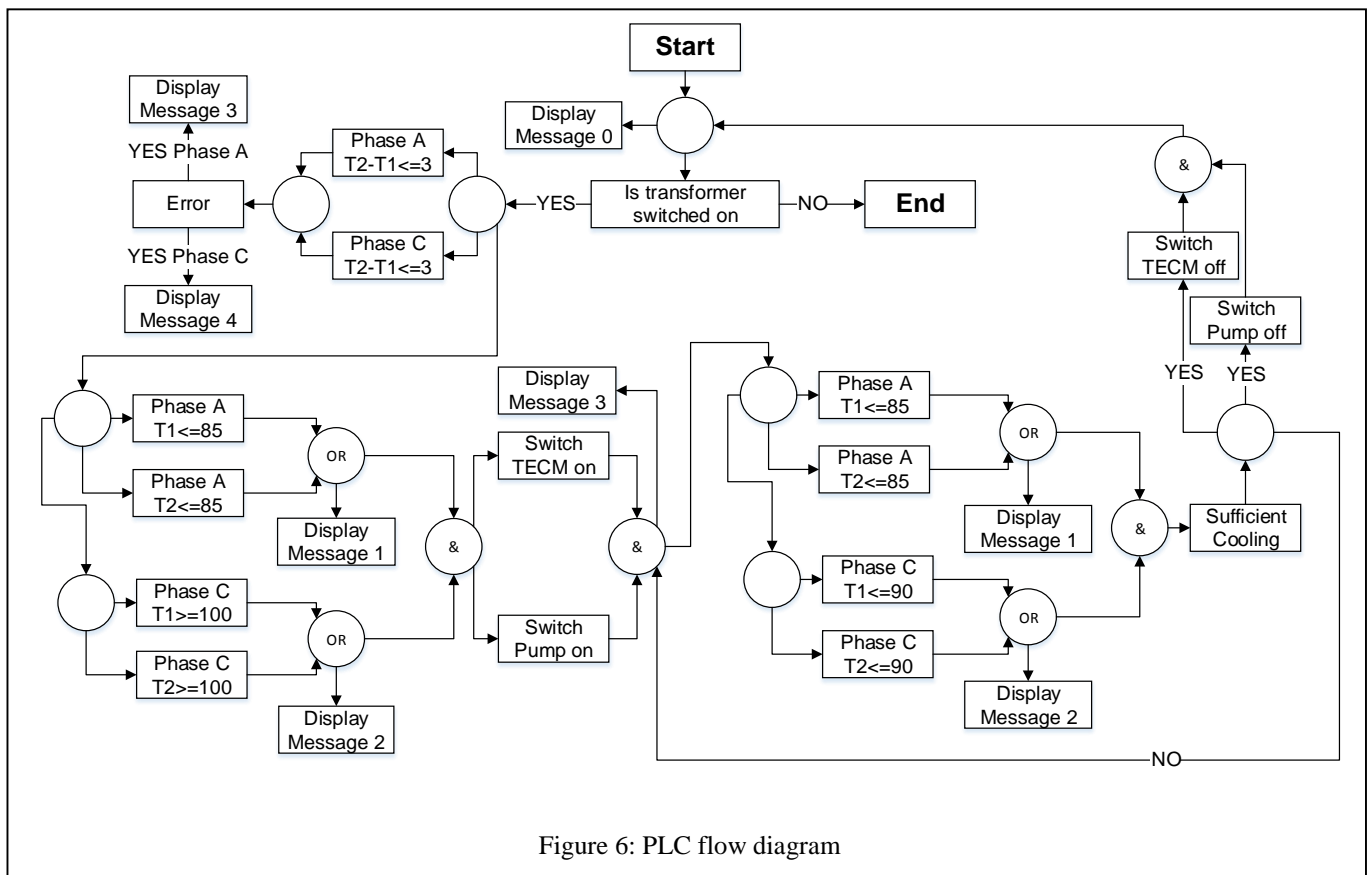


Figure 6: PLC flow diagram

Once implementation was complete the testing could be initiated. There are three main tests that have to be conducted and then calculations must be done based on the test results to determine whether the system is more efficient. The three tests are listed below.

- Test 1: The first test is to do an open and a short circuit test of the transformer. This is to calculate the core and copper losses of the transformer.
- Test 2: The second test is performed to obtain the base values for each phase. The controller is set to only obtain the values. The base values are the temperature, current and voltage. The values are obtained in 5 minutes intervals for 400 minutes. The efficiency is then calculated which is the base efficiency.
- Test 3: The final test is performed to obtain the cooling values for each phase. The controller limits are set based on the base values obtained in test 2. The values are the temperature, current and voltage. The values are obtained for 5 minutes intervals for 400 minutes. The efficiency is then calculated for this test and was compared to the efficiency of test 2.

4. EXPERIMENTAL RESULTS

This section discusses the results of the three tests that were performed. The tests were performed on the prototype as shown in figure 7. The figure shows the complete integrated system. The TECM is placed against the tube for more heat conduction. The tube can be seen is

coiled around phase C. It can also be seen that the TECM is connected to the pump and to the tube. The PT100 sensors can be seen are connected to the PLC.

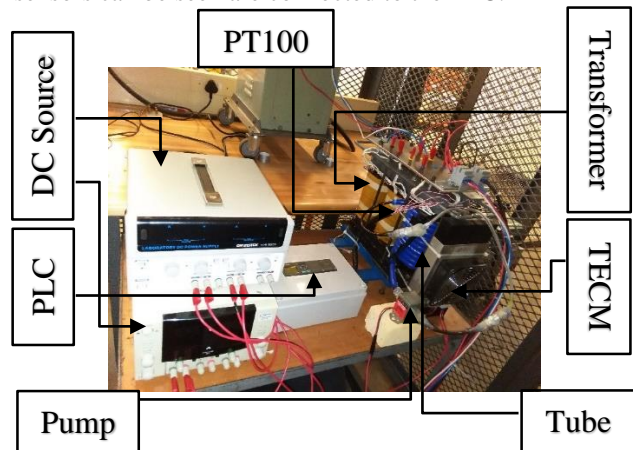


Figure 7: Complete integrated system

The result of the first test is shown in table 2. It shows the total losses of the core, copper.

Table 2: System losses

Losses	Power (W)	
	Experimental	Simulated
Open Circuit (Core)	110	105
Short Circuit (Copper)	54	50
Total	164	155

These losses form part of the input power. The second test show the temperature and current vs time for the base values. It can be seen that phase A and B is operated at half the load and phase C at full load. It can also be seen that the temperature of phase C increases much faster than phase A and B and stabilise at approximately 340 minutes. Phase C temperature satirises at approximately 105 °C. Figure 8 shows the baseline test.

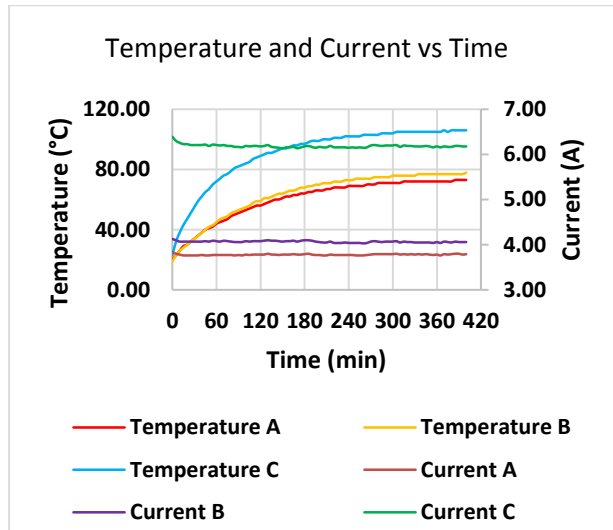


Figure 8: Baseline Test

The third test show the temperature and current vs time for the post implemented (cooled) values. It can be seen that phase A and B is operated at half the load and phase C at full load. It can also be seen that the temperature of phase C increases much faster than phase A and B and stabilise at approximately 340 minutes. It can be seen that phase C reach a 100 °C and then cool down to 90 °C. Figure 9 shows the post implementation (cooled) test.

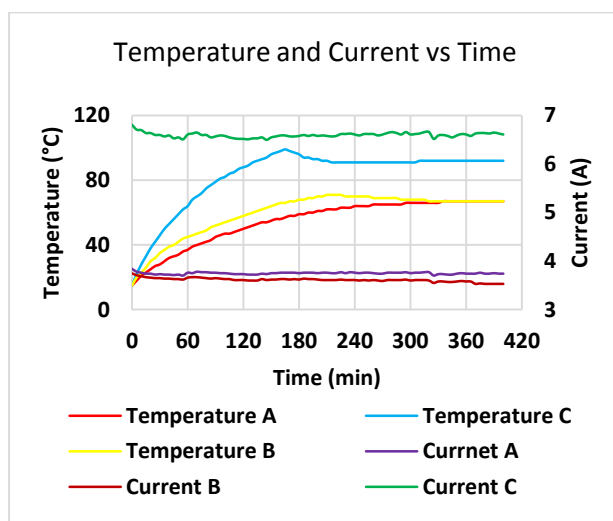


Figure 9: Post Implementation (Cooled) Test

Thus from the tests conducted, the efficiency of the baseline and post implementation values are calculated and

is shown in table 3. The efficiency does not include the use of the renewable energy source. Table 3 also shows the difference between the baseline and the post implemented (cooled) test.

Table 3: System Efficiency

Test	Efficiency (%)
Baseline	88.49
Post implementation (Cooled)	89.39
Difference (Saving)	0.9

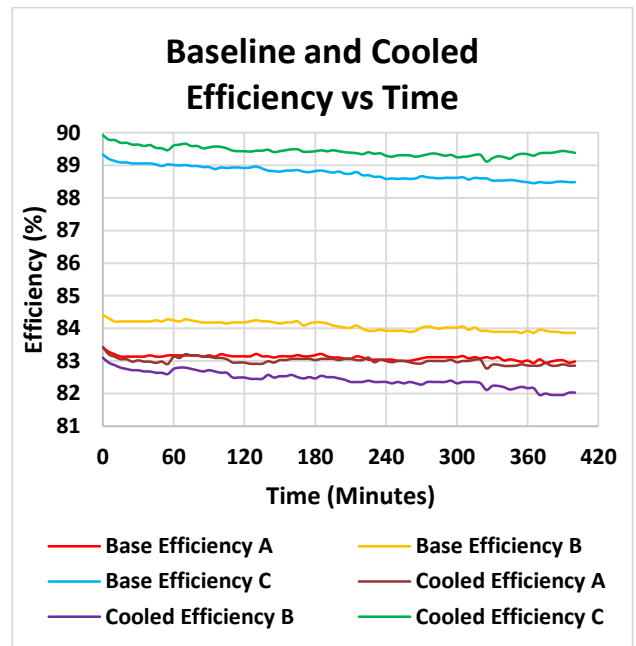
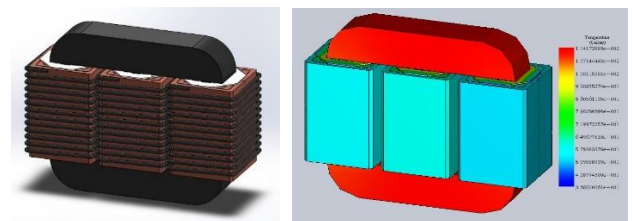


Figure 10: Baseline and Cooled Efficiency

Figure 10 shows the baseline and post implemented efficiency of the transformer. It supports table 3 that there is an increase in efficiency, 0.9 %, when the transformer is being cooled down.

5. DISCUSSION

The results can be interpreted for an actual transformer used for residential use. If all the phases were to be operated at full load and have a TECM for each phase and cooled with ethylene glycol. Figure 10a shows the implemented transformer and figure 10b shows the results of implemented transformer.

Figure 11: 3 TECM cooling transformer, 1 per phase
a) Implementation b) Results

As can be seen on figure 10b, the temperature is approximately 115 °C after is cooled down compared to approximately 155 °C before it is cooled down. The PLC can be set to switch separately for example if only one phase reach the upper limit temperature the specific phase can be cooled down on or it can be set if one phase reach the upper limit temperature all the phases can be cooled down.

The transformer was operated from the Eskom power grid, but as mentioned the TECM, PLC, pump and sensors was operated using solar energy. The simulations done for the solar power are based on the prototype that is implemented. Thus this means that the four components has a total output power 160 W. It was decided that the transformer operate for 24 hours a day, resulting in 2.9 kW/day. The solar panels to use was decided to be 300 W which is more than enough since only 160 W is needed. The batteries that was used is ten 12 V, 110 Ah battery.

The calculations for the batteries were done when the least irradiation is available which is in June as can be seen from figure 11. The figure also shows the available energy from the solar panels and the required energy from the consumer. The simulations were done using PVSyst®.

The price for the required solar panels are R 10,998 and the batteries are R 38,603 based on quotations received during 2015 [13, 14].

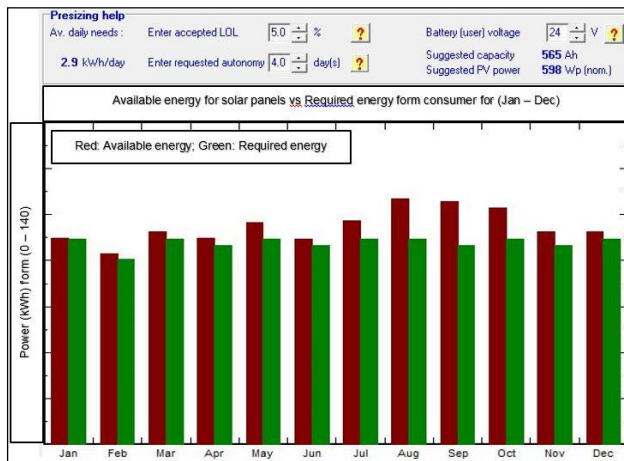


Figure 12: Solar power simulation

6. CONCLUSION

The main purpose of this project was to design a controlled cooling system for a three-phase power transformer with support of renewable energy. As can be seen from the results the cooling system decreases the temperature of the transformer which in result increase the efficiency of the transformer.

If the transformer would have been operated at full load, three TECMs would have been used for the cooling purposes of the transformer as indicated in figure 11. The

total decrease in temperature would be approximately 30 °C.

Since most of the components were available for use, a budget of only R 12,000 was required. If all of the components were to be bought, a total of approximately R 80,000 would be required for the prototype implementation. Like mentioned if the transformer would be operated at full load for all three phases, it would result in approximately R 100,000 if all the components have to be bought estimated on components prices during 2015.

7. REFERENCES

- [1] P. Debba, "Forecasts for electricity demand in South Africa (2010-2035) using the CSIR sectoral regression model," Pretoria, Jun. 2010.
- [2] T.C.H. Bonisa, "Eskom Holdings SOC Limited," Std Pp., Dec. 2013.
- [3] Electrical4u, "Transformers Cooling Systems and Methods." [Online]. Available: <http://electrical4u.com/transformer-cooling-system-and-methods/> [Accessed: Feb 2, 2015].
- [4] DA Discussion, "Electricity sector reform," Econ. Rep., Apr. 2008.
- [5] B. de Waal, "Mini TECM Solar Air Conditioning System," North-West - University Potchefstroom Campus, Potchefstroom, 2013.
- [6] H. Eilers, "Thermoelectric (TECM) Cooling Holder, a review on thermoelectric cooling modules: Installation design, performance and efficiency," North-West - University Potchefstroom Campus, Potchefstroom, 2012.
- [7] W.A. Pelsler and R. Gouws, "Design of an intelligent controller for a renewable energy efficient bulk storage tank", Proceedings of the Southern African Universities Power Engineering Conference, pp. 437-443, 2015.
- [8] Thermoelectric assembly, Liard technologies, America, 2010, pp. 4-5.
- [9] The need project, Secondary Energy Infobook, Manasas, 2009, pp. 42.
- [10] SAAEA, "New, most detailed solar resources maps of South Africa," 2012. [Online]. Available: <http://saaea.blogspot.com/2012/02/new-most-detailed-solar-resource-maps.html>. [Accessed Mar. 2015].
- [11] A. Amunrud, "Programmable Logic Controllers," Siemens, Pta, Paper. EE 367, Feb. 2002.
- [12] Reissmann Sensortechnik GmbH, "Product information," PT100, PT500, PT1000 datasheet, 2015. [Accessed Mar. 2015].
- [13] Imperial Crown Trading, "Solar Panel prices," Sustainable.co.za (Pty) LTD - Online Eco Store, 2014. [Online]. Available: <http://www.sustainable.co.za/catalogsearch/result/?q=poly>. [Accessed 31 May 2015].
- [14] The Lithium Battery Co., "24 V Lithium Battery," 2015. [Online]. Available: www.atbatt.com/sealed-lead-acid-batteries/b/volts-amps/m/12c-110ah.asp. [Accessed 14 September 2015].

STARTING OF CYLINDRICAL WOUND-ROTOR SYNCHRONOUS MOTOR FOR FAN LOADS

H.J.S. Roux and M.J. Kamper

Department of Electrical and Electronic Engineering, Stellenbosch University, Stellenbosch, South Africa

Abstract: For direct online starting of large (megawatt) fan loads the wound rotor slip-ring induction motor is often used in reducing starting currents while retaining good starting torque. In this paper a method is proposed and evaluated to switch and operate a wound-rotor slip-ring induction motor as a synchronous motor. In doing so it is envisaged to improve the power factor and efficiency of the motor. DQ-circuit analysis and modelling of the wound-rotor induction motor are used in MATLAB/SIMULINK to simulate the behaviour when switched to act as a synchronous motor. This is known as the synchronization process. SIMPLORER is used as a comparative tool to determine the validity of the results obtained from MATLAB/SIMULINK. Practical tests of this design were performed on a small wound-rotor motor system. The results of this system show great promise. It is shown that the efficiency and power factor of the motor increase and correspond with simulation results.

Keywords: Line starting, synchronous motor, fan load, synchronization switching.

1. INTRODUCTION

The majority of generated electrical energy in the world is converted to mechanical energy by means of electric motors. Electric motors, thus, represent a huge opportunity to reduce energy usage by improving these motor's energy efficiencies. The induction motor is the workhouse in the industry in converting the electrical energy into mechanical energy. These motors are generally used for their good start-up performance for applications such as industrial fans and pumps. These applications have the ability to reduce energy usage, while maintaining energy output by using new methods to control their characteristics and reduce losses.

In this paper the focus is on wound-rotor slip-ring induction motors which generally are used in industry for their high rotor-resistance start-up characteristics. However, these induction motors do not have as good power factor ratings. A synchronization technique is hence proposed to synchronize the motor with the grid-supply so as to operate the motor rather as synchronous motor with an improved power factor.

1.1 Proposed circuit

The proposed system makes use of the setup from both the wound-rotor induction motor and a synchronous motor. Figure 1 shows the circuit diagram of a general wound-rotor induction motor. The external resistances (R_{ext}) on the rotor side are used to reduce currents during start up. These resistances are typically removed during operation, thus short-circuiting the rotor.

Figure 2 shows the circuit diagram of a cylindrical wound rotor synchronous motor. In this connection the a- and b-phase rotor terminals are short-circuited and a DC voltage (V_f) is applied to the a and c phases causing a DC field current to flow in the rotor. With the correct DC field

voltage for best power factor and efficiency operation an external field resistor (R_{fe}) is not necessary.

Figure 3 shows the proposed circuit diagram for a wound-rotor synchronous motor. During start up the system is connected as a wound-rotor induction motor, initially with external rotor resistances as in Figure 1 but eventually with the rotor short-circuited. This connection brings the speed of the motor close to synchronous speed. When the switches are triggered at time t_1 , the system is connected as a synchronous motor as in Figure 2. This switching thus allows the system to have the characteristics of an induction motor at start up but the characteristics of a synchronous motor during operation. The switching time t_1 , however, is critical to ensure smooth transition from induction to synchronous motor operation, as is investigated in this paper.

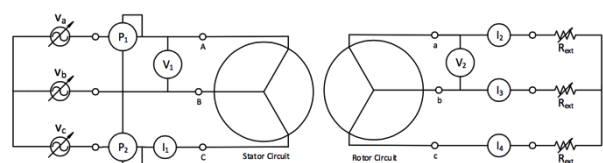


Figure 1: Circuit diagram of a wound rotor induction motor.

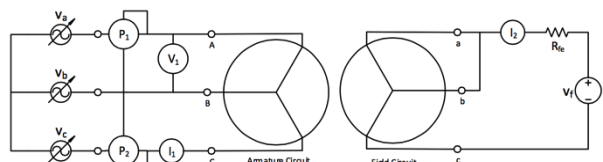


Figure 2: Circuit diagram of a synchronous motor.

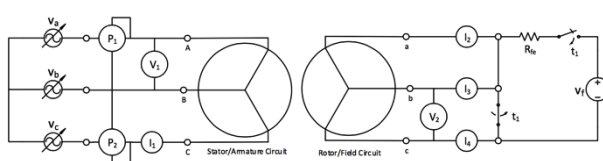


Figure 3: Proposed circuit diagram for the wound rotor synchronous motor.

2. DQ MODELLING OF WOUND-ROTOR MOTOR

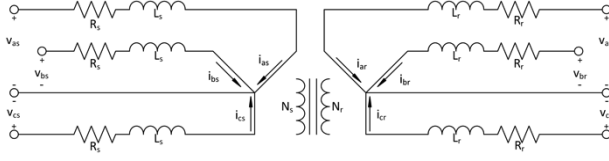


Figure 4: Circuit diagram of 3-phase wye-connected symmetrical induction motor.

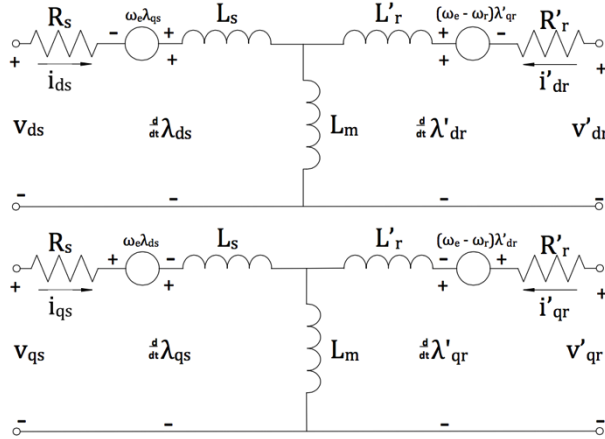


Figure 5: DQ equivalent circuits of the induction motor in the rotating reference frame.

Modelling motors for simulation purposes are best achieved through the use of circuit diagrams. For the proposed system a three-phase wye-connected stator and wound rotor circuit diagram, as shown in Figure 4, is used.

The equations mentioned in this section are derived from [1] and [2]. Inspecting Figure 4 and applying Kirchhoff's voltage law, we can determine the corresponding voltage equations of an induction motor, where core losses are ignored and the rotor terminals short-circuited, as

$$\mathbf{v}_{abcs} = \mathbf{R}_s \mathbf{i}_{abcs} + \frac{d}{dt} \lambda_{abcs}, \quad (1)$$

$$\mathbf{v}_{abcr} = \mathbf{0} = \mathbf{R}_r \mathbf{i}_{abcr} + \frac{d}{dt} \lambda_{abcr}. \quad (2)$$

Since coupling occurs between the stator and rotor circuits, it is better to refer the rotor quantities to the stator side to ease calculations. The equations for referring rotor quantities to the stator are

$$i'_r = \frac{1}{a_{eff}} i_r, \quad (3)$$

$$v'_r = a_{eff} v_r, \quad (4)$$

$$Z'_r = a_{eff}^2 Z_r, \quad (5)$$

$$a_{eff} = \frac{N_s}{N_r}. \quad (6)$$

The transformation of a motor to a dq0 axis system is useful when modelling motors, as it simplifies the equations. The dq0 transformation that is used throughout this paper is based on that of Park's transformation with the following angles used to transform the stator and rotor quantities respectively:

$$\theta_s = \omega_e t + \theta_0, \quad (7)$$

$$\theta_r = (\omega_e - \omega_r) t + \theta_0. \quad (8)$$

The angle θ_s is chosen to represent the angle between the axis of stator a-phase and that of the synchronous rotating dq0 reference frame, while that of θ_r representing the angle between the rotor a-phase and that of the synchronous rotating dq0 reference frame. The transformed stator and rotor voltage equations can then be expressed as

$$v_{ds} = R_s i_{ds} + \frac{d\lambda_{ds}}{dt} - \omega_e \lambda_{qs}, \quad (9)$$

$$v_{qs} = R_s i_{qs} + \frac{d\lambda_{qs}}{dt} + \omega_e \lambda_{ds}, \quad (10)$$

$$v'_{dr} = 0 = R'_r i'_{dr} + \frac{d\lambda'_{dr}}{dt} - (\omega_e - \omega_r) \lambda'_{qr}, \quad (11)$$

$$v'_{qr} = 0 = R'_r i'_{qr} + \frac{d\lambda'_{qr}}{dt} + (\omega_e - \omega_r) \lambda'_{dr}. \quad (12)$$

Note that the 0-sequence of the transformation under balanced and symmetrical conditions will give a zero result and is therefore ignored. The transformed flux-linkage equations can then be expressed as

$$\lambda_{ds} = L_s i_{ds} + \lambda_{md}, \quad (13)$$

$$\lambda_{qs} = L_s i_{qs} + \lambda_{mq}, \quad (14)$$

$$\lambda'_{dr} = L'_r i'_{dr} + \lambda_{md}, \quad (15)$$

$$\lambda'_{qr} = L'_r i'_{qr} + \lambda_{mq}, \quad (16)$$

$$\lambda_{md} = L_m (i_{ds} + i'_{dr}), \quad (17)$$

$$\lambda_{mq} = L_m (i_{qs} + i'_{qr}). \quad (18)$$

The torque of the motor can then be expressed as

$$T_{mech} = \frac{3}{2} \left(\frac{\text{poles}}{2} \right) (\lambda_{ds} i_{qs} - \lambda_{qs} i_{ds}). \quad (19)$$

The transformed voltage and flux-linkage equations introduce a new equivalent circuit, which represents the rotating dq0 reference frame as shown in Figure 5.

When operating this motor as a synchronous motor, the equations given above are still valid. However, since an external field voltage is applied to the rotor terminals, equation (2) can be rewritten as

$$\mathbf{v}_f = \mathbf{R}_r \mathbf{i}_{abcr} + \frac{d}{dt} \lambda_{abcr}. \quad (20)$$

This in turn affects equations (11) and (12) whereby the rotor voltages do not equate to zero. These voltage equations can then be found by transforming the applied field voltage matrix (\mathbf{v}_f) to the dq0 reference frame. Note that the field voltage matrix must be chosen in such a way so as to keep the 0-sequence equal to zero. With the setup shown in Figure 3 the field voltage matrix can be expressed as

$$\mathbf{v}_f = \begin{bmatrix} \frac{1}{3} v_f & \frac{1}{3} v_f & -\frac{2}{3} v_f \end{bmatrix}^T. \quad (21)$$

3. SIMULATION PACKAGES

The use of simulation packages, to determine whether a new design concept is possible, is vital in discovering possible flaws and shortcomings. MATLAB/SIMULINK is used to determine dq-transients while SIMPLORER is used to verify the results in the abc-reference frame.

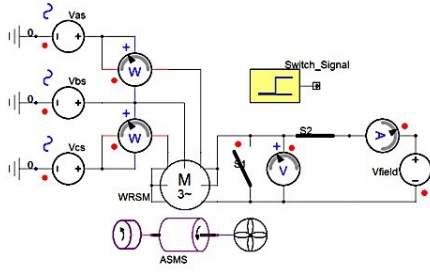


Figure 6: SIMPLORER circuit diagram for simulation.

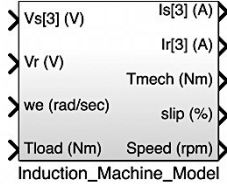


Figure 7: Block diagram of an induction motor in MATLAB/SIMULINK.

3.1. SIMPLORER

SIMPLORER is an easy to use simulation program whereby the user can build a circuit using basic components. Figure 6 shows the circuit built in SIMPLORER for simulation. The switch signal block controls the time when the system switches to a synchronous motor.

3.2. MATLAB/SIMULINK

MATLAB is an easy to use software program, which has the ability to simulate circuits given that the equations are programmed into a script file. This circuit analysis software is more time consuming than that of SIMPLORER, but a more in-depth understanding of the circuit is found.

The equations presented in Section 2 are important when considering the model of the motor in MATLAB/ SIMULINK. However, these equations contain a number of unknowns, such as the currents and flux-linkages. The conventional method to solve this problem is to consider the flux-linkages as the state variables and the current variables as dependant on these flux-linkage components. An iterative loop can be run to solve these states. Therefore, to make simulations easier, equations (9) to (18) are rearranged as follows:

$$\lambda_{ds} = \int [v_{ds} - R_s i_{ds} + \omega_e \lambda_{qs}] dt, \quad (22)$$

$$\lambda_{qs} = \int [v_{qs} - R_s i_{qs} - \omega_e \lambda_{ds}] dt, \quad (23)$$

$$\lambda'_{dr} = \int [v'_{dr} - R'_r i'_{dr} + (\omega_e - \omega_r) \lambda'_{qr}] dt, \quad (24)$$

$$\lambda'_{qr} = \int [v'_{qr} - R'_r i'_{qr} - (\omega_e - \omega_r) \lambda'_{dr}] dt. \quad (25)$$

The currents can be solved in terms of flux linkages as

$$i_{ds} = \frac{\lambda_{ds} - \lambda_{md}}{L_s}, \quad (26)$$

$$i_{qs} = \frac{\lambda_{qs} - \lambda_{mq}}{L_s}, \quad (27)$$

$$i'_{dr} = \frac{\lambda'_{dr} - \lambda_{md}}{L'_r}, \quad (28)$$

$$i'_{qr} = \frac{\lambda'_{qr} - \lambda_{mq}}{L'_r}, \quad (29)$$

$$\lambda_{md} = L_m (i_{ds} + i'_{dr}), \quad (30)$$

$$\lambda_{mq} = L_m (i_{qs} + i'_{qr}). \quad (31)$$

The angular velocity (ω_r) can be found as

$$\omega_r = \left(\frac{\text{poles}}{2} \right) \left(\frac{1}{J} \right) \int (T_{\text{mech}} - T_{\text{load}}) dt. \quad (32)$$

The equations discussed in this sub-section as well as equation (19) form the essential parts of modelling an induction motor in the dq0 reference frame. In Figure 7 the main SIMULINK block diagram is shown that contains the equations given in this sub-section.

4. SYSTEM PARAMETERS

Parameter estimation is vital to analyse, simulate and model the motor. In this section a summary of the parameters calculated from measured data is given. The rated performance of the motor used for experimentation is given in Table 1.

Table 1: Rated values for Siemens Induction motor.

V_{Rated} (V)	I_{Rated} (A)	P_{Rated} (kW)	$\cos(\theta)$ (pu)	f_{Rated} (Hz)	n_{Rated} (rpm)
220Δ/380Y	11.3/6.5	2.2	0.67	50	1390

4.1. Parameters of induction motor

Through the use of the DC, no-load and blocked-rotor tests the parameters of the given induction motor were determined as given in Table 2.

Table 2: Summary of Motor Parameters of the Siemens Induction Motor.

R_s (Ω)	R'_r (Ω)	$X_s = X'_r$ (Ω)	X_m (Ω)	R_c (Ω)
1.9333	2.7184	3.7623	76.4137	736.641

4.2. Parameters of synchronous motor

Investigating the effect of magnetic saturation in the motor, the measurements as in Table 3 were taken to determine the synchronous reactance.

 Table 3: Measurements taken at V_{rated} to determine X_{sat} .

V_{rated} (V)	I_f (A)	I'_a (A)	X_{sat} (Ω)	R_s (Ω)
220	8.5	1.5	84.678	1.9333

4.3. Load

The torque and power curves of the fan load attached to the motor for the investigation are shown in Figure 8.

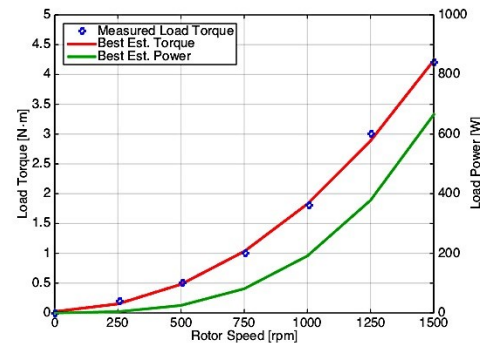


Figure 8: Torque and power curve of the fan load.

5. SIMULATION RESULTS

In Section 1.1 it is highlighted that the switching time to synchronize the induction motor as synchronous motor is critically important. The theory behind the choice of the switching time is discussed in this section together with the presentation of simulation results.

5.1. Synchronization switching

The rotor current waveforms of Figure 9 are used to reference the switching times (t_0 , t_1 and t_2) used to describe the starting of the synchronization stage. Note that the frequency of the rotor currents at switching is at a low slip frequency.

With the setup shown in Figure 3, the steady state condition will result in the field current being injected into the a- and b-phase, with the c-phase carrying the field current out of the rotor. With this assumption time t_1 in Figure 9 would indicate the best switching position, where in this instance the current amplitudes of the a- and b-phase are equal and the c-phase amplitude is at its maximum negative value. This is, however, not the case as the induced torque of the synchronous motor at this position is too low, resulting in the effect where the rotor's magnetic poles cannot follow the stator magnetic poles. This results then in the magnetic poles of the stator and rotor to slip over each other, creating a juddering rotation of the rotor and instability in the rotor currents as illustrated in Figure 10. Figure 11(A) illustrates the magnetic poles at this synchronization position.

With this knowledge, it is clear that a position should be chosen to increase the induced torque so as to accelerate the rotor to synchronous speed and lock the rotor's magnetic poles with the stator rotating magnetic field. If switching time t_2 in Figure 9 is considered, the induced torque of the motor will act in such a way that the rotor will decelerate due to the magnetic poles of the rotor leading the magnetic poles of the stator, as seen in Figure 11(B). Since the motor then decelerates, the magnetic poles of the stator and rotor will also slip over one another creating instability as illustrated in Figure 12.

If the process of synchronizing takes place at time t_0 , the induced torque will act in such a way that the rotor will accelerate due to the rotor poles lagging the stator poles, as seen in Figure 11(C). The rotor in this case will accelerate quickly in order to align its poles with that of the stator. Synchronizing at this switching position yields a stable transition, as illustrated in Figure 13.

To explain the switching-synchronization performance of the motor further, Figure 14 illustrates the current vector positions of the motors in the synchronous rotating dq reference frame, with the q-axis simply aligned with the supply voltage vector. Figure 14(A) illustrates the steady dq-state of an induction motor, while Figure 14(C) illustrates that of a synchronous motor. Figure 14(B) illustrates the transition current vector dq-state at start of syn-

chronization for the three synchronization switching times of Figure 9. It is clear from Figure 14(B) that switching at time t_2 will result in the worst synchronization performance as the current (and flux) vectors are completely out of phase. Switching at time t_0 the rotor current and flux vectors are advanced to create a more close to 90-degree angle between the stator and rotor vectors, hence inducing a strong acceleration torque.

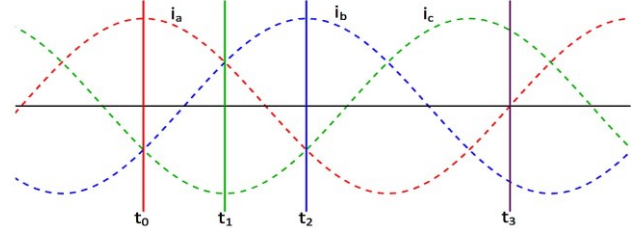


Figure 9: Rotor currents of 3-phase induction motor.

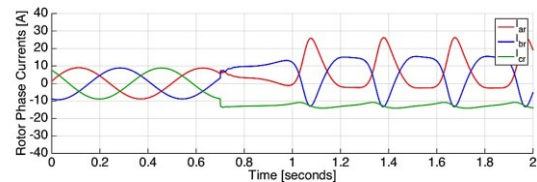


Figure 10: Simulation of rotor currents with switching at time t_1 .

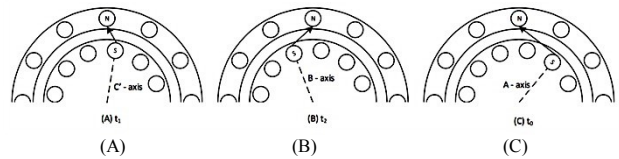


Figure 11: Stator and rotor magnetic poles at various synchronization positions.

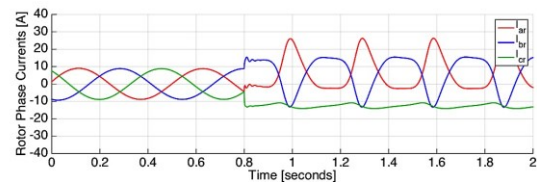


Figure 12: Simulation of rotor currents with switching at time t_2 .

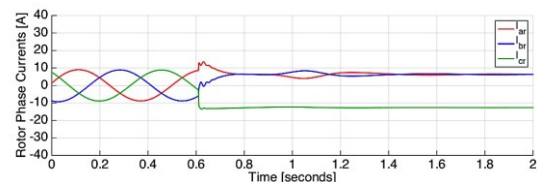


Figure 13: Simulation of rotor currents with switching at time t_0 .

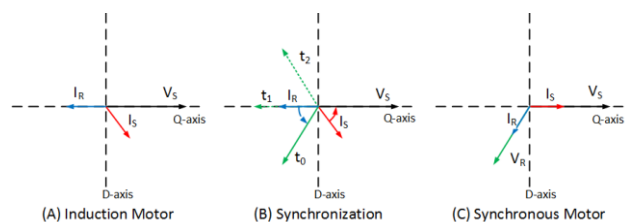


Figure 14: DQ motor current vector positions.

5.2. Starting and synchronizing

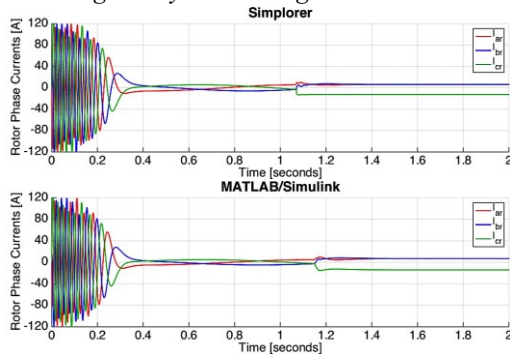


Figure 15: Simulation of the rotor phase currents at 380 V_{LL} direct-on-line start with SIMPLORER (top) and MATLAB/SIMULINK (bottom).

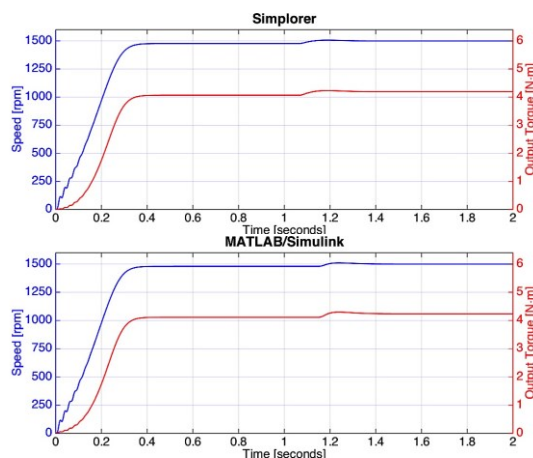


Figure 16: Simulation of the output torque and speed at 380 V_{LL} direct-on-line start with SIMPLORER (top) and MATLAB/SIMULINK (bottom).

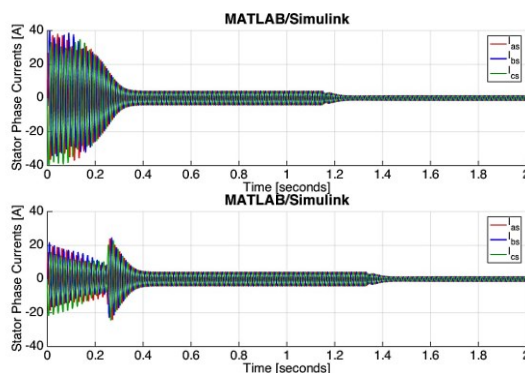


Figure 17: Simulation of the stator phase currents at 380 V_{LL} direct-on-line start without (top) and with (bottom) starting external rotor resistances.

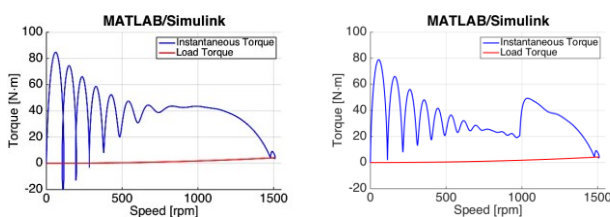


Figure 18: Simulation of motor and load torques versus speed at 380 V_{LL} direct-on-line start without (left) and with (right) starting external rotor resistances.

In Figure 15 it is shown how the rotor currents react at start and at synchronisation-switching, i.e. at 1.1 seconds for SIMPLORER and 1.15 seconds for MATLAB/SIMULINK. Once synchronization takes place, the rotor currents represent the injected field current of the synchronous motor.

Figure 16 shows the speed and output torque of the motor at start and at synchronization-switching. Here it can be seen that at the time after 1.1 seconds for SIMPLORER and 1.15 seconds for MATLAB/SIMULINK, the rotor accelerates to reach synchronous speed and lock into position as described in Section 5.1.

5.3. Use of external resistances for starting

Figure 17(top) illustrates the stator currents under a direct-on-line start of the motor. The synchronization of the motor can be seen occurs at 1.18 seconds. The stator currents before 0.3 seconds can be considered as high for the motor. External rotor resistances can be used at start-up to reduce these currents as can be seen in Figure 17 (bottom). The additional 10 Ω rotor phase resistance reduces these currents by almost 50%. In Figure 17(bottom) at time of 0.25 seconds the external resistances can be seen are short-circuited, with synchronization occurring at 1.3 seconds.

Figure 18 shows the torque induced by the motor and the torque applied by the load. Since the motor operates as an induction motor from start until it reaches steady state load and then is switched to operate as a synchronous motor, the induced torque of the motor at synchronization-switching changes to a new steady state synchronous motor torque at synchronous speed. In Figure 18(left) the start and synchronization of the motor are illustrated with the rotor short-circuited, while in Figure 18(right) external starting rotor resistances are used. In the latter case the external resistances are short-circuited at 1000 r/min as can be seen in the change in motor torque.

6. EXPERIMENTAL RESULTS

The induction motor used for experimentation can be seen in Figure 19(right) with the fan load mounted on the motor shaft in Figure 19(left). The overall system design for the electronic controlled switch is shown in Figure 20. A current sensor is used to measure the a-phase current of the rotor circuit to determine the correct time to switch to a synchronous mode state. The microcontroller calculates the correct time and transmits a signal to the switching contactors through an amplification stage.

Figure 21(left) displays the control circuit used for the synchronization. Here the Arduino Nano microcontroller used is shown on the left. The amplification transistor circuit can be seen in the middle at the bottom, while the output to the contactors at the bottom right. The ACS712-30A current sensor module, used to measure the a-phase rotor current, is shown in Figure 21(right).



Figure 19: Siemens induction motor (right) with the fan connected load (left).

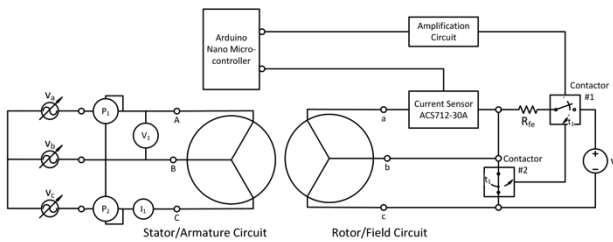


Figure 20: Diagram of the electronic switching system.

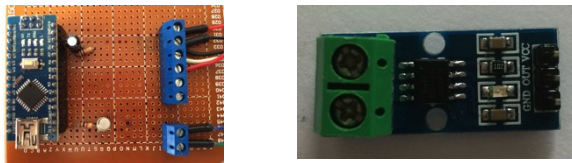


Figure 21: Control circuit of the Arduino microcontroller and amplification stage (left) and the rotor current sensor module (right).

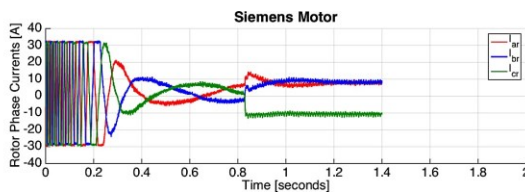


Figure 22: Measured rotor currents of the motor at direct-on-line start and synchronization.

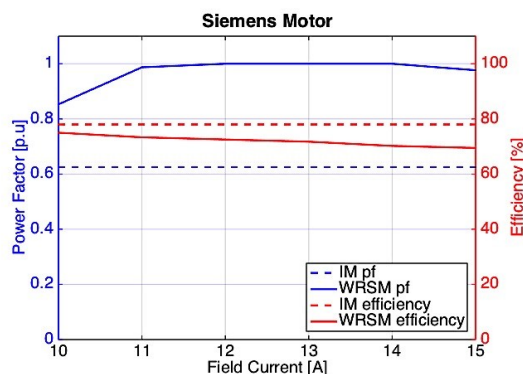


Figure 23: Effect of field current on efficiency and power factor correction at 220 V_{LL}.

Figure 22 illustrates the measured rotor currents of the motor with direct-on-line starting. The waveforms captured illustrate induction motor operation for times less than 0.84 seconds. It can be seen that the current amplitudes at start are much lower than simulated in Figure 15. The reason for this is that the current sensors can only measure up to 30 A and thus saturate at a 30 A value.

At 0.84 seconds the switch is activated and the motor synchronizes. Note how well the measured rotor current transients at synchronization correspond with the simulated currents of Figures 13 and 15. The results of Figure 22 confirm that the synchronization is stable.

In Figure 23 the effect of the field current on the power factor and efficiency of the synchronous motor is illustrated. These values were captured under minimal saturation at 220 V_{LL}. This figure illustrates that the power factor greatly improves from induction mode to synchronous mode of operation. The efficiency, however, is shown to be less and to reduce slightly in synchronous mode, but this is due to the use of the field resistance in Figure 3, which will not be the case in the actual application.

7. CONCLUSION

In this paper a method is proposed and evaluated whereby a cylindrical wound rotor motor be started as induction motor and then synchronized to the grid supply to operate as synchronous motor with a fan load. The following conclusions are drawn from investigation:

- The good agreement found between the simulation results of MATLAB/SIMULINK and SIMPLORER, plus the good agreement between the simulated and measured results confirm that the modelling and simulation of this system can be used with great accuracy to predict performance and stability of the system.
- The simulated and measured results of the proposed synchronization-switching process are shown to be quite promising. It is found and explained that switching at the correct rotor current state lead to stable transition from induction to synchronous motor mode.
- The electronic controlled switch system for synchronization is very simply and performed ideally. The implementation, thus, of such a system is relatively cheap and easy.
- Operating the motor as synchronous motor is shown to improve the power factor of the system. However, it is clear that the line-started-motor must rather be optimally designed for best synchronous motor operation, than using an induction motor design to operate as synchronous motor.
- Although further investigation is necessary, in general it can be concluded that the proposed system looks promising in terms of improving motor performance for large fan loads.

8. REFERENCES

- [1] Stephen D. Umans, *Fitzgerald & Kingsley's Electric Machinery*, 7th ed., McGraw-Hill, Ed. New York, United States of America: McGraw-Hill, 2014.
- [2] T.A. Lipo, "Electric motor analysis and simulation," Wisconsin Power Electronics Research Centre, University of Wisconsin-Madison, Research Report 2000.

Simulation Study of Generator Under-excitation Operation and Under-excitation Limiters

D.N.Ngema^{1*}, A.K.Saha¹

¹University of KwaZulu-Natal, Howard College Campus, Mazisi Kunene Road, Durban 4041, South Africa

*Email: 208528228@stu.ukzn.ac.za, saha@ukzn.ac.za

Abstract: This paper presents simulation studies on loss of field excitation and under-voltage protection using a multifunction generator software relay that resembles commercially used relay for protection of power utility generators in power plants. The paper includes underexcitation operation with respect to under excitation limiters. The underexcitation limiter models studied are suitable for use in large power system stability studies. These models are compatible with current IEEE recommended excitation system models. The simulation case studies are performed on real-time digital simulation platform. The simulation results have been presented and analysed in this paper.

1 INTRODUCTION

Most modern voltage regulators employed on large synchronous machines have the capability to do much more than just regulate machine terminal voltage to a pre-set level. These voltage regulators typically employ various auxiliary control, limiting, and protective devices which are designed to enhance performance and reliability. The voltage regulator limiting functions generally have no effect on excitation output during most normal operating conditions. It is only during severe conditions in which the excitation system, synchronous machine, or power system have been pushed near or beyond defined operating limits that these limiters act to modify excitation output [1]. Underexcitation limiters (UEL) have been available for use since way back. They were primarily designed for eliminating steady state and oscillatory problems arising from underexcited generator operation [2]. UEL were introduced to prevent generator operation below some excitation level that is associated with excessive armature core end heating caused by leakage flux and to prevent generator operation beyond the steady state stability limit [3]. When limiter models are applied, it is important that they be correctly represented with accurate model constants for each particular synchronous machine [1].

The purpose of this paper is to present underexcitation limiter model which can be applied to the excitation system models of synchronous machines and how they operate during loss of field and undervoltage disturbances on generators. RTDS is used as a platform to simulate the studies in which there is a generator connected to a grid. Field failure and under voltage conditions were simulated and tested with

multifunction generator software relay available on RTDS.

2 UNDEREXCITATION OPERATION

Generators may be operated in the under-excited region for the following reasons [2]:

- Based on dispatching to aid in system voltage regulation.
- As a result of the AVR's response to high system voltage.
- Failure in the excitation system resulting in a significant reduction in excitation thus forcing the unit into the under-excited region.
- Power system disturbances and restoration conditions in which load levels are greatly reduced.

2.1. Field failure protection (40)

Loss of excitation on a synchronous machine can be due to a variety of factors including but not limited to operator error, excitation system failure, a short in the field leads, accidental tripping of the field breakers, or flashover of the exciter commutator [4]. During loss of excitation, the synchronous generator, starts functioning like an induction generator. The rotor speed increases, active power output decreases, and the generator draws reactive power from system. High currents are induced in the rotor and stator current as high as 2.0 per unit is possible [5]. These high currents cause dangerous overheating in a very short time. To provide protection against this condition, a two-element offset mho relay is used to protect against loss of field. Properly set, this will detect a loss of field from full load down to almost no load. It is applicable to any type and size of generator, including hydro, gas turbine, steam, and diesel [4].

2.2. Under-voltage protection (27)

Under voltage conditions are not usually harmful to generators, so direct under voltage protection is not normally provided for such conditions. However, overheating due to extended operation at low voltages may damage the auxiliary motors for turbine generator sets. Auxiliary supplies are therefore sometimes monitored by under voltage relays that may trip the generator off line to protect the motors.

Where under voltage protection is required, it should comprise an under voltage element and an associated time delay. Settings must be chosen to avoid maloperation during voltage dips during power system fault clearance or associated with motor starting [6].

2.3. Underexcitation limiters

UEL acts to boost excitation so as to prevent operation that endangers the stability of the machine or severely lead to loss of synchronism due to insufficient excitation. Furthermore, UEL prevent operation that lead to overheating in the stator end region of the synchronous machine as defined by the underexcited region of the machine capability curve and lastly, prevent loss-of-excitation relays from operating during underexcited operation [7]. However, generators may be operated in the underexcited region due to operator action, excitation system failure and system disturbances [8]. For power system disturbances, operation in the underexcited region must be considered in the context of co-ordination with generator loss-of-excitation (LOE) protection settings. LOE relays may also operate for conditions that resemble loss of excitation, such as incorrect operator action or system disturbances [8].

Typically, UEL senses a combination of voltage and current of the synchronous machine or a combination of real and reactive power. The UEL output is applied to AVR either by adding it to the summing junction of the voltage regulator or to the HV gate so as to override the normal action of a regulator. The action of the UEL depends on the implementation function. Two UEL models have been developed, as follows [7][9]:

- Circular characteristic (Type UEL1)
- Single or multiple-segment straight-line characteristic (Type UEL2)

The circular characteristic UEL takes synchronous machine terminal output current and voltage phasor with both magnitude and phase angle as an input to the limiter. The piecewise linear characteristic UEL has either a straight-line or multi-segment characteristic when plotted in reactive vs. real power. The limiter senses reactive and active power as input in modelling [7][9]. The simulation results presented in this paper utilises a single straight-line characteristic underexcitation limiter.

2.4. RTDS

The RTDS configuration used for the studies conducted in this paper is illustrated in fig. 1. A real time digital simulator is a power system tool which provides facilities for simulations that takes place in real-time.

Further, physical equipment such as relays, generator controls etc. can also be connected and tested before use on a real system [5].

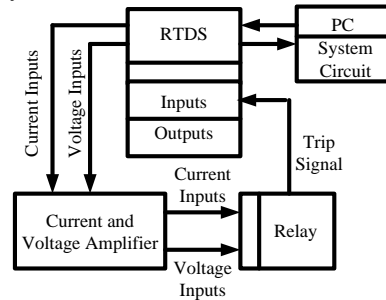


Fig. 1: RTDS connection diagram [10]

The RSCAD software is used to build and compile models of a power system to be simulated using RTDS. It is the interface between the user and the simulator. System models are built in the sub-program DRAFT and monitored in another sub-program RUNTIME. Due to the accuracy of this simulator and the ability of it to interact with real equipment, control and power systems can be designed, modelled and tested realistically. The system is modelled on RSCAD and simulated on RTDS [10].

3 SYSTEM UNDER STUDY

The phase-domain synchronous machine model is used for the studies conducted in this paper. It allows the adjacent excitation system to be modelled solely as an electrical circuit which forms part of the electromagnetic transient solution. This is advantageous in a sense that the electrical equipment supplying the generator field circuit can now be represented in detail using power system components which enables modelling and testing of more realistic contingencies.

This paper uses a power system network rated at 555 MVA, operating at 24 kV line-to-line voltage connected to an infinite bus through a step-up transformer and 400 kV transmission lines as shown in Fig. 2. The generator system is equipped with IEEE governor, power system stabilizer and an excitation system is modelled separately for the purpose of the studies conducted in this paper.

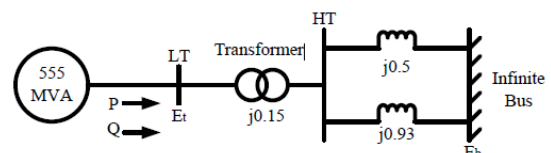


Fig. 2: System under study [9][11]

4 SOFTWARE RELAY SETTINGS

Settings for the following protection elements are well according to IEEE standards for ac generators. Multifunction generator software relay is used for the protection case studies on RSCAD. The relay allows a variety of case studies based on generator protection by means of trip bit signals to ensure the user is aware which relay has operated in case of an abnormal condition.

4.1. Field failure implementation

The loss of field excitation element is suitable for providing the backup function to the generator excitation controls. The relay provides two offset mho elements (40Z1 and 40Z2) to provide excellent high speed detection of loss of excitation [10]. The loss of excitation characteristic refers to the locus of the apparent impedances as viewed from the generator terminals during a loss of excitation condition.

4.2. Under voltage implementation

Generators are usually designed to operate continuously at a minimum voltage of 95% of its rated voltage, while delivering rated power at rated frequency. Operating generator with terminal voltage lower than 95% of its rated voltage may result in undesirable effects such as reduction in stability limit, import of excessive reactive power from the grid to which it is connected, and malfunctioning of voltage sensitive devices and equipment [13]. The undervoltage element is suitable for providing detection of undervoltage conditions. The relay provides two elements for undervoltage detection with time delayed operation:

- Under-voltage relay with instantaneous and inverse time characteristics in which inverse time characteristics element is set at about 90% of its rated voltage with a time-voltage curve so that the operating time is about 9.0 s at 90% of the pickup setting while the instantaneous element is set about 70% of its rated voltage [7][11].
- Under-voltage relay with two stages of voltage pickup and definite time delay set points in which the first stage is typically set at 90% of generator rated voltage with a definite time delay of 10.0 seconds and the second stage pickup is set at 80% of generator rated voltage with a definite time delay of 2 seconds [7][11].

5 SIMULATION, VALIDATION OF RESULTS AND ANALYSIS

This section entails the simulation case studies conducted in this paper as well as analysis of each simulation result.

5.1. System running under normal operating conditions

Prior any test, the system was run and tested for stability. Under this condition, the generator was supplying 0.9 p.u. of active power and 0.436 p.u. of reactive power and generator terminal voltage of 1.0 pu. The results are illustrated in fig. 3 where generator parameters such as terminal voltage, field current, active and reactive power are shown.

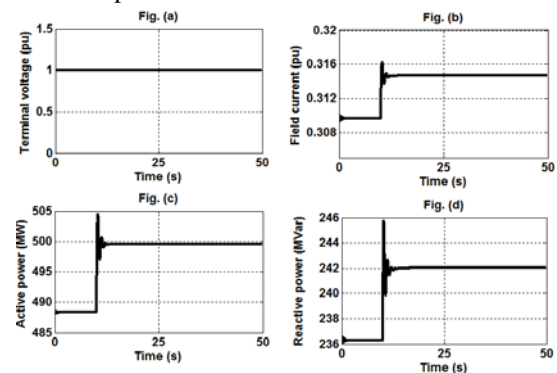


Fig. 3: Normal operating conditions.

Under normal conditions, the generator circuit breaker is closed and represented by logic 1 as illustrated in fig. 4(a) and there is no trip signal. In case of any fault detected, the breaker signal makes a transition from logic 1 to zero, and the trip signal transit from 0 to 1 to show that a trip has been issued.

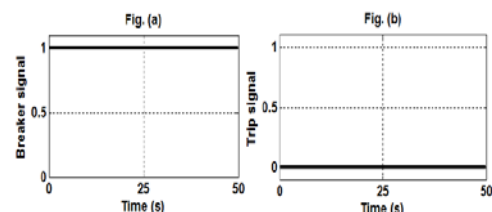


Fig. 4: Breaker and trip signal initial conditions

5.2. System response during field failure

Loss of field occurs when there is failure between the excitation system and the generator field. Misoperation of the field circuit breaker, short-circuit or open-circuit conditions in the excitation system are some of the possible causes of field failure condition. Two mho relays are used for detection of field failure. Both zone 1 and zone 2 trips the generator. The generator is tripped if the generator's apparent impedance remains within the mho characteristic for a selected period of time. Fig. 5 illustrates the system parameters when zone 1 was tested.

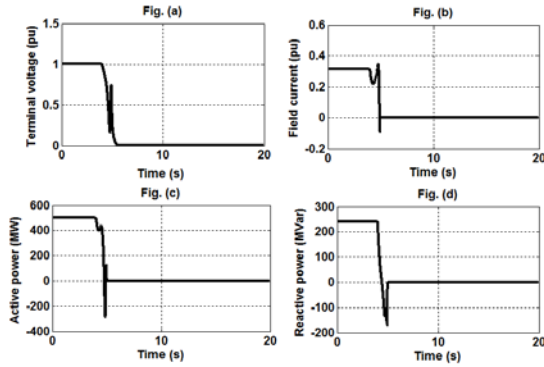


Fig. 5: Zone 1 field failure detection

Following zone 1 field failure detection, the relay issued a trip signal and the generator breaker opened instantly. This is shown in fig. 6. Simulations were performed in which the generator operating point was forced into the underexcited region to observe the impedance relay. Zone 1 was set with a delay very small to allow the impedance locus to detect field failure conditions in a short period of time. This is illustrated in fig. 7 and fig. 9 for zone 1 and zone 2 respectively.

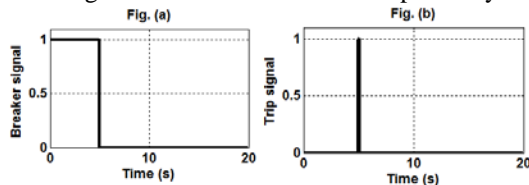


Fig. 6: Breaker and trip signal response for zone 1 detection

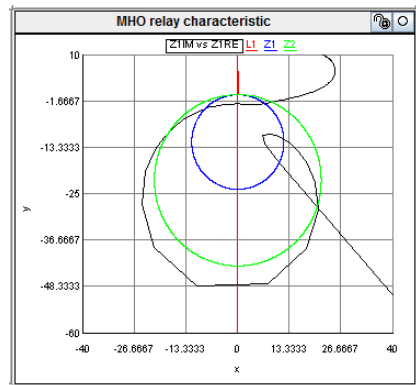


Fig. 7: MHO relay characteristic for zone 1 testing

Zone 1 trip from heavy load conditions whereas zone 2 detects light load conditions. Fig. 8 illustrates the system parameters such as generator terminal voltage, field current, active and reactive power output when zone 2 level testing was conducted. When the machine was forced to operate beyond minimum limits, the voltage to current ratio was reduced causing the generator positive sequence impedance measured at the stator terminals to decrease and enter the fourth quadrant of the R-X plane where it terminates inside the circular characteristic of the MHO relay characteristics, causing the relay to detect loss of field excitation.

The mho impedance characteristic for zone 2 is show in fig. 9.

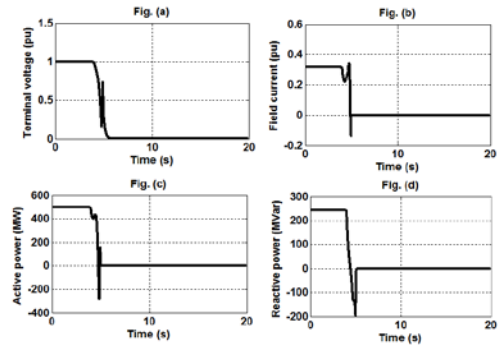


Fig. 7: Zone 2 field failure detection

Any fault detection results in a trip signal being issued by the relay to open any relevant circuit breaker for protection. Fig. 8 shows the breaker and trip signals.

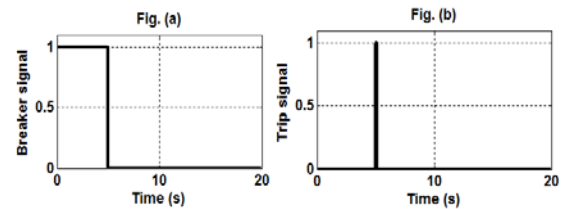


Fig. 8: Breaker and trip signal response for zone 2 detection

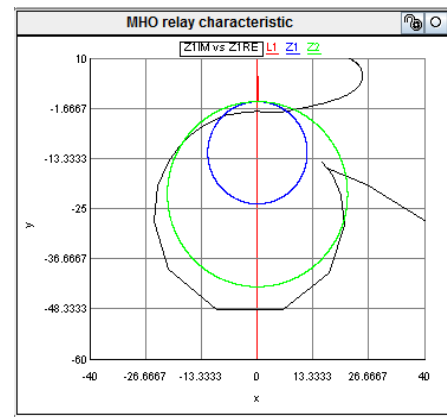


Fig. 9: MHO relay characteristic for zone 2 detection

Depending on the time delay settings of the relay, zone 1 and zone 2 are tested. Both levels are detected by the relay and the response in the system parameters is similar except that zone 1 trip before zone 2 because of impedance magnitude and time delay settings.

5.3. System response during under voltage

The relay offers two under voltage detection levels. The first case is set at 90% of the system phase voltage and the second case is set at 80%. Both levels trip the generator.

To test the generator under voltage level 1, the generator was operated at 89.5% of rated voltage below the 90% set level. When level 1 was detected, the generator reactive power decreases (fig. 8(d)) while active power remains, the decrease in reactive power forces terminal voltage of the machine also to decrease to a relay pickup value. As the level detection persists, a trip signal is sent and the circuit breaker trips (fig. 11) and the generator shuts down.

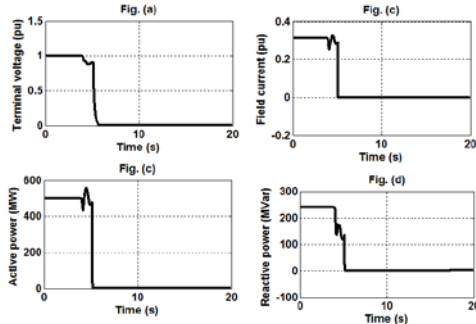


Fig. 10: System behaviour during under-voltage level 1 testing

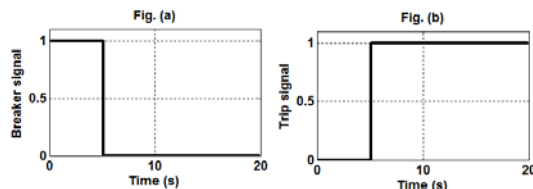


Fig. 11: Breaker and trip signal response for under voltage level 1 detection

Level 2 is tested by running the generator at 79.39% of the rated voltage while the pickup setting of the relay is 80%.

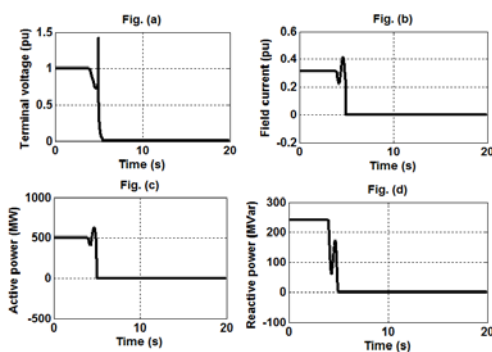


Fig. 12: System behaviour during under voltage level 2 testing

The system behaviour and the breaker and trip signals during level 2 testing of the undervoltage relay is shown in fig. 12 and 13 respectively.

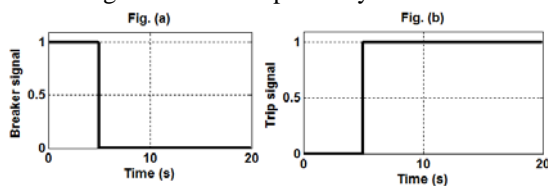


Fig. 13: Breaker and trip signal response for level 2 under voltage detection

5.4. UEL testing

Initially the system is run without any fault implementation. Fig. 14 illustrates the system parameters and the limiter parameters under this condition.

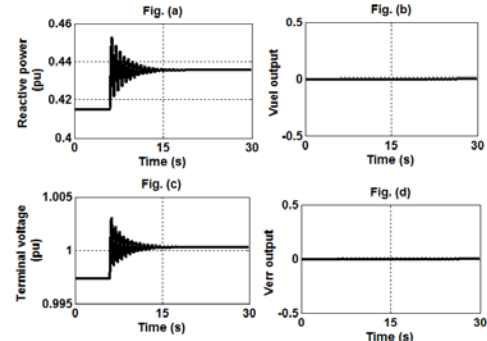


Fig. 14: System behaviour with UEL under full excitation level

Fig. 15 and 16 illustrates the system behaviour as well as the limiter output signal when under excitation limiter was included in the system without any protection backup. Reactive power, terminal voltage, limiter and AVR output were monitor when the system was subjected to different excitation levels. From the set of simulation results obtained, the functionality of the UEL is illustrated by the terminal voltage of the machine remaining between 0.9 pu and 1.0 pu although the excitation level were reduced to about 60% of the machine normal excitation levels. However, with the reduction in excitation, there are a lot of fluctuations in the system as it become more prone to instability.

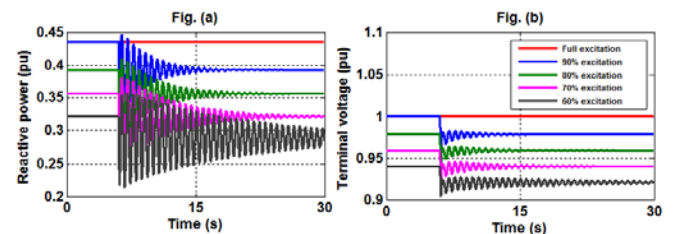


Fig. 15: Reactive power and terminal voltage response during UEL testing with no backup protection

When the limiter is not in operation, the output is zero, and there is no signal added into the AVR summing point, however with changes in the excitation level, the limiter operates to boost the excitation levels into acceptable values.

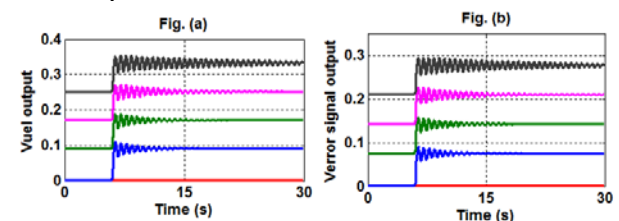


Fig. 16: Vuel output and AVR summing junction output response during UEL testing with no backup protection

Four different excitation levels were tested with loss of field and under-voltage element as backup protection. Fig. 17 and 18 illustrates the response for the different levels. Ideally, level 1 of under-voltage element trip the generator at about 89.5% and level 2 at about 79.3% excitation level as tested in the first section. When the elements were tested with the UEL, the limiter prevented the apparent impedance from entering the LOE relay characteristic, by producing a steady-state terminal voltage rise and the under-voltage relay did not operate at 90%, 80% and 70% as the limiter could produce a steady state voltage rise. However, at 60% excitation levels, the machine parameters were fluctuating and after a delay, the level 1 under-voltage relay operated since the machine terminal voltage was below the level 1 relay pickup setting.

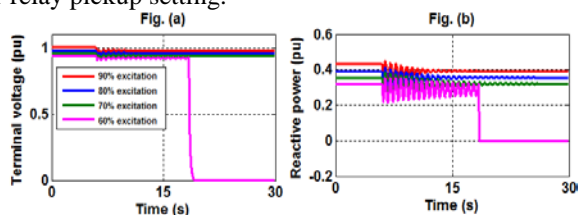


Fig. 17: Terminal voltage and reactive power during UEL testing with loss of field and under-voltage backup protection

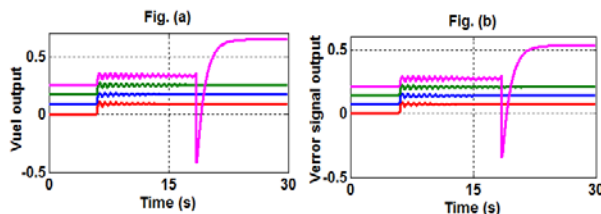


Fig. 18: Vuel output and AVR summing junction output response during UEL testing with loss of field and under-voltage backup protection

The generator breaker and trip signals following level 1 detection are shown in figure 19.

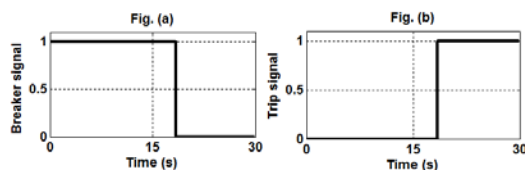


Fig. 19: Breaker and trip signal response

6 CONCLUSION

The generator protective functions studied in this paper are the ones which are closely coordinated with respect to underexcitation limiters and are employed to protect the generator. The simulation results and analysis have been presented in the paper. Limiters embedded in generators AVR do not trip the system but prevent the generator from operating in operation zones that are thermally dangerous to the machine.

UEL prevents the generator from operating in the prohibited underexcited region by sending an error signal to the AVR. This error signal in turn increases the AVR voltage reference so that ultimately the generator output voltage will be increased. The consequence of an UEL taking action is therefore to increase the generator output voltage.

7 REFERENCES

- [1] IEEE Task Force on Excitation Limiters, "Underexcitation Limiter Models for Power System Stability Studies," *IEEE Trans. Energy Conversion*, vol. 10, September 1995
- [2] G.R.Berube and L.M. Hajagos, 'Coordination of Underexcitation Limiters and Loss of Field Excitation Relay with Generator Capability',
- [3] J. R. Ribeiro, "Minimum Excitation Limiter Effects on Generator Response to System Disturbances," *IEEE Trans. Power Delivery*, vol. 6, March 1991.
- [4] N.G. Chothani, A.K. Desai, M.B. Raichura and A.S. Chaturvedi: "Development of generator protection using multifunction numerical relay in laboratory", *International Journal of Advanced Research in Electrical, Electronics, and Instrumentation Engineering*, Vol. 3, Issue. 4 pp. 8569-8575, April 2014.
- [5] W.A.Pullman, 'SEL-300G Generator Relay, [Installation Manual]' Schweitzer Engineering Laboratories Inc., 2007.
- [6] Alstom Group: "Network protection & automation guide, chapter 17, generator and generator-transformer protection", Alstom Grid, pp. 17-1-17-35. May 2011.
- [7] IEEE Std 421.5™-2005: "IEEE Recommended Practice for Excitation System Models for Power System Stability Studies", IEEE, 3 Park Avenue New York, NY 10016-5997, USA, 16 February 2007
- [8] G.R.Berube and L.M. Hajagos, R.E.Beaulieu 'A Utility Perspective on Under-Excitation Limiters'
- [9] P. Kundur: "Power system stability and control", Electric Power Research Institute, McGraw-Hill, Inc., New York, ISBN-13:978-0-07-035958-1.
- [10] RTDS: "Manual Set", Real Time Digital Simulation, pp. 1-517, November 2006
- [11] A.K. Saha: "Simulation study of generator under-voltage and over-voltage protection", submitted for Southern African Universities Power Engineering Conference, 2016.
- [12] Power Systems Relaying Committee: "IEEE guide for AC generator protections – C37.102 TM - 2006", IEEE Power Engineering Society, IEEE, 3 Park Avenue, New York, NY, 10016-5997, USA, pp. 1-177, November 2006.

INDUCTION MOTOR EFFICIENCY TEST METHODS: A COMPARISON OF STANDARDS

S Deda*, JA de Kock**

* MEng Student- School of Electrical, Electronic and Computer Engineering, North-West University Potchefstroom

** Professor- School of Electrical, Electronic and Computer Engineering, North-West University Potchefstroom

Abstract

The efficiency data provided by manufacturers is measured or calculated according to different national and international standards. These standards use different means to incorporate the stray load losses and use different test methods; thus, the efficiency values obtained from different testing standards can vary. This leads to problems in competition and a potentially confusing situation for manufacturers and customers [1]. Hence, there is a need to compare the standards and highlight the possible variations leading to these differences, their causes and recommend where possible, solutions on how they can be eliminated.

1 INTRODUCTION

Energy efficiency has been a matter of global interest in the past two decades. Resources are being channelled towards developing and improving the efficient use of electrical energy. Energy prices have been rising and countries are struggling to meet the ever increasing demands of their consumers. Most electrical energy is consumed by electrical drives.

Determining induction motor efficiency is of prime importance to three groups of people namely, the manufacturers, customers and legislators [2]. Stray load losses (SLL) must be accurately determined during efficiency testing.

Customers are concerned with the total energy loss a machine makes or the efficiency of a machine, as this will determine the running cost of the machine. Therefore, the accuracy of declared machine efficiency is paramount and efficiency values, which obscure the real losses, are misleading [3]. Knowing the exact value of motor losses is not only important for saving energy, but also to keep the motor heating within specified limits to ensure maximum machine life [4]. Furthermore, legislators need to be enlightened so that they enact policies that promote efficient energy conversation, and if need be, even put up incentives, which encourage the manufacture and acquisition of more efficient electrical machines. A brief survey of motors, which enter the South African market, will highlight the importance of having accurate efficiency values.

2 SOUTH AFRICA'S LOCAL MARKET

South Africa's electric motor industry market is largely supplied by Brazilian, European and Chinese manufacturers. It is important to know which standards are being used to measure/calculate the efficiency of motors being supplied to the local market.

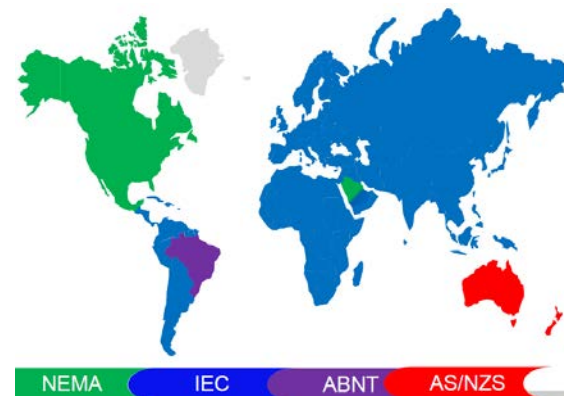


Figure 1: International standards used in different parts of the world [6]

Machines of the same rating, but from different manufacturers usually have different efficiency values. It results from the variations found in the methods used to determine the efficiency.

The work presented in this paper focuses on a comparison of standards. Losses in motors and differences in the test methods will be discussed, which give rise to different efficiency values between the standards.

3 LOSSES IN MOTORS

Induction machine losses can be subdivided into conventional losses (iron losses, ohmic

losses, friction and windage losses) and SLL, in the stator and rotor, under load and no-load conditions. Figure 2 gives a summary of losses and their respective locations.

3.1 Conventional losses

The conventional losses are:

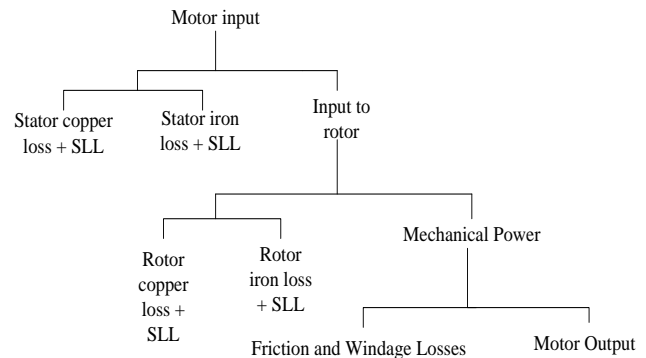
- a) Ohmic losses in the conductors that are a function of the current and resistance, they increase rapidly with the load current and can be reduced e.g. by increasing the cross sectional area of the stator and rotor conductors,
- b) Iron losses that occur mainly in the steel laminations of the stator and the rotor due to hysteresis and eddy currents, varying with flux density and frequency. They can be reduced e.g. by using thinner laminations, sharp punching tools or laser cutting and improved magnetic materials,
- c) Mechanical losses are due to friction in the bearings and – in case of slip ring machines – brush friction losses, the ventilation and windage losses. They can be decreased by using low friction bearings, improved and optimized ventilation and fan design.

3.2 Stray load losses

The stray load losses result from stray flux, the step-like (non-sinusoidal) distribution of the air gap flux density due to the arrangement of the winding and the cage in the slots, inter-bar currents [5] and mechanical imperfections in the airgap. The eccentric field induced voltages in the parallel paths of the stator windings give rise to equalizing currents, which also contribute to SLL. They can be reduced by optimal design and careful manufacturing [6].

The main components of stray load losses in squirrel-cage induction motors are:

- a) Fundamental-frequency stray load losses in the stator which consist of:
 - i) Skin effect (first and second order) in the stator winding,
 - ii) Stray load losses in the end region of the stator and rotor windings due to axial flux components, and
 - iii) Eddy current losses especially in high saturation areas in the stator housing and in metallic parts e.g. the bearing brackets.



- b) Higher frequency stray load losses in the rotor and stator include:

- i) The skin effect in the rotor cage, harmonic rotor currents due to the third space harmonic caused by iron saturation,
- ii) The losses due to inter-bar currents in cages with skewed rotor slots,
- iii) The tooth pulsation losses in the rotor and the stator caused by the distortion of the air gap flux density distribution due to the slot openings,
- iv) The surface losses in the rotor and the stator,
- v) The losses in the stator winding due to harmonic currents and circulating currents in delta connected stator windings due to the third space harmonic caused by iron saturation, and
- vi) The iron losses in the stator core due to the third space harmonic caused by the distortion of the field distribution due to iron saturation.

Induction motor efficiency test methods use different methods to determine efficiency, which are basically classified under direct or indirect methods and are affected by how the stray load losses are accounted for.

4 EFFICIENCY DETERMINATION METHODS

The methods of efficiency determination vary greatly in terms of their complexity, overall performance and the suitability for the plant conditions. Manufacturers provide efficiency values on the nameplates of their machines. This data is calculated or measured using different national or international standards.

These standards use different methods and assumptions to incorporate the stray load losses, thus the efficiency values obtained from different testing standards can differ by several percent. This leads to problems in competition and to a confusing situation for customers [1].

Figure 2: Induction motor losses

The IEEE/ANSI, IEC and AS/NZS standards are leading the process of critically evaluating the efficiency and the stray load losses in induction motors. These standards currently provide several methods and procedures for efficiency measurements in accordance with the type and the machine rating, with the desired accuracy, etc. In the direct (input-output) method the mechanical power is determined through an accurate measurement of speed and torque and used in [12], [13] and [7]. In the indirect method (segregation of losses) the loss components are determined individually and used in [12], [13] and [7]. The Calorimetric method is also used in the Australian standard [7]. This method is accurate, but very expensive and time consuming. The IEC 60034 standard [13] has an additional Eh-Y test to determine SLL. Previous versions of the IEC standard proposed a fixed allowance to represent SLL, for example 0.5% of input power. Both [12] and [13] require no-load, full-load, and part-load tests. The IEEE approach requires no-load tests over a range of voltages and a wider range of loads for the part-load conditions. The AN/NZS standard is closer to the IEC standard, thus the focus is of this comparison on the IEEE and IEC standards.

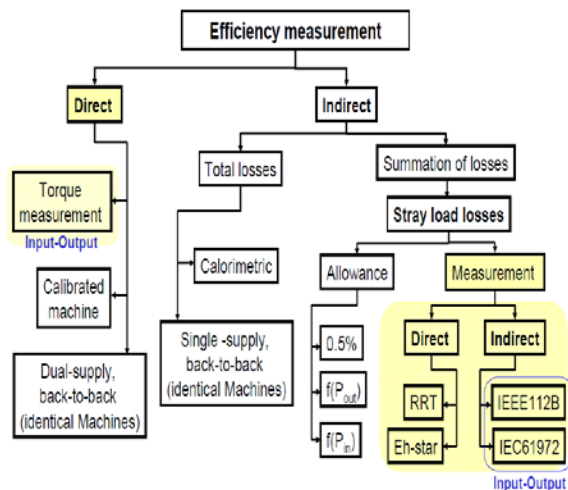


Figure 3 Test Methods [10]

Some methods of efficiency measurement and losses determination are presented in Figure 3. Differences in the standards are found in the test conditions and can be classified into four categories listed below:

4.1 Power Supply

The maximum deviation from rated voltage during testing of the machine is critical because efficiency varies with voltage [8] and differs between standards (see table 1).

Table 1: Power supply variations

Parameter	IEEE	IEC	AN/NZS
Max. THD (%)	5	1.5 ¹	-
Max. Voltage Unbalance (%)	0.5	0.5 ²	-
Max. Deviation from Rated Voltage (%)	-	-	0.5
Max. Deviation from Rated Frequency (%)	0.1	0.1	0.3

4.2 Instrumentation

Instrumentation requirements are generally the same, although IEC speed accuracy may need to be averaged against the other standards to bring about same results (see table 2).

Table 2: Instrumentation

Parameter	IEEE	IEC	AS/NZS
Instrument transformer (%)	±0.3	±0.3	±0.3
Power (%)	±0.2	±0.2	±0.2
Voltage (%)	±0.2	±0.2	±0.2
Current (%)	±0.2	±0.2	±0.2
Torque (%)	±0.2	±0.2	±0.2
Speed (rpm)	±1	±0.1	±1
Frequency (%)	±0.1	±0.1	±0.1
Resistance (%)	±0.2	±0.2	±0.2
Temp (°C)	±1	±1	±1

4.3 Test Procedure

The IEC gives an option to use resistance or temperature detectors while the AS/NZS has no room for temperature measurements as shown in Table 3. Temperature variations influence the skin effect in the motor conductors, thus altering efficiency results. When bearing loss stabilization is not done, the test shall be performed in a specific order where the load test is followed by the no-load test.

4.4 Computation of Results

Table 4 highlights similarities and differences in the computation of results. Higher efficiency values are expected when voltage drop is considered, although there will not be a significant difference for large motors.

Moreover, human error is a source of getting different results when testing for efficiency. Repeatability of tests and execution of the tests contribute to human error. Different people

running the same test using same standard and test bench will yield different results [9].

Table 3: Test Procedure

Step	IEEE	IEC	AS/NZS
Motor Temperature by detector	Yes	Optional	No
Measurement of motor resistance value	Any of 3	All 3	All 3
Temperature test at rated load	Yes	Yes	Yes
Measurement of motor temperature during load test	T_{detector}	$R_{\text{stator before}}$ $R_{\text{stator after}}$	$R_{\text{stator before}}$ $R_{\text{stator after}}$
Load test	Yes	Yes	Yes
Bearing loss stabilization	Yes	No	Yes
No-load test points	Min 6 Variable values	8 Fixed Values	Min 6 Variable values
Measurement of motor temperature during no-load test	T_{Detector}	$R_{\text{stator before}}$ $R_{\text{stator after}}$	$R_{\text{stator before}}$ $R_{\text{stator after}}$

The main difference of the mentioned methods, beside measurement equipment and setup, is the determination of the stray load losses. Stray load losses are difficult to predict analytically and measure accurately, because they constitute only a small fraction of the total power losses in an induction machine.

The most used methods can be subdivided in:

a) Direct measurement of SLL:

- i) Reverse rotation test in [10] method E and [11]
- ii) Eh-star method in [13]

b) Indirect measurement of SLL:

- i) Input-output method with loss segregation (residual loss method) in [12] and [11]
- ii) Calorimetric method with segregation of losses is used in [7].

Measurement of SLL using input-output test in the residual loss method in IEC 60034-2 Ed. 4 and IEEE 112B, calorimetric and reverse rotation test (RRT) methods need calibrated measurement equipment of high accuracy and a coupled load. Furthermore, it is time and energy consuming. On the contrary, the Eh-star method is an economical alternative test.

Table 4: Computation of results

Step	IEEE	IEC	AS/NZS
------	------	-----	--------

Calculation of motor rated load resistance	$t \leq t_{\text{table}}$	$t = t_0$	$t \leq t_{\text{table}}$
Calculation of motor load points resistance	Based on T_{detector}	$R_{\text{stator before}}$ $R_{\text{stator after}}$ $R_{\text{stator linear}}$	$R_{\text{stator before}}$ $R_{\text{stator after}}$ $R_{\text{stator average}}$
Core losses computation considering voltage drop in the stator	Yes	Yes	Yes
Correlation coefficient of the residual losses	0.90	0.95	0.95
Correction of windage / friction losses	No	Yes	No
Correction of input power	No	Yes	No
Coefficient for temperature correction	234.5	235	235

5 A COMPARISON OF THE TEST METHODS

5.1 Direct Methods for Total Loss

This method is used in [12] and [11].

Advantages

- i) Real physical behaviour due to the direct losses assessment from the input-output test.
- ii) [11] considers the load dependent-iron losses.

Disadvantages

- i) IEEE112 method B considers iron losses to be independent of the load, thus affecting small motors (with big stator resistance) more.
- ii) [12] method B and [13] considers the friction and windage losses to be independent of the changing speeds during the load test, leading to a small error in the SLL especially for motors with higher slip values.
- iii) Coupling of the machine with the load and use of the dynamometer is necessary.
- iv) Since the losses are the differences of nearly equal/output power quantities, the upper limit of efficiency to be evaluated with sufficient accuracy should be 95% to 96%.
- v) Procedure takes considerable time.

5.2 Indirect Methods for Total Losses

a) Reverse Rotation Test

Advantages

- i) Physically correct determination of the fundamental SLL in the stator at the removed rotor test except neglecting of small iron losses.

Disadvantages

- i) The consideration of load-dependent friction and windage losses affects the efficiency determination, e.g. method E in [12] and [13], but not the SLL.

- ii) Accuracy of instrumentation is important as load has to be coupled to a calibrated dynamometer.
- iii) No real physical load situation of the machine.
- iv) At the slip $s=2$ the magnetisation current is small, so low main flux and no main flux iron saturation. The zig-zag stray flux dominates.
- v) Different harmonic slip in the 5th and 7th air gap field harmonic causes different SLLs.
- vi) RRT generally yields high SLLs
- vii) Two test procedures are generally needed.

b) Eh-star method

Advantages

- i) No coupling of the machine with the load and no dynamometer needed.
- ii) Simple and short test.
- iii) No difference of nearly equal power quantities to be measured, so no efficiency limits.
- iv) Main flux too small, though it is bigger than RRT due to the positive sequence system.

Disadvantages

- i) No real physical load situation of the machine.
- ii) Complicated theory.
- iii) Auxiliary power resistor R_{eh} and maybe a switch for the symmetric start-up are necessary.
- iv) Loss component due to three times stator frequency circulating current in delta-connected winding, caused by the saturation harmonic, is not included.

c) Equivalent No-Load Method

Advantages

- i) No coupling of the machine with load and no dynamometer are necessary, thus less expensive and saves time.
- ii) Method is not complicated.
- iii) Fundamental current effects, e.g. current displacement, are considered.

Disadvantages

- i) Rotor fundamental current is missing, so the SLL are bigger than at rated condition.
- ii) Machine is highly saturated during test, so the main flux dependent SLL are bigger than at rated condition.
- iii) Voltage must be higher than the rated voltage to reach the rated current at no-load.
- iv) Resistive losses must be measured accurately.
- v) High frequency losses mainly localized in the rotor, so the rotor fundamental current may be of minor influence [12].

The direct method for calculating efficiency (measurement of the input and output power) suffers from measurement uncertainty, therefore it is limited for motors of lower efficiency. The indirect method is less sensitive to measurement errors and seems to be, depending on the measurement accuracy of the total power losses P_d , useful also for higher efficiency machines. In the efforts to improve the efficiency of the induction machine the stray load losses should be taken into account accurately. Due to the unavoidable measurement errors, the indirect determination of the stray load losses by measuring the input and output power is generally not accurate enough for the small value of the stray load losses at high efficiencies. Therefore, the direct measurement methods of the stray load losses could be useful at high efficiencies, but difficult to execute. A simple and fast test, like the eh-star method, is required for the stray load losses measurement, e.g. during the process of the optimisation of the motor design.

6 CONCLUSION

Recently most standards were revised as illustrated by the minor differences tabulated in this document. However, small differences still exist, mainly in the way stray load losses are measured and these give rise to inconsistent efficiency results. Furthermore, different people running the same tests under the same conditions will yield different results, a consequence of human error [9]. There is need to work towards a full harmonization of the standards so as to create a level global platform. Moreover, it will result in improved energy conservation.

7 BIBLIOGRAPHY

- [1] M. Aoulkadi and A. Binder, *Evaluation of Different Measurement Methods to Determine Stray Load Losses in Induction Machines*, IEEE Industrial Electronics Magazine, 2008.
- [2] E. B. Agamloh, "A Comparison of Direct and Indirect Measurement of Induction Motor Efficiency," *IEEE*, p. 36, 2009.
- [3] C. Glew, "Stray Load Losses in Motors: A Challenge to Academia," in *EMD97*, UK, 1997.

- [4] A. Jalilian, *Calorimetric measurement of induction motor harmonic losses*, Australia: University of Wollongong, 1997.
- [5] R. Carlson, C. A. d. Silva, N. Sadowski and M. Lajoie-Mazenc, "An Analysis of Inter-bar Currents on a Polyphase Cage Induction Motor," *Revista Controle & Automação*, vol. 15, no. 4, pp. 476-484, Novembro e Dezembro 2004.
- [6] J. Pyrhoen, T. Jokinen and V. Hrabovcova, *Design of Rotating Electrical Machines*, 1st ed., United Kingdom: John Wiley and Sons. Ltd, 2014, pp. 266-278.
- [7] A. Standard, "Rotating Electrical Machinery," Standards Australia, New South Wales, 1907.
- [8] A. Boglietti, A. Cavagnino, L. Ferraris and M. Lazzari, "Impact of the Supply Voltage on the Stray-Load Losses in Induction Motors," *IEEE Transactions On Industry Applications*, vol. 46, no. 4, pp. 1374-1380, July/August 2010.
- [9] W. Deprez, "Energy Efficiency of Induction Machines: A critical assessment," Leuven Catholic University, Belgium, 2008.
- [10] IEEE, "Standard for Standard Test Procedure for Polyphase Induction Motors and Generators". Patent 978-0-7381-9251-2, 26 07 2014.
- [11] IEC, "Rotating Electrical Machines. Part 2-1 Standard Methods for Determining the Losses and Efficiencies from tests (excluding machines for traction vehicles)". France Patent IEC 60034-2-1, 27 06 2014.
- [12] M. Aoukadi, "Experimental Determination of Stray Load Losses in Cage Induction Machines," <http://tuprints.ulb.tu-darmstadt.de>, Darmstadt, 14. 07. 2010.
- [13] "<http://www.wegelectricalmotors.com>," Manufacturers Distributor, Inc., 2011 . [Online]. Available: <http://www.weg-electricalmotors.com/about.html>. [Accessed 10 October 2015].
- [14] D. Basso, "WEG Motor Global Energy Efficiency Legislations 2015 and beyond," WEG Electric Corp , 2014.
- [15] A. M. a. Generators, "Low Voltage Motors- Motor Guide," ABB Motors and Generators, 2014.
- [16] H. Li and R. S. Curiac, "Designing More Efficient Large Industrial Induction Motors by Utilizing the Advantages of Adjustable-Speed Drives," *IEEE Trans. on Industry Applications*, vol. 46, no. No 5, pp. 1805-1809, September/October 2010.
- [17] M. Benhaddadi, G. Olivier and B. Dima, "Energy savings by means of generalization adjustable speed drive utilization," in *Canadian Conference on Electrical and Computer Engineering*, 2007.

8 BIOGRAPHIES



Simon Deda received his BEng Mechatronics at Chinhoyi University of Technology, Zimbabwe in 2011. He has worked for Zimbabwe Power Company at

Hwange Power Station and Industrial Electrics in the motor rewind section of the company. Currently he is studying to an MEng Electrical and Electronics at North-West University in South Africa. Research interests are energy efficiency improvements in the design, operation, and repair of electric machines



Jan A de Kock holds a B Eng, M Eng and PhD in Electrical Engineering from Stellenbosch University in South Africa. He is Professor in Electrical Engineering at the North-West University, in South Africa.

His academic and consulting interests include power system dynamic performance, power quality, protection performance and optimization studies, improvements of generator dynamic response, induction and synchronous machine transient performance, and high speed bus transfer system.

Electromagnetic design of active magnetic bearings for a 30 000 r/min PMSM

K. Swanepoel and A.J. Grobler

School for Electrical, Electronic and Computer Engineering, North-West University, Potchefstroom, South Africa E-mail: swanepoel.keith@gmail.com

Abstract: Overheating of the permanent magnets (PM) on a permanent magnet synchronous machine (PMSM) is a big problem as this can lead to the demagnetization of the PMs. This is currently the problem with the PMSMs nicknamed the TWINS. This problem can be solved by replacing the ball bearings with a low loss alternative: active magnetic bearings (AMB). The parts that will be considered in the electromagnetic design of the AMBs include: 1) The material stresses in the rotor laminations. 2) The rotordynamic behaviour to determine the required electromagnetic forces. 3) Electromagnetic design to ensure that the electromagnet will be able to produce the required forces. 4) Losses that will be produced by the electromagnet, to ensure that it is sufficiently low. 5) Theoretical implementation of the electromagnet, this is to ensure that it would be possible to implement the electromagnet on the desired application.

Keywords: Active magnetic bearing, rotor, electromagnet, laminations, stress analysis, rotor dynamic analysis, losses.

1. INTRODUCTION

Overheating of the permanent magnets on a permanent magnet synchronous machines (PMSM) is a big problem as this can lead to the demagnetization of its permanent magnets. The PMSM nicknamed the TWINS used for research at the McTronX lab of the North-West University can't be operated at its full load for extensive periods due to excessive heat generated by friction in its ball bearings [1]. This problem can be solved by replacing the ball bearings with active magnetic bearings (AMB). An AMB provides a low loss alternative to ball bearing by eliminating mechanical friction. This is done by suspending the rotor with electromagnets. AMBs provide other advantages than low loss. This includes actively controlling the stiffness and damping of the bearings to ensure stable levitation over a greater speed range. This project focuses on the electromagnetic design of an AMB system.

2. ACTIVE MAGNETIC BEARINGS

Active magnetic bearings use magnetic fields to levitate a rotor in a desired position. The main advantages of AMBs are that it produces lower losses compared to ball bearings, as well as the rotor dynamic behaviour can be actively controlled to produce the desired results. Figure 1 shows the architecture of a typical AMB system. A sensor senses the position of the rotor, this information is used by the controller to adjust the current through the coils on the electromagnet. The amplifier increases the power of the control signal to ensure that enough power is delivered to the electromagnet. Backup bearings are used to support the rotor in case any of the electrical components fail. It should however be noted that this article mainly discusses the electromagnetic design of an AMB but the interfaces with the other components was also considered.

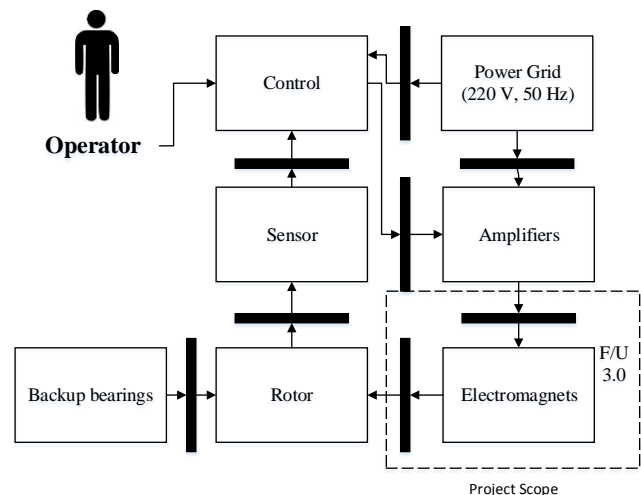


Figure 1: Architecture of an AMB system

3. DETAIL DESIGN

Figure 2 illustrates the design process that was followed in the electromagnetic design of an AMB system. Firstly a stress analysis was performed on the lamination stacks that will be shrink fitted to the rotor. This is to ensure that it will be able to withstand the stresses experienced at 30 000 r/min. Secondly a rotor dynamic analysis needs to be performed to determine the force needed by the electromagnets to counteract the unbalance force created by the unbalance on the rotor. These forces produced by the rotor dynamic analysis is used as an input to calculate the size of the electromagnets. The losses that will be present in the magnetic material on the rotor needs to be determined. This is to verify that the implementation of an AMB will significantly reduce the losses producing heat in the rotor. This is to ensure that the permanent magnet (PM) on the rotor do not demagnetize when the machine is operating at 30 000 r/min. Next the achievable stiffness and damping needs to be verified. Lastly the

designed electromagnets needs to be theoretically implemented to verify that there will be enough space to implement it in.

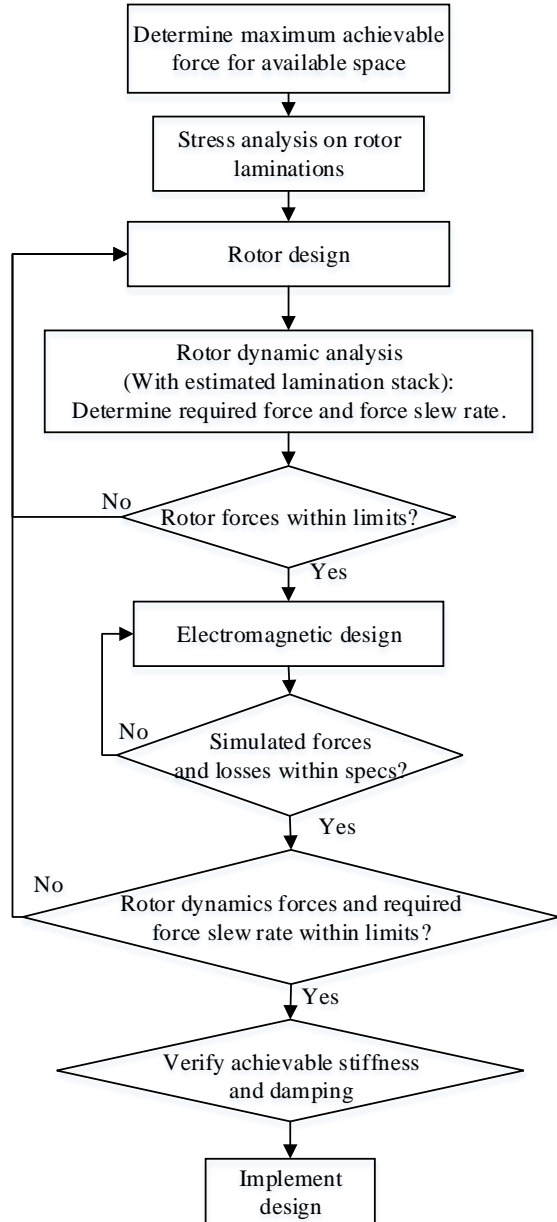


Figure 2: Design process

3.1 Stress analysis

A stress analysis was conducted on the lamination material that needs to be shrink fitted onto the shaft of the TWINS. This is to ensure that the lamination stack can withstand the stress that it will experience when the rotor is rotating at 30 000 r/min and to ensure that it will not lose contact with the shaft.

It was concluded out of the stress analysis that if a shrink fit with an interference of $8\mu\text{m}$ between the radius's is made, that the lamination stack will not lose contact with the shaft or break under the stress that it will experience.

This shrink fit needs to be manufactured with a maximum tolerance of $\pm 1\mu\text{m}$. This is to ensure that the laminations will not lose contact with the shaft with a minimum interference and will not break with a maximum interference.

3.2 Rotor Dynamic Analysis

A rotor dynamic analysis was performed to determine the force that will be required by the electromagnets to counteract the force created by the unbalance on the rotor.

The amount of unbalance that will be present on the rotor is determined by the balancing standard G that the rotor is to be balanced to [2]. The permissible unbalance that may be present on the rotor is given by (1).

$$U_{per} = \frac{9.549(G \cdot m)}{N_r} \quad [\text{kg} \cdot \text{mm}] \quad (1)$$

This unbalance can be located at two critical positions namely a) static unbalance of U_{per} in the centre of the rotor or b) a dynamic unbalance of $0.5 U_{per}$ on the centre of the journal of the AMBs. Note that the dynamic unbalance that will produce the maximum unbalance forces is when $0.5 U_{per}$ is located 180° out of phase with each other.

When the rotor is rotating with an angular velocity of ω , the centrifugal force F_{ub} acting on the additional piece of mass will be [3].

$$F_{ub} = \frac{U_{per}}{1000} \cdot \omega^2 \quad (2)$$

This can be used to determine a preliminary supporting stiffness of the bearing. The required stiffness is approximated by taking the maximum force that will be experienced by the rotor and dividing it by the distance that the rotor is allowed to displace from its centre. The stiffness is given by (3).

$$k = \frac{0.5 \cdot (F_{ub} + F_w)}{0.2 \cdot r_{rbb}} \quad (3)$$

Where r_{rbb} is the distance from the rotor to the backup bearing, this is called the clearance of the rotor. It is specified that the rotor is not allowed to displace more than 20 % of the clearance due to the fact that the backup bearing will not be 100 % aligned with the stator of the AMB, meaning that the clearance level will be a little less than r_{rbb} on one side of the rotor.

The rotor dynamic analysis was firstly done with a balancing of G1 for maximum added material to see if this would be sufficient. This produced a permissible unbalance of $U_{per} = 1.34 \times 10^3 \text{ kg} \cdot \text{mm}$ and a stiffness of $k = 569 \text{ N/mm}$. It was seen that highest unbalance force is produced by a static unbalance. It was however seen that this will produce an unbalance force of 1020 N at 30 000 r/min. This is more than the allowed force meaning that the rotor needs to be balanced with a smaller eccentricity.

Next a balancing standard of G 0.1 was used to determine if this would be sufficient. This yielded the following parameters: $m = 4.36$ kg, $U_{per} = 1.34 \times 10^4$ kg.mm, $k = 569$ N/mm. This produces a force of 121 N that will be required by the electromagnets to counteract the unbalance forces at 30 000 r/min as shown in Figure 3. This force is achievable by the electromagnets with the available space.

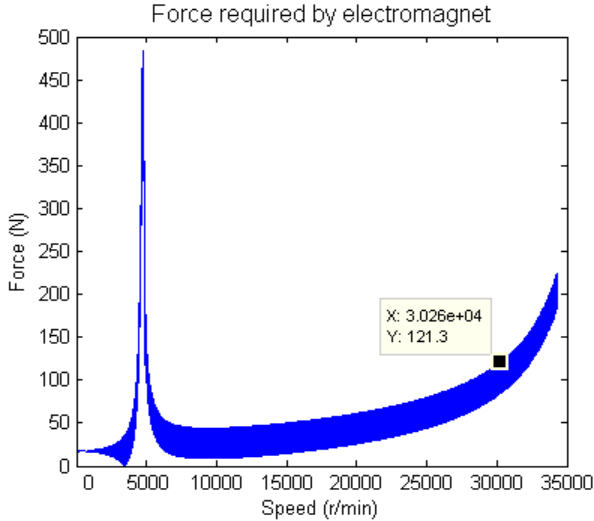


Figure 3: Force required by electromagnets

It can be seen that a critical frequency is present at 5 000 r/min this however falls outside the operating range of the machine. The critical frequency can also be shifted by changing the supporting stiffness of the AMB's [4].

It was decided out of the rotor dynamic analysis that the AMB's needs to be designed to be able to produce 150N and the and a supporting stiffness of 500 N/mm. The supporting stiffness however does not influence the electromagnetic design. The supporting stiffness is mainly influenced by the control parameters.

3.3 Electromagnetic Design

The required force determined by the rotor dynamic analysis and the available space on the existing rotor of the TWINS determines the size and shape of the electromagnets. The required stiffness and damping of the AMB does not influence the design of the electromagnets. It largely dependent on the control of the current through the coils of the electromagnets. The design steps that was used to design the electromagnets was based on the design process for a heteropolar radial bearing outlined in [5].

The geometry of an 8 pole heteropolar radial bearing is shown in Figure 4. This will be used to specify the size and shape of the electromagnet that needs to be designed.

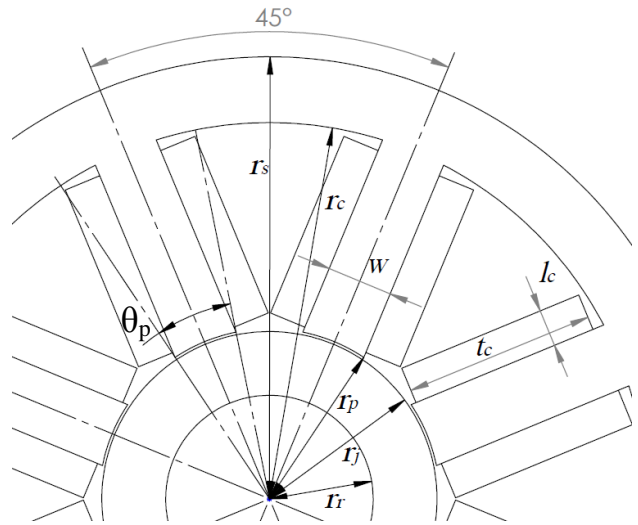


Figure 4: Electromagnet geometry

Symbols relating to the design is shown in appendix A:

The design choices that were made is listed below:

1. Material: M270-35A lamination material will be used to construct the journal and stator of the electromagnet. This is to reduce eddy current losses.
2. Quadrant coil control will be used: Meaning that two coils will be connected in series, this is to reduce the number of power amplifiers needed.
3. No flux splitting will be used between coil pairs, this is called a NNSSNNSS configuration: This is to simplify control.
4. Air gap $g_0 = 0.5$ mm: This represents a typical air gap.
5. Bias linearization: Each coil will be bias with a biasing current. This is to linearize the force produced by a coil pair as well as to improve the slew rate of the AMB for a given amplifier voltage [6].

Journal sizing:

The maximum force needed by the electromagnet that was obtained from the rotor dynamic analysis dictates the airgap area of each pole leg. A maximum operating flux density of 1 T was chosen to ensure that the magnetic material is operated in its linear range. Using an 8 pole heteropolar configuration as shown in Figure 4, the air gap area is obtained by using (4).

$$A_g = \frac{2 \cdot F_{max} \cdot \mu_0}{\eta \cdot B_{sat}^2 \cdot n \cdot \sigma} \quad (4)$$

$$A_g = 226.7 \times 10^{-6} \text{ m}^2$$

The scaling constant σ can be shown to be 0.231 for an 8 pole stator and 0.25 for an 4 pole stator. A derating factor (η) of 0.9 was used to account for magnetic leakage and fringing effects. This air gap area was used to determine the pole width and the axial length of the journal. The pole width and axial length is related by (5).

$$A_g = w \cdot l \quad (5)$$

The iron ratio was used to vary the pole width for a certain journal radius. The iron ratio is defined as the ratio between the total pole angle and the circumference as shown in (6).

$$f_i = \frac{n \cdot \theta_p}{2\pi} \quad (6)$$

The pole width produced for a given journal radius and iron ratio is given by (7).

$$w = 2(r_j + g_0) \sin\left(\frac{\pi \cdot \theta_p}{n}\right) \quad (7)$$

To avoid saturation of the journals magnetic materials radial length ($r_j - r_r$) needs to be more than the width of the stator legs:

$$r_j \geq r_r + f_s \cdot w \quad (8)$$

The pole width and axial length was calculated by varying the journal radius from its minimum to maximum value, this is to determine which radius will produce the best axial length. This was done for a variety of iron ratios as shown in Figure 5. It was decided to use the maximum journal radius ($r_j = 31.5$ mm) with an iron ratio of $f_i = 0.5$. This is to reduce the axial length of the journal, as it was seen that the axial space available on the rotor of the TWINS is limited.

The number of laminations per electromagnet if a lamination material with a thickness of 0.35 mm is used is given by (9).

$$N_{lam} = \frac{l}{0.35} \quad (9)$$

$$N_{lam} = 53$$

A lamination stacking factor of 0.9 was used to determine the axial space that needs to be left for the electromagnet. This produces an axial length of $l = 20.61 \text{ mm} \approx 21 \text{ mm}$.

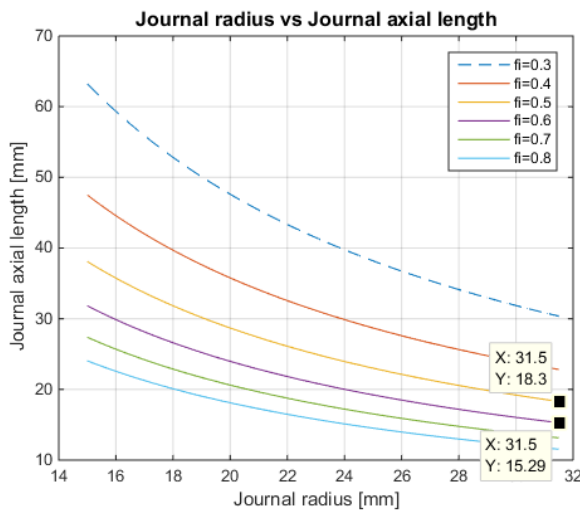


Figure 5: Journal radius vs Journal axial length

Coil design:

The coil can now be designed by using the desired flux density with the reluctance of the air gap. The parameters of the coil is shown in Figure 4.

The number of coil turns needed to produce the desired flux density (defined to be 1 T) is defined by using (10).

$$N = \frac{B_{sat} \cdot g_0}{\mu_0 \cdot I_{max}} \quad (10)$$

$$N = 80$$

I_{max} is 5 A which is the maximum current available by the available amplifiers. The area around the stator pole needed for the coil can be determined by using (11). A current density of $3 \times 10^6 \text{ A/m}^2$ was used as this is a very conservative value, it was seen from previous designs that this is a good choice to prevent overheating of the stator. A copper packing factor (f_c) of 0.5 was used to ensure the coils can easily fit inside the stator. The coil area is determined by using (11).

$$A_v = \frac{N \cdot I_{max}}{f_c \cdot J_{rms}} \quad (11)$$

$$A_v = 265 \times 10^{-6} \text{ m}^2$$

The coil thickness can be determined by using (12).

$$t_c = r_p \cdot \tan\left(\frac{\pi}{n} - \frac{w}{2}\right) \quad (12)$$

$$t_c = 7.1 \text{ mm}$$

And the coil length as:

$$l_c = \frac{A_v}{t_c} \quad (13)$$

$$l_c = 37.6 \text{ mm}$$

Stator sizing:

Next the coil radius can be determined with (14):

$$r_c = \sqrt{(l_c + r_p)^2 + \left(\frac{w}{2} + \frac{A_v}{l_c}\right)^2} \quad (14)$$

$$r_c = 70.82 \text{ mm}$$

The stator back iron meaning the length $r_s - r_c$ needs to be equal or more than the pole width to avoid saturation of the back iron.

$$r_s = r_c + f_s \cdot w \quad (15)$$

$$r_s = 83.2 \text{ mm}$$

Amplifiers sizing:

Amplifier sizing was done to determine if the available amplifiers would be sufficient. The required VA rating of the amplifiers is determined by the required force slew rate is of the AMB's and is given by [7]:

$$\left| \frac{dF}{dT} \right| = F_{max} \cdot 2 \cdot \pi \cdot f_{max} \quad (16)$$

$$\left| \frac{dF}{dT} \right| = 471.2 \times 10^3 \text{ N/s}$$

The required VA rating of the power amplifiers is given by (17).

$$V_{A_{\max}} = \left| \frac{dF}{dT} \right|_{\max} \frac{4 \cdot g_0}{\beta \cdot n} \quad (17)$$

$$V_{A_{\max}} = 245.12 \text{ VA}$$

The voltage required by the power amplifiers is given by (18).

$$V_{\max} = \frac{V_{A_{\max}}}{I_{\max}} \quad (18)$$

$$V_{\max} = 49.02 \text{ V}$$

The available amplifiers will be sufficient as its rated voltage is 51 V.

Rotor dynamic analysis:

The rotor dynamic analysis was redone for the designed journal geometries. It was seen that the required force from the AMBs was reduced from 121 N to 85 N with a reduction from 4.36 kg to 3.58 kg in the mass of the rotor. The electromagnet was however not redesigned, as it was advised that if a rotor is sent to be balance it normal comes back with a greater unbalance than specified. This cannot however be easily proven meaning that the rotor cannot be sent back without repaying for the balancing.

3.3 Simulation

The maximum force that the electromagnet can produce in a direction was verified with a FEMM simulation. This was done by fully turning on the top coil meaning that the current through the coil will be equal to 5 A, which is the maximum current available by the power amplifiers. The bottom coil was fully tuned off and the two coils on the side was biased with the biasing current ($I_b = 2.5 \text{ A}$). Figure 6 shows the FEMM simulation of the designed 8 - pole electromagnet.

It can be seen that the simulated force on the rotor is 165.2 N. This is very close to the expected value which the bearing was designed for. This is however not a problem as this only means that the bearing will be able to deliver a little more force than expected. This increase in force is due to the fact that the pole area was increased by 10 % to account for leakage and fringing effects. This means that the pole area could have only be increased by say 5 %. This will however not be changed as the force can be decreased by effect not included by the simulation if the bearing is implemented.

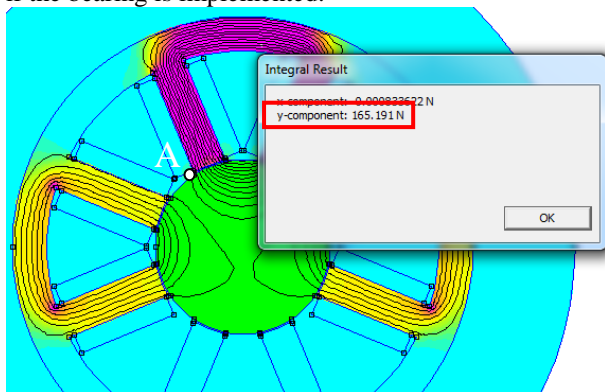


Figure 6: Force simulation 8 pole magnetic bearing

Figure 7 shows the magnetic flux density around the circumference of the starting at point A in Figure 6 and moving in a clockwise direction around the rotor.

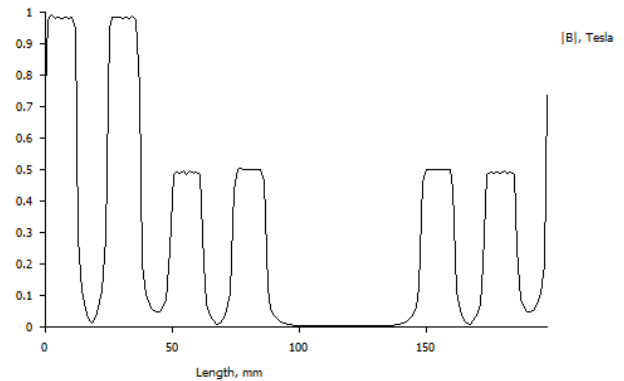


Figure 7: Flux density over circumference of rotor

It can be seen that the Flux density at the top pole is 1 T and at the side poles it is 0.5 T. This is what was expected as the bearing was designed to deliver maximum force at 1 T, and a biasing ratio of 0.5 was used to bias the side coils.

3.4 Losses

The primary objective of this project is to reduce the losses created in the bearings of the TWINS this is to ensure that the permanent magnet on the HS-PMSM does not demagnetize when it is operated at full speed for long periods of time. It is known that the losses in the ball bearings of the TWINS at full speed are approximately 150W [1].

The losses in the electromagnet that is of main concern is the iron losses in the magnetic material of the rotor. This is because these losses will be responsible for the heating of the rotor. Other losses that will be present on the rotor includes windage losses, this is due air resistance that will tend to slow the rotor down. This loss is however not of concern as it will not heat up the journals of the AMB. The windage loss will rather act as a load on the motor. The air resistance on the journal of the AMB can however not be lowered as the size of the journal is set, this is due to the fact that the journal was designed to produce an AMB with a small axial length.

The iron losses that is generated in the journal of the AMB consists of two loss types namely eddy-current losses and hysteresis loss. Eddy currents will be induced in the journal due the change in magnetic flux seen by the rotor. These current will generate heat as it flows in a material that has a resistance. Eddy current loss can be reduced by constructing the journal with laminated sheets. Hysteresis loss is produced when the magnetic material travels on its BH curve [8].

The losses in the rotor was determined by using a MATLAB® program written by Dr. David Meeker. This program uses FEMM to calculate the eddy-current, hysteresis and windage losses produced in the journal of

the AMB. The losses in the stator was calculated by using the method explained in [8]. The results can be seen in Table 1.

Table 1: Losses for different materials

	M235-35	M270-35	M400-50
Losses in rotor:			
Iron loss	15.78 W	17.05 W	29.42 W
Windage loss	16.94 W	16.94 W	16.94 W
Losses in stator:			
Copper loss	15.43 W	15.43 W	15.43 W
Iron loss	5.44 W	5.54 W	10.48 W
Total loss	53.59 W	54.96 W	72.27 W
Cost of material	-	R 4654	R 2796

As previously stated the losses in the ball bearing of the twins is 75 W per bearing this causes the rotor to overheat which will result in the demagnetization of the PM. It was decided that the losses in the M400-50 lamination material is too high. The M270-35 will rather be used as the main objected of this project is to minimize the losses in the bearings. The cost difference between the M270-35 and M400-50 is not considered to be too high. It is of more concern that the losses in the rotor is reduced as much as possible.

4. SYSTEM MODELING

It was verified by using a non-linear AMB model that it would be possible to deliver the desired stiffness and damping with the designed electromagnets. A PD control model was used to verify the achievable stiffness and damping [9]. Figure 8 shows the response of the rotor to a step input of 50 μm .

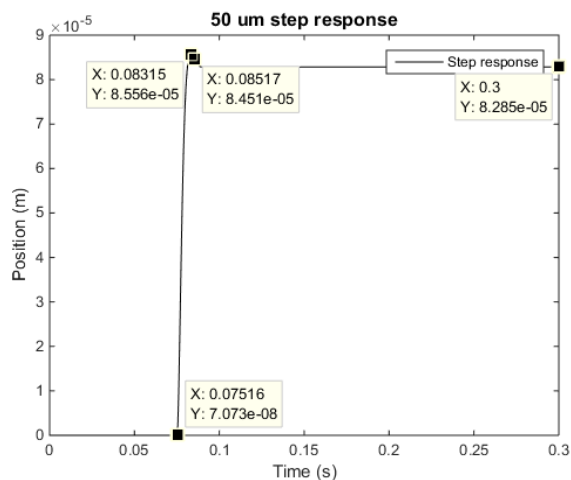


Figure 8: 50 μm step response

The equivalent stiffness and damping of the AMB can be determined by using the percentage overshoot (P.O.) and settling time (T_s) of the rotor to a step response [9]. From Figure 8 the P.O can be determined to be 3.27 % and the settling time (to within 2 % of the final value) can be shown to be 0.0102 s. This produces an equivalent stiffness $keq = 510.55 \text{ N/mm}$ and an equivalent damping of $deq = 1.4 \text{ N}\cdot\text{s/mm}$.

5. PHYSICAL IMPLEMENTATION

The electromagnets that was designed needs to be attached to the TWINS. If this is not possible the design would not have any significance. Figure 9 shows the TWINS as they are configured at the moment.

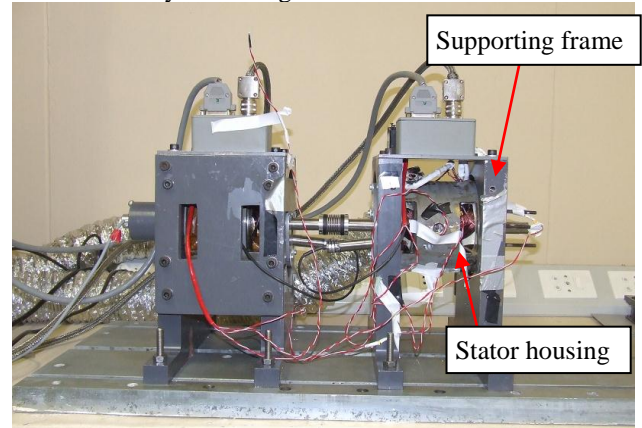


Figure 9: Photo of TWINS

The AMB can be implemented on the TWINS by removing the supporting frame of the TWINS and fastening the electromagnets housing to the stator housing of the TWINS as can be seen in Figure 10.

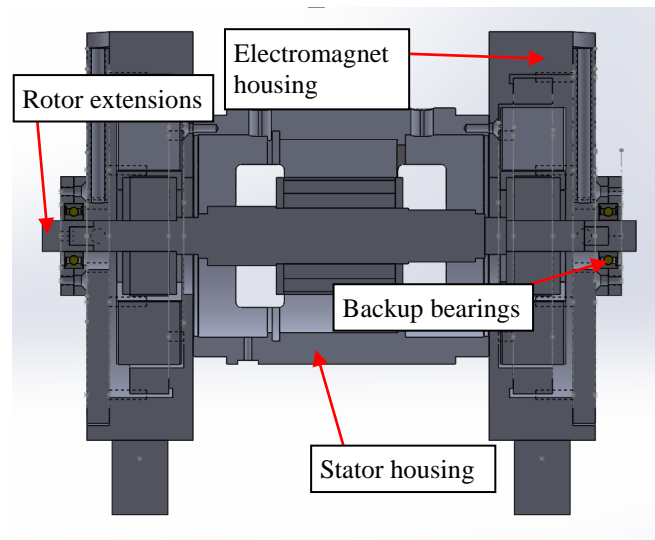


Figure 10: Sectional view of full assembly

It was concluded that the rotor needs to be made longer. This can be done by machining the tips of the rotor smaller and shrink fitting an extension piece to the ends of the rotor as can be seen in Figure 10.

6. CONCLUSION

It was concluded that it will be possible to replace the ball bearing of the TWINS with an AMB. A lamination stack with a radius of 31.5 mm can successfully be shrink fitted to the rotor of the TWINS without it losing contact or breaking at 30 000 r/min. From a rotordynamic point of view the rotor has to be balanced at G 0.1 this is to ensure that the unbalance forces produced by the rotor is within practical limits to the force that can be counteracted by the AMB's. The unbalance force with a balancing of G 0.1 was found to be 84.63 N, it was however decided that the AMBs will be designed to produce 150 N. This is to account for unbalance forces that can be higher than expected.

The geometries of the electromagnet that was designed to produce the necessary force is listed in Table 2.

Table 2: Electromagnet parameters

Parameter	Value
Shaft radius (r_r)	8.25 mm
Journal radius (r_j)	31.5 mm
Pole radius (r_p)	32 mm
Coil radius (r_c)	70.8 mm
Stator outer radius (r_s)	83.2 mm
Axial length (l)	21 mm
Pole with (w)	12.4 mm
Number of turns (N)	80

It was seen that it would be possible to use the available power amplifiers in this design as it VA rating is more than the required VA rating.

It was determined that lamination material M270-35 need to be used to lower the losses in the magnetic material on the rotor. The losses on the rotor of the TWINS due to the bearings will be reduced from 75 W to 17 W if the ball bearing is replaced by AMB's.

It was determined that a supporting stiffness of $k_{eq} = 511 \times 10^3$ N/m and an equivalent damping of $d_{eq} = 1.4 \times 10^3$ Ns/m can be obtained if a PD controller is used.

The design electromagnet will be able to be fitted to the stator housing of the TWINS it was however concluded that the rotor will need to be machined off to a thickness of 16.5 mm this is to produce the correct clearance lever between the rotor and backup bearings.

7. Appendix A

The symbols used in this article is shown below:

U_{per}	Permissible unbalance
G	Balancing standard
m	Mass of rotor
r_{rb}	Rotor clearance
N_r	Rotor speed (r/min)
r_s	Stator outer radius

r_c	Coil radius
r_j	Journal radius
r_p	Pole radius
r_r	Rotor shaft radius
g_o	Air gap
A_g	Air gap area
w	Pole width
n	Number of poles
l	Axial length
N_{lam}	Number of laminations
N	Number of coil turns
σ	Scaling constant
f_i	Iron ratio
θ_p	Pole angle
f_s	0.5 for flux splitting / 1 for unsplit flux
β	Biasing ratio
f_c	Copper packing factor
A_v	Coil area
t_c	Coil width
l_c	Coil length

8. REFERENCES

- [1] A.J. Grobler, S.R. Holm, and G. van Schoor, "Thermal modelling of a high speed permanent magnet synchronous machine," in *Electric Machines & Drives Conference (IEMDC), 2013 IEEE International*, 2013, pp. 319–324.
- [2] Balance quality requirements of rigid rotors: the practical application of ISO 1940/1, 2001.
- [3] H. Bleuler, M. Cole, P. Keogh, R. Larssonneur, E. Maslen, Y. Okada, G. Schweitzer, A. Traxler, G. Schweitzer, E. H. Maslen, and others, *Magnetic bearings: theory, design, and application to rotating machinery*. Springer Science & Business Media, 2009.
- [4] J. J. Janse Van Rensburg, "Development of a Flywheel Energy Storage System: Uninterrupted Power Supply (FLY-UPS)," Master's thesis, North-West University, Potchefstroom, South Africa, 2008.
- [5] P. Allaire, C.R. Knospe, et al, "Short course on magnetic bearings", Alexandria Virginia, United States of America: University of Virginia 1997.
- [6] D. C. Meeker, "Optimal solutions to the inverse problem in quadratic magnetic actuators," Ph.D. dissertation, University of Virginia. 1996.
- [7] E. Maslen, "Magnetic Bearings," Personal notes.
- [8] B. S. Guru and H. R. Hiziroglu, *Electric machinery and transformers*, vol. 726. Oxford University Press New York, 2001.
- [9] S. Myburgh, "The development of a fully suspended AMB system for a high-speed flywheel application," Master's thesis, North-West University, Potchefstroom, South Africa, 2007.

DESIGN OF A PLC-BASED VARIABLE LOAD, SPEED CONTROL SYSTEM FOR A THREE-PHASE INDUCTION MOTOR

B. Coetzer* and R. Gouws*

*North-West University, School of Electrical, Electronic and Computer Engineering, Potchefstroom, Email: brendancoetzer@ymail.com

Abstract: Industries make use of PLCs to control bulk electronic devices and it is found that combining them with motor drives such as VFDs, the efficiency of induction motors are rapidly improved. Eskom in association with suppliers has spent much time and resources on this. To address this problem, a PLC-based control system was designed for a three-phase induction motor. The system is designed using a PLC for intelligent control on a three-phase induction motor and DC generator. The motor is tested at four different control speeds (rpms), of which each of these rpm reference values are tested on three different load condition provided by the generator. The intelligent control system for the three-phase induction motor in combination with the assembled product turned out to be very effective. The theoretical and practical results were compared and the system in whole showed positive efficiency results. Eskom with their resources may implement such a system and will definitely see energy efficient results in the long term.

1 INTRODUCTION

Industries have rapidly changed in the last years, and make use of programmable logic controllers (PLCs) to control bulk electronic devices such as motors, trains, etc. [1]. A PLC is used to connect with computers to monitor load and electricity consuming devices. Combining the control of a PLC with the use of motor drives give efficient results, which is the main objective in the industry.

South Africa needs more generation capacity just like any other country in the world, of which the national electricity supplier, Eskom, can provide the country with. This supplier mentioned uses drive systems in many applications because of the energy efficiency benefit; they are used for process control and energy conservation. Drive systems are quickly becoming the most used method for speed control in the industry. They control the speed of alternating current (AC) induction motors and are considered as the most energy efficient way of controlling the speed of a motor. They have the ability to vary voltage and frequency simultaneously, thus the frequency of the induction motor can be

controlled from 0 to 400 Hz which is 0 to 24000 rpm [1]. This concept is important because in the end the more efficient the motor drive system, the more efficient the conveyor system that it controls [2].

The use of conveyor systems in the industry are considered as material handling and is an important sector of the industry, but it consumes a considerable proportion of the total power supply in South Africa, up to 10% of the total demand. Although their electricity usage is considered as a ridiculous fact, their high efficiency of transportation is the main attraction. As mentioned above, energy efficiency is important and keeping this in mind the main goal is to better the energy consumption or energy cost of the material handling sector. This can only be done if the energy efficiency of belt conveyors is improved, as they are the main energy consuming components of material handling systems [2].

The energy efficiency of belt conveyors can be improved through proper control of motor drive systems to better the efficiency vs load curve through different load conditions that may occur in the mining industry with conveyor systems.

After this brief background it is clear that the problem to be addressed is to improve the energy efficiency of induction motors which the supplier and so many people has spent much time and resources researching techniques on [3].

Therefore this paper focuses on designing a PLC-based variable load, speed control system for a three-phase induction motor.

2 LITERATURE REVIEW

In this section the main components used in the design phase of the project will be discussed. These components are the controller and motor drive. The other components discussed in the original literature study are the induction motor, speed sensors, current transducers, dc generator and possible solutions for the project. In the literature study a variety of components available in the industry were discussed; however in this literature review on the

main components chosen for the design will be the discussion.

2.1. PLC

Programmable logic controllers (PLCs) are microprocessor-based control systems designed for automation processes used in industrial environments. It has memory to that is programmable for the internal storage of user-orientated instructions such as arithmetic, counting, logic, sequencing, and timing. PLC's can be programmed to sense, activate, and control industrial equipment. It therefore has a number of I/O points which allow electrical signals to be interfaced. Input- and output devices are that are part of the process are connected to the PLC and the control program is entered into the PLC memory.

In the task at hand it controls through analog and digital inputs and outputs the varying load-constant speed operation of an induction motor. A PLC keeps monitoring the inputs and activating the outputs as they are needed. This PLC is composed of hardware building blocks called modules as shown in figure 1. These modules plug directly in a proprietary bus which is consumed of a central processing unit (CPU), a power supply unit, input-output modules (I/O), and a program terminal [4], [5], [6].

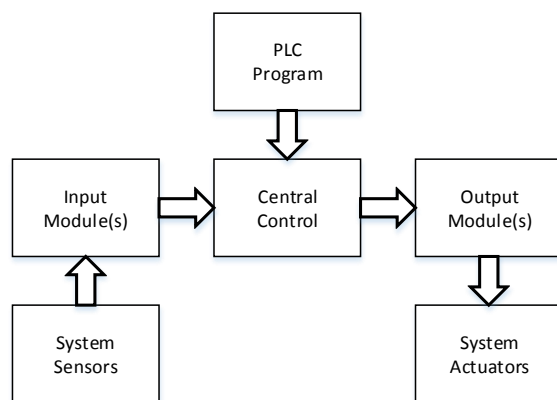


Figure 1: Main Unit and Expansion Modules

In table 1 a brief overview of the PLC used in the project is given [6]. When looking at the inputs, there are 8 available of which inputs 1, 2, 7 and 8 can be used as analog inputs.

Table 1: PLC Specifications

Product	Specifications
PLC LOGO! 0BA8	Maximum Temperature +70 °C Minimum Temperature -40 °C 8x Inputs and 4x Outputs Output Current 10 A Voltage 24 V

2.2. VFD

A variable frequency drive (VFD) is one of a few types of motor controllers. This type drives an electric motor by varying the frequency supplied to the electric motor. The frequency supplied is directly related to the motor's speed in revolutions per minute (rpm), this means that if the frequency is increased, the speed of the motor increases simultaneously. If the motor gets power directly from the three-phase power supply it will run at rated rpms, but if this wants to be avoided the VFD is used to ramp down the frequency of the motor to meet the requirements of the motor's load [7].

VFDs can be used in various areas in the practice, but in this project the sole area of focus is on a conveyor system [1]:

- Saving energy by slowing down the production line from 100% to 80%.
- Using a small PLC, the conveyors is stopped or slowed down when there are no products on them.
- When the products start to move, the conveyor could be started up slowly adjusting the acceleration time.
- Because of the gentle start up, no damages are caused to the products on the conveyor belts.
- If the VFD senses that it is in idle mode, it can go into a sleep mode for a small amount of time until it needs to start up again.

VFDs are supplied by an AC voltage which they convert to DC voltage and then back to an AC voltage. This all happens in the power conversion step 1, with the use of isolated-gate bipolar transistors (IGBTs) or silicon-controlled rectifiers (SCRs). The IGBT switches on and off to create an AC voltage waveform using PWM switching. In the power conversion step 2, electrical energy is set mechanical power and control over the motor is done via frequency or voltage changes. This process is shown in figure 2 [8].

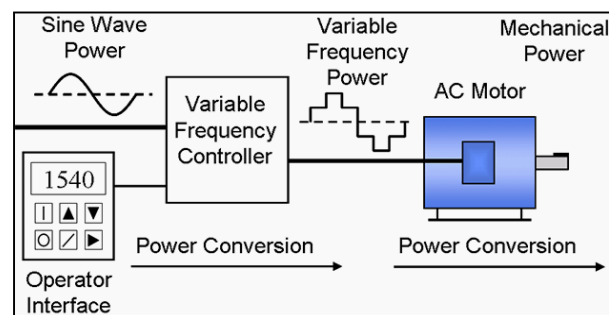


Figure 2: VFD System

2.3. REMAINING COMPONENTS

The remaining components used in the project were all briefly discussed in the literature study. All components used in the project were chosen using a process called a trade-off study, where a specified criteria was set out for

each component. The component choices are listed in table 2.

Table 2: Components Used

Component	Chosen Product
Controller	PLC
Motor Drive	VFD
Current Sensor	Split-Core Current Transducer
Speed Sensor	Inductive Proximity Switch
Load	DC Generator
Possible Solutions	PLC-Based Control

3 METHODOLOGY

In order to successfully complete the project, the engineering design process was followed. This was done by getting a background on the project, identifying the problem, confirming the specifications with the client, doing thorough research on the components to be used that will fit the needs of the project perfectly, designing and simulating the product, testing each sub system followed by the system in whole, and processing the end results. By following this process step by step, the results in the following section were obtained. This section however will focus on the methods used to obtain those results.

When the literature study was completed and the components in table 2 were chosen, the design of the final product was initiated. This could only be done if the right components were chosen for sensing and turning the induction motor with the PLC and so forth. The VFD used is a WEG CFW 08 Vector Inverter which was perfect for the induction motor whose specifications are given in table 3. The speed sensor used is an inductive proximity switch as mentioned in table 2. The switches diameter allows it to be attached 4 mm from the shaft of the motor for nominal sensing. The bigger the diameter of these switches, the further they can sense [9]. The control program of the system is designed to produce set-point reference values representing curtain rpm values. The proximity switch is used to count pulses as the shaft of the motor turns and in turn help get the motor speed up to the pre-set set-point value.

Table 3: Induction Motor Specifications

Name	Function
Connection Type	Y
Input Voltage	380 V
Input Current	6.63 A
Input Frequency	50 Hz
Rated Power	3.0 kW
Number of Poles	4
Rated Speed	1410 rpm

The control system referred to is called a closed-loop control system and is shown in figure 3. In using this setup a constant speed operation configured with speed feedback, load current feedback as well as stator current

feedback can be obtained. The induction motor drives a variable load represented by the DC generator, is fed by an inverter (VFD), while the PLC controls the inverter V/f output [4].

The three-phase power supply is connected to a rectifier pulse-width modulation (PWM) inverter representing the VFD. This in turn is connected to the induction motor on the high voltage side, giving it the relevant power to operate, and is then connected to the PLC on the other through low voltage inputs enabling control of the motor. As mentioned and seen in figure 3, a speed sensor is attached to the shaft of the motor to regulate speed, along with two current sensors of which one is attached to the stator of the motor and one to the load.

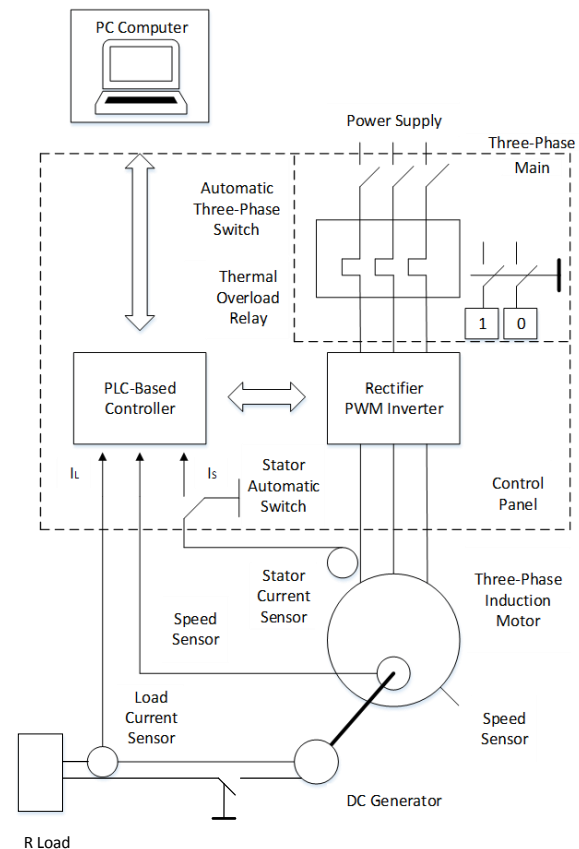


Figure 3: Electrical Diagram of Experimental System

The current sensors are merely a part of the system for data feedback to calculate the efficiency of the motor. These current sensors are split-core current transducers and are mainly used for automation and supervision of distributed PLCs or remote control systems [10].

The flowchart of the control system is given in figure 4 and indicates all relevant information sent and received from the sensors as well as the PLC and VFD.

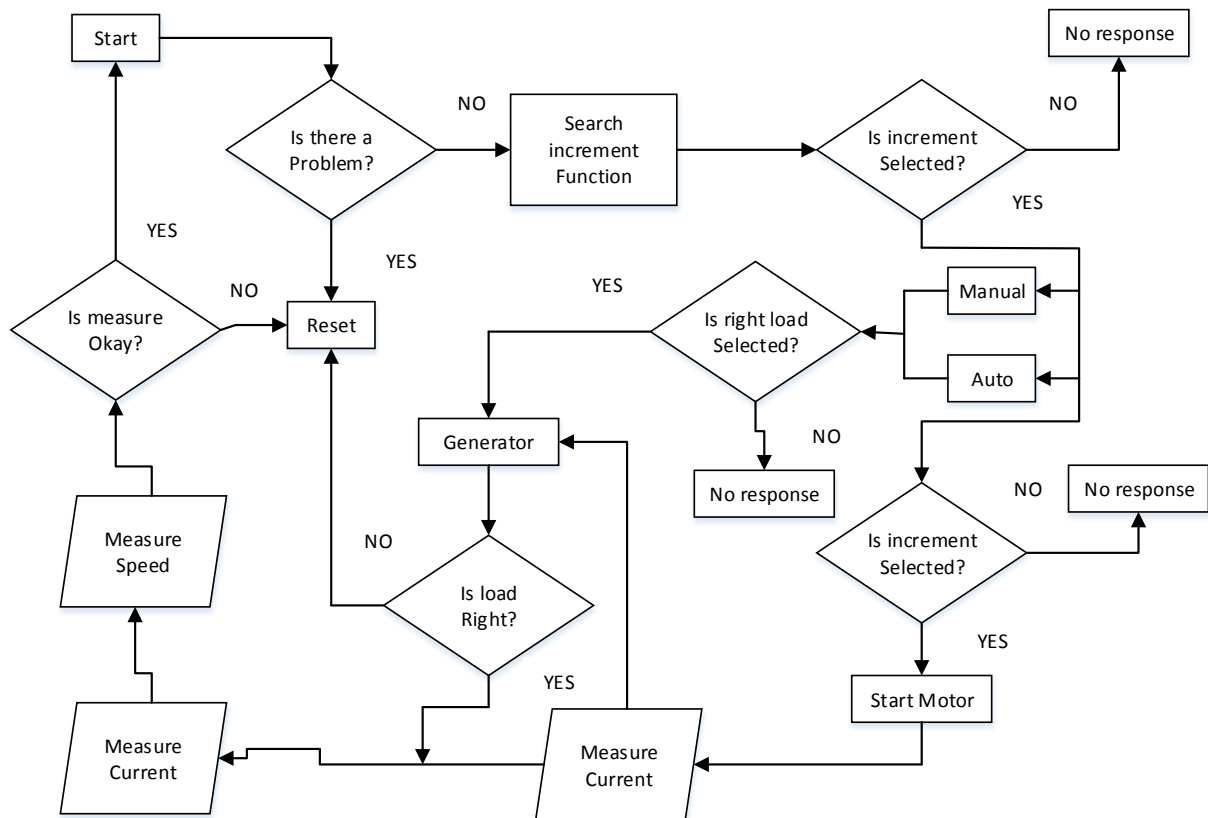


Figure 4: Flow Chart of Control Program

$$f = 47 \text{ Hz}$$

4 RESULTS

4.1. CALCULATIONS

In this section the experimental results of two different control systems will be compared. These system are a PLC with VFD control system and VFD only control system.

The practical results started off by first checking what the voltage generated by the DC generator was before applying any load to the system. This was done to see that when eventually applying the load, that the same voltage is still generated, which in turn means that the motor is running at a constant speed. Because of this being a DC load system, the normal ohm rule was used to calculate the current drawn by the system. All results obtain data on PLC and VFD control and only VFD control.

The rated speed of the motor as discussed in table 3 is 1 410 rpms and by using this information, combined with the knowledge that only four different rpm values will be tested, the following calculation was made.

$$N_m = \frac{120f}{p} \quad (1)$$

Working from 50 Hz and dividing it by four concluded in using 12.50 Hz intervals. These intervals were most accurately chosen according to what the reference values sent from the control program to the VFD allowed. In table 4 these values with their frequencies are listed.

Table 4: Reference Values and Frequencies

Reference Value	Frequencies (Hz)
265	12.5
515	25.3
761	37.5
900	47

The reference values were chosen from 0 – 1000 and were guided by the proximity switch with a 4 – 20 mA signal sent to the VFD to reach the set point values. This in turn allows 16 mA to still be used as 4 mA leaves the motor at standstill. Using this allowable 16 mA, the speed is calculated.

$$N_{calculated} = \left(\frac{1\,410}{16} \right) \times 4 = 352 \text{ rpm} \quad (2)$$

If this rpm value were to be used, it would have been according to the 47 Hz calculated in equation 1. This was

not the case as the 380 V, 6.63 A, Y-connected the motor was started on uses a supply of 50 Hz as stated in table 3. This is why intervals of 12.5 Hz more or less were used, thus the rpm value started on was.

$$N_{used} = \frac{120 \times 12.5}{4} = 375 \text{ rpm} \quad (3)$$

Starting with the generator, it requires 330 V_{DC} on the field of the motor and 310 V_{DC} on the armature. This was not needed on the armature, as voltage was generator and a load in the form of resistors was connected. The load at first would have been 64 Ω, 128 Ω and 256 Ω, but with tolerance kept in mind the load in the end was 63.8 Ω, 127 Ω and 222 Ω. These are the load condition mentioned. Also working on a 50 Hz supply, the synchronous speed of the induction motor calculated was 1 500 rpm. Now there were four rpm values measured at each load condition, which are considered as full-load rpm values each on their own. These rpm values are seen in table 5.

Table 5: Frequencies with Related RPM

Frequencies (Hz)	RPM
12.5	375
25.3	745
37.5	1 120
47	1 423

The set out rpm values measured at the load conditions are also the reference values for the system. With the PLC and VFD control system, this set out rpm values were sustained perfectly doesn't matter what the load conditions were. With only the VFD control system, this unfortunately could not be done. The motor slip for both of these control systems were then calculated using equation 4.

$$s = \frac{N_s - N_m}{N_s} \quad (4)$$

The efficiency of each system was then calculated using their related slip value.

$$\eta = \frac{1 - s}{1 - \left(s \times \frac{R_1}{R_2}\right)} \quad (5)$$

Where R_1 and R_2 are the stator and rotor resistance respectively.

4.2. CHARACTERISTICS

The range in which the speed vs. torque characteristics was taken can be seen in figure 5 and was the topic of discussion in table 5. However, the results show that the configuration where only the VFD controls the motor that the speed is not kept on a constant rpm value with the

varying loads. This results in not generating the same voltage as with PLC control on the system, where a constant speed was held. The surprising fact was that on higher rpm values with PLC control, the motor still kept a constant speed operation on any of the three load conditions tested. This however narrowed down on lower speeds and the difference between the two control methods was very small.

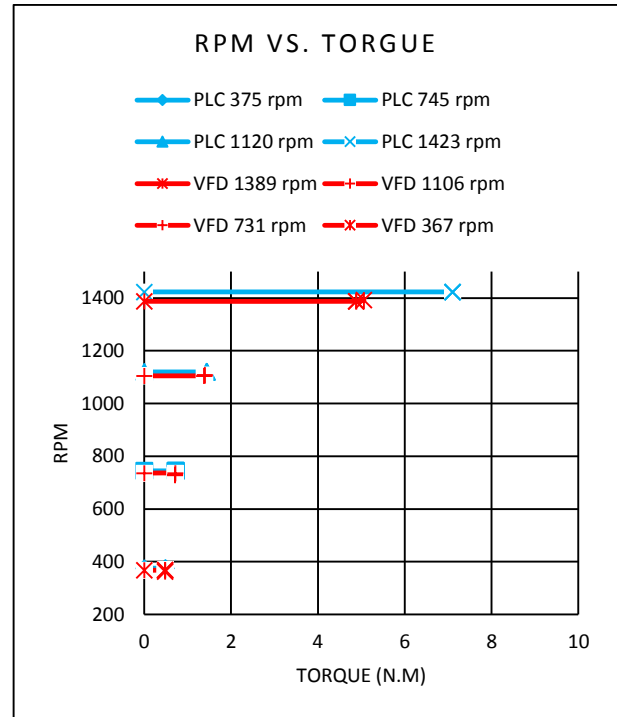


Figure 5: RPM vs. Torque Characteristics

Using the previous torque data of both systems and comparing it with the efficiency of both configuration systems, interesting results were obtained. First looking at the configuration system where only VFD control was done on the motor. It's seen in figure 6 that as the torque grew constantly, the efficiency grew less constant on higher rpm values and different loads. This leaves the system questionable as a motor in practice runs at synchronous speed or even sometimes 80 % higher. Whereas looking at the PLC control configuration, there is a constant efficiency vs. torque grow. This system also showed higher efficiency values in all cases than that of the VFD configuration.

With the three load conditions tested, it's seen in figure 7 that on the lower rpm side the efficiency bettered with about 1 %. This happened for the first two rpm values, whereas with the second last rpm value it changed to 2 % and finale to 3 % on the final rpm value. What makes the results with the PLC and VFD control system so satisfactory, is that each individual efficiency is maintained no matter what the load conditions were. This is mainly because the rpm values were kept constant by using the proximity switch to permanently count pulses,

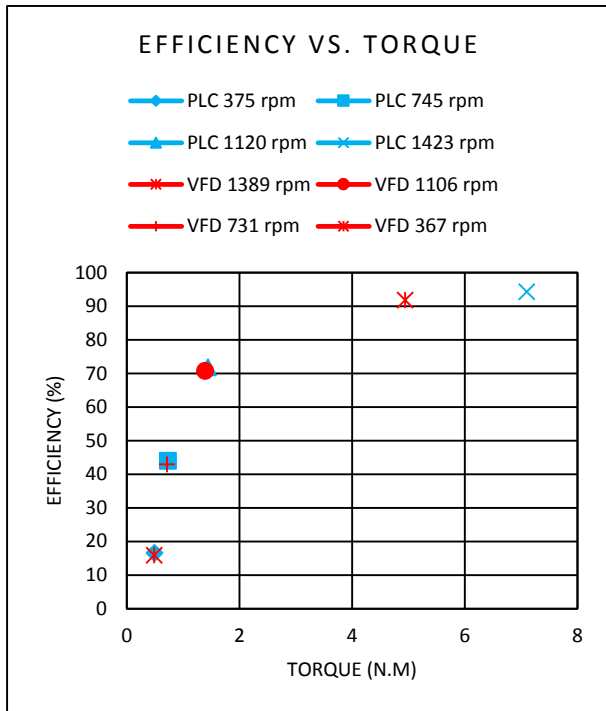


Figure 6: Efficiency vs. Torque Characteristics

and not allowing the motor to slow down on either of the three load conditions tested. This was not the case with just the VFD control system, as the frequency set out did not correspond with the rpm values measured and was lower than this expected value. This concludes that the VFD control system is not an as effective system relating with the PLC and VFD control system. The efficiency vs. load characteristics curve in figure 8 show that the efficiency improved even more with higher load conditions.

4.3. CONTROL PROGRAM

In this section just a fraction of the control program is given, just to illustrate how it was done. The program in figure 9 starts the motor using input 1 running through a set/reset function block to take control over output 1. The reset uses the stop and overload (O/L) inputs through an OR gate to put the system to a stop when trouble occurs. The stop and O/L inputs are wired normally close (N/C) according to rules set by law. In this part of the program auto incrementation of speed (rpms) on the motor is activated using a pushbutton connected to the system. Auto incrementation means that the program will automatically run through each speed set out for the motor and will stay on that speed for a set time using an edge triggered wiping relay which is function block B009. In this section of the program the same edge triggered wiping relay is used to count time for the speed of the motor, but instead of speed being adjusted automatically one of the pushbuttons is used to activate manual incrementation of the set out speeds. This means that the student can choose how long he would like to

remain on a speed for testing purposes. The OR gate following input of the pushbutton, uses the input and the edge triggered wiping relay for activation to start progress on the up/down counters B003-B007 and B014 which is the reset.

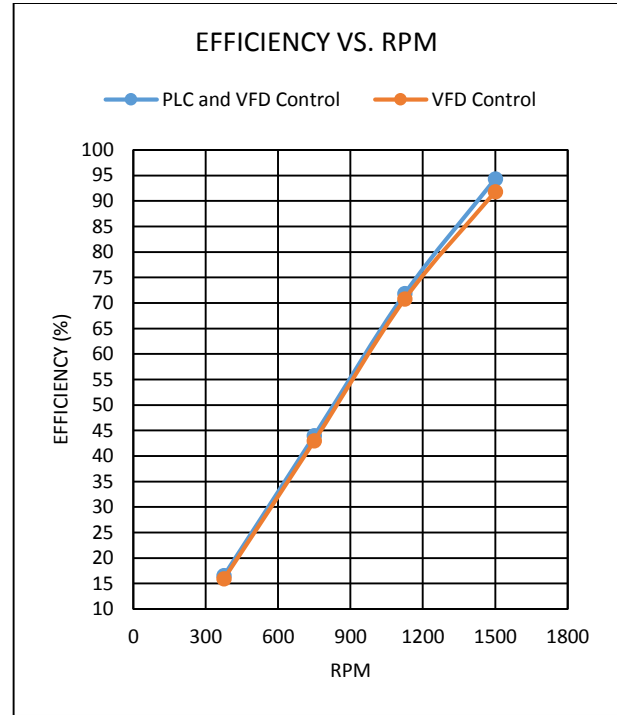


Figure 7: Efficiency vs. RPM Characteristics

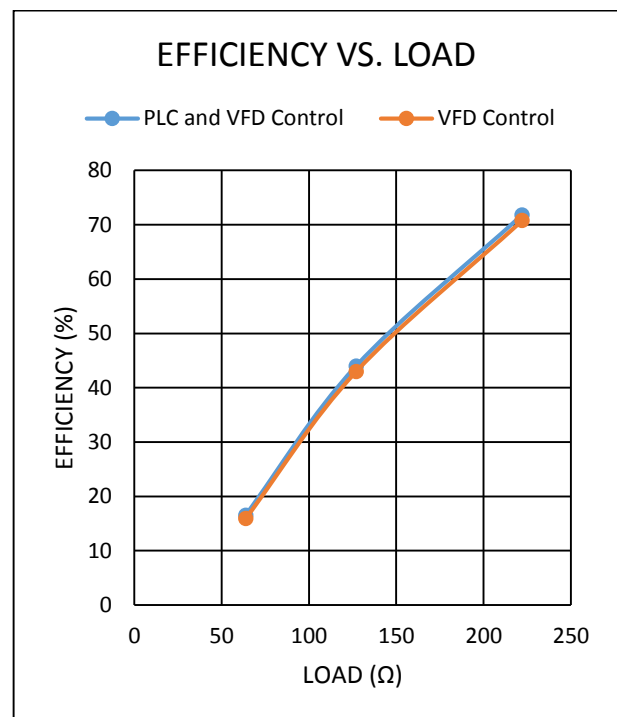


Figure 8: Efficiency vs. Load Characteristics

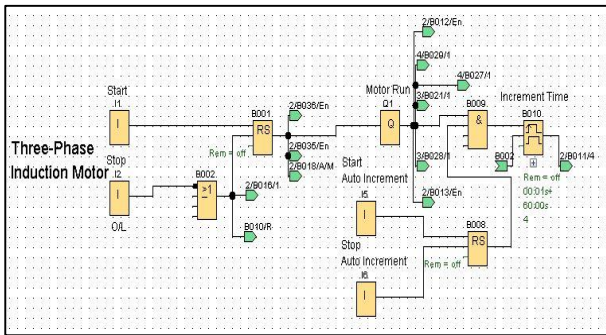


Figure 9: Start, Stop and Auto Increment

Following each counter is memory bit flag which represents a value for each reference speed set out. In figure 10 the discussed program is illustrated.

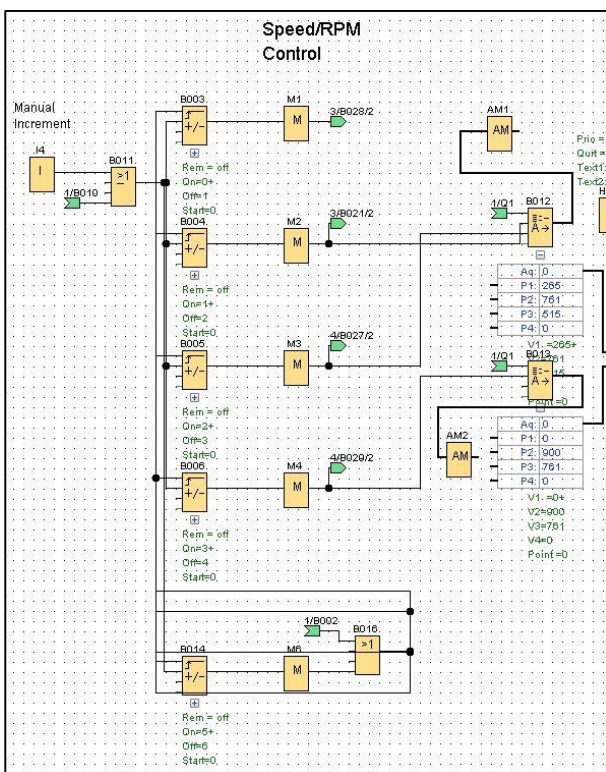


Figure 10: Manual Increment

5 CONCLUSION

The results show that this project can be interpreted in a real system as intended. The project, which is shown in figure 11 is in practice an example of a conveyor system in the mining industry.

It's seen that the motor operates in a more efficient state on or close to the synchronous speed. This causes the motor slip to be less with control on the system and at a constant value. When using this system in the mining industry, more intelligent and faster PLCs will be used like Siemens S7-300, S7-400 PLCs, etc. This opens more



Figure 11: Experimental Project

doors for improvement in the efficiency. They have more inputs and outputs to handle multiple systems like discussed in this article.

With the experimental results completed and discussed in section 4.1 and 4.2, the PLC and VFD control system is found to be more efficient than just the VFD control system. On the first two rpm values that tests were done on, there was a system efficiency increase of 1 %, whereas with the third and fourth rpm values the system efficiency increase went up to 2 % and 3 % respectively. As three-phase induction motors are constantly used at their synchronous speeds in the mining industry, an increase in efficiency of 91 % to 94 % is expected.

6 REFERENCES

- [1] ESKOM, "Variable Speed Drives (VSDs) – saving energy in the industrial sector," Sensible flow saves, Sep. 2010. E. H. Miller, "A note on reflector arrays," *IEEE Trans. Antennas Propagat.*, to be published.
- [2] S. Zhang, X. Xia. "Modeling and energy efficient optimization of belt conveyors," *Applied Energy*, pp. 1, 2011.
- [3] ESKOM, "The Energy Efficient series: Towards an energy efficient mining sector," Feb. 2010.
- [4] M.G. Ionnides. "Design and Implementation of PLC-based Monitoring Control for Induction Motor," *Academia.edu*, p. 8, Sep. 2004.
- [5] H.N.Y. Birber. "Design and Implementation of PLC-Based Monitoring Control System for Three-Phase Induction Motor Fed by PWM Inverter," *International Journal of Systems Applications, Engineering & Development*, vol. 2, no. 3, 2008.
- [6] M. Snyhed. (2014, Oct.). "Siemens LOGO! 8 logikcontroller is now in stock at RS Components," [Online]. http://www.electronic-supply.dk/announcement/view/40512/siemens_logo_8_logikkontrollere_er_nu_pa_lager_hos_rs_components#.VPVtScSmiSo, [August. 5, 2015].
- [7] C. Hartman. "What is a Variable Frequency Drive?", 20, March. 2014. [Online]. <http://www.vfds.com/blog/what-is-a-vfd>, [August. 5, 2015].
- [8] S. Prabhakaran. "LT/Medium/HT Variable Speed Drives in the Industry," 2014. [Online]. <http://electrical-engineering-portal.com/lt-medium-ht-vfd-part-2>, [August. 5, 2015].
- [9] Switches International. "Inductive Extended," [Online]. <http://www.switches.co.za/products/proximity-switches/inductive-extended/>, [September. 4, 2015].
- [10] RS Components. "Split Core Current Transducer, 20 A rms, 30 V dc," [Online]. <http://za.rs-online.com/web/p/current-transducers/0198778/>, [September. 9, 2015].

INNER LOOP CURRENT CONTROLLER DESIGN FOR A SOLAR ARRAY SIMULATOR

TB. Tapfumane^{*}, H du T Mouton[†] & A.J. Rix[‡]

Department of Electrical and Electronic Engineering, University of Stellenbosch, Private Bag X1, Matieland, 7602 South Africa

^{*} Email: 16881249@sun.ac.za

[†] Email: dtmouton@sun.ac.za

[‡] Email: rix@sun.ac.za

Abstract: In this paper the design and modelling of a PI Current Controller and Pulse Width Modulator (PWM) implemented on Field Programmable Gate Arrays (FPGA) for a Solar Array Simulator System are described. The Solar Array Simulator System should accurately simulate the I-V curve characteristics of different arrays under various environmental conditions i.e sun's eclipse, rotation, intensity, temperature etc. This entails that the controller should be fast and accurate and the simulator system should remain stable under all possible loads i.e any grid tie DC/AC inverter. The analysis of the continuous signal control processes closely approximates highly over-sampled digital current controllers. The small signal model of the Pulse Width Modulator (PWM), illustrates how the duty cycle behaves with small perturbations in reference current. A small signal model based method is derived and presented that enables the design of a stable controller.

Key words: FPGA, Small signal model, Bifurcation, PWM.

1. INTRODUCTION

Over the years, PI controllers have been used for a wide range of applications in power electronics. Using bode plots and root locus methods, a PI controller can be designed and fine tuned such that it satisfies the gain and phase margin requirements for a specific application. For the system in Fig. 1, the inner loop current control of the system that controls the inductor current, makes use of a PI controller that ensures good steady state tracking and responds to changes in the reference quickly. In order to obtain a bandwidth that enhances performance of the controller and rejection of disturbances, a larger bandwidth is needed [2].

The realisations of digital implementation of control algorithms for most commercial systems were performed using DSP/microprocessors. The sampling rate of the microprocessor is in the order of the switching frequency. Thus sampling of the current and reference signals happens once or twice for every switching period. During the sampling process and pulse width modulation, signal delays are incurred [3]. Due to the transport delays, severe gain margin restriction is imposed on the controller. To avoid the inherent transport delays incurred by sequential processing by DSPs, high speed parallel processing FPGAs are used.

The FPGA technology is flexible, complex and enables fast parallel signal processing [8]. This new digital technology solution has been embraced in power electronics for implementation in digital control algorithms. For this paper, a Cyclone V device manufactured by Altera is used. The discretised PID controller is implemented on

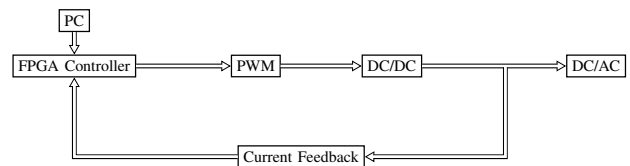


Figure 1: Solar Array Simulator System

a dedicated FPGA programmed using VHDL. When using FPGAs, the sampling rate is significantly higher than the switching frequency and thereby reduces the effect of the incessant transport delays as the digital signal closely approximates the analogue signal [4]. The sampling rate is typically 1000 times the switching frequency.

The main function of the Solar Array Simulator is to emulate the power transfer characteristics curve of a solar panel or an array of panels. The grid tie inverter connected to the DC/DC converter functions under an (MPPT) algorithm that ensures that it operates at maximum power point. The Solar Array Simulator is composed of an inner current loop and an outer voltage loop. The final aim in building the system involves controlling the output voltage.

In this paper the design and stability of the inner current control loop are described. A small signal model of the PWM is used to design for a range of K_p and K_i values for which the DC/DC converter system will be stable. Simulation is conducted in the Matlab environment in order to simulate the current feedback control loop.

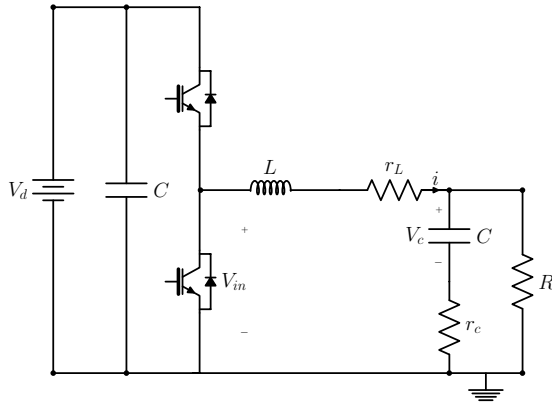


Figure 2: Synchronous Buck Converter

2. CONVERTER TOPOLOGY

The topology implemented by the Solar Array Simulator System is known as synchronous buck converter depicted in Fig. 2. The best performances of any high-gain DC/DC converter in Photovoltaic systems greatly depend on the employed topology and the corresponding control strategy [7]. The converter is rated at 20 kW with oversized IGBT modules and a gating signals' driver system that is isolated for electrical protection. The converter offers robustness in overload conditions or any control errors. It is designed to operate under loading with different operating conditions of a grid tie inverter.

3. MATHEMATICAL MODELLING OF THE SYSTEM

The resistors r_L and r_c in Fig. 2, are inductor and capacitor parasitic resistances. C and R represents the capacitive and resistive load characteristics respectively introduced by the grid tie DC/AC inverter. In order to simulate and analyse the behaviour of the system, a mathematically based description of the circuit is derived.

By analysing the circuit the following equation is obtained:

$$\begin{aligned} V_{in}(s) &= sLI(s) + r_L I(s) + V_c(s) + sr_c CV_c(s) \\ V_{in}(s) &= I(s)(sL + r_L) + V_c(s)(sr_c C + 1) \\ I(s) &= \frac{V_{in}(s) - V_c(s)(sr_c C + 1)}{sL + r_L} \end{aligned} \quad (1)$$

From analysing the circuit:

$$V_c(s) + sr_c CV_c(s) + sRCV_c(s) = RI(s)$$

Therefore

$$V_c(s) = \frac{RI(s)}{sC(R + r_c) + 1} \quad (2)$$

Fig. 3 is the block diagram representation of the

PWM current regulator as described by the mathematical model derived. $I^*(s)$ is the reference current, $G_c(s)$ is the compensator transfer function and $V_{in}(s)$ is the input voltage to the filter network per switching cycle. The comparator gives a PWM output by comparing the sawtooth carrier signal $C(s)$ to the modulating signal. Transfer functions in Fig. 3, $G_1(s)$, $G_2(s)$ $G_3(s)$ are obtained from the mathematical model derived in Eq.(1) and Eq.(2). The transfer functions are described as follows:

$$G_1(s) = \frac{1}{sL + r_L} \quad (3)$$

$$G_2(s) = \frac{R}{sC(R + r_c) + 1} \quad (4)$$

and

$$G_3(s) = sr_c C + 1 \quad (5)$$

The system designed should be stable for all loading characteristics introduced by the grid tie DC/AC inverter.

4. SMALL SIGNAL MODEL

Many commercial control loop designs use the average linear models which do not always predict the stability margins correctly. A deeper look at the underlying mechanisms that determine the behaviours of the naturally sampled control loops suggests otherwise[4]. An approach to design that overcomes the shortcomings related to the average model is identified. The approach is based on analysing the behaviour of the duty cycle with small signal perturbations in the reference current. The small signal model is analogous to the impulse generation and sampling behaviour of the PWM. Thus the sampling behaviour in z-domain is used to analyse small signal model stability. [4].

Fig. 4, represents the PWM replaced by the small signal z-domain model of the PWM. According to the small signal model, the comparator produces a series of impulses. The input signal to the comparator is sampled every time it intersects the sawtooth carrier signal. Only the sawtooth signal is used as a carrier for the small signal model as triangular waves do not work with small signal model. At the point of intersection, an impulse is produced. In order to analyse the system using the small signal model, the control loop is temporarily broken between the impulse generator and the sampler. The model is then analysed as if an impulse is generated around the loop from the output of the second half of the broken link. The sampler situated at the input of the first half of the broken link will sample the impulse response. A z-transform of the sampled impulse response is taken using impulse invariance method in order to come up with a transfer function of the system that sits around the PWM generation block. The open loop transfer function derived is therefore used for stability analysis.

After carrying out a block diagram manipulation, the open

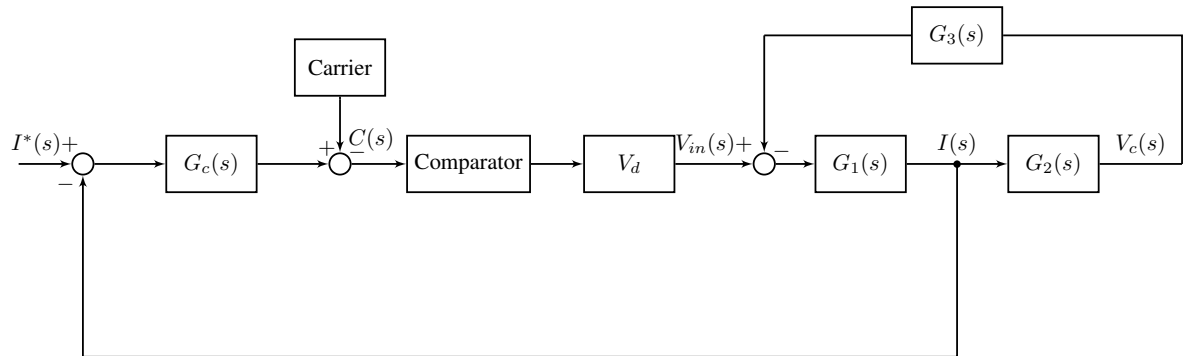


Figure 3: Pulse width modulator current regulator

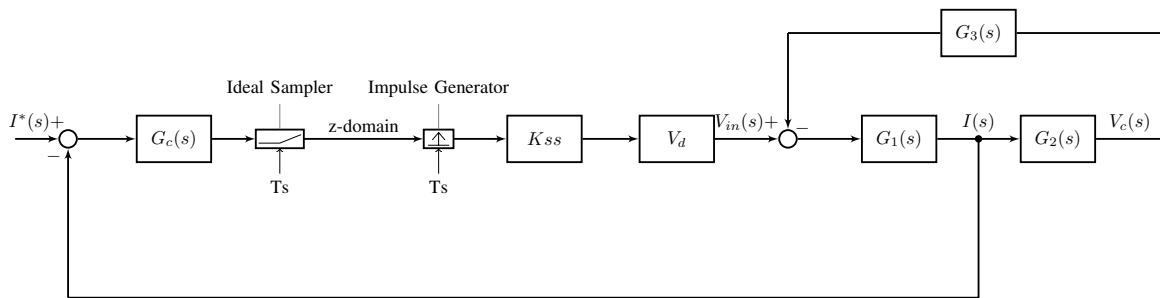


Figure 4: z-domain model of PWM current regulator

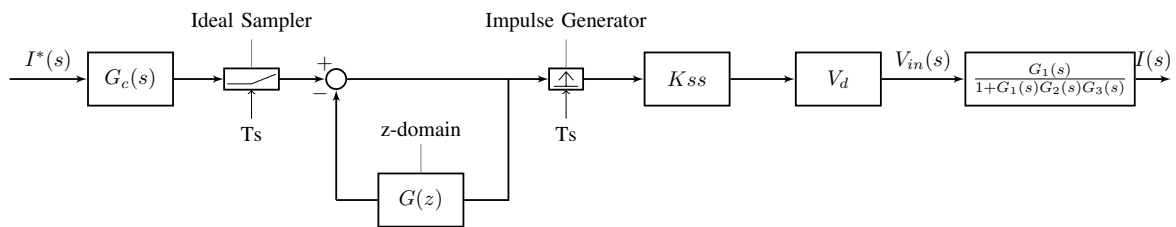


Figure 5: Manipulated feedback loop

loop transfer function of the model in Fig. 3, is:

$$G(s) = \frac{G_c(s)V_d K_{ss} G_1(s)}{1 + G_1(s)G_2(s)G_3(s)} \quad (6)$$

The transfer function of the PI controller, $G_c(s)$ is given by:

$$G_c(s) = K_p + \frac{K_i}{s} \quad (7)$$

The average model suggests that the PWM block has unit gain but considering the small signal model it seems that this is not necessarily the case [6]. The small signal gain, K_{ss} , is the equivalent gain of the sampling operation and impulse generation done by the PWM block [5]. The small signal gain depends on the slope of the compensator output signal just before it intersects the carrier signal. It is described by Eq.(8),

$$K_{ss} = \frac{f_s}{f_s - |\dot{r}_o|} \quad (8)$$

where f_s and $|\dot{r}_o|$ denote switching frequency and the slope of the PWM reference prior to intersection with the carrier signal respectively. It is accurate up to several multiples of the switching frequency [6]. The model block diagram in Fig. 4 is manipulated to produce the block in Fig. 5. The only feedback loop in Fig. 5 is the z-domain control feedback loop. The stability of the system thus depends only on the stability of the z-domain feedback loop. The closed loop transfer function of the model in Fig. 5, is shown in Eq.(9).

$$\frac{I(s)}{I^*(s)} = \frac{G_c(s)V_d K_{ss} G_1(s)}{(1 + G(s))(1 + G_1(s)G_2(s)G_3(s))} \quad (9)$$

5. PI CONTROLLER DESIGN

Table 1: System Parameters

Parameters	Values
DC-bus voltage (V_d)	900 V
Load Inductance (L)	2.08 mH
Parasitic resistance (r_L)	0.4 Ω
Switching frequency (f_s)	20 kHz
Transport delay (t_d)	0 μ s
Sampling frequency (f_{sample})	20 MHz
Load Capacitance (C)	1000 μ F
Load resistance (R)	40 Ω
Parasitic resistance (r_c)	0.6 Ω

The system parameters for the current regulator system of the Synchronous Buck Converter in Fig. 2 are shown in Table 1.

The performance of the PI controller is determined by the values of K_p and K_i [1]. In order for the system to meet the required phase and gain margins that suit the system's desired performance, the values of K_p and K_i need to be designed for. The approach to design for K_p and K_i values involve transforming the open loop s-domain

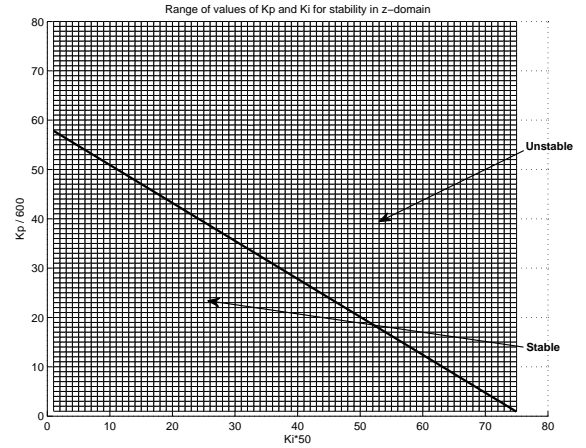


Figure 6: Range of values of K_p and K_i for stability

transfer function to z-domain in order to accurately analyse the values of K_p and K_i that will ensure the stability of the system. When transforming from s-domain to z-domain, impulse invariance method is used. As the PWM block emits an impulse that propagates around the loop, the impulse response is sampled by an ideal sampler. Taking the z-transform of these samples into consideration leads to the impulse invariance method being used. In order to transform to z-domain, the theoretical open loop transfer function $G(s)$ in Eq.(6) is used. It is expanded into partial fractions of the form:

$$G(s) = \sum_{n=1}^N \frac{A_n}{s + p_n} \quad (10)$$

where $-p_1, -p_2, \dots, -p_N$ are s-domain poles. The discrete time system transfer function obtained by taking the z-transform of the impulse response of $g(t)$ is as follows:

$$G(z) = \sum_{n=1}^N A_n e^{p_n T_s} \frac{e^{-p_n T_s}}{z - e^{-p_n T_s}} \quad (11)$$

The first sample of $g(t)$ ($k = 0$) is always zero as practical systems always have a small propagation delay hence it is not included in the derivation of $G(z)$.

In the s-domain, a 2-dimensional nested for loop, looping around small values K_p and K_i is made. For every K_p and K_i value, the open loop transfer function is transformed to z-domain and the maximum of the absolute value of the closed loop poles is determined. The stability or instability of the system is analysed by checking whether or not the poles lie in the unit circle. As can be observed from the mesh plot in Fig. 6, the plot is demarcated by a bold line into upper and lower regions. The upper region is unstable and the lower region is the stable. On the plot, axial values of the x axis are divided by a factor of 600 and y axis values are multiplied by 50 in order to obtain a wide range of K_p and K_i values that ensure stability.

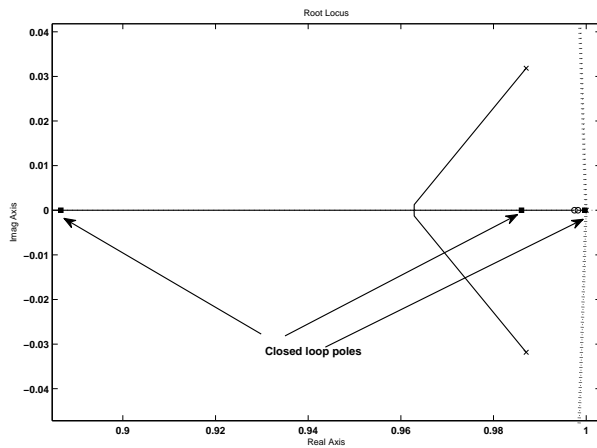


Figure 7: z-domain root locus

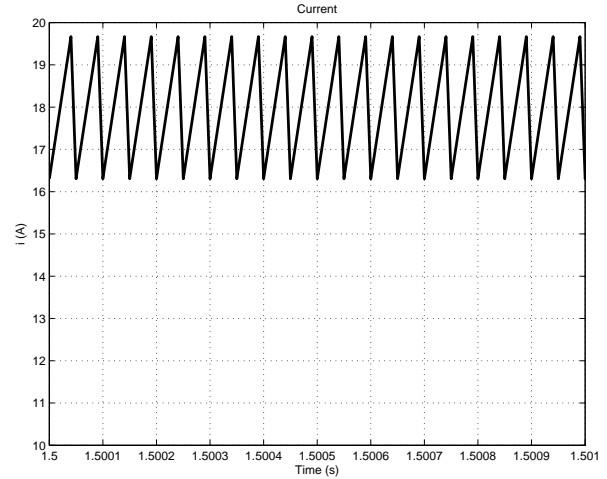


Figure 10: Output Current

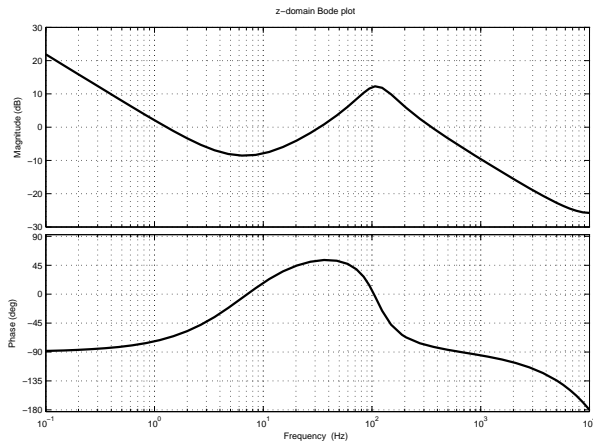


Figure 8: Bode plot

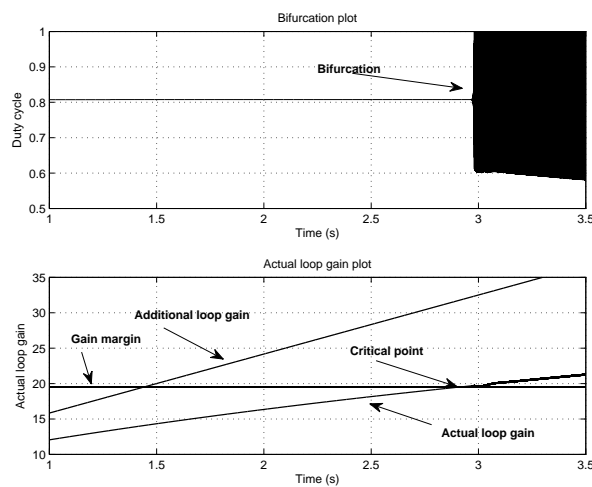


Figure 9: (a):Bifurcation diagram as a function of time(b):Actual loop gain as a function of time

From the plot, values are chosen that guarantees stability and critical damping i.e 0.0048 and 0.35 for K_p and K_i respectively and then used in simulation. The root locus is depicted in Fig. 7 and the poles are located inside the unit circle, signifying stability. In Fig. 7 it can be observed that one pole is most influential as the other two poles are each placed close to zeros, hence the two poles have very small influence on the time domain behaviour of the system. The bode plot is depicted in Fig. 8. The gain and phase margins are 25.8 dB and 98.5° respectively.

6. MODEL VERIFICATION AND RESULTS

6.1 Model Verification

A simulation was conducted in order to simulate the model in Fig. 4. The simulation was performed in order to verify the small signal z-domain model. An additional loop gain K_a was inserted into the loop and gradually increased. This was done in order to find the value loop gain that would make the system unstable by observing the point where the first bifurcation takes place. The bifurcation diagram in Fig. 9a, shows the point of period doubling where the system becomes unstable. In simulation the small signal gain, K_{ss} , which depends on the gradient of the compensator signal prior to intersection with carrier signal, was also taken into account. As K_a is increased, K_{ss} decreases. Therefore the actual loop gain of the system is the product of the small signal, K_{ss} , and the additional loop gain, K_a . In Fig. 9b, the point labelled critical point, corresponds to the bifurcation point in Fig. 9a. When taking a closer look at Fig. 9b, it can be observed that when the actual loop gain just crosses the gain margin at critical point, the first bifurcation occurs. The critical point value is 19.4984 which is the same as the theoretical value of the gain margin of 19.4984. This shows that the small signal z-domain model accurately predicts the stability of the current feedback loop.

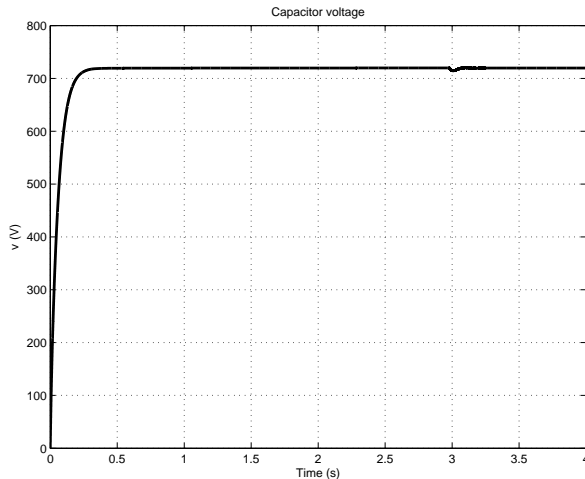


Figure 11: Output Voltage

6.2 Current regulation

The simulated output current perfectly tracks the reference current of 18 A, as shown in Fig. 10 with 30% ripple as designed for. The load characteristics introduced by the grid tie DC/AC inverter are modelled as a resistive and capacitive network with parameters in Table 1. With a reference current of 18 A, the load voltage is simulated as 720 V, as depicted in Fig. 11. This validates the mathematical model derived and the approach to PI controller design.

7. CONCLUSION

In this paper, a current controller is rigorously designed and tested in simulation for application in a DC/DC converter for connection with different types of grid tie DC/AC inverters. The techniques utilised in the design, enable perfect tracking of the current reference signal. The transformation technique to z-domain for stability check, proved fundamental in PI controller design as it guarantees the stability of the system under all operating conditions. Natural sampling behaviour of the PWM can be accurately modelled with the z-domain techniques. The approach of implementing the impulse invariance method for s-domain to z-domain transformation, assures correct small signal analysis of the PWM.

Future work will be focused on the design of the outer voltage control loop.

REFERENCES

- [1] Kiam Heong Ang, Gregory Chong, and Yun Li. "PID control system analysis, design, and technology". In: *Control Systems Technology, IEEE Transactions on* 13.4 (2005), pp. 559–576.
- [2] Luca Corradini, Walter Stefanutti, and Paolo Mattavelli. "Analysis of multisampled current control for active filters". In: *Industry Applications, IEEE Transactions on* 44.6 (2008), pp. 1785–1794.
- [3] Kjell Ljøkelsøy and Olve Mo. "Fast current controllers using FPGAs". In: *Proceedings of the 10th European Conference on Power Electronics and Applications, EPE*. 2003, pp. 2–4.
- [4] Toit Mouton et al. "Modelling and design of single-edge oversampled PWM current regulators using z-domain methods". In: *ECCE Asia Downunder (ECCE Asia), 2013 IEEE*. IEEE. 2013, pp. 31–37.
- [5] Lars Risbo. "Discrete-time modeling of continuous-time pulse width modulator loops". In: *Audio Engineering Society Conference: 27th International Conference: Efficient Audio Power Amplification*. Audio Engineering Society. 2005.
- [6] Lars Risbo, Mikkel CW Høyerby, and Michael AE Andersen. "A versatile discrete-time approach for modeling switch-mode controllers". In: *Power Electronics Specialists Conference, 2008. PESC 2008. IEEE*. IEEE. 2008, pp. 1008–1014.
- [7] Liu Yang Taizhou Bei Ping Wang and Zhe Zhou. "Dynamic Sliding Mode Evolution PWM Controller for a Novel High-Gain Interleaved DC-DC Converter in PV System". In: *Journal of Applied Mathematics* 2014 (2014), p. 11.
- [8] Terasic Technologies. *DE1-SoC User Manual*. English. Altera. 113 pp. URL: <http://www.terasic.com.tw/cgi-bin/page/archive.pl?Language=English&No=836&PartNo=4> (visited on 05/27/2015). April 8, 2015.

A TORQUE AND TEMPERATURE TELEMETRY SYSTEM FOR A ROTATING

P.J. Friend* and A.J. Grobler†

* School for Electric, Electronic and Computer Engineering, Faculty of Engineering, NWU, Potchefstroom, South Africa E-mail: bianca.friend@live.co.za

† School for Electric, Electronic and Computer Engineering, Faculty of Engineering, NWU, Potchefstroom, South Africa E-mail: andre.grobler@nwu.ac.za

Abstract: This paper focuses on the design of a system that can measure the temperature of the magnets in the rotor of a permanent magnet motor and also measures the torque transferred through the shaft. The need for such system exists as the magnets can demagnetize if the magnet temperatures exceed the specified values. It is difficult to measure these temperatures directly. There are various torque sensors available but they are expensive. This system is more favourable in laboratory conditions as modifications will have to be made to the motor. Similar products are available, but there isn't one that combines these two measurements. By making a single device that measures both temperature and torque, it is more cost effective. This system can be used to test newly designed motors and can help in developing and verifying temperature models of the motor. The system was designed to measure five temperatures using resistive temperature devices (RTDs) and the torque with strain gages connected in a full-bridge. The system operates from two 2600 mAh Li-ion batteries connected in parallel. The system was manufactured and tested on a 7.5 kW line start permanent magnet synchronous motor (LS PMSM). The system was tested and functions correctly at 1500 r/min. The temperature measurements are within 2°C of the temperature measured with a calibrated thermocouple, and the torque measurements are within 2 Nm of the torque measured with a commercial torque meter.

Key words: temperature measurement, torque measurement

1. INTRODUCTION

Monitoring critical temperatures in electric motors is a key part of preventing shortened life span due to excessive thermal stresses [1]. High temperatures of permanent magnets (PM) cause demagnetization that leads to failure or a reduction in performance. Exceeding the thermal limits of the windings can damage the insulation varnish. Permanent magnet synchronous machines (PMSM's) torque-speed characteristic is dependant on the temperature of the PMs. The PM remanent flux decreases with an increase in temperature thus reducing the torque capability of the machine [2]. Thus, it is important to know the temperature of the rotor to gain maximum utilization of a motor while assuring safe operation. When developing thermal models of motors, it must be tested and compared to actual values. It is difficult to measure the rotor temperatures directly. Thus an affordable device capable of measuring these temperatures and the torque would be of great use in the research and development area as it can be used to ensure the thermal models of a newly designed motor is correct.

Technologies used for directly measuring PM temperatures on the rotor, like telemetry systems, slip rings, etc., are expensive and therefore not used often [3]. Other methods for estimating the temperatures like model-based approaches and flux observers are discussed in [1], [3] and [4]. Contact measurement techniques give greater thermal information, but can't be done without making changes to the motor as the sensors must be fixed to specific parts of the rotor. The rotating instrumentation also needs to be

fixed onto the shaft. Despite this drawback, there are a few advantages in using contact techniques. It has a higher accuracy, and it is possible to measure multiple points simultaneously. It is possible to measure axial and radial temperature distribution. These methods are preferably used in laboratory setups. With this method, it is possible to get a relatively precise 3D thermal distribution of the rotor [5].

Torque is an important aspect in determining the performance of a motor. The efficiency of an electric motor can be determined if the torque and r/min are measured. There are various ways in which the torque of an electrical motor has been measured over the years. These methods include sliprings, rotary transformers, infrared telemetry and FM telemetry systems.

The most common temperature sensors are the resistive temperature device (RTD), thermocouple, thermistor and silicon chip sensors. Each type of sensor was designed for specific temperature ranges and environmental conditions [6]. For this application only an RTD, thermocouple and thermistor was considered as they have an appropriate temperature range.

The RTD's output is almost linear and has a smaller physical size than the thermistor and thermocouple. It is the most accurate and reliable of these three sensors. An RTD needs signal conditioning to measure the small difference in resistance. The disadvantage of the RTD is that it needs an excitation current. A thermocouple's advantage is that doesn't need a power source as it

generates an output voltage due to its temperature. It has a fast response but needs more complex signal conditioning as the output must be linearized and it needs a sensor to measure the "cold-junction" reference temperature for accurate readings. A thermistor is more sensitive than an RTD as it has larger changes in resistance for the same temperature difference. The thermistor is more likely to introduce errors due to self-heating if the excitation current is too high. A very small current is needed for high accuracy.

The data must be sent wirelessly to a stationary unit as the system is mounted on the shaft. There are various ways that can be used: Bluetooth, infrared and WiFi. If infrared is used, it must be mounted in the middle of the shaft. It has a lower power consumption and is more immune to electromagnetic interference than the other options. The use of infrared was presented in [5]. Both WiFi and Bluetooth are more tolerant to where it is placed, it can communicate further and can transfer data at higher speeds. The use of WiFi was presented in [2]. Bluetooth has a lower power consumption than WiFi, which is critical as the system will be battery powered and must be able to operate for at least 24 hours.

To be able to measure the torque of the motor, strain gages will be used to measure the strain on a shaft due to the torque applied to it. This is possible by using a half- or full-bridge configuration. The signal will be amplified to measure the small difference in resistance.

The data from the various temperature sensors and the torque must be saved to be able to use the data at a later stage. This data will be stored on the computer that the device is connected to, and backup storage will be on the device. This data can be stored on various types of devices like an SD card, EEPROM, etc. The main advantage of using an SD card is that a file system can be implemented on it. The SD card can thus be removed, and the data can be read on any computer. The main reason for the SD card storage is that if a computer doesn't have Bluetooth or if it failed the data can still easily be retrieved.

2. DESIGN

By considering the advantages of all the possible technologies discussed in the previous section the following components were chosen for the design:

- A microcontroller for the data processing
- RTDs to measure the temperature
- Strain gages to measure the torque
- RTD-to-digital converters chip for the signal conditioning of RTDs
- Instrumentation amplifier for the signal conditioning of the strain gages
- Bluetooth for transmitting the data
- A micro SD card for saving data
- Lithium-ion batteries to power the system
- A Lithium-ion battery charger

Figure 1 illustrates the basic interface of these components and where the different components will be mounted.

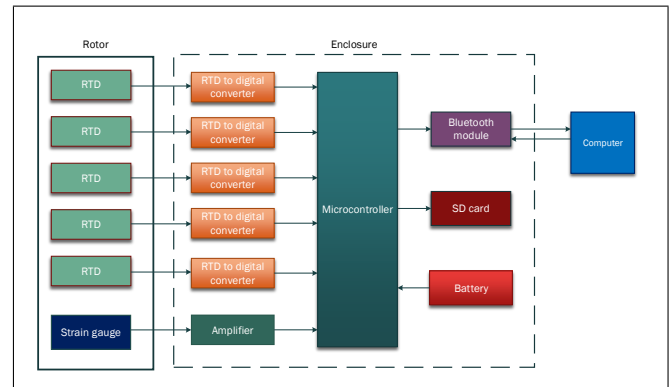


Figure 1: Basic design

2.1 Temperature measurements

A 3-wire RTD was chosen as the temperature sensor. For the signal conditioning of the RTD, a RTD-to-Digital converter IC (MAX31865) was chosen. The connection of the RTD, IC and microcontroller is illustrated in Figure 2. The datasheet suggests the reference resistor's resistance is approximately four times larger than the nominal resistance of the RTD. A 100 Ω RTD was used, and the closest resistor was 402 Ω . A resistor with a very low tolerance and that doesn't change much with temperature was chosen for the reference resistor.

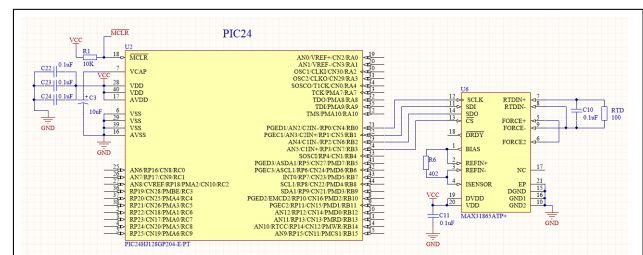


Figure 2: Schematic of RTD circuit

The IC that was used to measure the resistance of the RTD uses the SPI protocol to send the data to the micro-controller. With SPI devices can be connected in parallel, thus all five ICs use the same SPI channel where each IC has its own chip select pin. The program starts by configuring the pins. In this function all pins are set as digital, various pins are set to inputs, or outputs and the SPI pins are mapped. The SPI channel 1 of the micro-controller is set up in mode 3 with 8 bits communication and a clock rate of 230 kHz. The RTD IC must be set up next. This is done by writing to the configuration register of the IC. It was set up for a three wire RTD, to auto sample at 50 Hz and use the 50 Hz filter. There is a 20 ms delay because the IC samples at 50 Hz. A 16-bit value is read from the chip from two different registers. This is combined into a 16-bit value, and the LSB is discarded as it is a fault bit. The 15-bit value is

then converted to the resistance, and the temperature is calculated from the resistance.

2.2 Torque measurements

The rated torque of the motor that the system is designed for is

$$\begin{aligned} T &= \frac{P_o}{\omega} \\ &= \frac{P_o p}{4\pi f} \\ &= 47.75 \text{ Nm}, \end{aligned} \quad (1)$$

where P_o is the output power, ω is the speed in rad/s, f is the frequency and p is the number of poles of the motor [7].

The signal conditioning circuit and mechanical structure will be designed to measure a maximum torque of 100 Nm.

The rotor has a solid shaft made from steel. The strain when 100 Nm is applied will be very small, and a large gain is necessary. This makes the electronic design more complex. An additional shaft was designed to measure the torque on instead. Aluminium was chosen as it is soft and will deform more than other materials. The design of the shaft was an iterative process. A size was chosen, and the strain was calculated. The shaft was simulated to verify if the calculations were correct. In the simulation, the stresses on the shaft were also investigated. This was done to ensure that the shaft won't be exposed to plastic deformation. The simulation of the strain at 100 Nm is shown in Figure 3.

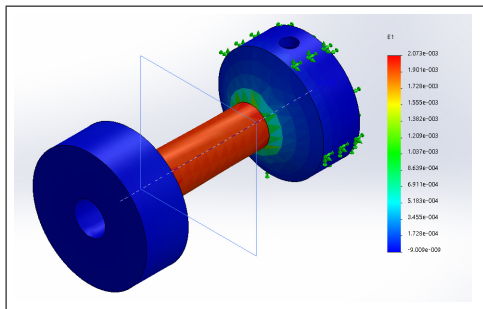


Figure 3: Simulation of strain on the shaft

After a few iterations, the dimensions of the middle of the shaft where the torque will be measured was chosen as an outer radius of 10 mm and an inner radius of 8 mm. The shaft is made from Aluminium 6082 which has a shear modulus of 26.4 GPa. Figure 4 shows a drawing of the final shaft that was designed.

To calculate the strain the polar moment of inertia is required. This is

$$\begin{aligned} J &= \frac{\pi}{2}(c_o^4 - c_i^4) \\ &= 9.274 \text{ nm}^4 \end{aligned} \quad (2)$$

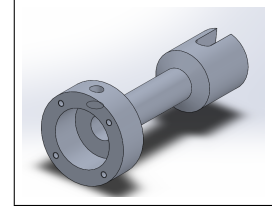


Figure 4: Shaft for measuring torque

where J is the polar moment, c_o is the outer radius and c_i is the inner radius of the shaft [8]. The torsional stress is

$$\tau = \frac{T_m c_o}{J} = 107.828 \text{ MPa} \quad (3)$$

and the torsional strain is

$$\gamma = \frac{\tau}{G} = 4.084 \times 10^{-3} \quad (4)$$

The strain at 100 Nm torque is

$$\epsilon = \frac{\gamma}{2} = 2.042 \times 10^{-3} \quad (5)$$

The strain and torsional strain is dimensionless. The amplifier has to be designed to be able to give the maximum output voltage at a strain of 2.042×10^{-3} .

The maximum change in resistance of the strain gages are

$$\begin{aligned} \frac{\Delta R}{R} &= GF \epsilon \\ \Delta R &= 1.45 \Omega \end{aligned} \quad (6)$$

where R is the nominal resistance of the strain gage and GF is the gage factor.

A full-bridge was chosen as the output voltage is twice the output voltage of a half-bridge and thus less amplification is necessary. A full-bridge is also less sensitive to the ambient temperature as all four of the strain gages' resistance changes the same with a rise in temperature. The output of the full-bridge is

$$\begin{aligned} V_{o1} &= V_a - V_b \\ &= \frac{R - \Delta R}{2R} V_{cc} - \frac{R + \Delta R}{2R} V_{cc} \\ &= -\frac{\Delta R}{R} V_{cc} \end{aligned} \quad (7)$$

An instrumentation amplifier must be designed to have an output voltage of 3.25 V when a 100 Nm torque is applied to the shaft. The voltage supply is 3.3 V. The nominal resistance of the strain gages are 350 Ω .

$V_o = 3.25 \text{ V}$ when $\Delta R = -1.45 \Omega$

$$V_{o1} = \frac{\Delta R}{RV_{in}} = 13.67 \text{ mV} \quad (8)$$

$$V_o = \frac{R_4}{R_3} \left(1 + \frac{2R_2}{R_1}\right) V_{o1} \quad (9)$$

Choose $\frac{R_4}{R_3} = 9$ then

$$\frac{R_2}{R_1} = 12.496$$

Standard resistor values or combinations thereof were chosen according to the ratios. The resistor values are

$$\begin{aligned} R_1 &= 1.2 \text{ k}\Omega \\ R_2 &= 15 \text{ k}\Omega \\ R_3 &= 1.5 \text{ k}\Omega \\ R_4 &= 12 \text{ k}\Omega \end{aligned}$$

The circuit was simulated, and the output of the instrumentation amplifier varies from 0 – 3.25 V for torque that varies from 0 – 100 Nm. Figure 5 is the designed circuit. The output voltage varies linear with a change in torque, and the output voltage is 3.25 V for 100 Nm torque. To convert the voltage to the torque, the following formula was used:

$$T_m = \frac{2V_{ADC}RGJ}{AV_{cc}RGF c_o} \quad (10)$$

where V_{ADC} is the voltage that was measured by the ADC and A is the gain of the instrumentation amplifier.

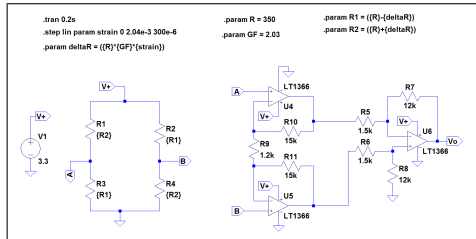


Figure 5: Circuit of instrumentation amplifier

The process of reading the torque will be briefly explained. An analog input pin is connected to the instrument amplifier and is used to digitize the torque signal. The ADC is configured with a 12-bit resolution and the voltage references set to V_{dd} and V_{ss} . The ADC is read, and the binary value is converted to a voltage value. From this voltage, the strain is calculated. The torque is then calculated from the strain.

2.3 Data storage

For the data storage a micro SD card was chosen as its physical size is small and it can be removed and the data can be read on a computer. A file system is implemented on the card that it saves the data as a text file that can be used afterwards. If the communication between the device and the computer fails, the data can still be accessed. The

card also uses SPI communication and it was decided to put the card on a separate SPI channel.

The SD card starts in SD bus mode and the controller must send at least 74 clock pulses with the chip select and data out pin high. The SD card will then go into SPI bus mode. Command 0 can be sent to reset the card and the card must respond with 1 to say it is in idle state. When this is received the micro-controller can send command 1 to initialize the card. The card must respond with a 0 to indicate the command was accepted. When the card is initialized, the micro-controller can now send a command to read or to write data. The card will send a response to say if the command was accepted and then the data can be sent.

2.4 Wireless communication

Bluetooth was chosen to transmit the data from the device to a computer. This eliminates the need for a receiver to be built as most computers have Bluetooth or a standard Bluetooth dongle can be bought if the computer doesn't. The Bluetooth in the device is version 3 but Bluetooth is backward compatible. Thus the device must work with a computer with any version of Bluetooth. The module uses UART communication to send and receive data from the microcontroller. The UART is set up with 8 bits, no parity and a baud rate of 115200. Data is read from the UART and also written to the UART. This enables the device to receive commands from the computer and also send data to the computer.

2.5 Micro-controller

Considering all the peripherals that the above functions require a microcontroller is required. A PIC microcontroller in the PIC24H family was chosen as it has at least 2 SPI channels, a UART channel, a 12 bit ADC channel and digital I/O pins. The 44 pin controller was chosen to ensure enough I/O pins for all the features.

2.6 Software

A basic GUI was written where the data that the computer receives from the device via Bluetooth is displayed. This program allows the user to save the data to a CSV file.

2.7 Power supply

The entire systems require a 3.3 V power supply. Thus, a 3.7 V lithium ion battery was chosen. The battery capacity must be large enough to power the system continuously for 24 hours. The current consumption was calculated as 71 mA. The power consumption of the micro SD card and the microcontroller could not be calculated, and it was assumed that the total power consumption will be approximately 80 mA. For an operation time of 24 hours, a 1920 mAh battery is needed. 2600 mAh batteries were purchased as they were most cost effective. Two of these batteries were used to help distribute the weight. The batteries can operate continuously for 65 hours.

A charger was built into the device to make it easier to charge the device as the batteries can be charged while in the device. A Li-ion charger IC was used to charge the batteries from a 5 V dc supply. A USB connector was used as any USB cellphone charger can be used for the power supply for the charger circuit. The circuit was designed that the charger charges one battery at a time with the use of a micro-controller. A basic 8-bit microcontroller was used as it only needed five digital I/O pins.

Figure 6 shows the schematic of the charger circuit. A Relay disconnects the batteries from the source and from each other when the 5 V dc power is attached. The microcontroller connects one battery to the charger and enables the charger. When the charger gives an output that the battery is fully charged, the microcontroller disables the charger and disconnects the battery. The other battery is connected and the charger is enabled. When both batteries are fully charged, both batteries are disconnected and the charger is disabled. By doing this it is possible to charge both the batteries with one single cell Li-ion battery charger. The batteries are charged at 500 mA and takes approximately 10.4 hours to recharge the batteries fully.

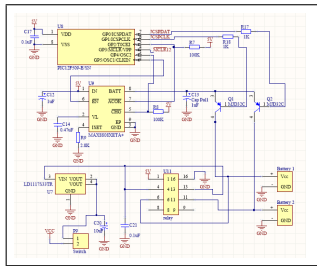


Figure 6: Schematic of charger circuit

2.8 Enclosure

An enclosure was designed that will be mounted to the shaft. The enclosure must be light as it is going to rotate at 1500 r/min. The enclosure is going to be 3D printed as the Bluetooth module can't be inside a metal casing. The size of the enclosure was determined by the diameter of the PCB and the height of the PCB when all components are attached. The mounting holes were determined from the shaft that is mounted to.

3. IMPLEMENTATION AND TESTING

3.1 Implementation

From the design, the PCB was manufactured and populated. Each RTD circuit, the instrumentation amplifier circuit and the Bluetooth can be disconnected from the supply voltage. Thus each section was tested individually. The tests consisted of first checking for any short-circuits and then testing the functionality. The faults that were detected was fixed before the entire system was tested. Figure 7 is a photo of the populated PCB.

The shaft that was designed to measure the torque on was manufactured from Aluminium 6082. The strain gages

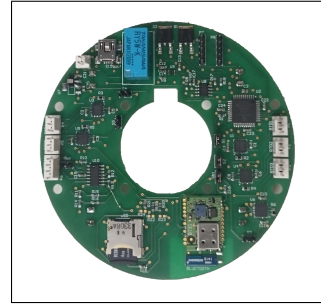


Figure 7: Populated PCB

were fitted at a 45° angle from the centre line with two on each side as shown in Figure 8. Lines were made on the shaft that was lined up with the markers on the strain gages to ensure it is at 45° .

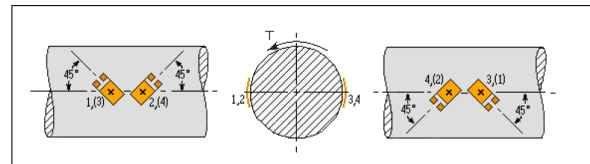


Figure 8: Placement of strain gages [9]

The enclosure of the device was 3D printed along with four brackets to help keep the batteries in place when rotating at 1500 r/min. The PCB with the batteries attached to it fits inside the enclosure. The wires for the RTDs and strain gages fit through the enclosure and is connected with connectors for easy assembling and disassembling the device. The enclosure is closed and fitted with four screws. The device as in Figure 9 can now easily be fitted to the rotor shaft.

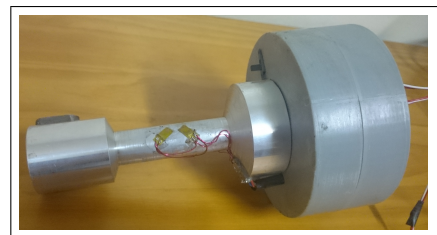


Figure 9: Device after it was assembled

The device is connected to the rotor by sliding it over the rotor shaft. A grub screw is used to fasten the device to the rotor shaft. The grub screw fits into the shaft key slot. Once the device is fitted to the rotor, there is no need to remove it regularly it as it can be charged while fitted to the rotor.

3.2 Test setup

For testing purposes, the device was fitted to a 7.5 kW LS PMSM. The other side of the device was connected to a torque meter. The torque meter was connected to a 7.5 kW dc machine. In this setup both the machines can be used as

the motor or the load. Figure 10 shows a photo of the test setup showing the main components. A variable resistor is connected to the machine that will be used as the load. This setup allows tests to be done at various speeds and at rated loads. The RTDs are not mounted in the rotor yet and the temperature will therefore be tested stationary.

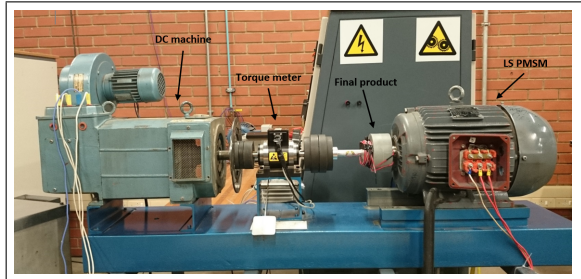


Figure 10: Experimental test setup

3.3 Temperature measurements

To test if the temperature measurements are correct, the RTD was exposed to various temperatures. A thermocouple of a multi-meter was placed directly next to the RTD that both of the sensors are exposed to the same temperature. For these tests, the multi-meter reading was assumed to be the actual temperature. The different temperatures that were measured are compared to the actual values. In Figure 11 the actual temperatures and the measured temperatures are plotted. This was done to determine the accuracy of the temperatures in the range that the system must be able to measure.

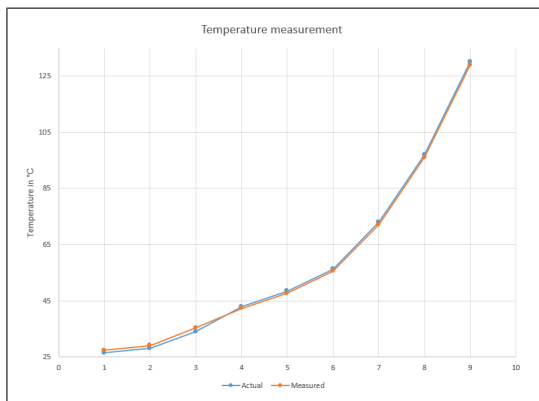


Figure 11: Measured temperature vs actual temperature

Due to the test setup it was difficult to compare the values as the temperature varied quickly. The test setup also limited the temperature that could be measured. Thus the measurements were taken from 26.5°C to 130°C. The largest difference was 1.4°C. From these values and the graph in Figure 11 it can be assumed that this accuracy will be the same for the entire temperature range that the device has to measure. With further calibration, a higher accuracy can be achieved.

3.4 Torque measurements

To measure the torque the system had to be completed first as the test was done while the shaft was rotating. The torque sensor that is fitted between the dc machine and the device was used to verify the torque measurements of the device. First the dc machine was used as the motor and resistors were connected to the terminals of the LS PMSM to function as the load. This was used to test the device at lower speeds to ensure it functions correctly before running it at 1500 r/min. The speed was slowly increased until 1500 r/min without the device failing.

To test the torque measurements the LS PMSM was used as the motor and a variable resistor was connected to the armature of the dc machine. The resistance was varied to change the torque. The torque that was measured had a ripple in and therefore only the peak values were plotted as it was the easiest to compare these values. The peak torque was varied from 4.5 Nm to 36 Nm and 11 measurements were taken. Figure 12 illustrates the actual torque and the measured torque.

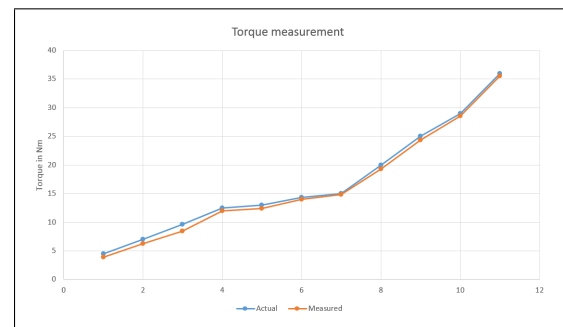


Figure 12: Measured torque vs actual torque

From Figure 12 it is clear that the device measures torque correctly. The measured values are slightly lower than the actual values. All measurements are within 2 Nm from the actual values. There is only one measurement that differs more than the rest. It is possible that the torque was changed before the system sampled on the exact maximum as it only measures every second. The maximum difference between the measured and actual values are 0.72 Nm, excluding the value discussed previously. To determine if it is necessary to calibrate the device for a better accuracy, longer tests must be taken where the RMS values are calculated and compared to the RMS values that the torque sensor displayed.

4. CONCLUSION

The device was tested on a 7.5 kW LS PMSM and functioned correctly while rotating at 1500 r/min. The rotor torque and temperature telemetry system could accurately measure the torque and temperatures. The system was implemented with only two RTDs but it can take up to five RTDs and all five circuits were tested. The temperature measurements are within 2°C of the actual values. The torque measurements are within 2 Nm of

the actual torque. The data was sent to a computer via Bluetooth. The Bluetooth had a stable connection and data was never lost or corrupted during tests. A GUI was used to display the values on the computer and save the data in a CSV file. The device can operate for 70 hours continuously. The micro SD card wasn't used when the tests for the power consumption was done. When the micro SD card is implemented the battery life will decrease but as it won't be constantly writing it won't use much power.

REFERENCES

- [1] T. Huber, W. Peters, and J. Bocker, "Monitoring critical temperatures in permanent magnet synchronous motors using low-order thermal models," in *Power Electronics Conference (IPEC-Hiroshima 2014 - ECCE-ASIA), 2014 International*, May 2014, pp. 1508–1515.
- [2] D. Fernandez, D. Reigosa, T. Tanimoto, T. Kato, and F. Briz, "Wireless permanent magnet temperature & field distribution measurement system for ipmsms." IEEE, 2015.
- [3] M. Ganchev, C. Kral, and T. Wolbank, "Compensation of speed dependence in sensorless rotor temperature estimation for permanent-magnet synchronous motor," *Industry Applications, IEEE Transactions on*, vol. 49, no. 6, pp. 2487–2495, Nov 2013.
- [4] A. Specht and J. Bocker, "Observer for the rotor temperature of ipmsm," in *Power Electronics and Motion Control Conference (EPE/PEMC), 2010 14th International*, Sept 2010, pp. T4–12–T4–15.
- [5] M. Ganchev, H. Umschaden, and H. Kappeler, "Rotor temperature distribution measuring system," in *IECON 2011 - 37th Annual Conference on IEEE Industrial Electronics Society*, Nov 2011, pp. 2006–2011.
- [6] B. Baker, "Temperature sensing technologies (an679)," Microchip Technology Inc., Tech. Rep., 1998.
- [7] B. Guru and H. Hiziroglu, Eds., *Electric Machinery and Transformers*, 3rd ed. Oxford University pres, 2001.
- [8] R. Hibbeler, *Mechanics of materials*, 9th ed. Pearson, 2014.
- [9] Measurement of force, torque, and other mechanical variables with strain gages. [Online]. Available: <http://bacula.nti.tul.cz/petr.sidlof/vyuka/LA1/strain-gauge-measurements.pdf>

An Investigation into Partial Discharges of XLPE Cable Insulation Defects.

I.K. Kyere¹, J.J. Walker¹⁺

¹Vaal University of Technology, Dept. of Power Engineering, Private Bag X021, Vanderbijlpark, 1900, South Africa

¹⁺Walmet Technologies (Pty) Ltd.

¹isaack@vut.ac.za; ¹⁺jerrywalker@walmet.co.za

Abstract: The high reliability and less maintenance of cables make them the primary choice for utilities. However, insulation defects inside cables can be a serious threat to safe operation and can lead to expensive disruption of supply. This paper investigates the effect of cavity geometry on partial discharge activity in XLPE cable insulation. The defects were spherical void and knife cut. Different experiments were made for PD measurements using the method of Phase-resolved partial discharge pattern (PRPD). The patterns obtained are discussed for the different partial discharge defects and the experimental results shows that partial discharge patterns strongly depends on the geometry of the void.

1 INTRODUCTION

Electrical insulation is one of the most important parts for any high voltage power system components. Electrical power systems include a large number of expensive and important power cables of different ages manufactured and installed over many decades [1]. The insulation quality plays a significant role in determining the reliability of the component. The quality of the insulation plays the most important role to ensure the reliability in power cables. Partial Discharge (PD) in cables provides useful information regarding the condition of the insulation as well as deterioration of the insulation [2].

Partial discharge is defined as a local dielectric breakdown that only partially bridges the insulation system between conductors under high voltage (HV) stress [3]. The main causes for the partial discharge are cavities within the solid and liquid dielectrics [4]. The aim of the insulation is to confine the electric field within the cable insulation for safe operation during the service life of the cable. The insulation should be able to perform its function for a variety of different system operating conditions such as temperature changes, load cycles, mechanical stresses, water ingress, etc. However, even if the insulation fulfils all required tests before installation and use, it may not maintain the same operation characteristics during the many expected years of service. There may be built-in manufacturing imperfections and workmanship errors that were not detected during commissioning tests [2]. Under specific conditions and due to high electric stress and existence of defects, partial discharges may take place in the cable

insulation. The presence of partial discharges in the insulation may degrade the insulation condition [5].

This paper presents the experimental results on the partial discharges in XLPE cable insulation using phase-resolved partial discharge measurements. The partial discharge measurement was conducted in solid insulation samples with known defects of spherical shape and knife cut shape in the insulation. This type of defects are typical of the defects imposed during the delivery and laying of cables and accessories due to lack of expertise of the personnel involved in assembling the cable system or lack of sufficient assembling guidelines provided by the manufacturer [6]. These defects causes partial discharge when the electric field in the void is higher than the inception field and there is an initial free electron to start an avalanche process [7].

The partial discharge data was presented in the form of Φ -q-n pattern where Φ is the phase angle of partial discharge occurrence, q the PD magnitude and n is the PD pulse number. The task was done using a digital ICMmonitor combined with a personal computer.

2 SAMPLE PREPARATION AND TEST SET-UP

For the samples used in these investigations, two artificial defects of different shapes and sizes were prepared. The sample used for these measurements consists of 11 kV XLPE insulated cable with semiconductive screen. Artificial defects were introduced in the XLPE through the semiconducting layer.

2.1. Spherical cavity

Figure 1 shows the test sample that was used in the experiment. The defect (cavity) was artificially created by drilling a hole of 1,5 mm diameter through the external semiconducting layer and 1 mm depth into the main XLPE insulation of the sample. This type of defect occurs as a results of failures in the cable extrusion process that causes a void in the insulation.

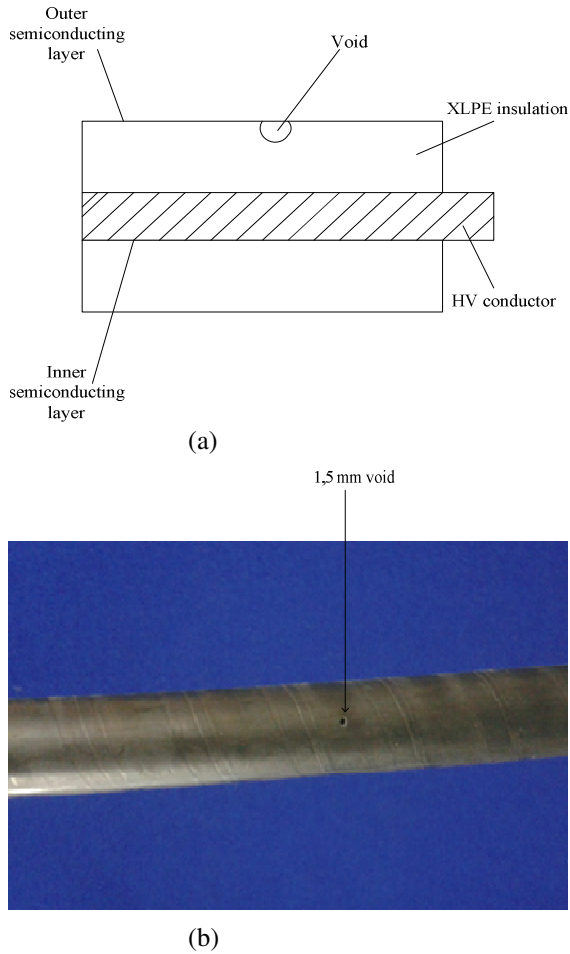


Fig. 1: (a) schematic diagram of the test sample, (b) Photograph showing the spherical void.

2.2. Knife cut

The partial discharges were generated using a 10 mm long knife cut through external semiconducting layer and 1 mm deep into the XLPE insulation as shown in Figure 2. This type of defect occurs due to improper handling of the splicing tool during preparation of the accessories.

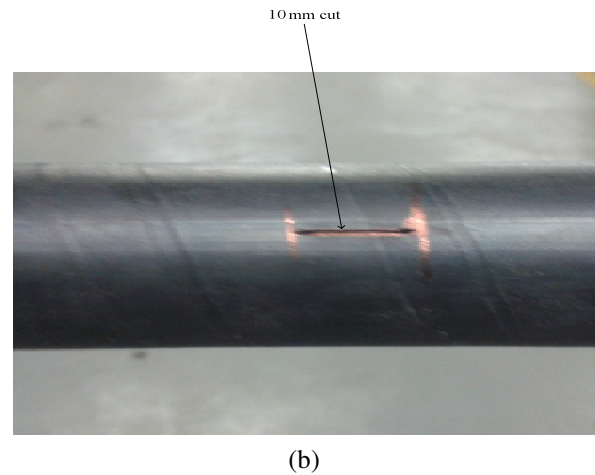
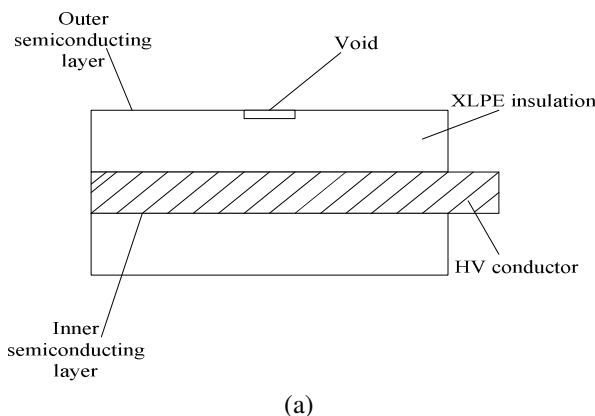


Fig. 2: schematic diagram of the test sample containing knife cut void, (b) A photograph of the cut in the insulation.

3 PARTIAL DISCHARGE MEASUREMENT SYSTEM

Partial discharges take place when a high voltage is applied to the samples. The circuit arrangement shown in Figure 3 below is the conventional PD test circuit in accordance with IEC 60270 [3]. In this method, it uses coupling capacitor (C_c) as part of the detection circuit. The advantage of the test system based on this method is that it has high sensitivity. However, the system need to be calibrated every time before testing to verify correctly measurement of specified PD magnitude. The circuit consists of 50 Hz ac power supply, the test sample, the Coupling Capacitor (C_c), the measuring impedance (Z_m) and the PD measuring device which consist of the ICMmonitor from Power Diagnostix and personal computer with software to evaluate and save the data.

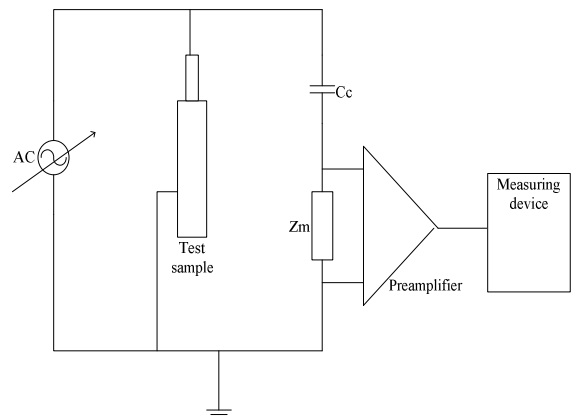


Fig. 3: Partial discharge measuring circuit

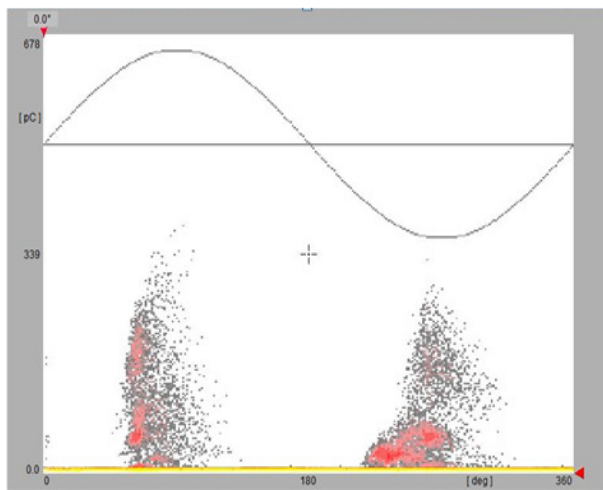
4 RESULTS AND DISCUSSION

Table 1 shows the measured PD data for spherical cavity of diameter 1,5 mm and 10 mm knife cut cavity within an XLPE insulation material of thickness 4 mm at 50 Hz, 2,5 and 3 kV ac sinusoidal applied voltages. The maximum charge magnitudes for spherical cavity are smaller than the knife cut cavity.

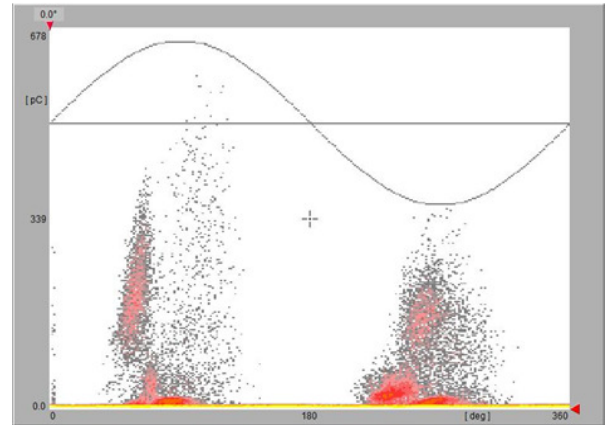
Referring to Table 1, each partial discharge measured is higher for the 3 kV than 2,5 kV applied voltages. The magnitude of the charge increases with cavity size since the cavity size determines the maximum propagation length of the avalanche parallel with the applied field as well as the size of avalanche head perpendicular to the applied field [8]. Therefore, the avalanche head can grow larger in a larger cavity, resulting in a larger partial discharge magnitude [9].

Tab. 1: Comparison of measured PD data between two different cavity sizes

Applied voltage (kV)	Spherical cavity (1,5 mm)		Knife cut (10 mm)	
	2,5	3	2,5	3
Maximum PD magnitude (pC)	284,6	339	329,4	864,7

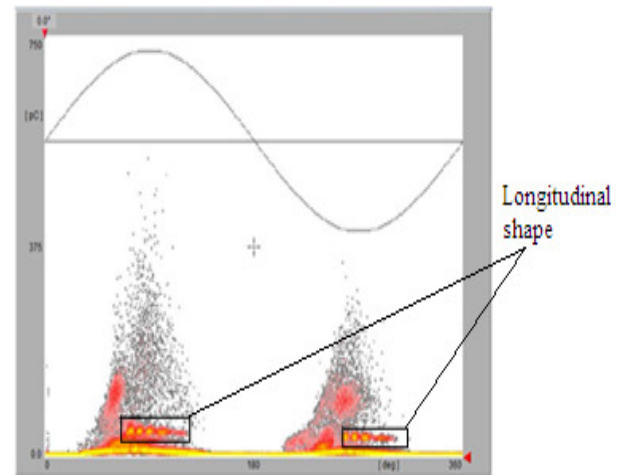


(a) 284, 6 pC at 2,5 kV

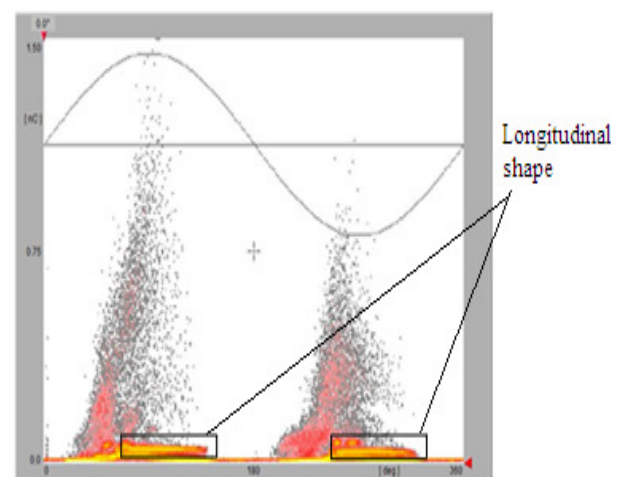


(b) 339 pC at 3 kV

Fig. 4: PRPD patterns obtained at different voltages of spherical cavity.



(a) 329, 4 pC at 2,5 kV



(b) 864, 7 pC at 3 kV

Fig. 5: PRPD patterns obtained at different voltages of knife cut cavity.

Various sets of phase-resolved patterns were obtained in this study. The measurements are carried out by varying the voltage to different levels. The phase-resolved plot displays all discharge pulses obtained during 60-second intervals at different magnitudes of applied voltages.

The horizontal axis is the phase angle where partial discharge pulses occurred while vertical axis is the partial discharge charge magnitude in pC. Each point has a colour, which represents the number of partial discharges that occurred with given amplitude and phase (a brighter colour indicates a higher number) [10]. Partial discharge magnitude increases with the applied voltage.

The PRPD patterns obtained from the experiments are presented in Figure 4 and 5. An increasing voltage of 0 – 3 kV is applied to measure the partial discharge activities of the test samples in Figure 1 and 2. Generally, it is seen that, partial discharge pulse appears in both positive and negative half cycles of the applied voltage.

Figure 4 shows typical PRPD patterns of spherical cavity recorded in our laboratory. It can be observed from this pattern that, the maximum partial discharges was about 284,6 pC at 2,5 kV applied voltage as depicted in Figure 4(a). In addition, this PRPD pattern also shows that, the pattern in the positive half is slightly higher than the negative half cycle. To observed PD activity within an enclosed cavity between the solid insulation and copper, the material operates as anode and cathode in the positive and negative half cycles. The cathode material provides free electrons to initiate partial discharges which then create plasma on the surface of the insulation. Plasma accelerates partial discharge activity as it is a very good source of free electrons. As a result, there is a likelihood of partial discharge activity taking place when the insulation material is acting as a cathode [15]. In the positive half cycle the insulation acts as a cathode and the copper acts as an anode. More electrons are supplied by the insulation, hence greater number of partial discharges in the positive half cycle as shown in figure 4. The pattern in Figure 4 also indicates that the cavity is located closer to the earthed electrode.

In the presence of longitudinal discharge activity, the PRPD pattern was different from what was seen with the spherical cavity. A typical PRPD pattern resulting from the longitudinal discharges measured is shown in Figure 5. This pattern was recorded at the same applied voltage of 2,5 kV with the maximum partial discharge of 329,4 pC as depicted in Figure 5(a).

Referring to Figure 5 the number of partial discharge is higher than that of Figure 4. This is due to the larger cavity geometry, resulting in higher initial free electrons in the cavity to initiate discharges, resulting in larger probability of partial discharge to occur. When the void is located close to earth electrode, the electric field on

the surface of the void is unsymmetrical. The discharge patterns of cavity discharge at positive and negative cycles of the applied voltage are also unsymmetrical [16]. In addition, another feature of this PRPD pattern in the form of longitudinal shape could be seen by the high intensity of partial discharge distribution pattern and marked by a solid line rectangle in Figure 5.

As the applied voltage was gradually increased to 3 kV, the PRPD patterns increases as depicted in Figure 4 (b) and Figure 5(b). With increasing voltage the maximum magnitude also increases with respect to the void size and shape.

Referring to figure 5 (a and b), the number of partial discharge is higher. This is due to higher initial free electrons in the void to initiate discharges, resulting in larger probability of partial discharge to occur. Therefore, within one cycle of the applied voltage, more PDs occur, which can be seen by the high density of partial discharge distribution pattern. However, there is a smaller number in the patterns of Figure 4 (a & b) compare to Figure 5 (a and b), due to lower initial free electrons to cause the occurrence of partial discharge in the other void. Hence, most of partial discharges occur after certain time delay when the inception field has been exceeded. Thus, there are a lower number of partial discharges per cycle, which can be seen by the low density of partial discharge distribution in sample containing the spherical cavity [11].

5 PARTIAL DISCHARGE INCEPTION VOLTAGE

Theoretically, the PD inception voltage (PDIV) according to [12] is calculated by:

$$V_{inc} = \frac{V_g}{\epsilon_r} [t + t_1 (\epsilon_r - 1)] \quad (1)$$

Where, V_g is the breakdown strength of the void and relative permittivity, ϵ_r for XLPE is 2.3.

Therefore, void inception voltage is given by:

$$V_v = \frac{V_{app}}{[1 + \frac{t-t_1}{\epsilon_r t_1}]} \quad (2)$$

Where, V_{app} is the applied voltage across the sample.

t is the thickness of the sample containing the void.

t_1 is the thickness of the void.

From equation (2), void inception voltage for the samples can be calculated as:

Spherical void:

$$V_v = \frac{3000}{[1 + \frac{4-1,5}{2,3(1,5)}]} = 1,74 \text{ kV}$$

The measured inception voltage, V_{in} is higher for the spherical cavity than the knife cut cavity. The cavity wall that is parallel with the applied field may influence the inception field, E_{inc} , where smaller cavity size increases the contact between avalanche head and the cavity wall, thus increasing E_{inc} [13]. The higher inception field in a smaller cavity is also due to the reduction of initial electron generation rate, resulting in longer statistical time lag and discharge occurs at higher voltage level [14].

The results of the calculated values are compared with the measured values and are presented in Table 2. However, the inception voltage in knife cut was not calculated since there is no define formula to calculate the inception voltage in knife cut.

Tab. 2: Comparison of PD inception voltages

Defect type	Measured	Calculated
Spherical void	1,8 kV	1,74 kV
Knife cut	1 kV	

6 CONCLUSION

Two artificial defects that represent different types of installation defects are applied to the test set – up and investigation is done by studying the effect of cavity geometry on partial discharge.

The results from these investigations primarily demonstrated that partial discharge phase characteristics and partial discharge number exhibit different tendency for each pattern. It is also observed that, each pattern has a unique feature resulting in an explicit identification potential for different defects. The results also indicated that partial discharge probability strongly dependent on the geometry of the cavity.

7 REFERENCE

- [1] P. Hyvonen: "Prediction of insulation degradation of distribution power cables based on chemical analysis and electrical measurements". DTech. Thesis, Helsinki University of Technology. 2008.
- [2] A. S. Ayub, W. H. Siew, and J. J. Soraghan: "Online Condition Monitoring of Partial Discharge in HV Underground Cables". University of Strathclyde, UK, 2001.
- [3] IEC60270, "Standard. High – Voltage Test Techniques – Partial Discharge Measurements," 2000.
- [4] M. Fidan and H. Ismailoglu: "A novel partial discharge calibrator design via dual microcontroller and high speed DAC". ELECO 2007, session A6, High Voltage Engineering, pp. 169-172. 8 December 2007.
- [5] S. Suwarno and H. Sutikno: "Model and Computer Simulation of Partial Discharge Patterns in Natural Liquid Insulation for High Voltage Application". International Journal of Mathematical Models and Methods in Applied Sciences, Issue 5, Volume 5, 2011.
- [6] S. M. Gargari: "Pattern Recognition and Knowledge Extraction for On-line Partial Discharge Monitoring with Defect Location," PhD project at Eindhoven University of Technology (TU/e) at Eindhoven, the Netherlands, pp22, 2012.
- [7] H. Illias, T. S. Yuan, AB H. Abu. Bakar, H. Mokhlis, G. Chen, and P. L. Lewin, "Partial Discharge Patterns in High Voltage Insulation," Inproceedings of IEEE International Conference on Power and Energy (PECon), Kota Kinabalu Sabah, Malaysia, pp. 751-755, 2-5 December 2012.
- [8] T. Do, O. Lesaint, and J. L. Auge, "Streamers and partial discharge mechanisms in silicone gel under impulse and ac voltages," *IEEE Transactions on Dielectrics and Electrical Insulation*, vol. 15, no. 6, pp. 1526-1534, 2008.
- [9] P. Das and S. Chakravorti: "Studies on partial discharge simulation based on a stochastic model considering the variation of discharge area and temperature of the void surface," *International Journal for Computational Methods in Engineering Science and Mechanics*, vol. 10, no. 5, pp. 393-405, 2009.
- [10] M. Conti: "Development of artificial intelligence systems for electrical insulation defect identification through partial discharge measurements". Ph.D. Thesis. Bologna, Italy: University of Bologna. Department of Electrical Engineering, pp. 8-9. 2003.
- [11] H.A. Illias, G. Chen, A.H.A. Bakar, H. Mokhlis and M.A., Tunio: "Partial discharges within two spherical voids in an epoxy resin". 2013 *J. Phys. D: Appl. Phys.* 46 335301, pp. 1-10. 29 July 2013.
- [12] B. RAMACHANDRA and R.S. NEMA: "Characterisation of partial discharge pulses in artificial voids in polypropylene films used in capacitors," *Proceedings of Conference Record of the 1996 IEEE International Symposium on Electrical Insulation*, Montreal, Quebec, Canada, June 16-19, pp. 517-520, 1996.
- [13] H. P. Burgener, T. H. Teich, and K. Frohlich: "Simulations of partial discharges of small microcracks parallel to the electrical field in polymeric materials," *Conference on Electrical Insulation and Dielectric Phenomena*, pp. 146-150, 2002.
- [14] A. Cavallini, F. Ciani, G. Mazzanti, and G. C. Montanari: "First electron availability and partial discharge generation in insulation cavities: effect of light irradiation," *IEEE Transactions on Dielectrics and Electrical Insulation*, vol. 12, no. 2, pp. 387-394, 2005.
- [15] H.A. Illias, M.E. Othman, M.A. Tunio, A.H.A. Bakar, G. Chen, and P.L. Lewin: "Measurement and simulation of Partial Discharge activity within a void in a Polymeric Cable model," In proceedings of 2013 IEEE International Conference on Solid Dielectrics, Bologna, Italy, pp.105 – 108, June 30 – July 4, 2013.
- [16] H. Illias, T. S. Yuan, AB H. Abu. Bakar, H. Mokhlis, G. Chen and P. L. Lewin: "Partial Discharge Patterns in High Voltage Insulation". In *proceedings of IEEE International Conference on Power and Energy (PECon)*, Kota Kinabalu Sabah, Malaysia, pp. 751-755. 2-5 December 2012.

INVESTIGATION OF BREAKDOWN VOLTAGE OF DIFFERENT TRANSFORMER OILS

K.P. Zondi*, L Pather* and AG Swanson*

* Discipline of Electrical, Electronic and Computer Engineering, University of KwaZulu-Natal, King George V Ave, Durban, 4041, South Africa

Abstract: Mineral oils have been used for over decades as an insulating material for power transformers. Recently, ester-based oils have been introduced as potential substitutes for mineral oils. To understand the impact of this change, it is necessary to compare the dielectric strength of these oils, which are natural esters, synthetic esters and mineral oil. The purpose of this report is to present an investigation of the breakdown voltages of different transformer oils. These insulating liquids were assessed using standard test method for electrical breakdown; both AC and lightning breakdown voltage test of these oils were carried out according to ASTM standards. On mineral oil and synthetic esters, the carbon path formed between the electrodes. Natural esters released lots of bubbles during an experiment. The experimental results were compared with those from previous research, and they were comparable.

Key words: Breakdown voltage, insulating oil, AC power frequency voltage, natural esters, synthetic esters, mineral oil and shell diala, power transformers.

1. INTRODUCTION

Mineral oil has been used for over 150 years as an important insulating material for transformers. Mineral oil can be potentially hazardous to the environment, due to its high flammability, less thermal stability and toxicity. Cases of transformer explosion may cause spill of oil or water stream. Ester based oil insulating have been introduced as substitutes for mineral oils, with biodegradable characteristics and it is an environmental solution to the insulating material of the transformers.

Transformer oils, as an essential component of transformer insulation, should withstand not only power frequency AC voltage but also transient impulse voltage (such as lightning impulse and switching impulse). AC breakdown test is normally used for oil quality check and lightning breakdown test as basic insulation level (BIL) is used as a criterion for large power transformer insulation design, and it is also generally regarded to be predominated by the oil intrinsic properties [1].

Oil insulators mainly serve two purposes in the operation of the transformer; as an insulating material and as a coolant. Briefly explained below [2];

- To insulate different parts at different electrical potential. The oil penetrates into and fills the spaces between wound insulation layers.
- To act as a coolant with the main task of absorbing the heat from the core winding, then transmitting it to the outer surface of the transformer

Transformer oil is the type of oil that is stable at high temperatures and has excellent electrical insulating properties. Its functions are to insulate, suppress corona and arcing and to serve as a coolant. The oil provides part of the electrical insulation between internal live parts, the

transformer oil must remain stable at temperatures for an extended period. As the transformer's life span increases, the oil degrades or ages, and this affects the oil's properties namely; breakdown voltage, viscosity, flash and pour point, moisture content, interfacial tension and the dielectric strength of the oil. Two types of oils are currently used in transformers, namely; mineral oil and ester based oil.

2. THEORY

This section is a literature review that discusses basic theoretical background of the electrical, chemical and mechanical characteristics of transformer oil and discusses the previous researches.

2.1. Mineral Oil

Petroleum oil has been used for transformer oil for decades. The source and production process of petroleum oil are described as follows:

Crude petroleum

- Petroleum oil is obtained from bituminous materials and is extracted from sources of crude petroleum. It contains a mixture of hydrocarbons and a small portion of sulphur and nitrogen [3], being yellow up to black in colour.
- Paraffin:
Methane (CH₄) is a gas, normal butane (C₄H₁₀) and isobutene;
- Naphthenic
It has ring structure with six carbon atoms (within six-membered rings) or 14 carbon atoms (within three-membered rings).
- Aromatics

It has six-membered ring structure, falls into two groups: mono-aromatics (single rings) and poly-aromatics (two or more).

2.2. Ester Based Oil

Esters are the synthesized organic compound of acids and alcohol [3]. Generally, there are two main type of esters:

Natural esters

It is derived from single, double or triple unsaturated fatty acids. The optimal condition is reached by using a fluid with a high single unsaturated fatty acids concentration. Natural esters can be produced from edible seed-based oil such as alcohol glycerol (triglycerides).

Synthetic Ester.

The synthetic ester is created from an acid and an alcohol, commonly known as polyol (pentaerythritol). The most recent products used in transformer insulation are MIDELE 7131 (M&I Company) and Elantas BecFluid 9902.

The advantages of ester based oil can be acknowledged from its performance [4]:

- Lubricity
- High solvency
- Low vapour pressure, low volatilities, high flash point
- Thermal stability
- Hydrolytic stability

Natural ester fluid needs some additives such as antioxidant or metal deactivators, to improve the performance and oxidation stability. They ensure that the combination between the natural ester fluid and additive material is in the range of minimum environmental and health safety target [5].

2.3. Transformer oil insulating properties

The oil used in transformers is hydrocarbon mineral oil. It is mainly composed of four generic classes of organic compounds, aromatics, paraffin's, naphthenes and olefins. Transformer oil gives a better insulation when aromatics, paraffin's, naphthenes and olefins are present at the right proportion. For better insulation transformer oil is desired to have more of saturated paraffin's and less of aromatics, naphthenes and olefins. For more stability, more aromatics and naphthenes are necessary. To get both insulating property and stability at the same time, there must be an optimum mix of four organic components. This can be obtained by careful refining of crude oil. Animal oils form fatty acids and attack the fibrous insulating materials and hence it might not be wise to use them in transformers [6].

Table 1: Basic properties of insulating oils

Properties	Units	Mineral Oil	Midel 7131	FR3	Shell Diallya
Density @ 20°C	kg/dm ³	0.882	0.97	0.92 (25°C)	0.881
Viscosity @ 40°C	mm ² /s	8.7	28	34	8
Pour point	°C	-60	-60	-21	-60
Flash Point	°C	144	275	316	135
Acidity	mgKOH/g	<0.01	<0.03	0.04	0.01
Water content	mg/kg	<20	50	30	<30
Breakdown (AC)		2.5mm	2.5 mm	2.0 mm	2.0 mm
- Before treatment	kV	40 – 60			>30
- After treatment	kV	>70	>75	>56	> 70
Dielectric dissipation @ 90°C		<0.001	0.03	3.0(100°C)	0.001

Assuming that the ratio of a breakdown voltage and gap distance is linear.

Table 2: Estimation of breakdown voltage in 1 mm gap

Type of Oil	Actual Breakdown (2.5mm or 2mm) kV	Expected Breakdown(1 mm) kV
Mineral Oil	70	28
Midel 7131	75	30
FR3	56	28
Shell Diallya	70	35

2.4. Dielectric Measurement

Generally, insulating material is expected to deteriorate under normal operating conditions. The aging rate of the oil can be influenced by external aging stresses: thermal stress, which is recognised as the change in temperature insulation during long term operation. Mechanical stress, the aging process relies on the tension, compression or torsion. Ambient stress is environmental dependant. Electrical stress leads to partial discharge and dielectric breakdown heating due to presence of conductive contaminants.

Breakdown in oil

Dielectric breakdown voltage test is a measure of the electrical stress that insulating oil can withstand without breakdown. The test is performed using a test vessel that has two electrodes mounted in it, with a gap between them. A sample of the oil to be tested is put into the vessel and an AC or impulse voltage is applied to the electrodes. This voltage is increased until the oil breaks down that is, until a spark passes between the electrodes.

Breakdown phenomena

Breakdown phenomena in oil is analysed by electro-optical means [14]. The conduction process commences through an injection of the charge at a point of field enhancement at the cathode. The avalanche process is started in the low density region created by the energy dissipated in the former conduction process. Electrons leave the cathode and their number increases due to the collision process under high electric field on their way to

the anode. They create a narrow filamentary channel as they leave the cathode plane.

Influence of bubbles

Gas bubbles can be produced during a heating process in insulating oil as the product of gas and water contamination. In this case, the bubbles may be a source of discharges in oil with uniform electric field E .

$$E = \frac{3\epsilon E}{3\epsilon + 1} \quad (1)$$

Where:

E = electric field

ϵ = relative permittivity

Spherical bubbles occur in low density in oils. The higher electric field and low electric strength on the bubbles, may initiate the discharge process on the enclosed gases in the bubbles. Effective spherical bubbles can be developed within a space where a sphere is highly conducting compared to the surrounding liquid.

Moisture in the oil delivers charge carriers and decreases the withstand strength. Acids as the aging by-product also deliver charge carriers through dissociation processes. They are surface active and decreasing the surface tension. This will also lead to the development of bubbles and weaken the dielectric strength.

The effect of contamination

The presence of contaminating particles in insulating oil may lead to a decrease of the breakdown strength. A breakdown at relatively low voltage can happen if the oil is heavily contaminated with fibres which can form a bridge of fibres between the electrodes along the highest field intensity. Moreover, in the case that a wet fibre exists in electrically stressed oil, it will cause a stream of water or vapour along with a breakdown channel, further decreasing the electric strength of the oil [6].

Different test methods

The investigation of breakdown voltage of the oils can be tested with different test methods, which are: rising voltage, up and down and multiple level method.

Rising voltage method

Rising-voltage method can be performed using all types of voltage [1]. For a single test, the applied voltage should be increased from an initial voltage level at a constant rate till the breakdown occurs. Repeat the single test procedure after a certain rest interval, until a significant number of breakdown voltages are obtained.

Up – and – down method

Up-and-down method, proposed by Dixon and Mood, permits an estimation of 50% probability breakdown voltage, when the breakdown voltage is normally distributed [1]. It is widely used in impulse breakdown tests to save testing time and also has the advantage that getting the breakdown voltage at a certain breakdown probability of 50%. The voltage is initially raised from an initial value at which with certainty no breakdown would occur, in steps of a fixed amplitude ΔU , until the first breakdown occurs. Next, the voltage is reduced by the same step ΔU until no breakdown occurs, and then raised again until breakdown occurrence, and so on so forth. After a significant number of useful shots, the 50% breakdown voltage can be calculated by simple averaging the applied voltages

Multiple – level method

Multiple-level method, also known as constant-voltage method, can be performed using all types of voltage. For impulse tests, they represent the ‘classic’ method of determining breakdown probability [1]. Apply a certain number of shots at different voltage levels and record the corresponding number of breakdowns at each voltage level. Based on the results, draw the cumulative frequency function.

2.5. Statistical analysis

Statistical techniques can be used to estimate the lowest likely breakdown voltage from the dispersion of the AC breakdown voltage data. This involves assuming that the dielectric failure follows a distribution and estimating the withstand voltage at the required probability [7]. Many factors influence the breakdown voltage of a dielectric [8]. Kulkarni notes that “the breakdown voltage of a dielectric material is a statistically distributed quantity which is a function of its physical/chemical properties and impurities present in it” [9]. A frequently used model is the weak link theory [10] where impurities and particles are swept into regions of high electric stress by dielectrophoretic forces [9]. Impurities and particles tend to line along the electric field lines creating a weak link in the oil gap.

Equation 2 and 3 shows the standard deviation and the mean of the sample data, which is breakdown voltage. The mean is simple the average of the breakdown voltages, and the standard deviation determine how is the data dispersed from the mean.

$$\bar{X} = \frac{1}{n} \sum_{i=1}^n x_i \quad (2)$$

$$s = \sqrt{\frac{\sum_{i=1}^n (x_i - \bar{X})^2}{n-1}} \quad (3)$$

Where:

- \bar{X} = Mean of the data
 x_i = i_{th} breakdown voltage
 s = standard deviation, and
 n = number of values in the data sample

Using the ASTM D1816 standards, the data can be validated by analysing it statistically. According to ASTM standards, after the investigation of breakdown voltages, the calculations must be done to determine a statistical behavior of each transformer oil [11].

Using the breakdown voltage values determined above, the range of five breakdown voltage must not exceed the values indicated as follows:

- 1 mm gap setting: Range must be less than 120% of the mean of five breakdown voltages
- 2 mm gap setting: Range must be less than 92% of the mean of five breakdown voltages

3. DESIGN

3.1. Test vessel design

The test vessel was designed to permit easy removal of electrodes for cleaning and polishing, verification of the shape is within the specified tolerance, and permit easy adjustment of the gap spacing. The capacity of the test vessel is 1000 ml. The test vessel was constructed with a material that is not soluble in or attacked by any of the cleaning or test liquids, and non-absorbent to moisture and cleaning or test liquids. The breakdown must be observed, the desirable material is transparent. The electrodes are VDE to plane, the dimensions of the electrodes are shown on figure 1. The gap distance is controlled by the nylon bolts and nuts mounted on the Perspex on top of the vde electrode, as shown on figure 2. The plane and VDE electrode are made up of brass and stainless steel respectively.

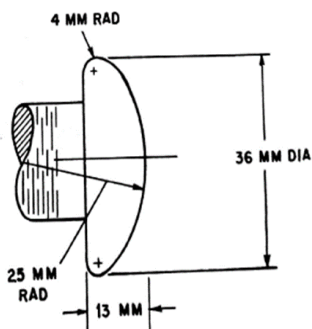


Figure 1: VDE Electrode dimensions

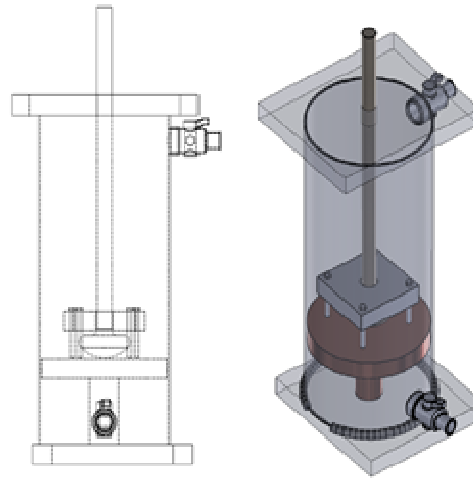


Figure 2: Engineering drawing of a test vessel

Preparing the test vessel

The vessel should be washed with soap thoroughly after every test, to remove all the oil on the testing vessel. The vessel is put into the oven, for drying up and to remove any moisture on the vessel. After thorough cleaning and drying, the vessel must be flushed with new oil of type to be tested.

3.2. Experimental setup

The circuit breaker is connected to the mains, it act as a switch that protect the circuit from damages that can be caused by overload or short circuit. The variac is used to gradually increase the voltage from the mains to the transformer. The transformer is a step transformer, it steps up voltage up to 64 kV. There are two measuring capacitor that calibrates the oscilloscope, since the oscilloscope output more accurate results than a voltmeter, the ratio of these capacitors is calculated below. The water resistor with a resistance of 200kΩ is used as a charging resistor to limit the current during the discharge / breakdown of the oil on the test vessel, since it can handle a fair amount of energy, with very high peak powers. The test vessel is connected in series with the water resistor. The ratio on the measuring capacitors is 400. As shown on the figure below

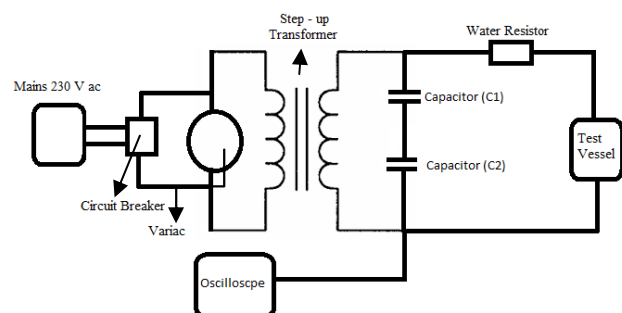


Figure 3: AC setup

3.3. Test procedure

- Allow the sample and the test vessel to equilibrate to ambient temperature, which is between 20°C and 30°C.
- Before pouring oil on the vessel, the gap distance must be accurately measured. Figure 35 and figure 36 shows the method that was used to measure the gap distance.
- Using a small portion of the sample to rinse the test cell. Drain the rinse. Within 30 seconds of the rinse, fill up the test vessel slowly with the remaining portion of the sample. The vessel must be closed with a baffle to allow no air to be in contact with oil.
- Wait at least 3 minutes but not more than 5 minutes between filling vessel and applying the voltage for the first breakdown, the waiting is for the bubbles to disappear on the oil, since the bubbles are formed during the filling of the vessel.
- Remove the earth stick on the circuit, switch on the breaker and apply the voltage increasing from zero at the rate of 0.5 kV/s until the breakdown occurs, record the highest rms voltage value that occurred immediately prior to each breakdown. Conduct another 29 breakdowns waiting at least 60 s but no more 90 s before applications of voltage for successive breakdown. The oil is stirred after every 3 breakdown to avoid the formation of carbon fibre across the electrodes.
- This experimental procedure is according to ASTM D1816 standards [11].

13	31.40	23.76	8.37	6.11
14	29.98	21.21	14.14	5.54
15	31.40	24.89	8.26	5.77
16	33.66	35.64	7.92	6.00
18	32.53	35.64	5.88	5.77
17	32.53	34.22	8.15	5.66
19	32.53	19.80	6.79	6.45
20	28.28	15.56	7.01	6.58
Mean	24.88	28.62	9.19	6.04
Stdv.	7.10	4.44	2.90	0.58
% range	88.42	67.2	111.43	33.78

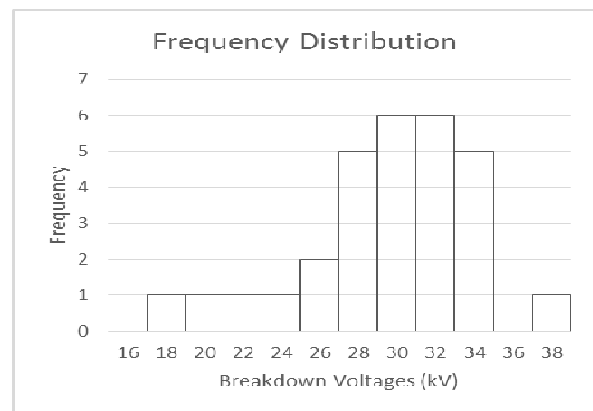


Figure 4: Frequency distribution of FR3

4. RESULTS AND ANALYSIS

The table below shows the recorded values of breakdown voltages of different transformer oil, midel 7131, synthetic ester, uninhibited mineral oil and shell dialla.

Table 3: breakdown voltages of different transformer oils

Number of shots	Transformer oil type (kV / 1.00 mm)			
	Midel 7131 ester	syn. natural ester	Mineral Oil	Shell Dialla
1	23.48	28.00	6.08	5.43
2	25.74	17.25	6.79	6.45
3	25.74	20.08	6.96	6.58
4	26.87	17.25	5.94	5.66
5	26.59	19.09	11.88	7.24
6	31.68	21.07	16.12	7.24
7	27.44	20.08	10.47	5.54
8	27.15	16.97	12.45	5.20
9	28.85	26.59	9.33	5.54
10	29.70	37.05	12.45	6.56
11	31.11	24.32	9.96	5.77
12	29.98	19.09	8.77	5.77

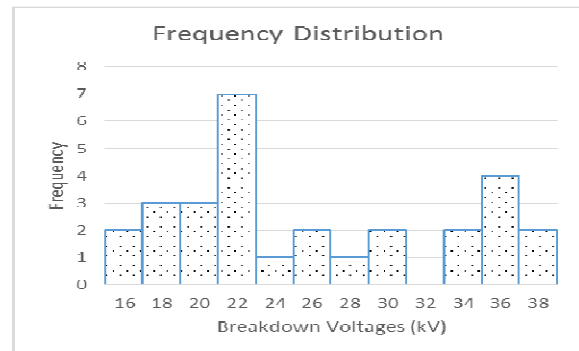


Figure 5: Frequency distribution of Midel 7131

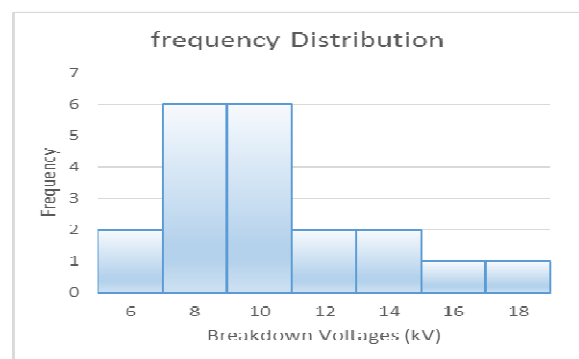


Figure 6: Frequency distribution of Mineral oil

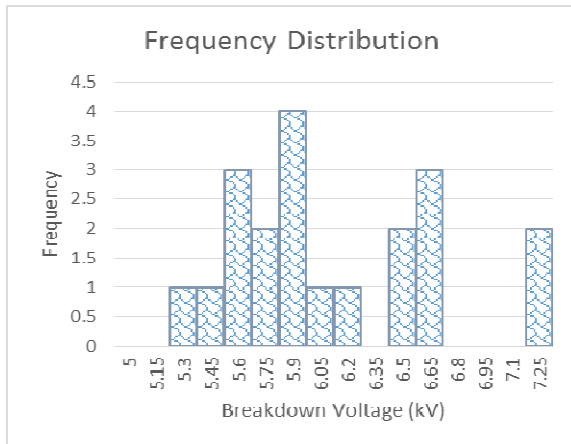


Figure 7: Frequency distribution of shell diala

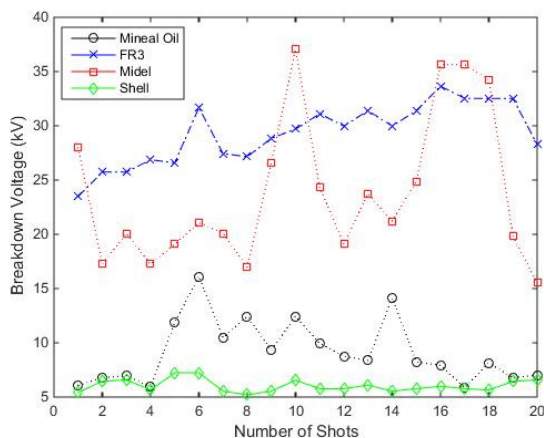


Figure 8: breakdown voltage per number of shots

The gap distance was held at 1.00 mm. FR3 does not create a carbon path between the electrodes, it only forms a lot of bubbles. On mineral oil, shell diala and midel the carbon path was forming between the electrodes, but shell's carbon path was not that dense compared to that of mineral and midel, few bubbles were formed.

Natural esters behaved in a way that was noted by Adamczewski, that the dielectric strength of oil can improve with repeated breakdowns, as discharge remove weak links such as gas bubbles and impurities from the liquid and electrode surface [12]. From figure 8, it can be observed that the oil gets better and better as the oil is being stressed with AC voltage.

Synthetic esters behaved in a way that was assumed by Naidu, that each breakdown is an independent event due to liquid self-healing [13], although the care must be taken to ensure that sufficient time is given to allow breakdown products to disperse and gas to expel [14]. Midel does not continuously gets better but it shows a trend of an increase of breakdown strength, due to the fact that this oil easily forms the weak link between the electrodes explains the lower breakdown voltages, this also explains the higher standard deviation.

Mineral oils were not inhibited, this insulating fluid underwent an oxidation degradation in the presence of oxygen. The presence of inhibitors on the oil is to prevent oxygen from reacting with the oil, thus advancing the ageing rate of the oil [15], and this explains the low breakdown voltages for mineral oil.

Shell diala oil, have a low dielectric strength than it was expected. There is a lot of pre discharge occurring on this oil during the experiment. The breakdown voltages of shell does not deviate more from the mean. Shell has chemical additives, inhibitors, which makes the oil to be ageing resistive.

Mineral oil and shell diala after being tested, they were flushed out with the new oil, which is contaminants free, to remove contaminants on the vessel, and test the new oils were tested, to verify the previous results, since these two oils were breaking down on low voltages.

Midel 7131 and FR3 were investigated under both AC and lightning impulse conditions, both did not breakdown under impulse conditions, which is a good intrinsic property of the oil, since the oils must not only withstand AC power frequency voltage, but also transient impulse voltage [1].

The range to mean percentage should be less than 120% for 1 mm gap for the breakdown test to be acceptable. Midel 7131, FR3, mineral oil and Shell has the range to mean percentage of 88.42, 67.2, 111.43 and 33.78 respectively, all the oils were in acceptable range according to ASTM D1816 standards.

5. CONCLUSION

A comprehensive comparison of breakdown properties between mineral oil, synthetic ester Midel7131, natural ester FR3 and shell diala were carried out in this paper. The investigation was carried out under ASTM standards, the design of the test vessel deviated from these standards, to make a gap distance to be easily controllable, and avoid the opening of the vessel during the experiment or stirring the oils. Mineral oil and shell diala were only stressed with AC voltage not with lightning impulse, because of the low breakdown voltages of these oils. Midel and FR3 withstood against lightning impulse, their dielectric strength was investigated under AC power frequency voltage. Midel's breakdown voltages were all over the place between 16 kV and 38 kV, this was due to the formation of carbon path between the electrodes, whilst FR3 was improving with repeated breakdowns.

The breakdown voltage is regarded as one of the most crucial elements, the oil paper insulating system can only be reliable when the condition of the oil is known, a routine oil testing and analysis, can determine the condition of the oil. Any significant reduction in the dielectric strength may indicate that the oil is no longer

capable of performing its vital functions on the transformer.

6. REFERENCES

- [1] Liu, Q.; Wang, Z.D.; Perrot, F., "Impulse breakdown voltages of ester-based transformer oils determined by using different test methods," in *Electrical Insulation and Dielectric Phenomena, 2009. CEIDP '09. IEEE Conference on*, vol., no., pp.608-612, 18-21 Oct. 2009.
- [2] Du, Y.; Mamishev, A.V.; Lesieutre, B.C.; Zahn, M.; Kang, S.H., "Measurements of moisture solubility for differently conditioned transformer oils," *Dielectric Liquids*, 1999. (ICDL '99) Proceedings of the 1999 IEEE 13th International Conference on, vol., no., pp.357, 360, 1999.
- [3] R. Eberhardt¹, H. M. Muhr¹, W. Lick¹, F. Baumann², and G. Pukel², "Comparison of Alternative Insulating Fluids," *IEEE - Annual Report Conference on Electrical Insulation Dielectric Phenomena*, pp. 591-593, October 26-29, 2008.
- [4] P. McShane, "Relative Properties of the New Combustion-Resistant Vegetable-Oil- Based Dielectric Coolants for Distribution and Power Transformers," *IEEE Transactions on Industry Applications*, vol. 37, No. 4, pp. 1132-1139, July/August 2001.
- [5] E. Yulastuti, "Analysis of dielectric properties comparison between mineral oil and synthetic ester oil", Dept. Elect. Eng., Delft Univ. Delft. Msc Report., Jun. 2010.
- [6] Osbert Joel C, "Transformer Oil and its properties", 30 October 2014.
- [7] Martin, D.; Wang, Z.D., "Statistical analysis of the AC breakdown voltages of ester based transformer oils," in *Dielectrics and Electrical Insulation, IEEE Transactions on*, vol.15, no.4, pp.1044-1050, August 2008
- [8] Blume, *Transformer Engineering 2nd edition*, John Wiley & Sons, New York, USA, 1951
- [9] S. V. Kulkarni and S. A. Khaparde, *Transformer Engineering Design and Practice*, Marcel Dekker Inc, New York, 2004
- [10] K. Nelson and C. Shaw, "The Impulse Design of Transformer Oil-Cellulose Structures", *IEEE Trans. Dielectr. Electr. Insulation*, Vol.13, I pp. 477-483, 2006
- [11] *Standard test method for Dielectric breakdown voltage of insulating oils of petroleum origin using VDE Electrodes*, ASTM D1816-04, 2003.
- [12] M. S. Naidu, V. Kamaraju, *High Voltage Engineering (2nd Edition)*, McGraw-Hill, New York, 1996
- [13] "Envirotemp FR3 Fluid testing guide", Section R900-20-12, Cooper Power Systems, Waukesha, 2004.
- [14] E. Yulastuti, "Analysis of dielectric properties comparison between mineral oil and synthetic ester oil", Dept. Elect. Eng., Delft Univ. Delft. Msc Report., Jun. 2010.
- [15] Wada, J.; Ueta, G.; Okabe, S.; Amimoto, T., "Inhibition technique of transformer insulating oil degradation - evaluation of the effectiveness of oxidation degradation inhibitors," in *Dielectrics and Electrical Insulation, IEEE Transactions on*, vol.20, no.5, pp.1641-1648, Oct. 2013

Partial Discharge Analysis of Failed ZnO Surge Arrester Varistors Elements at eThekweni Electricity

M. Gumede^{*1} and F. D'Almaine².

¹Durban University of Technology, Durban, 4001, South Africa

*Email: makhosonkegumede32@gmail.com

*Email: dalmaine@dut.ac.za

Abstract: This paper presents the Partial discharge results that were attained during laboratory experiment on 132kV surge arrester varistor elements supplied by eThekweni Electricity. The tests were undertaken at the UKZN high voltage laboratory. The tested varistor elements measured diameter 2cm and height of 1.3cm. To make sure that accurate results were achieved during measurement, the surface of the varistor was polished before initiating measurements, the aim was to remove any dust particles that could affect results. During the test experiments, good results were obtained, and the results attained during test compared favourably with each other.

1 INTRODUCTION

It is well known that moisture ingress has been the most common cause of degradation in ZnO varistor elements [1], [2]. This can possibly cause internal partial discharges on the surface area of ZnO varistor elements [1] as shown in Figure 1.



Fig 1: Internal partial discharge [1].

Therefore, there is a need to monitor the condition of such insulators closely. Any damage needs early detection to avoid further degradation leading to complete breakdown. In the last century, when high voltage was first introduced; partial discharge was recognized as a result of the ageing process. The degree of degradation is measured through partial discharges. [3], [4], [5].

It was observed that 'partial discharge' action is both an indication of degradation in the insulation systems of power apparatus - irrespective of the network stress - and a stress mechanism in itself [6]. Such problems cause the strength of partial discharge to increase, and may eventually lead to failure of the apparatus in the system [7], [8]. The thermal stress created by a partial discharge may be sufficient to cause damage to polymeric materials. Partial discharges generally cause progressive deterioration of insulating materials, which eventually lead to breakdown of electrical insulation [7].

2 PD OCCURRENCE

During the lifetime of gapless arresters, the internal components are continually exposed to stresses that can

lead to partial discharge. This partial discharge is the major cause of failure of high voltage surge arresters [9]. Partial discharges are mostly caused by a local field enhancement, due to imperfections in the insulation, such as gas filled inclusions or voids (see Figure 2(a)) and cracks. Partial discharges dissipate energy, generally in the form of heat. Heat energy dissipation may cause thermal degradation of the insulation, although the level is generally low [10].

PD causes progressive deterioration of insulating materials, ultimately leading to electrical breakdown. The cumulative effect of partial discharges within solid dielectrics is the formation of numerous, branching, partially conducting discharge channels, and a process called treeing [11]. [12] It has been reported that according to PD analysis the discharges most probably occurred in voids or cavities in the moist interface between the polymeric arrester housing and inner parts [12].

3 INTERNAL PARTIAL DISCHARGE

Where cavities are present in the solid dielectric of insulation systems, the field strength is greater inside than in the surrounding medium. When the voltage across the cavity exceeds the ignition voltage, a partial discharge breakdown will result. Usually, a pulse-shaped discharge occurs in the cavity, when alternating voltage of sufficient amplitude is applied [13]. Over a long period of time, internal partial discharges can cause surrounding dielectric deterioration under certain circumstances; erosion can even cause complete breakdown and destruction [14]. Figure 2(a). shows the proposed equivalent circuit for pulse shaped partial discharge [15].

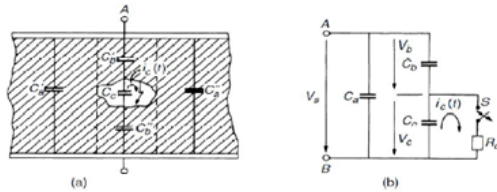


Fig 2 (a): Scheme of an insulation system comprising a cavity and (b) Equivalent circuit [15].

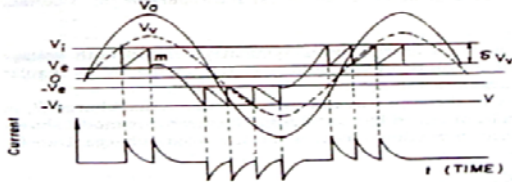


Fig 3: voltage waves in the equivalent circuit for pulse-shaped internal partial discharges [16].

4 DIAGNOSING THE PD ON INSULATION

In the last 25 years, a large amount of research has been performed on dielectric materials, to study their fortitude under electrical, mechanical, thermal, and other stresses [17]. When dealing with partial discharges, at least three stages of information handling are needed to collect sufficient data for an evaluation [18]. Nazemi reported that there are different types of PD charge measuring devices composed according to the classification in Figure 4, where the given bandwidths are approximate benchmarks according to the application range and the measurement conditions.

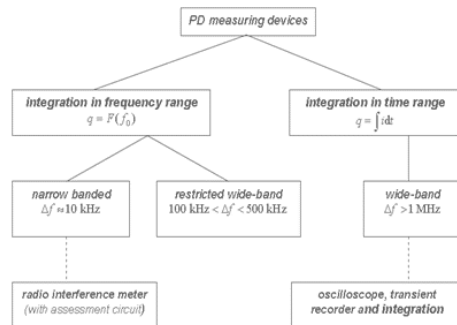


Fig 4: three stages of information handling are needed to collect sufficient data for an evaluation (Nazemi).

The different devices, which are available on the market, possess additional components in many cases, e.g. oscillographic demonstrations of PD pulses over an elliptic base line. Displays on the oscilloscope for some typical discharges are shown in Figure 5. Together with corresponding waveforms arising out of external discharges as well as from contact noise (Nazemi).

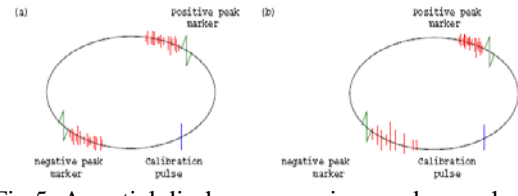


Fig 5: A partial discharge superimposed on a phase representation of a voltage waveform [19].

5 RESEARCH METHODOLOGY

PD measurements on zinc oxide varistor elements were performed in the HVAC Laboratory at University of KwaZulu Natal (UKZN) situated on the Howard College Campus. The tests were carried out using the AC voltage power transformer 220V/66kV and a coupling capacitor rated at 200kV and 0.001 μ F. The plate-plate (Rogowski profile) was used to connect the ZnO varistor across the coupling device and a 20M Ω resistor. The oscilloscope output results (pulses) were fed into a wide band amplifier and pulse display. The most important partial discharge measurements were to determine the onset voltage (U_e) and the extinction voltage (U_a). The laboratory tests were performed using conventional apparent charge measurement according to IEC 60270. IEC 60099-4 states that PD level limit should be 10pC.

5.1 Partial Discharge Test Circuit

The circuit in Figure 6 was designed to have a specific resonance frequency in the range of 50 kHz to 100 kHz. The pulses were fed into a wide band amplifier, and the output pulses were displayed on a CRT screen, superimposed on the supply sine wave, in order to detect the points on the wave where the discharges occur relative to the zero crossings. The positive and negative half waves are often displayed as an ellipse.

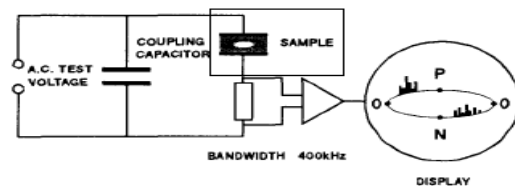


Fig 6: Test circuit for partial discharge measurement.

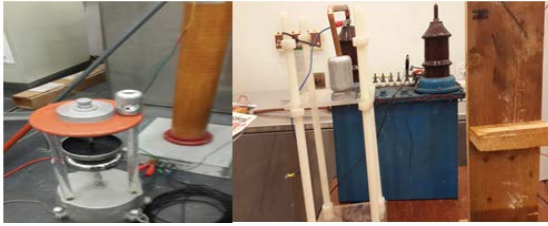


Fig 7: HV Final circuit diagram for partial discharge (PD).

The measured partial discharge intensity is displayed either in pC or in μV in accordance with IEC 60 270 / IS 6209. According to IEC 60 270, the measured quality must be multiplied by a correction factor, which considers the circuit characteristics of the complete test arrangement. With the built-in correction circuit, it is possible to incorporate the factor into the display. The HiPotronics DXX-7000® system was used to read true pC over all ranges of the system.

The actual partial discharge intensity was read directly without calculations. When switched on the correction factor was displayed directly. The (PC) pulses were tapped from the analogue output terminal and displayed on the built-in oscilloscope. The transient amplifier was connected in parallel with the DXX-7000®. The use of the transient field was necessary to give protection, when the intermittent pulse of interference occurred during measurements.

5.1 Main Test Circuit

The test object that was used to test varistor element is shown in the circuit diagram below (see Figure 8). The plate electrode was connected in parallel with 1nF, 200kV coupling capacitor. Before setup, the plates were polished to prevent the generation of apparent partial discharge during the measurements.

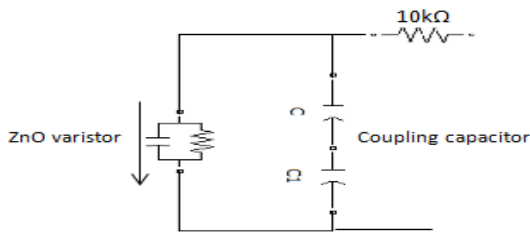


Fig 8: Test circuit diagram for PD.

6 PARTIAL DISCHARGE RESULTS

To verify results achieved during measurement, the surface of the varistor was polished before initiating measurements, and several breakdowns (overvoltages) initiated to remove any dust particles. The voltage applied to the varistor block for partial discharge measurements was calculated by counting number of

blocks in the arrester and dividing by its rated voltage (see Figure 9).



Fig 9: Varistor blocks that were tested.

The voltage applied during the partial discharge measurement was calculated as shown below on equation (1).

$$V_{ap} = \frac{V_r}{N_v} \quad (1)$$

V_{ap} applied voltage to varistor

V_r rated voltage of the surge arrester (kV)

N_v number of varistors element inside the arrester

$$V_{ap} = \frac{V_r}{N_v} = \frac{120}{37} = 3.25 \text{ kV}$$

Throughout PD measurement a voltage of 3.25 kV was applied to the varistors, unsatisfactory results were obtained (as presented on Figure 10.) because the varistors were conducting. Due to this the voltage was adjusted to be 2.5 kV. By utilising the PD technique, the varistor elements tested were suspected of PD activity considering the attained waveforms.

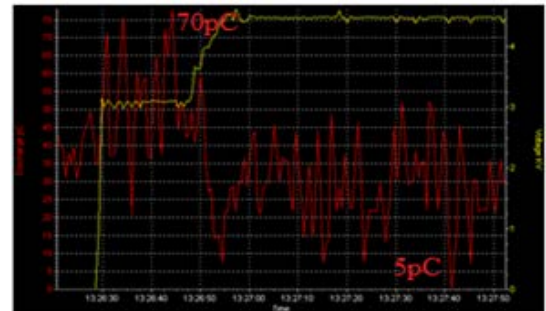


Fig 10(a): PD measurements (time versus apparent charge).

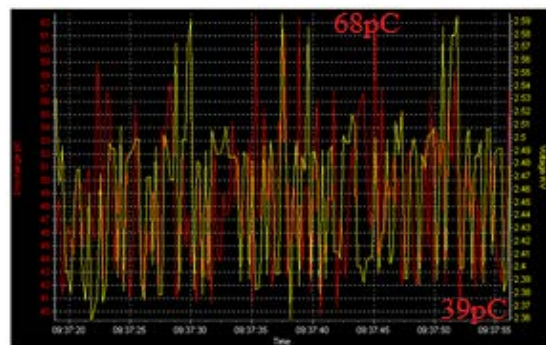


Fig 10 (b): PD measurements (time versus apparent charge).

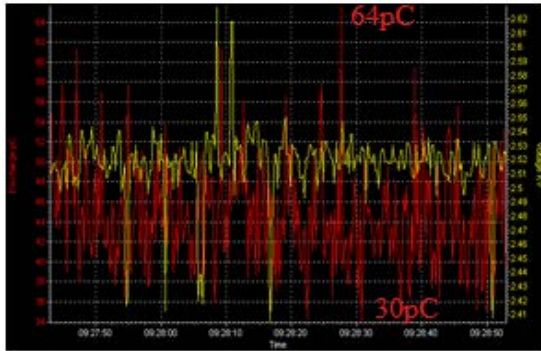


Fig 10 (c): PD measurements (time versus apparent charge).

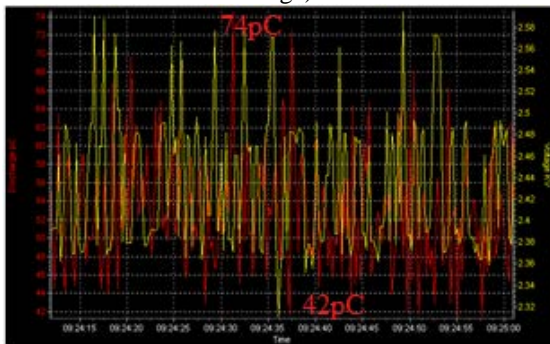


Fig10 (d): PD measurements (time versus apparent charge).

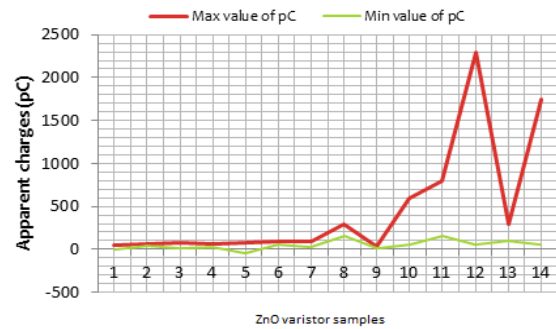


Fig 11: Comparison of partial discharge samples experimental results at laboratory.

Figure 11 graphs above present the comparison of partial discharge samples experimental results that were performed at laboratory, the results obtained were indicated the high amount of apparent charge especially from sample number ten up to fourteen.

It was concluded that partial discharge is the source of degradation in this family of ZnO arrester.

7 VISUAL ANALYSIS RESULTS ON SURGE ARRESTER

The results obtained during the visual inspection of the surge arresters of manufacturer A, (see Figure 12 show the samples that were taken during analysis). The moisture ingress through the sealing collar causes serious problems such as surface discharges. These factors can eventually end with a full breakdown over the insulation system. Water treeing inside the sealing collar was noted as were cracks on the ZnO blocks closest to the sealing, punctures.

Tab. 1: Comparison of partial discharge results at laboratory.

Samples	Max value of apparent charge (pC)	Min value of apparent charge (pC)
1	50	-5
2	68	39
3	70	5
4	64	30
5	74	-42
6	90	53
7	94	30
8	300	150
9	38	10
10	600	50
11	800	150
12	2300	50
13	300	100
14	1750	50

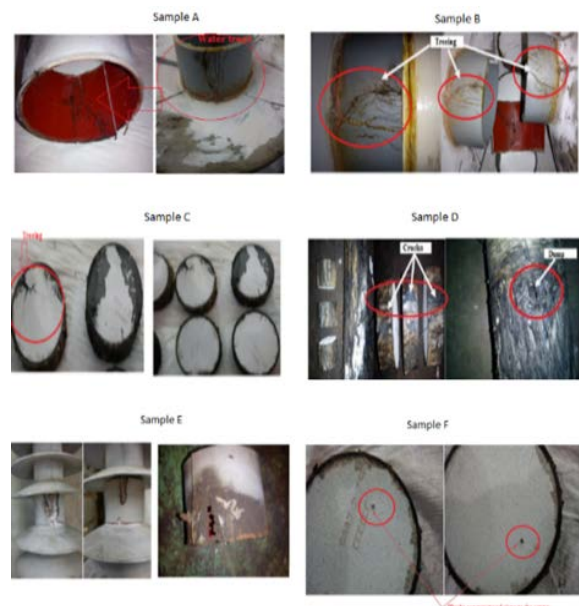


Fig 12: Surge arrester samples results that were taken during visual analysis [20].

8 CONCLUSION

The surge arresters measured were found to be in an unsatisfactory condition. PD measurements using the above tests was valuable in obtaining sufficient information concerning the failure of surge arresters. It was observed that partial discharge action is an indication of degradation in arrester varistors according to results that were obtained during experiments in the laboratory.

It was noted that the moisture ingress in the sealing collar is the source of partial discharge inside surge arrester. Electrical treeing is a significant degradation mechanism in polymers that can lead to premature failure of high voltage equipment.

9. ACKNOWLEDGEMENT

The authors gratefully acknowledge the help given by Dr A Swanson of UKZN in the compilation of this paper.

9 REFERENCES

- [1] Chrzan, Krystian Leonard. "Influence of moisture and partial discharges on the degradation of high-voltage surge arresters." *European transactions on electrical power* 14, no. 3 (2004), pp. 175-184.
- [2] Alghamdi, A. S., and S. J. Dodd. "The Influence of Absorbed Moisture on Partial Discharge Patterns Measured During Tree Growth in an Epoxy Resin." In *Solid Dielectrics, 2007. ICSD'07. IEEE International Conference on*, 2007, pp. 623-626
- [3] Kuffel, John, E. Kuffel, and Walter S. Zaengl. *High voltage engineering fundamentals*. Newnes, 2000.
- [4] Okubo, H., K. Kato, N. Hayakawa, M. Hanai, and M. Takei. "Functionally Graded Materials and their Applications to High Electric Field Power Equipment." In *CIGRE SC D1 Colloquium*, Budapest. 2009.
- [5] Bartnikas, R. "Partial discharges. Their mechanism, detection and measurement." *Dielectrics and Electrical Insulation*, IEEE Transactions on 9, no. 5 (2002): 763-808.
- [6] Kemp, I. J. "Partial discharges and their measurement." *Advances in High Voltage Engineering* 40 (2004): 139.
- [7] Amin, Mohammad, Mohammad Akbar, and Salman Amin. "Hydrophobicity of silicone rubber used for outdoor insulation (an overview)." *International Conference Rev. Adv. Mater. Sci*, 2007, pp10-26.
- [8] Sreejaya, P. "Study of Solid Dielectric Degradation Using Partial Discharge Test." In *Electrical Insulation and Dielectric Phenomena, 2008. CEIDP 2008. Annual Report Conference on*, pp. 408-412. IEEE, 2008.
- [9] Fonseca Badillo, M., L. Negrete Navarrete, A. González Parada, and A. Castañeda Miranda. "Simulation and analysis of underground power cables faults." *Proceeded Engineering* 35 (2012), pp. 50-57.
- [10] Cho, H. G., U. Y. Lee, S. W. Han, J. U. Cheon, and K. J. Lim. "The Performance of Tracking Aging and Surface in Polymer Insulator." *International Conference in Electrical Engineering (ICEE)*, Korea. 2002.
- [11] Mobedjina, Minoo, Bengt Johnnerfelt, and Lennart Stenström. "Design and testing of polymer-housed surge arresters." In *GCC CIGRE 9th Symposium, Abu Dhabi*, 1998, pp. 28-29.
- [12] K. Lahti, K. Kannus and K. Nousiainen. "Behaviour of the DC leakage currents of polymeric metal oxide surge arresters in water penetration tests." *Power Delivery, IEEE Transactions on* 13, no. 2 (1998), pp.459-464.
- [13] Kil, Gyung-Suk, Ju-Seop Han, Jae-Yong Song, and Hwang-Dong Seo. "Measurement Method of the Resistive Leakage Current for Lightning Arrester Diagnosis." *Transactions on Electrical and Electronic Materials*, 2005, Vol.6, No. 2.
- [14] Hinrichsen, Volker. "Monitoring of High Voltage Metal Oxide Surge Arresters." *VI Jornadas Internacionales de Aislamiento Electrico, Bilbao* (1997): 22-23.
- [15] ABB "Surge arrester selection and application guide" 12th International Conference on Electricity Distribution: Contributions (7 v.), pp. 2-14, 1993.
- [16] K. Chrzan, K. Feser, W. Kohler, D. Q i u, "Behaviour of Zinc Oxide Surge Arresters under Pollution" *IEFE Transactions on Power Delivery* Vol. 6, No. 2, April 1991.
- [17] Mr. C. K. Vibhakar and Prof S. A. Kanitkar "Investigation and modeling of epoxies aging tests under the effect of variation of parameters on partial discharge (PD)," 2009 Third International Conference on Power Systems, Kharagpur, INDIA December 27-29 PAPER ID 251.
- [18] F. H. Kreuger, E. Gulski and A. Krivda, "Classification of Partial Discharges", *IEEE Transactions on Electrical Insulation* Vol. 28 No. 6, December 1993.
- [19] J .R Lucas "Measurement of high voltage" *High voltage engineering*, 2001, pp116.

[20] Gumede M, and Frederick. G. d'almaine, "Surge arrester faults and their causes at EThekweni electricity" International Journal of Electrical Engineering, Vol 2 N.o 1. 2014.

Understanding Altitude in the Study of Air Gap Breakdown under High Voltage

P. Naidoo

University of the Witwatersrand, Johannesburg, South Africa
pat@patnaidoo.co.za

Abstract: The disruptive discharge voltage of external insulation is dependent upon the prevailing atmospheric conditions; among other factors. The dielectric strength of air is directly influenced by air density (pressure and temperature) and humidity. A key study variable is air pressure; decreasing with increasing altitude. This paper examines the topography of the earth and recommends the boundary within which experimental studies on altitude correction for air gap breakdown voltages should be focused. The proposed upper limit is 5500m. For the range 3000 to 5500m, it is recommended that published work on specific site test results be surveyed and generalised for application. The local laboratory investigation be focused on the altitude range 0 to 3000m. The South African laboratories are located at altitudes of 0m and 1500m and are ideally positioned to make a substantial contribution to the study.

Index Terms—Altitude, Air Pressure, Air Gaps, High Voltage

1 INTRODUCTION

In an endeavour to contribute to the ongoing worldwide search for better knowledge on altitude correction factors, the high voltage research programme at the University of the Witwatersrand, Johannesburg has research activities into understanding the influence of air density on air gap breakdown under direct voltage. The plan is to design a high voltage test arrangement with the ability to vary the air pressure in the test chamber. The variable pressure test chamber could be a custom built container, a high voltage porcelain bushing housing or a high voltage surge arrester housing. A rod - plane air gap configuration would be placed in the custom built housing. The plan is to initially hold humidity and temperature as a constant in the experimentation. The variable will be air pressure; decreasing with increasing altitude.

Given the complexities associated with preparing the variable pressure test chamber, the concurrent influence of many parameters in the breakdown process and the errors associated with repeatable high voltage test and measurements given that atmospheric conditions change continuously with time, it is recommended that we consider establishing boundary conditions for experimentation.

A disruptive discharge voltage measured in a given test condition at temperature t , pressure p and humidity h may be converted to the value which would have been obtained under the standard reference atmosphere conditions of temperature t_0 , pressure p_0 and humidity h_0 . The engineering practice is to apply correction factors as directed in the IEC 60060-1 standard [1].

Several practicing engineers [2] – [6] have directed attention to that of uncertainties in the application of the correction factors as recommended by the IEC Standard [1].

Calva et al [2] have demonstrated that the IEC 60060-1 standard correction factors are not adequate for dc voltage measurements at high altitudes. Their experimental work has shown that for the case of a rod to plane gap at 2240m above sea level, there is a difference greater than 10% between experimental data and the calculated value as per the correction factor procedure of IEC 60060-1 standard. They explain that this difference is due to the physical model employed which is based on the field of propagation of streamers; assuming that the propagation field of the pre-breakdown streamers varies linearly with the air density.

Wu et al [3] working at an original manufacturer of high voltage plant and equipment notes that atmospheric conditions influence the dielectric strength of air in a complicated way; simplified and generalized solutions may cause uncertainty especially when different recommendations are given in different standards without adequate clarification. The team refers to examples whereby the atmospheric correction recommended by a standard (IEC 60071-2) is most suitable for insulation co-ordination and the determination of type test voltage but uncertain for application to plant and equipment design with respect to altitudes.

Gutman et al [4], reporting to Cigre 2014 Paris Session, recommends that additional work should be done in understanding atmospheric correction of dielectric strength of external insulation for the development of UHV AC and DC transmission systems up to the altitude of 5000m.

Gutman et al [4] further recommends that although both air density and humidity have influence on the dielectric strength of air, the study can be limited to that of air

density which plays a major role as the variations are large as compared to changes in temperature.

Allen [5] notes that neither the IEC or IEEE procedures for the adjustment of measurement of high voltages to a common atmospheric density are suitable for air gaps less than 0.5m.

Yujian et al [6] concurs with Gutman et al [4]. Their emphasis was to determine the correction factors for air density versus altitude by on site experimentation. Yujian et al [6] proposed an interpolation method with data obtained by experimentation with switching impulse flashover voltage of rod plane air gaps at different altitudes; 55 meters, 2200 and 3000 m, 4300 meters and 5000 meters above sea level.

Gora et al [7] of the School of High Voltage Engineering at the University of Witwatersrand reported on their study of altitude correction factors on short air gap DC breakdown voltage. The study focused on relative air densities corresponding to altitudes of 1700m to 4500m above sea level. Their results showed a decrease in breakdown voltage as pressure decreases but only up to a threshold point beyond which an increase in breakdown voltage at very low pressures was observed. They corrected their results according to the IEC 60060-1 standard and their conclusion was that the corrected results did not resemble the trend of a decrease in breakdown voltage as relative air density decreases.

Presently, different approaches exist in the IEC standards on how to take into account atmospheric parameters in the design and specification of high voltage electrical plant and equipment. The different approaches are often contradictory and yield significant differences in design specifications and operational performance.

Gutman et al [4] notes that it is complicated to achieve an accurate and detailed approach for air density/altitude correction on the basis of the available knowledge. A reasonable target would be to find an approach that combines simplicity with reasonable accuracy for the two broad categories of air gaps and clean insulators. For the case of air gap breakdown, the discharge develops in the form of corona, streamers and leaders and for the case of insulators in polluted conditions, the major part of the discharge develops on the surface of the insulator covered by the electrolyte.

The setting of boundary condition for altitude will assist in focusing the efforts of investigations. High altitude corrections are known to be inconsistent because of the number of factors that influence the discharge process. The first task is to understand altitude in the workings of high voltage electrical power systems.

2 UNDERSTANDING ALTITUDE

The literature review was on the topography of the earth. Henry [8] records that a feature of the outer part of the earth is the distinct division between land, water and air; lithosphere, hydrosphere and atmosphere.

Hydrosphere accounts for 71% of the total earth's surface area and the remainder of 29% is made up of the continents of lithosphere [8]. Much of the continents have been topographically mapped.

With sea level used as the datum or reference level of elevation, the average height of land above sea level is 840 meters and the average depth of the oceans is 3800 meters below sea level. The average height above sea level for electrical power systems is thus 840m.

The results of hypsography, a study of the distribution of elevation on the surface of the earth, is given in table 1 [9]. Table 2 lists the biosphere altitude limits for the living earth [10].

Table 1: Hypsography Results of the Distribution of Elevations on the Surface of the Earth; with outliers [9].

Altitude (meters)	% of the Earth Surface
0 – 1000	20.9
1000-2000	4.5
2000-3000	2.0
3000-4000	1.1
4000-5000	0.5
Total	29%
Outliers	
8848 meters 5100 meters	Mount Everest La Rinconda Mining Community, Southern Peru

Table 2: Biosphere Altitude Limits

Altitude (meters)	Biosphere Limits
4500	Limit of cultivation
5500	Limit of human habitation
6000	Limit of higher plants
6200	Limit of terrestrial animals

From table 1 and 2, a clear conclusion is that the upper boundary limit of interest will be an altitude of 5500m.

Deducing from Table 1, we prepare table 3 to show the expected spread of high voltage electrical power systems globally. This is a first pass deduction and further literature review will be required to substantiate the deduction. However, Table 3 has a message.

Why do we seek a generalised solution for altitudes from 0 m sea level to the upper boundary limit of 5500m? The spread of locations of the global high voltage electrical power systems will be as follows:

Table 3: Expected Spread of High Voltage Electrical Power Systems Globally

Altitude (meters)	Expected Spread of HV Electrical Power Systems Globally
0 - 1000	72%
1000-2000	15,5%
2000-3000	6,9%
3000-4000	3,9%
4000-5000	1,7%

72% will be found in the lower altitude ranges of 1000m; 87, 5 % will be in the 0 to 2000m region and 94.4 % will be in the region less than 3000m. Only 5, 6% will be located in the altitude region above 3000m.

A first recommendation is that we explore and employ the work done by investigators in the altitude range of 3000 to 5000m. Yujian et al [6] notes that the commonly used altitude correction methods of IEC 60060 and IEC 60071-2 are suitable for altitude of 2000m and below. For higher altitudes, Yujian et al recommends that actual tests be conducted in the required areas by using the same test arrangements. Their work was performed using rod-plane test arrangements at Beijing (55 meters above sea level), Xining (2200 and 3000 meters above sea level), Yangbajing in Tibet (4300 meters above sea level) and Tanggula in Qinghai province (5000 meters above sea level) and the discharge voltage characteristics were obtained. Several other investigators, notably in the People's Republic of China, in the Qinghai – Tibet locality, have done extensive on site testing and have recorded their results. Their data is available and should be explored and employed for a contribution in the specific altitude range of 3000 – 5000 m. This is a practical recommendation given the complexity of the experimentation.

A second recommendation is that we focus the research into further understanding air gap breakdown in three specific altitude ranges viz. 0 to 1000m; 1000m to 2000m and 2000 to 3000m. Many authors have agreed that the current IEC Standards are suitable for application in the altitude range of less than 2000m. This will provide a solid foundation to build upon. It has added relevance to local research and investigations; the locality of the three available laboratories in South Africa are within the recommended altitude ranges. The University of Kwa Zulu Natal HVDC Test Facility is at sea level of 0m. The University of the Witwatersrand HVDC test facility is in Johannesburg; Johannesburg is located at an altitude of 1753 m above sea level. The SABS HV Test Facility is at the Apollo Converter Station; Apollo is located at 1540 m above sea level. The Apollo site has plans for a 1 MV direct voltage test facility.

3 CONCLUSION

Air gap breakdown occurs because of a concurrent of factors that intervene in the discharge process. It varies widely from time to time and from locality to locality.

Calva et al [11] notes that in seeking high altitude correction factors, the observed decreasing humidity found at higher altitudes has to be taken into account. It is known that the most amount of water vapour is located close to sea level and decreases rapidly with increasing altitude. The combined effects of reduced density and air dryness affects the breakdown level of air insulation in comparison to the sea level values.

To launch the investigations, we shall commence with understanding the effects of air pressure. The recommended research scope is as follows:

- The boundary conditions for study is set from 0 m to 5500m. 5500m is an upper bounded limit.
- The average height above sea level of global electrical power systems is 840 m. This effectively means that the bulk of the application of the IEC standards will be in the range less than 1000m, possibly even less than 2000m. For applications above 2000m, it can be considered to be unique or a special case that could warrant actual experimentation at the selected site. We should keep focus on the range less than 2000m and build upon the strong foundation of the existing IEC Standards.
- For the upper range of 3000m to 5500m, it is recommended that we survey and report on the experimentation (actual tests) conducted at the many high altitude sites. Published results are available from authors of the transmission utilities of State Grid of China and China Southern of the People's Republic of China.
- For the range of 0 to 3000m; it is recommended that we set up local experiments for detailed investigations into the mechanism of air gap breakdown under direct voltage. We can explore varying environmental conditions and experimental configurations. The effort can start with the prevailing atmospheric air pressure and atmospheric conditions at the local university laboratory.

The research time table is 2015 to 2020.

4 ACKNOWLEDGMENT

The creative idea emanated from the workings of Cigre. The paper of Gutman et al [4], as presented to the proceedings of Cigre 2014 Paris Session (Study Committee D1) summarises the state of research into the influence of density on air gap breakdown. The planned research is a contribution to a thesis in partial fulfilment of the requirements of the degree of Doctor of Philosophy (Electrical Engineering). The supervisors are Professors Cuthbert Nyamupangedengu and Ian Jandrell.

5 REFERENCES

- [1] IEC 60060-1, "High Voltage Test Techniques, Part 1: General Definitions and Requirements", *International Electrotechnical Commission Publication*, Edition 3, 2010.
- [2] Calva P A, Espino F P, "Correction Factors for Positive dc Voltages". *IEEE Transactions on Dielectrics and Electrical Insulation*, Vol.5, p541 – 544, No 4, August 1998.
- [3] Wu D, Li M, Kvarngren M, "Uncertainties in the Application of Atmospheric and Altitude Corrections as Recommended in IEC Standards", *Proc. 16th International Symposium on High Voltage Engineering*, Paper A-15, Cape Town RSA, 24-28 August 2009.
- [4] Gutman I, Pigini A, Rickmann J, Fan J, Wu D, Gockenbach E, "Atmospheric and Altitude Correction of Air Gaps, Clean and Polluted Insulators: State-of-the-Art within Cigre and IEC", *Cigre Paper D1-213*, Paris, 2014.
- [5] Allen N L. "Correction Procedures for High Voltage Measurements under a Variable Air Density", *IEE Proc.-Sci.Meas.Technol.*, Vol153, No.5, September 2006.
- [6] Yujian D, Weiming L, Jianbin F, Qingfeng Li, Jun Z, Zhiyi S, "Altitude Correction of Switching Impulse Flashover Voltage of Rod Plane Air Gaps", *Paper OB2-01, 18th International Symposium on High Voltage Engineering*, Seoul Korea, August 25- 30, 2013.
- [7] Gora T, Nyamupangedengu C, Jandrell I R, "Investigating the Effects of Altitude (Air Density) on the HVDC Breakdown Voltage of Rod Plane Air Gaps", *Proc. of the 19th ISH*, Pilsen, Czech Republic, August 2015.
- [8] Henry L. *Dynamic Earth*. McGraw Hill, USA, 1973.
- [9] Marcel L. *The Meteorology and Climate of Tropical Africa*. ISBN 1-85233-643-9.
- [10] Merrits D, de Wet A, Menking K. *Environmental Geology*. W.H.Freeman and Company, USA, 1998.
- [11] Calva Chavarria P A, Robledo-Martinez A, "Effect of Humidity on DC Breakdown Voltages in Ambient Air at High Altitude", *Proc. Of IEEE Conference on Electrical Insulation and Dielectric Phenomena*, San Francisco, October 20-23, 1996.

DYNAMIC ANALYSIS OF PHOTOVOLTAIC PLANT USING CUSTOM MODELLED PV SYSTEM

N. Mazibuko^{1*}, A.K. Saha²

¹Group Technology & Commercial Engineering, Power, Eskom, 2157 Sunninghill, South Africa.

²School of Electrical, Electronic & Computer Engineering, UKZN, 4041 Durban, South Africa.

*Email: MazibuNu@eskom.co.za

Abstract: This work evaluates the developed Photovoltaic model for integration impact and South African grid code compliance. Several important requirements are examined for a modelled photovoltaic system connected to a typical power station electrical auxiliary network. Load flow, fault level and contingency analyses are done with and without the photovoltaic system connected. The various testing to validate established controls are performed for frequency response requirement tested for the active power reduction during the event of an over-frequency, the low Voltage Ride Through (LRVT) and High Voltage Ride Through (HVRT) requirements. The results indicated the PV model capabilities to remain compliance to the requirements of (South African Grid Code) at the Point of Connection (POC). A steady state analysis is conducted with the PV plant to evaluate any violation with the voltages at all busbars for typical power station distribution network. Scenarios for an n-1 contingency are tested for voltage variations and must be within allowable limits. The PV plant fault contribution is found to be limited by PV inverter to 120% of nominal current of inverter thus a proposition that the inverter has controllability of fault current and only positive sequence current was notably injected during fault contribution

1 INTRODUCTION

The potential in renewable energy connected on utility grid is growing especially for wind and solar power. Thus, technical specifications shall be enforced to ensure safe interconnection of renewables onto the grid. The grid connection code objective is to specify minimum technical and design grid connection requirements for Renewable Power Plants (RPPs) connected to or seeking connection to the South African electricity transmission system (TS) or distribution system (DS) [1]. An appropriate point of connection shall be recognised on the basis of secure network operation taking the generating plant into consideration, and at which the requested power can be received and transferred [1]. Thus, assessment of the connection possibility under

disturbances at the network connection be tested for short-circuit power, and operation mode of the renewable plant. This paper presents the essential aspects to be taken into consideration for the connection of renewable plant to the power station distribution network so to maintain the security and reliability of network operation and evaluate requirements in accordance with SAGC.

1.1 Connection points

For this study a short conductor connecting the PV plant to the power station auxiliary load at different busbar levels is tested and at these different positions steady state analyses is done evaluating for any violations. A small difference at all the various connections is seen when comparing all bus node voltages. The voltage at lower voltage ratings tends to rise at the connected bus node but within acceptable limits. This can be avoided by having multiple point of connection. However depending on the connection point the daily variations in solar irradiance can cause reverse flow in reticulation system that could cause error in operation of protection relays thus, care should be taken when choosing connecting point. In this case the connection point suitable is the 11 kV busbar which is the next voltage level stepped down from generator output voltage of 22 kV, therefore the flow of power is in one direction and enhances the impact of PV plant to the generator for the purpose of the study shown by Figure 1. Further analyses are to be done to provide knowledge of any operational risk with PV plant connected.

With the PV system connected to an 11kV bus shown by Figure 1, grid code compliance will be tested at this connection point for various topics discussed below as per the requirements from SAGC.

1.2 PV model specification

The PV plant will consist of five feeders and each feeder with six inverters rated 0.5 MVA, power factor = 0.95 lagging with maximum power $P=0.475$ MW each. The inverter is connected through a step-up transformer 0.4/11 kV, 0.5 MVA, YNyn, 5%.

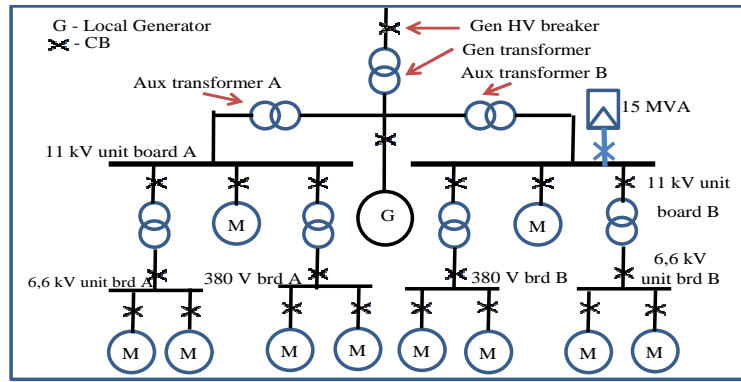


Figure 1: Auxiliary system for testing the PV system [5]

2 GRID COMPLIANCE FOR PV PLANT

The grid code integration requirement is an essential guideline for the design, control and operation of grid connected with PV energy system. In normal operation, the PV system is required to produce maximum within satisfactory injection currents e.g. IEC 61000 specification [3]. For high PV penetration level scenario, grid connected PV systems will impose new challenges to the distributed electrical network. The challenge lies in the atmospheric nature fuelling the PV sources and the response of PV systems from abnormal grid conditions. Thus, induce instability on the network. To overcome the above issues, the grid requirements act as guardline. The SAGC requires that the systems connected to the medium or high-voltage networks should be capable of riding through voltage sag and at the same time to provide reactive current to the faulted grid [1]. When the grid voltage level is higher than the specified ones defined, the PV systems should maintain connected to the distributed grid and inject reactive power to support the grid. For Renewable power plant to be in compliance with the South African grid code relevant controls are established to meet the requirements. This paper will only focus on the requirements for category B & C of the SAGC, renewables rated in the range 1-20 MVA and above respectively [1].

2.1 Frequency response

- When the frequency on the National Interconnected Power System (NIPS) is higher than 52 Hz for longer than 4 seconds, the RPP shall be disconnected from the grid.
- When the frequency on the NIPS is less than 47.0 Hz for longer than 200ms, the RPP may be disconnected.
- The RPP shall remain connected to the NIPS during rate of change of frequency of values up to and including 1.5 Hz per second, provided the network frequency is still within the minimum operating range indicated in Figures 2.

For the nature of the power station electrical auxiliary network and RPP the PV plant will not be participating in

the frequency control but will have the controllability to reduce its power output in the event of higher frequency limits exceeded as seen in figure 2 [1].

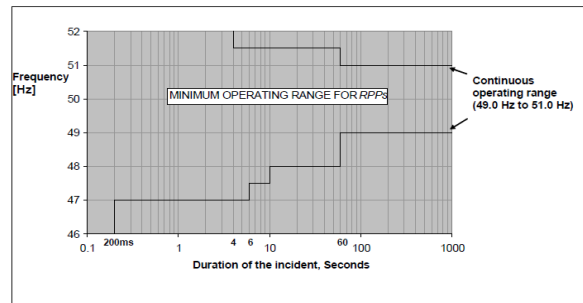


Figure 2: minimum frequency operating range of a RPP (during a system frequency disturbance)

2.2 Voltage response

LVRT & HVRT capabilities: In order to demonstrate the LVRT capability of a RPP, dynamic simulation studies based on the established model are performed. And the results of these simulation studies shall demonstrate:

- The RPP is capable of staying connected as long as voltage is above the lower limit curve (and below the upper limit curve) according to Figure 4 of SAGC (area A, B and D)
- The RPP injects reactive current as specified Figure 6.

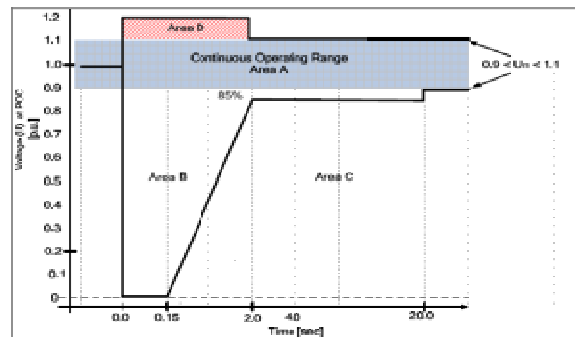


Figure 3 : voltage ride through capability for RPP of category A3, B and C

Disconnection is only allowed once Area C in Figure 4 is reached. The control of reactive current should follow the characteristics of Figure 6 with a tolerance of $\pm 20\%$ after 100 ms. The supply of reactive power has first priority in area B, while active power has second priority. If possible maintain active power supply during voltage drop but a drop is allowed. To test the Low Voltage Ride Through capabilities, worst case operating conditions of RPP is assumed for:

- Operation at maximum active power output
- Operation at maximum. voltage which leads to maximum voltage dips
- Operation at maximum. or minimum. reactive power

To test the High Voltage Ride Through capabilities, worst case operating conditions of RPP is assumed for:

- Operation at maximum active power output

- Operation at minimum voltage which leads to maximum voltage rise
- Operation at maximum or minimum reactive power

The results are tabled below and shown in Figure 4 and Figure 5 where a three phase fault is applied at 7 second. The reactive current is tabled and marked in Figure 5 in red circles. The High Voltage Ride Through results are also tabled below Table 1.

The results obtained in Table 1 show the active power is reduced to zero for a bigger voltage drop and maximum reactive current is injected to the point of connection. The reactive current negative sign denotes that reactive power leaves the PV plant and positive absorbs reactive power. In Figure 5 the voltage does not reach absolute zero this is due to the reactive current support [2].

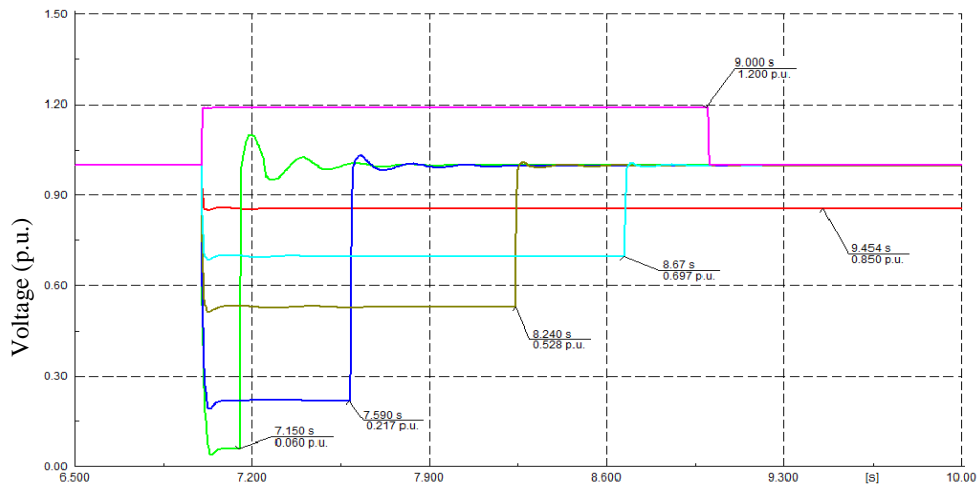


Figure 3: Voltage Ride Through capability of PV farm

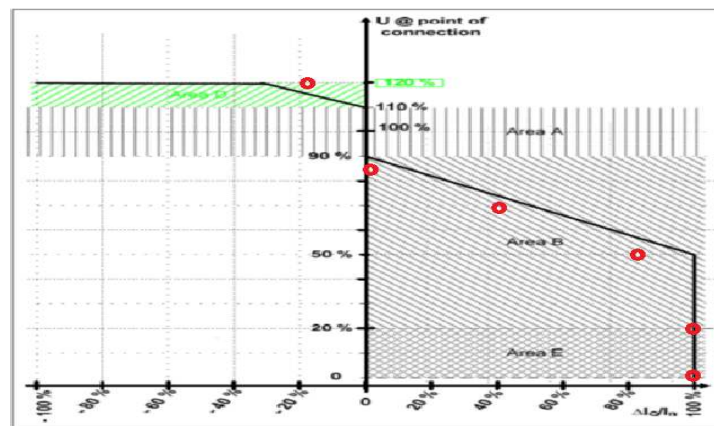


Figure 4: Requirements for reactive power support, IQ during voltage drops or peaks at the POC

Table 1: Voltage ride through capabilities

Voltage (p.u)	Fault duration (s)	Active Power (p.u)	Reactive current (p.u)	Stable (Y/N)
0	0.15	0	-1	Y
0.2	0.59	0	-1	Y
0.5	1.24	0.15	-0.801	Y
0.7	1.67	0.46	-0.409	Y
0.85	20	0.86	-0.018	Y
1.2	2	1	0.182	Y

2.3 Reactive power capabilities

Requirement for category B: RPP shall be designed to supply rated power (MW) for power factors ranging between 0.975 lagging and 0.975 leading for a PV plant rated 15 MVA and must be available from 20% of rated power measured at the point of connection as shown in Figure 7. The RPP must be capable to operate in the hatched area as shown in Figure 7 & Figure 8[1].

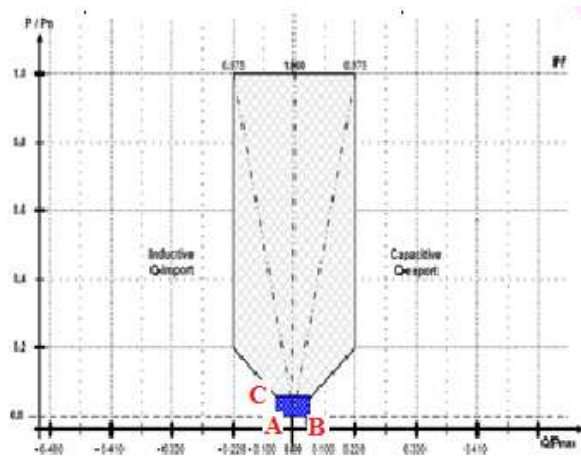


Figure 5: Reactive power requirements for RPPs of category B

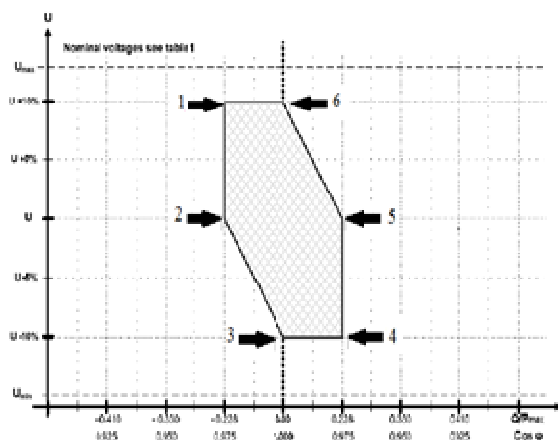


Figure 6: Requirements for voltage control range for RPPs of category B

Figure 7 point A and B are equivalent in (Mvar) to -5% and 5% respectively and point C is equivalent in MW to 5% rated MW output and the reactive power requirement over full generation range 22.8% corresponds to 0.975 power factor for leading and lagging.

The exercise to check if the PV plant complies with reactive power requirement is done for every point of operation of the PV plant. Aided by the power factor station controller to set the power output and reactive set points. The grid code requires at least 0.975 lagging and 0.975 leading and voltage to be within the range $\pm 10\%$. The control is at the point of connection. Table 2 show results of PV plant at point of connection to meet all requirements without violations from the PV inverter. Observation for leading pf the PV inverter voltage rises within the limits considering the cable length from the last PV array inverter will not be expanded. Since the PV inverter manufacture recommends voltage operation should be within $\pm 10\%$. So care should be taken when expending the PV plant.

Now to test for voltage control capabilities of the PV plant against grid code requirements shown by Figure 8 [1]. An external grid connected to the PV plant aids changing the voltage of the point of connection and a station control is to be used to control the power factor at the point of connection.

Table 2: Results of Photo voltaic farm connected

Power	Required Q @ POC	Required Q @ POC	Reactive power met? (Y/N)	Voltage @ POC	Voltage @ Inverter	Actual Q @ POC
P=5%	Q=5% (ind)	0.65Mvar	Y	1.02	1.02	0.5
P=5%	Q=5% (cap)	0.65Mvar	Y	1.01	1.01	0.5
P=20%	Q=22.8% (ind)	3Mvar	Y	1.01	1	3
P=20%	Q=22.8% (cap)	3Mvar	Y	1.02	1.04	3
P=100%	Q=22.8% (ind)	3Mvar	Y	1.01	1	2.99
P=100%	Q=22.8% (cap)	3Mvar	Y	1.03	1.04	3

Table 3 results of PV farm at various voltages and power factor

Point	V @ POC	PF @ POC	Q @ POC	Actual PF @ POC	Voltage @ inverter	Grid Compliant (Y/N)
1	1.1	0.975 (lag)	3 Mvar	0.975	1.11	Y
2	1	0.975 (lag)	3 Mvar	0.975	1.02	Y
3	0.9	1	0	1	0.9	Y
4	0.9	0.975 (lead)	-3Mvar	0.975	0.89	Y
5	1	0/975 (lead)	-3Mvar	0.975	0.99	Y
6	1.1	1	0	1	1.1	Y

From the table 3 the obvious voltage violation are at the maximum and minimum voltage limits of the PV inverter when operated at 1.1 p.u and power factor is 0.975 lagging the maximum voltage limit is exceeded, and also when operated at voltage 0.9 p.u. and power factor is 0.975 leading the minimum voltage limit is exceeded. Therefore compensation is needed. Where a minimum shunt reactor rating of 2.1 Mvar when modelled show improvement and the PV inverter voltages stay within limits specified by manufacture.

2.4 Reactive power and voltage control functions

The requirements of reactive and voltage control only applies to category B and C. The RPP must be equipped with reactive power control function, and voltage control function capable to controlling reactive power and voltage at the point of connection. But one control function can be activated at a time: Voltage control, Power factor control & Reactive power control. In this study only voltage control function is used [1].

Voltage control: The voltage control requirement is such that the voltage setpoint shall be commenced two seconds and completed no later than 30 seconds after receipt of an order to change the setpoint. The accuracy of the voltage setpoint shall be within $\pm 0.5\%$ of nominal voltage and the accuracy of the control must not deviate by more than $\pm 2\%$ of the required reactive power according to the droop characteristic as shown in Figure 9 [1]. The control shall not be limited to perform the control within its dynamic range and voltage limit with the droop configured. The droop is the voltage change in p.u caused by the change in reactive power (p.u). When the voltage control has reached the RPP's dynamic design limit, the control function shall await possible overall control from the tap changer or other voltage control functions [1].

Overall voltage coordination shall be handled by the network service provider in collaboration with the system operator. The voltage control function has been displayed above to be working in accordance to the requirements [3].

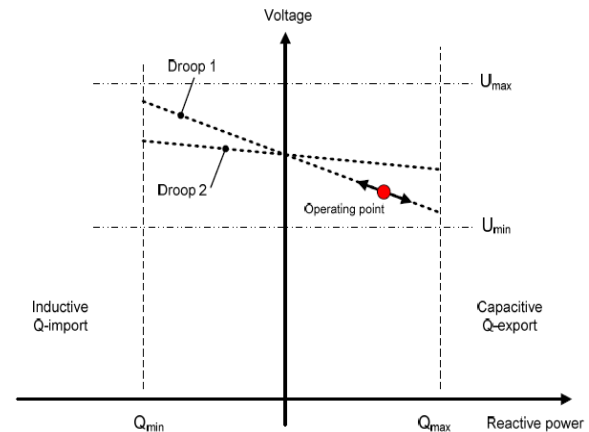


Figure 9 voltage control for the RPP

The regulation method of the voltage at the connection point of the PV system is employed by reactive power with voltage as input. Therefore, the consumption of reactive power is dependent by voltage variation. The general relation between reactive power of a PV system and the grid voltage is defined as follows:

$$droop = \frac{\Delta Q}{V - V_n} \quad (1)$$

where droop is the slope factor (kVar/V) and V_n is the nominal voltage ΔQ is the required reactive power limit.

3 POWER SYSTEM ANALYSIS

Steady state of RPP and local generator testing is performed to evaluate any possible electrical risks associated with PV system to ensure secure network operation taking all possible cases into consideration. The analysis results of the auxiliary network shown below.

3.1 Case: N-1 transformer contingency

An n-1 case where the aux unit transformer feeding 11 kV Unit Board A is isolated /disconnected and the tie link between busbar 11 kV board A and 11 kV board B is closed to maintain supply on the other rest of the auxiliary network and load flow showing busbar voltages is tabled below and show the PV plant improves the voltage in a situation for an n-1 contingency.

Table 4: Voltages at aux transformer n-1 contingency

Busbar (voltage)	Local generator (p.u)	Local gen & PV farm (p.u)
0.38 kV	1.04	1.05
6.6 kV	1.01	1.02
11 kV	0.99	1
22 kV	1.02	1.02

3.2 Case: Fault and voltage analyses

A load flow and fault level analysis is tabled below with busbars results.

Table 5: Fault levels

Busbars	Local generator		Local gen & PV plant	
	3-phase fault (kA)	1-phase fault (kA)	3-phase fault (kA)	1-phase fault (kA)
0.38kV	34.777	33.32	34.779	33.317
22kV	214.92	0.01054	214.92	0.01054
6.6kV	22.366	0.327	22.371	0.3273
11kV	25.97	0.308	26	0.8258

Table 6: Busbar voltages different loading

Busbar	Local generator (p.u)		Local gen & PV plant (p.u)	
	50% aux load	Max aux load	50% aux load	Max aux load
0.38kV	1.09	1.07	1.09	1.07
6.6kV	1.06	1.04	1.06	1.04
11kV	1.04	1.02	1.04	1.02
22kV	1.02	1.02	1.02	1.02

The tabled results show the PV plant contribution is significant for single phase fault at the point of connection. The single phase fault is increased to 0.825 kA from 0.308 kA. Since the dq-axis based current control scheme enables the current control in a balanced condition, the three phase fault current generated by the PV inverter is limited by the q and d axis reference values of the current controller, but for unbalanced fault, a single line to ground fault is not effectively controlled during

the fault condition but limited to 120% of the inverter-rated current [3], which is also seen in this case [2] [6].

The PV plant shows no contribution to voltage violation as seen in Table 6 but for a low auxiliary loading, with the PV plant connected, the voltage of 0.38 kV borders around the boundary of low voltage limit of $\pm 10\%$ reaching 1.09 p.u. at half load.

4 DISCUSSION AND CONCLUSION

In this paper the integration of the PV plant and power station electrical auxiliary network has been successfully tested utilizing the developed voltage controller. The dynamic behavior was investigated according to SAGC for category B & C. The LVRT & HVRT were tested under various voltage dips to satisfy the requirements. The results displayed the capabilities of the PV model to remain connected and supply desired reactive power to the point of connection thus, assisting in grid stability. The frequency response requirement effectively adjusted in case of over frequency event. Thus, encouraging high PV penetration level without compromising much on network operations and stability of network. A steady state analysis revealed no major concerns with only the low busbar voltages rising close to limit when the PV plant is connected thus, the PV plant voltage control considered such variation to suit the requirements of the auxiliary network. The rating limit of the PV plant is found to be dependent to the spinning reserve capacity to take over the maximum output power of the PV plant. If the variations are large they may cause system stability issues. The optimum PV penetration level may depend on size of the local power station generation.

5 REFERENCES

- [1] N. E. R. o. S. A. (NERSA), "Grid connection code for renewable power plants (rpps) connected to the electricity transmission system (ts) or the distribution system (ds) in south africa," Eskom Transmission Division, Germiston, 2012.
- [2] T. Neumann and I. Erlich, "Short circuit contribution of a Photovoltaic power plant," *Institute of electrical power systems*.
- [3] S. Kim, J. Jeon, C. Cho, E. Kim and J. Ahn, "Modeling and simulation of a grid-connected PV generation system for electromagnetic transient analysis," *Solar Energy*, vol. 83, pp. 664-678, 2009.
- [4] I. Banu and M. Istrate, "Study on three-phase photovoltaic systems under grid faults," *electrical and power engineering*, vol. 8, pp. 1132-1137, 2014.
- [5] P. Smit and G. Coetzee, "Power station electrical plant-auxiliary power system training manual," Eskom Generation Group, 2008.
- [6] K. Manohar and P. Rani, "Mppt and simulation for a grid-connected photovoltaic system and fault analysis," *The international journal of engineering and science*, vol. 1, no. 2, pp. 158-166, 2012.

Optimised Model of a Solar/Wind/Diesel Hybrid Generation System for Rural Application

E. Hamatwi^{1*} and I E Davidson²

¹University of KwaZulu-Natal, Discipline of Electrical Engineering, Durban 4001, South Africa

² University of KwaZulu-Natal, Eskom Centre of Excellence in HVDC Engineering, Durban 4001, South Africa

*Email: esterhamatwi@gmail.com

Abstract: The last century has demonstrated that every facet of human development is woven around a sound and stable energy supply regime. A critical focus over the last two decades has been on developing suitable technologies to meet the challenges of remote and rural settlements that are geographically isolated, and sparsely populated. Recent technological advances like solar-wind hybrid systems provide viable solution alternative to alleviate the energy scarcity experienced by isolated communities, as these systems are easy to install, robust, low maintenance, modular and cost effective for power generation. Hybrid renewable power generation and storage systems are considered to be an effective option for electrifying remote and isolated areas which are far from conventional grids. In this research investigation, a solar-wind hybrid system, with energy storage and a back-up diesel generator was modeled, simulated and optimized for a rural area in KwaZulu-Natal Province, South Africa. Simulations results obtained show that the optimal system comprises of a 200kW solar array, 10 wind turbines rated at 10kW each, a 40kW diesel generator, an 80kW converter and 96 batteries. The optimal system's net-present-cost and cost of energy are \$1,004,701 and \$0.533/kWh. This indicates that remote settlements can be electrified using hybrid systems as they have lower operating costs and more environmental friendly.

Index Terms—Optimization, Solar-PV, HOMER, Hybrid Energy Systems, wind energy, green-house gases,

1 INTRODUCTION

It is estimated that 17% of the world's population currently live in rural areas that are geographically isolated, sparsely populated and with no electricity access [1], [2]. According to the 2011 Census conducted for the KwaZulu-Natal Province, Statistics South Africa estimates that 54% of the total Provincial population lives in rural areas and this puts considerable pressure on the provision of social services such as electricity supply [3]. 48% of the households in the rural and informal settlements have no electricity access [4]. Further, it was recorded that Umzinyathi district has the highest number of informal settlements adding up to 91% with no electricity access. South Africa's generation capacity is mainly coal based due to large coal reserves. However, due to the increasing demand

and lack of capital for investments in coal-based generation, the government plans to change this and expects renewable energy (RE) sources to represent 20% of the installed capacity by 2030 [5]. Eskom, South Africa's dominant electric utility has been largely responsible for electricity distribution in rural area and smaller towns [6]. However, with electricity demand outstripping supply, high transmission and distribution costs it is expected that many remote households will remain unconnected to the conventional electricity generation and distribution networks in the foreseeable future [7], [8].

Renewable energy is a preferred solution to fossil fuels and their deployment in off-grid systems is growing steadily in both developed and developing countries [1], [8]-[10]. A power generating system which combines two or more sources of energy is called a hybrid system [11], [12]. Hybrid energy systems are increasingly considered as a viable option to electrify remote and sparsely populated areas [13]-[16]. Seasonal variations of wind and solar resources can complement each other [2], [17]. A consistent exploitation of the complementarities of these two sources of energy with battery storage with back-up diesel generator appear necessary to maintain an optimum level of electricity production in favourable sites [2], [5].

Many hybrid systems have been proposed in the past for electrification of remote areas or grid connected sites. Green [5] carried out a survey in Maphephetheni district, KwaZulu-Natal to investigate the experience of 50 households with access to both solar home system (SHS) and grid electricity. The results indicated that over 50% of households preferred SHS to grid electricity. Lal [2] proposed a hybrid PV/wind and micro-hydro/diesel system for a rural area in Sundargarh district. The simulation results concluded that the availability of different RE sources could replace the conventional energy sources as a feasible solution for distribution of electric power for stand-alone applications at remote and distant locations thus reducing the dependence on diesel generating units.

Daud [15] and Ngan [18] analyzed the potential implementation of a hybrid PV/ wind/diesel system for a house in rural Palestine and Southern Malaysia respectively. They analyzed different scenarios of hybrid systems in HOMER software. Based on the simulation results, the most economic scenario comprised of a PV/wind turbine/battery system with diesel generator as back-up supply.

Saheb-Kaussa [19] carried out a technical, economic and environmental analysis of a PV-wind hybrid system connected to a conventional grid. The study concluded that the hybrid system has a low cost of energy and the rates of greenhouse gas (GHG) emissions are significantly reduced compared to the conventional system. Tahri [20] designed an optimal wind/PV/diesel hybrid power system for a village in Merane, Chlef, Algeria. The paper concluded that a hybrid renewable energy system presents a better alternative to electrify remote areas over conventional grids.

This research investigation aims at determining the optimal hybrid renewable energy system configuration for electrifying a remote rural area in Umzinyathi district in KwaZulu-Natal Province, South Africa. The approach used in this study can be applied to similar rural settlements.

2 LOAD EVALUATION

2.1. Load Forecasting

To obtain the average load and energy consumption data for a remote rural area, it is required that load forecasting be carried out for the proposed study area. The electrical loads of the area were classified as domestic (households) and community/rural industries/shops. The area is estimated to have 80 houses and 15 shops. Load forecasting was carried out through a survey conducted through interviews and questionnaires.

The interval estimation criterion was used for sample size selection. The sample size is calculated using (1):

$$ss = \frac{z^2 \times P(1-P)}{C^2} \quad (1)$$

Where:

ss - Sample size;

z - Z-score for the selected confidence level from the z-score table;

P - Standard deviation;

C - Confidence interval chosen.

The new sample size needed is calculated using (2):

$$ss_{new} = \frac{ss}{1 + ss - 1/P_{op}} \quad (2)$$

Where:

ss_{new} - New sample size;

ss - Sample size calculated from (1);

P_{op} - The population considered in the study.

The 95% confidence level was chosen with the confidence interval of 5%. The standard deviation (P) was also chosen to be 0.5. From the z-score table, the z-score value close to 0.95 (95% confidence level) is 1.96. Therefore, the household load sample size was computed as follows:

$$ss = \frac{1.96^2 \times 0.5(1-0.5)}{(\frac{5}{100})^2} = 384.16 \quad ; \quad ss_{new} = \frac{384.16}{1 + \frac{384.16}{80}} = 66 \text{houses}$$

The commercial load sample size was computed as follows:

$$ss = \frac{1.96^2 \times 0.5(1-0.5)}{(\frac{5}{100})^2} = 384.16 \quad ; \quad ss_{new} = \frac{384.16}{1 + \frac{384.16}{15}} = 14.47 \approx 15 \text{shops}$$

2.2. Load Assessment

All shops were selected for survey conduction and since the total number of houses is less than 100 (first rule of thumb in sample sizing); all houses were considered for more accurate load forecasting. The information obtained from shop owners and household residents were their current sources of power and the electrical appliances that they are likely to use if they had access to electricity. The total load demand and power consumption (energy) is computed as follows:

Total load (W) = Power rating (W) x Quantity

Total Energy (Wh) = Total load (W) x Hours of use

The average load per house and per shop is calculated using (3):

$$\text{Load / house}_{avg} (kW) = \frac{\text{Demand}_{Tot} (W)}{\text{Houses}_{Tot} \times 1000W / kW} \quad (3)$$

Where:

Demand_{Tot} - Total load demand;

Houses_{Tot} - Total number of houses

The average power consumption (energy) per household and per shop is calculated using (4):

$$\text{Energy / house}_{avg} (kWh) = \frac{\text{Energy}_{Tot} (Wh)}{\text{Houses}_{Tot} \times 1000Wh / kWh} \quad (4)$$

Where:

Energy_{tot} - Total energy consumption;

Houses_{Tot} - Total number of houses

Table 1 illustrates the estimated load demand for the study area. The maximum load demand for the households and shops is 1.68kW/day/household and 0.35kW/day/shop respectively.

Tab. 1: Estimated Load Demand for the Study Area

Type of load	Per Unit (kW)	Quantity	Total load (kW)
Household	1.68	80	134.4
Shops	0.35	15	5.25
Total			139.65

Table 2 illustrates estimated power consumption for the study area. The maximum power consumption for the households and shops is 6.79kWh/day/household and 4.85kWh/day/shop respectively.

Tab. 2: Estimated Power Consumption for the Study Area

Type of load	Per Unit (kW)	Quantity	Total load (kW)
Household	6.79	80	543.2
Shops	4.85	15	72.75
Total			615.95

3 SYSTEM MODELLING

3.1. Geographical site location and climate database

The latitude and longitude coordinates of the study area are 28.17°S and 30.22°E respectively. The latitude and longitude coordinates for the study area are required to obtain the site insolation data and wind speed data from the surface solar energy website of National Aeronautics and Space Administration (NASA) [21]. The annual solar radiation and annual average wind speed for the study area obtained from NASA are $5.14\text{kWh/m}^2/\text{d}$ and 3.5 m/s respectively.

3.2. HOMER Code Implementation

Hybrid Optimization Model for Electric Renewables (HOMER) is a micro-power optimization software developed by Mistaya Engineering, Canada for the National Renewable Energy Laboratory (NREL) USA [22]. HOMER is an optimization software for both off-grid and grid-connected hybrid energy systems. HOMER's flexibility makes it useful for rural electrification projects through its three principal tasks: simulation, optimization, and sensitivity analysis.

3.3. Energy Analysis

1.1.1. Load profile

Fig. 1 shows the daily electrical load requirement on an hourly basis for the household and commercial loads obtained through the survey. There is a base load of 16.16kW . Small peak loads of 54.00kW occur from 7am-8am and 44kW from 13pm to 14pm. The daily peak load of the study area is 91 kW with the scaled annual average energy consumption of 615 kWh/day .

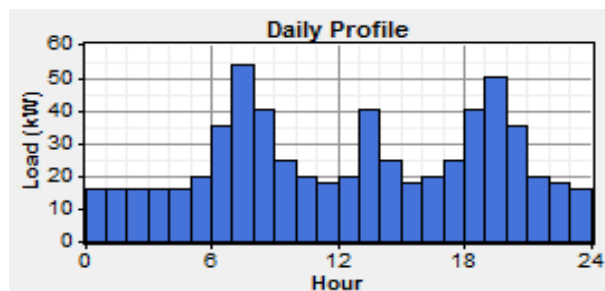


Fig. 1: Daily load profile for the study area

1.1.2. Solar radiation profile

Fig. 2 shows the solar resource profile for the study area over one year period. It has been observed that the solar intensity ranges from $3.66\text{kWh/m}^2/\text{d}$ to $6.43\text{ kWh/m}^2/\text{d}$. The scaled annual solar radiation is $5.13\text{ kWh/m}^2/\text{d}$.

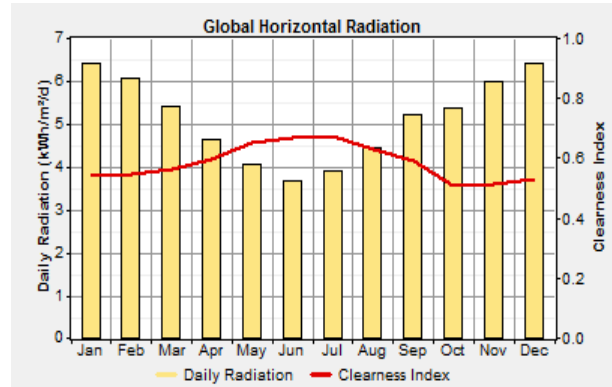


Fig. 2: Monthly average solar radiation and clearness index

1.1.3. Wind resource data

Fig. 3 illustrates the wind resource profile for the study area over one year period. The annual average wind speed is 3.5 m/s .

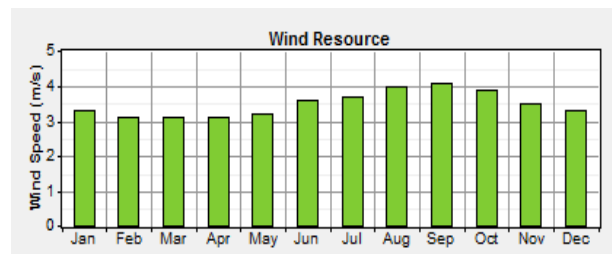


Fig 3: Monthly average wind speed

3.4. Economic analysis and reliable constraints

HOMER uses total Net Present Cost (NPC) to represent the life cycle cost of the system. This includes all costs and revenues that occur within the project lifetime. In this study, an annual interest rate of 10% was considered, which is common in many developing countries [23]; A project lifetime was taken as 20 years. Sensitivity analysis assesses the behaviour of the system when certain parameters change their values. Annual solar radiation, average annual wind speed, diesel fuel price and maximum annual capacity shortage (MACs) were taken as sensitivity variables.

3.5. System equipment configuration

The input data into the HOMER software include: sizes of the components under consideration, acquisition cost, replacement cost, operation cost, maintenance cost and the expected lifetime. Table 3 shows the data used, which were obtained from two suppliers of solar energy equipment in South Africa, Solar-World company and Green World store. Solar-World is a worldwide leading manufacturer and it relies on Germany and United States as its centre of excellence for solar technology, thereby ensuring sustainable product quality.

Tab. 3: System Components

Component	Size	Capital Cost (\$)	Replacement Cost (\$)	O&M cost (\$)	Lifetime
PV panels	0-300 kW	946.00 per kW	756.00 per kW	0.00	20 years
Battery bank	225Ah per 6V	148.00 per battery	119 per battery	2 per year	845kWh throughput
Diesel Gen	0-150 kW	124.00 per kW	99.00 per kW	0.01 per hour	25000 operating hours
Converter	0-160kW	171/kW	156/kW	20/year	15 years
Wind turbine	10kW	4006.00 per turbine	3204.00 per turbine	50 per year	20 years

3.6. Modelling of Hybrid Energy System Components

1.1.1 Solar Photovoltaic generator modelling

The solar panels convert solar radiation directly into DC electricity. According to standard practices, the solar panels are to be sized 10-30% above the load size for security of supply[24]. In this study, the solar panels are sized to be 20% above load size. The projected lifetime for the PV array is 20 years. The PV system considered has no tracking system. Solar panels generate more power when they are placed at an angle equal to the latitude of that site location[24]. Therefore, in this study, the slope angle for the panels is 28.17°.

1.1.2 Wind energy generator modelling

In wind mills, the energy in the wind turns the blades around a rotor. The rotor is connected to the main shaft, which spins a generator to generate electricity. In this study, a 10kW AC BWC Excel-S wind turbine was used in the simulation with a projected lifespan of 20 years.

1.1.3 Diesel generator modelling

The diesel generator acts as a backup power supply in hybrid systems. In this study, the diesel back-up system is operated at times when the output from wind and solar systems fails to satisfy the load and when the battery storage is depleted. For better performance and efficiency, the diesel generator will always operate between 80 and 100% of their kW rating [2]. In this study, a Perkins diesel generator rated at 150kW was considered. Diesel fuel price has a significant impact on the running cost of the equipped diesel generator. The prevailing diesel price is US\$ 1.26/L and this was taken as the reference price for the diesel fuel in this investigation.

1.1.4 Converter modelling

In the proposed scheme, the converter contains both rectifier and an inverter. The inverter converts the DC power from the PV generator and the battery bank to AC power, while the rectifier converts the AC power from the diesel generator into DC power for battery

charging [2]. Based on standard practices, the inverter size is to be 20-30% above the peak load to cater for losses experienced during the rectification and inversion processes [24]. In this study, the inverter efficiency was assumed to be 90% for all sizes considered.

1.1.5 Charge controller modelling

Charge controllers are used to protect the batteries from over-charging and over-discharging. They are used to sense when the batteries are fully charged or being critically discharged. When the batteries are fully charged, the amount of energy flowing from the energy source to the batteries is decreased or cut-off completely. On the other hand, when the batteries are being critically discharged and the solar resource is poor, the back-up diesel generator will be prompted to charge the batteries.

1.1.6 Battery bank modelling

Deep-cycle storage batteries are used to store the energy generated by the PV panels for backup purposes when the total system generation is lower than the load demand. The battery state of charge (SOC) refers to the cumulative sum of the daily charge/discharge transfers [2]. Depth of discharge (DOD) is a measure of how much energy has been withdrawn from a storage device, expressed as a percentage of full capacity[2]. The type of battery used for the proposed system is Trojan T105 deep cycle battery because of its favourable characteristics designed suitable for remote area applications and its favourable price[25]. Each battery has a rating of 6V, a nominal capacity of 225Ah, 1.35kWh with battery life time throughput of 845kWh.

4 RESULTS AND DISCUSSIONS

4.1. Model of the PV/Wind/Diesel hybrid system

Fig. 4 shows the schematic diagram of the PV/wind/diesel hybrid model and its components. As indicated, the scaled annual energy consumption is 615kWh/day and the peak power is 91kW.

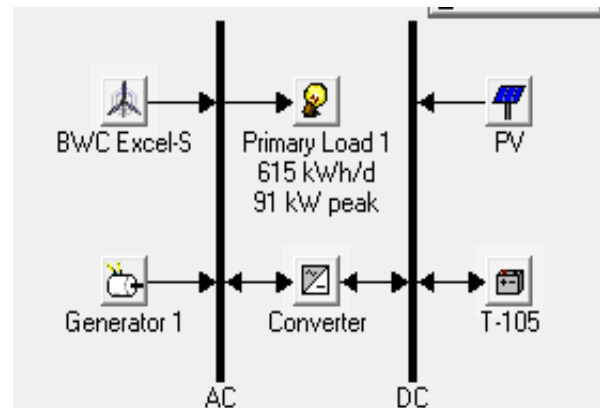


Fig. 4: Schematic diagram of the hybrid system

The PV generator and wind energy generator are the main electricity generating systems. The DC electricity generated from the PV array is fed to the DC bus while the AC electricity from the wind generator is fed to the AC bus. The bidirectional converter acts as a rectifier and inverter concurrently. The battery bank acts as the energy storage system for the proposed hybrid system. The decision to operate the diesel generator is taken when the battery is discharged to its depth of discharge level and there is no sufficient energy generated from the PV and wind system to supply the load. This switching process is carried out by the battery charge controller which in HOMER software is incorporated in the battery bank block.

4.2. Optimization results

HOMER software simulates every combination system configuration in search space and sorts the feasible ones based on the total Net Present Cost (NPC). The system with the least NPC is chosen as the optimum system. As shown in Fig. 5, the optimal system comprises of a 200kW solar array, 10 wind turbines rated at 10kW each, a 40kW diesel generator, an 80kW converter and 96 batteries. The Net Present Cost (NPC) of the system is \$1 004 701 and the Cost of Energy (CoE) is \$0.533/kWh.

Double click on a system below for simulation results.

Fig. 5: Optimized results by categories

4.3. Electricity production analysis

Fig. 6 shows the contribution of electrical energy production by various sources in the hybrid system. The PV array, wind turbines and diesel generator generated 68%, 16% and 16% of the total energy respectively. The system's renewable fraction is 84%.

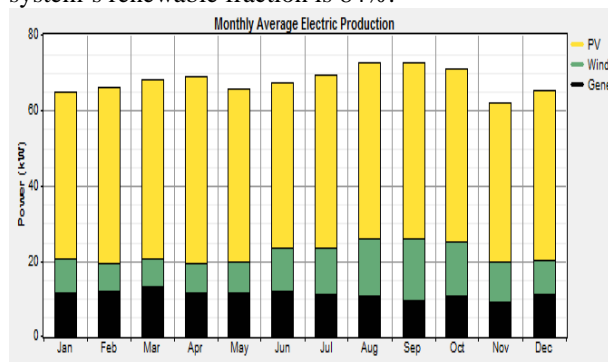


Fig. 6: Contribution of electrical energy production by various sources in the hybrid system

4.4. Economic comparison of PV/wind/diesel and PV/diesel hybrid system

Fig. 7 illustrates the economic comparison of the two systems performed based on the cash flow summary obtained from HOMER simulation software. The PV/diesel hybrid system was taken as the base case and compared to the current system which is the PV/wind/diesel hybrid system. From the simulation results, it is shown that although the capital cost of the current system is high as compared to the base case, it has minimal total Net Present Cost (NPC), operating and maintenance costs. Whereas for the base case, the initial capital cost is low but the operating and maintenance costs are very high. This means that the current system is more cost effective in a long run compared to the base case.

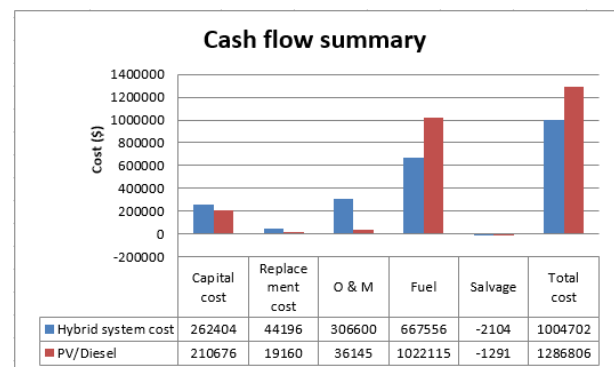


Fig. 7: Economic comparison of the base system and the current system

4.5. Environmental analysis

By generating the amount of GHG (in kg/year) emitted by the modeled system, HOMER simulation software enables an environmental impact analysis to be carried out. In this investigation, the amount of the GHGs emitted by both the PV/wind/diesel hybrid system and the PV/diesel hybrid system were compared to identify the system that is more environmental friendly. Table 4 clearly illustrates that the solar/wind/diesel hybrid system significantly reduces the amount of GHG emitted as compared to the solar/diesel hybrid system. This is due to the reduced dependency on diesel generating units.

Tab. 4: Annual Green House Gases Emissions

Pollutant	GHGs emissions (kg/yr.)	
	PV/wind/diesel	PV/diesel
Carbon dioxide	63 338	96 979
Carbon monoxide	156	239
Unburned hydrocarbons	17.3	26.5
Particulate matter	11.8	18
Sulfur dioxide	127	195
Nitrogen oxide	1 395	2 136
Total	65 045	99 593

5 CONCLUSION

In this paper, a solar-wind hybrid system with energy storage and a back-up diesel generator was modeled, simulated and optimized in HOMER software for a rural settlement in Umzinyathi district in KwaZulu-Natal Province, South Africa. Based on the simulation results, the optimal system comprises of a 200kW solar array, 10 wind turbines rated at 10kW each, a 40kW diesel generator, an 80kW converter and 96 batteries. The Net Present Cost (NPC), Cost of Energy and payback period of the optimal system obtained, are \$1 004 701, \$0.533/kWh and 5 years respectively. With the current cost of energy in KwaZulu-Natal being \$0.96/kWh[26], it is clearly visible that the proposed system will deliver reliable power at a much cheaper price. Comparing the results, the PV/wind/diesel hybrid system with 84% renewable energy (RE) penetration is cost effective in a long run and it would avoid or eliminate the addition of 35 tons of GHGs emissions compared to the PV/diesel hybrid system.

6 REFERENCES

- [1] R. Kempener, O. L. d'Ortigue, D. Saygin, J. Skeer, S. Vinci, and D. Gielen, *Off-Grid Renewable Energy Systems: Status and Methodological Issues*. Abu Dhabi, United Arab Emirates: IRENA Innovation and Technology Centre, 2015.
- [2] D. K. Lal, B. B. Dash, and A. K. Akella, "Optimization of PV/wind/micro-hydro/diesel hybrid power system in HOMER for the study area," *International Journal on Electrical Engineering and Informatics*, vol. 3, 2011.
- [3] R. R. Pillay, S. Pillay, and G. Apelgren-Narkedien, "2014/2015-Annual Performance Plan," Pietermaritzburg 28 March 2014.
- [4] A. Ngyende, "KwaZulu-Natal: Informal Settlements Status (2013)," Johannesburg 2013.
- [5] J. M. Green and D. I. Zwebi, "From SHS to grid electricity in low-income rural households," *Journal of Energy in Southern Africa*, 2006.
- [6] M. Bello, C. Carter-Brown, S. Salvoldi, K. Leask, C. Mushwana, B. Magoro, *et al.*, "Eskom's initiatives to support renewable energy grid integration," in *Energize Journal*, South Africa, 2010.
- [7] R. Sen and S. C. Bhattacharyya, "Off-grid electricity generation with renewable energy technologies in India: an application of HOMER," *Renewable Energy*, vol. 62, pp. 388-398, 2014.
- [8] I. E. Davidson, H. Muashekele, and N. Mukapuli, "Benguela Community/UNAM Wind Power Demonstration Project—Experiences in Implementation," *Journal of Energy and Power Engineering*, vol. 8, pp. 1067-1072, 30 June 2014.
- [9] G. K. Venayagamoorthy, I. Jayawardene, P. Arunagirinathan, R. Singh, and I. E. Davidson, "Grid Operations with High Penetration of Photovoltaic Systems," presented at the 3rd Southern African Solar Energy Conference, SASEC2015, South Africa, 2015.
- [10] M. M. Bello and I. E. Davidson, "Spatial Modelling and Dynamics of a PV-Powered Fuel Cell Generator for Renewable Energy Application," in *Inaugural IEEE Power Engineering Society Conference in Africa*, Durban, South Africa, 2005, pp. 125-131.
- [11] P. Nema, R. K. Nema, and S. Rangnekar, "A current and future state of art development of hybrid energy system using wind and PV-solar: A review," *Renewable and Sustainable Energy Reviews*, vol. 13, pp. 2096-2103, October 2009.
- [12] S. Sinha and S. S. Chandel, "Review of software tools for hybrid renewable energy systems," *Renewable and Sustainable Energy Reviews*, vol. 32, pp. 192-205, April 2014.
- [13] M. R. Khan and E. D. Brown, "DC nanogrids: A low cost PV based solution for livelihood enhancement for rural Bangladesh," presented at the 2014 3rd International Conference on the Developments in Renewable Energy Technology (ICDRET) Dhaka, Bangladesh, 2014.
- [14] S. Teleke, L. Oehlerking, and M. Hong, "Nanogrids with energy storage for future electricity grids," *T&D Conference and ...*, 2014.
- [15] A. K. Daud and M. S. Ismail, "Design of isolated hybrid systems minimizing costs and pollutant emissions," *Renewable Energy*, vol. 44, pp. 215-224, 2012.
- [16] T. H. Rocky, R. Islam, and U. K. Saha, "Nano solar grid (NSG): A solution for rural market power crisis," *Green Energy and Technology* (....), 2014.
- [17] I. Khan, P. K. Halder, and N. Paul, "Renewable Energy Based Hybrid Nano-Power Station for Remote Isolated Island," presented at the 4th Global Engineering, Science and Technology Conference, Dhaka, Bangladesh, 2013.
- [18] M. S. Ngan and C. W. Tan, "Assessment of economic viability for PV/wind/diesel hybrid energy system in southern Peninsular Malaysia," *Renewable and Sustainable Energy Reviews*, vol. 16, pp. 634-647, 29 September 2012.
- [19] D. Saheb-Koussa, M. Koussa, and N. Said, "A Technical, Economic, and Environmental Performance of Grid-Connected Hybrid (Photovoltaic-wind) Power System in Algeria," *The Science World Journal*, vol. 2013, p. 12, 3 October 2013.
- [20] T. Tahri, A. Bettahar, and M. Douani, "Optimization of a Hybrid Wind-PV-Diesel Standalone System: Case Chlef, Algeria," *International Journal of Mathematical, Computational, physical, Electrical and Computer Engineering*, vol. 7, 2013.
- [21] K. R. Ajao, O. A. Oladosu, and O. T. Popoola, "Using HOMER power optimization software for cost benefit analysis of hybrid-solar power generation relative to utility cost in Nigeria," *International Journal of Research and Reviews in Applied Sciences*, vol. 7, April 2011.
- [22] P. Lilienthal, T. Lambert, and P. Gilman, "Getting Started guide for HOMER Version 2.1," National Renewable Energy Laboratory, Colorado 2005.
- [23] A. Kassam, "HOMER Software Training Guide for Renewable Energy Base Station Design," 2010.
- [24] F. M. Vanek, L. D. Albright, and L. T. Angenent, *Energy Systems Engineering: Evaluation and Implementation*, 2 ed. New York: Mc Graw Hill, 2012.
- [25] Z. G. Giday, "Technical and Economic Assessment of solar PV/diesel Hybrid Power System for Rural School Electrification in Ethiopia," *International Journal of Renewable Energy Research*, vol. 3, September 2013.
- [26] Eskom Tariffs & Charges 2015/16 [Online]. Available: <http://www.eskom.co.za/CustomerCare/TariffsAndCharges/WhatsNew/Documents/Tariff%20brochure%20v9%20lowres.pdf>

A STUDY ON SYNCHRONIZATION OF SINGLE PHASE INVERTERS IN SOUTH AFRICAN GRID WITH HIGH DEGREE OF PENETRATION OF RENEWABLE ENERGY

M.M. Sibanyoni* and S.P. Chowdhury**

* M.M Sibanyoni, Enel Green Power RSA, Operation and Maintenance, 102 Rivonia Road Sandton, Johannesburg, South Africa E-mail: mm.sibanyoni@webmail.co.za or Maxwell.sibanyoni@enel.com

** S.P. Chowdhury, Tshwane University of Technology Dept. of Electrical Engineering Faculty of Engineering and the Built Environment, Pretoria 0001, South Africa E-mail: spchowdhury2010@gmail.com

Abstract: The South African Renewable Energy Independent Power Producer Procurement Programme (REIPPPP) is currently in its fourth round with a capacity of 5 243 MW already procured. With the increase in renewable energy installations together with some municipalities allowing commercial and residential sectors to feedback energy to the grid, results in new problems which need to be studied so that measures can be put in place to address them. This research seeks to address the synchronization problems with high degree of penetration of renewable energy generation by solar installations on residential and commercial buildings. This research will be focused on different phase locked loop systems for synchronization of single phase PV inverters. Several possible phase locked loop synchronization methods will be modeled and developed in Matlab Simulink to find the best possible method in the present context of South African grid regulations. This study will develop better single phase inverters to alleviate the current problems of grid synchronization with higher level of solar PV generation to the national grid. It will surpass the difficulties of higher noise sensitivity of the conventional single phase PLL systems for synchronization [9]. The present energy crisis of South Africa needs more generation augmentation predominantly from solar energy. The synchronization problems of high degree of penetration of solar PV energy to the South African grid will be addressed for a better solution.

Keywords: Phase lock loop (PLL), synchronization, solar inverter, PV generation, Point of common coupling (PCC),

1. INTRODUCTION

The cost of solar photovoltaic (PV) installations has reduced significantly over the past 4 years since South Africa started its Renewable Energy Independent Power Producer Procurement Programme (REIPPPP). This ambitious renewable energy drive to diversify on its energy mix with PV generation, being among the targeted generation mix, has led to South Africa being now ranked within the top 10 countries listed in 2014 in the world with PV generation installed capacity of 800MW [6].

Traditionally, the grid-connected PV systems are small scale at a residential level and designed to disconnect from the grid within a certain time tripping by a grid fault. However due to the thriving scenario of large-scale grid-connected single phase PV systems in many distributed installations, the disconnection could cause adverse conditions and negatively impact the reliability, stability, and availability of the distributed grid [10]. To address some of these faults on the grid, solar inverters need to be able to ride through certain faults on the system such as low voltage. The control methods together with grid synchronization techniques are responsible for the generation of appropriate reference signals in order to handle ride-through grid faults [2]. Thus, it is necessary to evaluate the behaviors of grid synchronization methods and control possibilities under grid faults.

Energy in South Africa has reached a crisis level and the country is facing load shedding that is estimated to last for the next three years.

Combined with the global climate change targets to reduce the CO₂ footprint, there is a sudden rush to increase the installation of renewable energy systems in South Africa. The South African energy infrastructure is ageing and requires maintenance and new infrastructure development. When renewable systems or embedded generators are connected to the grid, problems unique to the South African grid scenario are presented. Therefore there is a need to design appropriate systems that will be able to address such specific conditions.

Each utility has its own requirements that need to be met before an embedded generator can be synchronized to the grid. During synchronization many factors have to be considered such as frequency difference, voltage difference and phase angle difference. In order to provide a stable and reliable national grid in South Africa from the renewable energy stand point, inverters that are designed need to be able to provide grid support during faults and normal operation. Therefore it is important that new methods of synchronization and grid support systems are researched for the South African grid scenario. There is an increase of residential PV solar installations in South Africa with more municipalities set to allow feedback to the grid. With the problem of load shedding currently faced by the South African grid system, more advanced inverters that can work off grid are currently

being installed. More residential buildings are having solar systems installed to avoid load shedding and also to minimize their electricity bill as electricity tariffs in South Africa keep on increasing. Most South African residential buildings or houses have a single phase system hence there is a pressing need to research on the synchronization methods for single phase systems for better solutions with robust systems having higher degree of fault ride through capability. Therefore, this study seeks to delve into single phase inverters not the three phase ones.

2. HYPOTHESES

In contrast with the conventional single phase PLL methods, better synchronization methods for single phase inverters with lower noise sensitivity and higher degree of voltage ride through capability can offer better solution for handling high degree of penetration of single phase PV generation to the present South African grid.

3. LITERATURE REVIEW

The margins for the paper should be as given below:

The basic structure of any PLL consists of three blocks: a phase detector (PD), a loop filter (LF) and a voltage controlled oscillator (VCO) [11]. The input of the PLL is a continuous time sinusoidal signal or the zero crossing signals which is compared with output of the VCO in the PD. The high order harmonics in the phase error can be filtered out with the LF and the output modifies the frequency of the VCO. The feedback action is such that the phase error is forced to zero. When zero error is achieved, the input signal is sampled exactly at zero crossings and the PLL is locked [4]. All PLLs have this basic structure and differ mainly through the various methods in the implementation of the PD.

The basic structure of the PLL is given in Fig. 4.

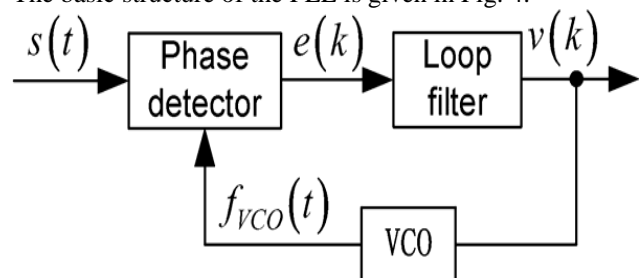


Fig.4. Basic structure of the PLL.

Usually, the main difference among different single-phase PLL topologies is the orthogonal voltage system generation technique. There are different ways of generating the orthogonal voltage system for a single-phase system. The common methods used in the technical literature make use of the transport delay block, Hilbert transformation, Inverse Park transformation. However, these methods have one or more of the following shortcomings: frequency dependency, high complexity,

nonlinearity, poor or no filtering. Therefore, more attention should be paid on single-phase PLL systems [5].

Four typical single-phase PLL topologies will be described which are the T/4 Delay PLL, PLL based on Inverse Park Transform (IPT-PLL), Enhanced PLL (EPLL) and Second Order Generalized Integrator based PLL (SOGI-OSG). The former two methods are trying to build a “dq” system by incorporating an Orthogonal Signal Generator system, while EPLL and SOGI-OSG methods are based on the combinations of adaptive filters with a sinusoidal multiplier and an Orthogonal Signal Generator (OSG) system, respectively [3]. Other single-phase PLL solutions will be reviewed along with none PLL methods will also be reviewed to achieve the goal of developing a better synchronization method that will best suit the South African grid requirements.

The T/4 Delay PLL is an approach that takes the input voltage v_a as the “ α ” component in a “ $\alpha\beta$ ” system, while the “ β ” component can be obtained simply by introducing a phase shift of $\pi/2$ rad with respect to the fundamental frequency of the input voltage. Thus, the Park transform can be employed to detect the phase error,

Where:

$$V_g = V_m \sin(\theta) = V_m \sin(\omega t + \varphi) \quad \text{In which} \quad (1)$$

V_g = Input signal

V_m = Amplitude

θ = Phase

ω = Frequency

φ = Phase angle of the input signal v_g ,

$\Delta\theta = \theta - \hat{\theta}$ = is the detected phase error

$\hat{\theta}$ = locked phase,

The error $\Delta\theta$ is very small in steady state [2]. However, due to the dependence of the input signal period, this kind of PLL technique is not suitable for single-phase systems subjected to voltage sags or frequency variations. In order words, the frequency variation is a challenge to the robustness of T/4 Delay PLL technique.

Below is the structure of the T/4 delay PLL Fig. 5.

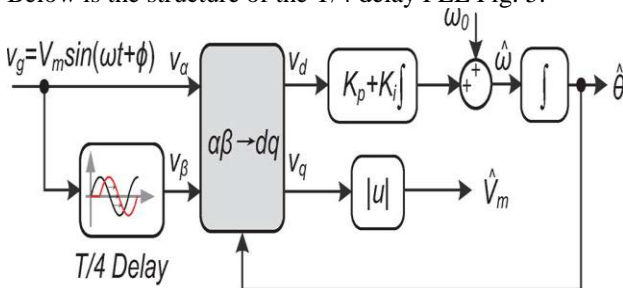


Fig.5. Structure of the T/4 delay PLL.

The Inverse Park Transform ($dq \rightarrow \alpha\beta$) can be used to generate the “ β ” component in order to build an OSG

system, the inverse Park transform based PLL is a good candidate for single-phase applications because it is easy to implement with only two additional low-pass filters compared to conventional PLL methods [2]. A single

phase voltage (v_a) and an internally generated signal (v_β) are used as inputs to a Park transformation block ($\alpha\beta \rightarrow dq$). The d axis output of the Park transformation is used in a control loop to obtain phase and frequency information of

the input signal. v_β is obtained through the use of an inverse Park transformation, where the inputs are the d and q-axis outputs of the Park transformation ($dq \rightarrow \alpha\beta$) fed through first-order low pass filters. However, the incorporated LPFs in this PLL solution must be adequately tuned in order to guarantee the performance.

The Enhanced PLL (EPLL) is essentially an adaptive band pass filter, which is able to adjust the cutoff frequency as a function of the input signal. The EPLL PD system consists of an adaptive filter and a multiplier in such a way that it can enhance the capability with information about the amplitude of the input signal to extract phase error. The objective of enhanced PLL is to track the input voltage in terms of amplitude V_m and

phase angle θ using conventional PLL method to regulate phase error ϵ , the phase angle θ can be locked easily. Thus, the task of adaptive filter is to estimate the amplitude according to the error signal e and the locked phase $\hat{\theta}$. Assuming the PI controller is tuned well and the phase angle is locked, in this case, the adaptive process is to modify the filter parameters in order to minimize a so-called objective function in this way that the amplitude is estimated. One important feature of EPLL concluded from the above discussion is that the

output signal \hat{v}_i is locked both in phase and in amplitude compared to the conventional PLL methods. However it should be noted that the performance, such as the stability and the speed of the estimation process, is exclusively dependent on the control parameter k_a [3].

Another adaptive filtering based PLL solution is using second order generalized integrator (SOGI) to create the OSG system, commonly known as SOGI-OSG PLL. The input signal v is the grid voltage. As output signals, two sine waves (v' and qv') with a phase shift of 90° are generated. The component v' has the same phase and magnitude as the fundamental of the input signal (v). The input signal v (grid voltage) is filtered resulting two clean orthogonal voltage waveforms v' and qv' , due to the resonance frequency of the SOGI at ω (grid frequency) [5].

The SOGI-OSG PLL enables the system to accomplish the three main tasks which are the generation of the orthogonal voltage system, the filtering of the orthogonal voltage system without delay and making the OSG structure frequency adaptive. The SOGI-PLL has a very simple digital implementation and makes it attractive for

applications such as single-phase grid connected photovoltaic inverters. The disadvantage of this PLL is that, during grid voltage frequency changes the estimated frequency will contain a sinusoidal ripple component of twice the fundamental frequency. This error results in harmonic distortion of the unit vectors. The transfer function used in the SOGI block result in a transient frequency error during grid voltage amplitude changes. One method to avoid the unit vector distortion when the grid voltage frequency changes is to make the SOGI-PLL frequency adaptive. This means that the transfer functions used in the PLL must be continuously changed. This increases the complexity in the implementation [8].

The structure of the PD of the SOGI PLL is given in Fig. 6.

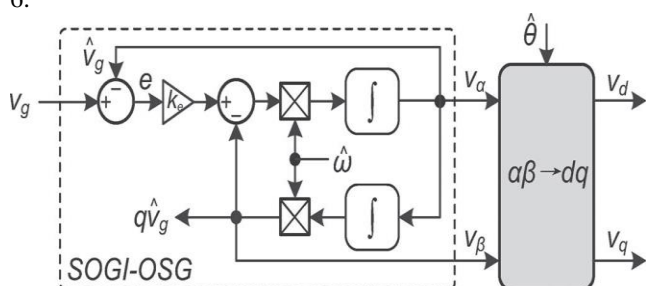


Fig.6. PD of the SOGI PLL.

15. CONCLUSION

This study will develop better single phase inverters to alleviate the current problems of grid synchronization with higher level of solar PV generation to the national grid. It will surpass the difficulties of higher noise sensitivity of the conventional single phase PLL systems for synchronization. The present energy crisis of South Africa needs more generation augmentation predominantly from solar energy. The synchronization problems of high degree of penetration of solar PV energy to the South African grid will be addressed for a better solution.

16. REFERENCES

- [1] Muhammad H Rashid. 2011. Power Electronics Handbook Third Edition. Butterworth-Heinemann. Elsevier's Science & Technology Rights Department in Oxford. UK. 711-750
- [2] Yongheng Yang, Frede Blaabjerg, and Zhixiang Zou. SEPTEMBER/OCTOBER 2013. Benchmarking of Grid Fault Modes in Single-Phase Grid-Connected Photovoltaic Systems. IEEE Transactions on industry applications, VOL. 49, NO. 5
- [3] Yongheng Yang and Frede Blaabjerg. 2012. Synchronization in Single-Phase Grid-Connected

Photovoltaic Systems under Grid Faults. 3rd IEEE International Symposium on Power Electronics for Distributed Generation Systems (PEDG)

- [4] Hua Geng, Jianbo Sun, Shuai Xiao and Geng Yang. May 2013. Modeling and Implementation of an All-Digital Phase-Locked-Loop for Grid-Voltage Phase Detection. IEEE Transactions on industrial informatics, VOL. 9, NO. 2

- [5] Mihai Ciobotaru, Remus Teodorescu and Vassilios G. Agelidis. 2008. Offset rejection for PLL based synchronization in grid-connected converters. IEEE 978-1-4244-1874-9/08

- [6] South Africa's Renewable Energy IPP Procurement Program: May 2014. Success Factors and Lessons

- [7] Saeed Golestan, Mohammad Monfared, Francisco D. Freijedo, and Josep M. Guerrero. JUNE 2013. Dynamics Assessment of Advanced Single-Phase PLL Structures. IEEE Transactions on industrial electronics, VOL. 60, NO. 6

- [8] Abhijit Kulkarni and Vinod John. 2013. A Novel Design Method for SOGI-PLL for Minimum Settling Time and Low Unit Vector Distortion. IEEE 978-1-4799-0224-8/13

- [9] Slobodan Lubura, Milomir Šoja, Srd-an Lale and Marko Ikić. April 2014. Single-phase phase locked loop with DC offset and noise rejection for photovoltaic inverters. IET Power Electronics. Vol. 7, Iss. 9, pp. 2288–2299

- [10] Lakshmanan.S.A, Amit Jain and B. S. Rajpurohit. 2014. Grid Voltage Monitoring Techniques for Single Phase Grid Connected Solar PV system. IEEE 978-1-4799-6046-0/14

- [11] Dong Dong, Bo Wen, Dushan Boroyevich, Fellow. Paolo Mattavelli, and Yaosuo Xue. January 2015. Analysis of Phase-Locked Loop Low-Frequency Stability in Three-Phase Grid-Connected Power Converters Considering Impedance Interactions. IEEE Transactions on industrial electronics, VOL. 62, NO. 1

- [12] Liansong Xiong, Fang Zhuo, Xiaokang Liu, Minghua Zhu, Ying Chen and Feng Wang. 2015. Research on Fast Open-loop Phase Locking Scheme for Three-phase Unbalanced Grid. 978-1-4799-6735-3/15

Potential in utilising ferrochrome furnace off-gas in South Africa: A techno-economic study

R. Murray^{1*}, J.A de Kock¹

¹North-West University (Potchefstroom Campus), Hoffman Street, 2520 Potchefstroom, South Africa

*Email: Ruanmurray1@gmail.com

Abstract: In South Africa the current electrical energy crises and the possibility of carbon tax forces ferrochrome (FeCr) smelters to improve the efficiency of the plant. This can be done by utilising the waste energy available at the plant. This paper presents a techno-economic evaluation of the utilisation of furnace off-gas, rich in carbon monoxide (CO), by using available technologies to convert waste off-gas energy into electrical energy – referred to as co-generation in this paper. The results from three case studies are used to determine the efficiency of the considered technologies (gas-engines, gas-fired boiler and gas turbines). A FeCr smelter in South Africa is used as a case study and the off-gas it produces analysed. The results, both the energy available in the FeCr furnace off-gas and the considered co-generation plants efficiency, are used to determine the potential of the various systems to generate electrical energy. Using the established potential an economic evaluation is conducted on both the existing co-generation plants (case studies) and the considered FeCr smelter co-generation plants. In this paper the potential of a co-generation plant is evaluated for implementation at a ferrochrome smelter. The most feasible system is identified using the results from the techno-economic analyses.

Index terms - Co-generation, electrical energy, ferrochrome smelter, gas-fired boiler, gas engines, gas turbines, off-gas, waste energy.

1 INTRODUCTION

Carbon dioxide (CO₂) emissions contribute to about 80% of the total greenhouse gas (GHG) emissions in South Africa [1], which has one of the most carbon-intensive economies in the world [2]. It was announced that carbon tax would be introduced as from January 2016, at a rate of R120/t on 20% to 40% of the carbon emissions – equated estimated rate of between R24/t and R48/t [3] [4].

With the introduction of carbon tax and the electrical energy supply from Eskom being regarded by some as unreliable, a smelter plant needs to look at ways to reduce its electrical energy consumption and with that carbon emissions. One option for doing this is to use waste energy (off-gas) to generate electrical energy.

2 PROBLEM STATEMENT

In this paper the potential in generating electrical energy from ferrochrome furnace off-gas is analysed. Details of the available off-gas (volume, composition and energy) are used to evaluate different co-generation plants. The efficiency of these co-generation plants are established with two case studies and from that the electrical energy that could be generated at the FeCr smelter determined.

The most feasible co-generation plant is identified using the electrical energy generation potential, as well as the estimated economic results, of each considered project.

3 FERROCHROME SMELTER

The studied ferrochrome (FeCr) smelter plant in South Africa has two submerged arc AC furnaces of 55 MVA each.

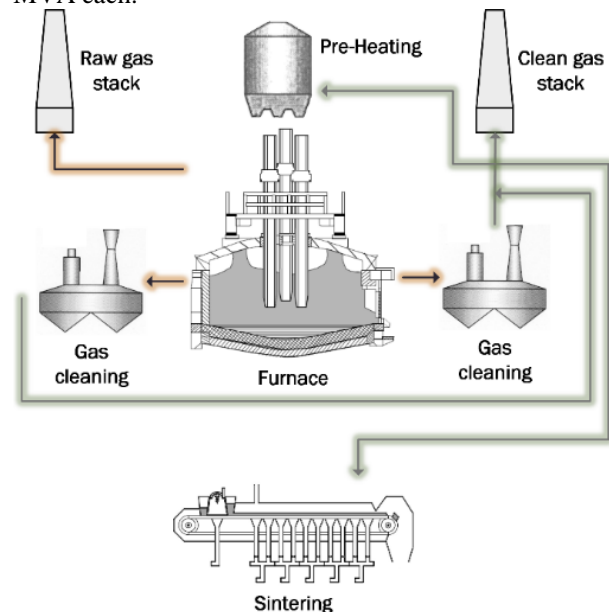


Fig. 1 Ferrochrome smelter off-gas flow diagram

In the process of producing FeCr a by-product in the form of CO-rich off-gas is formed. The off-gas, produced by the two furnaces, is supplied to the sinter plant (1 200 Nm³/h) and furnace pre-heaters (1 000 Nm³/h per pre-heater). In the pre-heaters the off-gas is used to supply thermal energy to the furnace feed, before it is fed to the furnace. Fig. 1 shows the flow of the produced off-gas

from the furnace, after which it is cleaned by venturi scrubbers and then supplied to the users.

3.1. Gas analysis

An off-gas analysis was conducted to determine the energy available. The characteristics (composition, volume and available energy) of the produced FeCr furnace off-gas is considered in this section.

3.1.1. Composition

The off-gas composition was measured by an independent stationary source emission specialist. The composition of the off-gas is given in Table. 1.

Table. 1: Ferrochrome furnace off-gas composition

Component	Volume (%)
CO	59
H ₂	5
CO ₂	16
N ₂	19
CH ₄	0.85

Using the gas composition shown in the table, the off-gas density is calculated as 1.2 kg/Nm³.

3.1.2. Volume

The off-gas volume, produced by the furnaces, was calculated using the assumption that 300 Nm³/h of off-gas is produced per furnace MW. This is done, because no flow meters are installed at the furnaces to measure the off-gas production. Independent measurements were done to verify this assumption.

Fig. 2 shows the monthly average load of each furnace and the total volume produced. The monthly produced off-gas volume was calculated using the daily energy consumption of the furnaces. From June to August a reduced off-gas production was noticed, caused by furnace shut-downs. The sinter plant also had a shut-down during April.

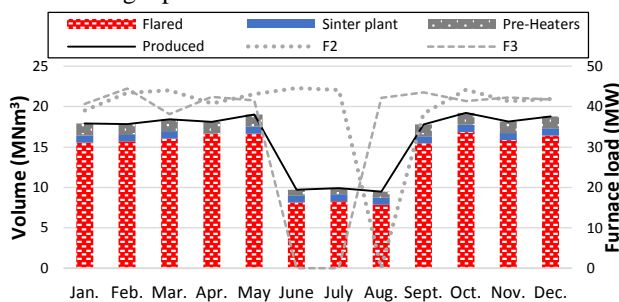


Fig. 2: Off-gas volume production at the FeCr smelter

As mentioned, the off-gas is used for a few purposes at the FeCr smelter. This includes the furnace pre-heaters (installed at each furnace), off-gas used to pre-heat furnace feed, and the sinter plant. Fig. 2 shows the off-gas utilisation and the remaining volume flared at the furnaces.

On an annual basis 194.3 MNm³ (16 MNm³ monthly average) of off-gas is produced of which 9.6 MNm³ and

15.3 MNm³ is utilised by the sinter plant and pre-heaters, respectively. This means that an annual volume of 169.4 MNm³ is available (flared) for utilisation at the FeCr smelter plant.

3.1.3. Energy

Using the off-gas composition (Table. 1) and the lower heating values of CO (10.1 MJ/kg or 2.81 kWh/kg), H₂ (120 MJ/kg or 33.33 kWh/kg) and CH₄ (49.8 MJ/kg or 13.83 kWh/kg) [5], the calorific value (CV) of the off-gas was calculated as 1.78 kWh/kg. By using the off-gas density, this gravimetric CV can be converted to a volumetric value of 2.14 kWh/Nm³.

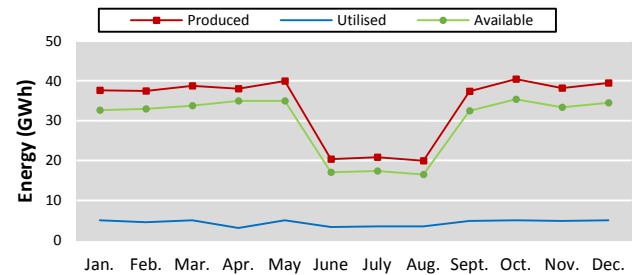


Fig. 3: Off-gas energy at the FeCr smelter

The volumetric CV and the produced off-gas volume was used to determine the off-gas energy (in GWh), given in Fig. 3. Again, a reduction in off-gas energy is noticed during the months of June, July and August (due to furnace shut-downs).

On an annual basis the off-gas energy produced equates to a total of 408 GWh (47 MW). Of this total, 53 GWh (6 MW) is used by the plant and 355 GWh (41 MW) flared at the furnaces. This means that 355 GWh of off-gas energy is available for electrical energy generation on an annual basis.

3.2. Electrical energy consumption

In Fig. 4 the monthly electrical energy consumption of the smelter plant is shown. It was also used in the following section to determine the carbon dioxide emissions.

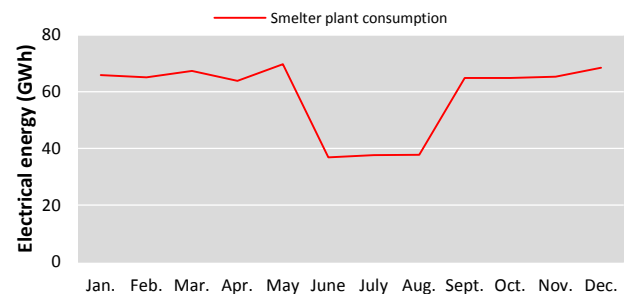


Fig. 4: Electrical energy consumption of the FeCr smelter plant

This figure shows that June, July and August were used for furnace shut-downs and maintenance. This resulted in a reduction in electrical energy consumption during those months. The furnace shut-downs were scheduled for these months as this is the high-demand

season, which means that electrical energy is charged at a higher rate during these months.

On average the smelter plant consumes 59 GWh of electrical energy per month. This results in a total annual consumption of 707 GWh (81 MW).

3.3. Carbon emissions

The annual carbon dioxide (CO₂) emission estimation is given in Fig. 5. In this figure two forms of emissions are shown. This includes the plant emissions, caused by the flaring of the produced off-gas, and the indirect emissions owing to electrical energy consumption. The latter was calculated using the smelter plant electrical energy consumption and a carbon emission factor of 1.09 kg of carbon dioxide per kWh generated by Eskom [6].

The annual plant emission equates to 287 kt of CO₂ and the indirect emissions add another 771 kt. This means that the plant is responsible for 1 058 kt of CO₂ emissions per annum.

Fig. 5 shows that if both furnace are operating in a specific month that an average of 100 kt of CO₂ is emitted.

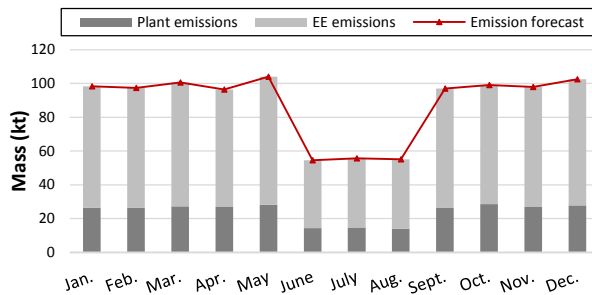


Fig. 5: Carbon dioxide emission estimation by the FeCr smelter

In the following sections the estimated off-gas energy available, electrical energy consumption and annual carbon emissions are used to determine the potential of co-generation plants at the FeCr smelter. The efficiency of two of the co-generation plants was determined by using the results from two case studies.

4 CASE STUDIES

Case studies were conducted on two smelter plants in South Africa, which use their off-gas to generate electrical energy. The off-gas, smelter plant and co-generation plant characteristics of each were established. A summary of these characteristic values (per annum) are given in Tab. 2.

In this table, smelter plant I represents an ilmenite smelter plant that produces Fe and TiO₂ and smelter plant II a ferromanganese (FeMn) smelter plant. Smelter plant I has two DC-arc furnaces (25 MW and 35 MW) and smelter plant II has four AC-arc furnaces (40 MW each).

Tab. 2: Summary of established smelter plant values and furnace off-gas characteristics

	Unit	Smelter plant I	Smelter plant II
CO	Vol. (%)	74	56
H ₂	Vol. (%)	16	9
CO ₂	Vol. (%)	2	14
N ₂	Vol. (%)	8	20
CH ₄	Vol. (%)	-	1
CV	kWh/Nm ³	2.76	2.17
Off-gas volume (produced)	MNm ³	83.2	420
Off-gas volume (available)	MNm ³	79.9	411.2
Off-gas energy (available)	GWh	226	893
	MW	25.8	102
Electrical energy consumption	GWh	523.5	1 364
	MW	60	155.7
Carbon emission forecast	kt	680	2 024

4.1. Co-generation plant layout

Both of the considered smelter plants have co-generation plants installed. Smelter plant I has a gas-engine co-generation plant and smelter plant II a gas-fired boiler with a steam turbine-generator.

4.1.1. Smelter plant I (TiO₂)

The co-generation plant, installed at smelter plant I, was designed to supply the off-gas to gas engine-generators. In this plant (see the layout in Fig. 6) the gas flows from the two furnaces into a dry-seal gas holder (3 200 m³), where the gas mixes. The off-gas is supplied to the engines via three gas trains (each rated at 8 000 Nm³/h), of which only two are required. The third gas train is used for emergencies and when maintenance is done on another gas train.

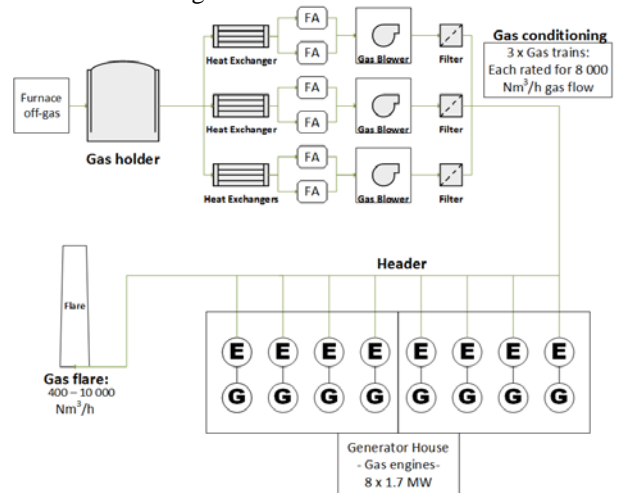


Fig. 6: Gas engine co-generation plant layout at the TiO₂ smelter plant

Each gas train has a heat exchanger (to reduce temperature and moisture), two parallel connected flame arrestors (protects gas holder), a gas blower (increases

the gas pressure and temperature) and also a filter (removes particles greater than $3 \mu\text{m}$ and reduces the dust load to under 10 mg/Nm^3). In order to regulate the header pressure some gas needs to be flared at the co-generation plant.

Eight gas engine-generator sets (1.7 MW each) were installed. They generate electrical energy at 11 kV and supply electrical energy to the smelter grid.

4.1.2. Smelter plant II (FeMn)

The second co-generation plant has a simpler layout, (see Fig. 7). In this co-generation plant the furnace off-gas, from the four furnaces, is fed to a gas-fired boiler. The boiler-produced steam is fed to a 50 MW steam turbine-generator. Low-pressure steam exists the steam turbine and flows to a dry-cooling condenser, where the steam is reduced to water. This water is again fed to the boiler.

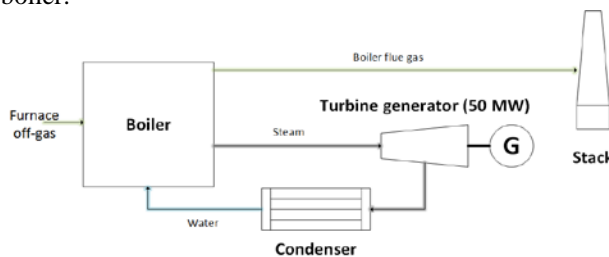


Fig. 7: Gas-fired boiler co-generation plant layout at the FeMn smelter plant

Fig. 7 shows the basic layout of this co-generation plant and only includes the major components. The boiler in this figure includes an economiser, evaporators, boiler drum, boiler furnace, super heaters, attemperators and an LP heater. The thermal energy in the boiler flue gas is utilised by the economiser and super heaters before being emitted via the plant stack.

4.2. Technical evaluation

Data regarding the performance of each co-generation plant was gathered and analysed. Tab. 3 shows the annual results for the two plants.

Tab. 3: Technical evaluation results of the co-generation plants

	Unit	Smelter plant I	Smelter plant II
Plant size	MW	13.6	50
Off-gas energy to plant	GWh	226	743
	MW	25.8	85
Off-gas energy to generating unit(s)	GWh	170	743
	MW	19.4	85
Electrical energy exported	GWh	63.6	174.6
	MW	7.3	20
System efficiency	%	28	23
Electrical savings	%	12	13
Carbon reduction	kt	70	191
	%	10	9
Plant utilisation	%	76	89
Off-gas utilisation	%	72	80

Of the two plants, the gas-fired boiler plant (at smelter II) produced the most off-gas energy and also generated more electrical energy. The gas engine plant (smelter I) has the greater efficiency (calculated by comparing the off-gas energy supplied to the plant with the electrical energy generated and exported the smelter grid).

A large volume of the off-gas is flared by the gas engine co-generation plant to regulate the header pressure and because of an insufficient number of engines. This causes a reduction in the system efficiency (engine-generators have an efficiency of 37%). It also results in a lower off-gas utilisation, which is the percentage of the available off-gas that is used by the co-generation plant.

The gas-fired boiler co-generation plant has a greater percentage plant utilisation, because it has four furnaces supplying it with off-gas. This plant utilisation was determined by calculating the percentage of the year in which the co-generation plant generates electrical energy, not necessarily at full load.

The results show that both co-generation plants reduces the electrical energy purchased from Eskom and also causes a reduction in secondary carbon emissions, by similar percentages.

4.3. Economic evaluation

An economic evaluation was done for each plant using the results in the previous section. In this economic evaluation the estimated project cost of each plant was calculated for 2015, using adjusted project costs. The results for each project are shown in Tab. 4.

Tab. 4: Economic evaluation results for the co-generation plants

	Unit	Smelter plant I	Smelter plant II
Capital cost	R (million)	300	465
Operating cost	R (million)	20	42
NPV	R (million)	-79	373
IRR	%	5.5	21.27
SPP	Years	11.75	4.67
DPP	Years	24.03	6.64

A discount rate of 10% and a project lifespan of 15 years was used. The only cash inflow of each project was the electrical energy savings per annum. In the cash flow projection major services and required shut-downs were taken into account.

From these results the gas-fired boiler co-generation plant (smelter II) has the greater project and operating costs. Even with the greater costs, this project has the better net present value (NPV), internal rate of return (IRR), simple payback period (SPP) and discounted payback period (DPP). The DPP takes into account the time-value of money and the SPP does not.

The gas-fired boiler project is the better performer of the two, if both the technical and economic results are taken into account. This is mainly because more off-gas (energy) is available at smelter plant II. The gas engine plant has the higher efficiency and also the lower project and operating cost. In the following section the case study

data is used to determine the potential of similar co-generation plants at the considered FeCr smelter.

5 CO-GENERATION PLANTS

Three co-generation plants were considered for implementation at the FeCr smelter. Two of which are similar to the plants discussed in the case studies (gas engines and gas-fired boiler). The third is a gas turbine plant, which has not yet been implemented in South Africa, but some details were gathered regarding turbines that could be used for this purpose.

5.1. Layout

First a gas-engine co-generation plant with 12 units (based on the available off-gas) was considered. Fig. 8 shows a simple layout of this plant. This plant has a larger gas holder, more engines and four gas trains, when compared to the case study. The gas holder is installed after the gas cleaning plants (GCPs).

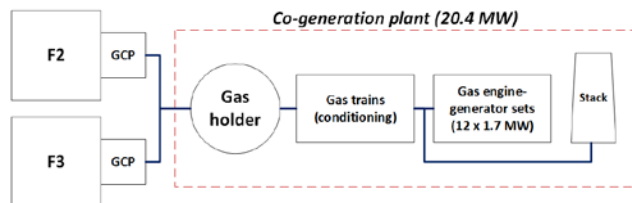


Fig. 8: Basic layout of a possible gas engine co-generation plant at the FeCr smelter

The second plant (Fig. 9) is also similar to the gas-fired boiler plant, discussed previously. The only difference is that a smaller steam-turbine generator and boiler are required, because the FeCr smelter only has two furnaces (less off-gas is produced).

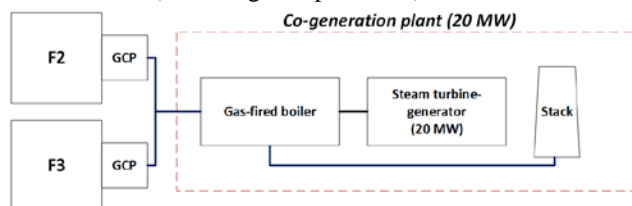


Fig. 9: Basic layout of a possible gas-fired boiler co-generation plant at the FeCr smelter

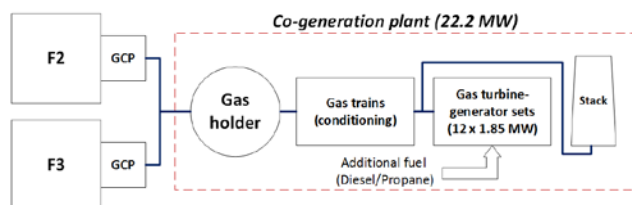


Fig. 10: Basic layout of a possible gas turbine co-generation plant at the FeCr smelter

As mentioned, a third plant (turbines) was also considered for implementation at the FeCr smelter. A gas turbine plant would require additional high CV fuel, propane or diesel, for the full time of operation. The

required fuel would be around 1 025 Nm³/h of off-gas, with an additional 440 ℓ/h of diesel or 178 m³/h of propane. This equates to 31.2 Mℓ of diesel or 12.6 Mm³ of propane per annum.

The gas turbine plant (Fig. 10) has a gas holder and gas condition trains with 12 turbine-generators (1.85 MW each).

5.2. Potential

Tab. 5 shows the potential of the considered co-generation plants, where the electrical energy generation is calculated using the established system efficiency and the available off-gas utilised. Because of the additional high CV fuel the gas turbine plant would generate the most electrical energy.

All of the plants have an installed capacity of around 20 MW and would save the FeCr smelter between 12% and 19% on its electrical energy purchases.

Tab. 5: Potential of each co-generation plant at the FeCr smelter plant

	Unit	Engines	Boiler	Turbines
Plant size	MW	20.4	20	22.2
System efficiency	%	28	23	19
Electrical energy generation	GWh	99	81	124
	MW	11.3	9.2	14
Electrical saving	%	14	12	19
CO ₂ emission	kt	108	88	135
reduction	%	10	8	13

The system efficiency shown in the table, takes into account reduced plant and off-gas utilisation. This is also the reason why the turbine plant has a lower efficiency, because the turbines would not be able to utilise all of the available off-gas and additional turbines (also additional propane/diesel) would be required.

It is also worth mentioning that the gas engine plant has the potential to have an improved efficiency. The gas engine-generators have an efficiency of 37% and the 12 engines will be able to utilise all of the available off-gas. This means that the system efficiency could be increase to at least 32%, if the minimum volume of off-gas is flared at the co-generation plant. This would result in electrical energy generation of 113 GWh (12.9 MW), resulting in a 16% saving and additional CO₂ emission reductions.

In the following section the results, shown in Tab. 5, are used to conduct an economic evaluation on the considered co-generation plants.

6 ECONOMIC EVALUATION

In the economic evaluation calculations a discount rate of 10% was used for each project with a project lifespan of 15 years. All the capital costs were converted to a present value (2015) and the operating and

generating costs to a future value (2016). In these results no carbon tax was taken into account.

6.1. Costs and results

Tab. 6 shows the results for each project. The results show that the gas turbine plant has the highest capital cost, operating cost (includes capital for additional propane/diesel) and electrical energy generation cost. The boiler plant has the lowest capital cost and the gas engine plant the lowest operating cost per annum.

Tab. 6: Economic evaluation results for the considered co-generation projects at the FeCr smelter

	Unit	Engines	Boiler	Turbines
Capital cost	R (million)	491	421	550
Operating cost	R (million)	31.3	36.8	304
Generating cost	R/kWh	0.32	0.46	2.48
NPV	R (million)	-25	-180	-1 957
IRR	%	9.2	2.0	-
SPP	Years	8.65	14.25	-
DPP	Years	16.51	63	-

The considered gas turbine plant would be uneconomical, mainly because of the additional fuel and the added capital cost. For this reason the gas turbine plant is disregarded in the following sections.

A gas engine plant would be the most feasible option.

6.2. Cash flow

The 15-year cash flow for each project is given in this section. The major maintenance and services required for each plant were included in these cash flows.

Fig. 11 and Fig. 12 shows the cash flows of both the gas engine and gas-fired boiler plants. With the gas engine plant major services occur during years 5, 6, 11, and 12. The boiler plant has a boiler inspection every two and a half years, during which the plant has a two month shut-down.

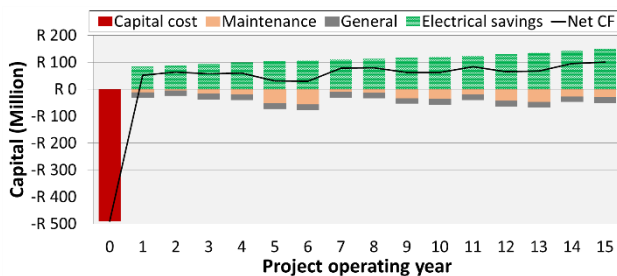


Fig. 11: Gas engine co-generation project cash flow projection

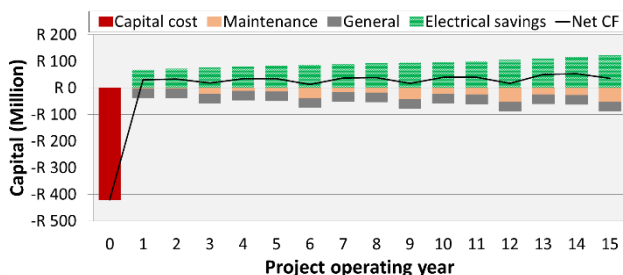


Fig. 12: Gas-fired boiler co-generation project cash flow projection

In both of the cash flow graphs the annual operating expenses are divided into general expenses and maintenance costs. The only cash flow income is represented by the electrical savings, where the same annual cost per kWh is used for each project.

The net cash flow (CF) is positive for each of the 15 years, which means that the plants have a positive annual revenue. Of the two, the gas engine plant has a more positive cash flow.

6.3. Generating costs

Using the established cash flows, the annual generating cost per kWh was calculated (see Fig. 13).

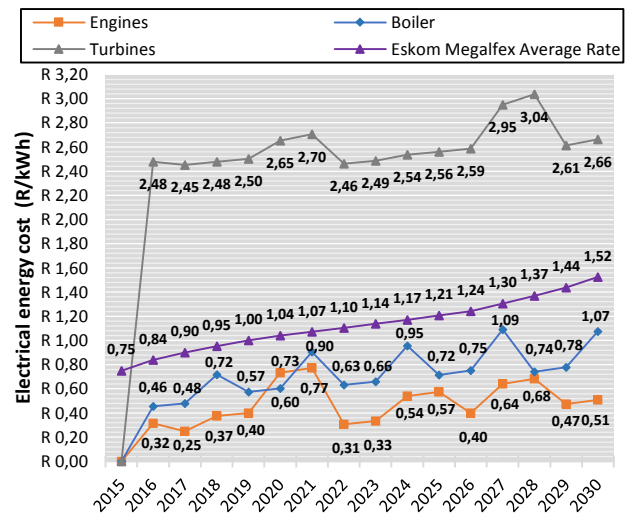


Fig. 13: Electrical energy generating costs for the considered co-generation plants at the FeCr smelter

In this figure both of the gas engine and gas-fired boiler co-generation plants can be seen to generate electrical energy at a cheaper rate, if compared to the average estimated Eskom Megaflex tariff forecast. Of the three, the gas engine plant generates electrical energy at a cheaper rate.

6.4. Sensitivity analyses

Sensitivity analyses were conducted for each project to establish what influence a change in certain parameters would have on the NPV and IRR of each project.

The change in each project's NPV and IRR because of the change in the electrical energy price (Eskom), off-gas utilisation, plant utilisation, system efficiency and the capital cost are shown in Tab. 7 and Tab. 8.

Of all the considered variables, the change in the system efficiency has the greatest effect on both the NPV and IRR. With a system efficiency of 32% for the gas engine plant, for example, a NPV of R90 million (R115 million increase) and an IRR of 12.8% (3.6% increase) could be achieved

Tab. 7: NPV sensitivity of considered co-generation projects at the FeCr smelter

	Gas engines			Gas-fired boiler		
	-10%	0%	+10%	-10%	0%	+10%
R/kWh	-R106	-R25	R56	-R247	-R180	-R144
Gas util.	-R115	-R25	R64	-R254	-R180	-R106
Plant util.	-R133	-R25	R82	-R225	-R180	-R107
System eff.	-R315	-R25	R265	-R470	-R180	R109
Capital cost	R24	-R25	-R74	-R138	-R180	-R222

Of all the considered variables, the change in the system efficiency has the greatest effect on both the NPV and IRR. With a system efficiency of 32% for the gas engine plant, for example, a NPV of R90 million (R115 million increase) and an IRR of 12.8% (3.6% increase) could be achieved.

Tab. 8: IRR sensitivity of considered co-generation projects at the FeCr smelter

	Gas engines			Gas-fired boiler		
	-10%	0%	+10%	-10%	0%	+10%
R/kWh	6.4%	9.2%	11.8%	-1.9%	2.0%	5.2%
Gas util.	6.0%	9.2%	12.0%	-2.3%	2.0%	5.5%
Plant util.	5.4%	9.2%	12.6%	-2.4%	2.0%	5.6%
System eff.	-2.8%	9.2%	17.8%	-13.8%	2.0%	14.0%
Capital cost	10.9%	9.2%	7.8%	3.4%	2.0%	0.8%

7 RESULTS AND DISCUSSION

The results from the two case studies showed that the gas-fired boiler with the steam turbine generator was the best performing plant. This was because the four furnaces at the FeMn smelter produced a greater volume of off-gas.

Similar co-generation plants were identified for implementation at the FeCr smelter. Here, the gas engine plant was the most feasible option. This was mainly because of the greater efficiency of the system, which results in more electrical energy generation.

This gas engine plant could generate 99 GWh of electrical energy per year, at R0.32/kWh (2016), and would cost around R421 million in 2015. With a 28% system efficiency the NPV is equal to -R25 million and the IRR 9.2%. The project also has a DPP of 16.51 years. An improved efficiency (32%) would result in an NPV of R90 million, an IRR of 12.8% and a DPP of 11.76 years.

In the economic evaluations no carbon tax was considered. If carbon tax was implemented at a rate of R48/t (R120/t on 40% of emissions) in 2016, the FeCr smelter plant could save a further 5-10% (R1.8 million to R3.4 million) per annum on carbon tax. This was calculated on the 287 kt direct emissions at the FeCr smelter.

8 CONCLUSION

This paper shows that there is a lot of potential in using ferrochrome furnace off-gas to generate electrical energy. By doing this the smelter plant will reduce the

amount of electrical energy purchased from Eskom and the CO₂ emissions for which the FeCr smelter is responsible.

A gas engine co-generation plant was identified in this paper as the most feasible option for doing this at the FeCr smelter. The economic performance of this investment would improve if carbon tax is implemented. A good plant design could also result in an improved efficiency and with that an improved feasibility.

Only certain technologies were considered in this study and other options do exist for utilising the furnace off-gas, which can also be evaluated. Some additions can also be made to the systems considered, e.g. the engine flue gas can also be used for heating purposes or for additional power generation. Further studies would be required to determine the feasibility of such options.

This paper shows that energy is available for utilisation at smelter plants and that well-established technologies exist for doing this. A FeCr smelter plant was considered in this study, but the results can be adapted and used for other smelter plants.

It is clear that co-generation plants can improve the overall efficiency and profitability of a smelter plant in South Africa.

9 ACKNOWLEDGMENTS

The authors would like to thank Namakwa Sands, Meyerton and Boshhoek smelters, Opra Turbines and Clarke energy.

10 REFERENCES

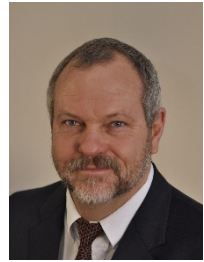
- [1] A. Pegels, "Renewable energy in South Africa: potentials, barriers and options for support," *Energy Policy*, vol. 38, no. 9, pp. 4945-4954, 2010.
- [2] T. Alton, R. Davies, F. Hartley, K. Makrelov, D. Ubogu, C. Arndt and J. Thrulow, "Introducing carbon taxes in South Africa," *Applied Energy*, vol. 116, pp. 344-354, 2014.
- [3] L. Peyper, "Government's mind made up on carbon tax.," in *Finweek*, 2013.
- [4] National Treasury, "Carbon Tax Policy Paper," May 2013. [Online]. Available: <http://www.treasury.gov.za/public%20comments/Carbon%20Tax%20Policy%20Paper%202013.pdf> f. [Accessed 1 September 2015].
- [5] W. W. Pulkrabek, *Engineering fundamentals of the internal combustion engine*, Harlow, Essex: Pearson Education, 2014.
- [6] Eskom, "CDM calculations," January 2015. [Online]. Available: http://www.eskom.co.za/OurCompany/SustainableDevelopment/Pages/CDM_Calculations.aspx. [Accessed 5 September 2015].

AUTHORS BIOS AND PHOTOGRAPHS



Ruan Murray holds a BEng (2013) in Electrical and Electronic Engineering from North-West University, Potchefstroom campus, in South Africa. He was a post-graduate (MEng) student, focusing on waste energy utilisation, at the North-West University, Potchefstroom campus, in South Africa. His academic interests

include energy efficiency, system optimisation and power quality. He is now an employee at Glencore Alloys.



Jan A. de Kock holds a BEng (1985), MEng (1987) and PhD (1991) in Electrical Engineering from Stellenbosch University in South Africa. At present he is a Professor in Electrical Engineering at the North-West University, Potchefstroom campus, in South Africa. His academic and consulting interests include power system dynamic performance. Power quality, protection performance, and optimisation studies, improvements of generator dynamic response, induction

and synchronous machine transient performance, high speed bus transfer systems and energy efficiency. He is the author of a number of papers and the co-author of a book.

Presenting author: The paper will be presented by R. Murray

NMMU South Campus Ring Feeder Protection: Design and Analysis

Llewelyn Grobler
Electrical Department
Nelson Mandela Metropolitan University
Port Elizabeth, South Africa
s211251399@live.nmmu.ac.za

Anthony Marks
Electrical Department
Nelson Mandela Metropolitan University
Port Elizabeth, South Africa
Anthony.Marks@nmmu.ac.za

Abstract—The increasing demand for continuous and reliable supply of electricity in distribution networks has taken its toll and the old fashioned radial systems is rapidly being replaced with ring feeders. The ring feeder system ensure that the supply of electricity to any substation within that ring will be reliable and always available even if any feeder in that ring is disconnected. Ring feeder systems pose problems with the protection design for the system. This is dependent on the size of the ring and the maximum tripping time the supply authority issued to the client. Larger ring feeder system poses slower tripping times for the most upstream relays when normal IDMT over current and earth fault protection is applied. Analysis on ring-feeder protection design with the use of directional overcurrent, directional earth fault and differential feeder protection discussed. DigSilent Power Factory used to do the analysis on the protection design.

Keywords— ring feeder protection; differntial protection; directional protection; back-up protection; time zone differential protection

I. INTRODUCTION

This The MV distribution network of NMMU's South Campus in Port Elizabeth consists of four MV rings [1]. Two rings are sole parallel feeders to one substation, the other ring consists of only two substations and then the last ring has nine substations with four radial feeders [1]. The current protection equipment installed are very outdated electromechanical relay technology [1]. This implied already slow tripping times from the grading margin of 0.4s applied to the protection design [1]. With the use of ring, feeder's reliability of the supply exists but the protection may be compromised [2]. Ring feeder systems poses problems with grading, timing and selectivity of the protection design [2]. The two main solutions to the problem is by implementing directional overcurrent and directional earth fault protection or by implementing feeder differential protection [1].

With directional protection the need of voltage measurement comes in to paly while with differential protection the need of fiber optic communication mediums between the relays are needed [2, 3].

With the aim to get in below the maximum tripping time issued by the supply authority the analysis with the directional protection for on three different ring layouts is shown and grouping of the substations were done to improve the trip time [1]. The first layout considered is the existing layout of the system. The creation of two alternative layouts, for the purpose

of increased reliability and selectivity of the directional protection scheme has been modeled [1]. The different layouts were modelled on DigSilent Power Factory and full analysis was done on the results gathered [1].

With the differential protection the analysis was done by an (n-1; n-2; n-3) scenario explanation [1].

II. FEEDER DIFFERENTIAL PROTECTION

The "In-Zone-Fault" is a fault on the protected object, the equipment or cable, that the differential protection scheme protects [2, 4, 5]. "Out-of-Zone-Fault" is when a fault occurs outside the protected zone, it is a fault that is not between the differential relays, or differential CT's [2, 4, 5].

The new digital differential protection relays have two back up over current and earth fault settings [3, 6]. The 1st setting applied is a back-up protection setting that will be enabled when the communication medium has been lost. When the system is running and the communication medium was broken for some, the relay will then ignore differential protection and go over to normal over current and earth fault protection [3, 6]. The 2nd setting is a back-up protection setting that is active while the differential protection is active, this setting is used to protect the equipment or feeder that are on the network in the case of extreme out of zone faults [3]. When there is a through fault (out-of-zone-fault) and the magnitude of the fault current is above the cable rated fault current or above the other equipment rated fault current level this back-up protection will then trip the breakers on both sides of the differential protection zone. Both these back-up protection settings have inverse curves and a high-set element protection function [3, 6]. The differential protection can trip in a time as low as 50ms [3].

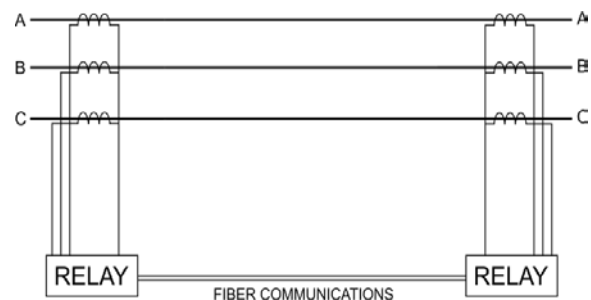


Fig. 1. Feeder Differential Protection via Fiber [1]

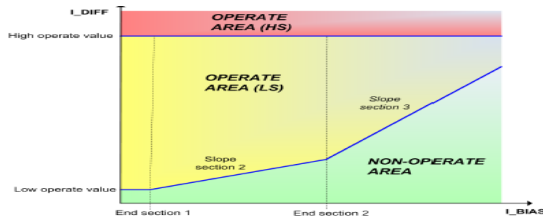


Fig. 2. Operating Characteristics of the differential protection [3]

III. DIRECTIONAL PROTECTION

Directional protection is a protection method that will look at the fault direction [7-9]. The direction of the fault is determined by the angle between the voltage and the current of each phase [7-9]. The relay can be set-up to either look in the forward or reverse direction [7-9]. With a setting applied, the relay will ignore faults in the reverse direction and trip for faults in the forward direction, or vice versa. The directional protection scheme needs a VT measurement input to the relay to determine the direction of the fault [7-9].

IV. GRADING MARGIN

The grading margin is a time delay between relays to compensate for the following:

- CB arc clearing time
- Relay Overshoot
- Relay and CT errors [2]

The Grading Margin proposed by NPAG is 0.4 – 0.3 seconds [2, 10]. As technology changes, so does the relays, CB's, CT's and grading margin change. The new acceptable grading margin for digital microprocessor relays combined with new fast tripping CB's is 0.2s [11, 12].

The Practical Power System Protection Book and the Electric Distribution Systems Book shows that if newer modern digital relays are used the grading margin can be taken down from 0.4 seconds 0.2 seconds [11, 12].

V. OVERCURRENT PROTECTION

The relay can operate on different curves such as, SI – Standard inverse curve, VI – Very inverse curve and EI – Extreme inverse curve [2, 13]. This means that the relay will operate in a certain amount of time under fault conditions depending on the fault size [2, 13]. The greater the fault the quicker the relay will initiate a trip. The relay will also have a definite time setting or also known as the high set stage of operation. Here much higher fault current will trip as fast as possible, usually in 50ms [2, 13].

VI. EARTH FAULT PROTECTION

Earth Fault protection is a protection method that protects either a feeder or other MV equipment against heavy earth fault currents [2, 14]. To use earth fault protection the protection design does not need a separate earth fault relay [2, 14]. The connection of the residual circuit is across the zero sequence filter of the relay [2, 14]. The earth fault element will operate exactly like the above-mentioned overcurrent elements, also

with different tripping curves and plug setting set by the engineer [2]. The plug bridge setting must be set in such a way that the relay would not trip on zero sequence current that flows because of imperfections in the CT's. Usually the setting should not be lower than 10% of nominal current [2, 14]. The PBS setting for earth fault was calculated by using 30% of the rated current of the cable [2].

VII. SOLUTIONS

A. Alternative 1 – Directional Protection Ring Layout

This layout of the rings is the actual layout of the substations at present. The system with this layout was modelled on DigSilent Power Factory.

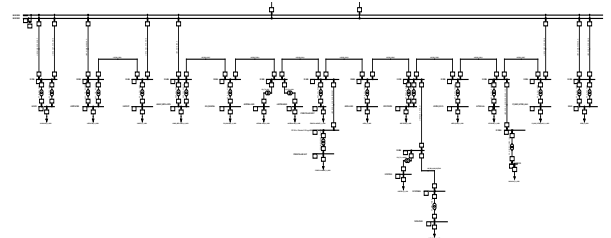


Fig. 3. Existing layout of the NMMU Substations [1]

B. Alternative 2 – Directional Protection Ring Layout

With this layout, the large ring was split in two rings, one ring with four substations and the other with five substations. The system with this layout was modelled on DigSilent Power Factory.

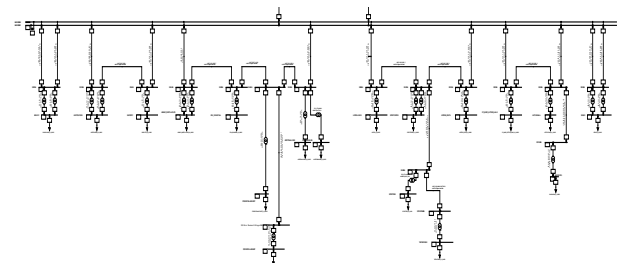
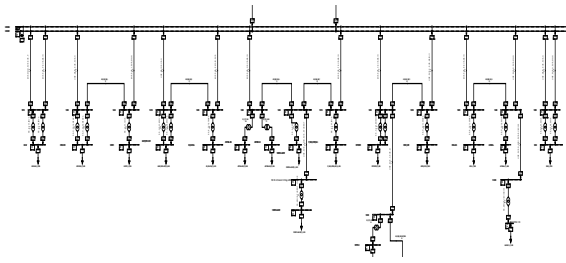


Fig. 4. Layout of the NMMU Substations for the 2nd Alternative Solution [1]

C. Alternative 3 – Directional Protection Ring Layout

This layout has two parallel feeders, four rings with two substations and one ring with three substations. The system with this layout was modelled on DigSilent Power Factory.

Fig. 5. Layout of the NMMU Substations for the 3rd [1]

D. Alternative 4 – Differential Time Zone Protection

This layout of the rings is the actual layout of the substations at present. This is the same layout as the Alternative 1 layout.

VIII. ANALYSIS

A. Curves Crossing

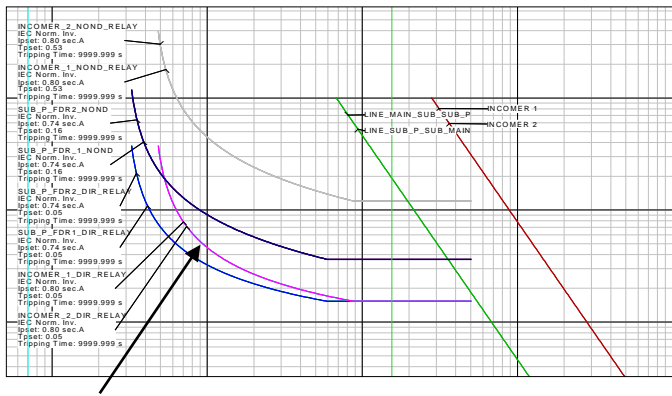


Fig. 6. Over Current Plot – Ring P [1]

The curves that is shown here is the curves of INCOMER-1-DIR-RELAY and INCOMER-2-DIR-RELAY. The curves, which are on top of each other, are allowed to cross with other curves. These curves are for the most upstream cable protection and it crosses with more downstream relay curves. These curves were shown to prove that they would not trip for faults, which is opposite to their chosen direction. Therefore, all the other plots that follows will have the same statement applied to these two curves.

B. Alternative 1

1) RING O – Anti-Clockwise Over Current Directional Protection

With the ring open, a symmetrical fault at 50% of LINE-SUB-F-SUB-MAIN was simulated. With LINE-SUB-F-SUB-MAIN open the all the current will flow through LINE-MAIN-SUB-SUB-H and so will the fault current.

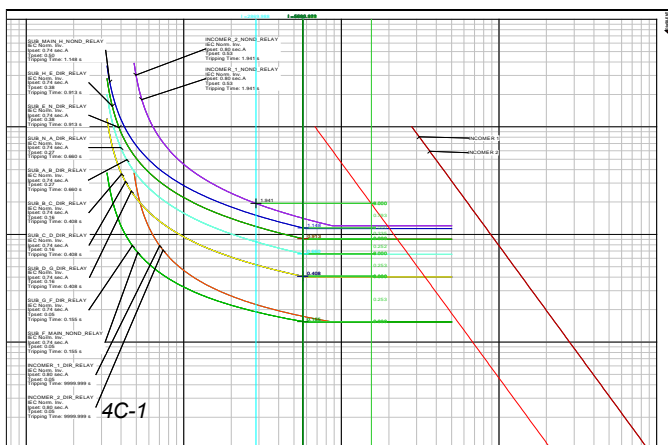


Fig. 7. Over Current Plot – Ring O [1]

TABLE I. TRIP TIME TABLE

Relay	Trip Time
INCOMER_1_NOND_RELAY	1.941s
INCOMER_2_NOND_RELAY	1.941s
SUB_MAIN_H_NOND_RELAY	1.148s
SUB_H_E_DIR_RELAY	0.913s
SUB_E_N_DIR_RELAY	0.913s
SUB_N_A_DIR_RELAY	0.660s
SUB_A_B_DIR_RELAY	0.660s
SUB_B_C_DIR_RELAY	0.408s
SUB_C_D_DIR_RELAY	0.408s
SUB_D_G_DIR_RELAY	0.408s
SUB_G_F_DIR_RELAY	0.155s
SUB_F_MAIN_NOND_RELAY	0.155s
INCOMER_1_DIR_RELAY	NO TRIP
INCOMER_2_DIR_RELAY	NO TRIP

The directional relay SUB-F-MAIN-NOND-RELAY and SUB-G-F-DIR-RELAY will trip in 0.155s, if the fault is not cleared then SUB-D-G-DIR-RELAY, SUB-C-D-DIR-RELAY and SUB-B-C-DIR-RELAY will trip in 0.408s. The grading between these relay groups is 0.253s.

If the fault still exists then SUB-A-B-DIR-RELAY and SUB-N-A-DIR-RELAY will trip in 0.66s, thus a grading margin of 0.253s is present. If the fault is still not cleared then SUB-E-N-DIR-RELAY and SUB-H-E-DIR-RELAY will trip in 0.913s, thus a grading margin of 0.252s is present.

If the fault is still not cleared then SUB-MAIN-H-NOND-RELAY will trip in 1.148s, thus a grading margin of 0.235s is present. This shows that the grading margin requirement for this project of 0.2s has been fulfilled. The Incomers (1&2) will trip together in 1.941s if all the previous mentioned relays fail to clear the fault.

The Incomers have a long time delay to trip because it has been graded with the downstream relays of Ring O. The Cable Damage curves show that the cable will be protected by the relay settings applied.

2) RING O – Anti-Clockwise Directional Earth Fault Protection

With the ring open, an asymmetrical fault at 50% of LINE-SUB-F-SUB-MAIN has been simulated.

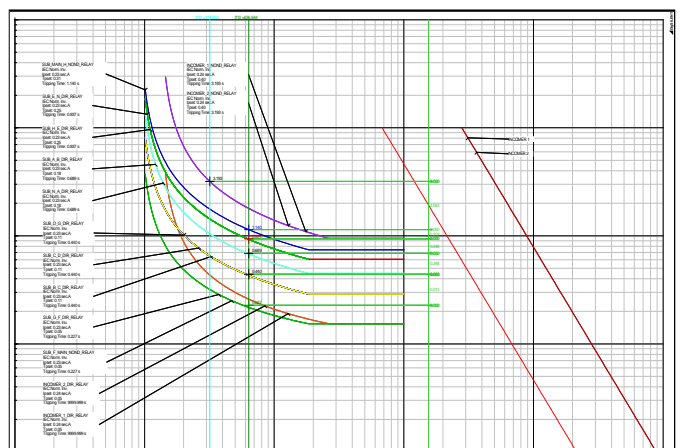


Fig. 8. Over Current Plot – Ring O [1]

TABLE II. TRIP TIME TABLE

Relay	Trip Time
INCOMER_1_NOND_RELAY	3.193s
INCOMER_2_NOND_RELAY	3.193s
SUB_MAIN_H_NOND_RELAY	1.140s
SUB_H_E_DIR_RELAY	0.937s
SUB_E_N_DIR_RELAY	0.937s
SUB_N_A_DIR_RELAY	0.689s
SUB_A_B_DIR_RELAY	0.689s
SUB_B_C_DIR_RELAY	0.440s
SUB_C_D_DIR_RELAY	0.440s
SUB_D_G_DIR_RELAY	0.440s
SUB_G_F_DIR_RELAY	0.227s
SUB_F_MAIN_NOND_RELAY	0.227s
INCOMER_1_DIR_RELAY	NO TRIP
INCOMER_2_DIR_RELAY	NO TRIP

The directional relays of the parallel Ring O are looking in the anti-clockwise direction. Therefore only the relays looking at the fault will trip. The directional relay SUB-F-MAIN-NOND-RELAY and SUB-G-F-DIR-RELAY will trip in 0.227s, if the fault is not cleared then SUB-D-G-DIR-RELAY, SUB-C-D-DIR-RELAY and SUB-B-C-DIR-RELAY will trip in 0.440s. The grading between these relay groups is 0.213s.

If the fault still exists then SUB-A-B-DIR-RELAY and SUB-N-A-DIR-RELAY will trip in 0.689s, thus a grading margin of 0.248s is present.

If the fault is still not cleared then SUB-E-N-DIR-RELAY and SUB-H-E-DIR-RELAY will trip in 0.937s, thus a grading margin of 0.248s is present.

If the fault is still not cleared then SUB-MAIN-H-NOND-RELAY will trip in 1.140s, thus a grading margin of 0.203s is present. This shows that the grading margin requirement for this project of 0.2s has been fulfilled.

The Incomers (1&2) will trip together in 3.193s if all the previous mentioned relays fail to clear the fault. The Incomers have a long time delay to trip because it has been graded with the downstream relays of Ring O.

C. Alternative 2

1) RING HEAN – Clockwise Over Current Directional Protection

The ring will be opened at LINESUB-H-SUB-MAIN. With the ring open, a symmetrical fault at 50% of LINESUB-H-SUB-MAIN has been simulated.

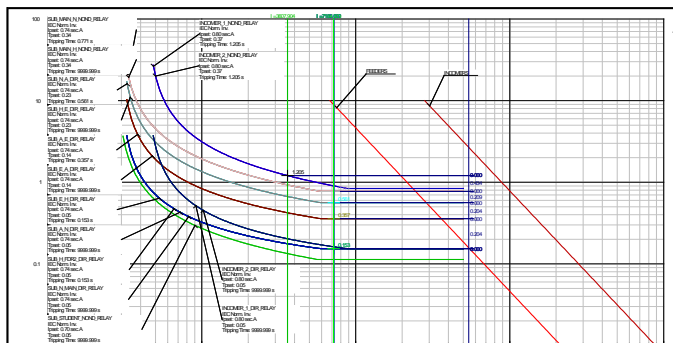


Fig. 9. Over Current Plot – Ring O [1]

Relay	Trip Time
INCOMER_1_NOND_RELAY	1.205s
INCOMER_2_NOND_RELAY	1.205s
SUB_MAIN_H_NOND_RELAY	NO TRIP
SUB_MAIN_N_NOND_RELAY	0.771s
SUB_N_A_DIR_RELAY	0.561s
SUB_H_E_RELAY	NO TRIP
SUB_E_A_DIR_RELAY	NO TRIP
SUB_A_E_DIR_RELAY	0.357s
SUB_E_H_DIR_RELAY	0.153s
SUB_A_N_DIR_RELAY	NO TRIP
SUB_H_FDR2_DIR_RELAY	0.153s
SUB_N_MAIN_DIR_RELAY	NO TRIP
SUB_STUDENT_NOND_RELAY	NO TRIP
INCOMER_1_DIR_RELAY	NO TRIP
INCOMER_2_DIR_RELAY	NO TRIP

TABLE III. TRIP TIME TABLE

In this instance, the directional relays of the parallel Ring HEAN are looking in the clockwise direction. Therefore only the relays looking at the fault will trip. The directional relays SUB-E-H-DIR-RELAY and SUB-H-FDR2-DIR-RELAY will trip in 0.153s; if the fault is not cleared then SUB-A-E-DIR-RELAY will trip in 0.357s. The grading between these two relays are 0.204s. If the fault is still not cleared then SUB-N-A-DIR-RELAY will trip in 0.561s, thus a grading margin of 0.204s is present.

After the previous SUB-MAIN-N-NOND-RELAY will trip in 0.771s, with a grading margin of 0.209s. This shows that the grading margin requirement for this project of 0.2s has been fulfilled.

The Incomers (1&2) will trip together in 1.205s if both the previous mentioned relays fails to clear the fault. The Cable Damage curves shows that the cable will be protected by the relay settings applied.

2) RING HEAN – Clockwise Directional Earth Fault Protection

The ring will be opened at LINESUB-H-SUB-MAIN. With the ring open, an asymmetrical fault at 50% of LINESUB-H-SUB-MAIN has been simulated.

TABLE IV. TRIP TIME TABLE

Relay	Trip Time
INCOMER_1_NOND_RELAY	1.692s
INCOMER_2_NOND_RELAY	1.692s
SUB_MAIN_H_NOND_RELAY	NO TRIP
SUB_MAIN_N_NOND_RELAY	0.875s
SUB_N_A_DIR_RELAY	0.641s
SUB_H_E_RELAY	NO TRIP
SUB_E_A_DIR_RELAY	NO TRIP
SUB_A_E_DIR_RELAY	0.432s
SUB_E_H_DIR_RELAY	0.153s
SUB_A_N_DIR_RELAY	NO TRIP
SUB_H_FDR2_DIR_RELAY	0.153s
SUB_N_MAIN_DIR_RELAY	NO TRIP
SUB_STUDENT_NOND_RELAY	NO TRIP
INCOMER_1_DIR_RELAY	NO TRIP
INCOMER_2_DIR_RELAY	NO TRIP

In this instance, the directional relays of the parallel Ring HEAN are looking in the clockwise direction. Therefore only the relays looking at the fault will trip. The directional relays

SUB-E-H-DIR-RELAY and SUB-H-FDR2-DIR-RELAY will trip in 0.153s; if the fault still exists then SUB-A-E-DIR-RELAY will trip in 0.432s. The grading between these two relays are 0.209s. If the fault is still not cleared then SUB-N-A-DIR-RELAY will trip in 0.641s, thus a grading margin of 0.209s is present.

After the previous SUB-MAIN-N-NOND-RELAY will trip in 0.875s, with a grading margin of 0.233s. This shows that the grading margin requirement for this project of 0.2s has been fulfilled.

The Incomers (1&2) will trip together in 1.692s if both the previous mentioned relays fails to clear the fault. The Cable Damage curves shows that the cable will be protected by the relay settings applied.

D. Alternative 3

1) RING NAF – Clockwise Over Current Directional Protection

The ring will be opened at LINESUB-H-SUB-MAIN. With the ring open, an asymmetrical fault at 50% of LINESUB-H-SUB-MAIN has been simulated.

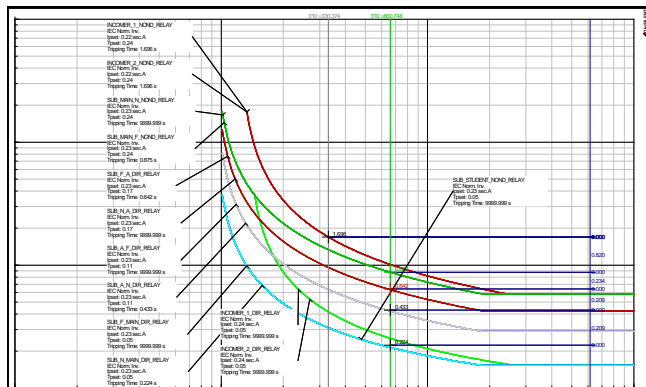


Fig. 10. Over Current Plot – Ring O [1]

TABLE V. TRIP TIME TABLE

Relay	Trip Time
INCOMER 1 NOND RELAY	1.696s
INCOMER 2 NOND RELAY	1.696s
SUB MAIN N NOND RELAY	NO TRIP
SUB MAIN F NOND RELAY	0.875s
SUB F A DIR RELAY	0.642s
SUB N A RELAY	NO TRIP
SUB A F DIR RELAY	NO TRIP
SUB A N DIR RELAY	0.433s
SUB N MAIN DIR RELAY	0.224s
SUB F MAIN DIR RELAY	NO TRIP
SUB STUDENT NOND RELAY	NO TRIP
INCOMER 1 DIR RELAY	NO TRIP
INCOMER 2 DIR RELAY	NO TRIP

In this instance, the directional relays of the parallel Ring NAF are looking in the clockwise direction. Therefore only the relays looking at the fault will trip. The directional relay SUB-N-MAIN-DIR-RELAY will trip in 0.224s, if the fault still exists then SUB-A-N-DIR-RELAY will trip in 0.433s. The grading between these two relays are 0.209s. If the fault is still

not cleared then SUB-F-A-DIR-RELAY will trip in 0.642s, thus a grading margin of 0.209s is present.

After the previous SUB-MAIN-F-NOND-RELAY will trip in 0.875s, with a grading margin of 0.234s. This shows that the grading margin requirement for this project of 0.2s has been fulfilled.

The Incomers (1&2) will trip together in 1.696s.

2) RING NAF – Clockwise Directional Earth Fault Protection

The ring will be opened at LINESUB-H-SUB-MAIN. With the ring open, an asymmetrical fault at 50% of LINESUB-H-SUB-MAIN has been simulated.

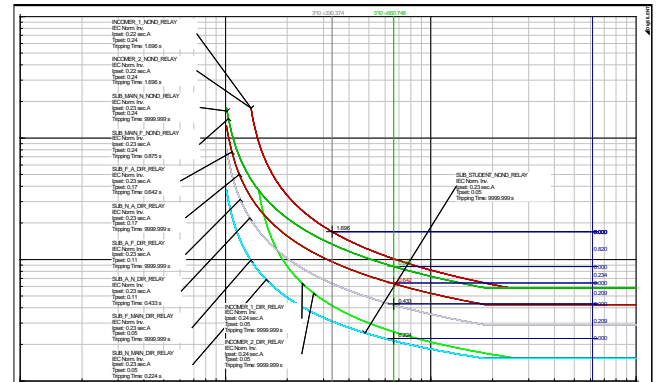


Fig. 11. Over Current Plot – Ring O [1]

TABLE VI. TRIP TIME TABLE

Relay	Trip Time
INCOMER 1 NOND RELAY	1.696s
INCOMER 2 NOND RELAY	1.696s
SUB MAIN N NOND RELAY	NO TRIP
SUB MAIN F NOND RELAY	0.875s
SUB F A DIR RELAY	0.642s
SUB N A RELAY	NO TRIP
SUB A F DIR RELAY	NO TRIP
SUB A N DIR RELAY	0.433s
SUB N MAIN DIR RELAY	0.224s
SUB F MAIN DIR RELAY	NO TRIP
SUB STUDENT NOND RELAY	NO TRIP
INCOMER 1 DIR RELAY	NO TRIP
INCOMER 2 DIR RELAY	NO TRIP

In this instance, the directional relays of the parallel Ring NAF are looking in the clockwise direction. Therefore only the relays looking at the fault will trip. The directional relay SUB-N-MAIN-DIR-RELAY will trip in 0.224s, if the fault still exists then SUB-A-N-DIR-RELAY will trip in 0.433s. The grading between these 2 relays are 0.209s. If the fault is still not cleared then SUB-F-A-DIR-RELAY will trip in 0.642s, thus a grading margin of 0.209s is present.

After the previous SUB-MAIN-F-NOND-RELAY will trip in 0.875s, with a grading margin of 0.234s. This shows that the grading margin requirement for this project of 0.2s has been fulfilled.

The Incomers (1&2) will trip together in 1.696s.

E. Alternative 4

1) Ring O – Time Zones

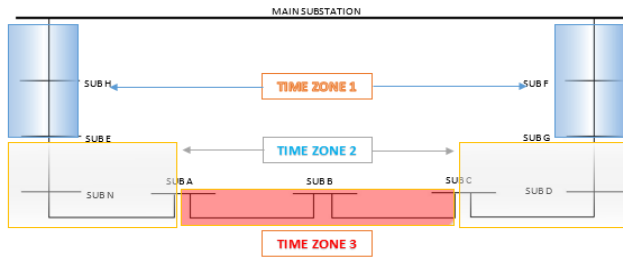


Fig. 12. Differential Time Zones

2) Differential Settings

TABLE VII. DIFFERENTIAL SETTINGS APPLIED

Function - Current Differential	
GROUP/PARAMETER	SETTING
Current Diff	Yes
Is 1	0.50In
Is 2	2.00In
K1	30%
K2	150%
I Diff Delay Type	DMT

TABLE VIII. BU OC/EF FIBER HEALTHY – TIME ZONE 1

GROUP/PARAMETER	SETTING
Function - Over Current	
PBS	0.74In
Curve Selection	DMT
Delay Time	800ms
Function – Earth Fault	
PBS	0.23In
Curve Selection	DMT
Delay Time	800ms

TABLE IX. BU OC/EF FIBER FAILED – TIME ZONE 1

GROUP/PARAMETER	SETTING
Function - Over Current	
PBS	0.74In
Curve Selection	DMT
Delay Time	200ms
Function – Earth Fault	
PBS	0.23In
Curve Selection	DMT
Delay Time	200ms

TABLE X. BU OC/EF FIBER HEALTHY – TIME ZONE 2

GROUP/PARAMETER	SETTING
Function - Over Current	
PBS	0.74In
Curve Selection	DMT
Delay Time	600ms
Function – Earth Fault	
PBS	0.23In
Curve Selection	DMT
Delay Time	600ms

TABLE XI. BU OC/EF FIBER FAILED – TIME ZONE 2

GROUP/PARAMETER	SETTING
Function - Over Current	
PBS	0.74In

Curve Selection	DMT
Delay Time	200ms
Function – Earth Fault	
PBS	0.23In
Curve Selection	DMT
Delay Time	200ms

TABLE XII. BU OC/EF FIBER HEALTHY – TIME ZONE 3

GROUP/PARAMETER	SETTING
Function - Over Current	
PBS	0.74In
Curve Selection	DMT
Delay Time	400ms
Function – Earth Fault	
PBS	0.23In
Curve Selection	DMT
Delay Time	400ms

TABLE XIII. BU OC/EF FIBER FAILED – TIME ZONE 3

GROUP/PARAMETER	SETTING
Function - Over Current	
PBS	0.74In
Curve Selection	DMT
Delay Time	200ms
Function – Earth Fault	
PBS	0.23In
Curve Selection	DMT
Delay Time	200ms

3) Ring O – Fault Analysis

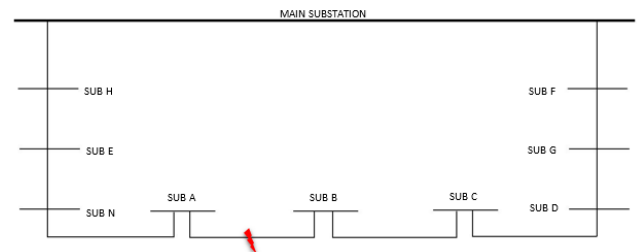


Fig. 13. Fault Location 1

Scenario “n-1”: Fiber is Healthy – With the fiber healthy the breakers on both sides of the line will trip in 50ms. If the breakers fail, the breaker fail function will trip both the breaker feeding the fault.

Scenario “n-2”: Fiber Failed Sub A and B – With the fiber failed both the breakers will trip in 200ms. If the breakers fail, the breaker fail function will trip both the breaker feeding the fault.

Scenario “n-3”: Fiber Failed between Sub A and B, and Breaker Fail function also failed – The breakers that has to clear the fault does not clear the fault. Now all the other feeders will see a through fault. The OC and EF setting applied while the fiber is healthy on them will now be triggered. Therefore the Time Zone 3 relays (Sub B – C) will trip first in 400ms, then the Tie Zone 2 Relays only on the left (Sub E – N, and Sub N – A) will trip in 600ms. This will result in only losing Sub N, A, B and C for an extremely rare fault where all the possible protection functions have failed.

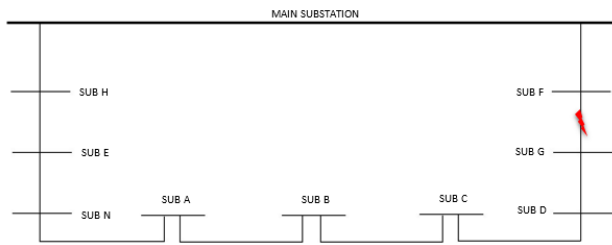


Fig. 14. Fault Location 2

Scenario “n-1”: Fiber is Healthy – With the fiber healthy the breakers on both sides of the line will trip in 50ms. If the breakers fail, the breaker fail function will trip both the breaker feeding the fault.

Scenario “n-2”: Fiber Failed Sub F and G – With the fiber failed both the breakers will trip in 200ms. If the breakers fail, the breaker fail function will trip both the breaker feeding the fault.

Scenario “n-3”: Fiber Failed between Sub F and G, and Breaker Fail function also failed – The breakers that has to clear the fault does not clear the fault. Now all the other feeders will see a through fault. The OC and EF setting applied while the fiber is healthy on them will now be triggered. Therefore the Time Zone 3 relays (Sub A – B and Sub B – C) will trip first in 400ms, then the Zone 2 Relays, (Sub E – N, Sub N – A, Sub G – D and Sub D – C) will trip in 600ms. Then Time Zone 1 will operate but only the relays between Sub F – G will trip in 800ms. This will result in losing most of the ring for an extremely rare fault where all the possible protection functions have failed.

The scenario explained is one that may never happen but it should still be considered for achieving complete protection of the network.

IX. CONCLUSION

The supply authority’s settings applied to the relays feeding NMMU Main Substation from Summer Stand Substation are OC TMS = 0.44s and EF TMS = 0.24s. The settings applied to the solutions needed to be below or similar those chosen by the supply authority.

With the solutions1, by using the ring as it is with directional protection the grading was done by grouping substations into groups that will trip simultaneously. This was done in order to achieve a setting below or similar to the supply authority’s setting. This was not achieved even with the grouping. The grading and tripping sequence was successfully achieved by applying the calculated settings. Another reason for the long tripping times was because of the radial feeders on Ring O and they cause problems with grading as the fault current is much higher when a fault is on them. Therefore this solution to a protection design for NMMU South Campus Distributions System is flawed.

With both solution 2 and 3, no substations were grouped to trip simultaneously. The correct tripping sequence and grading margin was achieved by using DigSilent functions to move the

tripping curves to achieve this. These two solutions may both be used for a working protection design for NMMU South Campus Distributions System. Both solutions are well below the setting of the supply authority.

The problem with using either solution 2 or 3 is that these solutions are very expensive. They would be plausible to implement as the routing of the cables can be done but the money involved may as well be the reason for not implementing either of these solutions.

The best economical and reliable protection solution for the system is to use the existing layout with the implementation of differential protection on all the feeders and the two main incomers, except for the radial feeders. The radial feeders will make use of normal overcurrent and earth fault protection. The tripping times for differential protection on the feeders can be set as low as 50ms. By implementing differential protection, the long tripping times at the incomers and the Ring O incomers will be much, much quicker, as it would now be 50ms. The tripping time between Sumer Strand 11kV and NMMU Main Sub 11kV will be significantly reduced.

REFERENCES

- [1] L. Grobler, "Refurbishment and Upgrade of the NMMU South Campus Substations and Network Protection," Nelson Mandela Metropolitan University 2015.
- [2] A. Engineers, Network Protection & Automation Guide, 2nd ed.: ALSTOM Grid, 2011.
- [3] ABB, "RED615 Current Differential," ed, 2015.
- [4] C. Labuschagne, N. Fischer, A. Guzmán, and K. Behrendt, "CURRENT DIFFERENTIAL PROTECTION," Journal of Reliable Power, vol. Volume 2, p. 144, 2011.
- [5] H. G. Wang, D. X. Du, Z. Q. Bo, X. Z. Dong, Z. X. Zhou, H. J. He, et al., "An Integrated Current Differential Protection Scheme," in Power System Technology, 2006. PowerCon 2006. International Conference on, 2006, pp. 1-6.
- [6] O. Rintamaki and J. Ylinen, "Communicating line differential protection for urban distribution networks," in Electricity Distribution, 2008. CIGRE 2008. China International Conference on, 2008, pp. 1-5.
- [7] M. Khederzadeh, "Back-up protection of distance relay second zone by directional overcurrent relays with combined curves," in Power Engineering Society General Meeting, 2006. IEEE, 2006, p. 6 pp.
- [8] B. Meyer. (2015, 18/03/2015). Directional Ground and Sensitive Ground Fault Systems [Manual]. Available: http://www.cooperindustries.com/content/dam/public/powersystems/resources/library/280_ReclosersControls/03046.pdf
- [9] A. Ukil, B. Deck, and V. H. Shah, "Smart distribution protection using current-only directional overcurrent relay," in Innovative Smart Grid Technologies Conference Europe (ISGT Europe), 2010 IEEE PES, 2010, pp. 1-7.
- [10] P. Hindle and J. Sanderson, "OVERCURRENT PROTECTION COORDINATION: A MODERN APPROACH FOR MODERN DEVICES," ed: IEEE, p. 65.
- [11] A. A. Sallam and O. P. Malik, Electric Distribution Systems: Wiley, 2011.
- [12] L. G. Hewitson, M. Brown, and R. Balakrishnan, Practical Power System Protection: Newnes, 2005.
- [13] K. Harker and I. o. E. Engineers, Power System Commissioning and Maintenance Practice: Institution of Electrical Engineers, 1998.
- [14] B. Ravindranath, Power System Protection and Switchgear: Wiley Eastern Limited, 1977.

Coordination between Overexcitation and Generator Over-voltage Protection with respect to Overexcitation Limiters

D.N.Ngema^{1*}, A.K.Saha¹

¹University of KwaZulu-Natal, Howard College Campus, Mazisi Kunene Road, Durban 4041, South Africa

*Email: 208528228@stu.ukzn.ac.za, saha@ukzn.ac.za

Abstract: This paper presents a brief review of generator excitation control and protection. The focus is mainly on the coordination between overexcitation control and protection with respect to overexcitation limiters. Over excitation limit plays a vital role in voltage stability studies of synchronous generators. The overexcitation limiter models studied are suited with current IEEE recommended excitation system models. The case studies are done on real time digital simulator and the simulation results have been presented and analysed in the paper using a software multifunction generator relay. The relay settings used are according to IEEE standards for ac generators.

1 INTRODUCTION

The operating requirements for synchronous generators are becoming more demanding in actual practice. One of these requirements is the use of the maximum reactive generating capability, which is mostly dictated by the rotor field winding thermal limit, also known as the overexcitation limit [4]. The impact of an appropriate use of this capability to maintain voltage stability in the power system has been widely recognized [3][4]. A modern excitation control system includes a number of control, limiting, and protective functions which assist in fulfilling the basic requirement of supplying and automatically adjusting the field current of a synchronous generator to maintain generator terminal voltage within the continuous capability [1]. Excitation system control and protection external to the excitation system needs to be coordinated so as not to limit the generator overexcitation capability [2]. During system disturbances, the excitation control/protection must allow the generator to operate within its short time capabilities.

2 GENERATOR EXCITATION CONTROL

The excitation system of a generator provides energy for the magnetic field that keeps the generator in synchronism with the power system. In addition to maintaining the synchronism of the generator, the excitation system affects the amount of reactive power the generator may absorb or supply [6]. An increase in the excitation results in an increase of the synchronizing torque of the machine thus increasing the reactive power

output and vice versa. In severe cases synchronism of the machine may be lost due to underexcitation. There are quite a number of control functions that can be applied to the excitation system. This includes but not limited to automatic voltage regulation (AVR), constant power factor regulation, and reactive power regulation [6]. In an absence of automatic regulation, excitation system may be operated using manual control, although the practice of such control has been avoided in the recent excitation systems. Automatic control modes allow excitation system to have supplementary controls. These supplementary controls ensure that even under automatic regulation of a primary parameter, the generator is always operated within its capability limits. Supplementary controls include [6]:

- Maximum and/or minimum excitation level limits
- Stator current limit to prevent stator thermal overload
- Volts per hertz limit to prevent equipment damage due to excessive flux levels
- Terminal voltage limit to prevent equipment damage due to excessive dielectric stress
- Line drop compensation to increase generator response to system voltage depressions
- Reactive power sharing controls for generators trying to regulate the same parameter
- Power system stabilizer to damp low frequency oscillations.

2.1. Overexcitation limiter (OEL)

The limiter is also referred to as maximum excitation limiter and field current limiter [2]. The function of OEL is to protect the generator field circuitry from excessive current versus time heating [7]. OEL setting should be coordinated with the generator capability in the overexcitation region and should also allow the exciter to respond to fault conditions where field current is boosted to a high level for a short period of time [7]. Limiting devices built to prevent field current from exceeding the machine capability are of different forms but all operate through the same sequence of events: detect the overexcitation condition, allow it to persist for a defined time-overload period, and then reduce the excitation to a safe level. The limiting action provided by OELs must offer proper protection from overheating due to high field current

levels while simultaneously allowing maximum field forcing for power system stability purposes [2]. The allowed overexcitation period may be fixed or vary inversely with the excitation level. A simple form of OEL has a fixed pickup point, a fixed time delay, and instantly reduces the excitation set point to a safe value. A more common type of overexcitation limiter combines instantaneous and inverse-time pickup characteristics [2]. A high setting provides almost instantaneous limiting at 1.6 times full-load current (FLC). A low setting of 105% of FLC in conjunction with a ramp timing function provides a limiting action with time delay dependent on the level of field current [1].

2.2. V/Hz limiter

V/Hz limiter limits the generator V/Hz ratio by limiting the generator voltage to a programmed setting. Steady state limit are $\pm 5\%$ of rated generator stator terminal voltage at rated frequency. The setting should permit short time excursions during transient conditions [7]. In case of the failure of this limiter, V/Hz protection serves as backup. The limiter operates by monitoring the voltage to frequency ratio i.e. when per unit V/Hz ratio exceeds the limiting value; a strong negative signal drives the excitation down. The limiter is typically set at 1.07 to 1.09 pu [1].

2.3. RTDS/RSCAD

Fig. 1 illustrates the RTDS configuration used for the generator studies presented in this paper. Real-time digital simulator is a very powerful power system tool which provides facilities for simulations that takes place in real-time. It further allows physical equipment such as relays, generator controls etc. to be connected and tested before use in real systems and also to observe the performance of the system and its components [8].

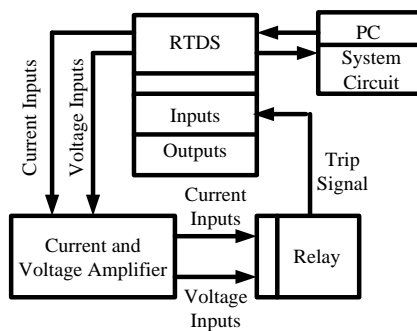


Fig. 1: RTDS connection diagram [10].

RSCAD software is used in conjunction with RTDS to build and compile models of a power system under study. RSCAD is an interface between the user and the simulator. System models are built in the sub-program DRAFT and monitored in another sub-program RUNTIME. Due to the accuracy of the simulator and

the ability to interact with real equipment, control and power systems can be designed, modelled and tested realistically [3].

3 SYSTEM UNDER STUDY

The power system network used for the studies is from [1]. This system is selected because it is a well-known standard model [9] for carrying out generator stability studies. The system also has documented parameters that are representative of both large generators and their associated controllers. This paper uses one generator system rated at 555 MVA, operating at 24 kV line-to-line voltage connected to an infinite bus through a step-up transformer and 400 kV transmission lines as illustrated in Fig. 2 [1]. The generator is equipped with IEEE governor, power system stabilizer and an external excitation system which is modelled specifically for excitation control studies.

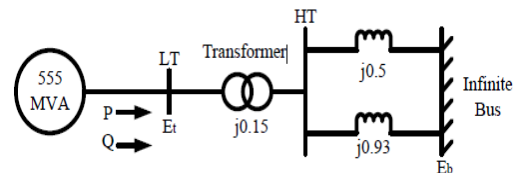


Fig. 2: System under study [1]-[10]

4 SIMULATION RESULTS AND ANALYSIS

Prior any test, the system is run and tested for stability. Under steady state stability, the generator supplies 0.9 pu active power, 0.436 pu reactive power and the terminal voltage of the machine is kept at rated voltage of 1 pu. This is illustrated in Fig. 3. As the generator is running under normal operating condition, the generator circuit breaker is closed (Fig. 4). In an event of a fault, the breaker status makes a transition from high (1) to low (0) which implies breaker opening.

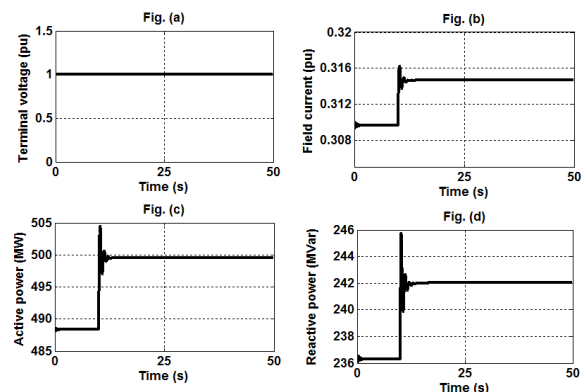


Fig. 3: Steady state operation

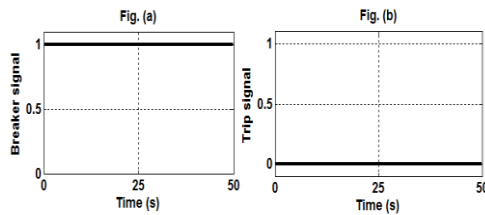


Fig. 4: Breaker and trip signals during steady state operation

4.1. Overexcitation protection (24) implementation

The volt per hertz element is suitable for providing over excitation detection on generators. The relay provides two elements for volts per hertz detection, the first element normally alarms and the second element trips. The relay uses the maximum phase voltage and calculates the ratio of volts per hertz and compares this to the setting thresholds. If the thresholds are exceeded longer than the time delay the element operates [8].

4.2. Overexcitation relay settings

The first element uses a definite time delay and the second element can be a definite time delay or inverse time characteristic. The level 1 setting is such that when the ratio of volts and hertz exceeds 1.05 pu, the relay delays for the time setting inside the relay and thereafter, an alarm signal is issued as a warning. Level 2 setting is a trip, when the V/Hz ratio exceeds 1.1 pu, the relay issues a trip signal after delaying as per the relay setting.

4.3. Overexcitation simulation results and analysis

Fig. 5 and 6 is an illustration of machine parameters when the machine was tested for level 1. The machine was run at 106% excitation level, and the V/Hz ratio measured at this level was 105.1% , an alarm signal was then issued as a warning (fig. 6) after the time delay set in the relay. At constant frequency, the machine terminal voltage is the same the V/Hz ratio as shown in fig. 5 (a). The field current, active power and reactive power output at 106.1% are shown in fig. 5 (b), (c) and (d) respectively.

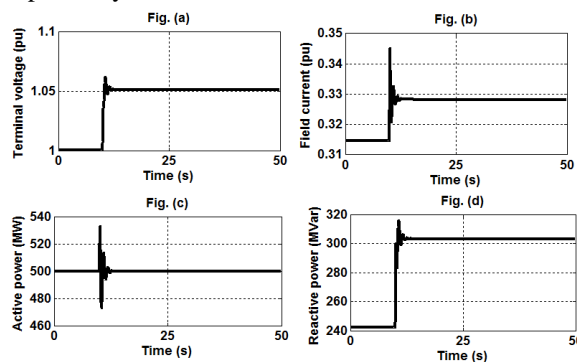


Fig. 5: System behaviour at 105% excitation

For level 2 testing, the machine is run at 111.4% above its normal excitation level while the setting was 110% with a time delay of 6s. The second level trips the generator. Fig. 6 illustrates the machine output parameters such as the machine terminal voltage, field current, active and reactive power at 110% excitation

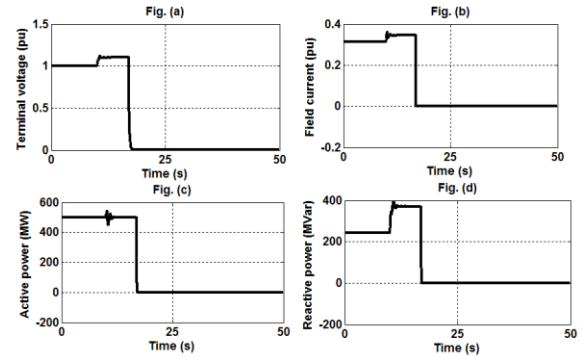


Fig. 6: System parameters at 110% excitation level operation

The level 2 setting was detected when the V/Hz setting was slightly above the machine setting at 110.8%. The breaker and trip signals are shown in fig. 7 (a) and (b) respectively.

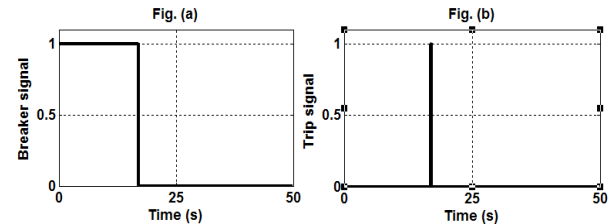


Fig. 7: Breaker and trip signals

4.4. Over voltage (59) implementation

The overvoltage element is suitable for providing detection of overvoltage conditions and providing backup protection. The relay provides two elements for overvoltage detection with time delayed operation. Overvoltage conditions are usually the result of a sudden loss of load. Small overvoltages cause large increases in excitation current and cause overheating [8].

4.5. Over voltage relay settings

The maximum phase voltage is chosen and compared to the first threshold; the negative sequence voltage is compared to the second threshold [5]. The first element is normally set for 106 – 110% of nominal voltage with a delay of 10-15 s. The second element has a quicker time delay [2]. The second level is set between 120-150% of the nominal voltage with a shorter time delay.

4.6. Over voltage simulation results

The generator was to set to run at 111.4% of rated voltage when the relay setting for level 1 was 110%.

The terminal voltage, field current, active and reactive power simulation results are shown in fig. 8(a), (b), (c) and (d) respectively. Both overvoltage levels setting trips the generator.

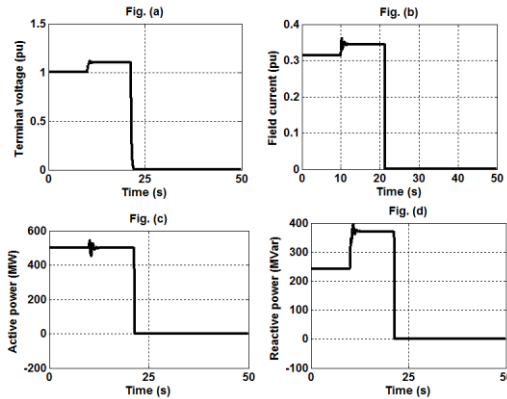


Fig. 8: System behaviour at 110% excitation level operation

The breaker and trip signals from the overvoltage relay level 1 and level 2 are shown in fig. 9(a) and 9(b) respectively.

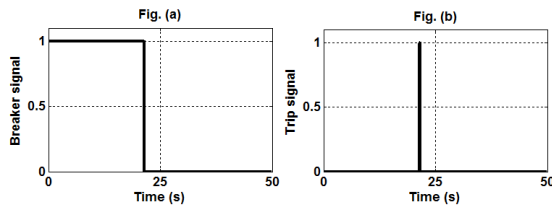


Figure 9: Breaker and trip signals

The level 2 relay setting was 140% with a time delay of 100 mS. The generator was run at 141.8% for the second level testing and the generator parameters obtained are shown in fig. 10.

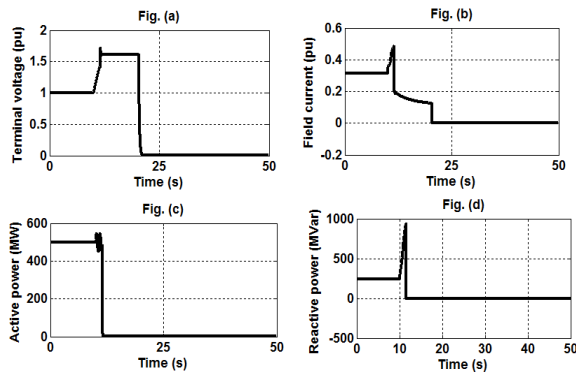


Fig. 10: System parameters at 140% excitation operation level

Fig. 11 illustrates the breaker and trip signals when level 2 testing was conducted. Since level 2 was set with a quicker time delay, the relay sends a trip signal much quicker than level 1.

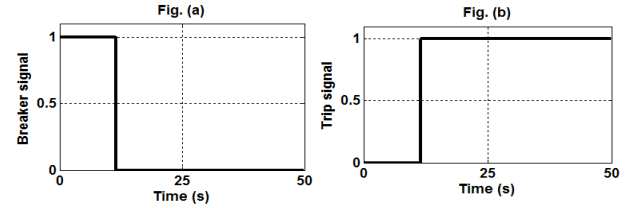


Figure 11: Breaker and trip signals

4.7. V/Hz limiter and protection

V/Hz limiters are used to protect the generator and step-up transformer from damage due to excessive magnetic flux resulting from low frequency and/or overvoltage. Excessive magnetic flux, if sustained, can cause serious overheating and may result in damage to the unit transformer and to the generator core [1].

4.8. V/Hz limiter model

The limiter controls the field voltage so as to limit the generator voltage when the V/Hz value exceeds a pre-set value. Fig. 12 shows the V/Hz limiter model.

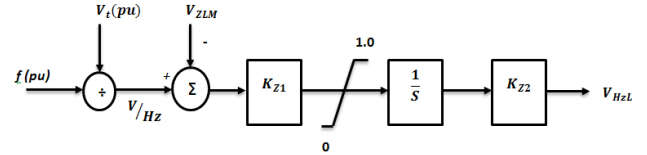


Fig. 12: V/Hz limiter model

When the V/Hz ratio exceeds the pre-set limiting value, a strong negative signal drives the excitation down. The limit is set typically below the overexcitation trip level of 110% [1].

4.9. V/Hz limiter testing

When the limiter is not in operation, the output remains at zero and when it start operating the output for the limiter changes and becomes more positive talking control in the AVR to drive the excitation down to acceptable levels as shown in fig. 13.

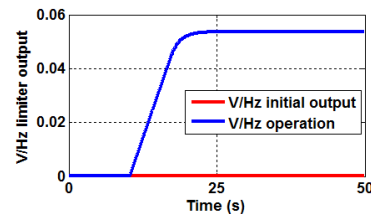


Fig. 13: V/Hz limiter output operation

When level 2 was tested without the V/Hz limiter, the relay tripped the machine when 110% level setting was reached. However, in the presence of the limiter this is different. When the machine was run at 111.4% the limiter made a transition from zero to a more positive value, driving the excitation down to 105% which is set when modelling the limiter. The limiter operation is illustrated in fig. 14 by the machine

parameters such as the machine terminal voltage, field current, active and reactive power.

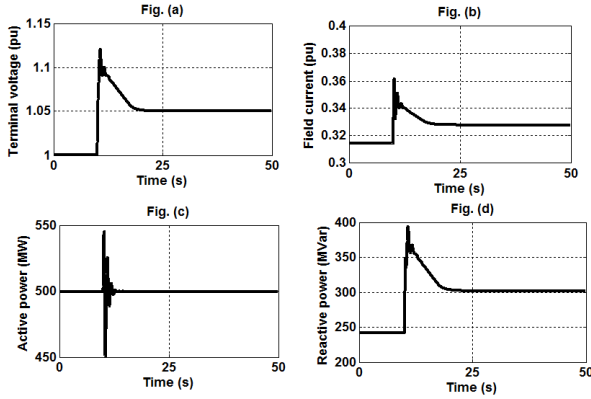


Fig. 14: V/Hz limiting operation

4.10. OEL and protection

OEL limits the excitation system from supplying excess field. The OEL control is a takeover type function that replaces the AVR input to the firing circuits. When the OEL is not in control, its output is fixed at full level, which will insure the AVR signal will always be in control while acting through a summing junction.

4.11. OEL limiter

The modelling of the over excitation limiter considers field current as inputs to the limiter, the field current of the machine is measured and compared with the limiter setting thresholds. When not in operation, the limiter output is zero (fig. 16), as excitation levels changes the output of the limiter changes continuously. Depending on the excitation levels, the limiter will operate and drive the excitation down to acceptable levels.

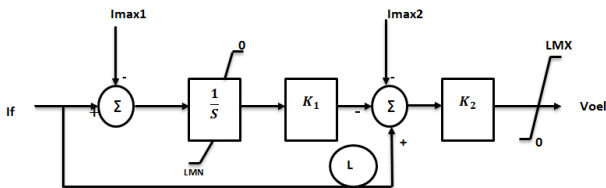


Fig. 15: OEL limiter

4.12. Simulation results

The machine was run in three different excitation levels in a presence of the limiter. When testing over voltage or overexcitation protection, 110% is normally set as a trip level in the relay as discussed earlier. However, the limiter was able to drive down the excitation level to 105.8% for the machine was excited by 120%, 140% , and 160% in a short period of time before any trip could be detected by the relay. Fig. 17, 18, 19 and 20 illustrates terminal volatge, field current, reactive power and active power respectively under different excitation levels.

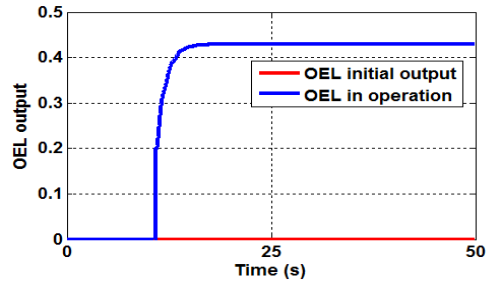


Fig. 16: OEL operation

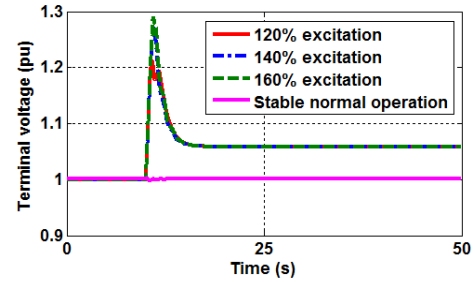


Fig. 17: Terminal voltage under different excitation levels

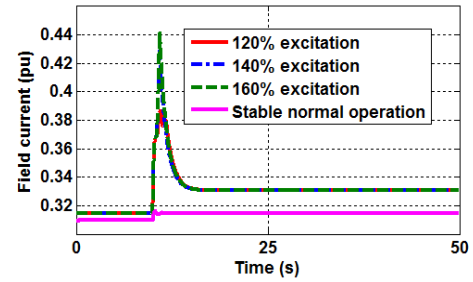


Fig. 18: Field current under different excitation levels

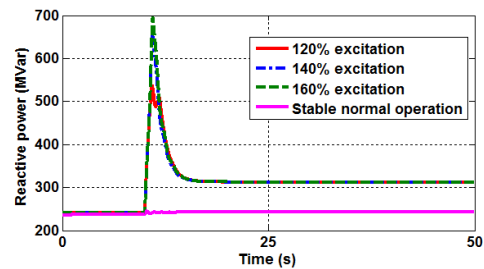


Fig. 19: Reactive power under different excitation levels

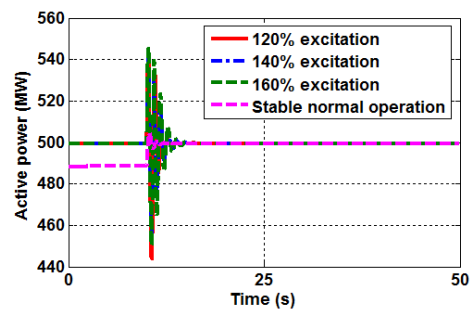


Fig. 20: Reactive power under different excitation levels

5 CONCLUSION

The paper presented the simulation studies of generator overexcitation and over voltage protection elements with and without overexcitation and V/Hz limiters. The results obtained conforms theoretical studies of these protection elements. Irrespective of the existence of such studies, the basic idea is the provision of education and simple training based on generator protection studies as well as the usage of RTDS in power system studies.

The same system configurations and methods can be used to connect any commercially available relays used for generator protection.

6 REFERENCES

- [1] P. Kundur: "Power system stability and control", Electric Power Research Institute, McGraw-Hill, Inc., New York, ISBN-13:978-0-07-035958-1.
- [2] IEEE Std 421.5™-2005: "IEEE Recommended Practice for Excitation System Models for Power System Stability Studies", IEEE, 3 Park Avenue New York, NY 10016-5997, USA, 16 February 2007
- [3] Power Systems Relaying Committee: "IEEE guide for AC generator protections – C37.102 TM - 2006", IEEE Power Engineering Society, IEEE, 3 Park Avenue, New York, NY, 10016-5997, USA, pp. 1-177, November 2006.
- [4] Eli Pajuelo, Ramakrishna Gokaraju and M. S. Sachdev, *Life Fellow, IEEE*: "Coordination of Overexcitation Limiter, Field Overcurrent Protection and Generator Control"
- [5] RTDS: "Manual Set", Real Time Digital Simulation, pp. 1-517, November 2006.
- [6] Working Group J6 of the Rotating Machinery Protection Subcommittee, Power System Relaying Committee: "Performance of generator protection during major system disturbances", *IEEE Transactions on Power Delivery*, vol. 19, no. 4, pp. 1650-1662, October 2004.
- [7] Working Group J-5 of the Rotating Machinery Subcommittee, Power System Relay Committee: "Coordination of generator protection with generator excitation control and generator capability", *IEEE Power Engineering Society General Meeting*, 2007, no. 4, pp. 1-4244-1298-6/07
- [8] RTDS, Applications, closed-loop testing of physical devices, <http://www.rtds.com/applications/closed-loop-testing/closed-loop-testing.html>
- [9] R. D, "Protective relaying for power generation systems," in Taylor and Francis group, 2005.
- [10] A.K. Saha: "Simulation study of generator under-voltage and over-voltage protection", submitted for Southern African Universities Power Engineering Conference, 2015.

Analysis and Solutions of Overcurrent Protection Issues for Distribution Networks with Distributed Generation Integrated

S.S. Mahendula^{1*} and A.K. Saha²

School of Electrical, Electronics and Computer,

University of KwaZulu-Natal,

Howard College Campus,

King George V Avenue, Durban, South Africa

Email: ¹208513369@stu.ukzn.ac.za, ²saha@ukzn.ac.za

Abstract: The Traditional radial distribution systems protection system is based on time and current coordination overcurrent protection. This protection scheme is direct affected by distribution generators. The distributed generators can be used to supply the load demand if the distribution network is operating in the islanded mode. In this paper, protection issues associated with connection of distributed generators are addressed in a context of radial distribution feeder systems. Analysis of the study based on traditional overcurrent protection and how it can be adjusted to protect the distribution networks with distributed generators are discussed. The paper also discusses different strategies that can be adopted to mitigate the problems of coordinating protection devices in case of the distributed generators connected.

1 INTRODUCTION

With a steady growth in electrical power demand in utilities, more power generation capacity is required. Renewable energy is becoming the main source of alternative energy generators. It is expected that 20% of power generation will be through renewable sources by 2020 [1]. In Denmark, about 40% of the total generation capacity is based on the distributed generation units, which is connected to the electrical distribution systems from 400V to 60kV [2]. A general electricity company of Libya (GECOL) extended its generation with distributed generations (DGs) to meet the needs for fast solution to overcome the increased demand [3]. The distributed generators (DGs) based on renewable energy sources assist in lowering the greenhouse gas emission. These DGs have benefits for both utilities and consumers because they have advantage of improving the voltage profile by reducing the power losses in the distribution network. Moreover, these DGs reduce transmission and distribution costs as they will be located close to the customers [1, 4].

One of the major advantage of higher DG unit is the possibility of operating in islanding mode. Islanding refers to the condition of distribution network being electrically isolated from the power system due to upstream fault but continue to be energized by DG connected to it [5]. The installation of DGs to radial

distribution systems (RDS) have disadvantages such as over-voltage, fluctuation and unbalance of the system voltage if the coordination with the supply utility is not properly done. Moreover, the addition of DGs alters the short circuit levels in the RDS and this can affect the protection unit settings. Since some DGs are connected to the distribution network via the power transformers and converters, therefore harmonics will be injected into the system. The increased in power injection from a DG can increase the power losses in the distribution system, depending on the RDS configuration and the penetration level of the DG [4].

The protection system of traditional distribution networks is based on the time and current coordination of overcurrent protection elements affected by DGs. The coordination of these protection elements is the most challenging part for the distribution system with the presence of DGs. In order to overcome the problems of miscoordination of protective elements, the new developments on traditional protection schemes must be implemented which includes [5]:

- The method of changing all protection devices and their settings. This method is costly and economically irrational and it is avoided by many utilities because it requires the system to be reconfigured to accommodate the adjustments.
- The second method is to apply a Fault Current Limiter (FCL) in series with any DG. This method only check if the fault has occurred and adjust the FCL impedance to limit the DG fault current. When DG has no effect on the short circuit currents, the FCL method change the protection system to operate the same as the traditional one.
- Finally, is to use adaptive protection schemes, these protection schemes are based on local or non-local information. The Adaptive local protection updates protection elements settings based on local information whereas in non-local adaptive protection scheme, the information is gathered through smart grid infrastructures from all over the power grid [3, 5]. This can be done by using a remote control for updating feeder relays and reclosers.

This research focuses on key issues associated with radial distribution systems overcurrent protection scheme with the integration of DGs. Section 2 of this paper discusses the impact of distribution generations (DGs) to the distribution network. Section 3 explain the effects of DGs on protection system based on investigated case study. Section 4 discusses the methods of preventing detection problems in distribution system in the presence of DGs.

2 IMPACT OF DISTRIBUTED GENERATION

2.1. Fault Analysis

In a radial distribution system without distributed generators, the overcurrent protection is straight forward because the fault current can only flow in one direction, similarly the fault current contribution for RDS with single small DG unit is not large. However, the fault contribution of many small DG units is large because the rate of change of fault currents rely on the abilities of distributed generation connected. The availability of DG lowers short circuit current levels through some areas in the distribution network, and this can lead to the loss of sensitivity of the protection elements [3]. This causes the system to be unreliable and unsafe to the customers. Most of the fault current contribution comes from the synchronous generators, and variable wind turbine generators. Fault current contribution for asynchronous and inverter based generators can be neglected [3].

The fault current depends on the sources of the short circuit power [5]. The short circuit power of the transmission grid is higher than that of small DG connected to distribution network. Therefore, when distribution network is isolated due to the fault on the upstream, the protection relay will see the fault current that is much less than that of when the distribution network is connected to the transmission grid.

Table 1, shows the contribution of the MVA synchronous generator to the general electricity company of Libya (GECOL) distribution network. All data about distribution lines, loads and turbine generator have been presented in [3]. The installation of synchronous generator (Gas turbine type) was done because of the shortage of power in the utility generation. The unit was installed at the HOTEL substation and the fault current between the two line connecting MENA and HOTEL substations was observed. It was noted that the fault current contribution of the DG reduces the current flowing between the two lines connecting MENA and HOTEL substations. The results shows that increasing the ratings of the DG unit affect the fault currents in the network. This is can be

further demonstrated by adding variable wind turbine as the distribution generator.

Tab. 1: Fault current from Mena bus to Hotel bus for both lines [3].

DG contribution	Two lines MENA-HOTEL fault Current(kA)
0 MVA	12.886
9 MVA	12.812
17.5 MVA	12.758
24 MVA	12.726

This is further demonstrated in [6] by considering the fault current in each section of the distribution system when a three phase fault is occurred at the end of the line. Fig.1, shows the fault current in each line sections [6], for both grid connected and islanding mode conditions. There is huge difference in the fault current for these two conditions, this is due to the fact that overcurrent protection system is designed to operate in transmission grid connected mode therefore causes the protection element to take longer time to clear a fault when the distribution system is isolated from the transmission grid. This is a big problem to the customers because when the fault not cleared fast, there might be loss of generations in the system [6].

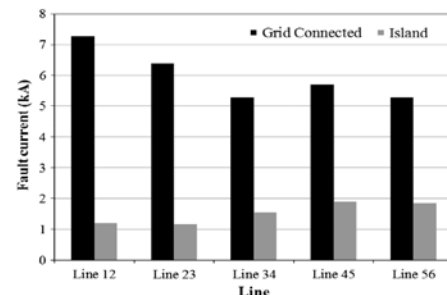


Fig.1: Fault current each line when a three-phase fault occur at the end of the line [6].

2.2. Effects of DG on Protection System

The connection of DG to distribution network reduces the transmission grid contribution to the total fault current. This can make the short circuit levels to be undetected due to the fact that the transmission grid contribution to the short circuit current never reaches up the pickup value of current for feeder protection element. This reduction to transmission grid contribution cause protection elements such as overcurrent relays, directional relays, and reclosers to malfunction and mis-coordinate. Most of these protection issues strongly depend on the protection elements scheme and distribution system configuration [7]. Mis-coordination issues can lead to false tripping of protection devices in the distribution network. And these false tripping problems usually occur in the distribution networks that are using underground cables

as well as overhead lines, whereas mis-coordination and recloser problems occur in the distribution networks that are using overhead lines [7]. Most of protection elements operation relies on detecting an abnormal current to the distribution network. To overcome this problem, a distance or overcurrent protection can be used with adaptive setting method [3, 6, and 8].

3 THE INVESTIGATED DISTRIBUTION SYSTEM

Fig.2, shows radial distribution system considered in this investigation. The sub transmission grid circuit of the investigated system consist a line to line voltage of 34.5 kV, 100 MVA, and distribution transformer of 100 MVA, 34.5/12.47 kV, with an impedance of 6%. Each of the 0.5 MVA loads are supplied by feeder 1, feeder 2, feeder 3, and feeder 4 on their corresponding locations. The data for distribution system transmission lines is given in Table 2. The system is integrated with a constant wind turbine generator (WTG). The WTG is a 1.6MW synchronous generator with connected via power electronic converter. The data and the model for the WTG are given in [9].

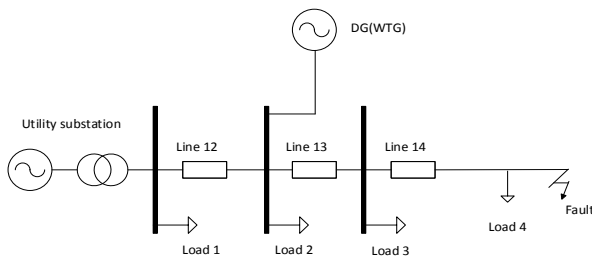


Fig.2: Distribution network with a wind generator [10].

Tab. 2: Distribution line data [10]

Line	Resistance(Ω)	Inductance(H)
Line12	2.94	0.02057
Line23	5.88	0.04115
Line3F	8.82	0.06172

In this study of load power flow, the wind speed is assumed to be constant, which implies that the distributed generator delivered constant power to the grid system. The connection of distributed generator is radial to the distribution network and protection elements are based on fault currents levels. The model of Fig.2, is simulated using PSCAD/EMTDC and the distributed generator was connected to each feeder, while the fault was created at the end of the line. Then, the currents, bus voltages and active power are measured in order to find the effect of DG in the distribution network. This help in getting the necessary settings for protection scheme [11]. The results are

compared with those one without the wind turbine connected.

3.1. Impact of DG on Short Circuit Levels of the System

3.1.1. Without DG

The system have been tested with different fault types including balanced and unbalanced. In the following analysis Fig.3, represents the currents in each feeder circuit when three phase fault is applied at the end of the line. It can be deduced that this is the steady state value of the current when there is fault in the system and it can be used as a detection level in overcurrent protection scheme. After the fault occurs, the current in each feeder rise considerably thus, become larger than the pickup setting. The rise in short circuit level can be easily detected by protection device installed in the system [12]. This primary protection device will then issue a signal to a switching device to trip the fault.

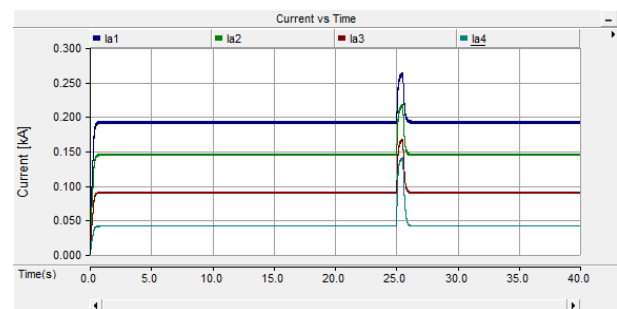


Fig.3: Currents in each feeder when three-phase fault applied at 25s for a duration of 0.5s.

3.1.2. With DG

Fig.4, shows the real and reactive power waveforms of the distribution generator when connected to the distribution network. It can be seen from Fig.4, that when a DG feed the grid system with the active power, the reactive power drop to zero.

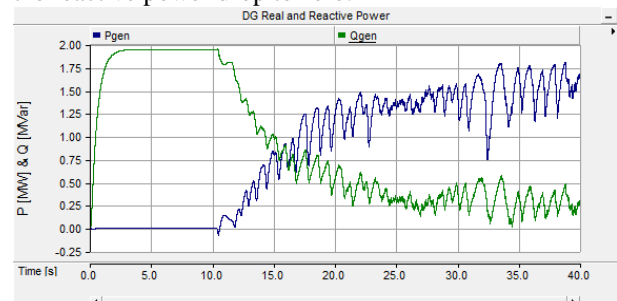


Fig.4: Active and Reactive power of the wind turbine distributed generator when connected with the grid.

Fig.5, shows a short circuit levels when the DG is connected on feeder 1 which is located between the utility substation and the fault. It can be observed from

Fig.5, that the fault current in feeder decrease with the presence of DG in the network. This is due to the underreach term introduce by a DG. The reduction of short circuit level in the line between substation and feeder one can cause minimum tripping of the upstream breaker close to the utility and it can cause coordination problems [13].

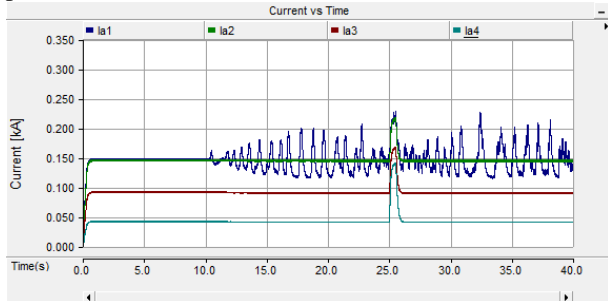


Fig.5: Currents in each feeder when DG connected to feeder 1.

The inclusion of DG in a distribution network destruct the short circuit levels of the network. The fault currents are increased when compared to that of normal conditions at which no distributed generator was installed. Table 3 shows the test results for short circuit levels when DG is connected at different locations on the distribution network. The results reveal that connecting the DG close to the fault (feeder 4) reduces the short circuit levels in the upstream feeders. It can be then concluded that distance of a DG from the fault location is one of the factors that influence the fault currents in the network. And the results also reveal that the fault contribution caused by one DG is not enough but it can cause an increase in fault current which can leads to mis-coordination of system protective devices.

Tab. 3: Short circuit levels on the distribution network during fault.

	<i>Currents Levels</i> [kA]			
	<i>Ia1</i>	<i>Ia2</i>	<i>Ia3</i>	<i>Ia4</i>
Without DG	DG on Feeder 1			
	0.261	0.215	0.166	0.139
With DG	0.219	0.216	0.167	0.140
With DG	DG on Feeder 2			
	0.234	0.194	0.171	0.143
With DG	DG on Feeder 3			
	0.250	0.208	0.167	0.139
With DG	DG on Feeder 4			
	0.256	0.211	0.162	0.136

Fig.6, shows the short circuit levels when DG is connected at Feeder 3. It can be observe from Fig.6, that all the short circuit level on the upstream part of the distribution network suddenly drops lower levels. And this have the negative impact on the upstream protection elements since it require adjustments in it pickup current settings. The short circuit level on the downstream device increases, this is due to the fact that DG introduce it own current which sums up with that one flowing in feeder 4. Again larger currents level can damage the protection elements.

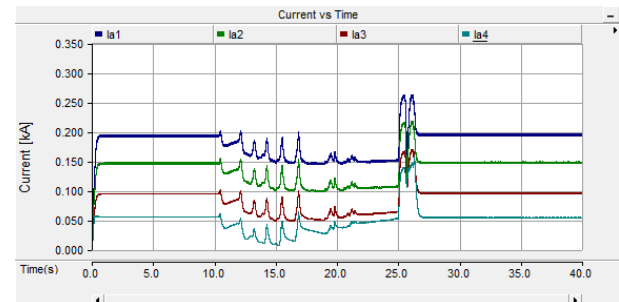


Fig.6: Currents in each feeder when DG connected to feeder 3.

Fig.7, shows the results of short circuit levels when DG is connected feeder 4 and the fault is applied between feeder 2 and 3. During fault, the current I_{a4} flows in the opposite direction with DG. This is due to the fact that the active power is negative produce by distributed generator. This has a big impact on the protection device because it can see the negative current and never respond to the fault. Presence of DGs in the network cause blinding of protection which occurs when the overcurrent protection device refuse to trip for fault [14]. Therefore, fault current can continue to flow until it exceed it limit and destroy the breaker.

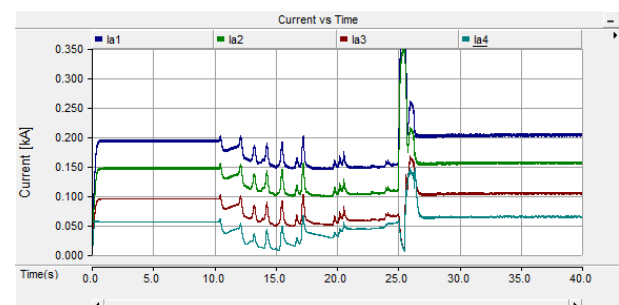


Fig.7: Currents in each feeder when three-phase fault applied between feeder 2 and 3.

3.2. Harmonic Impact of Distribution Generator

This section discusses the harmonics impact of distribution generators to the distribution network. Harmonics distortion of DG have an impact on system power quality thus causing the power quality to depend on the size of DG, total capacity of DG relative to the system, and the type of DG [15]. The harmonic

distortion is a biggest power quality concern because it can reduce the system performance. Non-linearity equipment such as converters, transformers and rotating machines are the main cause of harmonic distortion in electrical power systems [15,16].

The inclusion of DG to the distribution network changes the voltage profile along the feeder by changing the directions and magnitude of real and reactive power flow. This DG impact on voltage profile can be negative or positive depending on the DG configuration and its location [16]. Fig.8, shows the voltage profile when DG is connected to feeder 2 of the investigated distribution network. The results show that the voltage is lower on the feeder with distributed generator than that without distributed generator included in the network. To avoid this problem, an DG must be moved to the upstream feeder and to add voltage regulator controls to compensate the DG output [16].

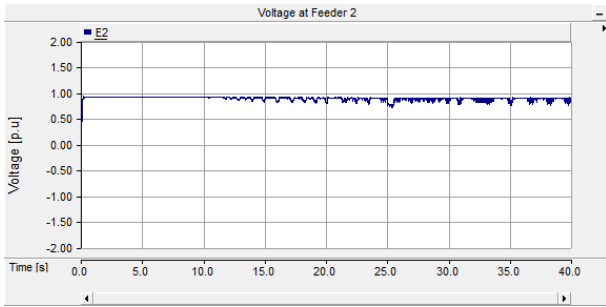


Fig.8: Voltage profile at feeder 2 when DG is connected at feeder 2

4 PREVENTION OF OVERCURRENT PROTECTION PROBLEMS

The first attempt to prevent fault detection problems is to adjust the settings of the protection devices manually. However, this attempt reduces the pick-up current and the sensitivity of the protection systems but it also leads to false tripping in case of fault occurring in the neighbouring feeder [3, 14]. Second attempt is to add a new protection device with an additional time delay to allow more time delay for areas that have DGs, this method is costly and it does not guarantee that faults are cleared on time unless they match the short circuit power of transmission grid [6].

Since the reduction to transmission grid contribution to the total fault current causes protection devices to malfunction, an attempt of using an adaptive method is well suited for distribution networks. This method allows the traditional settings of protection devices to be adaptively selected and this is a direct online method. The protection system has to be able to adapt its parameters to new configurations, and it also has to be able to maintain: Sensitivity, selectivity, reliability and velocity for perfect coordination [17]. The DGs impact on these settings (underreach) is compensated by using an adaptive

method. The method is valid for both cases when the distribution network is isolated from the utility and when it is connected to the utility. When the distribution network is isolated it is said to be operating in islanding mode, and therefore the settings are adaptively switched to island mode protection system settings. And when the distribution system is connected to the utility, once any fault occurs on the feeders, the current will rise, and fault detection mechanism to the system will switch back to detect the fault. The compensation of the current is calculated by using Kirchhoff's voltage law (KVL) of three sequence networks (positive, negative and zero) of the network. The calculated compensated current is digitally added to relay measured current in the secondary side to correct the underreach [5]. Equation (1) shows how the fault current level is changed with the installation of DG [5].

$$I_F = I_{FN} - I_U \quad (1)$$

Where,

I_F is the total fault current seen by overcurrent relay including underreach component (DG).

I_{FN} is the total fault current seen by the overcurrent relay with no underreach component (DG).

I_U is the current caused by underreach component and is termed as compensation current.

Fig. 2, shows currents seen by a relay for three phase fault when there's no adaptive system and when there is. These results were obtained from the test system which is part of a distribution network, of Himmerlands Elforsyning, in Aalborg, Denmark [5]. The distribution network uses wind turbine generator (WTG) as the distributed generator. The model is based on micro-grid, and the overcurrent protection relays (IEC 255-3) is used. Dotted lines represent uncompensated currents and bolds for compensated. Brown for no DG case, Blue for WT1=0.5 MW and WT2=0 MW, Red for WT1=2 MW and WT2=0 MW and finally green for WT1=2 MW and WT2=1 MW, K=+10%.

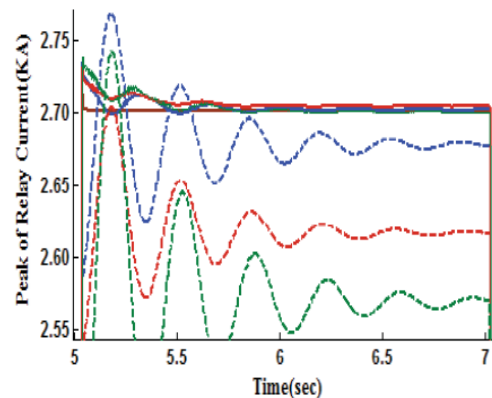


Fig.9: Currents seen by overcurrent relay for three phase fault [5].

5 CONCLUSION

The presence of distribution generators in distribution network is beneficial to the customers and also challenging in the protection system of the network. Radial Distribution systems overcurrent protection is affected by the impact of the DG which cause the current levels of the network to drop. False tripping, blinding of protection, and miscoordination are the main impacts on traditional overcurrent protection. The investigated distribution network study reveal that new technology of protection is needed for improving traditional overcurrent protection. The presented solutions show that by improving the protection elements settings, used of fault current limiters and the addition of directional elements, the problems of DG can be mitigated.

REFERENCES

- [1] M.Dewadasa, A.Ghosh and G.Ledwich,"Protection of distributed generation connected networks with coordination of overcurrent relays," IEEE Industrial Electronics Soc., pp. 924-929, 2011.
- [2] C.Liu,Z.Chen and Z. Liu,"A communication-less Overcurrent Protection for Distribution System with Distributed Generation Integrated," in Proc. IEEE Power Elec. For Distributed Gen. Syst. (PEDG), pp. 140-147, 2012.
- [3] A.Elhaffar, N.El-Naily and K.El-Arroudi,"Management of Distribution System Protection with High Penetration of Distributed Generations," International Conf. on Energy and Management.Ast Istanbul,Turkey,vol.1.no.,pp.1-8,Sep. 2014.
- [4] K.Vijeta and D.V.S.S Siva Sarma,"Protection of Distributed Generation connected Distribution system," Advances in Power Conversion and Energy Technologies (APCET),Int. Conf.,pp.1-6,2012.
- [5] R.Jafari,M.S. Naderi,G.B.Gharehpetian and N. Moaddabi,"Compensation of DGs Impact on Overcurrent Protection System of Smart Micro-Grids,"International Conf. and Exhibition on Electricity Distribution (CIRED),no.0924.,pp.1-4,2013.
- [6] P. Mahat, Z. Chen and B. Bak-Jensen,"A simple Adaptive Overcurrent Protection of Distribution Systems with Distributed Generation,"IEEE Trans. Smart Grid,vol.2,pp.428-437,Sep.2011.
- [7] A.K. Tiwari,S.R.Mohanty and R.K. Singh,"Review on Protection Issues with Penetration of Distributed Generation in Distribution System,"in Proc. International Electrical Engineering Congress (IEECON),pp.1-4,March.2014.
- [8] A. Sinclair,D.Finney,D.Martin and P.Sharma,"Distance Protection in Distribution Systems:How it Assists with Integrating Distributed Resources,"IEEE Trans. Industry Applications,vol.50,no.3,May/June.2014.
- [9] B.Upputuri, "PSCAD based Wind Turbine Application,"[online].Available:https://www.academia.edu/6071105/PSCAD_Power_System_Simulation_WIND_TURBINE_APPLICATIONS_TECHNICAL_PAPER
- [10] P.M. Anderson,Power System Protection, vol. I. New York: Wiley, 1999, p. 226.
- [11] H.B. Funmilayo and K.L. Butler-Purry,"An Approach to Mitigate the Impact of Distributed Generation on the Overcurrent Protection Scheme for Rdial Feeders,"Power System Conf. and Exposition(PES),pp.1-11,March.2009.
- [12] P.S.Babu, S.V. Jayaram Kumar and P.R. Krishma Chaitanya,"Digital Relay Based Adaptive Protection for Distributed Systems with Distributed Generation," International Journal of Energy Science(IJES),vol.1,no.2,pp.72-77,2011.
- [13] H.B. Funmilayo and K.L. Butler-Purry,"Overcurrent Protection Issues for Radial Distribution Systems with Distributed Generators,"Power and Energy Society General Meeting,pp.1-5,July.2009.
- [14] A.R. Haron,A. Mohamed,H. Shareef and H.Zayandehroodi,"Analysis and Solutions of Overcurrent Protection Issues in a Microgrid," IEEE Int. Conf. on Power and Energy (PECon),December.2012.
- [15] A.F. Abdul Kadir,A. Mohamed and H.Shareef," Harmonic Impact of Different Distributed Generation Units on Low Voltage Distribution System,"IEEE Int. Electric Machines and Drives Conf. (IEMDC),pp.1201-1206.May.2011.
- [16] A.F. Sarabia,"Impact of Distributed Generation on Distribution Systems,"Masters.dissertation,Dept.Eng,Univ.Aalborg,Den mark,June.2011.
- [17] A.F. Contreras,G.A. Ramos and M.A. Rios,"Methodology and Design of an Adaptive Overcurrent Protection for Distribution Sytems," Int. Journal of Electrical and Computer Science,vol.12,no.05,October.2012.

Implementation of Steam Turbine and Governing System using Programmable Logic Controller for Power Systems Studies

A.K. Saha

University of KwaZulu-Natal, Mazisi Kunene Road, 4001, Durban, South Africa

E-mail: saha@ukzn.ac.za

Abstract: This paper presents modelling and implementation of IEEE Type 1 governor and turbine model on real-time digital simulator and programmable logic controller for power system studies. Real-time digital simulator enables studying power systems in real-time scenarios whereas governor and turbine model implemented on a programmable logic controller provides a true sense of analogue signals that resemble actual ones associated with electric generator, governor and turbine at utility power plants. The simulation results obtained from mathematical model on real-time digital simulator were compared with that on a programmable logic controller for normal operating condition, load change, changes in grid frequency and for if there is any abnormal condition in the system to which the generator is connected. It has been found that the model implemented on programmable logic controller provides almost the same response with changing conditions as is obtained from real-time digital simulator mathematical model which is very useful for power systems education and training.

1 INTRODUCTION

Steam turbines are widely used as prime movers in many fields including power generating stations to convert stored energy of high pressure and high temperature steam into rotational energy, which in turn is converted into electrical energy using a generator [1], [2] and governing system of a steam turbine is an important element as it guarantees turbine unit to operate safely and stably. Not only that, it has direct influences on the economic efficiency and reliability of turbine unit [2,] [3]. Hence, the basic functions of a steam turbine governing system can be categorised as: normal speed/load control, over-speed control and over-speed trip. Further, controls for the turbine include a number of other functionalities such as start-up/shutdown controls, synchronisation, loading of steam turbine generating units and auxiliary pressure control [1], [4]. Therefore, for accurate analysis of power system stability, governing system has to be modelled as accurately as possible [3].

As the turbine control system is one of the key control elements in the dynamic performance of steam power generating units [4], this work considers modelling of IEEE Type 1 speed governor and steam turbine that is useful to study power system steady-state and stability issues. The mathematical model of governor and steam turbine are implemented first on RSCAD software of real-time digital simulator (RTDS)

system and thereafter the same were implemented on a PLC being connected in-hardware-loop with RTDS that replaced the mathematical model. The models were tested and verified with changing operating conditions on the generator connected to it.

Section 2 of this paper discusses about governor and steam turbine model while section 3 provides relevant information of RTDS and PLC. Section 4 presents the system configuration considered for the work with simulation results and analyses illustrated in section 5. Finally, the work is concluded in section 6.

2 GOVERNOR AND STEAM TURBINE MODEL

The steam turbine governing system used in power plant is a complex system concerning some non-linear parts, such as time-lag, inertia, disturbance, dead-time and saturation [5]. There are turbine and governor models for load frequency control and also there are recommendations on functional and performance characteristics related to speed/load control systems for steam turbines generator units that may be interconnected to power systems. According to IEEE recommended practice, a speed-load control system, speed-load reference changer, valve position limiter are the most important ones for a governor model. The speed-load control includes means that allows steady-state speed regulation whereas the speed-load changer allows speed or power output of the turbine to be changed. The speed-load control system should be capable of controlling, with stability, the speed of the turbine at power output between zero and maximum, inclusive, when the generator is operating isolated or in parallel with other generators. The valve position limiter limits the degree of opening of the control valves to any value with the full range of valve travel while the turbine is in operation [6], [7].

A typical governor model for steam turbines has two main sections, governor and steam control valve, whose output is effective control valve area in response to speed deviation of the machine, and a section modelling the turbine, whose input is steam flow and output is mechanical power applied to the generator rotor [8]. For this work, IEEE Type 1 speed governor and steam turbine model is considered [9], [10] which are shown in Fig. 1 and Fig. 2 respectively. The turbine portion of the model can be used to non-reheat, tandem compound and cross compound arrangements. For cross compound configuration, two torque signals are available as output

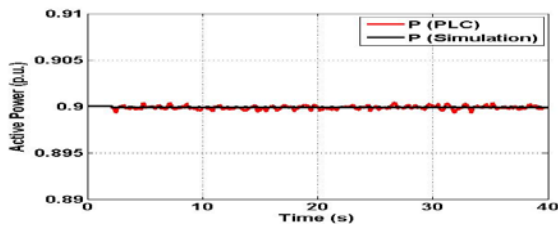


Fig. 6: Generator active power (normal operation)

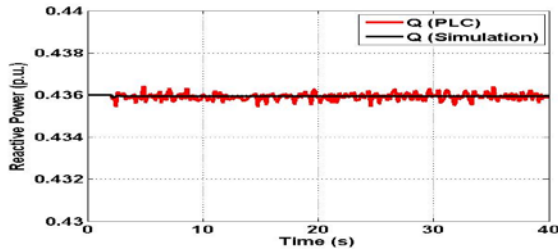


Fig. 7: Generator reactive power (normal operation)

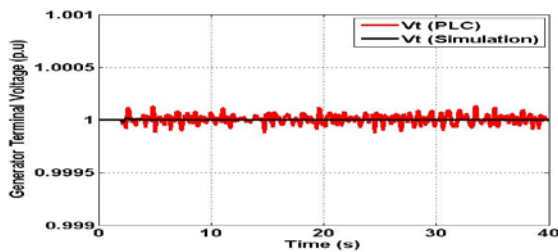


Fig. 8: Generator terminal voltage (normal operation)

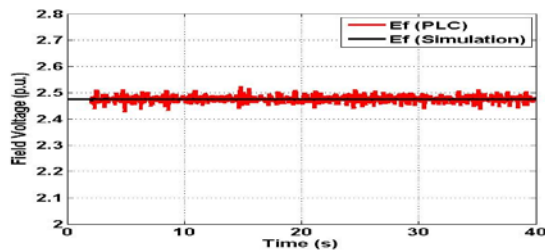


Fig. 9: Generator rotor voltage (normal operation)

The corresponding generator terminal and rotor voltages are shown in Fig. 8 and Fig. 9 to illustrate that the terminal voltage is held at its rated value and rotor voltage is maintained constant during the normal operation at this particular loading on the generator. Turbine torques and generator rotor angles were also observed and illustrated in Fig. 10 and Fig. 11 respectively that ensure stable operation of the generator system while supplying electrical power to the grid.

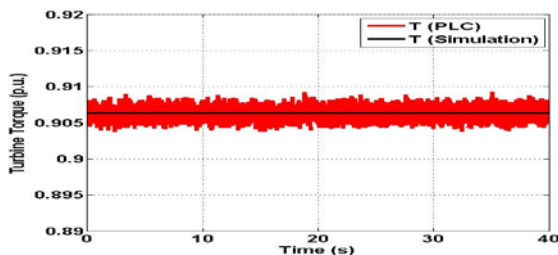


Fig. 10: Turbine torque (normal operation)

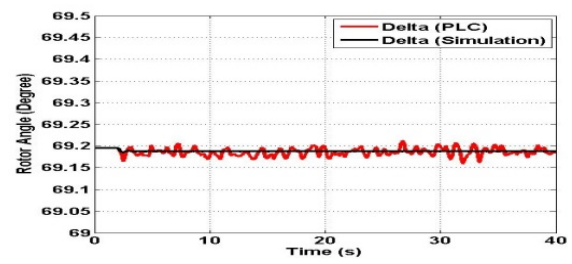


Fig. 11: Generator rotor angle (normal operation)

5.2. Changing Load on the Generator

In this case, the load reference on the generator was changed from its initial value of 0.9 p.u. to 0.5 p.u. With change in load reference, it has been found that governor turbine model responded as desired to reduce the active power supplied by the generator to 0.5 p.u. as shown in Fig. 12. The responses from simulation and PLC were found to be exactly the same which conform the proper implementation and response from the governor turbine models. The change in reactive power due to change in active power is illustrated in Fig. 13 while generator terminal and rotor voltages are illustrated in Fig. 14 and Fig. 15 respectively which demonstrates that due to changes in power the terminal voltage initially changes, but the exciter/AVR functions to stabilise the terminal voltage to its rated value of 1 p.u. fast enough. The corresponding turbine torques and rotor angles were also observed and found to be as expected which are illustrated in Fig. 16 and Fig. 17 respectively.

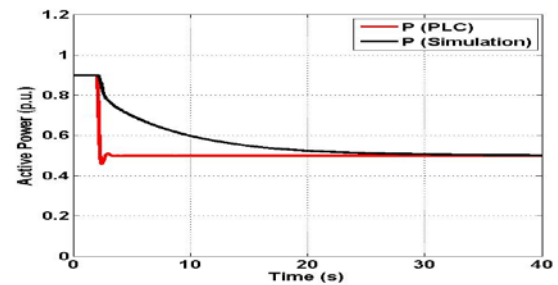


Fig. 12: Generator active power (0.9-0.5 p.u.)

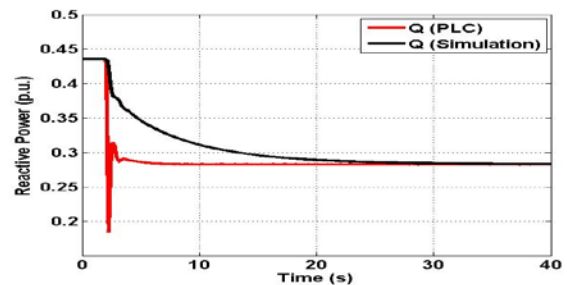


Fig. 13: Generator reactive power (0.9-0.5 p.u.)

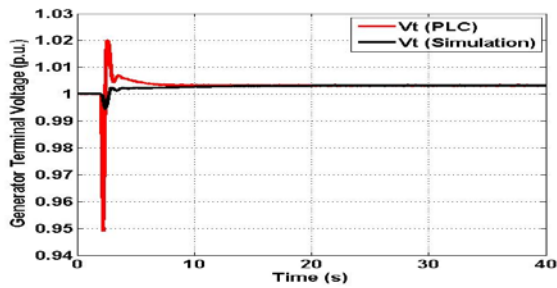


Fig. 14: Generator terminal voltage (0.9-0.5 p.u.)

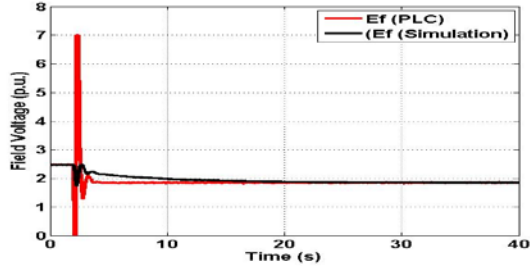


Fig. 15: Generator rotor voltage (0.9-0.5 p.u.)

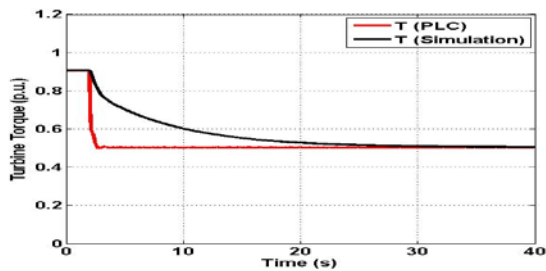


Fig. 16: Turbine torque (0.9-0.5 p.u.)

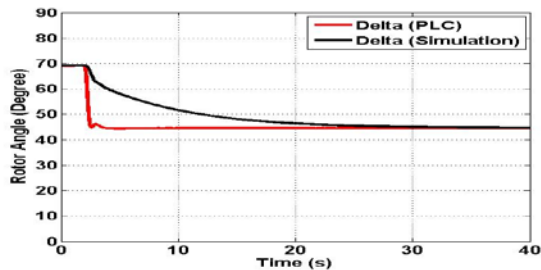


Fig. 17: Generator rotor angle (0.9-0.5 p.u.)

5.3. Changing Grid Frequency

In this case, the system frequency was changed to test the performance of the governor and turbine model.

5.3.1. Change in Grid Frequency from 60 Hz to 59.5 Hz

As a result of step change in grid frequency by 0.5 Hz, the changes in generator active powers and reactive powers are shown in Fig. 18 and Fig. 19 respectively to show that there has been an increase in active power as the frequency was reduced and the powers from both simulation and PLC model providing the same output. Generator terminal voltages, rotor voltages, turbine

torques, rotor angles and changes in rotor angles were also observed and shown in Fig. 20-24 respectively.

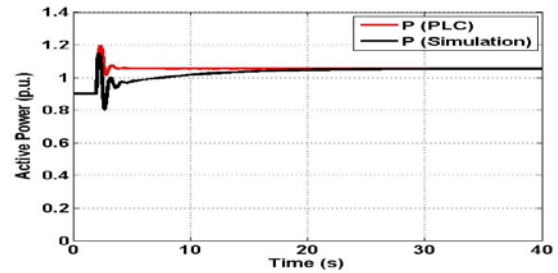


Fig. 18: Generator active power (60-59.5 Hz)

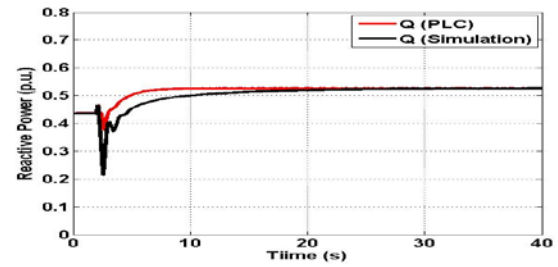


Fig. 19: Generator reactive power (60-59.5 Hz)

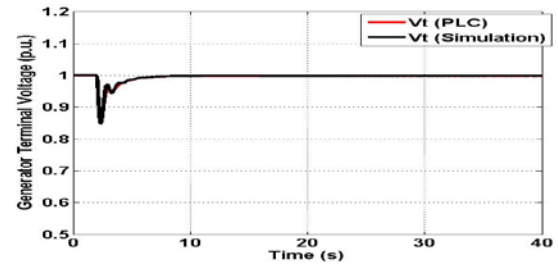


Fig. 20: Generator terminal voltage (60-59.5 Hz)

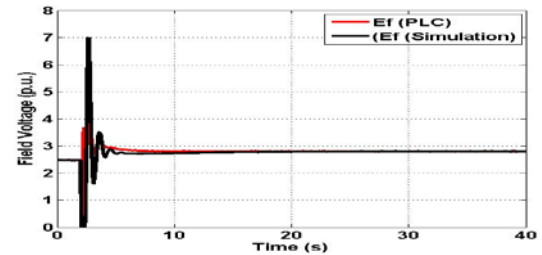


Fig. 21: Generator rotor voltage (60-59.5 Hz)

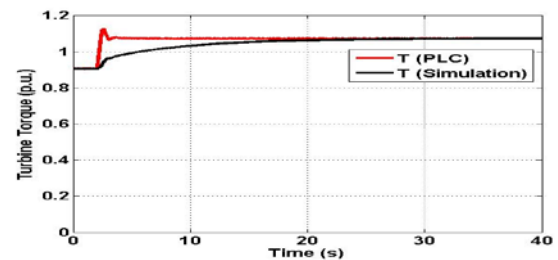


Fig. 22: Turbine torque (60-59.5 Hz)

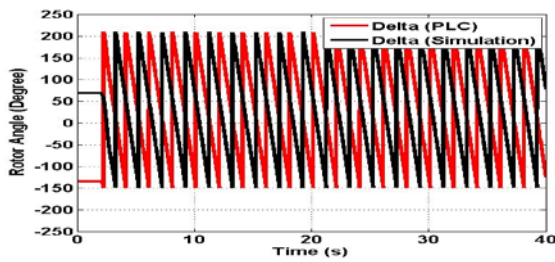


Fig. 23: Generator rotor angle (60 - 59.5 Hz)

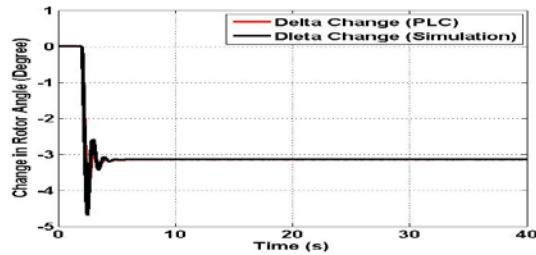


Fig. 24: Changes in rotor angle (60 - 59.5 Hz)

5.3.2 Change in Grid Frequency from 60 Hz to 60.5 Hz

With a step increase in grid frequency by 0.5 Hz, changes in active powers are shown in Fig. 25 and it is as expected as the active delivered by the generator should decrease with increase in frequency picked up by the governor associated with it and turbine model will set the corresponding torque which is illustrated in Fig. 29. Generator reactive power change, terminal voltage, rotor voltage, rotor angle and changes in rotor angles were again observed and compared for simulation and PLC model as illustrated in Fig. 26-28 and Fig. 30-31 respectively.

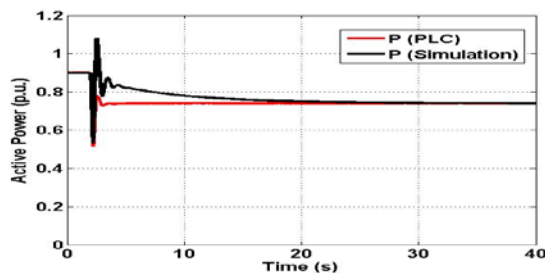


Fig. 25: Generator active power (60-60.5 Hz)

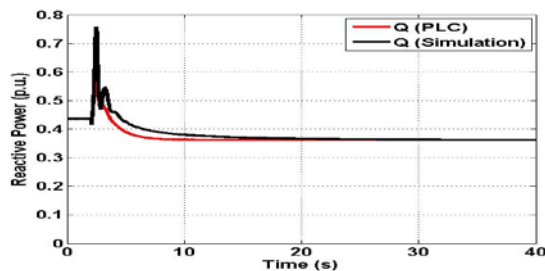


Fig. 26: Generator reactive power (60-60.5 Hz)

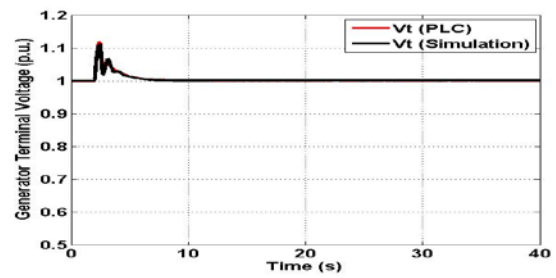


Fig. 27: Generator terminal voltage (60-60.5 Hz)

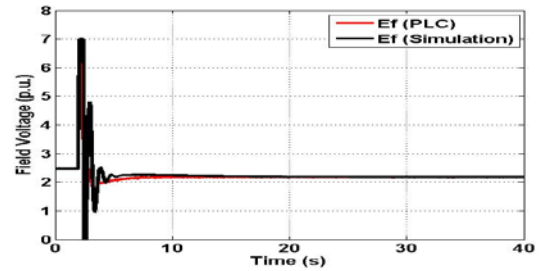


Fig. 28: Generator rotor voltage (60-60.5 Hz)

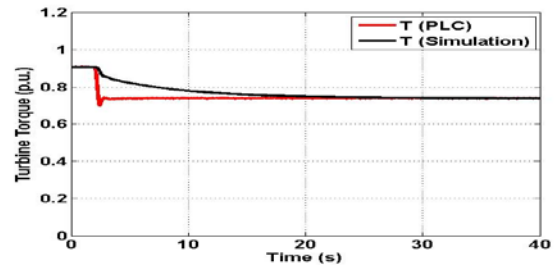


Fig. 29: Turbine torque (60-60.5 Hz)

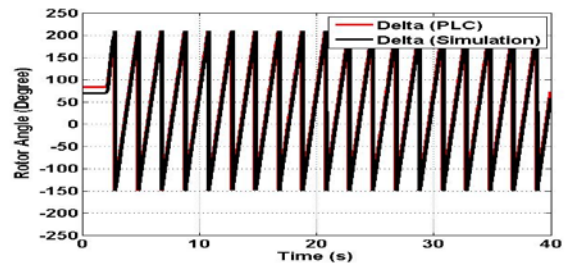


Fig. 30: Generator rotor angle (60-60.5 Hz)

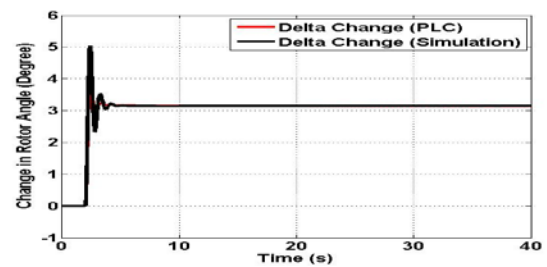


Fig. 31: Changes in rotor angle (60-60.5 Hz)

5.4. Loss of One of the Transmission Lines

This test case was conducted to ensure that the generator and its controls are capable of maintaining transient stability which mainly depends on generator loading, fault location, fault clearing time, post-fault transmission system reactance, generator reactance, generator inertia, generator internal voltage or field

excitation and infinite bus voltage. Therefore, in this case, a fault was introduced on the bottom transmission line of the parallel transmission lines and then the fault was cleared by switching off the breakers associated with it. The results were observed with simulation and PLC models as shown in Fig. 32-37 and they depict that the model can maintain the power transmission without losing stability.

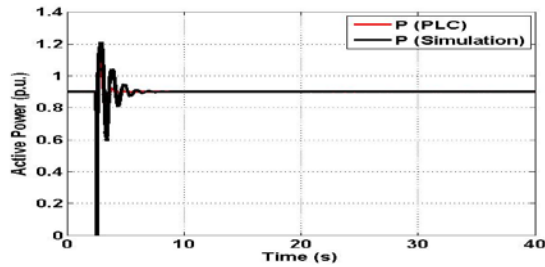


Fig. 25: Generator active power (fault on line)

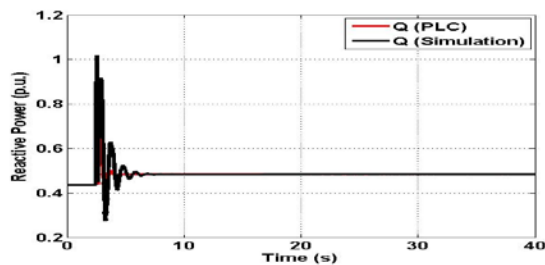


Fig. 26: Generator reactive power (fault on line)

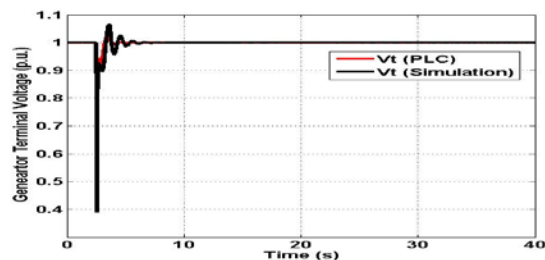


Fig. 27: Generator terminal voltage (fault on line)

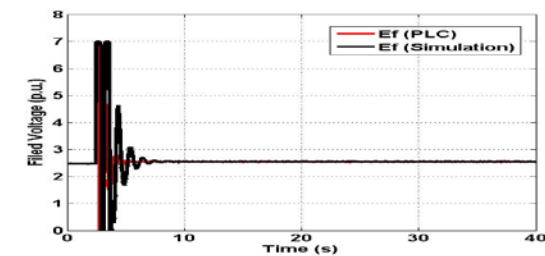


Fig. 28: Generator rotor voltage (fault on line)

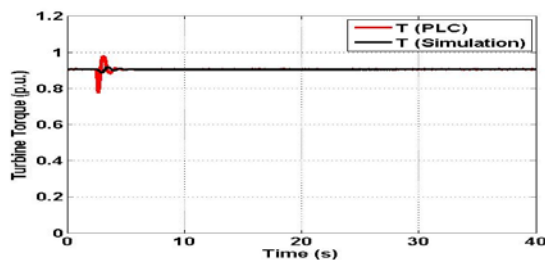


Fig. 29: Turbine torque (fault on line)

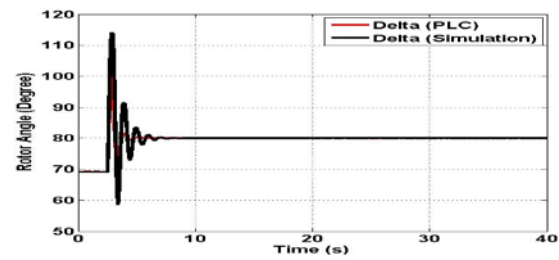


Fig. 30: Generator rotor angle (fault on line)

6 CONCLUSIONS

The paper presented modelling and implementation of governor and turbine, IEEE Type 1 and compared the performances considering various operating conditions such as changes in load reference to generator, changes in grid frequency and faults in one of the transmission lines to which the generator is connect to test its transient stability. The results obtained from simulation model and PLC were found to be as expected for all the case studies considered including transient stability case. Such a model is very useful in understanding the basic operation of generator, its controls and especially their implementation using programmable logic controllers that provides a true analog signal that resemble actual signals in utility power generators when they are in operation and subjected to changes in load, frequency and disturbances in transmission systems. Therefore, this model can be taken as one that could be introduced into electrical power systems education that encourages learning using real-time simulation and almost a practical power system.

7 REFERENCES

- [1] P. Kundur: "Power system stability and control", *Electric Power Research Institute*, McGraw-Hill, Inc., New York, ISBN-13:978-0-07-035958-1.
- [2] G. Han, L. Chen, J. Shao, and Z. Sun: "Study of fuzzy PID controller for industrial steam turbine governing system", *Proc. of Communication and Information Technology, ISCIT*, 2005, pp. 1228-1232.
- [3] Y. Tao, F. Yongxin, R. Yong, T. Lei, L. Yanghai: "Parameter identification of steam turbine speed governor system", *Proc. of Power and Energy Engineering Conference (APPEEC)*, Asia-Pacific, 2012, pp. 1-8.
- [4] H. Nademi, and F. Tahami: "Robust controller design for governing steam turbine power generators", *Proc. of International Conference on Electrical Machines and Systems, ICEMS*, 2009, pp. 1-5.
- [5] S. Wang, Y. Jiang, and H. Yang: "Chaos optimization strategy on fuzzy-immune-PID control of the turbine governing system", *Proc. of the IEEE/RSJ, International Conference on the Intelligent Robots and Systems*, October 9-15, 2006, Beijing China, pp. 1594-1598.
- [6] IEEE Standard Boards: "IEEE recommended practice for functional and performance characteristics of control systems for steam turbine generator units", *The Institute of Electrical, and Electronics Engineers, Inc.*, 1992, USA, ISBN-1-55937-189-7, pp. 1-28.
- [7] AIEE-ASME Committee Report: "Recommended specifications for speed-governing of steam turbines intended to drive electric generators rated 500 kW and larger", *Transactions of the*

- American Institute of Electrical Engineers, Power Apparatus and Systems, Part III*, Vol. 76, Issue: 3, 1957, pp. 1404-1411.
- [8] F.P. de Mello: "Boiler models for system dynamic performance studies", *IEEE Transactions on Power Systems*, Vol. 6, Issue: 1, 1991, pp. 66-74.
- [9] RTDS: "Manual Set", *Real Time Digital Simulation*, pp. 1-517, November 2006.
- [10] A. Bobon, S. Paszek, P. Pruski, T. Kraszewski, and M. Bozarska: "Computer-aided determining of parameters of generating unit models based on measurement tests", *Przegląd Elektrotechniczny (Electrical Review)*, ISSN: 0033-2097, R. 87 NR, 5/2011, pp. 17-21.
- [11] RTDS: "Manual Set", *Real Time Digital Simulation*, pp. 1-517, November 2006.
- [12] RTDS: Applications, closed-loop testing of physical devices, <http://www.rtds.com/applications/closed-loop-testing/closed-loop-testing.html>
- [13] Simatic S7-1200 Programmable controller, System Manual, Siemens AG, Industry Sector, Germany, 11/2011, pp. 1-796.

A simulated energy monitoring system to enable undergraduate engineering students to grasp fundamental energy generation principles

P.E. Hertzog and A.J. Swart

Department of Electrical, Electronic and Computer Engineering, Central University of Technology, Private Bag X20539, Bloemfontein, South Africa, 9300. Email: phertzog@cut.ac.za

Abstract: Engineering students must be equipped with the right graduate attributes in order to contribute effectively to the socio-economic growth of their communities. These vital attributes may be demonstrated by students through the use of various educational technologies, including computer based simulations. The purpose of this paper is to describe the design of a simulated energy monitoring system that was developed at the Central University of Technology to enable freshmen engineering students to grasp fundamental energy generation principles relating to solar energy. This system enables students to grasp principles of energy flow in a typical PV system, as well as the importance that power efficiency exerts on the overall performance of the system. The majority of students exposed to this system have indicated that they enjoyed the simulations, having applied new knowledge in a practical environment.

Keywords: LabVIEW, PV, education, visual, kinaesthetic

1. INTRODUCTION

“During my travels in Iraq, Israel, Gaza, Brazil, Indonesia, Japan, Europe and all over the United States, I have seen and heard the voices of people who want change. They want the stabilization of the economy, education and healthcare for all, renewable energy and an environmental vision with an eye on generations to come” [1]. These words by the musician, Michael Franti, point to society’s desire for a more sustainable future. This sustainable future requires energy monitoring, in order to ascertain the level and quality of sustainability. This monitoring leads to energy management which refers to an efficient and effective use of energy to minimize cost, improve energy efficiency, and reduce greenhouse gas [2]. This efficient and effective use of energy often requires some or other form of control.

Dynamic modelling and computer based simulations (CBS) are valuable tools for product and process understanding, design, optimisation and control [3]. This aspect of control is especially important in renewable energy systems in order to mitigate energy losses and improve system efficiency. Moreover, interactive CBS can provide an “interactive-learning environment” in which participants can apply what they have just learned in a dynamic scenario, receiving instant feedback and being able to reflect on what can be improved through trial and error [4]. This improvement of the system is once again achieved through some or other control mechanism, where students can almost instantaneously visually observe the effects of their decisions. This brings to mind the various learning styles of students.

CBS created in software packages, such as MATLAB or LabVIEW, appeals to a wide range of student learning styles, including inductive, sequential, active and visual learning styles. In fact, previous research has shown how an ARDUINO board can be integrated with MATLAB to achieve specific learning objectives and provide a

successful engineering experience for freshman engineering students [5, 6]. Academics therefore need to adjust their preferred teaching styles to accommodate the diverse learning styles of students [7] and to understand the connection between particular forms of educational technology and their effects on learning and teaching styles [8]. CBS are therefore key educational technologies which may be used to achieve this goal.

CBS are used in the training of engineering students when it is difficult or impossible to expose them to real life contexts or equipment. Research has shown that CBS can provide opportunities for students to perform experimental manipulations that would be inaccessible in real-life [9]. However, simulations are not ideal and it is therefore important for the academic to understand the limitations of this educational technology. Only then can appropriate guidance be provided to students in order to help them bridge the gap between the theoretical and practical instruction. Some disadvantages of using CBS in engineering education are that they can be expensive, time consuming to develop and difficult to grade [10]. Advantages of CBS can include the fact that it allows the student to freely vary specific parameters and observe the related effects, explore theoretical principles or systems under extreme conditions, allow for a detailed analysis of systems and are easily reproducible [11].

The purpose of this paper is to describe the design of a simulated energy monitoring system (SEMS) that was developed at the Central University of Technology (CUT) to help train freshmen engineering students in a renewable energy course. This SEMS is designed to help engineering students grasp fundamental principles of energy generation, which include energy efficiency, electrical energy flow, energy storage in a battery, energy usage and energy optimisation. The paper firstly explains the main energy generation principles, followed by the context of this study. Thereafter, the SEMS is introduced and explained followed by succinct conclusions.

2. ENERGY GENERATION PRINCIPLES

To enable students to grasp the operation of an energy generation system, with specific reference to a standalone PV system, requires understanding of energy flow, efficiency and storage. A simple analysis of the energy flow in a system is important in order to gain insights into the conversion process [12]. Maintaining a good energy efficiency is furthermore important for battery longevity [13], which is where the generated energy is stored.

The flow of electrical energy refers to the movement of electrons from the generating source to the storage device and associated loads. Students must be able to observe the input and output powers associated with each section of the energy system, thereby keeping track of the electrical energy flow. The main input power from the sun to the generating source (being the PV module in this case) is indicated in Watts/square meter (W/m^2) while the energy that is stored in the batteries (storage device) is indicated in Ampere hours (Ah). During direct sunlight hours, electrical energy will flow from the source to the storage device and then to the loads. During non-direct sunlight hours, students must be able to observe how the storage device is depleted, as it alone supplies energy to the load. The efficiency of the various components in the system plays a major role in the overall performance of the system, and is calculated using Equation 1.

$$\eta = \frac{P_{out}}{P_{in}} \quad (1)$$

Where

η = Efficiency of component

P_{out} = Output power

P_{in} = Input power

However, students tend to better understand complex processes, like the flow of energy in energy generation systems when they actively participate in the simulation of these systems [14, 15]. This helps them to visualize the operation of the different sections within the system, thereby moving away from purely abstract thinking. Abstract thinking is difficult, as it takes a great deal of time to become familiar with theory at any level of depth [16]. However, the use of active experimentation in CBS (part of Kolb's Learning Cycle [17]) enables students to engage with the theory, eventually resulting in abstract conceptualization. The importance of helping students grasp these different energy generation principles is mandated by the logarithmic growth in renewable energy, including the construction of many solar farms.

3. CONTEXT OF THIS STUDY

In November 2013, the first solar farm of 75 MW (near Kalkbult) was connected to the South African National Grid [18]. Kalkbult was the first of many to follow. The Renewable Energy Independent Producers Procurement Programme, directed by the Department of Energy, has

approved many projects for the Northern Cape, which is one of the provinces from where many CUT students emanate. This provides CUT with a unique opportunity to provide effective training to freshman engineering students regarding the operation, installation and maintenance of these renewable energy systems. This opportunity aligns itself with Vision 2020 of CUT which aims to be a centre of knowledge, innovation and excellence producing a critical mass of innovators that directly contributes to prosperity-creation [19]. One way of achieving this vision is by graduating an industry-ready workforce that possesses the right graduate attributes. These include problem solving, engineering design, communication, teamwork and technical competence.

Freshman engineering students at CUT may choose to enrol for a number of different National Diplomas or Certificates where these graduate attributes may be demonstrated. The National Diplomas usually requires a minimum of three years to complete, while the certificate requires one year of full time study. The certificate is designed to empower engineering students with the right graduate attributes to contribute to the socio-economic development of communities, societies and industry. The Higher Certificate in Renewable Energy Technologies (HCRET) has been offered at CUT since January 2014 and was specifically developed to supply technical competent people to the renewable industry in the Northern Cape and Free State. The HCRET is the first pre-graduate course in renewable energy that was approved by the South African Qualification Authority (SAQA) [20]. Successful completion of the HCRET indicates that students have been able to demonstrate the acquisition of specific learning outcomes (and subsequent graduate attributes) relating to the operation, design and installation of PV and Small Wind energy systems [21]. Digital Literacy, Academic Literacy, Mathematics I A and Mathematics I B are compulsory modules in this certificate (see Table 1), offered by service departments at CUT. The module entitled "Health and Safety: Principles and Practice" is offered by a professional service provider from within this field.

Table 1: Modules for HCRET [7]

Semester 1	Semester 2
Digital Literacy	Health and Safety: Principles and Practice
Academic Literacy and Communication Studies	Electrical Installation Practice
Mathematics I A	Power Generation and Storage
Electrical Engineering I	Solar Energy Systems II
Applied Physics of Energy Conversion	Small Wind Generation
Solar Energy Systems I	Mathematics I B

The SEMS was developed for the Solar Energy Systems II module which features 5 main sections. The introduction to solar energy covers basic concepts,

principles, and definitions of energy generation. The next section introduces students to the different solar system configurations, including grid-tied and stand-alone systems. The third section covers aspects relating to PV system design, where the student must be able to design a complete PV system. Finally, AC and DC electrical measurements are discussed; students must be competent in their ability to safely do AC and DC measurements on a PV system. Many parts in the syllabus of Solar Energy Systems II can be addressed by the use of simulation.

4. LABVIEW SIMULATION INTERFACE

Figure 4 shows the LabVIEW user interface of a stand-alone PV system that was designed to be the control panel of the SEMS. The first section represents the energy source, namely the sun. The simulation illustrates a 24-hour cycle and can be used in two modes. In the first mode, the sun follows its daily orbit and the energy output follows the form of a bell-shaped curve reaching its peak at around 12H00. In this mode, the student has no control over the energy from the sun and the simulation reflects the normal daily radiation available from the sun, peaking at 1000 W/m^2 . In the next mode, the student may manipulate the energy source to visually observe its effect on the subsequent sections.

The second section represents the PV array. This is where the student can change the output of the array from 0 to 1000 W. If, for example, a 100 W module is selected and the input from the sun is set at the Standard Test Condition (STC) of 1000 W/m^2 , then the output of the module will be 100 W. The output of each section is shown in Watts to enable students to grasp energy efficiency principles. The dust and mismatch factor of the PV array is another setting in the PV array section. The typical value for dust and mismatch on a PV array is 15% [22], with students being able to control it in the SEMS with values between 8 and 15%.

The third section illustrates the charge controller that will charge the batteries as well as protect them from discharging beyond a recommended limit. Modern charge controllers have typical efficiencies of 97% [23]. Students may control the efficiency of the charger by varying it between 50 and 100%, again being able to visually observe its effect on subsequent sections.

The fourth section is the battery bank (storage device). The efficiency of the battery may also be altered between 80 and 100%, which is in line with current technology providing battery efficiencies of around 85%. It must be noted, though, that battery efficiencies are highly dependent on charging and discharging regimes as well as one the depth of discharge [24]. The battery's voltage, charge and state of charge are also indicated in this section.

The fifth section is the inverter where the student may once again set its efficiency between 80% and 100%.

Current technology allow for inverter efficiency's in the order of 97% [25]. However, it must be noted that inverter efficiency is dependent on the AC load and may vary greatly over the operating range of the inverter [26].

The sixth section shows the losses in the wiring which can be controlled between 0% and 20%. Wiring losses include losses in electrical connections in the system as well as resistive losses that are affected by the length and diameter of the wires that are used [27].

Students may control the size of the load in the seventh section (0 to 200 W), visually observing the flow of energy from the storage section. The control panel of the SEMS is directly linked to the block diagram window available in LabVIEW, and is discussed in the next section.

5. LABVIEW SIMULATION CIRCUIT

The SEMS displays data for a one day period of 24 hour. If the simulation runs too quickly, then the student will not have time to interpret what is visually shown nor have time to control the various sections in order to optimize energy efficiency. This is set using the main loop time which is shown in Figure 1 to be 200 ms. It can also be seen that the main loop will repeat a total of 144 times at 200 ms each, resulting in a total simulation time of 28.8 s. This provides sufficient time for students to interact with the simulation, visually observing the effects of their decisions implement by the various controls. The simulation is set so that each sample represents 10 minutes of the 24 hour day. Three important parameters of the system is logged in the time domain over a 24 hour period and displayed on the control panel. These include the power from the PV array, the charge in the battery and the power to the load.

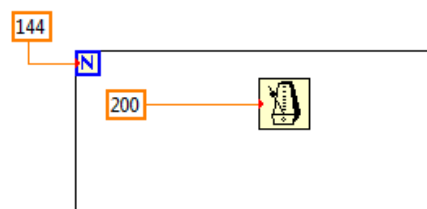


Figure 1: Loop timing in milliseconds

Figure 2 presents the components which are required for section 1 of the SEMS shown in Figure 1. A small part of the matrix that represents the values of the output of the sun is visible. The matrix consists of a set of 144 values that represents the bell-shaped curve of the sun's normal daily output.

Figure 3 illustrates the components of the second section shown in Figure 4. Here, the value of incoming solar radiation is divided by 1000, which equates to the STC of 1000 W/m^2 . This implies that if the incoming solar radiation is 1000 W/m^2 , then the sizing factor will be 1. This sizing factor is multiplied by the power rating of the

PV module to calculate the arrays output. Dust and mismatches in the array are expressed as a percentage in this section, which may also be controlled by the student. To calculate the correct multiplication factor, the control value is deducted from 100 and then divided by 100. This factor is then multiplied by the calculated PV output. As an example a dust and mismatch factor of 10% will result a multiplication factor of 0.9.

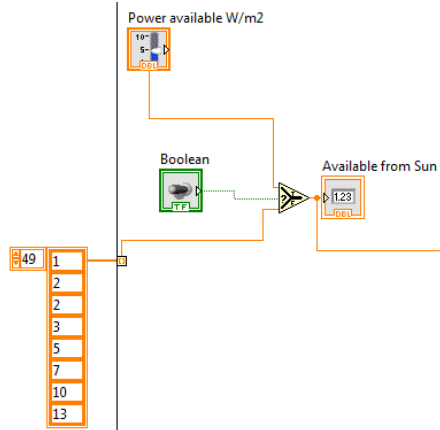


Figure 2: LabVIEW circuit of simulation mode selection

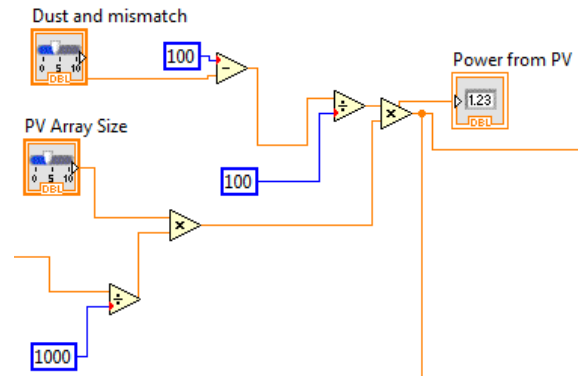


Figure 3: LabVIEW circuit of PV array

To calculate the output of the charge controller, the value of the PV array's output is multiplied with the efficiency of the charge controller (which may be controlled by the student) as shown in Figure 5. The same procedure is followed regarding the battery in order to obtain its efficiency factor as shown in Figure 6. This factor is multiplied with the output of the charge controller to determine how much of the input energy can be extracted from the battery after the losses have been accounted for.

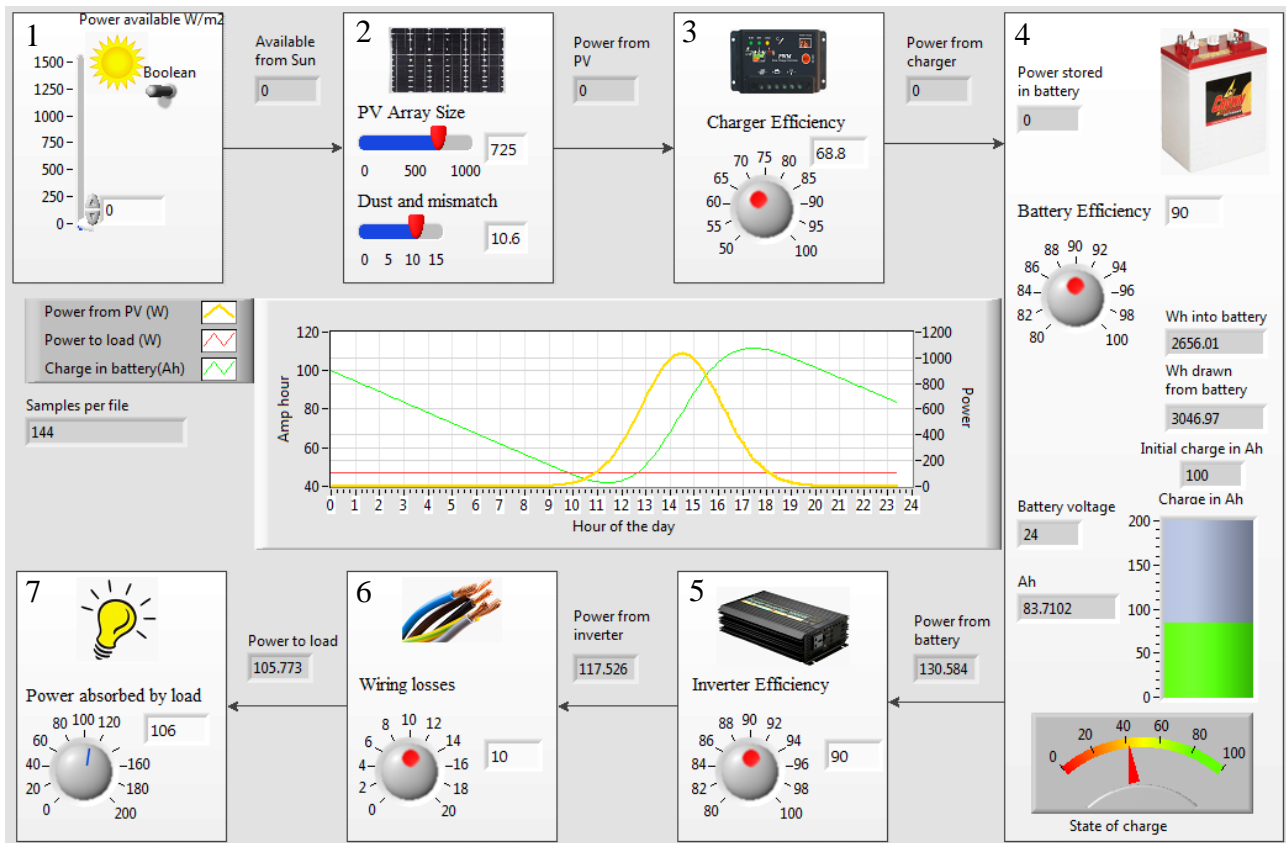


Figure 4: LabVIEW simulation user interface

Energy stored in the battery is indicated in Ah by firstly converting the incoming power from the charger to Wh. This calculation is shown in Figure 7. LabVIEW has a function that calculates the average value of all the previous samples in the execution of the loop. This

average value is then multiplied with the hour value indicated by the total samples in Wh. In the simulation, each sample represents 10 min of the day. Taking the samples from the beginning of the simulation (indicated by the letter i in Figure 7) and dividing it by six results

in an hour variable. The amount of energy stored in the battery (24 V) can be calculated by using the energy flowing into the battery and that flowing out to the load (may be controlled by the student). A simple calculation is done by dividing the Wh with the battery voltage to obtain the Ah as shown in Figure 8. The wiring losses are calculated in the same way as the dust and mismatch factor.

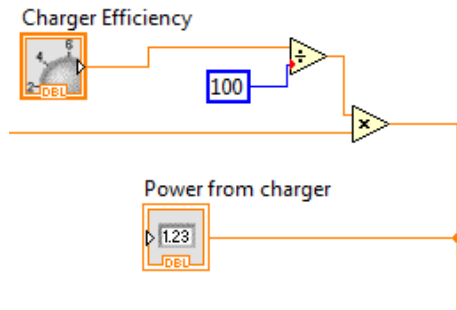


Figure 5: LabVIEW circuit of charge controller

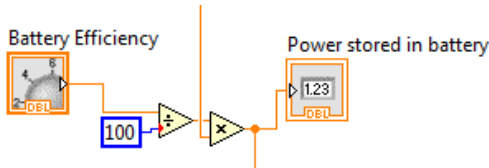


Figure 6: LabVIEW circuit of battery efficiency

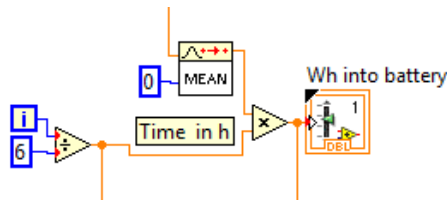


Figure 7: LabVIEW circuit of Wh calculation

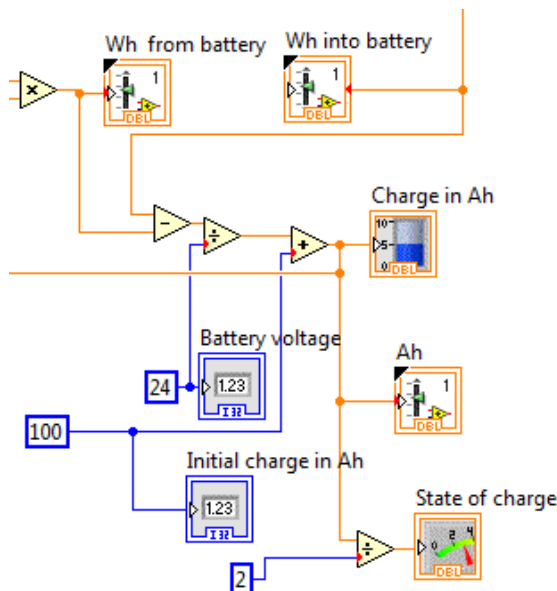


Figure 8: LabVIEW circuit of Ah calculation

The possible results of the simulation are shown in the next section. It highlights the control of the energy source, the different efficiencies and the size of the load.

6. RESULTS AND DISCUSSION

The following important energy monitoring principles are demonstrated with this SEMS:

1. energy flow,
2. efficiency of components in the system,
3. storage of energy,
4. the effect of optimisation and
5. the usage of energy.

Figure 9 illustrates the first principle of energy flow over a 24 hour period. The result shows a constant load (50 W) with normal solar radiation present (bell shaped curve that peaked in this simulation at 14H30). The state of the battery decreases from 100 Ah to around 47 Ah at 11H00, as the constant load is draining the 200 Ah battery. The state of the battery then starts to increase to 185 Ah as solar radiation is present. The 47 Ah point represents 23.5% state of charge (76.5% depth of discharge) that will influence the useful lifetime of the battery. Battery life is influenced by the depth of discharge(DOD), number of cycles, and charge/discharge rates [28]. Discharging to about 80% DOD will severely reduce the battery life of lead acid batteries[29]. The third principle of energy storage is also demonstrated with this result.

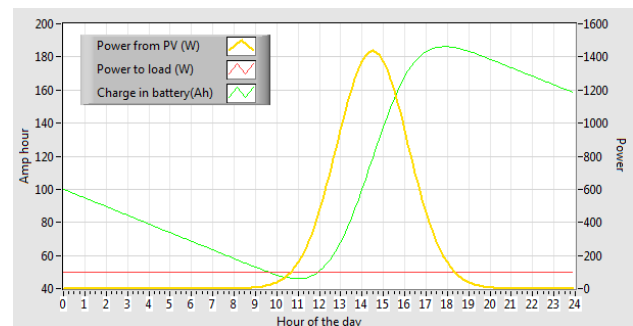


Figure 9: Simulation results of energy flow

The second principle, relating to energy efficiency of the components, is shown in Figure 10. Here, the efficiency of the charge controller was changed from 77 to 84% and the efficiency of the inverter was changed from 89 to 99%. All the other settings, as used in Figure 9, were retained. The result indicates that the state of the battery did not go below 50 Ah and that the battery was fully charged at 16H00. These results also address the principle of optimisation, as higher efficiencies result in a fully charged energy storage system. Fully charged systems can also be an indicator of energy surplus[30].

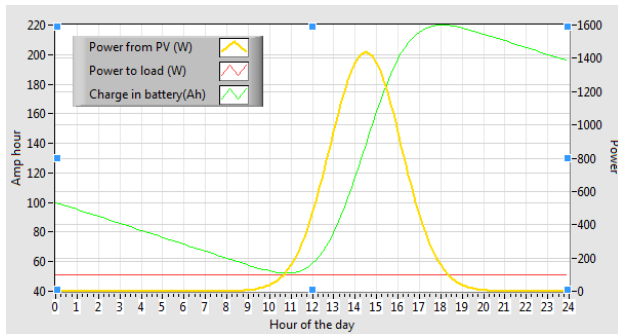


Figure 10: Simulation result of optimization

In order to address the last principal, named energy usage, required using all the settings from Figure 10 in Figure 11, with the exception of the load setting (changed from 100 W to 200 W). The effect of a higher load on the system indicates a 0% state of charge of the battery at 11H00, resulting in a total shutdown on the system. This is an indication of poor design and will result an unusable system[31].

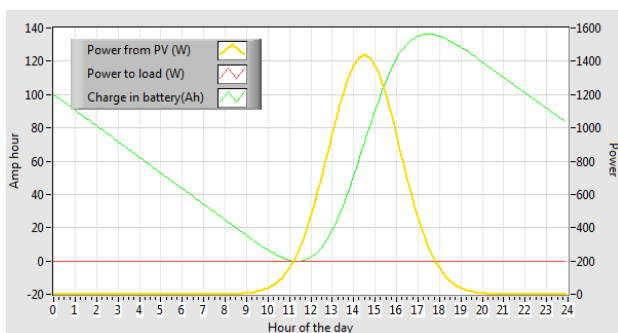


Figure 11: Simulation results with a higher load

Student perceptions are an important indicator to evaluate the success of any educational tool. Three questions were posed to the registered students in the Solar Energy Module at the end of the course (n=10). 90% of the students indicated that they really enjoyed the simulations that were done in the laboratory. Student satisfaction and enjoyment is important in order to maximise learning and to ensure program viability [32]. 80% of the students then indicated that they were able to apply new knowledge in a practical environment by doing the simulations, thereby suggesting that they were able to integrate their theoretical and practical instruction. All the students finally indicated that the simulations were not too difficult, thereby suggesting a good level of difficulty for these engineering students.

7. CONCLUSION

The purpose of this paper was to describe the design of a simulated energy monitoring system (SEMS) that was developed at CUT to help train freshmen engineering students in a renewable energy course. The control of specific parameters in the PV system helped students to conceptualize important energy generation principles, such as electrical energy flow, efficiency, storage, usage and optimisation. Student perspectives revealed student

satisfaction with the SEMS. A time lag study may further enhance the reliability and validity of these results, as this study was only limited to one group of students in one semester. However, the call by society for a more sustainable future may very well be achieved by graduating students with the right attributes that may be demonstrated by using specific and relevant CBS.

8. ACKNOWLEDGMENT

This work is based on the research supported in part by the National Research Foundation (NRF) of South Africa. Any opinions, findings, conclusions or recommendations expressed in this material are that of the author(s) and the NRF does not accept any liability in this regard.

9. REFERENCES

- [1] BrainyQuote. (2015). *Michael Franti Quotes at BrainyQuote.com*. Available: <http://www.brainyquote.com/quotes/quotes/m/michaelfr a472140.html>
- [2] A. Esmat, A. Magdy, W. ElKhattam, and A. M. ElBakly, "A novel Energy Management System using Ant Colony Optimization for micro-grids," in *Electric Power and Energy Conversion Systems (EPECS), 2013 3rd International Conference on*, 2013, pp. 1-6.
- [3] N. Perrot, I.-C. Trelea, C. Baudrit, G. Trystram, and P. Bourguine, "Modelling and analysis of complex food systems: state of the art and new trends," *Trends in Food Science & Technology*, vol. 22, pp. 304-314, 2011.
- [4] R. Krishnamurthy, A. Bhagwatwar, E. W. Johnston, and K. C. Desouza, "A Glimpse into Policy Informatics: The Case of Participatory Platforms That Generate Synthetic Empathy," *Communications of the Association for Information Systems*, vol. 33, p. 21, 2013.
- [5] U. Mohammad, "An Introductory Engineering Course for Freshman Students-From Programming to Implementation," in *ASEE NCS 2014, American Society for Engineering Education*, Oakland University, 2014.
- [6] P. E. Hertzog and A. J. Swart, "A customizable energy monitoring system for renewable energy systems," presented at the SAUPEC 2015, University of Johannesburg, 2015.
- [7] R. M. Felder and L. K. Silverman, "Learning and teaching styles in engineering education," *Engineering education*, vol. 78, pp. 674-681, 1988.
- [8] A. F. Grasha and N. Yangarber-Hicks, "Integrating teaching styles and learning styles with instructional technology," *College Teaching*, vol. 48, pp. 2-10, 2000.
- [9] D. I. Lewis, "The pedagogical benefits and pitfalls of virtual tools for teaching and learning laboratory practices in the Biological Sciences," 2014.

- [10] E. Cakici and S. Mason, "Parallel machine scheduling subject to auxiliary resource constraints," *Production Planning and Control*, vol. 18, pp. 217-225, 2007.
- [11] C.-S. Lam and M.-C. Wong, *Design and Control of Hybrid Active Power Filters*: Springer, 2014.
- [12] A. Nechibvute, A. Chawanda, P. Luhanga, and A. R. Akande, "Piezoelectric Energy Harvesting Using Synchronized Switching Techniques," *International Journal of Engineering and Technology*, vol. 2, 2012.
- [13] R. Torbensen, K. M. Hansen, and T. S. Hjorth, "My Home is My Bazaar-A Taxonomy and Classification of Current Wireless Home Network Protocols," in *Engineering of Computer Based Systems (ECBS-EERC)*, 2011 2nd Eastern European Regional Conference on the, 2011, pp. 35-43.
- [14] I. M. Greca, E. Seoane, and I. Arriasecq, "Epistemological issues concerning computer simulations in science and their implications for science education," *Science & Education*, vol. 23, pp. 897-921, 2014.
- [15] J. Blackledge and M. Barrett, "Evaluation of a Prototype Desktop Virtual Reality Model Developed to Enhance Electrical Safety and Design in the Built Environment," 2012.
- [16] C. P. Casanave and Y. Li, "Novices' Struggles with Conceptual and Theoretical Framing in Writing Dissertations and Papers for Publication," *Publications*, vol. 3, pp. 104-119, 2015.
- [17] D. A. Kolb, *Learning Cycle and Learning Style Inventory*. London: Prentice Hall, 1984.
- [18] S. Giglmayr, A. C. Brent, P. Gauché, and H. Fechner, "Utility-scale PV power and energy supply outlook for South Africa in 2015," *Renewable Energy*, vol. 83, pp. 779-785, 2015.
- [19] T. Sanandaji and P. T. Leeson, "Billionaires," *Industrial and Corporate Change*, vol. 22, pp. 313-337, 2013.
- [20] P. Hertzog and A. Swart, "Design and development of practical instruction for freshmen engineering students in a renewable energy course," in *1st International Conference on Scholarship of Teaching and Learning (SoTL) in Higher Education*, Bloemfontein, 2015.
- [21] P. Hertzog and A. Swart, "Enhancing freshman engineering student's experiences of photovoltaic module operation using educational technologies," presented at the 11th International Conference on EDUCATIONAL TECHNOLOGIES, Dubai, United Arab Emirates, 2015.
- [22] A. Kabade, A. Rajoriya, and U. Chaubey, "Solar Pump Application in Rural Water Supply-A Case Study from Ethiopia," *International Journal of Energy Engineering*, vol. 3, p. 176, 2013.
- [23] T. L. Gibson and N. A. Kelly, "Solar photovoltaic charging of lithium-ion batteries," *Journal of Power Sources*, vol. 195, pp. 3928-3932, 2010.
- [24] C. Belhadj-Yahya, "Performance monitoring of solar stand alone power systems," in *Energy Conference and Exhibition (EnergyCon)*, 2010 IEEE International, 2010, pp. 412-416.
- [25] Y. Yao, D. Lu, and D. Verstraete, "Power loss modelling of MOSFET inverter for low-power permanent magnet synchronous motor drive," in *Future Energy Electronics Conference (IFEEC)*, 2013 1st International, 2013, pp. 849-854.
- [26] S. Ozdemir, U. S. Selamogullari, and O. Elma, "Analyzing the effect of inverter efficiency improvement in wind turbine systems," in *Renewable Energy Research and Application (ICRERA)*, 2014 International Conference on, 2014, pp. 572-575.
- [27] I. Santiago, M. López-Rodríguez, A. Gil-de-Castro, A. Moreno-Munoz, and J. Luna-Rodríguez, "Energy consumption of audiovisual devices in the residential sector: Economic impact of harmonic losses," *Energy*, vol. 60, pp. 292-301, 2013.
- [28] (2 October 2014). Available: <http://en.climate-data.org/location/394/>
- [29] H. Bindner, T. Cronin, P. Lundsager, J. F. Manwell, U. Abdulwahid, and I. Baring-Gould, *Lifetime modelling of lead acid batteries*, 2005.
- [30] T. Ma, H. Yang, and L. Lu, "Performance evaluation of a stand-alone photovoltaic system on an isolated island in Hong Kong," *Applied Energy*, vol. 112, pp. 663-672, 2013.
- [31] C. L. Khang and Y. C. Liang, "Development of photovoltaic system planning software," in *Sustainable Energy Technologies (ICSET)*, 2012 IEEE Third International Conference on, 2012, pp. 200-204.
- [32] S. P. Stokes, "Satisfaction of college students with the digital learning environment: Do learners' temperaments make a difference?," *The Internet and Higher Education*, vol. 4, pp. 31-44, 2001.

ANALYSIS FOR IMPROVING REDUNDANCY AND RELIABILITY OF THE GRAAFF-REINET NETWORK

Anthony Marks

Department of Electrical Engineering
Nelson Mandela metropolitan University
Port Elizabeth, South Africa
Anthony.marks@nmmu.ac.za

Asekho Mbambiso

Control Plant Maintenance Dept.
Eskom Distribution
Uitenhage, South Africa
MbambiA@eskom.co.za

A-J Phillips

Plant Maintenance Department
Eskom Distribution
Uitenhage, South Africa
PhillipAJ@eskom.co.za

Abstract— According to the Eskom network planning reliability guidelines, a Power system network that is reliable is a network performing its purpose adequately for the period intended under the operating conditions encountered. [1]The degree of reliability may be measured by the interruption frequency, duration, and severity (magnitude of adverse effects on consumer supply availability). [2] The Graaff-reinet network has been identified as one of the networks not conforming thus due to the limited flexibility in terms of the 66kV supply source and transformer capability loadings in the three supplied substations. This has resulted in customers experiencing a number of outages causing the measured performance of the network to be poor according to the National Energy Regulator (NER). [3] The major concern to this network is the reliability, for a distribution system it plays a vital role in ensuring continuity of supply to the consumers. This paper aims to present the issues related with the network in terms of transformer loading, reliability of the supply, protection studies and improving redundancy of the network. DigSilent software has been used to simulate the Power flow studies of the network and the Short circuit analysis on the improved protection setting coordination.

Keywords- Reliability; Redundancy; Load Forecasting; Load Flow analysis; Short circuit Analysis; Protection settings coordination.

I. INTRODUCTION

The Graaff-Reinet network consists of a 66kV radial network supplied from Hangklip Substation supplying into Spandau, Aberdeen and Skietkop substations. The network in total supplies predominantly 5147 customers. Currently Spandou Substation transformer is carrying more loads compared to the two Substations supplying into Nieu-Bethesda area, Graaff-Reinet Umasizakhe location and mostly large power users (LPU's). The 22 kV MV Reticulation on this network consist of Normally Open points (NOP) interconnecting system between the three substation for back feeding capability.

The current supply to the substations in the Graaff-Reinet network is a 66kV radial feed system supplied from Hangklip Substation. Due to the radial feed between Skietkop and Aberdeen a loss of the Hangklip/Skietkop 66kV line results in

loss of supply to a large number of customers. Restoration of supply by Switching the NOP's on the MV reticulation network takes time due to the operation involved and the transformer at Spandou Substation operating already at above 80 % loading cannot maintain supply to all the customers affected.

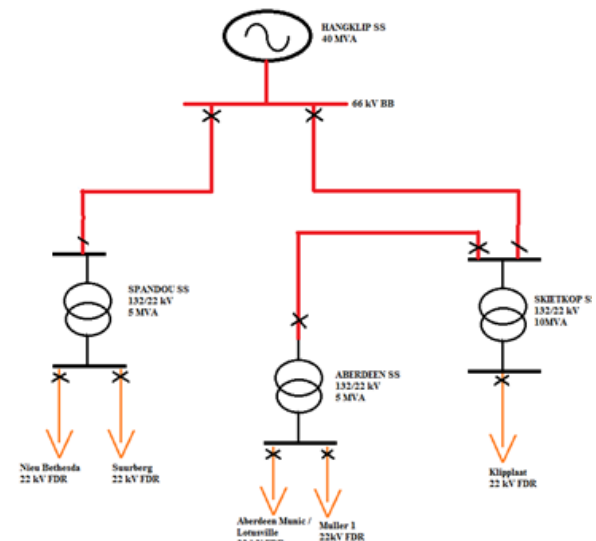


Figure 1: SLD overview of the Graaff-reinet network

A. PROBLEM AREAS

- Poor network performance due to the duration and frequency of interruptions on the network. The customers are affected by all outages (planned and unplanned) on this network from both transformer and line outages. Resulting in Eskom being penalized by NERSA.
- Transformer loading capabilities risk on load forecast. The load recorded on the transformer in 2012 Spandou Transformer was 80.8% and now 87% (peak). With the increase in the load over the years the flexibility for back feeding on the MV reticulation.

- The protection philosophy used in the 66kV network does not provide backup and selectivity as there is no protection schemes at the end of the line plus the 66kV line at Skietkop Substation is a Tee in. This results in a fault on the Skietkop/Aberdeen 66 kV line trips the breaker at Hangklip SS for the Skietkop Feeder bay breaker.

II. DATA COLLECTION

A. DESIGN ASPECTS

The existing Graaff-reinet network was proposed with 3 solutions to the identified problems. This paper only studies the existing network and preferred solution that was found to best improve the reliability, flexibility and redundancy of the network. The preferred solution of creating a ring feed network by having 65km line between Aberdeen and Spandou Substation this creates flexibility and provides alternative supply for any line outages. The transformer Capability is increased by an additional transformer at Aberdeen substation and some of Spandou load transferred to Aberdeen. Thus the pre-determined design Aspects:-

- 65km long HARE conductor with the maximum temperature of 50 degrees Celsius and current rating of 280 Amps. The Short time current rating and short circuit current rating are 534 A and 8.97kA respectively. [4]
- A 5MVA Transformer (66/22 kV YNd1) to be connected with the transformer at Aberdeen will be sufficient for the forecasted 2032 Maximum Demand of 69.3 Amps.
- The total load to be transferred from the Spandou/Suurberg 22kV line is from structure 184 – 245, the installed VA including the T-off line is 2046 kVA transferred to the Aberdeen Munic Feeder.

B. LOAD FORECASTING

The power system network loading data was obtained from Data Acquisition System (DAS) in order to analyze the current and the past loading of the network. The loading collected is used to construct a geo based load forecast from 2012-2032, this forecast takes into consideration the type residential are the network is situated in (urban or rural) and potential for the developments that will result in new electrifications. [5] Table 1 shows the data that was collected and predicted for all the transformer in the network based on the two feeders supplied in the network to construct the graph shown in figure 2.

Below figure 2 gives the load forecasted demand on the Spandou Transformer and the recorded likely forecast load in 2032 is 4.96 MVA and high optimistic demand of 5.68 MVA. Compared to the other Aberdeen and Skietkop substation this substation is the one that poses more growth beyond name pate rating.

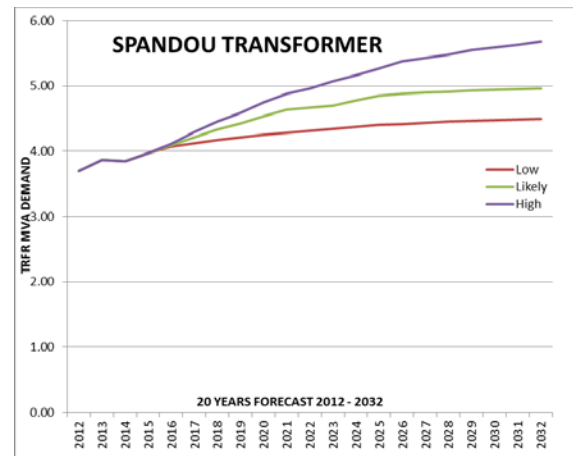


Figure 2: 2012-2032 forecasted load of the Spandou TRFR

Skietkop Substation load forecasted demand on the 10 MVA Transformer load and recorded likely forecast load in 2032 is 3.14 MVA and high optimistic demand of 3.24 MVA

Aberdeen Substation load forecasted demand on the 5MVA Transformer load and recorded likely forecast load in 2032 is 2.92 MVA and high optimistic demand of 3.09 MVA.

	Scenario	2012	2013	2014	2015	2016	2017	2018	2019	2020	2021	2022	2023	2024	2025	2026	2027	2028	2029	2030	2031	2032
Aberdeen 66/22kV 5MVA trfr	High	2.5	2.8	2.7	2.7	2.7	2.7	2.8	2.8	2.8	2.8	2.8	2.9	2.9	2.9	2.9	3.0	3.0	3.0	3.0	3.1	3.1
Skietkop Trf 1 - 10MVA 66/22 kV	High	2.82	2.9	3.0	3.0	3.0	3.0	3.0	3.0	3.0	3.1	3.1	3.1	3.1	3.1	3.1	3.2	3.2	3.2	3.2	3.2	3.2
Spandau Trf 1 - 5MVA 66/22 kV	High	3.7	3.9	3.9	4.0	4.1	4.3	4.5	4.6	4.8	4.9	5.0	5.1	5.2	5.3	5.4	5.4	5.5	5.5	5.6	5.6	5.7
Graaff Reinet 1 66kV Line	High	12.754	12.85	13.19	13.41	13.6	14.37	14.73	15.09	15.37	15.56	15.677	15.8	15.9	15.9	16	16	16.1	16.3	16.4	16.5	

Table 1: 2012/2032 Load Forecast Data of the Graaff-reinet network

III. ANALYSIS AND INTERPRETATION

This section is analysis of the power flow for existing and preferred network. To perform accurate modelling of the network on DigSilent power factory simulation package data from the name plate of currently installed equipment was gathered by visiting the substations. Data stipulated on equipment name plate was compared with library created by Eskom in DigSilent power factory.

Simulation of the network a number of assumptions and decisions are taken to best represent the network.

- Application of onload automatic transformer tap changers for Voltage Regulation (Set point 1 p.u).
- Hangklip 66kV BB1 is set to 1.05p.u (Regulated for outages).
- Use current load versus the 20year load forecast
- In terms of the line and transformer loadings, the author refers to :-

$$\%L (TRFR) = \frac{S_{DEMANAD}}{S_{RATED}} \quad \%L (LINE) = \frac{I_{LOAD}}{I_{RATED}} [6]$$

The Short Circuit simulation for the protection analysis to be done the *complete method* of calculation is used on DigSilent. This method is commonly known as the Superposition method. The method initially checks for a healthy load flow within the circuit before the short Circuit can be applied. [7] In this method the loads can have an influence in the short circuit current calculated. [7]

A. CURRENT NETWORK

Existing graaffreinet network is shown in figure 3, this network is a radial feed into the substation and any loss of 66kV line results in a consequence of a loss of supply to number customers. The simulation performed show the power flow with the loading implemented for the forecasted load. Table 2 show the results for the power flow and the transformer at spandou is operating above the rated MVA loading at 5.7MVA. As a results of these loading back feeding and transformer outages can no be done with out affecting customers.

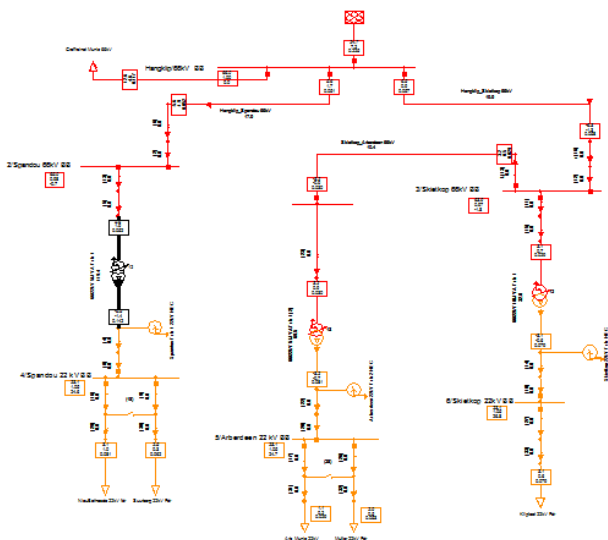


Figure 3: Existing Graaff-reinet Network at 2032 forecasted loading

	% Loading	Tap position	I HV (kA)	I MV (kA)	Apparent Power (MVA)
Skietkop Trfr 1	31.38	3.92	0.027	0.082	3.17
AberdeenTrfr 1	65.95	5.89	0.029	0.085	3.23
Spandou Trfr 1	113.98	5.14	0.050	0.149	5.70

Table 2: Existing network load flow results

A. PREFERRED NETWORK

This section is an analysis of solution which created a ring network on the 66kV and the increasing of the transformer loading at Aberdeen substation with the load transferred from Spandou. Figure 4 shows the simulation of the solution on DigSilent under current loading conditions. The table 3 is the results which show the Busbar voltage drops, the transformer line loadings. The results are for the current and at the forecasted 2032 loading. From the table it can be seen the

voltages are above the 95% acceptable voltage drop according to the NRS Quality of supply standards. [3] Also looking at the results the transformer loading is acceptable below the maximum loading ratings.

The analysis on the chosen solution by the author is assessed and compared to others and it was a preferable solution in terms of the following aspects: -

- Maintain firm & reliable supply for forecasted load.
- Transformer and Line rated loading limits not exceeded.
- Ability to maintain redundancy in terms of outages.
- Busbar Voltage drops acceptable in terms of NRS and QOS guidelines.
- The Voltage regulation of tap changers within limits.

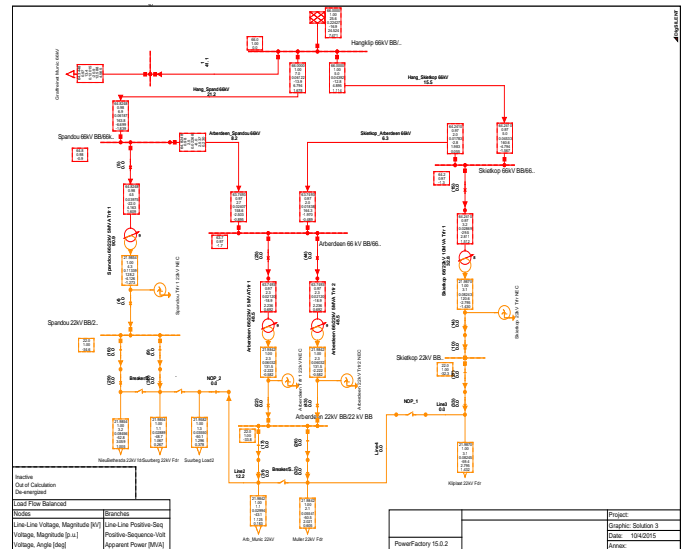


Figure 4: Preferred Graaff-reinet Network Configuration

Solution 3	2015	2032
	u(max)	u(max)
Aberdeen 22kV BB	1.00	1.00
Aberdeen 66kV BB	0.98	1.02
Skietkop 22kV BB	1.00	1.00
Skietkop 66kV BB	0.98	1.02
Spandou 22kV BB	1.00	1.00
Spandou 66kV BB	0.99	1.03
Loading percentages	% L	% L
Aberdeen Trfr 1 & 2	33.28874	57.24307
Skietkop Trfr	30.83436	32.85648
Spandou Trfr	61.62245	73.61004
Hang/Spandou line	14.98918	20.64467
Hang/Skiet line	12.26318	16.10879
Skiet/Aberd line	3.649218	6.865885
Spand/Aberd line	6.373517	9.311314

Table 3: Preferred solution power flow results

The table 4 shows the results of the transformer loading from the simulation for scenarios of having transformer outages in turn. From the table the tap changer positions are also shown for the voltage regulation of the transformers to the feeders and monitoring the limits of 1- 17 taps. The Skietkop transformer outage results in the transformers at Spandou and Aberdeen operating above 80% but still below the maximum rated loading. These transformer loadings can be accepted for planned outage as long the transformer Hot Spot Temperatures are closely monitored and as an addition application of forced air cooling systems to limit rise in Temperatures.

Solution 3 (TRFR OUTAGES)	Aberdeen OUT	Skietkop OUT	Spandou T2 OUT
% Loading			
Aberd 66/22kV 5MVA T1	63.01 (T9)	89.04 (T11)	73.49(T10)
Aberd 66/22kV 5MVA T2	0	89.04 (T11)	73.49(T10)
Skiet 66/22kV 10MVA T1	55.12 (T9)	0	55.63(T9)
Spand 66/22kV 5MVA T1	79.92 (T9)	80.26 (T8)	0

Table 4: Preferred network transformer outages

B. PROTECTION ANALYSIS

Figure 5 shows the new protection coordination and philosophy that will be used in the graffreinnet network. Fundamental requirements for protection are that it should have selectivity, sensitivity, speed, reliability and stability. [6] this philosophy applied ensures that these fundamentals are implemented, The 66kV line uses distance protection which is used as the main protection that will be applied in both ends of the line to ensure increased selectivity and reliability on the network. The backup protection on the lines is the directional IDMT overcurrent and earth fault protection this protection is not analysed in this paper.

The transformer protection uses Differential protection as the main protection and for back up HV IDMT OC, HV& MV IDMT EF fault that will be analysed in the transformer protection section.

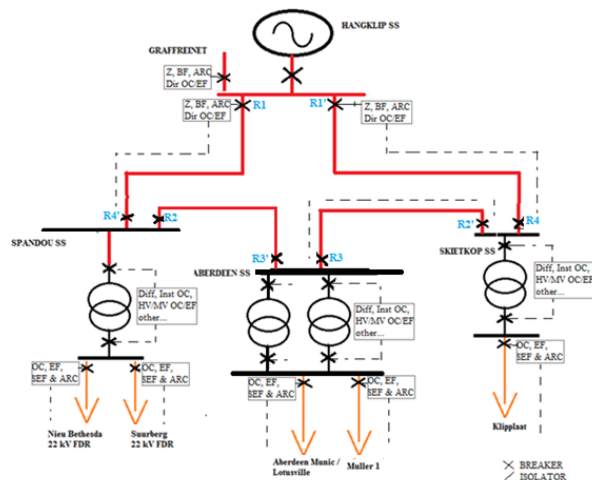


Figure 5: Preferred network protection coordination

1) DISTANCE PROTECTION

The Main protection for the 66kV lines is the distance protection which SEL321 Relay is used. [8] The Distance protection elements on the relay consist of Mho phase Overcurrent characteristics and the Ground Distance protection which can be set to be either Mho or quadrilateral characteristics. These elements on the settings respectively are referred to as PMHOZ, GMHOZ and QUADZ with different zone setting for each. [8]The characteristic for each zone requires input for the reactive reach (X) which is set the same as in Mho and the setting for the resistive reach (R). [9] The quadrilateral characteristics are used by the author for earth fault settings as it has an extended resistive reach which increases the sensitivity for high resistance faults.

Table 5 is a settings calculation for the new 66kV line between Spandou and Aberdeen. To calculate the settings firstly a CT ratio is chosen to be above the maximum current rating of the line but because this is a lightly loaded line with a maximum current that will flow through is 79 A maximum and 280A rated current so a CT ratio of 200/1 is chosen. The distance protection zone reach settings are calculated in the secondary impedance, so the primary impedance of the line is converted to secondary using the CT/VT ratio.

$$\text{CT Ratio} = 200/1 = 200$$

$$\text{VT Ratio} = 66000/110 = 600$$

$$\text{CT/VT ratio} = 200/600 = 0.333$$

Primary impedance: -

$$Z_1 = 36.1 \angle 54.7 \quad Z_0 = 105.7 \angle 69.1$$

If the Secondary Impedance $Z_s = Z_p * (\text{CT/VT})$ [10]

Secondary Impedance:-

$$Z_1 = 12.1 \angle 54.7 \quad Z_0 = 35.12 \angle 69.1$$

	ZONE 1	ZONE 2	ZONE 3	ZONE 4
Direction	Forward	Forward	Reverse	Forward
Line length (%L)	80 %	120 %	80 %	150 %
Delay (sec)	0.04	0.4	4	2.5
(cycle)	2	20	200	125
Z LL ($Z_1(\text{sec}) \%L$)	9.6	14.5	9.6	18.2
R-reach	5.5	8.94	5.5	10.5
X-reach	7.84	12.66	7.84	14.86

Table 5: Distance Protection Setting for Spandou/Aberdeen 66kV line

The time delays on the setting are Z1 80% is Instantaneous; Z2 120% is 0.4s; Z3 80% reverse is 4s and Z4 150% is 2.5s. These setting are used in both the EF and OC settings. [9]

a) Short Circuit Analysis Spandou/Aberdeen 66kV line

The settings calculated for the new line above are used to simulated a 3ph short circuit fault at 90% of the line length from Aberdeen. Relays installed on both ends of the line and the settings for the zone reaches are the same for both relays but looking at opposite direction towards the line. From Figure 6 below shows the fault simulated with the tripping times in the red boxes.

The relay named R1 (Spand/Aberd @ 10%) is supposed to see it on Zone 1 instantaneous, R2 (Aberd/Spand @ 10%) the fault is on the Zone 2 operating region and the time delay of the relay is 0.4 sec. R3 Aberd/Hangk main relay sees the fault on the reverse direction at a time delay of 4sec act as a backup and also R4 is on zone 4 at 2.5 sec time delay. The Results from the simulation R1 tripped in 0.015sec that has passed as it is an acceptable instantaneous tripping time; relay R2 tripping time is 0.415sec also a pass.

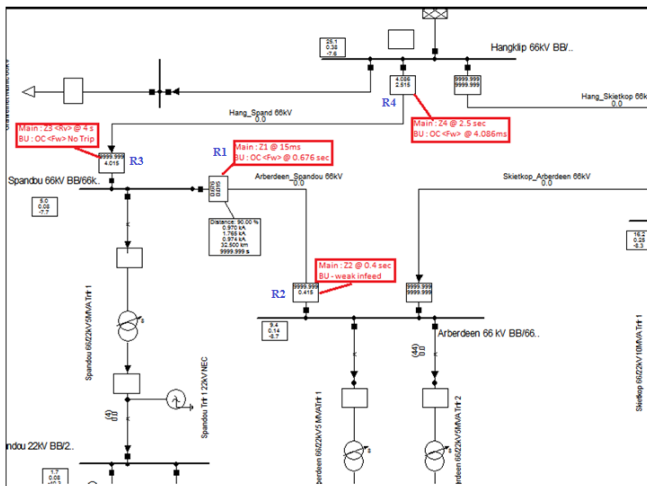


Figure 6: 3ph Short Circuit at 10% of Spandou/Aberdeen 66kV line

Figure 7 is the Impedance tripping characteristics for the relays in Spandou/Aberdeen line. The result box in red and the characteristic are the relay on the Aberdeen side seeing the fault at 90% on Zone 2 at 0.415sec and the shown in Green is the relay on the Spandou side seeing the fault on its zone 1 at 10% of the line length tripping time 15ms.

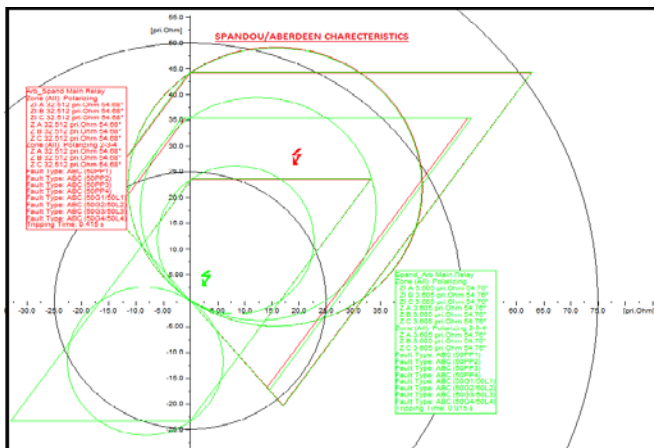


Figure 7: 3ph fault Impedance Tripping Characteristics

2) TRANSFORMER IDMT OC & EF PROTECTION

The protection settings to be analyzed are for HV IDMT OC & EF also MV IDMT EF on the Aberdeen transformers. These are the backup settings used for the non-unit protection on the transformer. In order to calculate this setting the existing feeder settings are used for grading the transformers for EF and OC with the existing 22kV feeder bays, thus the Tripping time delays are recalculated on the existing feeder. See Table 6 for the results of the settings that were calculated and are to be tested.

$$S = \sqrt{3} V * I \quad [66/22 \text{ kV } 5\text{MVA}]$$

$$I_{FL_{HV}} = 43.$$

$$I_{FL_{MV}} = 131 \text{ A}$$

$$HV \text{ CTR} = 100/1$$

$$MV \text{ CTR} = 200/1$$

ED SETTINGS	CTR	IDMT OC	IDMT EF
22kV FEEDERS			
Aberdeen Munic 22kV	200/1	PSM - 0.5 TM - 0.33	PSM - 0.4 TM - 0.2
Muller 22kV	200/1	PSM - 0.5 TM - 0.33	PSM - 0.4 TM - 0.3
TRANSFORMER IDMT			
22kV (MV) IDMT	100/1	N/A	PSM - 0.4 TM - 0.5
66kV (HV) IDMT	200/1	PSM - 0.66 TM - 0.6	PSM - 0.45 TM - 0.85

Table 6: Graded Trfr IDMT OC & EF Settings

a) Transformer HV IDMT EF

This Analysis is a single phase to ground fault simulated at the HV terminals of Aberdeen Trfr 2. The expected tripping time for a current magnitude of 653.44 A is 2.165 sec at Relay 1, looking at the figure below the relay trips correctly for the setting calculated. The Relays 3, 4 & 5 are Directional relays on the lines. The Fault on the HV of the Trfr is in reverse of Relay 5 hence there is no tripping and in the forward direction of Relay 3 & 4. Relay 6 is an MV EF Relay and cannot see the fault hence there is no tripping.

$$t = \frac{0.14 * TM}{PSM^{0.02} - 1} = \frac{0.14 * 0.85}{653.44/45^{0.02} - 1} = 2.165 \text{ sec}$$

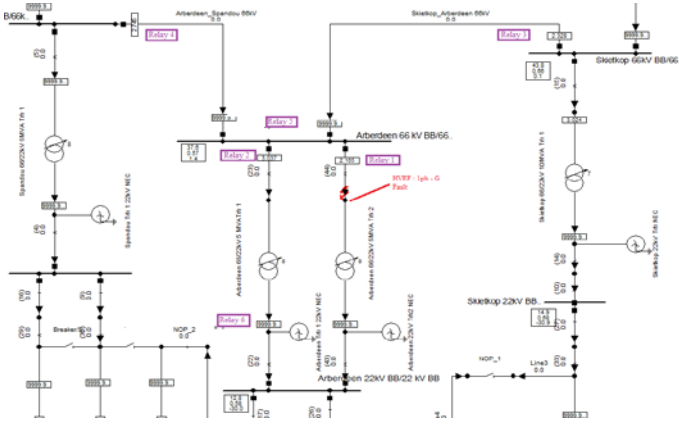


Figure 8: Single phase to Ground fault on Trfr 2 HV Terminals

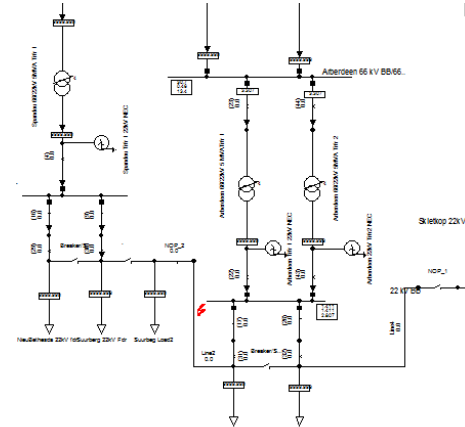


Figure 10: 3ph short circuit on Aberdeen 22kV Busbar

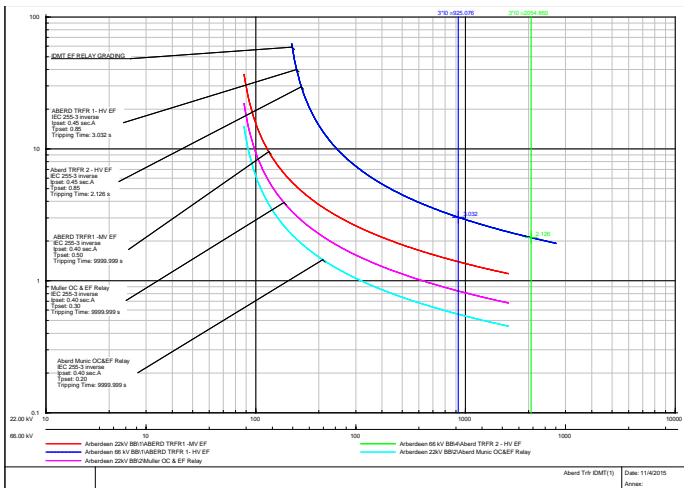


Figure 9: IDMT Characteristics for single phase to Ground EF

b) Transformer IDMT OC

The Current IDMT OC setting for Muller and Aberdeen Munic feeder are the same and the HV IDMT OC on the Transformer is graded with these two bays for the time. A three phase short circuit is simulated on the 22kV BB at Aberdeen Substation (figure 10), the Fault magnitude seen by the HV IDMT OC of the transformer is 230.43 A. To verify the tripping time the tripping time of the relay as per the calculation below the time delay should be 3.31 sec, looking at the characteristics the relay trips correctly. See figure 11 for the results of the characteristics tested for the EF.

$$t = \frac{0.14 * TM}{PSM^{0.02} - 1} = \frac{0.14 * 0.6}{230.43/66^{0.02} - 1} = 3.32 \text{ sec}$$

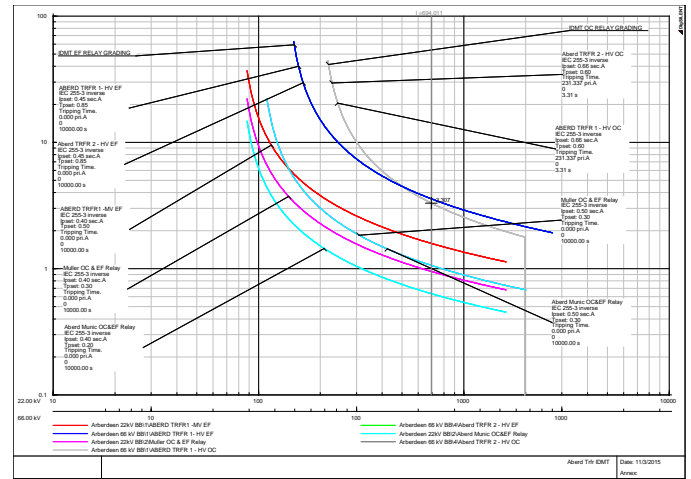


Figure 11: IDMT Characteristics for 3ph OC fault

NOTE: Figure 11 show the IDMT graded characteristics for both the both the overcurrent and the earth fault settings. This is for both transformers in parallel and the 22kV feeders downstream.

3) TRANSFORMER DIFFERENTIAL PROTECTION

The main protection implemented on the transformer is Differential protection and the relay used to protect the transformer is SEL 387 Differential relay. The relay settings that were calculated are applied on the relay and are tested using Test universe software. This Software drives a CMC256 Hardware which used to simulate fault conditions on the relays. To simulate differential protection on the relay two sets of 3 phase currents are used to inject on the HV and MV elements. The test that will be explained by the author is the Operating characteristics tests and through fault test.

a) Operating Characteristics Testing

Figure 12 shows the view for operating characteristics test done on the relay for a three phase fault (L1-L2-L3). From the characteristics the operating and restraining areas are indicated to show how the relay is supposed to behave. On the left side of the test view is the test points that were selected randomly. First test points are on the operating region of the characteristics with the expected instantaneous tripping time-

of (tnom) 40ms a tolerance of +/- 10% is accepted and the points are shown as passed green tick. Second set of points is testing the blocking restraining region test with expected tripping time N/T (no trip) for tnom and the relay response actual time (tact) is also a no trip thus the pass.

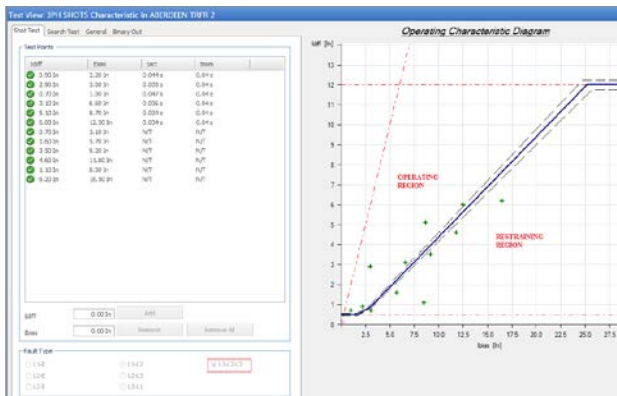


Figure 12: Differential protection Characteristics test results 3ph fault

External Fault Blocking Tests

Differential Protection is applied as transformer unit protection, the protection is supposed to operate for fault internal to the transformer or the zone of HV an MV CT's. The differential configuration test view shown in figure 13 is a simulation test for and external fault. During these external fault types the relay is supposed to block any relay operation due to differential protection. The Fault analyzed for this test is a 3phase fault on the MV side of the transformer and the currents injected are indicated on the Current Distribution Single line in figure 14.

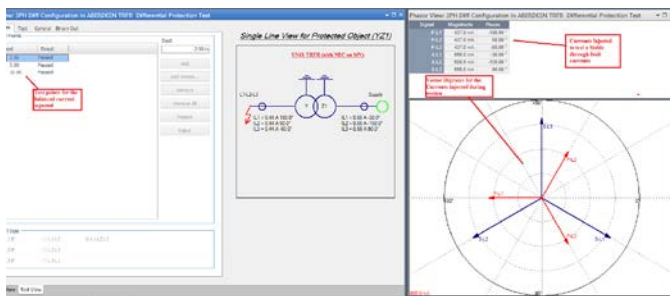


Figure 13: Differential protection test for External faults

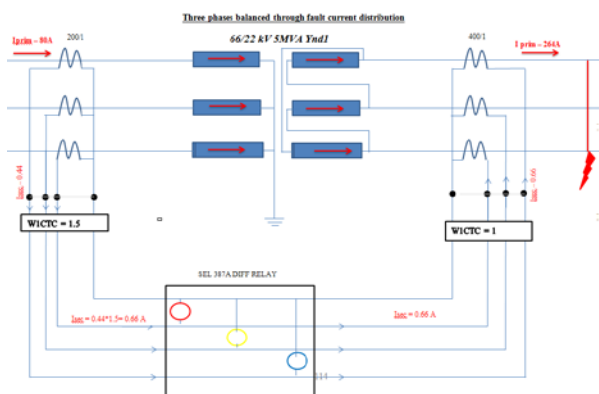


Figure 14: Current distribution for a 3ph fault on the Trfr MV

IV. CONCLUSION

Maintaining Continuity of supply and Quality of supply to the customers, these are one of the things that Eskom as an electrical utility is being monitored on by the National Energy Regulator (NERSA) and if not maintained will be penalties that the company encounters as annual targets are set. The Key Performance Indices' (KPI's) poorly performing on SAIDI and SAIFI due to the lack of reliability and flexibility during outages will be improved with the implementation of the new improved network.

The ring feed network is a good advantage in power system network design as this solution introduces a flexible network during line outage. It is evident from the analysis performed; meaning also the power system Plant maintenance does not have to be compromised to improve in power system performance for SAIDI and SAIFI.

The Increased Capacity of the transformer was a strategically solution to ensure the future forecasted load for all the substations is maintained for 20 years more. The transformer Capacity is highly critical as Spandou Transformer is already running close to full load and does not accommodate the forecast. In the analysis of at the existing network with the radial system, looking at the protection coordination the Customers on the 22kV reticulation Also experience unfortunate outages due to line and transformers.

RECOMMENDATIONS :-

- Implementation of Solution 3 by creating a ring on the 66kV network and increased TRFR capacity will improve the reliability of the system.
- The load Transfer on Suurburg 22kV Feeder to limit the loading on the Spandou TRFR to be done as this is a cost effective way to solve TRFR overloading at both substations and maintaining flexibility.
- The analyzed protection philosophy to be applied and the protection relays to be upgraded to Microprocessor relay technology, these relays are advantageous as they all continuous monitoring based on relay operation units and events recording. This makes it easier to analyze protection performance.
- Installation of Protection Remote Engineering Access panels on each substation, to be linked via Telecommunication channels to a local protection offices Computer. This Remote Access panel will be connected to all the relays at that Substation and The Protection Technician will be able to access the relay from the office. This will help when emergency setting have to be applied and Obtaining faults distance during operational event. This Saves Costs on driving and minimizes lengths on outages.

ACKNOWLEDGMENT

The author wishes to acknowledge the contribution of the following individual for their valued participation in this research: - My Manager Sandisiwe Smondile for providing me with Eskom resources for this research and mentors Mr.

Anthony Marks and Mr. A-J Phillips. The authors are grateful and wish to acknowledge Eskom for the financial support in ensuring that the project is successfully completed.

V. BIBLIOGRAPHY

- [1] Eskom : T. Kleynhans, "Network Planning Reliability Guidline," Eskom, Midrand, 02-2011.
- [2] R. B. L. Goel, "Determination of Reliability Worth for distribution system planning," *IEEE Transactions on Power Delivery*, vol. 09, no. 3, pp. 1577-1583, 1994.
- [3] SABS, Technology Standards SA, ESKOM, "NRS 048-2 :Quality of Supply," Standards SA, Pretoria, 2003.
- [4] Eskom : DX Engineering, "Network Planning Guidline for Lines and Cables," Eskom (Controlled Disclosure), Gauteng, 2014.
- [5] D. C. C.-B. S. Hashe, "GEO-BASED LOAD FORECAST STANDARD: UID 34-1284," Eskom, 2012.
- [6] ALSTOM, Network Protection and Automation Guide, UK: Alstom Grid, May 2011.
- [7] D. PoweFactory, "Chapter 22 : Short Circuit Analysis," in *User Manual*, Gomoringen, Germany, DigSilent GmbH, 2013, pp. 427-440.
- [8] D. PowerFactory, "Relay Model SEL 321 v001," DigSilent GmbH, Germany, 2012.
- [9] Eskom - Distribution protection council, "Protection Guide : Line Distance protection upto 132kV," Controlled Disclosure, Jhb, 2006.
- [10] SCHWEITZER ENGINEERING LABORATORIES, "SEL321 Data Sheet," SELINC, USA, 2008.

DESIGNING AND INTEGRATING A SOLAR GRID-TIE AND OFF-GRID SYSTEM INTO ONE SYSTEM

D. Diedericks*, O. Dobzhanskyi* and R Gouws*

**North West University, School of Electrical, Electronic and Computer Engineering, Potchefstroom Campus, odobzhanskyi@gmail.com*

Abstract. Because of population growth and continuous development in rural areas and cities, the utility electricity grid supplier in South Africa, Eskom, is finding it difficult to meet the power demand during certain period. The fact that Eskom cannot meet the power demand is a direct cause of what is known as load shedding. To avoid such a problem renewable energy sources should be implemented in an entire power generation system. The most commonly used and known renewable energy source is the sun. The paper presents the design and integration of a solar grid-tie and off-grid system into one system. The system is aimed to deliver a specified amount of power at a specific time in case if the system is operated in off-grid mode. The system integrates such devices as: PV modules, charge controller, energy storage, Powador inverter, PLC control unit, and a power meter. The system is able to power a load whenever the utility grid is unavailable. Also, the system is capable to feed power into the grid that may generate some form of income for the user from the electricity utility provider.

Key words. Grid-tie, Off-grid, Inverter, Photovoltaic, Power, Voltage, Current.

1. INTRODUCTION

It is crucial for Eskom to provide power for receivers continuously without interruption. Sometimes Eskom is not capable of maintaining constant power supply for its customers. It happens when load shedding occurs. Load shedding can occur unexpectedly and cause financial losses for financial institutions or a great deal of discomfort for the average home owner.

The preceding problems have created the need to use and implement renewable energy sources. In this project solar energy is used as a renewable energy source. The phrase, solar energy, is widely used to describe the energy from the sun and it is also the preferred phrase used to describe the sun as a renewable energy source.

Photovoltaic, first introduced in 1954, is a technology that is used to convert the solar energy from the sun into usable electrical energy. Since the first introduction of photovoltaic to generate electricity from the energy from the sun, the technology has come from strength to strength. The first system that was introduced was a small stand-alone system capable of supplying a load with only a few watts. Today huge solar plants exist all over the world that is capable of delivering megawatts of power. These systems are also known to be connected to the utility electricity grid [1].

Whenever these systems are connected to the utility electricity grid, it is known to be a grid-tied system. A

grid-tied system can be described as a system that generates electricity; this is mainly done through photovoltaics that are connected to a grid-tie inverter.

A grid-tie system is known to be able to supply the surplus power not used by the load connected to the inverter to the utility electricity grid. Therefore, these systems are becoming more and more desirable. Many grid-tie inverters are not able to act as a standalone inverter and cause power outages whenever the utility electricity grid becomes unavailable.

The solution to supplying a load with power whenever the utility electricity grid is unavailable is to install an off-grid system. Off-grid systems are almost identical to grid-tie systems in architecture with the major differences being that the off-grid system is not connected to the utility electricity grid, and an off-grid inverter is used in the place of a grid-tie inverter. The off-grid system is, therefore, able to supply a load with power whenever it is needed.

2. MATERIALS AND METHOD

2.1. Inverter

In the case of a grid-tie system the inverter plays an important role in the utility electricity distribution grid. The inverter is used as the interface between the renewable energy and the utility electricity grid. An inverter that is capable of seamlessly switching between grid-tied and stand-alone mode is the desirable in the scope of this project as the system will be able to operate as either a grid-tied or off-grid system [2].

The utility electricity grid supplier prescribed the Powador 2002 grid-tie inverter to be used. The Powador 2002 cannot be used as a standalone inverter and will only be functional as long as the utility electricity grid is available [3].

Inverters are used to convert direct current received from the PV modules or the energy storage device that is connected to the input of the inverter into alternating current that can be used to power AC loads. The loads to be powered by the inverter can vary from small to relatively large residential loads. Many different types of inverters do exist and the type of the inverter will be determined by the capabilities and characteristics of the inverter.

The Powador 2002 grid-tie inverter used in the design is part of the Powador 02 series from KACO. The Powador 2002 is a galvanically isolated string inverter that consists of connections necessary for communication on a single circuit board. The communication includes RS485, S0 and a fault finding relay. The Powador 2002 has a wide input voltage range which makes the planning of a PV installation quite flexible.

The Powador 2002 grid-tie inverter consists of a LCD display that is used to supply the operator with important information regarding the state of the inverter as well as the state of the utility electricity grid. User interface is also present on the Powador 2002 in the form of two buttons to control the information that is displayed on the display of the inverter. The casing of the inverter is made from aluminum and the inverter has a total weight of 14.5 kg.

The control and interfacing between the grid-tie and off-grid systems are most important for the success of such an interfaced system. By using the correct off-grid inverter along with an effective control unit and system the transition between grid-tie mode and off-grid mode can be achieved seamlessly [4].

2.2. Photovoltaics

Photovoltaics (PV) are one of the most widely used energy sources in remote areas where electricity is unavailable. Photovoltaics are also known to be quite cost-effective along with great reliability as well as durability. In some case PV systems are known to be connected to the utility electricity grid to supply power to loads. These PV systems are installed by the utilities to lessen the amount of power to be supplied by

installed power plants during high peak hours of power demand [4].

Mono-crystalline, the poly-crystalline and the amorphous silicon panels are three types of PV panel modules that is available. The poly-crystalline panel is also known as a multi-crystalline panel [5]. All of the before mentioned panels have different appearance, composition and efficiency.

2.3 Charge controller

Charge controllers are used in PV systems in order to primarily protect the energy storage devices, which typically are batteries in common systems from overcharging and over discharging. Any system that consists of characteristics that would allow excessive overcharging and/or over discharging requires a charge controller. Failing to install a charge controller in such systems will directly lead to a shortened battery lifetime and decreased load availability.

Some systems consisting of small, predictable and continuous loads may be designed without a charge controller present in the system architecture. The algorithm that is implemented by the charge controller in order to prevent overcharging and over discharging of the batteries installed in the system will determine the effectiveness of the protection supplied to the battery. These algorithms will also affect the overall efficiency of the system in ensuring that load demands are met.

2.4. Energy storage device

The energy collected from the use of PV modules while the sun is shining needs to be stored for use in the periods whenever the sun is not available, i.e. during night time or on cloudy days. The energy storage device to be used is a battery. The batteries used to store the energy can be used to power loads during the day or night, on a continuous basis, without even considering the weather conditions [6, 7].

Although batteries are essential in any standalone PV system, they are considered to be the weakest point of the system. Batteries have the lowest life expectancy of all the components used in a standalone PV system. Certain requirements need to be met by the batteries used in standalone PV systems. These requirements will include an ability to withstand numerous charge and/or discharge cycles along with a low self-discharge rate. The last requirement will be that the batteries must have little need for maintenance or maintenance free [8, 9].

Deep cycle batteries are designed and manufactured with much thicker plates than other types of batteries. These thicker plates used in the deep cycle battery will allow the battery to be discharged as much as 80% of its capacity time after time.

Other batteries are manufactured from plates often referred to as sponge plates. The design of deep cycle batteries do not allow for instant power but rather for

power over a length of time. For the best results concerning lifespan vs cost for deep cycle batteries it is recommended by most manufacturers that the average discharge cycle of the battery is kept to about 50% of its capacity [10].

2.5 Control unit (PLC)

A PLC is a device, commonly referred to as a type of computer, which is used in the control and/or automation of electromechanical processes. These processes can represent any process to be performed by means of flipping a switch to the automation of an assembly line in a factory. PLC's are programmed by means of logic, as the name suggests, and acts on digital or analog states of systems.

The PLC makes use of a human interface by means of software that is installed on a computer and by connecting the PLC by means of its communication ports to the computer the user will be able to program the device to perform certain tasks depending on the state of the system. It can be seen that the unit has eight input ports at the top of the unit and four output ports in the form of relays. The amount of input and output ports can be extended by connecting modules to the side of the PLC. It is not necessary to reprogram the unit in order to connect. Figure 1 shows the functioning of the PLC system.

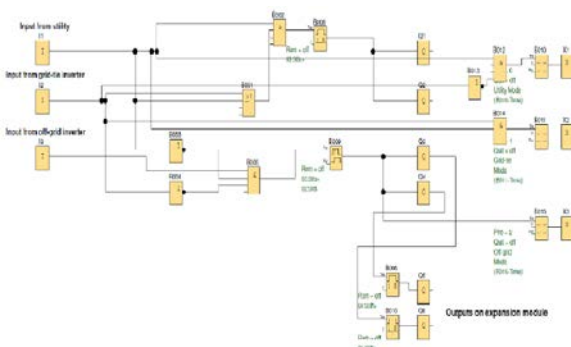


Figure 1: Detailed program loaded into the PLC

A screenshot of the detailed program loaded into the PLC is contains different blocks. In order to put more insight on how the program is functioning. Those blocks will be briefly discussed.

The input from the utility grid is connected to an OR and AND operation block which in turn is connected to a time delay. The time delay is set to close the output relays after 3 seconds. This is done to let the utility grid settle after becoming available again. Also there is a message block which is used to display the mode in which the system is operating. The message block on the PLC's LCD screen whenever the utility grid is available displays: Utility mode.

The input from the grid-tie inverter is connected to the same OR operation block as previously mentioned to supply the AND operator with the correct input. If system is operating in a grid-tie mode, LCD screen of the PLC displays: Grid-tie mode.

2.6 Power meter

Digital power meters are considered more accurate than mechanical power meters in the sense that they consist of pulse outputs that pulse at certain rate depending on the power consumed by the load. These pulse outputs range from one pulse per Wh to even 5 pulses per Wh depending on the accuracy of the meters. The most common digital power meter to be used in most applications uses a conversion rate of 1000 pulses per kWh consumed.

The pulse outputs of these meters can even be exported to event controller units which are used to log the pulses and communicate the data to a remote server in the case where the meters are installed in remote areas. This method is widely used by measure and verification companies to measure and verify power usage at certain sites.

3. RESULTS

Detailed conceptual design of the combined solar grid-tie and off-grid systems is shown in figure 2. This system can be divided by into two subsystems. Two sub systems are incorporated by the PLC which responsible for switching between grid-tie and off-grid mode respectively depending on the availability of the utility electricity grid.

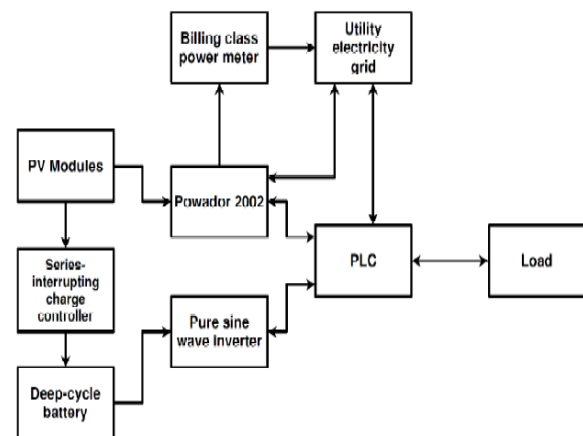


Figure 2: Detailed conceptual design of the combined solar grid-tie and off-grid system

The grid-tie inverter along with DC supplies emulating PV array is shown in figures 3.

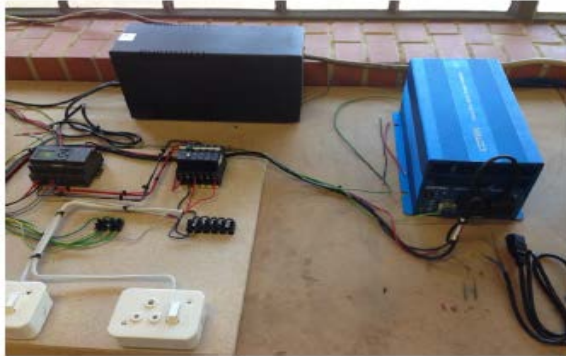
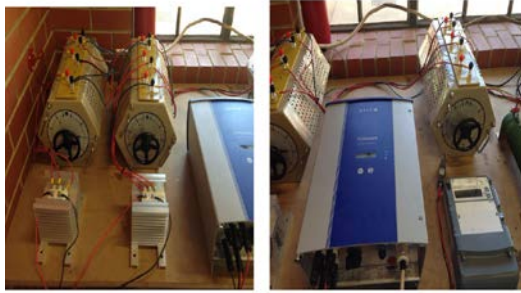


Figure 3: The grid-tie inverter with DC supplies

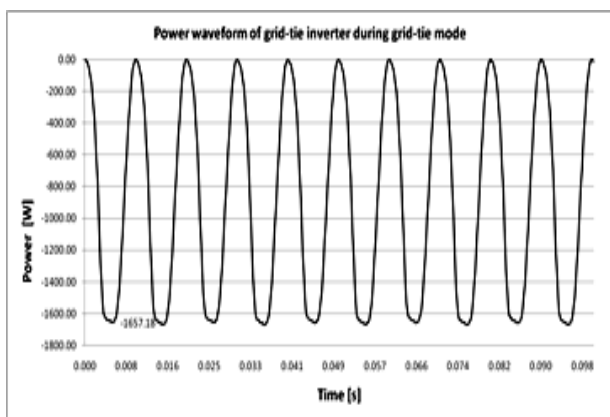


Figure 4: Power waveform of grid-tie inverter during grid-tie mode.

The waveform that is displayed in figure 4 is the power fed back into the grid from the grid-tie inverter to the utility grid. As it was previously mentioned the power can be seen to negative which is proof that the power is fed into the grid. At the bottom of the graph depicting the power waveform a data label indicating the value of the power fed into the grid can be seen to be -1657.18 W. This is again proof that the grid-tie inverter operated in grid-tie mode at the time of this measurement and verifies the capabilities of the grid-tie inverter to continuously delivers power to the grid-tie system as long as the PV system is available.

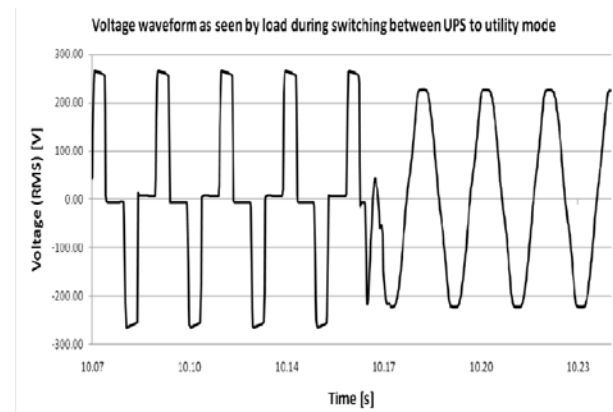


Figure 5: Voltage waveform as seen by the load during switching between UPS to utility mode

The voltage waveform of the system is displayed in figure 5. The first part of the voltage waveform represents the voltage supplied to the load from the UPS. It can thus be seen that the first part of the voltage waveform is modified sine wave. The modified sine wave from the UPS has a RMS voltage value of roughly 225 V as was measured using a multimeter. The point where the utility grid becomes available again can be seen in the middle of the voltage waveform displayed in figure 5.

At the point where the utility grid becomes available again it can be seen that the voltage drops for only a few milliseconds. The load will not be affected too much by this voltage drop in the sense that it is literally only for a split second.

The last part of the voltage waveform shown in figure 5 represents the voltage waveform of the utility grid. The voltage waveform of the utility grid has a RMS voltage value of close to 222 V as can be seen from figure 5.

The general shape of the current and power dissipation waveforms is expected to take the same shape as that of the voltage waveform and the figures displaying these waveforms are to follow along with the respective discussions surrounding these waveforms.

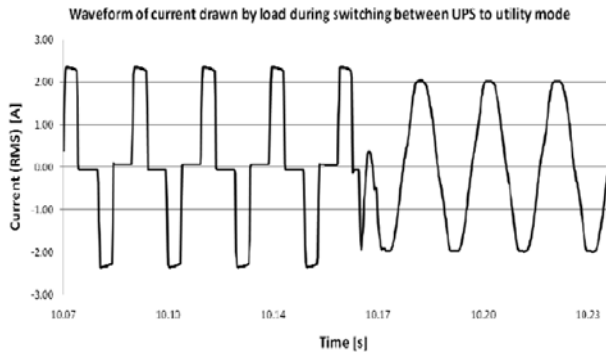


Figure 6: Waveform of current drawn by the load during switching between UPS to utility mode

As was expected the waveform of the current drawn by the load, displayed in figure 6 takes on the general shape of the voltage waveform displayed in figure 5. The RMS value of the current drawn by the load mentioned earlier is in the range of 2A and this value was again verified by means of a multimeter and theoretical calculations.

The power dissipation waveform of the resistive load connected to system is shown in figure 7.

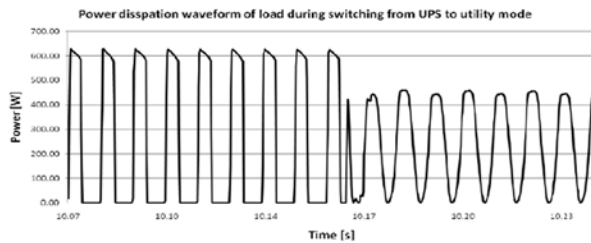


Figure 7: Power dissipation waveform of load during switching between UPS to utility mode

The value of the power dissipated by the load can be seen from the data label on the graph to be around 450 W. The load is pure resistive and therefore the power dissipated is real power and no reactive power exists in the system at this point. The value of the power dissipated by the load was verified by means of a power meter as well as theoretical calculations.

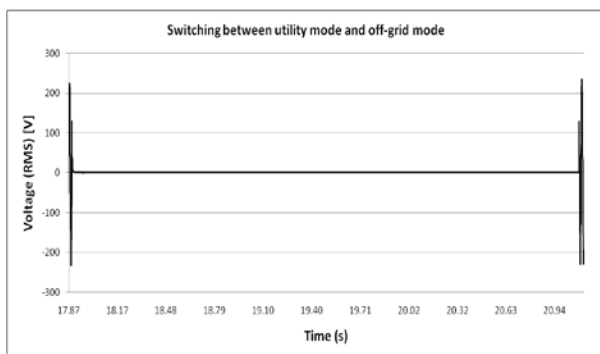


Figure 8: Voltage waveform as seen by load during PLC switching from utility mode to off-grid mode

The voltage waveform displayed in figure 8 shows the voltage seen by the load and is used to verify the time it takes the PLC to switch from utility mode to off-grid mode. It is important to keep in mind that the PLC was designed to switch to off-grid mode 3 seconds after the utility grid became unavailable. It can be seen from the voltage waveform that the PLC was active in utility mode and the voltage measured during the switching was zero at the instance where the utility grid became unavailable at round about 17.9 seconds on the graph.

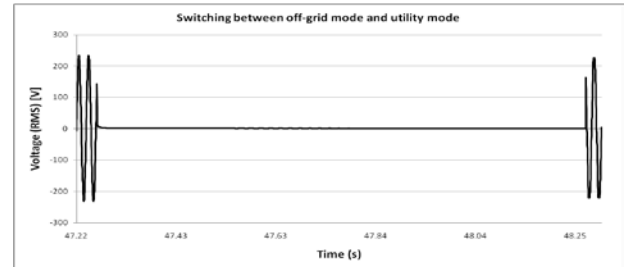


Figure 9: Voltage waveform as seen by load during PLC switching from off-grid mode to utility mode

The voltage waveform displayed in figure 9 is the switching from off-grid mode to utility mode at the moment where the utility grid becomes available again and the PLC switches back to utility mode. It can be seen from the graph contained in figure 8 that off-grid mode is switched off at round about 47.3 seconds. Utility mode is switched on at roughly 48.3 seconds on the graph and thus the graph in fig. 5 verifies the correct operation of the PLC in the sense that the PLC was programmed to allow for only second between switching from off-grid mode back to utility mode.

The power dissipation waveform of the resistive load connected to the system is displayed in figure 10. The value of the power dissipated by the load can be seen from the data label on the graph to be 718.75 W. The load is pure resistive and therefore the power dissipated is real power and no reactive power exists in the system at this point. The value of the power dissipated by the load was verified by means of a power meter as well as theoretical calculations.

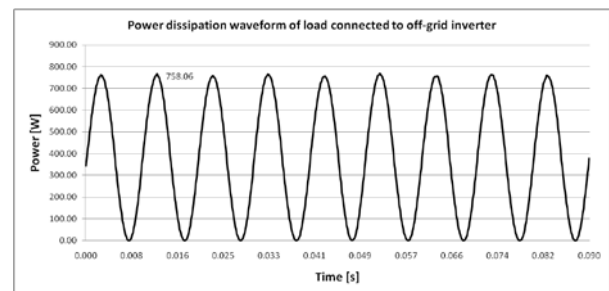


Figure 10: Power dissipation waveform of load in off-grid mode connected to a resistive load.

4. CONCLUSION

From the results obtained from the test conducted on the solar grid-tie and off-grid system it can be concluded that a solar grid-tie and off-grid system is quite feasible and that these systems can be implemented quite successfully. It can be predicted that in the future these type of systems will become more and more desirable in the sense that the system is able to power a load whenever the utility grid is unavailable and the system is able to feed power into to grid that may generate some form of income for the user from the electricity utility provider.

By implementing other technologies along with the technologies used in the current system, the system can be improved. Some of the technologies used in the implemented system can even be replaced by other technologies. Future developments regarding certain technologies and components will make these types of systems more and more feasible.

5. REFERENCES

- [1] T. Kheng Kwang and S. Masri: "Single phase grid tie inverter for photovoltaic application," *2010 IEEE Conf. on Sustainable Utilization and Development in Engineering and Technology*, pp. 23-28, 20-21 Nov. 2010.
- [2] H. Gu, Z. Yang, D. Wang and W. Wu: "Research on control method of double-mode inverter with grid-connection and stand-alone," *5th International Conf. on Power Electronics and Motion Control, IPEMC 2006. CES/IEEE*, vol.1, pp. 1-5, 14-16 Aug. 2006.
- [3] KACO New Energy, "Operating instructions for the operator Powador 2002 / 3002 / 4202 / 5002 / 6002", 2006. [Online].
- [4] C. V. Nayar: "Control and interfacing of bi-directional inverters for off-grid and weak grid photovoltaic power systems," *IEEE Power Engineering Society Summer Meeting, 2000*, vol.2, pp. 1280-1282 vol. 2, 2000
- [5] O. Asowata, J. Swart, and C. Pienaar: "Optimum tilt and orientation angles for photovoltaic panels in the Vaal Triangle," *Power and Energy Engineering Conference (APPEEC), 2012, Asia-Pacific*, pp. 1-5, 2012.
- [6] A. Luque, and S. Hegedus: "Handbook of photovoltaic science and engineering," West Sussex: Wiley, 2005, ch. 17.
- [7] S. Borowy, and Z. M. Salameh: "Methodology for optimally sizing the combination of a battery bank and PV array in a wind/PV hybrid system," *IEEE Trans. on Energy Conv.*, vol. 11, June 1996, pp.367-373.
- [8] P. Kumar Soori, L. Parthasarathy, M. Okano, A. Mana: "Intelligent off-grid photovoltaic supply systems," *World Academy of Science, Engineering and Technology Journal*, vol. 16, pp. 141-145, 2008.
- [9] L. Rebecca, Lankey, F. C. McMichael: "Life-cycle methods for comparing primary and rechargeable batteries," *Environmental Science & Technology*, vol. 34, no. 11, pp. 2299-2304, 2000.
- [10] "FEZ Panda II Board," 2011. [Online]. Available: http://www.ghielectronics.com/downloads/FEZ/Panda_I/FEZ_Panda_II_UserManual.pdf

Measurements and Multipath Characterization of Power Line Communication Channel

Steven O. Awino and Thomas J. O. Afullo

Department of Electrical, Electronic & Computer Engineering
University of KwaZulu-Natal, Mazisi Kunene Rd,
Durban, South Africa

Email: {stevewn06@gmail.com, Afullo@ukzn.ac.za}

Abstract—In this paper, we present measurement and analysis results of the in-door low-voltage Power Line Communication (PLC) network time variant and multipath characteristics under different unknown network topologies in the frequency band of 1-30 MHz. Based on the measurement results, a conventional method of estimating the Root Mean Square (RMS) delay spread and other delay parameters from the average impulse response delay profiles is used to extract the multipath characteristic parameters and associated coherence bandwidths for each network. From the results obtained, the RMS delay spread is observed to increase with the complexity of the network topology, which leads to a reduction in the coherence bandwidths. The results obtained are also compared to models of similar approach and found to be comparable.

Index Terms—Coherence bandwidth, maximum excess delay spread, mean excess delay, multipath propagation, Power Line Communication (PLC), RMS delay spread

I. INTRODUCTION

The in-door low-voltage power line network allows for the building of an in-house telecommunication network in the most cost effective way in that no extra costs of installations are incurred. This is due to the ubiquitous network providing connectivity points in the houses and buildings connected to the grid [1], [2], [3], [4]. However, the power line network characteristics that include varying impedance, noise, attenuation, signal scattering and reflections due to numerous branching points, are the most unfavourable conditions for data transmission [5]–[7]. The reason being that the power line network was designed for distribution of electrical energy [2]. These signal reflection and scattering characteristics in the PLC environment result in the receiver receiving a superposition of multiple attenuated and phase-shifted copies of the transmitted signal. This therefore calls for channel models, multipath and time variant characterization which play one of the most important roles in the design and analysis of PLC systems [1], [8], [9]. The common approach used in this research to investigate the multipath and time variant characteristic of the power line channel, is the extraction of multipath parameters from a large set of measurement data, a procedure which [10], [11], [12] and [13] have also used in their works among other researchers.

Even though multipath characterization of the in-door low-voltage PLC propagation channel has been performed and reported by several researchers, these reports are mainly based on simulated statistical characterization of the power line channel impulse response with few experimental results available [10]. Although characterization of the power line channel requires a comprehensive evaluation of its impulse response, characterization through the known channel multipath propagation parameters that include Root Mean Square (RMS) delay spread, mean excess delay and maximum excess delay spread have proved useful [10], [14], [15], [16], [17]. The work presented herein focuses on the analysis and characterization the PLC channel multipath and time variant nature of the PLC channel using the above mentioned multipath propagation parameters in typical networks with unknown network topologies and configurations through measurements. All these mentioned parameters are defined and discussed in the subsequent sections.

This paper is organized as follows: In Section 2, the theories of multipath propagation and the resulting mathematical model is introduced. Measurement set-up and procedures are outlined in Section 3, while the results are presented in Section 4. In Section 5, the multipath parameters are obtained from the measurement results and the rms delay spread values also presented. Discussion of the results obtained is presented in Section 6 and conclusions drawn in Section 7.

II. MULTIPATH PROPAGATION IN PLC CHANNEL

The power line channel is regarded as a multipath environment due to the multiple reflections and scatterings of signals at impedance discontinuities resulting in transmitted signals reaching the receiver not only through the direct path but also through delayed and attenuated paths [18], [1], [14], [16]. To understand, analyse and characterize this multipath phenomenon, we resort to determining the multipath parameters that provide important information on the data transmission rates and dispersive characteristics of the power line channel [10], [19], [20]. As shown in Fig. 1, the power line channel can be characterized as a linear time variant

(LTV) system [17], [20] with input, $x(t)$ and output, $y(t)$, assumed to comprise N discrete paths of propagation with each path having an amplitude attenuated by a factor α_k , a phase-shift θ_k , a propagation delay τ_k and noise factor $n(t)$ [17], [18], [21].

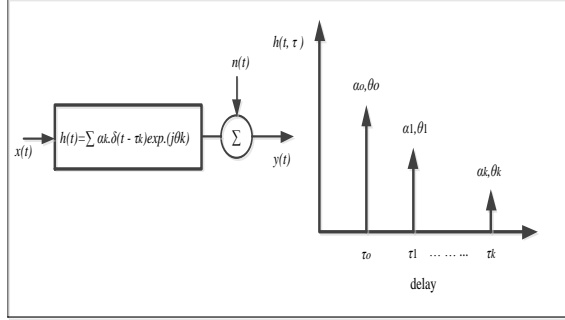


Fig. 1. Mathematical model of the channel

Mathematically, the power line network channel impulse response can be represented as [17], [18]:

$$h(t) = \sum_{k=1}^N \alpha_k \delta(t - \tau_k) e^{j\theta_k} \quad (1)$$

where $k = 1, 2, 3, \dots, N$ is the number of paths, with δ being the Dirac delta function [17], [18]. The phase-shift, θ_k is given as [18]:

$$\theta_k = \arctan \left(\frac{\text{Im}\{\alpha_k\}}{\text{Re}\{\alpha_k\}} \right) \quad (2)$$

The impulse transfer function is composed of a sum of N Dirac delta pulses which are delayed by τ_k and have frequency dependent phase-shifts [18].

III. MEASUREMENT SET-UP AND PROCEDURES

Measurements were done using a 9 KHz-13.6 GHz Rohde & Schwarz ZVL13 Vector Network Analyzer (VNA) shown in Fig. 2 to obtain the channel complex frequency responses in the frequency band of 1-30 MHz. Calibration were done for system error correction before the start of measurements to ensure integrity and accuracy of our measurement results. Measurement set-up at all the locations were as Fig. 2.

A frequency sweep range of 1-30 MHz was set on the VNA, and the S_{21} parameter selected as a measurement parameter. Designed and constructed couplers presented in [7], [10] as shown in Fig. 2 were used to connect the 50 Ω impedance ports, port 1 and port 2/RF input of the VNA to the power line network. An RF stimulus signal was then transmitted at output port 1 into the network and measured RF signal from the network received at port 2/RF input (response signals). The couplers provided isolation, impedance matching and filtering of the high frequency low voltage RF stimulus signal from the high-voltage low frequency power line network.

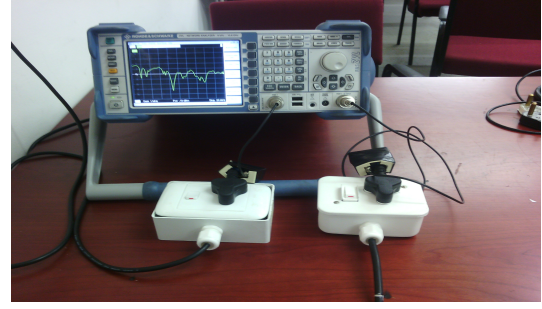


Fig. 2. Couplers connected to the analyzer ports through BNC to N-connectors

Using the impulse response approach of (1), extensive measurement of the transfer functions in the following listed selected locations were done. Although the purpose of this measurements was to fully characterize the multipath propagation phenomena in PLC channel, in this paper only results of the multipath delay spread are presented. The following locations were investigated:

- Second Year EEC Engineering Laboratory: In this location, a workstation was composed of a function generator, a digital multimeter, an oscilloscope and a trainer. The network connection was such that three workstations were connected to a single circuit breaker at the Distribution Board (DB) forming a single network. Thus measurements were done for two combined networks which translated into six workstations.
- Second Year Engineering Computer Laboratory: In this laboratory, the network connection was such that six workstations were connected to a single circuit breaker at the DB board forming a single network. A workstation had a CPU and a monitor. Measurements were done for six workstations.
- Office: Based on the knowledge of power supply network connections from the other locations from the DB boards, a random check on the network connections in several offices were done and it was found that the offices had single networks. The problem was fully establishing as to whether the power supply circuits in a single office were connected to a single circuit breaker at the DB or were just a loop from another next office since the installation schematics were unavailable. The selected office had the most used office equipment in the engineering north building that included, an electric paper shredder, computer station, photocopier machine, a scanning machine, a laptop and a fax machine. And thus only this selected office result is presented.
- Electrical Engineering workshop: This workshop had the most complex network amongst all the locations. Most heavy machinery had their own isolators or connected to a specific circuit breaker from

a sub distribution board. With such connections, the network was composed of several sub-networks terminating at different circuit breakers at the main DB and isolators.

At each location, the transmitter and receiver positions of the PLC channel were carefully chosen on the basis of number of networks interconnected together, sufficient terminal loading conditions and network topology. The Inverse Discrete Fourier Transform (IDFT) of the frequency responses were then taken to obtain equally the same number of impulse responses in the time domain.

IV. DATA ANALYSIS AND CHANNEL RESPONSE RESULTS

A. Channel Frequency Response (CFR)

We performed channel transfer measurements in the frequency domain through acquisition of the S_{21} parameter with a VNA from the various channels. From the basic definition of the channel frequency response as the ratio of the voltage at the receiver port of the VNA to the voltage at the transmit port of the VNA [11], [22], we denoted the S_{21} parameter as the channel frequency response $H(f)$ and are as shown in Fig. 3, 4, 5 and 6.

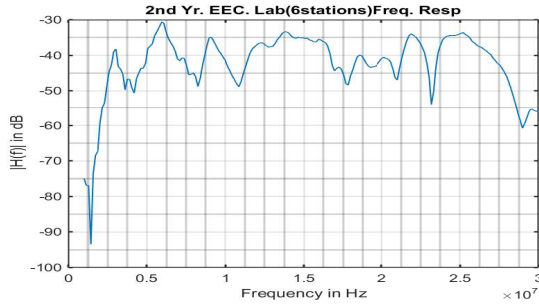


Fig. 3. Frequency response profile for Second Year EEC Engineering laboratory (six workstations)

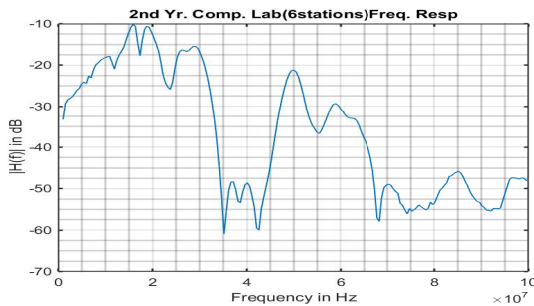


Fig. 4. Frequency response profile for Second Year EEC Engineering computer laboratory (six workstations)

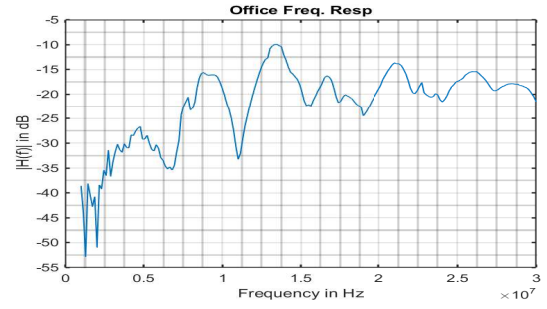


Fig. 5. Frequency response profile for the office

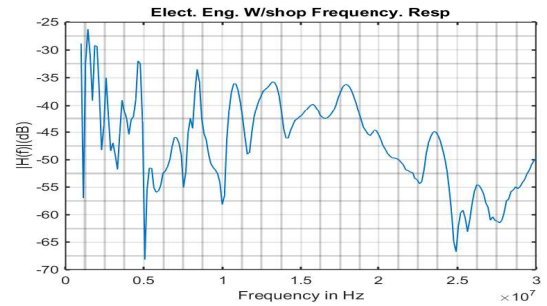


Fig. 6. Frequency response profile for Electrical Engineering workshop

B. Channel Impulse Responses (CIR)

Because of our interest in the time-variant multipath characteristics of the channel, the measured channel transfer functions $H(f)$, were then transformed to the CIR, $h(t)$. This transformation were accomplished through the Inverse Discrete Fourier Transformation (IDFT) in Matlab. The following procedures were adopted with the term m referring to the frequency samples within the frequencies of $f_1 = 1$ MHz, and $f_2 = 30$ MHz:

- Windowing of the measured CFR data: Our focus on the CFR were in the frequency range from f_1 to f_2 . The measured CFR were defined in the discrete frequency domains from f_1 to f_2 . This resulted in a total of $m + 1$ discretized data samples.
- IDFT were then done to obtain the real CIR at time instant $t = rT$, where $r = 0, \dots, R$, $R = 2m$, and T being the resolution in time. Thus the CIR were defined in discrete time domains with temporal resolution $\Delta t = 1/[(m + 1)\Delta f]$ with Δf being the resolution bandwidth.
- Each obtained CIR data were then normalized by their respective mean and standard deviations.

Fig. 7, 8, 9 and 10 are the processed CIR results for all the locations.

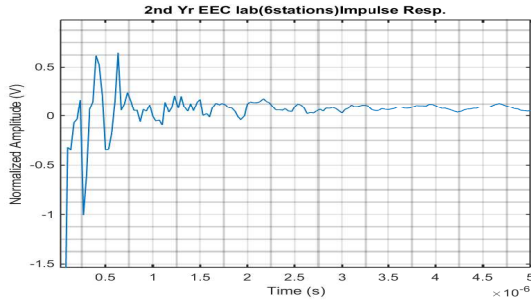


Fig. 7. Impulse response profile for Second Year EEC Engineering laboratory (six workstations)

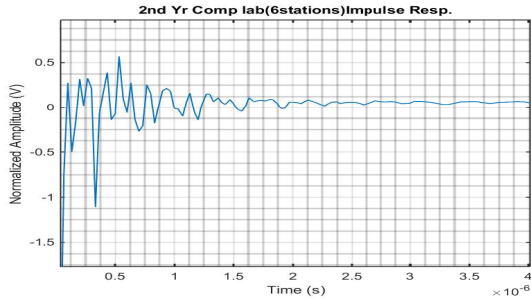


Fig. 8. Impulse response profile for Second Year EEC Engineering computer laboratory (six workstations)

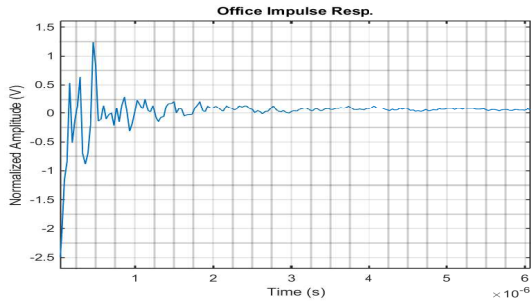


Fig. 9. Impulse response profile for the office

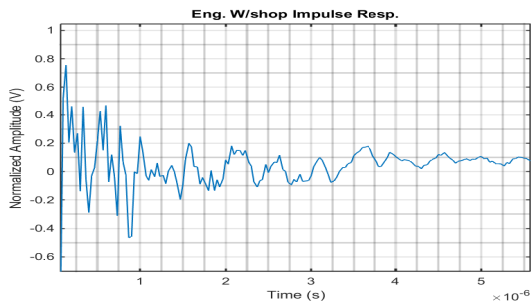


Fig. 10. Impulse response profile for Electrical Engineering workshop

From these channel transfer functions, deep and narrow notches occur and are spread over the whole frequency range. These notches are due to the multiple

reflections at the points of discontinuities and impedance mismatches. In addition, the length of the impulse responses and the number of the peaks that occur, vary considerably and depend on the network topology, terminal loading profiles and the environment.

V. MULTIPATH PROPAGATION PARAMETERS

In order to compare different multipath channels and develop general guidelines for PLC systems, multipath parameters are used to quantify the multipath and time variant channel [21], [23], [24]. Next, the key multipath and time variant parameters that include: mean excess delay, RMS delay spread and maximum excess delay spread are discussed. In addition, the relationship between the coherence bandwidth and the RMS delay spread of the networks is also studied statistically.

A. Mean Excess Delay ($\bar{\tau}_e$)

This is the first moment of the power delay profile and is given by [17], [21]:

$$\bar{\tau}_e = \frac{\sum_k a_k^2 \tau_k}{\sum_k a_k^2} = \frac{\sum_k P(\tau_k) \tau_k}{\sum_k P(\tau_k)} \quad (3)$$

where τ_k , a_k , and $k = 1, 2, 3, \dots$, are the signal arrival delay, amplitude of delay arrival and delay position respectively in the received power delay profile, while the power delay profile is defined as $P(\tau_k) = |h(\tau_k)|^2 / \int_0^\infty |h(\tau)|^2 d\tau$ [17], [21], [24].

B. Root Mean Square (RMS) Delay Spread (τ_{rms})

This is the square root of the second central moment of the power delay profile. It gives an account for the energy dispersion in the impulse response of the channel [20]. It is defined by [21]:

$$\tau_{rms} = \sqrt{\bar{\tau}^2 - \bar{\tau}_e^2} \quad (4)$$

Where $\bar{\tau}^2$ is the second moment of the power delay profile given as:

$$\bar{\tau}^2 = \frac{\sum_k a_k^2 \tau_k^2}{\sum_k a_k^2} = \frac{\sum_k P(\tau_k) \tau_k^2}{\sum_k P(\tau_k)} \quad (5)$$

These delays are measured relative to the first arriving signal at the receiver at delay $\tau_0 = 0$. Equations (3) and (4) rely only on the relative amplitudes of the multipath components within $P(\tau_k)$ [21], [23], [24].

C. Maximum Excess Delay Spread (τ_X)

Maximum excess delay, is defined to be the time delay during which the multipath energy falls to X dB below the maximum in the power delay profile. It is defined by $\tau_X - \tau_0$, where τ_0 refers to the first arriving signal and τ_X is the maximum delay at which a multipath component is within X dB of the arriving multipath component with the highest amplitude and does not necessarily arrive at τ_0 [21], [23], [24].

Maximum excess delay defines the temporal extent of the multipath that is above a particular threshold [44], [45]. In this work, the noise floor threshold was set at

0.125 V in the $h(t)$ graph delay profile to differentiate between received multipath components and noise. Table I shows the statistics of the extracted multipath parameters from the various CIR delay profiles.

TABLE I
STATISTICS OF THE EXTRACTED MULTIPATH DELAY PARAMETERS

Locations	Parameters (μs)			
	τ_o	$\bar{\tau}_e$	τ^2	τ_{rms}
EEC Eng. lab.(6stns)	0.250	0.623	0.553	0.406
Computer. lab.(6stns)	0.094	0.493	0.311	0.261
Office	0.125	0.464	0.270	0.234
Workshop	0.063	0.446	0.543	0.587

It is important to note that the RMS delay spread and mean excess delays are defined from a single power delay profile that is a temporal average of consecutive impulse response measurements collected and averaged over a local area.

D. Coherence bandwidth (B_c)

While the RMS delay spread is a natural quantity caused by the reflected and scattered propagation paths in the power line network channel, the coherence bandwidth, (B_c), is a relation derived statistically from the RMS delay spread. Coherence bandwidth is used as a statistical measure of the frequency band within which the channel can be considered “flat”. This means the spectral components within this range of frequencies have approximately equal gain and linear phase. Coherence bandwidth is defined in terms of correlation function of the frequency response ($R(\psi)$), given as (6) [12], [25]. It measures the correlation magnitude between the channel response between two spaced frequencies.

$$R(\psi) = \int_{-\infty}^{\infty} H(f)H^*(f + \psi)df \quad (6)$$

where ψ is the frequency shift and * refers to the complex conjugate. Table II shows the computed coherence bandwidths based on 0.5 and 0.9 correlation levels

TABLE II
COHERENCE BANDWIDTH VALUES FOR 0.5 AND 0.9 CORRELATION LEVELS

Locations	Parameters (KHz)	
	$B_{0.5}$	$B_{0.9}$
EEC lab.(6stns)	492.610	49.261
Comp. lab.(6stns)	766.283	76.628
Office	854.700	85.470
Workshop	340.716	34.072

VI. DISCUSSION OF RESULTS

Based on measurement results, we defined the complexity of the networks based on the different terminal loading conditions and circuit connections at the distribution boards. A circuit running from and to the same circuit breaker at the distribution board were considered

single networks, while the circuits that terminated at different circuit breakers were considered to form parallel connected networks.

From inspection of Table II, a clear and consistent dependence of the RMS delay spread on the loading conditions of the different power supply networks in the different locations were noted. The RMS delay spread values increased with increased loading profiles in the different power supply networks, and hence a reduction in the coherence bandwidths. This reduction in bandwidth witnessed is not a favourable condition for broadband data transmission and thus very suitable coding and modulation schemes are called for to mitigate against such conditions in PLC.

The dependence of the delay spread on the network topology and configuration is an important observation in this study that would thus greatly influence PLC system design. A review results obtained in previous works shows good agreement. In this regard, the results obtained here, were compared to results reported USA (1.8 - 30 MHz), for band A (1.7 - 30 MHz) from France, and frequency band B from Brazil (2 - 100 MHz) as presented in [26], [27], [13] respectively among other researchers as shown in Table III.

TABLE III
COMPARISON OF RMS DELAY SPREAD VALUES

Parameters(μsec)	UKZN	[26]	[27]	[13]
Minimum	0.234	0.090	0.026	0.039
Maximum	0.587	1.810	1.039	0.493
Mean	0.385	0.530	0.309	0.148
Standard dev.	0.162	0.290	0.212	0.064

From Table 5.3, our mean RMS delay value of $0.368\mu s$ were lower than $0.530\mu s$ reported in [26] but higher than $0.309\mu s$ and $0.148\mu s$ reported in [27] and [13] respectively. This could be attributed to the difference in the terminal loading conditions and network topology at these locations. The minimum, maximum and standard deviations also compared well with the other presented results.

VII. CONCLUSIONS

In this paper, measurements and analysis of the multipath characteristics of the power line network channel for selected locations within the University of KwaZulu-Natal were investigated and presented. From the analysis, it is evident that the power line channel is a time varying channel due to the ever varying channel impedance, mismatched branching points, and terminal load impedances causing scattering in the transmitted signal, thus leading to multipath fading propagation. In addition, we have also compared our mean delay with results from other regions employing a similar approach and found the results to be in good agreement with them.

REFERENCES

- [1] M. Zimmermann and K. Dostert, "A multipath model for the power line channel," *IEEE Trans. On Commun.*, vol. 50, no. 4, pp. 553–559, Apr. 2002.
- [2] S. O. Awino and T. J. O. Afullo, "Power line communication channel modelling using parallel resonant circuits approach," in *Proceedings of South Africa Telecommunication Networks and Applications Conference (SATNAC)*, ser. Western Cape, South Africa, 6-9, Sep. 2015, pp. 353–357.
- [3] J. Anatory, N. Theethayi, M. M. Kissaka, and N. H. Mvungi, "Broadband power line communications: Performance analysis," *World Academy of Science, Engineering and Technology*, pp. 832–836, 24 2008.
- [4] A. M. Nyete, T. J. O. Afullo, and I. Davidson, "On rayleigh approximation of the multipath plc channel: Broadband through the PLC channel," in *Proceedings of South Africa Telecommunication Networks and Applications Conference (SATNAC)*, ser. Nelson Mandela Bay, Eastern Cape, South Africa, 31 Aug.-3 Sep. 2014, pp. 265–270.
- [5] M. Tanaka, "High frequency noise power spectrum, impedance and transmission loss of power line in japan on intrabuilding power line communications," *IEEE Trans. On Consumer Electronics*, vol. 34, no. 2, pp. 321–326, May 1988.
- [6] H. Meng, Y. L. Guan, and S. Chen, "Modelling and analysis of noise effects on broadband power line communications," *IEEE Trans. On Power Delivery*, vol. 20, no. 2, pp. 630–637, Apr. 2005.
- [7] M. Zimmermann and K. Dostert, "Analysis and modelling of impulsive noise in broad-band power line communications," *IEEE Trans. On Electromagn. Comp.*, vol. 44, no. 1, pp. 249–258, Feb. 2002.
- [8] J. Anatory and N. Theethayi, *Broadband Power-Line Communication Systems: Theory and Applications*. WIT Press, 2010.
- [9] M. P. Sibanda, P. A. J. van Rensburg, and H. C. Ferreira, "Impedance matching with low-cost, passive components for narrowband PLC," in *Proceedings of IEEE Int. Symposium on Power-Line Communications and Its Applications (ISPLC)*, ser. Udine, Italy, 3-6, April 2011, pp. 335–340.
- [10] M. Mosalaosi and T. J. O. Afullo, "Dispersive characteristics for broadband indoor power line communication channels," in *Proceedings of South Africa Telecommunication Networks and Applications Conference (SATNAC)*, ser. Nelson Mandela Bay, Eastern Cape, South Africa, 31 Aug.-3 Sep. 2014, pp. 313–317.
- [11] F. Versolatto and A. M. Tonello, "PLC channel characterization up to 300 MHz: Frequency response and line impedance," in *Proceedings of IEEE Global Telecommunications Conference (GLOBECOM)*, ser. Anaheim, California, USA, 3-7, Dec. 2012, pp. 3525–3530.
- [12] H. Gassara, F. Rouissi, and A. Ghazel, "Statistical characterization of the indoor low-voltage narrowband power line communication channel," *IEEE Trans. On Electromagn. Comp.*, vol. 56, no. 1, pp. 123–131, Feb 2014.
- [13] M. Tlich, A. Zeddami, F. Moulin, and F. Gauthier, "In-door power line communications channel characterization up to 100 MHz-part II: Time-frequency analysis," *IEEE Trans. On Power Delivery*, vol. 23, no. 3, pp. 1402–1409, Jul. 2008.
- [14] D. Anastasiadou and T. Antanakopoulos, "Multipath characterization of in-door power line networks," *IEEE Trans. On Power Delivery*, vol. 20, no. 1, pp. 90–99, Jan. 2005.
- [15] L. Liu, T. Cheng, and L. Yanan, "Analysis and modelling of multipath for indoor power line channel," in *Proceedings of IEEE Conference on Advanced Communication Technology*, ser. Phoenix Park, Korea, 17-20, Feb. 2008.
- [16] G. Huang, D. Akopian, and C. L. P. Chen, "Measurement and characterization of channel delays for broadband power line communications," *IEEE Trans. On Instrumentation and Measurements*, vol. 63, no. 11, pp. 2583–2590, Nov. 2014.
- [17] H. Hashemi and D. Tholl, "Analysis of the rms delay spread of indoor radio propagation channel," in *Proceedings of IEEE Int. conference on Commun., ICC'92*, ser. Chicago, USA, 14-18, Jun. 1992, pp. 875–881.
- [18] H. Philips, "Modelling of power line communication channels," in *Proceedings of Int. Symposium on Power-Line Communications and Its Application (ISPLC)*, ser. Vancouver, Canada, 6-8, Apr. 2005, pp. 14–21.
- [19] H. Li, Z. Bi, D. Liu, J. Li, and P. Stoica, "Channel order and rms delay spread estimation for AC power line communications," in *Proceedings of the Tenth IEEE Workshop on Statistical Signal and Array Processing*, ser. Pennsylvania, USA, 14-16, Aug. 2000, pp. 229–233.
- [20] A. M. Tonello, F. Versolatto, and A. Pittolo, "In-home power line communication channel: Statistical characterization," *IEEE Trans. On Commun.*, vol. 62, no. 6, pp. 2096–2106, Jun. 2014.
- [21] T. S. Rappaport, *Wireless Communications: Principles and Practice*. Prentice-Hall, Inc., 2002.
- [22] P. J. Pupaiaikis, *The Relationship Between Discrete-Frequency S-parameters and Continuous-Frequency Responses*, DesignCon, http://cdn.teledynelecroy.com/files/whitepapers/designcon2012_lecroy_s-parameters_discrete_frequency_continuous_response.pdf, 2012.
- [23] A. F. Molisch, *Wireless Communications*, 2nd ed. Wiley-IEEE Press, 2011.
- [24] U. Madhow, *Fundamentals of Digital Communication*. Cambridge University Press, 2008.
- [25] M. Mosalaosi, *Power Line Communication (PLC) Channel Measurements and Characterization*, ser. MSc. Dissertation. Durban, South Africa: University of KwaZulu-Natal, 2014.
- [26] S. Galli, "A simplified model for the indoor power line channel," in *Proceedings of IEEE Int. Symposium on Power-Line Communications and Its Applications (ISPLC)*, ser. Dresden, Germany, 29 Mar.-1 Apr. 2009, pp. 13–19.
- [27] T. R. Oliveira, C. B. Zeller, S. L. Netto, and M. V. Ribeiro, "Statistical modelling of the average channel gain and delay spread in in-home PLC channels," in *Proceedings of IEEE Int. Symposium on Power-Line Communications and Its Applications (ISPLC)*, ser. Austin, Texas, USA, 29 Mar.-1 Apr. 2015, pp. 184–188.

Steven O. Awino received his Bachelor's degree in Electrical and Electronic Engineering from the Technical University of Kenya, Kenya in the year 2013 and is presently studying towards his Master of Science degree in Electronics Engineering at the University of KwaZulu-Natal, South Africa. His research interests include Power Line Communication, RF & propagation and Broadcasting Systems.

Thomas J. O. Afullo received his Bachelor's degree in Electrical and Electronic Engineering (Hons) from the University of Nairobi in the year 1979, the MSEE from the University of West Virginia, USA in the year 1983 and the license in technology and PhD in Electrical Engineering from Vrije Universiteit (VUB), Belgium in the year 1989. He is currently a Professor and Discipline Academic Leader of Electrical, Electronic and Computer Engineering at the University of KwaZulu-Natal, Durban, South Africa

Improved Dynamic Response of Flying Capacitor Converter Using Finite Set-Model Predictive Current Control

A. M. Almaktoof^{1*}, A. K. Raji¹ and M. T. E. Kahn¹

¹Department of Electrical, Electronic and Computer Engineering, Cape Peninsula University of Technology, Symphony Way, Bellville 7535, Bellville Campus, South Africa

*Email: 213301091@mycput.ac.za

Abstract: In this paper a model predictive control (MPC) for three-phase, three-level, flying capacitor converter (FCC) is proposed. The use of an MPC three-phase, flying capacitor multilevel converter has two primary control aims; reference current tracking and flying capacitor voltage balancing, both of which are done concurrently by means of a multivariable control algorithms proposed in this work. The first proposed control algorithm is to control the output current of a three-level FCC using a finite set-model predictive current control (FS-MPCC) strategy. The second algorithm is a flying capacitor voltage balancing algorithm based on predictive control to solve the unbalanced flying capacitor voltage problems. A flying capacitor voltage-based algorithm is presented to balance the flying capacitor voltage in a complimentary way with the FS-MPCC algorithm. The control algorithm is tested with sinusoidal waveform and square current waveform references in order to check the dynamic response of the system in terms of the tracking behaviour of the reference currents and the ability to balance the flying capacitor voltages. Co-simulation is effected by means of MATLAB/Simulink with PSIM software, to assess the efficacy and robustness of an FS-MPCC for the three-level FCC inverter for resistive-inductive load (RL-load).

1 INTRODUCTION

Multilevel converters present great advantages compared with conventional two-level converters and attempt to address some of the limitations that the latter impose [1]–[3]. In the last couple of decades, the multitude of applications of multilevel converters found in most industrial domains, have been intensively researched. When high switching frequency pulse-width modulation (PWM), [2] is used with MLIs, these inverters offer significant advantages compared with conventional two-level converters [4]. These advantages are fundamentally focused on improvements in the quality of the output signals and a nominal power increase in the converter.

The flying capacitor multilevel converter was presented by Meynard and Foch in the 1990s as an alternative to the diode-clamped inverters [5]. The advantages of the FCC topology over other multilevel topologies such as diode-clamped converters and cascaded converters [2], [6], has of late featured prominently in the literature [7]–[9].

From the 1980s onward, model predictive control has been applied to power electronics [10], [11]; when compared to traditional PWM, MPC has distinct advantages [12]. The inherent discrete nature of power converters sets the stage for

implementing an MPC for power converters and motor drives. Since power converters have a finite number of switching states, the MPC optimization problem can be simplified by limiting the prediction of the system behaviour to only those switching states that are permissible. Following this simplification process, each prediction is used to evaluate a cost function (also known as a quality or decision function), the switching state with minimum cost is then selected and generated in the subsequent switching instance. This control method is referred to as a finite set-model predictive control method since the possible control actions (switching states) are finite. Many studies have been presented and successfully applied using an FS-MPCC scheme for three-phase multilevel inverters and drive applications [12]–[15]. Muller et al. [16] and Rodríguez et al. [17] present a matrix converter controller and an induction machine torque controller respectively.

In this paper, an FS-MPCC technique for an FCC inverter is presented. For MPC with FCC multilevel inverters, the two foremost control objectives are reference current tracking and balancing the voltages of the flying capacitor; these objectives are achieved at the same time by the multivariable control scheme. The MPC algorithm inputs are the measured currents and flying capacitor voltages, and the reference currents. The algorithm output corresponds with one of the switch states of the converter, without the application of a modulation scheme. A flying capacitor voltages algorithm based on predictive control (active control) is presented to balance the flying capacitor voltages because the natural balancing (passive control) of the capacitor voltages of FCCs fails in certain circumstances (as it is the case for PWM) [7]–[9].

This paper is organized as follows: Section 2 presents the system model that is used in this paper. The control scheme used to control the model of the power converter, is developed in Section 3. Results and discussions of the performance of the algorithm are presented in Section 4. The last section of the paper contains the conclusion.

2 SYSTEM MODEL

With only one flying capacitor per phase, a three-level flying capacitor inverter as depicted in Fig. 1 is the simplest one; its simplicity is the reason it was chosen for a clear analysis of the MPC. The three-level FCC uses two pairs of complementary controlled switches, (S_1, S'_1) and (S_2, S'_2) . These switches facilitate the connection of the flying capacitors, C_{1x} ($x = a, b, c$) in a series with the load. In Fig. 1 the load is represented here as an RL connection in series. In Table 1 a summary of the different switch states and their corresponding output voltage is presented. Considering the switch pair, i ($i=1,2$). When the upper switch of the

switch pair is closed, S_{ix} is 1. When the lower switch is closed, S_{ix} is zero. When the load is coupled in series with the flying capacitor, the voltage associated with the current flowing through the capacitor, changes. In a three-level FCC the voltage of the flying capacitor, C_{1x} must always be maintained at $v_{DC}/2$.

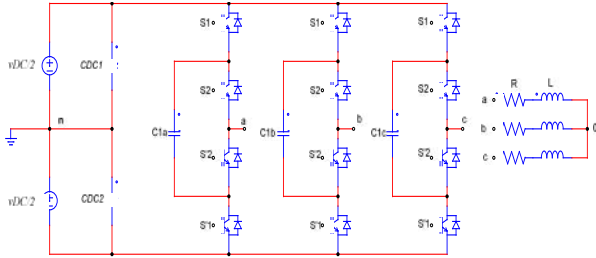


Fig. 1: Three phase, three-level FCC inverter with RL-load

Tab. 1: Switching states in one-leg of the three-level FCC

Voltage Level	complementary pair No 1		complementary pair No 2		Leg voltage (V_{an})
	S_1	S_1'	S_2	S_2'	
1	1	0	1	0	$v_{DC}/2$
2	1	0	1	0	0
	0	1	0	1	0
3	0	1	0	1	$-v_{DC}/2$

Because the maximum voltage stress occurs at $v_{DC}/2$, this requirement provides an optimal voltage rating of the switches. The transitional output voltage is generated by the two conditions of each phase. This allows a correction of the voltage of the capacitor for every possible direction, and furthermore, it presents a way of controlling the voltage of the capacitor.

3 FINITE SET-MODEL PREDICTIVE CONTROL OF FCC

An FS-MPCC does not require a modulator to determine the switching signals for the converter. Fig. 2 depicts an FC-MPCC incorporating an FCC inverter, where:

X_{ref} indicates the reference values for the predictive control,

$X(k)$ is the measured variables at time k and

$X(k+1)$ are the predicted values at time $k+1$, of n possible switching states.

The switching state minimizing the cost function is identified and selected from information obtained by considering the error between the reference and predicted values. The switching signals of the state selected, S are thereafter applied to the converter.

The effort of calculation increases exponentially with prediction horizon if the optimum inverter switching state is determined directly with a model-predictive control algorithm. To decrease the required computational effort arising from the switching possibilities, the switching state that delivers the best

voltage vector among 19 voltage vectors, is determined. A three-phase, three-level FCC can only deliver 19 different voltage vectors from a possible 64 switching states; this because 45 of the 64 states are redundant, leaving 19 different voltage vectors (see Fig. 3). With this redundancy, a finite-set model predictive control with greater than one prediction step can be implemented.

Fig. 2: FS-MPCC block diagram

In this study, the selection of the best voltage vector from the 19 delivered, is done with a prediction horizon of one prediction step. This facilitates a marked decrease in the amount of calculation required, as compared to carrying out the calculations for all 64 switching possibilities in one prediction step. In the implementation stage of an FS-MPCC for the control of a three-phase, three-level FCC, the estimation step, predictive step and optimization step have to be performed.

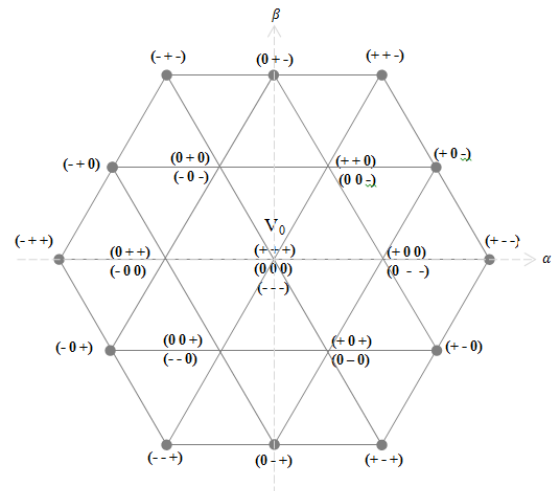


Fig. 3: Voltage vectors generated by a three-level converter

3.1. Estimation step

For the three-phase, three-level FCC system, $N1$ is defined as 1 because the goal is to finish all calculations in one update period and apply the selected switch state at the end of the update period. This means that when a measurement sample is taken at time instant k , it is possible to do all calculations required for the MPC and apply a newly defined switch state at time instant $k+1$. To enable prediction of the impact of future possible switch states, an estimate of the state variables at $(k+1)$ is required.

The measurements of the phase currents, $i_x(k)$ and the flying capacitor voltage, $v_{1x}(k)$ with $x = a, b, c$, are taken at time k . These measurements, in combination with the applied switch states $S_{ix}(k)$, are used as inputs of the system model to obtain the estimation of the state variables at $k + 1$. The switch states, $S_{ix}(k)$ remain unaltered throughout the update period, and any change in capacitor voltage is taken to be sufficiently small for it to be neglected when output voltage is calculated. With the aforementioned assumptions the equations below are derived for the voltage, v_{xn} between the output pole, x and the neutral point, n of the power supply for a three-level FCC:

$$v_{xn}(k+1) = (S_{2x}(k - 1/2) v_{DC} - (S_{2x}(k) - S_{1x}(k))v_{1x}(k)) \quad (1)$$

where the DC-link voltage, v_{DC} is measured.

The load phase voltage, v_{xo} (between the output pole and the neutral point) is determined from:

$$v_{on}(k+1) = \frac{v_{an}(k+1) + v_{bn}(k+1) + v_{cn}(k+1)}{3} \quad (2)$$

and

$$v_{xo}(k+1) = v_{xn}(k+1) + v_{on}(k+1) \quad (3)$$

where v_{on} is the star-point voltage.

The flying capacitor voltages and output currents at time $k + 1$ have to be estimated.

3.3.1 Output current estimation: At time $(k+1)$ the expression for the current can be determined by means of the Euler forward method, which yields a discrete-time equation which can be used to find the future load current. To derive the continuous-time, state-space equations for the load of each phase, consider the differential equation of the load current:

$$v_{DC}(t) = R \cdot i(t) + L \frac{di}{dt} \quad (4)$$

With the Clarke transformation applied to the load model, the load currents can be stated in relation to a simplified coordinate system having linearly independent axes, α and β . The values of α and β are defined as:

$$\alpha = 2/3 (a - 0.5 b - 0.5 c) \quad (5)$$

$$\beta = 2/3 (0 + 0.5 \sqrt{3} b - 0.5 \sqrt{3} c) \quad (6)$$

After applying the transformation, the continuous-time, state-space equation of the load takes on the following form:

$$\begin{bmatrix} \dot{i}_\alpha \\ \dot{i}_\beta \end{bmatrix} = \begin{bmatrix} -\frac{R}{L} & 0 \\ 0 & -\frac{R}{L} \end{bmatrix} \begin{bmatrix} i_\alpha \\ i_\beta \end{bmatrix} + \begin{bmatrix} \frac{1}{L} & 0 \\ 0 & \frac{1}{L} \end{bmatrix} \begin{bmatrix} v_\alpha \\ v_\beta \end{bmatrix} \quad (7)$$

The Euler forward equation (see equation 8) is used to derive a discrete-time equation system representation for the future load current; this is required to obtain a discrete-time system representation. The approximated derivation is as follows:

$$\dot{x} \approx \frac{x(k+1) - x(k)}{T_s} \quad (8)$$

Where: T_s is the sampling time, k is the current sampling instant, and x is the state variable.

The equation of the discrete-time load model is then expressed by:

$$\begin{bmatrix} i_\alpha(k+1) \\ i_\beta(k+1) \end{bmatrix} = \begin{bmatrix} 1 - T_s \frac{R}{L} & 0 \\ 0 & 1 - T_s \frac{R}{L} \end{bmatrix} \begin{bmatrix} i_\alpha(k) \\ i_\beta(k) \end{bmatrix} + \begin{bmatrix} \frac{T_s}{L} & 0 \\ 0 & \frac{T_s}{L} \end{bmatrix} \begin{bmatrix} v_\alpha(k) \\ v_\beta(k) \end{bmatrix} \quad (9)$$

3.1.2 Flying capacitor voltage estimation: A flying capacitor voltages algorithm based on predictive control is presented to balance the flying capacitor voltage in a complimentary way with the FS-MPCC method. It is important to mention that the flying capacitors C_1, C_2 and C_3 have to be charged to the voltage $v_{DC}/2$ so that the inverter is able to switch zero voltages. Selection of one of the zero switching states in a phase will result in an increase or decrease in the corresponding flying capacitor voltage; whether it increases or decreases will be determined by the direction of the current in the phase under consideration, as well as on the possibility of the selected voltage being zero. Choosing the switching states therefore, must be carried out so that the flying capacitor voltages remain continuously balanced. Once the most suitable voltage vector for the subsequent sampling cycle is determined, the optimum switching state generating this voltage vector, must be identified. The voltage of each of the three flying capacitors has to remain around the reference voltages $v_{DC}/2$. On condition that the flying capacitor voltage is not outside its limits, both switching combinations resulting in a voltage of zero, are permitted—for this situation, the switching state corresponding to zero that can be allocated with the least number of transitions, is selected. But, should the voltage of a flying capacitor stray outside the band assigned to the reference voltage, it is only the switching state that moves the voltage back within the limits of that band, that is permitted. The decision for which a zero switching state should be selected can be made, taking account of the direction of the current in that phase. The voltage band value was chosen to be 0.1% of the v_{DC} value in this study.

At the end of the time $(k + 1)$ the flying capacitor voltages have to be estimated. The switch state determines whether, and in which sense the load current passes through the capacitors; this is given by $(S_{2x}(k) - S_{1x}(k))$ in equation (10)

$$v_{1x}(k+1) = v_{1x}(k) - \frac{T_s}{2C} (i_x(k) + i_x(k+1)) (S_{2x}(k) - S_{1x}(k)) \quad (10)$$

where: C are the capacitor values of the flying capacitor, and x is a, b, c .

Equations (9) and (10) are used to predict the load current and flying capacitor voltage for each one of switching likelihood. For determining the subsequent value of the load currents and flying capacitor voltages, the cost function, g is calculated for every one of the 19 possible voltage vectors produced by the inverter. The voltage vector that results in a minimum cost function is chosen and implemented during the sampling instance that follows.

3.2. Predictive step

Starting at time $(k + N1)$, the controller has the capability to process any output during every update period, in order to bring the controlled variables nearer to their desired values. On the basis of estimates at time $(k + N1)$, the controller is therefore able to forecast the result of all feasible switch states over the whole prediction horizon between $(k + N1)$ and $(k + N2)$. The overall forecast horizon is defined by:

$$Np = N2 - N1 \quad (11)$$

Also, the output current and flying capacitor voltage are not determined by measurement, because the values estimated or forecast from the preceding step are applied. This leads to the subsequent group of equations being assessed for all feasible switching states for $i \in [N_1, N_2]$. In the case of the three-level converter, the output voltages are,

$$v_{xn}(k + i + 1) = (S_{2x}(k + i) - \frac{1}{2}) v_{DC} - (S_{2x}(k + i) - S_{1x}(k + i)) v_{1x}(k + i) \quad (12)$$

the star point voltage is :

$$v_{on}(k + i + 1) = \frac{v_{an}(k+i+1) + v_{bn}(k+i+1) + v_{cn}(k+i+1)}{3} \quad (13)$$

and the yielding phase voltages are:

$$v_{xo}(k + i + 1) = v_{xn}(k + i + 1) + v_{on}(k + i + 1) \quad (14)$$

To bring the controlled currents that much nearer to their reference, the controller can, from $i(k + 1)$ onwards, process any possible output. And with a long prediction horizon, the output currents in $\alpha\beta$ frame result to:

$$\begin{pmatrix} i_{\alpha}(k + n) \\ i_{\beta}(k + n) \end{pmatrix} = \begin{pmatrix} 1 - T_s \frac{R_L}{L_{fL}} & 0 \\ 0 & 1 - T_s \frac{R_L}{L_{fL}} \end{pmatrix} \begin{pmatrix} i_{\alpha}(k + n - 1) \\ i_{\beta}(k + n - 1) \end{pmatrix} + \begin{pmatrix} \frac{T_s}{L_{fL}} & 0 \\ 0 & \frac{T_s}{L_{fL}} \end{pmatrix} \begin{pmatrix} v_{\alpha}(k + n - 1) \\ v_{\beta}(k + n - 1) \end{pmatrix} \quad (15)$$

These currents influence the capacitor voltages

$$v_{1x}(k + i + 1) = v_{1x}(k + i) - \frac{T_s}{2C} (i_x(k + i) + i_x(k + i + 1)) (S_{2x}(k + i) - S_{1x}(k + i)) \quad (16)$$

From equations (13) and (14) it is apparent that in the system model, the phase output voltages of all

phases determine the phase voltage of the load. The outcome of this, is a set of equations that are convincingly linked. The results of all the switch state combinations are determined and applied in the optimization step; this is similar to the prediction phase where all the control actions have to be evaluated.

3.3. Optimization step

By assessing a cost function g , the best sequence can be chosen; this can however, only happen after the paths of the state variables for all possible control sequences have been computed. The sequence with the minimum cost is chosen, the first switch state is initiated by the controller at time $(k + N_1)$, and the algorithm is re-started producing what is called a receding horizon. The cost function assigns a cost to a deviation of state variables from their desired values, the reference values. In general, the cost is defined by the difference between the predicted variables and their reference. When adding all the cost functions for each predicted future state, the total cost function is obtained. For a three-phase, three-level FCC inverter, a straightforward cost function can be expressed as an absolute value term with a single prediction step; see equation (17).

$$g = |i_{refx}(k + 1) - i_x(k + 1)| + \lambda_{DC} |v_{1xref}(k + 1) - v_{1x}(k + 1)| \quad (17)$$

The respective reference values are i_{refx} and v_{1xref} for the phase current and the voltage of capacitor C_{1x} respectively, with the weight factor λ_{DC} expressing the relative importance of an error in the flying capacitor voltage compared to an error in the output current. The optimal switching operation is found when the total cost function, g is minimised, and cost function for a future predicted step n is

$$g = \sum_{n=1}^N |i_{refx}(k + n) - i_x(k + n)| + \lambda_{DC} |v_{1xref}(k + n) - v_{1x}(k + n)| \quad (18)$$

To simplify calculations in this study, the following approximation is taken in account: the current reference value is considered to remain unchanged, as shown in equation (19), with the prediction horizon of a short sampling time, T_s .

$$i_{ref}(k + n) \approx i_{ref}(k) \quad (19)$$

4 RESULTS AND DISCUSSION

The FS-MPCC strategy for a three-phase, three-level FCC was co-simulated using MATLAB/Simulink together with PSIM; this was done to evaluate the performance of the proposed control algorithm and to check the performance and robustness of the proposed control method. The FS-MPCC algorithm was evaluated with regard to two performance indicators: the effectiveness of reference current tracking and the ability to balance the flying capacitor voltages. In Table 2 the simulation values for the parameters used.

Tab. 2: Parameters used for the co-simulations

Parameter	Value
Load resistor, R	15 Ω
Load inductor, L	15 mH
Flying capacitor	560 μ F
DC-link voltage, v_{DC}	400 V
Weighting factor, λ	0.02
frequency	50 Hz
Sampling time, T_s	25 μ s

4.1. Sinusoidal waveform reference

The simulation result shows the control result for sinusoidal reference values. The load currents and load voltages are respectively shown in Fig. 4. The flying capacitor voltages can be seen in Fig. 5. The outcome of step changes on the amplitude of the reference currents is as follows: for i_α at time 0.035 s the amplitude changed from 14 A to 12 A, and for i_β at time 0.04 s the amplitude changed from 14 A to 10 A (see Fig. 4). Over the intervening time of the step change in the amplitude of the current i_β , the load voltage, v_β is kept at its maximum value until the reference current i_β is achieved.

The voltage balancing algorithm has the ability to maintain the voltages of the flying capacitors close to their reference voltages boundaries, as shown in Fig. 5. The proposed control algorithm can monitor sinusoidal reference currents; this ability is clearly demonstrated by the simulation. The predictive control method, as can be seen from this simulation, has a fast dynamic response with built-in uncoupling between i_α and i_β . And again, the algorithm shows exceptional monitoring performance, and the voltage balancing algorithm manages to keep the flying capacitor voltages within the proximity of their reference values.

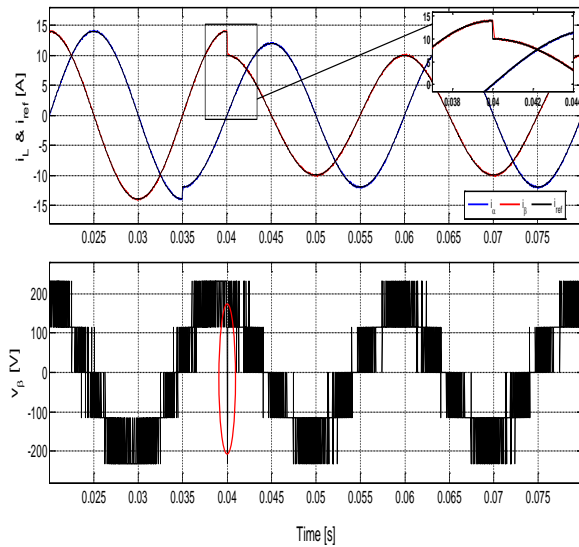


Fig. 4: Sinusoidal reference steps for load current and voltage

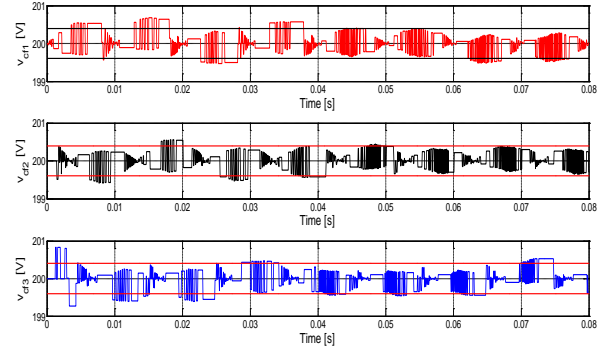


Fig. 5: Flying capacitor voltages during an RL-load step

4.2. Square waveform reference

One of the applications of a square current waveform is in a stepper motor driver when two functions are normally required: a controller to create step and directional signals. A square waveform in orthogonal coordinates was applied as a reference current in order to assess, the control algorithm in the model developed in this paper. The result for the square waveform in the amplitude of the references i_α and i_β was set to 2 A, and the flying capacitor voltages are shown in Fig. 6 and 7. The currents, i_α and i_β correctly followed the reference, while the current ripple remaining in steady state was effected by the controller frequency and finite switching. The flying capacitor voltages were maintained around their reference voltages by the voltage balancing algorithm; see Fig. 7.

This simulation demonstrated the fast, dynamic reaction of the predictive control method.

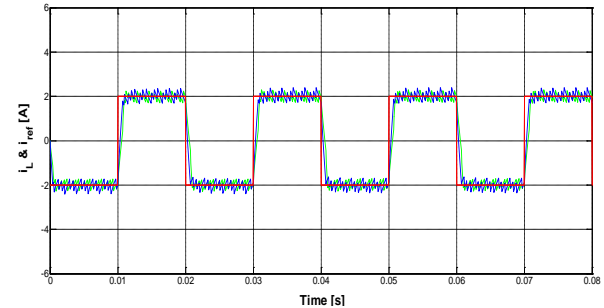
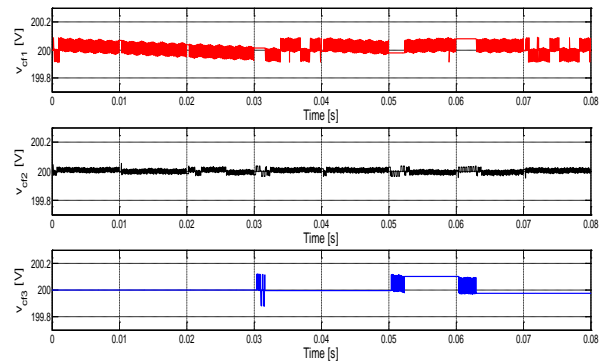


Fig. 6: Square waveform reference for load current


Fig. 7: Flying capacitor voltages with $T_s = 25 \mu$ s

5 CONCLUSION

The FS-MPCC strategy with one-step prediction time was presented to control the three-level FCC inverter for RL-Load. The best 19 different voltage vectors were selected and applied to the inverter, although there are 64 different switching combinations.

The minimization of the current and capacitor voltage errors by using a cost function provided a fast, dynamic response for load current control and guaranteed flying capacitor voltages balance. The proposed control strategy does not require a linear controller or the application of a modulation technique. Additionally it affords the designer the freedom to adjust the weighting factor λ_{DC} in order to fulfil the requirements in terms of reference current tracking and flying capacitor voltage balance. The FS-MPCC algorithm was subjected to two different conditions and evaluated in terms of reference current tracking and flying capacitor voltage balance. First condition, the sinusoidal waveform current reference tracking and sinusoidal waveform with a step change in the amplitude of the reference were investigated. For the second condition, the control algorithm was subsequently tested with square current waveforms in order to check the dynamic response; this reference current was a square waveform in orthogonal coordinates. For sinusoidal and square waveforms, the results showed that the algorithm displayed excellent tracking behaviour and a fast dynamic response with inherent decoupling between i_α and i_β at the step changes. Moreover, the voltage balancing algorithm, based on predictive control, was able to keep the flying capacitor voltages within the bounds of their reference values.

6 REFERENCES

- [1] M. F. Escalante, J. C. Vannier and Arzand'e A. "Flying capacitor multilevel inverters and DTC motor drive applications," *Industrial Electronics, IEEE Transactions on*, 2002, 49, (4), pp. 809–815.
- [2] J. S. Lai and F. Z. Peng, "Multilevel converters-a new breed of power converters," *Industry Applications, IEEE Transactions on*, 2002, 32, (3), pp. 509–517.
- [3] T. Meynard, M. Fadel and N. Aouda, "Modeling of multilevel converters," *Industrial Electronics, IEEE Transactions on*, 1997, 44, (3), pp. 356–364.
- [4] Y. Shakweh, "MV inverter stack topologies," *IEE Power Engineering Journal*, pp. 139–149, 2001.
- [5] T. A. Meynard and, H. Foch, "Multilevel conversion: High voltage choppers and voltage source inverters," *Proc. Int. Conf. Rec. IEEE PESC*, 1992, pp. 397–403.
- [6] S. S. Fazel, S. Bernet, D. Krug, K. Jalili, "Design and comparison of 4-kV neutral-point-clamped, flying capacitor, and series-connected H-bridge multilevel converters," *Industry Applications, IEEE Transactions on*, 2007, 43, (4), pp. 1032–1040.
- [7] F. Defay, A. M. Llor, and M. Fadel, "Direct Control Strategy for a Four-Level Three-Phase Flying-Capacitor Inverter," *Industrial Electronics, IEEE Transactions on*, 2010, 57, (7), pp. 2240–2248.
- [8] C. Feng, J. Liang, and V. G. Agelidis, "Modified Phase-Shifted PWM Control for Flying Capacitor Multilevel Converters," *IEEE Transactions on Power Electronics*, 2007, 22, (1), pp. 178–185.
- [9] H. A. Hotait, A. M. Massoud, S. J. Finney, B. W. Williams, "Capacitor voltage balancing using redundant states of space vector modulation for five-level diode clamped inverters," *Power Electronics, IET*, 2010, 3, (2), pp. 292–313.
- [10] R. Kennel, and D. Schroeder, "Predictive control strategy for converters," *Proc. Int. Conf. Proc. the third IFAC Symposium*, Lausanne, Lausanne, 1983, pp. 415–422.
- [11] A. M. Almaktoof, A. K. Raji, and Kahn M. T., "Modeling and simulation of Three-Phase Voltage Source Inverter using a Model Predictive Current Control," *International Journal of Innovation, Management and Technology (IJIMT)*, vol. 5, no. 1, 2014, pp. 9–13.
- [12] J. Rodríguez, and C. Cortés, "*Predictive control of Power Converters and Electrical Drives*," UK: A Johan Wiley & Sons, Ltd., 2012.
- [13] A. M. Almaktoof, A. K. Raji, and Kahn M. T., "Finite-Set Model Predictive Control and DC-Link Capacitor Voltages Balancing for Three-Level NPC Inverters," *Proc. Int. Conf. 16th International Power Electronics and Motion Control Conference and Exposition (PEMC 2014)*, Antalya-Turkey, September 21–24 2014(a), pp. 305–310.
- [14] A. M. Almaktoof, A. K. Raji, and Kahn M. T., "Software Simulation Integration in Enhancing Engineering Design in Power Conversion Studies," *Proceedings of the 23rd Southern African Universities Power Engineering Conference (SAUPEC 2015)*, pp. 63–68, on 28–30 January 2015, University of Johannesburg, Johannesburg, South Africa.
- [15] J. Li, F. Zhuo, X. Wang, et al., "A grid-connected PV system with power quality improvement based on boost + dual-level fourleg inverter," *Proc. Int. Conf. IEEE Int. Power Electronics and Motion Control*, Wuhan, China, 2009, pp. 436–440.
- [16] S. Muller, U. Ammann, and S. Rees, "New time-discrete modulation scheme for matrix converters," *IEEE Trans. Ind. Electron.*, 2005, 52, (6), pp. 1607–1615.
- [17] J. Rodríguez, J. Pontt, C. Silva, et al., "Predictive direct torque control of an induction machine," *Proc. Int. Conf. Power Electron. Motion Control*, Riga, Latvia, September 2–4, 2004.

BATTERY MONITORING AND TEMPERATURE CONTROLLER SYSTEM FOR THE 15E ORE-LINE ELECTRIC LOCOMOTIVES

S. Krishnamurthy and K.C Gabashane

Cape Peninsula University of Technology, Department of Electrical, Electronic and Computer Engineering, Center for Substation, Automation and Energy Management System, P.O Box 1906, Bellville – 7535, South Africa Email: ksenthilvpm@gmail.com and gabashanec@gmail.com

Abstract: The aim of this paper is to design and implement the DC battery monitoring system for the electric locomotives. The batteries used in the locomotives supply energy for the critical loads in case of the main power supply failure. The cost of the UPS system used in the electric locomotives is based on the price of the battery, therefore it is necessary to maintain and monitor the DC battery system used in the electric locomotives. This paper investigated the factors such as wide operating temperature range and rapid recharge capability in order to understand how the negative impact of poor performance batteries could be minimized. The Class 15E ore-line electric locomotive has eight 12V batteries connected in series, which provides 110V DC supply for nominal operating condition. The temperature of the batteries in the locomotives is measured using the temperature sensor LM35. The designed temperature control circuit and the developed software program in the Arduino environment is used to monitor and control the temperature of the DC batteries of the electric locomotives. The designed circuit for the temperature controller is implemented in the Proteus environment and a prototype of the hardware-based lab-scale system is built and tested. The designed temperature control circuit has a DC fan and its speed is proportional to the measured temperature, which reduces the high charging current and provide longer battery life, better reliability and reduce the battery failures due to the overheating.

Key words: 15E Electric Locomotive, Battery Monitoring System, LM35 Temperature Sensor, Arduino Temperature Controller, Battery Charging System, Three Phase Battery Charger, PWM Charge Controller and Fan Speed Controller.

1. INTRODUCTION

Battery [1] is an essential component of electric locomotive and is used to provide the startup current and emergency lighting, when the line supply fails. It has an electrochemical cell [2] which has composed of one or more cells, each containing a positive electrode, a negative electrode, separator, and electrolyte. It can be charged electrically to provide a static potential used to supply electrical loads, when the main supply of the utility fails. The battery is connected across the DC supply in Class 15E ore-line electric locomotives which has got eight 12V Batteries (G12) connected in series to provide a nominal 110V DC supply. The factors such as environmental ruggedness, a wide operating temperature range, rapid recharge capability, performance and reliability of the battery [3] are investigated in this paper. At present the DC battery used in the electric locomotives are failing due to high discharge currents which leads to overheating condition. Figure 1 shows the simple class 15E electric locomotive system.

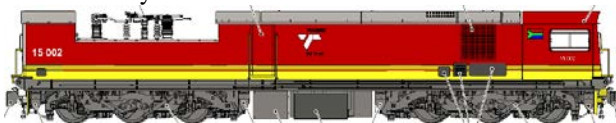


Figure 1: Class 15E-oreline electric locomotive

Therefore, the temperature control circuit is designed to monitor and control the ambient temperature of the battery. The review on a battery monitoring system used in the electric locomotive is given in this section. In paper [4], the authors investigated the modelling approaches for predicting the battery performance and discuss the demanding requirements and systems for battery management. A flexible architecture is implemented using fully-integrated active charge equalizer which has state-of-charge estimation and charge balancing. A distributed Battery Management System (BMS) used for Hybrid Electrical Vehicle (HEV) is described in [5]. The BMS has the characteristics of easy to expand, high precision, working reliability. In paper [6], the performance of a lithium battery pack is used for traction on electric vehicles and it describes how the charge is equally distributed among the cells. A three-level hierarchy BMS with test benching features was designed and discussed in [6]. This research investigated that a degradation of the battery caused by frequent charging and discharging that creates an accumulation of lead sulfate. Therefore, to improve battery management practices, a temperature monitoring and control method for the locomotives is proposed in this paper. The method had to be nondestructive, simple and cheap by using a temperature

sensor, electronic, supporting hardware and software devices in order to identify and decreasing sulfation, which in turn reduce the high charging current and ambient temperature of the DC batteries used in the electric locomotives.

This paper has five sections and is organized as follows: section 1 introduces the background of the battery monitoring system used in the electric locomotives. Section 2 describes the battery charging and discharging system used in the 15E Ore-line electric locomotives. Section 3 describes the battery monitoring system and its implementation in the lab-scale environment. Section 4 provides the designed temperature controller circuit for the 15E locomotives and its implementation part. Section 5 provides the conclusion and future work.

2. BATTERY CHARGING AND DISCHARGING SYSTEM USED IN 15E ORE-LINE ELECTRIC LOCOMOTIVES

This section describes the battery charging and discharging system used in the electric locomotives. The battery load testing method [4] is to determine the following factors:

- Whether the battery is fully charged?
- How much charge is left in the battery?
- Does it meet the manufacturer's specification?
- Has there been any deterioration in performance of its operation?

The discharge time of the battery is determined using Equation (1).

$$DT = \left(\frac{C}{IH} \right)^k \quad (1)$$

Where

DT is the discharge time

C is the rated capacity of the battery

I is the load current

H is battery charging unit in an hour

K is the peukert constant

The value of k which ranges from 1.05 to 1.15 for free maintenance (AGM) batteries, the typical net coulomb efficiency is 90%. The battery discharge test results used on 15E locomotive are shown in Figure 2.

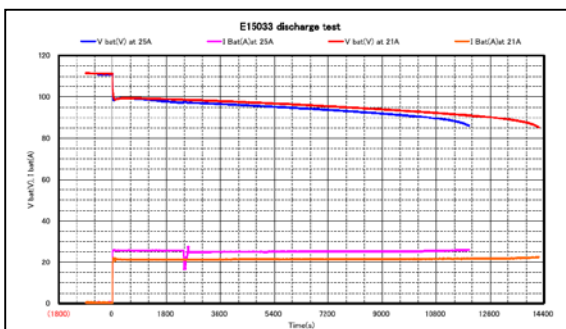


Figure 2: Battery discharge test results on Class 15E locomotive

A new set of the batteries is loaded on the class E15033 locomotive and the test is conducted on OREX line. The battery charger disconnects during the operation. The aim of this test is to find the time needed to discharge the battery for 80%. A deep battery discharge test could safely discharge the battery completely in order to check the status of the actual battery capacity. This test was initiated to compare the discharging test results of Hoppecke and Moll batteries. Test result indicates that Hoppecke battery SRC 12V 65 G battery with 65Ah capacity can supply power to full LV loads up to two hours and the Moll AGM 12V 95AH can supply the LV load for three hours. However, this discharge corresponds to 80 % Depth of Discharge (DOD). Moll battery has better performance in comparison with the rating of the Hoppecke battery capacity. Table 1 shows the specification of the Moll battery used in 15E Ore-line locomotives.

Table 1: Moll battery specification used in the Class 15E locomotives

Description	Rating
Nominal voltage per battery	12 Volts
Capacity (AH)	95AH C20
Discharge current (Locomotive load)	37.5 Amps at max & 25 Amps at continuous rating condition
Locomotive charging voltage	110.0 Volts

2.1 Peukert Equation

The discharge time of the battery is the ratio of the battery capacity over maximum load current. It is mathematically formulated and is given in equation (1).

The Peukert equation [7] is used to analyze the characteristics of a cell behavior. It is an empirical formula, which approximates how the available capacity of the battery changes according to the rate of discharge. Equation (1) shows that at higher currents, there is less available energy in the battery. The Peukert Number (k) is directly related to the internal resistance of the battery, where higher load current leads to more power losses and less available capacity of the battery.

In addition to that, the value of the Peukert number indicates, how well a battery performs under continuous heavy currents. A value close to 1 indicates that the battery performs well. i.e., higher the peukert number means more capacity is lost and the battery is discharged at high currents. The Peukert number of a battery is empirically determined using equation (1). A deep battery discharge test is safely conducted in order to check the actual battery capacity.

3. BATTERY MONITORING SYSTEM

Battery monitoring system is used to monitor the charging current of the battery. In this paper, the circuit shown in Figure 3 is designed to monitor the capacity of the battery. It has 3 LED's to display the battery voltage level as shown in Figure 4. The 15E ore-line electric locomotives has 8 batteries connected in series to provide 110V

nominal DC voltage, each battery is rated at 12V. The green LED is used to monitor the battery voltage for rated capacity condition (12V), when the battery voltage drops below 11V the yellow LED glow which indicates the battery drop from its rated nominal value. The red LED is used to identify, when the battery voltage drops less than 11V.

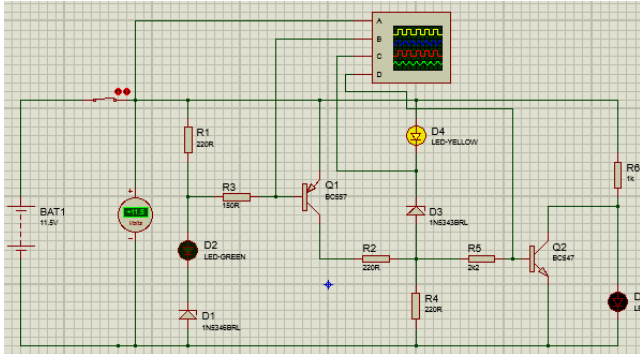


Figure 3: Battery monitoring system in Proteus environment

The base voltage (V_B) and base current (I_B) used in the battery monitoring circuit is shown in Figure 3 are calculated using equations (2) and (3) respectively. These parameters (V_B and I_B) are used to energize the transistors (Q1) and (Q2) for the operation of the circuit and Table 2 provides the 3 LED status which shows the battery capacity at different voltage levels.

$$V_B = V_{cc} - V_d - V_{BE} \quad (2)$$

$$I_B = \frac{V_B}{R_B} \quad (3)$$

Where

V_B is the base voltage in volts

V_{cc} is the voltage across the collector terminal

V_d is the voltage across the diode terminal

V_{BE} is the voltage across the base emitter terminal

I_B is the base current in Amps

R_B is the base resistance in ohms

Table 2: Battery monitoring system with LED status at different voltage levels across the battery terminals

Battery #	Battery Voltage	LED Status to monitor the battery voltages		
		Green	Yellow	Red
1	13.0	ON		
2	12.5	ON		
3	12.0	ON		
4	11.5		ON	
5	11.0		ON	
6	10.5		ON	
7	10.0			ON
8	09.5			ON

From Table 2, it is noted that the battery number 7 and 8 drops below the nominal rated values (11V), which is identified with the help of the status of the red LED. The 12V battery circuit used in Class 15E electric locomotive is designed in Multisim environment and is shown in Figure 4.

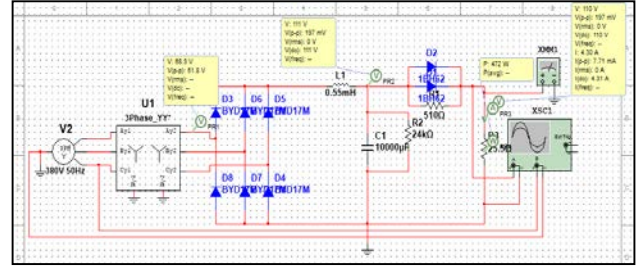


Figure 4: 12V battery circuit used in the locomotive is modelled in the Multisim environment

Constant voltage charging is one of the most common charging methods for lead acid batteries. The idea behind this approach is to keep a constant voltage across the terminals of the battery at all times. In Figure 4, Transformer (T38) step-down the 380V AC to 82V and is connected to the three-phase bridge rectifier circuit (U42) in order to provide the 110V DC. When a failure, such as grounding occurs in the secondary circuit of the rectifying transformer, Q82 detects the over-current and trips. An LC filter and diodes are provided between the output terminals of the rectifier circuit (U42) as shown in Figure 4. Where U42 is full-wave three phase bridge rectifier, and has a ripple with 6 times the input frequency which appears on the output voltage. It may affect the battery characteristics. In order to reduce the ripple, LC filter is used which has an inductance of 0.55mH (L10) and a capacitance of 10000 micro-farad (C10) as shown in Figure 4. i.e., reactances at 300 Hz are 1.036 ohms for L10 and 0.053 ohms for C10. Therefore, 300 Hz ripple is reduced as approximately to 5% and its simulation results is shown in Figure 8.

3.1 Problem formulation to find the different types of efficiencies of the batteries used in the electric locomotives

The energy efficiency of the battery is defined to find the performance of the battery and is given in equation (4).

$$\text{Energy Efficiency} = \left(\frac{V_D}{V_C} \right) \left(\frac{\text{IDTD}}{\text{ICTC}} \right) \quad (4)$$

Where

V_D is the discharge voltage of the battery

V_C is the charge voltage of the battery

IDTD is the battery discharge unit in A-hrs

ICTC is the is the battery charge unit in A-hrs

The coulomb efficiency of the battery is defined as the ratio of discharge current of the battery to the charging current and is given in equation (5).

$$\text{Coulomb Efficiency} = \frac{\text{discharge A} - \text{hrs}}{\text{charge A} - \text{hrs}} \quad (5)$$

The voltage efficiency of the battery is defined as the ratio of discharge voltage of the battery to the charging potential and is given in equation (6).

$$\text{Voltage Efficiency} = \frac{\text{discharge voltage}}{\text{charge voltage}} \quad (6)$$

Smoothing capacitor used in the power supply/battery charger and is determined using equation (7) as follows:

$$C = \frac{I_{\text{load}} (\Delta t)}{V} \quad (7)$$

Where

C is the battery capacity

I_{load} is the load current in Amps

Δt is the rate of change of time

V is the voltage across the battery terminal

The rectified voltage of the three phase battery charger of the class 15E electric locomotive is determined using equation (8).

$$V_{\text{dc}} = 3 \left(\frac{\sqrt{2}}{\pi} \right) (V_{\text{rms}}) \quad (8)$$

Where

V_{dc} is the DC voltage across the battery terminal

V_{rms} is the RMS voltage across the supply terminal

4. DESIGNED TEMPERATURE CONTROLLER CIRCUIT FOR THE CLASS 15E ELECTRIC LOCOMOTIVE

This section describes the circuit diagram and microcontroller configuration setting used in the 8-bit ATMEL. Figure 5 shows the block diagram of the temperature controller and battery monitoring system used in the 15E electric locomotives.

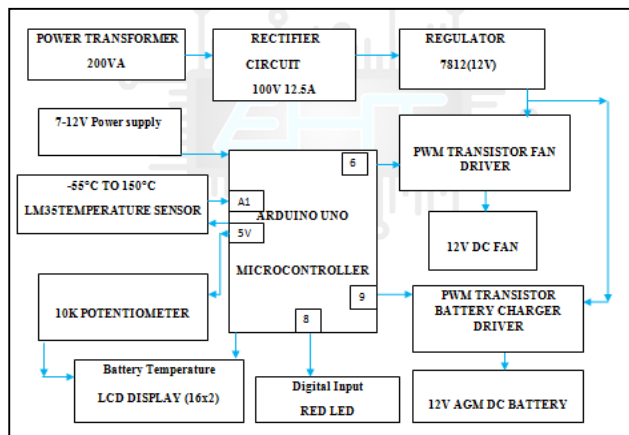


Figure 5: Block diagram of the temperature monitoring and control circuit used in the 15E ore line locomotives

The description of the operation of the designed temperature controller circuit as follows: 200VA capacity power transformer is used to generate 12V DC supply using a 7812 voltage regulator with the aid of the 100V, 12.5 Amps rectifier circuit. The output of the voltage regulator is used to supply the fan via the PWM switching mode on the transistor drivers [8]. The fan is used to cool

the temperature of the 12V battery used in the electric locomotives and its cubicle. The PWM transistor battery charger driver circuit is connected to pin 9 of the microcontroller circuit which in-turn used to control the charging current of the 12VAGM DC battery. In addition to that the temperature of the DC battery used in the electric locomotives is monitored using LM35 sensor and is connected to the pin A1 of the microcontroller. The temperature of the DC battery is monitored and displayed using the LCD display unit and its display quality is adjusted using the 10K potentiometer circuit. The microcontroller 5V pin is used to energize the display unit. When the battery temperature is above 49 degrees, which is monitored using the red LED and is connected to the pin 8 of the microcontroller unit as shown in Figure 7. Design of the battery charger unit for the 15E ore-line electric locomotive in Multisim environment.

This section describes the design of the battery charger circuit needed for the electric locomotives. This paper investigates the battery failure on the electric locomotives. It is identified that most of the cases the failures are due to inadequate maintenance of the constant voltage across the terminals of the batteries. Therefore, it is recommended to design the power supply unit of the DC battery. In addition to that providing the smoothing capacitor (C1) across the voltage regulator 7812 as shown in Figure 6.

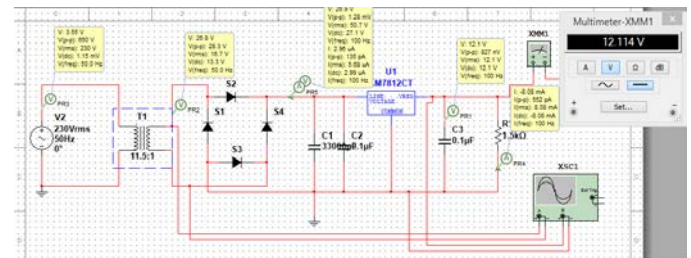


Figure 6: Designed circuit diagram of the DC battery charger used in the electric locomotives

Simulation result of the constant 12V output at 7812 regulator is shown in Figure 7.

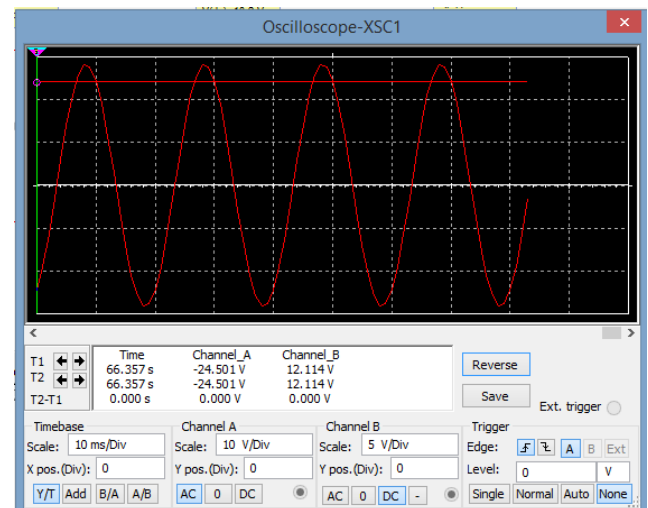


Figure 7: Constant 12V output on the voltage regulator terminal

This project designed to identify the rating of the smoothing capacitor needed in order to maintain the constant voltage across the battery terminals. The circuit is built and tested in the Multisim environment as shown in Figure 6. The smoothing capacitor ($C1=33000\mu\text{f}$) is used in the power supply unit and is capable to energize the voltage regulator 7812 circuit and provide a constant 12V supply across the battery terminals.

4.1 Description of the operation of the temperature controller and battery monitoring system used in the 15E locomotives

This section describes the operation of the hardware implementation part of the designed temperature circuit and battery monitoring system of the electric locomotives. Figure 8 shows the designed circuit diagram in the Proteus software environment. The idea of the ATME microcontroller [9] and [10] configuration is to drive the PWM transistor circuits (fan and battery charging units) according to the temperature monitored across the DC batteries using LM35 temperature sensor. The speed of the fan is controlled using the microcontroller, which is proportional to the temperature monitored at the battery cubicle of the electric locomotives.

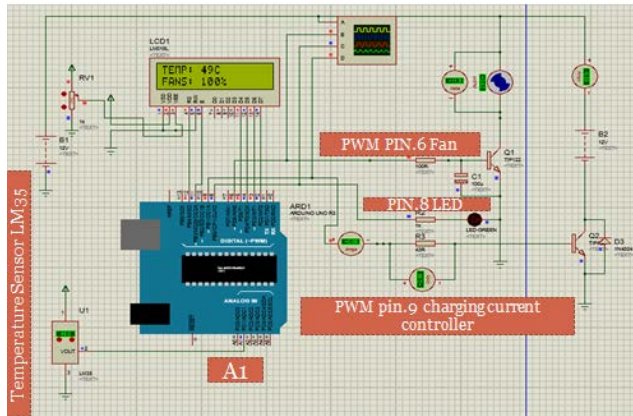


Figure 8: ATME microcontroller unit implemented and tested in the Proteus environment to control the temperature of the batteries used in the 15E locomotives

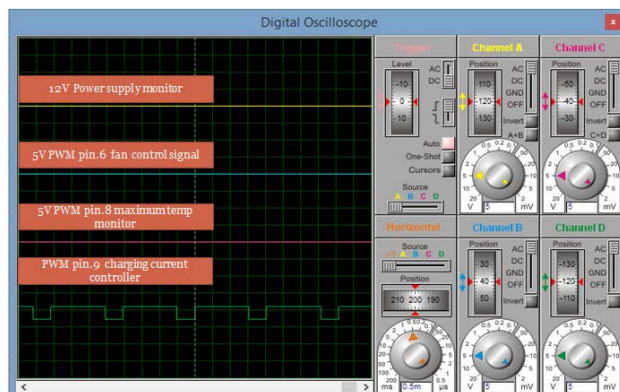


Figure 9: Simulation results of the battery monitoring

In addition to that the temperature monitoring system is implemented using the microcontroller and is displayed using LCD display as shown in Figure 9. The simulation result of the battery monitoring system is shown in Figure

9, it has four channel displays. Channel 1 has monitored the battery terminal voltage, channel 2 is monitored the PWM transistor fan drive circuit, channel 3 indicate the temperature status using the three LEDs (Green, Yellow and Red) and channel 4 is monitored the battery charging current as shown in Figure 9.

CONCLUSION

This paper designed and implemented the temperature monitoring and control circuit for the 15E ore line electric locomotives in the Proteus and Multisim simulation environments respectively and tested with a built-in lab-prototype model. The designed temperature controller circuit has 3 LED's (green, yellow and red) to monitor the capacity of the DC battery for different operating conditions. The designed control circuit equipped with DC fan and PWM controller for auto adjusts the speed of the fan, which is proportional to the operating temperature of the DC battery used in the 15E electric locomotives. It is proved that the test results of the designed circuit show that the temperature of the DC battery used in electric locomotives is monitored and controlled using 8-bit ATME microcontroller unit. The fan is used to cool the temperature of the DC battery, when the battery temperature set point exceeds its limits, then the fan starts to rotate and its speed is proportional to the temperature of the electric locomotive unit. The speed of the fan is controlled by the microcontroller unit. The future work will be recommended to implement the battery monitoring system and temperature controller for the 15E ore-line electric locomotives used for iron ore transportation by Transnet Engineering and Toshiba as the maintainer and manufacture of the electric locomotives within South Africa. This can reduce the high charging currents, increasing the life cycle of the battery and reduce the overall cost of the UPS system used in the electric locomotives and improve the overall reliability of the class 15E electric locomotives.

ACKNOWLEDGEMENT

The authors gratefully acknowledge the authorities of Cape Peninsula University of Technology, South Africa for the facilities offered to carry out this work. The research work is funded by the National research foundation (NRF) THRIP grant TP2011061100004 "CSAEMS development and growth" and ESKOM TESP project "Development of a method for real-time solution of the problem for optimal placement of capacitor banks in distribution networks".

REFERENCES

- [1] Ned Mohan, Tore M. Undeland, and William P. Robbins, "Power Electronics: Converters, Applications, and Design", 3rd Edition, Wiley, 2003.
- [2] Dietrich Berndt, "Maintenance-Free Batteries: Lead-Acid, Nickel/Cadmium, Nickel/Metal Hydride", Research Studies, 2nd Edition, 1998.

- [3] Thomas L. Floyd, "Electronic Devices: Conventional Current Version", Pearson International Edition, 8th Edition, 2007.
- [4] M. Brandl, M. Wenger, F. Baronti, G. Fantechi, and A. Thaler, "Batteries and Battery Management Systems for Electric Vehicles", Design, Automation & Test in Europe Conference & Exhibition, 2012, pp. 971-976.
- [5] L. Saigon and Z. Chengning, "Study on battery management system and lithium-ion battery," in International Conference on Computer and Automation Engineering. ICCAE '09, Mar. 2009, pp. 218-222.
- [6] F. Baronti, G. Fantechi, E. Leonardi, R. Roncella, R. Saletti, "Hierarchical platform for monitoring, managing and charge balancing of LiPo batteries," in Proc. Vehicle Power and Propulsion Conf., Sep. 2011, pp. 1-6.
- [7] Thomas Reddy, "Linden's Handbook of Batteries", McGraw-Hill, 4th Edition, 2010
- [8] P. Marian, "Fan Speed Controlled by Temperature and Arduino", Electro Schematics.
- [9] Massimo Banzi and Michael Shiloh, "Getting Started with Arduino: The Open Source Electronics Prototyping Platform", Maker Media, 3rd Edition, Dec 2014.
- [10] T. Sri, P. Rachana Rao, D. Anusha, and M. Sujala, "Battery charge controller using Arduino", BE Thesis, Jawaharlal Nehru Technological University, Hyderabad.
- [11] Abhik Datta, "Design of a Lead Acid Battery Charger System", BTech Thesis, National Institute of Technology, Rourkela, 2009.
- [12] Mark Slade, Daniel Christopher, Daniel Paul Martin, Ali Bibonge and Taverishima Tseghe, "Battery Management System (BMS) for a Solar Powered Racer", ECE 4007 Senior Design Project, Solar Jackets club at Georgia Tech, May 2011.
- [13] James P Dunlop, "Batteries and Charge Controller in Stand-Alone Photovoltaic Systems fundamentals and applications", Florida Solar Energy center, University of central Florida, 1997.

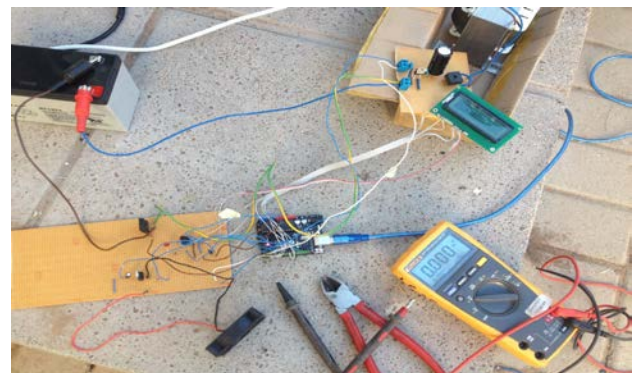
APPENDIX

A1: Abbreviations and Acronyms

AC	-----	Alternating Current
AGM	-----	Absorbed Glass Mat Battery
APU	-----	Auxiliary Power Unit
BMS	-----	Battery Management System
C	-----	Battery capacity
DC	-----	Direct Current
DT	-----	Discharge Time
H	-----	Battery Hourly Rating
I	-----	Current
I _B	-----	Base Current
I _{bat}	-----	External Load current
ICTC	-----	Charge A-hrs
IDTD	-----	Discharge A-hrs
k	-----	Peukert Exponent
LED	-----	Light Emitting Diode
LV	-----	Low Voltage
PWM	-----	Pulse Width Modulation
R _B	-----	Base Resistance

R _{soc}	-----	Internal Resistance
t	-----	Time
T	-----	Temperature
T _c	-----	Cycle Period
TCMS System	-----	Train Control Monitoring
T _o	-----	ON Time
UPS	-----	Uninterruptible Power Supply
V _B	-----	Base Voltage
V _{bat}	-----	Battery Voltage
V _{BE}	-----	Base Emitter Voltage
V _C	-----	Charge Voltage
V _{CC}	-----	Collector Voltage
V _d	-----	Diode voltage
V _D	-----	Discharge Voltage
V _{eff}	-----	Effective Voltage
V _s	-----	PWM Voltage
V _{soc}	-----	Battery EMF

A2: Prototype of the hardware structure of the temperature controller circuit for the DC batteries of the 15E electric locomotive



BIOGRAPHY



Dr. S. Krishnamurthy has BE and ME in Power System Engineering from Annamalai University, India and DTech in Electrical from Cape Peninsula University of Technology, South Africa. He has been a lecturer at the SJECT, Tanzania and Lord Venkateswara and E.S. College of Engineering, India. Since 2011 he has been working as a Lecturer at the Department of Electrical,

Electronic and Computer Engineering, Cape Peninsula University of Technology, South Africa. Dr S Krishnamurthy is a member of the Niche area Real Time Distributed Systems (RTDS) and of the Centre for Substation Automation and Energy management Systems supported by the South African Research Foundation (NRF). He is a member of the Institute of Electrical and Electronic Engineers (IEEE), Institution of Engineers India (IEI), Institution of Engineers Tanzania (IET), and South African Institution of Electrical Engineers (SAIEE). His research interest is in the fields of power systems, energy management systems, parallel computing, computational intelligence and substation automation.

Mr. K.C Gabashane has completed his BTech degree in Electrical Engineering from Cape Peninsula University of Technology (CPUT), Cape Town, South Africa. He works as a Technician at Transnet in Cape Town. His research focus areas are Electrical Power Systems, Power Electronics and its applications, Electric locomotives and Embedded systems.

Single phase to three phase variable frequency drive

D.Evan Rooyen, W. Kukard and A.J. Grobler

*School for Electrical, Electronic and Computer Engineering, North West University (NWU), Hoffman Street 11, Potchefstroom 2531, South Africa
E-mail: edvrooyen.work@gmail.com*

Abstract:

The design and synthesis of an inexpensive single phase to three phase amateur VFD was undertaken, with focus on the viability of construction. A three phase bridge (with needed sub-circuits) and DC rectification circuit was designed and integrated, where switching of semiconductors was controlled by an Arduino Uno. Initially the design seemed viable in terms of costs, however an isolation transformer was required to limit inrush current to avoid failure of semiconductors. This drastically increased construction cost of the VFD drive, making it uncompetitive with existing solutions already on the market. However with continued development, the product can still be improved to overcome the current short-comings.

Keywords: Variable frequency drive, pulse width modulation, inverter.

1. INTRODUCTION

For hobbyists owning old and technologically outdated equipment, it is often simply too expensive to replace these equipment in order to benefit from the advances of modern methods and technologies. There are notable benefits using three phase induction motors combined with variable frequency control instead of single phase induction motors. Single phase motors are more expensive, and the aging of operational capacitors lead to eventual start-up and running problems.

Changing the operational speed of the cutting spindle on older equipment (for example pedestal drill) is often a tedious task, where a mechanical belt and pulley configuration needs to be adjusted. This is a timely exercise that can be changed by being able to control the angular velocity of the motor while in operation.

By designing a less expensive single phase to three phase variable frequency drive, all the above problems could possibly be addressed. This article is focused on the design and synthesis of such a motor drive.

2. CONCEPTUAL DESIGN

For the functional operation of a VFD (see Figure 1), an incoming AC source needs to be rectified and filtered to form a DC bus. A three phase inverter bridge is needed to generate the output PWM pulses required to modulate the needed three phase output. The switching of the IGBT semiconductors need to be controlled by a microcontroller in order to be able to vary output frequency of the modulated sinusoidal voltage.

A low voltage regulated 5V/12V DC supply was designed, as required for the operation of the microcontroller and semiconductor drivers.

Optocouplers were introduced to provide isolation between the microcontroller and semiconductor drivers to avoid voltage surges caused by switching pulses of the semiconductors during operation from reaching the microcontroller.

A human interface needed to enable an operator to control the drive was designed, where this interface interconnects with the microcontroller.

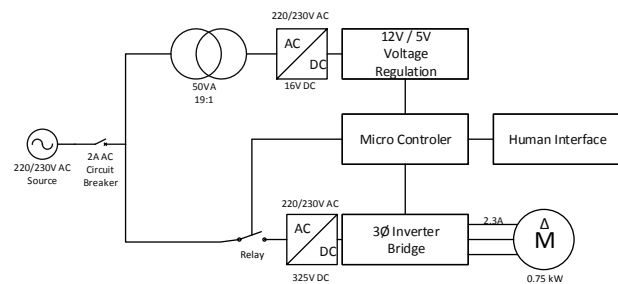


Figure 1: Conceptual design circuit overview

2.1 Inverter: Semiconductor trade off study

A trade off study was done, with important selection parameters being (and largest weights shown in brackets)

- Cost per unit
- Forward Potential blocking ability [0.2]
- Continuous current capability [0.2]
- Turn on / off delay time
- Total gate charge
- Switching loss

The power MOSFET IRG4PC30KDPbF was the second best contender, where the low cost of the unit made it an attractive option. However due to low power output thereof, the IRG4PH50UD IGBT were rather selected, having a better overall average score during the trade-off study.

2.2 Inverter: Semiconductor Drivers trade off study

A trade off study was conducted for proper driver selection. The models IR2113, IR2213 and IR2106 were compared. By using the parameters:

- Cost per unit [0.2]
- Maximum high side voltage [0.3]

- Current to Gate [0.3]
- Turn on/off propagation [0.2]

the IR2113 had the highest average due to fast switching times, high current output and cost competitiveness when compared to the other units. The second contender was the IR2213, which was countered by its higher cost.

2.3 Microcontroller trade off study

For selecting a microcontroller, a trade off study was conducted with the criteria:

- Amount of timers [0.2]
- Timer resolution
- Amount of PWM channels
- Turn on/off propagation
- Available on-board memory [0.2]

From selection criteria the PIC24F32KA304-I was initially chosen. This processor had the lowest purchase cost, along with the most available timers.

However during software implementation, a lookup table was used for storing the PWM switching data. Lookup tables are easier and faster (in terms of processing time) to implement compared to mathematically calculating numerical values as needed every cycle. Implementing the table had the drawback of placing heavy constraints on microcontroller memory, causing the PIC to be later replaced by the Arduino Uno with more available storage capacity.

3. DETAILED DESIGN

3.1 Interface console design

An interface was designed to enable a human operator with limited experience to be able to operate the drive. All pushbutton and POT outputs were passed through a passive low pass filter (approximately 125 Hz), to remove unwanted effects such as switch bounce.

Component values as shown below were obtained for the first order passive filter.

$$R = 13k\Omega$$

$$C = 0.1\mu F$$

The derived transfer function is given as [1]:

$$T(s) = \frac{V_{out}(s)}{V_{in}(s)} = \frac{1}{s + \frac{1}{CR}} \quad (1)$$

With substituted parameters, MATLAB® simulation yielded a result of -3dB cut-off frequency found located at 122Hz.

3.2 Inverter bridge design

For the inverter bridge, a design was used using 6 IGBT modules (see Figure 2). IGBTs as selected in the previous section were used, together with the selected drivers.

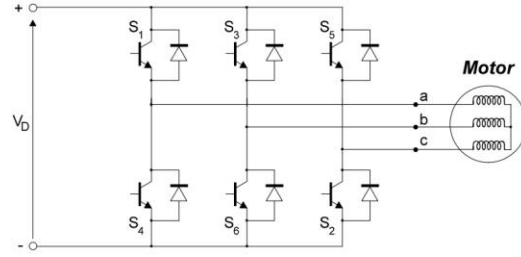


Figure 2: Three phase inverter [2]

Looking at only one half-bridge of the inverter (of three), fly-back diodes (D4 and D5) were added to provide back emf a dissipation path (shown in Figure 3).

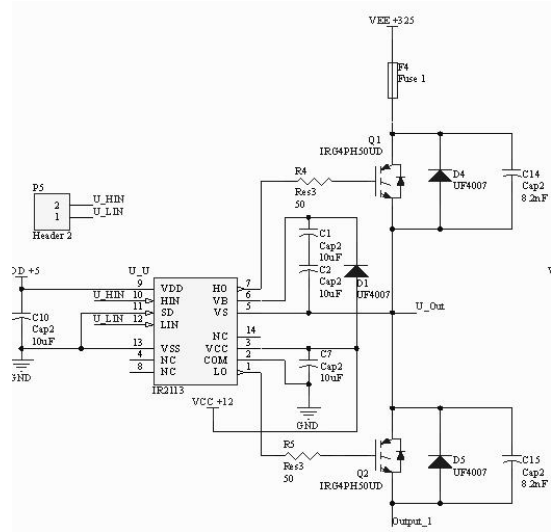


Figure 3: Conceptual design circuit overview

Also on a second iteration of the board, soft switching capacitors (C14 and C15) were added to reduce the dV/dt experienced during switching. Polypropylene capacitors were chosen due to their high pulse handling capacity (dV/dt) and maximum permissible pulse characteristic (k_o). Capacitor parameters were calculated using the same formula as would be used for calculating snubber capacitors [3]:

$$C_s = \frac{0.6I_d}{V_{LL}} \quad (2)$$

This yielded a capacitor size of $C_s = 0.0078\mu F$

3.3 Inverter thermal design

A thermal study was conducted in SolidWorks®. From the datasheet for the IRG4PH50UD IGBT, the parameters obtained were:

$$R_{\theta jc} = 0.64 \text{ } ^\circ\text{C/W [Junction to case]}$$

$$R_{\theta cs} = 0.24 \text{ } ^\circ\text{C/W [Case to sink; flat greased]}$$

$$R_{\theta sa} = 0.64 \text{ } ^\circ\text{C/W [Sink to ambient]}$$

Ambient temperature were taken at 25°C. Power generated in terms of switching loss were calculated by formula [3]:

$$P_s = \frac{1}{2} V_d I_o f_s (t_{c(on)} + t_{c(off)})$$

Substituting parameters:

$$V_d = 325 \text{ V}$$

$$I_o = 4 \text{ A}$$

$$f_s = 3.5 \text{ kHz}$$

$$t_{c(on)} = 46 \text{ n sec}$$

$$t_{c(off)} = 240 \text{ n sec}$$

Yields:

$$P_s = 0.65 \text{ W}$$

A convection rate of $6.349 \frac{W}{m^2 k}$ was used as calculated, with a contact resistance of $1.33 \frac{k}{W}$ used between the IGBTs and sink. Between the diode bridge and sink, a contact resistance of $2.2 \frac{k}{W}$ was used, with an estimated 15 Watt generated by the diode bridge. Simulation yielded the following results:

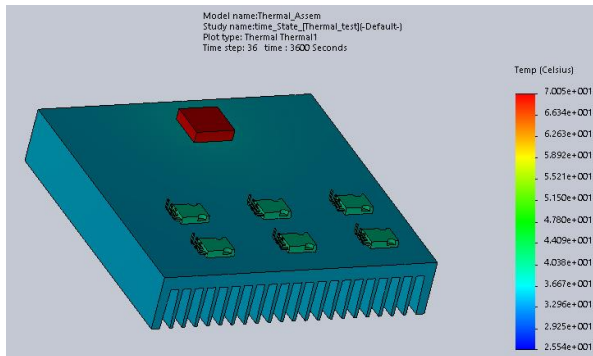


Figure 4: Temperature simulated at 3300 sec.

This clearly shows that the heat sink is adequate for the application, however the contact resistance between the diode bridge and heat sink have to be reduced by applying thermal paste.

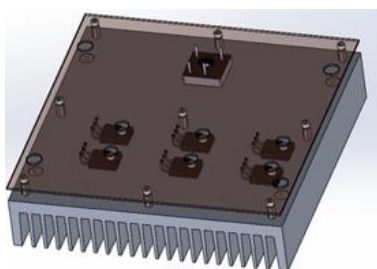


Figure 5: Finalised CAD design

The CAD assembly made it possible to determine where components should be placed (see Figure 5), and also made it possible to create a drawing indicating the necessary drilling schedule required during PCB manufacturing.

A second iteration PCB design was done in Altium® as shown in Figure 6. Note the merging of the 325V DC rectification circuit into the inverter bridge circuit, such that the diode bridge can also be placed on the available heat sink. Blue tracks are the bottom layer, and red tracks are the top layer. Components are marked green.

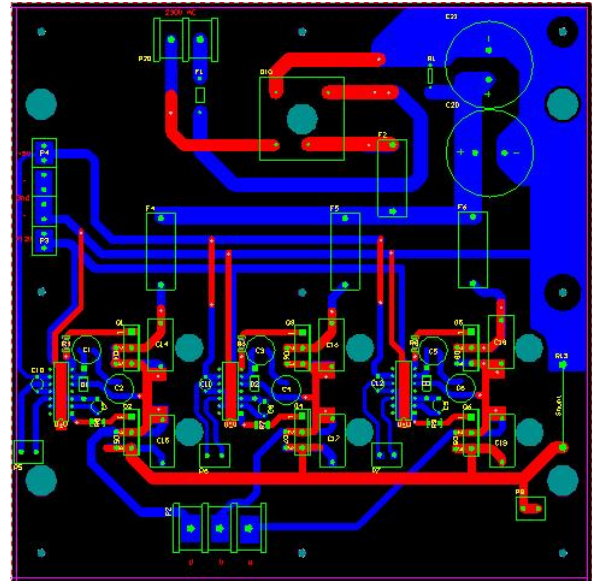


Figure 6: Finalised PCB design

3.4 Instrument Power Supply Unit (PSU) design

The instrument PSU consists of a 230/12V AC transformer feeding into the circuit where after it is rectified and filtered. This rectified DC was regulated by a 12V and 5V linear regulator.

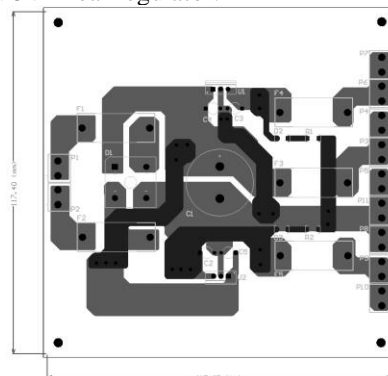


Figure 7: Finalised Instrument PCB design

3.5 Microcontroller to relay interface

A simple design was done to be able to drive a 12V DC relay field coil with the microcontroller. This relay

switches the 325V DC bus on or off, where the circuit can be seen in Figure 8.

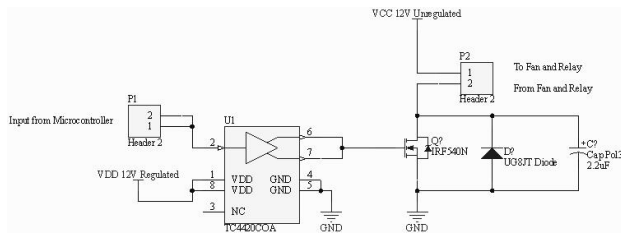


Figure 8: Relay field coil interface circuit

This design uses a driver, an IR540N MOSFET and fly back diode.

4. RESULTS

The constructed system can be seen in Figure 9. An isolation transformer had to be added to the system in order to limit high inrush current experienced by the inverter circuit, as this caused frequent component failures.

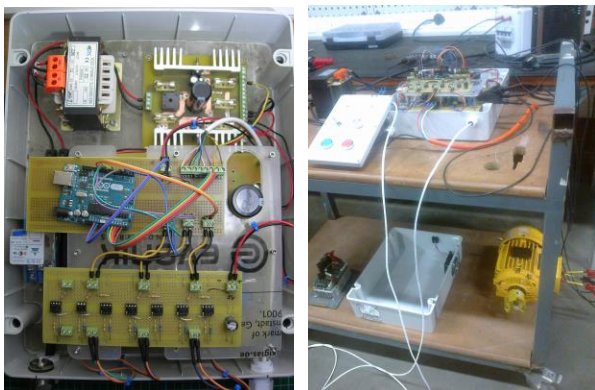


Figure 9: Complete circuit

4.1 Inverter Bridge output at 12V with resistor as load

Operating the circuit using star connected resistors (100Ω) as load at 12V, the following output voltage was obtained:

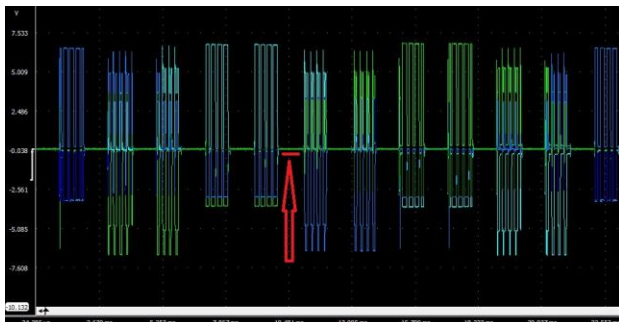


Figure 10: Captured output Voltage at 40Hz

Figure 10 was captured with the drive operating at 40Hz. Note the ample amount of ‘dead time’ indicted by the red arrow present between switching.

4.2 Inverter Bridge voltage output at 220VAC with motor as load

The rectification circuit was supplied with 220V AC input voltage, with a 0.75kW three phase induction motor connected to the inverter bridge as a load. The three phase asynchronous induction motor input terminals were connected in delta. By doing this, it was no longer necessary to generate the higher voltage levels necessary to drive the motor in a wye connection, greatly simplifying the circuit.

Output voltages captured using the TiePie® scope can be seen in Figure 11 for all three phases. Note the difference between the resistive load (Figure 10) and inductive load (Figure 11) on the measured waveforms. Ripples caused by back emf can be observed between switching instances where dead time is implemented.

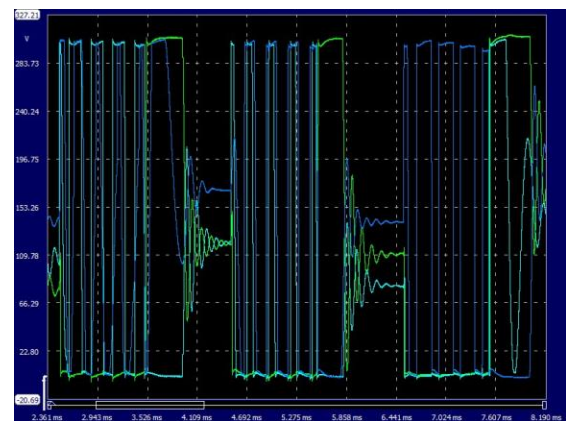


Figure 11: Captured output Voltage of U, V, W at 40Hz

4.3 Inverter Bridge current output at 220VAC with motor as load

Voltage of phase U (channel 1 / green) and line current of phase U (channel 2 / light blue) can be seen in Figure 12.

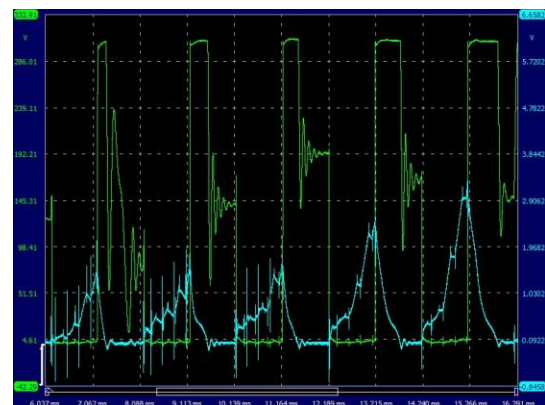


Figure 12: Captured current output of channel U at 40Hz

4.4 Single phase input voltage and current

Sampling the input current and voltage (main / source) of the entire circuit with the scope, the results can be seen in Figure 13

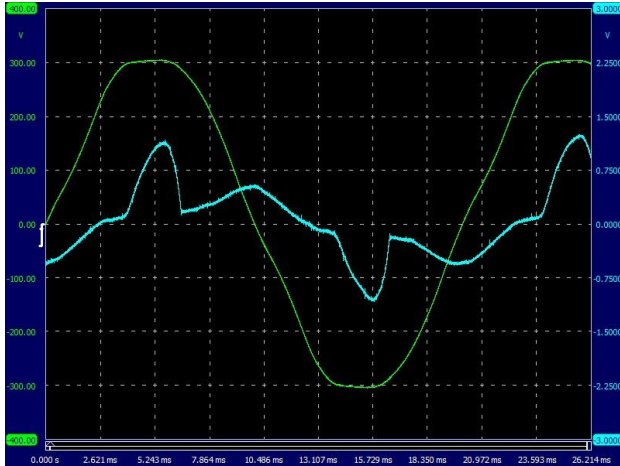


Figure 13: Captured input current and voltage of 220V AC supply

RMS power calculations of the scope was captured as 142.6 watt, as can be seen in Figure 14.



Figure 14: Captured RMS current and voltage input of 220V AC supply

Calculating the total harmonic distortion (THD) of the above with formula [4]:

$$PF = \frac{1}{\sqrt{1 + THD^2}} \quad (3)$$

A result of %THD = 77.63 were obtained. The IEEE standard 519 indicates that the limits on voltage harmonics are set at 5% for THD. Thus it is clear that corrective steps should be taken in future.

5. CONSTRUCTION COSTS AND FEASIBILITY

A complete cost breakdown was done. In summary, due to the isolation transformer that had to be added to the circuit, the costs of the system became uncompetitive with products already available on the market today. However, being able to remove the isolation transformer by providing an alternative solution to limiting the high inrush currents seen by the system, it is possible to reduce costs sufficiently to become cost competitive again. Further cost reductions and size reductions are possible,

where this should become the main focus of future design improvements.

6. CONCLUSION

An important lesson learnt during the development of the VFD was that there are very little to no tolerance for error or bad design in such a drive. Due to the magnitude of voltages present in the system, proper design and component operation is important.

Shoot through within the inverter semiconductors were a constant plague experienced with this project, which was responsible for slow development. This shoot through was not due to improper switching, but rather as seen in Figure 12 caused by current spiking experienced within the system. These current spikes managed to briefly become so high that it exceeded semiconductor ratings and caused failure. Failure of semiconductors caused by current spikes made the device 'remain open' at a constant resistance indefinitely. Remaining open created a short circuit condition, which was then interrupted by the fuse. If the short circuit condition was not properly stopped, the semiconductor allowed voltage spikes to be induced to the driver. Before the optocouplers were introduced, these induced spikes managed to completely damage a previous microcontroller.

7. DISCUSSION

Looking at the low power delivered to the motor, this can be attributed to:

- Unnecessary long dead time during switching
- PWM are limited to a maximum of 180 out of 255 to ensure stability during final demonstration.

Due to the PWM not being allowed to be fully driven up to 255, it means that a lower effective voltage potential is being delivered to the motor.

$$(220V \text{ AC (RMS)}) / 255 * 180 = 155V \text{ AC (RMS)}$$

This also attributes to the low power delivered by the drive. By being able to eliminate these restrictions, it is believed possible to increase power output to an estimated 300W. However 300W are not sufficient, and further design improvements may be required.

A Necessary improvement that is required to increase the robustness of the drive is being able to detect fault conditions occurring between itself and the motor. Thus the drive should be able to detect if there is a short circuit condition or even unhealthy mechanical operational condition on the motor side such as a failing bearing causing abnormally high current requirements by the motor.

Also, the drive must be able to detect if the incoming voltage from the mains experience conditions of overvoltage. This became clear before final demonstrations when the drive damaged semiconductors again the night before demonstration day. The failure was later found to be overcurrent, where this overcurrent was due to the mains in the laboratory reading 244V AC (RMS) compared to the designed operating conditions of 220/230V AC (RMS). This increased voltage was

enough to stimulate the above mentioned unfavourable operating condition.

Finally, cost savings should be done where possible to make the drive more feasible. Size reduction should also be considered, since the current design is not making optimally use of its available space.

8. REFERENCES

- [1] M Barnes, "Electromagnetic compatibility (EMC)" in Practical Variable Speed Drives and Power Electronics, First Edition: Newnes, 2003, pp 115-138
- [2] R Parekh, "VF Control of 3-Phase Induction Motors Using PIC16F7X7 Microcontrollers", Microchip, 17 February 2004. [PDF] Available: ww1.microchip.com/downloads/en/AppNotes/00889b.pdf. [Accessed: 2015/03/12]
- [3] N Mohan, T.M. Undeland, W.P. Robbins, Power Electronics, Third Edition: John Wiley & Sons, 2003
- [4] Don Tuite, "Reconciling Power-Factor Correction Standards Leads To Solutions", Electronic design, 2010. [Website] Available: <http://electronicdesign.com/energy/reconciling-power-factor-correction-standards-leads-solutions>. [Accessed: 2015/08/12]

DESIGN AND SIMULATION OF A DIGITALLY CONTROLLED CLASS-D AMPLIFIER

C.A. van der Merwe*, H.D.T. Mouton[†] and B. Putzeys[‡]

* Department of Electrical & Electronic Engineering, Stellenbosch University, Private Bag X1, Matieland, 7602, South Africa, E-mail: 16430778@sun.ac.za

[†] Department of Electrical & Electronic Engineering, Stellenbosch University, Private Bag X1, Matieland, 7602, South Africa, E-mail: dtmouton@sun.ac.za

[‡] Hypex Electronics B.V., Groningen, The Netherlands, E-mail: bruno@hypex.nl

Abstract: A modelling and design method for a digitally controlled class-D amplifier is presented. An equation is derived to determine the gradient of the PWM input signal and an accurate model of the PWM is used to calculate the small-signal gain of the comparator. Ripple compensation is implemented to minimise the distortion caused by the feedback signal. The amplifier is simulated in an environment similar to the FPGA which will be used to implement it. The simulation results are satisfactory and the next step will be to practically implement the system.

Key words: Quantization Noise, digital, amplifier, class-D.

1. INTRODUCTION

Class-D amplifiers have become very popular due to the fact that they can produce high quality audio and operate at very high efficiencies. The high efficiencies of these amplifiers negate the need for large heat sinks which are necessary for other classes of amplifiers. Thus, class-D amplifiers are usually quite small. Self-oscillating class-D amplifiers are the most compact due to the fact that no external circuitry is required to generate a PWM carrier signal as the circuit generates its own. One of the biggest disadvantages of self-oscillating amplifiers is, however, that the oscillation frequency varies along with the modulation index [3]. This can cause audible beat tones in multi-channel audio systems.

Both self-oscillating and externally clocked amplifiers have traditionally been controlled using analogue circuits. In this paper the design and simulation of a digitally controlled class-D amplifier will be discussed with the goal in mind to eventually implement the amplifier using only an output stage, FPGA and a simple analogue-to-digital converter. This will enable the amplifier to be even smaller than its analogue counterpart.

Along with the non-linearities of the output stage of class-D amplifiers, as discussed in [4], there are several other drawbacks to digitally controlled class-D amplifiers. The biggest of these drawbacks is the quantization noise which is induced into the system since the success of audio applications are commonly judged by the quality of their output. This paper discusses design methods to shape the quantization noise away from the audio band to ensure a high-quality output signal. An accurate PWM small-signal model from [11] will also be consulted to account for the high-frequency behaviour of the comparator so that stability margins can be determined accurately.

2. OVERVIEW OF THEORY AND BASIC OPERATION

2.1 Basic operation of Class-D amplifier

A basic class-D amplifier consists of a controller, comparator, power stage and output stage. The output stage is essentially a RLC low-pass filter when modelled due to the fact that the speaker is modelled using a resistor. The core concept of a class-D amplifier is the use of a comparator to create a PWM signal which drives the power stage. The low-pass filter then attenuates the high-frequency components of the PWM carrier signal. The power stage consists of two MOSFET transistors which are switched complimentary. The transistors are thus used as switches and not operated in their linear region. This ensures that class-D amplifiers have higher efficiencies than amplifiers with different configurations [2]. The basic configuration also includes a global negative feedback loop which can be seen in Fig. 1.

The global negative feedback loop is implemented to compensate for the non-linearities which occur in open-loop switching amplifiers [8]. These include pulse timing errors, low power supply rejection, and a load dependent frequency response [4]. Class-D amplifiers can either be self-oscillating, where the feedback is used to

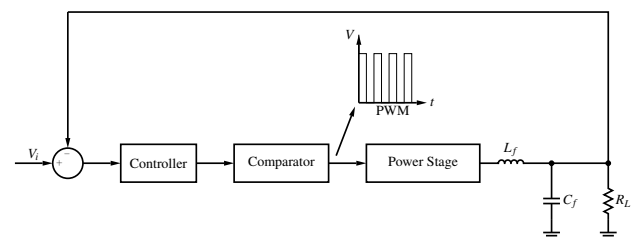


Figure 1: Basic Class-D configuration.

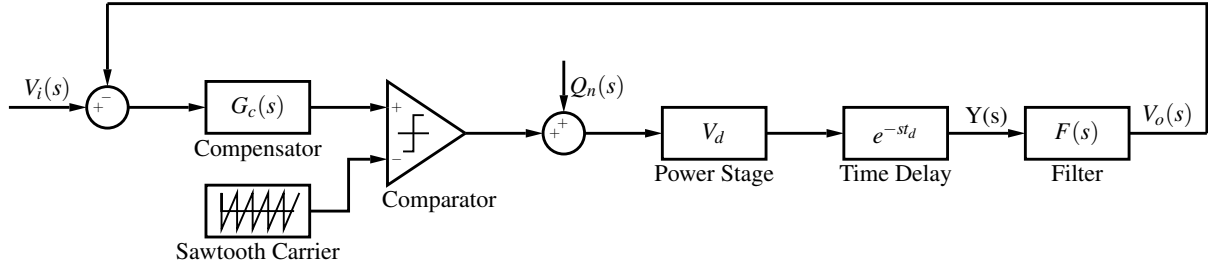


Figure 2: Transfer Function Model.

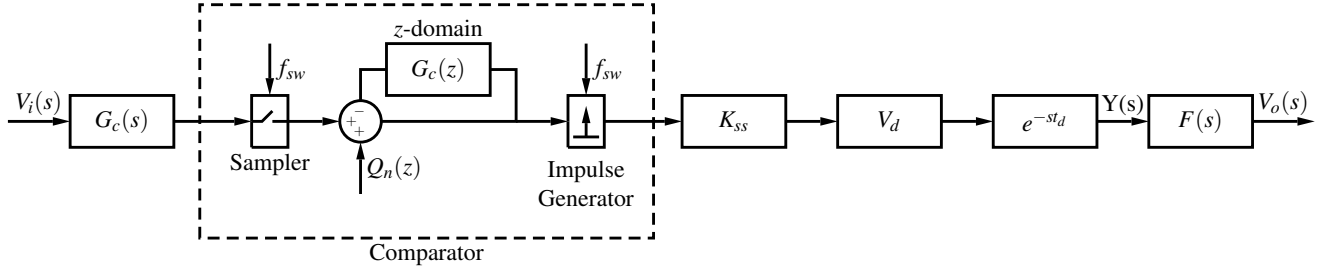


Figure 3: System model with z-domain comparator model included.

create the system's own PWM carrier by operating in a limit cycle [11], or the PWM carrier can be generated by external circuitry. The latter is the route that was chosen for the following work where the ground work is done to implement the external PWM carrier and the controller using an FPGA.

2.2 Quantization Noise

To ensure high quality audio, it is desirable to use a 24-bit counter for the system. It is however impossible to clock an FPGA at a high enough clock speed to achieve this. The switching frequency, and thus the sampling rate, will be increased to reduce the requirements of the quantizer. This process is known as oversampling [9]. The switching frequency was chosen as 768 kHz and will eventually be implemented in an FPGA which is clocked at 98.304 MHz. The system will thus make use of a 7-bit pulse-width modulator. The approximations that are made to restrict the analogue signals to a discrete range of values induce quantization noise into the system. A relatively cheap sigma-delta analogue-to-digital converter will be used in the feedback loop of the amplifier which will also add quantization noise.

There are multiple noise shaping techniques that can be used to reduce the effect of the quantization noise as discussed in [1]. However in the following work the controller design will be used to adequately attenuate the quantization noise by ensuring that the controller has an open-loop gain of 50 dB or more in the audio band [4]. The audio band is from 20 Hz to 20 kHz.

2.3 Modelling

The transfer function model of the system can be seen in Fig. 2. At first the conventional model of the PWM will be used where it is modelled simply as an equivalent gain [5]. The time delay function accounts for any delay the system might have including the delay of the A/D converter and FPGA which will eventually be implemented. The open-loop transfer function can be seen in (1).

$$G_{OL}(s) = G_c(s)V_d e^{-st_d} F(s) \quad (1)$$

It is shown in [11] and [12] that the traditional model of the PWM is however not accurate as it fails to account for the high-frequency behaviour of the comparator. This results in inaccurate stability margins. An accurate model, which can be seen in Fig. 3, was derived where the comparator is modelled as a sampling operation with the sampling frequency equal to the switching frequency of the system. The sampler is then followed by an impulse generator which also operates at the switching frequency of the system. The area between the sampler and the impulse generator is thus in the discrete-domain and the block diagram in Fig. 2 is manipulated to ensure that the stability of the system is now solely dependant on the $G_c(z)$ feedback loop. This is done because the discrete-domain is more accurate when it comes to analysing stability margins. The transfer function will be converted to the discrete-domain using methods which are discussed in section 2.5. In [6] a method is proposed to determine the correct PWM small-signal gain, K_{ss} . The value of K_{ss} can be determined using (2) where $\dot{f}(tp)$ is the gradient of the input signal to the PWM at the transition points of the

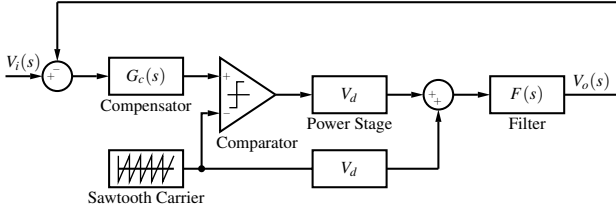


Figure 4: Simplified system with Ripple Compensation.

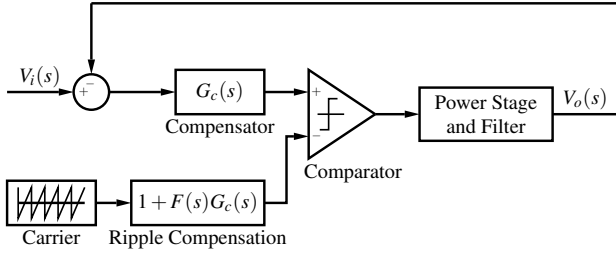


Figure 5: Practical Implementation of Ripple Compensation.

PWM carrier signal and the controller output.

$$K_{ss} = \frac{2f_s}{2f_s - \dot{f}(tp)} \quad (2)$$

The ripple component of the output signal causes aliasing of the high-frequency carrier components. This results in distortion of the output signal and a change in the PWM small-signal gain since the ripple gradient changes. There is a simple and effective way of solving the ripple feedback problem. The proposed method entails cancelling the unmodulated edge from the PWM signal by adding the sawtooth carrier signal to the output of the PWM as can be seen in Fig. 4 [10]. The unmodulated edges are effectively replaced by continuous linear slopes as they contain no information. This will ensure a more constant small-signal gain and will also minimise the aliasing error [6].

The implementation seen in Fig. 4 is however impractical. Using block diagram manipulation, Fig. 5 can be obtained from Fig. 4 illustrating that the proposed ripple compensation technique is equivalent to pre-distorting the PWM carrier signal. This is a very convenient method to implement the ripple compensation when implementing the controller using an FPGA, since the pre-distortion of the PWM carrier signal can be done off-line [8].

2.4 PWM Input Gradient

In this section an equation will be derived to determine the gradient of the PWM input signal. The value of the gradient at the transition points with the PWM carrier signal, denoted by $\dot{f}(tp)$ in previous sections, can then be calculated. The input of the system will be a DC signal to ensure that the PWM signal has a constant duty cycle. It will also be assumed that the input signal of the PWM is periodic. It is important to note that once the ripple compensation has been implemented, the input signal to the output filter will be a sawtooth waveform which can be

denoted by (3).

$$x(t) = \frac{2}{T_s}t, \text{ for } \frac{-T_s}{2} \leq t < \frac{T_s}{2} \quad (3)$$

The simplified system which is used for calculations can be seen in Fig. 6 where $Y(s)$ is the input signal of the PWM and $X(s)$ is the PWM output after ripple compensation has been implemented. The combination of $F(s)$ and $-G_c(s)$ is then decomposed into partial fractions in the form of (4).

$$G_n(s) = \frac{k_n}{s - a_n} \quad (4)$$

The differential equation for a single term is solved and applied to every partial fraction. The derivative of the outputs of every partial fraction is then added together to produce the output of the whole system. The fact that the PWM output has a constant duty cycle can then be used to determine the gradient of the PWM input signal at the transition point of the PWM carrier signal and the controller output using (5), where n is the number of partial fractions which the system in Fig. 6 is decomposed into.

$$\frac{dy}{dt} = \sum_{n=1}^N \left(\frac{2k_n e^{a_n t}}{e^{-\frac{a_n T_s}{2}} - e^{\frac{a_n T_s}{2}}} + \frac{2k_n}{a_n T_s} \right) \quad (5)$$

2.5 Impulse Invariance Method

The controller will be designed in the s-domain and then converted to the z-domain using the impulse invariance method as described in [11]. This method differs from the standard impulse invariance method in that it takes the first sample as zero since a practical system will never have a propagation delay of zero. To use this method, the continuous-time transfer function needs to be expanded into partial fractions in the form of (6).

$$G(s) = \sum_{n=1}^N \frac{A_n}{s + p_n} \quad (6)$$

Equation 7 is used to map the continuous-time transfer function to the z-domain [7]. It is clear that the propagation delay of the system, t_d , only affects the location of the z-domain zeros.

$$G(z) = \frac{1}{f_{sw}} \sum_{n=1}^N A_n e^{p_n t_d} \frac{e^{-p_n T_s}}{z - e^{-p_n T_s}} \quad (7)$$

2.6 Noise Transfer Function

The noise transfer function of the system is important as it indicates whether the system adequately attenuates the

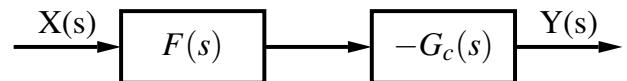


Figure 6: Simplified system for PWM input gradient calculation.

quantization noise induced by the PWM. For the average model in Fig. 2, the noise transfer function is described by (8).

$$NTF_1 = \frac{Y(s)}{Q_n(s)} = \frac{V_d e^{-sT_d}}{1 + F(s)G_c(s)V_d e^{-sT_d}} \quad (8)$$

The modified model in Fig. 3 can now be used to derive a more accurate noise transfer function where $Q_n(z)$ represents the quantization noise of the 7-bit pulse-width modulator. The small-signal closed-loop transfer function can be seen in (9).

$$V_o(\omega) = V_i(\omega) \left\{ \frac{G_c(j\omega)K_{ss}V_d e^{-j\omega T_d} F(j\omega)}{1 + G(e^{j\omega T_s})} \right\} + Q_n(\omega) \left\{ \frac{K_{ss}V_d e^{-j\omega T_d} F(j\omega)}{1 + G(e^{j\omega T_s})} \right\} \quad (9)$$

Where:

$$G(e^{j\omega T_s}) = G(z) = \mathcal{Z}\{G_c(s)F(s)K_{ss}V_d e^{-sT_d}\}$$

The \mathcal{Z} symbol refers to the z-transform using the impulse invariance method discussed in section 2.5. It is thus clear that the noise transfer function of the system, which includes the accurate PWM small-signal model, can be described by (10).

$$\frac{Y(\omega)}{Q_n(\omega)} = NTF(\omega) = \frac{K_{ss}V_d e^{-j\omega T_d}}{1 + G(e^{j\omega T_s})} \quad (10)$$

3. DESIGN

This section will cover the design of the controller and other parts of the system. Firstly, the LC low-pass filter was designed to have a cut-off frequency of 35 kHz. The system will operate with rail voltages of 30 V and a propagation delay of 210 ns. As previously stated, it is desirable for the system to have an open-loop gain of at least 50 dB over the audio band (20 Hz to 20 kHz). The system must also have a gain margin of at least 3 dB to accommodate any component inaccuracies. A root-locus design approach was followed to design the controller in the continuous-time domain and the open-loop bode plot of the system can be seen in Fig. 7.

The complex poles of the low-pass filter can be seen at 35 kHz. Two zeros were placed at 30.9 kHz for cancellation of the low-pass filter poles to ensure a stable control loop. Together with an integrator, two complex pole pairs were placed at the high frequencies of 1.15 MHz and 1.88 MHz to attenuate the quantization noise of the A/D converter. Two complex pole pairs were also placed at 10.6 kHz and 17.8 kHz with their associated zeros being placed at 42.1 kHz and 74.8 kHz. The damping ratios of these zeros are 0.157 and 0.572 respectively. The resulting system has a gain margin of -2.82 dB and a phase margin of 26.6 degrees. The system is then converted to the discrete-time domain using (7) to assess the stability of the system more accurately. The magnitude response of the

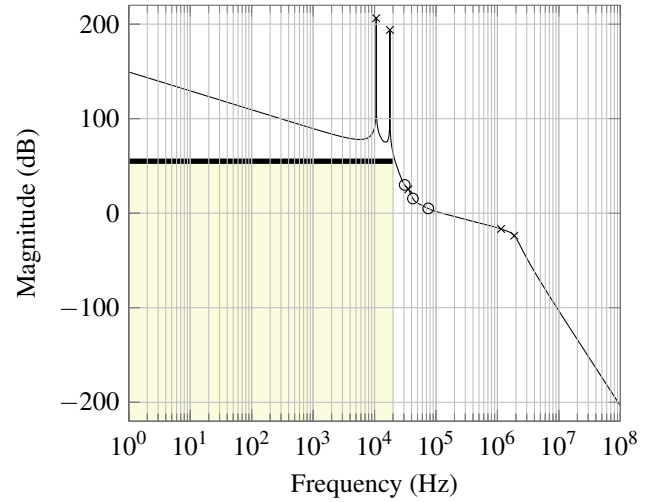


Figure 7: Magnitude of Continuous-time Open-Loop Bode Plot.

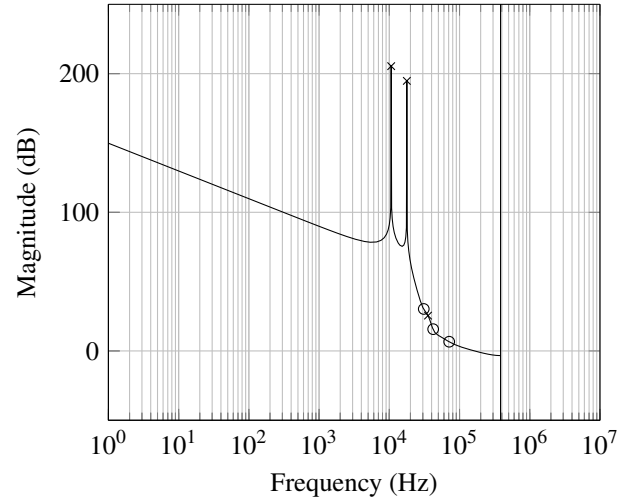


Figure 8: Magnitude of discrete-domain Open-Loop Bode Plot.

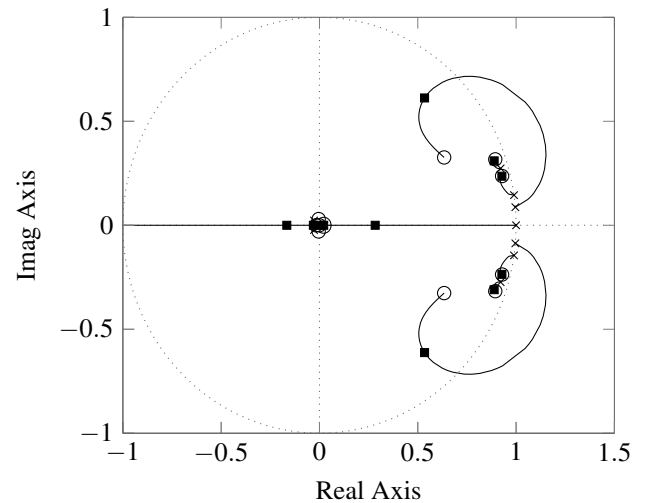


Figure 9: Root Locus in z -domain.

discrete-domain system can be seen in Fig. 8.

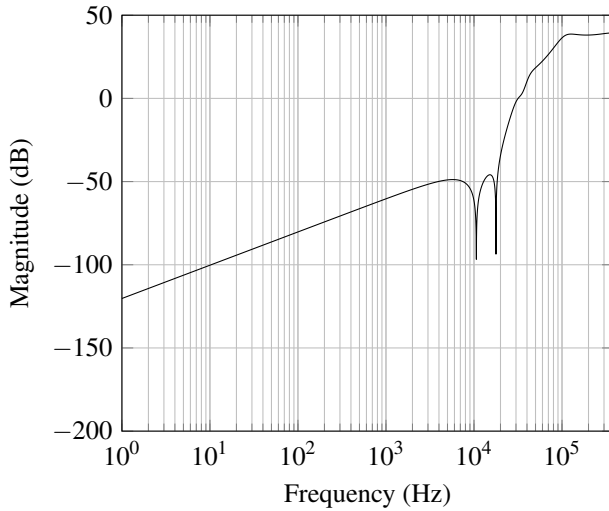


Figure 10: Noise-transfer function.

When the z-domain root locus — which can be seen in Fig. 9 — is examined, it is clear that the system is stable with a gain margin of -3.11 dB and a phase margin of 20.4 degrees. The system has an open-loop gain of more than 50 dB across the audio band. The noise-transfer function in Fig. 10 shows that the controller shapes the noise in such a way that the noise in the audio band is suppressed by at least -50 dB. The open loop zeros of the system translates to the poles of the noise-transfer function. This is illustrated clearly in Fig. 10 at 10.6 kHz and 17.8 kHz. The controller thus satisfies the criteria which was initially stipulated as requirements.

Once the design of the controller has been completed, it is possible to use (5) and the method discussed earlier to determine the gradient of the PWM input signal. The resulting plot is shown in Fig. 11. It is important to note

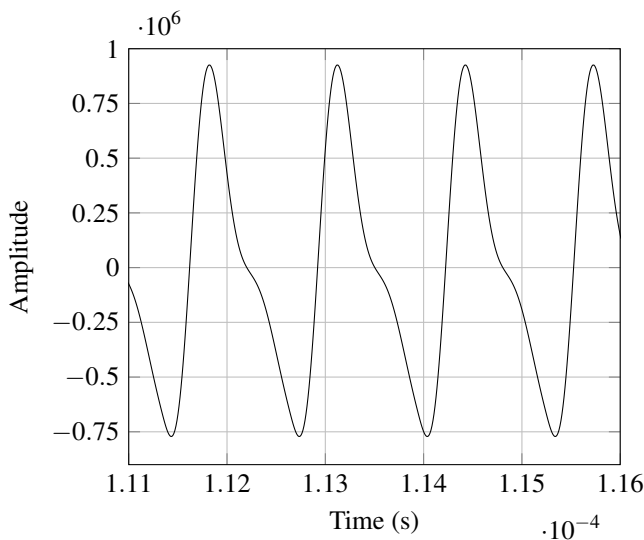


Figure 11: Calculated Gradient of PWM input signal.

that only the value of the gradient of the PWM input signal at the transition points of the PWM carrier signal and the controller output is of interest as this value has an influence on K_{ss} as can be seen in (2).

4. SIMULATION RESULTS

The simulation of the system was done using Simulink. The audio input is simulated using a 1 kHz sinusoid and the speaker of the amplifier was modelled using an 8.2Ω resistor. The simulation was clocked at 98.304 MHz to simulate the FPGA environment in which it will be implemented. A counter was used to simulate the sawtooth carrier signal. The gradient of the PWM input at the transition points of the PWM carrier signal and the controller output was measured as -1.883×10^5 . The PWM small-signal gain, which is determined using (2), is thus equal to 0.8946 . A gain of 1.117 is added to the controller gain to compensate for the PWM small-signal gain. The system was, at first, simulated without

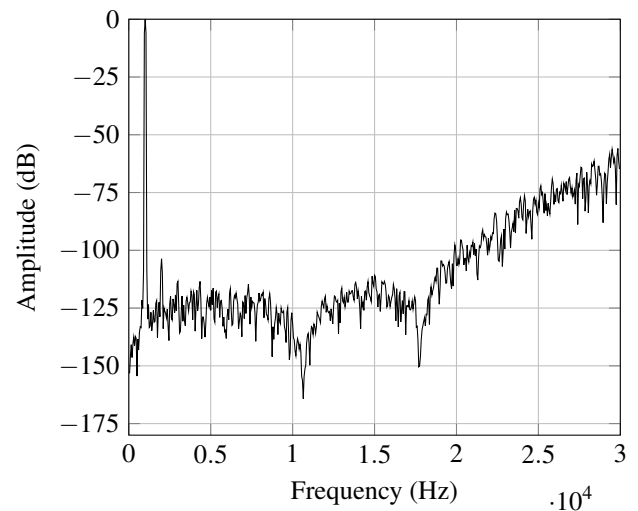


Figure 12: FFT over the audio band without ripple compensation.

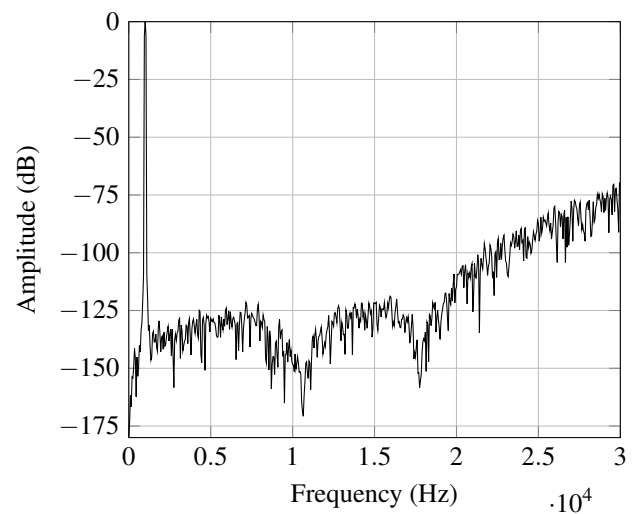


Figure 13: FFT over the audio band with ripple compensation.

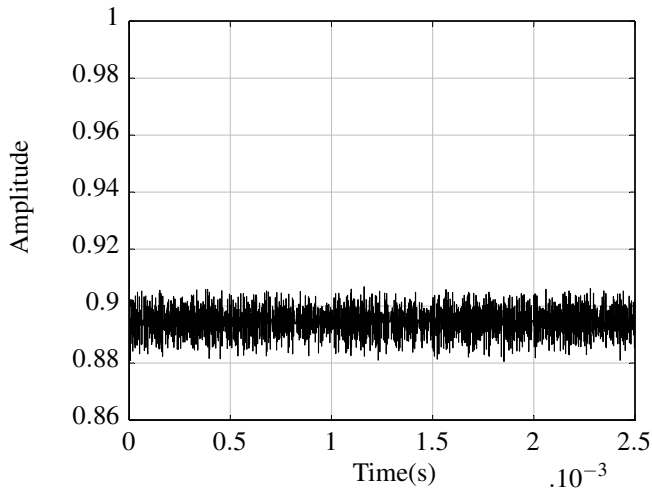


Figure 14: Small-signal gain with ripple compensation.

implementing ripple compensation. Fig. 12 shows the FFT of the output of the system over the audio band without ripple compensation. Ripple compensation was then implemented with Fig. 13, the FFT, and Fig. 14, the small-signal gain. It is important to note that the variation of the PWM small-signal gain is very small with the change in input signal of the amplifier once the ripple compensation is added. When comparing Fig. 12 to Fig. 13 it can be seen that the harmonic distortion which is caused by the feedback from the output is adequately attenuated by the ripple compensation.

The poles at 10.6 kHz and 17.8 kHz are clearly visible. The fundamental component of the sinusoid can be seen at 1 kHz. It is evident that the noise in the system is sufficiently attenuated over the audio band and the amplitude of the noise starts to rise outside of the audio band as expected.

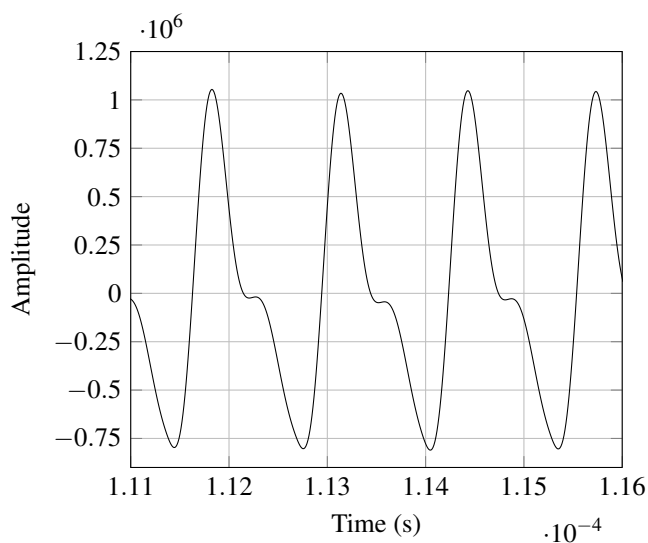


Figure 15: Simulated Gradient of PWM input signal.

Fig. 15 shows the simulated gradient of the PWM input signal. When comparing Fig. 15 to the mathematically

calculated gradient in Fig. 11, it can be seen that the graphs are very similar but do contain some differences. The slight differences in amplitude and form are due to the quantization noise which is induced into the system during simulation. When the simulation is performed at a higher frequency, the two graphs become identical. This confirms the credibility of the method proposed to mathematically determine the gradient of the PWM input signal. It is however clear that this method does not account for quantization noise.

5. CONCLUSION

A modelling and design method for a digitally controlled class-D amplifier was proposed. An equation was derived to determine the gradient of the PWM input signal and an accurate PWM small-signal model, which accounts for the high-frequency behaviour of the comparator, was used to ensure accurate stability margins. Ripple compensation was also implemented to negate the drawbacks of the feedback ripple. The controller was successfully designed and simulated to meet the pre-defined requirements. Future work will include a method to account for the quantization noise when mathematically calculating the gradient of the PWM input signal and practically implementing the controller using an FPGA.

REFERENCES

- [1] Ma Gerzon and Pg Craven, *Optimal noise shaping and dither of digital signals*, Audio Engineering Society Convention 87 **2822** (1989), no. i.
- [2] J Honda and Jonathan Adams, *Class D Audio Amplifier Basics*, International Rectifier Application Note AN-... (2005), 1–14.
- [3] Pieter Kemp, Toit Mouton, and Bruno Putzeys, *High-Order Analog Control of a Clocked Feedback Using Z-Domain Methods*, Audio engineering society convention 131, 2011, pp. 1–10.
- [4] Pieter Stephanus Kemp, *The Design of an Analogue Class-D Audio Amplifier Using Z-Domain Methods*, MSc, 2012.
- [5] Ned Mohan, Tore Undeland, and William Robbins, *Power Electronics: Converters, Applications and Design*, 3rd ed. (Bill Zobrist, ed.), John Wiley & Sons, Inc, 2003.
- [6] Toit Mouton, *Living on the Edge : Designing High Gain PWM Control Loops*, 2013.
- [7] Toit Mouton, Adriaan De Beer, Bruno Putzeys, and Brendan McGrath, *Modelling and design of single-edge oversampled PWM current regulators using z-domain methods*, 2013 IEEE ECCE Asia Downunder - 5th IEEE Annual International Energy Conversion Congress and Exhibition, IEEE ECCE Asia 2013 (2013), 31–37.
- [8] Toit Mouton and Bruno Putzeys, *Digital control of a PWM switching amplifier with global feedback*, 37th International Conference: Class D Audio Amplification (2009), 1–10.
- [9] John G. Proakis and Dimitri G. Monolakis, *Digital Signal Processing: principles, algorithms and applications*, Third Edit, Prentice-Hall International, Inc., New Jersey, 1996.
- [10] Bruno Putzeys, *Simple, Ultralow-Distortion Digital Pulse Width Modulator*, 120th aes convention, 2006, pp. 1–9.
- [11] Lars Risbo, Digital Audio, Video Division, and Texas Instruments Denmark, *Discrete-Time Modeling of Continuous-Time Pulse Width Modulator Loops*, AES 27th International Conference (2005), 1–10.
- [12] Lars Risbo, M. C W Høyerby, and M. a E Andersen, *A versatile discrete-time approach for modeling switch-mode controllers*, PESC Record - IEEE Annual Power Electronics Specialists Conference (2008), 1008–1014.

The Impact of HVDC Schemes on Network Transient Rotor Angle Stability

K.N.I. Mbangula^{1*}, O.E. Oni¹ and I.E. Davidson²

¹Discipline of Electrical Engineering, University of KwaZulu-Natal, Durban, 4001, South Africa

²Eskom Centre of Excellence in HVDC Engineering, University of KwaZulu-Natal, Durban, 4001, South Africa

*Email: imbangula14@gmail.com

Abstract: Compared to high voltage alternating current lines, the response of high voltage direct current schemes to system faults is faster and more controllable, thus making it more tolerable to system faults. By making use of the DlgSILENT PowerFactory software simulation tool, this paper investigates the impact of high voltage direct current schemes on the transient rotor angle stability of synchronous machines in an electrical network. The research is carried out on a two machine infinite busbar network. The transient rotor angle stability level of the network is measured by calculating the critical clearing time of the network under different network configurations. It was found that integration of the high voltage direct current schemes into the network improves the critical clearing time, which is an indication of improvement in the transient rotor angle stability of the network.

1 INTRODUCTION

Electric power systems serve to generate, transport and distribute electrical energy to consumers in an efficient, economic and reliable manner. Transmission systems are exposed to weather factors and subjected to system faults that may cause transient stability problems. Transient rotor angle stability is the ability of synchronous machines of an interconnected power system to remain in synchronism after being subjected to a severe disturbance, such as a short circuit on a transmission line. It depends on the ability to maintain or restore equilibrium between electromagnetic torque and mechanical torque of each synchronous machine in the system. The resulting system response involves large excursions of generator rotor angles and is influenced by the nonlinear power-angle relationship [1]. Transient rotor angle stability is measured by means of the critical clearing time (CCT) which is defined as the maximum time between the initiation and the isolation of a system fault such that the power system remains transiently stable [2], [3].

Various measures can be taken to enhance the stability of an electrical network. These measures can either be taken at generator level, transmission network level or at the low voltage distribution network level. The use of Flexible AC Transmission Systems (FACTS) devices are some of the measures used to prevent or mitigate against instability at network level [4]-[10]. High Voltage Direct Current (HVDC) transmission schemes are now widely regarded as suitable alternative to High Voltage Alternating Current (HVAC) schemes for long distance power transmission [11], [12].

Beside the basic function of bulk power transmission over long distances, HVDC system can be used in the interconnection of asynchronous systems; decoupling electrical networks to avoid cascading during faults. HVDC schemes may also be used to enhance transient rotor angle stability of an electric power system when operated in parallel to HVAC lines. In [13]-[15] it is shown that by making use of rapid control of HVDC converters for temporary increment of DC power during the fault and transient period, the system retarding torque can be improved. However, in [16] it was found that HVDC schemes in parallel with HVAC lines may deprive the AC system of the needed synchronizing torque during disturbances and may cause system instability if conventional control strategies are used for DC power modulation instead of using fast, advanced, robust, state of the art control techniques. It is further demonstrated in [17]-[19] that the simultaneous transmission of AC and DC power in one transmission line may lead to the improvement of transient rotor angle stability of the electric power system.

This paper reports on an investigation carried out to determine how high voltage (HV) transmission schemes employing different technologies impacts the transient rotor angle stability of an electric power system. The following four network scenarios were studied:

- (i.) Two machine infinite busbar system (TMIB) with two AC lines (case A)
- (ii.) TMIB system with three HVAC line in parallel (case B)
- (iii.) TMIB system with two AC lines and a line commutated converter (LCC-HVDC) scheme in parallel (case C)
- (iv.) TMIB system with two AC lines and a voltage source converter (VSC-HVDC) scheme in parallel (case D)

2 CONTROL METHOD

Transient rotor angle stability of an AC system can be improved by employing rapid control of the converters for DC power modulation during the transient period after the system has been subjected to a severe fault. The HVDC control system is required to detect the AC system conditions during the transient period, and to make use of the AC voltage drop caused by a fault in the AC system to derive a change in the DC current control signal, and add this control signal to the limited current reference of the converter. Alternatively, the control signal can be derived from the speed deviation signal of the generator using a controller (PI or PD). The control

signal is then used to increase or decrease the converter DC reference current, and thus controls the DC power flowing through the HVDC link during the transient period. The DC power is expected to return to its steady state value after successful power modulation. This helps with improving the system synchronizing torque. The schematic diagram of the TMIB is shown in fig. 1.

The simplified power-angle characteristics of the generators and the HVDC scheme in the parallel AC-DC system is shown in fig. 2. For simplicity of analysis, the two parallel generators (G1 and G2) are lumped up and assumed to be a single machine with an apparent power rating equal to the sum of the power ratings of the two machines. The network diagram of the TMIB system with a LCC-HVDC scheme in parallel is shown in fig. 3.

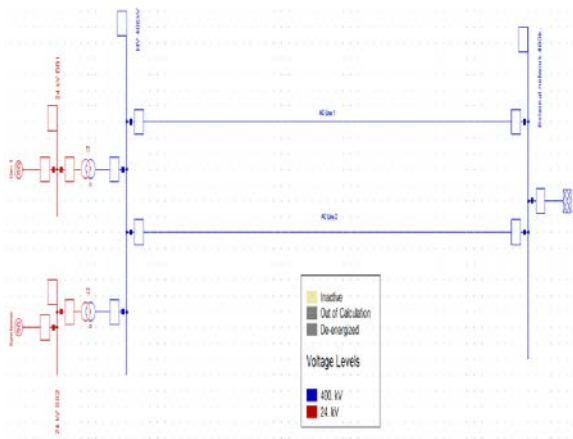


Fig. 1: TMIB System (case A)

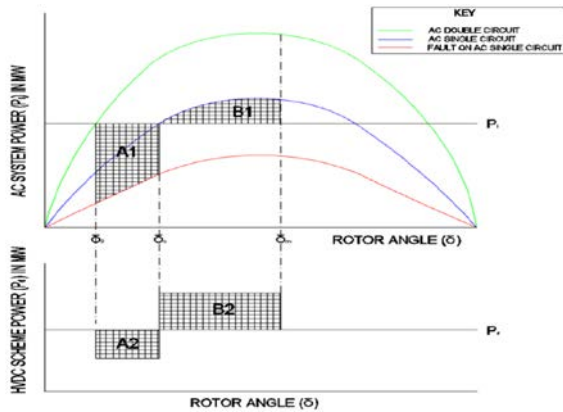


Fig. 2: Test network power angle characteristics

The analysis was carried out for a scenario where a solid three-phase short circuit occurred in one of the parallel AC lines (Line2). Table 1 shows the symbols for fig. 2 and their meanings.

Table 1: Symbols and their meaning.

Symbol	Designation
δ_0	Steady-state rotor angle
δ_c	Rotor angle when AC fault is cleared

δ_m	Maximum rotor angle at which the transient stability power limit is reached
P_M	Input mechanical power
P_i	AC system steady state power
P_d	HVDC scheme steady state power
P_i'	AC system transient power
P_g'	Generator transient power output
P_d'	DC power transferred via the HVDC link during the transient period
A1	Acceleration energy of the generator caused by the decrement of AC power transferred due to the fault
A2	Decrement of the DC steady state power P_d caused by the fault (generator acceleration)
B1	Retarding energy of the generator
B2	Increment of the DC power during and after the fault has been cleared (causing the generator to retard)

To ensure that the total acceleration area $A1+A2$ is not larger than the total retarding area $B1+B2$, which would cause the generator to continue accelerating and go out of step, it is important that fast and robust converter control is employed to increase the DC power being transferred via the DC link during the transient period. This acts as a counter measure to the net acceleration energy absorbed by the generator during the fault. This prevents the generator from stepping out and thus improving transient rotor angle stability of the machine. The DC power is increased by B_2 as specified by equation (1).

$$B_2 = (A_1 + A_2) - B_1 \quad (1)$$

Taking all the pre-fault and transient state powers of the system into consideration, equation (1) can be re-written in integral form as:

$$\int_{\delta_c}^{\delta_m} (P_d' - P_d) d\delta = \int_{\delta_c}^{\delta_m} [(P_i - P_i') + (P_d - P_d')] d\delta - \int_{\delta_c}^{\delta_m} (P_i' - P_i) d\delta \quad (2)$$

During steady state, the system is at an equilibrium point of operation and ideally the input mechanical power is equal to the generator output power i.e. $P_M = P_g$. During the transient state the total generator output power is the sum of the transient AC power and the transient DC power, i.e. $P_g' = P_d' + P_i'$. Using these relationships, equation 2 can be re-written as:

$$\int_{\delta_c}^{\delta_m} P_d' d\delta = \int_{\delta_0}^{\delta_m} P_M d\delta - \int_{\delta_0}^{\delta_c} P_g' d\delta + \int_{\delta_c}^{\delta_m} P_i' d\delta \quad (3)$$

Solving for the DC power flowing through the HVDC scheme during the transient period (P_d') from equation (3) it is found that:

$$P_d' \cong P_M \frac{\delta_m - \delta_0}{\delta_m - \delta_c} - \frac{1}{\delta_m - \delta_c} \left(\int_{\delta_0}^{\delta_c} P_g' d\delta + \int_{\delta_c}^{\delta_m} P_i' d\delta \right) \quad (4)$$

With P_d' known, both the steady state and transient state DC power of the HVDC link is known at a particular time instant, therefore, the increment in DC power required to

keep the generator in synchronism is known and is given by:

$$\Delta P_d = P_d' - P_d. \quad (5)$$

For simplification of analysis, it is assumed that the input mechanical power is constant. From equation (5-4) it can be seen that the required increment in DC power to prevent the machine from going out of step is dependent on the values of the generator output power and the power flowing in the AC lines during the transient period.

3 NETWORK MODEL

The study is carried out on the two machine infinite busbar network model shown in fig. 3. The studied LCC and VSC-HVDC schemes are shown in fig. 4 and 5. All the equipment parameters are presented in the appendix. A solid three-phase fault was simulated at the end of the AC transmission line 2 and the CCT of the network was determined for the different network operation scenarios. The transient stability level of the network was then determined from the obtained CCTs.

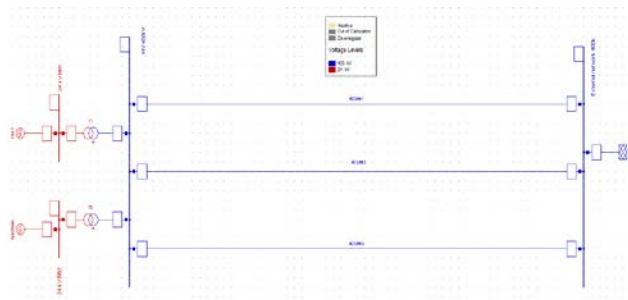


Fig. 3: TMIB System with HVAC in parallel (case 2)

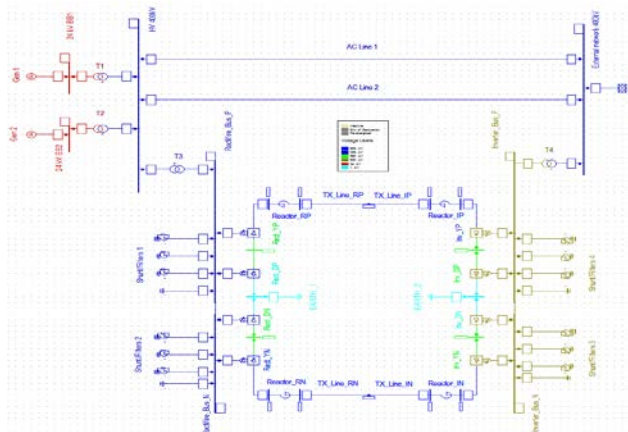


Fig. 4: TMIB System with LCC-HVDC (case 3)

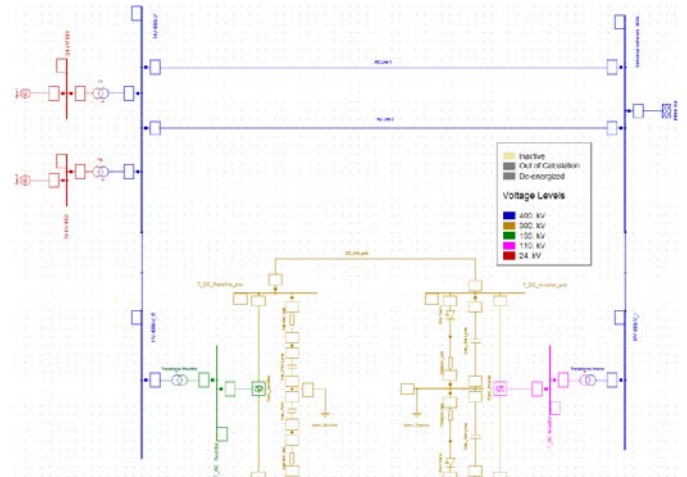


Fig. 5: TMIB System with VSC-HVDC (case 4)

4 RESULTS AND DISCUSSIONS

4.1. Case 1

Figs. 6 and 7 show the response of the rotor angle, rotor speed and the power angle characteristics of gen 1 when a solid 3- ϕ fault occurs on AC line 2 in case 1.

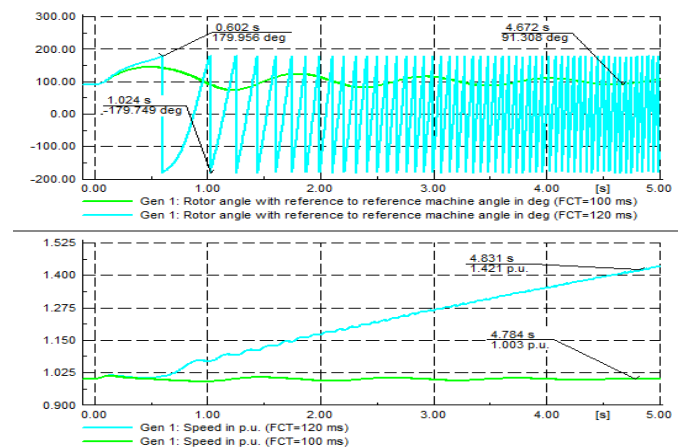


Fig. 6: Rotor angle and speed

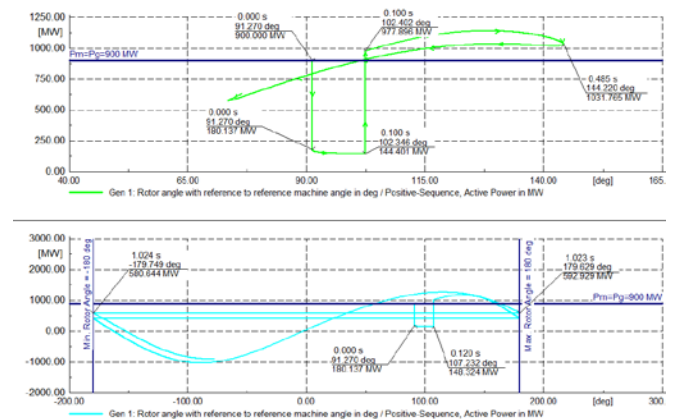


Fig. 7: Gen 1 Power-Angle Characteristics

From the obtained results it can be observed that when the fault is cleared in 100 ms, the machine rotor angle undergoes some oscillations, the amplitude of oscillation is damped out over time and the rotor angle settles at a new point of equilibrium, which is a sign that the machine remains transiently stable after successful clearance of the fault. When the Fault is cleared at 120 ms, it can be observed that the speed of the rotor continues to increase indefinitely and the machine goes out of step due to pole slip. From these results it can therefore concluded that the CCT for case A is 100 ms.

4.2. Case 2

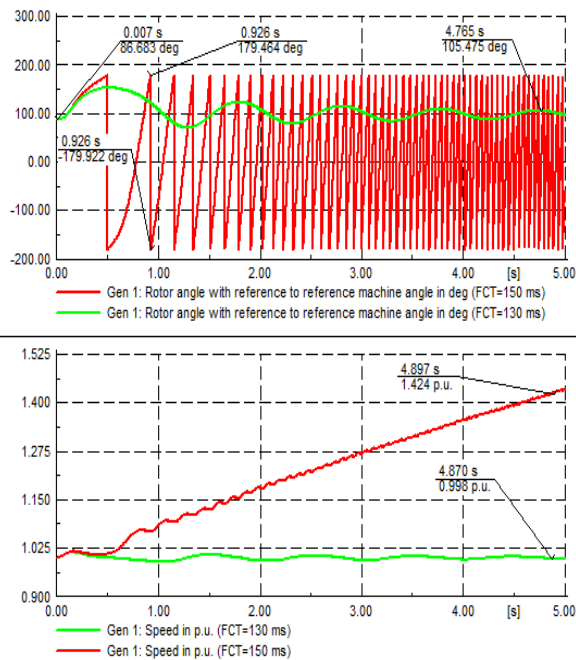


Fig. 8: Rotor angle and speed

In case 2 a third HVAC line was placed in parallel with the two HVAC lines, with equal apparent power flowing in all three lines. From the simulation results shown in fig. 8 it can be observed that Gen 1 remains transiently stable when the fault is cleared at 130 ms and loose synchronism due to pole slip when the fault is cleared at 150 ms. It can therefore be said that the CCT of Gen 1 is 130 ms in case B.

4.3. Case 3

In case 3 an LCC-HVDC scheme is connected in parallel to the two HVAC lines. Fig. 9 shows the rotor angle and rotor speed response for the simulated solid three-phase at the end of line AC 2. Fig. 10 shows the response of the DC power at the inverter before, during and after the fault. From fig. 9 it can be seen that Gen 1 remains transiently stable when the fault is cleared at 250 ms and goes out of step for a fault duration of 270 ms. Similarly, fig. 10 shows that for a fault duration of 250 ms, the operation of the inverter is stable and the inverter DC power recovers to its steady state power of 248 MW

after the fault has been cleared. For a fault duration of 270 ms, the operation of the inverter is unstable.

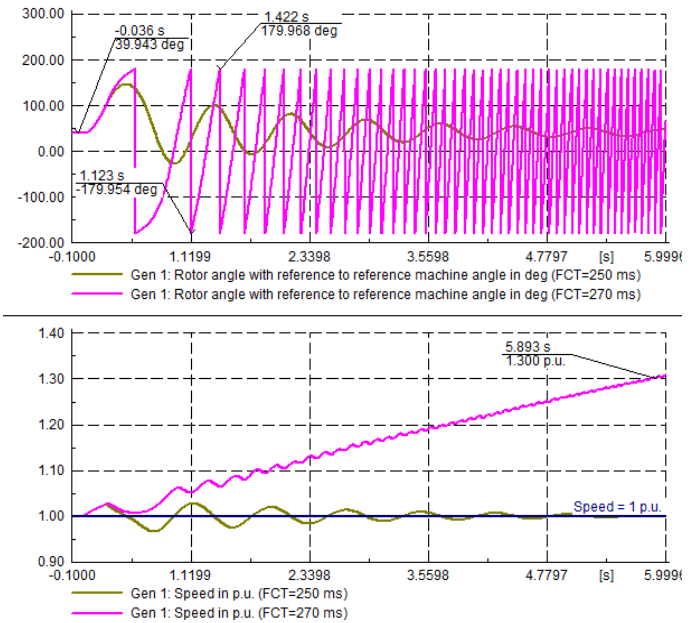


Fig. 9: Rotor angle and speed

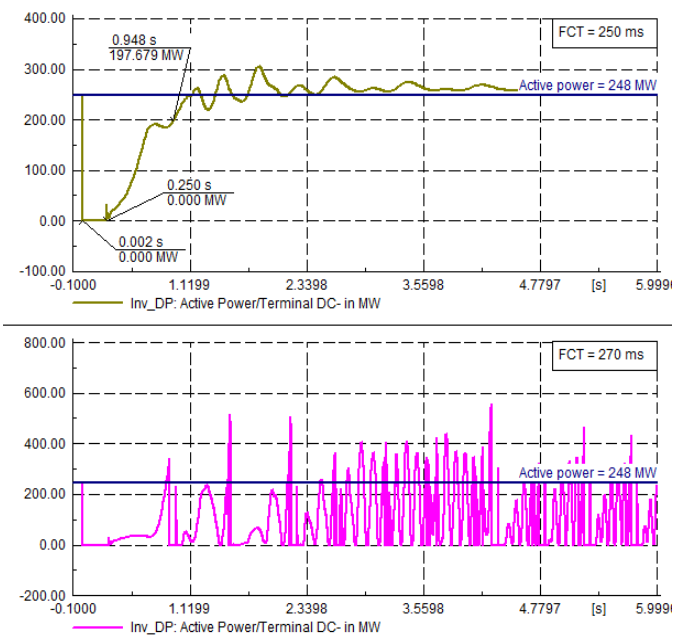


Fig. 10: LCC-HVDC Inverter active power response

From the response of the transferred DC power flowing through the LCC-HVDC inverter it can be seen that for a FCT of 250 ms (stable operation), the DC power collapses to zero MW due to commutation failure of the converter valves during the fault duration, and then recovers after the fault has been cleared. From fig. 10 it can be seen that the DC power fault recovery time (FRT), which is defined as the time from the instant the fault has been cleared to the time the DC power is restored to 80%

of its steady state value, is 700 ms approximately during stable operation. From the obtained results it can be concluded that the CCT of Gen 1 is 250 ms for case 3.

4.4. Case 4

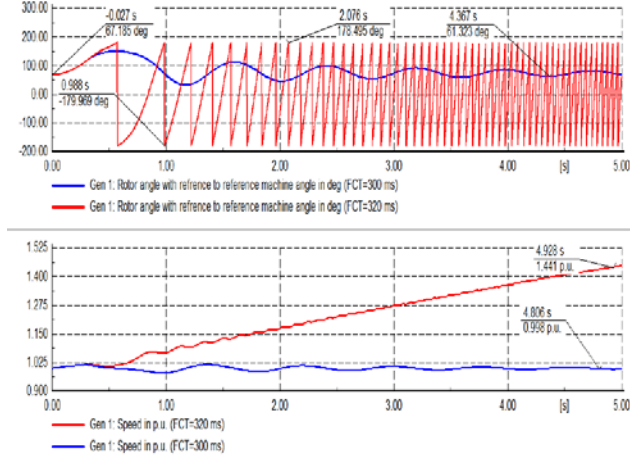


Fig. 11: Rotor angle and speed

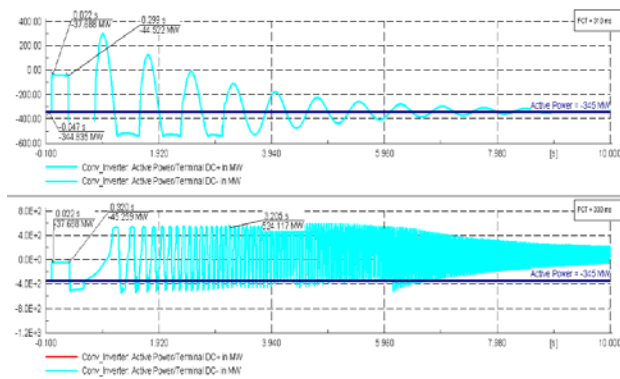


Fig. 12: VSC-HVDC inverter DC power

Fig. 11 shows the rotor angle and speed response of Gen 1 when a VSC-HVDC scheme is connected in parallel. From the obtained results it can be seen that the machine remains stable when the simulated fault is cleared at 300 ms, when the fault duration is increased to 320 ms, the machine loses synchronism due to pole slip. The CCT of Gen 1 is therefore 300 ms for case D. The CCTs for all the studied network operation scenarios is given in table 1. From fig. 12 it can be observed that for stable operation (FCT of 310 ms), the DC power flowing through the inverter of the VSC-HVDC scheme does not collapse to zero during the fault period. It can also be seen that the DC power of the VSC-inverter is instantly restored to 80% of its pre-fault value after the fault has been cleared. This is an indication that the response of the VSC controllers is faster, compared to those of the LCC controllers. This means that the retarding power contributed by the VSC-HVDC system is greater than that contributed by the LCC-HVDC system during the transient period.

Table 2: CCT Summary

Study Case	CCT
Case A	100 ms
Case B	130 ms
Case C	250 ms
Case D	300 ms

5 CONCLUSIONS

The results presented in section 4 show that the two HVDC schemes improve the transient stability of Gen 1 by absorbing part of the excess power supplied by the generators during the fault and transient periods, and therefore contributing to the system retarding power which allows the generators to maintain a stable state of operation. From the obtained results, it can further be concluded that the parallel VSC-HVDC scheme improves the transient rotor angle stability of the generator more compared to the LCC-HVDC scheme. This is so because, compared to the LCC-HVDC scheme, the VSC-HVDC scheme has the ability to improve the system synchronizing power more during and after the fault has been cleared. When a HVDC scheme is placed in parallel with HVAC transmission lines, and the converter controllers are set such that the amount of DC power flowing through the converters is well regulated in a way that the DC power contributes to the total retarding power of the system, the HVDC scheme can be used to improve the system CCT and therefore improving the transient rotor angle stability of the system generators.

6 APPENDIX

Table 3: Generator parameters

Parameter	Value
Nominal Apparent Power	950 MVA
Nominal Voltage	24 kV
Power Factor	0.9
Connection	YN
X_d	1.81 p.u.
X_q	1.71 p.u.
Inertia Constant	6.3
Stator Resistance (rstr)	0.003
Leakage Reactance (Xl)	0.15

Table 4: Transformer parameters

Parameter	Value
Rated Power	1000 MVA
Nominal Frequency	50 Hz
Rated Voltage (LV)	24 kV
Rated Voltage (HV)	400 kV
Vector Group and Phase Shift	YNd1
Positive Sequence Impedance	0.15 p.u.
Zero Sequence Impedance	0.15 p.u.

Table 5: AC transmission line parameters

Parameter	Value
Rated Voltage	400 kV
Rated Current	2 kA

Type	Overhead line
Positive and Negative Sequence Impedance	$R=0.05 \Omega/\text{km}$ $X=0.25 \Omega/\text{km}$
Zero Sequence Impedance	$R=0.2 \Omega/\text{km}$ $X=1 \Omega/\text{km}$

Table 6: LCC-HVDC scheme parameters

Converters			
Rectifier		Inverter	
Rated voltage	AC 375 kV	Rated AC voltage	210 kV
Rated voltage	DC 250 kV	Rated DC voltage	250 kV
Rated current	DC 2 kA	Rated DC current	2 kA
Rated power	600 MW	Rated power	600 MW
Control mode	Current	Control mode	voltage
Current set point	2 kA	Voltage set point	-1 p.u.
Firing angle	15 degrees	Extinction angle	20 degrees
Rectifier Transformer		Inverter Transformer	
Min. turns ratio	0.7	Min. turns ratio	0.9
Max. turns ratio	1.4	Max. turns ratio	1.3
Tap control mode	Alpha-control	Tap control mode	Gamma-control
DC Line			
Rated voltage	500 kV		
Rated current	2.5 kA		
Length	600 km		
Smoothing reactor	650 mH		

Table 7: VSC-HVDC scheme parameters

Converters			
VSC-Rectifier		VSC-Inverter	
Rated voltage	AC 155 kV	Rated voltage	AC 110 kV
Rated voltage per pole	DC 300 kV	Rated voltage per pole	DC 300 kV
Rated power	900 MVA	Rated power	900 MVA
Control mode	P-Q	Control mode	DC voltage
Active Power set point per pole	300 MW	Voltage set point	-1 p.u.
Modulation	Sinusoidal PWM	Modulation	Sinusoidal PWM
DC Line			
Rated voltage	300 kV		
Rated current	1.3 kA		
Length	400 km		

7 REFERENCES

- [1] P. Kundur, J. Paserba, V. Ajjarapu, G. Andersson, A. Bose, C. Canizares, et al., "Definition and classification of power system stability IEEE/CIGRE joint task force on stability terms and definitions," *Power Systems*, IEEE Transactions on, vol. 19, pp. 1387-1401, 2004.
- [2] "Proposed Terms & Definitions for Power System Stability," *Power Apparatus and Systems*, IEEE Transactions on, vol. PAS-101, pp. 1894-1898, 1982.
- [3] P. Anderson and A. Fouad, *Power system control and stability*. Hoboken: John Wiley & Sons, 2003.
- [4] S. Panda and R. N. Patel, "Improving power system transient stability with an off-centre location of shunt FACTS devices," *JOURNAL OF ELECTRICAL ENGINEERING-BRATISLAVA*, vol. 57, p. 365, 2006.
- [5] H. Wang and F. Swift, "A unified model for the analysis of FACTS devices in damping power system oscillations. I. Single-machine infinite-bus power systems," *Power Delivery*, IEEE Transactions on, vol. 12, pp. 941-946, 1997.
- [6] Kumar and G. Priya, "Power system stability enhancement using FACTS controllers," in *Emerging Trends in Electrical Engineering and Energy Management (ICETEEEM)*, 2012 International Conference on, 2012, pp. 84-87.
- [7] K N I Mbangula and I E Davidson, "Power System Modelling and Fault Analysis of NAMPOWER'S 330KV HVAC Transmission Line". *Journal of Energy and Power Engineering*, USA, Vol. 8, 2014, pp.1432-1442.
- [8] S. R. Kumar and S. S. Nagaraju, "Transient stability improvement using UPFC and SVC," *ARPN Journal of Engineering and Applied Sciences*, vol. 2, pp. 38-45, 2007.
- [9] J. Arrillaga, Y. H. Liu, and N. R. Watson, *Flexible power transmission: the HVDC options*. England: John Wiley & Sons, 2007.
- [10] K N I Mbangula and I E Davidson, "System Modelling and Fault Analysis of a HVAC Transmission Line Using DigSilent Powerfactory Software Tool". In *Proceedings of the 1st Eskom-EPPEI Students' Conference*, Midrand, May 5-6, 2014
- [11] C. Taylor and S. Lefebvre, "HVDC controls for system dynamic performance," *Power Systems*, IEEE Transactions on, vol. 6, pp. 743-752, 1991.
- [12] T. Machida, "Improving transient stability of AC system by joint usage of DC System," *Power Apparatus and Systems*, IEEE Transactions on, pp. 226-232, 1966.
- [13] K. To, A. K. David, and A. Hammad, "A robust co-ordinated control scheme for HVDC transmission with parallel AC systems," *Power Delivery*, IEEE Transactions on, vol. 9, pp. 1710-1716, 1994.
- [14] J. Hazra, Y. Phulpin, and D. Ernst, "HVDC control strategies to improve transient stability in interconnected power systems," in *PowerTech*, 2009 IEEE Bucharest, 2009, pp. 1-6.
- [15] Y. Phulpin, J. Hazra, and D. Ernst, "Model predictive control of HVDC power flow to improve transient stability in power systems," in *Smart Grid Communications (SmartGridComm)*, 2011 IEEE International Conference on, 2011, pp. 593-598.
- [16] Hammad, "Stability and control of HVDC and AC transmissions in parallel," *Power Delivery*, IEEE Transactions on, vol. 14, pp. 1545-1554, 1999.
- [17] K. P. Basu, "Stability enhancement of power system by controlling HVDC power flow through the same AC transmission line," in *Industrial Electronics & Applications*, 2009. ISIEA 2009. IEEE Symposium on, 2009, pp. 663-668.
- [18] K N I Mbangula and I E Davidson, "Detailed power system transient stability analysis using expert system concepts and stability improvement of a large multi-machine HVAC network using HVDC technologies," *Proceedings of the 23rd South African Universities Power Engineering Conference* Johannesburg, South Africa, 28-30 January 2015.
- [19] K N I Mbangula, I E Davidson and R Tiako, "Improving Power System Stability of South Africa's HVAC Network Using Strategic Placement of HVDC Links". *Proceedings of the CIGRE International Symposium 2015 Development of Electricity Infrastructures for Sub-Saharan Africa*, Cape Town, South Africa, October 26-30, 2015.

STABILITY ENHANCEMENT OF HVAC NETWORKS USING SUPPLEMENTARY CONTROLLERS WITH HVDC LINKS

S M'builu Ives*,** and AG Swanson**

**Eskom Holdings SOC Limited, Group Technology Engineering, South Africa E-mail: mbuilus@eskom.co.za.*

*** Discipline of Electrical, Electronic and Computer Engineering, School of Engineering, University of KwaZulu Natal, Durban.*

Abstract: This paper reflects the basic principles of supplementary control and demonstrates the controls of High Voltage Direct Current (HVDC) transmission together with the supplementary control of Power Oscillation Damping (POD) Controllers and Model Predictive Controllers (MPC), to improve power system dynamic performance through case studies using MATLAB. A four generator, two area AC network is simulated unstable and tested showing the impact of the HVDC link with two types of supplementary control and two different feedback control signals in improving system stability. The damping ratios and the mode decay time, with emphasis on the inter-area mode, are presented for the different case studies. The results indicate that the damping and the decay time improved with the integration of the POD and the MPC as supplementary control to the LCC HVDC link. Two feedback control signals are tested with both types of controllers to demonstrate the best signal for controller applications. The time domain simulations with faults introduced on the AC tie line demonstrate the improvement of mode decay or recovery time of the real power. The results of this study indicate that parallel HVDC links with supplementary control (POD and MPC) could be used to improve dynamic system performance. The MPC showed more flexibility as it maintains power system stability with changes in system operating conditions. This is however achieved through calculating the predicted control action with consideration to the applied system constraints on the control effort of the HVDC link.

Keywords: LCC, Stability, MPC, POD, HVDC, Power angle, firing angle, MATLAB, PST

1. INTRODUCTION

Published literature indicates that High Voltage Direct Current (HVDC) links may be used to enhance power system stability [1]. Inter area oscillations are a typical phenomenon in large interconnected systems and HVDC schemes can serve as powerful tools to damp these oscillations. Due to the various benefits; Eskom is studying the impact of implementing more HVDC schemes in various areas of the country. According to Witzmann, the damping of inter area oscillation between (Zimbabwe Electricity Supply Authority) ZESA and Eskom is demonstrated showing the improved damping with the introduction of a POD.

This supplementary controller assists by taking advantage of the quick change in HVDC power flow modulation and overload capability which improves the damping of the inter area oscillations thus making better use of the installed capacity[2]. This added advantage of network stability enhancement and fault current limiting further contributes to the techno-economic feasibility.

This study incorporates the application of power modulation control including the study of the POD performance and the study of the performance of a Model Predictive Controller (MPC). This MPC controls the power transfer through the HVDC link however the DigSILENT software was useful in understanding the problem of small signal stability and the integration of the LCC HVDC into the grid. It is limited due to the complexity of extracted state space model, around which the control design is based. Power Systems Toolbox (PST) was considered the most appropriate tool in investigating and designing the controllers as the state space model is directly accessible. In addition to the MATLAB tools used to design the controller, a number of design analysis tools are provided within the Power System Toolbox itself [3] [4]. A two area network with an integrated HVDC system is investigated. The model is commonly used in literature than that used by Rogers in reference [3]. The model was purposely unstable to allow a study of the effectiveness of the controllers. More details are found in reference [3].

2. METHODOLOGY

When designing a controller, it is important that the correct control signal and measurement points are selected as the mode disturbance must be observable and the control signal must be controllable.

The research methodology adopted for this study is as follows:

- The two area ac network as implemented and the performance specifications of this network is established by detailed modelling to represent an unstable network with the damping of the inter area mode being negative. The studies involved time domain fault analysis and eigenvalue analysis.
- A parallel HVDC link is connected across bus 7 and bus 9 and the changes in damping are studied. This study also involved time domain fault analysis. A disturbance is introduced and cleared in order to move the system out of steady state operating condition causing the rotors in the two areas to exchange the excess energy generated by the fault.
- A POD is introduced to the unstable base network as supplementary control and two different feedback signals are tested for effectiveness, the results are graphical displayed and analysed.
- Two different MPC cost functions are integrated into the unstable base case and the same two feedback signal are tested for effectiveness in terms of stability enhancements. The MPC is tuned accordingly in order to get the desired stable system.

3. BACKGROUND

The HVDC link cannot be entirely effective in bringing significant stability enhancement without the use of supplementary controllers. Therefore these supplementary controllers and the basic HVDC link are defined.

3.1 Basic LCC HVDC operation

Devices that may be used for economic design and improvement of system stability without compromising system performance include. The basic operation of the LCC HVDC bridges convert ac power into dc power at the rectifier terminal and the inverse at the inverter terminal to allow power flow to the ac network. The advanced controls keep the direct voltage at specific levels for the transfer of power from or into the ac grid. The setting of the firing angle determines the size and polarity of the direct output voltage after rectification.

The rectifier's output voltage differs to the inverter's input voltage due to a volt drop caused by the resistance of the transmission line [5].

HVDC control benefits: The HVDC control is the heart of the HVDC scheme as it is fast acting with controlled dynamics. HVDC control is more advanced than an AC system such as the control of electrical generators [5]. The correct design of HVDC control allows the fast acting control system to assist the weak ac network to recover from faults and as such avoiding voltage instability or voltage collapse as well as optimising the power flows within the network. The control requirement for HVDC power transmission related to control functionality is determined from the HVDC system objectives and varies between different projects. The control requirements include the following attributes [5]:

- Flexibility in the control of power,
- Fast control response,
- Stability under all operating conditions,
- Good transient recovery,
- Promotion of AC system performance,
- Robustness in the AC system events,
- Maintaining symmetrical valve firing in the steady state,
- Prevention of repetitive commutation failure in inverters,
- Reactive power control.

3.2 Power Oscillation damper

Damping of power oscillations can be achieved by using the ability of the HVDC scheme to control the active power accurately and fast. The HVDC link can be controlled by rapidly ramping the dc power down to reduce generation or load unbalance of the ac system on both sides. It can rapidly ramp up power through its overloading capabilities which can be used to assist to improve system stability [2]. A power oscillation damper, POD, can be used as a supplement control to modulate the HVDC power transmission and provide damping to the low frequency power oscillations. Power modulation function derives a measurement of the power oscillation in the connected ac system from the ac bus waveforms such as frequency and phase angle but the active power for the effective generator is the input signal selected in Figure 1.

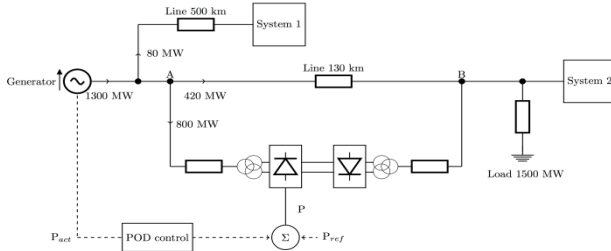


Figure 1: A typical system for damping power oscillation using HVDC POD control [2].

In Figure 1, if a fault is applied on line A-B, the HVDC keeps its scheduled power without any additional measures introduced, and the power oscillation depends on the natural system damping. The gain and the phase angle as well as the limits are added to the system configuration and the output signal is the reference of the power controller. It is then emphasised that increased system damping can be introduced by the appropriate power modulation of a parallel HVDC link [2]. The POD however is a damping controller that is designed around a linearized state space model for a nominal operating condition which is represented as a transfer function in most software packages. The feedback signals selected plays an important role in terms of its controllability. However based on the system residues taken on various control signals, the optimal control signal is the real power flow and angle difference across the ac corridor of Figure 2, and the compensator will be designed for both feedback signals to illustrate and confirm the selection of the signals

3.2.1 Damping criteria of a POD

When designing a POD, the following requirements must be met:

- Pole-placement: The closed-loop poles corresponding to the inter-area modes should be placed in the left half of the complex s-plane in order to confirm that the inter-area oscillations are stable and settle within a specified time [7]. Damping ratio: A minimum damping ratio must be maintained for critical modes but different utilities have different minimum values
- Settling time: The oscillations must settle out in a chosen time specified by the operating guidelines of a certain utility.
- Robustness: Robust control handles uncertain system parameters and disturbances outside the nominal operating point therefore making the controller more flexible [9].
- Control effort: Minimisation of control effort is essential to effectively utilise the dynamic range available for the highly expensive power electronic HVDC actuators with very limited short-term overload capacity [8].

- Controller structure: If there are multiple HVDC links in a system with individual PODs, it is important that the PODs are designed in a coordinated way to achieve the overall design specifications effectively; since there is a risk that the controller would not work in unison requiring larger control effort [8].

3.3 Model Predictive Control

The POD cannot be depended on entirely to maintain the stability of a power system after a large disturbance or changes in system operating conditions. The damping controllers are designed around a linearized state space model for a nominal operating condition. The MPC uses a process model to perform clear predictions of future plant behaviour and the calculation of suitable corrective control action needed to take the predicted output as close as possible to the desired target value thus providing high performance control systems [10].

According to reference [11], [12], [13], Model Predictive control (MPC), can manage control constraints and therefore shown to be valuable for adapting the reference settings for FACTS and HVDC to avoid transients. These strategies can maintain an acceptable system response without any prior knowledge of the disturbance [14]. The main advantage of MPC is that it considers the constraints on the control effort while calculating the predicted control action [6][15]. MPCs are software based and can be represented as cost functions.

3.3.1 MPC Cost Functions

Cost functions penalises deviations of the predicted control output from a reference trajectory and it predicts the deviations of each output over a predicted horizon. This cost function as seen in Equation 1, calculates the weighted sum of squared deviations from its reference. The goal of the controller is to minimize in Equation 1. Bemporad et al defines the cost function used in the MPC prediction to be [6][16]:

$$Vy(k) = \sum_{i=1}^P \sum_{j=1}^{ny} \{ j [r_j(k+i) - y_j(k+i)] \}^2 \quad [1]$$

Where k is the current sampling interval, $(k+i)$ is a future sampling interval (within the prediction horizon), P is the number of control intervals in the prediction horizon, ny is the number of plant outputs, j is the selected output, and the term $[r_j(k+i) - y_j(k+i)]$ is a predicted deviation for output j at interval $k+1$.

However this paper will use a cost function to an implemented MPC in order to adapt the current order (rectifier) of a LCC HVDC as a corrective control scheme. The objective is to reduce the loading of the AC tie line when exposed to various operating conditions. The

current order (rectifier) of the LCC HVDC is the control input of the proposed controller.

At every discrete time instant k the MPC algorithm calculates a sequence of control actions that minimizes a certain cost function over a time horizon P . The first control action of this sequence is applied at instant k and at the next time step the process is repeated.

4. CHARACTERISTICS OF THE STUDY SYSTEM

4.1 The Two Area System unstable Network

The network consists of two similar areas connected by weak parallel ac ties, as shown in Figure 2. Each area consists of a set of coupled generator units, each having a rating of 900 MVA [1]. The generators, transformers and transmission system parameters are found in reference [1].

The system operating within area 1, exporting 600MW to area 2 are electrically loaded according to reference [1]. The generators are equipped with an IEEE type DC1A DC excitation system model [1]. The loads of areas 1 (L_7) and 2 (L_9) are 976 MW and 1767 MW respectively. The Cigre benchmark model is integrated between Bus 7 and Bus 9. The model represents a monopolar 500 kV with 12-pulse converters at both rectifier and inverter ends. The location was selected according to reference [17] as it demonstrates that a path with the most inter-area oscillation content is referred to as the ‘dominant oscillation path’ of the network. In this study the HVDC was transmitting approximately 100 MW of power, the inverter properties: DC voltage of 504.3 kV, gamma /extinction angle of 18 deg and the line current of 0.2 A and the rectifier properties: DC voltage of 504.466 kV, Alpha angle of 29.3212deg

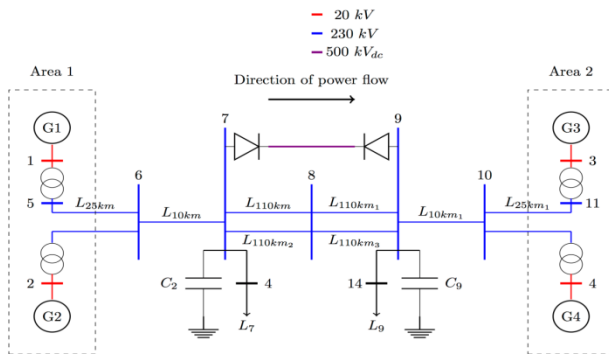


Figure 2: Two Area Network [1]

The load flow and eigenvalue analysis of the power system were performed where the inter-area and local modes were identified.

- Figure 3 shows the unstable network under heavy loading after an event/fault has been applied.
- Figure 4 shows the eigenvalue analysis (inter area mode of oscillation) of the unstable network

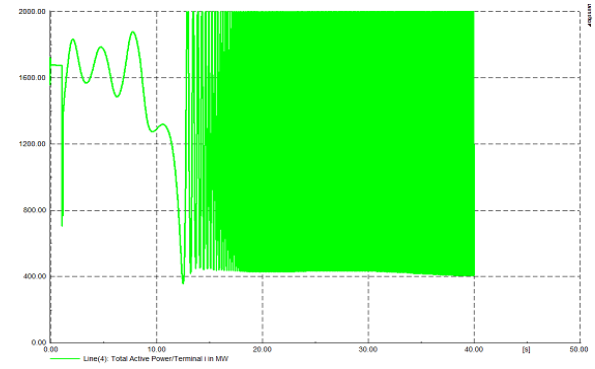


Figure 3 : Time domain of the Real Power: Heavy Loading between bus 7-9

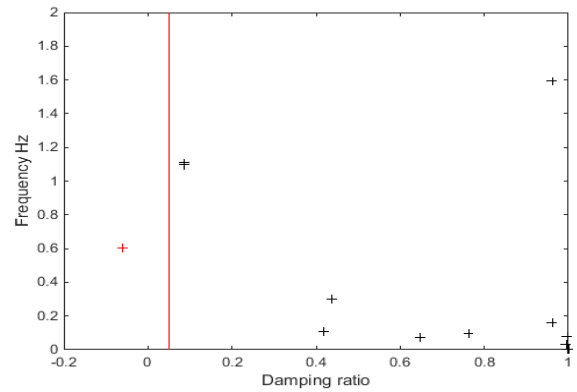


Figure 4: Eigenvalue analysis of the unstable network

Modes with a damping ratio of less than 3% can be accepted but with caution as it may lead to instability [7]. The minimum acceptable level of damping is not clearly known but a damping ratio which is negative causes the mode to become unstable [1].

4.2 The POD design structure

The supplementary controller was used to move the unstable mode by moving the poles to the left half of the plane. Decent separation can be attained by a suitable choice of feedback signals or by retuning existing controllers in the system [18]. The feedback control signals that were reviewed are real power L10km between bus 6 and 7 (as per Figure 2) and voltage angle difference (between bus 7 and 9 as seen in Figure 2). The sensitivity of the system to dynamic feedback can be achieved through a transfer function (POD) where the system stability is taken back to steady state or nominal operating point. This transfer function consists of a washout filter and a lead compensator. The washout filter eliminates the effect of the steady state voltage magnitude and the control moves at high frequencies.

The lead/lag compensator has the effect dragging the poles into the left half plane and this positive shift on the phase has an additive effect of the open loop transfer

function, hence the term lead compensator. However the poles and zeros must be designed correctly such that they bring damping to the inter area mode. The lead/lag compensator adds up to 90 degrees (and with positive feedback at the inter area frequency; it is used to stabilise the mode. This is seen in the following transfer function (POD):

$$G(s) = K \left(\frac{T_w}{1+sT_w} \right) \left(\frac{1+sT_2}{1+sT_1} \right) \left(\frac{1+sT_2}{1+sT_1} \right) \quad [2]$$

The transfer function has the following parameters for the selected signals as seen in Table 1.

Table 1: POD transfer function details feedback signals

Term	Real Power	Angle
T1	0.04	0.05
T2	0.02	0.02
Tw	10	10
K	0.6	2.4

4.3 The MPC design structure

MPC allows for the current timeslot parameters to be optimised while keeping the future timeslot in account through parameter optimisation of a known time horizon; however the implementation is applied on the current time interval with consideration to constraints. The MPC can however expect future events and take control actions accordingly [19]. The other benefits are seen below

- It can be used to handle a multivariable system
- Permits constraints to be enforced on both Manipulated variable (MV) and Controlled variable (CV) in order to operate closer to constraints.
- Permits time delays, inverse response, difficult dynamics, changing control objectives and sensor failure. (predictive) [10].

The MPC is designed using the Matlab. The number of each subclass of signals specifications such as Manipulated variables and unmeasured disturbance is viewed as seen in Figure 4.

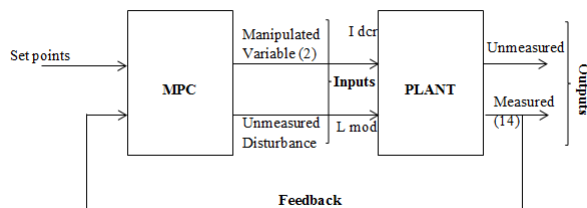


Figure 4: The MPC structure for the study

4.3.1 The MPC cost functions

Two alternative cost functions have been considered in the paper with selected feedback signals based on input-output controllability analysis relating to its residue and the location is based on the dominant oscillation path [17]. The added benefit of an MPC is its ability to manage control constraints, while taking note of future events and implementing in the current timeslot without any computation complexity. The real power order constraints set to ≥ 20 MW. The cost functions are seen below in Equation 3 and Equation 4 with the parameters seen in Table 2

$$Vy(k) = \sum_{i=1}^p \{j[pf2(L110km3)[pf2(L110km3)ss]\}^2 \quad [3]$$

$$Vy(k) = \sum_{i=1}^p \{j[Vad B7-B9(k+i)] - [Vad B7-B9 ss]\}^2 \quad [4]$$

Where pf2 is the real power on the receiving end of the line L110km3 and Vad is the angle difference between bus 7 and 9.

Table 2: The MPC Parameters

Parameters	Quantity
Constraints on the manipulated variable	Min = 0; Max = 20; RateMin = -1; RateMax = 1
Weighting on manipulated variable	1
Rate Weight	0.1
Prediction horizon	10
Control horizon	3
Nominal values	As per state space model

Equation 3, shows the cost function where the real power across the AC tie line (L110 km3 on the receiving terminal of the transmission line as per Figure 2) is selected as the output and they capture the deviations from its steady state in order to control it to its reference steady state value by adjusting the current order of the LCC HVDC converter scheme. Equation 4 shows the voltage angle across the corridor (voltage angle difference between bus 7 and 9) as per Figure 2 and it functions the same way hence a comparison of the two cost functions will be shown with the effect on the AC tie lines after a disturbance. The MPC will however operate more effectively when tuned by adjusting the controller's settings.

5. RESULTS AND DISCUSSION

Non-linear time domain simulations were performed to validate the dynamic response after a disturbance for the following cases. The effectiveness is based on the mode decay time which is the time taken for the real power signal to return to its steady state after the disturbance:

- The POD integrated into an unstable base case network- real power and voltage angle difference feedback signals
- The MPC integrated into an unstable base case network- real power and voltage angle difference feedback signals

5.1 Case 1: The POD integrated into the unstable base case network- real power feedback signal and voltage angle difference across the AC corridor

The feedback signals are real power at Line L10km (as per Figure 20) and the voltage angle difference (between bus 7 and 9 as seen in Figure 20). The damping ratio has improved to 0.36 (as seen in Figure 37) which is a significant improvement and is visible in the impulse response (time domain simulation) which relates the decay time of an oscillation after an event. The mode decay time in Figure 5a is approximately 26s and is a major improvement when compared to the unstable Base case in Figure 3a. With the integrated POD, the real power signal settles about 26s after the event.

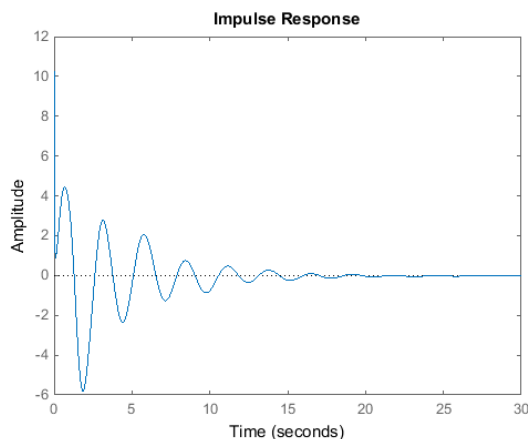


Figure 5 a: Impulse response with and without POD - Power signal

The damping ratio increased to 0.42 of the inter area mode which again correlates to a reduction in the mode decay time of 5s as the power of system settles in 21s after the disturbance (fault or step change). This is seen in the time domain response plots in Figure 5b

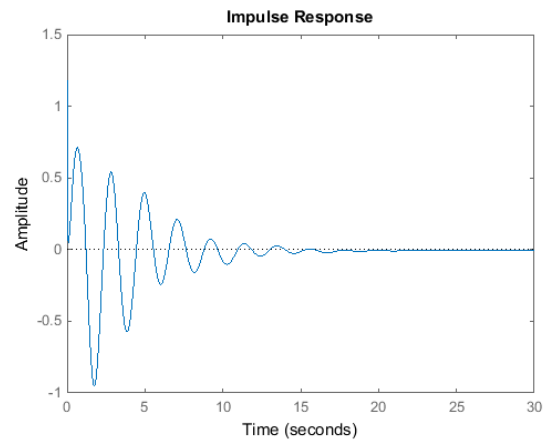


Figure 5 b: Impulse response with and without POD - Voltage angle difference signal

5.2 The MPC integrated into an unstable base case network- real power and voltage angle difference feedback signals

The disturbance or impulse are applied on the at Bus 7 (as per Figure 20) The first cost function (Equation 3) using real power across the AC tie has poorer performance as it does not restore the DC voltage of the Rectifier to almost its pre event value (504.466 kV) but on the other hand, the second cost function (Equation 4) restores the DC voltage of the Rectifier to its pre event value (504.267 kV) in a shorter period of time (Figure 6b thus showing superior performance over the first MPC (Figure 6a) based on the real power. The first MPC cost function using real power across the AC tie has inferior performance as it does not restore the DC voltage of the Rectifier to almost its pre event value (504,466 kV) but however the second MPC cost function restores the DC voltage of the Rectifier to its pre event value (504.267 kV) in a shorter period of time (18s) thus showing a slightly better performance over the first MPC based on the real power (23s). These MPC Cost functions penalises deviations of the predicted control output from a reference trajectory and it predicts the deviations of each output over a predicted horizon.

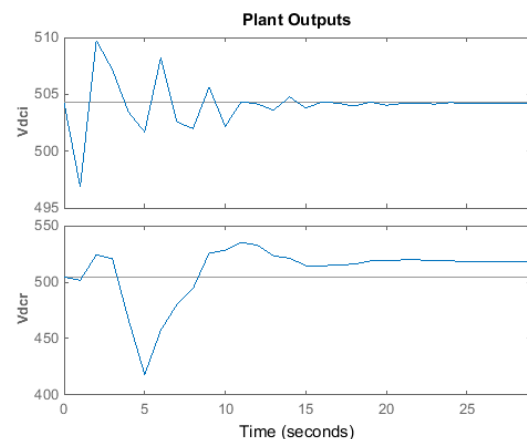


Figure 6 a: The HVDC voltage: Rectifier and Inverter: Real power.

Figure 7 below, shows the behaviour of the dc line current which is the current order to the Rectifier after the event. It is clearly evident from Figure 7 that the voltage angle difference feedback signal has a lower overshoot value of 1.22 compared to the Real power which was 1.35 but this control action is understood from the real power output response as seen in Figure 8 where the real power (Pf2-13 is Line110km1 between bus 8 and 9 which is the line receiving real power as seen in Figure 2) is observed.

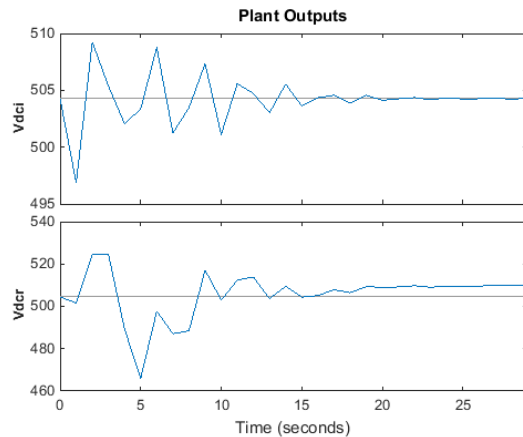


Figure 6b: The HVDC voltage: Rectifier and Inverter: Voltage angle difference

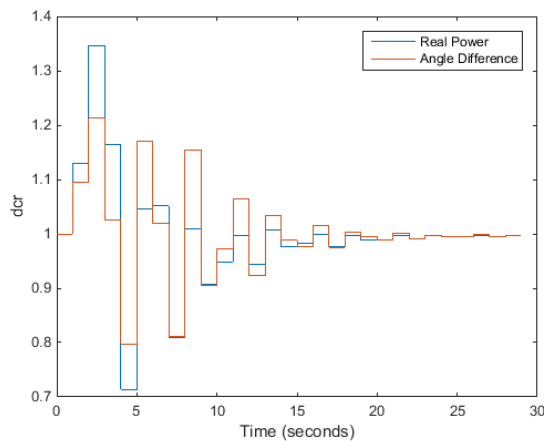


Figure 7: A Comparison of the two feedback signals input response

The comparison of the two feedback signals clearly show that the voltage angle difference is a slightly more effective signal in enhancing stability as the mode decay time is approximately 18s (voltage angle difference across the AC corridor) compared to 23s (Real power across the AC tie) however the real power feedback signal does return to steady value as seen in Figure 8. The lower overshoot of the voltage angle difference feedback signal is again seen in the Figure 8 and this will prevent the premature activation of over current protections on the transmission lines.

However, the MPC is effective in automatically relieving the burden on the AC lines by adapting the HVDC current order to rectifier after a load event or disturbance. Consequently to this, the amplitude of the rotor angle oscillations of the generators decreased with MPC based corrective control therefore enhancing small signal stability

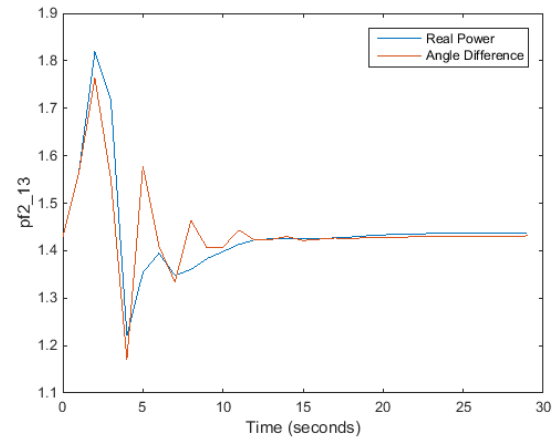


Figure 8: A Comparison of the feedback signals real power output response

6. CONCLUSION

This paper presented the use of supplementary control by using power oscillation damping control and predictive control through single LCC HVDC links on a simulated unstable system. The POD design specifications and MPC design structure was outlined. The POD design represented as a transfer function was defined and the MPC represented as cost functions are explained. Simulations studies with two feedback control signals are demonstrated. Stability studies using eigenvalue analysis and time domain plots showed the effectiveness of the POD and MPC with two different feedback control signals i.e. real power across the AC tie and voltage angle difference across the AC corridor.

The voltage angle difference feedback control signal proved to be more sensitive to changes in the system and contributed to improving system stability, hence increased damping and reduced settling/mode decay time after a disturbance or event is evident. The MPC using the Voltage angle difference proved to be the more effective by relieving the burden on the AC lines through the adjustment of the HVDC link controls following a disturbance as a result power system stability is sustained and the MPC's flexibility to new operating conditions while considering system constraints is demonstrated through the calculation of the predicted control action required.

As Eskom is pursuing investing in HVDC lines at various locations, this analysis presented will be used to facilitate

the process of supplementary controllers being selected to enhance system stability with the performance of parallel HVDC links in terms of the techno-economic feasibility. Eskom will then have the full advantage of transporting bulk power but at the same time mitigating the effects of small signal stability on the National grid and internationally under any operating conditions and considering system constraints.

7. FUTURE STUDIES

The Model predictive control should be analysed on a more complex network which is more realistic. The benefits and factors affecting predictive control performance will be noted for possible future installations of HVDC schemes. The models will be validated against literature.

8. ACKNOWLEDGEMENTS

The authors would Eskom for their support of the university through the Eskom Power Plant Engineering Institute programme.

9. REFERENCES

- [1]. P. Kundur. *Power system stability and Control*, 1st ed. McGraw-Hill, 1994
- [2]. R.Witzmann, Damping of Inter area modes
- [3]. G.Rodgers, Power System oscillations, 1999
- [4]. J.H.Chow and K.W.Cheung, "A toolbox for power system dynamics and control engineering education and research," IEEE Transactions on Power Systems, vol. 7, no. 4, pp. 1559 - 1564, 1992.
- [5]. Eskom Power Series, *HVDC Power Transmission , Basic principles, planning and convertor technology*, Crown Publications, ISBN 978-0-9921781-0-9, Johannesburg, 2012
- [6]. Adaptive HVDC control System and Power Oscillation Damping Methods: Theoretical Developments. EPRI, Palo Alto, CA:2012.1024321
- [7]. Cigré task force 07 of advisory group 1 of study committee 38. Analysis and control of power system oscillation Cigré, Dec 1996
- [8]. B.Pal and B.Chaudhuri, Robust Control in Power Systems, New York: Springer Science+Business Media, Inc., 2005.
- [9]. J.Ma, T.Wang, W.Yan and Z.Wang, "Design of wide-area robust damping controller based on the non-convex stable region for inter-area oscillations", Beijing: State Key Laboratory of Alternate Electrical Power System with Renewable Energy Sources, North China Electric Power University, 2013
- [10]. None, "Model Predictive Controller," Chemical Engineering department, 2002.
- [11]. D.Q.Mayne and J.B.Rawlings, Model predictive control: theory and design, Madison, Wis.: Nob Hill Pub., 2009.
- [12]. J.J.Ford, G.Ledwich and Z. Dong, "Efficient and robust model predictive control for first swing transient stability of power systems using flexible AC transmission systems devices," IET Generation, Transmission and Distribution, vol. 2, no. 5, pp. 731-742, 2008.
- [13]. Y.Phulpin, J.Hazra and D.Ernst, "Model predictive control of HVDC power flow to improve transient stability in power systems," in IEEE International Conference on Smart Grid Communications (SmartGridComm), Brussels, 2011.
- [14]. M.Glavic, D.Ernst and L.Wehenkel, "A reinforcement learning based discrete supplementary control for power system transient stability enhancement," Engineering Intelligent System for Electrical Engineering and Communications, vol. 13, no. 2, pp. 81-88, 2005.
- [15]. L.A.Wehenkel, Automatic learning techniques in power systems, Boston: Mass :London Kluwer Academic, 1998.
- [16]. A.Bemporad, M.Morari and L.Ricker, Model Predictive Control Toolbox- Getting Started Guide, Natick, MA: MathsWorks, 2015.
- [17]. S.Mvuyana, J.VanColler and T.Modisane, "Identification of Power System Oscillation Paths in Power System Networks," in 22nd South African Universities Power Engineering Conference, Kwazulu Natal, 2013.
- [18]. A.M.Kulkarni and U.P.Mhaskar, "Power Oscillation Damping Using FACTS Devices: Model Controllability, Observability in Local Signals and Location of transfer function zeros," IEEE, vol. 21, no. 1, 2006.
- [19]. None, "<https://en.wikipedia.org/wiki/Modelpredictivecontrol>," Wikipedia, 2015. [Online]. [Accessed 18 August 2015].

Finite Element Analysis of Mechanical Oscillation of Power Line Conductors

E.E. Ojo¹ and M. N. Ijumba²

¹Electrical Engineering Discipline, School of Engineering,
University of KwaZulu-Natal, Westville Campus,
Private Bag X54001, Durban 4001, South Africa
E-mail: st_evansojo@yahoo.co.uk

²Electrical Engineering Discipline, School of Engineering,
University of KwaZulu-Natal, Howard College Campus,
Private Bag X54001, Durban 4001, South Africa
E-mail: mutatinak@gmail.com

Abstract: Wind-induced vibration has long been a topic of interest in the area of power line design. This phenomenon has been extensively investigated by researchers using concepts from aerodynamics, fluid mechanics, rigid body dynamics and vibration analysis. These investigations have provided a better understanding of the conductors' dynamic behaviour. Various analytical models have been developed, describing the dynamic characteristics of conductors' wind-induced vibration. Research investigations have shown that wind-induced vibration that occurs on overhead transmission line is a very complex phenomenon and the conductor response exhibits non-linear characteristics, hence to obtain an exact analytical solution to conductor vibration has remained elusive. Approximate solutions have become the alternative.

1 INTRODUCTION

In the 1920s the phenomenon of wind induced vibration was noticed on transmission lines. This has attracted numerous researches [1][2][3][4]. In an overhead transmission lines, the conductor is most flexible components, hence is most susceptible to the dynamic forces of nature such as wind. Also the conductor is most expensive component of any power line. Base on this, adequate attention is given because of the colossal cost that will be incurred if the conductors are damaged. Most damage result from the mechanical vibration due to the aerodynamic effect from wind.

Transmission line conductor is a flexible due structure due to its helical arrangement, making more prone to vibrations. This vibration which is cyclical in nature and with the static stress tends to produce a bending stress on conductor. This bending stress, if not controlled eventually result to fatigue failure.

The purpose of this paper is to present a developed model finite element analysis model for the conductor. This model will be used to determine the natural frequencies, mode shapes and the free vibration response

2 ANALYTICAL MODEL

Most researches that are carried out to investigate this phenomenon of conductor vibrations, model the

conductor either as taut string or beam. Most often, the vibrating conductors are modeled as a simply supported beam with acceleration, variable linear density, and variable section modulus, subjected to either point or distributed loading. Modelling the conductor as a simply supported beam, the equation of motion of the conductor with axial loading (tensioned at both ends) as described in [3][4][5][6][7][8][9][10] is given as

$$EI \frac{\partial^4 y(x,t)}{\partial x^4} - S \frac{\partial^2 y(x,t)}{\partial x^2} + \rho A \frac{\partial^2 y(x,t)}{\partial t^2} = f(x,t) \quad (2)$$

Where EI is flexural rigidity or bending stiffness, S is the tension, ρ is the density, $y(x, t)$ is transverse displacement, A is the cross-sectional area, $f(x, t)$ is the external force, defined as $f(x, t) = F \sin \omega_d t$

Let $y(x, t) = X(x)e^{-i\omega t}$ $i = \sqrt{-1}$

The homogenous part of the equation

$$EI \frac{\partial^4 y(x,t)}{\partial x^4} - S \frac{\partial^2 y(x,t)}{\partial x^2} + \rho A \frac{\partial^2 y(x,t)}{\partial t^2} = 0$$

Boundary conditions:

$$y(0, t) = \frac{\partial y(0, t)}{\partial x} = 0, \text{ at } x = 0$$

$$y(l, t) = \frac{\partial y(l, t)}{\partial x} = 0, \text{ at } x = l$$

Initial conditions:

$$y(x, 0) = y_0(x) \quad \text{at } x = 0$$

$$\frac{\partial y(x, 0)}{\partial t} = \dot{y}_0(x) \quad \text{at } x = 0$$

To find the natural frequencies are by finding the solution to equation (2), assuming that the mode shape is the same as the pinned-pinned eigenfunction with no external force.

$$Y(x, t) = \sin \frac{n\pi x}{l} \cos \omega_n t \quad (3)$$

The natural frequencies becomes

$$\omega_n^2 = \left(\frac{n\pi}{l} \right)^2 \frac{S}{A\rho} + \left(\frac{n\pi}{l} \right)^4 \frac{EI}{A\rho} \quad (4)$$

In [11], it was inferred that to improve on this conductor models, some form of non-linear concepts should be introduced when modelling the conductor dynamic behaviour. The mechanical oscillation of conductors is characterized by non-linearity either from its geometry or damping. In the case of Aeolian vibration, because of

the small displacement, the non-linearity is mostly attributed to its damping mechanism.

Based on the work of C. Hardy [12], when the conductor flexes, the strands of the conductor slip against each other; this relative motion generates frictional forces that provide damping. Secondly, conductors can damp out energy by internal energy losses at microscopic (molecular) level within the core and individual strands of the conductor and this known as metallurgical or material damping. The combination of these energy dissipative processes by a conductor is known as conductor self-damping. During bending, the energy dissipation due to frictional effects around the area of contacts induced by the sinusoidal forcing function coupled with the material damping tends to limit the amplitude of vibration.

Considering the conductor as visco-elastic beam and with the two forms damping as explained in [11]. If the conductor obeys the stress-strain relationship as given below

$$\sigma = E\varepsilon + \beta \frac{\partial \varepsilon}{\partial t}$$

Hence the equation of motion for the transverse vibration of the conductor will be the form

$$EI \frac{\partial^4 y(x,t)}{\partial x^4} - S \frac{\partial^2 y(x,t)}{\partial x^2} + \beta I \frac{\partial^5 y(x,t)}{\partial x^4 \partial t} + \quad (5)$$

$$C \frac{\partial y(x,t)}{\partial t} + \rho A \frac{\partial^2 y(x,t)}{\partial t^2} = f(x,t)$$

Using the Rayleigh Method for the above damped nonlinear equation for the conductor, the damping coefficient is obtained as

$$\zeta_n = \frac{\int_0^l \left(\beta EI(x) \left[\ddot{X}_n''(x) \right]^2 dx + C \left[\dot{X}_n''(x) \right]^2 dx \right)}{2 \int_0^l \rho A(x) \dot{X}_n''^2(x) dx}$$

3. FINITE ELEMENT METHOD

The concept of finite element method is very powerful numerical tool for the evaluation of dynamic systems problems such power line Aeolian vibration. This method is a computational technique that can be employed to evaluate the dynamics of systems response. Though, a conductor is continuous system but to analyse the transverse vibration using the FEA method involves discretizing the system into its finite elements. Then equations will be obtained for each finite element. Assembling these finite element equations are used to formulate equations that will be used to generate equations for the inertial, stiffness, applied force, and damping forces in matrix and vector form. In system dynamics, the mass, stiffness and damping matrices of the system are required to solve the required dynamic response and then determine the dynamic parameters.

3.1 Finite Elements

The FEA for the conductor formulation starts with the standard finite element formulation for the beam shown below. In this method the space dimension was approximated by the higher-order approximation finite element (cubic polynomial) with respect to time i.e. cubic Hermits polynomial. To this regard, the finite element interpolation functions as time dependent such that u is approximated by

$$u = \sum_{i=1}^4 c_i N_i = c_1 x^3 + c_2 x^2 + c_3 x + c_4 \quad (6a)$$

$$u(x) = N_1(x)u_1 + N_2(x)\theta_1 + N_3(x)u_2 + N_4(x)\theta_2 \quad (6b)$$

Where

$$N_1(x) = 1 - \frac{3x^2}{L^2} + \frac{2x^3}{L^3}, \quad N_2(x) = x - \frac{2x^2}{L} + \frac{x^3}{L^2}$$

$$N_3(x) = \frac{3x^2}{L^2} - \frac{2x^3}{L^3}, \quad N_4(x) = -\frac{x^2}{L} + \frac{x^3}{L^2}$$



Fig 1a: Straight Beam

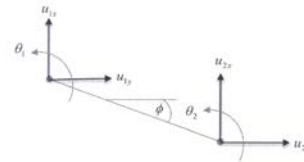


Fig 1b: Deformed Beam Element

Thus if $[N] = [N_1, N_2, N_3, N_4]$

Then $[A] = [N'_1, N'_2, N'_3, N'_4]$ and $[B] = [N''_1, N''_2, N''_3, N''_4]$ (7)

3.2 Finite Element Formulations

Some physical phenomena can be described by differential equation that relates certain quantities to their derivatives with respect to time and space variables. The weak formulation is used to derive the finite element equation and this is obtained from the equation of motion describing conductor vibration. The Galerkin's method (method of weighted residual) is then used to develop the finite element formulation for the conductor. By using the Galerkin's variational principle to this time dependent problems, considering the boundaries conditions, the finite element model is obtained. Hence, damped equation (5) for the transverse vibration of the conductor is used. The weak formulation for the finite element equation is obtained firstly by multiplying equation (5) by the finite element interpolation functions defined by equation (6) to obtain:

$$\int_0^l \left(EI \frac{\partial^4 y}{\partial x^4} u - S \frac{\partial^2 y}{\partial x^2} u + \rho A \frac{\partial^2 y}{\partial t^2} u - fu \right) dx = 0 \quad (8)$$

Secondly, carrying out the integration by parts twice on equation (8) and taking into account the finite-element

discretize model as defined by the number of finite elements in the system domain.

Hence, the resultant equation is obtained as:

$$EI \int_{\mathfrak{R}} \frac{\partial^2 y}{\partial x^2} \cdot \frac{\partial^2 u}{\partial x^2} dx + S \int_{\mathfrak{R}} \frac{\partial y}{\partial x} \cdot \frac{\partial u}{\partial x} dx + \beta I \int_{\mathfrak{R}} \frac{\partial^3 y}{\partial x^2 \partial t} \frac{\partial^2 u}{\partial x^2} + \quad (9)$$

$$C \int_{\mathfrak{R}} \frac{\partial y}{\partial t} u + \rho A \int_{\mathfrak{R}} \frac{\partial^2 y}{\partial t^2} u dx - \int_{\mathfrak{R}} f u dx = 0$$

Where \mathfrak{R} is the element domain

From the weak formulation, the equations for the finite element in terms of the stiffness, mass, damping matrices and force vector are given as:

$$[K^e] = EI \int_{\mathfrak{R}} \frac{\partial^2 y}{\partial x^2} \cdot \frac{\partial^2 u}{\partial x^2} dx + S \int_{\mathfrak{R}} \frac{\partial y}{\partial x} \cdot \frac{\partial u}{\partial x} dx \quad (10a)$$

$$[M^e] = \rho A \int_{\Omega} \frac{\partial^2 y}{\partial t^2} u dx \quad (10b)$$

$$[F^e(t)] = \int_{\mathfrak{R}} f u dx \quad (10c)$$

$$[D^e] = \beta I \int_{\mathfrak{R}} \frac{\partial^2 y}{\partial x^2} \cdot \frac{\partial^2 u}{\partial x^2} dx + C \int_{\mathfrak{R}} \frac{\partial y}{\partial t} u dx \quad (10d)$$

Using equations (7), equations (10) become:

$$[K^e] = \left(EI \int_{\mathfrak{R}} B^T B + S \int_{\mathfrak{R}} A^T A \right) y \quad (11a)$$

$$[M^e] = \left(\rho A \int_{\mathfrak{R}} N^T N \right) \ddot{y} \quad (11b)$$

$$[F^e] = \int_{\mathfrak{R}} f [N]^T \quad (11c)$$

$$[D^e] = \left(\beta I \int_{\mathfrak{R}} B^T B + C \int_{\mathfrak{R}} N^T N \right) \dot{y} \quad (11d)$$

Considering the equations (11d), it can be seen that before the equation can be implemented the damping constants have to be determined first. Based on the classical work done by H.H Cudney and D.J. Inman [13], they outlined the procedures to estimate the values for each damping model and also for combination of the both models. The evaluation of the damping constants C and β is done by the least squares method also known as the pseudo-inverse routine. For the values of both C and β is evaluated by

$$\begin{bmatrix} \zeta_1 \\ \zeta_2 \\ \vdots \\ \zeta_n \end{bmatrix} = \begin{bmatrix} \frac{1}{2\omega_1} & \frac{\omega_1}{2} \\ \frac{1}{2\omega_2} & \frac{\omega_2}{2} \\ \vdots & \vdots \\ \frac{1}{2\omega_n} & \frac{\omega_n}{2} \end{bmatrix} \begin{bmatrix} C \\ \beta \end{bmatrix} \quad (12)$$

The values for damping coefficients and natural frequencies can be obtained from the experimental values such those document in [11].

4 The System Matrix

Conductor transverse vibration is a classic example of such practical problems in which in the differential

equation, position and time dimension have to be considered. Hence, the method use for the finite element approximation of the dynamic type element of time and space dependent equation (time dimensions). The conductor vibration can be model by a beam element.

When strung under tension, the overhead transmission lines conductors support its weight thereby sagging and sag/span ratio depends on the axial tensions at both ends. When subjected to transverse vibration, each member of the conductor is subjected to both axial and bending loads. Due to fact that the sag/span ratio is small, the axial and transverse deformations can be decoupled. Therefore, modelling for transverse vibration for pure bending only, the axial effect can be neglected.

Fig. 3 shows the discretized model of a single span of conductor. The conductor is discretized into n number of nodes and $(n-1)$ number of elements.

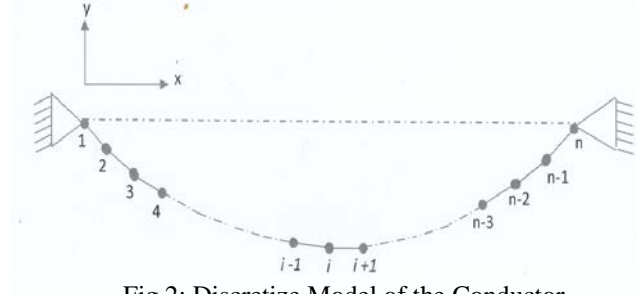


Fig 2: Discretize Model of the Conductor

The deformed beam element shown fig. 1b can mapped to form discretize model shown above. To achieve this, the 2 D beam formulation done for the straight beam (fig 1a) is extended to 2-dimensional cases (fig 1b) of conductor on the bases that the axial deformation is neglected. The displacement of a 2D beam element expressed in the 2D global coordinate system for the conductor can be written as follows

$$u = \begin{bmatrix} u_1 \\ \theta_1 \\ u_2 \\ \theta_2 \end{bmatrix} = \begin{bmatrix} \Delta x & \Delta y & 0 & 0 & 0 & 0 \\ 0 & 0 & 1 & 0 & 0 & 0 \\ 0 & 0 & 0 & \Delta x & \Delta y & 0 \\ 0 & 0 & 0 & 0 & 0 & 1 \end{bmatrix} \begin{bmatrix} u_{x1} \\ u_{y1} \\ \theta_1 \\ u_{x2} \\ u_{y2} \\ \theta_2 \end{bmatrix} \quad (13)$$

Where $\Delta x = \frac{x_2 - x_1}{L^e} = \cos \phi = c$ and

$$\Delta y = \frac{y_2 - y_1}{L^e} = -\sin \phi = -s$$

Using the deformed finite element shown above with reference to the beam element the stiffness matrix, mass matrices and load vector for the conductor are obtained as follows

$$K_C^e = [T]^T [K_B^e] [T] \quad (14a)$$

$$K_C^e = [T]^T [M_B^e] [T] \quad (14b)$$

$$f_C^e = [T]^T [f_B^e] \quad (14c)$$

Where $[T]$ is transformation matrix and is defined as

$$[T] = \begin{bmatrix} c & -s & 0 & 0 & 0 & 0 \\ 0 & 0 & 1 & 0 & 0 & 0 \\ 0 & 0 & 0 & c & -s & 0 \\ 0 & 0 & 0 & 0 & 0 & 0 \end{bmatrix}$$

The assembly of finite element equations derived above to form the system finite element equation requires the satisfaction of the boundary conditions as defined in the diagram of the discretize domain (figure 2). Therefore, the assembled global equation must satisfy the boundaries conditions of simply supported beam i.e.

$$u_1 = \theta_1 = u_n = \theta_n = 0$$

The above transformation results to damped equation for the transverse vibration of conductor. Thus, the system matrix equation was obtained as:

$$[M]\{\ddot{y}\} + [C]\{\dot{y}\} + [K]\{y\} = [F] \quad (15)$$

5 Matlab Implementation

A modified MATLAB code [14] for beam element was used to simulate above finite element equation for the conductor. The code was modified to include the transformation function. Code was written to determine the conductor static profile from which the coordinate used to determine the angle of deformation along the sag. Another code was written based on modal analysis to obtain the eigenvalue, mode shape and natural frequencies. Also another code was developed, using the least square method to obtain the damping constant (β and C) according to equation (12).

These Matlab programs were implementation and used to simulate this numerical problem developed above for the vibrating conductor. The code was simulated to find the solution to the displacement field developed from FEA. The implementation was done for Tern conductor and physical properties are document in [11].

This computer program simulation was used to generate the dynamic response for free vibration for three different axial tensions. The MATLAB results and the work that is documented in [15] were compared.

6 RESULTS

The finite element analysis modeling of transmission lines conductor simulation can be found in [14], in which the simulations of the conductor vibrations were done using ABAQUS software. In this study Matlab software was used for the conductor vibration simulation for Aeolian vibration. Thus, finite element analysis for the mechanical oscillation for transmission line conductors was simulated using the code for deformed beam properties.

In similar manner as done for conductor vibration using ABAQUS, the eigenvalues were searched and computed in the frequency range for both conductors. For purpose of comparison for the Tern conductor, the first ten

natural frequencies for the conductor were obtained and are recorded in table 1 in comparison to the values obtained for the analytical model at tensions 20%, 25%, and 30% of its UTS.

To compute the damping constants, the modal damping from the experimental values in [11] was used. Using the experimental resonance frequencies values, the least squares method (pseudo-inverse routine) was used to compute the damping constants using Matlab. These obtained values were then used as proportional damping constants to simulate the conductor vibration for damping.

The Matlab simulation results for the eigenvalues and the natural frequencies for both conductors are presented in the tables below.

Table 1: The comparison of natural frequencies values obtained from analytical, FEM and experimental result for Tern conductor

Table 1a: Natural Frequencies at 20% UTS

Mode	Natural Frequency (Hz) 20% UTS		
	Analytical Model	FEM	Exp. value
1	4.521	4.450	5.237
2	9.044	8.900	10.212
3	13.570	13.354	14.613
4	18.099	17.810	19.13
5	22.634	22.272	22.929
6	27.175	26.739	29.022
7	31.723	31.214	32.992
8	37.062	35.698	37.70
9	40.180	40.1692	42.211
10	44.682	44.699	45.829

Table 1a: Natural Frequencies at 25% UTS

Mode	Natural Frequency (Hz) 25% UTS		
	Analytical Model	FEM	Exp. value
1	5.510	5.422	5.463
2	11.021	10.845	9.098
3	16.535	16.27	17.435
4	22.051	21.698	23.678
5	27.571	27.130	28.746
6	33.097	32.567	34.415
7	38.628	38.010	38.109
8	45.967	43.461	45.22
9	49.714	48.921	51.073
10	55.271	54.390	56.2

Table 1a: Natural Frequencies at 30% UTS

Mode	Natural Frequency (Hz) 30% UTS		
	Analytical Model	FEM	Exp. value
1	5.034	4.953	6.785
2	10.069	9.909	10.224
3	15.107	14.866	15.829
4	20.148	19.826	21.134
5	25.193	24.790	26.833
6	30.244	29.760	31.815
7	35.302	34.737	36.249
8	41.262	39.721	42.274
9	44.702	44.716	45.613
10	49.702	49.721	51.527

Also, the free vibration of the conductor was done to obtain its response when the conductor is subjected to some form of impact or displacement and the amplitude of vibration decay with time due to damping. A diagram of the decay is shown in fig. 3.

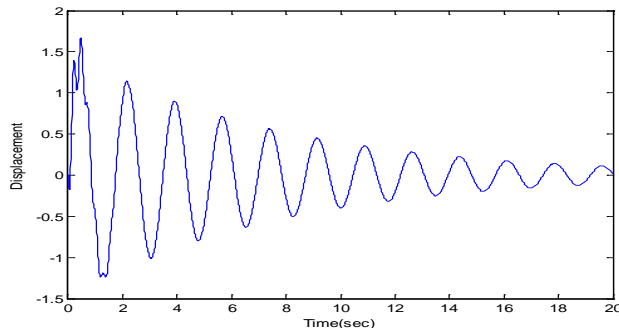


Fig 3: Free Vibration of Conductor

7 CONCLUSIONS

The dynamic characteristic of conductors' vibration is very complex process. In this paper, a finite element model for the conductor in 2-D was developed. Finite-element analyses were used to determine the nonlinear response of the conductor system to dynamic loading from wind. The FEM implementation of a simply supported conductor model for the transverse vibration of conductor was presented for three different conductor stringing tensions.

Matlab was used to simulate the dynamic behaviour of conductor for free vibration i.e. impulse loading. The results obtained from the simulation were used to verify the effects of axial tension variations on the conductor natural frequencies. The parameters obtained from the above, to some degree of accuracy can be used to predict the response of conductors to wind loading. This present work is being extended to implement a FEM model that includes the axial effects.

8 REFERENCES

- [1] T. Varney, "The Vibration of Transmission line Conductors," AIEE, pp 799-807, 1928
- [2] Tompkins, J.S., L.L. Merrill and B.L. Jones. "Quantitative Relationships in Conductor Vibration Damping". AIEE Transactions, Part III (Power Apparatus and Systems) vol.75, pp. 879-84. October. 1956.
- [3] R. Claren and G Diana, "Mathematical Analysis of Transmission Line Vibration" IEEE transactions on power apparatus and systems, vol. pas-88 No. 12, December, 1968
- [4] EPRI "Transmission Line Reference Book: Wind-Induced Conductor Motion" Final Report, November, 2006
- [5] F.B Faquharon and R.E McHugh, "Wind Tunnel Investigation of conductor Vibration of Rigid

Model" IEEE, Transaction Paper, Pp. 871-7, October 1956

- [6] G. Diana and M. Falco, "On the Forces Transmitted to a Vibrating Cylinder by a Blowing Fluid" Meccanica, vol. 6 pp. 9-22, 1971
- [7] C.B. Rawlins, "Wind Tunnel measurement of the Power Imparted to a Model Vibrating Conductor" IEEE Transactions of Power Apparatus & Systems, Vol, PAS-102, No 4, April, 1983, pp 963-972
- [8] Cigrè Study Committee 22-Working Group 01, "Report on Aeolian Vibration" Electra, no 124, pp-101, May 1989
- [9] J. Vecchiarelli, I.G. Currie and D.G. Havard, "Computational Analysis of Aeolian Conductor Vibration with a Stockbridge-type Damper" Journal of fluids and Structures 14, 489-509, 2000
- [10] L. Möcks . and J. Schmidt , "Survey on measurements of mechanical self-damping of ACSR conductors" CIGRESC22-89 (WG-11)TF1-2, 1989
- [11] E. E. Ojo "Dynamic Characteristics of Bare Conductor" Msc in Electrical Engineering Dissertation, University of KwaZulu-Natal, 2011
- [12] C. Hardy, "Analysis of Self-damping Characteristic of Stranded Cables in Transverse Vibrations" CSME Mechanical Engineering Forum, 1990
- [13] H. H Cudney and D. J Inman "Determining Damping Mechanisms in a composite beams by Experimental Modal Analysis" State university of New York at Buffalo, Amherst, NY 14260, April 27, 1989.
- [14] Y.W. Kwon and H. Bang,, "Finite Element Method using Matlab" 2nd Edition CRC Pressperiodic coefficients," Ph.D. dissertation, Dept. Aerosp. Eng., Univ. Maryland, College Park, 1997.

STUDY OF PHOTOVOLTAIC INTREGRATION IMPACT ON ESKOM POWER STATION DISTRIBUTION SYSTEM USING CUSTOM MODELLED PV SYSTEM

N. Mazibuko^{1*}, A.K. Saha²

¹Group Technology & Commercial Engineering, Power, Eskom, 2157 Sunninghill, South Africa.

²School of Electrical, Electronic & Computer Engineering, UKZN, 4041 Durban, South Africa.

*Email: MazibuNu@eskom.co.za

Abstract: This paper presents the results of transient stability due to an impact from a solar plant connected to the power station reticulation system. The rapid variation in power injection by PV system due to changing weather events and other factors such as tripping out the PV system will introduce power fluctuation in the reticulation system and frequency instability. Thus need to evaluate the impact of rapid power variation of the PV system due to changes of irradiance and temperature, also tripping the PV system and simulating a three phase fault. This will illustrate the stability impact of the PV system and the responses of high PV penetration level therefore will relatively reduce the local generator power output. In particular, the PV impact on the transient stability is expected to be more serious considering close proximity of the connected PV system to the generator. In this work, the potential impact of significant PV penetration on the transient stability is assessed by simulation using PowerFactory

1 INTRODUCTION

The photovoltaic system is able to supply electric energy to a given load by converting direct solar energy through photovoltaic effect [1]. The application of grid connected photovoltaic power systems is growing rapidly, with numerous grid connections of PV systems. This growth in PV penetration may introduce other challenges for the system operators to ensure reliable and secure grid operations. With the increasing PV penetration it is important to understand the implications on the system stability and dynamic performance [2]. Because of the unpredictable weather patterns which significantly affect the solar power output, especially if the solar irradiance drops sharply from 100% to 20% within a very short time, will cause major problems for frequency stability.

This paper will present case studies assessing the impact of connecting a PV system onto the power station reticulation system. A PV model developed in PowerFactory is used for stability studies connected to a typical Eskom power station electrical auxiliary network.

2 SIMULATION MODEL

2.1 Power system model

Fig. 1 show a typical power station reticulation network which is used for simulation analysis. The power is distributed on various voltage levels that are associated

with the function of the system. The typical Eskom auxiliary power is distributed with voltages of 11 kV, 6.6 kV and 400 V as seen in Fig. 1 [3]. Power plants need to have an extensive auxiliary power system that supplies power to the power station electrical auxiliary network to provide reliable power to all of the support equipment in the power plant. It is similar to the distribution system in an industrial plant, but it has certain special requirements and limitations. When the unit is generating, it can supply power to its own auxiliaries, when not generating, it must be provided with an external power source [3] [4]. This source must also be capable of supplying the cold start. The main function of the power station electrical auxiliary system is to supply electrical power to the equipment and auxiliaries needed to generate electrical power.

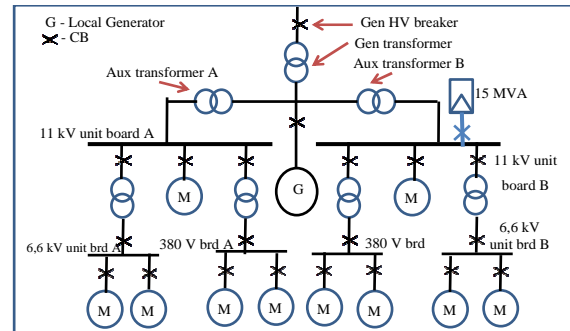


Figure 1: PV connection in distribution network

2.2 Modelling of PV array

PV cell can be characterised by an I-V curve which is influenced by solar irradiance, temperature and load. PV cells are described by a current source shown in equation (1) [5].

$$I = I_{ph} - I_0 \left(e^{\frac{V + IR_s}{nV_t}} - 1 \right) - \frac{V + IR_s}{R_p} \quad (1)$$

where I_{ph} and I_0 are the photocurrent and the reverse saturation current respectively,

$$V_t = nN_s k T / q \quad (2)$$

Equa...(2) is the thermal voltage of the module with a number of N_s cells connected in series, q represents the

electron charge, k is the Boltzmann constant, T means the temperature of the P-N junction and n represents the ideality factor of the diode. I is output current from the cell and V is output voltage of the cell.

Fig. 2 show the solar cell modelled as a current source, I_{ph} which is the generated current from photovoltaic effect and a reverse saturation current, I_0 which is modelled as anti-parallel diode. R_s is the series resistance which is the body resistance of the cell, electrode resistance, the conductor resistance and the surface resistance. R_{sh} is the parallel resistance which makes up for the surface leakage current along the edge of the cell and the leakage current [6].

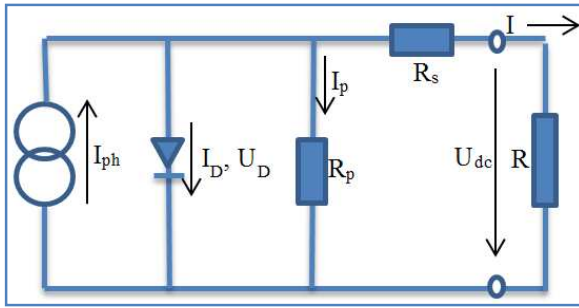


Figure 2: Equivalent model of a PV cell

A basic building block is the PV module which consists of a number of series connections of solar cell typically 36 cells designated for 12 Volts, but for grid connected modules many solar cells are connected to meet the required voltage [5].

The described physics of PV based on mathematical model is shown by Fig. 2 and equation (1). In order to make sense and utilise the PV model practically and be interpreted by PowerFactory the following expressions are implemented:

Equation (3) describe the open circuit voltage with, the open circuit voltage V_{oc-STC} is at STC and V_{oc} is at solar cell operating temperature, K_v temperature coefficient for open circuit voltage provided by the manufacture, at operating conditions of different temperatures is expressed as follows [5] [6]:

$$V_{oc} = V_{oc-STC} [1 + k_v (T - T_{STC})] \quad (3)$$

The photo-current I_{ph} depends on solar irradiance and cell temperature and is expressed as shown below by equation (4) [5] [6]:

$$I_{ph} = I_{ph-STC} [1 + k_i (T - T_{STC})] \frac{E}{E_{STC}} \quad (4)$$

Where I_{ph-STC} is photo current at STC and K_i is temperature coefficient of short circuit current. K_i is

basically the change of short circuit current with respect to temperature [5] [6]:

The saturation diode current is proportional to the temperature raised by power of three as shown by equation (5) below [8] [9]:

$$I_0 = AT^3 e^{\left(\frac{-E_g}{nkT}\right)} \quad (5)$$

Where A is temperature coefficient and E_g is the band energy in eV defined below as [10]:

$$E_g = 1.16 - 7.02e^{-4} \frac{T^2}{T - 1108} \quad (6)$$

The ideality factor is shown by [11] as a unit less parameter defining the extent to which the solar cell acts as an ideal diode. The ideality factor is not affected by the weather conditions therefore n at STC is the same at operating conditions [11].

The temperature of the cell is a function of ambient temperature, solar irradiance, the module back-surface temperature and cell temperature is shown below:

$$T_c = T_m + \Delta T \frac{E}{E_{STC}} \quad (7)$$

Where T_c is the cell operating temperature in $^{\circ}\text{C}$, T_m is the collected back-surface operating temperature of module in $^{\circ}\text{C}$ and ΔT is a constant temperature between cell and module back-surface and is 3°C [5].

The thermal voltage is influenced by temperature as shown in equation (8):

$$V_t = V_{t-STC} \frac{T}{T_{STC}} \quad (8)$$

The parallel resistance which represents the leakage current is affected by the irradiance proportionality defined by [12] [11] used in this paper shown in equation (9) but in [5] the proportionality is inverse.

$$R_p = \frac{R_{p-STC}}{E/E_{STC}} \quad (9)$$

And lastly the series resistance was concluded by [11] [9] that it is better it not influenced by operational weather conditions which will simplify the calculation process. But in this paper the series resistance is analytically established from the other four parameters obtained under various operating conditions.

2.3 PV system model

Directly connecting a PV array to the grid has compatibility problems with grid frequency. Therefore an interface mechanism to convert dc output from PV to ac output synchronized with the grid is necessary. The interface mechanism is a typical DC-AC converter (inverter) which inverts the DC output current from the PV array into a synchronized sinusoidal waveform [13]. Another challenge is the matching of power extraction from sun with the load. PV array is a nonlinear system that is influenced by solar irradiation and weather conditions. To match the nonlinear output, a maximum power point tracking (MPPT) technique is implemented and it keeps the grid-connected system to operate at maximum power point. The MPPT algorithm is applied inside the inverter controls; therefore, the grid-connected PV system efficiency is increased [14].

Fig. 3 show the interfacing through pulse-width modulation (PWM) voltage source converter used as PV inverter. The inverter controls the active and reactive power injected from the PV array, the PV array is represented with a constant current source connected to a DC busbar in parallel with DC link capacitor. The elements in DigSilent are noted as DC source current (ElmDci), Pulse Width Modulation converter (ElmVscmono) and compensation shunt capacitor (ElmShnt) [15].

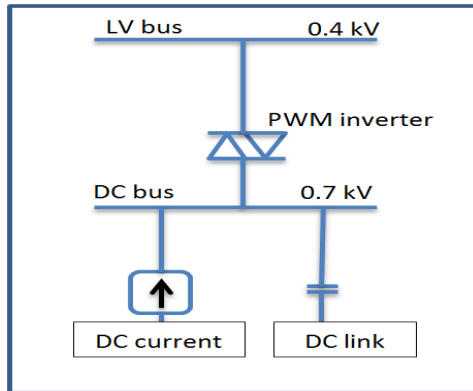


Figure 3: PV model

Maximum power point tracking: The maximum power point tracking is a control mechanism which regulates the DC voltage in such a way that maximum possible power output is delivered with respect to the weather conditions [16] [17]. An MPPT is fully an electronic system that varies the operating point of the modules to achieve optimal operating point and is embedded inside the inverting interface. There are several MPPT algorithms available for use, implementing different techniques. The Perturbation & Observation (P&O) method and Incremental Conductance (incCond) were implemented in the model; however, the latter method was used for dynamic simulation as it does not produce oscillations profile when the solar irradiance remains unchanged [18].

The incCond algorithm is based on the observation that the equation (9) holds at maximum power point

$$di_{pv}/dv_{pv} + i_{pv}/v_{pv} = 0 \quad (9)$$

The algorithm starts the first cycle by obtaining measurements of current values of $I_{pv}(n)$ and $V_{dc}(n)$ and corresponding values $I_{pv}(n-1)$ and $V_{dc}(n-1)$ and the changes are approximately $\Delta I_{pv} = I_{pv}(n) - I_{pv}(n-1)$ and $\Delta V_{dc} = V_{dc}(n) - V_{dc}(n-1)$ and these changes dI_{pv}/dV_{dc} are equated in equation (9) ($dI_{pv}/dV_{dc} + I_{pv}/V_{dc}$) and if this equation yields a negative value means the operating point on the P-V curve is to the right of the maximum power point and the voltage V_{dc} will be increased in steps towards maximum point and if yields positive value then operating point is to the left of the maximum point therefore the voltage V_{dc} will be decreased in step towards the maximum point.

3 INTEGRATION OF PV MODEL

The PV model with the MPPT implemented is integrated to the power station reticulation system shown in Fig. 4. The PV model is modelled under the steady state meaning irradiation and cell temperatures are constant during the simulation period. However, when subject to disturbances the transient stability is analysed in a time period of seconds at constant weather activities.

In this case the suitable connection point is the 11 kV busbar which is the next voltage level stepped down from generator output voltage of 22kV, therefore the flow of power is in one direction and the impact of PV plant to the generator is maximized considering close connection proximity. Two different levels of penetration level are considered in this work, the amount of generation of 15MVA and 7.5MVA.

4 CASE STUDIES

Two different levels of penetration are to be considered in the study one with a penetration of 15 MVA and 7.5 MVA which is supplying 24 % & 12 % respectively of the auxiliary load for an 810 MVA rated machine. Various case studies are looked at with the two PV penetration level. At higher penetration of the PV the local generator is expected to oscillate more.

The output power of the PV system varies every minute due to weather activities which is a negative impact on the stability especially if the variations are large e.g. sharp drop rate of irradiance from 1000 to 200 W/m² in just a few seconds which is a huge generation loss in a short space of time. The objective of the ramping rate test is for the cloud effect over the PV panels.

The PV system penetration level is demonstrated at cases where the PV plant will be subject to internal fault and short circuit faults which is inevitable to any engineered components and safety measures to protect against further damage is to trip out the faulted part therefore both the scenario when the PV plant is tripped out is evaluated at

different penetration levels as mentioned. And when the PV plant is subject to short circuit fault lasting for 0.15 sec and then cleared located at the PV plant busbar. The generator power, load angle, frequency and PV power output of the generator are monitored and analyzed.

4.1 Effect of irradiance change in stability

The effect of a large cloud suddenly covering 80% sunshine for the PV panels dropping the irradiance from 1000 W/m^2 to 200 W/m^2 in less than a minute is investigated at different irradiance ramping rates (-1000 W/m^2 , -400 W/m^2 , -200 W/m^2) per second to determine impact on stability. A drop of the magnitude 10 MW within a short time can have significant impact on the local generator stability.

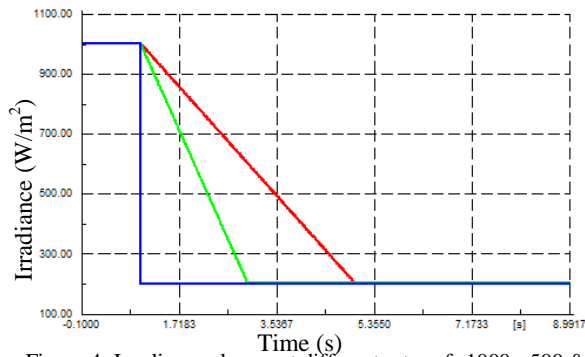


Figure 4: Irradiance change at different rates of -1000, -500 & -200 (W/m^2)

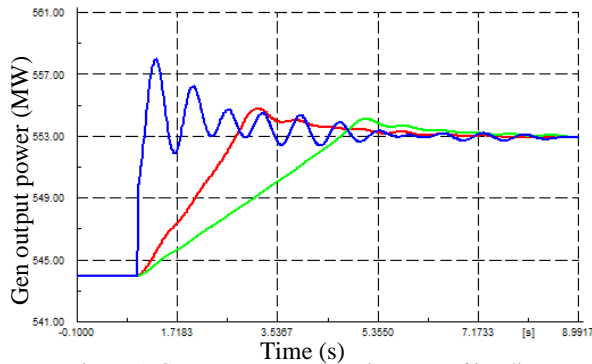


Figure 5: Generator output at various rate of irradiance

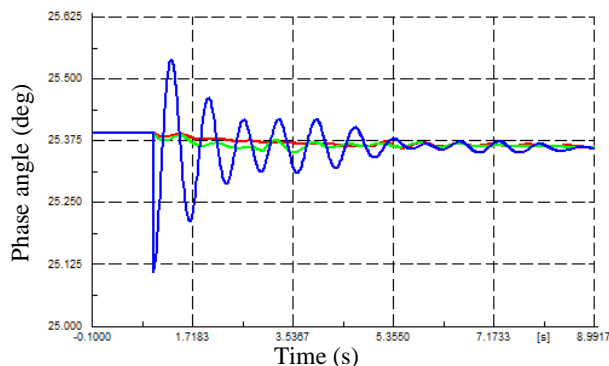


Figure 6: Phase angle of generator at various rate of irradiance

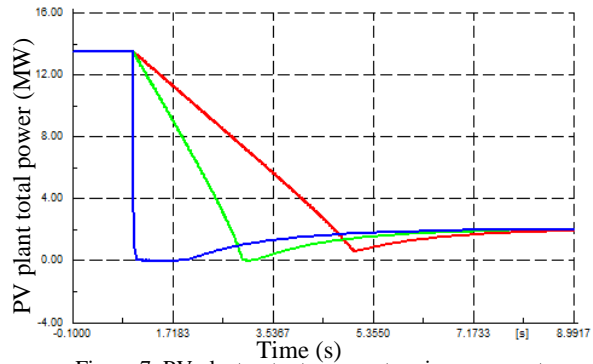


Figure 7: PV plant output power at various ramp rate

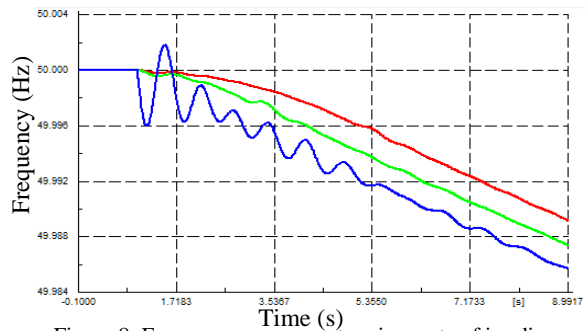


Figure 8: Frequency response at various rate of irradiance

Fig. 5 shows the change of irradiance from 1000 W/m^2 to 200 W/m^2 at different ramping rates, change in generator power output is shown in Fig. 6, generator load angle on Fig. 7, PV plant output power changes and frequency response are shown in Fig. 8 and Fig. 9 respectively.

The local generator output power shown in Fig. 6 can be seen picking up the PV plant lost generation load at different ramping rates and for a quick drop rate (blue curve) the output power is seen to oscillate and eventually settles to a level which compensates the difference of the lost and available PV generation. But for slower irradiance drop rate (red curve) trivial oscillations are seen. Load angle shown in Fig. 7 show the significant of drop rate which is seen for a quick drop rate irradiance the oscillations are severe when compared with slower drop rate.

But in reality outside of simulation a big cloud will not instantly cause a sudden drop of irradiance for a 15 MVA PV plant considering the size of a cloud and the speed the cloud can travel with. Therefore, the drop will not be as quick as indicated on simulation. Therefore, Changes in atmospheric conditions are not likely to cause severe oscillation that can impose stability threats.

Fig. 8 shows the PV plant drops to zero for a second for quickest drop rate and due to the available irradiance the PV plant steadily picks up and continues to produce power according to the available 200 W/m^2 of irradiance and the PV system does not oscillate as it does not have rotary machinery.

Fig. 9 shows the frequency response, and oscillations are seen for quickest drop rate and the significant is that the frequency drops quicker to a lower level for higher drop rate which is undesired but other control mechanism such as the governor will respond and maintain the frequency to be stable.

4.2 Effect of tripping a PV farm

This case study is considering worst case scenario by disconnecting the PV plant operating at full capacity 13.5 MW at the closest possible point of connection to the generator and the effect of the change in loss of the PV plant at various penetration levels is to be observed below. The PV plant output power suddenly drops from 13.5 to 0 MW but at that time the local generator continues to supply power and in the event the PV plant is tripped the generator is subject to sudden load increase and must compensate the sudden increase in load that was supplied by the PV plant. The output power and frequency of the local generator is shown on Fig. 10 and Fig. 11 respectively where the red curve is local generator output supply when the PV plant is supplying 13.5 MW and green curve is local generator output supply when PV plant supplying 6.75 MW.

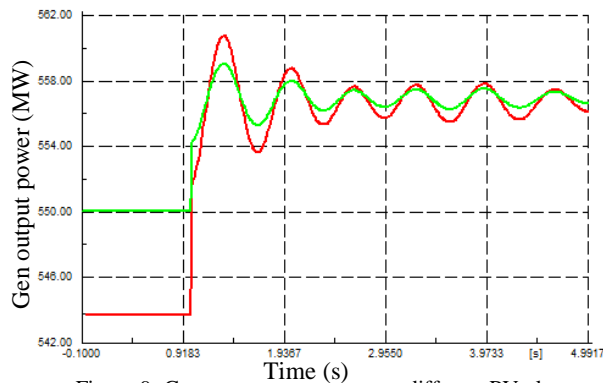


Figure 9: Generator output power at different PV plant penetration level

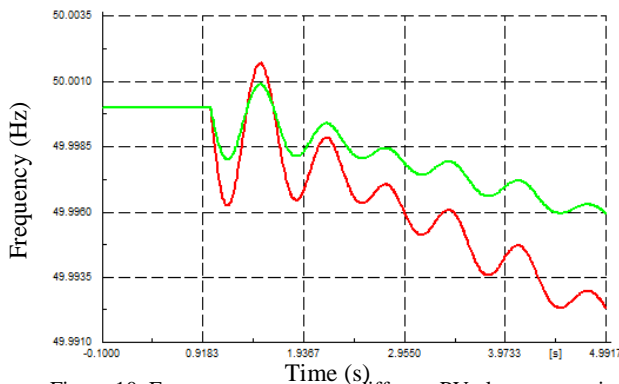


Figure 10: Frequency response at different PV plant penetration level

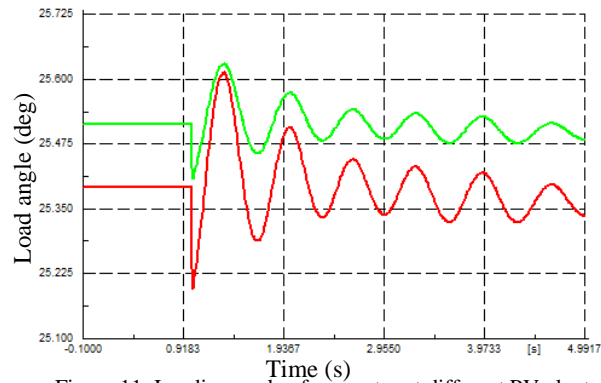


Figure 11: Loading angle of generator at different PV plant penetration level

Fig. 10 shows power from the local generator and the quick loading increase change due to the plant disconnecting results in oscillations as observed and the generator power output power settles at the new level. The local generator has produced the extra power of the lost PV generation therefore total generation is increased at a short space of time. It is also observed that at a higher penetration level the higher the magnitude of oscillations in comparison with less penetration level as seen with the red (Higher MW) & green (Lower MW) curves.

Fig. 11 show that penetration level of PV plant has a significant impact on the generator frequency. With the increase in PV penetration level the more severe the impact on the system stability as the frequency decays faster. Therefore increased PV penetration may make system to be unstable at the presented conditions.

The governor reaction function is to mitigate frequency deviation but the response time is slow therefore not adequate for a large fast drop therefore PV penetration level should be a guidance limit considering the reserve margin of each local generator unit to take over the total lost PV plant power output. Specifically the operating point of generator in terms of load angle should consider the PV plant output power for example shown in Fig. 12 the first swing (red curve) is high when PV plants is disconnected but the margin of the electrical inertia is high enough to bring the swing back and dampen the oscillations.

4.3 Effect of a fault at the PV bus

In this case study a three phase short circuit fault is applied at the PV bus. The fault is applied through a small R/X ratio and lasted for 0.15 s. The solar irradiance is maintained constant at 1000 W/m² therefore maximum power output from the PV plant. Due to the fault the voltage shoots down to zero till fault is cleared in 0.15.

Fig. 12 show the PV power drops to zero until the fault is cleared. When the fault is cleared the output power went back to produce maximum capacity. During the fault Fig. 14 shows the output power from the local generator drops and when the fault is cleared it shows oscillations but dampens after some time. The PV power response does

not oscillate as it does not have rotary machines and it settles faster than the local generator.

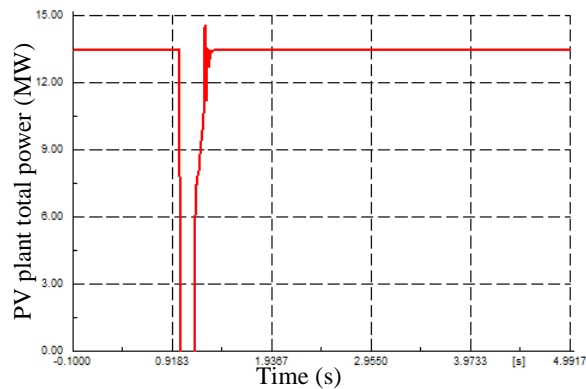


Figure 12: PV power response (MW)

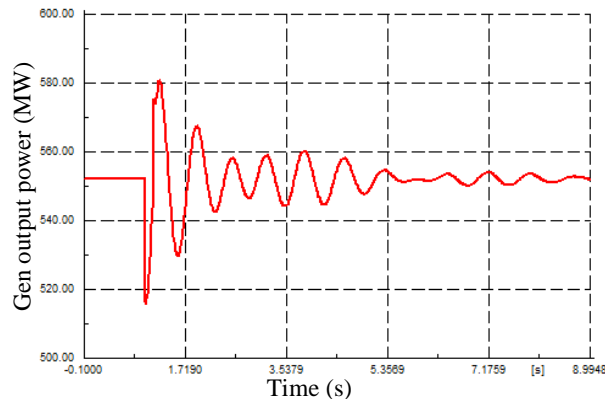


Figure 13: Generator output power after three phase fault

5 DISCUSSION AND CONCLUSION

A significant increase in the penetration of PV generation has a significant impact on the stability of the local generator. The more PV penetration level connected to the auxiliary network the more susceptible to stability problems. This can be counteracted by having enough reserve generation margin of the local generator to avoid unstable condition due to PV plant.

The evaluated scenarios demonstrate that in such case the integration of PV system does contribute to transient problems but assist in running the generator at lower capacity, saving costs and reduced emissions. The connection of PV plant to a load busbar does help in reducing frequency oscillation as seen to be not severe and oscillates within limits for worst case of tripping out the PV plant. The PV system had minimal impact on the voltage as it did not violate any limits but if penetration level is increased the voltage control and compensation shall be considered. However, this concludes the benefits of integrating PV plant on power station distribution to be beneficiary in terms of running the generator at lower capacity thus reduced emissions and costs. Negative results are drawn from transient results corresponding to PV plant inconstant power output.

6 REFERENCE

- [1] J. Duffie and W. Beckman, *Solar engineering of thermal processes*, New Jersey: John Wiley & Sons, 2013.
- [2] R. Shah, N. Mithulananthan and R. Bansal, "Oscillatory stability analysis with high penetrations of large-scale photovoltaic generation," *Energy Conversion and Management*, vol. 65, pp. 420-429, 2013.
- [3] G. Castleberry, "Power plant electrical distribution system," PDH-Course E184, 2008. [Online]. Available: www.PDHcenter.com.
- [4] P. Smit and G. Coetzee, "Power station electrical plant-auxiliary power system training manual," Eskom Generation Group, 2008.
- [5] V. Quaschnig, *Understanding Renewable Energy Systems*, UK and USA: Earthscan, 2005.
- [6] P. Würfel, *Physics of Solar Cells from Principles to New Concepts*, British Library, 2005.
- [7] G. M. Masters, *Renewable and Efficient electric power systems*, New Jersey: John Wiley & Sons, 2004.
- [8] W. S. e. al, "Improvement and validation of a model for photovoltaic array performance," *Solar energy*, vol. 80, pp. 78-88, 2006.
- [9] M. d. Blas, J. Torres, E. Prieto and A. Garcia, "Selecting a suitable model for characterizing photovoltaic devices," *Renewable energy*, vol. 25, pp. 371-380, 2002.
- [10] K. Ishaque, Z. Salam and H. Taheri, "Simple, fast and accurate two diode model for photovoltaic modules," *Solar energy materials & solar cells*, vol. 95, pp. 586-594, 2011.
- [11] M. A. Green, *Solar Cells*, The University of New South Wales, 1998.
- [12] F. Schimpf and L. E. Norum, "Grid connected converters for photovoltaic state of the art, ideas for improvement of transformerless inverter," *Nordic Workshop on Power and Industrial Electronics*, pp. 9-11, 2008.
- [13] M. Casaro and D. Martins, "Grid-connected PV system using a three-phase modified dual-stage inverter," *IEEE*, vol. 978, no. 1, pp. 167-173, 2009.
- [14] D. GmnH, "DigSilent PowerFactory 15 user manual," DigSILENT GmbH, Gomaringen, 2013.
- [15] K. Hussein, I. Muta, T. Hoshino and M. Osakada, "Maximum photovoltaic power tracking: an algorithm for rapidly changing atmospheric conditions," *IEEE proc. of generation, transmission and distribution*, vol. 142, pp. 59-64, 1995.
- [16] M. P. A, A. Mellit and V. Lughi, "Explicit empirical model for general photovoltaic devices: experimental validation at maximum power point," *Sol Energy*, no. 16, pp. 101-105, 2014.
- [17] T. Eswar and P. Chapman, "Comparison of photovoltaic array maximum power point tracking techniques," *IEEE transaction on energy conversion*, vol. 22, no. 2, pp. 439-449, 2007.
- [18] C. Hau and C. Shen, "Comparative study of peak power tracking techniques for solar storage system," *IEEE*, vol. 98, no. 9, pp. 679-685, 1998.

Secured Smart Grid Network for Advanced Metering Infrastructure (AMI)

Philani Khumalo¹

Department of electronic Engineering
DUT
Durban, KZN
philanipk@gmail.com

Bakhe Nleya²

Department of electronic Engineering
DUT
Durban, KZN
bakhen@dut.ac.za

Abstract — Smart Grids are generally modern electric power network technology systems used by power utility to optimise the efficiency of power supply. While it is good practice to introduce technology of Smart Grid, the use of digital technology introduces security threats on Smart Grid systems. Smart Grids mostly have a sophisticated network arrangement and private sensitive information therefore there is a need to secure them. Energy theft is one of the biggest fears related to the Smart Grid application. This paper will discuss Smart Grid security technology challenges, and possible effective solutions. Particularly overcoming Smart Grid security challenges we need a robust communications protocol that will implement security functionalities. The solutions of this aspect should include but not be limited to encryption of messages, minimizing delays due to cryptographic processes, and guaranteeing integrity of these messages with negligible latency. Smart Grid is a part of Advanced Metering Infrastructure (AMI) and the whole network need to be secured. Advanced Encryption Standard (AES) will be implemented to enhance security of this network. Using OPNET and Java NetBeans 8.2 compiler it will be proven that the AES or modified AES will best serve the Power Line Communications (PLC) smart grid security challenges.

Key words — Power line Communications, Smart Metering, Smart Grid, Advanced Encryption Standard, Advance Metering Infrastructure, PLC security.

I. INTRODUCTION

Power Line Communication (PLC), uses the existing power lines to transmit information or data. The information is transferred on a conductor that is simultaneously used for carrying Alternative Current (AC) power to consumers. A diversity of power-line communication technologies are required for diverse usage, ranging from home automation to internet access. Many data rates and frequencies are used in diverse PLC applications and there is a number of technical problems that are mutual on this technology. The major concern on (AMI) is the security of data. Since PLC uses existing electrical power grid infrastructure it is most popular and less costly. Security of information over PLC network has become a focus by many organizations. Challenges of network protocols used will be discussed and various levels of safekeeping schemes with the intention to address security challenges. The data must be safeguarded by robust encryption

and authentication. The protocols, bandwidth, reliability, and accessibility are important aspects because these are the core components of the robust network. PLC would be a perfect candidate because it is comparatively inexpensive as compared to fibre and the infrastructure already exists. The PLC network advantages is that the medium carries power which makes these medium resistant to cable tapping attacks[1].

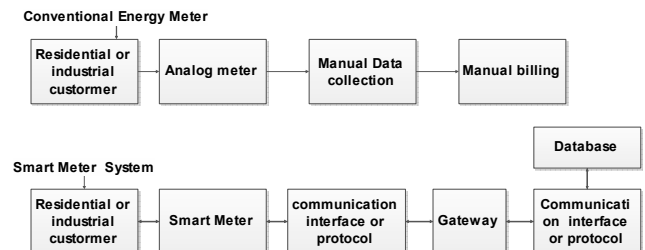


Fig. 1 Architecture of analogue and smart meter[2]

II. ADVANCED METERING INFRASTRUCTURE

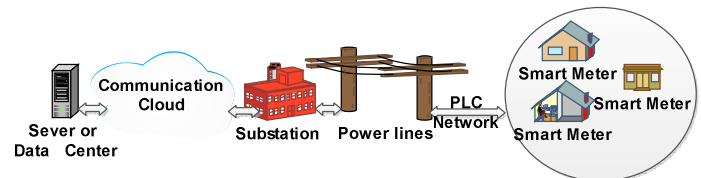


Fig 2 Typical AMI network

Figure 2 above shows a typical AMI network drawing. The smart meters are connected at the customer houses and they communicates via PLC using the existing power lines to the nearest substation, from the substation to the data management center it uses a different communication medium which can be fibre or wireless.

A. Advanced Metering

Smart metering is a solution for the supplier and consumers due to intelligence it provides. The smart meter on the customer side will provide information about consumption behavior. Information can be sent by the supplier to the smart meter for the customer to access i.e. monthly consumption therefore eliminating the need for sending billing letters [3].

On the other hand the supplier will have information on meters when being tampered with by customers, remaining power for usage on prepaid consumers and notifies on power outages. Smart meter will give the customers real time consumption. If the customers can see how much they consume in real time, it will be up to them to monitor, save and change their usage behavior by reducing non-essential appliances. Smart meter will reduce the cost of personnel to be sent to all house hold to manually read meters.

Billing can be executed remotely, by downloading the usage and bill the customers. The restrictions commands can also sent remotely when the customer have not paid they utility bill. Smart metering provides two way communications, the supplier can use the meter to send the message to the customer and the message can be displayed on the meter display.

B. Advantages of Smart Metering (Smart Grids)

- The smart meters report when it is tampering with
- The smart meters report power outage
- The household power can be restricted via smart meter commands
- Load shedding can be executed remotely
- The smart meter help in real time consumption
- The smart meter can penalize peak hour users
- The smart meter can help in power saving
- The smart meter can reduce energy theft

C. Disadvantages

- Expensive.
- Security issues.
- Less jobs.
-

D. PLC standards consideration

Table 1 below shows the PLC standard as part of AMI. The table show standards of different PLC bands, technology frequency and data rate [6]

TABLE I. PLC STANDARDS

Bandwidth	Standards used	Technology	Frequency	Data Rate
Narrow band	Prime	OFDM	42-90kHz	21-128kbps
Narrow band	PLC G3	OFDM	35-90kHz	2.4-34 kbps
Broad band	P1901	OFDM	2-3MHz	100 Mbps
Narrow band	Homeplug	OFDM	2-30MHz	3.8 Mbps
Narrow band	IEC	SFSK	60-76 kHz	1.2-2.4kbps

The protocols that are used on PLC are: X10, CE Bus etc. Some of these protocols are outdated and they have inadequate security features on them. The bandwidth and speed is also a limiting factor on the communications network and needs to be addressed. Most PLC's currently make use of Orthogonal

Frequency-Division Multiplexing (OFDM) technology. OFDM is a method of encoding digital information on multiple carrier frequencies.

OFDM has industrialised into a popular structure for wideband digital communication, whether wireless or over copper wires. OFDM is used in applications such as digital television and audio broadcasting, Internet access, wireless networks and power line networks etc [2]. IEEE P1901 is standard for high speed devices via AC power line [3]. IEEE P1675 is a standards for connecting Broadband Power Line (BPL) devices underground and overhead power line distribution lines [4][6].

III. PLC CHANNEL

A. Power Line Channel Noise

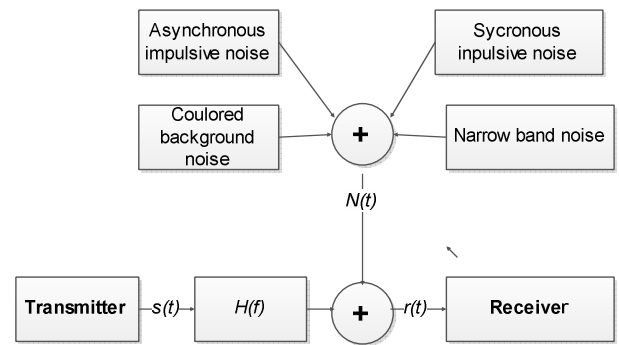


Fig 3 Channel noise introduced on PLC network [7]

The Power Line Communications channel problem is that the channel is mostly exposed to severe noise interference; unlike other transmission channels it does not represent an Additive White Gaussian Noise (AWGN) channel [8][12]. The noise interference situation is much more compound because it does not only work with broadband noise, but also narrow band interference and diverse types of impulsive disturbance occur as portrayed in figure 3. When dealing with PLC smart grid the all types of noise need to be accounted for and suppressed [12].

B. The Transfer function of PLC multipath signal

When designing a PLC smart grid network the PLC channel and PLC transfer function need to be understood. Understanding the channel will enable easy design and security protocol implementation on the channel. Zimmerman developed an echo model that has an extra signal attenuation factor on his equation. The model proves and represents the superposition of signals from N unlike paths, a weighting factor g_i and length d_i characterizes each different path individually. Additionally, the values a_0 , a_1 , and k are utilised to model frequency dependent attenuation. Equation (1) defines a general transfer function of the power line channel [9].

$$H(f) = \sum_{i=0}^N g_i e^{-(a_0+a_1 f^k)d_i} e^{-j2\pi f \frac{d_i}{v_p}} \quad (1)$$

IV. AMI SECURITY

A. PLC Security

In the design of AMI and PLC system security, important security features needs to be considered as well as protocol used channel capacity and data transmission speed. Deficiency of security in AMI system can make electrical distribution untrustworthy [4]. To define attacks on the AMI four components that need to be looked at are: Smart meter, AMI Head End, Communication Network and Meter Data Management System (MDMS). To identify the attack at a specific node, it is important to understand what kind of security service is running on that precise node. The attacker will manipulate or alter a specific controlled data to gain admission to a forbidden area to perform malicious operation and destroy the network or steal information [5] [6].

B. The Security Rules and Design of a System

• AMI Authentication:

An AMI data is required to be protected against the eavesdropping and tampering.

• Authentication and coupling:

The AMI devices should be able to authenticate themselves right after they are installed in order to not allow meter spoofing. The smart meters shall constantly re-authenticate in the back ground.

• Key management:

There should be an enhanced cryptosystem to secure data and establishment of encryption keys e.g. Advanced Encryption Standard (AES).

• Flexibility and extensibility:

The AMI should be open for future expansion without any difficult of hardware change.

• Security strength:

The security algorithms should ensure high security strength.

• Forward secrecy:

Different keys should be used in each session, and they must not be able to be derived from the exposed key.

C. Threats Modeling

To define the threat model we need to identify the intruder and define counter measures to mitigate the dangerous threats [10]. The following are the identified threats:

- Tampering application on AMI nodes.
- Authenticate bypass in smart meters
- Firmware manipulation.
- Masquerade the control center.
- Man in the middle attacks

- Buffer overflow through AMI firmware.

D. The Threats of security domain

- Privacy of data must be no compromised or bridged.
- Tempered of data or message must be discouraged during transmission.
- Unverified equipment on the network
- Data unavailable when it is required by an authorized person.

E. The Intruder Motives

- Disruption of services.
- Stealing of electricity.

TABLE II. PLC SECURITY THREATS VULNERABILITY AND IMPECT SUMMARY TABLE[2]

Treats	Vulnerabilities	Impact
Tamper	Management Applications	Distribution of communication
Masquerade	Lack of Authentications and encryption	Impersonate the control centre and send unauthorized commands
Authentication bypass	Poor proper metering protocol	Manipulate the parameters of the meter
Buffer overflow Firmware manipulation	Firmware assumption Firmware poor access control	System not stable Attacker shut down the meter

F. Security recommendations

• Control for buffer overflow.

Use stack canaries to sense for buffer overflow if the canary value is altered attack can be detected before execution.

• Control for Firmware

Encrypt firmware, validate firmware integrity and authentication before it gets located to the boot loader [2].

• Control for Authentication.

Metering protocols like AES must be used to support authentication. Depending on the requirement the modified AES can be used since it provides fast encryption and authentication scheme.

G. PLC Physical Security

PLCs are naturally more secure than wireless due to its physical medium. PLC network is a danger due to the presence of AC voltage on them. The differences in the Signal to Noise Ratio (SNR) and Channel frequency response between different nodes in the network makes it more difficult to retrieve information from intercepted signal [9]

H. PLC Semantic Security

Cryptography denies intruders access to data exchange on the network, the information is encoded using Encryption key before transmission and this makes data useless to the intruder or someone who eavesdrop it [11].

Authentication access to the network gained after identifying the user.

Integrity control the data sent will be identified if it was changed or not.

Confidentiality Data travelling across a network should not be viewed by an intruder.

Two cryptography techniques:

- Asymmetric – private key cryptography and public key cryptography.
- Symmetric–key cryptography single key is used to encrypt and decrypt information. The key must be available on both ends (transmitter and receiver).

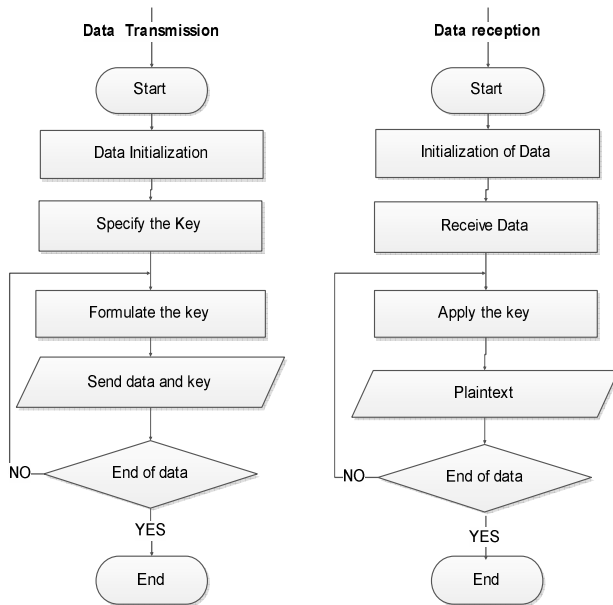


Fig 4 Security Algorithm flow chat [12].

Figure 4 show the flow chat on the security algorithm

I. Cryptology

Cryptology is the scientific study of cryptosystems, and it is divided into two categories.

- Cryptography which is the design of cryptosystems.
- Cryptanalysis is the study of how to hack the cryptosystems.

These two features of cryptology are closely linked when setting up a cryptosystem. The study of its security plays a significant role. There are numerous reasons for this, for example the privacy of data. When conveying data, we do not want an eavesdropper to comprehend the information conveyed. The same is true for kept data that should have privacy against unapproved access, for example by hackers. Authentication is the equivalent of a signature where the receiver of a data wants evidence that the data comes from a certain party and not from someone else. Integrity means that

the receiver of certain message or data has indication that no alterations that have been made on the data received. The safety of the data will be performed by means of cryptographic techniques [13] [14].

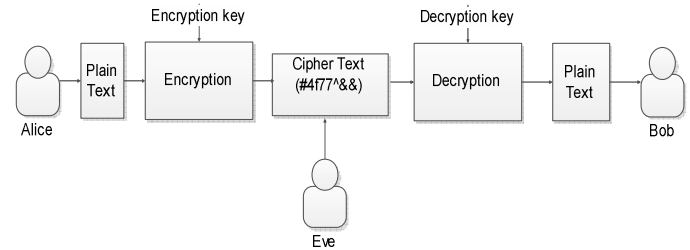


Fig 5 Encryption block diagram

Figure 5 above shows how the encryption process is executed when Alice sends plain text to Bob and there is an Eavesdropper listening to the conversation.

V. AES CRYPTOSYSTEM

The challenge of data transmission on the PLC network is securing the network from the adversary. The security can be implemented using Advance Encryption Standard (AES) to encrypt and decrypt data. The data have to be authenticated to verify if the data received comes from the trusted source and the data is not tempered with during the transmission. Lost packets that are retransmitted and repeated data is authenticated [15]. The smart meters are authenticated before it is requested for data, to prevent the meter spoofing and impersonation. There is less security on the smart meter build-in software that is why there is a need to secure data on the transmission network. The study has been conducted on few encryption protocols like RSA, 3DES and AES has proven to be the best with respect to data block size against data execution time. AES has been proven to be the fastest and efficient encryption method [16]. AES provides low-cost and low frequency encryption essentially and appropriate for security and low resource applications. The AES algorithm is a part of the Rijndael algorithm scheme. The AES algorithm utilises 128 bit block and other three diverse sizes of keys 128, 196 and 256 data bits. AES uses symmetric key algorithm that means that the key that is utilized for encryption and decryption of data is the same and he cipher text created by the AES encryption is of the same size as the plain text [15]. AES also make use of multiplication state matrix called GF (2⁸) the equations below depicts this.

$$m(x) = x^8 + x^4 + x^3 + x + 1 \quad (3)$$

The key and input data are referred to as state and are structured in a 4x4 matrix of bytes. Figure 7 shows how 128 bit key is distributed into byte matrix.

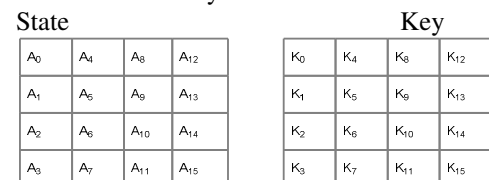


Fig 6 Structure of the Key and the State [19]

A. AES Encryption and Decryption.

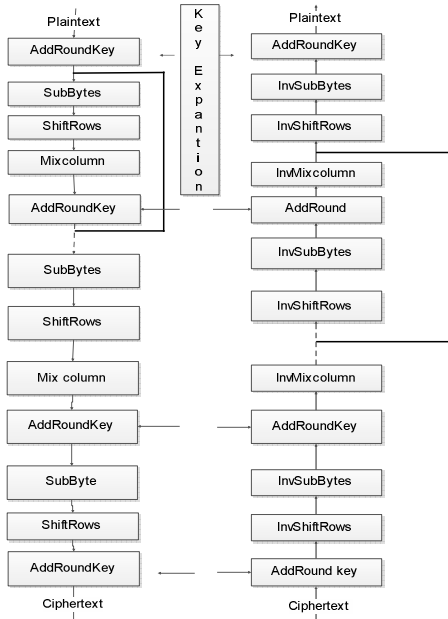


Fig 8 Flowchart of AES Algorithm [20]

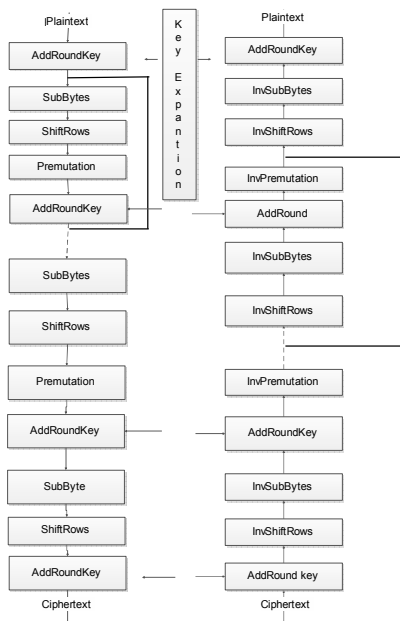


Fig 7 Flowchart of Modified AES Algorithm [20]

Table 3 one below shows us the key length number of rounds and the required number of keys.

TABLE III. SUMMARY TABLE FOR KEYSAND ROUND]

Key length	No. of rounds	No. of keys
128	10	11
192	12	13
256	14	14

The AES encryption consist of ten rounds. After the first key is added round key 0. The initially 9 rounds are similar the only different is the final round. The first 9 rounds are made up of 4 changes. The last round does not have MixColumns change. There are four straightforward steps named layers that are executed on the incoming data while performing the encryption process these are: ByteSub, ShiftRow, MixColumn and AddRoundKey [18].

B. AES Decryption

The four steps that are executed on encryption are reversed in a decryption structure. The decryption process is as follows

- The InvShiftRow
- The InvByteSub
- Add RoundKey
- The InvMixColumn

C. AES Modification to Enhance Speed

AES is one of the fastest encryption scheme but it can be a bit slower when processing big data files. To minimise more calculation an AES was investigated and modified, to lessen the calculation time of encryption and decryption. Lessening the calculation of the algorithm will improve the encryption performance. This led to development of a modified AES. The aim to modify AES is to lessen computation time but not compromising security of data. Modified AES algorithm provide improved encryption speed. AES has the block length data and the key length. The three alternatives are 128, 192, or 256 bits. We selected 128 bits key since it is the most applied in encryption of PLC. To defeat big calculation on encryption process the Mixcolumn step is skipped and the permutation is used. Other three junctures remain unchanged [17].

D. AES Results and Analysis

We used OPNET and NetBeans 8.0.2 Java compiler to verify the efficiency of the modified AES encryption and decryption. Using this test analysis it shows that the modified AES is faster than the original AES. A few data sizes were simulated using AES and Modified AES and the results were compared. The program was run on the compiler and the results are depicted below.

Start program

==Java==

plain: test text ABC

cipher: -104 48 9 29 -121 21 47 -114 -118 44 -25 25 -86 -109 -112 109

decrypt: test text ABC

TABLE IV. ENCRYPTION AND DECRYPTION TIME

Method	Total Time [%]	Total Time
main		248 ms (100%)
aesmodified.AESModified.main (String[])		248 ms (100%)
aesmodified.AESModified.encrypt (String, String)		247 ms (99.2%)
Self time		1.54 ms (0.6%)
aesmodified.AESModified.decrypt (byte[], String)		0.317 ms (0.1%)
aesmodified.AESModified.<clinit>		0.027 ms (0%)

TABLE V. ENCRYPTION ANALYSIS TIME

file size	AES (ms)	Modified (ms)	Efficiency (ms)
16 bit	290	247	43

VI. COMPARISON OF AES CRYPTOSYSTEM WITH DES

Both AES and DES use block cipher scheme. The AES and DES use symmetric cryptosystems. Both encryption schemes make use of substitution tables called S-boxes. AES and DES encryption and decryption process are same. Despite these resemblances of AES and DES, there are essential and important differences between their algorithms. The DES algorithm is based on the Feistel cipher arrangement. DES uses 64-bit block size and 56-bit key length and it is attacked a lot as its key is too short to provide robust security. The AES algorithm on the other hand does not use Feistel cipher. AES has three layers, each with its own function. The AES also is 128-bit block twice the length used by DES and is represented by 4 x 4 array of bytes. Another difference between this two is rounds required. DES needs 16 round and the AES needs 9, 11 or 13 rounds. For a 128-bit block and a 128-bit key, no attacks were found for more than six rounds. Three additional rounds, and final round, were added security enhancement on AES. [16]

VII. CONCLUSION

The AES algorithm is an enhancement security over the DES and other cryptosystem. The AES offers a very high level of security efficient. Though AES will need improvements to keep up with current threats AES will still be strong for a decades to come. Due to AES flexibility and variable length block of 128, 192 or 256 bits it is possible that in future, that AES block size be stretched beyond 128, 192 and 256 bit length. AES is a modern block cipher and it provides excellent long term security against brutal force attacks. AES is efficient in software and hardware. Concluding AES is the best solution for PLC security [15] [16].

References

- [1] K. Adak, J. Mohamed, S.H. Darapuneni, "Advanced metering infrastructure security" university of Colorado, Bolder 2010 Dec 06
- [2] J.J. Lee, C.S. Hong, J.M. Kang and J.W. Ki Hong "Power Line Communication network trial and management in Korea" *int j. Mgmt* 2006.

- [3] L.F. Montoya "Power Line Communication performance overview of the physical layer of available protocols" University of Florida.
- [4] F.N. Pavlindou, H.A. Latchman, A. J. Hanvick, R.E Newman "Power line communications and applications" *int commun. Sys* May 2003
- [5] G. Bumiller "System architect for power line communications and consequences for modulation and multiple access" Grohhabersdorf, Germany 2010
- [6] R Newman S. Gavette L. Yonge and R. Anderson "Protecting domestic power line communications" in *proceeding of the second symposium on Usable privacy Security* (SOUPS July 2006)
- [7] *Transmission of data using power line carrier communications* Volume 2 6sity ed IJCCT ISSN:2249-7838
- [8] V Pparushuri, and A Duresi, "Secure power line communications" Pittsburg, PA USA 2006 Dec 14.
- [9] S. Lee, "Security issues of power line multihome network for seamless data transmission" *international journal of Advanced Science and Technology* vol 37 December 2011.
- [10] S. Ju, M. Choi, C. Kim and Y. Lim, "Security Architecture for advanced metering Infrastructure" *Advance Computer Science (ACSIJ)* July 2013
- [11] K. S. Al Mawali "Techniques for Broadband power line communications: impulsive noise mitigation and adaptive modulation" RMIT University July 2011.
- [12] "Making the smart grid smarter with embedded java" Oracle March 2011.
- [13] Naira Escudero Sanchez, *The Rabin Cryptosystem*, University of Paderborn
- [14] S. Hammeed, F Riaz R Moghal, "Modified Advanced Encryption Standard For Text And Images", computer science journal volume 1 issue 3, December 2013
- [15] Salim M Waddi N Zinal, "Rapid Encryption Method Based on AES Algorithm for Grey Scale HD Image Encryption", ICEEE 2012
- [16] Uli Kretzschmar, "AES 128 AC Implementation for Encryption and Decryption". SLAA397A July 2009.
- [17] P Kawle, A Hiwase, G Bagde E Tekam. R Kalbande "Modified Advanced Encryption Standard", ISSN:2231, volume 4, issue 1 March 2014.
- [18] G Singh, "A study of Encryption Algorithm (RSA DES 3DES and AES) for information Security", IJCA Volume 67-No 19 April 2013
- [19] Mukti Winanda, A Satriawan, Y S Gondokryono, "Smart Grid Secure Data Transmission for High Voltage Grid." ICITSI 24-27 November 2014
- [20] VC. Gungor, D Sahin T Kocak, S. Ergut, C Buccella, C Cecati, GP Hanke, "Smart Grid Technology: Communications Technologies and Standards".

ZP Khumalo (Pr Tech Eng) was born in Kosi Bay on 06 January 1978. He received his BTech degree in Electronic engineering from Durban University of Technology in 2013 and currently studying towards Master of Engineering. His research interests include Power Lines Communications, Smart metering, SCADA system and artificial Intelligence

DC Optimal Power Flow through the Linear Programming – in Context of Smart Grid

A. Goudarzi^{1*}, M. Kazemi² and A.G. Swanson¹ and M. H. Nabavi³

¹University of KwaZulu-Natal, Howard College, 4001 + Durban, South Africa

²Mapua Institute of Technology, Intramuros, 1002 + Manila, Philippines

³Department of Electrical Engineering, Tabriz Branch, Islamic Azad University, Tabriz, Iran

*Email: goudarzia@ukzn.ac.za

Abstract: In a real-time electricity market, where the contribution of distributed resources is increasing, the utilization of fast and robust tools to compute locational prices becomes vital. This paper proposes a method for distributed resources based on linear programming to solve the direct current optimal power flow. In this manner, minimum generation cost, bus angles, line flows and locational marginal prices have been achieved subject to the system constraints and social welfare. To demonstrate the capability of the proposed method two scenarios have been studied on a 4-bus test system with and without considering grid congestion. It was found that the results converged precisely with a low computation time. The main feature of this method is its simplicity and robustness which allows the utilization of this method in a smart grid with a variety of customers.

Keywords: DC optimal power flow, Smart Grid, Locational Marginal Prices, Optimal Scheduling, Market Clearing Price

Nomenclature

P_{Gi}, Q_{Gi}	active and reactive power generation at bus i
P_{Di}, Q_{Di}	active and reactive power demand at bus i
$P_{Gi}^{min}, P_{Gi}^{max}$	minimum and maximum active power generation at generator i
$Q_{Gi}^{min}, Q_{Gi}^{max}$	minimum and maximum reactive power generation at generator i
I_i	current at bus i
V	vector of bus voltages
I	vector of currents at buses
Y	bus admittance matrix
V_i	i^{th} element of vector V
G_{ij}	conductance of ij bus
B_{ij}	susceptance of ij^{th} bus
N_B	number of buses
N_G	number of generators
N_D	number of load demands
f_{P_i}	cost function of active power
f_{Q_i}	cost function of reactive power
LMP	locational marginal price
B	$N \times N$ admittance matrix with $R=0$
P	$N \times 1$ vector of bus active power
P_B	$M \times 1$ vector of branch flows (M is the number of branches)
D	$M \times M$ matrix where b_{ii} is equal to the

susceptance of line i and non-diagonal elements are zero

A	$M \times N$ bus-branch incidence matrix
P_i	active power of the system
Q_i	reactive power of the system
θ_i	Voltage angle at bus at bus i

1 INTRODUCTION

Optimal power flow, which determines power generation cost and transmission loss subject to practical constraints, is inherently nonlinear and non-convex. It has always been a challenging problem in power system operation. For simplicity, the majority of previous works use linearization and approximation methods such as small angle approximation and relaxation methods. In a smart grid, where intermittent energy such as photovoltaic plant supplies, direct current optimal power flow (DC-OPF) is practically important [1].

Locational marginal pricing (LMP) is an important method which can use AC-OPF and DC-OPF and has been utilized in most power markets ISOs such as PJM, New York, New England, California and Midwest. DC-OPF model is a linearized model of AC-OPF due to its simplicity, efficiency and fast response and is still preferred compared to AC-OPF [2], [3].

The authors of [4],[5] used decentralized DC-OPF method to solve the decentralized SC-OPF problem which is an iterative algorithm. The result of their studies demonstrated that DC-OPF has a fairly good result regarding congestion patterns compared to the full ac system model and they found that dc approach is substantially faster.

Reference [6] introduced a quadratic approximation of the OPF for power distribution system which is based on the linear power flow. The proposed method does not take into account PV nodes.

The authors of [7] used DC power flow to show the usefulness of this tool especially when power flow controlling devices such as phase shifting transformers are considered. In their study, they found a relatively small error between AC and DC-OPF which was caused by the approximation of a sine function.

Therefore, the focus of the present study is to investigate the effects of transmission lines constraint and congestions on the customers in the context of

smart grid. To have an accurate and thorough investigation on payment to loads (customers) and generators a new formulation of LP-DC-OPF has been applied to a 4-bus test system with 2 different scenarios.

2 PROBLEM FORMULATION

2.1. AC Power Flow

The classical power flow (PF) problem can be formulated with considering four main decision variables for each bus of the power system. These variables are as follows [9]:

$$x = \begin{bmatrix} P_i \\ Q_i \\ V_i \\ \theta_i \end{bmatrix} \quad (1)$$

The active and reactive power of the system with respect to equality constraints can be calculated by the following formulation:

$$\sum_{i=1}^{N_B} P_i = \sum_{i=1}^{N_G} P_{G_i} - \sum_{i=1}^{N_D} P_{D_i} \quad (2)$$

$$\sum_{i=1}^{N_B} Q_i = \sum_{i=1}^{N_G} Q_{G_i} - \sum_{i=1}^{N_D} Q_{D_i} \quad (3)$$

Subject to inequality constraints

$$\begin{aligned} P_{G_i}^{min} &\leq P_{G_i} \leq P_{G_i}^{max} \\ Q_{G_i}^{min} &\leq Q_{G_i} \leq Q_{G_i}^{max} \end{aligned} \quad (4)$$

According to Kirchhoff's law for determination of the current at each bus [9]:

$$I = YV \quad (5)$$

subject to

$$I_i = \frac{(P_i - jQ_i)}{|V_i|} e^{j\theta_i} \quad (6)$$

$$\begin{aligned} V_i &= |V_i| e^{j\theta_i} \\ Y_{ij} &= |Y_{ij}| e^{j\delta_{ij}} = G_{ij} + jB_{ij} \end{aligned} \quad (7)$$

Subsequently, the active and reactive power of the system can be expressed based on the equations [10]:

$$P_i = \sum_{j=1}^{N_B} |V_i| |V_j| (G_{ij} \cos(\theta_i - \theta_j) + B_{ij} \sin(\theta_i - \theta_j)) \quad (8)$$

$$Q_i = \sum_{j=1}^{N_B} |V_i| |V_j| (G_{ij} \sin(\theta_i - \theta_j) - B_{ij} \cos(\theta_i - \theta_j)) \quad (9)$$

Therefore, the objective function of AC-OPF can be simply proposed by summation of cost functions of active and reactive power injections for each generator [11]:

$$\min_{P_i, Q_i, V_i, \theta_i} \sum_{i=1}^{N_G} f_{P_i}(P_{G_i}) + f_{Q_i}(Q_{G_i}) \quad (10)$$

2.2. DC Power Flow

The most frequently used solution for calculation of the power flows through the transmission lines and power grid injections is the ACPF, where the high level of analysis and detailed information of the power grid is carried out. The ACPF is a very time consuming method for the large scale of a power grid with N buses and $2N$ resulting non-linear equations that have to be solved iteratively for each time step [12]. The main idea of DCPF is to simplify the task and reduce the calculation time of ACPF by considering several approximate assumptions. DCPF is non-iterative method and it is completely convergent but less accurate than ACPF. This non-iterative nature of DCPF causes to significant reduction in computation time which makes it a very useful method for the real time analysis of large systems.

The following assumptions are considered to formulate the DCPF [13]:

1) The resistance of transmission lines is significantly less than the reactance. Therefore, the resistance terms of the impedance will be ignored

$$Z = R + jX \quad (11.A)$$

$$Y = G + jB \quad (11.B)$$

$$Y = \frac{1}{Z} = Z^{-1} \quad (11.C)$$

$$R \ll X \quad (11.D)$$

The power flow equations can be rewritten:

$$P_i = \sum_{j=1}^{N_G} |V_i| |V_j| (B_{ij} \sin(\theta_i - \theta_j)) \quad (12)$$

$$Q_i = \sum_{j=1}^{N_G} |V_i| |V_j| (-B_{ij} \cos(\theta_i - \theta_j)) \quad (13)$$

2) Since the difference in angles of the voltage phasors at sending and receiving buses are less than 10-15 degrees, therefore we say that the angular separation across any transmissions lines are negligible ($\sin(\theta) = \theta, \cos(\theta) = 1$).

$$P_i = \sum_{j=1}^{N_G} |V_i| |V_j| (B_{ij} (\theta_i - \theta_j)) \quad (14)$$

$$Q_i = \sum_{j=1}^{N_G} |V_i| |V_j| (-B_{ij}) \quad (15)$$

3) Ignoring the reactive power of the system ($P_i \gg Q_i$).

4) Ignoring the transmission line losses.

5) The tap settings of the transformers are neglected (means in-phase and phase-shifting transformers are considered like transmission lines).

6) Bus voltage magnitudes are fixed to 1.0 per unit.

According to aforementioned assumptions, only active powers of the system and voltage angles are the remaining variables of DCPF. Therefore, the power balance equation of DCPF will be converted to set of linear equations

$$P_i = \sum_{j=1, j \neq i}^N (B_{ij}(\theta_i - \theta_j)) \quad (16)$$

where the above equation as well as power of branch flows can be represented in the matrix notation as follows:

$$\theta = [B']^{-1} P \quad (17)$$

$$P_B = (D \times A) \times \theta \quad (18)$$

It should be noted, as in power flow the angle of slack bus is equal to zero therefore in B' matrix the first row and column must be removed. Consequently, the objective function of DCOPF by reducing the optimization variables can be derived as below

$$x = \begin{bmatrix} P_i \\ \theta_i \end{bmatrix} \quad (19)$$

$$\min_{P_i, \theta_i} \sum_{i=1}^{N_G} f_{P_i}(P_{G_i}) \quad (20)$$

The DCPF estimates the approximate values of the system in comparison to ACPF which is able to carry out very detailed information of the power grid, but it has three main advantages over the classical Newton-Raphson PF [8]:

1) The admittance matrix (the system matrix, B) is almost half the size of the full problem.

2) Since the problem can be solved in a linear and non-iterative way, a single run is required to obtain the problem solution which has a significant reduction on the calculation time as well as real time analysis.

3) The admittance matrix of the system is totally independent from the system state, so it is required to be derived only once as long as the topology of the system has no changes.

It is worth noting that by considering the first and second advantages of DCPF, the calculations would be

obtained 7 to 10 times faster than AC. Consideration of the third advantage which has a huge effect on the calculation time, the multiple solutions are required since the inverse of the admittance matrix has to be solved only for a single run.

2.3. DC-OPF Based on Linear Programming

While the DCPF attempts to find two variables; power flows in the transmission lines and the angles of bus voltages, DC-OPF gives this ability to user to have the optimal dispatch of the generating units at the same time. This feature is a handy tool for power system planners and operators which they tend to have a holistic overview of the system with respect to all of the load fluctuations in the real time systems. In this regard, the following section explains the principles of linear programming (LP) and then it illustrates how DCOPF can be embedded into LP concept.

LP has found many usages in the industry where system planners and operators want to utilize and optimally manage limited resources in a suitable way. The main application of linear programming is to find the maximum or minimum of some quantity such as cost or profit while the system is involved with different sets of linear equations. This mathematical approach of finding extremum values of a quantity is widely known as optimization. LP is a classical optimization method which deals with types of problem that are presented in forms of linear functions which subsequently they can be optimized with respect to a set of linear constraints where the functions are known as objective function. The basic principles of LP can be defined as [14], [15]:

$$\min Z = \sum_{i=1}^n c_i x_i = c_1 x_1 + c_2 x_2 + \dots + c_n x_n \quad (21)$$

subject to

$$\begin{aligned} a_{11}x_1 + a_{12}x_2 + \dots + a_{1n}x_n (\leq, =, \geq) b_1 \\ a_{21}x_1 + a_{22}x_2 + \dots + a_{2n}x_n (\leq, =, \geq) b_2 \\ \vdots \\ a_{n1}x_1 + a_{n2}x_2 + \dots + a_{nm}x_n (\leq, =, \geq) b_n \\ x_1 + x_2 + \dots + x_n \geq b_n \end{aligned} \quad (22)$$

where the set of LP constraints can be stated in terms of summation notation as below

$$\sum_{i=1}^n \sum_{j=1}^m a_{ij} x_j (\leq, =, \geq) \sum_{i=1}^m b_i \quad (23)$$

subject to

$$l_j \leq x_j \leq u_j \quad (24)$$

which can be simplified and rewritten in matrix notation

$$A_{eq} x (\leq, =, \geq) b_{eq} \quad (25)$$

Where Z is the objective function, c_i is per unit cost of i^{th} variable, x_i is i^{th} decision variable and $(\leq, =, \geq)$ defines the types of the constraints. The \leq constraint indicates the upper limit of available resources, while

the \geq constraint defines a minimum value is targeted to be obtained in the final solution, where the $=$ constraint strictly specifies a decision variable should be exactly equal to what desired amount. a_{ij} is the constraint coefficient of x_j in the i th main constraint, b_i is the right-hand side constant of main constraint i , n is number of the decision variables, m is number of the main constraints, l_i is the lower bound of i th decision variable, u_i is the upper bound of i th decision variable, A_{eq} is the linear equality constraint matrix and b_{eq} is the linear inequality constraint vector.

The optimization process is highly dependent on the nature of problem, the study demonstrates how the DCOPF can be smoothly embedded into LP concept. The linear equality constraint matrix (A_{eq}) can be divided into six sub-matrices per below [17]:

$$1) P_b = (D \times A) \quad (26)$$

$$2) \text{ form } B' \text{ matrix} \quad (27)$$

subject to

$$\begin{cases} \text{if } i = j \rightarrow B_{ii}' = b_i + \sum_{j=1, j \neq i}^N b_{ij} \\ \text{otherwise} \quad B_{ij}' = -b_{ij} \end{cases} \quad (28)$$

$$3) E = (\text{eye}(N_B, N_B)) \times (-1) \quad (28)$$

$$4) Z_1 = \text{zeros}(N_\theta, N_B) \quad (29)$$

$$5) Z_2 = \text{zeros}(N_B, N_G) \quad (30)$$

$$6) G = \text{zeros}(N_{node}, N_G) \quad (31)$$

subject to

$$\begin{cases} \text{if } N_{node_i} = N_{G_i} \rightarrow G = -1 \\ \text{otherwise} \quad 0 \end{cases}$$

Where D is $M \times M$ susceptance matrix (where the B_{ii} is equal to the susceptance of line i and non-diagonal elements are zero), A is the node-arc incidence matrix, b_{ij} is susceptance between bus i and bus j , E is an eye matrix multiply by -1, N_B is the number of branches, Z_1 and Z_2 are the zeros matrix, G is a $N_{node} \times N_G$ matrix and N_{node} is the number of nodes (buses).

It is important to mention, that the size of A_{eq} is $M \times N$ where the M is equal to number of generators, branches and nodes (means $M = (N_G + N_B + N_{node})$) and N is equal to number of branches and nodes (means $N = (N_B + N_{node})$). Subsequently, A_{eq} can be formed in the following order:

$$A_{eq} = \begin{bmatrix} Z_2 & E & P_b \\ G & Z_1 & B' \end{bmatrix} \quad (32)$$

The vector dimensions of inequality constraint is $N \times 1$ where N is equal to number of branches and nodes (means $N = (N_B + N_{node})$). In order to form b_{eq} , all the values which are assigned to number of branches are zero, while all the values which are assigned to number of nodes are equal to the corresponding load demand at

that particular node. Also, it is required that all the values of load demand must be represented in the negative value to maintain the equality constraint of power flow. Therefore b_{eq} matrix can be represented as:

$$b_{eq} = \begin{bmatrix} N_{B_1} \\ N_{B_2} \\ \vdots \\ N_{B_i} \\ N_{node_1} \\ N_{node_2} \\ \vdots \\ N_{node_i} \end{bmatrix} = \begin{bmatrix} 0 \\ \vdots \\ 0 \\ P_{D_1} \\ P_{D_2} \\ \vdots \\ P_{D_i} \end{bmatrix} \quad (33)$$

By solving the LP-DCOPF values of x which are generators schedule, branch flows and bus angles will be calculated. The study has used inequality constrained minimization interior point method to solve the linear programming which can be found in [16].

3 RESULTS AND DISCUSSION

In order to demonstrate the procedure of problem formulation as well as the practicality of the proposed LP-DC-OPF, the methodology has been applied to a four bus test system [18]. Tables 1 and 2 illustrate the test system details where the single line diagram of the test system is depicted in Fig. 1. For simplicity of the calculation all the values of the test system are given in per unit. The considered test system has three generating units with total load 4.3075 p.u [18]. The directions of power flows through the branches are selected arbitrarily. To have an accurate investigation of proposed method, the study has considered two different scenarios to show the capability of the proposed method with respect to load fluctuation and transmission lines constraints in real time systems. The proposed method of the study has been implemented on MATLAB 2013a and executed on a personal computer with the following specifications, Intel® Core™ i7-3770 (3.40 GHz), 8.00 GB RAM (DDR5) and Windows 10 operating system. The study has indicated the procedure of the solution set up before analysis of the scenarios to have a better understanding about process of the proposed method.

Table. 1: Transmission lines characteristics

Branch No.	Nominal Flow		Admittance (p.u.)	Capacity (p.u.)
	From	To		
1	1	4	-j10	500
2	1	2	-j10	500
3	2	3	-j10	500
4	3	4	-j10	500
5	1	3	-j10	500

Table. 2: Generators' characteristics

Gen No.	Pmin (p.u.)	Pmax (p.u.)	Marginal Cost (\$/MWh)
1	0.50	3.50	10.55
2	0.50	2.50	8.45
3	0.50	2.90	8.80

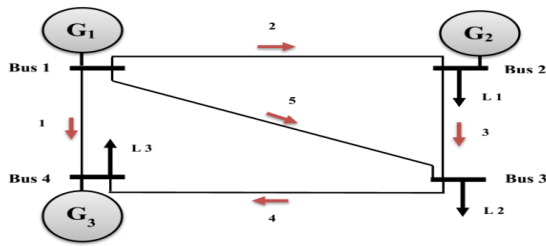


Figure. 1: 4-bus single line diagram

3.1. First Scenario

The LMP is one of the most effective analyses to evaluate the behaviour of the power grid in any electricity market especially for the day-ahead and real-time bases; therefore it is required to calculate the LMP of each bus of the network for every five minutes. In this situation, it is vital to have a quick and efficient tool like LP-DC-OPF to do the fast and optimal calculation. In the first scenario, the study assumed there is no transmission line constraint. The branch flows are strictly within the branch capacities, therefore the transmission lines has no effect on the economical dispatch of a lossless system in the proposed LP-DCOPF. To maintain the system security and adhere to this assumption, the study has assigned 500 p.u for the lower and upper bounds of all transmission lines which effectively makes the capacities equal to infinity in the per unit scale. The results of LP-DC-OPF are shown in the Table 3, where totals system demand is equal to 4.3075 p.u. The proposed method has successfully calculated the optimal scheduling of the generating units, branch flows, bus angles and LMPs. Also, by having the LMPs it is very easy to calculate the amount of payment to generators (PTG) as well as amount of payment to loads (PTL) or customers. The optimal and fast calculation of PTG and PTL has a key role in smart grid (SG) because the system operator is able to propose a suitable demand response program (DRP) for the consumer at each location of the system based on these values. As it can be seen from Table 3, all LMPs have the same value since the network has no transmission line constraint. Therefore, the marginal prices are equal at every node of the system, where the generators would be paid based on the market clearing price which is 8.8 \$/p.u. It is important to mention, that PTG and PTL are equal to the total generation cost (37.906 \$/h), it means the market has settled in the same price of PTG and PTL since the branch flows can vary in an infinite bound. To show the practicality of the proposed method, the study has considered another different load point at 4.6075 p.u to examine the efficiency of LP-DC-OPF where the results are shown in Table 4. By increasing the load demand in this case accordingly the schedule of generating units has been changed. The total cost of generation, PTG and PTL have increased to 40.546 \$/h while LMPs are remained 8.8 \$/p.u since the generator

number 2 has cleared the market price. The evaluation Power balance violation (PBV) ensures that equality constraint of economic dispatch has been maintained intact, where in the both cases of this scenario the PBV is equal to -3.14×10^{-12} (which is small enough to be neglected). The elapsed time is less than 0.27 second for the both cases.

Table. 3: Results of LP-DCOPF without considering transmission lines constraints (load = 4.3075 p.u.)

No.	Gen Dispatch	Line Power Flows	Bus Angles	LMPs	PTG	PTL
1	0.5000	0.0034	0.0125	8.8000	4.4000	9.2400
2	2.5000	-0.3178	0.0443	8.8000	22.0000	24.2660
3	1.3075	1.1322	-0.0689	8.8000	11.5060	4.4000
4	0.0000	0.8109	0.0122	8.8000	0.0000	0.0000
5	0.0000	0.8144	0.0000	0.0000	0.0000	0.0000
Total Cost (\$/h)	37.9060			Total	37.9060	37.9060

Table. 4: Results of LP-DCOPF without considering transmission lines constraints (load = 4.6075 p.u.)

No.	Gen Dispatch	Line Power Flows	Bus Angles	LMPs	PTG	PTL
1	0.5000	-0.1091	0.0125	8.8000	4.4000	9.2400
2	2.5000	-0.2803	0.0405	8.8000	22.0000	26.9060
3	1.6075	1.1697	-0.0764	8.8000	14.1460	4.4000
4	0.0000	0.9984	0.0234	8.8000	0.0000	0.0000
5	0.0000	0.8894	0.0000	0.0000	0.0000	0.0000
Total Cost (\$/h)	40.5460			Total	40.5460	40.5460

3.2. Second Scenario

This scenario investigates the effects of transmission lines constraint and congestions on the customers in context of smart grid. The study has considered two test case studies to have a precise investigation on payment to loads (customers) while the capacity of the main transmission line of the system which accommodates the highest power flow within the system has been significantly limited. According to our calculation in the previous scenario, branch number three carries the highest power flow with 1.1322 and 1.1697 p.u for the first and second test case respectively. Therefore, to see the effect of congestion in transmission line the capacity of this line has been limited to 0.5 p.u which is less than 55% of its actual value. Thereafter, the results are shown in Tables 5 and 6 with respect to two different load points (4.3075 and 4.6075 p.u). It is observable by limiting the branch number three; LMPs are noticeably changed at each node with a specific marginal price. But the most important result is that, the amount of payments to generators and loads are less than total cost. The is due to the proposed method optimizing the system based on the bids that have been offered by the generators or power plant owners but the market has settled according to LMPs. This is based on the idea that most of the electricity markets around the world has adopted or adopting the principal of payment at market clearing price in order to discourage the market participants to offer their bids in the higher price.

Another noticeable fact that can be concluded by the results, the prices paid by loads are higher than by generators from 0.287 to 0.35 \$/h respectively for case 1 and 2. This exceeding amount should be paid by customers due to transmission line congestion effect. The PBVs for case 1 and case 2 are 1.42×10^{-12} and -8.83×10^{-11} respectively. In the both cases of the second scenario the elapsed time has remained less than 0.27 second which indicates the fast convergence of the proposed method of the study.

Tab. 5: Results of LP-DCOPF with considering transmission lines constraints (load = 4.3075 p.u.)

No.	Gen Dispatch	Line Power Flows	Bus Angles	LMPs	PTG	PTL
1	0.5000	-0.6287	0.0125	8.7125	4.3563	8.8725
2	1.2356	0.3144	-0.0189	8.4500	10.4410	24.5073
3	2.5719	0.5000	-0.0689	8.8875	22.6325	4.4000
4	0.0000	1.4431	0.0754	8.8000	0.0000	0.0000
5	0.0000	0.8144	0.0000	0.0000	0.0000	0.0000
Total Cost (\$/h)	38.3485			Total	37.4298	37.7798

Tab. 6: Results of LP-DCOPF with considering transmission lines constraints (load = 4.6075 p.u.)

No.	Gen Dispatch	Line Power Flows	Bus Angles	LMPs	PTG	PTL
1	0.5000	-0.6287	0.0125	8.7125	4.3563	11.4075
2	1.5356	0.3144	-0.0190	8.4500	12.9760	24.5073
3	2.5719	0.5000	-0.0690	8.8875	22.6325	4.4000
4	0.0000	1.4431	0.0753	8.8000	0.0000	0.0000
5	0.0000	0.8144	0.0000	0.0000	0.0000	0.0000
Total Cost (\$/h)	40.8835			Total	39.9648	40.3148

4 CONCLUSION

In this paper, a new formulation of DC-OPF through the linear programming has been represented and successfully employed to solve the optimal power flow problem. The proposed method demonstrates the efficient and fast calculation of line power flows, bus angles, generators dispatch and LMPs with respect to system constraints and social welfare. The practicality of the LP-DC-OPF through to two scenarios was investigated; the first scenario with two base cases and second scenario with line congestion cases. It was found out that when the grid had congestion on the transmission line in the second scenario, market prices would be settled in the different amount at each node of the test system which results the significant changes in LMPs. Also, it has a direct effect on the payments that should be provided by the customer side, where the exceeding amount of market settlement that should be paid by the customers. Therefore, in the modern set up of power system or more specifically in context smart grid where the grid is more customer orientated, the efficient and fast calculation of system details and price transactions in market place is became absolutely vital. In order to facilitate this aim, the system operator needs

an efficient tool in the real time systems to consider several scenarios of the demand response and substitute options to deal with these kinds of issues. It is believed that the proposed LP-DCOPF is a very fast and precise tool to handle the OPF problem in the smart grid context.

5 REFERENCES

- [1] Chee Wei Tan, Cai, D.W.H and Xin Lou, "DC optimal power flow: Uniqueness and algorithms" *smart grid communication conf.*, pp. 641-646, 2012.
- [2] B.V. NarenBharatwaj, A.R. Abhyankar, and P.R. Bijwe, "Improved loss distribution and modelling in DCOPF: Uniqueness and algorithms" *Energy, Automation, and Signal international conf. IEEE*, pp. 1-6, 2011.
- [3] H. Saboori, S. Dehghan, and S. Jadid, "DCOPF-based LMP calculation considering line reactive flows" *Electrical Engineering, 2010 18th Iranian conf.*, pp. 1-6, May 2010.
- [4] P.N. Biskas, A.G. Bakirtzis, "Decentralized security constrained DC-OPF of interconnected power systems" *Generation, Transmission and Distribution, IEE Proc.*, vol. 151, no. 6, pp. 747-754, Nov 2004.
- [5] P.N. Biskas, A.G. Bakirtzis, "A decentralized solution to the security constrained DC-OPF problem of multi-area power systems" *Power Tech, 2005 IEEE Russia, Conf.*, pp. 1-7, Jun 2005.
- [6] A. Garces, "A quadratic approximation for the optimal power flow in power distribution systems" *Electric Power System Research, Elsevier.*, pp. 222-229, 2016.
- [7] D. Van Hertem, et al, "Usefulness of DC power flow for active power flow analysis with flow controlling devices" *AC and DC Power Transmission, 2006. ACDC 2006. The 8th IEE International Conference on*, pp. 58-62, 28-31 March 2006, IET.
- [8] H. Saadat, *Power System Analysis*, McGraw Hill, 1999.
- [9] J. J. Grainger and W. D. Stevenson, Jr., *Power System Analysis*, McGraw Hill, 1994.
- [10] S. Nabavi, et al., "Congestion Management Using Genetic Algorithm in Deregulated Power Environments," *International Journal of Computer Applications*, Vol. 18, pp. 19-23, 2011.
- [11] K. Purchala, "Modelling and Analysis of Techno-Economic Interactions in Meshed High Voltage Grids Exhibiting Congestion", Ph.D. Thesis, University of Leuven (KU Leuven), December 2005.
- [12] T. J. Overbye, X. Chang and Y. Sun, "A comparison of the AC and DC power flow models for LMP calculations" *System Sciences, 2004. Proc. of the 37th Annual Hawaii International Conf.*, pp. 1-9, 5-8 Jan 2004, Hawaii.
- [13] G. Anderson., *Modelling and analysis of electric power systems*, ITET ETH Zurich, 2004.
- [14] W. J. Stevenson., *Operations Management*, McGraw-Hill, 2014.
- [15] Tamas Terlaky., *Interior Point Methods of Mathematical Programming*, Springer US, 1996.
- [16] McCalley, J. "E553- Transmission system effects: losses" Lecture notes, Iowa State University, Iowa, USA, fall, 2012.
- [17] Viray, Zigfed N. C. "Economic dispatch considering loss and optimal power flow." Lecture notes, Mapua Institute of Technology, Manila, Philippines, October, 2010.
- [18] Philippine Electricity Market Corporation. (2006, Jan.). The WESM Price Determination Methodology. [Online]. <http://www.wesm.ph/UserFiles/File/Revised%20PDM.pdf>

Smart Grid Penetration at the eThekweni Municipality

V. Ramprith^{1*} and I.E. Davidson²

¹eTE Municipality, Electricity Unit, 1 Jelf Taylor Crescent, Durban, 4000, South Africa

² University of KwaZulu-Natal, Eskom Centre of Excellence in HVDC Engineering, Durban 4001, South Africa

*ramprithv@elec.durban.gov.za

Abstract: The world's population is increasing rapidly and is projected to reach 8 billion within the next few decades. Urban migration is on the increase and it is estimated that more Africans will reside in urban rather than rural areas by 2030. eThekweni, as a leading city in Africa has to establish practices to ensure that it utilizes its current resources optimally and sustainably to provide for the present and cater for future energy and resource requirements. The role of smart grid systems as an electricity industry enabler has been recognized throughout the world. The effective introduction and implementation of smart grids is also regarded as a major enabler to realize some of the key objectives at local, provincial and national government levels. This paper addresses the level of smart grid penetration at the eThekweni Municipality, using various performance indices. Results obtained are presented and discussed.

1 INTRODUCTION

A smart grid (SG) is a modernized electrical grid that uses analogue [1] or digital information and communications technology to gather and act on information, such as the behaviours of suppliers and consumers in an automated fashion. It aims to improve the efficiency, reliability, economics, and sustainability of the production and distribution of electricity [2]. The term "SG" refers to optimizing, automating and modernizing of the electrical network so that it monitors, protects and automatically optimizes the operation of its interconnected elements. In the eThekweni Electricity (eTE) context, this includes the electricity purchase points from Eskom; DG injection points; the high-, medium- and low voltage networks as well as the industrial, commercial and domestic consumers and their applications and devices.

The SG is characterized by a bi-directional flow of electricity and information to create an optimized and automated self-healing network. It would incorporate the benefits of distributed computing and modern communication systems to deliver information in real-time which enables the almost instantaneous balance of supply and demand. SGs will be designed to ensure reliability, security, quality, availability and will also aim to improve economic productivity, minimize environmental impact, maximize safety and improve quality of life in general.

2 SG TECHNOLOGY DEPLOYMENT AT ETE

Significant investment has gone into modernizing the existing electricity grid infrastructure at eTE to make it smarter, albeit with varying degrees of success.

2.1 Communication Systems

The communication system is often referred to as the backbone of a SG [3]. The adding of intelligence to the network would result in the automation of the various grid functions; and automation is not possible without communications networks that enable a two-way flow of data [4]. Traditionally, electric utilities owned and controlled their communications networks for mission-critical applications due of concerns about reliability, safety; security and cost. Even where the capital and operational cost is greater than a nonutility alternative, the guarantee of reliability, safety and security inherent in a proprietary utility-owned network often trumps cost concerns [4].

The eTE communication network strategy has been formulated for a period of 20 years, from pre 1995 up until 2015 [3]. The strategy catered for an, integrated, private, multi-tier, hierarchical communication network and follows the electrical network in terms of tiers which follows a similar principle. eTE Communication Systems fairs favourably when compared to first world standards and caters for all communication requirements across the various SG applications.

2.2 Distribution Automation (DA)

Distribution automation (DA) refers to integration of various technologies and protocols that enables the electrical distribution system to be remotely controlled, monitored and operated. eTE has embarked on various DA projects as part of the SG Initiative to all distributor substations (DSS), ring main units (RMU), auto-reclosers (AR), through fault indicators (TFI), kiosk and miniature substations (MSS). This is being done in conjunction with other projects to improve reliability, increase efficiency, optimize asset utilization and maximize performance of the electrical distribution system, thereby increasing visibility of the entire grid and providing safe, reliable and high quality power to consumers.

There are currently many DA initiatives and projects that are being implemented across eTE and progress is at an advanced stage in many cases. The major benefits arising out of the DA initiatives in the context of SG is the increased visibility of the electrical system and the ability to remotely control, operate and monitor the electrical network.

2.3 Advanced Distribution Management System

eTE historically operated on a manual outage management process. The control rooms have large mimic wall boards which represent the electrical network. The ERP Ellipse system is used to log faults by creating a “Work Request” and thereafter a “Work Order” is manually created in order to trace the work carried out. The processes currently used are time consuming and provide little or no real time information to customers. The current process is functioning adequately due to a committed team who strictly adhere to the business process. However there are major challenges faced, such as:

- The inability of the Contact Centre to respond accurately to the consumer on faults
- The reporting back of the work progress details from the field staff is delayed.
- Linking process is inefficient
- Cumbersome process of creating work orders
- Backlog for completion of work orders

An Advanced Distribution Management Systems (ADMS) solution was therefore sought to address these and other challenges. In the business case, eTE stated that it is vital to promote technological advancements and improve operational efficiencies. The intention is to integrate the solution with eTE’s operational systems thereby radically improving business processes and assisting to deliver a world class distribution service to the residents of the eTE Municipality.

2.4 Distributed Generation

It is evident that distributed generation (DG) and SGs will become permanent features of our world society, and energy storage will be a critical component. Widespread acceptance will fundamentally change the way consumers procure and control their energy use. Consumers worldwide are turning to DG in various forms, with energy storage as a key consideration for the future. The interconnection of DG sources onto the electrical network is currently classified as one of the methods that a utility can demonstrate as implementing SG systems. The eTE Municipality has embarked on several projects from a municipal perspective and others restricted to the Electricity Unit. Current and future DG projects at various eTE sites are shown in Table 1.

Table1: eTE DG Projects

Current DG Project	Generation Capacity
Marianhill LFS	1 MW
Bisasar Road LFS	6.5 MW
Dube Tradeport PV	0.5 MW
Hazelmere CPV	0.5 MW
VAWT	30 KW
Co Gen (Tonga-Hulett)	1 MW
Total	+/-10 MW

Future DG Project	Generation Capacity
Wind Generation	300 KW
Hydro	8 MW
Gas Peaking Plant	42 MW
PV	14 MW
Landfill Gas	2 MW
Waste Water Works: CH ₄	8 MW
Mini Hydro	1 MW
Ocean Current Generation	6 MW
Total	81.3 MW

The eTE Municipality has embarked on various renewable energy (RE) and DG projects that support SG. The impact of these are quite minimal currently when compared to generation capacity and energy consumption trends. The technologies and principles of RE and DG are, however being demonstrated and has paved the way for future development and larger scale implementation in the future. The various projects prove that eTE has accepted that DG is now an integral part of the system and has shifted its mindset in embracing this concept.

2.5 Advanced Metering Infrastructure (AMI)

eTE is currently in the process of rolling out a modern smart metering (SM) system. It has engaged the consultancy services of Accenture to assist with this process. A summary of the programmes, action items and some of the achievements to date include [5]:

- Establishment of an AMI Programme
- Customer Marketing and Stakeholder Plan
- Implementation Plan
- Business Case benefits identification
- Solution Conceptual Blueprint
- Smart Meter Operational Centre (SMOC) Support Structure defined
- AMI related Business Processes documented
- Request for Proposals (RFPs) for Metering Devices, MVMS, MDMS, Field Installation
- User Cases (requires product vendors input)
- Design of manual business processes

- Customer Communication Approach and Plan
- RFP Evaluation and Contracting
- Vendor Solution Design Implementation and Integration and Training
- Customer and Stakeholder Communication
- Field Deployment (~10,000 installations)
- Technical Infrastructure Finalized
- Systems Implementation
- Automated Smart Meter Billing
- Rapid Field Deployment (Remaining meters)
- Middleware to support first phase functionality
- Rollout of remaining capability enabled through automation

SM is probably the area where the benefits of SG systems can be most clearly demonstrated. It is however, unfortunate that during this study, eTE was still at a very embryonic stage in this regard. eTE is making huge strides in achieving its SM objectives but it will be at least a few years until the required systems are in place to realize maximum benefits.

2.6 Smart Street Lighting

The two main interventions that eTE has implemented to support the SG objective is the implementation of light emitting diode (LED) street lighting and the rollout of a lighting telemanagement project. eTE had carried out various projects that compared the various lighting technologies which included sodium, mercury, metal halide, induction and LED. LED technology provided satisfactory results and the city also received grant funding from various sources to specifically implement LED street lighting. eTE aims to implement Smart Street Lighting, the benefits of which are stated below:

- Enables smart cities
- Advanced monitoring
- Remote control
- Reduce maintenance costs
- Reduced energy consumption
- Improve information availability
- Reduced greenhouse gases
- Improve customer satisfaction

The use of LED for various applications has increased exponentially over the past few decades and is even being hailed as the future of lighting by many. The suppliers and manufacturers are claiming various advantages which include a compact size, longer life spans, lower maintenance, improved design capabilities, colour rendering features and increased luminous

efficacies, amongst others. LEDs are changing the tradition of photometry and are being continuously improved to maximize benefits.

eTE is also currently in the process of rolling out a lighting telemanagement system. A pilot project for the implementation of an Owlet Telemanagement system for 20 light fittings on Umgeni Road is currently underway. The Owlet lighting telemanagement system is used to manage, control, monitor and meter outdoor lighting systems [6]. The main objectives of the system are to reduce greenhouse gas emissions, reduce energy consumption, improve reliability and minimize maintenance costs. Individual lighting points can be controlled and the system is based on open technologies. A central repository collects and stores date and time stamped critical information such as energy consumption, operating states and failures which could also be geographically categorized. The layout of a street light management system is shown in figure 1.



Figure 1: Typical Street Light Management System [6]

The implementation of small scale Smart Lighting systems at eTE has demonstrated that there is potential for huge development and benefits in this area. The move from high intensity discharge (HID) to LED technologies provides huge energy savings in itself and further benefits could be achieved by intelligently controlling and monitoring these lighting systems. The big question mark in this area is the reliability and the ability of these mostly electronic and microprocessor based systems to withstand the harsh climatic and environmental coastal conditions over prolonged periods. The high vibration levels, especially in the industry intensive areas will pose further challenges to these systems.

2.7 Asset Management (AM)

eTE has developed an AM Policy and Strategy which is applicable to the electricity assets of the eTE Municipality and includes transmission, sub-transmission and reticulation assets. These have been developed with due consideration of statutory and legal

requirements, organisation goals as well as stakeholder requirements. eTE has been assisted largely in all processes relating to AM by Pragma, which is a consultant company specialising in the field of AM. This aggressive drive will immensely assist eTE in achieving its SG objectives.

An intention would be to reduce the amount of time spent on non-tactical maintenance, thereby increasing investment in tactical maintenance. The optimum maintenance mix (OMM) for each equipment type will need to be defined and implemented and a layout is illustrated in figure 2. The concept of reliability centred maintenance (RCM) is based on assessing the various maintenance options and determining the optimum strategy on assets so that it fulfils its operational requirements. The OMM methodology is based on RCM and aims to simplify the RM process by starting with criticality analysis that identifies focus areas. OMM combines some RCM steps to simplify the development of Asset Care Plans (ACP).

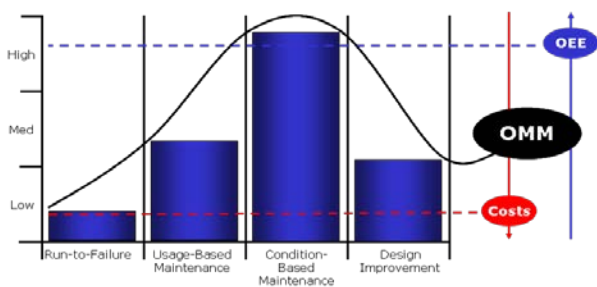


Figure 2: Asset Care Plan Layout [9]

The AM reports provide a clearer picture of the state of the electrical network and the seriousness of the challenges facing the organization. There is a huge disparity between tactical and non-tactical maintenance which indicates that field staff are concentrating more of their efforts on faults and breakdowns, thereby neglecting the planned maintenance work. The lack of planned maintenance work ultimately results in more faults and breakdowns and this coupled with the huge volumes of theft, vandalism and third party cable damage poses serious challenges for the municipality. The AM and SG systems are however, providing the organization with a much clearer picture of the situation.

3 PERFORMANCE ANALYSIS OF ETE SMART SYSTEMS

The impact assessment used empirical data developed from the SG projects with information on how SG technologies were being applied and also

determined the value of the technology to better inform future decisions. The focus areas were peak demand and energy consumption, operational improvements, maintenance improvements, system losses, system. Indices that provide accurate and unambiguous information on system technical performance are important tools in the management of electrical network performance [7]. These indices could provide the foundation for dialogue between major stakeholders.

3.1 Frequency of sustained connection point interruptions

The system average interruption frequency index (SAIFI) for sustained connection point interruptions (CPI) are given by [7]:

$$\text{SAIFI-CPI} = \frac{\sum (\text{No of sustained CPI})}{\text{Total no. Of CP}}$$

SAIFI statistics as illustrated in figure 3 indicate a decrease in this performance indicator from 2011 until 2014, however there was a huge peak in 2013, indicating the largest number of sustained connection point interruptions.

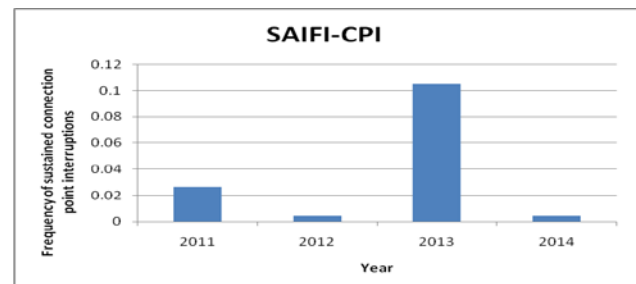


Figure 3: Historical eTE SAIFI Statistics

3.2 System event severity indices

The severity of an interruption event or an involuntary customer load reduction event is quantified by the associated energy-not-supplied, in MWh (in the case of end-use customers In the case of loads, the severity of an individual interruption event is given as: [7]

$$\text{SMn} = \frac{\text{Est energy not supplied (MWh)} \times 60}{\text{System annual max demand (MW)}} \text{ min}$$

The statistics as illustrated in figure 4 indicates a drop from 2011 to 2014 in system minutes measured for energy not supplied. This is positive and probably the biggest indicator in demonstrating that the implementation of SG is having a positive impact on the management of the electrical network. The peak in 2013

is due to the large number of interruptions that occurred in that year.

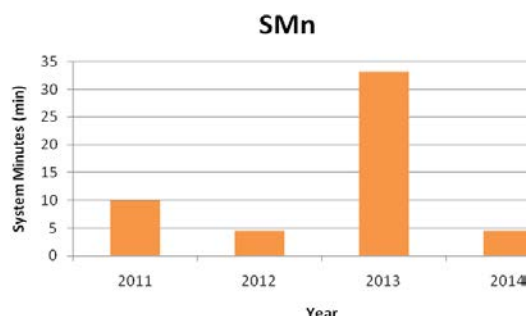


Figure 4: Historical eTE System Minutes Statistics

3.3 Capital and Operating Expenditure

The capital and operating expenditure for the past 7 financial years is depicted in figure 5. The capital expenditure was R419m in 2007 and has risen to R526m in 2013, with a peak of R683m in 2009. The operating expenditure on the other hand has been on a constant uptrend and has increased from R1.03bn in 2007 to R2.27bn in 2013 which equates to a 220% increase in just a period of 7 financial years. The operating costs used for this exercise excludes the cost for the purchase of electricity from Eskom which accounts for approximately 60% of the total eTE expenditure per annum.

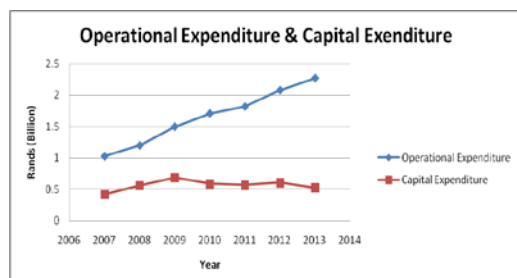


Figure 5: Capital and Operating Expenditure

The financial statistics indicates a fairly static capital budget spend which indicates that eTE is somewhat progressive in this regard but there is only a slight increase year on year. This is actually misleading as eTE had actually intended to spend much more on capital projects but had to declare significant savings due to corporate instructions. The operating budget, on the other hand is on a constant uptrend, largely owing to the large number of faults that occur on the network. As indicated earlier in this study, one of the main objectives of the implementation of SG systems is to drive down costs. The financial statistics however indicate results to the contrary. This does not necessarily mean that SG is not having a positive impact on the system, but rather

that there are many more factors that are driving up the costs that are beyond the control of the SG systems.

3.4 Electricity Tariffs

Figure 6 shows the historical electricity tariff rates at eTE for the residential, commercial and industrial sectors. It can be seen that the tariffs have been on a steady rise from 2008 to now, with the residential tariff rising by 226%, the commercial tariff by 249% and the industrial tariff by 266% during the past 7 financial years (2008 – 2014).

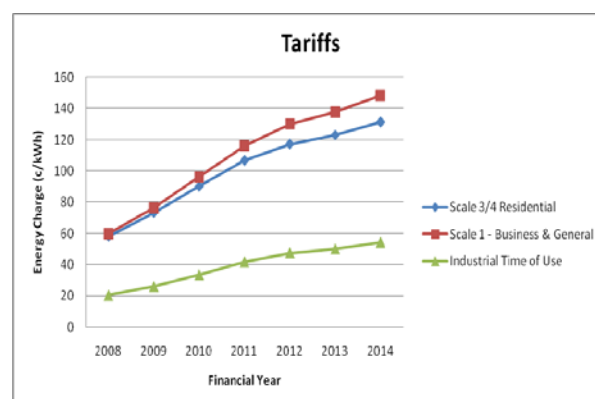


Figure 6: Historical Tariff Rates

ETE is classified as an electricity distributor as it purchases electricity from Eskom and thereafter sells to its customers. In order to make this transaction feasible and sustainable, the eTE tariffs are to some extent a reflection of the Eskom tariffs and any price increase imposed on by Eskom will have a resultant increase in the eTE tariffs. It was also pointed out earlier in the study that an objective of the implementation of SG is to make services more affordable to the consumers, however the consistent increase in tariff rates indicates otherwise. The other method where consumers could save money is by better managing their load requirements and power consumption. There is already a TOU tariff available for the industrial and commercial customers where consumers could enjoy significant savings by moving their loads into the standard and off-peak periods and the metering infrastructure is already in place to support this. A residential TOU tariff was published and advertised approximately four years ago, but the metering infrastructure is unfortunately not yet in place to support this tariff.

3.5 System Losses

The total losses at eTE as illustrated in figure 7, has been fluctuating between 5 and 6.22% over the past 12 financial years. The figure is calculated by taking the difference between the energy purchased and sold. This

value would therefore include the technical as well as the non-technical losses. A total energy loss of 667 412 169 kWh was experienced during the past financial year. The resultant revenue impact was R396 million which was a 9% increase from the previous financial year.

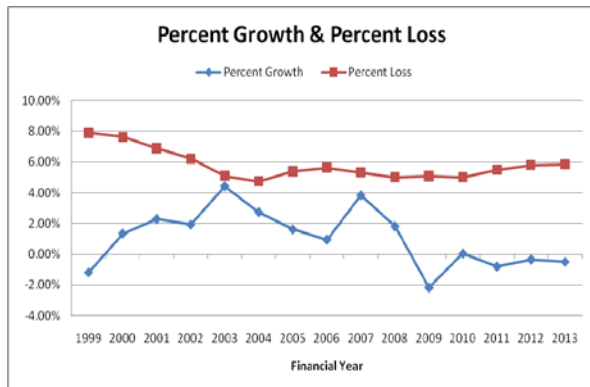


Figure 7: System Losses and Sales Growth

The overall system losses dropped from around 8% in 1999 and has averaged between 4.5 to 6% from then till date. It is however, noted that there has been a steady uptrend over the past seven financial years and this is cause for great concern as it is largely an indicator of the increase in volumes of illegal electricity connections. Non-technical losses (NTL) are a huge revenue loss [10]. The SG systems are able to detect these anomalies in the systems but the socio-economic battle is a far greater challenge for the municipality.

4 SG IMPACT ASSESSMENT AT ETE

An invitation was extended by South African SG Initiative (SASGI) to all metropolitan municipalities in South Africa to be considered for the first SG Maturity Model (SGMM) assessment. eTE was chosen for this assessment which was to be sponsored through the South African National Energy Development Institute (SANEDI). The following generic observations were made by the Navigator which was based on the analysis of results received from SEI and his insight and knowledge: [8]

- The technology implementation is not aligned and integrated into a SG strategy;
- The survey results reflect the absence of an integrated technology deployment approach.
- The adoption of a SG vision, strategy and technology deployment plan will significantly elevate the SG maturity level of the eTE;

- While the utility's SG maturity level lags the Peer Community as well as that of the SGMM community, there is a level of correlation.
- The maturity level in respect of the Customer domain somewhat did not dovetail with the utility's stated objectives;
- The Grid Operations (GO) and the Value Chain Integration (VCI) indicated significant maturity and were closest to the Peer and the SGMM community.
- The high focus on information security from the outset on all projects was commendable

5 CONCLUSION

The SGMM results indicated that there have been significant progress made in several domains of eTE. It also emerged that the lack of a formalized SG vision, implementation strategy and technology plan resulted in various initiatives not been aligned to its objectives. The level of impact of SG systems varies in different areas of the business with varying degrees of success. It is evident that eTE is quite progressive in its approach and has embraced the concept of SG and is striving to become one of the leaders in SA in this regard.

6 REFERENCES

- [1] Hammerstrom DJ et al, Testbed Demonstration Projects, Pacific Northwest GridWise, www.pnl.gov/main/publications
- [2] US Department of Energy, SG, Office of Electricity Delivery and Reliability, 1000 Independence Avenue, SW, Washington DC,, <http://energy.gov/oe/services/technology-development/smart-grid>
- [3] Jagannath S, Communication Networks Overview, Current and Future Projects, eTE Electricity, 2014
- [4] McDonald JD, SG Subject Matter Expert, Institute of Electrical and Electronic Engineers
- [5] Mashinini G, AMI (AMI) Programme Overview, eTE Electricity, 2014
- [6] BekaSchreder, The Owllet Telemanagement System, Nightshift Intelligent Digital Streetlighting, www.beka.co.za, owl@beka.co.za
- [7] Dold A and Others, NRS 048-8:2009, Quality of Supply, Measurement and Reporting of EHV and HV Network Interruption Performance, 2009, : <http://www.nrs.eskom.co.za>,
- [8] de Beer W, eTE SG Maturity Assessment, South African National Energy Development Institute (SANEDI), 2014, wj.debeer@yahoo.com, www.SANEDI.org.za
- [9] Jagessar S, Pragma, Asset Management Strategy for eTE Electricity, 2012, sanjay.jagesar@pragmaworld.net
- [10] I E Davidson, "Evaluation and Effective Management of Non-Technical Losses in Power Systems". *The Transactions of the South African Institute of Electrical Engineers*, Vol. 94, No.3, Sep. 2003, pp. 39-42.

SMART GRID APPLICATION USING ETSI M2M: DOMESTIC ELECTRIC WATER HEATERS

A.H. Cloete, J.W.K. Brown, M.J. Booysen R. Steinke and T. Magedanz

Department of E&E Engineering
Stellenbosch University, South Africa
South Africa

Fraunhofer FOKUS
TU Berlin
Germany

Corresponding email: mjbooyesen@sun.ac.za

Abstract: Energy supply constraints have increasingly been in the spotlight recently, especially in South Africa. Concurrently, advances in machine-to-machine (M2M) communications and cloud computing have opened a multitude of opportunities for the so-called smart grid, and have shifted the traditional paradigms of what is controlled and how these things are controlled. Water heating, which is the prime contributor to household electricity use, is one application that provides opportunities for new and more efficient control and reporting through these technologies. However, to exploit the substantial gains from such opportunities, M2M blocks need to be in place, and such systems need to conform to standards to fully realise the potential benefits. The dominant standard is currently the ETSI standard, which has two main compliant implementations: OpenMTC and OM2M. This paper proposes a smart grid configuration using the ETSI M2M standard to exploit new means of control of and reporting on domestic electric water heaters in the South African context. A pilot study application was set up with the proposed configuration and some of the novel results are described and results given to demonstrate the system and its benefits.

Key words: ETSI M2M, Smart grid, domestic electric water heater, OM2M, demand-side management, ESKOM, RESTful architecture.

1. INTRODUCTION

Due to the shortage of energy supply capacity, South Africa has been experiencing regular black-outs since early 2008, adversely affecting the country's economy. [1, 2]. In an attempt to lower peak demand, Eskom significantly raised energy prices for redistributors (municipalities) during peak times. In response, municipalities installed ripple control units in residences to switch electric water heaters (EWH) in bulk. [3] Although so-called peak shaving reduces the demand on the grid, typical installations use one-way communication, which does not take into account user behavioural patterns and user comfort. Furthermore, the energy storing nature of EWHs presents an attractive opportunity for large scale intelligent demand-side management for load balancing given suitable connectivity and control [4]. In fact, several load balancing schemes have been suggested in the past. However in order to be practical, a two-way communication infrastructure and intelligent analysis is needed to connect each control unit to an automated decision making agent. Such a system of distributed communicating devices requiring little human administration, is known as machine-to-machine (M2M) communications.

Up until recently, no commonly accepted standards existed for M2M communications, meaning that end-to-end M2M solutions were developed on a per case basis for each new application often resulting in duplicate effort. Moreover, these tailored solutions are fragmented and cannot be used for cross-domain interoperability. Consequently, they

became known as *vertical* implementations. However, in 2008 the European Telecommunication Standards Institute (ETSI) started working on M2M standards that specify a common *horizontal* framework that builds on the successes of the world wide web architecture [5].

The ETSI M2M architecture was designed to work across all industry segments including healthcare, transportation, retail, consumer etc. ETSI especially paid attention to the energy sector. A summary of typical use cases is presented in [6]. The term "Smart Grid" however, encompasses a plethora of distinct applications that covers generation, transmission, distribution and end-customer as described in [7]. The objective of the work presented in this paper is the design an EWH M2M system that fits into the ETSI reference architecture, and with particular focus on the requirements of the end-user: the consumer of hot water. The greater purpose of the proposed system, i.e. for connecting EWHs to the Internet, is three-fold: 1. To provide remote control; 2. To provide eco-feedback (real-time feedback for increased user awareness); and 3. To enable large-scale analysis of EWH efficiency and user behaviour.

1.1 Contribution

This paper proposes a design of an M2M architecture for large-scale EWH monitoring and controlling, which is compliant to the ETSI M2M standards. A prototype implementation of this design is presented and the benefits and challenges are discussed. Also presented are some novel presentations of analytical results obtained during a pilot study.

The rest of this paper is structured as follows. Section 2. discusses some of the related work. Section 3. gives a brief overview of the ETSI M2M standards and how it fits into a smart grid infrastructure. Section 4. discusses the system design. Section 5. presents the results of testing and using the system. Finally section 6. concludes the paper.

2. RELATED WORK

Extensive research has been conducted on EWH usage and several techniques have been proposed for improving efficiency [4, 8–10]. However, none of the suggestions proposed an architecture for large-scale deployment to test and implement the proposed techniques and most resort to simulation. This section shortly discusses some of the work that has been done on EWHs in the context of Smart Metering and Smart Grid.

2.1 EWH efficiency

In [11], the authors developed a proof-of-concept EWH monitoring system and deployed it to 18 household EWH's. The purpose of the study was to validate an EWH model presented, and investigate the impact of human-in-the-loop feedback. The M2M network in this paper is built on a proprietary platform called Trinity SMART. Each device connects to the access network using a cellular modem that is installed with custom firmware from Trinity. The problem with this type of architecture is that the quality of service (QoS) is wholly dependent on the platform vendor. Furthermore, all data collected is confined to the internal infrastructure, making it difficult to incorporate into 3rd party applications. This type of architecture is a typical example of a *vertical solution*, which is ubiquitous in the M2M industry. A smartphone application was developed in [12] that accesses the Trinity platform and gives real time feedback of each EWH to its user. The work hypothesises that environmental impact can be greatly reduced by simply providing customers with more timeous and higher-resolution feedback of their usage. The authors admit that functionally of the application is inhibited due to proprietary API restrictions.

Similarly, the authors of [13] emphasise that concise and timely feedback is essential to those who wish to change their behaviour for the sake of energy conservation. The work proposes a system that measures the energy consumption of individual household appliances where each smart meter interfaces with a custom central household gateway. User interface is provided via a mobile device that also connects to the local gateway. No access is provided from outside. Showcasing modern technology (RESTful interface with a database) this article serves as an example of a valuable contribution, which did not gain traction, arguably due to a lack of interoperability.

2.2 Use of ETSI M2M in Smart Grid

The introduction of the ETSI M2M standards aroused interest in both the academia and industry for its application to Smart Grid. One implementation of ETSI

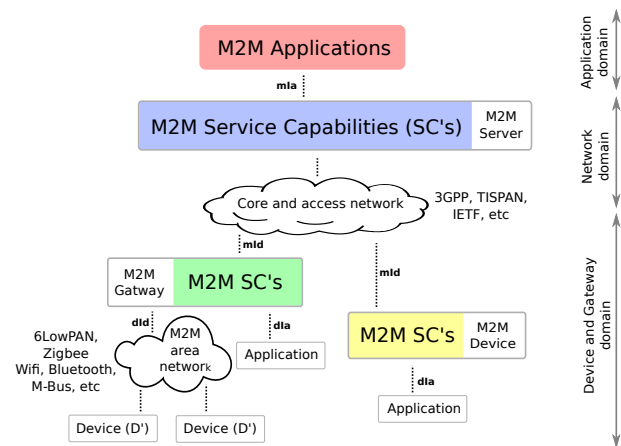


Figure 1: ETSI horizontal architecture

M2M, called OpenMTC, is presented in [14]. OpenMTC is utilised as a Smart Energy platform that facilitates large-scale deployment of real-world experiments in a collaboration project called TRESCIMO (Testbeds for Reliable Smart City M2M Communication). The partners include Eskom, the CSIR and UCT [2].

3. ETSI M2M OVERVIEW

This section introduces the ETSI M2M architecture to provide the necessary background to understand how the proposed EWH monitoring system fits into the architecture.

3.1 Reference architecture

After conducting an in-depth study in 2008, in various application domains, ETSI listed a set of generic requirements for M2M communications. The effort resulted in technical specification documents [15–17] finalised in 2012.

In essence, ETSI defined a middleware layer they called *Service Capability Layers* (SCLs), which abstracts the underlying communication layer to provide a common interface. Each SCL is a software module that provides a specific service such as security, remote management, addressing, etc. and may be shared by various applications. Figure 1 shows the high level functional architecture as defined in [16]. Notice that the architecture defines *servers*, *gateways* and *devices*, each containing some or all of the SCLs. The architecture also accommodates legacy devices and protocols through the use of interworking proxy units (IPUs). Alongside these SCLs, ETSI proposed a standard hierarchy for device access that ensures a constant format across all M2M domains [18]. The maintenance and extension of ETSI M2M were handed over to *OneM2M* [19] in 2013, founded specifically for this purpose.

REST: Since the nature of M2M distributed systems is more about tangible states than about exposed methods [20, p. 112], ETSI decided to adopt a REST architecture

for the new standards. The term REST originates from REpresentational State Transfer, which means:

- End-point nodes should be thought of as objects (called *resources*) instead of actions;
- Each resource has a globally unique ID (*URI*);
- Each resource remembers *only* its own state;
- State should be represented and transferred as web documents; and
- Access to the state of each resource is constrained to only four actions: *create*, *retrieve*, *update*, *delete* (CRUD).

Since no resource is responsible for remembering the state of any other resource than itself, the REST architecture is called *stateless*. Statelessness is important, since it enables horizontal scaling, that is, performance can be added by simply adding more machines. Statelessness also enables network caching which greatly aids resource contained devices by either allowing data to be retrieved even when a device is offline or limiting the amount of requests to an individual device. A highly scalable architecture is a key prerequisite for M2M.

3.2 OM2M: An open implementation of ETSI M2M

Shortly after the release of the ETSI M2M standards, an open-source project initiated by LAAS-CNRS, called *Open M2M* or *OM2M* started work on a reference implementation of the standards [21]. The result was a modular and extensible framework that includes the implementation of SCs for both server and gateway devices [22].

3.3 OpenMTC: A standard-compliant ETSI M2M implementation

OpenMTC development was started by Fraunhofer FOKUS and TU Berlin. It is a prototype implementation of an M2M middleware. It aims to provide a standard-compliant platform for M2M services [14, 23]. The implementation can be deployed as single instance or as part of a server gateway(s) system [24]. OpenMTC supports HTTP and CoAP and is capable to support transport protocol selection [25].

4. DESIGN

This section presents the design for an EWH M2M network that can be built using either of the OM2M or OpenMTC platforms.

4.1 Requirements and constraints

Although only the minority of households in South Africa have DSL access, cellular access is ubiquitous and still growing. Therefore, to be feasible, device connectivity needs to be established via the cellular access network.

To ensure optimal network utilisation, the transaction period must be as close as possible to network latency.

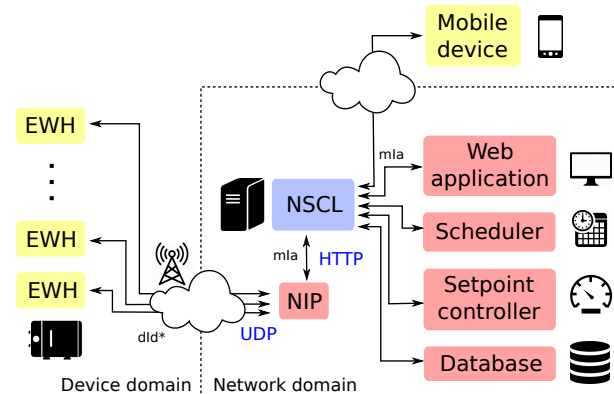


Figure 2: The proposed architecture for EWH M2M

According to [18], Smart Grid applications can be classified into four categories according to network latency: *protection* (1 - 10 ms), *control* (100 ms), *monitoring* (1 s) and *reporting and billing* (1 h). Under this classification an EWH falls under controlling and monitoring, requiring a maximum communication latency between 100 ms and 1 s. However, the large thermal mass of a typical EWH means that noticeable state changes can take up to an hour to occur. Including the requirement for data analysis, user behaviour and eco-feedback, preliminary experiments showed that a reporting period of 1 minute is sufficient.

4.2 M2M architecture

Figure 2 shows the high level layout of the proposed architecture. For reference, the colours indicated correspond to that of Figure 1. A discussion of each component follows below.

EWHs: Represented here are the hardware monitor and control units at each site. The unit was designed to be retrofitted to existing EWH installations without compromising the structural integrity. A custom unit was developed that measures four temperatures, two water flow rates, power consumption and leakage. The unit controls electrical power to the element and water flow to the EWH. The processor on the control unit performs basic operations on sensor data to calculate energy and flow rate. It also implements a failsafe control scheme in the event of a communications failure. Apart from immediately cutting both water and power supply to the unit when a leak is detected, the primary function of the processor is to aggregate and format the data that is transmitted, and to decode instructions that are received. The unit reports a measurement point via a cellular modem to the NIP located at a central server once a minute.

Communication and protocols: Several lightweight protocols targeted specifically at M2M/IoT were designed alongside the M2M standards, the most prominent of which is the Constrained Application Protocol (CoAP)

[26]. CoAP is a *request/response* type protocol that can be viewed as binary implementation of HTTP but has additional M2M features such as multi-casting and discovery. CoAP also transports over UDP, is better suited than TCP for M2M because it is light-weight, and scales well [27]. Furthermore, many M2M applications are usually tolerant to packet-loss. We opted to use CoAP in our design, however at the time of this writing we were not able to implement the full CoAP protocol. We therefore implemented a proof-of-concept custom protocol that borrowed two features from CoAP: UDP for low network load, and a queuing mechanism for NAT (network address translator) traversal. The queuing mechanism involves sending a command *piggybacked* on the response/acknowledge of a client device request. This mechanism allows a device behind a firewall or NAT to be reached.

NIP: The purpose of the Network Interworking Proxy is to translate the custom UDP protocol message from every EWH into a standards compliant HTTP request to the NSCL. Proxy units are defined as part of the ETSI M2M standards as a means to support legacy, or non-standard protocols. Since UDP is a connectionless protocol this application is single threaded and easily scalable.

NSCL: The *Network Service Capability Layer* provided by OM2M, forms the core of the architecture. The NSCL contains all of the SC modules provided by OM2M, and includes:

- *Application enablement* providing the REST API;
- *Generic communication* providing HTTP and CoAP access;
- *Reachability, addressing and repository* providing storage and subscription management;
- *Security*

Setpoint controller and Scheduler: These applications were developed as simple example applications that are now made possible thanks to the underlying extensible architecture.

To enable centralised control of a multitude of EWHs, the temperature controller is moved into the cloud. The module compares each data point received with a temperature reference point and if necessary requests a change in element state at the EWH. In the event of communication failure, each EWH unit reverts to a safe local control loop. The EWH is also able to ignore an element request from the Setpoint controller if it violates a safety restriction. This mechanism is depicted in Figure 3 and is extended in Figure 4.

The Scheduler simply contains a *list* of setpoints which it forwards to the Setpoint controller every 15 minutes. Owing to the well-defined interface, this application can easily be extended to actively change the schedule, say, for an individual based on a learned usage behaviour, or for

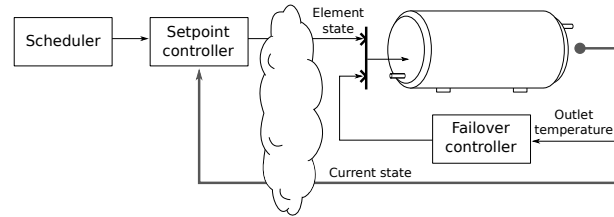


Figure 3: EWH temperature control scheme

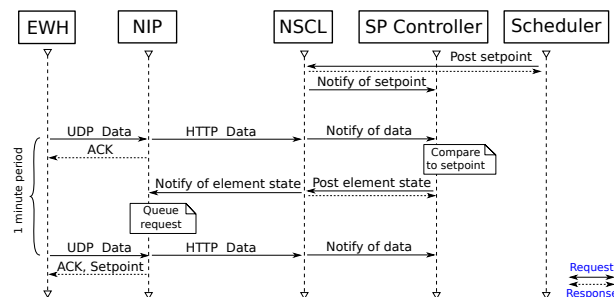


Figure 4: Typical EWH M2M transactions

an entire suburb based on grid load predictions. Figure 4 depicts the timing diagram for a complete transaction from Scheduler to EWH. The queuing mechanism is also highlighted here again.

Database: This application subscribes to inbound data from the NSCL and upon notification stores it in a relational database for future analysis.

User interfaces: A simple web application was developed as a portal to demonstrate EWH interface. Once a user has logged in, the web application queries the NSCL to display a dashboard for EWH status and control.

Alongside the web application, the Android application in [12] was adapted for monitoring and control. The uniform interface to the NSCL allows this application to perform queries against the NSCL in the *exact* same way as the web application. No duplicate effort is therefore required for the same functionality on a different platform.

5. RESULTS

The proposed system was implemented in a pilot study of 6 households. A lab unit was also set up for experimentation.

As stated in the introduction, one goal of the pilot project is to collect initial data for analysis. Presented here are visualisations of some of the data obtained, along with a preview of the information made available through analysis.

Figure 5 shows a plot of EWH temperatures for one household over 24 hours with element state for reference (top), as well as a balloon plot of the hot water usage events during that same day (bottom). Detail concerning

the events is presented in Table 1. The energy cost per event was estimated by calculating the *effective* energy of the consumed water using the volume and temperature of each event.

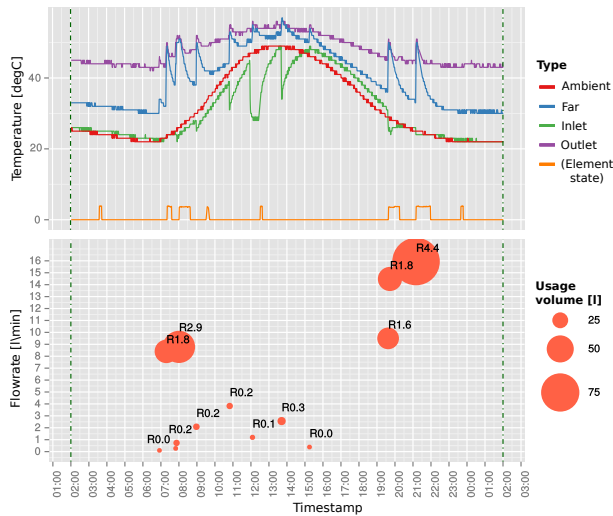


Figure 5: Temperature and event data for EWH (A) on 28 October

Event time	Volume (litres)	Duration (minutes)	Temp (°C)	Energy (kWh)
07:18	42.0	5	48.8	1.23
08:00	61.4	7	51.4	1.96
19:37	37.9	4	49.7	1.05
19:43	43.4	3	49.3	1.23
21:10	95.6	6	50.3	2.93

Table 1: Summary of events

Figure 6 gives the daily energy breakdown for a particular household EWH over the month of October. The measured electrical energy consumption is given along with an estimation of the effective consumed energy and standing losses.

Table 2 gives the average daily packet loss per EWH in the pilot study.

EWH	A	B	C	D	E	F
Packet-loss (%)	4.5	0.9	2.6	0.7	6.9	0.9

Table 2: Average daily UDP packet loss per EWH

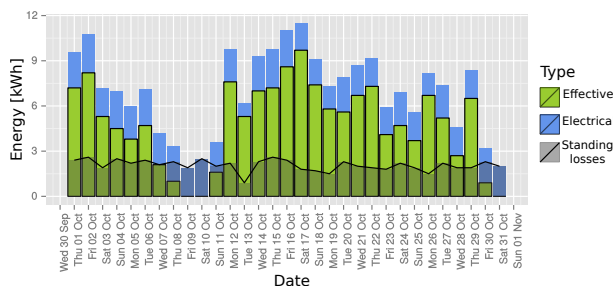


Figure 6: Daily energy consumption profile of a household EWH for October

Each data-point is 219 bytes long, which results in roughly 10 megabytes per EWH per month.

Figure 7 shows the result of an experiment conducted on an EWH over 24 hours to validate the correct operation of the Scheduler and Setpoint controller. The Setpoint controller controls against the *outlet* temperature. To emphasise the control, the EWH was drained for 25 minutes at 12:00 to cool the EWH down. After the event, the figure clearly depicts the outlet temperature following the scheduled temperatures. Note that Setpoint controller has 2°C of hysteresis around the reference point.

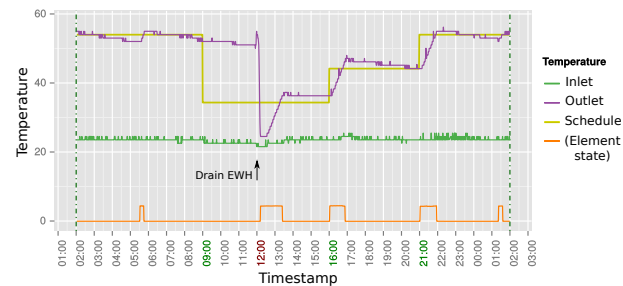


Figure 7: Laboratory experiment showing Schedule control performance over 24 hours

6. CONCLUSION

Energy constraints have resulted in various interventions and innovations, including demand side management and eco-feedback. A major contributor to household energy use is electrical water heaters (EWHs). The multitude of vertical smart metering (and other M2M) solutions have necessitated the recent release of the ETSI standards for M2M, which enable scalable and compatible infrastructures. This paper described the design of an ETSI compliant EWH solution that uses cellular technology, and which aims to provide a platform for eco-feedback, large-scale analysis, and remote control. The results show the historically *dumb* EWH can be transformed to provide new insight, access, and control in an extensible centrally controlled smart grid application.

REFERENCES

- [1] R. Inglesi and A. Pouris, "Forecasting electricity demand in South Africa: a critique of Eskom's projections," *South African Journal of Science*, vol. 106, pp. 50 – 53, 02 2010.
- [2] H. Madhoo, A. Khatri, T. Willemsse, D. Oosthuizen, and L. Coetzee, "Future internet concepts for demand management," in *Domestic Use of Energy (DUE), 2015 International Conference on the*, March 2015, pp. 19–26.
- [3] B. Rautenbach and I. Lane, "The multi-objective controller: a novel approach to domestic hot water load control," *Power Systems, IEEE Transactions on*, vol. 11, no. 4, pp. 1832–1837, Nov 1996.

- [4] M.H. Nehrir and B.J. LaMeres, "A multiple-block fuzzy logic-based electric water heater demand-side management strategy for leveling distribution feeder demand profile," *Electric Power Systems Research*, vol. 56, no. 3, pp. 225 – 230, 2000.
- [5] H. Anton-Haro and M. Dohler, *Machine-to-machine (M2M) communications : architecture, performance and applications*. Cambridge, UK Waltham, MA: Woodhead Publishing, 2015.
- [6] "Machine-to-machine communications (m2m); smart metering use cases," ETSI, ETSI TR 102 691 V1.1.1.
- [7] G. Lu, D. Seed, M. Starsinic, C. Wang, and P. Russell, "Enabling smart grid with etsi m2m standards," in *Wireless Communications and Networking Conference Workshops (WCNCW), 2012 IEEE*, April 2012, pp. 148–153.
- [8] C. Diduch, M. Shaad, R. Errouissi, M. Kaye, J. Meng, and L. Chang, "Aggregated domestic electric water heater control - building on smart grid infrastructure," *2012 IEEE 7th International Power Electronics and Motion Control Conference - ECCE Asia conference proceedings : June 2-5, 2012, Harbin, China*.
- [9] K. Al-jabery, D. C. Wunsch, J. Xiong, and Y. Shi, "A novel grid load management technique using electric water heaters and q-learning," *IEEE International Conference on Smart Grid Communications*.
- [10] K. Lajoie and D.A. Halamay and T.K.A. Brekken, "Residential water heaters as a grid-scale energy storage solution using model predictive control," *IEEE Conference on Technologies for Sustainability (SusTech)*.
- [11] M.J. Booysen and J.A.A. Engelbrecht and A. Molinaro, "Proof of concept : large-scale monitor and control of household water heating in near real-time," *International Conference on Applied Energy ICAE 2013, Jul 1-4, 2013, Pretoria, South Africa*, 2013.
- [12] P.J.C Nel and M.J. Booysen and A.B. van der Merwe, "ICT-enabled solutions for smart management of water supply in Africa," *Proceedings of the 1st International Conference on the Use of Mobile ICT in Africa*, 2014.
- [13] M. Weiss, F. Mattern, T. Graml, T. Staake, and E. Fleisch, "Handy feedback: Connecting smart meters with mobile phones," in *Proceedings of the 8th International Conference on Mobile and Ubiquitous Multimedia*, ser. MUM '09. New York, NY, USA: ACM, 2009, pp. 15:1–15:4.
- [14] A. Elmangoush, R. Steinke, A. Al-Hezmi, and T. Magedanz, "On the usage of standardised m2m platforms for smart energy management," in *Information Networking (ICOIN), 2014 International Conference on*, Feb 2014, pp. 79–84.
- [15] "Machine-to-machine communications (m2m); m2m service requirements," ETSI, ETSI TS 102 689 V2.1.1.
- [16] "Machine-to-machine communications (m2m): Functional architecture," ETSI, ETSI TS 102 690 V2.1.1.
- [17] "Machine-to-machine communications (m2m); mia, dia and mid interfaces," ETSI, ETSI TS 102 921 V1.3.1.
- [18] T. Predojevic, A. Al-Hezmi, J. Alonso-Zarate, and M. Dohler, "A real-time middleware platform for the smart grid," in *Green Communications, 2014 IEEE Online Conference on*, Nov 2014, pp. 1–6.
- [19] OneM2M. [Online]. Available: <http://www.onem2m.org/>
- [20] D. Boswarthick, O. Elloumi, and O. Hersent, *M2M communications a systems approach*. Hoboken, N.J: Wiley, 2012.
- [21] OM2M - Connecting things. [Online]. Available: www.eclipse.org/om2m/
- [22] M. B. Alaya, Y. Banouar, T. Monteil, C. Chassot, and K. Drira, "OM2M: Extensible ETSI-compliant M2M Service Platform with Self-configuration Capability," *Procedia Computer Science*, vol. 32, no. 0, pp. 1079 – 1086, 2014, the 5th International Conference on Ambient Systems, Networks and Technologies (ANT-2014).
- [23] A. Elmangoush, H. Coskun, S. Wahle, and T. Magedanz, "Design aspects for a reference M2M communication platform for Smart Cities," *2013 9th International Conference on Innovations in Information Technology, IIT 2013*, no. MARCH 2013, pp. 204–209, 2013.
- [24] M. Corici, H. Coskun, A. Elmangoush, A. Kurniawan, T. Mao, T. Magedanz, and S. Wahle, "OpenMTC: Prototyping Machine Type communication in carrier grade operator networks," *2012 IEEE Globecom Workshops, GC Wkshps 2012*, pp. 1735–1740, 2012.
- [25] A. Elmangoush, R. Steinke, T. Magedanz, A. A. Corici, A. Bourreau, and A. Al-Hezmi, "Application-derived communication protocol selection in M2M platforms for smart cities," *2015 18th International Conference on Intelligence in Next Generation Networks*, pp. 76–82, 2015.
- [26] Z. Shelby, K. Hartke, and C. Bormann, "The constrained application protocol (coap)," Tech. Rep. 7252, June 2014.
- [27] S. Abdul Salam, S. Mahmud, G. Khan, and H. Al-Raweshidy, "M2m communication in smart grids: Implementation scenarios and performance analysis," in *Wireless Communications and Networking Conference Workshops (WCNCW), 2012 IEEE*, April 2012, pp. 142–147.

Mitigation of Electromagnetic Interference Generated By GPIB Control-Network In Ac-Dc Transfer Measurement System

M.M. Hlakola^{1*}, E. Golovins¹, D.V. Nicolae²

Abstract— The field of instrumentation electronics is undergoing an explosive growth, due to its wide range of applications. The proliferation of electrical devices in a close working proximity can negatively influence each other's performance. The degradation in the performance is due to electromagnetic interference (EMI).

This paper investigates the negative effects of electromagnetic interference originating in the General Purpose Interface Bus (GPIB) control-network of the ac-dc transfer measurement system. Remedial measures of reducing measurement errors and failure of range of industrial devices due to EMI have been explored. The ac-dc transfer measurement system was analyzed for the common-mode (CM) EMI effects. Further investigation of coupling path as well as more accurate identification of noise propagation mechanism has been outlined. To prevent the occurrence of common-mode (ground loops) which was identified between the GPIB system control circuit and the measurement circuit, a microcontroller-driven GPIB switching isolator device was designed, prototyped, programmed and validated. This mitigation technique has been explored to reduce EMI effectively.

Keywords— *CM, EMI, GPIB, ground loops*

I. INTRODUCTION

Growing complexity of electronic and communication devices leads to emergence of various electromagnetic interference (EMI) sources that hinder the stable operation of these devices. EMI is a spurious electromagnetic energy that pollutes electronics and electrical equipment. The ac-dc transfer measurement system stability and accuracy are limited by electromagnetic interference. The high-accuracy low frequency ac-dc measurements are particularly susceptible to the conducted EMI, which can be produced in the measurement circuit by differential-mode (DM) and common-mode (CM) current and voltage components originating from the external sources coupled with the measurement circuit [1]-[2].

The negative effects of EMI are obstruction, degradation and limitation of the effective performance of electronics and electrical devices. The interference occurs in electronic devices on the operation of another by means of electromagnetic energy transfer.

The conducted EMI passes through supply lines, electronic control networks and interconnecting wires and cables. It is desirable to find effective measures of dealing with the conducted EMI problems to avoid measurement uncertainties and costly equipment failures in industry. To secure an interference-free environment, mitigation technique(s) are desired to overcome the EMI problem. In this paper, the negative impact of the common-mode EMI (ground loops) on the ac-dc transfer measurement system will be outlined. The technical solution to prevent ground loops has been explored and validated.

II. AC-DC TRANSFER MEASUREMENT SYSTEM.

The ac-dc transfer measurement system joins up to 5 different instruments and a PC with the Automated Measurement System (AMS) control software into a network of the IEEE 488.2 (GPIB) interfaces

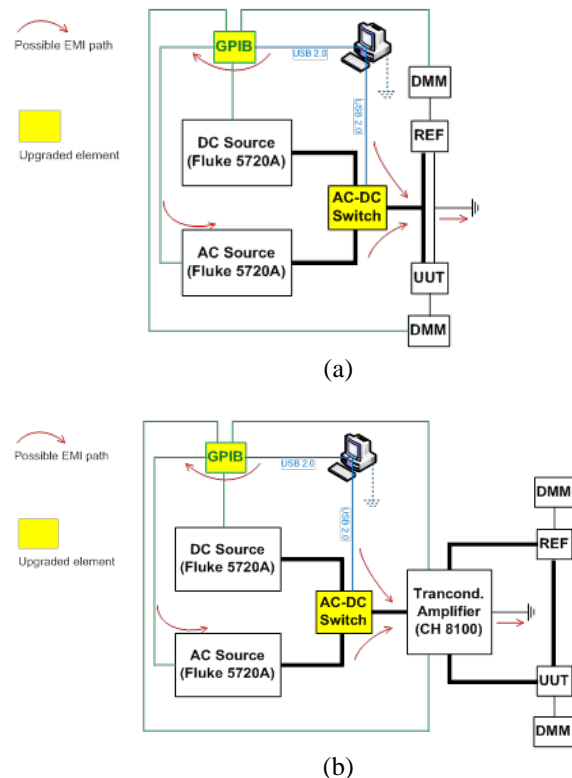


Fig.1. Schematic diagrams of ac-dc transfer measurement system: (a) for voltage measurements; (b) for current measurements [3]

The diagrams on Fig.1. assume that the dc source is not susceptible to the conducted EMI in contrast to the ac source which is with more likelihood considered to contain coupling between the control and generation circuits, involving multiple reactive components

III. PROBLEM IDENTIFICATION

It was experimentally observed that the control-plane currents originating in the GPIB can penetrate the measurement plane through coupling between the ac source's GPIB flowing towards the central ground point and cause thermal converter response observed at the measurement instrument even when no measured signal is applied at the input [4]-[5]. Figure 2 shows one of the hypothetical ground loops that could get formed in such a configuration

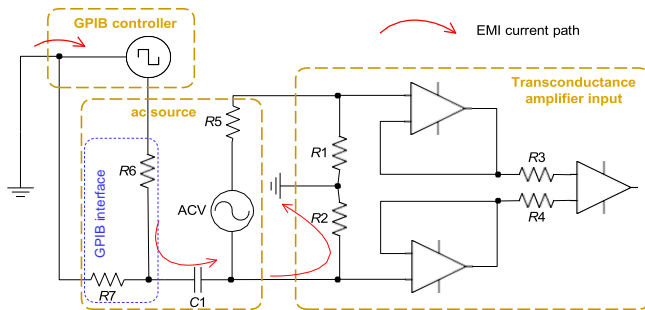


Fig 2: Ground loops through coupling between the GPIB bus and primary measurement network

The differential input of the transconductance amplifier leaves possibility of the output current gain fluctuation due to the EMI-induced Lo-to-ground voltage noise. It is therefore necessary to comprehend the ground loops in the ac-dc measurement system through common-mode (CM) interference error analysis so that a custom solution could be designed to prevent loop occurrence in the measurement plane. The critical requirement to this solution is a non-intrusive design with regard to the measurement plane that would exclude measurement accuracy deterioration

IV. MITIGATION OF EMI GENERATED FROM THE GPIB CONTROL NETWORK.

A programmable GPIB bus isolator implementing the automated GPIB channel switching has been developed at the AC-DC Difference Laboratory. The ultimate goal of the isolator is to prevent any EMI path through the GPIB bus, the risk of ground loop occurrence and EMI-induced error when the meter processes a measured sample. The following concepts were adopted in the approach to the GPIB isolator and its control module design:

- +12 Vdc supply to power both the channel switching array and control module of the isolator;
- Complete electric cut-off of each of the 24 wires in the GPIB bus using relay circuit breakers;

- Arduino Uno R3 MCU with the USB 2.0 interface for reconfigurable channel selection in accordance with the requested instrument's GPIB address.

The basic schematic diagram of the switching isolator control module is shown in figure 3. The circuit is characterised by the following features:

- Electrical isolation of the MCU digital outputs from the rest of the module through the use of optocoupler; provides protection against high voltages and low level noises that could produce errors in the output
- Capacity to expand the maximum number of programmatically switched GPIB channels, determined by the number of vacant MCU digital outputs (up to 7 channels).

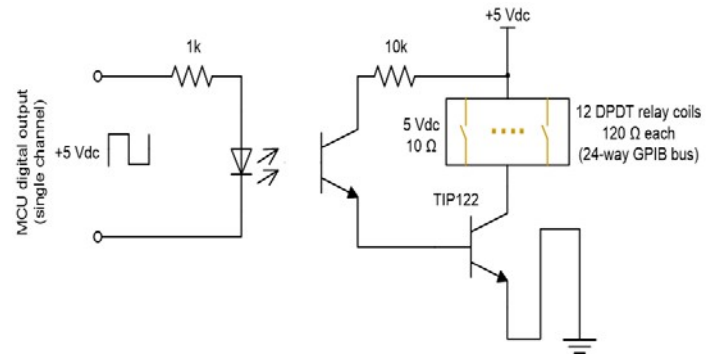


Fig 3: Basic schematic diagram of the switching isolator control module [6]

A photo of the developed GPIB isolator device is shown on fig. 4



Fig. 4: Programmable GPIB switching isolator (up to 7 channels)

The time diagram contains a sequence of the following control stages through the GPIB network (initially all GPIB

channels are disabled and dc input is set in the meter). The basic operation of the isolator is outlined below:

- (1). setting the ac source output level (GPIB Channel 1 enabled);
- (2). switching from dc to ac (all GPIB channels disabled);
- (3). setting the dc source output level (Channel 0 enabled);
- (4). reset meter's filter (Channel 2 enabled);
- (5). measured sample processing by the meter (all channels disabled);
- (6). read processed meter's response to the ac input (Channel 2 enabled);
- (7). Switching from ac to dc (all GPIB channels disabled), etc.

A simplified measurement system is consisting of a network of 3 instruments is considered: dc source (channel 0), ac source (channel 1) and meter (channel 2).

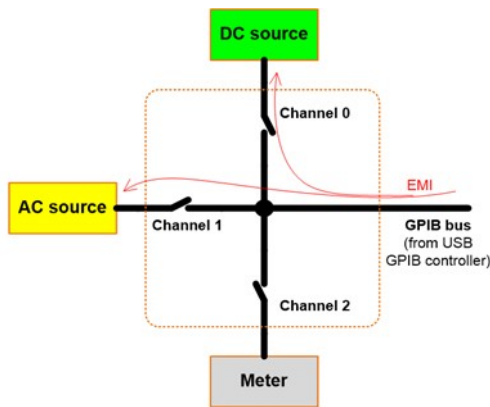


Fig. 5: Three-instrument GPIB network

The input of the isolator is attached to the GPIB controller with the PC connection and the switched outputs are connected with the GPIB interface modules on the instruments. The meters measures instruments in two periodic states of the measurement system configuration: dc input and ac input. The operation of the isolator is given by the time diagram on Fig. 6.

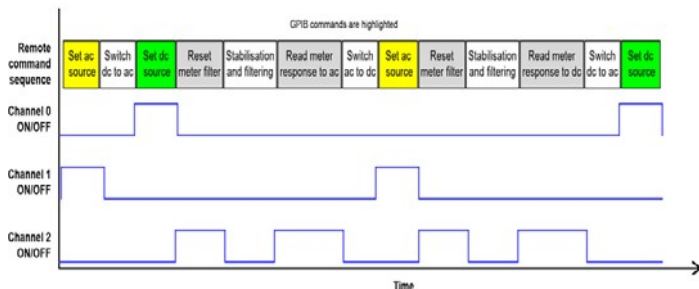


Fig. 6 isolator switching time diagram

V. VALIDATION OF THE UPGRADED AC-DC TRANSFER MEASUREMENT SYSTEM

The upgraded ac-dc transfer measurement system has been validated. The list of equipment used in the measurement system is given as follows:

- 2 Fluke 5720A calibrators, s/n 7790203 (dc source) and 6700201 (ac source);
- 2 Keithley 182 digital nanovoltmeters, s/n 0685929 and 0685931;
- Clarke-Hess 8100 transconductance amplifier, s/n 411;
- common-mode noise isolator
- cables, adapters and connectors

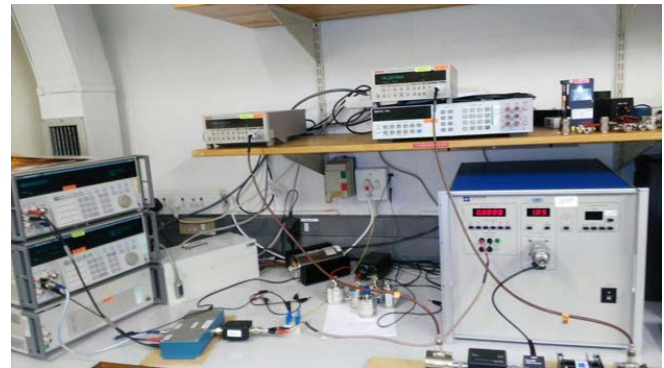


Fig. 7: Upgraded ac-dc current transfer measurement system

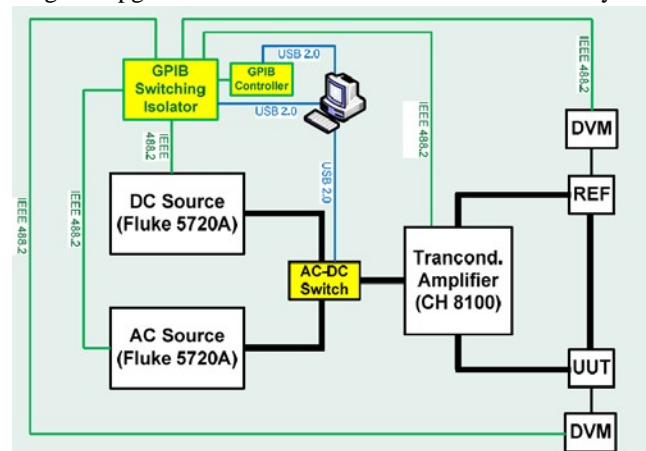


Fig.8: Schematic diagram of the ac-dc current transfer measurement system

The implementation of GPIB isolator for CM mitigation has been verified by obtaining the ac-dc current transfer difference measurements for unit-under test (UUT) thermal current converters against the reference (REF) national thermal current converters standard. Ten measurements were obtained for 0.01Arms current input at various frequencies (KHz) for the UUT and REF. Measurements results compare well with the NPL-certified results

TABLE 1. AC-DC current transfer difference

No.	Freq. (KHz)	NMISA verification		NPL calibration	
		UUT ($\mu\text{A/A}$)	Uncertainty ($\pm\mu\text{A/A}$)	Ac-dc diff. ($\mu\text{A/A}$)	Uncertainty ($\pm\mu\text{A/A}$)
1	0.01	44	41	34	12
2	0.02	10	41	12	11
3	0.04	1	39	5	11
3	0.1	-4	40	3	11
5	1	-1	39	2	11
6	5	-2	40	1	11
7	10	0	40	0	13
8	20	2	40	1	14
9	50	-2	42	2	15
10	100	-4	43	10	22

The ac-dc current transfer measurement results are graphically plotted:

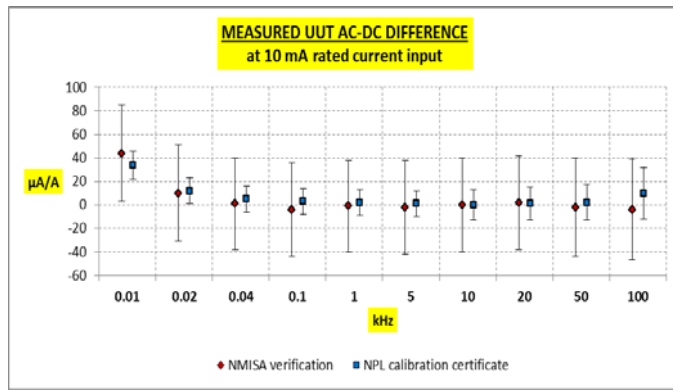


Fig 8: Validation of the NMISA verification against the NPL calibration certificate

There is good correlation between the NMISA verification and NPL certified ac-dc current transfer difference measurements. General comparison shows improvement in achieved uncertainties. The resultant values fall well within the certified uncertainty margins.

VI. SUMMARY

The paper presents an effective GPIB isolator which reduces EMI in ac-dc transfer measurement system. The EMI source and propagation path have been outlined and discussed. A GPIB isolator was successfully designed and implemented to reduce the measurement errors and failure of range of industrial devices due to EMI in the ac-dc measurement system. The ac-dc current transfer measurement system has been upgraded and verified. Measurement data shows significantly improved stability and repeatability.

VII. PROJECT IMPACT

Potential reduction of the ac-dc difference measurement uncertainty through the developed EMI mitigation

mechanisms will have a major impact on the NMISA alternating voltage and current calibration and measurement capability that will directly benefit the South African network of accredited calibration laboratories, industry and Department of Trade and Industry (dti) Technical Infrastructure through the traceability dissemination at higher test uncertainty ratios (TURs).

VIII. ACKNOWLEDGMENT

We are thankful to the NMISA and NRF for working resources and support. The Development of the device was carried out by E. Golovins and F. Prinsloo whose efforts in this regard are gratefully acknowledged. We would also like to acknowledge the authors whose published work has been referred to in this paper.

REFERENCES

- [1] A. E. Ruehli and H. Heeb, —"Circuit models for three- dimensional geometries including dielectrics", IEEE transactions on Antennas and Propagation, Vol. 40, pp. 1507-1516, 1992.
- [2] T. Weiland, —"A discretization method for the solution of Maxwell's equations for six components fields", Electronics and Communication, (AEU), Vol. 31, pp. 116-120, 1977.
- [3] DCLF/U-0005: Procedure for Calibration of AC-DC Voltage Transfer Standards.
- [4] D. Deaver, —Calibration and traceability of a fully automatic ac measurement standard' in Proc. Of NCSL Workshop & Symposium, 1991.
- [5] Noise Reduction and Isolation. White Paper. Measurement Computing: [http://www.mccdaq.com/PDFs/specs/Noise-Reduction.pdf]
- [6] E Golovins, F. Prinsloo, A.M Matlejoane" NMISA-14-00267: Improvement of ac-dc transfer difference calibration and measurement capabilities", pp 23-26, 2015

M. M. Hlakola is with University of Johannesburg and National Metrology Institute of South Africa, Electrical Metrology, DCLF Section (phone: 012 841 1700; e-mail: mhlakola@nmisa.org).
E. Golovins is with National Metrology Institute of South Africa, Electrical Metrology, DCLF Section (e-mail: egolovins@nmisa.org).
D.V. Nicolae is with the Electrical Engineering Technology Department, University of Johannesburg, (e-mail: dnicolae@uj.ac.za.).

National Metrology Institute of South Africa (NMISA), National Research foundation (NRF), University of Johannesburg (UJ)

Android Based Vehicle Tracking System with Collision Detection

T. Mvindi¹ and F. Adlam^{1*}

¹Nelson Mandela Metropolitan University (NMMU)
Port Elizabeth, South Africa

*Email: Frank.Adlam@nmmu.ac.za

Abstract— An android based vehicle tracking system is designed and implemented for the sole purpose of tracking the location of a vehicle in real-time. This system uses Global Positioning System (GPS) technology to continuously acquire latitude and longitude coordinates which are processed by the main controller which is an STM32F4 discovery board microcontroller. The crash detection is done by using an accelerometer which comes onboard the STM32F4 discovery board, by measuring the G-Forces from this sensor the crash detection functionality is implemented. Global System for Mobile communication/ General Packet Radio Service (GSM/GPRS) technology forms the backbone of the proposed project as this enables internet connectivity to be achieved through use of Hypertext Transfer Protocol (HTTP) communication. A GSM/GPRS module is used to transmit the acquired coordinates to a web server at regular intervals and these coordinates are then stored in a database and are accessible from an android application. PHP webpages are used to relay and manage this transfer of data between the android smartphone and the microcontroller. An android smartphone application is developed which continuously retrieves the vehicle location coordinates which are processed and then using the Google Maps API are interpreted to a geographic position that is displayed on the map. The android application is capable of displaying the status of the vehicle in terms of crash detection which is also fed from the tracking system which will be on the vehicle.

Keywords-Vehicle tracking systems;GPS technology; GSM/GPRS technology; STM32F4 discovery board; Google Maps API; Android; PHP webpages;

I. INTRODUCTION

The technological advancements over the past years have resulted in the development of a number of products and systems that are used to track the locations of vehicles. These devices are usually in the form of handheld devices which can be installed onto a vehicle and update the driver of their current location or it might be a system located at a remote location doing the monitoring. Such systems are in use in areas such as Vehicle recovery, Fleet management, Surveillance etc. The challenge presented in this project is the creation of an easy to use, affordable and reliable solution which still meets the standard of a product which can be implemented in industry.

Many vehicle tracking systems have been created over the years and most vehicles are now manufactured with modules that allow their location to be determined for navigation purposes. South African companies such as MiX Telematics Africa (Pty) Ltd have designed similar systems which are used for tracking and recovery, crash alert and other services[1]. They use a combination of RF and GSM technologies with

GPS for their systems[1]. RF communication is used as it can provide the location of a vehicle even in areas where GPS might be out of reach such as covered places which include buildings, garages etc.[1].

The proposed project uses GPS technology only as it can still provide the required location coordinates with high accuracy and has advantages over RF communication such as less power requirements. A GPS module will provide location and timing data which is used with the Google Map API to find the precise location on a map [2]. The GPS module selected should be highly sensitive and capable of tracking the location even when it is in motion. To improve the sensitivity of a GPS module it can have an active GPS antenna connected to it, this also aids in the positioning of the module as a longer antenna cable can be used.

The proposed project also uses a GSM module because of its use of GSM/GPRS technology which is one of the most used communication technique with low cost and high reliability [3]. This module can be used to connect to the internet which makes it suitable for routing vehicle coordinate data to the android application in real time. There are many applications where GSM/GPRS modules have been used to communicate with web services for purposes of control or monitoring hence the proposed project is achievable [4]. The GSM module achieves internet connectivity through the use of AT commands which are sent to it from the main controller. These commands, which are also referred to as Hayes commands were originally developed by Hayes Microsystems for use with modems [5]. Over the years different manufacturers have adopted their use which has become very common in GSM/GPRS technologies such as modems and phones.

The Google Company provides a web map service which will be used in an android application to display the vehicle location on a map [6]. The Google Maps API is a JavaScript technology based application programming interface (API) offered by Google and it provides a lot of processing map service [7] [8]. It automatically handles all map related operations which will be done as per developed application such as zooming in on the map, displaying it and making it easy for user interaction. Technological advancements have meant that there has been an increase in the number of people who use smartphones therefore this platform is easily available to any user [9]. Implementing a vehicle tracking system using

an android based smartphone application and GPS/GSM/GPRS technology can provide better service and a cost effective solution as this will allow for a more dynamic user interface to be developed [9].

Similar systems have been created which use technologies which might be considered inferior in comparison with GSM/GPRS technology, these are systems which use SMS technology to forward location coordinates from the vehicle to a remote monitoring device such as a cell phone or a tablet. This approach means that for every single location coordinate there will be a corresponding SMS to carry it, which not only results in tremendous costs of operation but also a very unreliable and slow system.

II. USER INTERFACE

The features of the tracking system the author proposed and the intended functions can be grouped in terms of the tracking hardware, the web server and the android application. No user interaction is needed with the web server because everything is handled automatically using PHP web pages. The proposed vehicle tracking system therefore has two sections with user interaction, these are:

A. Data Collection and Tracking System

This system comprises of the hardware whose function is to collect location coordinates and vehicle status data from respective sensors and relay this information to an online web server. As shown in the block diagram in fig. 1 this section requires no user input with the only interface to the user being an LCD screen which serves as a display for showing the status of the tracking process.

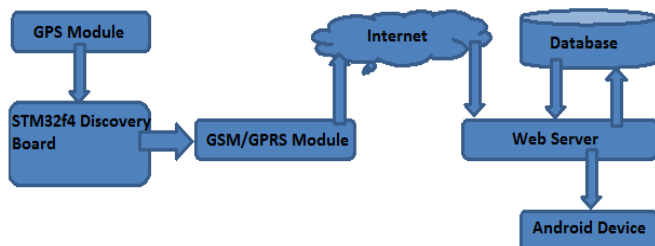


Figure 1. Vehicle Tracking System Block Diagram

B. Android Application

The use of an android smartphone was chosen because it provides an easy to use visual interface on which the vehicle location and status are displayed. Their availability, cost and ease of use are better compared to alternatives hence their use.

To use the android application no technical background is required as the user is only required to enter their login details which will be provided and once logged in the rest of the functions are made available for

- Displaying the location of the vehicle in real-time
- Displaying the status of the vehicle
- Tracking the location history of the vehicle for any date

III. IMPLEMENTATION DETAILS

Implementation of the project prototype is done in sections. These include the hardware section and the software section which formed the backbone of this project as most of the work done was in software.

A. STM32F4 Discovery Board

This board is used in the project mainly because it has a LIS3DSH ST MEMS 3-axis accelerometer which is used as part of the crash detection functionality. It forms the main controller of the whole data collection process as it is responsible for acquiring GPS data from the GPS module and then transmitting it to the web server via the SIM900 GSM module. The IDE used to program this controller is Keil IDE and this is achieved using C programming language. This microcontroller can be powered by an external application power supply of 3 V or 5 V making it more flexible compared to other boards which are mainly powered by 5V[10].

B. GSM/GPRS Module

The GSM module shown in fig. 2 is used to provide communication between the STM32F4 discovery board and the online web server in the form of HTTP communication. It is controlled and configured via its UART by the STM32F4 discovery board using AT commands to initialize, execute and terminate the internet connection. The normal operating voltage of the module is from 3.2V to 4.8V. The peak working current can rise up to 2A during maximum power transmitting period, resulting in a voltage drop. The power supply used should have a supply rating of 2A to provide sufficient peak current as the module will automatically power down when the voltage drops below 3.1V[11]. How this module establishes a connection between an online server and the main controller is explained in section F titled HTTP communication.



Figure 2. GSM module with attached antenna and MTN sim card

C. GPS Module

The Adafruit GPS module shown in Fig.3 is capable of returning location coordinates in the form of an NMEA strings by tracking up to 22 satellites with a sensitivity of -165dBm [12]. It can do up to 10 location updates a second hence is suitable for high speed, high sensitivity logging or tracking. Power usage is incredibly low at only 20 mA during

navigation. The GPS module can be interfaced to a controller with a single wire via USART to feed NMEA data. NMEA data is National Marine Electronics Association (NMEA) specification that defines the interface between various electronic devices and also defines GPS receiver communication[13]. To improve the sensitivity of the GPS module it can have an active GPS antenna connected to it, this also aides in the positioning of the module as a longer antenna cable can be used.



Figure 3. GPS module

This module will be connected to the STM32F4 discovery board which will receive the NMEA sentence containing the location data and parse it to the respective coordinates before transmission to the online web server. The NMEA sentence with the "\$GPRMC" header is the most useful one in the proposed project as it provides location data and also the speed at which the module is moving which translates to the speed of the vehicle since the module will be mounted on it. This sentence has the following format, with each comma separating parameters:

`$GPRMC,194509.000,A,4042.6142,N,07400.4168,W,2.03,221.11,160412,,,A*77`

The STM32 discovery board's USART is initialized to a baud rate of 9600 baud as the transmission is done at that rate between the two modules. It is responsible for processing the received NMEA sentence to get the GPS location coordinates and its speed among other parameters. The pin configuration used is such that RX of the GPS module connects to PB7 which is the USART1 receiver on the STM32F4 discovery board.

D. Online Web Server and Database

To achieve communication between the data collection section of the project and the android client application a web server is necessary to buffer and relay information between the two sections. An online web server was used because it is easily accessible from anywhere in the world and is much more secure and reliable than hosting one on your own as it will be vulnerable to computer crashes, will have limited uptime as the computer is switched off at some point and also a high risk of data lose due to theft or damage of the PC. The author purchased the domain name <http://scientium.co.za/> to host the

web server and managed to make it accept, save and transmit data successfully. The web server design can therefore be categorized into stages for acquiring and saving vehicle data from the STM32F4 discovery board, sending data to the android application and database maintenance.

Data storage and maintenance on the online web server is done through the use of an online phpMyAdmin database. The author created two tables on the database, one for handling of the android application login information and another one for handling of the vehicle location and status data. The web server was configured to accept data coming from the STM32F4 discovery board and arrange it into the correct table and columns in the database with the format shown in TABLE 1.

TABLE 1. SIMPLIFIED DATABASE STRUCTURE

Name	Type	Default	Extra
ID	int(64)	None	Auto Increment
VehicleID	varchar(256)	NULL	
Latitude	varchar(256)	NULL	
Longitude	varchar(256)	NULL	
GForce	varchar(256)	NULL	
Speed	varchar(256)	NULL	
GPSTDataStatus	varchar(256)	NULL	
VehicleStatus	varchar(256)	NULL	
EntryDate	timestamp	NULL	

For the android application to process data, it is transmitted from the web server in JSON format as this makes the processing of the data easier and manageable. The programming of this part of the project is done in PHP. The program flow is implemented in a way that a connection to the online database is first negotiated through a unique username and password before the data can be stored into it. Storage is done at every instance new data arrives from the STM32F4 discovery board instead of refreshing the webpage periodically. This is the same approach used for sending data to the android application, it is done per request.

E. Android Client

This section of the project forms the user interface (UI) of the project and performs the necessary steps for the location of the vehicle to appear on a map on an android device. An android device which runs such an application requires a valid internet connection since every vehicle location and status data is stored on the online database. To be able to display the vehicle's location on an android application, the Google Maps API is used and is updated in real time using HTTP requests to the server which respond with the location and status data. The android application uses four activities with each activity handling different functionalities of the project. These activities include:

1) Login Activity

This activity is responsible for the user login into the android application. It is designed such that the user enters their vehicle identification and password so that they gain access to the

tracking application if these details match the ones saved on the web server's database. The vehicle identification i.e. the unique number which is used for purposes of this project to uniquely identify possible vehicles being tracked simultaneously and the associated password will guarantee access. Upon entering the wrong credentials the users will be prompted to enter the correct ones by means of a message which appears onscreen.

2) Vehicle Location Activity

The vehicle location activity is passed the verified vehicle ID from the login activity. This unique ID is used to get location and status data from the web server, it acts as the key to retrieving the data from the server's online database. Two threads will be running at any stage of this activity with the one in the background continuously retrieving data and the foreground one displaying the map. Data is retrieved from the online database by filtering it based on the current date and vehicle identification. After being received, the data is processed to get the latitude and longitude values which are passed to the foreground thread to update the location shown on the map. This cycle continues until the user logs out of the application or changes to the vehicle status or route trace activity.

3) Vehicle Status Activity

The android application gives the user the option to select the vehicle status. It shows the current speed at which the vehicle is moving at and also the highest or maximum speed which has been reached by the vehicle. It also shows the GPS data status which can be OK or NOK and the G-Force measured by the accelerometer on-board the STM32F4 discovery board. When the G-Force exceeds a pre-set value then a crash is assumed to have happened. This will result in the displayed vehicle status being updated from OK to NOK and a message appears onscreen informing the user of the incident.

4) Route Trace Activity

The author also implemented a trace route functionality which gives the path taken by the vehicle on the selected date. This function requires the user to first select a date using a date dialog after which the vehicle data is filtered from the online server for that particular day. The smoothness of the mapped route depends entirely on the network service provider and the provided network speeds, a high latency network connection therefore results in a mapped route which is rough as the coordinates from the STM32F4 discovery board arrive widely spaced compared to under a low latency network connection.

F. HTTP Communication

The Hypertext Transfer Protocol (HTTP) enables communication between clients and servers and works as a request-response protocol between the client and server[14]. Initialization of the GSM communication involves making sure the module is connected to the network and setting up bearer profile which is used for the TCP/IP communication, a specification protocol which defines the exchange of data over the internet. The client application connects with a web service and submits database commands which then process the requests and send the results back to the client in the HTTP response messages[15]. Once this step is successful the

initialization of the HTTP communication is done prior to the HTTP data exchange. The HTTP communication is done through a TCP/IP connection which operates at port 80. This connection is achieved by configuring the GPRS module to bearer profile 1 which enables GPRS communication. The network service provider MTN was used to provide the internet service:

```
USART_puts(USARTx, "AT+SAPBR=3,1,\"CONTYPE\","GPRS"
S\"r\n");
USART_puts(USARTx, "AT+SAPBR=3,1,\"APN\","internet\"r
\n");
USART_puts(USARTx, "AT+SAPBR=1,1r\n");
```

The module responds to the AT commands by returning an OK if the command is successful. The HTTP GET method is used in this project to transmit data as this method directly adds the data to the URL. Although the length of a URL is limited to 2048 characters compared to a POST method which has no restrictions, the data transmitted is way less than 2048 it fits in the URL. To use this method the HTTP service is first initialized and the parameters set using the AT commands:

```
USART_puts(USARTx, "AT+HTTPINITr\n");
USART_puts(USARTx, "AT+HTTPPARA=\"CID\",1r\n");
sprintf(dataParameter, "AT+HTTPPARA=\"URL\", \"http://scie
ntium.co.za/PutVehicleData.php?VehicleID=19&Latitude=%s
&Longitude=%s&GForce=%f&Speed=%s&GPSDataStatus=
%s&VehicleStatus=%s\"r\n",
GPS_Latitude, GPS_Longitude, GForce, GPS_Speed, GPSDataS
tatus, VehicleStatus);
USART_puts(USARTx, dataParameter);
```

Once the data has been successfully transmitted the module responds with:

```
OK
+HTTPACTION:0,200,XX
```

With XX indicating the number of bytes transmitted. To terminate the HTTP service the following AT command is executed:

```
USART_puts(USARTx, "AT+HTTPTERM\n");
```

IV. RESULTS

As shown in TABLE 2 the location and status data is stored into the columns Latitude, Longitude etc. on the web server's online database. The column "ID" is the index which shows the row number. This index in auto incremented each time a new entry is received from the STM32F4 discovery board, the index shown in TABLE 2 starts at 421 suggesting that there are at least 420 other entries before the displayed ones. The "VehicleID" columns shows the unique number which identifies each vehicle being tracked at that moment. The "Latitude" and "Longitude" columns store the latitude and

longitude coordinates respectively. These coordinates are still in NMEA format and are converted into decimal values in the android application. The “Speed” column shows values in knots and the conversion to kilometers per hour is done on the android client application before they are displayed onscreen. The “GPSDataStatus” columns are responsible for storing the status of the GPS coordinates received from the GPS module. The “VehicleStatus” column shown is displaying “NOK” which suggest that a vehicle crash has been detected, the android application will pick on this and display a message onscreen informing the user.

TABLE 2. VEHICLE DATA STRUCTURE IN THE DATABASE

ID	VehicleID	Latitude	Longitude	GForce	Speed	GPSDataStatus	VehicleStatus	EntryDate
421	19	3400 1917S	02540 0423E	4.206000	0.03	OK	NOK	2015-09-30 00 23:45
422	19	3400 1917S	02540 0423E	4.206000	0.02	OK	NOK	2015-09-30 00 23:47
423	19	3400 1917S	02540 0423E	4.206000	0.01	OK	NOK	2015-09-30 00 23:49
424	19	3400 1917S	02540 0423E	4.206000	0.04	OK	NOK	2015-09-30 00 23:50
425	19	3400 1917S	02540 0423E	4.206000	0.00	OK	NOK	2015-09-30 00 23:52

The results shown in Fig.4 to 6 are the screens which were displayed on the android smartphone during the testing of the vehicle tracking system prototype. These show that communication between the data collection on board the vehicle and the android application via the web server was successful. The vehicle’s geographic location can therefore be tracked from anywhere on earth since the application gets the location data from a webserver via the internet.

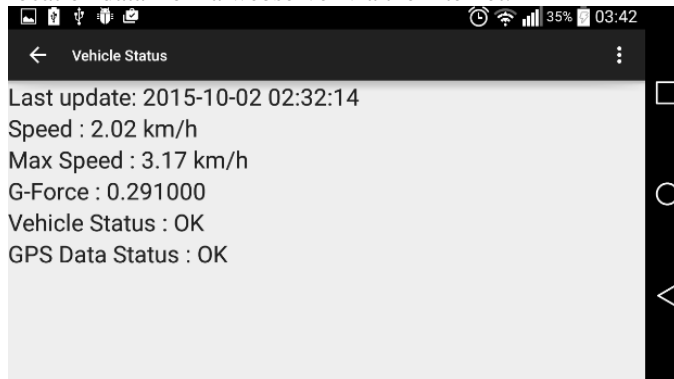


Figure 4. Vehicle Status Screen

Fig. 5 shows the location of the vehicle and a timestamp displaying the date and time at which the data was sent from the tracking system onboard the vehicle.

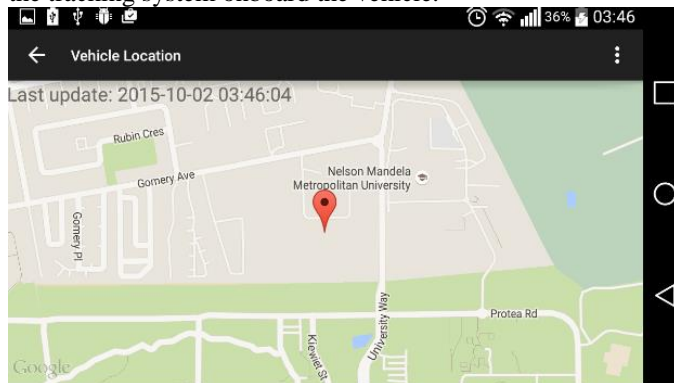


Figure 5. Vehicle Location Screen

Fig. 6 shows a trace of the route which the vehicle took on a selected date. This path is displayed from the vehicle’s starting point to its stopping point. Once the application has completed mapping all the available data for the selected date it displays the message “Route Mapping Complete”.

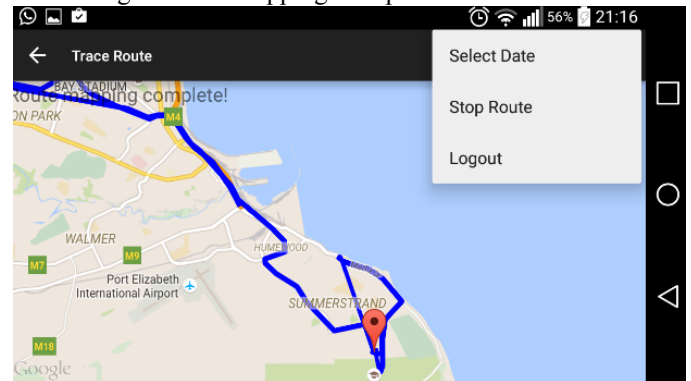


Figure 6. Trace Route Screen

V. CONCLUSION

Based on the analysis of the results obtained from the created prototype and the android application, the author concludes that it is possible to use an android device to actively track your vehicle over the internet. This method is more convenient and reliable since all the data is stored on a database for access at any time hence the entire vehicle location history can be tracked. Since the most smartphone users use the Android OS this makes the Vehicle Tracking System accessible to anyone with ease and no technical knowledge or background is required to operate it. The implemented project solves the problems which were raised in the project’s problem statement. It was required that the user be able to locate their vehicle and view its status using a visual interface, this was developed and is in the form of the android based application. The other problem which was solved is the need to provide the location of the vehicle accurately at any time of the day in real time to provide live tracking and monitoring. In addition to this the author also added functionality which allows the user to trace the vehicle location on other selected dates. The crash detection functionality was also implemented to meet the expected standard. In general the author concludes that the project was a success.

ACKNOWLEDGMENT

The author would like to thank the following persons and companies for their assistance in implementing the project, be it in terms of advice, suggestions etc. Frank Adlam, Nelson Mandela Metropolitan University’s Electrical Engineering department, S4 Integration, classmates, friends and family for their valuable support.

REFERENCES

- [1] M. T. A. P. Ltd. (2015, 18). Available: <https://www.matrix.co.za/>

- [2] M. S. Amin, J. Jalil, and M. B. I. Reaz. (2012, 18-19 May 2012). Accident detection and reporting system using GPS, GPRS and GSM technology. *Informatics, Electronics & Vision (ICIEV), 2012 International Conference on*, 640-643. Available: <http://0-ieeeexplore.ieee.org.wam.seals.ac.za/xpls/icp.jsp?arnumber=6317382>
- [3] W. Yang, J. Liu, J. Wang, M. Shen, X. Wang, and Z. Li. (2006, 22-26 Oct. 2006). The Application of GSM and GPRS Technology in Monitoring System for HVDC System Earth Pole. *Power System Technology, 2006. PowerCon 2006. International Conference on*, 1-5. Available: <http://0-ieeeexplore.ieee.org.wam.seals.ac.za/xpl/articleDetails.jsp?tp=&arnumber=4116184&queryText%3DGSM+technology>
- [4] Mithila. (2014, 18 June). *Connect with webservice via SIM900 and control LEDs (Arduino)*. Available: <https://www.youtube.com/watch?v=bDBOlELNLA>
- [5] Z. Qian, D. Luo, and s. Wu, "Analysis and Design of A Mobile Forensic Software System Based on AT Commands," in *Knowledge Acquisition and Modeling Workshop, 2008. KAM Workshop 2008. IEEE International Symposium on*, 2008, pp. 597-600.
- [6] E. Denaxas, S. Mpollas, D. Vitsios, C. Zolotas, D. G. Bleris, G. M. Spanos, *et al.* (2013, 16-19 April 2013). Real-time urban traffic information extraction from GPS tracking of a bus fleet. *Computational Intelligence in Vehicles and Transportation Systems (CIVTS), 2013 IEEE Symposium on*, 58-63. Available: <http://0-ieeeexplore.ieee.org.wam.seals.ac.za/xpls/icp.jsp?arnumber=6612290>
- [7] L. He and Z. Lai. (2010, 3-5 Dec. 2010). The study and implementation of mobile GPS navigation system based on Google Maps. *Computer and Information Application (ICCIA), 2010 International Conference on*, 87-90. Available: <http://0-ieeeexplore.ieee.org.wam.seals.ac.za/xpls/icp.jsp?arnumber=6141544>
- [8] G. Developers. (2015, 23 April). *Introduction to Google Maps Android API v2*. Available: <https://developers.google.com/maps/documentation/android/intro>
- [9] L. SeokJu, G. Tewolde, and K. Jaerock. (2014, 6-8 March 2014). Design and implementation of vehicle tracking system using GPS/GSM/GPRS technology and smartphone application. *Internet of Things (WF-IoT), 2014 IEEE World Forum on*, 353-358. Available: <http://0-ieeeexplore.ieee.org.wam.seals.ac.za/xpls/icp.jsp?arnumber=6803187>
- [10] STMicroelectronics, "STM32F405xx STM32F407xx," ed: STMicroelectronics, 2012.
- [11] ElecFreaks. (2015, 23 June). *EFCOM Pro GPRS/GSM Module*. Available: http://www.electfreaks.com/wiki/index.php?title=EFCOM_Pro_GPRS/GSM_Module
- [12] l. ada. (2015). *Adafruit Ultimate GPS*. Available: <https://learn.adafruit.com/adafruit-ultimate-gps>
- [13] M. Shoab, K. Jain, M. Anulhaq, and M. Shashi, "Development and implementation of NMEA interpreter for real time GPS data logging," in *Advance Computing Conference (IACC), 2013 IEEE 3rd International*, 2013, pp. 143-146.
- [14] N. Tomar and M. S. Gaur, "Information theft through covert channel by exploiting HTTP post method," in *Wireless and Optical Communications Networks (WOCN), 2013 Tenth International Conference on*, 2013, pp. 1-5.
- [15] T. Kvamme and S. Ahmed, "SQL Tunnelling through HTTP," in *Computer and Information Technology (ICCIT), 2010 13th International Conference on*, 2010, pp. 181-186.

Design and development of a remote solar power control, battery monitoring system and internet logging capability

J. Bothma¹, N de Lange² and F. Adlam^{1*}

¹Nelson Mandela Metropolitan University (NMMU)

Port Elizabeth, South Africa

²Department of Research and Development Microcare Solar Components

Port Elizabeth, South Africa

*Email: Frank.Adlam@nmmu.ac.za

Abstract

Improper utilization of the battery bank in a solar power system will lead to a reduction in lifespan and increase in maintenance for the battery bank as well as an overall increase in cost in operating the solar power system. By implementing a battery monitoring system (BMS) such problems can be reduced or completely removed. The BMS offers the ability to analyse the solar power system given monitoring for example: battery state of charge (SOC), time remaining in the battery, charge current and discharge current. The BMS also has the ability to control all charge sources and loads connected to the battery bank with the purpose of projecting the battery bank from undesired conditions.

This paper covers all aspects that had been taken into consideration in the design and development of the solar power controller and BMS. This BMS and all related designs of the BMS is property of Microcare solar components.

Keywords: Battery monitoring system (BMS): Microcontroller unit (MCU): State of charge (SOC): Maximum power point tracker (MPPT): Analog to digital converter (ADC)

1. Introduction

This paper covers all aspects that had been taken into consideration in the design and development of the solar power controller and BMS.

Off-grid solar power systems consist of solar panels charging batteries through charge regulators and inverters, converting the battery bank DC voltage into a usable AC voltage for the load. This allows the individual or corporation to reduce or erase their dependence on a power grid. A large, expensive battery bank is needed for this system to operate with reliability and to maintain the load throughout night times.

This chapter covers aspects of the BMS that needs to be taken into consideration in later stages of design. The author states a brief overview of the aspects which is considered in the design and how the interpretation of the information affected the design of the BMS.

As shown in

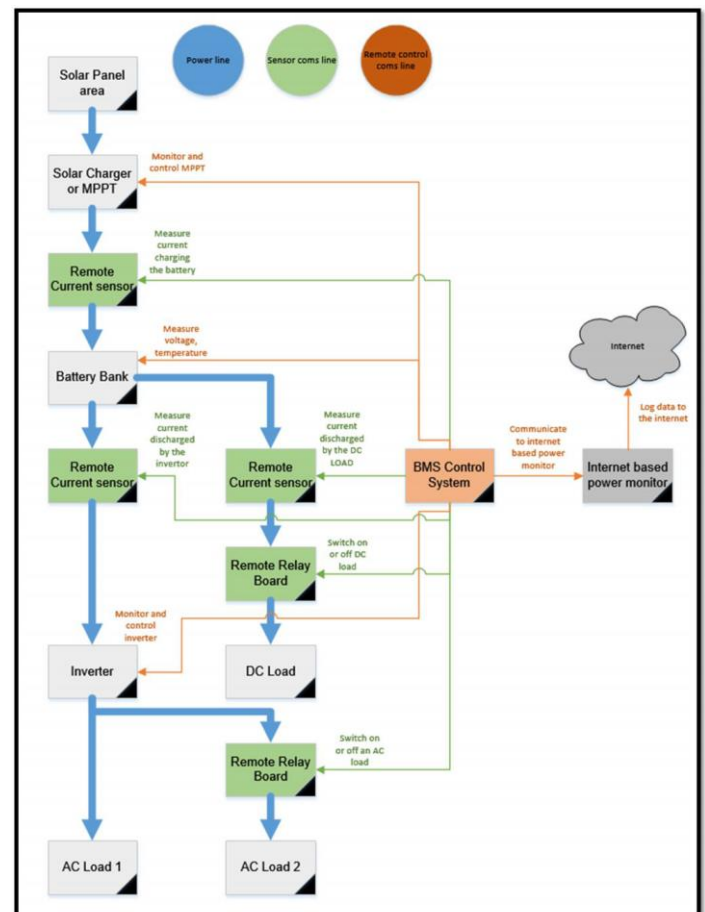
Figure 1 a detailed connection diagram of the BMS. The BMS would have current sensors placed in line with all charging or discharging devices connected to the battery bank. The battery bank would provide power to the BMS and the same cables would be used to detect the voltage of the battery bank. The BMS would have control of relay modules that can be signalled to switch specific loads on or off depending on the conditions of the battery bank. The BMS has communication to the Microcare MPPTs and inverters, giving it the ability to monitor the state of those devices and power them on or off as needed. Finally, there should be a communication connection between the BMS and the Microcare Web-logger to allow for internet logging of the BMS's data.

In

Figure 1 the blue lines represents power cables connected to power components. The green lines represents

communication cables between the remote sensors and the BMS.

Figure 1: Detailed Connection Diagram



Factors that can have a negative influence on the lifespan of a battery include:

- Discharging a battery too deeply.
- Leaving a battery bank at a low state of charge for an extended period.
- Applying a load greater than the rated discharge of the battery.
- Allowing a battery bank to overheat during the charge cycle.
- Allowing a battery bank to become unbalanced, thus undercharging some batteries and overcharging others.

The BMS monitor these factors, and enforce certain actions to prevent or correct these problems. Possible steps that such a monitoring system can implement, include:

- Disconnecting all loads to the battery when it reaches a maximum battery bank discharge point.
- When the BMS finds that the battery bank has not been fully charged for an extended period, it should prevent lower priority loads from running.
- The BMS should warn the user of loads that exceed that of the battery rating and possibly disconnect those loads for a set amount of time.
- The BMS should monitor the temperature of the battery bank while it is being charged and instruct the charge regulator to reduce charge if the battery bank's temperature becomes in excess of its rated operating conditions.
- When a battery bank becomes unbalanced the BMS should inform the operator of the problem and attempt to correct the problem by equalizing the battery bank.

2. Peukert's Exponent

A key feature of a BMS is to accurately measure the state of charge (SOC) of the battery bank, as well as to predict the estimated time remaining in the battery bank when a constant load is applied. The Peukert's Exponent calculation as can be seen in Figure 2, takes into account the size of the battery bank and the relative size of the load applied to the battery bank, for more accurate calculations, including the effect of other factors on the battery. [6]

Battery manufactures rate their batteries in terms of a 20 hour rate of discharge, for example a 20 Amp hour battery is rated to provide 1 Amp to the load for 20 hours when fully charged. When discharging the same battery at 20 Amps not considering the Peukert's Exponent the battery should be able to provide to the load for 1 hour, but when the Peukert's Exponent with a number of 1.19 (a good modern lead acid average) we find that the battery is only be able to provide power to the load for 34 minutes or less before being completely discharged. [7]

By implementing the Peukert's Exponent into the BMS software, the system was able to accurately predict the SOC and the time remaining in the battery bank in any situation, including situations where the load would discharge the battery in less than 20 hours.

$$C_{n1} = C_n \left(\frac{I_n}{I_{n1}} \right)^{pc-1}$$

3. Unbalance in a Series Battery Bank

A DC load such as an inverter normally stop discharging when the batteries become too low, but when a battery bank is unbalanced the inverter is not able to detect that one of the batteries has reached a dangerously low point. When a battery is discharged to deeply it can cause irreversible sulfation in the battery, which reduces the capacity of the battery. Sulfation can also cause the battery plates to warp and bend, which can cause internal faults to the battery, this can bring down the whole battery bank and solar power system. [8]

When charging a battery with a device such as an MPPT, the batteries are brought to a voltage at which it should reach 100 % SOC and kept at that voltage for the time it should take for the battery to reach 100 % SOC. When a battery bank is imbalanced, fuller batteries have a higher voltage across them compared to the flatter batteries. The higher voltage battery warms up and the excess heat can cause damage to the battery. The flatter battery would need more time at a set voltage to reach full state.

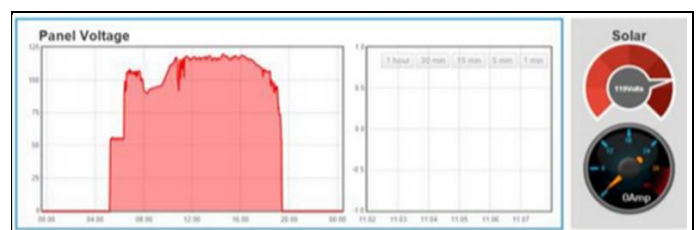
For the BMS to reduce the problem, it needs to know the voltages of the batteries in the system. When the BMS detects an unbalance in the battery bank, it must indicate to the battery charger that a equalise charge is required. The BMS would monitor the temperature of the battery bank and indicate to the MPPT, to reduce charge when the battery bank gets hot, to avoid damage to the fuller batteries. If the battery equalise is not successful the BMS should notify the user to take further steps to recharge or replace problematic batteries.

4. Web-Logger Device

The Microcare web-logger was used as an internet-of-things connection to the BMS. This is a small Linux based computer that needs to be provided with an internet connection using an Ethernet port. The BMS then sent data packets using the Microcare communication protocol on an RS485 bus. The BMS would then upload the data to the website under a given serial number provided for the BMS. [9]

The user can use the data provided from the BMS on graphs, gauges and dials on the website. As shown in Figure 3.

Figure 3: Screenshot of Internet Based Power Monitor Website



5. Design Considerations of Sensor Module

The main purpose of the sensor module is to accurately measure current flowing in and out of the battery bank, and the voltage the battery bank is operating at.

In general, a 200 Amp sensor was selected as this sensor is the closest match to the most popular solar product sold by Microcare, namely the 5 kW 48 Volt bidirectional inverter. (5000 Watt / 40 Volt = 125 Amp).

The selection of a Hall Effect sensor for current measurement is the Allegro ACS758xCB. [10]

It was selected for having a Nominal Power loss due to the 100 $\mu\Omega$ resistance, galvanic isolation in the Hall Effect sensor of up to 4800 and a much lower cost than the alternatives.

The voltage divider used to measure the voltage of the battery bank consist of the following: two 100 k Ω resistors in series going from the battery voltage sense pin to the MCU's ADC pin and a 10 k Ω resistor going to battery negative. All the resistors are 1% tolerance. There is also a 10 nano ferrite ceramic capacitor connected as a noise filter to the MCU.

A resistor based temperature sensor was added to the sensor module to allow users to monitor the temperature surrounding the battery bank. The sensor should be located as close as possible to the battery bank to allow the temperature sensor to measure the temperature surrounding the battery bank. A battery over-temperature-error is used as an indicator to turn off chargers or loads.

A relay control circuit has also been added to the Sensor module to allow for control of devices such as lights. The relay is located off board to reduce cost when it is not needed.

- The final completed sensor module can be found in Figure 5.

6. Design Considerations of Relay Module

The main purpose of relay module is to allow the BMS to control external conditions, for instance starting a generator, turning on a battery charger and turning lights on and off, or any other combination of these.

A 6 Volt relay was selected because the supply voltage on the MC_COMS bus is 8 Volt. This is not high enough to reliably switch a 12 Volt relay. The 16 Amp double pole relay capability is a good middle-sized relay that can be used for the following. In a 230V AC system ($16 * 2 * 230$) it can be used to switch resistive loads of up to 7 kW, alternatively it can be used to switch larger contactor of other applications.

The relay circuitry consists of two sets of transistor circuits per relay. The start transistor puts the full 8 Volts of the MC_COMS bus onto the coil of the relay for approximately 20ms. At this point the relay is considered on. The second relay switches the 8 Volts to the coil through a 220 Ω resistor. The first relay turns off for the remainder of the time that the relay should stay on for. When the relay must turn off, the secondary stay on relay turns off as well. Using this method of relay switching reduces the power consumption of each of the 4 relays on the relay module from (8.2Vx8.2V/90 Ω) 747 milliwatt per relay, down to (8.2Vx8.2V/310 Ω) 216 milliwatt per relay.

- The final completed relay module can be found in Figure 6.

7. Design Considerations of Control Module

The main purpose of the control module is to interpret all information gathered by the sensors, display the information to the user in a sensible way and control the external devices based on the sensor information.

A Graphical LCD display has been selected for the control module because compared to a multiline display (for example A 2 line 16 character or a 4 line 20 character display) that the author has used in the past. The selected 64 by 128 dot display has the ability to display $64 / 8 = 8$ lines and $128 / 6 = 21.3$ characters. This allows for a greater amount of information to be displayed at once. Using this graphic display has the added advantage of allowing for a graphic user interface and menu systems that is more user friendly.

MC_Coms is the communication protocol of all Microcare solar products (1-15KW inverters, 20-10Amp MPPT charge controllers and the Microcare web-logger). For this reason this communication protocol has been selected for this project. The communication protocol can be used in non-bus interfaces such as RS232 or bus interfaces such as RS485. The RS485 interface is used in the control module.

Having an accurate track of time is essential to this project as some logging facilities, for instance measuring kWh and Ah going in and out of the battery and graphing the information onto the display, require accurate timekeeping. This control module also offers a 2 year computed log which would not work if the control module were not able to retain the time when power source is removed from the control module. The selected RTCC is the microchip MCP79400. [13]

The selected flash chip is the Atmel AT25M01. Some of the key features relevant to this project is A 100Year retention and 1,000,000 write cycle capability to ensure that this is not a future point of failure in this control module. Having 1,048,576 bits programmable memory space was an ample amount of space for the control module. [14] See Figure 4.

The design has been changed to surface mounted devices to facility a compact design that can easily be hung on a wall in a house or in a cupboard. The main advantage of using surface mount components besides the obvious reduction in size, is the cost of components, cost of labour and a reduced PCB size.

An audio buzzer has been added to the PCB. This was used on button presses for feedback on button press, and during error condition to indicate to the user that there is a problem with the battery bank or the BMS and that attention need to be given.

A matrix keypad membrane switch label has been designed by the author. It also houses indication LEDs which indicate simple states of operation to the user from a distance or at a glance.

SMD components tend to be cheaper than their through-hole counterparts due to the reduced material cost and higher volume of manufacturing. Generally SMD PCBs are stencilled with solder paste and after components have been added the PCB is placed in a reflow oven to solder all components at once, this involves less labour than that of the through-hole method of soldering every pin individually.

- The final completed control module can be found in Figure 7.

N/O COM N/C N/O COM N/C N/O COM N/C N/O COM N/C
 OUT 1 OUT 2 OUT 3 OUT 4

MICRO CARE
 SOLAR COMPONENTS

BATTERY MONITOR
 4 CHANNEL RELAY

MC
 COMS

MC
 COMS

[illegible]

Figure 7: Assembled Control Module

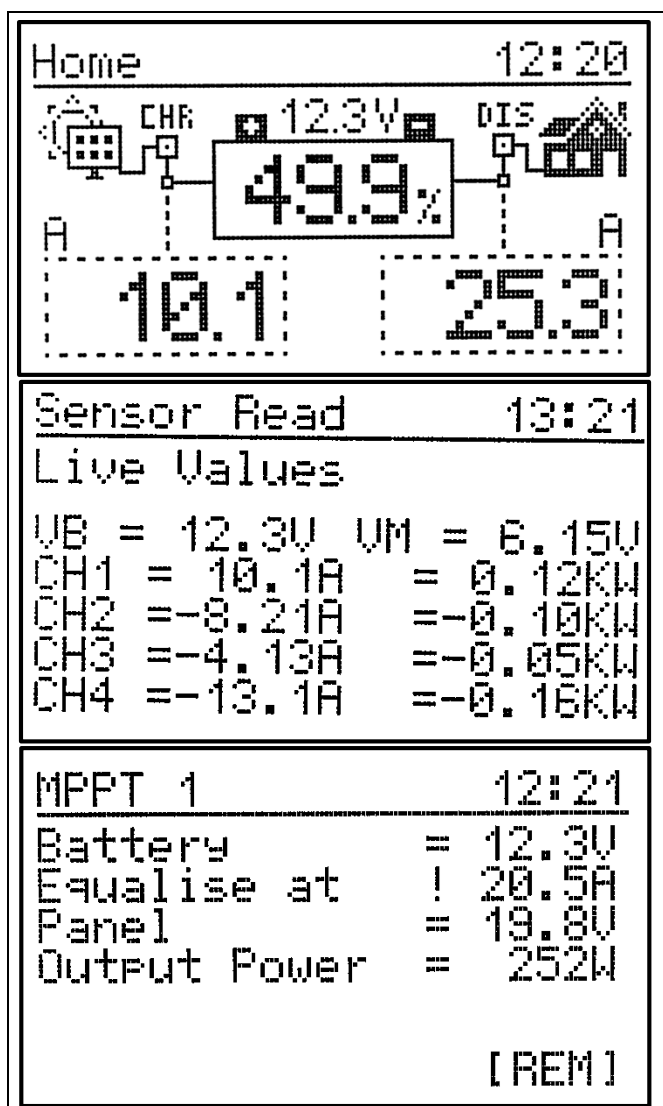


8. Real-Time Displays

The real-time displays are used to give a current state on how the battery bank and solar system as a whole is functioning. This allows the user to view the following information as it happens:

The battery bank voltage. Current flowing in and out of the battery bank from various sources. Power flowing in and out of the battery bank from various sources. The current time of the day. The estimated time of operation remaining in the battery bank, if the current load remains stable. The estimated percentage that the battery bank is at. The amount of Amp hours, that needs to put back into the battery bank for full charge. The middle-point voltage of the battery bank. Individual current and power through each of the four possible sensor modules. The temperature around the battery bank. The estimated amount of Amp hours remaining in the battery bank. The status of all 8 possible relays, "on" or "off". The panel voltage, battery bank voltage, charge current, charge status and charge power of all 5 possible connected Microcare MPPT charge controllers to the BMS. The output voltage, battery bank voltage, charge or discharge current, output current, output power, operating temperature and operating status of all 5 possible Microcare inverters connected to the BMS. An indication whether or not the Microcare web-logger is connected to the BMS, and if it is functioning correctly.

Figure 8: Real Time Displays Screenshot

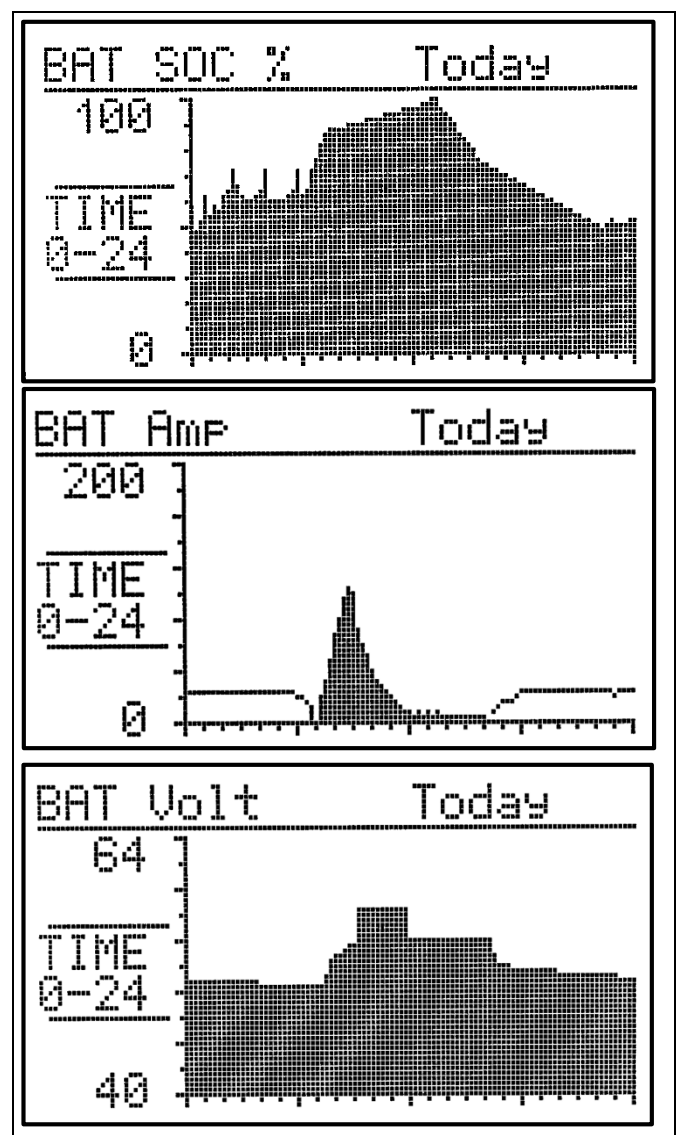


9. Graph Displays

The graph displays are used to give a more complete full day view of the state on how the battery bank and solar system as a whole are functioning. This allows the user to view the following information which happened throughout the day for a duration of 31 days.

The percentage of the battery bank throughout the day, to identify problem areas in over discharge or underutilization. The battery bank voltage throughout the day, to identify correct charging and any possible under voltage conditions. The current being charged into the battery bank throughout the day, to monitor the correct operation of the charge source. The current being discharged out of the battery bank throughout the day, to identify problems with the loads. The temperature near the battery bank throughout the day, to identify if the battery bank is working at accepted temperature levels.

Figure 9: Graph Displays Screenshot



10. Conclusions

This designed BMS has great abilities in data logging and to the trained user it would be a useful tool in ensuring a long life for any large solar battery bank. The remote monitoring and control functionality is useful, but only if the control module is located in a more convenient location than the rest of the solar system. For example, if the inverter and MPPT is located in a garage and the control module is placed in the house. There is the disadvantage that it is only able to operate with other Microcare products, but this is only because of the selected communication protocol being used is Microcare specific.

Using a PIC24 was mainly motivated because of the authors past experience with the manufacturer and software tools, but the MCU proved to be a limiting factor in this project as the available program memory of the MCU forced the author to have to rewrite software in order to fit the newer software. The graphic display did prove to help in visualising larger amounts of data in the form of graphs, but it was only capable of low resolution.

Acknowledgments

- Nelius De Lange - Microcare mentor
- Frank Adlam - University mentor
- Winston Dyson - Enclosure designer

References

- [1] A. a. P. B. Auswamaykin, "Design of Real Time Battery Management Unit for PVHybrid," in *Design of Real Time Battery Management Unit for PVHybrid*, Rajamangala, SciRes, 2004, pp. 186-193.
- [2] G. Burley, "Microcare - Solar," Microcare, 28 January 2015. [Online]. Available: <http://microcare.co.za/solar/>. [Accessed 20 April 2015].
- [3] Q. Barnard, "powermonitor," QBSOft, 20 January 2015. [Online]. Available: <https://powermonitor.co.za/user/view>. [Accessed 20 April 2015].
- [4] S. A. S. Dennis Doerffel, "A critical review of using the Peukert equation for determining the remaining capacity of lead-acid and lithium-ion batteries," *Journal of Power Sources*, vol. 155, no. 2, pp. 395-400, 2004.
- [5] SmartGauge Electronics, "smartgauge.co.uk," SmartGauge Electronics, 20 January 2008. [Online]. Available: <http://www.smartgauge.co.uk/peukert2.html>. [Accessed 20 April 2015].
- [6] S. C. C. M. Yao Ching Hsieh, "Balance discharge for series-connected batteries," *Power Electronics Specialists Conference*, vol. 4, no. 35, pp. 2697-2702, 2004.
- [7] Allegro Micro Systems LLC, "ACS758," Allegro Micro Systems LLC, 07 04 2015. [Online]. Available: <http://www.allegromicro.com/~media/Files/Datasheets/ACS758-Datasheet.ashx?la=en>. [Accessed 15 09 2015].
- [8] Riedon Inc, "RS Series," Riedon Inc, 01 08 2014. [Online]. Available: http://riedon.com/media/pdf/DC_Current_Shunt.pdf. [Accessed 15 09 2015].
- [9] Microchip Technology Inc, "MCP79400," Microchip Technology Inc, 28 10 2013. [Online]. Available: <http://ww1.microchip.com/downloads/en/DeviceDoc/20005009D.pdf>. [Accessed 15 09 2015].
- [10] Atmel Corporation, "AT25M01," Atmel Corporation, 07 07 2015. [Online]. Available: <http://www.atmel.com/Images/Atmel-8824-EEPROM-AT25M01-Datasheet.pdf>. [Accessed 19 09 2015].

A Review of DSTATCOM for Power Quality Improvement

O. Ajayi, R. Tiako

University of KwaZulu-Natal, King George V Avenue, 4041 Durban, South Africa

*Email: olukoladeajayi@yahoo.com

Abstract: The Distribution Static Synchronous Compensator (DSTATCOM) is a custom power, shunt connected device used in the electric power distribution system for the mitigation of power quality problems. This Paper presents a brief review of the DSTATCOM and its application for the improvement of Power Quality in the electric power distribution system. The review examines the basic structure of DSTATCOM, various inverter topologies, control techniques and existing modified architecture. The motivation of this review is to present the DSTATCOM technology on a broad spectrum to researchers and engineers who are concerned with the improvement of power quality in the distribution system.

1 INTRODUCTION

This Power quality is increasingly becoming a major concern between utility experts and consumers of electric power. With the advancement in technology, domestic and industrial processes are becoming automated and as such, their controls which is mainly micro-processor based depend on quality electric power for smooth operation. Malfunction or total breakdown of the control devices as a result of poor power quality causes a disruption in the automation process which can have a severe economic impact [1]. Power quality problem is an all-encompassing word for multitude of disturbances that occur along the power transmission and distribution line such as outage (Interruption), momentary interruption, voltage Sag, voltage Swell, impulsive transient, oscillatory transient, steady state voltage variation (over/under), voltage Imbalance and voltage Harmonics [2]. The most frequently occurring power quality problems as reported in [3] are harmonic distortion and voltage dip (sag/swell).

With rapid developments occurring in the electronics industry, power electronics devices have been developed with high power capability for application in the power transmission and distribution systems. Static Synchronous Compensator (STATCOM) which belongs to the Flexible AC Transmission System (FACTS) family of power electronics devices, it was developed for mitigation of power quality problems in the transmission system. Other members of the FACTS family include SVC and UPFC. Distribution-STATCOM (DSTATCOM) which belongs to a group of power electronic devices referred to as Custom Power Device (CPD) was developed for mitigation of power quality

problems in the distribution system. Examples of other custom power devices are DVR and UPQC [4], [5].

DSTATCOM is a high speed switching device capable of reactive power control, voltage regulation and can mitigate other power quality problems in the distribution system [6]. Operation of DSTATCOM in Voltage control mode and current control mode is reported in [7]. Optimal sizing and allocation of DSTATCOM has been employed using various algorithms such as differential evolution algorithm, bat algorithm and particle swarm optimization technique as reported in [8], [9], [10].

This Paper aims at presenting a concise review of DSTATCOM by highlighting previous research materials that had been written by various researchers on DSTATCOM.

This paper is divided into five sections. Section 2 talks about DSTATCOM architecture, working principle, operation modes and diverse applications. Various inverter topologies are discussed in section 3. Section 4 covers DSTATCOM control topologies. In section 5, conclusions are drawn as well as consideration of future scope.

2 DSTATCOM

The static synchronous compensator (STATCOM) is a fast acting shunt compensator for reactive power control in transmission system [11]. When STATCOM is applied in the distribution system it is called distribution STATCOM (DSTATCOM) [10]. STATCOM and DSTATCOM have similar configuration but have different operating characteristics. STATCOM is required to inject a set of three balanced quasi-sinusoidal voltages that are phase displaced by 120 degrees while DSTATCOM must be able to inject an unbalanced and harmonically distorted current to eliminate unbalance in the load current or supply voltage [12].

2.1. DSTATCOM Architecture

This D-STATCOM is a shunt connected custom power device consisting of a filter, Voltage Source Converter (VSC), a DC energy storage device and a coupling transformer. It is connected at the point of common coupling (PCC) in parallel to the power distribution system through the coupling transformer. A schematic diagram of the arrangement of DSTATCOM is shown in Fig. 1 below.

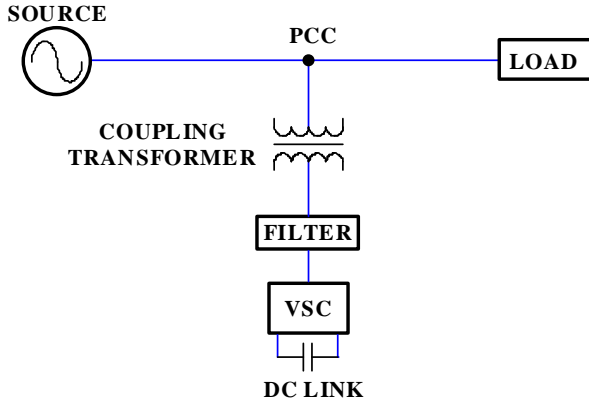


Fig. 1: Schematic diagram of DSTATCOM

The VSC is a power electronic device which comprises of self-commutating solid-state turn-off devices such as IGBTs and MOSFETs with a reverse diode connected in parallel to them. The switching of the solid state devices is based on PWM as reported in [13]. The VSC can generate a sinusoidal voltage at the required magnitude, phase angle and frequency.

A DC voltage source on the input side of VSC is generally achieved by a DC capacitor. The output voltage from the VSC is a multi-stepped AC voltage waveform, almost a sinusoidal waveform [14]. A DC bus capacitor may also be used with two split sections having equal or unequal values [15]. Also, according to [15], the capacitor and DC bus voltage are calculated as:

$$V_{dc} = \frac{2\sqrt{2}V_{LL}}{\sqrt{3}m} \quad (1)$$

$$C_{dc} = \frac{6aVIt}{[V_{dc}^2 - V_{ph}^2]} \quad (2)$$

Where m is the modulation index, V_{LL} is the ac line voltage, I is the phase current, V_{ph} is the phase voltage, t is the time by which the dc bus voltage is to be recovered.

Coupling transformer is used to provide isolation between the VSC and the PCC while also providing neutral current compensation caused as a result of the presence of unbalanced loads in the power system [16].

The filter is used to separate high frequency noise from the generated voltage at the PCC [17]. It is usually a first order high pass filter consisting of a resistor and capacitor connected in series as reported in [10].

2.2. Working Principle of DSTATCOM

The primary objective of DSTATCOM is to obtain harmonic neutralized and controllable three-phase AC output voltage waveforms at the point of common coupling (PCC) to regulate reactive current flow by generation and absorption of controllable reactive power by the solid-state switching algorithm.

The VSC converts the DC voltage across the storage device into a set of sinusoidal AC voltage at the required amplitude, frequency and phase angle. The generated voltage is injected into the power system through

the point of common coupling through the coupling transformer.

As reported in [18], adjustment of the phase and magnitude of the D-STATCOM output voltages allows effective control of active and reactive power exchanges between the D-STATCOM and the ac system.

DSTATCOM operates in the injection and absorption mode. In the injection mode, the reactive power is supplied into the grid while in absorption mode; the active power is taken from the grid. Consequently, if the magnitude of voltage crosses the limit, there exists the condition of voltage swell. Under this condition the extra voltage needs to be removed from the grid. Hence the DSTATCOM acts as an additional load so that the excess voltage is safely absorbed from the power grid. However, when a voltage sag condition takes place where the grid voltage is less than the nominal value, the 'missing' voltage is injected into the grid [19].

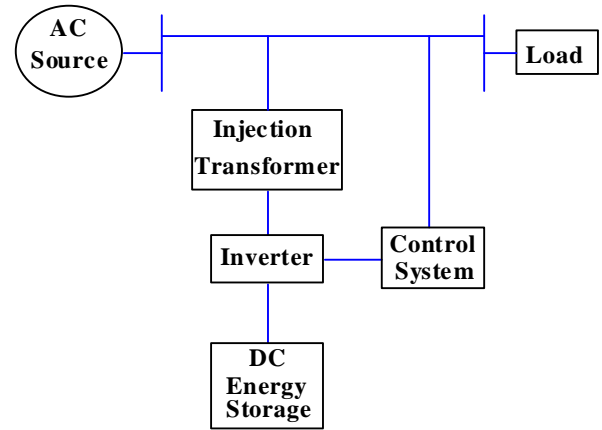


Fig. 2: Block diagram of DSTATCOM System

2.3. Voltage and current control mode of the DSTATCOM

Electrical Distribution system suffers from both current and voltage related power-quality problems, which include poor power factor, distorted source current and voltage disturbances. DSTATCOM is instrumental in mitigating the effects of both types of power quality problems when it is connected at the point of common coupling. In the current control mode (CCM), it injects reactive and harmonic components of load currents to make source currents balanced sinusoidal and also keeping it in phase with the PCC voltage. In voltage-control mode the DSTATCOM regulates PCC voltage at a reference value to protect critical loads from voltage disturbances, such as sag, swell, and unbalances [20].

2.4. Application of DSTATCOM

Various DSTATCOM applications have been reported in literature. Application of a DSTATCOM to solve power quality issues arising from high energy demand loads in an all-electric ship power system [21], the application of a Distribution Static Compensator

(DSTATCOM) to an existing industrial facility to solve power quality problems such as voltage flicker that occurs during the starting of a large motor [10], integrating DSTATCOM into a PV energy system to mitigate the effect of power fluctuations [22] are reported in literature.

3 DSTATCOM TOPOLOGIES

Extensive work has been carried out over the years by researchers into the optimization of DSTATCOM to make it more efficient and fast acting in tackling low power factor, voltage sag, voltage flicker, reactive power consumption and other power quality problems present in the distribution system. Power quality experts' approach comprises of improving and enhancing the performance of the components that make up the DSTATCOM system. When each component is fully optimized to its full capacity, its overall effect can be felt on the performance of the entire system. This section reviews different DSTATCOM topologies that have been reported in literature.

3.1. Inverter Topology

The inverter is an electronic device responsible for conversion of direct current across a DC energy storage device into alternating current which is injected into the power system to correct power quality problems [23]. This makes it a vital component of the DSTATCOM system. The inverter can be current based commonly referred to as Current Source Inverter (CSI) or voltage based commonly referred to as Voltage Source Inverter (VSI) [20]. The VSI uses DC voltage from the energy storage device (capacitor) as source and converts it into AC voltage waveform while the CSI makes use of the DC current from the energy storage device (inductor) as source and converts it into AC current waveform [24]. The schematic representation of the CSI and VSI based DSTATCOM is shown in Fig. 3.

CSI based DSTATCOM is developed as a suitable option in high power application. However VSI based DSTATCOM system is the best suited for medium power application [25]. VSI based DSTATCOM gives more harmonic reduction as compared to CSI based DSTATCOM [20]. The use of inductors as the energy storage device in CSI based DSTATCOM induces high conduction losses which are the main reason why the CSI topology is not widely used as the VSI topology [13]. Recent research reveals the development of superconducting magnetic energy storage technology which is aimed at addressing the problem of conduction losses in the CSI topology [11]. The VSI topology is most widely used due to its simple design of the power and control circuits, light weight, flexible operation and its cost effectiveness [26].

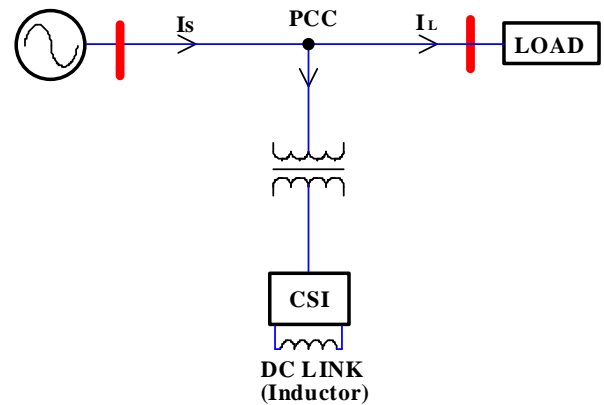


Fig. 3(a): Current source inverter configuration

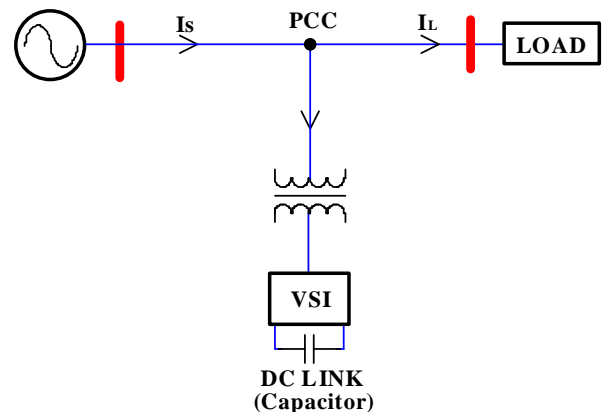


Fig. 3(b): Voltage Source inverter configuration

3.2. Multilevel Inverter Topology

Multilevel Inverters (MLI) are widely known for their high-voltage and high-power capability replacing the classical thyristor-based cyclo-converters, and line and load commutated current-fed converters.

The most common MLI topologies reported in literature are: Diode-Clamped MLI topology (also referred to as Neutral Point Clamped – NPC), Capacitor-Clamped MLI topology (also known as The Flying Capacitor topology) and Cascaded H-Bridge (CHB) MLI topology [27], [28], [29].

A multilevel inverter based DSTATCOM is a choice application in power quality improvement because it reduces the device voltage, lowers output harmonics and suppresses switching losses by increasing the number of output voltage levels.

Other MLI based DSTATCOM topologies are also reported in [30].

3.3. Supply System Classification

DSTATCOM is predominantly used in the distribution system as its name implies. The distribution system which can either be 3-phase 3-wire, 3-phase 4-wire or single phase 2-wire features various DSTATCOM topology in accordance with the topology of the supply system. There are some power quality problems which persist due to the configuration of the power supply topology.

In many residential buildings and some industrial facilities, power is distributed through a three-phase, four-wire (3P4W) systems. The nonlinear and unbalanced loads in these systems may result in excessive neutral currents, which may potentially damage the neutral conductor and distribution transformer while affecting the safety of the consumers [31].

Application of DSTATCOM to mitigate the effect of power quality issues such as excessive neutral current, voltage sag, harmonic distortion which arise due to peculiarities of the power supply system are reported in [32].

3.4. Transformer Topology

Transformers are used in the DSTATCOM to provide isolation of the VSC device from the power system and to provide neutral current compensation. Researchers in [18] reports that the transformer also help to provide isolation between the inverter legs to prevent the dc storage capacitor from being shorted by switches in different inverter legs. Common transformer topologies reported in literature are zig-zag, star/delta, T-connected and star/hexagon [33].

4 CONTROL STRATEGIES

Control strategy is the heart of DSTATCOM operation and major determinant of its performance [34]. DSTATCOM control involves two distinct operations.

Generation of Reference signals: There are two methods involved in the generation of reference signals which are: frequency domain and time domain methods as reported in [35]. The Time domain is faster and easy to implement but the frequency domain present a better detection performance over the time domain method [36]. Some of the reference signal generation techniques reported in literature are Synchronous reference frame (SRF), Instantaneous reactive power (IRP), Symmetrical Component Theory, Proportional Integral Controller [37].

In [38] SRF was used in conjunction PWM for the control operation of a 6-leg VSC DSTATCOM. It reports is the most widely used method as the reference signal extracted as free from harmonics due to the action of two low pass filters. The IRP theory also known as the p-q theory was initially proposed by [39] and it is

based on the transformation of three phase quantities to two phase quantities in α - β frame and the calculation of instantaneous active and reactive power in this frame. Other signal generation techniques are reported as follow Average unit power factor theory [40], Adaline based neural network [13], sliding mode control. Advanced and modified techniques have played a significant role in the operation of DSTATCOM are reported in [37]. Comparative studies depicting various strength, weakness and performance of different control techniques are reported in [10].

Generation of a suitable switching signal: This is considered to be the most significant part of the control operation of DSTATCOM due to its high influence on the compensation performance of DSTATCOM [41]. The most reliable way of achieving this is through the use of PWM which is divided into Open loop and closed loop. According to [13] the open loop method is further subdivided into SPWM and SVPWM. Also, the closed loop method is further classified into Hysteresis Current Control (HCC) and Linear Current Control (LCC) as reported in [13].

5 CONCLUSION AND FUTURE SCOPE

A review of DSTATCOM for the improvement of power quality is carried out. An overview of DSTATCOM topologies and control techniques is considered. Classification of DSTATCOM was also done based on supply system.

DSTATCOM has attracted a lot of attention and currently receiving a lot of research interests due to its capability of mitigating power quality problems effectively. Extensive research is being carried out to make DSTATCOM performance better while bringing down implementation cost. Researchers are looking to develop new topologies and control strategies and also modification of existing ones in order to mitigate power problems existing in the electrical power distribution system.

6 REFERENCES

- [1] R. A. K. a. S.K.Joshi, "A review on power quality problems and solutions," *Elixir International Journal*, pp. 39 (2011) 4759-4762, 28th september 2011.
- [2] Y. Arora, "A REVIEW ON POWER QUALITY PROBLEMS AND ITS SOLUTION AT DISTRIBUTION END USING DIFFERENT INTERFACING DEVICE," *International Journal of Emerging*

- Trends in Engineering and Development*, vol. 5, p. 2249-6149, September 2014.
- [3] M. H. J. Bollen, "Review: What is power quality?," *Science Direct*, vol. 66, 2003.
- [4] C. a. J. P. P. Rajeev Kumar, "Mitigation of Power Quality Problems Using FACTS Devices: A Review," *International Journal of Electronic and Electrical Engineering*, vol. 7, pp. 255-262, 2014.
- [5] J. Alexander Domijan, Alejandro Montenegro, Albert J. F. Keri, Senior Member, IEEE, and Kenneth E. Mattern, "Custom Power Devices: An Interaction Study," *IEEE TRANSACTIONS ON POWER SYSTEMS*, vol. 20, p. 8, May 2005.
- [6] Y. Y. Ahmet TEKE, Mohammad Barghi LATRAN, "Step by Step Design Procedure of a Distribution Static Synchronous Compensator (DSTATCOM)," *Haziran 2015*, vol. 30, pp. 117-131, 2015.
- [7] M. K. Mishra, Ghosh, A. and Joshi, A, "Operation of a DSTATCOM in voltage control mode," *Power Delivery, IEEE Transactions on*, vol. 18, p. 6, Jan 2003.
- [8] K. R. T. Yuvaraj *, K.R. Devabalaji, "DSTATCOM allocation in distribution networks considering load variations using bat algorithm," *Ain Shams Engineering Journal*, 28 August 2015.
- [9] H. S. Jazebi S, Vahidi B., "DSTATCOM allocation in distribution networks considering reconfiguration using differential evolution algorithm," *Energy Convers Manage*, vol. 52, 2011.
- [10] A. G. S. Om Prakash Mahela, "A review of distribution static compensator," *Renewable and Sustainable Energy Reviews*, vol. 50, p. 15, 29 May 2015.
- [11] R. S. B. Singh, A. Chandra, K. Al-Haddad, "Static synchronous compensators (STATCOM): a review," *IET Power Electronics*, 22nd April 2008.
- [12] S. Singh, "An Extensive Survey on Distribution Static Compensator (DSTATCOM)," *International Journal of Emerging Technology and Advanced Engineering*, vol. 4, pp. 2250-2459, 2014.
- [13] A. T. Mohammed Barghi Latran, Yeliz Yoldaş, "Mitigation of power quality problems using distribution static synchronous compensator: a comprehensive review," *The Institution of Engineering and Technology*, 23 Jan. 2015.
- [14] V. V. B. Hande, A.Y. ; Ankushe, R.S. ; Patil, D.R., "Voltage regulation with adaptive control algorithm for DSTATCOM " *Power and Energy Systems Conference: Towards Sustainable Energy*, 2014, p. 13, 2014.
- [15] M. Srikanthan S., Mahesh Kumar, "DC Capacitor Voltage Equalization in Neutral Clamped Inverters for DSTATCOM Application," *Industrial Electronics, IEEE Transactions*, vol. 57, p. 7, 2010.
- [16] A. SreenivasaraoD, DasB., "Neutral current compensation in three-phase, four-wire systems:a review," *Electric Power System Research*, vol. 86, p. 10, 2012.
- [17] P. RohillaY, "T-connected transformer integrated three-leg vs c-based 3p4w dstatcom for power quality improvement," *2013 Nirma University international conference on engineering (NUIcone)*, p. 7, 2013.
- [18] S. K. a. M. R. R. S. P. Gawande, "Design Consideration for Configuration, Topology & Control Schemes of DSTATCOM Implemented on Distribution Systems," *Lecture Notes on Information Theory*, vol. 1, September 2013.
- [19] R. J. SHIVARAJ S, PRAVEENA ANAJI, "Improvement of Power Quality of a Grid Connected Distributed System Using DSTATCOM," *International Journal of Scientific Engineering and Technology Research*, vol. 04, p. 3, May 2015.
- [20] V. F. P. Natália M. R. Santosa, "Three-phase STATCOM based on a single-phase current source inverter," *2nd International Conference on Advances in Energy Engineering (ICAEE2011)*, p. 5, 2011.
- [21] P. M. a. G. K. Venayagamoorthy, "An Adaptive Control Strategy for DSTATCOM Applications in an Electric Ship Power System," *IEEE TRANSACTIONS ON POWER ELECTRONICS*, vol. 25, 2010.
- [22] B. B. B. a. Y. Li, "Reviewing DSTATCOM for Smart Distribution Grid Applications in Solving Power Quality Problems," *Proceedings of the 17th International Conference on Automation & Computing, University of Huddersfield, Huddersfield, UK*, 2011.
- [23] S. B. KOTLA SUMA, "T-STATCOM based Cascaded Multilevel Converter with IGBT Technology," *International Journal of Scientific Engineering and Technology Research*, vol. 04, p. 5, 2015.
- [24] P. P. Dash, Kazerani, M. , "A multilevel current-source inverter based grid-connected photovoltaic system," *North American Power Symp., Boston*, p. 6, 2011.
- [25] P. P. Dash, Kazerani, M., "Harmonic elimination in a multilevel Current-Source Inverter-based grid-connected photovoltaic system," *38th IEEE Annual Conf. Ind. Electronics Society, Montreal, Montrea*, p. 5, 2012.

- [26] K. D. R. Chinmayee Tripathy, Prasanna Kumar Karjee, "Cascaded H-Bridge Multilevel Inverter Based DSTATCOM Using Fuzzy Logic Controller in MATLAB Simulink," *IJRSI*, vol. 2, April 2015.
- [27] S. Srikanthan, Mishra, M.K., Rao, R.K.V., "Improved hysteresis current control of three-level inverter for distribution static compensator application," *IET PowerElectron*, vol. 2, p. 9, 2009.
- [28] R. E. Betz, Summerst, T., Furneyt, T., "Symmetry compensation using a H-bridge multilevel STATCOM with zero sequence injection," *41st IEEE Ind. Conf. Applications, Tampa*, vol. 4, p. 7, 2006.
- [29] J. Rodríguez, Franquelo, L.G., Kouro, S., "Multilevel converters: An enabling technology for high-power applications," *IEEE Proceedings*, vol. 97, p. 31, 2009.
- [30] A. Shukla, Ghosh, A., Joshi, A., "State feedback control of multilevel inverters for DSTATCOM applications," *IEEE Trans. Power Deliv.*, vol. 22, p. 9, 2007.
- [31] V. Khadkikar, "Enhancing electric power quality using UPQC: A comprehensive overview," *IEEE Transactions on Power Electronics*, vol. 27, p. 13, 2012.
- [32] G. GuptaR, JoshiA., "Control of cascaded transformer multilevel inverter based {DSTATCOM}," *Electric Power System Research*, vol. 77, p. 10.
- [33] S. A. J. A. Barrenal, J. M. Canales' M. A. Rodriguez1, L. Marroyo, "Design, Analysis and Comparison of Multilevel Topologies for DSTATCOM Applications."
- [34] B. Singh, Al-Haddad, K., Chandra, A., "A review of active filters for power quality improvement," *IEEE Trans. Ind. Electron*, vol. 46, p. 11, 1999.
- [35] A. M. Massoud, Finney, S.J., Williams, B.W., "Review of harmonic current extraction techniques for an active power filter," *11th Int. Conf. Harmonics Quality Power, 12-15 September 2004*, p. 5, 2004.
- [36] Sepulveda C, Espinoza J, Figueroa M, Melin P., "All-on-chip dq-frame based d-statcom control implementation in a low-cost fpga," *IEEE Transactions on Electronics*, p. 659-69, 2013.
- [37] J. SinghB, KothariD., "New control approach for capacitor supported {DSTATCOM} in three-phase four wire distribution system under non-ideal supply voltage conditions based on synchronous reference frame theory.," *International Journal of Electric Power Energy System*, vol. 33, p. 17, 2011.
- [38] R. V. Bangaraju J, Jayalaxmi A., "Unit template synchronous reference frame theory based control algorithm for dstatcom," *JInstEng(India)*, p. 41, 2014.
- [39] Sahu. G, "Real time implementation of digital filter on control strategy of dstatcom for load compensation under distorted utility condition.," *IEEE Asia Pacific conference on postgraduate research in microelectronics and electronics(PrimeAsia)*, p. 164-9, 2013.
- [40] S. A. Kumar P, Kummari N., "p-q theory based modified control algorithm for load compensating using dstatcom.," *IEEE 16th international conference on harmonics and quality of power*, p. 591-5, 2014.
- [41] R. S. Herrera, Salmeron, P., Hyosung, K., "Instantaneous reactive power theory applied to active power filter compensation: different approaches, assessment, and experimental results," *IEEE Trans. Ind. Electron*, vol. 55, p. 184 - 19, 2008.

VALIDATION OF THE BREAKDOWN MECHANISM BETWEEN ROTATED ARCING HORNS

BA Smith* and AG Swanson

* Discipline of Electrical, Electronic & Computer Engineering, School of Engineering, University of KwaZulu Natal, Durban E-mail: basmith1991@gmail.com

Abstract: Arcing horns are fitted onto line insulation with the primary purpose of protecting the insulator against potential damage as a result of flashover. Additionally, the resulting spark gap performs a role in the insulation co-ordination of the transmission system. Adverse weather conditions result in the rotation of the arcing horns and necessitates the need for an investigation into how the performance of the insulator may be affected as well as the co-ordination. This study serves as a supplemental investigation to the insulation co-ordination model developed and involves an experiment to find the critical flashover (CFO) voltage of rotated arcing horns on a polymeric insulator by means of an up-down U_{50} test. The results of the experiment are then compared to the theoretical CFO gap values for each point of rotation obtained by means of a leader progression model (LPM). Comparison of the results show that a correlation can be drawn between the measured and the theoretical CFO values by means of a multiplicative factor.

Key words: Arcing horns, flashover mechanism, leader progression model

1. INTRODUCTION

Service interruptions to transmission line systems is often as a result of an earth fault caused by external overvoltages such as lightning. Backflashover across an insulator occurs as a result of a direct strike to a transmission tower or shielding event causing a steep rise of the tower potential and subsequent breakdown of the spark gap. Arcing horns are set in place on either side of the line insulation for protection as well as performing a role in the insulation co-ordination of a transmission system in order to further help protect non self restoring insulation such as the internal insulation of transformers.

In the case where arcing horns have been rotated through an angle (θ) it is vital to understand the flashover mechanism that exists between these units in the presence of an insulator.

In practise, physical approaches and integration methods can be utilised to determine the U_{50} voltage for a given gap distance and geometry after which a CFO value may be obtained.

In this paper, two insulators, namely 88 kV and 22 kV, fitted with arcing horns were subjected to U_{50} testing at different points of rotation using a $1.2 \times 50 \mu\text{s}$ waveform using a Marx generator. A leader progression model, developed in MATLAB, was then used as a reference to compare the laboratory results.

2. BACKFLASHOVER

For lightning events, the outages resulting from back-flashover are more commonly occurring than those caused by a shielding failure. [3] Positioning of shield wires on overhead transmission lines is designed in such a way that should a lightning strike terminate on the phase

conductor the amplitude of the resulting impulse waveform experienced by the insulator would be insufficient to cause a flashover. When lightning strikes the shielding wire the shielding impedance coupled with that of the surge and ground impedances of the tower will produce a heightened potential on the cross arms of the tower. Factors mentioned in [7] and [10] can however influence the waveform experienced by the insulator on transmission systems. These factors should be noted and taken into account when conducting experiments with laboratory induced impulses which are largely unaffected by these external factors. Factors may include:

- The electromagnetic coupling of the shield wires with that of the conductors can result in a portion of the voltage being observed on the phase conductor.
- Depending on the travel time, the reflections of the earthing resistance and soil ionisation can result in the voltage being reduced across the insulator string.
- Reflections from other towers may also result in destructive interference of the voltage across the string although, due to the travel time this is usually insignificant.

A diagram of backflashover and the associated processes can be found below:

3. FLASHOVER MECHANISMS

There have been many models used to realise flashover [9] such as the volt-time method, equal area criterion, leader propagation model and the non-linear inductance

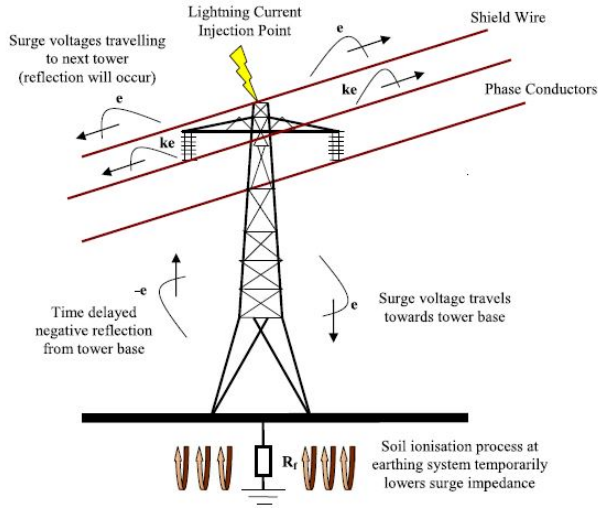


Figure 1: Direct strike to a tower [10]

method. In [4], [12], [5] [11] it was decided to utilise the leader progression model (LPM) in order to theoretically calculate CFO voltages for each gap rotation.

3.1 Leader progression model

The leader propagation method is an iterative method used for estimating flashover in a number of gap configurations and geometries as demonstrated in [11]. In [4] it was used to compare CFO voltages on high voltage polymer insulators of 110, 120 and 440kV fitted with arcing horns on both ends.

The method can be shown in the Figure and proceeds in two stages prior and subsequent to leader onset.

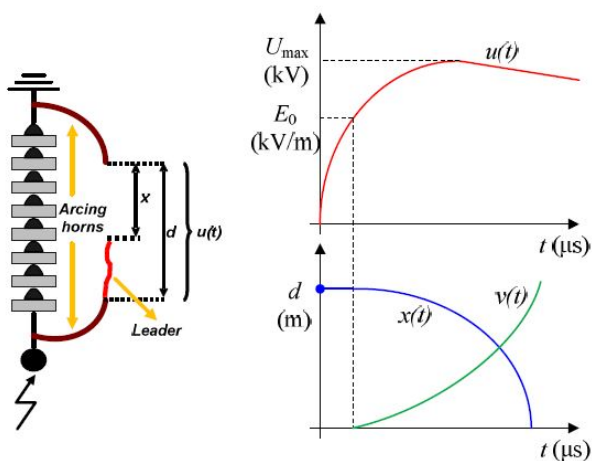


Figure 2: Leader progression model [4]

Leader Onset:

Provided that equation 1 below remains valid the leader

will not begin its progression across the gap and the arcing distance will remain fixed at the initial value of d.

$$\frac{U}{d-l} < 500 \frac{kV}{m} \quad (1)$$

Leader development process:

Once the voltage gradient E_0 is exceeded the leader will begin to progress at a velocity calculated by the following equation found in [11] for a rod-rod gap with an impulse of either polarity.

$$\frac{dl}{dt} = k \times d \times \left(\frac{U(t)}{d-l} - E_0 \right) \quad (m/s) \quad (2)$$

Where k and E_0 are constants dependant on the geometry and minimum distance, d of the gap. The expression $(d-l)$ is the revised gap distance in the presence of a developing leader under the instantaneous voltage $U(t)$ of the impulse waveform.

The length of the developed leader can then be calculated by the addition of each incremental step

$$\int \frac{dl}{dt} = x_{leader} \quad (3)$$

and the flashover criterion is fulfilled when

$$x_{leader} > d \quad (m) \quad (4)$$

which implies that the gap has been bridged.

3.2 Flashover of smaller gaps

Considering the arcing horn arrangements for both insulators it was noted that the initial gap spacing was less than the valid minimum distance as quoted in [11] of 1 meter. It was therefore necessary to include an equation from [6] which governs the spark over voltage for both positive and negative polarity valid for gaps less than 1 meter as shown below:

$$V_{sp} = 2 + 534 \times d \quad (kV) \quad (5)$$

3.3 Rotation of arcing horns

In order to assimilate the movement under adverse weather conditions an expression for the gap distance of the rotated arcing horns needed to be found. This was done using spherical co-ordinates assuming one horn remained still throughout while the other rotated in a horizontal manner through an angle θ . it can be shown that the gap distance produced by a single arcing horn rotating under any angle θ with an initial gap setting of x, a vertical arcing horn radius r, can be governed by:

$$d_{gap}(x, r, \theta) = \sqrt{(x^2) + (r - r \cos \theta)^2 + (r \sin \theta)^2} \quad (6)$$

3.4 Non atmospheric conditions

The disruptive discharge on external insulation is dependant on atmospheric conditions.

Humidity correction factor:

The humidity correction factor, k , found in [8] for impulse voltages may be expressed as:

$$k = 1 + 0.01(h/\delta - 11) \quad (7)$$

where h represents the absolute humidity and δ the temperature correction factor. For gaps less than 0.5 m however, the humidity correction factor shall not be applied.

Air density correction factor:

Pressure and temperature perform a role influencing the U_{50} voltage and can not be neglected.

$$\delta = \left(\frac{b}{b_0}\right) \times \left(\frac{273 + t_0}{273 + t}\right) \quad (8)$$

where b_0 is seen to be the standard atmospheric pressure and t_0 the standard room temperature.

4. EXPERIMENT

The purpose of the experiment in the laboratory was obtain the CFO value for each gap spacing by the means of an up-down method as mentioned in [8] and [12] in order to ascertain the respective U_{50} for each point of rotation.

4.1 Apparatus

The insulator-arcing horn test arrangement was connected as the device under test (DUT) to a 7 stage Marx impulse generator capable of reaching $125kV_{dc}$ per stage. The test setup is shown below.

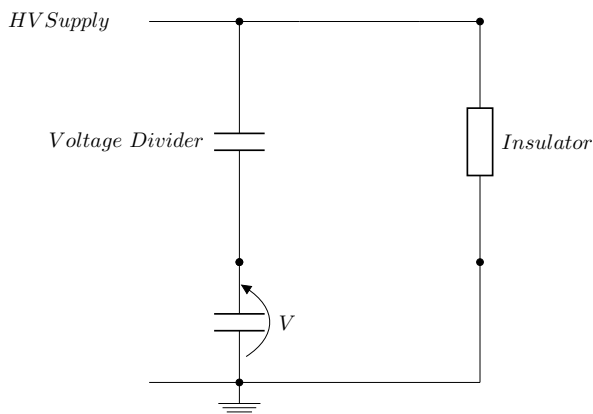


Figure 3: Set up for arcing horn testing arrangement [10]

The two test arrangements can be found below:

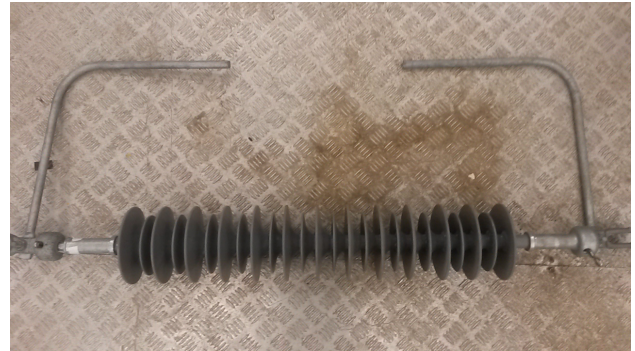


Figure 4: 88kV insulator set up

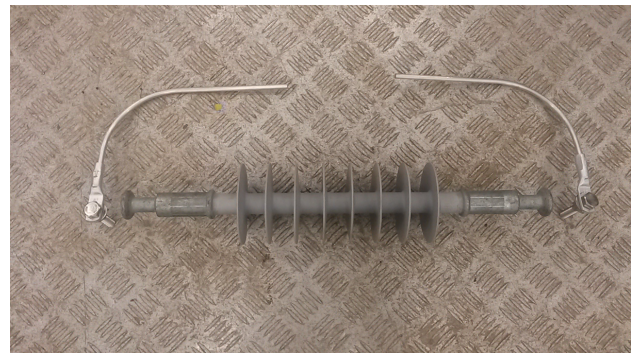


Figure 5: 22kV insulator set up

It should be noted that the arcing horns which were fitted onto the smaller 22kV insulator were dimensioned in a ratio with those dimensions of the 88kV. The initial air gap of the 22kV arcing horns was calculated to correspond to the ratio of the dry arcing distance between the end fittings of the insulators. The vertical radius of the smaller arcing horn was then calculated to satisfy the initial gap condition. The insulator dimensions can be found below.

4.2 Insulator Dimensions

• 88kV insulator

Dry arc distance: 785mm
Initial arcing horn separation (x): 400mm
Arcing horn vertical radius (r): 350mm

• 22kV insulator

Dry arc distance: 280mm
Initial arcing horn separation (x) : 150mm
Arcing horn vertical radius (r): 207mm



Figure 6: Arcing horns for each set up

4.3 U_{50} testing

The insulators were subjected to an up-down test wherein a total of 20 (N) impulse shots were applied to the spark gap with an initial voltage level, V_i . For each flashover, voltage level V_{i-1} was applied and each withstand V_{i+1} . The number of withstands and flashovers were then summed and the U_{50} voltage was then calculated as follows as per the [1] and [2].

$$U_{50} = \frac{\delta \times k \times \left(\frac{\sum(n \times V_i)}{N} \right) \times s_{measure} \times d_{ratio}}{1000} \quad (kV) \quad (9)$$

where $s_{measure}$ is the scaling ratio of the impulse measurement circuit and d_{ratio} represents the capacitive divider. The results were recorded for both polarities of impulse.

5. RESULTS

5.1 U_{50} testing results

The results of both the positive and negative impulses across the arcing horn air gap were recorded for rotations up to 90 degrees at which point the leader development in the gap was constantly breaking down to the fitting and not the opposing arcing horn.

5.2 Leader model results

The leader progression model results were simulated in MATLAB by applying double exponential impulses to an air gap dimensioned for each arcing horn point of rotation. The amplitude of each exponential waveform was increased until flashover occurred in the gap. For each point the time to breakdown was noted and the crest amplitude recorded. It was then possible to plot corresponding V-t curves for each gap distance. According to [4] the CFO values can be found at a time to breakdown of about $16\mu s$. The values of the crest voltage amplitude can be found in Tables 1 and 2 below.

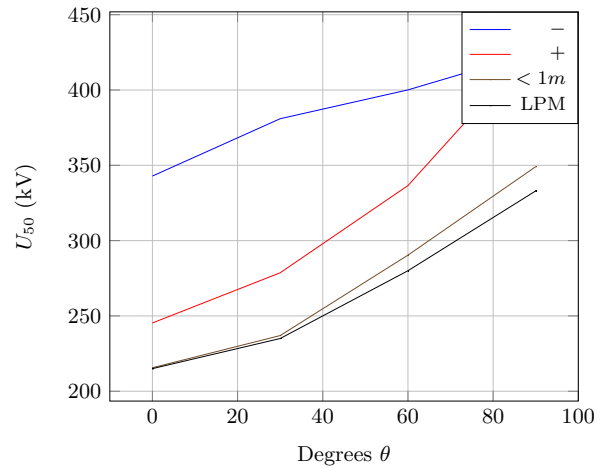


Figure 7: Results of 88kV insulator testing

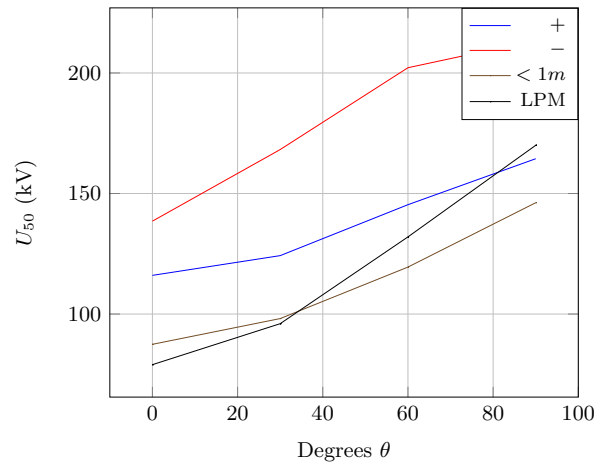


Figure 8: Results of 22kV insulator testing

5.3 One arcing horn vs. two

During testing it was noticed that not all the flashovers were taking place in the arcing horn gap but rather to the end fitting of the insulator; this was particularly more apparent in the 22kV insulator. A U_{50} test was then conducted on both set ups carrying one arcing horn fitted to the live side.

Due to a strain on supply the negative impulse U_{50} voltage could not be attained for the 88kV insulator. The same experiment was conducted on the 22kV insulator.

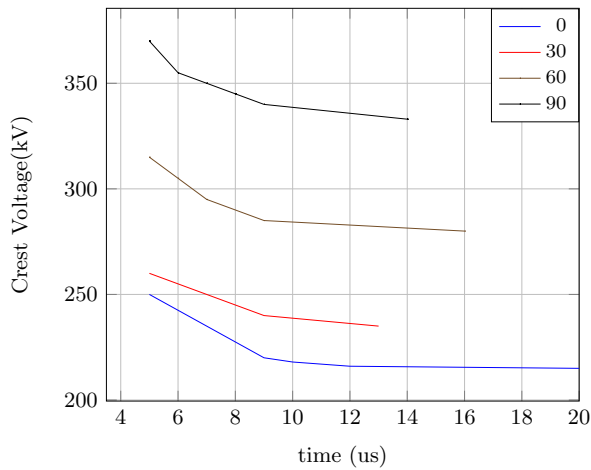


Figure 9: V-t curve result for 88kV insulator

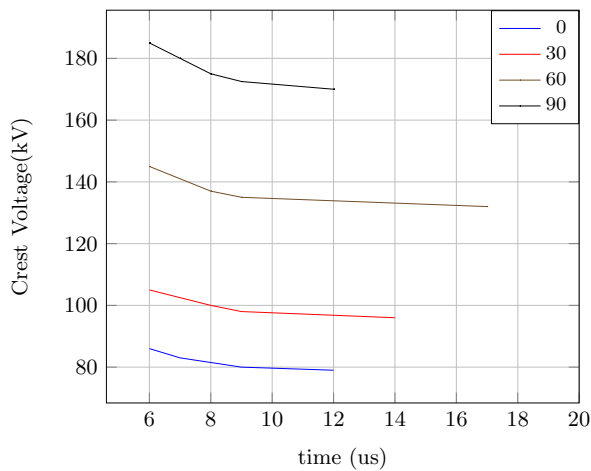


Figure 10: V-t curve result for 22kV insulator

6. DISCUSSION

The results from both the laboratory testing as well as the integration method models have been compared in Figure 7 and Figure 8 for both set ups. On both occasions it can be noted that the negative polarity impulse was the most difficult to breakdown as anticipated by [4]. This can be attributed largely to the different mechanisms associated with positive and negative lightning found in [3].

6.1 Comparison of results

In both cases, the positive and negative impulses recorded higher level of U_{50} voltages when comparing to both the leader progression method as well as the sparkover voltage

Rotation	Time (μ s)	Crest amplitude (kV)
0	20	215
30	13	235
60	16	280
90	14	333
One horn	16	280

Table 1: Results for 88kV LPM method

Rotation	Time (μ s)	Amplitude (kV)
0	12	79
30	14	96
60	17	132
90	12	170
One horn	17	132

Table 2: Results for 22kV LPM method

for gaps less than 1 meter. This could possibly be attributed to a number of factors.

- The insulator plays a role in the distribution of the electric field distribution
- The original breakdown mechanism used in the development of leader velocities in [11] was different to that conducted in the experiment.

It is worth noticing the similarity in the results recorded from the leader progression model and the equation from literature for gaps less than 1 meter and thus a multiplicative factor for each polarity based on both tests was developed. This was done by taking an average correlation value between both polarities and comparing it to that of the LPM. For positive polarity the multiplicative factor, $k_{pos} = 1.2$ and the negative multiplicative factor, $k_{neg} = 1.5$. These multiplicative factors could perhaps account for the role of the insulator in the development of the electric field between the arcing horns.

7. CONCLUSION AND RECOMMENDATIONS

The breakdown mechanism between rotated arcing horns is not one that has had much investigation. Current literature only provides integration methods which deal mainly with gaps over 1 metre in length and are, according to [11] not always completely accurate. Although, as expected, the breakdown voltages increase for increasing degree of rotation there does come a point when the breakdown between the arcing horns ceases to exist and the breakdown to the insulator fitting begins. The exact point is difficult to pinpoint due to the complexity of the breakdown mechanism which itself depends on many physical attributes. Mathematically, the point at which this takes place is 60° although experimentally, the U_{50} closest to that of the one horn experimental result is

	Positive Impulse (kV)	Negative Impulse (kV)
U_{50}	440.98	n/a

Table 3: U_{50} test on an 88kV insulator

	Positive Impulse (kV)	Negative Impulse (kV)
U_{50}	192.38	221.77

Table 4: U_{50} test on an 22kV insulator

measured closer to 90°. Future work could include a more detailed simulation perhaps using more than one method to compute the CFO value in order to fully validate the laboratory results for both polarities of impulse.

8. ACKNOWLEDGEMENTS

The authors would like to thank Eskom for the funding of the university through the Electrical Power Plant Engineering Institute programme. The authors would like to thank eThekweni Municipality for the use of the equipment.

REFERENCES

- [1] IEC 60060-1. *High-voltage test techniques - Part 1: General definitions and test requirements*. September 2010.
- [2] IEC 60060-2. *High-voltage test techniques - Part 2: Measuring systems*. November 2010.
- [3] EPRI. *Chapter 6- Improving the Lightning Performance of Transmission Lines, Overhead Transmission Line Lightning and Grounding Reference Book*. Palo Alto, 2013.
- [4] D. Filipovic-Grcic, B. Filipovic-Grcic, D. Brezak, I. Uglesic, and A. Tokic. Leader progression model application for calculation of lightning critical flashover voltage of overhead transmission line insulators. In *Lightning Protection (ICLP), 2012 International Conference on*, pages 1–8, Sept 2012.
- [5] F.M. Gatta, A. Geri, S. Lauria, M. Maccioni, and F. Palone. Tower grounding improvement vs. line surge arresters: Comparison of remedial measures for high-voltage subtransmission lines. *Industry Applications, IEEE Transactions on*, PP(99):1–1, 2015.
- [6] G. Gela. Sparkover performance and gap factors of air gaps below 1 meter. Technical report, Electric Power Research Institute, 1998.
- [7] A.R. Hileman. *Insulation coordination for power systems*, volume 19. Sept 1999.
- [8] IEEE. Ieee standard for power systems - insulation coordination. *IEEE Std 1313-1993*, pages i–, 1993.
- [9] P. Sarma Maruvada. *Chapter 8 - Corona and Gap Discharge Phenomena, EPRI AC Transmission Line Reference Book - 200 kV and Above*. EPRI, 2005.
- [10] I. Cotton b M.Z.A. Ab Kadir a. Application of the insulator coordination gap models and effect of line design to backflashover studies. In *Electrical Power and Energy Systems* 32 , 443449, 2010.
- [11] A. Pigini, G. Rizzi, E. Garbagnati, A. Porrino, G. Baldo, and G. Pesavento. Performance of large air gaps under lightning overvoltages: experimental study and analysis of accuracy predetermination methods. *Power Delivery, IEEE Transactions on*, 4(2):1379–1392, Apr 1989.
- [12] C.F. Wagner and A.R. Hileman. Mechanism of breakdown of laboratory gaps. *Power Apparatus and Systems, Part III. Transactions of the American Institute of Electrical Engineers*, 80(3):604–618, April 1961.

IMPULSE BREAKDOWN OF SF₆-N₂ GAS MIXTURES

C. Babunandan*, M.D. Brown* and A.G. Swanson*

* Discipline of Electrical, Electronic and Computer Engineering, School of Engineering, University of KwaZulu-Natal, King George V Ave, Durban 4041, South Africa Email: chash182@gmail.com

Abstract: The streamer breakdown of SF₆:N₂ mixtures are investigated analytically and through Bolsig+, a Boltzmann equation solver. The breakdown voltages at gas pressures of 1, 2, and 3 bar of pressure, respectively, proved to be similar for both methods. Where the electron energy was altered due to the presence of nitrogen. The experimental procedure for impulse breakdown of compressed gases, uses sphere-plane electrodes and lightning impulse in both positive and negative polarity for each mixture of SF₆:N₂ at different gas pressures. The breakdown voltage for 50% SF₆-50%N₂ mixtures, as well as lower partial pressures of SF₆, appear to be higher with increased pressure of the gases. The impulse breakdown voltage produces different values when positive and negative polarities are inputted. The impulse breakdown voltages with lower partial pressures of SF₆ in the mixtures, are considerably higher than pure SF₆, therefore, mixtures with lower percentages of SF₆ can be used in GIL and GIS.

Key words: Impulse breakdown, lightning impulse, SF₆:N₂ mixtures.

1. INTRODUCTION

Gas-insulated equipment has become an integral part of power and distribution systems throughout the electrical industry using Sulphur hexafluoride (SF₆) more than any other gas. SF₆ is one of the most dominant gases in the electrical industry due to its electrical properties. SF₆ is a strong electronegative gas, that has good dielectric strength and arc-quenching properties, will allow SF₆ to be widely used in gas insulating substations (GIS), where SF₆ will be used throughout the substation as a means of insulation [1].

The problem lies in the fact that, despite the performance as an insulator, SF₆ has significant environmental impacts if it is leaked into the atmosphere, due to it being a potent greenhouse gas. Therefore, SF₆ is one of the gases that are included in the Kyoto Protocol, with a global warming potential that is given as 22800 times greater than CO₂ [2]. This motivates the need to investigate alternative combinations of gases that can produce similar electrical characteristics that make SF₆ a good insulator, without having a harmful effect on the environment. Other insulators used besides air and SF₆ include, N₂ and CO₂.

This design investigates the breakdown of gases, and applies the theoretical to Matlab, a software package that will show the breakdown voltages for different gas mixtures for uniform electric field, in accordance to the code written, and Bolsig+ is used to verify the Matlab results. Lastly, impulse breakdown of SF₆:N₂ mixtures is experimented in order to find out whether lower partial pressures of SF₆ in N₂ will be able to replace pure SF₆ in certain electrical applications.

2. THEORY

In order to understand the breakdown of gases under different pressures and different gap distances, simulations by means of Matlab and Bolsig+ can be done. Using Baumgartner's premise, it is stated that each gas contributes to the α and η in proportion to its partial pressure. Since, different combination of gases are to be used at different partial pressures to find a combination that matches the breakdown voltage of pure SF₆, Baumgartner's premise is used. Therefore in the case of mixing SF₆ and N₂, the equation for the streamer breakdown is as follows, provided that the partial pressure of SF₆ is denoted as pS , and that of N₂ is pN [3]:

$$\alpha - \eta = 0.28 pS (E - 8.89 \times 10^6 p) + 5.32 \times 10^5 p \times pN \exp\left(\frac{-2.08 \times 10^7 p}{E}\right) \quad (1)$$

Where:

p is the total pressure [bar]

pS is the partial pressure of SF₆

pN is the partial pressure of N₂

E is the electric field [V/m]

α is the ionisation coefficient [/m]

η is the attachment coefficient [/m]

The Bolsig+ software is a Boltzmann equation solver that can be used to obtain the ionisation and attachment coefficients of different gases or combination of gases at different partial pressures. These results are imported to Matlab, and code should be written to obtain the effective ionisation coefficient. Importantly Bolsig+ allows the user to capture the coefficients over a wider energy range.

The results for 50 %SF₆:50%N₂ mixtures were as follows:

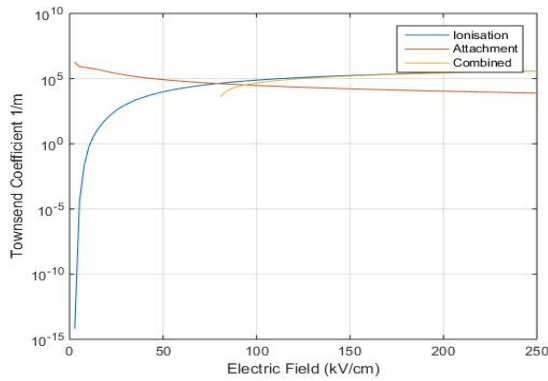


Figure 1: Townsend coefficients for 50%SF₆-50%N₂

Breakdown will occur when the streamer criterion is met:

$$\int (\alpha - \eta) dx = 18 \quad (2)$$

By writing the relevant code, using Equations (1) and (2), where the DC voltage is defined by a range and the electric field is given by:

$$E = V/S \quad (3)$$

Where:

V is the DC voltage range used, and
S is the gap distance between the electrodes, which is 2.54mm.

The breakdown is calculated for both the analytical expression and the results from Bolsig+ in Figure 2. It can be seen that the results are similar.

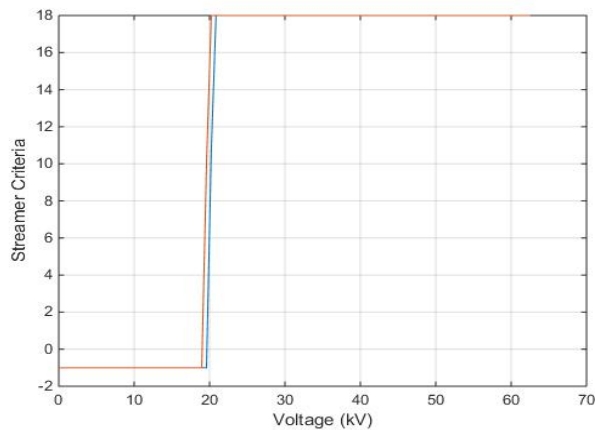


Figure 2: Breakdown voltage for analytical versus Bolsig+

The breakdown voltages for mixtures of gases of 100% N₂, 75% N₂ - 25% SF₆, 50% N₂ - 50% SF₆ and 100%

SF₆ are illustrated in Figures 3-5 at pressures of 1,2 and 3 bar respectively. Table 1 summarises the results.

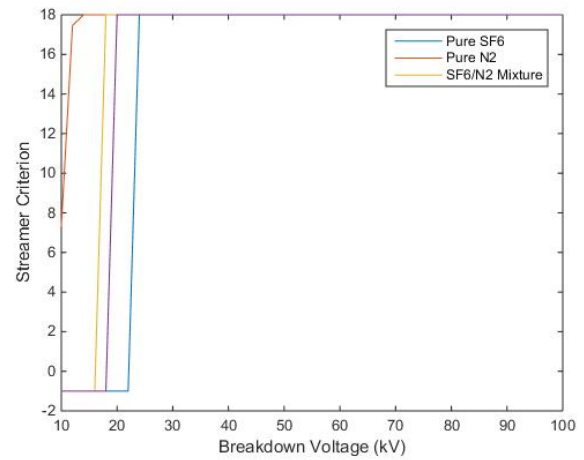


Figure 3: Breakdown voltages for 1 bar

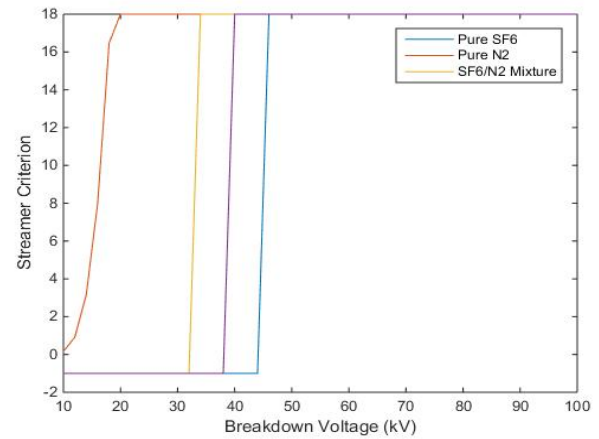


Figure 4: Breakdown voltages for 2 bar

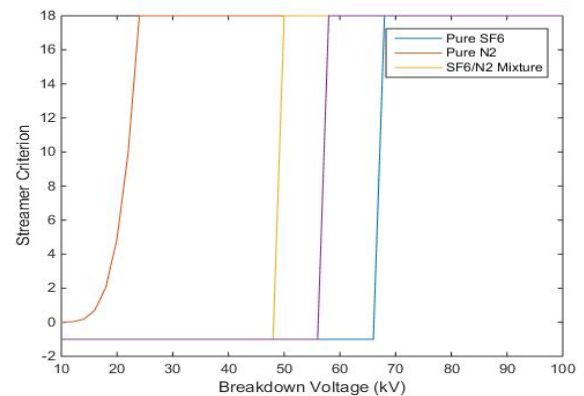


Figure 5: Breakdown voltages for 3 bar

Table 1: Breakdown voltages for different gas mixtures

SF ₆ /N ₂	1 bar	2 bar	3 bar
0 %	14kV	20kV	24kV
25 %	18kV	34kV	50kV
50 %	20kV	40kV	57kV

100 %	24kV	46kV	68kV
-------	------	------	------

From each graph it can be noted that the breakdown voltage of pure nitrogen is significantly lower than that of pure sulphur hexafluoride, and with merely 25% of SF₆ in the mixture, the breakdown voltage increases drastically in comparison to pure nitrogen. The difference between breakdown voltages for pure nitrogen compared to the 25% SF₆ mixture, is higher with an increase in pressure.

3. EXPERIMENTAL PROCEDURE

The purpose of the experiment is to measure the impulse breakdown voltages of different gas mixtures at different gas pressures. This was conducted using the ASTM D2477 [5], for the preparation of the gas and the construction of the gas vessel, whereas, the Up-Down Method [6] was used for recording and calculating the breakdown voltage.

1.1 Experimental procedure

The circuit set up is shown in Figure 6 with the following apparatus:

- Transformer- a step-up transformer rated 220V:64 kV was used.
- Circuit-interrupting equipment- a circuit breaker with the rating of 15A was used to protect both the transformer and the voltage control equipment.
- Voltage-control equipment- a variac was used as a means of voltage control rated at 15kVA.
- Voltmeter- connected to the secondary side of the transformer.
- Diode- to charge the capacitor and change the polarity of the lightning impulse
- Water resistor- used to limit the charging current

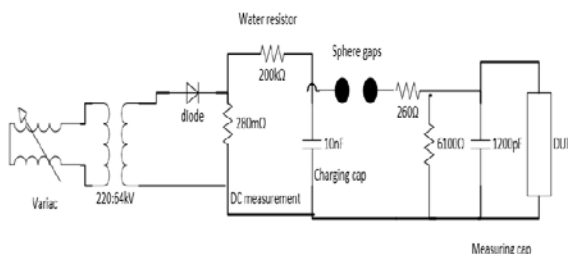


Figure 6: Testing arrangement

The high voltage side of the transformer is connected to the voltage impulse generator (1.2/50μS) [7] which has front time and tail time resistors, along with a charging and measuring capacitor. The sphere gaps produce the impulse and the breakdown voltage is measured by means of a scope. The block labelled DUT contains the

gas vessel built which houses the sphere and plane electrodes, as well as the gas.

1.2 Gas vessel and preparation of the gas

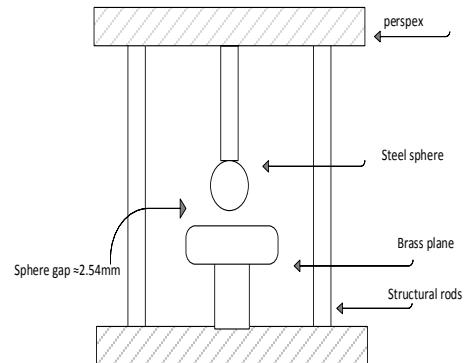


Figure 7: Design of the gas vessel containing the electrodes

The sphere-plane electrode set-up at a gap distance of 2.54 mm is used to create a quasi-uniform electric field. The gas mixtures are obtained by mixing the gases at different partial pressures, using Dalton's law of partial pressures is used to prepare gas mixtures for the tests, and in order to enhance the accuracy of mixing ratio, the test chamber should be inflated with SF₆ gas which has low content first, then inflated with N₂ gas.

The mixtures should be left to stand for a minimum of 2 hours (12-24 hours more effective) before breakdown measurement is done in order to obtain a uniform gas mixture [8]. The gas vessel needs to be purged before the mixtures can be prepared, using the following method from the standard ASTM D2477 [4].

Fill the cell as follows:

- Evacuate the cell to a pressure of less than 0.1 bar.
- Fill the cell with the gas to be tested to atmospheric pressure or slightly above.
- Again evacuate the cell to a pressure of less than 0.1 bar.
- Fill the cell with the gas to be tested to either the calculated pressure.

Before filling the chamber with a gas or a gas mixture, it was first evacuated by a rotary vacuum pump, the partial pressures as well as the total pressure were measured using two mechanical gauges [9]. Gas pressures of 1 bar-3 bar are used in this experiment.

1.3 Up-down Method and calculations

- For the impulse voltage generator, the spark gaps were adjusted such that, if breakdown occurs, the gap distance decreases, however if the mixture withheld the input voltage, the gap distance should be increased. This was done for 20 shots to obtain an impulse breakdown voltage range, using an oscilloscope to identify if breakdown has occurred and its voltage range.
- For the Marx generator set up, by means of an impulse voltmeter and multimeter, the voltage was set and the gaps between the generator were closed via a switch, if breakdown occurred the input voltage (DC) is to be decreased, and if it withstood, then the voltage level was increased. The voltage was increased or decreased in steps of 1/2kV. This worked in the same manner as the spark gap distance changing, for 20 shots. The time interval between adjacent two tests were a minimum of 1 minute in order to recover the dielectric strength of gas [8].
- The calibration factor for the impulse voltage divider and the Marx generator was 559 and 856 respectively, using the capacitor divider ratio

4. RESULTS

The experimental recordings were used in the following way. Here an average of the voltage ranges are used, this average is multiplied by the calibration factor to obtain the U50 result for each gas mixture at different partial pressures [6], [7], [8].

Table 2: Breakdown voltages for different gas mixtures

SF6%	U50 (kV) Negative			U50 (kV) Positive		
	1 Bar	2 Bar	3 Bar	1 Bar	2 Bar	3 Bar
0	19,12	21,10	25,13	19,19	22,14	25,58
12.5	23,89	39,35	42,57	19,03	26,95	31,89
25	32,51	43,93	45,56	22,17	28,10	29,79
50	28,87	33,40	41,39	24,39	33,21	41,88
100	40,38	40,68	47,77	28,39	37,25	46,61

These results were plotted in order to understand the trends for negative lightning impulse breakdown voltages and positive lightning impulse breakdown voltages. The waveforms were as follows:

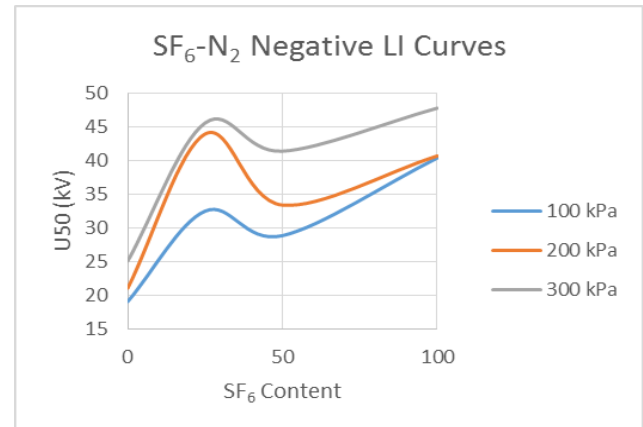


Figure 8: Breakdown voltages at different partial pressures of SF6 for a negative lightning impulse

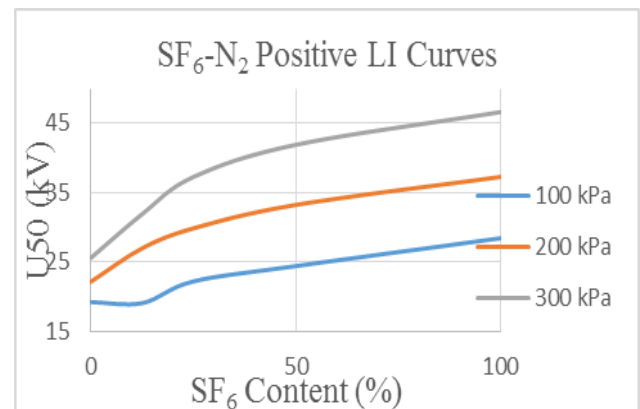


Figure 9: Breakdown voltages for different mixtures of SF6 for a positive lightning impulse

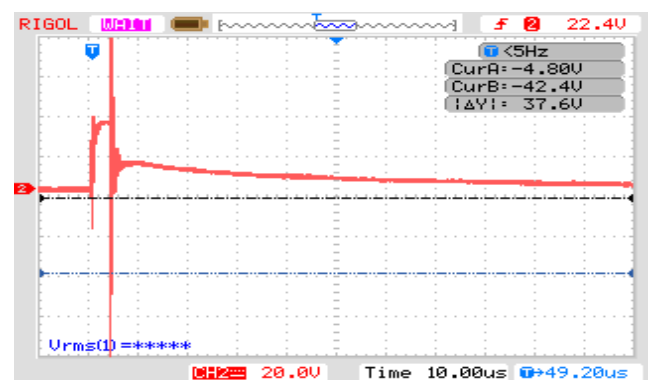
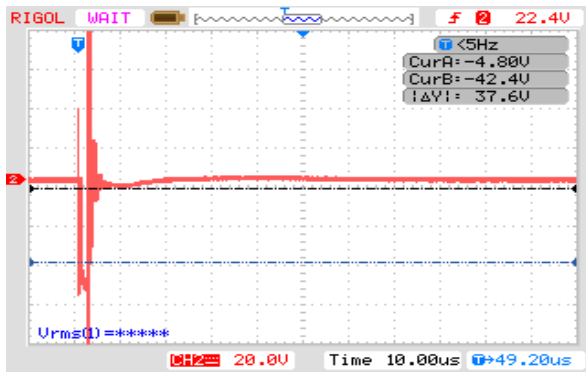


Figure 10: Breakdown curve for 12.5% SF6

Figure 11: Breakdown voltage curve for pure SF₆

5. DISCUSSION

From Figure 10 and Figure 11, the breakdown voltages for positive lightning impulse and negative lightning impulse the breakdown voltages are shown respectively. Table 3 shows that the positive lightning impulse has a resultant breakdown voltage that is higher than that of the negative lightning impulse for nitrogen. From the experiment it can be seen that for 12.5% sulphur hexafluoride in the gas mixture and higher, the negative lightning impulse results are greater than the positive lightning impulse results. The breakdown voltage for each gas mixture increases with the increase in gas pressure, for both positive and negative lightning impulses. From Table 2 it can be noted that the breakdown voltage for 12.5% of sulphur hexafluoride is significantly higher than that of pure nitrogen. For figure 10, it can be seen that the breakdown for 12.5% of SF₆ in the mixture, upon breakdown, the oscilloscope graph forms a standard lightning curve, which is usually shows that the mixture has withstood breakdown at that voltage level, as compare to pure sulphur hexafluoride in Figure 11, which merely breakdown. This could be the result of SF₆ recombining at 12.5% of SF₆, which can be due to arc-quenching, which is interesting as this does not happen for pure sulphur hexafluoride. This needs to be investigated further.

6. CONCLUSION

From the graphs and results it can be seen that there is a significant increase in breakdown voltage with the introduction of sulphur hexafluoride to the mixture, this coincides with the DC results given in Table 1. The impulse breakdown voltages increase with higher gas pressures, where 50 % SF₆:50% N₂ at 3 bar, has a higher breakdown voltage than pure SF₆ at 1 and 2 bar of pressure. This shows that by increasing the pressure, the breakdown voltage can be similar to pure SF₆. Due to the presence of nitrogen, SF₆ will not liquefy at higher pressures, therefore these gas mixtures can be used in applications that require a high breakdown voltage, without very good arc-quenching properties.

7. REFERENCES

- [1] L. G. Christophorou, J. K. Olthoff and D. S. Green, "Gases for Electrical Insulation and Arc Interruption: Possible Present and Future Alternatives to Pure SF₆," *NIST Technical Note 1425*, pp. 1-26, 1997.
- [2] Y. Kieffel, A. Girodet, F. Biquez, P. Ponchon, J. Owen, M. Costello, M. Bulinski, R. Van San and K. Werner, "SF₆ Alternative Development For High Voltage Switchgears," *CIGRE Technical Brouchure D1-305*, 2014.
- [3] *Electrical discharge in gases*, Johannesburg: University of the Witwatersrand..
- [4] A. Pedersen, "Criteria For Spark Breakdown in Sulphur hexafluoride," *IEEE TRANSACTIONS ON POWER APPARATUS AND) SYSTEMS*, Vols. VOL. PAS-89, no. No.8, pp. 1-4, December 1970.
- [5] *Standard Test Method for Dielectric Breakdown Voltage and Dielectric Strength of Insulating Gases at Commercial Power Frequencies*, ASTM D2477-02, 2007.
- [6] S. Meijer, J. Smit and A. Girodet, "Comparison of the of the Breakdown Strength of N₂, CO₂ and SF₆ using the Extended Up-and-Down Method," *IEEE, Villeurbanne Cedex, France*, 2006.
- [7] E. Kuffel, and J. Berg, *Breakdown Voltage Characteristics of SF₆/CF₄ Mixtures in Uniform*, Winnipeg, Manitoba: University of Manitoba.
- [8] Y. Qiu and E. Kuffel, "DIELECTRIC STRENGTH OF GAS MIXTURES COMPRISING," *IEEE Transactions on Power Apparatus and Systems*, Vols. Vol. PAS-102,, no. No. 5,, pp. 1-6, May 1983.
- [9] A. Singhasathein , A. Pruksanubal , N. Tanthanuch and W. Rungsevijitprapa, "Dielectric Strength of Breakdown Voltage," Thailand, 2013.

MEAN ENERGY, ELECTRON DRIFT AND EFFECTIVE IONISATION COEFFICIENTS IN SF₆-N₂ AND SF₆-CO₂ MIXTURES FROM BOLSIG+

M.D. Brown, A.G. Swanson and L. Jarvis

Dept. of Electrical, Electronic and Computer Engineering, University of KwaZulu Natal, King George V Ave, Durban, 4041, South Africa

Abstract: The electron energy distribution function, electron drift velocity and number density reduced effective ionisation coefficients are calculated for SF₆-N₂ and SF₆-CO₂ mixtures. Bolsig+ is the Boltzmann equation solver used to calculate the swarm parameters in conjunction with the cross-sections from the LXCat database. Results show a significant decrease in the electron energy distribution function, mean energy, electron drift velocity and effective ionisation coefficient of the SF₆ mixtures as the SF₆ content is increased. SF₆-N₂ mixtures appear more attractive for replacement of pure SF₆ than SF₆-CO₂ as it possess a lower mean energy, lower electron drift velocity and lower effective ionisation coefficient. In addition the critical field strength $(E/N)_{lim}$ is higher for the SF₆-N₂ mixtures and the effective ionisation coefficients of the SF₆-N₂ mixtures tend to converge towards that of pure SF₆ at higher E/N values. The critical field strength from Bolsig+ shows good agreement with published results from Christophorou and van Brunt.

Key words: EEDF, mean energy, drift velocity, effective ionisation coefficient

1 INTRODUCTION

Since the 1960s Sulphur Hexafluoride (SF₆) has been widely used in the electrical industry due to its superior electrical, thermal characteristics and physical characteristics [1] [2]. Unfortunately SF₆ is the most potent greenhouse gas known, with a global warming potential (GWP) of almost 24 000. Due to its lifespan of 3200 years the SF₆ released into the atmosphere is cumulative and permanent [2] [3].

As a result considerable effort has been exerted to find a replacement for SF₆. However, to date the problem remains unsolved [4]. Christophorou et al [5] believe that at the moment the most viable alternative is to replace pure SF₆ with a SF₆ mixture that decreases the greenhouse impact. While the initial number of potential SF₆ mixtures appear to be vast, the requirements a gaseous medium must meet (such as low toxicity, no ozone depletion potential (ODP), low GWP, chemical inertness and non-flammability) significantly reduce the number of mixtures to be considered.

Binary mixtures of SF₆-N₂ and SF₆-CO₂ (amongst others) exhibit a synergy effect: where the component gases act together to improve the dielectric performance of the mixture to greater than the sum of the components [6], [7], [8]. In particular SF₆-N₂ is regarded as an ideal alternative to pure SF₆ as its performance is superior to that of SF₆-CO₂ being less sensitive to conductive particles and surface roughness than pure SF₆ [4].

In this paper the Boltzmann equation solver Bolsig+ is used to calculate the mean energy, electron drift velocity and the number density reduced effective ionisation

coefficients for varying SF₆ content of SF₆-N₂ and SF₆-CO₂ mixtures.

2 SET-UP

Given the fundamental collision cross-section data the Boltzmann equation may be used to solve for the electron energy distribution and electron coefficients of a given discharge.

Developed by Hagelaar and Pitchford [9] Bolsig+ is a user friendly Boltzmann equation solver for calculating the EEDF and the electron coefficients to be used by a fluid model. Using the cross-sections from the LXCat database the input parameters for Bolsig+ were:

Gas Temperature (K): 293
Ionisation degree: 1E-05
Electron density (1/m³): 1E+20

Electron-electron collisions were included.

Hagelaar and Pitchford [9] show that the inclusion of the electron-electron collisions results in the EEDF tending towards a Maxwellian distribution function with their influence being greatest for an ionisation degree greater than 10⁻⁶. They also believe that the most important consequence of the electron-electron collision for fluid models is that they increase the rate coefficients of the ionisation and excitation coefficients by repopulating the tail of the EEDF. However, the rate coefficients are only increased at low electron energies due to the cross-section for electron-electron collisions dropping off with increasing electron energy. As a result for discharges where the ionisation degree is low or the mean electron energy is high the influence of the electron-electron collision may be ignored for simplicity sake. Breakdown in gaseous insulation tend to have electrons with high energy so the electron-electron collision may be ignored.

Further information on the operation and behaviour of Bolsig+ can be found in [9].

3 RESULTS AND DISCUSSION

3.1 Effective Ionisation Coefficients of Pure SF₆

The results from the Boltzmann equation solver Bolsig+ for the number density reduced effective ionisation for pure SF₆ are compared to experimental results from Christophorou and van Brunt [10] and experimental results from Qiu and Xiao [11] in Figure 1. It can be observed that the number density reduced effective ionisation coefficient $(\alpha - \eta)/N$ increases with an increasing reduced electric field strength. The results obtained using Bolsig+ are in good agreement with these previously published experimental values.

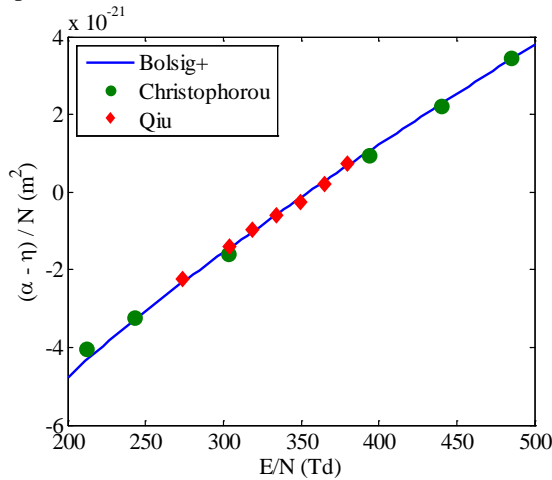


Figure 1: Effective ionisation coefficient as a function of E/N for pure SF₆.

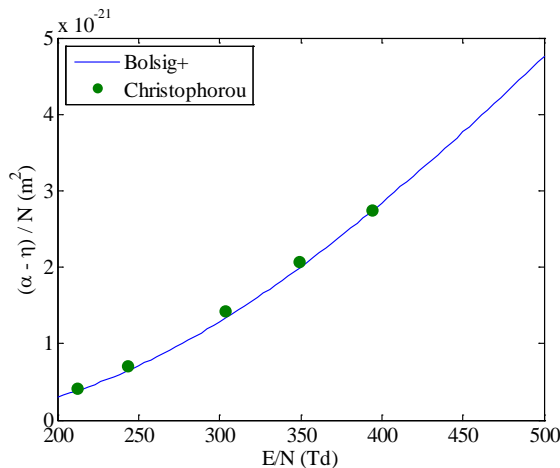


Figure 2: Effective ionisation coefficient as a function of E/N for N₂

3.2 The Electron Energy Distribution Function (EEDF)

Figure 3 shows the mean energy (ϵ) as a function of SF₆ content for SF₆-N₂ and SF₆-CO₂ mixtures for an E/N of 500 Td.

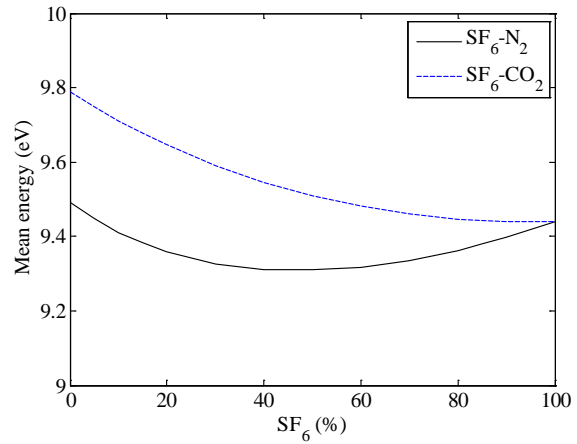


Figure 3: Mean electron energy as a function of SF₆ content for SF₆-N₂ and SF₆-CO₂

The mean energy of the SF₆-N₂ has a trend of decreasing with increasing SF₆ content, however, there appears to be a minimum mean energy occurring at 50% SF₆ content after which an increase in SF₆ results in a slight increase in mean energy. The mean energy of the SF₆-CO₂ mixture decreases with increasing SF₆ content with the lowest mean energy occurring at 100% SF₆ content.

The changes in the mean energy of the mixtures as the SF₆ content increases occurs due to the EEDF altering. It should also be noted that the mean electron energy of the SF₆-N₂ mixture is lower than the mean energy of the SF₆-CO₂ mixture.

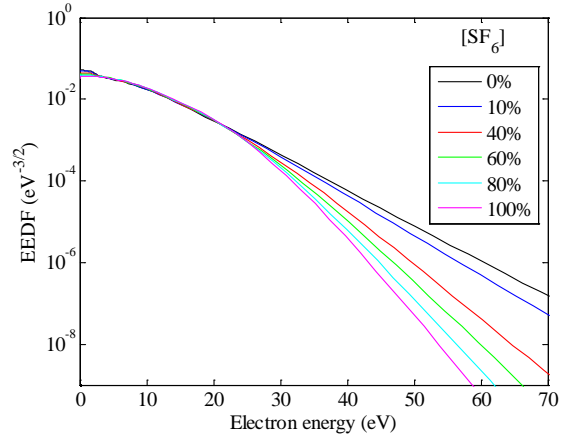
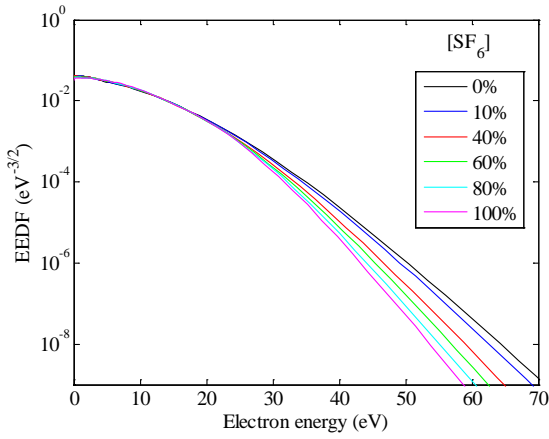


Figure 4: EEDF for SF₆-N₂ at 500 Td

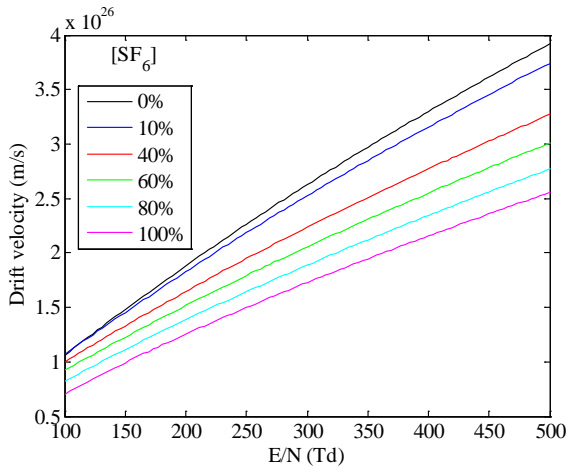
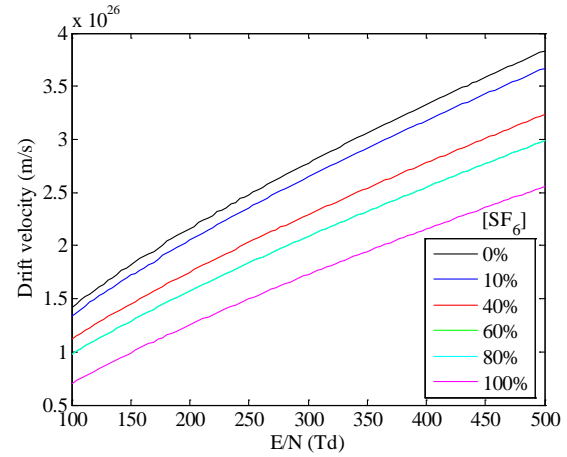
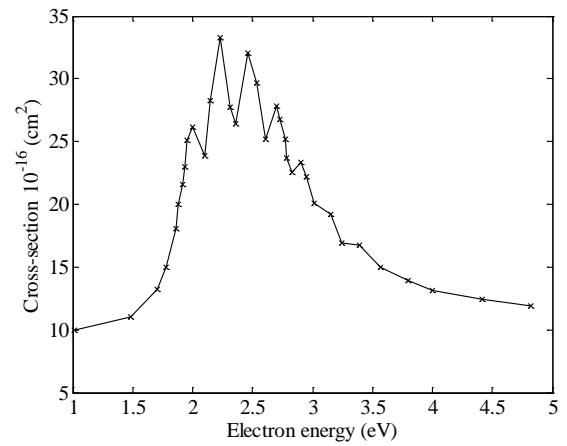
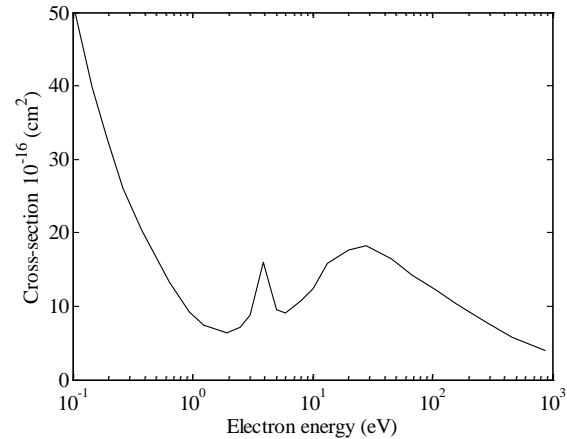
Figure 4 shows the effect of increasing SF₆ content in a SF₆-N₂ mixture has on the EEDF. It can be seen that for the E/N of 500 Td the increase of SF₆ content in the mixture alters the EEDF by shifting it to the left. The increase of SF₆ content also results in the decrease of the EEDF in the vicinity of the origin of energy space $\epsilon = 0$ [12]. This net decrease in the EEDF as the SF₆ content increases results in a net decrease of the mean energy. The minimum mean energy observed in Figure 3 is as a result of what occurs in the EEDF (Figure 4) between 5 eV and 22 eV. Between these two points the EEDF increases as the SF₆ content increases. The point at which the increasing portion of the EEDF balances the decreasing portion of the EEDF is observed as the minimum in Figure 3.


Figure 5: EEDF for SF₆-CO₂ at 500 Td

The addition of SF₆ in the SF₆-CO₂ mixture has the effect of decreasing the EEDF. While the EEDF differs imperceptibly near $\varepsilon = 0$, it shifts to the left as shown in Figure 5. This reduction of the EEDF results in a decreasing mean energy as the SF₆ content increases.

3.3 Drift Velocity

The electron drift velocity as a function of the reduced field for SF₆-N₂ and SF₆-CO₂ mixtures are illustrated in Figure 6 and Figure 7. Both figures show that as the electric field strength increases (E/N) so does the drift velocity. With increasing SF₆ content the drift velocity is lower in the SF₆-N₂ and SF₆-CO₂ mixtures with the reduction of drift velocities becoming more pronounced at higher electric field strengths. It is also of interest that at lower electric field strengths the SF₆-N₂ mixtures tend to exhibit lower drift velocities than the SF₆-CO₂ mixture while the opposite is true at higher electric fields. This difference may be attributed to the electron energies at which the electron scattering cross-sections for the two additive gases peak. The total electron scattering cross-sections for N₂ and CO₂ are shown in Figure 8 and Figure 9. The electron scattering cross-section for N₂ peaks between 2 eV and 3 eV while for CO₂ the electron scattering cross-section has peaks below 0.1 eV, at 4 eV and at 40 eV. The numerous peaks of N₂ at low energies efficiently slow down the electrons at low electric fields while the peaks of the CO₂ at higher energies enable the reduction of electron speed at higher electric fields.


Figure 6: Drift velocity in SF₆-N₂ mixtures

Figure 7: Drift Velocity in SF₆-CO₂ mixtures

Figure 8: Total electron scattering cross-section of N₂ [13]

Figure 9: Total electron scattering cross-section for CO₂ [14]

3.4 Effective Ionisation Coefficients

The number density reduced effective ionisation coefficients $(\alpha-\eta)/N$ are calculated for 0%, 10%, 40%, 60%, 80% and 100% content of SF₆ in SF₆-N₂ and SF₆-CO₂ mixtures. The results, as a function of the reduced field strength, are displayed in Figure 10 and Figure 11. Both figures illustrate that the effective ionisation coefficient increases with increasing electric field strength. The increase of the reduced electric field strength favours

ionisation as the ionisation cross-section is greatest while the attachment cross-section is lowest at high electric field strengths. It can also be observed that for a given electric field strength the effective ionisation coefficient decreases as the SF₆ content increases for both the SF₆-N₂ and SF₆-CO₂ mixtures. This reduction in the effective ionisation coefficient is due to the increasing electronegativity of the mixtures. In addition the increase of the SF₆ content in the SF₆-N₂ and SF₆-CO₂ mixtures causes the EEDF to shift to the left, as shown in Figure 4 and Figure 5, resulting in a reduction of the mean electron energy. Due to the electron attachment cross-section being greatest at low energies this reduction in the EEDF results in a lower effective ionisation coefficient.

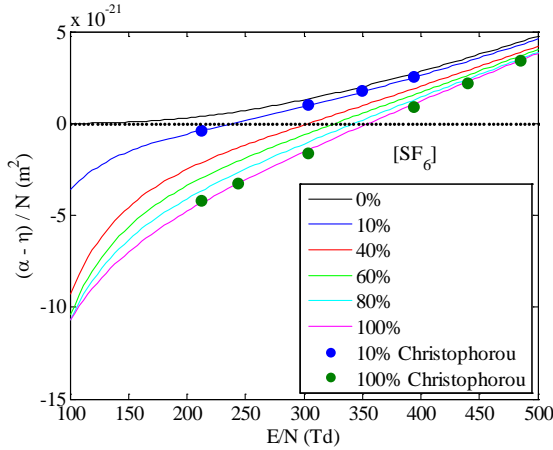


Figure 10: Effective ionisation coefficient in SF₆-N₂ mixtures

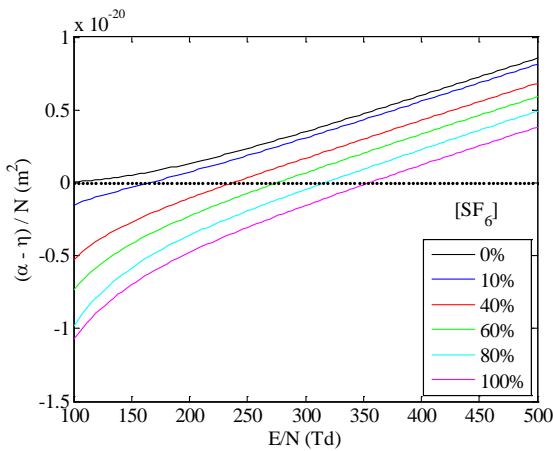


Figure 11: Effective ionisation coefficient for SF₆-CO₂

Comparison of Figure 10 and Figure 11 show a marked difference in the SF₆-N₂/CO₂ mixture behaviour at high E/N values. Past the critical electric strength value, (E/N)_{lim}, the effective ionisation coefficients for the SF₆-N₂ mixtures converge while for the SF₆-CO₂ mixtures do not converge. The cause of the convergence may be as a result of the energies at which the scattering occurs in N₂ and CO₂. Due to the scattering in N₂ peaking at low energies as the electric field increases there are less electrons in its scattering range resulting in a diminished effect of the scattering and a convergence of the effective ionisation coefficient to that of pure SF₆. CO₂ on the other hand has a strong scattering cross-section at higher electron energies so in order for convergence of the

effective ionisation coefficients to be observed would require a higher electric field.

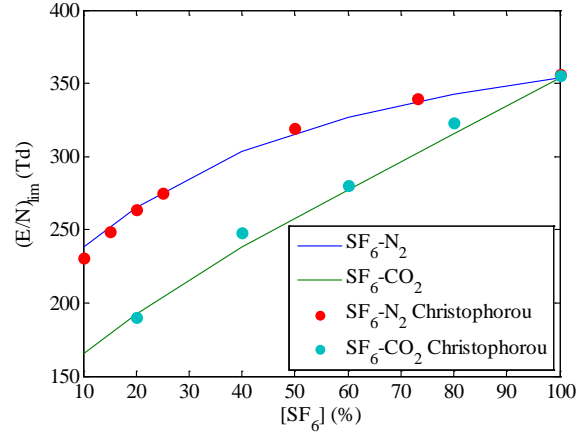


Figure 12: Critical field strength for SF₆-N₂ and SF₆-CO₂

The critical electrical field strength (E/N)_{lim} for the SF₆-N₂ and SF₆-CO₂ mixtures compared with results from Christophorou and van Brunt [10] are plotted in Figure 12 as a function of the SF₆ content. It can be seen that the critical field strengths obtained from Bolsig+ are in good agreement with the experimental data.

4 CONCLUSION

In this paper the number density reduced effective ionisation coefficients, EEDF, mean energy and the electron drift velocity for SF₆-N₂ and SF₆-CO₂ mixtures are calculated using the Boltzmann equation solver Bolsig+ over the number density reduced electric field 100 Td to 500 Td. Comparison of electron coefficients obtained from Bolsig+ and experimental results show good agreement further validating the use of Bolsig+ for solving electron coefficients for fluid models.

Comparison of the SF₆-N₂ and SF₆-CO₂ mixtures confirm from a physics point of view that the replacement of pure SF₆ by a SF₆-N₂ mixture is more viable than replacement by a SF₆-CO₂ mixture within the electric field range of most relevance.

As the SF₆ content in the gas mixtures increase the EEDFs tend to decrease by shifting to the left resulting in a reduction of the mean energy of the mixtures. The mean energy of the SF₆-N₂ mixtures is lower than that of the SF₆-CO₂ mixture.

The drift velocity increases with increasing electric field and reduces with increasing SF₆ content. At a fixed E/N SF₆-N₂ mixtures tend to possess a lower drift velocity than the SF₆-CO₂ mixtures.

The effective ionisation coefficients decrease with increasing SF₆ content and increase with increasing electric field strength. A comparison of the critical electric field strengths of SF₆-N₂ and SF₆-CO₂ show that (E/N)_{lim} is much higher for the SF₆-N₂ mixture than for the SF₆-CO₂ mixture.

5 REFERENCES

- [1] T. Govender, "Identifying Defects in SF₆/N₂ Mixtures using External UHF Couplers and Neural Network Analysis," University of the Witwatersrand, Johannesburg, 2011.
- [2] D. Jeong, S. Woo, K. Seo and J. Kim, "A Study of the Insulation Property for Development of Eco-friendly GIS Under SF₆/N₂ Mixtures," in *1st International Conference on Electric Power Equipment*, Xi'an, 2011.
- [3] M. Koch, "Prediction of Breakdown Voltages in Novel Gases for High Voltage Insulation," 2015.
- [4] W. Sun, Y. Li, D. Zheng, R. Guo and X. H. Du, "Insulation Characteristics of SF₆/N₂ Gas Mixtures and Applied Researches," in *IEEE Annual Report Conference on Electrical Insulation and Dielectric Phenomena*, 2013.
- [5] L. Christophorou, J. Olthoff and D. S. Green, "Gases for Electrical Insulation and Arc Interruption: Possible Present and Future Alternatives to Pure SF₆," U.S Department of Commerce, Washington , 1997.
- [6] M. Zhou and J. Reynders, "Synergy between SF₆ and Other Gases to Enhance Dielectric Strength," University of Witwatersrand, Johannesburg.
- [7] M. Zhou and J. Reynders, "AC and Negative Lightning Impulse Voltage Breakdown Characteristics of Gas Mixtures in a Coaxial Cylinder Gap," University of the Witwatersrand, Johannesburg.
- [8] Y. Qiu and Y. Feng, "Investigation of SF₆-N₂, SF₆-CO₂ and SF₆-Air Substitutes for SF₆ Insulation," in *IEEE International Symposium on Electrical Insulation*, Montreal, 1996.
- [9] G. Hagelaar and L. Pitchford, "Solving the Boltzmann Equation to Obtain Electron Transport Coefficients and Rate Coefficients for Fluid Models," IOP Publishing, 2005.
- [10] L. Christophorou and R. Van Brunt, "SF₆/N₂ Mixtures," *IEEE Transactions on Dielectrics and Electrical Insulation*, vol. 2, no. 5, pp. 952-1003, 1995.
- [11] Y. Qiu and D. Xiao, "Ionisation and Attachment Coefficients Measured in SF₆/Ar and SF₆/Kr Gas Mixtures," *Journal of Physics D: Applied Physics*, vol. 27, pp. 2663-2665, 1994.
- [12] L. Wei, D. Yuan, Y. Zhang and Z. Tan, "Electron Drift, Diffusion and Effective Ionisation Coefficients in SF₆-CHF₃ and SF₆-CF₄ Mixtures from Boltzmann Analysis".
- [13] Y. Itikawa, "Cross Sections for Electron Collisions with Nitrogen Molecules," *Journal of Physics and Chemistry*, vol. 35, no. 1, pp. 32-53, 2006.
- [14] Y. Itikawa, "Cross Sections for Electron Collisions With Carbon Dioxide," *Journal of Physics and Chemistry*, vol. 31, no. 3, pp. 749-767, 2002.

LIGHTNING OVERVOLTAGE PROTECTION AND NETWORK PERFORMANCE OF DISTRIBUTION TRANSFORMERS- CASE STUDY: SWAZILAND ELECTRICITY COMPANY

M.T. Maziya* and K.O. Awodele**

* Swaziland Electricity Company, Mhlambanyatsi Rd, Swaziland

E-mail: Mphumuzi.maziya@sec.co.sz

** University of Cape Town, Faculty of Engineering and the Built Environment, Department of Electrical Engineering

E-mail: kehinde.awodele@uct.ac.za

Abstract: This paper investigates how improving lightning protection for pole mounted transformers improves the reliability of the distribution network in the Swaziland Electricity Company network.

A Pole mounted distribution transformer, just like any other component of the distribution network, is prone to failure and it takes the longest time to install compared to the other components. Its reliability therefore has a significant impact on the system and customer indices. When exposed to stressful conditions electrically, mechanically or chemically, the withstand capability of a pole mounted distribution transformer is reduced. It was discovered that Swaziland falls within a high lightning intensity area with high ground flash densities per square kilometre per year, and for this reason, effective lightning protection of the distribution network is critical. Lightning overvoltages were found to be the major contributor to total failure of the pole mount distribution transformers in the Swaziland Electricity Company's distribution network. The lightning protection is improved through the separating of the secondary and primary earths and the installation of LV neutral surge arrestors at KaPhunga, feeder 5030 in Swaziland. The performance of the network after these improvements is determined through the use of failure modes and effects analysis to calculate the network reliability indices.

Keywords: pole mounted distribution transformer, surge arrestors, lightning impulses, point of failure, reliability

1. INTRODUCTION

Over the years, transformers, especially pole mounted have been damaged by lightning related incidents and a number of lightning protection methods have been developed, and improvements are made where necessary. A major milestone in the reduction of lightning related transformer failures was the bringing of primary surge arrestors closer to the protected unit [1]. Diverted primary surges and secondary direct strikes have necessitated the installation of LV surge arrestors [1, 2, 3]. For improved performance of lightning protection, [3] advocated for the minimisation of the primary surge arrestor leads, and the practical implementation of this yielded positive results. [4] has noted that a majority of faults in the Swaziland Electricity Company's network are found in the distribution network, hence a lot of outages. One of the reasons pointed out was that there are a lot of radial feeders in Swaziland, so a single event results in outages of a lot of load points [5]. Whilst the distribution network has a lot of components contributing to the overall reliability of the distribution network, transformers are the mostly affected during lightning strikes, and they have a high unit cost. Improved lightning protection and maintenance can prolong the useful life of a transformer [6], and contribute positively to the performance of the distribution network. The absence of LV surge arrestors on the Swaziland Electricity Company's network was found to be the major contributor to pole mount transformer failures [4]. This paper therefore looks at the

effectiveness of installing LV surge arrestors on part of a feeder (KaPhunga – feeder 5030) as part of lightning protection for improved network performance.

The structure of the paper is as follows: section 1 is the introduction, section 2 gives the background information, section 3 is the methodology, section 4 is results and analysis, whilst section 5 is the conclusion.

2. BACKGROUND

2.1 Lightning History and transformer failures

Swaziland is a severe lightning area [7] with lightning flash ground density of more than 9 per square kilometre per year [8]. Shown below is an isokeraunic map of Southern Africa,

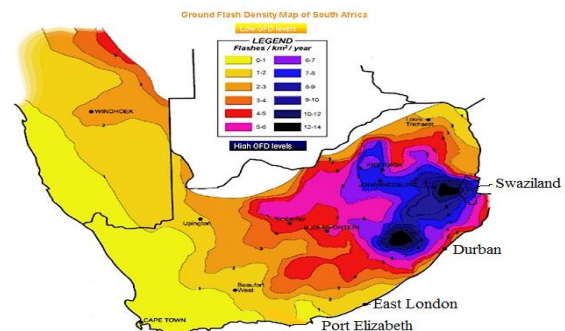


Figure 1: Isokeraunic Map of Southern Africa [9]

When the isokeraunic map for the world is considered, Swaziland together with parts of KwaZulu Natal receives the highest amount of lightning in the world [9].

The effects of lightning are more prevalent on the distribution network, compared to the transmission network. The distribution network consists of the 11 kV network and the 400 V network. Outages on the network after a storm in 2015 are shown in Figure 2 below,

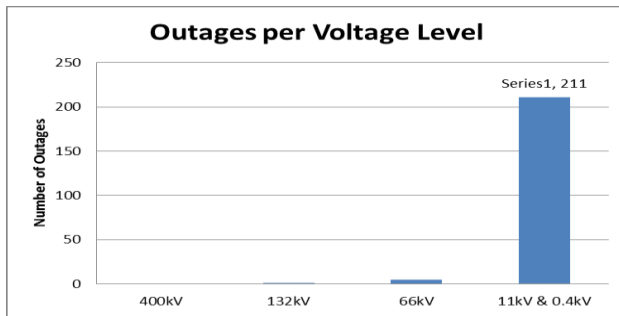


Figure 2: Outages after storm on 11 August 2015

The pole mount transformers have the highest failure rates in the distribution network compared to any other component, and the failures were discovered to be high during the summer months where there was a lot of rainfall, hence lightning as shown in Figure 3 below,

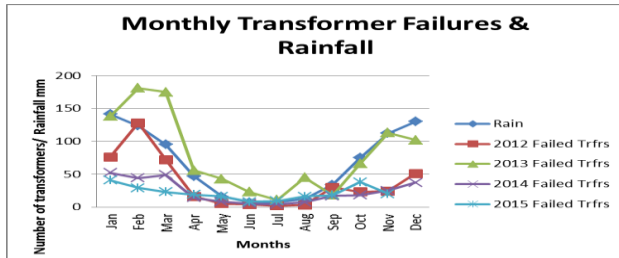


Figure 3: Relationship between rainfall (through thundershowers) and failed transformers

Lightning can damage a transformer through direct strikes on the primary or secondary of the transformer [2] and damage the windings or bushings. Surges may also be diverted from the primary of the transformer to the secondary. Lightning overvoltages are the major contributor to transformer failures as shown in Figure 4 below,

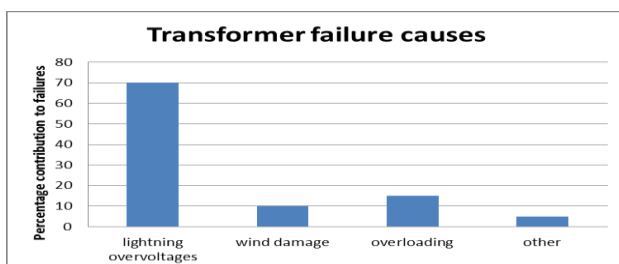


Figure 4: Lightning is major contributor to transformer failures

A. KaPhunga Feeder 5030

KaPhunga area is a mountainous area between the Highveld and the Lowveld of Swaziland. It loses a lot of pole mount transformers whenever there is a thunderstorm. In May 2015, KaPhunga had 91 pole mount transformers that were installed and between January 2015 and May 2015, 13 of the 91 transformers had been lost through lightning overvoltages and were replaced afterwards.

2.2 Reliability Evaluation of KaPhunga

The LV neutral surge arrestors will therefore be installed on this network as a pilot. The failure mode effects and analysis will then be used to calculate the network indices to see the extent in improvement in the reliability indices by improving the reliability of the pole mount transformer. The indices that will be calculated are system average interruption frequency index (SAIFI), customer average interruption frequency index (SAIDI), and system average interruption duration index (CAIDI). The indices are calculated as follows,

$$SAIFI = \frac{\sum \lambda_i N_i}{\sum N_i} \quad (1)$$

$$SAIDI = \frac{\sum U_i N_i}{\sum N_i} \quad (2)$$

$$CAIDI = \frac{\sum U_i N_i}{\sum N_i \lambda_i} \quad (3)$$

Where λ_i is the failure rate, N_i is the number of customers at load point i and U_i is the annual outage time [6]. The indices will be calculated for the network before LV surge arrestor installation and after surge arrestor installation.

3. METHODOLOGY

3.1 Surge Arrestor installation

As previously mentioned, lightning strikes can be on the primary or secondary side of the transformer. If the secondary neutral is earthed on the transformer tank as the surge arrestors, then diverted surges from the primary are likely to occur.

To prevent diverted surges, earth the neutral of the transformer at a different point from the surge arrestors. To prevent failure of the LV neutral bushing, install a surge arrestor at the separate earth point.

In trying to improve lightning protection on KaPhunga feeder 5030, hence the performance of this network, the following will be done:

1. Separate secondary earth from primary earth.

2. Install secondary surge arrestors on the neutral away from the transformer tank.

A practical test system to separate the primary and secondary earths as well as install the LV surge arrestor was designed for practical installation.

Below is the practical implementation of the system,

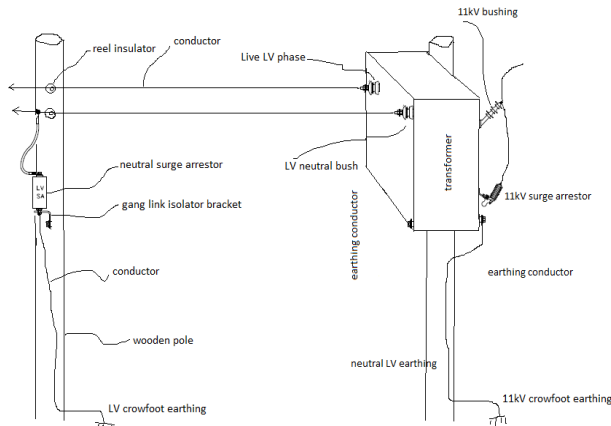


Figure 5: Separate earths and a surge arrestor

Material needed: surge arrestors, scrap gopher conductor, earth spikes, earth clamps, scrap gang link brackets and bolts, conductive cement

Method:

- Step 1: Bolt bracket into pole below the neutral conductor. This bracket is where the surge arrestor will be suspended.
- Step 2: Mount surge arrestor and connect gopher earth lead to crowfoot earth. Connect other end to the neutral conductor.
- Step 3: Use crowfoot method of earthing and join earth lead to the crowfoot. Earth resistance values at structures where the LV surge arrestors were installed are shown below,

3.2 Reliability Evaluation

With the secondary surge arrestor installed, the pole mount transformer is protected from overvoltages either on the primary or secondary. The indices for the network of KaPhunga shown below are calculated,

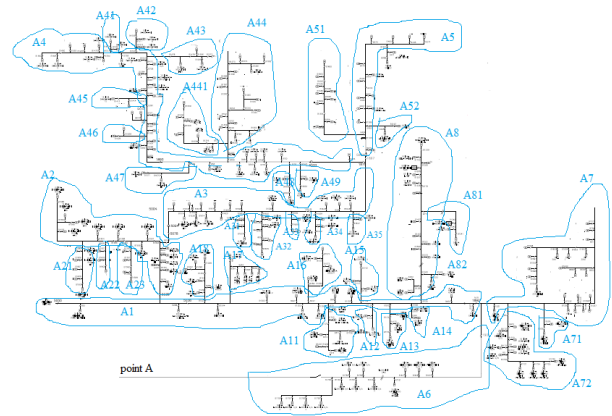
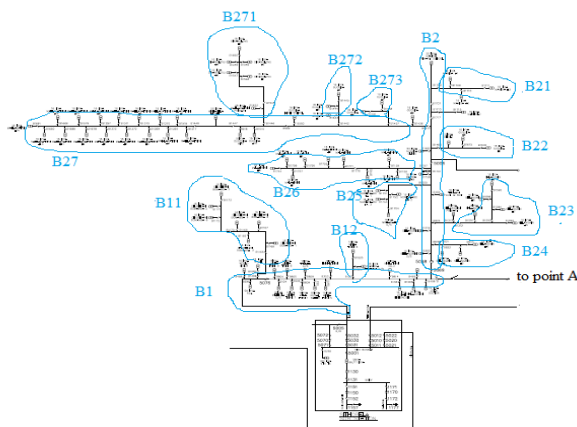


Figure 6: KaPhunga network single line diagram

In the calculation of indices, the following facts and assumptions are taken into account.

1. Switching time is 2 hours. This allows for travel, taking into account the terrain of the place as well as the time for switching.
2. Repair time for the 11 kV main line and the branches is assumed to be 5 hours.
3. Replacement time for transformers, isolators and reclosers is 7 hours under normal conditions. Components are replaced and faulty ones are repaired and kept as spares.
4. Assume mink conductor on the main line and gopher conductor for branches. Take all branches to be 50m with fuse drop outs for overcurrent protection.
5. The main 11kV line has some air break switches (gang links) along its length for switching purposes. Throughout its length, the line is divided into sections A1 – A8, B1 – B2. These section have subsections, for instance subsections linked to section A1 are A11, A12 and so on, whilst those linked to B1 are B11, B12, B13 and so on.
6. The probability of failures, as stated in [6] will be used and are as follows;
 - a. 11/0.4 kV transformers: 0.015 per year. From gathered statistics over a period of 3 years, the failure rate per year for 3 years is 0.015, 0.029 and 0.058, so if we take an average of the three, we get 0.037. Although more data is required to come up with the failure rate for our network transformers, 0.037 will be used for transformers as a failure rate for transformers per year before surge arrestor installation.
 - b. Mink conductor: 0.065 per km
 - c. Reclosers and isolators 0.006 per year
7. There are no alternate feeds for the network.

8. The high fuse rating for transformer laterals makes the laterals behave as if there are no fuses, hence transformer faults also affect line sections to which they are connected. When correct fuses are used, transformer faults only affect that load point to which it is connected.

Having practically installed LV neutral surge arrestors, and calculated the reliability indices, the results are analysed below.

4. RESULTS AND ANALYSIS

A. Installation of neutral surge arrestors at KaPhunga

Separating the primary and secondary earths was effective in eliminating diverted primary surges [2] to the secondary of the transformer. There was then an observed pattern of failure of the transformers with such an arrangement, and this was the failure of the LV neutral bushing. This is because when there is a primary strike, the primary surge arrestor discharges into ground, and the transformer tank potential rises as a function of the surge current and the footing resistance in the process. Footing resistances of the transformers where surge arrestors on LV were installed are shown in Figure 7 below.

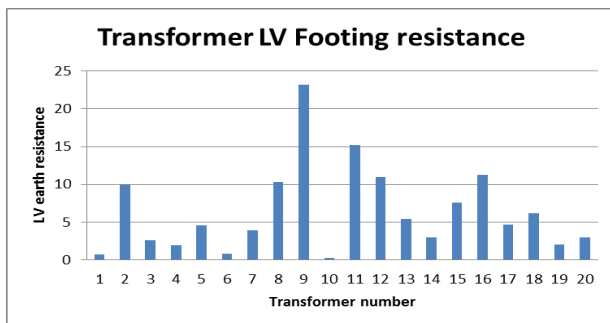


Figure 7: Footing resistances at transformer structures

The mean earth value was 6.3Ω with a standard deviation of 5.6. According to the SEC's standards, a value of 10Ω or less is desired for footing resistances.

Because the neutral bushing is earthed at a different point from the primary, a flashover results due to the large difference in potentials (tank and tip of LV neutral bushing) as seen by the LV neutral bushing [10]. The neutral bushing is stressed to the point of failure as a result of this overvoltage [10].

The LV neutral surge arrestors that were installed on 20 transformers at KaPhunga in May 2015 to reduce the large potential difference as seen by the neutral bushing during primary strikes as explained above, was effective. It is difficult to quantify the improvement in terms of outages on the feeder as the LV surge arrestors were not installed on all the transformers at KaPhunga. The figure

below is used in voltage calculation across the LV neutral bushing after surge arrestor installation,

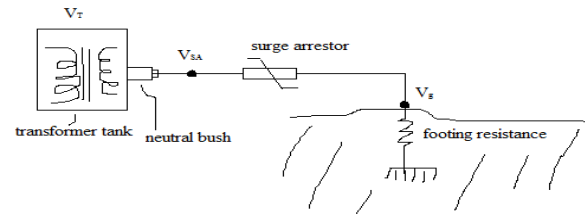


Figure 8: Effect of neutral surge arrestor when tank voltage rises during a primary strike

The voltage as seen by the neutral surge arrestor is,

$$V_{bush} = V_t - (V_{sa} + V_g) \quad (1)$$

Where V_t is tank voltage, V_{sa} is voltage across surge arrestor and V_g is voltage across footing resistance.

Between May and November 2015, there were 14 thunderstorms at KaPhunga area where the LV neutral surge arrestors were installed, and there were no transformers that had surge arrestors that were damaged. Only transformers without neutral surge arrestors were damaged. The neutral surge arrestors on the LV are therefore effective in reducing failure of the neutral bushing, hence the pole mount distribution transformer. Table 2 below shows the results after implementation of the surge arrestors,

Table 2: Transformer failures before and after LV surge arrestor installation

	(Jan – May) 2015	(May – Nov) 2015
No. of thunderstorms	17	14
No. of failed transformer without surge arrestor	13	11
No. of failed transformer with surge arrestor	Surge arrestors not yet installed	0

The total number of failed transformer between January and November 2015 at KaPhunga area was 24. Out of the 24 transformers, 17 had the LV neutral bushing damaged. Out of the 17 that had a damaged neutral bushing, three had no protection on the primary due to damaged primary surge arrestors. The remainder of the transformers that were damaged failed because of overload.

B. KaPhunga Network Reliability

The obtained failure modes and effects analysis results for KaPhunga area are shown in Table 3 below.

Table 3: Improvement in indices after installing LV neutral surge arrestor

	$\lambda=0.037$	$\lambda=0.015$	%
	Before surge arrestor installation	After surge arrestor installation	
SAIFI	9.13000	3.58668	60
SAIDI	24.54839	13.4277	45
CAIDI	2.68876	3.74377	39

The reliability indices improve when surge arrestors are installed on the network at KaPhunga. The system performance improves significantly especially through the reduction of system interruptions and system outages. There is however, a slight increase in customer outage durations.

5. CONCLUSION

A field transformer is exposed to a number of stressors, like overloading, overcurrent, harmonics, inrushes, over-excitation, to mention but a few, during its useful life which reduce its withstand capabilities [11]. In the Swaziland Electricity Company's distribution network, total failure of field transformers was found largely to be brought about by lightning overvoltages during the summer months, after the transformer had been exposed over time to stressors. The failures are not localised, rather are a function of the amount of rainfall, hence thundershowers received.

The reliability indices improve when the failure rate of transformers also improves through the installation of LV neutral surge arrestors. There was an improvement in both system and customer indices, which can be translated to commercial gains. The percentage change in system indices is large compared to customer indices. For instance the system interruption indices and system outage durations reduce by approximately half.

Based on the collected field data, and FMEA results, the following are recommended to ensure a further improvement on transformer reliability and lightning protection,

- Earth the LV neutral at a separate point from the transformer tank, and install a surge arrestor at the earthing point. This exercise should be rolled out throughout the entire Swaziland Electricity Company's distribution network.
- Revise the 11kV surge arrestor specification, so that the lightning impulse residual voltage under nominal discharge current is changed from 40 kVp to any value between 70 kVp and 75 kVp, so that the safety margin is between 20 and 25 % of the BIL as per section 4.7.3.2 of NRS 039-1:2008
- Conduct pole mounted transformer audits to identify overloaded ones and uprate where necessary.
- Use variety of transformer manufactures to avoid single mode of failure.
- Reduce primary fuses from 30A to 5A

6. ACKNOWLEDGEMENTS

The authors gratefully acknowledge the provision of support, data and research infrastructure provided by Eskom Holdings through TESP, Swaziland Electricity Company and the University of Cape Town in carrying out this research.

7. REFERENCES

- [1] M. Darveniza and D. R. Mercer, "Lightning protection of pole mount transformers." *IEEE Transactions on Power Delivery*, Vol. 4, No. 2, pp. 1087-1095, April 1989
- [2] G. L. Goedde, S. S. Kershaw and R. N. Schettler, "Low Voltage, High Energy Arrestor for Secondary Application." *U.S. Patent*, vol. 5, pp. 220-480, June 1993
- [3] R. Billinton and J. Billinton, "Distribution system reliability indices," *IEEE Transactions on Power Delivery*, vol.4, no.1, pp.561,568, Jan 1989
- [4] M. T. Maziya and K Awodele, "Investigation and Analysis of Causes of the Causes of 11/0.4 kV Distribution Transformers' High Failure Rate: Case Study - Swaziland Electricity Company." *South African Universities Power Engineering Conference*, Johannesburg, January 2015
- [5] C. W. Plummer, G. L. Godde, E. L. Pettit, J. S. Godbee and M.G. Hennessey, "Reduction in Distribution Transformer Failure Rates and Nuisance Outages with Improved Lightning Concepts." *IEEE Transactions on Power Delivery*, Vol. 10, No. 2, pp. 768-777, April 1989
- [6] R. Billinton and P. Wang, "Teaching Distribution System Reliability Evaluation Using Monte Carlo Simulation," *IEEE Transactions on Power Systems*, vol.14, no.2, pp.397-403, May 1999
- [7] M. F. Stringfellow and F. R. Met, "Overhead distribution lines and surge arrestors for severe lightning areas," *South African Institute of Electrical Engineers, Lightning performance of overhead lines*, South Africa, 1982
- [8] M. Gijben, The Lightning Climatology of South Africa," *South Africa Journal Of Science*, vol. 108, no. 3, Jan 2012
- [9] "Live Line Technology." <http://www.liveline.co.za/images/gfd-1.jpg>. Accessed 13 March 2015
- [10] J. P. Holtzhauzen., W. L. Vosloo. *High Voltage Engineering Practice and Theory*. Stellenbosch, Cape Town: University of Stellenbosch, 2014, pp. 26-56
- [11] D. Hongzhi, R. Heywood, J. Lapworth and S. Ryder: "Why transformers fail." *Euro TechCon*, Stretton-United Kingdom, 200

A SIMULATION STUDY OF THE INRUSH CURRENT PERFORMAMNCE OF AMORPHOUS CORE AND C.R.G.O. TRANSFORMERS

J. Naidoo*, ** and AG. Swanson**

* Network Optimisation, Eskom, KZN OU, 01 Portland Road, Mkondeni, Pietermaritzburg, 3201, South Africa

** Discipline of Electrical, Electronic and Computer Engineering, University of KwaZulu-Natal, Howard College, Durban, 4041, South Africa

Abstract: The purpose of this document is to provide an analysis of how inrush currents affect amorphous core transformers and cold rolled grain oriented (CRGO) steel core transformers, respectively. Similar single phase, 16 kVA, transformers with core materials of the amorphous and CRGO are simulated using ATP. The results show that the amorphous core transformer has a higher inrush current than the CRGO core transformer due to the lower saturation point.

Key words: Inrush currents, amorphous core transformer, CRGO steel core transformer

1. INTRODUCTION

Amorphous core transformers are known to be energy efficient, has lower CO₂ emissions and a better operational cost than other similarly rated transformers. It has been established that the amorphous core transformer have the potential to reduce transformer core losses by up to 80% than silicon steel transformer under linear loads. The lower losses are due the ease of magnetisation of the material that lower hysteresis loss, and the high resistivity and thin sheets of the material which lower the eddy current losses [1].

There is a significant amount of switching on the MV distribution network which means that transformers may be subject to inrush currents. As radial electromagnetic forces are proportional to the square of the current, the difference between the amorphous and CRGO core transformers need to be understood [1].

The aim of this paper is to compare and analyse the inrush currents for amorphous core transformers and CRGO steel core transformers and draw conclusions thereon. Amorphous core and CRGO steel core are simulated using a circuit model on ATP for inrush currents.

2. INRUSH CURRENTS

Inrush currents occur during energisation of the transformer. According to [2], inrush currents have predominately second harmonics (i.e. a frequency of 100 Hz).

The design peak flux density (B_p) is usually 10–20% below saturation in typical power transformers. At energisation, the core will be driven strongly into saturation, which requires a very high exciting current. This exciting current is called the inrush current and can

be in orders of magnitude more than the normal load current for the transformer [3].

These currents depending on their magnitude could cause damage to the windings and conductor insulation because of associated mechanical stresses.

High inrush currents cause nuisance fuse or breaker interruptions, arcing, as well as failure of primary circuit components such as switches. High magnetizing inrush current in transformers also necessitate over-sizing of fuses or breakers. Another negative effect of high inrush current is the injection of noise and distortion back into the main supply [4].

There are three factors that determine the transformer's inrush current from [2]:

- The residual flux in the transformer core (B_R).
- The point on the voltage wave at which the transformer is energized.
- The magnitude of the ratio of the source impedance to the transformer impedance.

In a distribution system, the source impedance is small compared to the impedance of the transformer.

The transformer can be represented by the magnetic circuit illustrated in Figure 1. Consider the flux in the centre limb, under normal conditions the flux flows through the core.

The reluctance of the core is related to the permeability of the material, the length and the cross-sectional area [3]:

$$R = \frac{l}{\mu A} \quad (1)$$

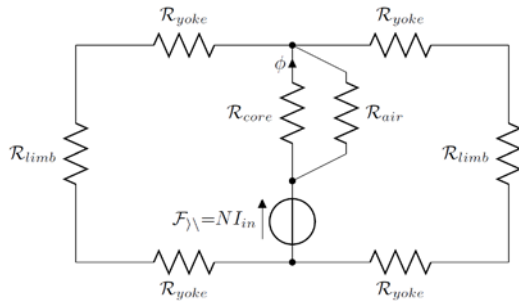


Figure 1: Magnetic circuit.

The equivalent electrical representation of the transformer is shown in Figure 2. Only the primary is considered in this case as this is where the magnetising current is drawn from as the secondary is not drawing any load current. The magnetising inductance is determined by the flux which is high under nominal conditions. It tends towards a low inductance when the core is saturated, which leads to a higher magnetising current drawn by the transformer [2, 4].

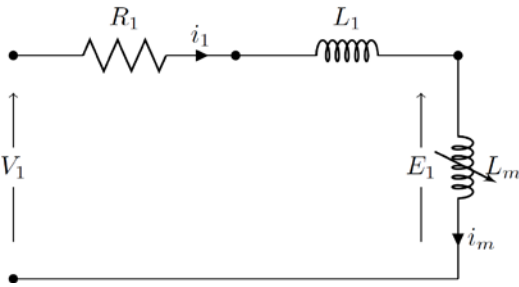


Figure 2: Electrical circuit.

For applied sinusoidal voltage [5]:

$$V_p(\omega t + \theta) = i_0 R_1 + N_1 \frac{d\Phi_m}{dt} \quad (2)$$

Where:

V_p = peak value of applied voltage

θ = angle at which voltage is switched on (degrees)

i_0 = instantaneous value of magnetising current

Φ_m = instantaneous value of flux at any time t

R_1 = primary winding resistance (Ω)

N_1 = primary winding turns

The inrush flux in the core consists of the normal AC component as well as a DC component due to the switching angle and the residual flux in the core [4, 5]:

$$\Phi_m = (\Phi_{mp} \cos \theta \pm \Phi_r) e^{\frac{-R_1 t}{L_1}} - \Phi_{mp} \cos(\omega t + \theta) \quad (3)$$

Where:

Φ_{mp} = instantaneous peak value of flux

Φ_r = residual flux

L_1 = inductance of primary winding (H)

The worst case of over-flux occurs at the zero crossing of the voltage, leading to a doubling of the flux which then drives the core into saturation [5]:

$$\Phi_{air} = \mu_0 H A_w = (2\Phi_{mp} + \Phi_r - B_{sat} A_c) \quad (4)$$

Where:

Φ_{air} = flux in air

μ_0 = permeability of space

μ_r = relative permeability

A_w = mean area enclosed by a winding turn

B_{sat} = saturation flux density

A_c = net core area

2.1 First peak calculation

For a single phase transformer, the maximum first peak inrush current is [5]:

$$H = \frac{N_1 i_{0max}}{h_w} \quad (5)$$

Where:

N_1 = number of turns for the energised winding

i_{0max} = maximum first peak inrush current

h_w = height of the energised winding (m)

Therefore [5]:

$$\begin{aligned} i_{0max} &= \frac{h_w H}{N_1} = \frac{h_w (2\Phi_{mp} + \Phi_r - B_{sat} A_c)}{\mu_0 A_w N_1} \\ &= \frac{h_w A_c (2B_{mp} + B_r - B_{sat})}{\mu_0 A_w N_1} \end{aligned} \quad (6)$$

Where:

B_r = residual flux density

B_{mp} = maximum peak flux density

Inductance of the magnetising branch (L_μ) of the transformer is calculated as follows [2]:

$$L_{\mu} = \frac{N^2 A \mu_0 \mu_r}{l} \quad (7)$$

Where

N = number of turns; constant

A = area of core; constant

l = length of core; constant

$\mu_0 \mu_r$ = permeability of material; depends on B-H curve operating point and from [2]:

$$\mu_0 \mu_r = \frac{B}{H} \quad (8)$$

From equation (8), permeability of material is proportional to the B to H ratio. After saturation, this ratio approaches zero. This explains how saturation impacts inrush currents.

3. SPECIFICATIONS AND PROPERTIES

The aim of this simulation is to determine how the different transformers behave under inrush currents. The transformers used in the simulations have the following specifications: The flux-linkage and current curves for the transformers are illustrated in Figure 3; it is evident that the amorphous core is more easily magnetising and that it has a lower saturation point than the CRGO.

Table 1: Specifications of the transformers

Specification	Amorphous core	CRGO steel core
Rating (kVA)	16	16
Phase	Single	Single
Voltage (V)	22000/240	22000/240
Core material	2605SA1	M-5
Design flux density (T)	1.3	1.3
Saturation (T)	1.56	2.08

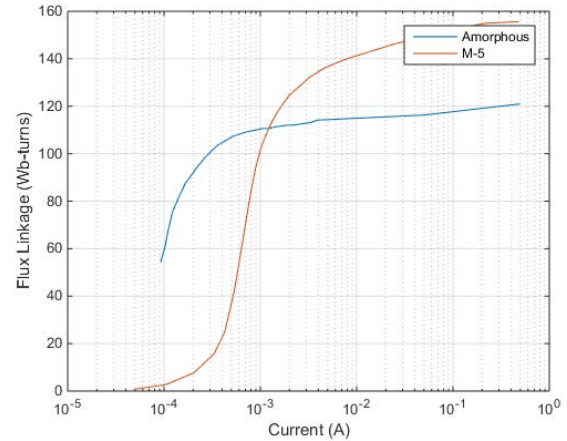


Figure 1: Flux linkage-current curve for amorphous core and CRGO steel core transformers [6].

4. ANALYSIS

Lin et al have solved the inrush problem from the fundamental equations [6], Ebner [7] and Chiesa [8] have solved the inrush problem though an ATP/EMTP model and this approach is used in this paper. The models (see figure 4) were simulated using Type 93 pseudo non-linear inductance using the information shown in Figure 3 and with a residual flux linkage of 50 Wb-turns (approximately half the peak flux linkage). The value of the resistance is 250 Ω and the value of the inductance is 4.5 H (to limit the numerical oscillations a damping factor of 10 was used).

The results are displayed below:

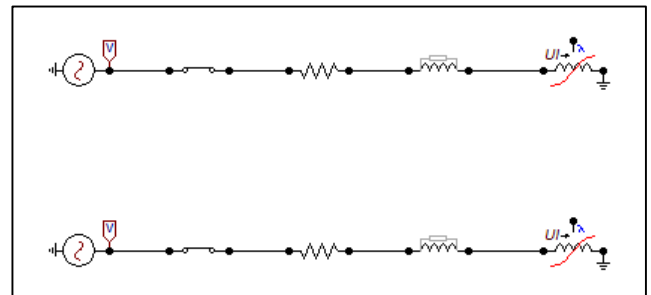


Figure 4: ATP model of the two transformers.

The source voltages and the voltage across the magnetising inductance are illustrated in Figure 5. The corresponding inrush currents and flux linkages are illustrated in Figures 6 and 7. A summary of results from ATP and equation (6) are illustrated in Table 2.

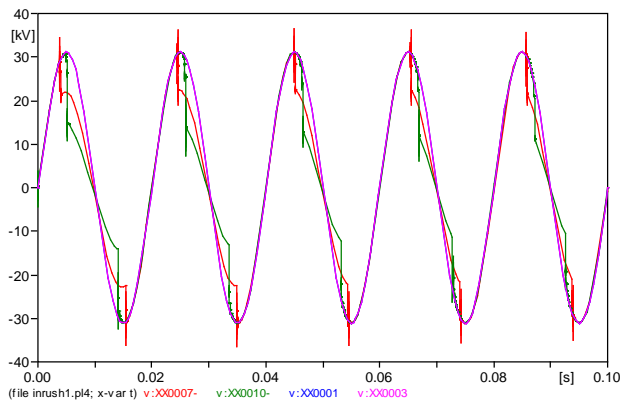


Figure 5: ATP simulation results for source voltages (v: XX0001 (CRGO steel) and v: XX0003 (amorphous)) and magnetising voltages (vXX0007- (CRGO steel) and vXX0010- (amorphous)) during inrush currents.

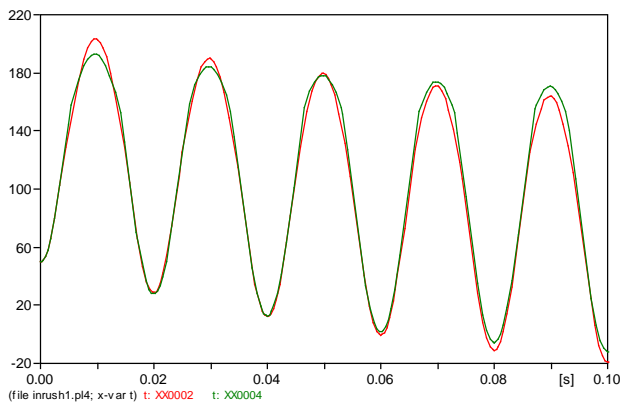


Figure 6: Flux linkage (t: XX0002- (CRGO steel) and XX0004- (amorphous)) during inrush currents.

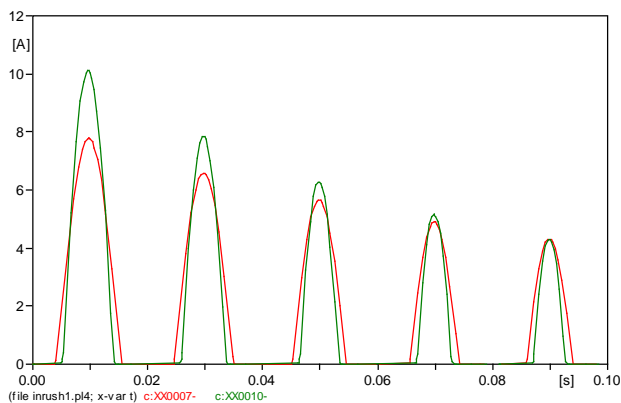


Figure 7: ATP simulation results for currents (cXX0007- (CRGO steel) and cXX0010- (amorphous)) at the magnetising inductances during inrush currents.

Table 2: Calculated and ATP results for inrush currents

Results	Calculated	ATP	Difference
CRGO steel core	6.5871 A	7.8 A	1.21 A
Amorphous core	9.5147 A	10.11 A	0.6 A

5. DISCUSSION

Figure 5 illustrates the source voltages and the voltages across the magnetising inductance.

Figure 6 illustrates the flux linkage through the transformer; the residual flux of 50 Wb-turns is evident. It is also evident that the peak flux for the first cycle is 200 Wb-turns, which pushes the core into a saturated state. The corresponding inrush current is illustrated in Figure 7.

Referring to Figure 5, it shows why it is important to include the resistance and winding inductance as the high currents will reduce the voltage across the magnetising branch, this leads not only to limiting the current but also the decay of the flux linkage and current over time. This is in line with the information shown in Equations 2 and 3.

There is an expected error between the calculated and ATP simulation results (see Table 2) where the calculated results were obtained by using equation (6). The ATP results are assumed to be more accurate as it accounts for flux leakage around the winding and the damping resistance of the circuit, however, this will be verified once the transformers are tested.

It is evident that the amorphous core transformer has a higher inrush current of approximately 30% when compared to the CRGO core transformer. The transformer's rated current is 0.73 A and the inrush currents are 14 times higher than this. This is significant as the forces exerted are proportional to the square of the current and this will have an impact on the mechanical stresses of the transformer. This is particularly important on a distribution system where the transformers are switched often.

6. CONCLUSION

Inrush currents are higher in the amorphous core transformer; this is due to the lower saturation point (see figure 3 and 7). The inrush current will have an impact on the mechanical stresses of the transformer and needs to be investigated.

7. ACKNOWLEDGEMENTS

The authors would like to thank Eskom for their support of the research through the TESP programme. The authors would like to thank Group Transmission and

Sustainability, Research Testing and Development for their support of the project.

The authors would like to thank Revive Electrical Transformers for providing information on the transformers.

8. REFERENCES

- [1] M. Mohan, "An overview on amorphous core transformers," *Journal of Emerging Trends in Engineering and Applied Sciences*, vol. 3, no. 2, pp. 217-220, Jan 2012.
- [2] S. Hodder, B. Kasztenny, N. Fischer and Y. Xia: "Low Second-Harmonic Content in Transformer Inrush Currents – Analysis and Practical Solutions for Protection Security", *Southern African Power System Protection Conference*, Johannesburg, South Africa, pp. 1-5, November 2014
- [3] R. M. Del Vecchio, B. Poulin, P. T. Feghali, D. M. Shah and R. Ahuja: *Transformer Design Principles, With Applications to Core-Form Power Transformers*, Taylor and Francis Group, LLC, second edition, 2010
- [4] <http://www.electrical4u.com/magnetizing-inrush-current-in-power-transformer/>; date accessed: 10 November 2015
- [5] S.V.Kulkarni and S.A.Khaparde: *Transformer Engineering; Design and Practice*, Marcel Dekker, Inc., first edition, 2004
- [6] C. Lin, C. Cheng, C. Huang, and J.-C. Yeh, "Investigation of magnetizing inrush current in transformers. i. numerical simulation," *Power Delivery, IEEE Transactions on*, vol. 8, no. 1, pp. 246{254, Jan 1993.
- [7] A Ebner, "Transient Transformer Inrush Currents due to Closing Time- and Residual Flux Measurement-Deviations if Controlled Switching is used," Unpublished, date accessed 15 November 2015 http://www.eeh.ee.ethz.ch/uploads/tx_ethpublications/ebner_transient_transformer_inrush_currents_EMTP2007.pdf
- [8] N Chiesa, *Power Transformer Modeling for Inrush Current Calculation*, PhD Thesis, Norwegian University of Science and Technology, 2010

ECONOMIC ADVANTAGES OF STIRLING-DISH CONCENTRATED SOLAR POWER OVER THE MOLTEN SALT POWER TOWER TYPE CONCENTRATED SOLAR POWER USING SYSTEM ADVISOR MODEL

C Chukwuka * and K A Folly *

* Faculty of Engineering and the Built Environment University of Cape Town, South Africa.

Abstract. Following the recent announcement by the South African Department of Energy to diversify the country's electricity generation away from the fossil based generation to renewable energy sources, the question of which technological options and the merits of these options are available in the current renewable energy markets. Concentrated Solar Power technologies considered are the molten salt power tower, parabolic trough and Stirling dish technologies. The first two are already fully developed and market ready however the last option which is the Stirling Dish type was least developed despite the fact that it has been shown to be the most efficient and economical than the rest. In this paper, we review the features of the Stirling dish CSP and then compare the cost implications of the Stirling dish CSP with that of the Molten Salt Power Tower situated in Cape Town, South Africa.

Keywords: solar multiple, concentrated solar power, systems advisor model, national energy regulators of South Africa, Renewable Energy Feed-in tariff, capacity factor, molten salt energy storage

1. INTRODUCTION

Concentrated solar thermal energy technology has been proven to be reliable and cost efficient method of generating electricity. The most common technologies are the molten salt power tower, parabolic trough and Stirling dish technologies. Parabolic troughs have dominated the concentrating solar power market thus far followed by molten salt power tower however, Stirling dish systems are anticipated to surpass parabolic troughs by producing power at more economical rates and higher efficiencies. A Stirling dish system recorded a world record in solar-to-electric energy conversion efficiency of 29.4 % in 1984 [1]. Since then, there has been an interest in the potentials for these systems to produce inexpensive and reliable renewable electric power to the market in the near future. Stirling Energy Systems is expected to install the largest solar-electric power plant in the world over the next several years after initial testing of a 40 dish 1 MW test pilot project [2]. Stirling dish systems have not been researched as extensively as other solar technologies such as photovoltaics or solar hot water heaters, and literature on these systems is difficult to find. Data on the performance of Stirling dish systems have typically not been accessible to the public, and few Stirling dish systems have been constructed to date. Despite these limitations, data were obtained from Sandia National Laboratory for the WGA Mod 2-2 Stirling dish system in order to validate models of Stirling dish power systems developed during the course of the present study.

2. OVERVIEW

The first part is based on the technical configuration of the plant while the second deals with the software used for the simulations.

2.1 Concentrated Solar Power

Concentrated solar power plants basically contain solar collector fields that focus the incident solar rays on a central receiver shown in figure 1. The incoming solar flux is converted to heat by the receiver; this heat is then sent to the storage tanks usually the molten salt tanks for storage. The amount of heat energy stored by the salt is determined by the size of the tanks measured in hours of thermal energy [1]. From the salt tanks, steam is generated and sent to the turbine for onward conversion to electricity.

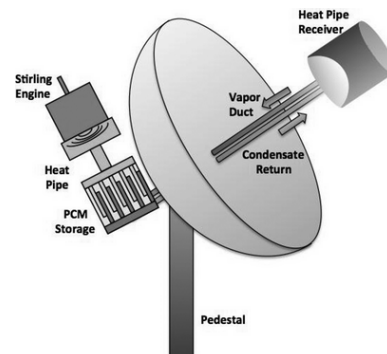


Figure 1: Dish Stirling Operation Diagram [2]

There are currently different designs of CSP: the parabolic trough which is by far the most developed, the Fresnel type, Stirling dish and the power tower type which is known for its high efficiency because of its ability to reach very high temperatures up to 2000° C.

2.2 Dish Stirling

A dish-Stirling system consists of a parabolic dish-shaped collector, receiver and Stirling engine. The collector focuses direct normal solar radiation on the receiver, which transfers heat to the engine's working fluid. The engine in turn drives an electric generator. A dish-Stirling power plant can consist of a single highly reflective solar concentrator dish or a field of dishes, a solar receiver cavity and a Stirling engine. Stirling engine was invented by Scottish Robert Stirling in 1816, believing that steam engine was too complicated and dangerous [3]. This engine runs on a gas expansion and contraction, usually helium, hydrogen, nitrogen or air. This gas is transported through a cooling cycle in a cold focus, it is contracted, and then, in a hot focus, it is expanded. Thus a thermodynamic cycle takes place. Within the cycle, it highlights the importance of a regenerator, which is based on absorbing and transferring heat at constant volume changes of the cycle. The engine can work without the regenerator, but it allows higher efficiencies.

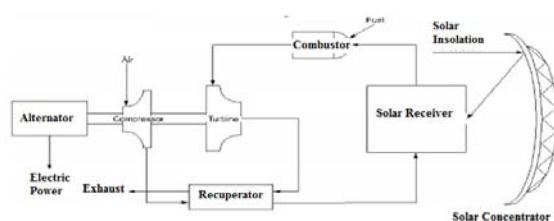


Figure 2: Schematic of a Solar Dish Engine

2.3 Dish-Stirling System

The Stirling engine is an external heat (or combustion) engine that converts heat from the absorber to mechanical power in a manner similar to internal combustion engines. Unlike internal combustion engines, however, heat is applied externally to the piston heater head in a Stirling engine. Because the Stirling engine relies on an external source for heat input, the cycle itself operates as a closed system since the working fluid is contained within the cylinders and not vented to atmosphere like exhaust gases from internal combustion engines. The addition of a regenerator into a Stirling engine improves the efficiency of the engine by pre-cooling the working fluid as it moves from the expansion space to the compression space, and pre-heating the working fluid as it moves from the compression space into the expansion space. The working fluid is often hydrogen which is heated to over 700 °C with a maximum pressure around 20 MPa yielding a thermal-to-mechanical efficiency of approximately 40 % [4]. The compression space is cooled by a refrigerant loop that circulates a secondary fluid through a common automotive radiator with forced air cooling provided by a fan. Cliques Solar India offers two commercially available parabolic dishes, the ARUN 100 and the ARUN 160 which are basically the same but with different sizes.

2.4 Advantages and Disadvantages of Stirling Dish

Advantages of Stirling Engines [5] are maximum potential efficiency for a heat engine operating between the same temperatures up to 32 % compared to 15 % of power tower technology; flexible fuel usage such as biomass, solar, geothermal, waste heat, and fossil fuels; lower nitrogen oxides pollution compared to internal combustion engines; quiet and minimal vibration; piston-free Stirling engines have very high reliability; Stirling engines allow for operation as a refrigerator or a heat pump; they have the highest specific work output for any closed regenerative cycle. They are modular which is achieved by the fact that Stirling dish has a turbine attached to each concentrator dish. Stirling dish can be placed in sloppy terrains and hills. They are reliable, low noise, low cost of power and have good commercial properties.

Disadvantages; Stirling engines often have a slower response to an increase or decrease in load; Lower specific power output so added weight and volume would be less practical for automotive purposes; hydrogen or helium seals can be problematic for kinematic Stirling engines. They produce electricity without the use of energy storage hence it tends to compare with PVs. Issues with the mechanical support of the dish and its tracking system are still debated. More research with materials as opposed to the steel which are currently being used. The main research of dish-Stirling system is to optimize the key parts of system and reduce the system costs.

2.5 Parabolic Concentrator

The concentrator for the Stirling dish systems uses parabolic mirrors mounted on a structure that tracks the sun by pivoting on two axes. The parabolic concentrator must be sized to deliver about four times more thermal energy than the rated electrical output due to an average net system efficiency of around 25 % [6]. Existing Stirling dish systems have been built to provide 10 kW and 25 kW electric with an approximate diameter of the parabolic dish being 7.5 and 11 meters respectively [7].

The solar reflectance of the silvered mirrors ranges between 91-95 % for current Stirling dish systems fabricated by four manufacturers [8]. The most durable mirror surfaces employ silver/glass mirrors. Attempts to produce low cost reflective polymer films have had limited success in the past. ReflecTech has recently developed a polymer reflective film (ReflecTech™) that has excellent optical properties with a 94.5 % mirror reflectivity and costs R17.4 (\$1.30) per square foot in large volume [9]. The most innovative parabolic mirrors use stretched-membranes where the reflective membrane is stretched across a hoop or rim and a second membrane is placed behind the first. A partial vacuum then pulls the first membrane into a parabolic shape.

The dual-axis solar tracking is accomplished through azimuth-elevation tracking or polar tracking. Azimuth-elevation tracking rotates the concentrator in a plane parallel to the earth (azimuth) and in another plane perpendicular to the earth (elevation). For polar tracking, the concentrator rotates in a plane parallel to the rotation of the earth at a constant rate of 15° per hour, and the declination axis rotates perpendicular to the polar axis by slowly varying between plus and minus 23.5° over the year. Larger Stirling dishes have used azimuth-elevation tracking and smaller Stirling dish systems have used polar tracking.

2.6 Receiver

The Stirling dish receiver absorbs thermal energy from the parabolic concentrator and transfers the absorbed thermal energy to the working fluid in the Stirling engine. The receiver must accommodate a large thermal input as well as a solar flux over a thousand times greater than the direct solar radiation from the sun. A Stirling receiver consists of an aperture and an absorber. The aperture in a Stirling receiver is located at the focal point of the parabolic concentrator to reduce radiation and convection losses, and can have concentration ratios of over 13,000 suns. The size of the aperture has diameters ranging from about 14 to 20 cm to ensure an appropriate fraction of the concentrated solar energy is intercepted by the aperture. The intercept factor, which is the fraction of the energy from the collector that enters the aperture and is not blocked due to the receiver housing, is often between 94 and 99 %.

2.7 Stirling Engine Types

There are two common types of Stirling engines that have been used for power production: the kinematic and the free-piston engine. Kinematic engines have the power piston connected to the crankshaft by a connecting rod, which is attached to a cross-head to eliminate lateral forces against the cylinder walls. A linear seal is used between the cross-head and piston to seal the region between high and lower pressures to allow the bearing surfaces to remain lubricated in the low-pressure area while preventing fouling of the heat exchanger surface in the high-pressure region [10]. Kinematic Stirling engines are currently being used in the Stirling dish systems by all of the major manufacturers.

An alternative design to the crankshaft with the cross-head is to use a swash plate or wobble plate drive. A slanted drive surface is connected to the drive shaft at an angle and moves the fixed piston push rods up or down while the drive surface rotates. The stroke length can be controlled by varying the drive surface angle with respect to the axis of rotation. The STM 4-120 engine uses a variable-angle swash plate to control the power of the engine by using a variable stroke as previously stated.

Free-piston Stirling engines do not have the power piston connected to a crankshaft, but rather cycle back and forth between the working fluid and a spring which is often another gas. The displacer is allowed to bounce on gas or mechanical springs, which are incorporated into the Beale free-piston design. The spring and mass system control the frequency, piston stroke, and timing between the two pistons. Power is generated by attaching a magnet to the power piston and moving it past stationary coils that act as a linear alternator, or the engine can be used to drive a hydraulic pump. Free piston Stirling engines only have two moving parts, no dynamic seals are required to seal the high and low pressure region since electricity is generated internally, and oil lubrication is not required. This enables the free-piston engines to have a lower cost, longer life, and minimal maintenance with respect to kinematic Stirling engines. A 6 kW free piston Stirling engine system was tested by Cummins Power Generation and Sunpower to have a 28 % demonstrated efficiency operating with a 629°C expansion space temperature. The free-piston Stirling dish system by Sunpower had a comparable net efficiency to the SBP kinematic engine system, but no free-piston Stirling dish systems are currently planned for direct solar dish applications.

2.8 Stirling Engine Configurations

Two sets of configurations are discussed in this section.

2.8.1 Mechanical Configuration

Various machine components have been combined to provide the Stirling cycle. The cycle provides a constant-volume process during the transfer of the working fluid between the hot and cold space of the engine and provides a constant-temperature heating and cooling process during compression and expansion. The compression and expansion processes of the cycle generally take place in a cylinder with a piston. A displacer shuttles the working fluid back and forth through the heater, regenerator, and the cooler at constant volume. The displacer that moves to cold space displaces the working fluid from the cold space causing it to flow to the hot space and vice versa. There are three basic engine design configurations that have been used for Stirling engines. These include alpha, beta, and gamma configurations.

The alpha configuration uses a separate cylinder for the expansion and compression space. A displacer is not used rather two pistons, called the hot and cold pistons are used on either side of the heater, regenerator, and cooler. These pistons move uniformly in the same direction to provide constant-volume heating or cooling processes of the working fluid. When all the working fluid has been transferred into one cylinder, one piston will be fixed and the other piston moves to expand or compress the working fluid. The expansion work is done by the hot

piston while the compression work is done by the cold piston as shown in figure 3.

In the beta-configuration, a displacer and a power piston are incorporated in the same cylinder. The displacer moves working fluid between the hot space and the cold space of the cylinder through the heater, regenerator, and cooler. The power piston, located at the cold space of the cylinder, compresses the working fluid when the working fluid is in the cold space and expands the working fluid when the working fluid is moved into the hot space as shown in figure 4.

While gamma-configuration uses separated cylinders for the displacer and the power pistons, with the power cylinder connected to the displacer cylinder. The displacer moves working fluid between the hot space and the cold space of the displacer cylinder through the heater, regenerator, and cooler. In this configuration, the power piston both compresses and expands the working fluid as shown in figure 5. The gamma-configuration with double-acting piston arrangement has theoretically the highest possible mechanical efficiency. This configuration also shows good self-pressurization. However, the engine cylinder should be designed in vertical type rather than horizontal in order to reduce bushing friction [11].

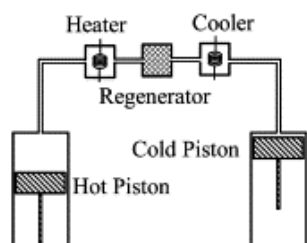


Figure 3: The Alpha Engine

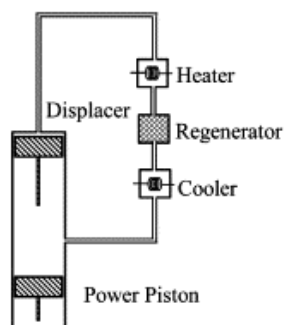


Figure 4: The Beta Engine

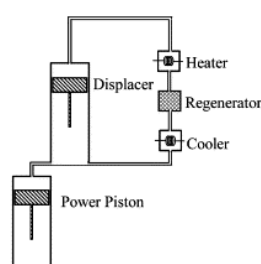


Figure 5: The Gamma Configuration

2.8.2 Low Temperature Differential Engine Configuration

A low temperature differential (LTD) Stirling engine can be run with small temperature difference between the hot and cold ends of the displacer cylinder. It is different from other types of Stirling-cycle engines, which have a greater temperature difference between the two ends, and therefore the power developed from the engine can be greater. LTD engines may be of two designs. The first uses single-crank operation where only the power piston is connected to the flywheel, called the Ringbom engine. This type of engine, that has been appearing more frequently, is based on the Ringbom principle. A short, large-diameter displacer rod in a precise-machined fitted guide has been used to replace the displacer connecting rod. The other design is called a kinematic engine, where both the displacer and the power piston are connected to the flywheel. The kinematic engine with a normal 90° phase angle is a gamma configuration engine. Some characteristics of the LTD Stirling engine are as follows;

Displacer to power piston swept volumes ratio is large; (2) diameter of displacer cylinder and displacer is large; (3) displacer is short; (4) effective heat transfer surfaces on both end plates of the displacer cylinder are large; (5) displacer stroke is small; (6) dwell period at the end of the displacer stroke is rather longer than the normal Stirling engine; (7) operating speed is low.

2.9 Stirling Engine Working Fluids

Working fluids commonly used in Stirling engines consist of air, helium, or hydrogen. The selection of a specific working fluid is based on the following fluid properties: thermal conductivity, specific heat, density, and viscosity. A working fluid with a higher thermal conductivity, density and higher specific heat will improve the heat transfer capabilities of the gas and improve the efficiency of the heat exchangers. A working fluid with a lower density and viscosity will reduce the pressure drop through the regenerator, working space, and dead space and consequently improve the engine efficiency [12]. Prandtl and Grashof describe the two dimensionless numbers related to heat transfer. Increasing both of these numbers would improve the heat transfer capabilities of the heater and cooler and therefore improve the efficiency of the engine.

3 SYSTEM ADVISOR MODEL (SAM)

SAM, originally called the 'Solar Advisory Model' was developed by the National Renewable Energy Laboratory in collaboration with Sandia National Laboratories in 2005 [13]. It was first used internally by the U.S. Department of Energy's Solar Energy Technologies Program for systems-based analysis of

solar technology improvement opportunities within the program. The first public version was released in August 2007 as version 1, making it possible for solar energy professionals to analyze photovoltaic systems and concentrated solar power parabolic trough systems in the same modelling platform using consistent financial assumptions. Since 2007, two new versions have been released each year. Adding new technologies and financing options. In 2010, the name of this package was changed to 'Systems Advisor Model' to reflect the addition of non-solar technologies.

The outputs are levelized cost of energy, power purchase price, rate of return and other financial targets, payback period and net present value, hourly, monthly and annual average predictions of the system performance including net electric output and efficiencies, annual cash flow table with cost details and customizable graphs. The levelized cost of energy (LCOE) in cents per kilowatt-hour accounts for a project's installation, financing, tax, and operating costs and the quantity of electricity it produces over its life. The LCOE makes it possible to compare alternatives with different project lifetimes and performance characteristics. The real LCOE accounts for the effects of inflation over the life of the project. The nominal LCOE excludes inflation from the calculation. Abstract – The purpose of the abstract is to summarize the contents of the paper. The abstract is thus a short, focused paragraph that tells the reader of the paper the following: the subject area and the particular research problem being tackled in the paper; the particular approach to the problem that is considered in the paper; the main findings and conclusions of the paper. The abstract should not be used to provide an introduction to the subject area. As a guideline, think of the abstract as a description of your paper intended for readers who are working in the same broad area as you are; after reading your abstract, they should be able to decide whether or not your paper is of further interest to them.

3.1 Inputs

The climate input page shows detailed weather information of the location of the plant. In this case, Cape Town weather data is selected. The weather data of Cape Town is shown in table 1.

Table 1: Weather Data of Cape Town

Location Details	
City	Cape Town
Time zone	GMT+2
Elevation	47m
Latitude	-33.98
Longitude	18.6°
Annual Weather Data Information	
Direct Normal Irradiance (DNI) kWh/m ²	1923.9

GlobalHorizontalIrradiance kWh/m ²	1900.7
Dry-bulb temperature °C	16.5
Wind speed (m/s)	5.1

4 SIMULATION RESULTS

Using the same input data shown in table 1, two sets of simulations were ran with SAM simulation software. The first one is the Stirling dish CSP while the second one is a power tower CSP. The results of these simulations are shown in tables 2 and 3 respectively using Dollar-Rand current exchange Rate as 13.46.

Table 2: Summary of a Stirling Dish CSP Output Data

Metric	Value
Annual Energy	132,630,392 kWh
Capacity factor	15.1 %
Levelized COE (nominal)	R1.30/kWh
Levelized COE (real)	R1.06/kWh
Electricity cost without system	R698 166.8
Electricity cost with system	R-494 182 08.4
Net savings with system	R503 407 76.88
Net present value	R-1244932521.12
Net capital cost	R393 571 003 0.08
Equity	R118 159 023 1.92
Debt	R275 499 710 7.2

Table 3: Molten Salt Power Tower CSP Output Data

Metric	Value
Annual Energy	373,537,280 kWh
Capacity factor	42.6%
PPA price (year 1)	R2.17/kWh
PPA price escalation	1.00 %
Levelized PPA price (nominal)	R2.54/kWh
Levelized COE (real)	R2.44/kWh
Net present value	R349 302 048.28
Internal rate of return (IRR)	11.00 %
Year IRR is achieved	20
IRR at end of analysis period	11.00 %
Net capital cost	R112 356 921 43.36
Equity	R560 898 917 6.32
Size of debt	R562 646 025 6.32

5 DISCUSSION

Two types of concentrated solar power plants were modelled using System Advisor Model. The capacity factors of 15.1 % (Power Tower) and 42.6 % (Stirling Dish) obtained is a clear indication of the effects of the energy storage that is lacking in the Stirling dish scenario. Stirling dish by design does not incorporate energy storage medium hence limitation is placed on the capacity factor. Whereas the power tower used in this simulation consists of a six hour molten salt energy storage. Lower levelized cost of energy was obtained for the Stirling Dish

technology R1.06 compared to the Levelized Cost of Energy R2.44/kWh.

GaAs, InP, and GaSb,” *Journal of crystal growth*, 71(3), 551-558, 1985

[12] National Renewable Energy Laboratory Help files December, 2011

CONCLUSION

In conclusion Stirling Dish technology shows lots of promises because of its inherent competitiveness in achieving low cost of electricity and high overall conversion efficiency compared with other CSP technologies however the fact that its comes with no energy storage medium makes it less attractive compared to technologies such Photovoltaic panels and wind turbine. Hence, more research is needed in order to overcome this hurdle.

REFERENCES

- [1] Andraka, C. E., Rawlinson, K. S., Moss, T. A., Adkins, D. R., Moreno, J. B., Gallup, D. R., and Johansson, S., “Solar heat pipe testing of the Stirling thermal motors 4-120 Stirling engine,” *IEEE Proceedings of the 31st Intersociety in Energy Conversion Engineering Conference, IECEC*, Vol. 2, pp. 1295-1300, 1996
- [2] Stirling Energy Systems, Inc; “Solar Dish Stirling Systems Report For NREL CSP Technology Workshop,” March 7, 2007
- [3] Sonntag, R. E., Borgnakke, C., Van Wylen, G. J., & Van Wyk, S. “*Fundamentals of thermodynamics*,” Vol. 6, New York: Wiley, 1998.
- [3] Teagan, Peter, W., “Review: Status of Markets for Solar Thermal Power Systems,” May 2001.
- [4] Urieli, I., and Berchowitz, D. M. “*Stirling cycle engine analysis*,” Adam Hilger, Bristol, 1984
- [5] Diver Jr, R. B. *U.S. Patent No. 6,597,709*. Washington, DC: U.S. Patent and Trademark Office 2003
- [6] Li, M., and Dong, J.; “Modelling and Simulation of Solar Dish-Stirling Systems,” *IEEE transaction in Power and Energy Engineering Conference (APPEEC), Asia-Pacific* pp. 1-7, 2012,
- [7] Mancini, T., Heller, P., Butler, B., Osborn, B., Schiel, W., Goldberg, V., and Moreno, J., “Dish-Stirling systems: An overview of development and status,” *Journal of Solar Energy Eng*, 125(2), 135-151, 2003.
- [8] 3M™ Solar Mirror Film 1100 Technical Data book, 2012
- [9] W. Stine and R. Diver; “A compendium of Solar Dish/Stirling Technology,” Sandia National Laboratories, Albuquerque, NM, USA, Contract No. 67-3678, 1994
- [10] Kongtragool, B., and Wongwises, S., “A review of solar-powered Stirling engines and low temperature differential Stirling engines,” *Renewable and Sustainable energy reviews*, 7(2), 131-154, 2003.
- [11] Jordan, A. S., “Estimated thermal diffusivity, Prandtl number and Grashof number of molten

Evaluation of an empirical model for a flat plate solar collector

Nothando Ndlovu^{1,2}, Michael Simon¹ and Stephen Tangwe¹

Fort Hare Institute of Technology, University of Fort Hare, Alice, South Africa

E-mail: ndlovun@ufh.ac.za

Abstract: Empirical modelling has been widely used to model systems due to its relatively simple methodology. In particular, multi linear regression (MLR) has been employed as a technique to empirically model solar collectors during collector testing procedures. In this study, a simple MLR model for a flat plate solar collector is presented. The model predicts the hot water temperature at the collector outlet for a system installed in Alice, South Africa from four input variables namely solar radiation, ambient temperature, relative humidity and collect inlet temperature. The system consists of two flat plate collectors each of 2m² gross area installed in parallel. The fluid outlet sensor of the two collectors is positioned to measure the combined temperature from both collectors. Weather data, temperature and flow data were collected on clear sky days during two winter month. Model validation was done by evaluating the correlation coefficient (R-squared), and the percentage mean absolute error (PMAE). These were determined to be 0.93 and 5.83 respectively. These results indicate that the model can be successfully used to predict the collector outlet temperature using the given input parameters. This approach has the advantages of simplicity and can be easily implemented with very little computational time.

1. Introduction

Solar water heaters have become important as a cleaner and sustainable alternative for residential and commercial water heating purposes. The solar collector, which forms the main component of the system, captures solar radiation, converting it to heat. Due to the dependence of the collector on ambient conditions (solar radiation and ambient temperature), the interaction of climatic conditions is important in determining the collector outlet temperature of solar collector systems. As a result, the performance of a given solar collector will vary when installed in different locations. The key parameter of interest in designing solar collectors is the energy delivered by the system over its lifetime [1] and [2].

²Nothando Ndlovu:ndlovun@ufh.ac.za

To determine the energy delivered by the tank, the hot water outlet temperature achieved by the collector should be sufficiently high to counter heat losses from pipes between the collector and the tank. For a solar collector designer, knowledge of this collector outlet temperature is important. Mathematical models have been used to predict collector temperature as well as estimate its long-term performance. The advantage of building models is that data collected over a short monitoring period can be used to predict a systems long term performance. Performance prediction is important for designers particularly for comparison of system performance for various locations, and encouraging construction of quality systems. In addition, performance prediction provides consumers with valuable information about the operation of the system.

Generally, there are two types of models and these are namely white box models also known as physical models, and black box models. The former typically involves the formulation of a complex set of mathematical equations. These form the basis of simulation software such as TRNSYS. A set of equations developed numerically describe the various parts of a solar systems and are embedded in the library of components. White box models require skill and expertise and are generally time consuming. Examples of studies modelling the performance of solar water heaters using white box models have been done by [3] and [4].

Black box models on the other hand make use of historical data to predict system performance. Artificial neural network (ANN) is one type of black box model that has been used to model solar water heater performance. Kalogirou and Pantelio employed a neural network for modeling a domestic water heating system [5]. Farkas and Geczy-Vig developed an ANN model to determine the output temperature and the performance of flat plate solar collector. They used the inlet and outlet fluid temperature as input and output parameters respectively [6]. Sozan et al.,2008 used ANN to specify the performance of flat plate collector by using meteorological parameters [7]. ANN can achieve high accuracies; however this method requires training of the network which can increase computational time.

Multi linear regression is a type of black box modelling technique which uses ordinary least squares optimization method to predict an output from one or more inputs. It is a simple form of an artificial neural network model, but has the merit of easily predicting the variation of each input parameter with the desired output [8]. It can be easily applied to any dataset at a low computational time. Regression modelling though a simple modelling technique has not been extensively researched in solar thermal technology for the prediction of collector temperatures. This work therefore aims to evaluate the accuracy of a MLR model in determining the outlet hot water temperature of a flat plate solar collector. This study uses easily measurable quantities as inputs, namely solar radiation, ambient temperature, relative humidity and collector inlet temperature and this can facilitate the work of design engineers and researchers in the solar thermal industry.

2. Experimental setup

The collector system comprised of two identical flat plate collectors each of 2m² gross area installed on the roof of the Solar Watt House, at the University of Fort Hare Alice Campus (32°South, 26°East). The piping system is such that the collector configuration is parallel. Cold water from the main supply pipe divides into two and feeds into the inlet of the both collectors. In this array arrangement water enters both collectors at the same temperature and exits at a similar temperature. The performance of the collector array is the same as the performance of the individual collector [9]. The solar system is of open –loop, thermosyphon type installed with a 200litre storage tank.

2.1. Materials and description

The data acquisition system consisted of two 12-bit temperature sensors with an accuracy of $\pm 0.2^\circ\text{C}$ and a resolution of 0.03°C , and a pulse flow meter which measured flow at a rate of 3.785litres/pulse. A silicon pyranometer with an accuracy of $1.25\text{W}/\text{m}^2$ was employed for the measurement of global solar irradiance. An ambient temperature and humidity sensor with an accuracy of $\pm 0.2^\circ\text{C}$ measured ambient temperature and relative humidity. The temperature sensors measured collector inlet temperature and the hot water temperature from the collectors. All the sensors were connected to a Hobo U30/Non Remote Communication data logger which automatically sensed configuration settings of every sensor via HOBOWare Pro software. Measurements were logged at 1minute interval and averaged over 10minutes.

2.2. Schematic setup

The installation of the collectors is shown on figure 1 while figure 2 shows the full schematic of the setup. For the purposes of this study data from T2, T3 and F1 was collected. T2 and T3 show the temperature sensors measuring the collector cold water inlet temperature and the collector hot water outlet temperature respectively. F1 was used to measure the collector thermosyphon flow rate. The tank had a 2kW element which was disabled during period of monitoring.



Figure 1. Solar collectors on roof top

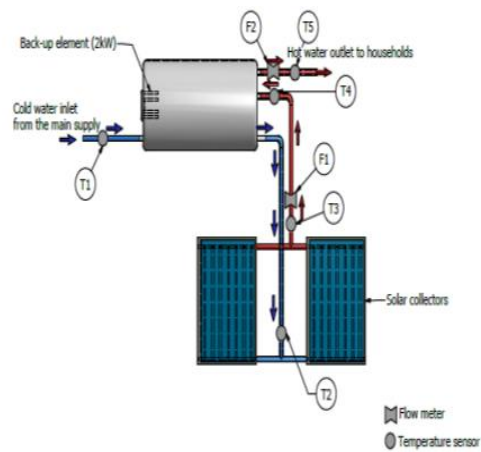


Figure 2. Schematic showing position of sensors

3. Methodology

In this study the relationship between collector outlet temperature (T_{co}) and four predictor variables, solar radiation (I), ambient temperature (T_a), relative humidity (Rh) and collector inlet temperature (T_{ci}) is investigated. Equation (1) presents the MLR form of the model.

$$T_{co} = \alpha_0 + \alpha_1 I + \alpha_2 T_a + \alpha_3 Rh + \alpha_4 T_{ci} \quad (1)$$

Where $\alpha_1 - \alpha_4$ represent the regression coefficients for the individual parameters and α_0 represents the model intercept. These coefficients are determined by applying ordinary least squares method in which a function L is minimized with respect to the model coefficients as shown in equation (2).

$$L = \sum_{i=1}^n (y_i - y_i^*)^2 \rightarrow \min \quad (2)$$

Where y_i is the measured value and y_i^* is the value calculated by the model and n is the number of

observations. L is the sum of residual (error) squared for the measured data set used in model fitting [10]. The residual is defined as the difference between observation y_i and the fitted value y_i^* . This correlation forms the basis of the prediction model. The parameter identification was performed using OriginLab soft-ware.

3.1. Data collection and partitioning

For the parameter estimation, data was collected from the 17th-20th June 2014. These days were characterised by sunny 'clear sky' conditions.

To select only appropriate data values, the data was partitioned using two main criteria:

- When the difference between the collector inlet and collector was below than 10°C , and when the collector outlet temperature was less than 35°C this data was removed from the analysis. From observation of the dataset, there was no collector flow when temperatures were in this range hence no heat collection. Data from the input parameters data in this range was also excluded in the analysis
- Data averages between 4pm and 7am were excluded from the analysis. From observation of the dataset, these corresponded to periods when there was no collector flow and also include night time when the collector shuts down. The data used in the study therefore represents time when the thermosyphon collector system was in operation. During the monitoring period the maximum average flowrate was 0.045kg/sec and the minimum average flow was 0.0063kg/sec .

4. Results and discussions

This section presents the results of the parameter estimation, comparison of the modelled and measured results as well as the model validation results. Table 1 shows the values of the parameter estimates. It can be seen from the positive values of the coefficients that the collector outlet temperature increases with a unit increase in ambient temperature, solar radiation, relative humidity and collector inlet temperature. For optimum energy collection however, T_{ci} should be low. A low inlet temperature increases the temperature difference between the hot and cold section, thereby increasing energy collection. The correlation coefficient (R^2) from the parameter estimation was 0.93. This is close to unity and shows good model fit. This high correlation coefficient shows that the collector outlet temperature of the flat plate collector can be predicted for any given day using the relation in equation (3).

Figure 3 shows a scatter plot of the modelled temperature against measured temperature. As observed, lower temperatures show more scatter compared to higher temperatures due to the fact that at the lower temperatures the incident angle of solar radiation is large. This impairs the performance of the collector [11].

Table 1. Results of parameter estimation

α_0	α_1	α_2	α_3	α_4	R^2
1.167	0.044	0.669	0.056	0.33	0.93

$$T_{co} = 1.167 + 0.044I + 0.669T_a + 0.056Rh + 0.33T_{ci} \quad (3)$$

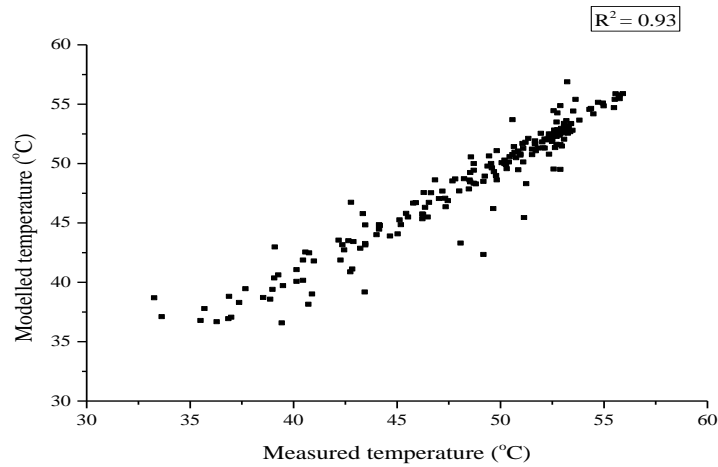


Figure 3. Modelled versus measured collector outlet temperature

4.1. Model Validation

A separate set of data excluded in the model development was for model validation. This was taken from selected days from the month of July 2014. Results from 19 July 2014 are presented below. Figure 4 shows the comparison between the measured and modelled collector outlet temperatures. The solar radiation and ambient temperature on this day are shown in figure 5. The maximum solar radiation and ambient temperature were 575.6 W/m^2 and 26.6°C respectively while corresponding measured maximum collector outlet temperature was 56°C . As seen, the modelled collector temperature generally follows the measured temperature with slight variances at higher temperatures. The maximum percentage error between the modelled and measured temperature was 5.83% which is in the range of acceptable values in engineering applications.

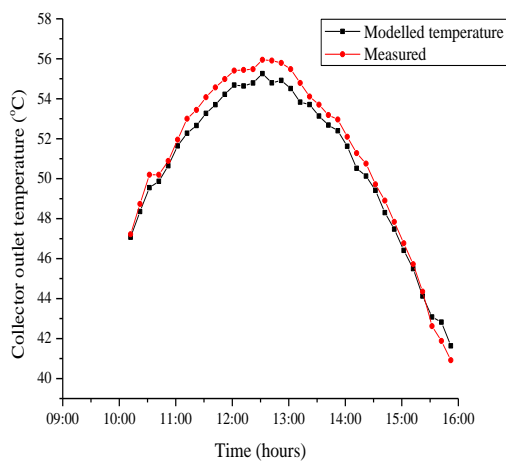


Figure 4. Measured and modelled collector outlet temperature

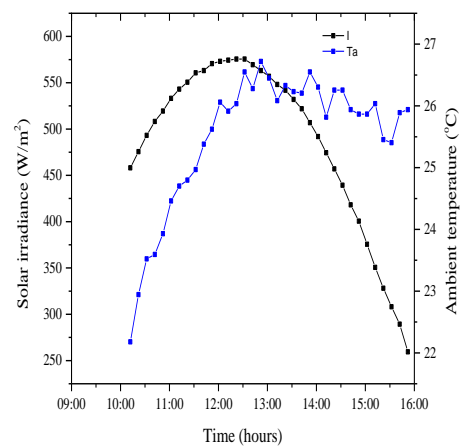


Figure 5. Solar radiation and ambient temperature

5. Conclusions

The collector outlet temperature (T_{co}) is an important parameter as it determines the energy collection capability of a system. In this work, T_{co} is used as a performance index to predict the performance of a flat plate collector from solar radiation, ambient temperature, relative humidity and collector inlet temperature. The objective was to predict the performance of the collector using a multi linear relation of the input and output parameters. A mathematical model was developed and the results obtained were compared with experimental measurements. The MLR model predicts results that compared reasonably well with the experimental data. A correlation coefficient of 0.93 and a mean absolute error of 5.83 were obtained. The results obtained are satisfactory and show that solar collectors can be modelled using MLR with high accuracy.

Acknowledgments

The authors would like to acknowledge ESKOM and Fort Hare Institute of Technology for the purchase of the solar water heater and the sensors and data logger that were used to undertake this research.

6. References

- [1] Bourges B, Rabl A, Leide B, Carvalho M, and Collares-Pereira M 1991 Accuracy of the European Solar Water Heater test procedure. Part I: measurement errors and parameters estimates *Solar Energy* **47** 11-16
- [2] Duffie J A and Beckman W A 2006 Solar engineering of thermal processes. 3rd ed. Hoboken, New Jersey: Wiley
- [3] Narasimhe G B, Gowda B P and Chandrashekar R 2014 Investigation of Mathematical modelling Assess the performance of a solar flat plate collector *Int. Journal of Renewable Energy Research*, **4** No.2
- [4] Abdunnabi M J R and Loveday D L 2012 Optimization of thermosyphon Solar water heaters Using TRNSYS. Part1: Improved Model Development and validation *Int. Conf. on Future Environment and Energy IPCBEE* **28** IACSIT Press Singapore
- [5] Kalogirou S A, Panteliu S and Dentsoras A 1999 Modeling of solar domestic water heating systems using artificial neural networks *Solar Energy* **65** 335–342
- [6] Farkas I and Geczy-vig P 2003 Neural network modelling of flat-plate solar collectors. *Computers and Electronics in Agriculture* **40** 78-102
- [7] Sozen A, Menlik M and Unvar S 2008 Determination of efficiency of flat-plate solar collectors using neural network approach *Expert Systems with Applications* **35** 1533-1539.
- [8] Stephen L T, Simon M and Meyer E L 2014 Mathematical modelling and simulation application to visualize the performance of retrofit heat pump water heater under first hour heating rating *Renewable Energy* **72** 203-211
- [9] Batabyal K 2013 *On the Performance prediction of solar water heating systems using artificial neural network*, A thesis submitted in partial fulfilment of the requirements of the degree of Master of Technology in Energy Science and Technology at Jadavpur University, West Bengal, India 24
- [10] Khaled A 2012 *On the Technical and economic performance of parabolic trough in Jordan*, A thesis submitted in partial fulfilment of the requirements of the Master in Renewable Energy and Energy Efficiency at University of Kassel Germany 69
- [11] Bolaji B O 2011 Mathematical Modelling and Experimental Investigation of Collector Efficiency of a thermosyphonic Solar water heating system. *ANUL XVIII*, NR. **3** ISSN 1453 – 7397 <http://anale-ing.uem.ro/2011/C8.pdf> Accessed 12 March 2014

Impact of Solar Power Generation on Economic Growth – The Role of Three-Dimensional Photovoltaic Structure

O.A. Mafimidiwo^{1*}, A.K. Sahar¹

¹University of KwaZulu-Natal, Howard Campus, 4041 Durban, South Africa

² University of KwaZulu-Natal, Howard Campus, 4041 Durban, South Africa

*Email: alicemafi@yahoo.co.uk

Abstract: For solar energy to be relevant to economic development, it must be able to compete relatively with the convectional energy sources. At present, solar power accounts in the world's power consumption is not competitive. One of the main criticisms of solar power is its high cost due to its low energy conversion efficiency. Of the various sources of solar energy technologies, this paper carried out study on thermal photovoltaic technology as solar energy study case. Using the appropriate materials selection and physics definitions, this paper utilises COMSOL Multiphysics, an engineering tool in the design, modeling and simulation of thermal Photovoltaic to investigate the effect of three-dimensional structure on generated power output. The study was made using and comparing the two and three-dimensional geometries and the findings were analysed and reported.

1 INTRODUCTION

Energy is the backbone of the global economy – an essential input to basically all of the goods and services of the modern world. A stable and reasonably priced energy supplies are fundamental to maintaining and improving the living standards of people anywhere in the world [1]. Energy is the oxygen of the economy as it is a primary factor to the building and maintenance of the factories and cities that provide us jobs, goods and services, and enjoyment of the amenities that make life more comfortable and enjoyable at homes - they all depend on the provision and availability of heat, light and power [2].

Renewable energy is an integral part of the energy industry and thus have a part to play in economic development. Record has it that Renewable energy in 2010 supplied an estimated 16.7% of global final energy consumption out of which estimated 8.2% came from modern renewable energy making up of hydropower, wind, solar, geothermal, biofuels, and modern biomass. This represents about 12.2% of the total renewable energy [3]. At present, Solar energy currently does little to abate GHG emissions, but it will play an important and ever-growing role in climate-friendly scenarios in the coming decades, given that necessary support incentives are given for aggressive and results-oriented researches that will lead to development of highly efficient and reliable energy sources [2, 4-8].

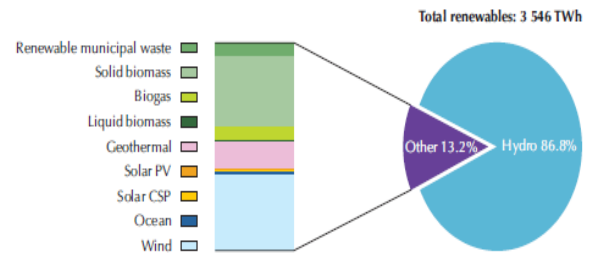


Figure 1: Renewable electricity generation in 2007 [[4]]

Renewable energy is still crawling on its knee and much is still required to be done or achieved on it in order for it to be relevant to economic development. Considering the solar energy as a percentage of the total renewable energy, then, solar energy requires breakthrough research.

The concern associated with solar power is that its costs is still much higher than conventional energy technologies, notwithstanding the fact that its costs had been reduced considerably in the recent past [9]. Furthermore, its low power output efficiency coupled with its adverse performance in bad weather conditions are not to its advantage at all. Considering the present development of renewable energy, in particular solar, renewable energy cannot be used in isolation for now as a major drive for any appreciable impact on the economy. How then can solar energy have meaningful contribution to the world's economic development?

2 IMPROVING SOLAR POWER GENERATION

Solar energy generation technologies are diverse in application - from Photovoltaic Solar Panels (PV) to Concentrated Photovoltaic Systems, Dye Sensitized Solar Cell, Solar Thermoelectric Effect and Concentrated Solar Power [10, 11]. The various photovoltaic technologies are at different levels of maturity, each with a significant potential for improvement. Notwithstanding the different PV technologies that have emerged to improve upon solar energy output, the conversion efficiency of the solar radiation into useful energy is yet to improve appreciably [12, 13]. Hence research activities are still on-going in order to address this problem.

Research has proved that three-dimensional photovoltaic (3DPV) structures can increase the generated energy density (energy per footprint area,

Wh/m^2) in a linear proportion to the configuration height, for a given day and location. These 3D structures includes shapes like a cubic box open at the top, a funnel-like shaped cubic box, a sphere, a parallelepiped or any other 3D shape and are in principle found capable of doubling the daily energy density [14, 15]. In addition, 3DPV technology by Fibonacci number method involves the arrangement of the individual solar cells of the three-dimensional PV module in a leaf-like manner or be stacked in a vertical configuration. The arrangement revealed that such a modular design has the benefits of having each solar cell receive the reflected light from the other cells, thereby maximizing power generation per installation area [16, 17]

Continuous and sustained research, development and demonstration efforts are necessary over the long term in order to accelerate efficient power generation, cost reductions and the transfer of the current mainstream technologies to the industry, to develop and improve medium-term cell as well as system technologies, and to design novel concepts that will bring them to industrial use [18]. In this paper, the design, modeling and simulation of thermal Photovoltaic (TPV) technology in energy generation is considered. The findings in this work could provide an insight that could help other researchers avoid long term switching cost in the future and make the solar systems performance more efficient, economical and stable [19, 20].

In this paper, a COMSOL Multiphysics model for a Photovoltaic/Thermal (PV/T) system is used to simulate the electromagnetic waves produced by the Sun through solving Maxwell's equations in both the two and three-dimensions in order to study the effect of the three-dimension with respect to the two-dimensions. Besides that, COMSOL is used in studying the material absorption capabilities and calculating the material absorption coefficient using its refractive index. In line with the above, a thermal analysis for the PV module and the Heat Transfer with Surface-to-Surface Radiation interface are used to investigate the influence of operating conditions (flame temperature) on system efficiency and the output power in a typical TPV system

For improved system efficiency, it is preferable to use high-efficiency PV cells, but this can be quite expensive. Hence, in order to reduce system costs, engineers and researchers try to work with smaller-area PV cells and then use mirrors to focus the radiation on them. However, there is a limit to how much one can focus the beams. If the radiation intensity becomes too high, the cells could overheat and burn out [21, 22]. Therefore, engineers have to try to optimize system geometry and operating conditions to achieve maximum performance and power output at minimum material costs.

2.1. Methodology

In PVT system, forced convection occurs on the top surface of the PV panel as well as through the pipe mounted to the backside of the panel. Therefore, the total convective heat transfer is a combination of the heat transfer at the surface of the panel and the heat transfer from the flowing water in the pipe. The engineering analysis software being used in this study, COMSOL Multiphysics version 5.1 contains an open system laminar flow and appropriate heat transfer physics package, capable of modeling the convective heat transfer in the water pipe on the backside of the PV panel, hence the thermal model was implemented in COMSOL environment. The defined geometric definitions, dimensions and meshing were initiated in 2D model using COMSOL Multiphysics. The 2D model of the thermal PV was then directly converted into the 3D model to ensure precise translation. The thermal properties for the various material used in the model are given in Tab. 1 and they remain the same even for the 3D modeling.

COMSOL Multiphysics is a powerful interactive environment for modeling and solving all kinds of scientific and engineering problems. It contains detailed features and techniques to assist the user throughout while working in the COMSOL Desktop environment as presented in Fig. 1.

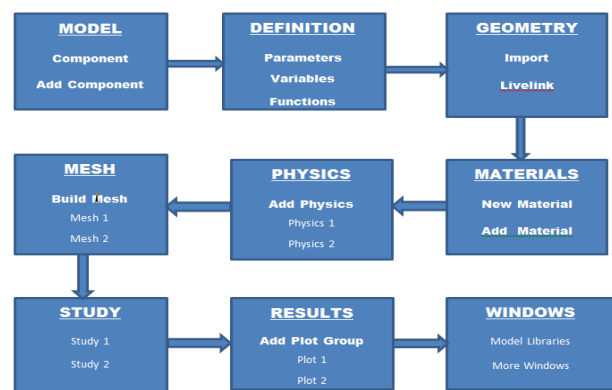


Fig. 1: Basic modeling workflow in COMSOL Multiphysics

It provides steps and detailed information on how to build model geometries (3D, 2D-Axisymmetry, 2D, 1D-Axisymmetry and 1D), how to create a mesh for the finite elements, how to create parameters and variables used within a model, how to add the physics and material properties, and how to solve and display the results

2.2. List of Materials used

The materials described below were used for the modeling and simulation and these include the emitter (with a specific temperature, T_{heater} , on the inner boundary), the mirrors, the PV cells and the insulation.

Radiation is taken into account on all boundaries and the insulation has low emissivity value, while the PV cells and the emitter are with high emissivity values with the mirror having the least. The materials definitions and properties were added from COMSOL Multiphysics library of materials.

3 MODEL DEFINITION

The PV cells convert some portion of the irradiation to electricity instead of heat. The materials properties are as described in Tab. 1 and the global definition for the heater is as described in Tab. 2. Heat sinks are placed on their inner boundaries to simulate this effect by accounting for a boundary heat source, q . The heat transfer equations for solid and fluid domains are defined in equations (1) and (2) respectively. The irradiation flux is G in (W/m^2) while η_{pv} is the PV cell's voltaic efficiency. This efficiency of the PV cell depends on the local temperature, with a maximum of 0.2 at 800 K as defined in (3).

Tab. 1: Material properties summary

Component	k [W/(m·K)]	ρ [kg/m ³]	C_p [J/(kg·K)]	ε
Emitter	10	2000	900	0.99
Mirror	10	5000	840	0.01
PV Cell	93	2000	840	0.99
Insulation	0.05	700	100	0.1

Fig. 2 depicts the materials make-up, the geometry and dimensions of the system under study. In order to reduce the temperature, the PV cells are water-cooled on their back side, at the interface with the insulation.

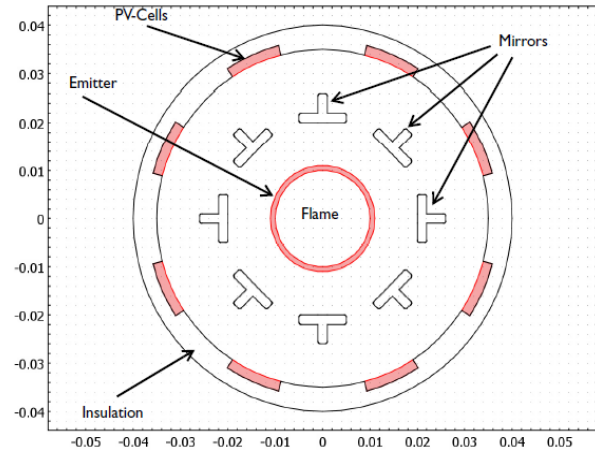


Fig. 2: Materials make-up, the geometry and dimensions of the Thermal PV System

The heat transfer equations for solid and fluid domains are described by equations (1) and (2) respectively

$$q = -k \nabla T \quad (1)$$

$$\rho C_p u \cdot \nabla T + \nabla \cdot q = Q + Q_{tesd} \quad (2)$$

$$\eta_{pv} = \begin{cases} 0.2 \left[1 - \left(\frac{T}{800 K} - 1 \right)^2 \right] & T \leq 1600 K \\ 0 & T > 1600 K \end{cases} \quad (3)$$

where:

ρ = the density,

C_p = specific heat capacity,

T = temperature, t is the time,

k = thermal conductivity,

q = heat transferred by conduction,

Q = internal heat generation,

u = fluid velocity

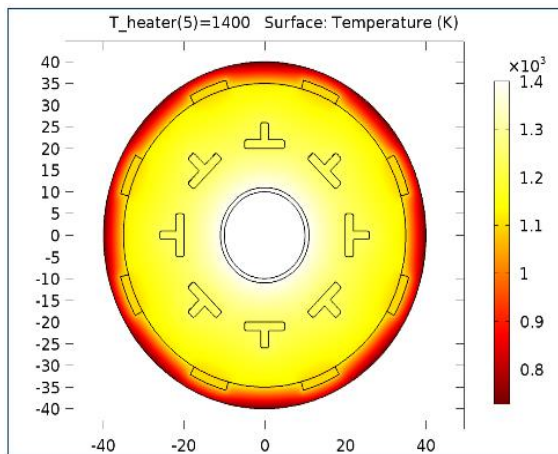


Fig. 3a: T_heater(5)=1400 Surface: Temperature (K) - 2D Thermal PV

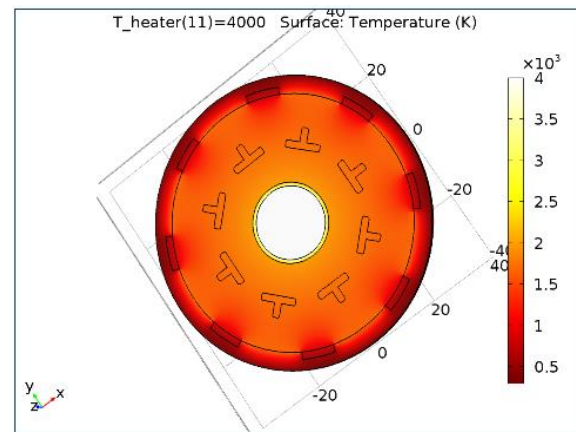


Fig. 3a: T_heater(11)=4000 Surface: Temperature (K) - 2D Thermal PV

3.1. 2D TPV Model

The model calculates the stationary solution for a range of emitter temperatures (1000 K to 2000 K) using the parametric solver. The PV temperature range is as described in Tab. 3 and the results obtained show that the device experiences appreciable temperature distribution that changes with operating conditions. Further parameters changes were effected. The results are post-processed and various graphs plotted, analysed and discussed.

Table 2: Global definition for the Heater

Parameters Name	Expression	Value	Description
T_heater	1000 [K]	1000 K	Temperature, emitter inner boundary

Table 3: Global definition for the PV Cell

Name	Expression	Unit	Description
eta_pv	$\text{if}(T < 1000[\text{K}], 0.2 * (1 - (T/500[\text{K}] - 1)^2), 0)$		Voltaic efficiency, PV cell
q_out	$\text{ht.Gm} * \text{eta_pv}$	W/m ²	Electric output power

3.2. 2D TPV Model Conversion to 3D TPV Model

The 3D TPV model was created directly from the already existing 2D TPV by browsing and exporting it into a new 3D geometry of COMSOL Multiphysics version 5.1 engineering software, using the same material properties. This ensures that the modeling parameters for 2D and the 3D of the TPV could be compared directly one to the other.

The same procedure of modeling and simulation was similarly followed for the 3D and the obtained results were post-processed and various graphs plotted, analysed and discussed. However, the number of points generated for the domain, boundaries, edges and points in the 3D modeling were quite more in the 3D than in 2D.

The device experiences an appreciable temperature distribution (stationary) with an emitter temperature of 2000 K that varies with operating conditions.

4 ANALYSIS AND RESULTS

The results obtained for the 2D and 3D simulations are expressed graphically. For the 2D model, the heater temperature was operated between 1000 K and 2000 K at local temperature range of 600 K and 1800 K as shown in Fig. 3a. For the 3D model, the heater temperature was between 2000 K and 4000 K at local temperature range of 450 K and 800 K as shown in Fig. 3b.

As the upper plot in Fig. 4a for the 2D model shows, the PV cells reach the temperature of approximately 1800 K, while that of 3D in Fig. 4b is at PV temperature of about 840 K. The PV temperature in 2D is significantly higher than their normal maximum operating temperature of 1600 K, above which their photovoltaic efficiency is zero as seen Fig. 5a. The heater temperature for the 2D cannot exceed 1400 K otherwise the efficiency becomes zero. The maximum PV efficiency attained is about 20% in Fig. 5a. For the 3D model, the PV cell temperature is 800 K at the heater temperature is as high as 3800 K. That means high temperature is quite safe for the cells in 3TPV as they do not get overheated as seen in Fig. 5b. The maximum efficiency obtained is also about 20% at Heater temperature of 2500 K. The output power in the 2D model in Fig. 6a is 7500 W/m² at 1200 K Heater temperature above which the output power drops sharply while that of the 3D model is 2200 W/m² at 3700 K and is fairly stable to Heater temperature of about 3800 K as shown in Fig. 6b.

From the analysis of these results, modeling the thermal PV system in 2D would be able to deliver more power output than going for the 3D model, provided care would be taken not to exceed Heater temperature of 1200 K.

Furthermore, the 2D model shall be more cost-effective than the 3D model as some money would be saved from the cost of fuel that would be needed to operate the heater to higher temperature of about 4000 K.

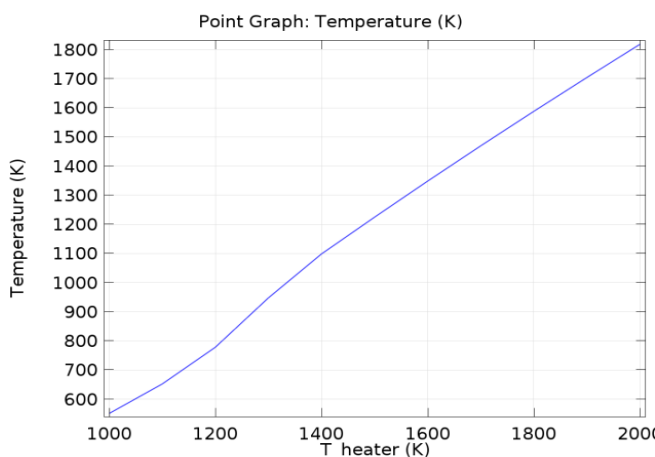


Fig. 4a: PV Cell Temperature for 2D Thermal PV Model

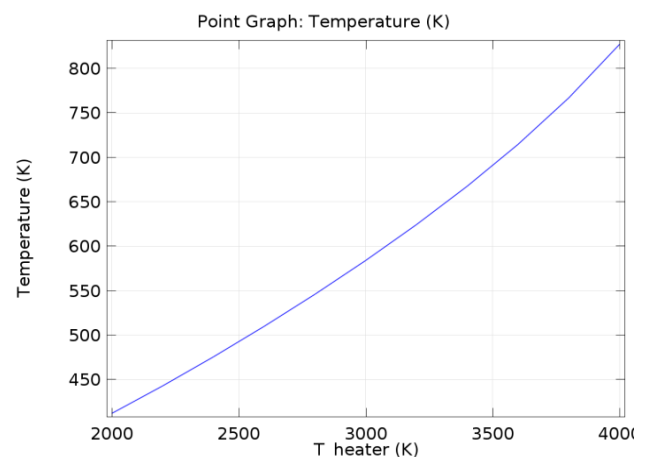


Fig. 4b: PV Cell Temperature for 3D Thermal PV Model

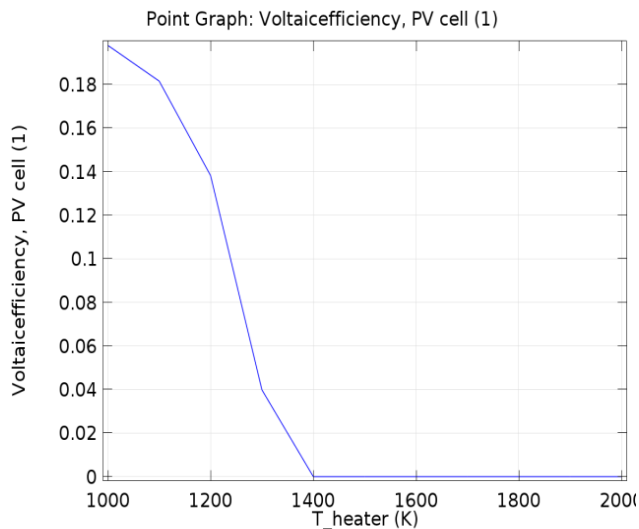


Fig. 5a: Voltaic Efficiency for 2D Thermal PV Model

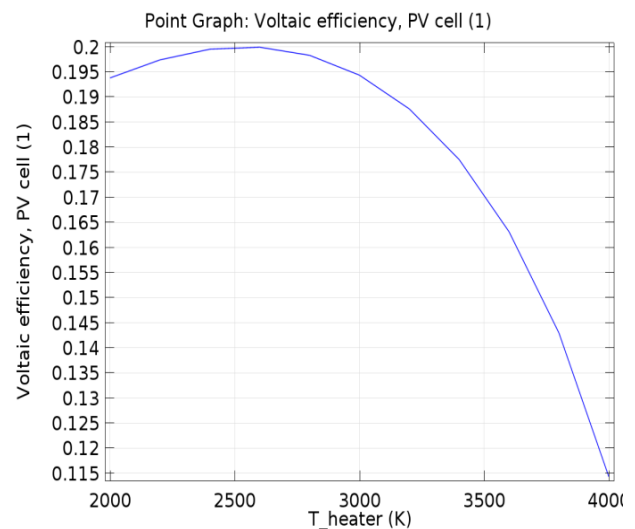


Fig. 5b: Voltaic Efficiency for 3D Thermal PV Model

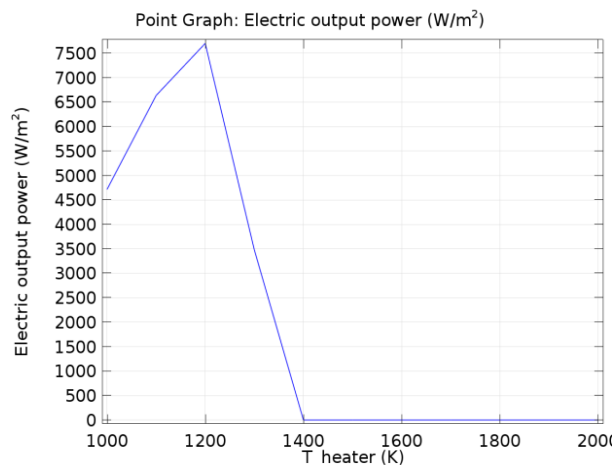


Fig. 6a: Electric Output Power for 2D Thermal PV Model

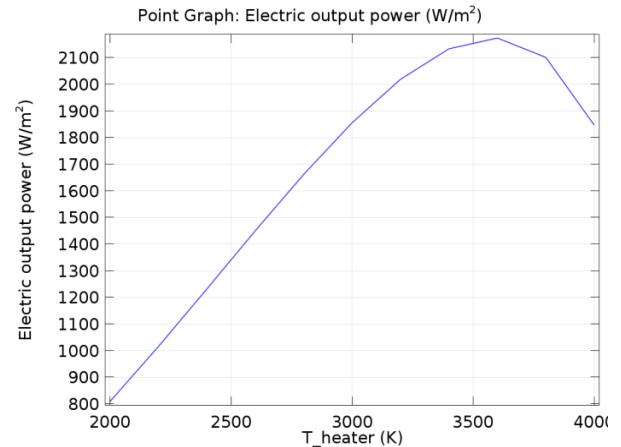


Fig.: 6b Electric Output Power for 3D Thermal PV Model

5 CONCLUSION

In conclusion, the choice of 2D thermal modeling over that of 3D modeling will be more favourable to contributing and impacting solar power generation on economic growth and therefore more preferable. This decision is for the simple fact that the design focus is to obtain optimum power output at the minimum cost possible. The benefit of this thermal modeling is that it can shortcut the prototype development time, optimize the operating conditions for the finalized TPV device and eliminates undue operational cost. It could also serve as a reference for Researchers who are interested in thermal solar energy and for Stakeholders who want to invest or work in this field.

6 REFERENCES

- [1] E. Yildirim, Ş. Saraç, and A. Aslan, "Energy consumption and economic growth in the USA: Evidence from renewable energy," *Renewable and Sustainable Energy Reviews*, vol. 16, pp. 6770-6774, 12// 2012.
- [2] S. G. Daniel Yergin, Daniel Bachman, John Larson, Ted Lyman, Nancy Meyer and Jan Randolph, "Energy for Economic Growth - The Oxygen of the Economy," World's Economic Forum 2012.
- [3] E. Martinot and J. Sawin, "Renewables global status report. Renewables 2012 Global Status Report, REN21," ed, 2012.
- [4] OECD/IEA, "Solar Energy Perspectives in Renewable Energy," in *Renewable Energy Technologies*, ed. Printed in Luxembourg by Imprimerie Centrale: IEA Publications, 9, rue de la Fédération, 75739 Paris Cedex 15, 2011, p. 1.
- [5] C. J. Dai Qinghui, "Improving the efficiency of solar photovoltaic power generation in several important ways," *IET Conference Publications*, pp. 1-3, 2009 2009.
- [6] M. Yahyavi, M. Vaziri, and S. Vadhva, "Solar energy in a volume and efficiency in solar power generation," in

- Information Reuse and Integration (IRI), 2010 IEEE International Conference on*, 2010, pp. 394-399.
- [7] M. Gharghi, B. Hua, G. Stevens, and S. Sivorththaman, "Three-dimensional modeling and simulation of p-n junction spherical silicon solar cells," *Electron Devices, IEEE Transactions on*, vol. 53, pp. 1355-1363, 2006.
- [8] M. Usama Siddiqui, A. F. M. Arif, L. Kelley, and S. Dubowsky, "Three-dimensional thermal modeling of a photovoltaic module under varying conditions," *Solar Energy*, vol. 86, pp. 2620-2631, 9// 2012.
- [9] R. Govinda, K. Lado, A. Patrick, and T. Govinda, "A review of solar energy: markets, economics and policies," *Policy Research Working Paper Series*, 2011.
- [10] I. E. Agency, "Solar Energy Perspectives," IEA Publications, 9, rue de la Fédération, 75739 Paris Cedex 15 978-92-6412-457-8, 2011 2011.
- [11] Y. Chu, "Review and comparison of different solar energy technologies," *Global Energy Network Institute (GENI), San Diego, CA*, 2011.
- [12] Q. Dai and J. Chen, "Improving the efficiency of solar photovoltaic power generation in several important ways.pdf," pp. 1-3, 2009.
- [13] N. M. Maricar, E. Lee, H. K. Lim, M. F. Sepikit, M. R. M. Maskum, M. F. Ahmad, *et al.*, "Photovoltaic solar energy technology overview for Malaysia scenario," in *Power Engineering Conference, 2003. PECon 2003. Proceedings. National*, 2003, pp. 300-305.
- [14] N. F. Marco Bernardi, Jin H. Wan, Rachelle Villalon and Jeffrey C. Grossman, "Solar Energy Generation in Three Dimensions," *The Royal Socceity of Chemistry*, pp. 1-5, 2012.
- [15] M. B. a. J. C. G. Bryan Myers, "Three-Dimensional Photovoltaics," *American Institute of Physics*, vol. 96, pp. 071902 - 071902-3 16 February 2010.
- [16] A. Yuji and T. Yachi, "A novel photovoltaic module assembled three-dimensional," in *Photovoltaic Specialists Conference (PVSC), 2010 35th IEEE*, 2010, pp. 002811-002816.
- [17] M. Yahyavi, M. Vaziri, and S. Vadhva, "Solar Energy in a Volume and Efficiency in Solar Power Generation.pdf," 2010.
- [18] D. Mills, "Advances in solar thermal electricity technology," *Solar Energy*, vol. 76, pp. 19-31, 1// 2004.
- [19] P. Valera, A. Esteban, M. de los Reyes Carrillo, R. Osuna, P. Menna, R. Gambi, *et al.*, "Solar energy: comparative analysis of solar technologies for electricity production," in *Photovoltaic Energy Conversion, 2003. Proceedings of 3rd World Conference on*, 2003, pp. 2482-2485 Vol.3.
- [20] I. E. Agency, "Solar Thermal Electricity - Technology Roadmap," p. 52, 2014 2014.
- [21] E. Skoplaki and J. Palyvos, "On the temperature dependence of photovoltaic module electrical performance: A review of efficiency/power correlations," *Solar energy*, vol. 83, pp. 614-624, 2009.
- [22] R. P. Collins, "Hybrid Solar Panel Efficiency Optimization with a Labyrinth Fin Arrangement," Rensselaer Polytechnic Institute, 2013.

The Extraction of Power and Fresh Water from the Ocean off the Coast of KZN utilizing Ocean Thermal Energy Conversion (OTEC) Techniques

M. Gumede^{*1} and F. D'Almaine².

¹Durban University of Technology, Durban, 4001, South Africa

*Email: makhosonkegumede32@gmail.com

*Email: dalmaine@dut.ac.za

Abstract: This paper investigate the available data on thermal energy resource around KZN south coast region (Port Edward) which ultimately can be used for generation of electrical power. The geographical location of this region is very suited to the development of renewable energy (Ocean thermal electrical conversion). OTEC is a promising renewable energy technology and has other applications such as the production of freshwater, seawater air-conditioning, marine culture and chilled-soil agriculture. The site of Port Edward is naturally suited for the establishment of alternate energy collection sources like OTEC. Since Port Shepstone lies just beneath the tropic of cancer and on the shore of the Indian ocean, the two vital elements: constant sunlight and large coastal areas needed for OTEC can easily be found in this region, hence by experimental design we want to prepare an OTEC site for a new and original development.

Keywords: OTEC and open cycle

1 INTRODUCTION

The new technologies for the extraction of valuable ocean resources have become significant following the increased scarcity of other relatively cheap sources i.e. oil [1], [2]. Furthermore global warming has shown the disadvantage of using other fossil fuels such as coal [3], [4], [5]. Any alternative to coal fired power station in South Africa would lead to a large saving in carbon based pollution.

A white paper emanating from the Department of Minerals and Energy indicates that the South African Government is committed to ensuring that renewable energy including wind, solar and ocean energy becomes a significant part of its energy portfolio. Considering the above and further categorizing ocean energy into its component parts viz. ocean currents, tidal currents, wave energy, thermal energy and energy derived from differences in salinity this paper examines the ocean thermal resource.

According to L.A. Vega (2003), the amount of solar energy absorbed by the oceans in a year is equivalent to at least 4000 times the amount currently consumed on earth. For an OTEC efficiency of 3%, in converting ocean thermal energy to electricity, we would need less than 1% of this renewable energy to satisfy the world demand [6]. The aim of this research is to identify an optimum site (or sites) off the coast of KwaZulu natal suitable for developing OTEC generating station on the shore.

2 BACKGROUND

OTEC technology was established in the 1880s. In 1881, Jacques Arsene d'Arsonval was the first to

introduce the term OTEC in France [23]. Georges Claude tried to build the first OTEC plant open-cycle shore at Matanzas Bay, Cuba [24]-[29]. The system generated 22-kilowatt (gross) of electricity with a low pressure turbine [23]. In 1956, French researchers designed a 3 MW plant for Abidjan on Africa's west coast [23], [30]-[32]. The plant was never completed because of competition with low-cost hydroelectric power.

In 1979, the Natural Energy Laboratory of Hawaii Authority (NELHA), started a closed-cycle floating OTEC experimental plant. The system produced 53 kW of gross power and 18 kW of net power. Hilbert Anderson and James (1962) focused on increasing component efficiency. In 1967 they originated their new "close-cycle". In 1982, Toshiba and TEPC (Japans) contributed to the development of the technology [13].

In 1993 NELHA installed an open-cycle OTEC plant at Kea hole Point, Hawaii, producing 50 kW of net power, surpassing the record set by the Japanese system (1982) [8],[14]. A 210 kW (gross) open cycle shore based OTEC plant facility off the island of Hawaii was designed built and run successfully by NELHA (US) for a period of 6 years (1993-1998) by the US Government with a net power production of 100 kW [15],[16]. This OTEC plant would also provide 1.25 Millions of Gallons per day of potable water to the base [8], [15], [17].

A private U.S. company has proposed the building of a 10 MW OTEC plant at Guam. Lockheed Martin's Alternative Energy Development team is currently in the final design phase of a 10 MW closed cycle OTEC pilot system which will become operational in Hawaii by 2012-2013 [18],[8]. This system is being designed to

expand to 100 MW commercial systems in the near future

Table 1: OTEC operation theory

Year	Task	Year	Task
1881	D'Arsonval (France) conceived of OTEC	1982	Kyushu Electric Power Co. succeeded with 50KW of power at Kagoshima, Japan
1926	Claude (France) began research for commercial use	1985	Saga University completed 75KW of power plant
1933	Claude built power generating ship (1200KW)	1988	Inauguration of Organization of OTEC Study (Japan)
1964	Anderson's proposal for a power generation in the sea	1989	Agency of Science and Technology (Japan) began study of utilization of Deep Sea Water (DSW) off Toyama in Japan Sea
1970	OTEC research results examined by the board of investigation into new power generation methods (Japan)	1990	IOA (international OTEC Association) was organized by Taiwan, USA and Japan)
1973	Saga University, Japan, commenced research study on OTEC technology-power generation	1993	210KW open cycle system completed in Hawaii
1974	OTEC research commenced as part of Sunshine project plan (Japan)	1994	Saga University constructed a new cycle plant
1974	ERDA project (USA) commenced	1995	Saga University started on testing new 4.5KW cycle plant (Kalina cycle, Uehara cycle)
1974	First international OTEC conference (USA)	1997	Signing of collaboration memorandum with National Institute of Ocean Technology (NIOT), India, on OTEC study
1977	Saga University succeeded with 1kw of power	2003	Saga University Completed 30KW multipurpose OTEC Plant in Imari, Saga, Japan
1979	Mini-OTEC (USA) succeeded with 50KW of power	2005	OPOTEC (Organization for the Promotion of the Ocean Thermal Energy Conversion) established in Saga, Japan
1980	Saga University performed experiments on the sea, off Shimane in Japan Sea	2013	A 1.25 MW OTEC power plant was built in Japan's Kumejima Island, which supplies 10% of the island's total electricity consumption
1981	Tokyo Electric Power Co., succeeded with 120KW of power on Nauru		



Fig 1: 210-Kilowatt Open-Cycle Ocean Thermal Energy Conversion Experimental Apparatus.

3 OCEAN THERMAL ENERGY CONVERSION

OTEC is a promising renewable energy which exploits the thermal gradient between warm, surface

seawater and deep, cold seawater to generate electrical energy. The ocean thermal energy conversion (OTEC) concept uses the temperature differences; about 22 °C, between the warm surface water 26 °C and the cold deep water 4 °C to operate a heat engine [4].

Table 1: OTEC operation theory		
Resource	Transfer Function	Product
T (°C)	Public Domain	kWh; H ₂ O, AC
Ocean Volume	24/7	

AC= air conditioning, H₂O = water, kWh = kilowatt-hour, m = meter, T = temperature.

OTEC has the least environment impact and is capable enough to provide thousands of megawatt which are urgently required in developing countries [5]. OTEC usually incorporates a low- temperature Rankin cycle engine which boils a working fluid such as ammonia to generate a vapour which turns the turbine to generate electricity, and then is condensed back into a liquid in a continuous process. Compared to other ocean energy technologies, OTEC has some advantages. It can

provide continuous base-load power, and it can also provide fresh water for irrigation or drinking water and cold water for refrigeration.

Resources for ocean thermal energy conversion are larger than for any other type of ocean energy. It is estimated that between 30000 and 90000 TWh/ year of power are extractable without having any negative impacts on the thermal characteristics of the oceans [7], [8], and [9]. The main resources can be found in the area between 30° S and 30° N, which means in tropical seas [10]. Figure 2 shows the temperature difference between water depths of 20 m and 1000 m, and the potential of areas showing a temperature gradient of more than 20°C.

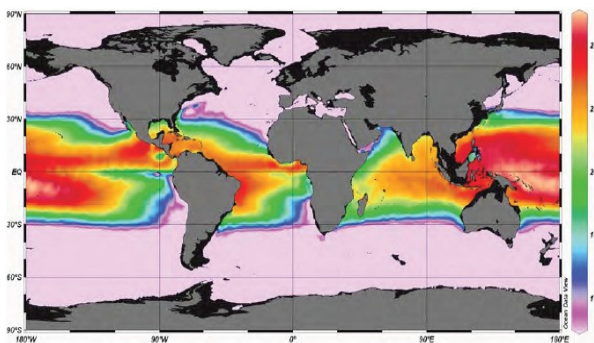
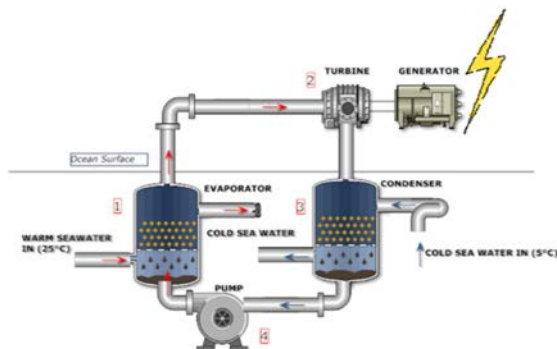


Fig 2: Worldwide Average Ocean Temperature Differences between 20m- and 1000-Metre Depths [11].

There are three main types of OTEC plant: open-cycle, closed-cycle and hybrid systems. Considering the above, this paper examines the thermal energy resource and, more specifically, the Ocean Thermal Energy Conversion (open close cycle) off the coast of KwaZulu Natal. In an open-cycle plant, warm surface water is flash evaporated and drives a turbine (Fig 3). Cool water is used to condense the vapour again. The condensed desalinated water can be used for various purposes (e.g. drinking water, irrigation). The cold water that has been pumped from the sea can feed air-conditioning systems after it has been used in the condenser. In addition, the cold seawater can also be used in aquaculture, since it is rich in nutrients.



1= Evaporator (25°C), 2 = Turbine, 3 = Condenser, 4 = Pumps.
Fig. 3: Simplified open-cycle OTEC process flow diagram

4 WATER MASSES IN PORT SHEPSTONE

The oceanic waters of the East Coast and within the proposed Exploration Area comprise numerous water masses. Surface waters are a combination of Tropical Surface Water from the South Equatorial Current, and Subtropical Surface Water from the mid-latitude Indian Ocean which regularly enters the Agulhas Current from the east at depths of between 150 m and 300 m. The surface waters are warmer than 20° C and of a lower salinity than the South Indian Ocean, Equatorial Indian Ocean and Central water masses present below. Conversely, the characteristics of surface water do vary due to isolation and mixing (Schumann, 1998). Water temperatures along the East Coast vary seasonally, and in relation to the distance offshore. The temperature increases offshore towards the centre of the Agulhas Current.

Gründlingh reported that seasonal variation (warmest in the Southern Hemisphere summer and coldest in winter) only occurs in the upper 50 m of the water column, with only insignificant variations occurring deeper down. According to Schumann (1998), water temperatures within the Agulhas Current may exceed 25° C in summer and 21° C in winter, and are enduringly warmer than the water inshore and offshore of the Current. Water temperatures also decrease with depth, with temperatures at 50 m below the surface being 4° C cooler than the surface in summer, and 1° C cooler in winter. Water under the current is, however, significantly cooler.

5 EFFICIENCY IN OTEC PLANT SITE

Equation 3 (Carnot's equation) was utilised to get an idea about the efficiency of OTEC. It is worth noting that while the temperature difference between the topmost and bottommost layers in tropical regions of the ocean is appreciable when compared with other ocean environments, it is still quite small. The ideal Carnot efficiency (η) for a heat engine operated with a heat source [8].

$$\text{Carnot equation: } w = \frac{T - T_o}{T} \cdot Q \quad (3)$$

Here,

W - Work obtained (energy)

T - Surface water temperature (K)

To - The deep water temperature (K)

Q - Thermal value

Typical example for tropical climate:

T - 25 °C

To - 4 °C

$$w = \frac{(273 + 25) - (273 + 4)}{(273 + 25)} \cdot Q = \frac{21}{298} \cdot Q$$

$$= 7. \% \cdot Q$$

6 AVAILABLE OCEAN POWER IN KZN SOUTH COAST

The site of KwaZulu natal (Port Shepstone) is naturally suited for the establishment of Ocean Thermal Energy Conversion (OTEC). OTEC are abundant in southern parts of the case-study region that southern parts. The south coast of KwaZulu Natal, the continental shelf is relatively close to the shoreline, approaching to within 3km in some places. More importantly, the steep drop in water depth up to 3000 metres can makes this worthy of research for ocean thermal energy conversion.

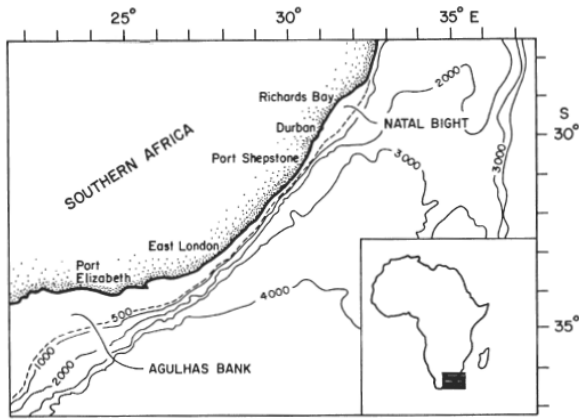


Fig 4: Map of Northern KZN coastline showing vicinity of 3000m depth contours to shore.

Maritime maps of the coast of KZN indicate possible sites where continental shelf is suitable close the shore. The University of Hawaii has tested this technology and an important by-product of this process is fresh water which could be interesting to a water-stressed country such as South Africa. Although OTEC might be viable for KZN, it is known to be very expensive.

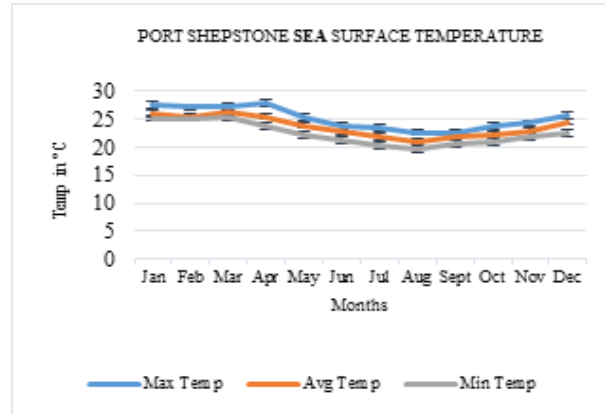


Fig 5: Port Shepstone sea temperature profile.

7 PRINCIPLE OF OTEC

OTEC is a heat engine with a low boiling point 'working fluid', e.g. ammonia, operating between the 'Cold' temperature T_c of the water pumped up from substantial depth and the 'hot' temperature,

$$T_h = T_c + \Delta T \quad (1) \quad , \text{ of the surface water}$$

The working fluid circulates in a closed cycle, accepting heat from the warm water and discharging it to the cold water through heat exchangers. As the fluid expands, it drives a turbine, which in turn drives an electrical generator. The working fluid is cooled by the cold water, and the cycle continues.

Alternative 'open cycle' systems have seawater as the working fluid, but this is not recycled but condensed, perhaps for distilled 'fresh' water; the thermodynamic principles of the open cycle are similar to the closed cycle. In an idealized system with perfect heat exchangers, volume flow Q of warm water passes into the system at temperature T_h and leaves at T_c (the cold water temperature of lower depths). The power given up from the warm water in such an ideal system is [12]:

$$P_o = \rho c Q \Delta T \quad (2)$$

8 OTEC ECONOMICS

OTEC power will be cost effective if the unit cost of power is comparable with other power plants such as wave, hydro and diesel. Conversely, it is imperative that all capital costs and continuing maintenance or service costs are included so that the individual technologies are compared on a level playing field.

Work carried out by Dr Luis Vega and his team in Hawaii has shown that for plants of the 1 MW range, the unit cost is considered comparable, see graph below.

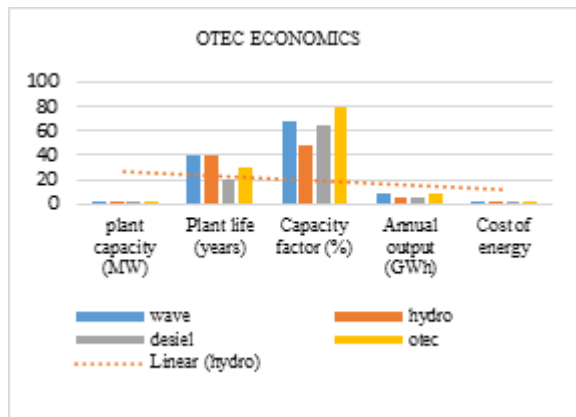


Fig 6: OTEC economics.

9 RESEARCH METHODOLOGY

In order to meet the objective of this research, the following technical approach will be evaluated:

- A site suitable for OTEC will be identified.
- Surface and sub-surface temperatures at this site will be measured over a period.
- A model of a suitable OTEC plant will be developed and simulated at DUT.

A physical small scale model will be built in the DUT laboratory and measurements will be compared with the simulation. A further step will be a pilot plant near Port Shepstone.

10 CONCLUSION

Fossil fuels will dry up in the near future, thus alternative energy sources have to be identified. OTEC power sources are gaining popularity across the world due to the demand of renewable energy. This report is aimed at presenting the proposal of OTEC on the KZN South Coast. Off the south coast of KwaZulu Natal, the continental shelf is relatively close to the shoreline, approaching to within 3km in some places. More importantly, the steep drop in water depth up to 3000 metres can make this worthy of research for ocean thermal energy conversion.

11 REFERENCES

- [1] Toossi, Reza. *Energy and the Environment: Resources, Technologies, and Impacts*. Verve Publishers, 2009.
- [2] Tooke, Mike. "Oil Peak—A Summary." April Retrieved 2 (2005).
- [3] Szpunar, Carole Bryda, and Jerry L. Gillette. *Environmental externalities: Applying the concept to Asian coal-based power generation*. Argonne National

Laboratory, Environmental Assessment and Information Sciences Division, 1993.

- [4] Hall, D. O., and J. House. "Biomass: an environmentally acceptable fuel for the future." *Proceedings of the Institution of Mechanical Engineers, Part A: Journal of Power and Energy* 209.3 (1995): 203-213.

- [5] Hansen, Ulf. "Technological options for power generation." *The Energy Journal* (1998): 63-87.

- [6] Kobayashi, Hiroki, Sadayuki Jitsuvara, and Haruo Uehara. "The present status and features of OTEC and recent aspects of thermal energy conversion technologies." *24th Meeting of the UJNR Marine Facilities Panel, Honolulu, HI, November*. 2001.

- [8] Harrison, Sara. "Ocean Thermal Energy Conversion." Submitted as coursework for Physics 240, Stanford University, November 28, 2010

- [7] Charlier & Justus (1993). Charlier, R. H. & Justus, J. R. (Eds): *Ocean Energies: Environmental, Economic and Technological Aspects of Alternative Power Sources*.

- [8] Fujita *et al.* (2012). Fujita, R., Markham, A. C., Diaz, J. E. *et al*: *Revisiting Ocean Thermal Energy Conversion*. *Marine Policy* 36 (463–465). DOI: 10.1016/j.marpol.2011.05.008.

- [9] Semmari *et al.* (2012). Semmari, H., Stitou, D. & Mauran, S.: *A Novel Carnot-Based Cycle for Ocean Thermal Energy Conversion*. *Energy* 43 (361–375). DOI: 10.1016/j.energy.2012.04.017.

- [10] Nihous (2010). Nihous, G. C.: *Mapping Available Ocean Thermal Energy Conversion Resources around the Main Hawaiian Islands with State-of-the-Art Tools*. *Journal of Renewable and Sustainable Energy* 2 (043104). DOI: 10.1063/1.3463051.

- [11]

- [12] *Ocean thermal energy conversion (OTEC)*, Chapter 14

Aquifer Underground Pumped Hydroelectric Energy Storage in South Africa

S.Y. Khan^{1*} and I.E. Davidson²

¹University of KwaZulu-Natal, Discipline of Electrical Engineering, Durban 4001, South Africa

² University of KwaZulu-Natal, Eskom Centre of Excellence in HVDC Engineering, Durban 4001, South Africa

*Email: sykconsult@gmail.com

Abstract: This paper proposes the use of underground pumped hydroelectric energy storage as a technical alternative for bulk energy storage in South Africa, as a potential contribution to the constrained electricity network with environmental and economic benefits. The use of aquifers for the implementation of this proposed scheme is explored. South Africa has large amounts of groundwater as well as transboundary aquifers which may be used for the proposed energy storage systems. An extensive literature review and document analysis of this alternative is carried out and results obtained from preliminary studies and assessment are presented and discussed.

1 INTRODUCTION

An aquifer or groundwater UGPHERS is a system whereby an integrated pump-turbine unit located below the surface of the aquifer water level is used to either pump water to the surface reservoir or to generate electricity when water is released from the surface reservoir back in to the aquifer [18].

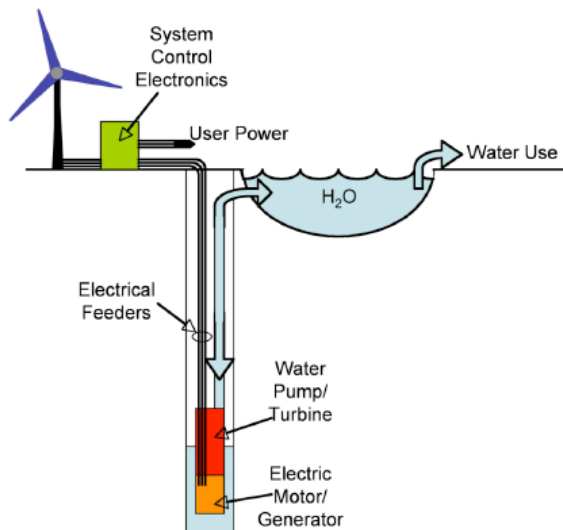


Figure 1 – Aquifer UGPHERS system concept illustration [5]

The weight of the water in the surface reservoir is stored as gravitational potential energy with respect to the aquifer. The volume of the surface reservoir and head height is directly proportional to the energy storage needs required by the application. This also dictates the

positioning of the integrated pump-turbine unit whereby for large UGPHERS installations, it is located below the lower reservoir in an effort to avoid water hammering issues [18].

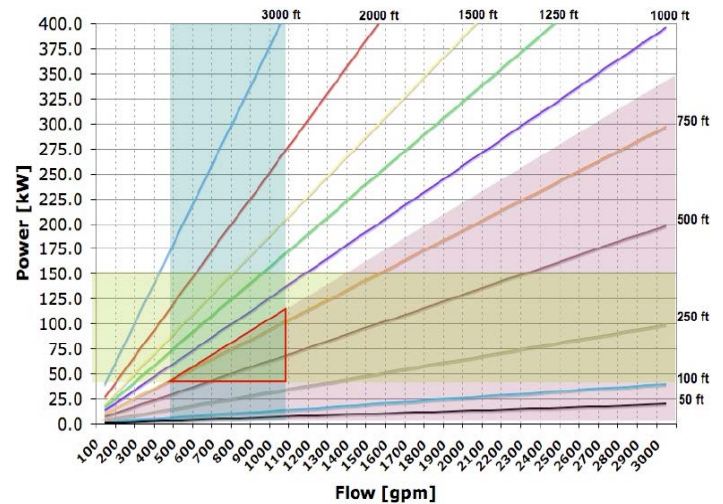


Figure 2 – Relationship of flow and head to power output and expected ranges [5]

A primary requirement of the aquifer UGPHERS system is a deep well to the groundwater. The well is constructed to meet flow demands by using an adequately sized water tube together with a conduit for the electrical feeders. The size and construction of the well directly impacts the size of the integrated pump-turbine assembly that can be installed and the water flow capacity [18]. This ultimately impacts the sizing of the system for maximum power. Where an unconfined aquifer is not deep enough, a well may be dug to interface with deeper confined aquifers [18]. Water flow capacity can be maximized through well modifications such as radial or horizontal.

2 AQUIFERS IN SOUTH AFRICA

South Africa is underlain by over 80% with relatively low-yielding, shallow, weathered and/or fractured rock aquifer systems. However, in the northern and southern parts of the country consisting of dolomitic and quartzitic aquifer systems, along with primary aquifers along the coastline, groundwater is able to be abstracted at relatively high rates [26]. Aquifer consumption in South Africa contributes only around 15% of the total volume of water consumed in the country [1].

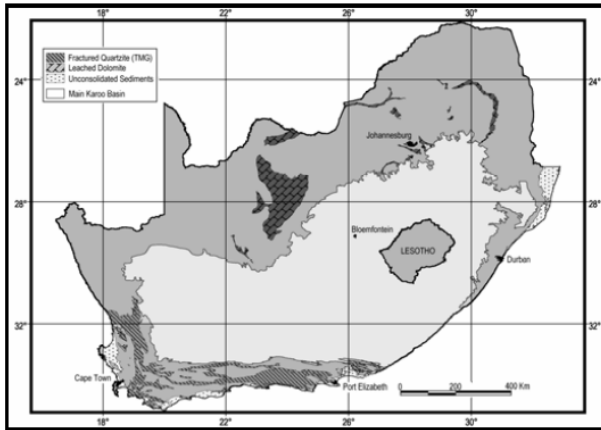


Figure 3 – Distribution of significant secondary and primary aquifer systems in South Africa [25]

The South African mean annual groundwater recharge volume from rainfall is 30,520Mm³ which is estimated using various empirical rainfall versus recharge relationships and the chloride-mass-balance [26]. The abstraction of the maximum volume (m³) of groundwater per unit area per annum without continued long term declining water levels, is known as the Groundwater Resource Potential (GRP). For South Africa, this ranges from a maximum of 47,727 Mm³/a to as low as 7,536 Mm³/a [26]. The Average Groundwater Exploitation Potential (AGEP) which utilizes the total volume of groundwater available for abstraction under normal rainfall conditions is recommended for water resource planning purposes. This is estimated at 19,073 Mm³/a which declines to 16,253 Mm³/a during drought conditions in South Africa [26].

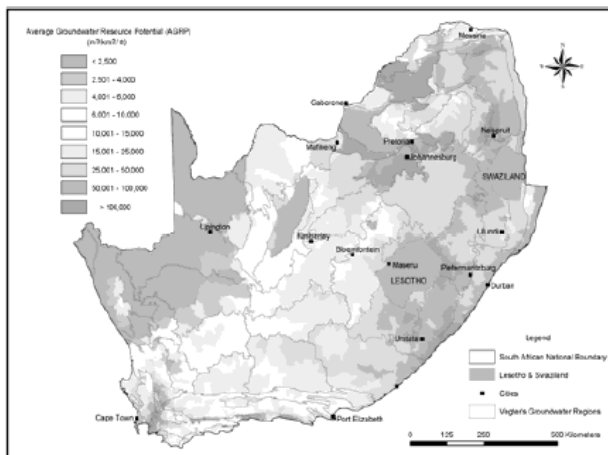


Figure 4 – Average groundwater resource potential for South Africa [25]

The Department of Water Affairs (DWA) South Africa has developed a series of aquifer maps based on aquifer classification, vulnerability and susceptibility, to provide the appropriate information to national water resource managers and planners. These maps are a vital source of information that can be used for identification

of aquifers suitable for implementation in a UGPHEs scheme. It is evident from Table 1 that an aquifer classified as a major aquifer system is the most suited for UGPHEs application although other important factors including the head height will also need to be considered.

South Africa has developed three aquifer maps namely aquifer classification, aquifer vulnerability and aquifer susceptibility to assist with the Reconstruction and Development Programme (RDP) in South Africa of which the role of groundwater resources is of high importance [24]. The aquifer classification map indicates the aquifer classification system of South Africa. The aquifer vulnerability map indicates the tendency or likelihood of contamination of the aquifer, while the aquifer susceptibility map includes both the aquifer vulnerability and aquifer classification, while also indicating the relative ease with which a groundwater body can be potentially contaminated.

The South African aquifers are classified as tabulated as follows [24]:

Aquifer Type	Description
Sole Source Aquifer System	An aquifer for which there is no available alternative source and which is used to supply 50% or more of domestic water for a given area.
Major Aquifer System	Able to support large abstractions with high water quality. Highly permeable formations with probable presence of fracturing.
Minor Aquifer System	Variable water quality with limited extent. Potentially fractured rocks with formations of variable permeability.
Non-Aquifer System	Negligible permeability regarded as not containing groundwater that can be in exploited. Water quality may not be good enough for use.
Special Aquifer System	Classified as special following due process by the Ministry of Water Affairs.

Table 1 – Aquifer system management classification

The maps indicate an abundance of aquifer systems in South Africa with certain potential to develop selected aquifer systems for UGPHEs schemes. These selected aquifer systems are discussed further in an effort to identify key knowledge gaps and to ascertain the extent and suitability of the aquifers for the implementation of UGPHEs schemes.

2.1. The South African Transvaal aquifer

The South African Transvaal aquifer (SATVLA) is one of the world's largest subterranean sedimentary aquifers with an area approximated from the Geosciences map of 500km by 250km and incorporating the area from Springs and Brakapan east of Johannesburg; to Lenasia south of the city; Zuurbekom, Carltonville and Magaliesberg on the West Rand; Kuruman in the Northern Cape and even as far as parts of Botswana as shown in Figure 5 [2], [7].

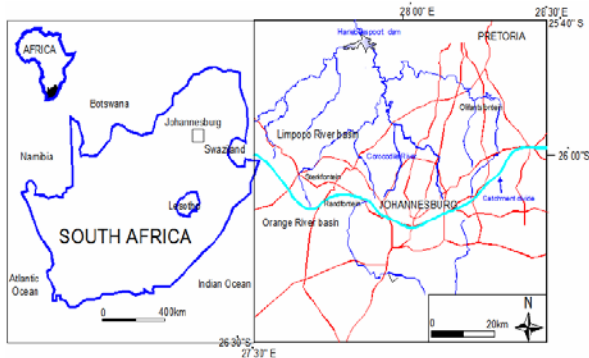


Figure 5 – Location map of the SATVLA area, Johannesburg at the north central part of the country (east-west solid line is water divide between Limpopo and Orange Rivers, blue lines represent streams and red lines represent roads) [2]

The area also includes the Bushveld Igneous Complex (BIC) shown in Figure 6 which is the world's largest known layered intrusion with an estimated area of 182,000 km² and hosts many billions of Terra liters of subterranean groundwater [7].

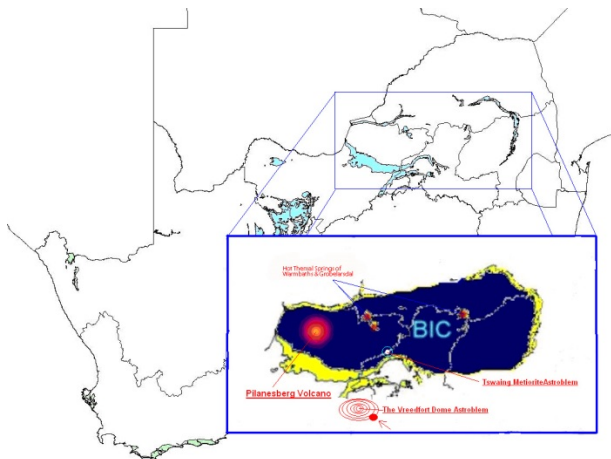


Figure 6 – Location map of the Bushveld Igneous Complex – [7]

The mean annual rainfall in the SATVLA area is between 600 to 700mm/year [14] and is an extremely important contribution to the groundwater recharge. The dolomitic aquifers have been identified as highly productive aquifers in the region [4], [6]. Mining in the

area pumped out 110ML/day of groundwater until 2008 [10] which has not affected the shallow groundwater. Recharge of the shallow aquifer is increased considerably due to surface discharge of pumped water to dams, reservoirs and local streams [21].

The SATVLA area holds much promise for the development of UGPHEs schemes from an aquifer vastness, availability of groundwater and groundwater recharge perspective. Further investigations will have to be carried out to ascertain depth to groundwater related to the head of the UGPHEs scheme which is a vitally important parameter in determining the power output.

2.2. The Karoo aquifer system

The main Karoo basin covers an area of approximately 500,000km² [3]. The upper shallow aquifer system (less than 300m deep) of the Karoo is relatively well understood due to detailed research over the years and groundwater exploration while deeper formations (greater than 300m to greater than 4,000m deep) and associated groundwater occurrences are relatively unknown. The occurrence of a continuous aquiferous zone from the shallow aquifer zone to the deep formations is considered highly unlikely [22].

The existence of undetected deep aquifers is a strong possibility which can only be confirmed by exploration drilling. Deep (up to 4,692m) exploration drilling in the 1960s and 1970s did indicate isolated occurrences of deep, saline groundwater in the Karoo formations and fresher underground water from the underlying Witteberg Group [27]. The Karoo area has only two known hot springs that are estimated to be more than a 1,000m deep [22].

The key knowledge gaps for the Karoo aquifer system is the presence or otherwise of deep aquifers, the hydraulic interconnectivity between the shallow aquifer and deeper formations, and the existence of upward migration of deep groundwater [22].

2.3. Aquifer under seabed

Deep Water Research (DWR) which is a marine research company from Cape Town in South Africa, has identified the possibility of fresh water aquifers occurring in significant volumes off the coast of South Africa, more specifically approximately 60km off Port Elizabeth which they claim could be very long term and consistent. Years of oil and gas exploration in the area revealed the possible existence of fresh water aquifers at least a kilometre beneath the seabed where a potentially abundant supply of fresh water was intersected by an exploration well off Port Elizabeth [13]. DWR has reached an agreement with oil and water exploration and sea spring water companies, to explore sites on the south, east and west coasts of South Africa including Namibia for the existence of aquifers under the seabed.

While this looks very promising from a water supply perspective for potable water and human consumption, the adaptation of an onshore aquifer system for use as a

UGPHES scheme will surely be challenging if at all possible. This is an area that will require future research from a technical and financial viability perspective.

3 AQUIFERS IN NAMIBIA

The Cuvelai-Etosha Basin (CEB) in central-northern Namibia represents the largest aquifer system in Namibia known as the Ohangwena II that extends into Southern Angola covering an area of approximately 100,000km². It is part of the much larger Kalahari basin which covers parts of Angola, Namibia, Zambia, Botswana and South Africa and is estimated to be able to supply the north of Namibia for 400 years at current rates of consumption [17], [19]. The Ohangwena II aquifer however, is still in the process of being investigated in terms of its sustainable capacity as well as the sustainable management of the transboundary resource. A project known as Groundwater Management in the North of Namibia (GMNN), is currently underway that will ultimately provide the relevant information and procedures required towards sustainable management and utilization of the aquifer [15].

The CEB which is the most densely populated area in Namibia and hosting approximately half the country's population relies on an inefficient open canal and pipeline network from Angola to provide drinking water supply for most of the population in the CEB. There is no doubting the potential of such a vast aquifer to be used for UGPHEs scheme/s, however utilizing the Ohangwena II vast aquifer for anything other than a sustainable resource for human consumption and other basic social needs will certainly be a challenge in itself considering the fact that Namibia is the most arid African nation south of the Sahara [17].

Namibia's electrical generating capacity is currently severely constrained. This is due in part to the fact that South Africa supplies nearly half of Namibia's electricity [11]. Namibia is currently actively embarking on ways to increase the electricity generation capacity in the country through the investigation of solar photovoltaic, wind, hydro and gas technologies. However, utilizing the Ohangwena II vast aquifer for a UGPHEs scheme can benefit both Namibia and South Africa in the long term. The GMNN project will provide important technical details which can be used to further investigate the aquifer's suitability for implementation of a UGPHEs scheme from a technical, economic and political perspective.

4 TRANSBOUNDARY AQUIFERS SHARED BY SOUTH AFRICA

Transboundary groundwater or shared aquifer resources refers to a volume of groundwater shared between two or more countries. Approximately 5,116km of land border and seven aquifers is shared

between South Africa and Namibia, Botswana, Zimbabwe, Mozambique, Swaziland and Lesotho [8]. The seven transboundary aquifers shared with South Africa have been identified for further investigation with only one of the seven consisting of only shallow and local aquifers [23].

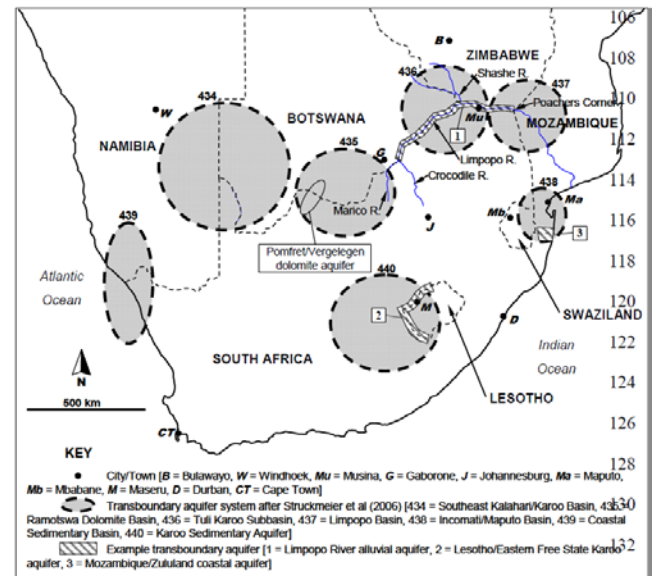


Figure 7 – Map of seven transboundary aquifer systems shared with South Africa [23]

Whilst this is encouraging from an electrical perspective through the development of UGPHEs schemes and cross boundary wheeling of electricity, the actual management of transboundary groundwater may be a challenge. Further consideration needs to be given to the nature of the aquifer itself in terms of its hydraulic properties which includes transmissivity.

4.1. Limpopo river alluvial aquifer

The northern border between Botswana, Mozambique, Zimbabwe and South Africa is created by the Limpopo River as shown in Figure 7. The irregular adjoining floodplain resulting from unconsolidated alluvial deposits that fill the river channel constitutes an international transboundary aquifer [8], [16]. The aquifer is currently tapped by using wellpoint systems, hand-dug wells, infiltration galleries and boreholes generally located on the river bank [12]. The town of Musina meets its municipal water demand by tapping off the Limpopo river through the use of boreholes and wellpoints while agricultural use by neighboring countries from this aquifer is negligible. Resource-poor farmers consider this aquifer as a valuable source of water that allows during dry periods for meeting and sustaining irrigation demands [8].

It must be noted that there is no evidence of the potential of this aquifer being fully explored. Deeper exploratory wells need to be drilled in an effort to understand the full extent of the aquifer and its potential to be adapted for use in a UGPHEs scheme.

4.2. Lesotho/Eastern Free State Karoo aquifer

The boundaries between western Lesotho and south-eastern South Africa are created by the Caledon, Senqu, Mokare/Clarens and Makhaleng rivers. The aquifer characteristics for this area comprise of the Burgersdorp Formation, Molteno Formation and the Elliot Formation [8].

The Burgersdorp Formation is a semi-confined to confined aquifer able to support borehole yields $<0.5\text{l/s}$ and with a mean transmissivity of $20\text{m}^2/\text{d}$ [9], [27]. Many boreholes have been dug in this formation and used for the supply of water to small rural communities and farms [8].

The Molteno Formation is classified as a semi-confined aquifer with an average transmissivity of $20\text{m}^2/\text{d}$ and is regarded as the best aquifer in this region. The borehole yields from the Molteno Formation are $>3\text{l/s}$ while there is also spring discharges as high as 0.5l/s [9], [27].

The Elliot Formation is an aquifer that is classified as poor due to its compact nature. The underlying Molteno Formation and aquifer are often in hydraulic continuity. The borehole yields are only 0.9l/s and transmissivity is $5\text{m}^2/\text{d}$ [9], [27].

The low borehole yields and low transmissivities of the transboundary aquifers between Lesotho and South Africa make this area unfavorable for the application of UGPHEs technology. It must be noted as with the Limpopo River Alluvial Aquifer, that there is no evidence of the potential of this aquifer being fully explored with the drilling of deeper exploratory wells [8]. Deeper drilling could yield aquifers with improved transmissivities and well yields suitable for implementation in a UGPHEs scheme.

4.3. Mozambique/Zululand Coastal aquifer

The Zululand coastal plain extends approximately 250km south of the Mozambique and South Africa border along the northeast coast of South Africa, and approximately 1,000km north towards and into Mozambique. Groundwater recharge figures for this area range between 5% and 18% across the plain [20]. Land use for this area which is sparsely populated, is limited to subsistence farming, nature conservation, irrigation farming using surface water and limited commercial forestry. The South African side of the boundary has a confirmed north-south groundwater divide which continues north towards and into Mozambique with the flow separated towards the coast (east) and the Pongola River (west) [8].

A primary aquifer with shallow groundwater levels underlies the entire plain giving rise to fresh water lakes which are used to support the water requirements of the majority of the local population. The aquifer capacity is estimated to be able to support a population $>500,000$ with the Uloa Formation being the most productive aquifer with transmissivity $>1,000\text{m}^2/\text{d}$ and borehole yields up to 30l/s [8]. Limited information is available

for the aquifer on the Mozambique side of the border however it is expected to be similar to that on the South African side [8].

It is envisaged that the demand for groundwater from this aquifer is unlikely to be significantly expanded in the future with little to no risk of competition for water between South Africa and Mozambique thereby negatively impacting the available water resources [23].

The vastness of this aquifer and excellent transmissivity presents a very promising opportunity for the development of a UGPHEs scheme that could greatly contribute towards the dire need for generating capacity in South Africa. There are however many parameters that will first need to be investigated to ascertain the viability of such a scheme in this area. One such parameter is the head height which is directly proportional to the power output. Due to the shallow groundwater levels, this could prove to be an obstacle.

5 COST ESTIMATE OF AN AQUIFER UGPHEs SYSTEM

There is no existing installation of an aquifer UGPHEs system hence the available associated costs are only an estimation. A cost estimation has however been done for a relatively small scale aquifer UGPHEs system rated at 50kW and providing 300kWh of energy, to be implemented for use in an irrigation scheme. The cost estimation was done for two different sites each with existing wells, however the second site requires well modifications. The cost estimate was performed in 2001 hence a 15% escalation per annum is added in an effort to align the cost with current economies of scale. The cost for site1 is estimated at R40,815,077 and for site2 R46,652,534 [18]. It is clear that the costs are dependent on site characteristics which include the availability of a surface reservoir, the amount of possible well modification that may be required, transmissivity and depth to water [18].

6 CHALLENGES FOR IMPLEMENTATION OF AQUIFER UGPHEs IN SOUTH AFRICA

The biggest challenge for the implementation of aquifer UGPHEs systems in South Africa is the fact that UGPHEs systems are a fairly new technology with regards to the number of global installations, hence practical experience in this field from an engineering and equipment perspective is limited. Extensive research and experimentation into the actual equipment and components of an aquifer UGPHEs system and their suitability for South African climatic and geological conditions will have to be undertaken prior to any specific installation being implemented.

7 CONCLUSION

South Africa has an abundance of groundwater which can be used for UGPHEs systems. The use of trans-boundary aquifers will be of benefit to South Africa, its neighbouring countries and to the South African Power Pool (SAPP). Future steps such as: identification of pilot sites, performing geological sampling tests, analyzing transmissivities, storativity values, field testing with a centrifugal pump/turbine to determine pump/turbine efficiencies and flow, should be conducted.

8 REFERENCES

- [1] "A Groundwater Mapping Strategy for South Africa," Directorate Geohydrology publication, Department of Water Affairs and Forestry, August 2002, Pretoria, South Africa.
- [2] Abiye, T.A., Mengistu, H., and Demlie, M.B., "Groundwater Resource in the Crystalline Rocks of the Johannesburg Area, South Africa," *Journal of Water Resource and Protection*, April 2011, Vol.3, pp.199-212, DOI:10.4236/jwarp.2011.34026.
- [3] Adams, S., Titus, R., Pietersen, K., Tredoux, G., and Harris, C., "Hydrochemical characteristics of aquifers near Sutherland in the Western Karoo, South Africa," *Journal of Hydrology*, January 2001, Vol.241, Issues 1-2, pp.91-103, DOI:10.1016/S0022-1694(00)00370-X.
- [4] Barnard, H.C., "An Explanation for the 1:500 000 Hydrogeological Map of Johannesburg 2526," Department of Water Affairs and Forestry, 2000, Pretoria, South Africa.
- [5] Barnes, F.S., and Levine, J.G., *Large Energy Storage Systems Handbook*, Taylor & Francis Group, LLC, Florida, USA, 2011.
- [6] Breidenkamp, D.B., and Xu, Y., "Perspectives on Recharge Estimation in Dolomitic Aquifers in South Africa," In: Xu, Y., and Beekman, H.F., Eds., *Groundwater Recharge Estimation in Southern Africa*, UNESCO, p.207, 2003.
- [7] Buchanan, M., "Hypothesizing the Highly Fractured Defuse South African Transvaal Aquifer (SATVLA)," IUCN WCPA Task Force on cave and Karst, Cave Research Organization of South Africa – CROSA, Hampshire, United Kingdom, 2005.
- [8] Cobbing, J.E., Hobbs, P.J., Meyer, R., and Davies, J., "A critical overview of transboundary aquifers shared by South Africa," *Hydrogeology Journal*, 2008, Vol.16, Issue 6, pp.1207-1214, DOI:10.1007/s10040-008-0285-2.
- [9] Davies, J., "Lesotho Lowlands water supply feasibility study – Hydrogeology," *British Geological Survey Report CR/03/176C*, 2003.
- [10] "Derivation of a Numerical Model for a Cumulative Water Balance of the Central Rand Basin," Ferret Report, Council for Geosciences, 2005, Pretoria, South Africa.
- [11] "Electricity Supply and Demand Management Options for Namibia. A Technical and Economic Evaluation," Ministry of Mines and Energy, Renewable Energy and Energy Efficiency Capacity Building Programme (REEECAP), March 2008 (<http://www.reeei.org.na/admin/data/uploads/Namibia%20Electricity%20Supply%20Demand%20Options.pdf>).
- [12] Hobbs, P.J., and Esterhuysen, C.J., "A preliminary evaluation of the groundwater resources of the upper Limpopo River valley, North West Transvaal," Department of Water Affairs and Forestry Report Gh3278, 1983, Pretoria, South Africa.
- [13] "Huge ancient freshwater aquifer under seabed," Posted by: Saving Water SA – partnered with Water Rhapsody conservation systems, May 2010, (<http://www.savingwater.co.za/2010/05/10/08/huge-ancient-freshwater-aquifer-under-seabed/>)
- [14] "Hydrology of Upper Crocodile River Sub-System," Department of Water Affairs and Forestry (DWAF), Report No. PA200/00/1492, Vol.1-2, DWAF, 1992, Pretoria, South Africa.
- [15] Jager, M., "Namibia – Groundwater Management in the North of Namibia," Technical Cooperation with Namibia Kalahari: Hydrogeology and Sedimentology of the Cuvelai-Etosha Basin, Southern African Science Service Centre for Climate Change and Adaptive Land Management (SASSCAL), BGR Projects, Project-No.: 2013.2472.2, (http://www.bgr.bund.de/EN/Themen/Zusammenarbeit/TechnZusammenarb/Projekte/Laufend/Afrika/2011_2013-2472-2_Namibia_Grundwassermanagement_en.html).
- [16] Jean Boroto, R.A., "Limpopo River: steps towards sustainable and integrated water resources management," Regional Management of Water Resources, Proceedings of a symposium held during the Sixth IAHS Scientific Assembly at Maastricht, The Netherlands, July 2001, IAHS Publication No.268, 2001.
- [17] Lohe, C., and Houben, G., "TC Namibia: Groundwater for the North of Namibia," BGR Projects, (http://www.bgr.bund.de/EN/Themen/Wasser/Projekte/laufen d/TZ/Namibia/ceb_fb_en.html).
- [18] Martin, G.D., "Aquifer Underground Pumped Hydroelectric Energy Storage," MScEng Thesis, Department of Electrical and Computer Engineering, University of Colorado at Boulder, Colorado, USA, December 2007.
- [19] McGrath, M., "Vast aquifer found in Namibia could last for centuries," *Science and Environment*, BBC World Service, 20 July 2012, (<http://www.bbc.com/news/science-environment-18875385>).
- [20] Meyer, R., Talma, A.S., Duvenhage, A.W.A., Eglington, B.M., et al., "Geohydrological investigation and evaluation of the Zululand Coastal Aquifer," Water Research Commission Report 221/1/01, 2001, Pretoria, South Africa.
- [21] "Numerical Modelling of Seepage Potential at Three Ingress Areas of the Central Rand Basin of the Witwatersrand Goldfields," Africa Geo-Environmental Services (AGES) Report, Council for Geosciences, 2005, Pretoria, South Africa.
- [22] Rosewarne, P., Woodford, A., Goes, M., Talma, S., O'Brien, R., Tredoux, G., Esterhuysen, C., Visser, D., and van Tonder, G., "Recent Developments in the Understanding of Karoo Aquifers and the Deeper Underlying Formations," Karoo Groundwater Expert Group, 2013, (http://gwd.org.za/sites/gwd.org.za/files/01_Peter%20Rosewarne_Recent%20Developments%20in%20the%20Understanding%20of%20Karoo%20Aquifers.pdf).
- [23] Struckmeier, W.F., Gilbrich, W.H., Gun, Jvd., Maurer, T., et al., "WHYMAP and the World Map of Transboundary Aquifer Systems at the scale of 1: 50 000 000," Special Edition for the 4th World Water Forum, Mexico City, March 2006, BGR, Hannover and UNESCO, Paris.
- [24] Vegter, J.R., "Groundwater Resources of South Africa: An explanation of a set of national groundwater maps," Water Research Commission Report No. TT 74/95, Pretoria, South Africa, 1995.
- [25] Vegter, J.R., Seymour, A.J., and Simonis, M., "Groundwater Resources of the Republic of South Africa. A Set of 7 Maps," Water Research Commission and Department of Water Affairs and Forestry, 2005.
- [26] Woodford, A., Rosewarne, P., and Girman, J., "How Much Groundwater Does South Africa Have?" National Groundwater Resource Assessment 2 (GRA 2), SRK Consulting and Department of Water Affairs and Forestry, South Africa, 2005, (http://www.srk.co.za/files/File/newsletters/groundwater/PDFs/1_A_Woodford.pdf).
- [27] Woodford, A.C., and Chevallier, L., "Hydrogeology of the Main Karoo Basin: Current Knowledge and Future Research Needs," WRC Report No. TT 179/02, 2002, Pretoria, South Africa.

DESIGN ASPECTS OF A MAGNETICALLY GEARED PERMANENT MAGNET MACHINE WITH AN OUTER-STATOR

PM Tlali, JDG van der Merwe, R-J Wang, S Gerber *

* Department of Electrical & Electronic Engineering, Stellenbosch University, Private Bag X1, Matieland 7602, South Africa, E-mail: 15894215@sun.ac.za; rwang@sun.ac.za; sgerber@sun.ac.za

Abstract: Magnetically geared permanent magnet (MGPM) machines are an attractive alternative for wind power applications because of their merits over other machine types. A prototype MGPM machine was constructed in a recent study. Although both theoretical and finite element methods predict high efficiencies on the design, the prototype's practical measurements differ to them by a significant margin due to mechanical problems experienced in the manufacturing process. This paper discusses some of the design improvements done on a previously designed and built machine prototype. It focuses mainly on the mechanical aspects of it, and has shown that careful consideration on that sector can help improve its efficiency.

Key words: Magnetically geared machines, permanent magnets, magnetic flux modulation.

1. INTRODUCTION

The constant increase in the demand of energy worldwide coupled with environmental concerns has been the major drive for rapid development in renewable energy power generation. Amongst others, wind energy has become one of the most promising renewable energy sources. There exists several different generator drive-train configurations for harvesting wind power. Two most common configurations are mechanically geared medium or high speed generator system and low speed directly driven generator (DDG) systems.

Although the mechanically geared high speed generator system enjoys the advantages such as an improved efficiency [1,2], compact and light weight, the reliability of the mechanical gearbox is still a major concern. Since the mechanical gearbox relies on physical teeth meshing mechanism for torque transfer, it is noisy and subject to wear. In addition, in the event of overload conditions, mechanical gearbox can easily be damaged. Therefore, condition monitoring and frequent maintenance are necessary, which is a challenging task especially in the offshore plants. On the other hand, the DDGs are more reliable and have less complex mechanical structure. But, the size and weight of the DDGs increase rapidly with high power rating [3].

As an alternative to the two common configurations currently implemented, magnetically geared permanent magnet (MGPM) machines have recently been proposed for wind power application [4–6]. The MGPM machines are essentially a combination of a coaxial flux modulated magnetic gear (CMG) and a conventional medium to high speed permanent magnet synchronous machine (PMSM). This enables a direct connection of the low-speed high-torque turbine onto the machine without an external gearbox. The whole system potentially can be light weight and small volume. Furthermore, because of the non-contact gearing principle of CMG, MGPM machines

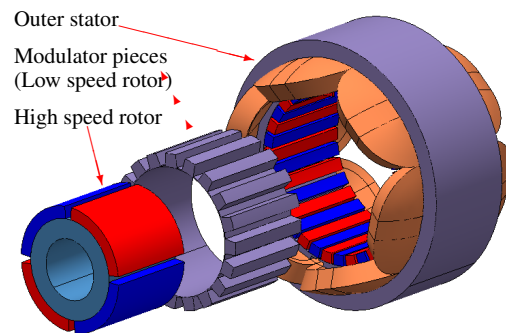


Figure 1: Outer-stator MGPM machine structure.

boast several advantages such as [4–6]: (i) quiet operation, (ii) inherent overload protection, (iii) little maintenance, and (iv) potential for high torque density and efficiency.

In an attempt to practically validate the potential merits of such a machine, the authors had previously designed and built a prototype of an outer-stator MGPM (OS-MGPM) machine for use in the wind power generation [7]. The machine showed satisfactory output characteristics as expected, and exhibited good efficiency from the finite element analysis (FEA) based computer simulations. It was however found that the mechanical losses had the major contribution to the machine's total losses. Moreover, the stator winding had a lower than designed fill factor due to difficulties in the winding process.

The main aim of this paper is to revisit the design and construction of the previously built OS-MGPM machine prototype. It is envisaged that with the improvement on both the electromagnetic and mechanical design aspects, the overall machine's losses can be significantly reduced resulting in improved efficiency.

2. MACHINE DESCRIPTION

The system layout of the OS-MGPM machine investigated is shown in Fig. 1. It consists of the following main components: the high-speed inner PM rotor, ferromagnetic low-speed flux modulator and an outer-stator with tooth concentrated non-overlapping windings. A set of PMs is also glued to on the inner surface of the stator.

In the same manner as in CMGs, the working principle of the OS-MGPM machine is based on the fact that the ferromagnetic pole-pieces modulate the magnetic fields from both sets of PMs. Then the PMs on either side of the modulator engages with the field harmonics of the same order to their pole-pair number. In this way, the magnetic torque is transferred between the two PMs sets and the modulator, two of them running at different speeds while one is fixed, forming the gearing action. Furthermore, the fundamental field harmonics from the inner PM rotor together with the stator PMs' modulated fields interacts with the stator windings to produce electrical power. For the magnetic gearing phenomena to take place, the number of PM pole pairs on the inner- and outer-rotors, p_h and p_l respectively, and the modulator pole-pieces (q_m) are related by the following equation [8, 9]:

$$q_m = p_l \pm p_h \quad (1)$$

And with the other set of stationary PMs fixed on the stator, the speed gearing ratio G_r between the inner PM rotor and the flux modulator is given by:

$$G_r = \frac{\omega_h}{\omega_m} = \frac{q_m}{p_h} \quad (2)$$

where ω_m and ω_h are modulator and inner rotor's speeds, respectively.

The employed electromagnetic design environment, main machine dimensions and other parameters are kept the same as in the previous prototype [7]. Most of the proposed changes were focused on the mechanical aspects of this machine. For the sake of clarity, the redesigned machine's key specifications are provided in Table 1.

3. DESIGN IMPROVEMENTS

3.1 Shaft Design

The shaft design process included an examination into the following elements: material selection, geometric layout, stress and strength, deflection and rigidity and vibration due to natural frequency. Critical areas were located and analyzed so as to meet the requirements of the shaft supported elements.

The shaft layout of the machine consists of the modulator and inner rotor coupled by the bearings as shown in Fig. 2, together with its free body diagram. To avoid complications imposed by this layout on static force analysis, the shaft components were grouped as one since the force will act simultaneously on both of them. But

Table 1: Machine key parameters.

	Parameter Description	Value
OS-MGPM	Outer diameter	140 mm
	Stack length	50 mm
	Air-gap lengths	0.7 mm
	Magnet remanence	1.39 T
	PM relative perm.	1.05
	Lamination material	M470-50A
Generator	Number of slots	6
	Number of poles	4
	Number of phases	3
	Winding layers	2
	Rated frequency	52.5 Hz
	Winding factor	0.866
Gear	Inner rotor pole-pairs	2
	Fixed PM pole-pairs	19
	Modulator pole-pieces	21
	Gearing ratio	10.5
	Rated speed	150 rpm

the torsional stress analysis due to rotational forces is done on the modulator shaft alone. The combination of the resultant forces acting on the shaft components and the machine's total weight obtained from 3D FEA is represented by F_y in the diagram. Then the corresponding resultant forces (F_{Ay} and F_{By}) at points A and B can be calculated by making use of equilibrium principle. In the diagram, the point 'C' is identified as the most vulnerable shaft point because it has the smallest diameter, and both torsional and bending stresses are more effective on that region. The selected shaft material was cold

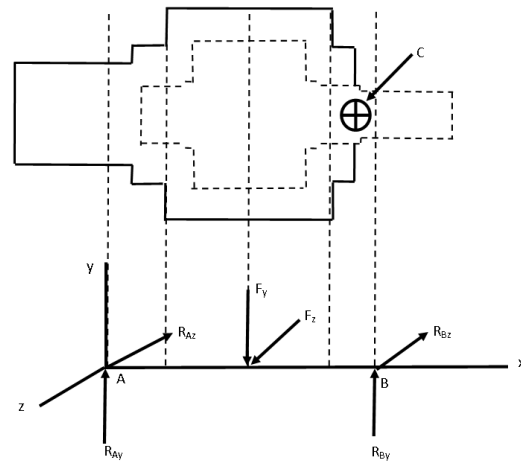


Figure 2: Combined shaft free body diagram.

drawn mild steel, grade 080M40, with the properties given in Table 2. Different types of stresses have been combined into mid-range von Mises stress equations, which is customized for shaft applications. For a solid and circular cross-section shaft with inertial geometry terms

Table 2: Shaft material properties

Hardness HB	108	Modulus of elasticity E (GPa)	895
Tensile strength (MPa)	700	True strain at fracture	0.96
Fatigue strength exponent b	-0.12	Fatigue strength coefficient σ_f (MPa)	465
Fatigue ductility coefficient ϵ_F	0.22	Fatigue ductility exponent c	-0.66

incorporated, these equations are expressed as [10]:

$$\sigma_a = K_f \frac{32M_a}{\pi d^3} \quad \sigma_m = K_f \frac{32M_m}{\pi d^3} \quad (3)$$

$$\tau_a = K_{fs} \frac{16T_a}{\pi d^3} \quad \tau_m = K_{fs} \frac{16T_m}{\pi d^3} \quad (4)$$

where M_a and M_m represents the mid-range and alternating bending moments, K_f and K_{fs} are fatigue stress concentration factors for bending and torsion, T_m and T_a are the mid-ranges and alternating torques, respectively, and d is the shaft diameter.

The maximum bending moment M_{max} occurs in the x-y axis (see Fig. 2), due to machine's weight, while axial forces are ignorable. The torque values obtained from electromagnetic FEA are given in Table 3.

Table 3: Torque values from electromagnetic FEA

M_a	1.0518 Nm	M_{max}	82.26 Nm
T_m	70 Nm	$M_m = T_a$	0

The fatigue stress concentration factors K_f and K_{fs} are respectively reduced from K_t and K_{ts} , which are obtained from the geometry and material specifications of the used shaft [10]. Equations (3) and (4) are then combined with the distortion energy failure theory of the von Mises stresses. For a solid and round rotating shaft, with axial loads neglected, these are calculated with equations below [10]:

$$\sigma'_a = (\sigma_a^2 + 3\tau_a^2)^{1/2} = \sqrt{\left(\frac{32K_f M_a}{\pi d^3}\right)^2 + 3\left(\frac{K_{fs} 16T_a}{\pi d^3}\right)^2} \quad (5)$$

$$\sigma'_m = (\sigma_m^2 + 3\tau_m^2)^{1/2} = \sqrt{\left(\frac{32K_f M_m}{\pi d^3}\right)^2 + 3\left(\frac{K_{fs} 16T_m}{\pi d^3}\right)^2} \quad (6)$$

Equations (3)-(6) are used together with the values of the analyzed machine in Table 3, the following results are obtained. Using the modified Goodman diagram, the failure curve of these alternating and midrange stresses can be evaluated, with fatigue failure criteria defined as [10]:

$$\frac{1}{n_f} = \frac{\sigma'_a}{S_e} + \frac{\sigma'_m}{S_{ut}} \quad (7)$$

where $S_{ut} \geq 1400$ MPa. Since the modified Goodman criteria does not guard against yielding, separate check was incorporated. A von Mises maximum stress (σ_{max}) is

Table 4: Shaft design factors

K_t	1.6	q_{shear}	0.93
K_{ts}	1.35	σ_a	2.014 MPa
K_f	1.504	τ_m	74.14 MPa
K_{fs}	1.294	σ'_a	2.014 MPA
q	0.84	σ'_m	128.4 MPA

calculated and then compared to the yield strength S_y (see eqn: (9)):

$$\sigma'_{max} = [(\sigma_m + \sigma_a)^2 + 3(\tau_m + \tau_a)^2]^{1/2} \\ = \sqrt{\left(\frac{32K_f(M_m + M_a)}{\pi d^3}\right)^2 + 3\left(\frac{K_{fs} 16(T_m + T_a)}{\pi d^3}\right)^2} \quad (8)$$

$$n_y = \frac{S_y}{\sigma'_{max}} > \frac{S_y}{\sigma'_a + \sigma'_m} \quad (9)$$

For steels of up to 1450 MPa, it is suggested that the endurance limit (S'_e) be in the ranges of 40 % to 60 % of the steel's tensile strength [10]. The endurance in the case of this prototype analysis is estimated to be 50 % of the tensile strength, i.e $S'_e = 0.5S_{ut}$. The Marin equation (S_e) was further employed to take into account various influences that different factors may have on the endurance limit. It includes quantified effects of the surface factor, size, loading, temperature and miscellaneous items [10].

$$S_e = k_a k_b k_c k_d k_e k_f S'_e \quad (10)$$

where k_a is the surface conditioning factor, k_b is dedicated to the sizing factor, k_c is the load factor, k_d is the temperature factor and k_e the reliability factor.

The reliability factor is the probability that a known stress will exceed the strength of a randomly selected component that is manufactured out of the same material. In the foregoing design, both k_c and k_e have been approximated as 1. The other factors are defined by the equations below, and their calculated values are given in Table 5.

$$K_a = a S_{ut}^b \\ K_b = \left(\frac{d}{7.62}\right)^{-0.107} \\ K_d = 0.9877 + 0.6507(10^{-3})T_C - 0.3414(10^{-5})T_C^2 \\ + 0.5621(10^{-8})T_C^3 - 0.6246(10^{-12})T_C^4 \quad (11)$$

The modified Goodman fatigue failure criteria can be

Table 5: Marin equation factors values

S_{ut}	700 MPa	K_a	0.795
S'_e	350 MPa	K_b	0.902
S_e	253 MPa	K_d	1.009

calculated from a combination of these results, while the fatigue factor n_f and the yielding factor n_y are evaluated from eqns (7) and (9). The values for these factors are provided in Table 6 for the designed shaft. It can be clearly seen that yield factor for the old shaft $n_{y,shaft}$ is less than

the maximum yield factor $n_{y,max}$. However, these factors are too high and indicate that the shaft was over-designed for the expected loads. The safety factor of the old shaft was 5.22, whereas it is expected to be 1.5 - 2.

Table 6: Shaft's Goodman fatigue factors

σ'_{max}	128.4 MPa	$n_{y,max}$	3.62
n_f	5.22	$n_{y,shaft}$	3.565

3.2 Bearing Selection

Stresses occur on both the inner- and outer-rings of a ball bearing as a result of its rolling mechanism of operation. The bearing life, defined as the total number of revolutions that it can withstand before it can fail or fatigue can be developed, is termed rating life. With the intended bearing life (L_D), predicted radial load (F_D) to withstand, and desired rotational speed (n_D) all known, the catalogue rating (C_{10}) can be calculated from eqn (12). The parameter (C_{10}) is then used to select a suitable bearing for certain application.

$$C_{10} = F_D \left(\frac{L_D n_D 60}{L_R n_R 60} \right)^{1/a} \quad (12)$$

where n_R is rated speed, L_R is rated life and $a = 3$ for ball bearings.

It was then realized that the old machine had oversized bearings. Since the bearing losses are directly proportional to its bore diameter, oversized bearings could unreasonably add more losses as smaller bearings could have been used instead. Furthermore, SKF energy efficient ball bearings were used instead of normal ball bearings as it was the case with old machine, which then have a potential of 10% bearing loss reduction. From the used bearing specifications in Table 7, it can be seen that the new bearings have small bore diameters while they can still handle almost equal load as the old ones.

Table 7: Bearing specifications

Bearing designation	Inner D(mm)	Outer D(mm)	Width (mm)	Load (kN)
E2.6302-2Z	15 ↓	42	13	11.4
6004-2RSH	20	42	12	9.95
E2.6303-2Z	17 ↓	47	14	13.8
6005-2RSH	25	47	12	11.9
E2.6204-2Z	20 ↓	47	14	12.7
6005-2RSH	25	47	12	11.9
E2.6208-2Z	40 ↓	80	18	30.7
6009-2RS1	45	75	16	22.1

↓ Indicates reduced bearing bore diameter.

3.3 Stator Winding

The stator coils were re-wound in an attempt to improve the fill-factor and reduce the end-windings' length. Due to

the same winding challenges previously met in the process during the first trial, the newly realized coils had 10 turns less than the old. On the other hand, the end-winding's lengths seemed to be much shorter as they were pulled tighter. The shorter end-windings' length promises less machine's total resistance. This clearly shows that closed-slots stator brings manufacturing challenges which could also be detrimental to the machine's performance. In this regard, alternative stator configurations (e.g. segmented stator) should be considered.

4. TESTING AND RESULTS

4.1 Bearing Losses

A test model was developed to measure the losses for each bearing individually without the interference of magnetic and electromagnetic active parts of the machine. This was done with the aim of separating the no-load core losses from mechanical losses. Unfortunately, only the big bearing's (E2.6208-2Z) losses were accurately measured due to the model's and measuring equipments' limitations. Hence, the amount of loss contribution of the other three bearings was still unknown. Figure 3 shows the comparison of the old and new big bearings' losses, together with their theoretical predictions. It can be seen that there is a huge difference between the practical losses of the two bearings. For a machine with such a small output capacity, this can directly be reflected by the reduced overall efficiency.

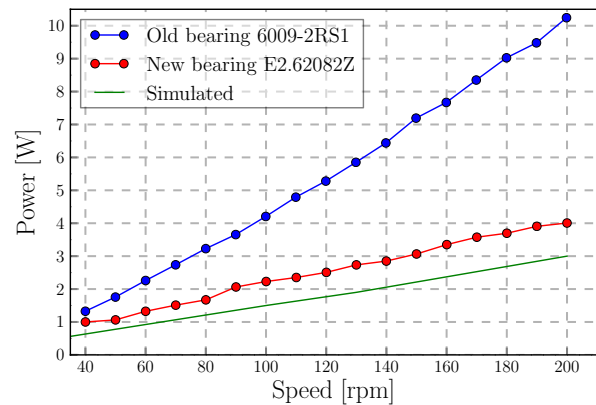


Figure 3: Comparison of two bearings' losses.

4.2 Stator Resistance

In order to find a practical value of the stator resistance, and check whether the three phases are properly balanced, a DC coil resistance test was done. The average per-phase resistance was found to be 5.8Ω , which is 1.5Ω less than that of the previous windings, as presented in Table 8. Although the current number of coil turns is slightly less than before, the big difference in the resistances is a result of shortened end-windings' lengths. It is believed that this will have a significant reduction in copper losses.

Table 8: Stator resistances

Old stator	New stator	Difference
7.3 Ω	5.8 Ω	1.5 Ω

4.3 No-load Losses

In order to see if the implemented changes did improve on the machine's performance, no-load loss tests were conducted. This was done with the machine's terminals open so that only the eddy current, hysteresis and mechanical losses can be measured, while excluding copper loss.

A comparison of these losses as predicted from FEA, and measured from the first and re-designed machines is given in Fig. 4. There is a big difference between FEA predicted and measured losses. However, the difference between the two versions of the machine is not significant. This can be attributed to the fact that the three other bearings running at high speed were not replaced since the proposed new bearings could not be acquired. It is understood that the losses would have drastically reduced if the energy efficient bearings with smaller bore diameters were used instead.

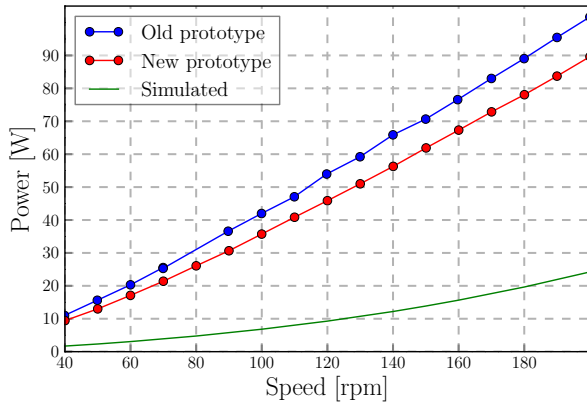


Figure 4: No-load loss comparison.

4.4 Open Circuit Voltage

By operating the prototype machine as a generator under no-load conditions, the induced back electro-motive force (EMF) was obtained. The stator EMF waveforms measured at an input speed of 150 rpm are plotted in Fig. 5. They are balanced in both the magnitude and phase displacement, proving that the stator windings were correctly configured. Furthermore, the output electrical frequency (f_e) is obtained to be 52.5 Hz, which is in good agreement with the theoretical calculations. Therefore, the speed and/or torque gearing principle can also be validated by calculation of the inner rotor's mechanical speed (n_h) from f_e and then comparing it to the input speed, as shown

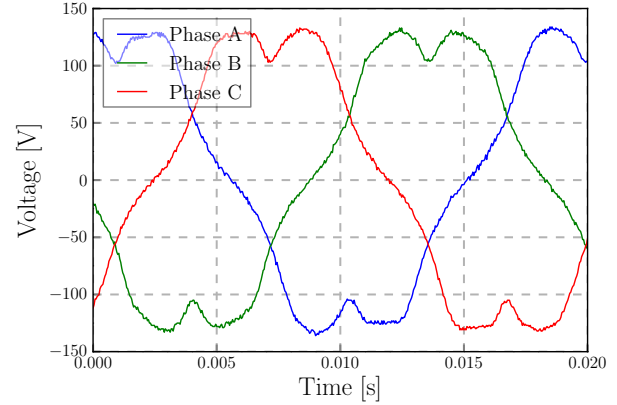


Figure 5: Electromotive force waveforms at 150 rpm.

below:

$$n_h = \frac{60 \times f_e}{p_h} = \frac{60 \times 52.5}{2} = 1575 \text{ rpm} \quad (13)$$

And the gear ratio is:

$$G_r = \frac{n_h}{n_l} = \frac{1575}{150} = 10.5 \quad (14)$$

where n_h and n_l are output and input speeds, respectively. A graph of open circuit voltage as a function of input speed is given on Fig. 6. From this, the practical machine's induction constant (k_m) is found to be 0.86. Also, the FEA simulated magnitudes are slightly higher than the experimental measurements due to 3D end effects.

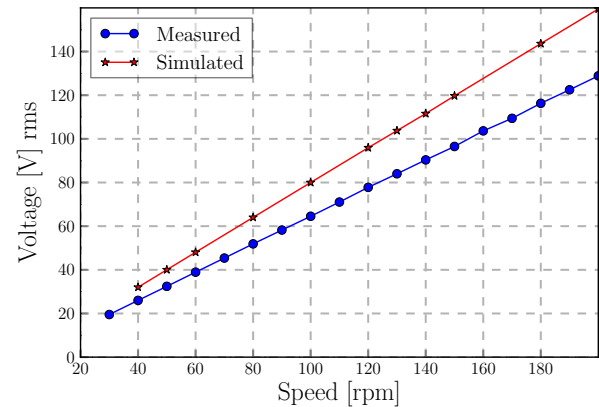


Figure 6: Phase rms voltage as a function of speed.

4.5 Load Tests

The output efficiency of the machine was determined by measuring the input mechanical and output electrical power at various operating speeds. Both the output active power and efficiency at rated current are presented in Fig. 7, as a function of speed and at two different constant loads. Since the power graph is plotted at a constant current, this means the copper losses are also fixed, hence

the efficiency has an increasing trend with increase in speed. The slope of an efficiency graph is initially steeper but flattens at higher speeds due to overwhelming friction and core losses.

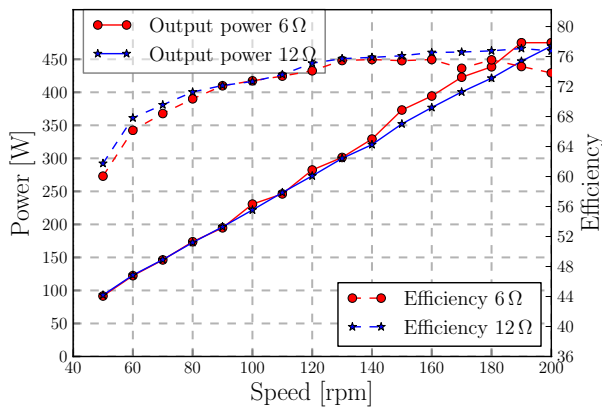


Figure 7: Output power and efficiency at rated current.

4.6 Overload Condition

The pull-out or slip torque of the machine is measured by overloading it until it's gear-part slips or becomes un-synchronized. Figure 8 illustrates the torque on the input side (modulator) as a function of time while the load is steadily increased. It can be seen that the torque increases until the gear slips at almost 60 Nm, which is actually the machine's stall torque predicted by FEA [7]. After the slip point, the torque oscillates between positive and negative magnitudes until the load is decreased well below its capability and the gear re-engages. The over-load condition occurs at almost twice the rated current. This further demonstrates the overload protection characteristic of the MGPM machines.

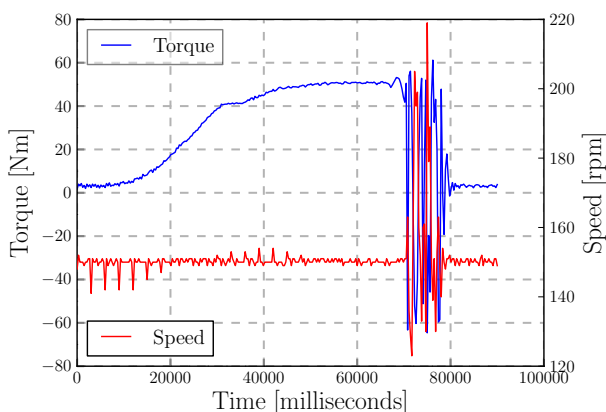


Figure 8: Overload test to illustrate machine's pullout torque.

5. CONCLUSIONS

In this paper, design improvements for an MGPM machine prototype were proposed and implemented.

It has been shown that careful consideration on the non-electromagnetic active components such as bearings and shaft can considerably reduce the losses. The over-load protection and contact-less power transmission are clearly the advantages of MGPM machines comparing with mechanically geared systems. However, to fully realize the superiority of these machines, the mechanical design optimization is just as important as the electromagnetic design.

REFERENCES

- [1] H. Polinder, F.F.A. van der Pijl, G-J. de Vilder, P.J. Tavner, "Comparison of direct-drive and geared generator concepts for wind turbines," IEEE Trans. Energy Convers., 21(3):725-733, Sept. 2006.
- [2] R.-J. Wang, S. Gerber, "Magnetically geared wind generator technologies: Opportunities and challenges," Appl. Energy, vol. 136:817-826, Dec. 2014.
- [3] D. McMillan, G.W. Ault, "Techno-economic comparison of operational aspects for direct drive and gearbox-driven wind turbines," IEEE Trans. Energy Convers., 25(1):191-198, Mar. 2010.
- [4] K.T. Chau, D. Zhang, J.Z. Jiang, C. Liu, Y. Zhang, "Design of a magnetic-geared outer-rotor permanent-magnet brushless motor for electric vehicles," IEEE Trans. Magn., 43(6):2504-2506, Jun. 2007.
- [5] K. Atallah, S. Calverley, R. Clark, J. Rens, D. Howe, "A new PM machine topology for low-speed, high-torque drives," in Proc. 18th Int. Conf. Elect. Mach. (ICEM), Vilamoura, Portugal, Sep. 2008, pp. 1-4.
- [6] L. Jian, K.T. Chau, J.Z. Jiang, "A magnetic-geared outer-rotor permanent-magnet brushless machine for wind power generation," IEEE Trans. Ind. Appl., 45(3):954-962, May/Jun. 2009.
- [7] P.M. Tlali, S. Gerber, R.-J. Wang, "Optimal design of an outer-stator magnetically geared permanent magnet machine," IEEE Trans. Magn., (early access).
- [8] K. Atallah, D. Howe, "A novel high performance magnetic gear," IEEE Trans. Magn., 37(4):2844-2846, Jul. 2001.
- [9] K. Atallah, J. Wang, D. Howe, "A high performance linear magnetic gear," J. Appl. Phys., 97(10):10N516-110N516-3, May 2005.
- [10] R.G. Budynas, J.K. Nisbett, *Shigley's Mechanical Engineering Design*, McGraw-Hill, 2008.

DESIGN AND OPTIMISATION OF A LINE-START SYNCHRONOUS RELUCTANCE MOTOR

Q. Smit*, A.J. Sorgdrager** and R-J. Wang**

* Stellenbosch University, Department of Mechanical and Mechatronic Engineering, Corner of Bosman Road and Victoria Street, Stellenbosch 7600, South Africa

Email: 16139844@sun.ac.za

** Stellenbosch University, Department of Electrical and Electronic Engineering, Corner of Bosman Road and Victoria Street, Stellenbosch 7600, South Africa

Email: ajsorgdrager@gmail.com; rwang@sun.ac.za

Abstract: In this study a line-start reluctance synchronous machine (LS-SynRM) was designed and optimised using a finite element method based approach. Simulation results showed that the optimised LS-SynRM when compared to an induction machine achieved better efficiency, but lower power factor and higher torque ripple. Based on the simulation results, a LS-SynRM prototype was manufactured and experimentally tested. The prototype did however not achieve synchronization under loaded conditions. Possible causes were discussed and relevant conclusions are drawn.

Keywords: Line-start motor, reluctance synchronous machine, induction machine, synchronisation, design optimisation, transient performance.

1. INTRODUCTION

As of 2013, rotating electrical machines consume 40% of global electrical energy and 70% in industry applications [1]. This resulted in energy efficiency with regards to rotating electrical receiving a considerable amount of attention in recent years. With the advent of IEC 60034-30 standard, there has been a big drive in electrical machine industry to look into alternative machine technologies that could meet with the forthcoming IE4 efficiency standard. Since synchronous machines tend to have better efficiencies than their asynchronous counterparts, the industry has seen a gradual shift towards synchronous operating machines.

Synchronous machines typically are not line-start machines and require expensive power inverter control systems for start-up. Conversely, induction machines can start simply by connecting to a constant frequency line-voltage. Line-start synchronous machines attempt to remove the weakness of synchronous machines by creating a hybrid motor that has high efficiency at steady-state operation and the ability to self-start. Different line-start electrical machine technologies have been proposed in literature. Amongst others, line-start synchronous reluctance machines (LS-SynRM) have received some attention [2-3].

In this paper, the design process and practical evaluation of a LS-SynRM including rotor concept selection, FEM based design optimisation, prototype construction and finally experimental testing are presented. The intended application of this machine is for fans and pumps loads operate for long periods of time at a constant speed.

2. CONCEPT DEVELOPMENT AND SELECTION

For this study a standard WEG 2.2kW 525V 4-pole three-phase premium efficiency cage induction motor (IM) is used as a reference motor. An LS-SynRM can utilize the

same winding configuration and design as an IM, thus the stator configuration of the reference IM is used for all LS-SynRM designs in the study. Figures 1 and 2 present the stator winding layout and the rotor design of the IM respectively.

For the LS-SynRM rotor design, three different concepts are considered. Concept 1 (Fig. 3) uses the existing squirrel cage structure of the reference IM as in Fig.2 with an internal flux barrier structure. Concept 2 (Fig. 4) has a typical flux barrier structure surrounded by a solid copper sleeve. Concept 3 (Fig. 5) adopts a complete SynRM rotor and simply inserts the cage conductors into the available spaces inside the flux barriers.

2.1 FEM Model

To evaluate the design concepts, two-dimensional (2D) finite element analyses (FEA) were conducted by using ANSYS' Maxwell v16 software package and the motor design toolkit plug-in. The software employs time-stepped transient FE simulation to determine the transient

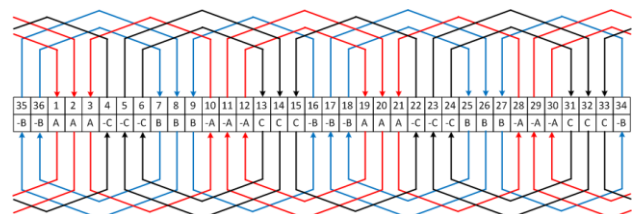


Figure 1: IM stator winding layout

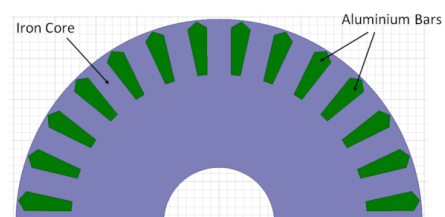


Figure 2: Reference induction machine rotor

synchronisation response and steady-state performances of electrical machines using the toolkit.

Considering the geometrical symmetry of the machine, it is necessary to model only one half of the machine by applying a positive periodical boundary condition. Assuming the magnetic field is fully contained within the stator, the magnetic vector potential along the outer surface of the stator is defined as 0 Wb.m^{-1} , which is the so-called Dirichlet boundary condition. The FE model of a LS-SynRM is shown in Fig. 6.

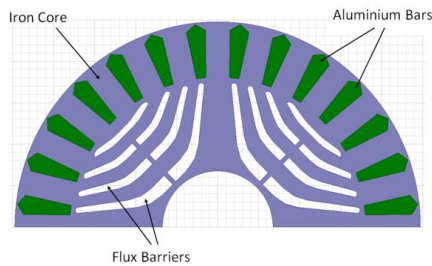


Figure 3: Rotor design concept 1

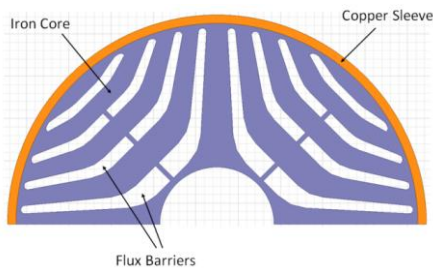


Figure 4: Rotor design concept 2

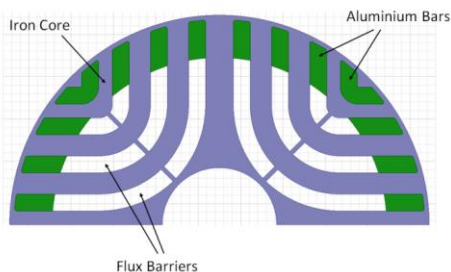


Figure 5: Rotor design concept 3

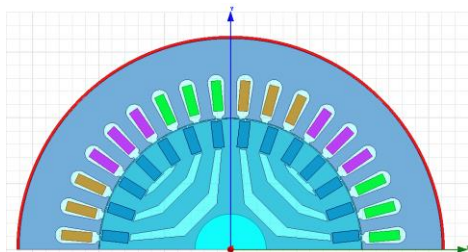


Figure 6: LS-SynRM's FEA model

2.2 Rotor Concept Selection

From the initial non optimized design analyses results as presented in Table 1, it appears that Concept 3 has the best steady-state performances. However, it requires unrealistically low conductivities in both cage conductor bars and the end rings in order to achieve synchronisation. The resulting end ring thickness and

conductor bar cross sections are not practically realisable, and therefore Concept 3 was excluded from the selection.

Concepts 1 and 2 both show good synchronisation ability. Concept 1 demonstrates better efficiency and power factor than Concept 2, while Concept 2 has lower torque ripple (Table 1). Concept 1 was selected for further design optimisation, since existing design techniques can be applied in the design of LS-SynRM to reduce the torque ripple [4-5].

Table 1: Performance comparison of different concepts

Rotor concept	1	2	3
Synchronisation	Yes	Yes	No
Efficiency (%)	87.3%	53.5%	95.1%
Power Factor	0.58	0.49	0.79
Torque ripple (%)	33.8%	5.9%	14.3%

3. CONCEPT REVISION AND DESIGN SPACE

The selected concept was further revised by changing the conductor bar cross section into a rectangular shape which allows for the insertion of standard aluminium flat bar instead of casting. Additionally, the number of flux barriers is reduced to three per pole which corresponds to the optimum number for torque ripple minimisation as proposed by Vagati [4-5].

Conductor slot openings are also added to give additional control over the torque ripple. After defining constraints, a total of 6 design variables (as shown in Fig. 7) remained to define the design space, of which 3 variables are required for defining the flux barrier size and width; 2 variables are needed to characterise the conductor bar cross section and a single variable defines the width of the conductor slot opening.

4. OPTIMISATION

As shown in Fig. 8, the optimisation was conducted in 3 sequential steps. Firstly, the conductor bar cross section was determined by selected the minimum cross section that could still successfully synchronise (with a safety factor of 50%). Cross sections were selected from a supplier's aluminium flat bar catalogue. Secondly, the flux barrier variables were optimised for efficiency and power factor using a full parametric sweep. Finally the conductor slot opening width was optimised to reduce torque ripple and further increase efficiency.

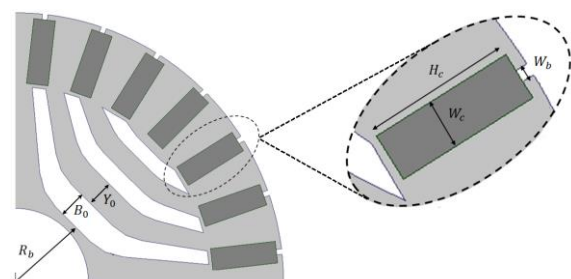


Figure 7: Optimisation design space showing 6 variables

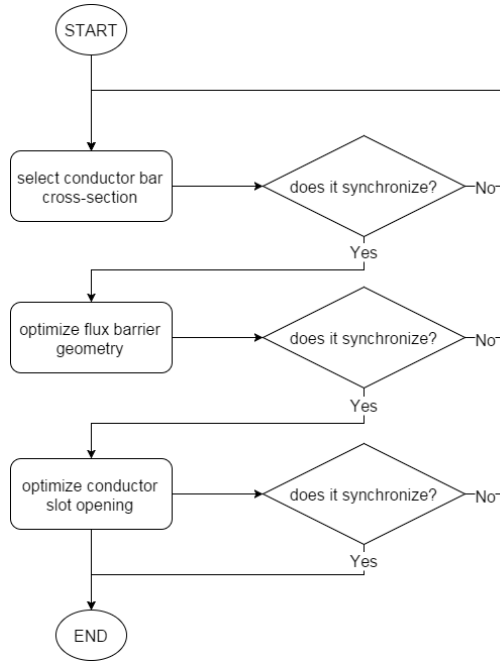


Figure 8: Optimisation design flow chart

4.1 Flux barrier optimisation

Table 2 shows the best performing flux barrier parametric sweep results ranked in terms of efficiency. Even though there are large differences in the geometry variables, the efficiency results are within $\pm 0.1\%$ of each other. The results with higher efficiencies also correspond to higher power factors and lower stator currents. This can be explained by the fact that; for LS-SynRM, the highest losses occur due to the I^2R losses of the stator windings and are therefore directly linked to the stator current.

The second ranked design is chosen as it has a larger bottom flux barrier radius (R_b), which corresponds to thicker and stronger ribs between the shaft and the bottom flux barrier. Additionally, the second ranked variation also has lower torque ripple.

4.2 Conductor slot opening optimisation

To select the slot opening width a parametric sweep was done to investigate the effects it has on both the rms line current and the torque ripple. The simulation results are presented by Fig 9. The point at which the supply current is the lowest (as indicated on the plot) is selected as the optimum width, this also corresponds to a relatively low torque ripple.

Table 2: Flux barrier geometry optimisation

	Geometry (mm)			Performance			
	B_0	R_b	Y_0	TR (%)	Eff. (%)	Phase Current (Arms)	PF
1	6	15	7	36.1	93.88	2.44	0.74
2	5	16	7	31.0	93.85	2.44	0.74
3	7	14	7	31.8	93.81	2.45	0.74
4	6	14	8	33.2	93.79	2.45	0.74
5	6	16	6	33.6	93.78	2.46	0.74

4.3 Geometry comparison

Fig. 10 compares the initial rotor geometry with the optimised rotor geometry. It can be seen that the optimised result favours a structure with almost perfect flux barrier alignment with the conductor bars. This is an intuitive result, since the conductor bars should essentially become extensions of the flux barriers due to the magnetic saturation of the webs between them resulting in improved reluctance torque and steady state performance.

4.4 Optimisation results

Table 3 shows the effectiveness of the optimisation process by comparing the performance of the optimised geometry with the initial unoptimised geometry and the simulated reference induction motor.

Table 3: Optimisation performance comparison

Performance	Initial	Optimised	Induction motor
Efficiency	92.46 %	93.69 %	92.95 %
Power factor	0.615	0.656	0.693
Torque ripple	29.6 %	29.9 %	18.7 %

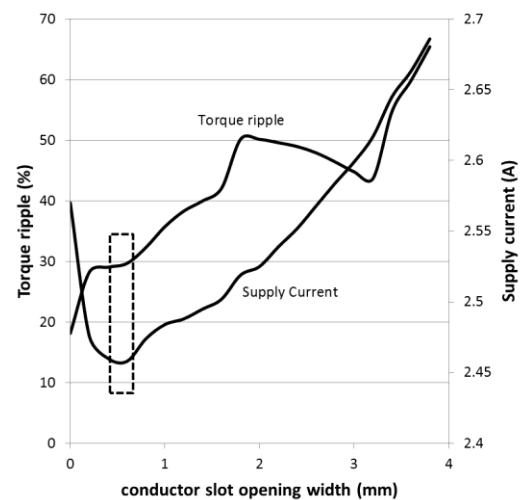
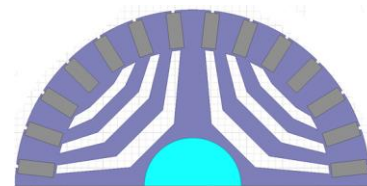
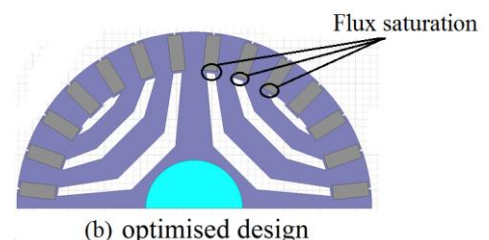


Figure 9: Effect of conductor slot opening width



(a) unoptimised design



(b) optimised design

Figure 10: Design geometry comparison

The optimisation process improved efficiency by more than 1% over the original geometry. Additionally, the efficiency is more than 0.7% better when compared to the simulated induction motor. The power factor and torque ripple of the optimised geometry is still worse than the reference IM, indicating that the LS-SynRM is only preferable in high efficiency applications where torque ripple and power factor are not a major consideration.

5. MANUFACTURING OF A PROTOTYPE

The optimised geometry was laser-cut using M400-50A electrical steel as shown in Fig. 11. The close-ups show that the quality of the laser cutting was relatively poor.

Figure 12 presents the manufacturing steps taken. The laminations were stacked onto a dummy shaft with the aluminium conductors positioned inside the conductor slots (Fig 12a). The end rings were pressed onto both sides of the rotor to secure the lamination stack (Fig 12b). A stacking factor of 0.95 is achieved for the 120 mm shaft. The end rings were then TIG welded using aluminium filler in order to improve the cage conductivity and overall rotor strength (Fig 12c). The dummy shaft was removed after which the machined shaft was inserted to ensure compatibility with the IM stator. Finally, compatible NHK bearing and keyways were fitted with the final rotor as presented in Fig 12d.

6. EXPERIMENTAL RESULTS

In this section the testing setup and results are described. Fig. 13 shows the test setup used for the prototype LS-SynRM.

A Norma 3000 power analyser is connected in series with all three lines of the input power supply using shunt resistors. This power analyser can measure the steady-state electrical input power and power factor very accurately; however it is unable to take transient measurements required during transient performance of the machine. The transient voltages and currents are measured using a TiePie Handy-Scope HS4 DIFF digital oscilloscope, which is connected to a PC via USB where they are interpreted by a software suite. The DR-3000 digital torque sensor is connected to the shaft and fan load with spider couplings. The torque sensor is connected to a PC via USB and results are interpreted by a software suite. The torque sensor is capable of taking transient or steady-state shaft torque, speed and output power readings.

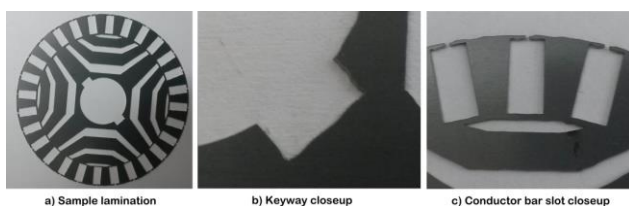


Figure 11: Rotor lamination

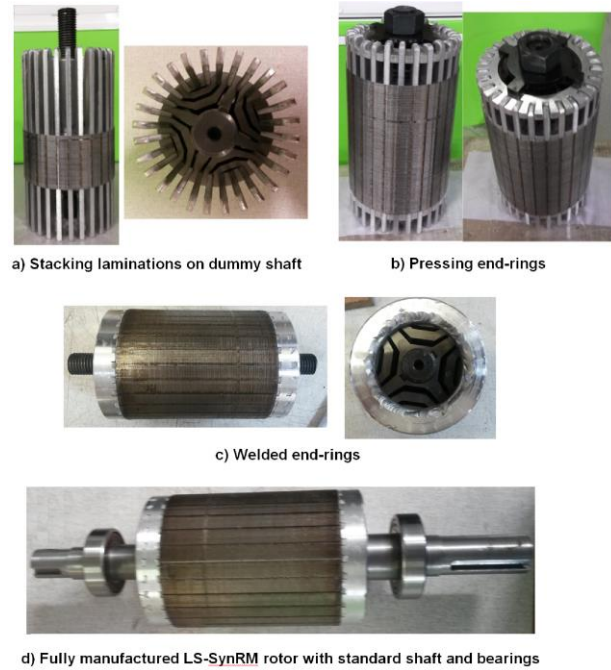


Figure 12: Manufacturing process for LS-SynRM rotor

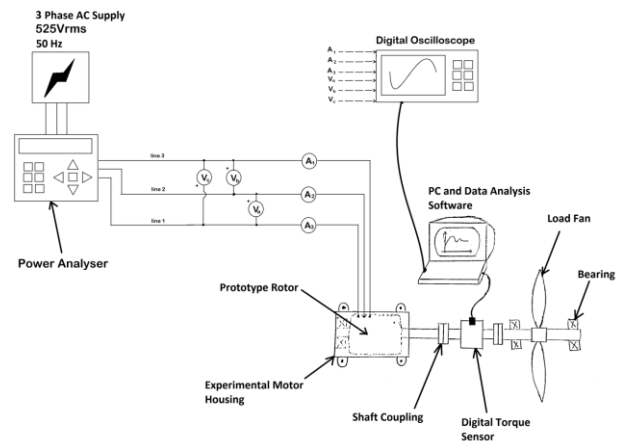


Figure 13: Experimental setup

Figure 14 shows the measured speed versus time characteristics of the LS-SynRM under no-load and full load conditions. The prototype motor was able to synchronise under the no-load condition, but was unable to synchronise while driving the fan load.

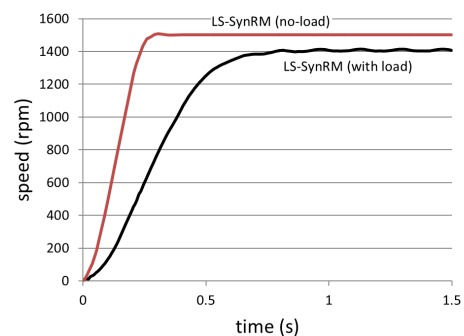


Figure 14: Measured speed versus time characteristics of the prototype LS-SynRM machine

7. ANALYSIS OF SYNCHRONISATION FAILURE

Since the prototype machine failed to synchronise contrary to the simulation prediction, further analysis on the possible causes was conducted. Considering the large effect of inertia on synchronisation, some evidence regarding its influence was investigated. The graph in Fig. 15 compares the measured speed versus time starting response of the induction motor with the simulated ones at different load inertia assumptions. The simulated response at the initial inertia assumption 0.11 kg.m^2 does not match the measured response well. However, if the inertia assumption is increased from the initial 0.11 to 0.17 kg.m^2 , the simulated response matches the measured response very well. This implies that the actual inertia of the load could be higher than the original assumption used in the design.

The graph in Fig. 16 shows the simulated speed versus time starting response of the LS-SynRM at various system inertia values. Clearly, the motor fails to synchronise with system inertia of 0.17 kg.m^2 , however at the slightly lower inertia of 0.16 kg.m^2 the motor can still synchronise. This result indicates the actual system inertia maybe be just outside synchronisation capability of the prototype machine.

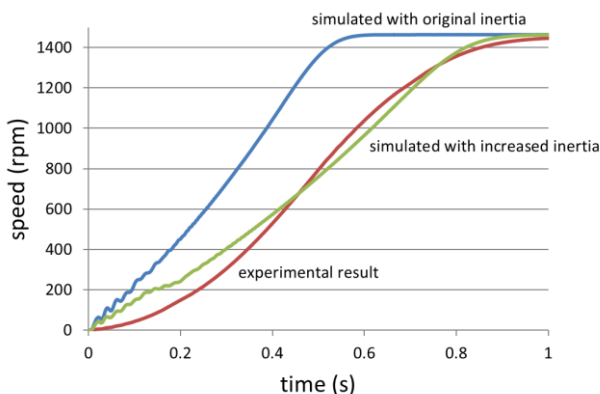


Figure 15: IM inertia comparison

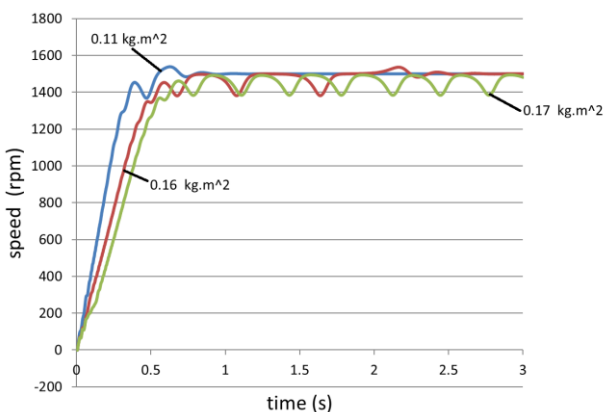


Figure 16: Simulated LS-SynRM at various inertias

8. CONCLUSION

Even though the prototype failed to synchronise, the most likely cause was determined to be the underestimation of load inertia. The FEM optimisation results showed that better efficiency than a typical induction machine can be achieved; however the power factor and torque ripple may still be inferior. The LS-SynRM should thus only be considered in high efficiency applications where power factor and torque ripple are not a major concern.

From a manufacturing perspective, the costs of LS-SynRMs should be similar to IMs as practically the same manufacturing process can be followed. This is a major advantage over other line-start alternatives such as the line-start permanent magnet machine which is generally more expensive than typical IMs.

9. RECOMMENDATIONS

In light of the failed synchronisation, recommendations are made with regard to future work. Firstly, the motor can be redesigned using the new inertia assumption by following the same process laid out in this paper. Secondly, the test load can be modified to reduce the inertia so synchronisation is achieved.

Once a synchronising is achieved, the effect of inserting magnets along the q -axis should be investigated as this could improve steady state performance without deteriorating synchronisation and torque ripple. The prototype's flux barriers were designed to ensure compatibility with rectangular magnets.

REFERENCES

- [1] J. Estima and A. Cardoso: "Efficiency Analysis of Synchronous Reluctance Motors." *International Conference on Engineering*. UBI2013. Nov 2013.
- [2] S.T. Boroujeni, N. Bianchi and L. Alberti: "Fast estimation of line-start reluctance machine parameters by finite element analysis," *IEEE Trans. Energy Convers.*, Vol. 26, No. 1, pp. 1–8, March 2011.
- [3] S.T. Boroujeni, M. Haghparast and N. Bianchi: "Optimization of Flux Barriers of Line-start Synchronous Reluctance Motors for Transient- and Steady-state Operation", *Electric Power Components and Systems*, 43:5, 594-606, 2015.
- [4] A. Vagati, G. Franceschini, I. Marongiu and G.P. Trogia: "Design criteria of high performance synchronous reluctance motors", *Industry Applications Society Annual Meeting, Conference Record of the 1992 IEEE*, vol. 1, pp. 66-73, October 1992.
- [5] A. Vagati, M. Pastorelli, G. Franceschini and S.C. Petrache: "Design of low-torque-ripple synchronous reluctance motors", *IEEE Industry Applications Society Annual Meeting*, Vol. 34, No. 4, pp. 758-765, July-August 1998.

DESIGN OF PERMANENT MAGNET SYNCHRONOUS GENERATOR FOR GEARED DIRECT-GRID-CONNECTED WIND GENERATOR DRIVE TRAIN

P. J. J. van Wyk, G. Dawood and M. J. Kamper*

* Department of Electrical & Electronic Engineering, University of Stellenbosch, Stellenbosch, South Africa E-mail: kamper@sun.ac.za

Abstract: In this paper the design and construction of a permanent magnet synchronous generator (PMSG) for use in a geared, direct-grid-connected wind generator drive-train are detailed. The dq equivalent circuits used to model the PMSG are given, as well as the finite element modelling procedure. The design optimisation of the PMSG is explained, and a prototype of an optimised 2.2 kW generator is constructed and tested. The measured results of the PMSG are shown to compare favourably with simulated results.

Key words: Permanent magnet, synchronous generator, finite element method, design optimisation, dq analysis, wind energy.

1. INTRODUCTION

With the rapid rise of wind energy generation in the last few decades several different types of wind generator drive trains have become commonplace. These drive trains always consist of at least a set of turbine blades and a generator of some sort, and often contains a gearbox and power electronic converters. Some common topologies are that of geared induction generators, either standard or doubly fed induction generators. Direct drive as well as geared, permanent magnet synchronous generators (PMSGs) are also quite prominent, but all require power electronic converters [1] to operate.

Direct grid connection of PMSGs is an attractive concept, since this removes the inefficiencies caused by power electronic converters, and also removes a potential point of failure in the system. Unfortunately, direct grid connection of a PMSG is quite difficult, since any variations in torque causes oscillations within the PMSG, which in turn negatively affects voltage quality. As such, several attempts have been made to introduce some form of damping into the drive train [2–4], but none of these methods seem to have gained much prominence.

An alternative method of directly connecting a generator is illustrated in the permanent magnet induction generator (PMIG), such as the one discussed in [5]. The PMIG consists of a standard cage rotor induction motor which contains an additional freely rotating PM rotor, which provides flux in the machine, and also improves the power factor of the machine. This concept is quite promising, since no gearbox or power electronic converters are present.

In [6–8] a new concept generator, based on the PMIG, was introduced. This new machine consists of a slip permanent magnet coupling (S-PMC) sharing a common PM rotor with a PMSG. This concept is called a slip-synchronous permanent magnet generator (SS-PMG), and is depicted in

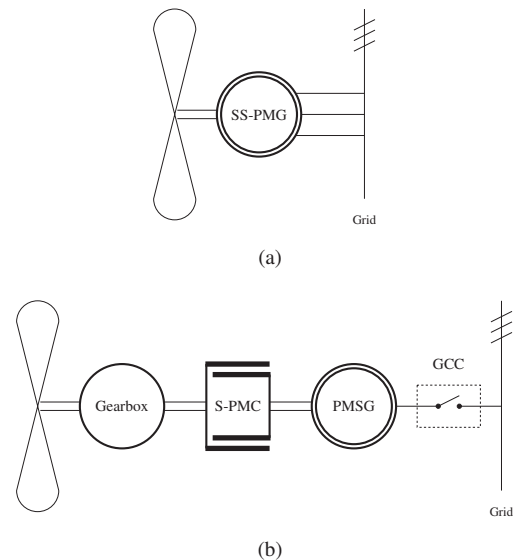


Figure 1: (a) Diagram representing the direct drive, direct grid-connected SS-PMG, and (b) the split drive train topology, consisting of gearbox, S-PMC and PMSG [10].

Fig. 1a. The machine is a direct drive, direct grid connected machine, with the turbine blades directly connected to the S-PMC, and the PMSG directly connected to the grid supply. The S-PMC provides the damping necessary for direct grid connection. The SS-PMG was further developed in [9, 10] to be split into a separate S-PMC and PMSG, and a gearbox was also introduced, to allow for flexibility in terms of speed selection. This option is shown in Fig. 1b. This splitting of the SS-PMG simplifies the construction of the drive train, and with speed selection available from using the gearbox a much smaller S-PMC and PMSG can be used. The S-PMC design and testing is investigated in great detail in [9] and [10].

The focus of this study is on the design and prototyping of the direct grid-connected PMSG. Direct grid connection

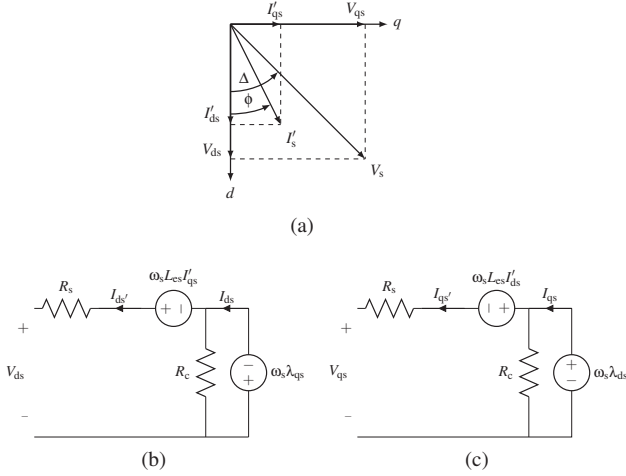


Figure 2: Equivalent circuit diagrams of the PMSG, with (a) the vector diagram for the dq currents and voltages, (b) d -axis equivalent circuit, and (c) q -axis equivalent circuit [10].

implies the connection of the PMSG output terminals to a constant voltage source of 230 V (RMS, line-to-neutral) at 50 Hz. Note that grid code requirements are not considered in this investigation, and only a proof-of-concept prototype is built and tested.

2. PMSG EQUIVALENT CIRCUIT

The PMSG investigated in this paper is modelled using steady state dq equivalent circuits. These equivalent circuits are given in Fig. 2. The d - and q -axis voltages (with positive current flowing out) are written as:

$$V_{ds} = -R_s I'_{ds} + \omega_s L_{es} I'_{qs} - \omega_s \lambda_{qs} \quad (1)$$

$$V_{qs} = -R_s I'_{qs} - \omega_s L_{es} I'_{ds} + \omega_s \lambda_{ds}. \quad (2)$$

I'_{ds} and I'_{qs} are the d - and q -axis currents as seen from the terminals of the machine. The per phase end winding leakage inductance is represented by L_{es} and R_s is the per phase copper winding resistance. L_{es} is calculated using a method detailed in [11], and R_s is calculated using the active copper area. R_c is the core loss resistance, and this is calculated using a method detailed in [12] along with loss-frequency curves. The d - and q -axis flux linkages are given by λ_{ds} and λ_{qs} , and these are provided as output by the finite element (FE) package. ω_s is the PMSG synchronous speed in electrical rad/s. I_{ds} and I_{qs} are the d - and q -axis currents which are provided as input to the FE package. The relationships between I_{ds} and I'_{ds} , and I_{qs} and I'_{qs} are given by

$$I_{ds} = I'_{ds} - \frac{\omega_s \lambda_{qs}}{R_c} \quad (3)$$

$$I_{qs} = I'_{qs} + \frac{\omega_s \lambda_{ds}}{R_c}. \quad (4)$$

The phase voltage at the PMSG terminals, V_s (peak, line-to-neutral), can be written in terms of the dq voltage

components using

$$\begin{bmatrix} V_{ds} \\ V_{qs} \end{bmatrix} = V_s \begin{bmatrix} \cos(\Delta) \\ \sin(\Delta) \end{bmatrix} \quad (5)$$

$$\Delta = \arctan\left(\frac{V_{qs}}{V_{ds}}\right) \quad (6)$$

with Δ being the angle between the d -axis and V_s as shown in Fig. 2a. In a similar fashion I'_s , which is the terminal peak line current of the PMSG, can be written in terms of the dq current components using

$$\begin{bmatrix} I'_{ds} \\ I'_{qs} \end{bmatrix} = I'_s \begin{bmatrix} \cos(\phi) \\ \sin(\phi) \end{bmatrix} \quad (7)$$

$$\phi = \arctan\left(\frac{I'_{qs}}{I'_{ds}}\right) \quad (8)$$

with ϕ being the angle between the d -axis and I'_s . Performance metrics of the PMSG are also considered. The torque generated by the PMSG is given by

$$T = \left(\frac{3}{2}\right) \left(\frac{p}{2}\right) (\lambda_{ds} I_{qs} - \lambda_{qs} I_{ds}) \quad (9)$$

where p is the number of poles in the machine. The apparent output power and real power of the PMSG are given by

$$S = \frac{3}{2} V_s I'_s \quad (10)$$

$$P_{out} = \frac{3}{2} V_s I'_s \cos(\theta) = P_{mech} - P_{losses} \quad (11)$$

$$\theta = \phi - \Delta \quad (12)$$

$$P_{mech} = P_{in} = T \omega_s. \quad (13)$$

The total machine losses are given by P_{losses} , and this consists of stator core/iron losses (P_c), winding copper losses (P_{cus}), and friction and windage losses (P_{fw}). The eddy current losses in the stator conductors and the core losses in the rotor core and permanent magnets are assumed to be negligible. The conductor copper losses, P_{cus} , are calculated using

$$P_{cus} = \frac{3}{2} I'^2_s R_s. \quad (14)$$

P_c is calculated using a method given in [12]. P_{fw} , calculated using a method from [13], is found to be almost negligible. Considering all the losses, the efficiency is calculated as

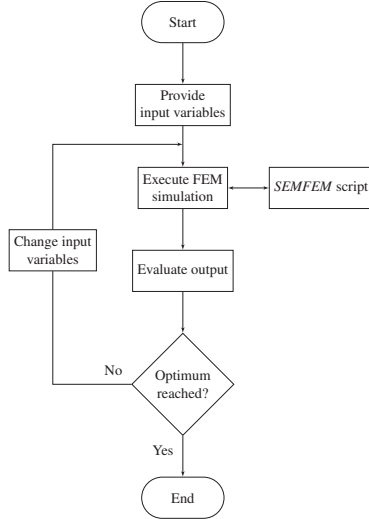
$$\eta = \frac{P_{in} - P_{losses}}{P_{in}}. \quad (15)$$

The transformations used in this analysis are given by

$$\mathbf{I}_{abc} = \mathbf{K}_p(\alpha) \mathbf{I}_{dq} \quad (16)$$

$$\lambda_{dq} = \mathbf{K}_p^{-1}(\alpha) \lambda_{abc}. \quad (17)$$

α is the electrical angle between the phase a axis and the rotor direct axis and \mathbf{K}_p is Park's transformation.


Figure 3: Flow diagram of the *VisualDoc* optimisation process.

3. SIMULATION OF PMSG

In this study static FE simulations are used to simulate the PMSG, using a custom in-house FE package called *SEMFE*. The PMSG is directly grid-connected, thus a fixed phase voltage of $V_s = 230$ V is applied to the machine terminals. This implies that the voltage magnitude is always fixed for any given load, but the current magnitude, as well as both voltage and current angles, are not known. These unknowns are determined iteratively using successive static FE simulations. To this end (1) and (2) are rewritten in terms of current as

$$I'_{ds} = \frac{-V_{ds} + \omega_s L_{es} I'_{qs} - \omega_s \lambda_{qs}}{R_s} \quad (18)$$

$$I'_{qs} = \frac{-V_{qs} - \omega_s L_{es} I'_{ds} + \omega_s \lambda_{ds}}{R_s} \quad (19)$$

To determine the current magnitude I'_s for a given load point copper losses for the load point are chosen, and I'_s calculated using (14). I'_s and V_s are kept constant when evaluating the load point. An initial simulation is run, and V_{ds} and V_{qs} is calculated using (1) and (2), from which Δ is calculated using (6). With a fixed V_s , new values for V_{ds} and V_{qs} are calculated using Δ and (5). Values for I'_{ds} and I'_{qs} are calculated using the new V_{ds} and V_{qs} values and (18) and (19). Using I'_{ds} and I'_{qs} together with (8), ϕ is calculated, which allows for the calculation of new values for I'_{ds} and I'_{qs} using the fixed I'_s and (7). These new I'_{ds} and I'_{qs} values are used as input for the next iteration. This process is repeated until convergence of the d - and q -axis currents.

4. DESIGN OPTIMISATION

Using the simulation method described, a simple optimisation of the PMSG is done using the *VisualDoc* suite. The objective function for the optimisation is minimizing the active mass, subject to several constraints.

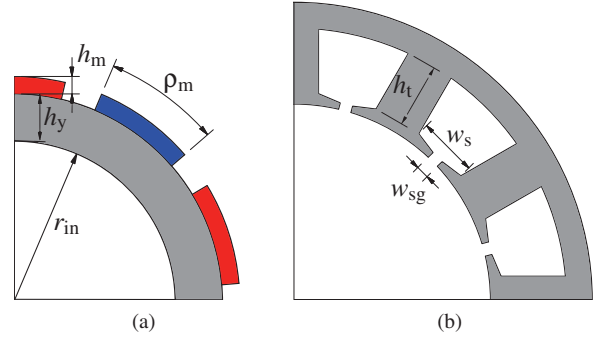


Figure 4: Dimensions used as optimisation input variables.

Table 1: Design variables and Optimised Values for PMSG.

Fixed Input	Value
Synchronous Speed	600 rpm
Outside Radius	92.5 mm
Optimisation Variables	Optimised Value
Axial Length - l_a	77 mm
Slot Width - w_s	18.5 mm
Slot Gap Width - w_{sg}	21.8% of w_s (4 mm)
Tooth Height - h_t	20 mm
Magnet Pitch - ρ_m	72.8% of pole pitch (26.2°)
Magnet Height - h_m	4.6 mm
Rotor Yoke - h_y	12.5 mm
Inside Radius - r_{in}	42.9 mm
Number of Turns - N_c	145
Rated Copper Losses - P_{cus}	130 W
Objective Function	Optimised Value
Active Mass (minimised)	9.92 kg

The optimisation process is illustrated in Fig. 3. Various input variables are optimised by *VisualDoc*. These input variables are illustrated in Fig. 4 and also given in Table 1 along with their optimised values. The optimised minimum active mass is also given in Table 1 as 9.92 kg. The permanent magnet mass, which isn't given in Table 1, is found to be just over 700 g. The axial length is 77 mm, and the outer radius of the machine is fixed at 92.5 mm. The constraints used in the optimisation are given in Table 2 along with their final values. The torque is 36.57 Nm, with all constraints sufficiently satisfied. Note that torque ripple and efficiency are exactly on the constraint limits, and it was observed that the 10/12 pole/slot combination used in this machine exhibited quite a high amount of torque ripple.

5. MEASURED AND SIMULATED RESULTS

A prototype of the optimised PMSG was built and tested. Unfortunately, some mechanical problems arose during the construction of the prototype. The desired fill factor of 0.4 could not be achieved, and a thinner wire gauge was used which reduced the effective fill factor to 0.32. This negatively influenced the machine performance.

Table 2: Optimisation Constraints.

Constraint	Limits	Values
Generated Torque	$36 < T < 38 \text{ Nm}$	36.57 Nm
Torque Ripple	$< 9\%$	9%
Efficiency	$> 93\%$	93%
Real Power Output	$> 2140 \text{ W}$	2141 W
Rated Power Factor	> 0.9	0.9767
Current Density	$< 5.5 \text{ A/mm}^2$	4.84 A/mm ²

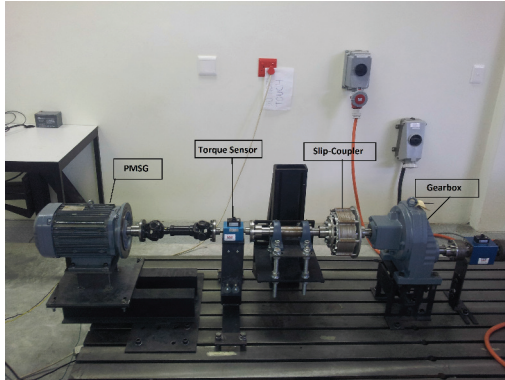


Figure 5: Set-up used for PMSG testing.

Additionally, an error was made during the manufacturing of the rotor shaft, resulting in an axial misalignment between the rotor and stator stacks of about 4 mm, hence further reducing machine performance. Despite these issues, a working prototype was successfully constructed and tested on the test set-up shown in Fig. 5. The test set-up consists of the PMSG with a torque sensor connected at the input drive side. The S-PMC (also referred to as a slip coupler), as well as the gearbox are also included in the set-up, although these two are not essential for these tests. A power analyser is connected to the output terminals of the PMSG. The measured results are compared to FE simulation results. The initial simulation results are attained from *SEMFEM*, which is the same static FE packaged used to perform the design optimisation. Additional transient FE results are attained from *Infolytica Magnet* to verify that the static simulations are correct. The voltage is initially considered, since it is very important that the voltage magnitude is correct for direct grid-connection. As can be seen in Fig. 6 the voltage matches quite well between the measured and simulated results.

Several direct grid-connected tests are performed to determine machine performance during actual operation. The torque versus load current characteristic is shown in Fig. 7. As can be seen there is a relatively good match between the measured and simulated results, with mostly a linear characteristic between torque and current. With a thinner wire used for the coils, the per phase coil resistance increases, resulting in higher copper losses, which has a negative effect on the efficiency. As can be seen in Fig. 8 the measured efficiency is lower than the simulated efficiency, as is expected. The efficiency curve follows

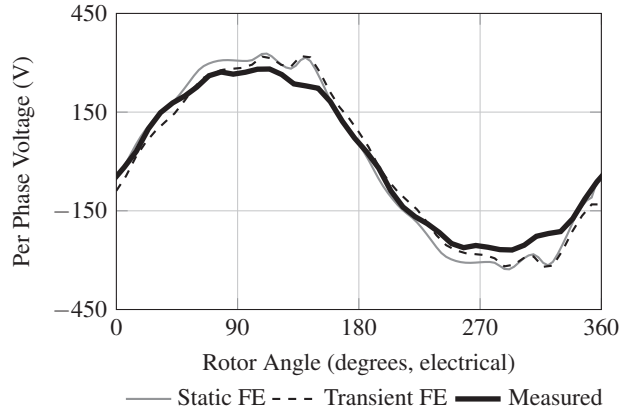


Figure 6: FE-calculated and measured induced voltage waveforms of the PMSG.

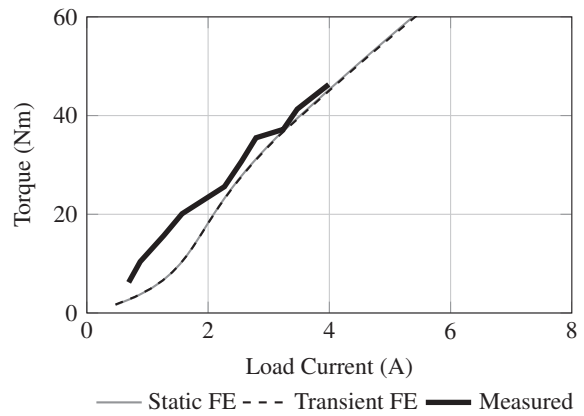


Figure 7: FE-calculated and measured torque versus load current of the grid-connected PMSG.

the same shape in both cases, and the measured efficiency is still above 80% for most of its operating range. It is expected that the measured current density will also be higher than the simulated value.

Another important characteristic for direct grid-connected operation is the power factor, which is shown in Fig. 9 for the grid-connected PMSG prototype. For both the measured and simulated values the power factor is above 0.9 for most of the machine operating range. The mismatch between the simulated and measured power factors at low torque loads as shown in Fig. 9, can be explained by the lower ampere/torque measured at low loads of the PMSG as shown in Fig. 7, which leads to a lower kVA supply and an increased power factor.

6. CONCLUSIONS

In this paper the optimum design of a grid-connected PMSG for a slip-coupled wind generator drive train is described and the construction, and testing results of a prototype generator are presented. The machine is shown to perform adequately, albeit not quite as good as the original design performance. The prototype achieved an efficiency above 80% and a power factor above 0.9 for most of its operating range. Thus it can be concluded

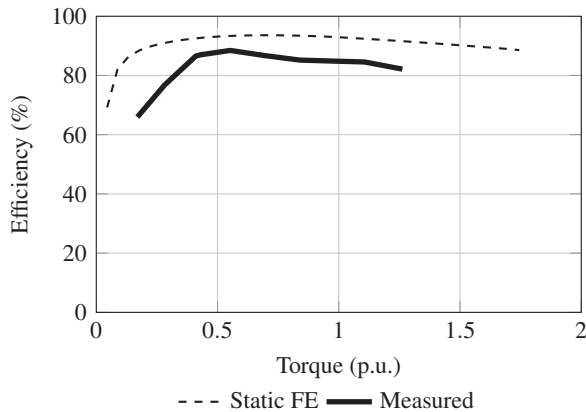


Figure 8: FE-calculated and measured efficiency versus per unit torque of the grid-connected PMSG.

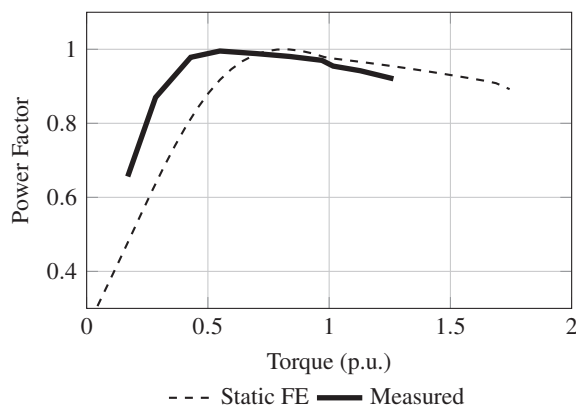


Figure 9: FE-calculated and measured power factor versus per unit torque of the grid-connected PMSG.

that the PMSG constructed in this investigation is entirely feasible for direct grid-connected operation. Further minor changes to the design may be required to meet the exact requirements of the grid code specifications. The next step in this investigation is to perform a full scale field test of the entire wind generator drive-train, with actual wind power then as input, and the PMSG directly grid-connected. It would be most enlightening to evaluate the system's performance during a field test, especially to observe the effects of torque transients on the PMSG output voltage and current quality.

REFERENCES

- [1] J. A. Baroudi and V. Dinavahi, "A review of power converter topologies for wind generators," in *Proc. IEEE International Electric Machines & Drives Conference (IEMDC 2005)*, San Antonio, Texas, USA, 2005, pp. 458–465.
- [2] A. J. G. Westlake, J. R. Bumby, and E. Spooner, "Damping the power-angle oscillations of a permanent-magnet synchronous generator with particular reference to wind turbine applications," *IEEE Proceedings - Electric Power Applications*, vol. 143, no. 3, pp. 269–280, 1996.
- [3] S. Grabic, N. Celanovic, and V. A. Katic, "Permanent magnet synchronous generator cascade for wind turbine application," *IEEE Transactions on Power Electronics*, vol. 23, no. 3, pp. 1136–1142, 2008.
- [4] C. Rossi, P. Corbelli, and G. Grandi, "W-CVT continuously variable transmission for wind energy conversion system," in *Proc. IEEE Power Electronics and Machines in Wind Applications (PEMWA 2009)*, Lincoln, Nebraska, USA, 2009, pp. 1–10.
- [5] T. Fukami, K. Nakagawa, Y. Kanamaru, and T. Miyamoto, "A technique for the steady-state analysis of a grid-connected permanent magnet induction generator," *IEEE Transactions on Energy Conversion*, vol. 19, no. 2, pp. 318–324, 2004.
- [6] J. H. Potgieter and M. J. Kamper, "Design of new concept permanent magnet induction wind generator," in *Proc. IEEE Energy Conversion Congress and Exposition (ECCE 2010)*, Atlanta, Georgia, USA, Sep. 2010, pp. 2403–2408.
- [7] —, "Design of new concept direct grid-connected slip-synchronous permanent-magnet wind generator," *IEEE Transactions on Industry Applications*, vol. 48, no. 3, pp. 913–922, May 2012.
- [8] —, "Optimum design and technology evaluation of slip permanent magnet generators for wind energy applications," in *Proc. IEEE Energy Conversion Congress and Exposition (ECCE 2012)*, Raleigh, North Carolina, USA, Sep. 2012, pp. 2342–2349.
- [9] P. J. J. Van Wyk and M. J. Kamper, "Simplified analysis technique for double layer non-overlap multiphase slip permanent magnet couplings in wind energy applications," in *Proc. IEEE International Electric Machines & Drives Conference (IEMDC 2015)*, Coeur D'Alene, Idaho, USA, May 2015, pp. 1317–1323.
- [10] P. J. J. Van Wyk, "Design and evaluation of medium speed geared direct grid-connected wind generator drive train with specific focus on slip permanent magnet coupling," Masters Thesis, University of Stellenbosch, 2015.
- [11] J. H. J. Potgieter and M. J. Kamper, "Calculation methods and effects of end-winding inductance and permanent-magnet end flux on performance prediction of nonoverlap winding permanent-magnet machines," *IEEE Transactions on Industry Applications*, vol. 50, no. 4, pp. 2458–2466, Jul. 2014.
- [12] M. J. Kamper, F. S. van der Merwe, and S. Williamson, "Direct finite element design optimisation of the cageless reluctance synchronous machine," *IEEE Transactions on Energy Conversion*, vol. 11, no. 3, pp. 547–553, 1996.
- [13] J. Pyrhonen, T. Jokinen, and V. Hrabovcova, *Design of rotating electrical machines*, 1st ed. Chichester: John Wiley & Sons, 2008.

DEVELOPMENT OF AN ANALYTICAL MODEL FOR A MOVING COIL TUBULAR PERMANENT MAGNET LINEAR OSCILLATORY MACHINE

D. K. Chembe, J. M. Strauss and P. J. Randewijk

Department of Electrical and Electronics, Stellenbosch University, Private Bag X1, Matieland 7602, South Africa E-mail: 18336078@sun.ac.za

Abstract: This paper presents a 2-D analytical model for determining predictive values of the open-circuit magnetic field distribution of surface mounted permanent magnet tubular linear short-stroke oscillatory machine. A resolution of Maxwell equations and separation of variables are used to solve two dimensional Laplace and Poisson equations to develop an analytical model. The presented model is for predicting the air-gap magnetic field in slot-less tubular linear permanent magnet machines and validation is carried out through finite element analysis

Key words: Analytical model development, tubular linear machine, free-piston application

1. INTRODUCTION

Moving coil tubular linear surface mounted permanent magnet oscillatory machine is a type of a short stroke (15 mm), single-phase linear oscillatory generator (LOG) which operate at fixed resonant frequency (mechanical eigenfrequency = electrical frequency). While there are three main types of linear oscillatory machines (LOMs) or (LOGs), the moving coil as compared to its counterparts, the permanent magnet (PM) mover and the iron mover, has a reduced mover mass as an advantage. Due to this, high frequency oscillations can be achieved. With air-coils, LOGs of moving coil type have smaller inductance which lead to larger power factors [1]. Although these machines have lower thrust density, high efficiency and high force density can be achieved according to Amara *et al* [2]. Fixed frequency and stroke length distinguishes linear oscillatory machines from other linear electromagnet machines which have variable frequency and long strokes [3].

Development of analytical models has been pursued due to demand for accurate and quick machine analysis [4]. Polinder *et al* [5] and Bianchi *et al* [6] have used the magnetic equivalent circuit (MEC) method to analyse to develop an analytical model for permanent magnet machines. Although the method they have used is very fast and accurate, it suffers from inaccuracy if there is any large variation in the geometrical parameters. Xu and Chang have proposed an improved MEC for the purpose of optimisation. Still, the improvements could not solve big challenge of MEC [7]. Although finite element method (FEM) is accurate and fast, it is not suitable for design optimization from premature design stages as it takes too long to converge as highlighted by Gysen *et al* [8], Wang *et al* in [9], [10], and others [11], [12], [13].

This paper develops an analytical model using Maxwell equations solutions, a method widely used for its speed and accuracy and for early machine design stages. Similar models have been developed by Wang *et al* (1999) [14],

(2007) [15], [16], Gysen *et al* [8], [17]. However, the models considered are not only for PM mover topologies but also for iron-cored machines. Yan *et al* proposed a model for a similar topology with Halbach arrays but with a short coil length and stroke length is not mentioned [18], [19]. Therefore, this paper proposes an analytical model for tubular machine topologies of double layered magnet structure but with longer coils in relation to magnet pole length and air-cored.

2. ANALYTICAL MODEL DEVELOPMENT FOR FIELD DISTRIBUTION DUE TO PERMANENT MAGNETS

Due to the tubular structure of the permanent magnet linear oscillating machine (LOM), the cylindrical coordinate system is adopted in the formulation of Laplace and Poisson equations [15]. The development of the analytical model is concentrated on radial magnetization topologies which are air-cored and slot-less. To accommodate analysis of the permanent magnet field distribution of the machine, the model is sub-divided into regions based on their magnetic characteristics. Magnetic vector potential expressions are formulated for each region such that Laplace and Poisson equations are satisfied. Together with boundary conditions applied to separate regions, coefficient solutions are obtained.

The following assumptions are implemented for simplicity of the analytical model:

1. Axial length of the machine is considered infinite so that the field distribution is axi-symmetric and periodic in the z-direction,
2. The armature is slot-less and the stator cores are assumed to have a relative permeability of 10,000 Henry per metre,
3. The relative permeability of the permanent magnet is assumed unity ($\mu_r = 1$).

In figure 1 the five sub-domains to determine the field distribution in the air gap are shown.

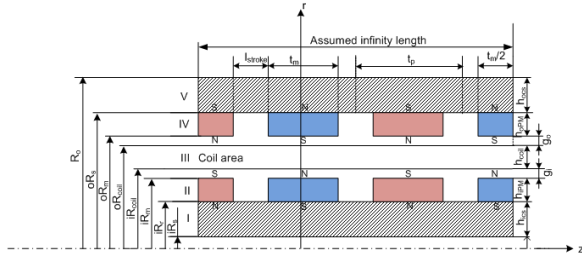


Figure 1: Sub-domains of LOM

The magnetic field analysis focusses on two main aspects of the machine: the regions consisting of permanent magnets and the regions without them. In this case, regions I, III and V have the magnetic flux density \mathbf{B} of the form:

$$\mathbf{B} = \mu_0 \mathbf{H} \quad (1)$$

whereas the regions II and IV containing the permanent magnets have \mathbf{B} of the form:

$$\mathbf{B} = \mu_0 \mu_r \mathbf{H} + \mu_0 \mathbf{M} \quad (2)$$

Where \mathbf{H} , \mathbf{M} are the magnetic field intensity and magnetisation vector respectively. The magnetisation vector is given by:

$$\mathbf{M} = M_r \mathbf{e}_r + M_z \mathbf{e}_z. \quad (3)$$

In equation (3) M_r and M_z , express the components of r and z coordinates respectively. In this case however, the machine being only radially magnetised will have the magnetisation vector in the radial direction only such that $\mathbf{M} = M_r \mathbf{e}_r$ as shown in the following diagram. In the

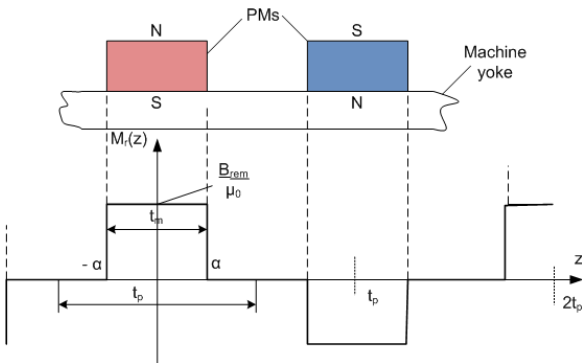


Figure 2: The machine is given with an enlarged linearised portion to show the magnetization radial component of the magnetic flux along the axial coordinate

Figure 2, τ_p, τ_m, B_{rem} the pole pitch, magnet length and remnant magnetisation respectively. M_r can be expressed

as a Fourier series expansion by:

$$M_r(z) = \frac{a_0}{2} + \sum_{n=1, \dots}^{\infty} a_n \cos(\omega_n z), \quad (4)$$

where $\omega_n = \frac{n\pi}{\tau_p}$ since the period is $2\tau_p$. From the figure displaying the radial component of the field, it is clear that.

$$a_n = \frac{1}{\tau_p} \int_{-\tau_p}^{\tau_p} f(z) \cos(\omega_n z) dz, \quad (5a)$$

which is equal to

$$a_n = \frac{2}{\tau_p} \int_0^{\tau_p} f(z) \cos(\omega_n z) dz. \quad (5b)$$

After mathematical manipulation and application of trigonometric identities, a_n is obtained as

$$a_n = \frac{2B_{rem}}{n\pi\mu_0} (1 - (-1)^n) \sin\left(\frac{n\pi\tau_m}{2\tau_p}\right), \quad (6)$$

where $(-1)^n = \cos(n\pi)$ whence,

$$a_{2n-1} = \frac{4B_{rem}}{(2n-1)\pi\mu_0} \sin\left(\frac{(2n-1)\pi\tau_m}{2\tau_p}\right). \quad (7)$$

The value of $M_r(z)$ is therefore equal to

$$M_r(z) = \frac{a_0}{2} + \frac{4B_{rem}}{\pi\mu_0} \sum_{n=1}^{\infty} \frac{1}{(2n-1)} \times \sin\left(\frac{(2n-1)\pi\tau_m}{2\tau_p}\right) \cos(m_n z), \quad (8)$$

where $m_n = (2n-1) \frac{\pi}{\tau_p}$.

2.1 Governing equations

The Governing equations are derived from Maxwell equations. The magnetic vector potential \mathbf{A} is used for the development of Laplace and Poisson equations, as it may be used in regions where current density \mathbf{J} is zero or non-zero. Noting that $\nabla \cdot \mathbf{B} = 0$ and taking into consideration that the divergence of the curl of any vector field is zero.

$$\mathbf{B} = \nabla \times \mathbf{A}. \quad (9)$$

As the vector field are related through the permeability μ as displayed in (1) and $\nabla \times \mathbf{H} = \mathbf{J}$ we obtain:

$$\nabla \times \mathbf{B} = \mu \mathbf{J}. \quad (10)$$

Inserting (9) into (10) results in:

$$\nabla \times \nabla \times \mathbf{A} = \mu \mathbf{J}. \quad (11)$$

This equation represents the axi-symmetric nature of the topology under scrutiny. If the current density $\mathbf{J} = 0$, then the equation (11) becomes a Laplace equation and represents non-magnet regions of the machine in regions

I, III and *V*,

$$\nabla \times \nabla \times \mathbf{A} = 0, \quad (12)$$

whereas a Poisson equation is obtained for permanent magnet machine regions of *II* and *IV* of the form

$$\nabla \times \nabla \times \mathbf{A} = -\mu_0 \nabla \times \mathbf{M}. \quad (13)$$

Due to the axi-symmetric nature of the magnetic field distribution of the tubular LOM, the magnetic vector potential has only the A_ϕ component and therefore, the Laplace and Poisson equations with respect to the sub-domains of the machine will appear as shown in (14) in cylindrical coordinate system. For the regions *I, III* and *V* the Laplace equations are:

$$\frac{\partial^2 A_{I\phi}}{\partial z^2} + \frac{\partial^2 A_{I\phi}}{\partial r^2} + \frac{1}{r} \frac{\partial A_{I\phi}}{\partial r} - \frac{1}{r} A_{I\phi} = 0 \quad (14a)$$

$$\frac{\partial^2 A_{III\phi}}{\partial z^2} + \frac{\partial^2 A_{III\phi}}{\partial r^2} + \frac{1}{r} \frac{\partial A_{III\phi}}{\partial r} - \frac{1}{r} A_{III\phi} = 0 \quad (14b)$$

$$\frac{\partial^2 A_{V\phi}}{\partial z^2} + \frac{\partial^2 A_{V\phi}}{\partial r^2} + \frac{1}{r} \frac{\partial A_{V\phi}}{\partial r} - \frac{1}{r} A_{V\phi} = 0 \quad (14c)$$

The Poisson equations for permanent magnet regions of *II* and *IV* are:

$$\frac{\partial^2 A_{II\phi}}{\partial z^2} + \frac{\partial^2 A_{II\phi}}{\partial r^2} + \frac{1}{r} \frac{\partial A_{II\phi}}{\partial r} - \frac{1}{r} A_{II\phi} = -\mu_0 \nabla \times \mathbf{M} \quad (15a)$$

$$\frac{\partial^2 A_{IV\phi}}{\partial z^2} + \frac{\partial^2 A_{IV\phi}}{\partial r^2} + \frac{1}{r} \frac{\partial A_{IV\phi}}{\partial r} - \frac{1}{r} A_{IV\phi} = -\mu_0 \nabla \times \mathbf{M} \quad (15b)$$

The magnetisation vector \mathbf{M} as described in equation (3), is related to the remnant flux density such that $\mathbf{M} = \frac{B_{rem}}{\mu_0}$. The value of \mathbf{M} as determined in equation (8) is key to getting the solution to the Poisson equation as expressed in equation (15) and will be demonstrated later.

2.2 Solution to the Laplace equation

With the application of separation of variables to the Laplace equation of equation (14), the magnetic vector potential is therefore assumed to be $A_{i\phi}(r, z) = R(r)Z(z)$, where i represents the regions *I, III* and *V*. Separation of variables is achieved by replacing A_ϕ into the Laplace equation (14) and dividing by $R(r)Z(z)$. The separated variables must be equivalent to a constant c_k .

$$\frac{1}{Z(z)} \frac{d^2 Z(z)}{dz^2} = - \left[\frac{1}{R(r)} \frac{d^2 R(r)}{dr^2} + \frac{1}{R(r)r} \frac{dR(r)}{dr} - \frac{1}{r^2} \right] = c_k, \quad (16)$$

it therefore follows that,

$$\frac{d^2 Z(z)}{dz^2} - c_k Z(z) = 0, \quad (17a)$$

which in short form can be written as

$$Z'' - c_k Z = 0, \quad (17b)$$

which is a second order linear differential equation so that the radial variable can be obtained as:

$$r^2 \frac{d^2 R(r)}{dr^2} + r \frac{dR(r)}{dr} + (r^2 c_k - 1) R(r) = 0, \quad (18a)$$

which in short form can be written as

$$r^2 R'' + rR' + (r^2 c_k - 1)R = 0. \quad (18b)$$

The solutions to the separated variables of $R(r)$ and $Z(z)$ depends on the case values of c_k . Three case values are obtained for which solutions are sort for and these are, $c_k = 0$, $c_k > 0$ and $c_k < 0$. The required solution for A_ϕ from the mentioned cases has to be periodic in z direction. Therefore, the solutions obtained for the case values of $c_k = 0$ and $c_k > 0$ are not periodic in z direction and are thus not considered. The case of $c_k < 0$, taken as $c_k = -k^2$, provides a solution which is periodic in z direction. Replacing c_k with $-k^2$ in equations (17) and (18) gives the general solution as,

$$A_\phi(r, z) = [A_0 I_1(mr) + B_0 K_1(mr)] \times \quad (19)$$

$$[C_0 \cos(mz) + D_0 \sin(mz)] \quad (20)$$

which can be rewritten as

$$A_\phi(r, z) = \begin{cases} [E_0 I_1(mr) + F_0 K_1(mr)] \cos(mz) \\ + \\ [G_0 I_1(mr) + H_0 K_1(mr)] \sin(mz) \end{cases} \quad (21)$$

In this solution, m is a real number defined by $k = jm$, whereas I_1 and K_1 are Modified Bessel functions of the first and second order respectively.

Due to the fact that the axial component of the magnetic flux density is very minimal at $z = 0$ which implies that $B_{z|z=0} = 0$. Also considering that I_1 and K_1 are independent of each other, E_0 and F_0 are taken as zero (0).

Therefore the general solution to Laplace equation is

$$A_\phi(r, z) = [a_n I_1(mr) + b_n K_1(mr)] \sin(mz). \quad (22)$$

To form a complete series solution, superposition principal is applied while considering that $a_n = G_0$ and $b_n = F_0$ to obtain

$$A_\phi(r, z) = \sum_{n=1, \dots}^{\infty} [a_n I_1(m_n r) + b_n K_1(m_n r)] \sin(m_n z). \quad (23)$$

This equation is the final equation for the homogeneous solution of Laplace equation.

2.3 Solution to Poisson equation

The Poisson equation (15) has a corresponding homogeneous equation's general solution equivalent to that of Laplace equation shown in equation (23). However the full solution can only be completed when the right side

of equation (15), $(\mu_0 \nabla \times \mathbf{M})$, is replaced by the harmonic expansion of the magnetisation vector solved in equation (8), since

$$\nabla \times \mathbf{M} = \frac{\partial M_r}{\partial z} \mathbf{e}_\phi. \quad (24)$$

The differentiation and multiplication with μ_0 leads to the solution of the whole right side of Poisson equation to be

$$\nabla^2 A_{\phi j} = \frac{4B_{rem}}{\tau_p} \sum_{n=1}^{\infty} \sin\left(\frac{(2n-1)\pi}{2} \frac{\tau_m}{\tau_p}\right) \sin(m_n z). \quad (25)$$

In this equation j represents the regions *II* and *IV*. The Poisson equation in cylindrical coordinate appears as

$$\frac{\partial^2 A_\phi}{\partial z^2} + \frac{\partial^2 A_\phi}{\partial r^2} + \frac{1}{r} \frac{\partial A_\phi}{\partial r} - \frac{1}{r} A_\phi = P_n \sin(m_n z). \quad (26)$$

Separation of variables is again applied in a similar way it has been handled for the Laplace equation. With $P_n = \frac{4B_{rem}}{\tau_p} \sin\left[(2n-1)\frac{\pi}{2} \frac{\tau_m}{\tau_p}\right]$, the anticipated result for the Poisson equation is

$$A_\phi = \sum_{n=1, \dots}^{\infty} [a_n I_1(m_n r) + b_n K_1(m_n r)] \sin(m_n z) + S(r, z). \quad (27)$$

After applying the separation of variables together with mathematical manipulation while taking into consideration that $S(r, z) = R(r)Z(z)$, we obtain the equation for $S(r, z)$ as

$$S(r, z) = R(r)Z(z) = \frac{\pi L_1(m_n r)}{2m_n^2} P_n \sin(m_n z). \quad (28)$$

where $L_1(x)$ is the solution to the inhomogeneous Bessel's equation and it is a Modified Struve Function according to Bowman [20]. Therefore, the solution to Poisson equation in this case becomes:

$$A_{\phi j} = \sum_{n=1, \dots}^{\infty} [a_n I_1(m_n r) + b_n K_1(m_n r)] \sin(m_n z) + \frac{\pi L_1(m_n r)}{2m_n^2} P_n \sin(m_n z). \quad (29)$$

The magnetic vector potential for all the regions has been obtained following the obtained Laplace and Poisson equations solved and displayed as:

$$A_\phi(r, z) = \begin{cases} \sum_{n=1, \dots}^{\infty} [a_{In} I_1(m_n r) + b_{In} K_1(m_n r)] \sin(m_n z) \\ \sum_{n=1, \dots}^{\infty} [a_{II n} I_1(m_n r) + b_{II n} K_1(m_n r)] \sin(m_n z) \\ + \frac{\pi L_1(m_n r)}{2m_n^2} P_n \sin(m_n z) \\ \sum_{n=1, \dots}^{\infty} [a_{III n} I_1(m_n r) + b_{III n} K_1(m_n r)] \sin(m_n z) \\ \sum_{n=1, \dots}^{\infty} [a_{IV n} I_1(m_n r) + b_{IV n} K_1(m_n r)] \sin(m_n z) \\ + \frac{\pi L_1(m_n r)}{2m_n^2} P_n \sin(m_n z) \\ \sum_{n=1, \dots}^{\infty} [a_{V n} I_1(m_n r) + b_{V n} K_1(m_n r)] \sin(m_n z) \end{cases} \quad (30)$$

The coefficients a_{in} and b_{in} have subscripts *I, II, III, IV* and *V* which represent the regions of analysis as shown

in Figure 1.

2.4 Solution to Magnetic Flux Density

The magnetic flux density is calculated from equation (9)

$$\mathbf{B} = \nabla \times \mathbf{A} = -\frac{1}{r} \frac{\partial r A_\phi}{\partial z} \mathbf{e}_r + \frac{1}{r} \frac{\partial r A_\phi}{\partial r} \mathbf{e}_z \quad (31)$$

A_ϕ is only a component of ϕ . From the equation (31) it is clear that $B_r = -\frac{\partial r A_\phi}{\partial z} \mathbf{e}_r$ and $B_z = \frac{1}{r} \frac{\partial r A_\phi}{\partial r} \mathbf{e}_z$. Therefore after differentiating the magnetic vector potential for the r and z results into:

$$B_r = \begin{cases} \sum_{n=1, \dots}^{\infty} -m_n [a_{In} I_1(m_n r) + b_{In} K_1(m_n r)] \cos(m_n z) \\ \sum_{n=1, \dots}^{\infty} -m_n \{ [a_{II n} I_1(m_n r) + b_{II n} K_1(m_n r)] \cos(m_n z) \\ + \frac{\pi L_1(m_n r)}{2m_n^2} P_n \cos(m_n z) \} \\ \sum_{n=1, \dots}^{\infty} -m_n [a_{III n} I_1(m_n r) + b_{III n} K_1(m_n r)] \cos(m_n z) \\ \sum_{n=1, \dots}^{\infty} -m_n \{ [a_{IV n} I_1(m_n r) + b_{IV n} K_1(m_n r)] \cos(m_n z) \\ + \frac{\pi L_1(m_n r)}{2m_n^2} P_n \cos(m_n z) \} \\ \sum_{n=1, \dots}^{\infty} -m_n [a_{V n} I_1(m_n r) + b_{V n} K_1(m_n r)] \cos(m_n z) \end{cases} \quad (32)$$

The values of the magnetic flux density in the radial direction can only be obtained and used after obtaining the coefficients. Boundary equations have to be applied in order to achieve the required results. The equations for the axial direction for the magnetic flux density B_z are obtained after differentiation and results into:

$$B_z = \begin{cases} \sum_{n=1, \dots}^{\infty} m_n [a_{In} I_0(m_n r) - b_{In} K_0(m_n r)] \sin(m_n z) \\ \sum_{n=1, \dots}^{\infty} m_n \{ [a_{II n} I_0(m_n r) - b_{II n} K_0(m_n r)] \sin(m_n z) \\ + \frac{\pi L_0(m_n r)}{2m_n^2} P_n \sin(m_n z) \} \\ \sum_{n=1, \dots}^{\infty} m_n [a_{III n} I_0(m_n r) - b_{III n} K_0(m_n r)] \sin(m_n z) \\ \sum_{n=1, \dots}^{\infty} m_n \{ [a_{IV n} I_0(m_n r) - b_{IV n} K_0(m_n r)] \sin(m_n z) \\ + \frac{\pi L_0(m_n r)}{2m_n^2} P_n \sin(m_n z) \} \\ \sum_{n=1, \dots}^{\infty} m_n [a_{V n} I_0(m_n r) + b_{V n} K_0(m_n r)] \sin(m_n z) \end{cases} \quad (33)$$

Dirichlet and discontinuous Boundary conditions are applied between the boundaries of the the machine displayed in Figure 1 so as to obtain the values of the coefficients in equations (30), (32) and (33). The boundary condition applied are:

$$A_I|_{r=iR_s} = 0 \quad (34a)$$

$$A_V|_{r=R_o} = 0 \quad (34b)$$

$$B_{rI}|_{r=iR_r} = B_{rII}|_{r=iR_r} \quad (34c)$$

$$B_{rII}|_{r=iR_m} = B_{rIII}|_{r=iR_m} \quad (34d)$$

$$B_{rIII}|_{r=oR_m} = B_{rIV}|_{r=oR_m} \quad (34e)$$

$$B_{rIV}|_{r=oR_s} = B_{rV}|_{r=oR_s} \quad (34f)$$

$$H_{zI}|_{r=iR_r} = H_{zII}|_{r=iR_r} \quad (34g)$$

$$H_{zII}|_{r=iR_m} = H_{zIII}|_{r=iR_m} \quad (34h)$$

$$H_{zIII}|_{r=oR_m} = H_{zIV}|_{r=oR_m} \quad (34i)$$

$$H_{zIV}|_{r=oR_s} = H_{zV}|_{r=oR_s} \quad (34j)$$

The magnetic flux density is related with the magnetic field intensity as

$$\mathbf{H} = \frac{\mathbf{B}}{\mu} \quad (35)$$

Upon application of the boundary equation ten simultaneous equation are formed and the coefficients are solved through a matrix of the form:

$$\begin{bmatrix} I_1(m_n i R_s) & \cdot & \cdot & \cdot \\ I_1(m_n i R_r) & \cdot & \cdot & \cdot \\ I_0(m_n i R_r) & \cdot & \cdot & \cdot \\ \cdot & \cdot & \cdot & \cdot \\ \cdot & \cdot & \cdot & \cdot \\ \cdot & \cdot & \cdot & \cdot \\ \cdot & \cdot & \cdot & \cdot \\ \cdot & \cdot & \cdot & \cdot \end{bmatrix} \begin{bmatrix} a_{In} \\ b_{In} \\ a_{IIIn} \\ b_{IIIn} \\ a_{IVn} \\ b_{IVn} \\ a_{Vn} \\ b_{Vn} \end{bmatrix} = \begin{bmatrix} 0 \\ \frac{\pi L_1(m_n i R_r)}{2m_n^2} P_n \\ \mu_f \frac{\pi L_0(m_n i R_r)}{2m_n^2} P_n \\ -\frac{\pi L_1(m_n i R_m)}{2m_n^2} P_n \\ -\frac{\pi L_0(m_n i R_m)}{2m_n^2} P_n \\ \frac{\pi L_1(m_n o R_m)}{2m_n^2} P_n \\ \frac{\pi L_0(m_n o R_m)}{2m_n^2} P_n \\ -\frac{\pi L_1(m_n o R_s)}{2m_n^2} P_n \\ -\mu_f \frac{\pi L_0(m_n o R_s)}{2m_n^2} P_n \\ 0 \end{bmatrix} \quad (36)$$

The final solution of the magnetic vector potential and the magnetic flux densities are obtained by replacing the calculated coefficients $a_{In}, a_{IIIn}, a_{IVn}$ and a_{Vn} together with $b_{In}, b_{IIIn}, b_{IVn}$ and b_{Vn} into the equations (30), (32) and (33) to get the particular solution for particular domains or regions of the machine for number of harmonics.

The magnitude of the magnetic flux density can be obtained from:

$$B_i(r, z) = \sqrt{B_{ir}^2(r, z) + B_{iz}^2(r, z)} \quad (37)$$

Since this equation provides us with the total flux density, the graph plot of the equation (37) shows the peak value of the total flux density obtained.

3. VALIDATION OF OPEN CIRCUIT MODEL WITH FINITE ELEMENT METHOD(FEM)

The 2D analytical model developed has been compared with finite element method (FEM) for particular dimensions of the linear double layered permanent magnet oscillating machine topology. NdFeb magnets with $B_{rem} = 1.39T$ and $\mu_r = 1.04$ were adopted for both the analytical model and the FEM. It should be noted that $\mu_r = 1$ was the assumed value for the magnets.

Periodic boundary conditions are used at the axial boundaries of the finite element model as well as for the continuous boundary conditions that was adopted between the stator and armature for desired solutions. Since the topology under study is a slot-less, coil-mover linear oscillatory machine, with surface mounted radially magnetised permanent magnets, the developed analytical model can only apply to such topologies. Figures 3 and 4 shows the comparison of results from analytical model and FEM in the permanent magnets, both lower and upper

and in the air-gap. In Figure 3 and 4 the radial and axial flux density distributions in the air-gap and in the both layers of permanent magnets are shown respectively. As can be seen from the figures below, the analytical model compares well with finite element results.

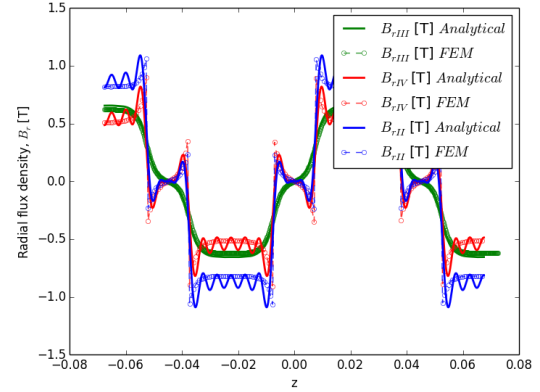


Figure 3: Radial component of flux density comparison as a function of z at $r = (iR_m + oR_m)/2$ is B_{rIII} in green (air-gap), at $r = (iR_r + iR_m)/2$ is B_{rII} in blue (inner PMs) and at $r = (oR_r + oR_m)$ is B_{rIV} in red (outer PMs)

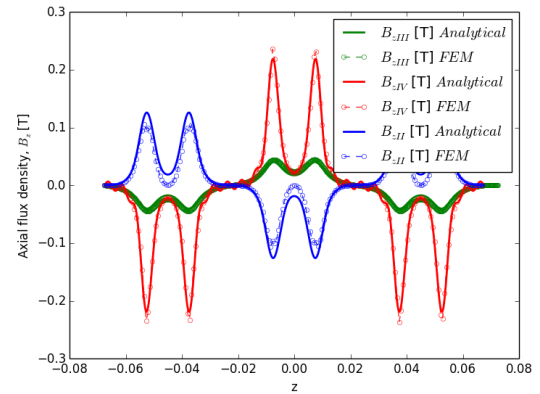


Figure 4: Axial component of flux density comparison as a function of z at $r = (iR_m + oR_m)/2$ is B_{zIII} in green (air-gap), at $r = (iR_r + iR_m)/2$ is B_{zII} in blue (inner PMs) and at $r = (oR_r + oR_m)$ is B_{zIV} in red (outer PMs)

4. DISCUSSION

Considering that the model uses the $(2n - 1)^{th}$ harmonic, it is observed that up to the 17^{th} harmonic, the model operates excellently well. However, over the 17^{th} harmonic the model begins to struggle. Nevertheless, this challenge is very particular to Bessel functions in cylindrical coordinate system on which scaling techniques for the coefficient a_{in} and b_{in} cannot be applied [8]. The effects of a finite number of harmonics can be well observed in the radial flux densities especially in the PMs.

Therefore, only solutions up to the 17th harmonic needs to be considered.

5. CONCLUSION

The analytical model has for the open-circuit magnetic field distribution has been successfully developed for a class of radially magnetised tubular linear permanent magnet oscillating machines. This model is ideal as a design tool for design optimisation and also for comparative studies. The model is further used to determine thrust force, flux-linkages and EMF for performance analysis which has not been shown in this paper. The model is validated with 2D finite element analysis and results show that the analytical model agrees very well with those of finite element method.

ACKNOWLEDGEMENT

The Author would like to thank the Africa for Innovation, Mobility, Exchange, Globalization and Quality (AFIMEGQ) and the Copperbelt University of Zambia for the sponsorship.

REFERENCES

- [1] I. Boldea, Linear Electric Machines, Drives, and MAGLEVs *Handbook*. CRC Press, Taylor and Francis Group, 2013.
- [2] Y. Amara, G. Barakat, and P. Reghem, "Armature Reaction Magnetic Field of Tubular Linear Surface-Inset Permanent-Magnet Machines", *IEEE Trans. Magn.*, vol. 47, no. 4, pp. 805811, 2011.
- [3] I. Boldea and S. A. Nasar, "Linear electric actuators and generators", *IEEE Trans. Energy Convers.*, vol. 14, pp. 712717, 1999.
- [4] Y. Amara and G. Barakat, "Analytical modeling of magnetic field in surface mounted permanent-magnet tubular linear machines", *IEEE Trans. Magn.*, vol. 46, pp. 38703884, 2010.
- [5] H. Polinder, J. G. Sloopweg, J. . Compter, and M. . Hoeijmakers, "Modelling a linear PM motor including magnetic saturation", *IEEE Power Electronics, Machines and Drives*, 2002.
- [6] N. Bianchi, S. Bolognani, and F. Tonel, "Design Criteria of a Tubular Linear IPM Motor", *IEEE Trans. Ind. Electron.*, vol. 3, pp. 17, 2001.
- [7] Z. Xu and S. Chang, "Improved moving coil electric machine for internal combustion linear generator", *IEEE Trans. Energy Convers.*, vol. 25, no. 2, pp. 281286, 2010.
- [8] B. L. J. Gysen, K. J. Meessen, J. J. H. Paulides, and E. A. Lomonova, "General Formulation of the Electromagnetic Field Distribution in Machines and Devices Using Fourier Analysis", *IEEE Trans.*, vol. 46, pp. 3952, 2010.
- [9] J. Wang, D. Howe, and G. W. Jewell, "Fringing in Tubular Permanent-Magnet Machines : Part I . Magnetic Field Distribution , Flux Linkage , and Thrust Force", *IEEE Trans. Magn.*, vol. 39, no. 6, pp. 35073516, 2003.
- [10] J. Wang, Z. Lin, and D. Howe, "Analysis of a short-stroke , single-phase , quasi-Halbach magnetised tubular permanent magnet motor for linear compressor applications", *IET Electr. Power Appl.*, vol. 2, no. January, pp. 193200, 2008.
- [11] H. Tiegna, Y. Amara, and G. Barakat, "Overview of analytical models of permanent magnet electrical machines for analysis and design purposes", *Math. Comput. Simul.*, vol. 90, pp. 162177, 2013.
- [12] X. Chen, Z. Q. Zhu, and D. Howe, "Modeling and Analysis of a Tubular Oscillating Permanent-Magnet Actuator", *IEEE Trans. Ind. Appl.*, vol. 45, 2009.
- [13] H. Tiegna, A. Bellara, Y. Amara, and G. Barakat, "Analytical modeling of the open-circuit magnetic field in axial flux permanent-magnet machines with semi-closed slots", *IEEE Trans. Magn.*, vol. 48, no. 3, pp. 12121226, 2012.
- [14] J. Wang, G. W. Jewel, and D. Howe, "A general framework for the analysis and design of tubular linear permanent magnet machines", *IEEE Trans. Magn.*, vol. 35, no. 3, pp. 19862000, May 1999.
- [15] J. Wang, D. Howe, and Z. Lin, "Comparative study of winding configurations of short-stroke , single phase tubular permanent magnet motor for refrigeration applications", *Ind. Appl. Conf. 2007. 42nd IAS Annu. Meet. Conf. Rec. 2007 IEEE*, pp. 311318, 2007.
- [16] J. Wang, D. Howe, and Z. Lin, "Comparative studies on linear motor topologies for reciprocating vapor compressors, in *Proceedings of IEEE International Electric Machines and Drives Conference, IEMDC 2007*, 2007, vol. 1, pp. 364369.
- [17] B. L. J. Gysen, E. A. Lomonova, J. J. H. Paulides and A.J.A Vandenput, "Analytical and Numerical Techniques for Solving Laplace and Poisson Equations in a Tubular Permanent-Magnet Actuator :, *IEEE Trans. Magn.*, vol. 44, no. 7, pp. 17511760, 2008.
- [18] L. Yan, I. Chen, and C. K. Lim, "Magnetic Field Modeling of Linear Machines with, *fluid power mechatronics*, *IEEE*, pp. 16, 2011.
- [19] L. Yan, L. Zhang, T. Wang, Z. Jiao, C. Chen, and I. Chen, "Magnetic Field of Tubular Linear Machines, *Prog. Electromagn. Res.*, vol. 136, no. November 2012, pp. 283299, 2013.
- [20] F. Bowman, "Introduction to Bessel Functions," *Handbook*. Longmans, Green and Co., 1938.

DESIGN AND OPTIMISATION OF AN IRONLESS DOUBLE-ROTOR RADIAL FLUX PERMANENT MAGNET MACHINE.

A. Joss and P.J. Randewijk

*Department of Electrical and Electronic Engineering, Stellenbosch University, South Africa
E-mail: 16450612@sun.ac.za*

Abstract: This paper consists of the multi-objective optimisation of an Ironless Double-Rotor Radial Flux Permanent Magnet (IDRFPM) machine. The electromagnetic aspects are mainly considered. A methodology regarding the multi-objective optimisation of the IDRFPM machine is presented. The objectives to be optimised include efficiency, torque and PM mass. The solutions of the optimisation process are also briefly discussed. Furthermore, eddy current losses due to the magnetic flux experienced by the coil windings are investigated.

Key words: multi-objective optimisation, permanent magnet electrical machines, eddy current losses

1. INTRODUCTION

This paper consists of the multi-objective optimisation of an Ironless Double-Rotor Radial Flux Permanent Magnet (IDRFPM) machine. The electromagnetic aspects of the machine are considered in the optimisation process. The magnets which are to be optimised are arranged in a quasi-Halbach topology. According to the authors' knowledge, no literature exists which comprehensively discusses the design optimisation of this machine. A methodology regarding the multi-objective optimisation of the IDRFPM machine is presented. The objectives to be optimised include efficiency, torque and PM mass. The results of the optimisation process are also discussed. A prototype machine exists, which was used as a benchmark for other possible solutions. The prototype machine was designed using only engineering intuition. For this paper, it is desired to obtain an improved machine design. Furthermore, eddy current losses due to the magnetic flux experienced by the coil windings are investigated, and the eddy current losses of the prototype machine are measured and compared to theoretical values.

2. GOAL

The goal of this study is to optimise the IDRFPM machine with regard to three competing objectives, namely efficiency (η), torque (τ) and PM mass (m). The existing prototype machine is used as a benchmark for the evaluation of new design solutions. The prototype machine is designed in [1] for a prototype car that would be entered in the Shell Eco Marathon competition.

The three competing objectives give rise to the term "Pareto optimal set". The aforementioned term is a set of solutions non of which are superior to the other. A solution is Pareto optimal if it is not possible to improve at least one objective function without causing another objective function to deteriorate. In this paper, the decision-maker is presented with a set of Pareto optimal

solutions a posteriori. This means the decision-maker does not articulate preferences beforehand, but rather manually selects a solution after completion of an approximate Pareto front. This way, amongst other things, the decision-maker can decide between similarly pleasing results and compare designs according to ease of manufacturing. Furthermore, it is possible for similar solutions in the objective space, $\mathbf{f}(\mathbf{x})$, to correspond with completely different solutions in the design space, \mathbf{x} .

In general, for any multi-objective function, it is desired to optimise a vector of objective functions

$$\text{Optimise } \mathbf{f}(\mathbf{x}) = [f_1(\mathbf{x}), f_2(\mathbf{x}), \dots, f_k(\mathbf{x})]^T \quad (1)$$

In this paper, the vector of multi-objective functions is described as

$$\text{Optimise } \mathbf{f}(\mathbf{x}) = [f_\eta(\mathbf{x}), f_\tau(\mathbf{x}), f_m(\mathbf{x})]^T \quad (2)$$

where \mathbf{x} is the design-space vector containing all the variables of concern which describe the machine's dimensions that need to be optimised.

3. MULTI-OBJECTIVE OPTIMISATION

A wide selection of multi-objective optimisation techniques are available, for example the Lexicographic Method, Bounded Objective Function Method, Normal Boundary Intersection Method, Normal Constraint Method, scalarisation (weighted) methods, and the Multi-objective Genetic Algorithm (MOGA) [2] [3] [4]. All the methods except for the last mentioned method, reduce the multi-objective optimisation problem to single-objective optimisation subproblems (where the weighted methods reduce the problem within a single step, and the other methods require sequential steps of single-objective solving or extra constraints to reduce the problem to a final single-objective problem). In contrast, MOGA can solve multi-objective problems directly and is

also not gradient dependant, but is however more complex to program [2].

No single method is best for all circumstances, therefore the method to be selected depends solely on the personal preferences and problem insight of the decision-maker [2], [3]. In this study, the Weighted Sum Method (WSM) is used due to the ease of implementation and relative acceptable results. In spite of these advantages, much literature exists explaining the pitfalls of using this method. The first pitfall is that this method is unable to capture Pareto optimal points situated on non-convex portions of the Pareto optimal curve. The second pitfall is that the method does not produce an even distribution of points on the Pareto curve when using consistent change in weights [5]. In [6], an adapted WSM method is revealed which determines uniformly-spaced Pareto optimal solutions, however this also adds more programming complexity and was avoided for this reason. The normal WSM is described as

$$f(\mathbf{x}) = \sum_{k=1}^n w_k f_k(\mathbf{x}), \quad (3)$$

where the weights (which can be selected otherwise) are chosen in this paper such that

$$\sum_{k=1}^n w_k = 1. \quad (4)$$

The multi-objective function (2) is then scalarised into the form of

$$f(\mathbf{x}) = w_1 \eta(\mathbf{x}) + w_2 \tau(\mathbf{x}) - w_3 m(\mathbf{x}), \quad (5)$$

where the weights w_1 , w_2 and w_3 are varied to produce a representation of the Pareto optimal set. The last term is subtracted because it is desired to minimise PM mass, while maximising efficiency and torque.

Furthermore, [5] discussed that it can be difficult to distinguish between setting weights to compensate for differences in objective function magnitudes as opposed to setting weights in order to indicate the relative importance of an objective. For this reason, it is advised to transform each objective function so that they all have similar magnitudes. Many different approaches exist to transform an objective function. One of the simplest, is to divide the objective function by its maximum achievable value [2], thereby the new transformed function has an upper limit of one and an unbounded lower limit. Practical realisable machines will not produce negative values of efficiency, torque or PM mass. The maximum value of each objective function can be obtained either by maximising only for the specific objective function or it can be determined by engineering intuition.

$$f_i^{\text{trans}}(\mathbf{x}) = \frac{f(\mathbf{x})}{|f_i^{\text{max}}(\mathbf{x})|} \quad (6)$$

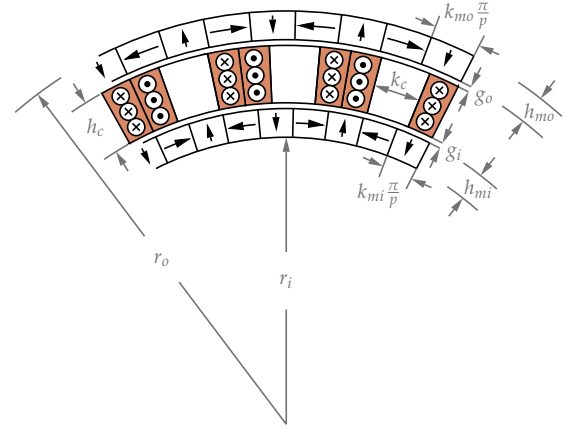


Figure 1: IDRFPM with design variables

4. IMPLEMENTATION OF OPTIMISATION

In order to insure that the weights operate as intended (indicating relative importance rather than compensating for difference in magnitudes), the objective functions in (5) are normalised with their ideal values. The ideal values of each objective function are determined by setting only a single weight to one, and all other weights to zero. Then only a single objective function is optimised without competing against other objective functions.

Figure 1 shows the 9 design variables that are considered. All the variables are defined in per unit relative according to a single absolute value r_o the outer radius. The optimisation process will realise that there is a mathematical relationship between variables h_{mo} , g , h , h_{mi} , r_i and r_o , due to the fixed value of r_o and the minimum value of r_i . The outer radius and stack length are kept constant so that it is possible to benchmark the optimised solutions with the existing prototype of IDRFPM machine. The air-gap width is also kept constant (equal to that of the prototype machine). The variable p denotes the number of pole pairs, k_m describes the ratio in width of the radially magnetised magnets compared to the tangentially magnetised magnets, whilst k_c denotes the ratio of the coil core width compared to the coil slot width. Only non-overlapping coils are considered in this paper. The current density is kept equal to that of the working prototype, thereby hopefully ensuring feasible machines with regards to cooling of the coils.

4.1 Single-Objective Optimisation

To optimise the single-objective function, an open-source Python-based package “pyOpt” was employed. Currently, only one of the methods in pyOpt are being used for this study, namely Sequential Penalty Derivative-free Methods for Nonlinear Constrained Optimisation (SDPEN). This method is ideally suited for engineering applications where the objective function are computed by simulation software and thus derivative information is unknown.

The original problem is solved by a sequence of approximate minimisations of an augmented function of which constraint violations are progressively penalised [7]. The 1-dimensional problem is solved using a line-search algorithm.

4.2 Overall Optimisation Process

The optimisation process to obtain the Pareto surface is described by the flow chart in Figure 2. The simulation is achieved by an in-house 2D FEM package, named SEMFEM.

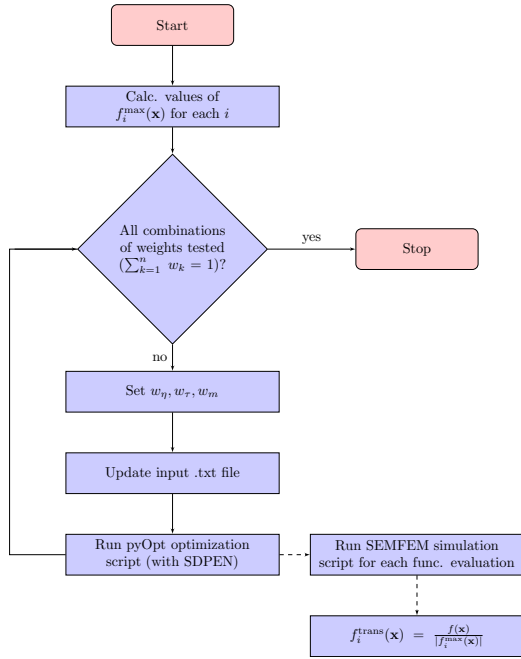


Figure 2: Flowchart of optimisation process

5. OPTIMISATION RESULTS

Figure 3 shows the solutions that were obtained when the process of Figure 2 is executed. The weights are altered using an increment size of 0.025, generating 861 solutions. The simulated output performance of the prototype is used as a benchmark. Any solutions, which in all aspects (efficiency, torque and PM mass), dominate the prototype machine's performance, are indicated with red dots. The prototype solution itself is indicated by the colour magenta. All other solutions are indicated with blue dots. From Figure 3 it is clear that machines exist which dominate the prototype output performance.

Table 1 shows the three solutions that were found, indicated by "1", "2", "3" which dominate the prototype machine, indicated by "P". For the purposes of the competition car, the gain in torque is probably the most appealing. Design solution 3 promises a slight reduction of the required PM mass (2.97%), with unchanged efficiency, but a 15.58% increase in output torque.

	P	1	2	3
Efficiency [%]	84.917	85.893	85.438	84.938
Torque [Nm]	22.644	25.611	24.601	26.172
PM Mass [kg]	2.488	2.469	2.309	2.414
w_η	-	0.450	0.425	0.400
w_τ	-	0.250	0.250	0.275
w_m	-	0.300	0.325	0.325
% η increase	-	1.150	0.613	0.024
% τ increase	-	13.104	8.643	15.584
% m increase	-	-0.775	-7.188	-2.973

Table 1: Simulated solution results which dominate the simulated prototype design

The percentage change of the design variables compared to the prototype design are indicated by Table 2. As shown, variables r_i and k_m remain mostly unchanged. As mentioned before, r_o is kept constant. It can also be seen that the general tendency is for the outer magnet thickness h_{mo} to decrease and the inner magnet thickness h_{mi} and coil thickness h_c to increase. It is interesting to see that for all three solutions, the ratio between the coil core and coil winding angle k_c settles at approximately 25% higher, and the number of pole pairs 43% (to 20 pole pairs) higher, than the prototype value. In future optimisations, it can be considered to keep the variables k_c and p constant to the aforementioned values, thereby speeding up the optimisation process.

Variables	P	$\Delta_1\%$	$\Delta_2\%$	$\Delta_3\%$
r_o	131 mm	0	0	0
r_i	109 mm	-0.211	0.516	-0.846
h_{mo}	55 mm	-8.014	-16.664	-10.595
h_c	9 mm	2.950	2.387	12.904
h_{mi}	55 mm	7.378	0.188	6.103
k_m	0.5 p.u.	-1.128	-1.454	-0.012
k_c	0.718 p.u.	24.737	24.419	26.447
p	14	42.857	42.857	42.857

Table 2: Design variable values (in % change) of the solutions compared to the prototype design (in indicated units)

6. EDDY CURRENT LOSSES

The IDRFP design which is considered in this paper, does not contain any materials in the stator that can be easily magnetised. More specifically, the stator consists only of copper windings cast in resin, which both pertain similar magnetic permeabilities than that of air (also known as a coreless or air-cored stator). For this reason, the magnetic flux path produced by the inner and outer permanent magnets is equally spread in the stator; meaning the copper windings experience a similar magnitude of flux density than that of the winding core "air". This is a quality that is unique to coreless machines, and serves as motivation to investigate the severity of the eddy current

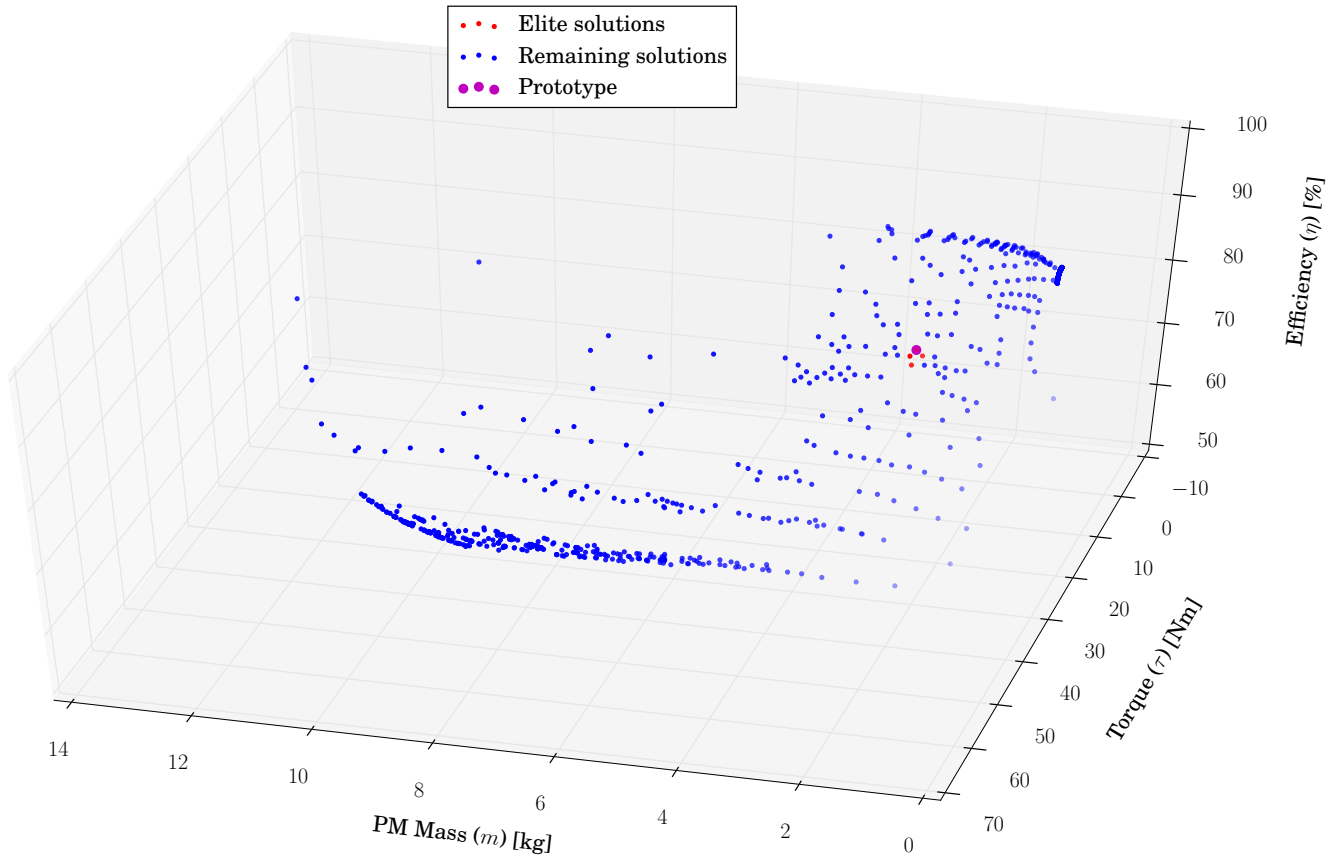


Figure 3: 3D Scatter plot of solution points approximating the Pareto front

losses for this particular machine. Once the approximate magnitude of the expected eddy losses is known, the designer can choose whether or not to include the eddy current loss calculations within the design optimisation process. For the purpose of the discussed optimisation process, it is desired to improve on the existing prototype. As mentioned earlier, the prototype machine is designed for a prototype car which will be entered in the Shell Eco Marathon competition. The competition restricts the maximum system voltage to 48V, therefore relatively large phase currents are required to deliver sufficient torque or power. For this reason, it is expected that conduction losses will be the most significant losses in the machine. It remains however important to investigate the eddy current losses when machines with different applications are envisioned.

Eddy currents are produced in the stator windings when the machine rotates; the stator coils cut the rotating magnetic flux paths, thereby inducing a voltage on the coil terminals but also a voltage within each conductor, the latter voltage generates eddy currents. These eddy currents circulate in small loops perpendicular to the radial direction. The magnetic flux which the stator coil windings experience, are shown in Figure 4. The white regions in the stator indicate the air-cored areas of the coils. Notice that the flux moving through the stator are both in the radial and tangential directions, and that the flux paths are not

affected by the relative position of the stator towards the rotors.

In [8], analytical methods are categorized according to the particular situation. The methods are categorized according to low frequency, high frequency and wide frequency problems. The penetration depth is calculated in order to determine the appropriate method. The penetration depth is approximated by,

$$\delta = \sqrt{\frac{2\rho_c}{\omega_e \mu}} \quad (7)$$

where ω_e is the magnetic field's angular frequency experienced by the conductor. Here we use $\mu = \mu_0$ as copper has an almost equal permeability than that of free space, thus $\mu_0 = 1.25664 \times 10^{-6}$. The resistivity of the copper conductor is given by $\rho_c = 1.73 \times 10^{-8} \Omega\text{m}$ at 25°C . As will be explained later, the resistivity at 25°C is used to verify the theoretical calculation with measured results from the prototype. The rated speed of the 28 pole machine is 300 rpm which equates to an electrical frequency of $f_e = 70\text{Hz}$. The penetration depth is then $\delta = 7.91213 \text{ mm}$.

According to [8], it is considered a low frequency situation when

$$d \leq 1.6\delta \quad (8)$$

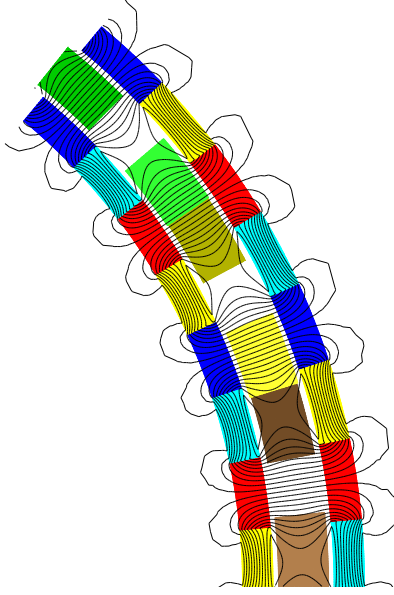


Figure 4: Conceptual IDRFP machine with magnetic paths shown, sizing is identical to that of prototype machine

is satisfied. The conductor diameter is denoted by d . In a low frequency situation, the assumption is made that the eddy currents induced within the windings do not noticeably change the applied magnetic field inside the conductor [9] [10]. This is the easiest route of determining the eddy current losses, if this is not the case then the eddy current induced magnetic field would also need to be taken into account.

The prototype machine was initially constructed using 1.6 mm before it was realized that the eddy current losses are too large. Consequently, a new stator was constructed which makes use of Litz wire. Each wire consists of 70 parallel strands, and a single strand has the diameter of 0.2 mm. The measured eddy current results are shown in Table 3.

Conductor Diameter [mm]	Strands	P_{eddy} [W]
1.6	1	30.5
0.2	70	0.6

Table 3: Measured eddy current losses at 300 rpm [1]

Equation (8) requires that the conductor diameter be less or equal than 12.6594 mm to be qualified as a low frequency problem. Thus for both scenarios of Table 3, the magnetic field induced by the eddy currents can be neglected.

Traditionally, the eddy current losses in windings for a low frequency situation are calculated using a classic equation derived by [11]. The limitations are that it assumes only a one-dimensional (thus only in the radial direction) pure sinusoidal flux component. The classic approximation of the eddy current losses of a single conductor in a transverse alternating field is described by [11] and [?] as

$$P_{eddy} = \frac{\pi l d^4 \hat{B}_{r1r}^2 \omega_e^2}{128 \rho_c}, \quad (9)$$

where l is the axial length of the conductor, \hat{B}_{r1r} is the peak value of the fundamental field density component in the radial direction (one-dimensional direction).

Equation (9) can be used to account for all conductors within the machine

$$P_{eddy} = N Q n_p \left(\frac{\pi l d^4 \hat{B}_{r1r}^2 \omega_e^2}{64 \rho_c} \right), \quad (10)$$

where N is the number of turns per coil per phase, Q is the total (including all three phases) number of stator coils, n_p is the number of parallel strands per turn. A factor two is also multiplied to account for the return path of each conductor.

A more accurate method is suggested by [10]. The method makes use of the classic equation (10), and extends its use to accommodate for both radial and tangential flux components and does not assume pure sinusoidal flux components. The extra information of the field density is then obtained by a two-dimensional FEM simulation and subsequently using the Fast Fourier Transform. This method is therefore known as the hybrid method. Furthermore, it provides for different values of flux densities to be used depending on the position of the particular winding layer. This is important because the flux densities are fairly higher closer to the magnets and from (10) the eddy losses are proportional to B^2 . The eddy current losses calculated using the hybrid method is described as

$$P_{eddy} = N Q n_p \left(\frac{\pi l d^4}{64 \rho_c} \right) \sum_{j=1}^l n_j \sum_{i=1}^n (i \omega_e)^2 \left(\hat{B}_{rij}^2 + \hat{B}_{tij}^2 \right) \quad (11)$$

where i denotes the harmonic number, j is the layer number, footprint r represents the radial component and footprint t denotes the tangential component. The number of conductors in a specific layer is denoted by n_j . The reader is encouraged to read [10] for a more elaborative explanation on the hybrid method.

6.1 Eddy Current Loss Results

The 2D magnetic field information was gathered at different layers using the previously mentioned SEMFEM package. Thereafter a Fast Fourier Transform was done to obtain the harmonic information. These values were then substituted into (11). The prototype stator windings consist

of 5 layers. It was decided that 15 harmonics is sufficient to capture the effect of the non-sinusoidal flux distribution in the machine's air gap. It should be mentioned that the the measured results of Table 3 was obtained by an open-circuit test at the rated speed of 300 rpm. Because it is an open-circuit test, the machine temperature is fairly low. Therefore, to match the measured results, the copper resistivity was assumed to be the resistivity at 25°C. This produces slightly higher than usual eddy current losses. Table 4 shows both measured and calculated losses.

d [mm]	Strands	$P_{eddy}(1)$ [W]	$P_{eddy}(2)$ [W]
1.6	1	30.5	27.58
0.2	70	0.6	0.47

Table 4: Measured $P_{eddy}(1)$ and calculated $P_{eddy}(2)$ eddy current losses at 300 rpm

The measured and calculated results match fairly well. The higher measured results could be attributed to wind and friction losses and eddy current losses at the end-windings. The prototype machine has a rated power of 700 W. It should be noted that the eddy losses for the 1.6 mm conductors are then 4.36% of the machine's rated power.

7. CONCLUSIONS

In this paper, it was desired to optimise an existing prototype machine, with emphasis on the motor efficiency, output torque and PM mass. The aforementioned objectives are usually competing objectives, and gives rise to the necessity of determining the Pareto surface. The basic theory behind multi-objective optimisation strategies was discussed and for this study, the Weighted Sum Method was introduced and implemented. The objective weights were varied such that the solution points approximate the 3-dimensional Pareto front. This allowed the decision-maker to select solutions which more accurately presents the desired preferences as compared to a priori articulation of preferences strategy. The optimisation process made use of the pyOpt open-source package to perform the single-objective optimisation. The electromagnetic simulation was performed using an in-house FEM package. The optimisation process considered 9 design variables, 2 of which were constant. The objective weights were varied according to a 0.025 increment size, which generated 861 solutions. These solutions were plotted on a 3-dimensional scatter plot (see Figure 3). From this plot, the decision-maker can easier select and visualise solutions which satisfy the desired output performance. In this case, it was only desired to out-perform the present prototype design. The prototype's simulated efficiency, torque and PM mass was used as minimum requirements and only solutions which satisfied all three objectives were considered. Regarding the prototype car for the Shell Eco Marathon, it is most desired to increase the output torque. A machine was found (amongst two others), which promises approximately 3%

less PM mass, unchanged efficiency and a 15.58% increase in torque.

The theory for eddy current losses and the importance thereof in the IDRFP machine was discussed. Two possible low frequency methods for approximating the eddy current losses were discussed. The first method is known as the classical analytical method and makes use of 1-dimensional flux density information and assumes a pure sinusoidal flux distribution. The second method extends the classical method to take into consideration 2-dimensional and non-pure sinusoidal flux density information. It also uses different flux densities depending on the position of the particular copper turn. This extra information is obtained via FEM simulation. The measured and calculated results matched fairly well. The slightly higher measured results can be attributed to wind and friction losses and eddy currents at the end-windings. It is clear that the use of Litz wire almost eliminates eddy current losses in the machine, thus it would not be necessary to include the eddy current losses in future optimisation processes. If however normal round copper wires are considered, the hybrid method ensures relatively accurate loss calculation which can then be included in the optimisation process.

8. FUTURE WORK

The coil mass can also be included in the optimisation process. At present, the design variable k_m is assumed to be identical for both outer and inner magnets. An investigation can be done to see if the optimisation process would choose them differently.

Currently, the peak flux density of the prototype in the air-gap is relatively low ($B_{pk} \approx 0.63T$). This is mostly due to the fact that the air-cored stator adds high reluctance to the magnetic path produced by the magnets. An increase in magnetic flux density could result in an increase in torque and power density of the machine. Therefore, a future investigation could be done on the use of Soft Magnetic Composite (SMC) materials within the coil cores. Modern SMC materials promise relative magnetic permeabilities of up to 850 and core losses as low as 6T/kg at a 1T flux density. However, the introduction of SMC materials possibly reintroduce other problems such as increased cogging torque and torque ripple, and an investigation of the stator layout would need to be done (the flux paths now depend on the relative position between the rotors and the stator, because the flux now favours moving through the SMC material).

ACKNOWLEDGEMENT

This work was supported by the Centre for Renewable and Sustainable Energy Studies (CRSES) and Stellenbosch University.

REFERENCES

- [1] G. I. Oosthuizen, "Design of an Ironless Double-Rotor Radial Flux Permanent Magnet Machine by," Stellenbosch University, Tech. Rep. November, 2015.
- [2] R. Marler and J. Arora, "Survey of multi-objective optimization methods for engineering," *Structural and Multidisciplinary Optimization*, vol. 26, no. 6, pp. 369–395, 2004. [Online]. Available: <http://link.springer.com/10.1007/s00158-003-0368-6>
- [3] L. S. de Oliveira and S. F. P. Saramago, "Multiobjective Optimization Techniques Applied to Engineering Problems," *Journal of the Brazilian Society of Mechanical Sciences and Engineering*, vol. 32, no. 1, pp. 94–105, 2010.
- [4] I. Das and J. Dennis, "Normal-Boundary Intersection: An alternate method for generating pareto optimal points in multicriteria optimization problems," *Society for Industrial and Applied Mathematics Journal on Optimization*, no. 8, pp. 631–657, 1998. [Online]. Available: <http://hdl.handle.net/2060/19970005647>
- [5] R. T. Marler and J. S. Arora, "The weighted sum method for multi-objective optimization: New insights," *Structural and Multidisciplinary Optimization*, vol. 41, no. 6, pp. 853–862, 2010.
- [6] I. Y. Kim, "Adaptive Weighted Sum Method for Multiobjective Optimization," pp. 1–13.
- [7] C. J. P. Newton, "Sequential Penalty Derivative-free Methods for Nonlinear Constrained Optimization," vol. 20, no. 5, pp. 2614–2635, 2010.
- [8] A. Van den Bossche and V. C. Valchev, "Inductors and Transformers for Power Electronics." Taylor & Francis Group, 2005, ch. 5.
- [9] A. V. D. Bossche, V. C. Valchev, and S. T. Barudov, "Practical Wide Frequency Approach for Calculating Eddy Current Losses in Transformer Windings," *IEEE ISIE*, no. 1, pp. 1070–1074, 2006.
- [10] R. J. Wang and M. J. Kamper, "Electric machinery," *IEEE Transactions on Energy Conversion*, vol. 19, no. 3, pp. 532–538, 2004.
- [11] G. W. Carter, "Electromagnetic Field in its Engineering Aspects," White Plains, NY, 1954.

Assessment of the Vibration Level at the Catenary value of 2100m for an OPGW using Endurance Limit Approach

M. Gizaw^{1*}, R. Loubser², I.E. Davidson¹ G. Bright² and R. Stephen³

¹Eskom CoE in HVDC Engineering, University of KwaZulu-Natal, Durban, South Africa

²Mechanical Engineering Discipline, University of KwaZulu-Natal, Durban, South Africa

³Eskom Holdings SoC Limited, South Africa

*Email: sykconsult@gmail.com

Abstract: Aeolian vibration is one of the critical problem areas to be addressed in transmission line design because it represents the main reason for fatigue failure of conductor strands or items associated with the conductor. This type of vibration is most severe when the conductor tensions are high, steady wind, and spans are long. Relative to phase conductors, Optical Ground Wires (OPGW) tends to vibrate at a very high level form of Aeolian vibration due to their position on towers, relatively light weight and low self-damping characteristics. The energy dissipated by a conductor is negatively impacted with a high tension values. As a result, OPGW may suffer large amplitude of vibrations at relatively high frequencies. Recent developments leads to a more scientifically based method of setting conductor tension for most commonly used conductor materials. Most conductor types, including OPGW, are not specifically covered by the recommendation of standard organization due to lack of documented laboratory and field evidence. In addition, there is a lack of sufficient evidence to indicate safe tension limits using this “new” approach for steel ground wires and OPGW. The Endurance Limit Approach in combination with laboratory test result is used in this paper for evaluating the vibration severity of an OPGW at catenary value of 2100m.

1. INTRODUCTION

Electric Power Utilities are replacing existing earth wire with OPGW where the mechanical integrity of the earth wire is suspected and needed to be replaced. The tension settings of between 5 and 10 % above the static tensile strength but below the maximum specified stringing tension set by the manufacturers of the cable and supporting hardware is mostly recommended [1]. This values are now become the concern of the Power companies. Suppliers of the cable and supporting hardware apparently cannot string their OPGW at a Tension-to-Weight ratio (H/w) required by their customers. Eskom, South Africa, strung the OPGW at same C-value as Earth wires which is a value of typically 2100m so that the clearances to phase conductors are the same and

assumed to be practical. Although suppliers would like to use smaller C-values which would be impractical from the perspective of Eskom transmission line design, because it would then be too close to the phase conductors and causing clearance or safety problems. The investigation and recommended Safe Design Tension by CIGRE for Single Conductor Lines with and without Stockbridge Dampers do not endorse the value (2100m) from the perspective of protecting the OPGW from Aeolian fatigue failure. The recommendation by CIGRE is valid only for ACSR, AAC, AAAC and ACAR conductors [2].

The structure of OPGW is not the same as other conductor type and there is no reliable data on its vibration features. Based on preliminary experimental data [3] and on similarity of OPGW creep to Aluminium alloy (A2) conductor, the OPGW tension constraints is set equal to those of A2. As far as the literature available to the author is concerned, there is lack of empirical evidence for evaluating the vibration severity and safe design tension recommendations on OPGW with respect to Aeolian vibration.

In order to realize allowable vibration conditions, this paper presents a probabilistic model for predicting Aeolian vibration response of OPGW conductors by using laboratory test setup with a test span length 85m,



Fig 1. Test span length 85m, at University of KwaZulu-Natal (UKZN) Vibration Research and Testing Centre

at University of KwaZulu-Natal (UKZN) Vibration Research and Testing Centre (VRTC), as per the standard (Electra No.62).

1.1. Energy Balance Principle (EBP)

As a vibrating conductor with fittings receive energy from the wind, its amplitude will obviously rise to a point at which its internal dissipation balances the energy input from the wind. This is expressed in the following equation of the EBP.

$$P_w = P_c + P_D$$

Where:

P_w is the power imparted by the wind; P_c the power damping of the conductor, and P_D the power dissipated by the damper.

To determine the free span amplitude terms for P_w , P_D and P_s are required.

$P_w = L f^3 D^4 F \left(\frac{A}{D} \right)$, wind input power. The value, $F(A/D) = 2.6 \left(\frac{A}{D} \right) + 81.2 \left(\frac{A}{D} \right)^2 - 76.5 \left(\frac{A}{D} \right)^3$ can be used as an approximation for $F(A/D)$

$$P_D = \frac{1}{2} \sqrt{Tm} \cdot V_u^2 \left(\frac{Y_{min}}{Y_{max}} \right) \quad \text{or} \quad P_D = 1/2 V_k^2 Re[Z],$$

$$P_c = k \frac{A^l f^m}{T^n} \quad \text{Considering Noiseux, } P_c = k \frac{A^{2.44} f^{5.63}}{T^{2.76}}$$

For the case of damped conductors, the balancing process must also account the energy dissipated by the damping device.

$$P_w = L f^3 D^4 F \left(\frac{A}{D} \right) = k L \frac{A^l f^m}{T^n} + \frac{1}{2} \sqrt{Tm} \cdot V_u^2 \left(\frac{Y_{min}}{Y_{max}} \right)$$

Aeolian vibration control is achieved if the system damping, defined as energy dissipated by conductor and damping device for all the system vibration modes, is high enough to limit the vibration amplitudes to within acceptable levels.

1.2. Conductor Stress and Strain

To define the stress on a stranded conductor, the cable vibration response is needed. To find this quantity, the equation of motion for conductors could be used. However, the solution will have some difficulties, because the equation contains terms for wind input energy and conductor self-damping, which cannot be equated mathematically in a simple manner. Therefore, vibration amplitude is approximately determined using the energy balance principle (EBP) [4]. Once the *rms* value of antinode displacement

$Y_{v,rms}$ is calculated using the EBP method, the nominal dynamic bending stress in the conductor at suspension clamps can be determined using the Poffenberger-Swart formula [5], based on the assumption that each individual wire flexes independently of the others. Based on the latter, the alternating bending stress in the conductor at a clamped extremity is:

$$\sigma_{b,rms} = 4\pi D E_{Al} \sqrt{\frac{T}{E I_{min}}} f Y_{v,rms}$$

$$\varepsilon_{b,rms} = \sigma_{b,rms} / E_{out}$$

Where: E_{out} the modulus of elasticity of the outer wire

The conductor curvature is defined as the second derivative of the conductor displacement and then, in no slippage hypothesis, the maximum bending strain (on the cable outer layer) is obtained through:

$$(\varepsilon_{max})_n = \frac{\partial^2 y_n(x)}{\partial x^2} \frac{D}{2}, \quad y_n = A_n \sin \left(\frac{2\pi}{\lambda_n} x \right),$$

It has long been known that the risk of fatigue failure due to fluctuating stress in the wire is slight in the case of bending strain values of less than 150µm/m [5].

1.3. Effect of Tension

In a stranded power cables the self-damping ability reduces as the conductor tension increases [5]. This will produce higher levels of vibration in the cable. The effect of tension on vibration level is illustrated by different research laboratories and analytical results. Both confirm that the effect of tensile load on the vibration level is very important, and concluded the same results. It is seen that when the tension is increased, the vibration response is increased (enlargement of the frequency spectrum and that of amplitude), especially for high frequencies. But it will be important to note here that the highest value of vibration response occur at low frequencies of vibration.

2. LITERATURE REVIEW

Various researches have been analyzed in relation to the allowable tension level of overhead conductors. The criteria for stringing the conductor are not

stabilized and the research is underway to date. On overhead line Engineering and industries, designs are trying to have different tests and research data but the safety model for protecting conductors from fatigue failure, because of wind speed 1-7m/s, which convince all is not existing in the standard.

From those the CIGRE EDS board investigating the results of the international research, observed that a conductor without damper were probably safe at an Every Day Stress level of about 18 to 20 %RTS. By that time it was argued that stringing all conductors to the same %RTS would produce a higher aluminum stress in conductors with a high steel-to-aluminum ratio than in those with a low steel-to-aluminum ratio, the inference being that the former would be subject to greater vibration. Different researchers were examining the trustworthiness of EDS panel recommendations, suggesting that a Tension-over mass criterion (catenary constant or H/w) be used instead of %RTS because the catenary value is related to aluminum stress, and thus to the self-damping properties of the conductor. And believed to be a better criteria to control fatigue life of conductors.

The research by Leblond & Hardy, 2000 [6] presented on the assessment of safe design tension with regard to Aeolian vibrations of single overhead conductors. Basically two different approaches were used in the modeling process. The conductor fatigue endurance limit and cumulative damage of the conductor. The research tried to show on how to assess safe design tension values for a given ACSR conductor by using the endurance limit approach. The paper [6] used the EBP to search for the rms antinode displacement (Y_{rms}). This value was used to calculate the nominal dynamic bending stress in a conductor at the suspension clamp by using the formula proposed by Poffenberger-Swart.

The numerical analysis by Vecchiarelli*, Currie and Havards, 2000 [7] has the capability to account for more than one spatial mode of conductor vibration, traveling wave effects, conductor resistance to bending and damper mass. A two part numerical analysis is performed in which the finite difference scheme was applied to simulate Aeolian vibrations of typical conductor with and without Stockbridge damper. The results are employed to investigate (a) Steady state form of conductor vibration, (b) the conductor bending amplitude near each span end as a function of vibration and damper location, and (c) the influence of conductor flexural rigidity and damper mass. The result of this finite difference scheme is compared with solutions of EBP method, see fig.2.

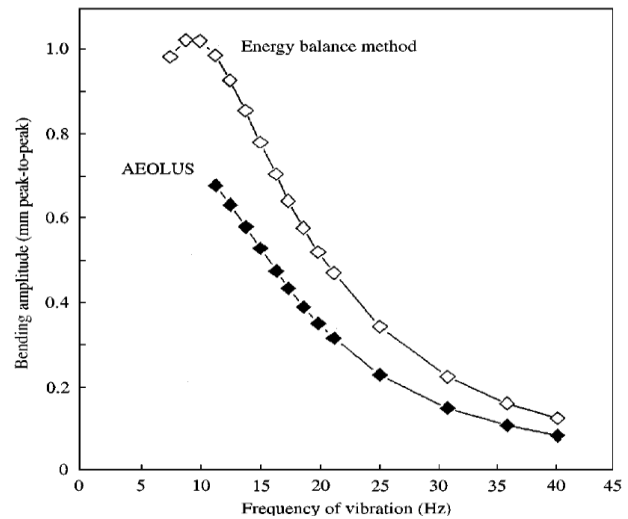


Fig. 2 Bending amplitude of 240/40 sq. mm ACSR (26/7) conductor as a function of Aeolian vibration frequency, based on Vecchiarelli*, Currie and Havards and energy balance method, 2000.

For mono frequency Aeolian vibration of a conductor without dampers, the numerical scheme by J. Vecchiarelli and EBP method yield similar solution for regions far away from the suspension clamp. However, the EBP method overestimates the conductor bending amplitude (Y_b) in the area near a clamp because this method do not consider flexural rigidity, which was measured in its worst-case scenario in the case of J. Vecchiarelli, (EI_{min}).

The uncertainties, overestimating of antinode displacement, on the EBP and the application of Poffenberger-Swart formula will create more doubt on the prediction of bending stress on the outer part of stranded conductors. The application of the endurance limit approach to assess safe design tension values for a given ACSR conductor will most probably mislead the appropriate stringing tension value of the conductor.

A research contributed towards the safe design tension value, to reduce fatigue failure of overhead conductors is by J.S.Barrett and Y. Motlis [8]. In this research of the single conductor without dampers was used to study how well the H/w criterion works. A sag-tension program runs were performed for a range of temperatures, representing different climates, and for various steel-to-aluminum ratios. If the H/w criterion works well, the value of initial H/w ought to remain constant. The research [8] proved that the application of the H/w value look to be a good stringing criterion for conductors without dampers in typical colder climate, between -5°C and -10°C , see fig 3.

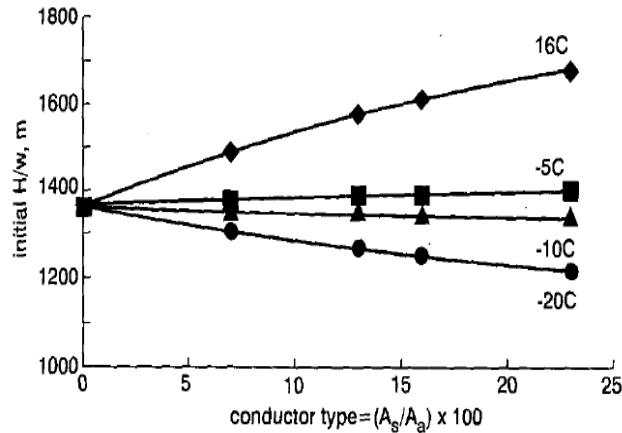


Fig. 3 Initial H/w for an initial aluminum stress of 37MPa both at the indicated temperature, category 4 terrain cover

3. EXPERIMENTAL WORK

A test as per the standard “Guide on conductor self-damping measurements” (Electra No. 62) was used for

accelerometers were applied on the test bench to generate data for the response to the input variable load at the shaker. One load cell at the shaker is used and a strain gauge to the opposite of the shaker at the fixed end of OPGW is located. A conductor of OPGW of spec: Diameter 13.5mm, Rated Tensile Strength of 60KN, Wight per unit length 459.4 Kg/Km, Modulus of elasticity with 111000 N/mm², Coefficient of linear expansion 15.5×10^{-6} and nominal Area of 86mm² was used for the test. To search for the vibration response of the conductor ($f_{y_{max}}$), the test runs at four different mechanical tension values (6.81KN, 7.76N, 9.33KN, 11.27KN) in a controlled temperature of 21°C. This will help to see the relationship between $f_{y_{max}}$ values with frequency of excitation so that it can be used to evaluate the vibration severity of the conductor. The fatigue endurance limit of the conductor in terms

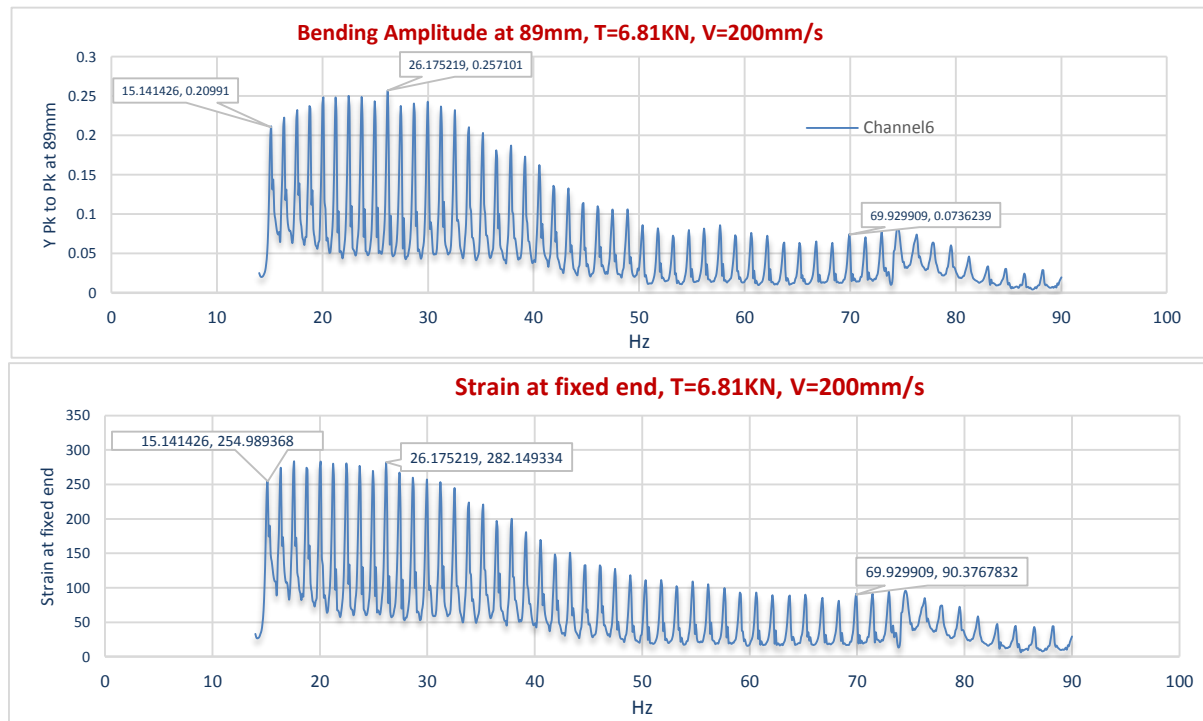


Fig.4 The bending amplitude response of the OPGW at 89mm and the strain Vs frequency correlations.

generating data in relation to the response of the conductor to Aeolian vibration. The shaker, with the capability of range of frequency 0-3000Hz, 690m/s²/50.8 mm (pk-pk), was used to cover a frequency range of 5Hz to 92Hz. A sweep rate of less than 0.5mm/s were given to the controller to vibration response of the conductor at the antinode location. Six

of $f_{y_{max}}$ can be plotted on the graph of $f_{y_{max}}$ Vs frequency of excitation. This can determine the critical vibration level easily. The maximum of the curves may be plotted as a function of the mechanical tensions. The safe design tension arises from the intersection of these curves with the fatigue endurance limit of the conductors. Finally, it was possible to see

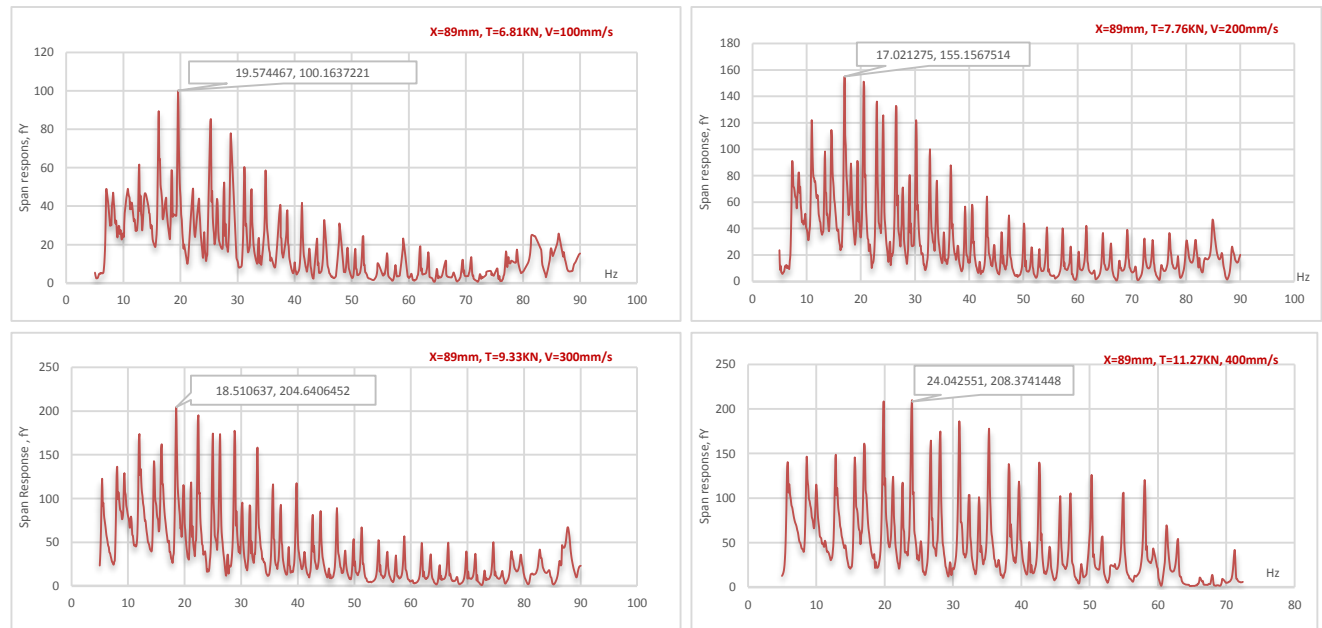


Fig.5 Product of maximum antinode amplitude by frequency as a function of frequency at tension value of 6.81kN, 7.76kN, 9.33kN, and 11.27kN

the vibrational response of the cable at the required stringing tension values.

It employs four accelerometer transducers at quarter locations along the conductor to determine the response of cable from the input power of the shaker. The OPGW was strung in the test span. The vibration response was measured at tunable resonance frequencies from 5 to 92 Hz. This is the frequency range to be expected in the wind speed range of 1 to 7 m/s with respect to the OPGW diameter. The frequency and peak to peak amplitude was measured with four different tension values at a constant antinode velocity of 100mm/s, 200 mm/s, and further tested for 300mm/s and 400mm/s wave velocity [9]. In the whole test, an OPGW cable is run with the respective loop velocity at four different tension levels, of catenary equals to 1513m, 1725m, 2074m, and 2505m. Test results are shown on Fig.4, 5 and 6 in terms of the basic parameters for the confirmation critical condition of the conductors' response to fatigue.

3.1 Vibration Amplitude Vs Strain of the OPGW

For whole test of the cable at different tension values, the relationship between the bending amplitude and strain values have similar pattern of the data complying with Poffenberger-Swart's analytical

model, which is reasonable to relate the response of stranded conductor at 89mm is good way of predicting the variable bending stress at clamped extremity of the cable. From [5] the estimated amplitude endurance limit for conductor type Alumoweld at a 25% tension is 0.96mm. Experimental result shows that all the tension values are under 25% RTS but the laboratory result showed the maximum bending amplitude of 0.406mm, which is less than the endurance limit of the material (see fig. 5).

3.2 Maximum antinode amplitude

The evaluation of dynamic loading of stranded conductors can be investigated by linking the maximum predicted bending stress amplitude with the fatigue endurance limit of the conductor at the constrained locations. The free loop amplitude of vibration, Y_{max} , multiplied by the instantaneous frequency of vibration is plotted with respect to frequency, for all loop velocity at stringing tension value of $C=1513m$, $1725m$, $2074m$, and $2505m$, respectively. The maximum response of the cable with the corresponding tension values are $f_{y_{max}}=100mm/s$, $155mm/s$, $204mm/s$, and $208mm/s$ for the respective tension values. When we compare this value with the endurance limit of the conductor type [3], Alumoweld, $f_{y_{allowable}}=276mm/sec$, it appears to be safe from fatigue failure because of wind. The design recommendation for stringing the OPGW with the

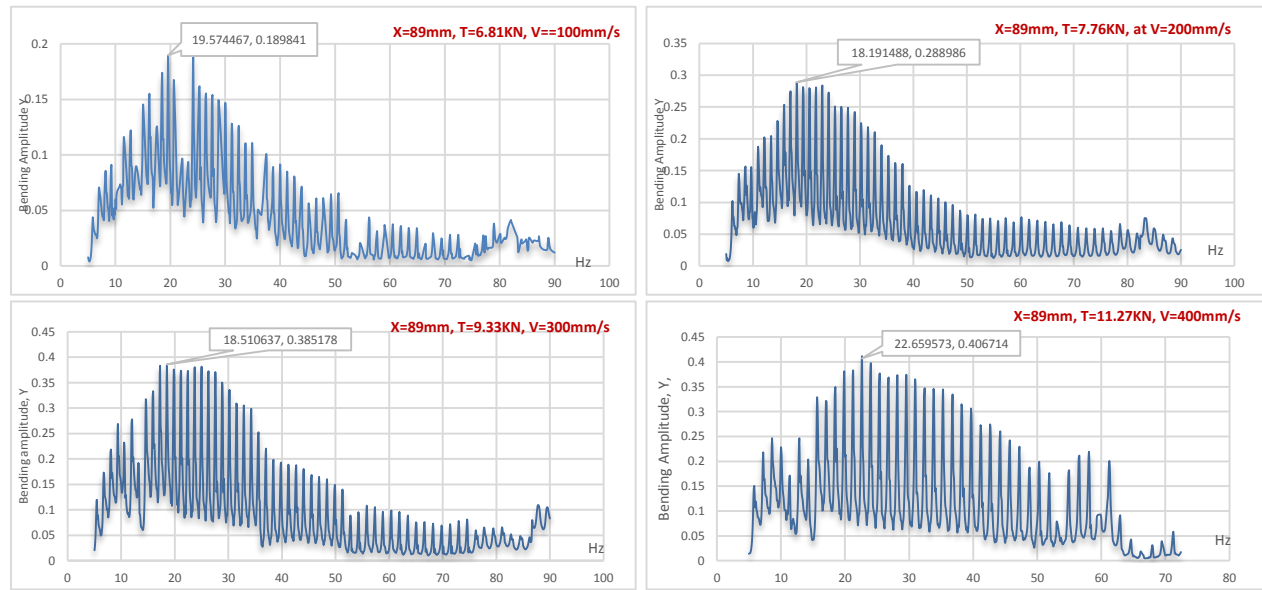


Fig.6 Laboratory test result for bending amplitude at 89mm with tension value 6.81kN, 7.76kN, 9.33kN, and 11.27kN with loop Velocity 200mm/s

same C-value to that of phase conductors, 2100m, may not have safety questions in relation to Aeolian vibration fatigue failure of the specified conductor. The maximum free loop amplitude for this catenary value is 142mm/s, which is relatively less than the allowable value according to [5].

The test result shows that the maximum vibrational level of the OPGW is under the value of endurance limit of the cable. Further, we can say that when the stringing tension increases, the response amplitude also increases especially for the high frequencies whereas its highest value occurs at the lowest frequencies, which is less influencing the load of vibration.

The test data shows that the vibration levels in terms of $f_{y_{max}}$ for smaller diameter of conductors like most OPGW's seems to have less response and low increment of value of the vibration when we compare with the big diameter of conductor types, for the increased value of tension. This will not make suitable to model an appropriate tension recommendation for low diameter OPGW conductors types. Conversely, the bending amplitude at 89mm from the fixed end abutment has significant increment of the value as we change the tension of conductor. This parameter most probably can be used evaluation the appropriate design tension value and an assessment of vibration severity of low diameter conductors, like OPGW's. The Maximum bending amplitude at 89mm of the specified OPGW for all test parameters have a good agreement with the values of strain measured at the constrained location of the cable. This shows the

relationship between the bending amplitude at 89mm and stress at the fixed end of the cable complying with Poffenberger-Swart formula, which is used for calculation of strain from bending amplitude data.

3.3 Assessment of the vibration level of the OPGW

The sweep test were performed at loop velocity of 100mm/s, 200mm/s, 300mm/s and 400mm/s to gather relevant data for the evaluation of vibration level tension value C=2100m of the OPGW. Both the free span vibration angle and the bending amplitude are widely used as indicators of vibration levels [3]. The response of the cable at the 89mm has relatively consistent and reliable value in comparison with the free span response of the OPGW. The reference [5] provides data for the endurance strength of the Alumoweld in terms of bending amplitude. So, it will be reasonable to examine the response of the cable by using this parameter.

It is practically difficult to find more test results, (i.e. stringing tension with the bending amplitude at 89mm), of the vibration response of an OPGW for the total degrees of freedom of the conductor at various levels of tension of the conductor, because of the limitation of vibration measuring equipment and the structural complexity of the conductor. To solve the problem of size compatibility, a mathematical method can be used to generate test results of Eigen vectors for unmeasured test parameters of predominant modes by taking tested Eigen vectors of few results of the parameters as a reference.

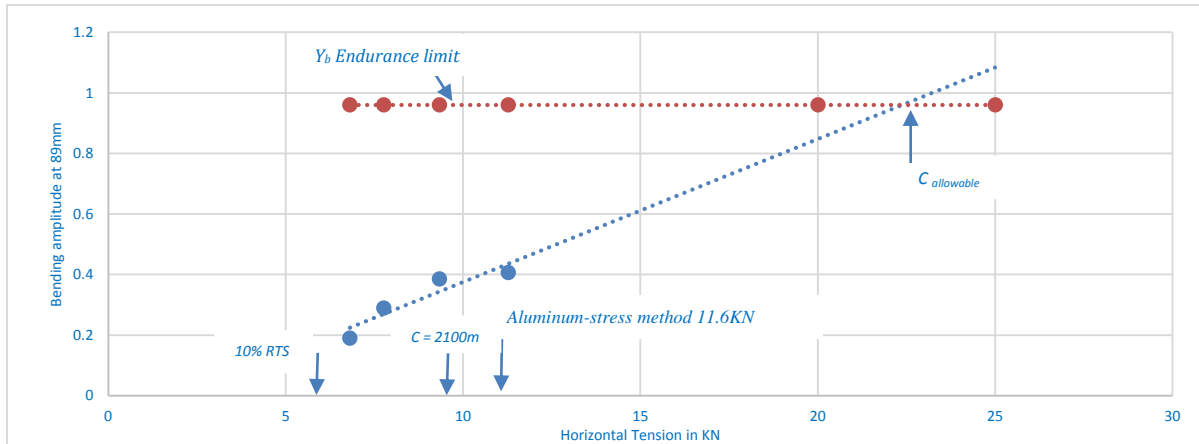


Fig.6 Laboratory test result for bending amplitude at 89mm with tension value 6.81KN, 7.76KN, 9.33KN, and 11.27KN with loop Velocity 200mm/s

As we can infer from test result shown on fig. 7, it was possible to have the maximum bending amplitude response of the cable with respect to the horizontal tension values. The considered tension values are let to vibrate within the recommended loop velocities and the maximum bending amplitudes are taken to relate with the tension values. The response of the cable at the 89mm from the fixed end showed bending amplitude, which is less than the recommended value (0.96mm). The OPGW at the horizontal tension at the c-value of 2100m fall under the 10KN, which can validate that the cable is safe from fatigue failure due to Aeolian vibration.

4. CONCLUSION

The experimental data in combination with endurance limit of the OPGW showed that the vibration level because of wind speed between 1-7 m/s or Strouhal frequency between 14-92Hz, have less impact on the fatigue failure of the OPGW at the tension value with the Catenary constant of 2100m. The conductor tension used in this test considered the OPGW specification indicated above. It is important to note that the vibration levels would be different for other materials of different strength. This is important, because it has sometimes been assumed in the field of line design that conductor strung for equal catenary values would vibrate the same, and would be equally likely, or unlikely, to suffer Aeolian vibration damage.

5. ACKNOWLEDGMENT

This research investigation has been supported by the Ministry of Education, Ethiopia; the Eskom CoE in HVDC Engineering and the University of KwaZulu-Natal.

6. REFERENCE

- [1] E. Marshall, "Fibre optic roll out on Eskom transmission system," in IEEE 2003, 10th International Conference on PP. 50 – 57
- [2] Electra 1999. "Safe design tension with respect to Aeolian vibrations, part 1: single unprotected conductors," Electra N° 186.
- [3] A.-L. Tukachinsky, "Selection of overhead conductors type and tension for Israeli terrain and weather conditions," in IEEE 2000, Conference Publications on pp. 308 – 313.
- [4] Cigre SC22-11: Modelling of Aeolian vibration of single conductors: Assessment of the technology. Electra 181 (1998), pp. 53 to 69.
- [5] EPRI Transmission line Reference Book: Wind Induced conductor Motion. Project 792, Palo Alto, CA, 2006
- [6] Leblond & C. Hardy, "Assessment of Safe Design Tension with Regard to Aeolian Vibrations of Single Overhead Conductors", Proc. of the ESMO 2000 Conference, Montreal, 8-12 October 2000, pp. 202-208.
- [7] J. Vecchiarelli, I. G. Currie, and D. G. Havard. "Computational analysis of Aeolian vibration with a Stockbridge-type damper," Journal of Fluids and Structures, Vol. 14, Issue 4, May 2000, Pages 489–509
- [8] J.S.Barrett and Y. Motlis, 'Allowable tension levels for overhead line conductors', IEE proc. Genre. Transm. Distrib. Vole 148 No. 1, January 2001, pp. 54-59
- [9] "IEEE Guide for Laboratory Measurement of the Power Dissipation Characteristics of Aeolian Vibration Dampers for Single Conductors". IEEE Std 664-1993.

POWER DISTRIBUTION SYSTEM RELIABILITY IMPROVEMENT THROUGH THE APPLICATION OF SMART TECHNOLOGY

GC Dumakude^{1*}, AG Swanson², R Stephen¹ and IE Davidson³

¹ Eskom Holdings SOC Ltd, Transmission, Block C 1st floor, 1 Langford road, Westville, 3630, South Africa

² Discipline of Electrical, Electronic and Computer Engineering, School of Engineering, University of KwaZulu-Natal, Durban

³ Eskom Centre of Excellence in HVDC Engineering, School of Engineering, University of KwaZulu-Natal, Durban, South Africa

*Email: dumakug@eskom.co.za

Abstract: This paper evaluates the application of smart technologies with the aim of improving the reliability of Eskom's medium voltage (MV) networks. The intent is to reduce the outage duration, frequency of outages, maintenance costs, and operational expenditure while improving overall system performance. Historical and predictive approaches are the two power system reliability assessments that are predominantly used. Both approaches are applied whereby expected performance is modelled, given the specific network topology, past performance, customer numbers, operating environment, etc. A number of network components including transformers, lines, isolators, and fuses are used and applied in a systematic manner to calculate expected downtime experienced by the customer supplied on different connections of the network with different smart technology interventions. To achieve this, a methodology is developed and verified using DigSilent PowerFactory simulations. Test network samples were selected on the existing networks from KwaZulu Natal Operating Unit (KZN OU). The application of smart technology has confirmed an improvement on overall outage duration while improving system performance.

1 INTRODUCTION

The distribution system is an important part of the total electric system, as it provides the final link between the bulk system and the customer. In many cases, these links are radial in nature and therefore susceptible to outage due to a single event. In general, many distribution systems have normally open points in a meshed configuration, so that the system is operated as a radial feed. However during fault conditions normally open switches can be operated so that the load can be restored to unaffected areas. The idea is to isolate the faulted part and connect the healthy part of the system as soon as possible to enhance overall system reliability. The reliability of a distribution system depends on a number of factors including the location (urban or rural), environment, the type of system and the type equipment installed. Events that affect the customer supply include failure rate of equipment and the duration of an outage. A number of traditional systems including devices such as over-current relays, reclosers, fuses and sectionalisers are commonly used to protect the distribution system [1-3].

Eskom distribution also uses these protective devices to minimise the customer impact per load point.

The Smart Distribution Grid has gradually become an obvious choice to face future challenges in the power system because it provides integration and greater visibility over traditional approaches. It delivers a system that can remotely monitor the condition of the equipment, diagnose the faulted section while employing measures that will keep system operating optimally [4-7].

2 APPROACH

Historical and predictive approaches are the two power system reliability assessments that are predominantly used [1]. Both approaches are applied whereby expected performance is modelled, given the specific network topology, past performance, customer numbers, operating environment, etc.

A number of specialised software packages are available in the market for reliability modelling of electrical networks including PowerFactory, ReticMaster, and PSS/E. These packages require detailed network models to model the expected reliability of power networks. KZN OU network engineers have introduced PowerFactory for the modelling of all MV networks. This is enabled by the Smallworld export to PowerFactory which was not available in the past. Furthermore there were other data incomplete issues that were experienced with Smallworld export to PowerFactory that were later resolved [2]. The accuracy of PowerFactory results were compared to calculations. Practical assumptions were made on the analytical approach with regards to failure rates, travel times to site; travelling speed for fault finding, repair times based on performance history of the feeders as well as interviews and interactions made with site engineers and operators.

Visits were made to different sites at Stanger Technical Service Centre (TSC) KZN OU to validate the information. A key assumption is that KZN OU MV networks are maintained and operated well according to Eskom maintenance standards and are fairly in a good condition. It was also noted that most substations have Remote Terminal Units (RTU), meaning that the fault finding and sectionalising time will be reduced through

remote switching. Network control operators will be able to pick up equipment alarms which make the substation more visible, which is key to any smart technology.

A number of network components including transformers, lines, isolators, and fuses are used and applied in a systematic manner to calculate expected downtime experienced by the customer supplied on different connections of the network with different smart technology interventions. The focus of this study is on the MV feeders connecting the distribution substations to the customers. Customer, substation equipment and sub-transmission networks are excluded.

This approach recognises the fact that key network components such as length of line, number of transformers, location of fuses and breakers, etc. have a significant impact on the reliability of a feeder [8], [9]. Therefore the outcomes from this approach provide the intended “realistic anticipated” performance based on the application of different technologies on the MV

network. The distribution network modelling includes all feeders up to 33 kV. The detailed steps are described below.

3 MODELLING METHODOLOGY

The distribution network modelling includes all feeders up to 33 kV. The detailed steps are described below.

3.1. List of smart technology evaluated

Table 3-1 presents a list of smart technologies that are currently available in the market to improve MV network reliability [10], [11]. Some of this technology is used already in utilities abroad. The combination of these smart technologies is commonly referred to as Distribution Automation (DA); which is one of the major aspects in smart grid [12].

Table 3-1: List of smart devices

Device	Impact on number of faults	Impact on duration	Impact on number of customer interrupted
Smart fuse saver	Will reduce number of faults by improving fuse failure rates, as a fuse tends to operate for temporary faults	Will reduce the outage duration where fuse has blown due to transient fault. Will also provide visibility to SCADA for all fuse operations without intervention from the customer.	No impact on number of affected customers
Transformer remote monitoring	No impact on number of faults	Will reduce the duration by a significant amount because it will provide visibility for all transformer interruptions without customer interventions.	No impact on number of affected customers.
Smart fault indicators	No impact on number of faults	Will reduce the outage duration by a significant amount	Will reduce the impact of number of customer affected, by quick identifying the faulted section. This will reduce the sectionalizing and fault finding time.
Automatic feeder switches	Will reduce the number of faults through self-healing	Will reduce the duration of the outage	Will reduce the impact of number of customers affected through self-healing
Fault Location Isolation & Service restoration (FLISR)	Will reduce the number of faults through self-healing and alternative source transfer	Will reduce the duration with a significant amount	Will reduce the impact of number of customers affected through self-healing
AMI & Smart meter for outage detection	No impact on number of faults	Will reduce the duration with a significant amount, by providing visibility all the way to the consumer.	No impact on number of affected customers.

3.2. Sample networks used

Eskom has nine Operating Units, it is important to note that even though sample networks were taken from KZN OU, this methodology is applicable to the rest of the OU's with similar network characteristics.

The sample networks used are selected from Pietermaritzburg and Empangeni zones. This is because both these are exposed to different environmental conditions and their characteristics are quite different. Wartburg NB 22 and 23 11kV overhead lines can be 100% backed from each other and they belong in Pietermaritzburg zone. Mtonjaneni NB1 11kV overhead line is a long rural network that belongs to Empangeni zone. Equipment details are as shown by table 3-2.

Table 3-2: Equipment details

Networks	Transformers	Switches	Overhead lines	Customers
Wartburg NB22 11Kv	62	94	50km	151
Wartburg NB23 11Kv	88	120	57km	266
Mtonjaneni NB1 22Kv	193	259	175km	925

3.3. Failure rates

Failure rates values used were taken from KZN OU. These assumptions were based on the historical analysis of the KZN OU MV network failures by the local engineers. High number of component exposure and long length of lines will have a higher exposure to faults hence failure rates for lines and cables are assigned per kilometre.

3.4. Fault path indicator application

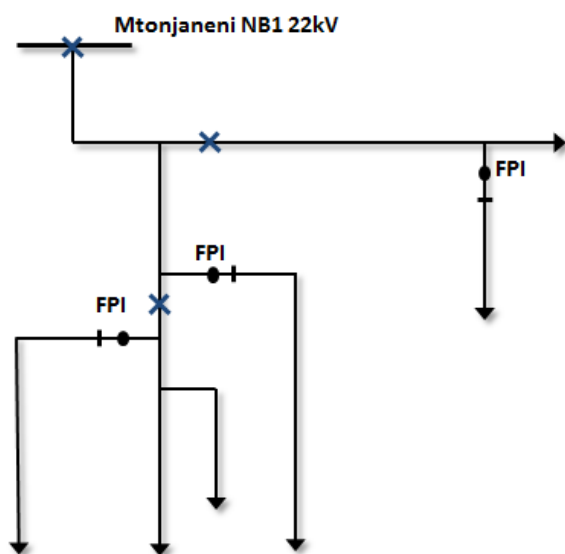


Figure 3-1: FPI application

On average protection zone has about of 15 switching points, with the fault path indicator these switching points are reduced to about 2 to 3 operations. This translates to about 90 minutes savings on sectionalising and fault finding.

According to [9], the simulation work done by the author indicates at least 20 minutes improvement on sectionalising time on the network with fault path indicators hence improving overall system performance.

The benefit of the Fault path indicators (FPI) are realized when installed on the long networks with high number of customers rather than network with fewer customers. Three FPI's were installed at Mtonjaneni NB1 22kV network on S75 in zone 1, S33 which is in zone 2 and S3222 in zone 3 as per figure 3-1.

3.5. Automated feeder switches application

Figure 3-2 shows the placement of automated feeder switches in different locations along the feeder. Automated feeder switches improve the reliability of the network by reducing the outage duration, frequency of interruptions as well as reducing the impact of the affected customer. This is a crucial step as the position of automated feeder switches has a big impact on SAIDI and SAIFI measures.

- At point number 1 there is the base network no automated switch added.
- Point number 2 is when the automated feeder switch was placed in line 3. Line 3 is a lateral line that feeds 300 customers as highlighted in figure 3-1.
- Point number 3 is where the automated feeder switch is placed in line 2; this lateral line feeds 100 customers.
- And point number 4 is when the automated feeder switch was placed in line 1; this portion of the network also feeds 100 customers.

Customer base and length of the line need to be taken into account when placing these switches. Also the number of customers that will be affected by a single breaker operation is significant. Line 3 is 20km long but because 300 customers will be affected it contributes poorly on SAIDI and SAIFI values. This is because of its position in the network; switch 1 will have to be open for any fault that may occur on line 1. This simply means, for optimal performance of the network, configuration and topology is key when it comes to the placement of any device on the network.

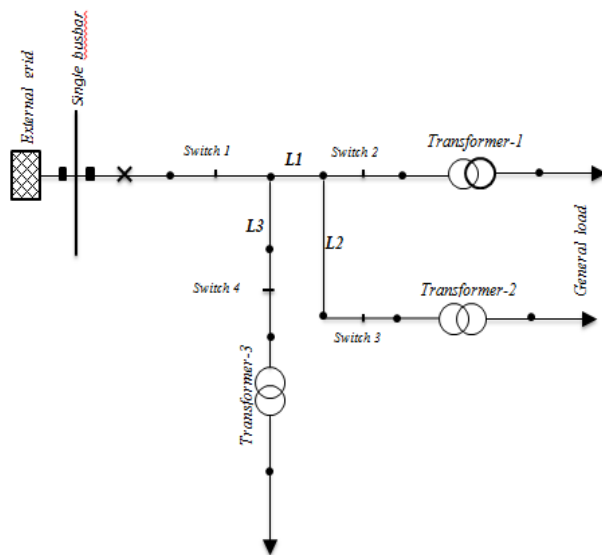


Figure 3-2: Automated feeder switch application

3.6. FLISR technology application

Wartburg network was modelled to see how the tie point switch (N/O) reacts during fault conditions. S66 is a tie point switch that can provide back feed capabilities to both the Wartburg NB22 and NB23 during abnormal conditions. The behaviour of the switches in the network model is crucial in reliability analysis. Basically automated feeder switches are circuit breakers controlled by relays or with communications from a control room. Analysis of key factors including network topology and characteristics is vital. Integration of auto reclosers with RTU reduces sectionalising time by isolating the downstream network through the remote switching. All loads on upstream breakers remain supplied. The estimated time for the operator to get to the first disconnecter and operate with the purpose of isolating the faulty section is 2 hours.

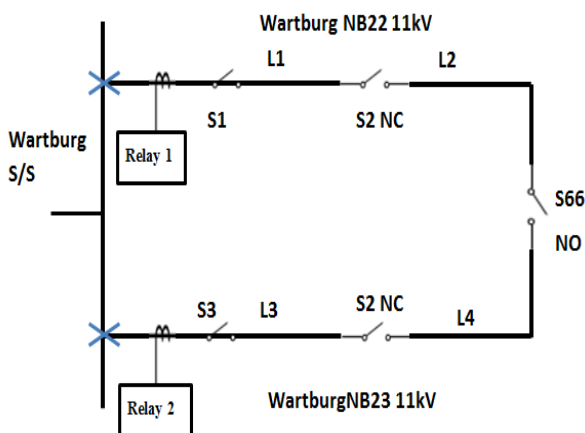


Figure 3-3: FLISR technology application

Figure 3-3 indicates Wartburg NB22 and NB23 networks with three manually operated switches for network isolation and load transfer. The relay 1 will trip for any permanent fault experience on Line 1 resulting to supply interruption on all loads in both lines 1 and 2. To restore load in the unaffected section of the network, in this case line 2, operators need to be dispatched and go to site to manually open switch 2 and then close switch 5. The assumption is that it takes an operator 2 hours to operate the first switch thus partially restoring load to the network which is fed by line 2. The network will be returned to its normal state once the fault in line 1 has been repaired.

With the automated feeder switches, the time to restore network to the unaffected section of the network will be reduced to 1 minute, this actuation time is taken from the global 'remote controlled' switch actuation time [13]

4 RELIABILITY INDICES

The degree of reliability may be measured by the frequency, duration, and severity. It is fairly common practice in the electric utility industry to use the standard IEEE reliability indices such as Customer Average Interruption Duration Index (CAIDI), System Average Interruption Frequency Index (SAIFI), System Average Interruption Duration Index (SAIDI), etc. for reliability measures. Eskom also use these indices to track and benchmark reliability performance against other utilities abroad. There are also internal indices that Eskom is using such as SAIDI-N and SAIFI-N where transformer interruptions duration and frequency are measured [14]. Reliability indices also allow customers and investors to make an informed decision about the security of supply.

4.1. Measure of unplanned outage

The overall outage duration for each fault can be broken down into single steps of events as mentioned on figure 4-1. SAIDI and SAIFI values are calculated from the moment the fault is captured in the system. The combination of these intervals represent the overall outage duration that is experienced by the customer from the moment the fault occurs.

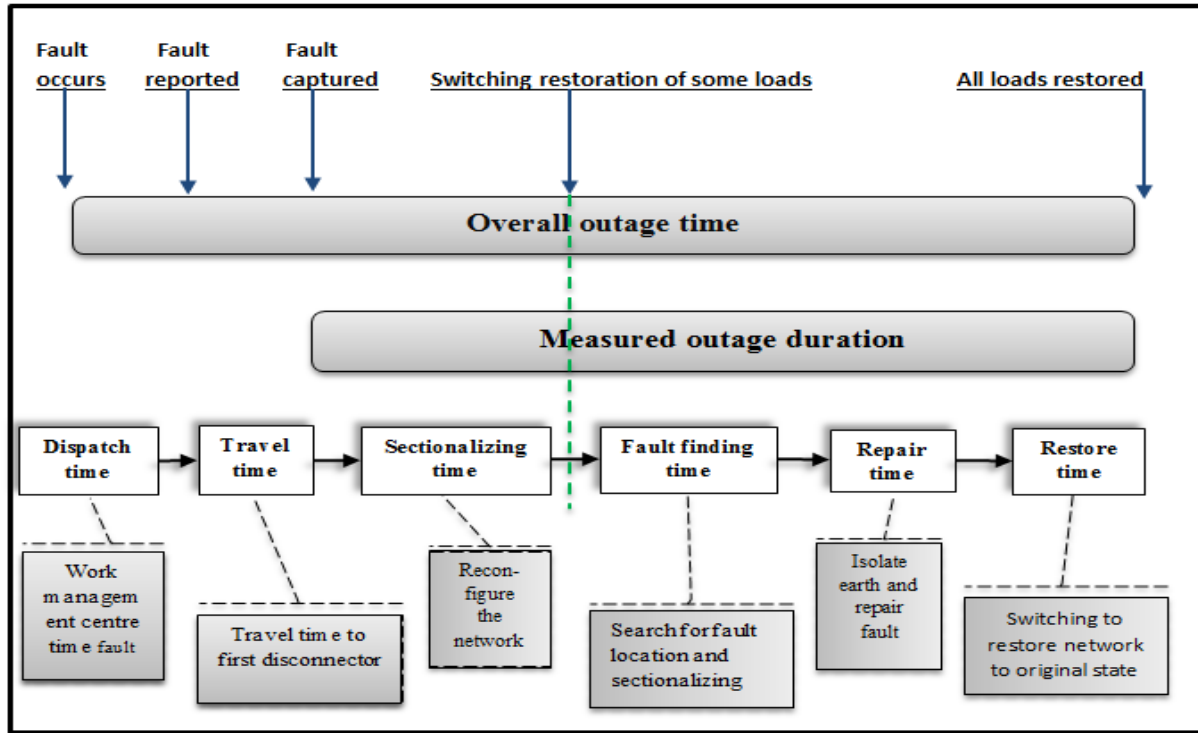


Figure 4-1: Overall outage duration

4.2. SAIDI and SAIFI approach

The unplanned SAIDI algorithm for a feeder was calculated as follows:

$$SAIDI = \frac{CID}{Cust_T} \quad (1)$$

$$CID = (line \times FR_L + Disc \times FR_D \times fuse \times FR_F) \times Cust_D + (line \times FR_L \times R_{timeL}) \times Cust_R (fuse \times FR_F \times FR_F) Cust_R (Disc \times FR_D \times R_{timeD} \times Cust_R) \quad (2)$$

The unplanned SAIFI algorithm is similar to SAIDI except that frequency is considered instead of duration.

$$SAIFI = \frac{CI}{Cust_T} \quad (3)$$

$$CI = (line \times FR_L \times Cust_D + fuse \times FR_F \times Cust_D) + (Disc \times FR_D \times Cust_D) \quad (4)$$

Where:

Line = total line length in km (km)

Fuse = total number of fuses on a feeder

Trfr = total number of transformers on a feeder

Disc = total number of isolators on a feeder

Cust_D = customer interrupted for dispatch, travelling and sectionalising time

Cust_R = customer interrupted for fault finding, repair and switching the line back to its original state

Cust_T = total number of customers in a specific feeder

CID = customer interruptions duration

CI = customer interruptions

FR_L = line failure rate (occ/km/a)

FR_D = Isolator failure rate (occ/a)

FR_F = fuse failure rate (occ/a)

FR_T = transformer failure rate (occ/a)

D_{time} = sum of dispatch, travelling and sectionalising time

R_{timeT} = sum of fault finding, transformer repair and switching the line back to its original state

R_{timeL} = sum of fault finding, line repair and switching the line back to its original state

R_{timeF} = sum of fault finding, fuse repair and switching the line back to its original state

R_{timeD} = sum of fault finding, isolator repair and switching the line back to its original state.

These indicators yield a good picture of the quality of service of the entire system. The bigger the value of these indicators, the poor the quality of the grid will be and vice versa. For each delimited segment *i* between two switches, if a fault occurs on the segment *i*, reliability indicators are calculated as follows [65]:

$$SAIDI(i) = \frac{D_{pc}(i) \times N_{cus}(i) \times N_{pc}(i)}{N_{tot}(i)} \quad (5)$$

$$SAIFI(i) = \frac{N_{cus}(i) \times N_{pc}(i)}{N_{tot}(i)} \quad (6)$$

$$ENS(i) = \frac{P_{pc}(i) \times T_{pc}(i) \times N_{pc}(i)}{N_{tot}(i)} \quad (7)$$

Where:

$D_{pc}(i)$ = outage duration for the segment i (min)

$N_{cus}(i)$ = number of customers experiencing an outage

$N_{pc}(i)$ = number of times an outage is experienced

$N_{tot}(i)$ = total number of customers

$P_{pc}(i)$ = the total rating of the outage

To calculate the total *IND* reliability indicator, where *IND* represents the SAIDI, SAIFI or ENS, the following formula is used:

$$IND = \sum_{i=1}^n IND(i) \quad (8)$$

Where n is the total number of segments in a system, the calculation of $D_{pc}(i)$, $N_{pc}(i)$, $N_{tot}(i)$ and $P_{pc}(i)$ depends on the switching device used, the location of the devices as well as the status of the system. For example, if the main feeder is sub divided into 3 segments such as A_1 , A_2 and A_3 . Equations are re defined as follows:

$$SAIDI(i) = \lambda \times L_i \times \left(T_d + T_m \times \frac{N_i}{N_1 + N_2 + N_3} \right) \quad (9)$$

$$SAIFI(i) = \lambda \times L_i \times \left(\frac{N_i}{N_1 + N_2 + N_3} \right) \quad (10)$$

$$ENS(i) = \lambda \times L_i \times (T_d \times P_{feeder} + T_m \times P_i) \quad (11)$$

Where:

λ = conductor failure rate

T_d = outage times for stages 1 and 2

T_m = outage time for stage 3

N_i = number of affected customers for A_1

L_i = conductor length for A_1

P_i = total affected power for A_1

P_{feeder} = total power for the whole feeder

L_{feeder} = total length for the whole feeder

SAIDI, SAIFI and ENS for the whole feeder are therefore equal to the amount of SAIDI, SAIFI and ENS for the three sub segments. Therefore:

$$SAIDI_{feeder-j} = \sum_{j=1}^3 SAIDI(i) \quad (12)$$

$$SAIFI_{feeder-j} = \sum_{j=1}^3 SAIFI(i) \quad (13)$$

$$ENS_{feeder-j} = \sum_{j=1}^3 ENS(i) \quad (14)$$

Where n is the number of feeders in a system, then:

$$SAIDI = \frac{\sum_{j=1}^n SAIDI_{feeder-1}}{n} \quad (15)$$

$$SAIFI = \frac{\sum_{j=1}^n SAIFI_{feeder-1}}{n} \quad (16)$$

$$ENS = \frac{\sum_{j=1}^n ENS_{feeder-1}}{n} \quad (17)$$

4.3. Results of different reliability improvements interventions

In long networks like Mtonjaneni NB1 22kV network the position of these switches along the network is very important for remote monitoring and control, as it trips and isolates the downstream network during fault conditions this is the section of the line closer to the affected load. Different positions were modelled and verified that optimum performance is achieved when it is placed at S330 as shown in figure 4-2.

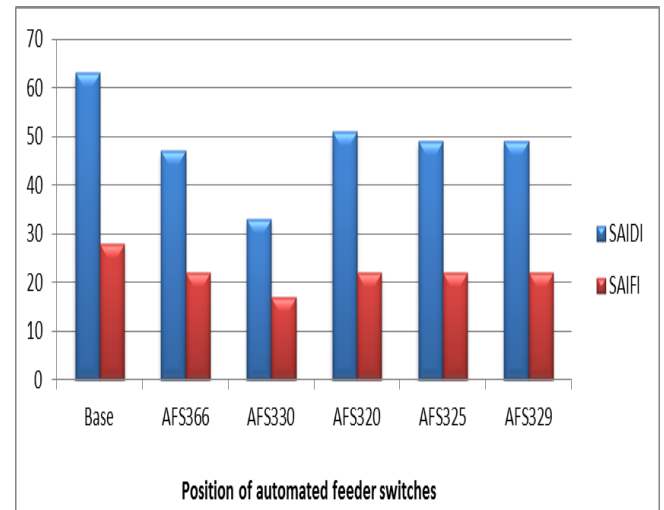


Figure 4-2: SAIDI and SAIFI for Mtonjaneni network

Automated feeder switches were also simulated in different locations along the Wartburg NB 22 and 23 11kV overhead lines, which can be back-fed from each as shown in figure 4-3.

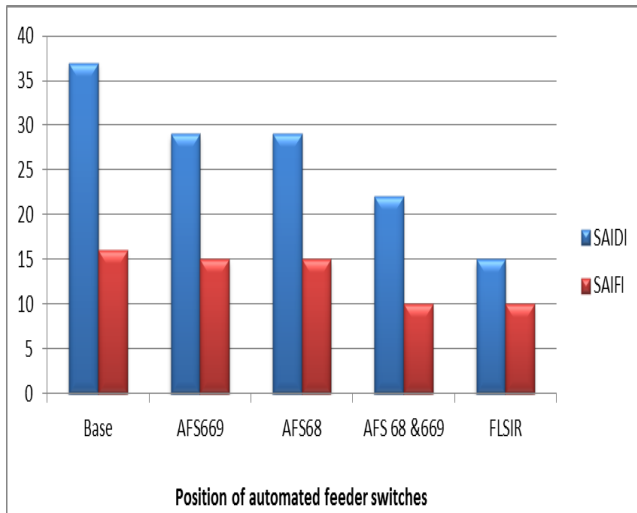


Figure 4-3: SAIDI and SAIFI for Wartburg network

As noted the automated feeder switches were installed at S669 and S68, thereafter the combination of these switches were simulated. The best performance is achieved when both these switches are installed. The improvement on SAIDI and SAIFI is 41% and 38% respectively

Three FPI's were installed at Mtonjaneni NB1 22kV network on S75 in zone 1, S33 which is in zone 2 and S3222 in zone 3 as per figure 4-4. Two FPI's are installed in Wartburg NB 22 and 23 11kV network, at S69 and S29 as demonstrated by figure 4-5. There is 46% and 21% improvement on SAIDI and SAIFI respectively in Mtonjaneni network.

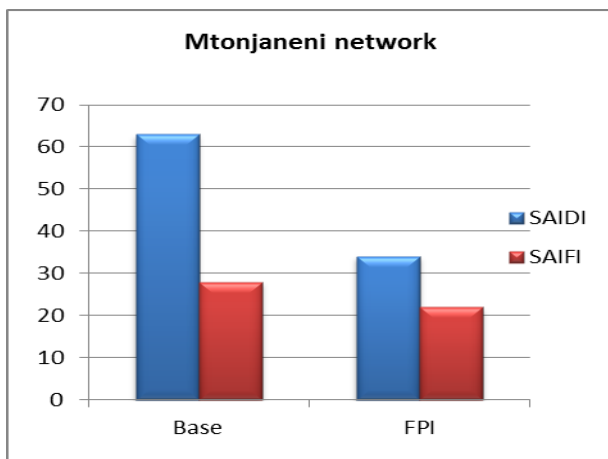


Figure 4-4: FPI for Mtonjaneni network

On the Wartburg network there is 46 % improvement on SAIDI and 7% improvement on SAIFI

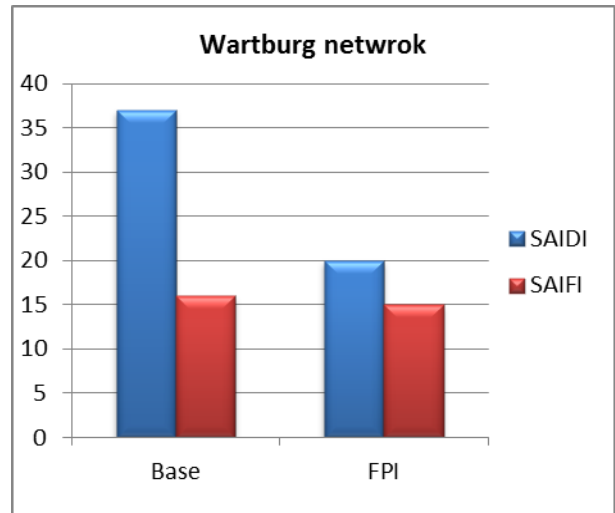


Figure 4-5: FPI for Wartburg network

The huge benefit of transformer remote monitoring is that if there is a transformer fault, it will be visible to the control centre so the operator will be dispatched to go and repair a faulted transformer right away, instead of doing sectionalising and fault finding prior the repairs.

When doing SAIDI and SAIFI calculations for a network, all possible faults and scenarios are placed in each component at a time. Transformer remote monitoring will only benefit transformer faults; all other faults duration will remain unchanged. Ideally this device will benefit those networks that are prone to transformer failures. This device was modelled on Mtonjaneni and Wartburg network as shown in figure 4-6 and 4-7.

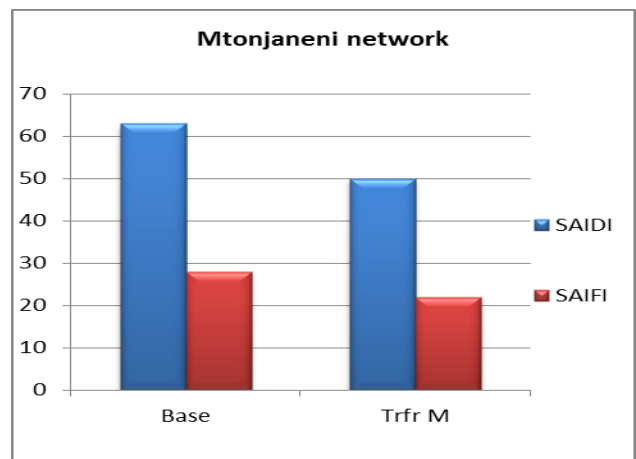


Figure 4-6: Mtonjaneni transformer remote monitoring

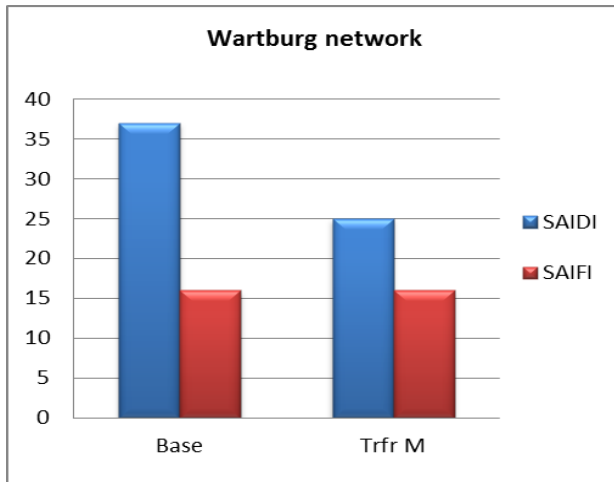


Figure 4-7: Wartburg Trfr. remote monitoring

At Mtonjaneni network there is 21% on both SAIDI and SAIFI. This improvement is not so significant as compared to automated feeder switches; the reason is that it only improved transformer related faults whereas SAIDI and SAIFI calculations are based on all possible faults on the system. For Wartburg network there is 32% change in SAIDI and no change in SAIFI.

4.4. Conclusion

It has been observed that results are network specific, different results may be obtained for different network configurations. Hence the performances of the studied Smart Grid cases varied in the simulated networks. What is more significant is the customer distribution in a network. The number of customers that are affected by a single breaker operation has a major impact to overall network reliability. As SAIDI is dependent on the number of customers and the fault duration, it becomes critically important to focus on the lines with high customers and long fault duration.

As smart grids mature and the rate of new installations increases, its marginal costs are likely to decline rapidly. Smart grid investment can always be economically justified and the huge capital costs are outweighed by the benefits that come with it. Its marginal costs decline with time as it matures.

5 ACKNOWLEDGMENT

The authors would like to thank Eskom for their support of the university through the Eskom Power Plant Engineering Institute programme.

6 REFERENCES

[1] P. P. Subban and K. O. Awodele, "Reliability Impact of Different

Smart Grid Techniques on a Power Distribution System," *IEEE*, vol. 1, pp. 1-9, 2013.

[2] L. Wang and S. H. Hyun, "A New Fault Location Method for Distribution System under Smart Grid Environment," *IEEE , The 6th International Forum on Strategic Technology*, vol. 1, pp. 1-4, August 2011.

[3] A. Bakirtzis, G. Bouhauras, D. Andreou and A. Labridis, "Selective Automation Upgrade in Distribution Networks Towards a Smarter Grid," *IEEE TRANSACTIONS ON SMART GRID*, vol. 1, no. 3, pp. 1-8, December 2010.

[4] M. X. JIA DongLi, SONG XiaoHui, "Study on technology system of self-healing control in smart distribution grid," *IEEE The International Conference on Advanced Power System Automation and Protection*, vol. 1, pp. 1-5, 2011.

[5] R. Billinton and R. N. Allan, *Reliability Evaluation of Power Systems*. New York and London: Plenum Press, 1996

[6] J. V. d. Merwe, M. Cameron and D. Gütschow, "Network Segmentation and Reliability Planning criteria," January 2014.

[7] F. Chan, *Electric Power Distribution System*, Vol 3 ed., Hong Kong, China: CLP Engineering, 2005.

[8] C. Carter Brown, N. Nunes and M.J.Cameron "Determining a relationship between Eskom Distribution network performance improvement and infrastructure investment cost" (C I R E D, 20th International Conference on Electricity Distribution, June 2009, pages 1-4)

[9] G. Dumakude, A. Swanson, R Stephen, I Davidson "Evaluation of smart technology for improvement of reliability in power distribution system"(SAUPEC conference, 2015, pages 1-7)

[10] J. Holmlund, "Practical experience of a self-healing grid," ABB, Finland May 20 2013.

[11] U.S. Department of Energy, "Reliability improvements from the application of Distribution Automation technologies," United States, pp. 1- 45, December 2012.

[12] C Carter Brown, "Quantifying the reliability impact of Smart Grid Technologies on Medium Voltage overhead networks," *Proceedings: 7th Southern African Regional Conference - CIGRE*, Johannesburg, pp. 1- 11, 2012.

[13] D. GmbH, "DigSILENT PowerFactory," DigSILENT GmbH, Gomaringen, Germany, User Manual 2014. N. Nunes "Distribution Network Performance KPI definition" (Eskom Standard, August 2010. pages 1- 29)

[14] M. Alvarez, R. Caire and B. Raison, *Smart Grids*, 1st ed., N. Hadjsaid and J. Sabonnadiere, Eds., Hoboken: John Wiley & Sons, Inc., 2012.

The Southern African Power Pool (SAPP) steady state security assessment using contingency analysis

Stacey J. T Mwale^{1*}, Innocent E. Davidson¹

¹University of KwaZulu-Natal, +27-31 Durban, South Africa

² University of KwaZulu-Natal, +27-31 Durban, South Africa

*Email: Stazhio@yahoo.com

Abstract: Many nations not only in Southern Africa but in Africa as a whole are faced with power deficits and inconsistent supply and distribution of electrical power. Reasons include lack of sufficient generating sources, faulty equipment and unforeseen disturbances in the network, negatively impacting both the quality of life and economic growth. A secure power system, however, is one capable of withstanding a wide variety of these disturbances and/or failures. This thesis assess the severity of possible disturbances that can occur in the SAPP (Southern African Power Pool) network by carrying out a contingency ranking then verifying these results by performing a contingency analysis in DIGSILENT PowerFactory. By so doing, the lack of security of the SAPP network in accordance with the N-1 criteria was affirmed. In this research, focus was given to two of the most critical and common failures to occur in a power system; the transmission line and generation unit failure. Both of which can cause alterations in the voltages of the transmission system and power flow. This research is particularly important because it allows appropriate measures to be put in place to mitigate the effects of unforeseen disturbances and failures that could occur in any given network.

1 INTRODUCTION

The Southern African Power Pool (SAPP) is an organisation whose primary aim is to provide reliable and economical electricity to its customers. It is a cooperation of 12 national electricity companies in the southern part of Africa and was the first formal international power pool to be created in Africa in 1995 [1]. The SAPP member countries include; Angola, Botswana, Democratic Republic of Congo, Lesotho, Malawi, Mozambique, Namibia, South Africa, Swaziland, Tanzania, Zambia and Zimbabwe (see Fig.1). SAPP has facilitated broadband infrastructure in Southern Africa in order to efficiently and effectively trade electricity among the countries utilizing cheap electricity generated by coal-fired thermal plants in South Africa and abundant hydropower potential in neighboring countries. The organization's other objectives include [2];

To increase power accessibility in rural communities.
Implement strategies in support of sustainable development priorities.

Provide a forum for the development of a world class, robust, safe, efficient, reliable and stable interconnected electrical system in the Southern African region
Harmonize relationships between member utilities.
Co-ordinate and enforce common regional standards of Quality of supply (QoS); measurement and monitoring of system performance.

Facilitate the development of regional expertise through training programs and research.

In order to effectively achieve its aims and objectives, the organization created a trading platform that enables the export and import of electrical power between the member states. This is carried out through three main trading platforms;

Bilateral trading - This involves the barter trade exclusively between two states without the use of hard currency for payment.

Day ahead trading market (DAM) - Contracts are made between buyer and seller for the delivery of power and the following day the price is set and the trade is agreed upon.

Post day ahead trading market (PDAM) - Unlike DAM, the price is set prior to deliver.

By 2013, SAPP comprised of a membership of 16 utility companies which also includes Independent Power Producers (IPP) and Independent Transmission Companies (ITC) from the 12 member countries. Whilst some of the utility companies are declared to be non-operational (NP), others are merely observers (OB).

2 POWER SYSTEM RELIABILITY AND SECURITY

Power system reliability is the measure of the capability of the electric power network to withstand sudden disturbances or unanticipated losses in the system components that can be caused by both natural and man-made events[3]. An operationally secure network is one that has a low probability of experiencing power outage or faults in the equipment. As the availability of electricity is of paramount importance in every sector of growth in our communities, it is of vast prominence that each power grid is of good reliance. A reliable and secure power grid is characterized by the following [4];

The voltages must be within the limits.

The grid must be able to withstand the loss of a generator.

Must be able to withstand the loss of a transmission line.

Must be able to retain stability during a short circuit.

The generating capacity must be greater than the load demand at any given time.

The transmission lines must not be overloaded.

A noticeable sign of an unreliable power grid is frequent power outages or blackouts. Despite modern electrical power grids being monitored by trained system operators equipped with sophisticated monitors and control systems such as SCADA, large, frequent and uncontrolled blackouts are affecting millions of customers around the globe.

2.1. Contingency Analysis

Power system steady state security is an instantaneous condition as it's a function of time and of the robustness of the system with respect to the imminent disturbances[5]. Some of the factors that threaten the reliability and security of the network include aging infrastructure of both the transmission and distribution networks[6]. One method of ensuring a reliable and secure power network is by careful monitoring, automation and information management. Such a tool that can be used to carry out a power system analysis in this regard is a contingency analysis (CA). CA is the study of the outage of elements such as transmission lines, transformers and generators, and investigation of the resulting effects on line power flows in the remaining parts of the system network. This tool is especially effective during the operation and planning stages to study the effect of contingencies. Contingencies refer to disturbances including transmission element outages or generator outages that may cause sudden and large changes in both the configuration and state of the system. They often result in severe violations of the operating constraints and in many cases lead to power outages [7]. Steady state contingency analysis aims at the assessment of the risk that certain contingencies may pose to an electrical network in real time. For any system to be considered secure it should conform to the N-1 criterion which certifies the networks ability to withstand any one disturbance. CA is also used as a study tool for the offline analysis of contingency events and as an online tool to show operators what would be the effects of future outages. This allows operators to be better prepared to react to outages by using pre planned recovery scenarios. During contingency analysis it should be noted that [8];

Security is determined by the system's ability to withstand equipment failure. Weak elements are those that present overloads in the contingency conditions (congestion). Standard approach is to perform a single (N-1) contingency analysis simulation. Contingencies

put the whole or part of the power system under stress and this occurs due to[9];

- Sudden opening of the transmission line
- Generator tripping
- Sudden change in the generation
- Sudden change in the load

2.2. Contingency Ranking and Selection

In practice, it is often not feasible to carry out a line outage on each independent transmission line in an exceptionally larger power system in an effort to study the overloading that will occur in the system. As is the case, a contingency ranking is applied to identify which lines have a higher probability of causing system overload. For purposes of this research the performance index (PI) index method was used in which the contingencies are ranked in severity of line over loads (PI_p) and the 'out of limit' voltages (PI_v) given by (1) to (3) [10]. And in order to get a reflection of the reactive power capacity constraints due to generator outages we will apply (4) [11].

$$PI_p = \sum_{i=0}^{NL} \left(\frac{W}{2n} \right) \left(\frac{P_i}{P_{i,max}} \right)^{2n} \quad (1)$$

Where;

PI_p – Active power index

P_i - power flow in MW

$P_{i,max}$ - MW capacity of the line

N_L - Number of lines in the system

W - Rean-non negative weighing factor = 1

n – Penalty function = 1

Where;

$$P_{i,max} = \frac{V_i V_j}{X} \quad (2)$$

Where;

V_i – voltage at bus i after load flow

V_j = voltage at bus j after load flow

X – Reactance of the line connecting bus

$$PI_v = \sum_{i=1}^{NB} \left(\frac{W}{2n} \right) ((|V_i| - |V_i^{sp}|) / \Delta V_i^{lim})^{2n} \quad (3)$$

Where;

PI_v – Reactive power index

V_i - voltage magnitude corresponding to bus i

V_i^{sp} – specified voltage magnitude corresponding to bus i

ΔV_i^{lim} – Voltage deviation limit

n – Penalty function = 1

N_B – Number of buses in the system

W – Real non-negative weighting factor = 1

$$PI_v = \sum_{i=1}^{NB} \left(\frac{W}{2n} \right) \left(\frac{|V_i| - |V_i^{sp}|}{\Delta V_i^{lim}} \right)^{2n} + \sum_{i=0}^{NG} \left(\frac{W}{2n} \right) \left(\frac{Q_i}{Q_{i,max}} \right)^{2n} \quad (4)$$

Where:

- PI_V – Reactive power index of generator outage
- V_i – voltage magnitude corresponding to bus i
- V_i^{sp} – specified voltage magnitude corresponding to bus i
- ΔV_i^{lim} – Voltage deviation limit
- n – Penalty function = 1
- N_G – Number of generating units
- W – Real non-negative weighting factor = 1
- $Q_{i\max}$ – Reactive power limit at bus i
- Q_i – Reactive power at bus i

2.3. N-1 Criterion

The N-1 criterion is one which is used to determine the security analysis of a power system following unpredicted faults and is an abstraction representing a single contingency or the outage of any one element following an incident. An ‘N-m’ contingency refers to the loss of m components in the power system where $m > 1$. As such, a first level contingency were only one component is lost during a fault is represented as N-1, a second level fault is represented as N-2 and so forth. Therefore, the total number of m^{th} contingencies that can occur in a power system is represented by the expression C_{Nm} , where; $m = 0, 1, 2, 3, \dots, N$ and N = number of elements. The total number of all possible contingencies that can occur in a power system is given by the equation;

$$TC_{Nm} = \sum_{m=0}^N C_{Nm} \quad (5)$$

Where;

$$C_{Nm} = \frac{N!}{m!(N-m)!} \quad (6)$$

Two of the most critical and common failures to occur in a power system are the transmission line failure and generation unit failure. Both of which can cause alterations in the voltages of the transmission system and power flow. This is why performing a contingency analysis allows one to determine which violations have been made after a disturbance occurs in the system. Even whilst the loss of a generation unit can cause additional dynamic problems usually affecting the frequency and operation output, this research is limited to the voltage and thermal violations that are reached during and after each contingency.

2.4. Voltage Violations

Voltage violations occur at the buses. A violation of the voltage at the bus bar indicates that the voltage post contingency at the bus bar has exceeded its acceptable limit of 0.95 – 1.05pu (per unit) of the nominal voltage. This standard is according to the IEEE which is a professional association to which all global standards succumb for a range of industries. When a voltage drop

occurs post contingency, meaning the voltage at the bus bar is below 0.95pu of the nominal voltage, there will be a spike in the reactive power as more of it will be injected into the bus in an effort to increase the voltage profile at the bus bar. Similarly, when a voltage rise occurs post contingency, exceeding the permissible 1.05pu of the nominal voltage, a drop in the reactive power will be experienced as more of it will be absorbed at the buses to maintain the nominal voltage.

2.5. Line MVA Limit / Thermal Overload Violation

When the MVA rating of the transmission line exceeds its given rating (which varies for each kind of transmission line) the line MVA is violated. Transmission lines are known to have some level of resistance which results in heat losses causing the transmission line to become hotter as more current flows through it. The maximum amount of current that can be transferred through a conductor whilst keeping the conductor’s temperature below its limit is what is specified as the maximum power in MVA, commonly referred to as the thermal rating of the line. Even while most lines are designed to withstand 125% of the thermal limit, some utilities declare a thermal limit ranging between 80% - 90% an alarm situation. For purposes of this research however, any line that exceeds 80% of its thermal limit will be considered an alarm situation whilst those surpassing 100% their thermal limit will be referred to as being overloaded.

Some of the factors that define the thermal rating of a line include;

- Current through a conductor
- Conductor characteristics
- Location – latitude, elevation, line direction, etc.
- Weather – wind speed/direction, air temperature, sun light.

3 SAPP NETWORK LOAD FLOW SIMULATION

3.1. Network building and design

The steps used in the building and load flow simulations of the SAPP network is as shown below;

Step 1: The SAPP network model was built using the DIgSILENT PowerFactory. The preliminary data that was used to construct the model was provided by SAPP and ESKOM (under a strict confidentiality agreement). A reduced equivalent model for each country was developed and represented as substations. This was done to eliminate computing constraints that were being experienced when the national grids of each country were integrated to form the SAPP network model. The models were reduced from a network consisting of transmission voltages of 11kV, 33kV, 88kV, 110kV, 132kV, 220kV, 275kV, 330kV and 400kV to a

HV model consisting of transmission voltages of 132kV, 220kV, 330kV and 400kV. The models were built such that only the transmission networks that are directly connected to the SAPP network were included. This resulted into a reduced 58 busbar network model on which simulations were run. The following procedure was adopted in developing the reduced order equivalent model of the SAPP model;

Step 2: The single line diagrams of the member states of SAPP were built using DIgSILENT PowerFactory.

Step 3: Data specifications of each component, namely: power transformers, transmission lines, generators, loads, reactors, are inserted using the raw data collected.

Step 4: The separate models are then interconnected to build one network, each country being represented as a substation in the SAPP mega station.

Step 5: The thermal ratings of the components and the voltage ratings of the busbars are set in DIgSILENT PowerFactory according to the SAPP requirements..

Step 6: The models are checked for connectivity to make sure that there will be a constant flow of power through each substation. The connectivity of the models are represented in seven different colours, each of which represent a split according to how many nodes are connected to that particular grid and also non connectivity.

4 LINE AND GENERATOR OUTAGE CONTINGENCY RANKING

The contingency ranking was computed using a MATLAB coding which depicts several line and busbar violations as formulated in Equation (1 – 4). The steps used are as shown below;

Step 1: Load flow is carried out in the networks pre-contingency state using the Newton Raphson iterative method under DIgSILENT PowerFactory.

Step 2: Generate a fault in any one of the transmission lines (L.1) in the network resulting in the outage of that line and run a load flow analysis.

Step 3: Using the generator, busbar and line profiles obtained from the post contingency analysis, apply necessary values to the MATLAB coding in order to get the PI_P and PI_V for the first line contingency C.L.1.

Step 4: Generate another line contingency (C.L.2) in a different transmission line and run a load flow analysis.

Step 5: Repeat steps 2 to 4 to acquire the PI_P and PI_V of the all the line contingencies in the network.

Step 6: Arrange the several indices to identify which contingencies are more critical. Six of the most critical line and generator contingencies are as shown in Fig.1 and Fig.2.

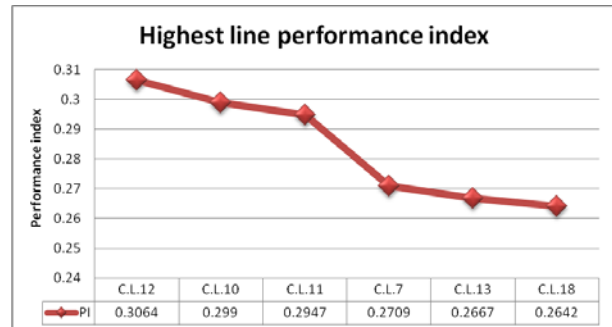


Fig.1. Highest rated line contingencies

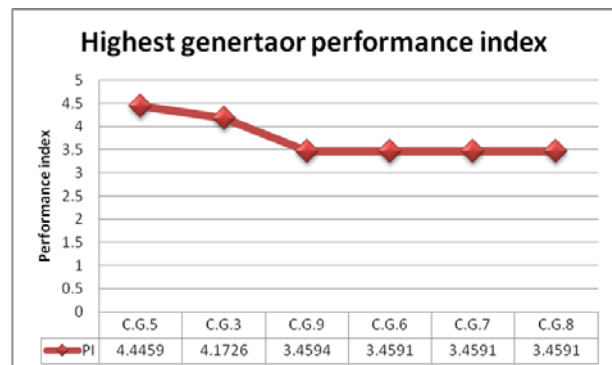


Fig.2. Highest rated generator contingencies

5 SAPP CONTINGENCY ANALYSIS RESULTS

The contingency analysis for each contingency case was carried out in the DIgSILENT PowerFactory. Example shown is the result that followed after a contingency was applied to the Goaborone South – spitskop 132kV transmission line that interconnects Botswana and South Africa. The figures depict the thermal loading, minimum voltage violation and maximum voltage violation results after the contingency occurs. Figure x shows that post contingency, the BPC substation is affected by dropping below the voltage limit represented by the blue colour. NAMPOWER substation shows a voltage drop occurs by the alteration of colour from green to blue in one section and from yellow to green in the other section. A section of the ZESA substation experienced a voltage drop below the security limit.

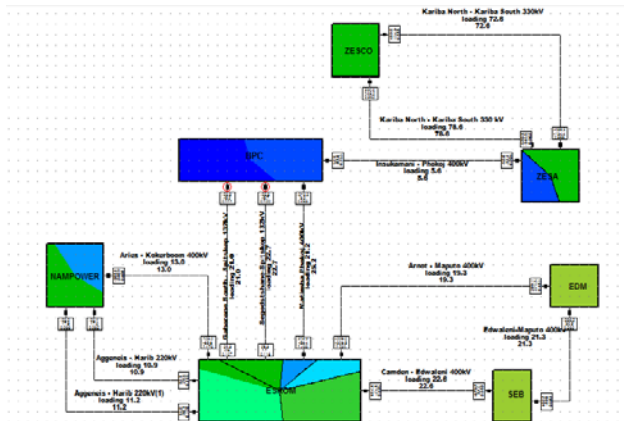


Fig.3. SAPP network post contingency

Fig.3 on the other hand shows that all the busbars in the BPC network experience voltage drops below the secure limit when under contingency C.L.10. This is represented by their blue colour.

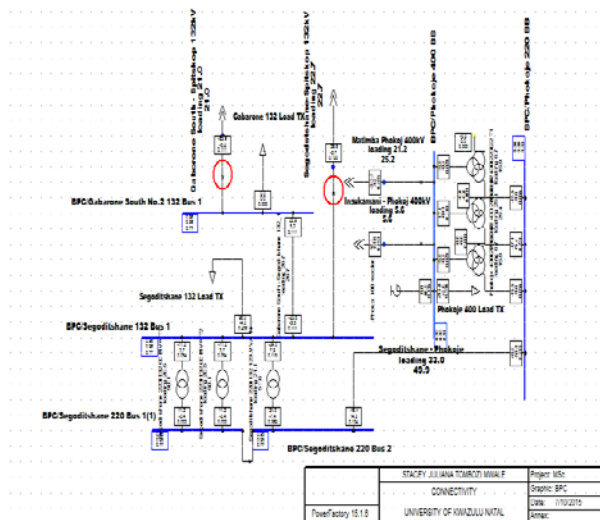


Fig.4. BPC substation network post contingency

Fig.4 displays the voltage violations caused from contingency C.L.10. A total of 8 busbars undergo a change of voltage levels post contingency. The first busbar, Segoditshane 220 Bus 1, is seen to have a base voltage of 0.954 p.u which then drops to 0.770 p.u post contingency. This change in voltage is represented by a differentiation in colour as the voltage drops from a voltage that is within the required security limits to one that is not. The bar in the graph is multi coloured, green in the far right side to show the voltage lies within the specified security limit to a dark red colour in the far left to indicate that the voltage now falls outside the required security limit. This proves true for the next three busbars that follow. The Phokojoe 220 BB busbar in the same graph however has a different set of colours. The bar corresponding to Phokojoe 220 BB is coloured bright red in the far right to show that its base case voltage of 0.877 p.u is not within specified limits and

drops further to 0.8833 p.u represented by a dark red colour in the far left of the bar. This analysis can be used to interpret the three busbars that follow which all have base voltages below the security limit and drop even further.

Component	Substation	Voltage Min. [p.u.]	Voltage Step [p.u.]	Voltage Base [p.u.]	Base Case and Post Voltage [0.770 p.u. - 0.964 p.u.]
Segoditshane 220 Bus 1	BPC	0.77	-0.18	0.95	
Segoditshane 220 Bus 2	BPC	0.77	-0.18	0.95	
Gaborone Sth No.2 132B1	BPC	0.77	-0.19	0.96	
Segoditshane 132 Bus 1	BPC	0.77	-0.19	0.96	
Phokojoe 220 BB	BPC	0.83	-0.04	0.88	
S. Phikwe 22 BB	BPC	0.83	-0.04	0.88	
Phokojoe 400 BB	BPC	0.91	-0.03	0.93	
Insakumani 400 Bus 1	ZESA	0.91	-0.03	0.94	

Fig.5. Post contingency voltage violation

6 CONCLUSION

The SAPP network was modelled and built using DiGSILENT PowerFactory. The entire SAPP network, consisting of 1407 busbars incurred computational constraints due to the size of the network. Therefore, the model was reduced to only include the path that is directly used by SAPP in the transferring of power from one member state to the next and consisted only 58 busbars. The simplified network was modelled to facilitate the HV network consisting of transmission voltage levels of 132kV, 220kV, 330kV and 400kV.

The contingency ranking method used in this paper to determine the severity of security violations in the SAPP network is very systematic and methodological and can be applied to several networks, both larger and smaller, in order to comprehensively study several types of first level contingencies. This is reflected in the correlation of results yielded from the MATLAB codes and the contingency analysis graphs simulated in DiGSILENT PowerFactory. The simulations were focused on the primary contingency disturbance (N-1 criteria) of the generators and transmission lines in the network because these are the highest recorded faults that are likely to occur in any power network. The vulnerability of the SAPP network is exposed after the contingency analysis simulation of the designed model. The results attained not only reveal the extent to which the power network is insecure in accordance with the SAPP transmission criteria but also reveal the severity with which each exact component is affected after each possible disturbance. These disturbances lead to differed levels of security severities that are characterised by voltage and thermal loading discrepancies.

7 ACKNOWLEDGMENT

Gratitude goes to the staff University of KwaZulu-Natal and my supervisor for allowing me the opportunity and assisting me in every way possible and the Eskom Electric Power Plant Engineering Institute (EPPEI) for the sponsorship to carry out my research.

8 REFERENCES

- [1] T. Aldrich, "The Southern African Power Pool: Meeting the sub-continent's electricity needs," in *Institute for global dialogue*, 2002.
- [1] L. Musaba, "The development of the SAPP competitive electricity market," in *Power Engineering Society Inaugural Conference and Exposition in Africa, 2005 IEEE*, 2005, pp. 188-194.
- [3] (2013). *SADC consumption/production*. Available: <http://www.google.co.za/url?sa=i&source=imgres&cd=&cad=rja&uact=8&ved=0CAkQjRwwAGoVChMI4avz4-DBxwIVyVoUCh1BWAc&url=http%3A%2F%2Fkitweonline.com%2Fbusiness-in-kitwe%2Fservices-and-resources%2Frenewable-energy-sources&ei=2xLbVaHSGsm1UcGwnfAD&psig=AFOjCNGrsFnY3ssZ-I3aCO-u9EqiUpMU0Q&ust=1440506971582770>
- [4] C. Singoi, "Zesco power system stability studies for 2011," Chalmers University of Technology, Goteburg, Sweden, 2011.
- [5] S. J. T. Mwale and I. E. Davidson, "A Steady-state Contingency Analysis of the SADC Regional Grid using the N-1 Criterion," *Journal of Energy and Power Engineering*, vol. 9, May 2015 2014.
- [6] A. Ipakchi. (2007) Implementing the smart grid: Enterprise information integration. *Grid-interop forum*.
- [7] A. J. Wood, B. F. Wollenberg, and G. B. Sheblé, *Power Generation, Operation and Control*: Wiley, 2013.
- [8] V. N. Pande, V. M. Jape, and M. D. Khardennis, "Transmission network expansion planning using contingency analysis," presented at the International conference on signal, Singapore, 2011.
- [9] P. Kundur, N. J. Balu, and M. G. Lauby, *Power System Stability and Control*: McGraw-Hill, 1994.
- [10] S. Ahmed, N. M. Zakaria, A. Ehali, and G. Biswas, "Contingency analysis and reliability evaluation of Bangladesh power system," BRAC University, Dhaka, Bangladesh, 2011.
- [11] B. Prusty, B. Pattnaik, P. Pandey, and S. Santosh, "Power system security analysis," *International journal of scientific and engineering research*, vol. 5, pp. 849-853, May 2014 2014.
- [12] A. A. Abdulrazzaq, "Contingency ranking of power systems using a performance index," *International research journal of engineering and technology* vol. 2, 02 May 2015.

A METHOD FOR MEASURING AND RECORDING CHANGES IN WOOD POLE IMPEDANCE OVER TIME

N.E. Khoza*, A. Beutel**, J. Van Coller***

School of Electrical & Information Engineering, University of the Witwatersrand, Private Bag 3, 2050, Johannesburg South Africa

*E-mail: * 1315266@students.wits.ac.za ** BeutelAA@eskom.co.za *** John.VanColler@wits.ac.za*

Abstract: The impedance of wood poles changes over time which suggests that the conductivity of the wood pole increases or decreases over time. These changes could be due to the occurrence of rain (moisture content), pollution deposited on the wood surface, treatment preservatives and aging. It is therefore important to study the variation of the wood pole impedance over time. The research will be focused mostly on bird safety in relation to wood pole impedance.

Wood cross-arms that have been normalised i.e. stored in the same way, same place and same treatment method will be used as samples. A single cross-arm will be tested by applying a voltage across it using different electrode configurations and the impedance will be calculated from the current measured.

The impedance of wood was measured and found to be in the range of 10^6 to $10^{11} \Omega$ for dry wood and 103 to 104 Ω for wet wood. The dielectric constant for dry wood at the power frequency range is between 1 and 10 and between 10^2 and 10^3 for wet wood. The range of wood impedance that would reduce the risk of bird electrocution was found to be between 121.3 - 126.6 k Ω .

The research work will also include the logging of weather data which will include wind pressure, rain events, temperature, humidity and wood moisture content. The data will be downloaded and analysed on a day to day basis for a period adequate to study the different prevailing weather seasons in South Africa.

Keywords: Wood pole, Impedance, Bird, Safety, Sapwood, Heartwood, Moisture content

1. INTRODUCTION

The MV networks (1 kV up to 33 kV) in Eskom mainly use wood or concrete poles. Steel poles are used less frequently on MV lines due to various factors such as cost per kilometre when compared to wood [1]. Composites, polymers, fibreglass and hybrids (combination of two different materials) are also being considered. These considered materials may offer better performance in terms of maintenance throughout the pole's life cycle [1].

Notwithstanding the different options and technologies available, wood poles still dominate the present networks. It is therefore important that the electrical characteristics of wood poles are understood. The research will focus on the impedance of wood poles and the impact thereof on the safety of large (often endangered) birds.

The impedance studies on wood poles will be performed over a period of time to determine how the impedance changes. This change will have a major impact on the birds that perch on these structures as the impedance influences the magnitude of leakage current that flows through the bird if it makes simultaneous contact between a phase conductor and the pole. The aim is to prevent bird electrocution. The range of wood impedance that would reduce the risk of bird electrocution is between 121.3 - 126.6 k Ω , assuming bird impedance range of 800-5700 Ω and a current of 100 mA. This wood impedance is typical for a wet wood pole [2]. Other impacts are pole-top fires due to leakage current flow in or on the wood and the possibility of earth potential transfer when performing work on live (energised) MV structures.

It is therefore important to measure the variation of the wood pole impedance during its lifespan and the effect it has on bird safety.

2. BACKGROUND

2.1. Bird safety (environmental)

The electrocution of birds on wood poles has been seen as "unlikely" since wood poles are seen to be non-conductive throughout their life span. Field experience has ruled this out.

There is, however, concern because of recent cases of the electrocution of large birds of prey (e.g. vultures, eagles etc.) that have occurred due to the bird bridging a phase conductor and the steel frame attached to the top of relatively new wood pole structures. The only conclusion that could be drawn was that the wood pole impedance was low enough to allow sufficient leakage current to flow through the bird, thereby electrocuting the bird.

A report prepared by the Endangered Wildlife Trust (EWT) in conjunction with Eskom [3] showed that 36 birds were electrocuted within a period of 2.5 years on wood pole structures of a new 22 kV line that was constructed in 2010/2011.

The structures where these mortalities occurred are of the A-Frame type shown in Figure 1. Figure 2 below shows the bird feathers and burn marks on the frame of the structure. It is therefore clear that the birds made contact with both the steel frame and the 22 kV phase conductor.

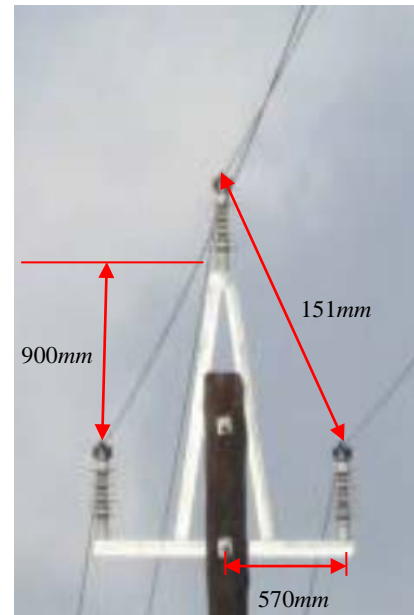


Figure 1: Intermediate A-Frame structure on the network [3]



Figure 2: Burn mark on the metal frame of the intermediate structure after a martial eagle was electrocuted [3]

The frame is not directly connected to earth via the earth conductor, but this earth conductor has a 500 mm wood gap inserted for insulation coordination purposes. This raises the question of how the metal frame got to be connected to earth through low impedance. The only reasonable explanation is that the wood pole was sufficiently conductive to allow a significant phase-to-earth leakage current to flow when contact was made. The electrocution mechanism could be similar to that illustrated in Figure 3.

The postulated mode of electrocution is a bird sitting on a cross-arm making contact with a phase conductor with its wing or sitting on an insulator and making contact with

the cross arm. This is therefore to be investigated in this project.

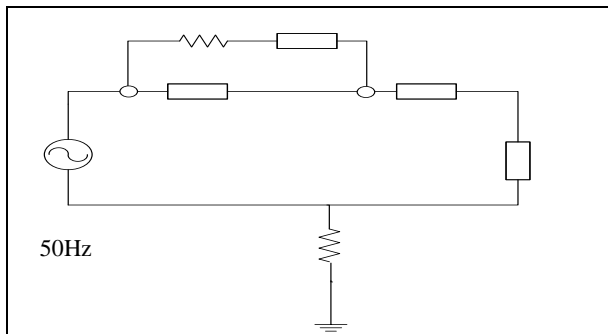


Figure 3: Equivalent circuit of a bird sitting on a metal cross-arm (A-Frame) and making simultaneous contact with the phase conductor and the cross-arm.

2.2. Wood pole fires

Wood pole fires may occur due to leakage current flowing across the insulator surface under lightly wetted pollution conditions and finding its way into or onto the wood pole. This may lead to charring, smouldering and eventually ignition of the wood pole. The fact that there is flow of current on the surface of the wood suggests that the wood has non-infinite impedance. This subject is therefore related to the research questions, but the subject of wood pole fires has been well researched and understood [4]. An example of a structure burnt in this way is shown in Figure 4.



Figure 4: Wood pole cross-arm after a fire caused by leakage current flow

2.3. Live working

Electrical shocks to linesmen have been reported on Chromated Copper Arsenate (CCA) treated poles [5]. The degree of hazard/risk of electrical contact depends on the resistance of the wood pole or contact resistance to the wood pole. It has been observed that all wood poles regardless of treatment, particularly when new; allow sufficient leakage current to flow through a person to

cause a significant shock [5]. The wood pole shock hazard during live working, ranging from worst to least, is:

- Creosote treated wood pole (due to the fact that it reduces the drying rate)
- CCA treated wood pole
- Untreated wood pole

However further results showed that even “rogue” untreated poles presented a worse situation than the average Creosote treated pole. Therefore no pole, regardless of its treatment, can be regarded as safe [5].

3. INVESTIGATION METHODOLOGY

The research methodology will consist of three sections; laboratory experiments, simulations and field experiments

The measurement direction will be along the grain. Wood cross-arms that have been normalised i.e. stored in the same way, same place and same treatment method (with creosote) will be used as samples.

3.1. Laboratory Experiments

Sample details

- Wood cross arm, 140mm diameter, creosote treated in 2012, strength class E55 (55MPa)
- Space between electrodes = 0.5m
- Coach screw penetration depth = 70mm
- Clout nail penetration depth = 12mm
- Copper strap width = 30mm

The electrode configurations applied in the experiments are shown in Figure 5.



Figure 5: Partially insulated coach screw penetration (left), nail penetration (centre), copper strap (strap)

Wood pole impedance measurements will be done in the different electrode configurations by applying DC and AC voltages separately.

Some of the configurations are shown in Figure 6 below.

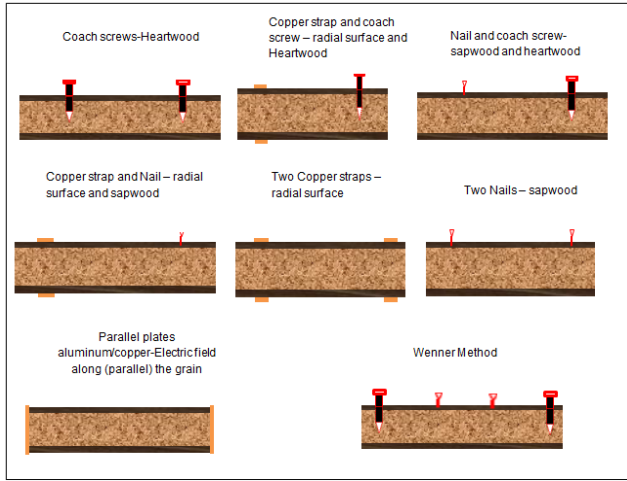


Figure 6: Proposed electrode configurations

The equilibrium moisture content of the wood samples will be determined using the oven dry method and wood impedance measurements will be performed at room temperature.

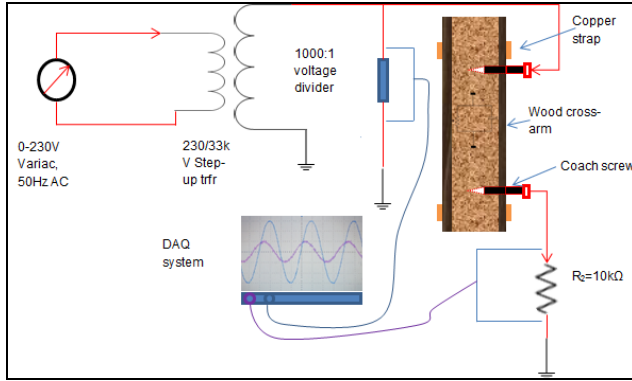


Figure 7: Typical experimental setup for measuring wood impedance

Studies of the dielectric properties of wood will be done using equipment with high accuracy such as the Omicron Dirana. The different electrode configurations as shown in Figure 6 will be used. The following parameters will be determined in these experiments; dielectric constant, capacitance, loss factor/power factor.

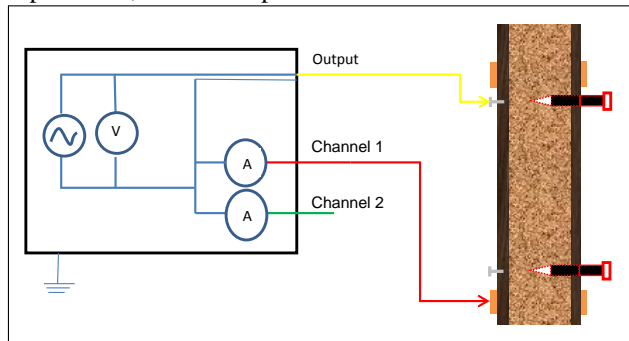


Figure 8: Typical experimental setup for performing a tan delta test on wood using the Omicron Dirana “in nail out strap” [6].

The dielectric constant is directly proportional to the total polarizability. The dielectric constant (DK) can be

simplified as follows [7] (symbols defined at the bottom of the page):

$$DK = a + \frac{b}{(1 + \frac{f}{f_0})} + \frac{c}{\frac{f^l}{f_0^l}} \quad (1)$$

a, b, c are the polarization coefficients:

f , is the frequency, in Hz;

f_0 is the frequency at which effectively half of the polarizations represented by the coefficient b have vanished;

l , is an exponent that may differ from 1.0 by small amounts, due to slight non-uniformity in the distribution of time constants c ;

f_0^l is unit frequency, inserted to make the coefficient c dimensionless;

High frequency instruments calculate the permittivity (ϵ) as;

$$\bar{\epsilon}_r(\omega) = \epsilon'_r(\omega) - i\epsilon''_r(\omega) = \epsilon'_r(\omega) - i\left[\epsilon''_r(\omega) + \frac{\sigma_0}{\epsilon_0\omega}\right] \quad (2)$$

The real part represents the capacitance of the test object, the first term in the imaginary part represents the dielectric loss and the second term represents the DC conduction losses [8, 9]. At high frequencies (>10 kHz) the dielectric constant decreases to typical values of homogeneous polar solids – interfacial polarization becomes insignificant and the polarization is predominately molecular [7]. At low frequencies (<10 kHz) the dielectric constant increases – interfacial (due to polarization at discontinuities of conductivity) polarization is predominant [7].

3.1.1. Wood cross-arm interactions

A bird perching on the cross-arm and making contact with the source is modelled as resistor in the different electrode configurations.

The impact of wood impedance will be studied taking into account the following conditions that are related to utility wood pole structure design;

- When there are gaps in the wood,
- Metallic hardware that traverses the heartwood e.g. spindles
- Shallow nails in close proximity to wood path gaps.

3.1.2. Dielectric properties of utility wood poles

The dielectric properties of wood will be studied in the frequency domain where the properties of water in the wood can be researched. The complex permittivity part of Equation (2) will be further analysed to study the resistive losses as a function of frequency.

3.2. Simulations

The wood pole sample(s) will be modelled as anisotropic material (2 layer model) using 3-D electrostatic software.

The two layers will be sapwood and heartwood. The inputs to the software will be the geometry of the wood, boundary conditions, permittivity conductivity, voltage or potential. The following assumption will be made during modelling, that the transition from sapwood to heartwood is immediate i.e. no transition layer. The output of the software, for example, capacitance will be compared with the laboratory experiments for consistency.

3.3. Field Experiments

A field setup of a cross-arm with known initial moisture content will be used. The best arrangement of electrodes will be used and measurements will be done at 50 Hz with a constant voltage source. The input voltage, the current from the output electrode and the angle between the two will be measured directly. The impedance will be calculated using Ohm's law $v(t) = R i(t)$

The mini weather station will be a combination of sensors that will be measuring wind data, weather data (temperature, dew point, humidity & rain)". The data recorded from these sensors will be downloaded and analysed on a day by day basis for a period adequate to study the major prevailing weather seasons in South Africa (summer and winter).

If certain weather data cannot be measured in this project they can be requested from the South African Weather Services. The equipment should have the correct Ingress Protection (IP) rating for dust and water in this outdoor use as described in IEC 60509:1989. The site chosen will be an Eskom site and the setup should be able to be used after this project.

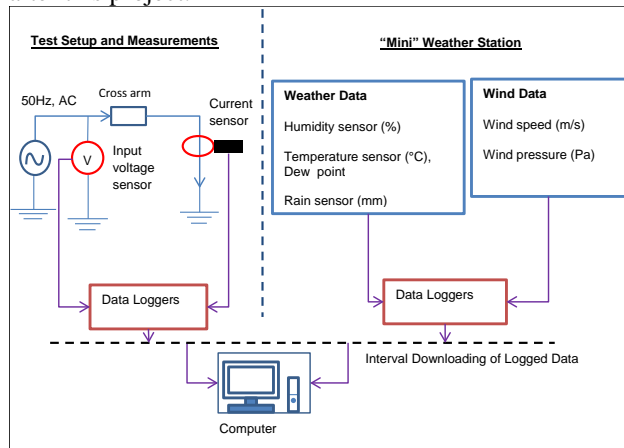


Figure 9: The proposed field experiment setup for measuring wood-pole impedance changes over time.

The field experiments have not yet been conducted, but the following is expected;

Older poles show lower impedance than newer poles [5, 12]. Poles with high moisture content have been found to have lower impedance. The heartwood moisture content is higher than the sapwood moisture content and does not get much influenced by weather changes [11]. There is relatively higher moisture content on the first meter above the ground line, mostly due to the moisture in the soil, and less at the top meter of the pole mostly due to air drying effects [6, 11]. Rain is known to reduce wood pole resistance and in turn increase the moisture content over

long periods of persistence [11]. Pollution on the wood surface (e.g. salt deposition, dust, soil, coal dust, chemicals etc.):_poles with salt deposited on the surface have been found to have lower impedance.

Very humid conditions promote leakage current flow meaning that the impedance is lower than under dry conditions [10]. The resistance of wood is expected to decrease with a rise in temperature, approximately halving for every 10-12 degrees Celsius increase [3, 6]. The treatment method has a much bigger influence on the electrical performance of the pole such that the wood species becomes a secondary effect [5]. The conductance is expected to drop on the sapwood surface. This is due to the Creosote's impregnation interactions with the hygroscopic properties of the sapwood [5]. High humidity and rain will increase the conductance on Creosote-treated poles [5].

4. RESULTS

4.1. Wood impedance

The measurements were performed for both wet and dry conditions. The wetting was achieved by sprinkling tap-water on the surface of the wood and readings taken as soon as possible.

The temperature, humidity and moisture content readings were taken during the experiment.

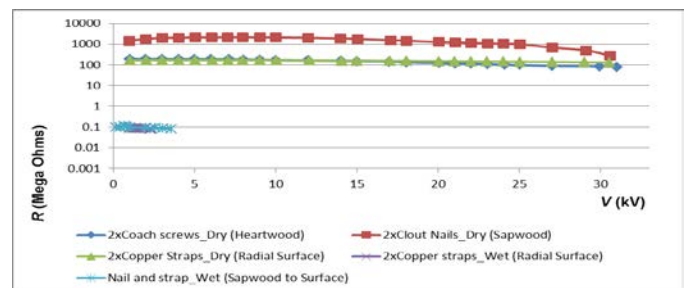


Figure 10: Typical results of a Creosote treated wooden crossarm obtained using the experimental setup of Figure 7.

4.2. Dielectric property – Permittivity

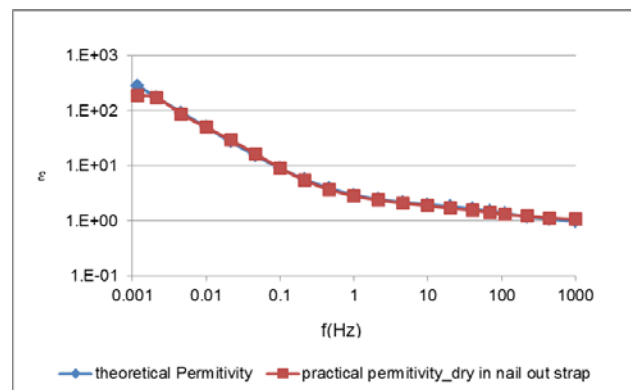


Figure 11a: The permittivity of dry wooden cross arm as a function of frequency from the setup of Figure 8

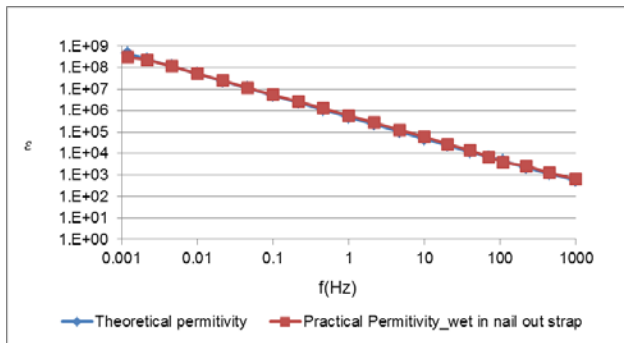


Figure 11b: The permittivity of a wet wooden cross-arm as a function of frequency from the setup of Figure

In Figures 11a and 11b, “in nail out strap” represents the way in which the electrodes were arranged in order to determine the permittivity between the sapwood and the radial surface of the wood cross arm in both dry and wet conditions.

5. DISCUSSION OF RESULTS

5.1. Wood impedance

The results, from Figure 10, generally show that wood poles have non-linear impedance characteristics. The impedance decreases as the voltage is increased. The impedance of the heartwood is lower than that of the sapwood, this is because the heartwood moisture content is higher than the sapwood moisture content and does not get much influenced by weather changes [11]. The magnitude of current flowing through the wood pole is influenced by the contact resistance of the electrode and the resistance of the pole itself [5].

5.2. Wood dielectric properties

The theoretical permittivity was calculated using Equation (1) after a few guesses of the polarization parameters. The drawback in these devices is that they do not take into account the DC conduction mechanism in the measured permittivity $\epsilon''(\omega)$ or dielectric loss $\chi''(\omega)$ [8,9].

6. CONCLUSION

The impedance of wood was measured and found to be in the range of 10^6 to $10^{11} \Omega$ for dry wood and 10^3 to $10^4 \Omega$ for wet wood. These findings are consistent with the findings of [2] and James [7]. The dielectric constant for dry wood at the power frequency range is between 1 and 10 and between 10^2 and 10^3 for wet wood. These findings are consistent with the findings of James [7] at room temperature (25 °C). The techniques of using electrodes and a voltage source may be used in determining the impedance of utility wood poles, however the drying factor introduced by the current flowing needs to be taken into consideration.

7. FUTURE WORK

Impedance measurements will be done taking into

account the weather conditions such as temperature, humidity, wind speed, dew point etc. A way to account for the drying introduced by the flow of current will be suggested. The measurement direction will be along the grain. Wood cross-arms that have been normalised i.e. stored in the same way, same place and same treatment method (with creosote) will be used as samples. The imaginary part of the complex permittivity equation will be analysed to determine the role which the water molecule plays in the conduction term. A full 3-D electrostatic simulation model will be developed to study the interaction of the wood poles with electric fields. A bird model will be included in the wood impedance measurement to determine the safety of raptors under different conditions. In order to study further the impedance of the two layers of the wood, the Wenner method for measuring soil resistivity, described in SANS 10199, will be applied on the wood cross-arm samples.

8. REFERENCES

- [1] R.White, “An assessment of the South African Utility Pole Market”, International Zinc Association Southern Africa (IZASA) Report, November 2001.
- [2] R. Kellogg, “Physical Properties of Wood,” in Wood: Its Structure and Properties, Forintek Canada, 1979, pp. 195-212.
- [3] C. Hoogstad, “A-frame structure incidents investigation Beaufort-West, Western Cape” Endangered Wildlife Trust Special Investigation Report, May 2013.
- [4] A. Beutel, H. Geldenhuys, B. McLaren, M. Ntshani, K.Thejane, A. Khatri, “Pole-Top Fires Risk Assessment: A South African Perspective”, CIRED 22nd International Conference on Electricity Distribution, Stockholm, June 2013.
- [5] M. Darveniza, “Chapter 6: Electrical Resistance of Wood and Leakage Current Effects,” in Electrical properties of wood and line design, Queensland, University of Queensland Press, 1980, pp. 117,121,123,125-127.
- [6] Omicron Dirana User Manual, Article Number: VESD0800 - Manual Version: DIRANA.AE.3.
- [7] W. L. James, “Dielectric Properties of Wood and Hardboard: Variation with Temperature, Frequency, Moisture Content, and Grain Orientation,” U.S. Department of Agriculture Forest Service Research Paper, 1975.
- [8] W. Zaengl, “Dielectric spectroscopy in time and frequency domain for HV Power Equipment, Part I: Theoretical considerations,” IEEE Insulation Magazine, vol. 19, no. 05, 2003.
- [9] T. Liu, “Dielectric Spectroscopy of Very Low Loss Model Power Cables,” submitted for PhD, University of Leicester, Leicester, 2010.
- [10] S. Pathak, “Leakage Current in Wooden Structures Used for Power Distribution,” Thesis for PhD, RMIT University, 2011.
- [11] R. Filter; J.D.Mintz, “An Improved 60 Hz Wood Pole Model”, IEEE/PES Transmission and Distribution Conference, New Orleans, Louisiana, 1989.

CURRENT CONTROL OF A GRID-TIED INVERTER WITH LCL-FILTER THROUGH MODEL PREDICTIVE CONTROL

J.M.C. Geldenhuys*, T. Mouton** and A. Rix***

Department of Electrical and Electronic Engineering, Stellenbosch University, Private Bag X1, 7602 Matieland, South Africa.

* Email: 16722590@sun.ac.za

** Email: dtmouton@sun.ac.za

*** Email: rix@sun.ac.za

Abstract: This paper presents a method to control the output current of a three-phase grid-tied inverter. To reduce harmonics caused by the inverter an LCL-filter is implemented to reduce the amount of current distortion injected into the grid. The approach presented is based on the finite control set model predictive control (FCS MPC) strategy and makes use of sphere decoding to make the process computationally efficient for long horizons. The aim is to minimise current distortion and switching frequency to reduce losses.

Keywords: finite control set model predictive control over long horizons, LCL-filter, grid-connected inverter, sphere decoding, current control.

1. INTRODUCTION

Model predictive control (MPC) has only recently become popular in power electronic applications due to previous limitations of real time processing capabilities. Direct MPC with reference tracking can be used to reduce switching frequency, consequently reduce losses and still maintain acceptable distortion levels. This is important for high power converters [1-2]. In this paper finite control set model predictive control (FCS MPC) over long horizons with sphere decoding is used for inner-loop current control. MPC over long horizons determine solution sequences that are close to optimal pulse patterns and perform better in the frequency domain than with a horizon of one. Sphere decoding removes the computational burden of long horizons by optimizing the search process [3-4].

The topology of the system is illustrated in Fig. 1. DC power is supplied from a renewable source to an inverter followed by a three phase LCL-filter to filter out harmonics caused by the inverter before the power is supplied to the grid [5].

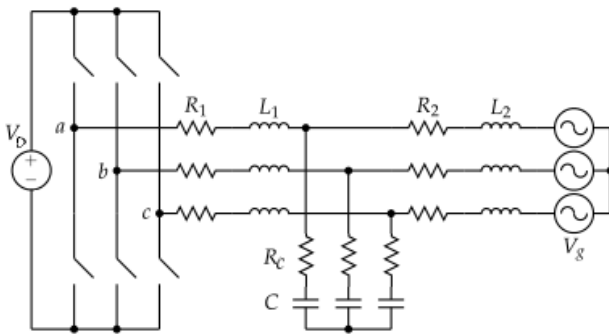


Figure 1: System topology

LCL-filters are desirable for grid-connected systems as a result of their high harmonic attenuation abilities compared to series inductor filters [6-7]. Fig. 2 shows the filter's setup, with i_1 being the output current of the inverter, i_2 the output current to the grid, which will be controlled with FCS MPC and sphere decoding, and u the switch state. At each time instance each phase leg of the system can assume one of two possible switch states listed in the finite control set $u_a, u_b, u_c \in \{-1, 1\}$.

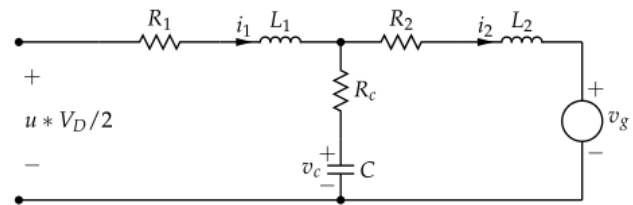


Figure 2: Per-phase model of the LCL-filter configuration.

2. SYSTEM MODELLING

The per-phase model in Fig. 2 is implemented mathematically into a MATLAB-based simulation to evaluate the strategy.

2.1 $\alpha\beta$ Reference frame

Three-phase quantities can be transformed from the abc reference frame $\xi_{abc} = [\xi_a \ \xi_b \ \xi_c]^T$ to the stationary orthogonal $\alpha\beta$ reference frame $\xi_{\alpha\beta} = [\xi_\alpha \ \xi_\beta]^T$ by using the transformation in (1) where K is the transformation matrix.

$$\xi_{\alpha\beta} = K \xi_{abc} \quad (1)$$

$$K = \frac{2}{3} \begin{bmatrix} 1 & -\frac{1}{2} & -\frac{1}{2} \\ 0 & \frac{\sqrt{3}}{2} & -\frac{\sqrt{3}}{2} \end{bmatrix} \quad (2)$$

2.2 Controller model

The continuous-time state-space model is given by (3) and (4) with the matrices F , G_1 , G_2 and C listed in the Appendix. State variable $x = [i_l \ i_2 \ v_c]^T$ consists of the input current from the inverter $i_l = [i_{la} \ i_{lb}]^T$, grid-side output current $i_2 = [i_{2a} \ i_{2b}]^T$ to be controlled and the capacitor voltage $v_c = [v_{ca} \ v_{cb}]^T$. The manipulated input variable $u = [u_a \ u_b \ u_c]^T$ represents the switch states for each phase leg. The grid voltage $v_g = [v_{ga} \ v_{gb} \ v_{gc}]^T$ is an external influence but to simplify the analysis it will be set to zero. The grid voltage will be incorporated into future investigations.

$$\frac{dx(t)}{dt} = Fx(t) + G_1 u(t) + G_2 v_g(t) \quad (3)$$

$$y = Cx(t) \quad (4)$$

The continuous-time model is then converted to the discrete-time model in (5) through exact discretization. Time is divided into fixed sampling intervals of length T_s and the current position in time is indicated by k . This model is evaluated at each time step k to determine the state x of the system at the next time step $k+1$. At each time instance k each phase leg of the system can assume one of two possible switch states listed in the finite control set $u_a, u_b, u_c \in \{-1, 1\}$.

$$x(k+1) = Ax(k) + B_1 u(k) + B_2 v_g(k) \quad (5)$$

2.3 Model predictive control

The discrete-time state-space model is used to predict the outcome for different switch state inputs of $u(k)$. Each outcome is put into the cost function in (6) comprising of the control objectives for the system. The first part of the cost equation represents the control objective to minimise the current-tracking error i_e between the grid-side current i_2 and the reference current. The second part in (6) implements the control objective to minimise the switching frequency to lower switching losses. The weighting factor λ_u controls the trade-off between these two control objectives. The prediction horizon length N represents the finite amount of time steps into the future over which the cost function predicts and evaluates the outcomes. The longer the horizon, the larger the set of possible switching sequences becomes. Equation (7) states the optimization problem of determining the optimal switching sequence $U_{opt}(k)$ by evaluating all the possible sequences $U(k)$ to identify the one resulting in the minimum cost. The first element u_{opt} of the sequence

is then applied at time step k before the next search for the optimal sequence is carried out at time $k+1$, this is known as the receding horizon policy [3-4].

$$J = \sum_{l=k}^{k+N-1} \|i_{e,abc}(l+1)\|_2^2 + \lambda_u \|\Delta u(l)\|_2^2 \quad (6)$$

$$U_{opt}(k) = \arg \min_{U(k)} J \quad (7)$$

For this system there are two possible switching states for each phase leg, -1 and 1, which amounts to 2^N possible switching sequences, illustrated in Fig. 3. For the three-phase setup this becomes 2^{3N} different sequences. As the horizon is enlarged the computational complexity grows exponentially. The most apparent approach is to do an exhaustive search where each of the end nodes in Fig. 3 is investigated to identify the solution with the lowest cost. This approach is only computationally feasible for short horizons.

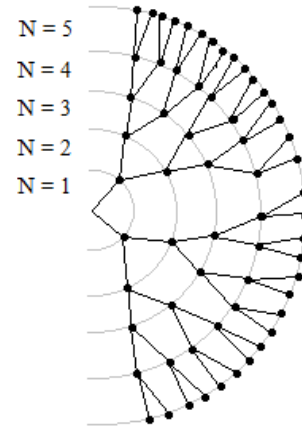


Figure 3: Exponential growth of possible switching sequences of one phase leg as the horizon N increases.

The problem of finding the optimum sequence to minimise the cost equation in (6) as in (7) is reformulated into an integer least-squares problem in vector form (8) [3-4].

$$U_{opt}(k) = \arg \min_{U(k)} \|HU(k) - \bar{U}_{unc}(k)\|_2^2 \quad (8)$$

Where:

$$Q = Y^T Y + \lambda_u S^T S$$

$$H^T H = Q$$

$$\bar{U}_{unc}(k) = HU_{unc}(k)$$

Q is a symmetric and positive-definite matrix for $\lambda_u > 0$ and further details on the derivation of Q can be obtained in [4]. H is a lower-triangular matrix derived by taking

the Cholesky decomposition of Q^{-1} . U_{unc} is the unconstrained optimum which is the optimum solution obtained by eliminating the integer constraints of the switch state u [3-4].

A comparison is illustrated in Fig. 4 of the optimization problem in (7) versus (8) for the three-phase case with a horizon of length $N=1$. Each possible switching sequence can be plot as a point onto a coordinate system. The number of dimensions is dependent on the number of switches in the system and the horizon length of predictions. In this scenario each axis represents the switch state in one of three phases and in this case the switching state is constrained to values -1 and 1. The cube of dashed lines represents the solution space before it is transformed. The points at its vertices indicated by diamonds represent all the possible constrained solutions U . The lone diamond point represents the unconstrained solution U_{unc} . After applying the H matrix as in (8) to transform the problem the solution space becomes skewed and scaled. This can be seen when looking at the cube of solid lines which gives an indication of the transformed solution space. The dots at its vertices represent all the transformed constrained solutions $\bar{U} = HU$, and U_{unc} becomes \bar{U}_{unc} .

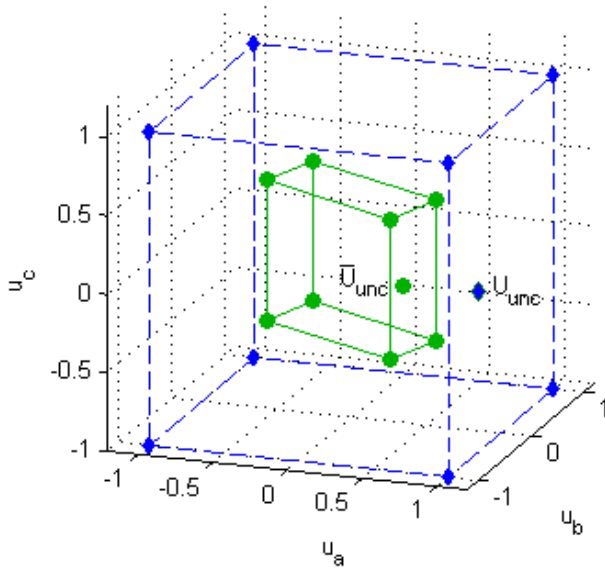


Figure 4: Visualization of the optimization problem in an orthogonal coordinate system (dashed line) and how the transformed problem (solid line) compares for a three-phase system with a horizon of $N=1$.

To obtain the optimal solution with (7) one must apply each of the possible constrained solutions in the orthogonal coordinate system (dashed lines in Fig.4) to the cost function to determine which gives the minimum cost. With (8) the euclidean distances from the unconstrained solution to each constrained solution point is calculated to determine the closest point. Both of these approaches deliver the same solution which will always

be the optimal sequence. They also both follow an exhaustive search which computationally intensive. The method of sphere decoding offers a more optimal approach and is discussed in the next section.

2.4 Sphere decoding

The aim of using the sphere decoding approach is to optimise the search for the optimal solution by eliminating as many sub-optimal solutions from the search as possible. A sphere is used to determine which solutions are closer to the optimal one. The sphere is centred around \bar{U}_{unc} , the transformed unconstrained optimum. The initial radius of the sphere should be chosen in such a way that it is small enough to eliminate as many candidate switching sequences as possible. It should also be large enough to avoid having an empty solution due to all solutions falling outside of the sphere. The search is based on a branch-and-bound approach and only explores branches of which the distance between that solution and \bar{U}_{unc} is smaller than the sphere's radius ρ as described in (10). When a solution is discovered within the sphere, the radius is tightened and the exploration process continues until there is only one solution point left within the shrunken sphere. The closest point is then declared the constrained optimum U_{opt} . A key role player in sphere decoding is the lower-triangular matrix H in (9) which allows (10) to be rewritten as (11). This makes solving each step a one-dimensional problem [3-4].

$$H = \begin{bmatrix} H_{11} & 0 & 0 \\ H_{21} & H_{22} & 0 \\ H_{31} & H_{32} & H_{33} \end{bmatrix} \quad (9)$$

$$\rho(k) \geq \|\bar{U}_{unc}(k) - HU\|_2 \quad (10)$$

$$\rho^2(k) \geq (\bar{U}_{unc1} - H_{11}U_1)^2 + (\bar{U}_{unc2} - H_{21}U_1 - H_{22}U_2)^2 + \dots \quad (11)$$

$$\rho_{ini}(k) = \|\bar{U}_{unc}(k) - HU_{ini}(k)\|_2 \quad (12)$$

The initial radius is determined by (12) where an initial estimate $U_{ini}(k)$ of what the optimal could be or is close to is inserted into the equation. The initial solution estimate is made by component-wise rounding of the unconstrained solution towards the finite control set values. Therefore each unconstrained switch value within U_{unc} is rounded to either -1 or 1, depending on which is closer. This is known as the Babai estimate [3-4].

In Fig. 5 the problem is viewed from above in the ab -plane. In the orthogonal coordinate system (dashed line) the unconstrained solution is equally close to the solution points $[1 \ -1 \ -1]$ and $[1 \ 1 \ -1]$. It may seem that

both these points would provide an optimal solution but this is not the case. In the transformed coordinate system (solid line) the unconstrained solution ends up being closer to the transform of $[1 \ 1 \ -1]$ as can be seen by the sphere excluding the transform of $[1 \ -1 \ -1]$. Therefore $[1 \ 1 \ -1]$ is the optimal solution sequence [3-4].

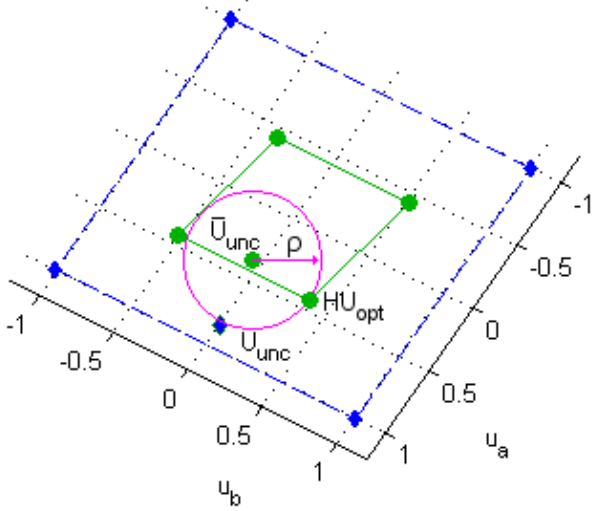


Figure 5: Top view of Fig. 4 showing the ab -plane to gain perspective on the sphere and the points which lay closest to its centre.

3. RESULTS

The mathematical model presented in Chapter 2 is implemented in a MATLAB-based simulation. Table 1 provides the parameter values specified for the LCL-filter. The dc-link voltage V_D is kept constant at 120 V. The three-phase grid-side current reference has an amplitude of 30 A and a frequency of 50 Hz. A horizon length of $N = 4$ and a sampling interval of $T_s = 10 \mu s$ is implemented. The weighting factor is set to $\lambda = 1 \times 10^{-8}$ and the resulting switching frequency is approximately 7 kHz.

Tab. 1: Parameters of the LCL-filter used in the simulation

Parameter	Value
L_1	2.33 mH
L_2	45 μ H
R_1, R_2, R_c	0.55 Ω
C	15 μ F

Fig. 6 shows the steady-state three-phase output current to be injected into the grid. Fig. 7 gives an up-close view of the a -phase current from Fig. 6. It can be seen that the actual current ripples over the smooth reference current due to the trade-off between switching frequency and current error to minimise the cost. Setting the weighting factor λ higher would result in less frequent switching and larger ripple. It was also observed that an increase in V_D increases the ripple size. A slight tracking error is

noticed between the average actual current and the reference current. This could be due to the inability of MPC to consider the past in making or adjusting its decision, as it is a predictive strategy that only focusses on the current values of the state variables and their predicted future behaviour. The tracking error is also reflected by the grid-side current spectrum in Fig. 8. The amplitude of the 50 Hz impulse is 29.42 dB, which is 0.12 dB below the 30 A reference. The current-tracking error of the fundamental component is therefore 1.35%. Higher up in the spectrum prominent sharp peaks occur at integer multiples of the switching frequency $f_s = 7$ kHz.

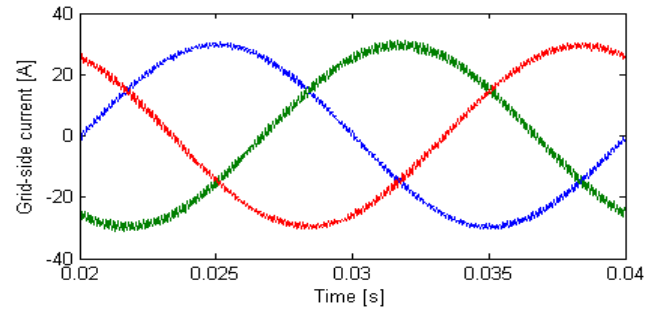


Figure 6: The three-phase steady-state grid-side currents i_{2a}, i_{2b}, i_{2c} .

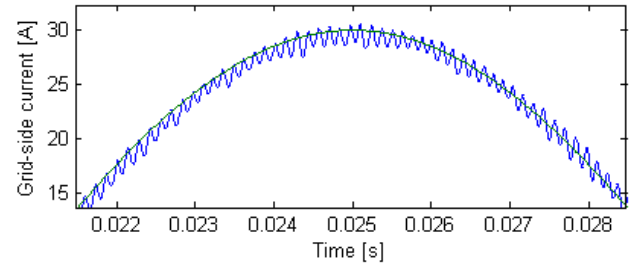


Figure 7: The a -phase grid-side current i_{2a} and its reference up-close.

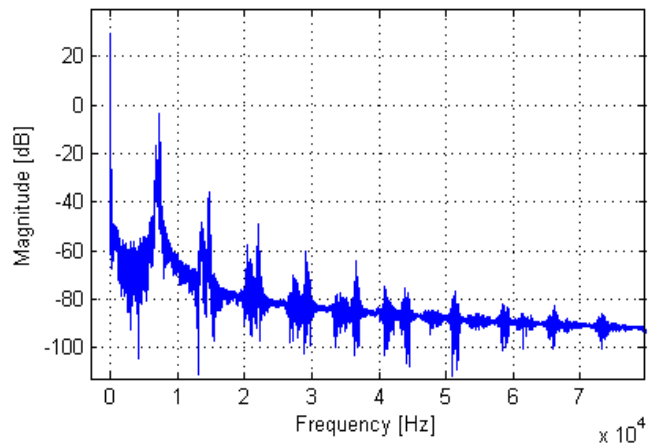


Figure 8: Spectrum of the a -phase grid-side current i_{2a} .

The response of the system to a step in the reference current is shown in Fig. 9. The time it takes to accurately track the new current reference is about as long as two switching instances.

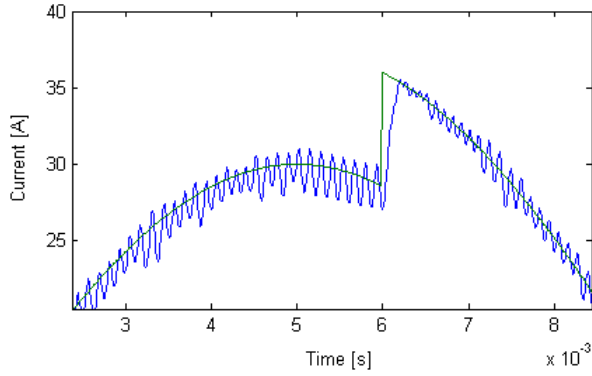


Figure 9: Reaction to a step in the sinusoidal current reference.

4. CONCLUSION

This paper presented a strategy to control the output current of a three-phase grid-tied inverter. The approach uses MPC with long horizons and incorporates sphere decoding to decrease the computational burden. The two control objectives are to minimise the current-tracking error and switching frequency. The mathematical model was presented and implemented in a MATLAB-based simulation with a horizon of $N = 4$. The outcome was satisfactory as the grid-side current was controlled successfully with a switching frequency of approximately 7 kHz and a current-tracking error of 1.35%.

5. APPENDIX

The matrices F , G_1 , G_2 and C from the state-space equations (3) and (4) follows:

$$F = \begin{bmatrix} \frac{R_c + R_1}{-L_1} & 0 & \frac{R_c}{L_1} & 0 & -\frac{1}{L_1} & 0 \\ 0 & \frac{R_c + R_1}{-L_1} & 0 & \frac{R_c}{L_1} & 0 & -\frac{1}{L_1} \\ \frac{R_c}{L_2} & 0 & \frac{R_c + R_2}{-L_2} & 0 & \frac{1}{L_2} & 0 \\ 0 & \frac{R_c}{L_2} & 0 & \frac{R_c + R_2}{-L_2} & 0 & \frac{1}{L_2} \\ \frac{1}{C} & 0 & -\frac{1}{C} & 0 & 0 & 0 \\ 0 & \frac{1}{C} & 0 & -\frac{1}{C} & 0 & 0 \end{bmatrix}$$

$$G_1 = \begin{bmatrix} \frac{V_D}{2L_1} & 0 & 0 & 0 & 0 & 0 \\ 0 & \frac{V_D}{2L_1} & 0 & 0 & 0 & 0 \end{bmatrix}^T \times K$$

$$G_2 = \begin{bmatrix} 0 & 0 & \frac{1}{L_2} & 0 & 0 & 0 \\ 0 & 0 & 0 & \frac{1}{L_2} & 0 & 0 \end{bmatrix}^T \times K$$

$$C = \begin{bmatrix} 0 & 0 & 1 & 0 & 0 & 0 \\ 0 & 0 & 0 & 1 & 0 & 0 \end{bmatrix}$$

6. REFERENCES

- [1] J. Scoltock, T. Geyer and U.K. Madawala: "Model Predictive Direct Current Control for a grid-connected converter: LCL-filter versus L-filter", *Industrial Technology (ICIT), 2013 IEEE International Conference*, pp. 576-581, February 2013.
- [2] J. Scoltock, T. Geyer and U.K. Madawala: "Model predictive direct power control for a grid-connected converter with an LCL-filter", *Industrial Technology (ICIT), 2013 IEEE International Conference*, pp. 588-593, February 2013.
- [3] P. Karamanakos, T. Geyer and R. Kennel: "Reformulation of the long-horizon direct model predictive control problem to reduce the computational effort", *Energy Conversion Congress and Exposition (ECCE), 2014 IEEE*, pp. 3512-3519 September 2014.
- [4] T. Geyer and D.E. Quevedo: "Multistep Finite Control Set Model Predictive Control for Power Electronics", *Power Electronics, IEEE Transactions on*, Vol.29 No. 12, pp. 6836-6846, December 2015.
- [5] A. Reznik, M.G. Simoes, A. Al-Durra and S.M. Mueen: "LCL Filter Design and Performance Analysis for Grid-Interconnected Systems", *Industry Applications, IEEE Transactions*, Vol.50 No. 2, pp.1225-1232, March-April 2014.
- [6] J. Scoltock, T. Geyer and U.K. Madawala: "A Model Predictive Direct Current Control Strategy With Predictive References for MV Grid-Connected Converters With LCL-Filters", *Power Electronics, IEEE Transactions*, Vol.30 No. 10, pp. 5926-5937, October 2015.
- [7] H. Miranda, R. Teodorescu, P. Rodriguez and L. Helle: "Model predictive current control for high-power grid-connected converters with output LCL filter", *Industrial Electronics, 2009. IECON '09. 35th Annual Conference of IEEE*, pp. 633-638, November 2009.

DESIGN AND DEVELOPMENT OF A LABORATORY MODEL OF DISTRUBUTION STATIC SYNCHRONOUS COMPENSATOR

T.E. Mabotja* and S.P. Chowdhury**

*Electrical Engineering Department, Tshwane University of Technology, Pretoria West Campus, Pretoria 0001, elton.mabotja@gmail.com

**Electrical Engineering Department, Tshwane University of Technology, Pretoria West Campus, Pretoria 0001, spchowdhury2010@gmail.com

Abstract: In recent years, the custom power technology, the low voltage counterpart of the more widely known flexible ac transmission system (FACTS) technology, aimed at high voltage power transmission applications, has emerged as a credible solution to solve many of the problems relating to continuity of supply at the end-user level. FACTS devices are proving to be very effective in using the full distribution capacity while increasing power system stability, efficiency and maintaining power quality and reliability of Power systems. As an important member of FACTS devices family, STATCOM has been at the centre of attention and the subject of active research for many years. In this project a D-STATCOM laboratory model is designed and developed for experimentation of reactive power compensation. Much literature on STATCOMs and other FACTS devices have been widely studied by analytical models and simulations done, but the physical functionality is unfamiliar for a lot of power researches. An understanding of the physical functionality and a design and development of a real single-phase D-STATCOM laboratory prototype is presented in this project. This is done to clearly demonstrate the D-STATCOM capabilities in reactive power compensation and voltage stability under sensitive load conditions. This prototype will be hugely useful by technical colleges, universities to build a low-cost laboratory set-up for students to undergo experiments and verify the power electronic theories behind reactive power compensation. This will encourage electrical engineering/technology students to build their own compensators to enhance their power electronics knowledge through experimental prototypes.

Keywords: Flexible AC Control Systems, Static Var Compensators, STATCOM, D-STATCOM and Pulse Width Modulation.

1. INTRODUCTION

The problem addressed in this project was to improve the power system's reactive power handling capability and prevent voltage instabilities with the use of Flexible AC transmission System (FACTS) device called a static synchronous compensator (STATCOM). In recent years, the increase in load demand and power transfers between utilities has elevated concerns about system voltage security [1]. Voltage sags and voltage collapses are the most prominent power quality problems faced by many industries and utilities. Research shows that it contributes to more than 80% of power quality problems that exist in power systems [2]. One of the major causes of voltage instability is the reactive power variations in a power system. A D-STATCOM is a controlled reactive power source. It is connected in shunt to the alternating current (AC) supply system by means of magnetic coupling. A D-STATCOM provides the desired reactive-power compensation by means of power electronic processing of voltage and current waveforms in a voltage-source converter (VSC) [3].

The engineering challenge in the project was to implement a small scale prototype emulation of a D-STATCOM to show its operation within a lab environment. This is due to the fact that STATCOM systems are normally used in high voltage transmission systems. Thus the challenge was to

achieve power compensation using a simple conversion circuit switching at low kHz frequencies.

2. LITERATURE REVIEW

Reactive power compensation is defined as the management of reactive power to improve the performance of utility power systems [4]. Holistically the problem of reactive power compensation in AC systems is related to load and voltage support. In load support the aim is to maintain a high system power factor so as to balance the real power drawn from the AC supply, to enhance voltage regulation, and to eliminate current harmonic components produced by large and fluctuating nonlinear industrial loads. Voltage support is generally required to reduce voltage fluctuation at a given terminal of a power system [4]. The major problem associated with power systems is voltage instability or collapse. A system is said to enter a state of voltage instability when a disturbance causes a progressive and uncontrollable decline in voltage such as voltage sags and voltage swells, which can occur because of the inability of the network to meet the increased demand for reactive power [5].

Figure 1 below show typical power quality problems with their typical percentage contribution.

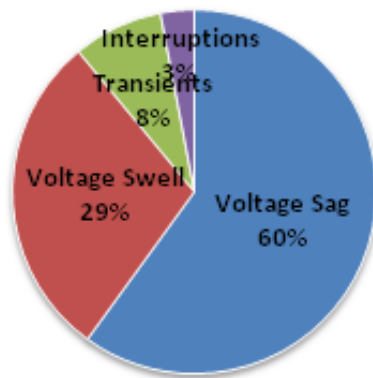


Figure 1: Power Quality problems (R. Madhusudan 2012) [6]

Voltage sags are considered as the most severe disturbances to the industrial equipment, and voltage swells can cause overheating, tripping or even destruction of industrial equipment. Studies show that a higher percentage of all disturbances in the electrical power distribution systems are voltage sags, transients, and momentary interruptions [7].

There are two main shunt connected flexible AC control systems (FACTS) devices which are used for reactive power compensation, static var compensators (SVCs) and Static synchronous compensators (STATCOM). SVC based systems use Thyristor Switched Capacitors (TSC) or Thyristor Controlled Reactors (TCR) as in figure 2 with fixed filters employing capacitive/inductive reactive power and harmonic filtering. SVC systems cause harmonic current problems while they solve reactive power problems. This requires constant shunt filters or special transformer connections for these systems.

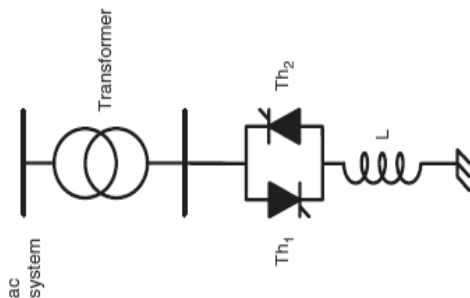


Figure 2: SVC layout (Mehta B.K 2012)[8]

The second is STATCOM as shown in figure 3 which is defined by IEEE as a self commutated switching power converter supplied from an appropriate electric energy source and operated to produce a set of adjustable multiphase voltage, which may be coupled to an AC power system for the purpose of exchanging independently controllable real and reactive power [2].

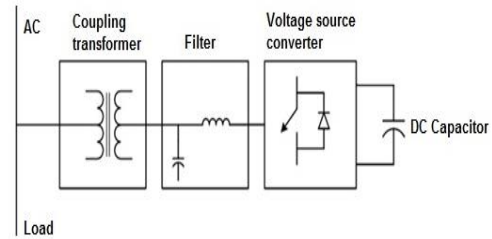


Figure 3: Basic STATCOM layout(Cetin 2007) [9]

Based on the researched study STATCOM shunt compensator has a greater advantage over SVCs. The STATCOM has a special characteristic that it does not depend on the AC system voltage and yet compensates for any deviation in power system voltage. It has emerged as a promising device to provide not only for voltage sag mitigation but a host of other power quality solutions such as voltage stabilization, flicker suppression, power factor correction and harmonic control.

STATCOM is defined by IEEE as a self-commutated switching power converter supplied from an appropriate electric energy source and operated to produce a set of adjustable multi-phase voltages, which may be coupled to an AC power system for the purpose of exchanging independently controllable real and reactive power. The STATCOM has the following three operating structural components [10].

- Static: based on solid state switching devices with no rotating components.
- Synchronous: analogous to an ideal synchronous machine with 3 sinusoidal phase voltages at fundamental frequency.
- Compensator: provided with reactive compensation [10].

To address reactive power compensation problems a shunt connected low cost single phase D-STATCOM system was designed. The STATCOM essentially consists of a single phase power electronics inverter (DC to AC converter), DC capacitor as DC input voltage for the IGBT inverters, low pass filtering circuit to filter out high frequency components of inverter output voltage and a coupling transformer that links the inverter output to the ac supply side. Figure 2 indicates a simple schematic of the designed system for reactive power compensation.

3. APPROACH

In designing D-STATCOM system a number of inverter topologies and control methods were considered. The core components in designing the inverter circuit are the power electronic switches. The inverter's magnitude and frequency of the output voltage must be controlled by a switching scheme.

Constant DC link voltage method was used as a control strategy. The input voltage to the inverter was kept constant and variation in the output voltage achieved by changing the duty cycle of the gating signal. The modulation technique of the gating signals was implemented using PWM switching scheme. SPWM or sinusoidal pulse width modulation is widely used in power electronics to digitize the power so that a sequence of voltage pulses can be generated by the on and off of the power switches. The pulse width modulation inverter has been the main choice in power electronic for decades, because of its circuit simplicity and rugged control scheme.

A. PWM controller

The pulse-width modulation (PWM) is the control method widely used in converters, and rough schematic of this is shown in Figure 4. In the diagram, the triangular signal (V_{tri}) is compared with horizontal straight line ($V_{control}$) [11].

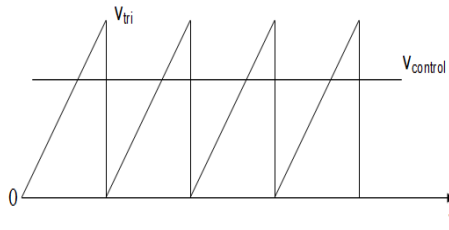


Figure 4: Simplified schematic of PWM control (Mohan 2003) [11]

The principle of operation is that for constant switching frequency, the switch control signal which controls the switching state (on or off), is generated by comparison a signal level control voltage $V_{control}$ with a repetitive triangular waveform with magnitude V_{tri} . When $V_{control}$ is above V_{tri} the switch turns on, and vice-versa. Hence, the frequency of repetitive triangular/sawtooth waveform with voltage magnitude V_{tri} establishes the switching frequency at which the switch will be operating. The switch duty ratio is then calculated in equation 1 as.

$$Duty_ratio = \frac{\tau_{on}}{\tau_s} \quad (1)$$

The amplitude and frequency modulation are calculated in equations 2 and 3 as.

$$m_a = \frac{V_{ctrl}}{V_{tri}} \quad (2)$$

$$m_f = \frac{f_{tri}}{f_{ctrl}} \quad (3)$$

The SG3524 pulse-width modulator chip controls the switching frequency in the inverter circuitry. The chip outputs two 180° out of phase square wave signals at a

maximum duty cycle of 45%. The dead gap between the waveforms is necessary to prevent the supply from shorting during IGBT turn-off periods. The switching frequency of PWM is dependent on the timing capacitance and the timing resistance. The frequency is related to R_T and C_T by the relationship in equation 4.

$$f_s = \frac{1.3}{R_T C_T} \quad (4)$$

B. Gate driver circuitry

In a full bridge converter topology, IGBT transistors will be configured as high-side and low-side switches, whereby two switches are on at a time. Thus to achieve these a gating circuit was designed as a driver to the switches. IR2101 IC circuit as shown in below was implemented as a gating circuit to the power electronic switches. Input to the driver circuit is from the SG3524 PWM controller low and high side pulse outputs. The IR2101 gate driver circuit translate the logic inputs from the PWM controller into low impedance outputs capable of driving the semiconductor devices.

The gate driver circuitry supplies gating pulses to the gate of the power electronic switches and also provides isolation between them. There are several approaches to perform gate drive isolation. The bootstrap circuit is used as a popular method in providing isolation in low power gate drivers. The circuit consists of a capacitor and a diode.

Another important parameter used in calculating the gate drive requirements is the gate capacitance charge. The gate capacitance has direct implications on the switching behaviour of the IGBT like the switching time, switching losses and short circuit capability. The gate charge is also used to calculate the charge current required to gate the IGBT, with the equation being.

$$I_g = \frac{C_g}{\tau_r} \quad (5)$$

From equation 5 the gate resistance is calculated in equation 6 as.

$$R_g = \frac{V_g}{I_g} \quad (6)$$

C. Inverter

The inverter is the core component in the D-STATCOM system and responsible for the actual reactive compensation and voltage stabilisation. A complete inverter systems as depicted on the block diagram in figure 5 comprises of the inverter topology, dc input side controlled (gating) unit and a filtered ac output side.

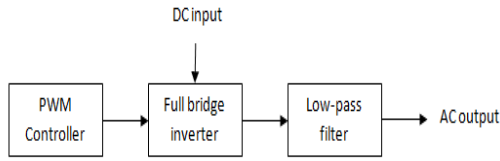


Figure 5: Inverter block diagram

There are multiple methods used in the construction of power inverters, but they all share a common idea of converting a DC input voltage to AC output as in figure 6.

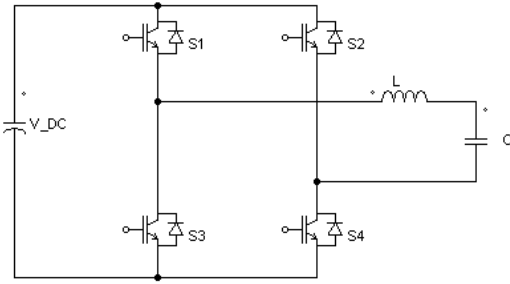


Figure 6: DC to AC converter (inverter)

The DC to AC inverter full bridge topology was implemented using IRGB15B60KD IGBT semiconductor switches. The switches were connected in an H bridge configuration and switched on using PWM control pulses from the gate driver circuit. S1-S4 and S2-S4 conducted alternatively to generate the positive and negative half cycles of the PWM AC output converted from the DC input. Only N-channel IGBT switches were used as they result in lower on resistance and thus reduced power losses.

The reliability and performance of the D-STATCOM system depends on the passive components of which the DC capacitor on the input terminal of the inverter is one of. In sizing the capacitance factors like the dc voltage ripple, transient voltage overshoot, harmonic distortions and current play a role and are taken into consideration. The capacitor is sized to handle the worst case scenario which is when the D-STATCOM system operates in capacitive mode [2]. The capacitor is sized using equation 7.

$$C_{DC} = \frac{V_s \Delta_L T}{V_{DC_{max}}^2 - V_{DC}^2} \quad (7)$$

Where V_s is the peak phase voltage, I_L is the rated inverter current, T the inverter period, and V_{DC} the DC voltage.

In order to eliminate high frequency harmonic components a 2nd order low-pass filter was designed and implemented on the inverter output. The filter allows only frequency components below the designed cut off frequency and rejects frequencies components above it. The designed 2nd order low-pass filter is designed with the formula.

$$f_c = \frac{1}{2\pi\sqrt{L_f C_f}} \quad (8)$$

To meet the requirements of filter bandwidth and system stability f_c is determined in the middle band.

$$2f_n \leq f_c \leq f_s/2 \quad (9)$$

Where f_n is the 50 Hz fundamental frequency and f_s is the switching frequency.

4. RESULTS

The designed and implemented D-STATCOM system is as shown in figure 7 below with the subsystems and integrated simulated and experimental results outlined.

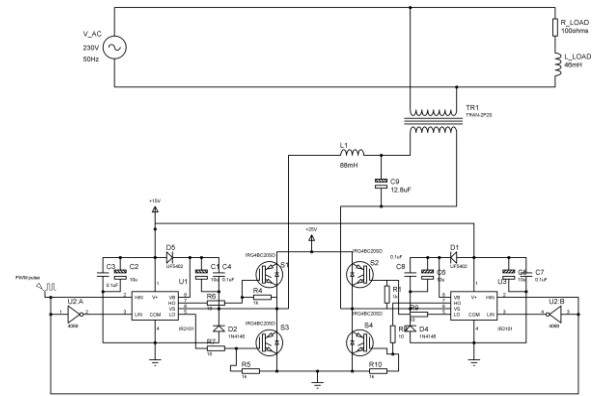


Figure 7: STATCOM system connected to AC mains and reactive load

The implemented PWM controller circuit is as shown in figure 8 below with the measured high side and low side pulse outputs complementary of each other with a voltage magnitude of 15.2 V and a duty ratio of 35%.

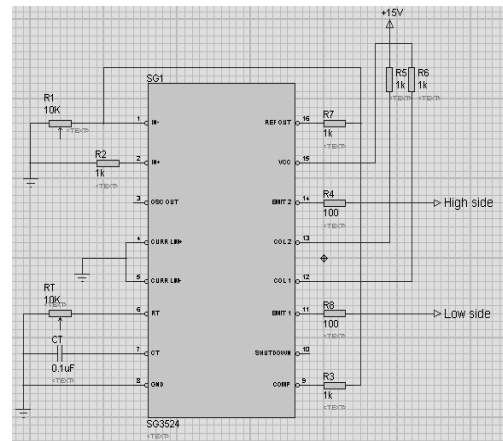


Figure8: SG3524 PWM controller

The PWM controller outputs were then integrated with the gate driver circuit and complementary low impedance gating signals generated. Figure 9 indicates the simulated and measured complementary waveforms of the IR2101 gate drive circuit.

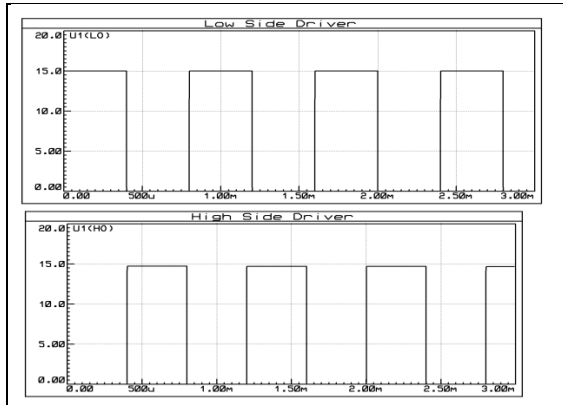


Figure 9: IR2101 gate driver waveforms (simulated)

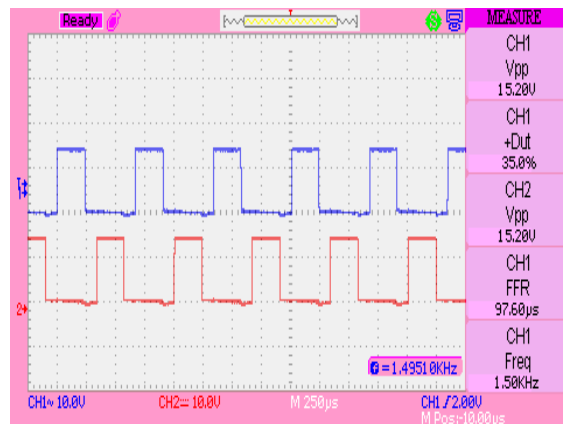


Figure 10: IR2101 gate driver waveforms (measured)

A dead time of 97.6 μ s as shown in figure 10 is more than enough not only as blanking period between the High and low pulse but to also allow for turn-on and turn-off switching transitions of the IGBT switches.

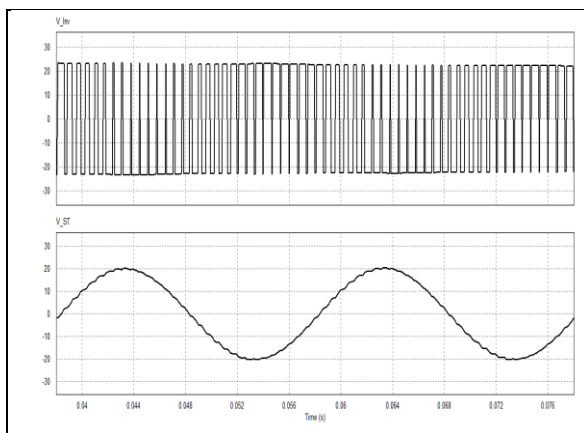


Figure 11: Inverter output voltage(simulated)

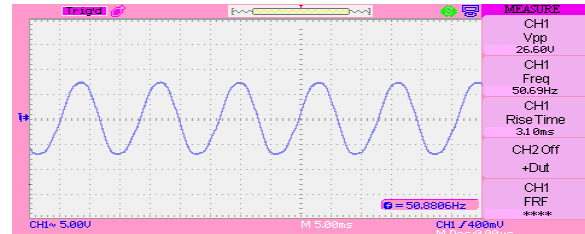
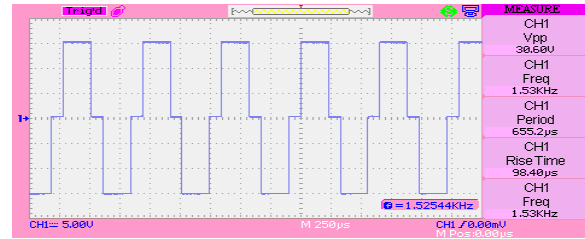


Figure 12: Inverter output voltage (measured)

The output of the inverter as shown in figure 11 is a quasi-square waveform with voltage magnitude of 30.6 V_{pk-pk} for an input voltage of 16 V. The measured dead time between any switching transitions (on-off-on) is 97.6 μ s. Figure 51 above shows the measured output of the filtered inverter output before step-up amplification. The waveform is sinusoidal with magnitude of 26.6 V peak to peak at a frequency of 50.69 Hz (1.38% deviation).

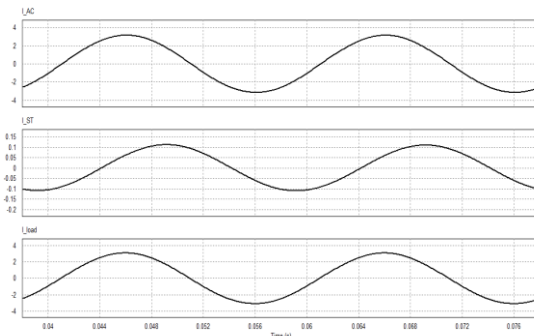


Figure 13: Supply Current, D-STATCOM output current, Load Current

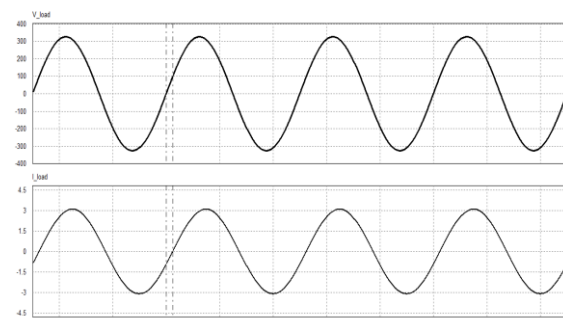


Figure 14: Load voltage and current

Figure 13 shows the line, load and STATCOM currents. The STATCOM current (I_{ST}) lags the load current by approximately 90°. This shows that the STATCOM is purely reactive while the line current is active (with small reactive components). Figure 14 shows the load voltage and

and current, with the current lagging the voltage (inductive load).

5. CONCLUSION

The basic principle of operation of a STATCOM system was studied to understand how it compensates for reactive power and mitigate voltage deviations. A small scale emulation of the system based on voltage source converters has been designed, and implemented. Simulations of subsystems and the entire STATCOM system are done to validate design and show operation of the system.

The designed PWM generator, gate driver, inverter and filtering circuits have worked properly. While the full laboratory experimental results of reactive power compensation are not fully documented, its principle of operation is shown as depicted in simulations results. A fully operational D-STATCOM, Demand Side Management and Power quality management are not only the responsibilities of the supplier but equally that of the end-user.

6. REFERENCE

- [1] M. Sarvi, H. Marefatjou, "Performance of SVC and UPFC in Static Voltage Stability Margin Enhancement in two Area Power System with Continuation Power Flow Method" *International Electrical Engineering Journal (IEEJ)*, Vol. (2012) No. 3, pp. 803 – 809
- [2] H. Masid, N. Moriun, S. Mahmud, A. Mohamed And S. Yusuf "Design of a prototype D-Statcom for voltage sag mitigation", in *Proc. 2004 National Power and Energy Conf.*, Malaysia, Nov. 2004, pp. 61-66.
- [3] M.R. Mathur and R.K. Varma, "Thyristor-Based FACTS Controllers for Electrical Transmission Systems (IEEE Press Series on Power Engineering)", *Wiley-IEEE Press*, 2002
- [4] E. Larsen and T. Weaver "FACTS Overview", *IEEE PES Working Group Report and CIGRE International Conference on Large High Voltage Electric Systems*, April 1995
- [5] J.W. Dixon and L. A. Morán, "Reactive power compensation technologies", *McGraw-Hill Education*, 2008
- [6] R. Madhusudan, and G.R Rao, "Modeling and Simulation of a Distribution STATCOM (D-STATCOM) for Power Quality Problems Voltage Sag and Swell Based on Sinusoidal Pulse Width Modulation (SPWM)", *IEEE-International Conference On Advances In Engineering, Science And Management (ICAESM -2012)*, March 30, 31, 2012
- [7] H. Sunita, N. Palukuru and P. Subrata, 'Global voltage stability analysis of a power system using network equivalencing technique in the presence of TCSC' *Leonardo Electronic Journal of Practices and technologies*, issue 16, January-June 2010
- [8] B.K. Mehta and P.J. Patel, 'Static voltage stability improvement in power systems using Statcom FACTS controller', *Journal of information, knowledge and research in Electrical Engineering*, vol 02, issue 02, November 2012
- [9] A Cetin, 'Design and implementation of a voltage source converter based STATCOM for reactive power compensation and harmonic filtering', April 2007
- [10] T. Masood, R.K. Aggarwal, A.Q Suhail, R.A. J. Khan, "STATCOM Model against SVC Control Model Performance Analyses Technique by Matlab" *ICREQP*, 10 Granada Spain, March 23, 2010
- [11] N. Mohan, T. Undeland and W. Robbins, "Power Electronics, Converter, Applications and design". *Wiley*. 2003.

MAXIMUM POWER POINT TRACKING CONTROLLER FOR A WIND ENERGY CONVERSION SYSTEM

C.P. Brand* and A.J. Grobler**

* School for Electric, Electronic & Computer Engineering, Hoffman Street 11, North-West University, Potchefstroom 2531, South Africa E-mail: ChristiaanBrand12@gmail.com

** School for Electric, Electronic & Computer Engineering, Hoffman Street 11, North-West University, Potchefstroom 2531, South Africa E-mail: Andre.Grobler@nwu.ac.za

Abstract: The energy crisis in South Africa is taking a turn for the worst as power utilities struggle to keep up with the demands of users. The use of alternative energy sources as a more permanent and stable alternative has become a more appealing option for most people. Wind energy conversion systems (WECS) are candidate technology for utilizing wind energy in South Africa. The system, designed in 2011, utilizes two induction machines (IMs) to form a grid connected induction generator system. The project was launched to build on this system by improving the power delivery capabilities by means of a maximum power point tracker (MPPT). The system was reconstructed and sensors for the induction generator voltage and current were designed. A perturb and observe algorithm was used to implement frequency control in the induction generator.

Keywords: wind energy conversion system, induction machine, maximum power point tracking, perturb and observe algorithm.

1. INTRODUCTION

The use of induction machines as generators that can be applied to a wind turbine system has become a popular method for utilizing wind energy to generate power. Although some systems that utilize IMs as generators for wind generation have been developed and proven to function quite well, they are often expensive and most people will not be able to afford such a system. This led to the need for a low cost wind generator system.

The most popular option for induction generators for wind generation is a self-excited induction generator (SEIG) system, which can be used in remote locations to generate power without being connected to a power distribution grid in order to work [3]. This is achieved by using a capacitor bank to supply the reactive power needed by the induction generator. This is shown in Figure 1.

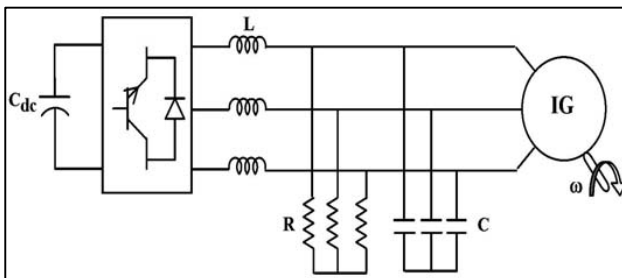


Figure 1: SEIG System [2]

The existing system makes use of a grid connected induction generator system, which means the system is dependent on a connection to the power grid to supply the reactive power the induction generator needs to function

[4]. The existing system has been set up as displayed in Figure 2.

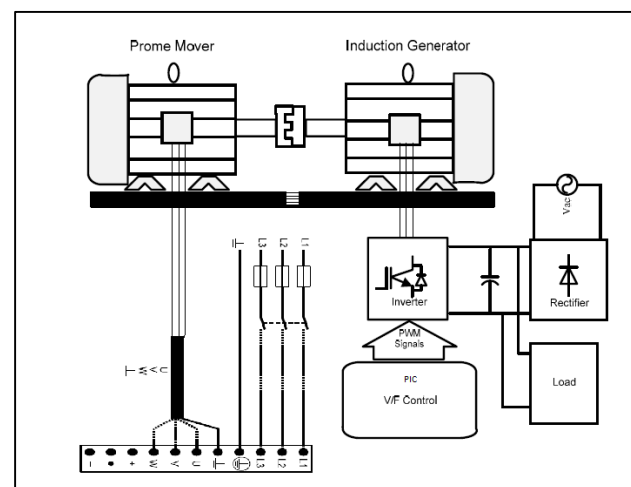


Figure 2: Existing System [4]

1.1 Main objective

The goal of this article is to implement a system that can utilize a normal IM to act as generator in a wind energy conversion system (WECS) as well as the development and implementation of a maximum power algorithm to extract the maximum available power from an induction generator system in a range of rotational speeds.

2. CONCEPTUAL DESIGN

The main system components of the system architecture is shown in Figure 3. These are the main power sources supplying the equipment with power, the two IMs mechanically connected, one operating as the prime mover the other as the generator, the PWM inverter supplying the generator with the voltage required by the stator, the load that will dissipate the power generated as well as the AC-DC rectifier.

The focus of this article is mainly the controller that will manage the PWM inverter as well as manage the calculations required by the MPP algorithm.

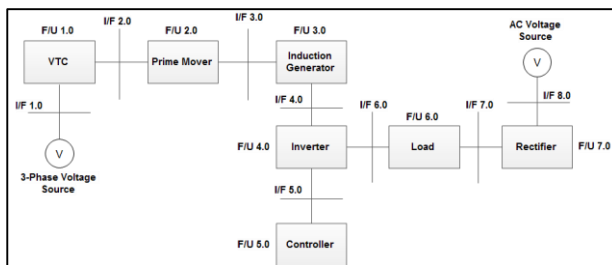


Figure 3: System Architecture

The trade-offs contain the possible solutions to each of the sub systems that need to be constructed as identified in the system architecture as shown in Figure 3.

2.1 MPPT algorithm trade-off

Three possible algorithms that could be used for maximum power point tracking have been identified. These were wind speed measurement (WSM), perturb & observe (P&O) and power signal feedback (PSF)[6].

The decision matrix used in the trade off study consists of a number of identified parameters weighed against each other based on importance. The identified parameters for the MPPT algorithm is:

- Ease of implementation (EOI): how easy the algorithm will be to implement in code.
- External component need (ECN): the amount of external equipment/sensors needed.
- Memory requirements (Memory): the amount of memory needed in a microcontroller.
- Convergence speed (Speed): time algorithm takes to determine maximum power and stabilize on that point.

A weight value (W) is then assigned to each of the identified criteria with the total value adding up to 1. Based on the selected option for an algorithm and the criteria to be evaluated for that option, a performance rating (R) between 0 and 10 is then given for each criteria. The resulting value of $R \times W$ is summed together for all criteria and a final rating for the selected option is achieved. The highest scoring algorithm is selected as the best suited for the application.

Table 1: MPPT Algorithm Trade-Off

Algorithm	WSM			P&O		PSF	
	W	R	WxR	R	WxR	R	WxR
EOI	0.15	4	0.6	8	1.2	5	0.75
ECN	0.3	2	0.6	9	2.7	4	1.2
Memory	0.15	5	0.75	9	1.35	4	0.6
Speed	0.4	8	3.2	7	2.8	8	3.2
	1.0	Total:	5.15	Total:	8.05	Total:	5.75

A perturb & observe algorithm was determined to be the best option. It is simple to implement and would require minimal external components.

2.2 Voltage sensor trade-off

Various devices were investigated in order to determine what could be used for the measurement of generator voltages. The options were narrowed down to the Eaton EVT4-420-24L, the MCR-VAC-UI-0-DC and the LEM LV25-600. The parameters used to evaluate the options were:

- Supply Voltage (SV): the dc voltage needed to drive the sensor, 5 V-15 V is ideal.
- Range: voltage range that can be measured.
- Accuracy: percentage of accurate measurement.
- Integration: how easy the device will integrate with other components.

Table 2: Voltage sensor trade-off

Voltage Sensor	EVT4-420-24L			MCR-VAC-UI-0-DC		LV25-600	
	W	R	WxR	R	WxR	R	WxR
SV	0.3	5	1.5	6	1.8	10	3.0
Range	0.2	6	1.2	7	1.4	7	1.4
Accuracy	0.3	8	2.4	6	1.8	8	2.4
Integration	0.2	7	1.4	7	1.4	8	1.6
	1.0	Total:	6.5	Total:	6.4	Total:	8.4

The LV25-600 voltage sensor was determined to be the best option. The device is produced by LEM and is shipped already fitted to a PCB with suitable connections. This will speed up the integration process.

2.3 Current sensor trade-off

Various devices were investigated in order to determine what could be used for the measurement of generator currents. The options were narrowed down to Allegro ACS770xCB and the LEM LTS 25-NP. The parameters used to evaluate the options were:

- Supply Voltage (SV): the dc voltage needed to drive the sensor, 5 V-15 V is ideal.
- Range: the current range that can be measured.
- Accuracy: percentage of accurate measurement.
- Integration: how easy the device will integrate with other components.

Table 3: Current sensor trade-off

Current Sensor		ACS770xCB		LTS 25-NP	
	W	R	WxR	R	WxR
SV	0.3	10	3.0	10	3.0
Range	0.2	7	1.4	8	1.6
Accuracy	0.3	8	2.4	9	2.7
Integration	0.2	8	1.6	8	1.6
	1.0	Total:	8.4	Total:	8.9

The LTS 25-NP current sensor was determined to be the most suitable option. The device is also produced by LEM but unlike the voltage sensor, it is not shipped on a PCB. The sensor can be integrated on the microcontroller PCB or a separate PCB can be designed. The implementation is discussed in Section 3.2

2.4 Microcontroller trade-off

Various microcontrollers were identified as possible solutions. The options were narrowed down to the STM32F303RE Nucleo board from ST Microelectronics and the dsPIC30F series manufactured by Microchip. The parameters used to evaluate the options were:

- Implementation: Ease at which the microcontroller can be implemented into the system.
- ADC channels (ADC/C): Sufficient channels in the ADC.
- ADC sampling speed (ADC/S): Sampling speed of the ADC channels.
- PWM channels (PWM): Ease of PWM motor control signal generation.

Table 4: Microcontroller trade-off

Microcontroller		STM32F303RE		dsPIC30F	
	W	R	WxR	R	WxR
Implementation	0.3	8	2.4	6	1.8
ADC/C	0.2	10	2	10	2
ADC/S	0.2	10	2	4	0.8
PWM	0.3	8	2.4	8	2.4
	1.0	Total:	8.8	Total:	7

The STM32F303RE Nucleo development board was determined to be the best option. The Nucleo board will ease the integration into the system.

3. DETAIL DESIGN

The outlining ideas for the project is generated by the conceptual design. These ideas are then further explored to create a more detailed solution to the specified problem. Each sub system is now explained in detail and component choices are justified.

3.1 Voltage sensor

The LEM LV25-600 voltage sensor will be used to detect generator voltages, convert these values to a suitable level in order for the microcontroller to receive the values and, together with the current values, calculate the generated power.

Figure 4 shows the circuit diagram, as received from the manufacturer, for the LV25-600 voltage sensor module as well as the needed configuration for the correct conversion ratio. The ± 15 V will be supplied by the voltage sources mounted within the final enclosure. The output will be connected to the microcontroller via a voltage divider in order to lower the output voltage from 5 V to 3.3 V which is the maximum voltage limit allowed as input to the ADC.

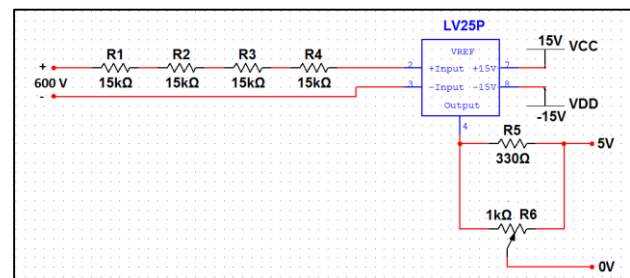


Figure 4: Voltage Sensor Circuit Diagram

Figure 5 shows a photo of the voltage sensor module mounted on the PCB with the needed peripherals and connectors. Each connector has been clearly labelled according to the circuit design.

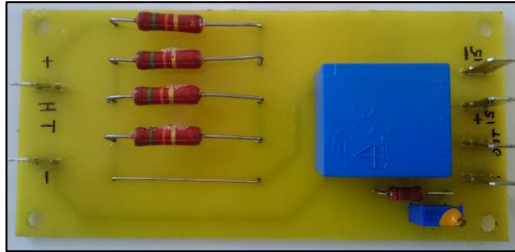


Figure 5: Voltage Sensor PCB

3.2 Current sensor

The LEM LTS 25-NP current sensor will be used to detect generator currents, convert these values to a suitable level in order for the microcontroller to receive the values and, together with the voltage values, calculate the generated power.

According to the sensor's datasheet, three current configurations are possible by connecting the 6 primary pins in different connections, shown in Figure 6.

Number of primary turns	Primary nominal current rms I_{PN} [A]	Recommended connections
1	± 25	
2	± 12	
3	± 8	

Figure 6: Recommended Connections

Figure 7 shows the three modes selectable with the double pole double throw (DPDT) switches. Mode 1 refers to the $\pm 25A$ nominal current rating, mode 2 refers to the $\pm 12A$ rating and mode 3 refers to the $\pm 8A$ rating.

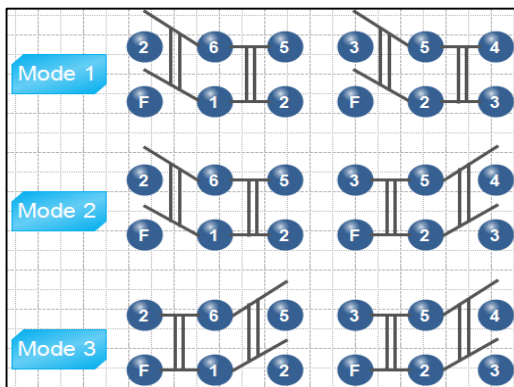


Figure 7: Three selectable modes

Figure 8 shows the PCB design. Externally mounted peripherals will ease the integration of the PCB with components such as the microcontroller and power sources. The power will be delivered by a voltage regulator that converts the 15 Vdc from the main supplies to the 5 Vdc required by the sensor.

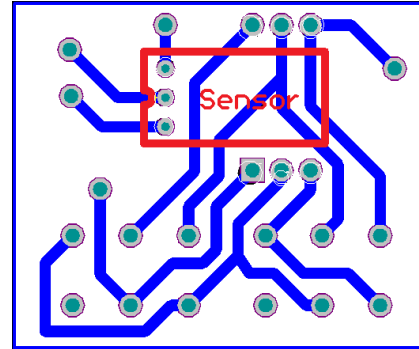


Figure 8: Current Sensor PCB Design

3.3 Microcontroller

The ST Microelectronics STM32F303RE Nucleo microcontroller will be used to generate the sinusoidal pulse width modulated (SPWM) signals required to drive the system. The SPWM signals are generated by means of a lookup table and three indexes controlling the phase placement of the three channels.

Figure 9 shows the method of generating PWM output using a sinusoidal control voltage. This method is implemented in the lookup table and saved within the microcontroller.

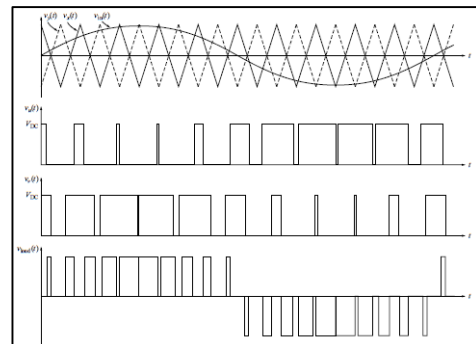


Figure 9: PWM output with sinusoidal control voltage [10]

The IGBT's in the PWM inverter are driven by a SEMIKRON™ SKHI61 driver. The driver requires SPWM signals to be at a voltage level of 5 V-15 V. As the microcontroller can only output the SPWM signals at a maximum voltage of 3.3 V a step up circuit is needed.

Figure 10 shows the design for the interfacing circuitry. By using a transistor pair to increase the output voltage to 15 V as well as a totem pole output stage, shown by Q1 and Q2, to lower the output impedance, the SPWM signals can be fed directly to the SKHI61 driver.

Although the SKHI61 driver provides protection by means of optocouplers, extra optocouplers have been included to protect the microcontroller outputs.

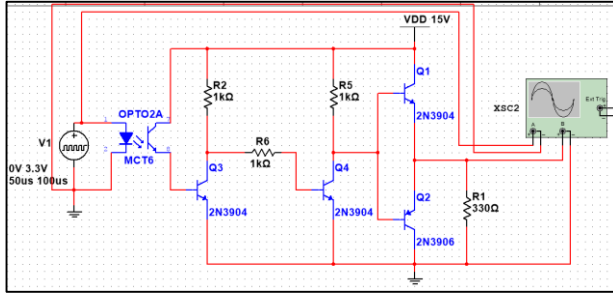


Figure 10: Voltage step up circuit

4. IMPLEMENTATION

4.1 Voltage sensor implementation

The microcontroller will sample the output voltage from the voltage sensor by means of an on-board ADC input. This will be a voltage value between 0 V – 5 V and should be reduced to a value between 0 V – 3.3 V. This was however found to be unnecessary due to the fact that during the system operation, voltages will not exceed 100 Vdc. By factoring in the conversion ratio calculated by (1) it can be seen that the voltage sensor output (2) will not exceed the 3.3 V level allowed by the microcontroller ADC.

$$r_{conv} = \frac{V_p}{V_s} \quad (1)$$

Where:

V_p = Maximum sensor voltage

V_s = Maximum allowed ADC voltage

r_{conv} = Conversion ratio

$$\begin{aligned} r_{conv} &= \frac{600V}{5V} \\ r_{conv} &= 120 \\ V_{max} &= \frac{V_{op}}{r_{conv}} \end{aligned} \quad (2)$$

Where:

V_{max} = Sensor output voltage

V_{op} = System operational voltage

r_{conv} = Conversion ratio

$$V_{max} = \frac{100Vdc}{120}$$

$$V_{max} = 0.833V$$

The conversion ratio will allow for a maximum voltage of 396 Vdc to be applied to the sensor before the maximum allowed voltage range of the ADC is reached as calculated by (3):

$$V_{s\ max} = V_{max} \times r_{conv} \quad (3)$$

Where:

$V_{s\ max}$ = Maximum sensor voltage

V_{max} = Maximum allowed ADC voltage

r_{conv} = Conversion ratio

$$V_{s\ max} = 3.3V \times 120$$

$$V_{s\ max} = 396Vdc$$

4.2 Current sensor implementation

As with the voltage sensor the microcontroller will also sample the output voltage from the current sensor by means of an on-board ADC input. The information provided is used to calculate the conversion ratio that needs to be implemented in the microcontroller.

Using the 12 ampere mode the output will be a value between 2.5 V – 3.1 V for positive flowing current and a value between 1.9 V – 2.5 V for negative flowing current. If no current is measured a constant voltage of 2.5 V will be measured at the output of the sensor. Using (4) the conversion ratio is calculated:

$$r_{conv} = \frac{\Delta V}{I_{max}} \quad (4)$$

Where:

ΔV = Voltage variation

I_{max} = Mode maximum current

r_{conv} = Conversion ratio

$$r_{conv} = \frac{600mV}{12A}$$

$$r_{conv} = 50mV / A$$

4.3 SPWM and interfacing circuitry implementation

The software design for the STM32F303RE Nucleo consisted of setting up the appropriate registers to drive the microcontroller's main clock at 72 MHz. The registers for timer 1 were set up to generate PWM on 6 different channels at a frequency of 10 kHz. The sinusoidal change in duty cycle was achieved by values in a lookup table. The output signals were individually verified in order to ensure the PWM inverter would function correctly.

The registers for the two analogue to digital converters were set up in order to sample two channels, one for the voltage and the other for the current. The rest of the MPPT algorithm was then implemented into the code. Testing of the algorithm was performed by supplying voltages and currents to the sensors and observing the variations in frequency.

Figure 11 shows the output SPWM signals as generated by the microcontroller. These represent the top signals for the three different channels. The difference in duty cycles between the three signals that can be seen represents the needed phase shift between the signals. The fourth signal found just beneath the third signal represents the complimentary bottom signal of channel 1. The duty cycle will vary according to the top signal for channel 1 but will always be phase shifted 180°.

The voltage level of the SPWM signals have been stepped up by the interfacing circuitry. Figure 11 shows that the interfacing circuitry can step up the voltage to 15 V which is accepted by the SEMIKRON™ SKHI 61 driver, but the final product only stepped up the SPWM signals to 5 V in order to power the entire board which includes the protection IC's with a single 5 V source. The SEMIKRON™ SKHI 61 driver also accepts 5 V input levels.



Figure 11: SPWM Output

The SPWM signal are then outputted to the PWM inverter through a ribbon cable. The different signals are connected to the cables by following the connection

diagram of the SEMIKRON™ SKHI 61 driver found in the datasheet.

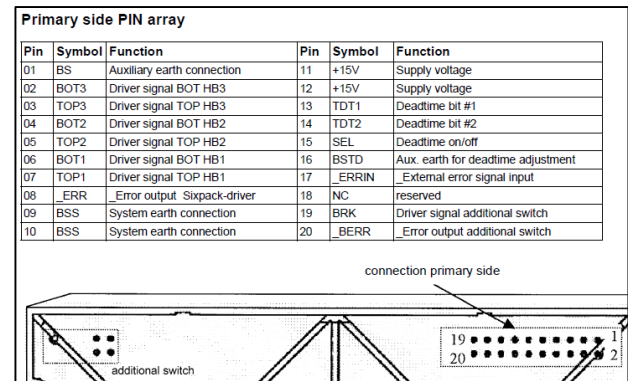


Figure 12: SKHI 61 Connection Diagram

5. TEST RESULTS

Two main test were conducted on the system. The first test was a constant frequency test in which the controller frequency was held constant at 46 Hz while the prime mover speed was set to a constant 1500 r/min (50 Hz).

The second test was a variable frequency test. The controller frequency was varied while the prime mover speed was held constant at 1500 r/min (50 Hz).

5.1 Constant frequency test

This test was conducted in order to measure the output from the system and ultimately determine whether the system does in fact generate power. The voltage and current measurements of both the ac source as well as the generator are taken.

By comparing the active power from the ac source with that of the generator it can clearly be seen from Table 5 that the power generated by the system exceeds that which is being supplied, proving that the system does indeed generate power.

Table 5: 46 Hz power calculations

Controller frequency (Hz)	Variac				Generator			
	S (VA)	Q (VAR)	P (W)	Phase angle (°)	S (VA)	Q (VAR)	P (W)	Phase angle (°)
46	304,39	57,04	299	10,8°	1068,06	214,98	1046,2	11,612°

5.2 Variable frequency test

This test was conducted in order to measure the generated power of the system in a range of controller frequencies. The calculated power should display the maximum power point for the system at a constant prime mover speed of 1500 r/min.

Table 6 shows the power calculations of the system with changes in frequency ranging from 48 Hz down to 40 Hz. Comparing the active power it can be seen that the maximum power point of the system at a constant prime

mover speed of 1500 r/min is at a controller frequency of 41 Hz.

Table 6: Variable frequency power calculations

Controller frequency (Hz)	Variac				Generator			
	S (VA)	Q (VAR)	P (W)	Phase angle (°)	S (VA)	Q (VAR)	P (W)	Phase angle (°)
48	308,7	7,76	308,6	1,44°	1065,99	285,95	1026,92	15,56°
47	299,91	12,25	299,66	2,34°	1113,32	371,82	1049,4	19,51°
46	304,39	57,04	299	10,8°	1068,06	214,98	1046,2	11,612°
45	340,62	6,42	340,56	1,08°	1109,23	277,92	1073,85	14,51°
44	305,27	9,59	305,12	1,8°	1137,73	296,19	1098,5	15,09°
43	363,06	11,4	362,88	1,8°	1173,03	400,82	1102,43	19,98°
42	340,87	18,2	340,38	3,06°	1160,92	392,1	1092,7	19,74°
41	399,08	17,55	398,69	2,52°	1232,65	544,99	1105,63	26,24°
40	372,5	21,05	371,9	3,24°	1186,2	489,84	1080,34	24,39°

Figure 13 shows the variation in generator power vs variations in controller frequency. From the graph the maximum power point at 41 Hz is clearly visible.

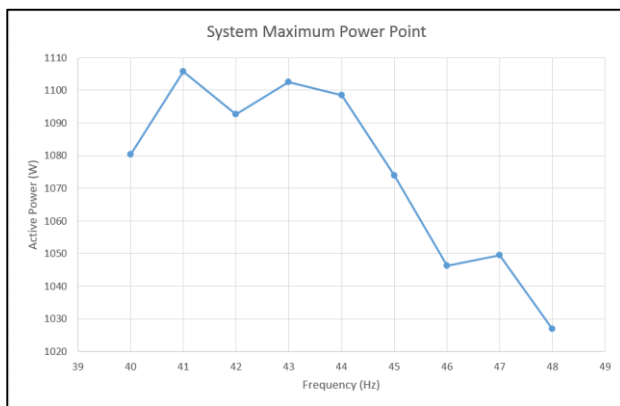


Figure 13: Maximum power point graph

6. CONCLUSION

The controller was implemented into the system and tests were done to ensure correct functionality. The generator and ac source voltages and currents were measured and the calculations were performed to determine the power generated. The results from the generator showed that 1046.2 W of active power was being generated while only 299 W of active power was being supplied by the ac source. This concluded that the system is capable of generating power.

The final product addressed all the objectives of the project. The controller was portable and easy to use. The system was tested and the maximum power point of the system was calculated at 41 Hz for a prime mover speed of 1500 r/min. The algorithm was unable to effectively track the maximum power point as the voltage and currents that were being measured weren't capable of providing sufficient information to calculate the power. The omission of the phase angle resulted in the power calculations of the controller not reflecting the true variations in power as introduced by the variations in speed from the system.

7. REFERENCES

- [1] Bhag S. Guru, Hüseyin R. Hiziroglu. Electric Machinery and Transformers. Oxford University Press, 2001.
- [2] J. Dheeraj, S. K. Singh, S. M. Kumar, "Voltage control of self-exciting induction generator using genetic algorithm", Dept. of Elect. Eng., National Institute of Technology, Haryana, India, 2009.
- [3] L. Louze, A. L. Nemmour, A. Khezzar, M. Hacil, H. Bouzekri, "Nonlinear control algorithm for a self-excited induction generator for wind power applications", Mentouri University, Constantine, Algeria, 27 Dec 2011.
- [4] A. J. Coetzee, "Drive for a low power induction machine", North-West University, South Africa, 2011.
- [5] D. García, J. Luis, "Modelling and control of SCIG with full power converter applied to windmills", University of Oulu, 30 Nov 2009.
- [6] S. M. Barakati, M. Kazerani, J. D. Aplevich, "A mechanical speed-sensorless maximum power tracking control for a wind turbine system including a matrix converter", IEEE, 2008.
- [7] F. J. Lin, P. K. Huang, C. C. Wang, L. T. Teng, "An induction generator system using fuzzy modelling and recurrent fuzzy neural network", IEEE transactions on power electronics, vol.22, no.1, Jan 2007.
- [8] S. M. Barakati, M. Kazerani, J. D. Aplevich, "Maximum power tracking control for a wind turbine system including a matrix converter", IEEE transactions on energy conversion, vol. 24, no. 3, Sep. 2009.
- [9] A. Ghaffari, M. Krstić, S. Seshagiri, "Power optimization and control in wind energy conversion systems using extremum seeking", IEEE transactions on control systems technology, vol. 22, no. 5, Sep. 2014.
- [10] PWM Techniques: A. Pure Sine Wave Inverter. Worcester Polytechnic Institute Major Qualifying Project. Advisor: Professor Stephen J. Bitar, ECE. 2010-2011.
- [11] M. Abdel-Salam, A. Ahmed, M. Abdel-Sater, "Maximum power point tracking for variable speed grid connected small wind turbine", IEEE International energy conference, 2010.
- [12] A. M. Bhandare, P. J. Bandekar, S. S. Mane, "Wind energy maximum power extraction algorithms: A review", IEEE, 2013.
- [13] R. Raedani, M. Hanif, "Design, testing and comparison of P&O, IC and VSSIR MPPT techniques", 3rd International conference on renewable energy research and applications, Milwaukee, USA, 19-22 Oct 2014..

Design and Implementation of a Power Line Carrier Communication System using Home Plug greenPHY for Demand Side Management (DSM)

A. Ogunleye, P.J Randewijk , R. Wolhuter

Department of Electrical and Electronic Engineering, Stellenbosch University, Private Bag X1,
MATIELAND, 7602,
South Africa

18832563@sun.ac.za, pjrandew@sun.ac.za, wolhuter@sun.ac.za

Abstract- Smart home and smart grid applications at the moment is a must for developing countries especially in Africa. Researchers, Technologist and Engineers should be at the fore front, championing the deployment of devices from the lab into our society. The 21th century power line will not only carry energy from point to point but also useful data. This paper explores how to build a power line communication system for a smart home using, a free web based APIs, libraries and tools (Tornado websocket, CSS3, JQuery, JavaScript, HTML5 and SVG) for the dashboard, a computing platform (Beaglebone Black), a power line module called the greenPHY produced by i2se group and an Energy measuring IC, CS5490 with 3V relays for switching purposes.

Keywords- Internet Of Things, Beaglebone Black, Tornado, JQuery, Home Plug GreenPHY, Relay and Power Measuring Unit, GPIO, GNU, API, DSM.

1. INTRODUCTION

Although, power line communication technologies have existed since 1950[1], the advancement in electronics, power distribution, modulation and signal processing has made it to be feasible to harness the usefulness of the Home Plug GreenPHY technology. Power Line Communication Carrier (PLC) is a trending technology that brings broadband communication and power into our various homes. Instead of having a dedicated communication medium for appliances consuming power from the AC mains, the same cables that supply power could also be used to communicate and control the appliance[2]. In June 2005 the international

regulatory body IEEE recognized the potential of power line communication and formulated the IEEE P1901 standard protocol[3]. The rate of data transmission for most modern smart grid power line communication is 4-10Mbps which is more than enough to send data from point to point [3][4]. The ability of a power line module to participate in unicast, multicast and broadcast makes different configurations such as; master-to-slave and slave to slave communication possible. A master power line module broadcasts commands to connected slaves on a network while slaves listen to the broadcast data and act on them as the case maybe. The usefulness of internet in our modern civilized nations can never be over emphasized. It is gradually changing the way we live our daily lives from internet banking to web-based home automation. PLC technology is used in smart home nowadays due to its bi-directional communication which is addressed on by this project. One of the greatest advantages of greenPHY is that it is interoperable with each other due to alliance and industrial standards agreed upon by designers. Energy efficiency, lower cost of deployment and scalability are some of the attractive characteristics of using Home Plug GreenPHY.

2. MOTIVATION

The aim of this paper is to demonstrate how to design a low cost home/office or industrial power line communication system using HPGP, GNU API for a dashboard and on the shelf components for RPMU. Power line module such as Home Plug GreenPHY in a

master-slave configuration coupled with an energy measuring IC e.g. the CS5490 and a web-based dashboard for real time control is a very appealing option. In the nearest future, power companies like ESKOM can send SMS to power consumers to switch off devices for more power at peak period (DSM) which is achievable with this system in place.

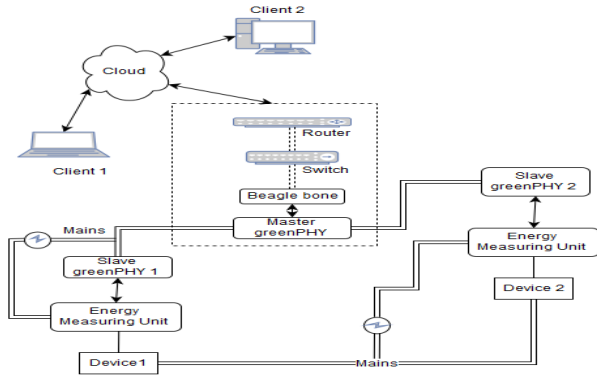


Fig 1: Diagram of the whole system.

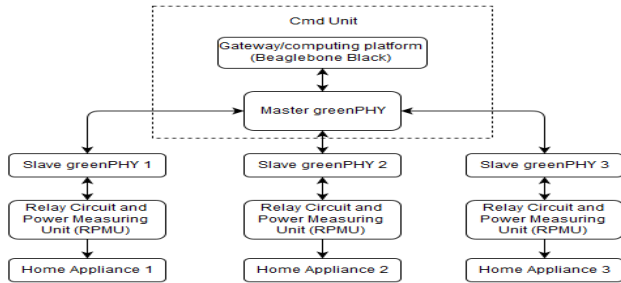


Fig 2: Block diagram of the power line smart home system.

3. THE DESIGN

There are many methods of achieving this type of smart home communication. Some have used Zigbee and different wireless technologies [5][6][7] or even the heterogeneous mixture of both wired and wireless technology in the same vicinity (home). In this design, the computing device (Beaglebone Black), greenPHYs, switch, router and a modem are combined together to form the command unit. The master greenPHY could have been excluded but the Beaglebone black cannot directly connect to the power lines to communicate with the slave greenPHY. The Relay and Power Measuring Unit (RPMU) is a PCB designed to communicate serially with the slave greenPHY, sending power, voltage and current from the connected home appliance on request. The data transmission diagram between the different subunits is shown in Fig 2. High-Level Data Link Control (HDLC) asynchronous serial protocol is also developed

to frame data transmission with fields containing a start flag, the destination address, command, data, Cyclic Redundancy Check (CRC) and End of Data. These sub units will be further discussed below in full details.

4. WEB INTERFACE

Since the internet is ubiquitous nowadays, users could monitor in real time how energy is consumed by their devices/appliances and can remotely control them from anywhere in the world. Getting data into the cloud has been made easy by making use of GNU web API and free web applications. For this project, Tornado websocket and some client side programming (CSS3, JavaScript, JQuery and HTML5) was used. A few line of code were written in Python to connect, configure and send the data from the Beaglebone black into the cloud. Tornado websocket manages the whole operation on the server side by generating JSON containing the data from the slave greenPHYs sending it to the client side for display. The client side of the web interface uses Scalable Vector Graphics (SVG) which is scalable; supported by 90% of existing browsers and it is appealing and intuitive to work with. The gauges were based on Raphael's library and justGage library which are MIT licensed and open source [8]. Clicking the "ON" and "OFF" button on the client side sends parameters to the websocket which in turn generates a command data packet (analogous to the industrially popular HDLC protocol) that is routed to the appropriate quarters from the command unit.

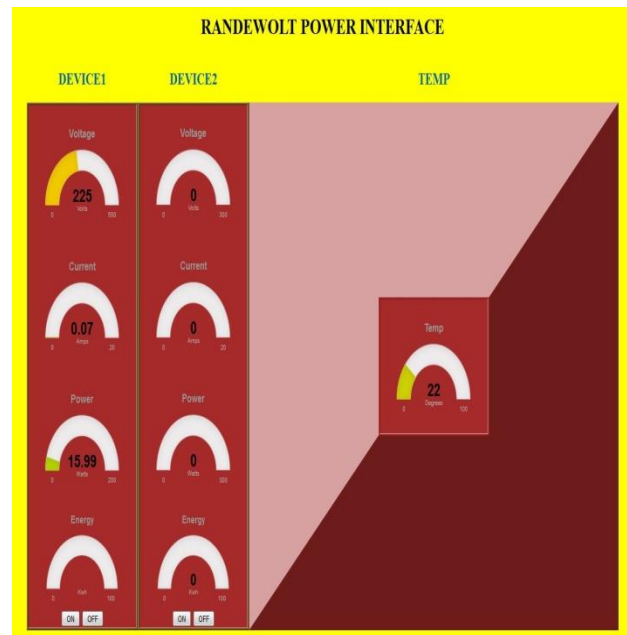


Fig 3: Web-Interface

5. THE COMPUTING PLATFORM

The computing platform is where data collation, handling and processing takes place. Any microcontroller would have done the job perfectly (Arduino, Atmel or Raspberry-pi) but we settled for a Beaglebone Black (BBB). Beaglebone black is based on ARM cortex-A8 processor that can run Ubuntu, Debian, Angstrom Linux or Android. It is a 32-bit microcontroller that has an on-board Ethernet port to connect it to the internet easily and 64 pin headers for UART, SPI and I2C serial protocols and other I/O functions. It runs at 1 GHz, has a 512 MB of RAM and internal storage of 4GB [9]. Although, any high level language could be used to write the program running on the Beaglebone, Python was chosen because of its fewer lines of code, simplicity and elegance. The UART serial interface was used because it is easy to implement compared to SPI. Adafruit library was used to implement the UART protocol. The Beaglebone Black computing platform generates the data that controls the slave greenPHY by the click of buttons on the dashboard which are mapped to specified strings of command data on the Beaglebone black. The data string is converted into hexadecimal strings which will finally forming a HDLC string. It performs its own CRC and appends it to the HDLC frame it created.

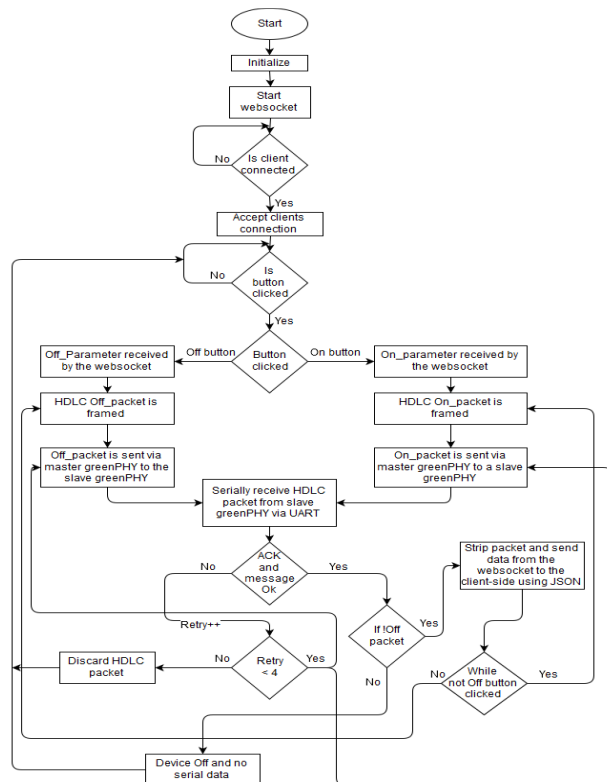


Fig 4: Flow diagram of the program running on Beaglebone black.

6. HDLC SERIAL COMMUNICATION PROTOCOL

HDLC is a data link layer communication protocol developed by International Organization for Standardization (ISO) for point to multipoint communication[10]. HDLC protocol was used in this design because of its simplicity compared to other protocols and was modified a little bit to suit the project. Normal Response Mode (NMR), a form of HDLC protocol which is also known as master-slave mode was implemented. It was written for the Beaglebone Black in Python and for the slave greenPHY in C. Initiation of the communication is preceded with starting flag of 1 byte which was represented with character “~” or “7E” in hexadecimal, followed by the address of the slave greenPHY also in hexadecimal, the function to be performed, the data, Frame Check Sequence (FCS) and the ending of the frame with carriage return and line feed “CRLF”. Cyclic Redundancy Check (CRC) was preferred to Longitudinal Redundancy Check (LRC) for the design because CRC is much more robust compare to LRC in error checking [11][12]. The HDLC frames are created on the Beaglebone Black and serially sent via UART to the master greenPHY destined for a slave greenPHY. The slave greenPHY validates the received frame by comparing its calculated CRC to the received frame CRC, and responds with its own constructed HDLC frame containing the data requested by the BBB command module.

The modified version of the HDLC used included a very important part of a protocol known as Modbus by including the “CARRIAGE RETURN” and “LINE FEED” to terminate every frame generated. The two functions performed by the slave greenPHY is switching of a relay and buffering of data from the RPMU. The size of pay-load of a HDLC frame is 100bytes for the project.

```

typedef struct HDLC{

unsigned char startFlag;

unsigned char slaveAddr;

unsigned char control;

unsigned char data[numbOfData];

unsigned char crc;

unsigned char *CRLF;

};
  
```

Starting Flag	Address	Control	Information	FCS(CRC)	Ending Flag
8 bits	8 bits	8 bits	N*8 bits	16 bits	8 bits

Fig 5: HDLC frame.

7. HOME PLUG GREENPHY (HPGP)

Management Message Entry (MME) is a greenPHY vendor specific protocol that allows it to communicate over the power lines and it is compliant with the HomePlug Powerline Alliance packet data frame. The I2SE greenPHY Stamp1 used for this project contains QCA7000 (Power line chip) and the MK20DX256VMC7 microcontroller that controls all the other operations of the PLC module. The QCA7000 is a special chip made by Qualcomm that sniffs out MME packets from the power lines, decodes it and sends it to the MK20DX256VMC7 microcontroller through SPI protocol[13]. The MME buffer carries along the Original source address, Original destination address, MME Version, I2se OUI, MME Subversion and Fragmentation Management Information[14]. The QCA7000 comes with its own program unlike the MK20DX256VMC7 that requires you to flash the chip with your own written firmware[13]. The time taken to send and receive MME between greenPHYs is 3seconds, this design we sped up by reducing the timer on the MK20DX256VMC7 to 0.5s to and fro. That has really improved the response time of the whole system because data is quickly sent, received and interpreted at the required end. The HDLC data frames use MME vendor based protocol as a vehicle on the power lines.

8. MASTER GREENPHY

In this design, the master greenPHY acts like a relay center (that is the interface between Ethernet and power line communication). Most of the work is done by the computing platform and the slave greenPHY. If a greenPHY is hooked to a power line, it starts searching for other greenPHYs on the network. AV Logical Network (AVLN) is only set up if there is another device on the power line and has the same Network Membership Key (NMK) [14]. NMK is a string of characters that is contained in greenPHYs to participate in an AV logical network if authenticated between greenPHYs. The major work of the master greenPHY in the design is to handle UART HDLC frames from the Beaglebone Black, store it into a buffer and copy it into the MME buffer to be sent to the slave greenPHY. It also collects data from the

slave greenPHYs, stores it into a buffer and sends it to Beaglebone Black through its UART.

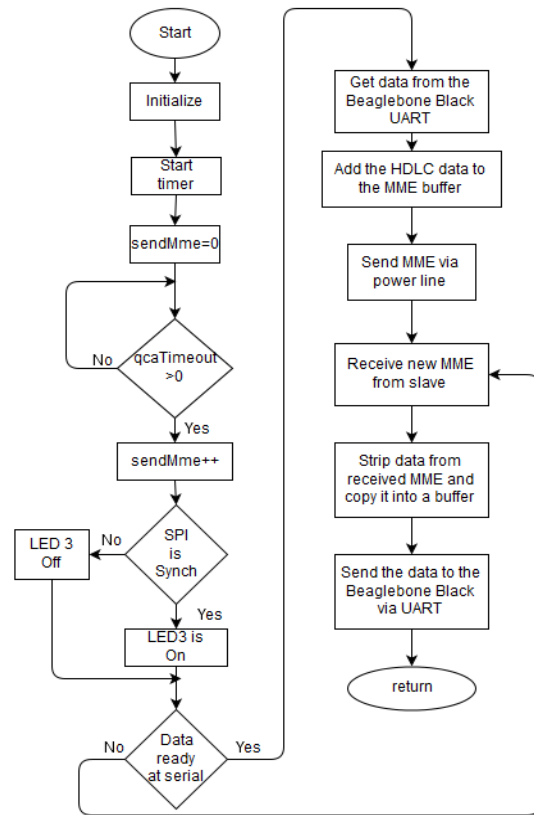


Fig 6: Flow diagram of the program running in the master greenPHY.

9. SLAVE GREENPHY

The slave greenPHY is responsible for receiving the voltage, current and power consumed by appliances from the RPMU in the smart grid system via its UART from the CS5490. It also receives data sent by the command unit via the power line MME protocol and acts on it. The collected data from the CS5490 chip on the RPMU is stored in a buffer and HDLC data packet is created and sent to the command unit. The firmware running on both the master and the slave greenPHY are almost similar. Validation of data takes place in the slave greenPHY by calculating the CRC of data received and comparing it with the CRC in the received HDLC data frame to check the data corruption that might have taken place during transmission. For both the master and the slave greenPHY, the buffers have to be cleared regularly after use to allow in new data and avoid compromising of data due to data overflow. A unique part of the flow chart of the slave greenPHY is the parser that takes parameters to control the GPIO.

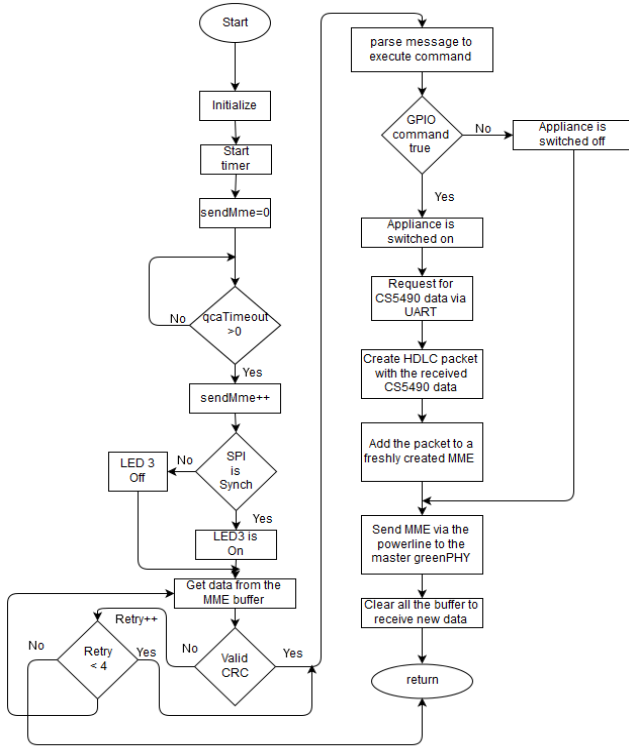


Fig 7: Flow diagram of the program running in the slave greenPHY.

10. RELAY, POWER AND MEASURING UNIT (RPMU)

For the design, a PCB was made using the CS5490 energy measuring chip, relays to switch on and off devices and optocouplers to isolate the mains AC voltage from interfering with delicate part of the circuit. The CS5490 has a 24-bit analog to digital converter with energy measurement accuracy of 0.1% a 3.3V 16-pin SOIC [15]. CS5490 was chosen for this project due to the fact that it has a UART serial interface which is a little bit easier to configure compared to SPI and I2C. The UART baud rate of the CS5490 chip by default is 600Baud. There are different ways of setting up the CS5490 e.g for current measurement (shunt, Rogowski coil, and current transformer), but the shunt method was settled upon for visible cash implementation. The CS5490 chip is calibrated and compensated as stated in [15] for accurate performance of the chip. The calibration and compensation code is saved in the slave greenPHY to be relayed to the CS5490 chip serially during start up of the whole system. A compact power source (TRACO POWER) was used to supply 3.3V from the 230V AC mains. The switching of the appliances was done by the use of 3V relays and FET as switches.



Fig 8: Relay and Power Measuring circuit.

11. TESTING AND MEASUREMENT

Using the timing in Python, the round time trip of the packet sent from the websocket to the slave greenPHY via the master greenPHY was measured and recorded for analysis. A time is set when a packet is immediately created and sent representing the start time and another time is set when a packet is received which represents the stop time. The difference in the start time and the stop time gives the round trip time. The system was tested with a master greenPHY communicating with a slave greenPHY on the power line system, while scaling down disturbances to a barest minimum because of simplicity and to benchmark the system. Vary times were recorded during each test sending 1-Byte of 10bits across the communication system.

The total estimated latency calculated:

$$Time = \frac{\text{Number of bits per byte}}{\text{Baud rate}}$$

$$Time = \frac{10}{19200} = 5.2 \times 10^{-4} \text{ s}$$

Time = 0.52ms times were recorded during each test.

T_{Beg} = Beaglebone sleep time, T_{PHY} = GreenPHYs delay,

T_{Ser} = Time for serial transmission, T_{Buf} = Time to store character. $T_{10Mb/s}$ = Time to travel via power line which is small.

$$T_{Est} = T_{Ser} + T_{PHY} + T_{Buf} + T_{Beg}$$

$$T_{Ser} = 2 \times 0.52\text{ms}, T_{PHY} = 500\text{ms}, T_{Buf} = 0.1\text{ms},$$

$$T_{Beg} = 100\text{ms}, T_{10Mb/s} = \text{negligible}, T_{Est} = ?$$

$$T_{Est} = 0.52 \times 2 + 500 + 0.1 + 100 = 601.14\text{milsec}$$

$$T_{Est} = 0.601\text{s}$$

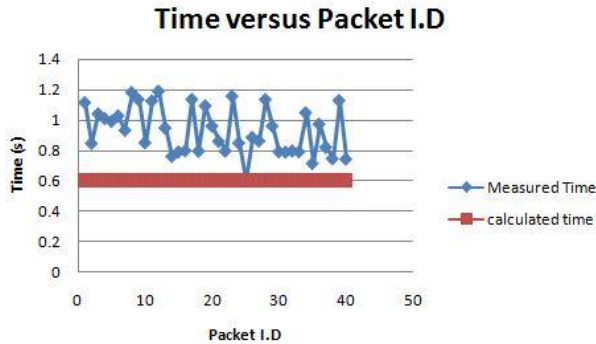


Fig 9: The latency of receiving packet.

An FFT on the signal was carried out using an oscilloscope to check for the contribution of a switching inverter added to powerline communication system and other disturbances.

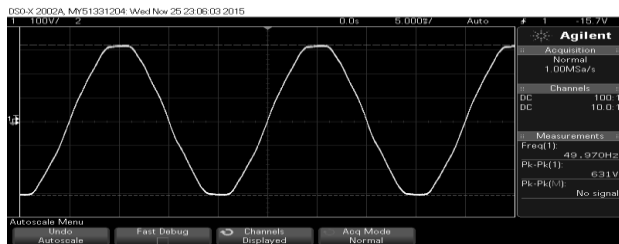


Fig10: Trace of the impure 50Hz measured from the mains with an inverter connected.

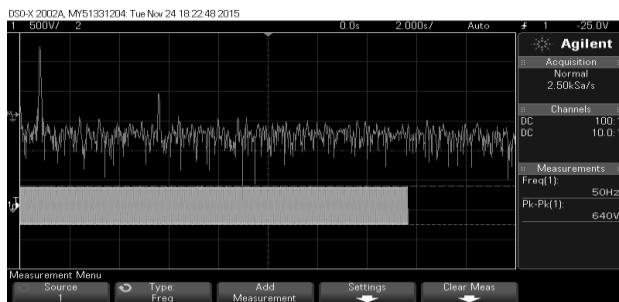


Fig11: Oscilloscope showing the FFT of the mains with a spike contributed by inverter at 15 KHz (span of 50 KHz).

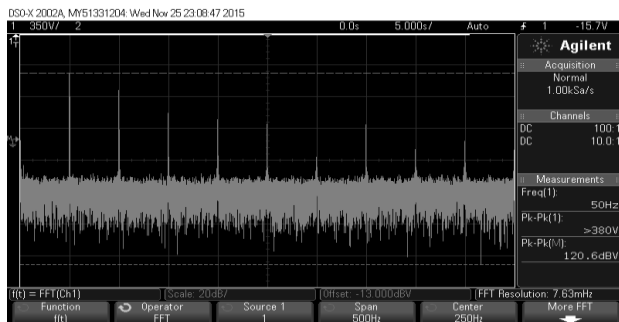


Fig12: The harmonics across the span of 500Hz including the 50Hz of the mains as the fundamental frequency.

12. CONCLUSIONS

This paper started to investigate a smart home/office based on the use of inexpensive, powerful and reliable components. Power line smart grid applications are attractive compared to other applications due to the fact that the system depends on the laid cables of a house or office where it will be implemented. Further work is in progress to assess the error robustness of the system.

13. REFERENCE

- [1] P. L. Communications, P. L. Communications, P. P. Communications, and P. L. C. Broadband, "Introduction to power line communications (PLC) | Kioskea.net," no. June, 2014.
- [2] P. P. Coax, "Understanding the New G . hn Standards & Technology Brief HomeGrid Forum Introduction HomePNA Alliance merged into HomeGrid Forum as of June 2013," no. April, 2014.
- [3] O. Logvinov, "Netricity by HomePlug," *HomePlug*, p. 20 pages.
- [4] H. P. Alliance, "The Standard for In-Home Smart Grid Powerline Communications : An application and technology overview Home Plug Green PHY™ 1.1 The Standard for Smart Grid Powerline Communications," no. October, pp. 1–17, 2012.
- [5] D.-M. Han and J.-H. Lim, "Smart home energy management system using IEEE 802.15.4 and ZigBee," *IEEE Trans. Consum. Electron.*, vol. 56, no. 3, pp. 1403–1410, 2010.
- [6] D.-M. Han and J.-H. Lim, "Design and implementation of smart home energy management systems based on zigbee," *IEEE Trans. Consum. Electron.*, vol. 56, no. 3, pp. 1417–1425, 2010.
- [7] H. Jun, W. Chengdong, Y. Zhongjia, T. Jiyuan, W. Qiaoqiao, and Z. Yun, "Research of intelligent home security surveillance system based on ZigBee," *Proc. - 2nd 2008 Int. Symp. Intell. Inf. Technol. Appl. Work. IITA 2008 Work.*, pp. 554–557, 2008.
- [8] B. Djuricic, "JustGage - nice & clean dashboard gauges," 2012. [Online]. Available: <http://justgage.com/>.
- [9] Beagleboard.org, "Beagleboard.org," *Beagleboard.org community*. [Online]. Available: <http://beagleboard.org/>.
- [10] A. Shankar and S. Lam, "An HDLC protocol specification and its verification using image protocols," *ACM Trans. Comput. Syst.*, vol. 1, no. 4, pp. 331–368, 1983.
- [11] H. S. Warren, "Cyclic redundancy check," *Hacker's Delight*, vol. 13, p. 306, 2003.
- [12] P. Koopman and T. Chakravarty, "Cyclic Redundancy Code (CRC) Polynomial Selection For Embedded Networks," *Int. Conf. Dependable Syst. Networks, 2004*, pp. 1–11, 2004.
- [13] S. E. G. October, "PLC-Stamp 1 (Preliminary Datasheet)," pp. 1–14.
- [14] M. M. Entry, "every 5 seconds the direction of a GPIO changes (without any debouncing) the state of a input GPIO changes (without any debouncing)," pp. 1–5.
- [15] O. Information, "Two Channel Energy Measurement IC," vol. 2013, 2013.

SYNCHRONIZATION CRITERIA OF LINE-START PERMANENT MAGNET SYNCHRONOUS MOTORS: A REVISIT

A. Chama, A.J. Sorgdrager R-J Wang *

* Dept of Electrical & Electronic Engineering, Stellenbosch University, Private Bag X1, Matieland 7602, South Africa E-mail: chama@aims.ac.za, ajsorgdrager@gmail.com, rwang@sun.ac.za

Abstract: A main challenge in designing a line-start permanent magnet synchronous machine (LS-PMSM) is the synchronization analysis and determination. Often the use of time-consuming transient time-step finite element (FE) simulations is unavoidable in the design process. An attractive alternative is to use an analytical synchronization model, which is efficient and can be included in an optimization procedure. However, the implementation of the energy based synchronization criteria is complex as there is little explanation of mathematical principles and function estimations in literature. This paper attempts to revisit and evaluate the viability of the analytical synchronization model.

Key words: Line-start motor, permanent magnet machine, synchronization, analytical modelling, finite element method, transient performance

1. INTRODUCTION

When designing a LS-PMSM, both steady-state and transient operations must be considered. This differs from common synchronous machines design approaches, where usually only the steady-state operation is considered, as a power electronic drive is used for precise motion control. The self-starting capability is a key advantage and also a design challenge for LS-PMSMs. Traditionally, the design of an LS-PMSM starts from the steady-state performance optimization. When the optimum design has been realized, the synchronization capability of the machine is then verified for the specific application. The design is considered a success if the machine synchronizes, otherwise, another design iteration is necessary.

There is extensive published work on steady-state design and optimization of LS-PMSMs using both classical machine theory or finite element method (FEM). For validating the synchronization performance of LS-PMSMs, the more favored approach is the use of transient time-step FEM simulations. However, this verification method is computationally expensive thus limiting the possibility for designers to incorporate it into an optimization procedure.

The use of an analytical synchronization model has been proposed by researchers such as Honsinger [1], Miller [2], Rahman [3–5] and Soulard [6]. This energy based synchronization criteria model is very efficient and can be readily implemented as part of an optimization framework, which will minimize the use of costly transient time-step FEM simulations. However, the implementation of the energy based synchronization criteria from past literature can be difficult to follow and repeat as authors used different notations and symbols for the same parameters without clearly defining them. There is also a lack of clear explanation of mathematical principles and function estimations applied to determine certain key parameters, which are required to determine an accurate synchronization conformation.

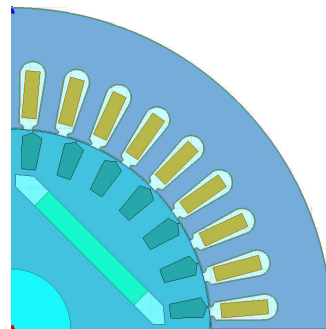


Figure 1: LS PMSM with interior radial flux PMs

The aim of this paper is to revisit the energy based synchronization criteria as presented in past literature. In doing so a detailed explanation of each component and implementation steps of the critical synchronization criteria for a LS-PMSM can be clarified. To check the viability of the analytical approach, the analytically determined synchronization status for several LS-PMSMs is further verified by comparing it to results obtained from transient time-step FEM simulations.

2. ANALYTICAL SYNCHRONIZATION CRITERIA

In this section, the analytical torque equations of a LS-PMSM based on classical electric machine theory are first presented, based on which an analytical synchronization model is then formulated and implemented. The relevant computational aspects are also described.

As shown in Fig.1, a LS-PMSM has a hybrid rotor, which contains both cage winding and PMs. The transient state of a LS-PMSM machine is rather complex as the behavior of the machine is affected by a number of torque components as illustrated in Fig.2, where T_c , T_b and T_s stand for cage torque, braking torque and synchronous torque respectively. According to [1, 5, 7], these torque

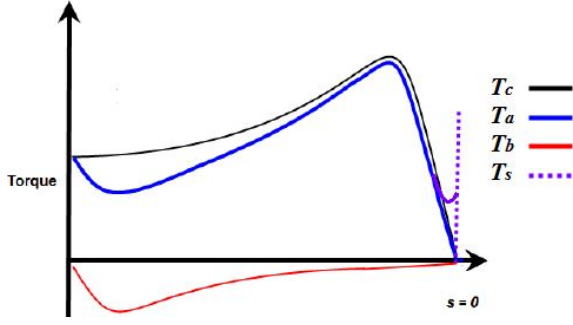


Figure 2: LS-PMSM torque components as a function of slip

components can be expressed as functions of the slip s and load angle δ in radians as follows:

$$T_b(s) = \frac{mpE_0^2 R_1}{\omega_s} \cdot \frac{[R_1^2 + (1-s)^2 X_q^2] (1-s)}{[R_1^2 + (1-s)^2 X_q X_d]^2} \quad (1a)$$

$$T_c(s) = \frac{mp}{\omega_s} \cdot \frac{s R_2' V_{ph}}{(s R_1 + c_1 R_2)^2 + (s X_1 + c_1 X_2)^2} \quad (1b)$$

$$T_s(\delta) = T_{s0} + T_{s1} \sin \delta + T_{s2} \sin 2\delta + T_{s3} \cos \delta + T_{s4} \cos 2\delta \quad (1c)$$

where the components of T_s are the coefficient of the trigonometrical functions in the explicit formulation of T_s , see (A.10), and $c_1 = \frac{1+X_1}{X_m}$. From (A.7)-(A.9), the average and instantaneous torques can be defined as follows:

$$T_a(s) = T_c(s) + T_b(s) \quad \text{and} \quad T_i(s, \delta) = T_s(\delta) + T_a(s) - T_l(s)$$

with $T_l(s) = T_{\text{rated}}(1-s)^2$ being the load torque; T_{rated} is the rated torque of the machine at synchronous speed. The instantaneous torque T_i follows the equation of motion in the $s - \delta$ plane, i.e.

$$-\frac{J\omega_s^2}{p} \times s \frac{ds}{d\delta} = T_i(s, \delta) \quad (2a)$$

The eqn. (2a) is a nonlinear ordinary differential equation and can be solved by the implicit Runge-Kutta-Fehlberg method. To implement the method, (2a) can be first written in the form:

$$\frac{ds}{d\delta} = -\frac{p}{J\omega_s^2} T_i(s, \delta) = f(s, \delta) \quad (2b)$$

Starting with an initial condition $s_0 = s(0) = 1$, the six-stage coefficient K_j is evaluated at each i^{th} iteration:

$$K_j = hf(s_i + \sum_{n=1}^{j-1} \gamma_{jn} k_n, \delta_i + \alpha_j h_j), \quad j = 1, \dots, 6,$$

where γ_{jn} and α_j are the coefficients of Butcher table for the Fehlberg's 4-5 order method. Next the forth and fifth order Runge-Kutta approximate solutions y_{i+1} and k_{i+1} of problem (2b) are computed. The local discretization error is then expressed as:

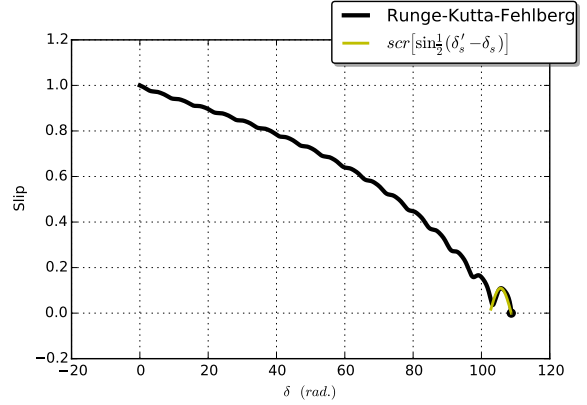
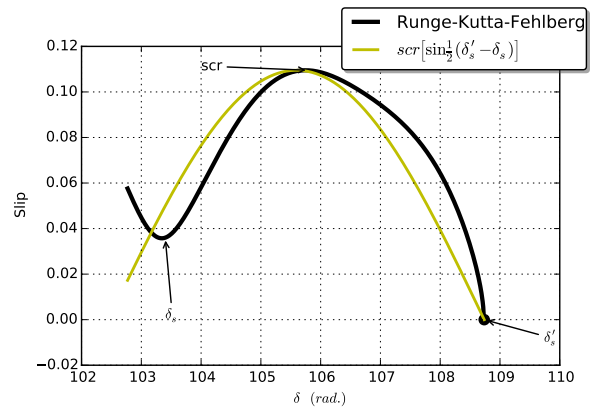


Figure 3: Slip as a function of the load angle: solution by an implicit iterative Runge-Kutta-Fehlberg method.


 Figure 4: Slip- δ function in the synchronization region

$$\tau = \frac{|y_{i+1} - z_{i+1}|}{h_{i+1}}$$

If τ is greater than the set tolerance in the implementation, then the approximation is accepted; else a new step size is chosen for a better convergence. The program terminates if the value $s = 0$ is found within a tolerance less than 10^{-10} .

Figure 3 shows the slip as a function of the load angle obtained by the numerical implementation of the Runge-Kutta-Fehlberg method. Figure 4 compares this implementation with the approximation of the synchronization region proposed in [5]. Clearly, there exists a good agreement between the two approaches. However, to the contrary of [5], where the proof and error estimate have been omitted, the proposed approximation is well known to have at least a fourth order of convergence. Choosing the mesh size h to be small enough would allow us to reach the critical synchronization state with a very small relative error.

One of the advantage of the direct resolution of the PDE's (2) is that it allows in certain context to easily recognize the synchronization capability of the machine without deeper treatment of the problem. Figures 5 and 6 show clear indication of non-synchronized machine, whereas Figure 7 shows that the machine does indeed synchronize to operate at rated conditions of the machine.

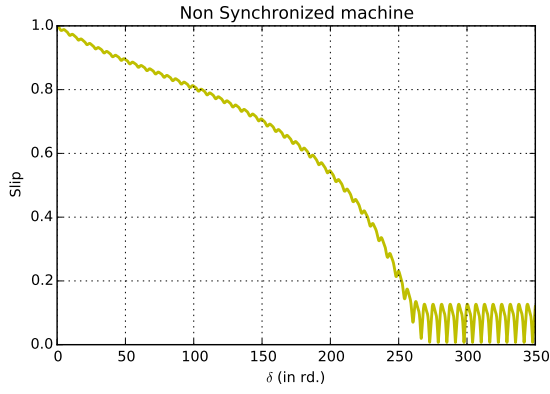
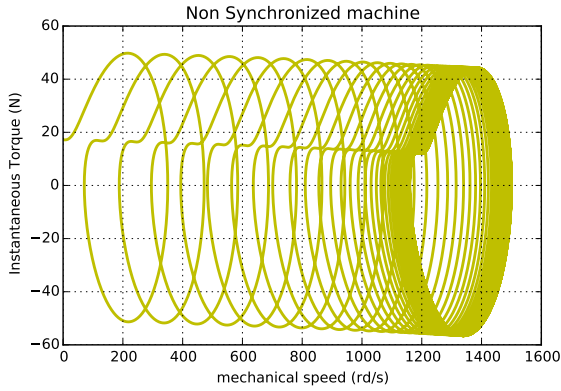

 Figure 5: Slip- δ curve of a non-synchronized machine.


Figure 6: Instantaneous torque of a non-synchronized machine.

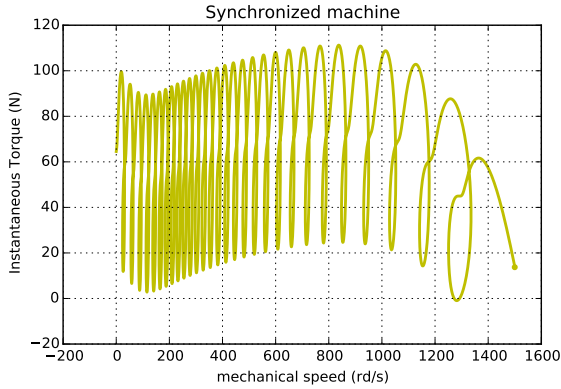


Figure 7: Instantaneous torque of a synchronized machine.

2.1 Synchronization Conditions

The critical synchronization state of the machine is determined within the domain $[\delta_s, \delta'_s]$ [7], which is depicted in Fig.4. The necessary kinetic energy E_k to pull the motor into synchronization is evaluated from the critical slip $s = s_{scr}$ to zero slip, $s = 0$:

$$E_k = \int_{s_{scr}}^0 -\frac{1}{p} J \omega_s^2 s \, dx = \frac{1}{2p} J \omega_s^2 s_{scr}^2 \quad (3a)$$

The synchronization energy from point δ_{scr} to δ'_s is

$$E_{syn} = \int_{\delta_{scr}}^{\delta'_s} T_i(s(\delta), \delta) \, d\delta, \quad (3b)$$

where δ_{scr} is the x -axis component of the critical point scr .

The machine synchronizes for situation when: $E_{scr} \leq E_{syn}$, otherwise it does not synchronize. A flow chart describing the implementation of synchronization criteria as discussed in [5] is shown in Fig. 8.

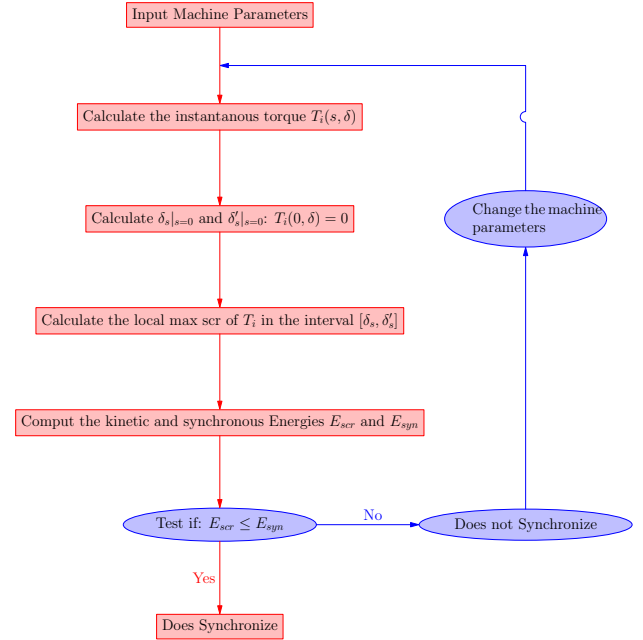


Figure 8: Flow chart describing the implementation of synchronization criteria in [5].

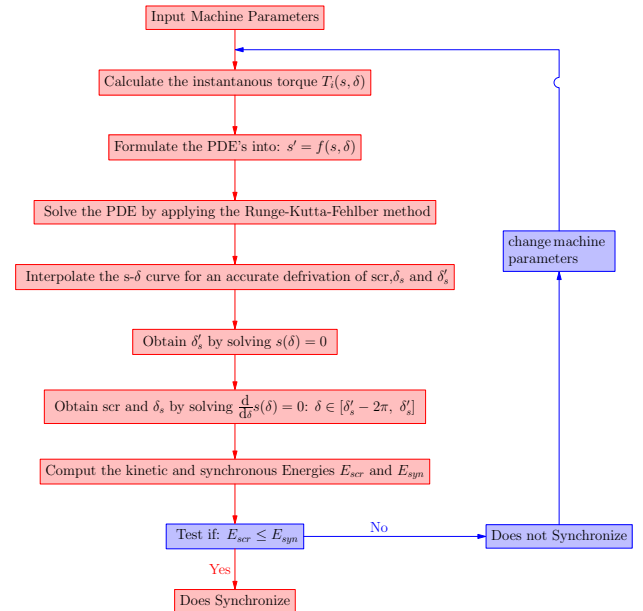


Figure 9: Flow chart describing the implementation of synchronization criteria using the proposed approach.

To evaluate the integrals (3a) and (3b), δ'_s need to be found by solving the equation $T_i(0, \delta) = 0$, the existence of solutions of which can be analyzed from a graphical representation of the instantaneous torque $T_i(0, \delta)$, see

Fig. 10. To obtain the critical slip the equation $T_i(s, \delta'_s - \pi) = 0$ has to be solved, see Figure 11. Note that s_{cr} must be the closest local maximum of the $s - \delta$ function to the origin $s = 0$ and δ'_s the second x-intercept of the curve of T_i .

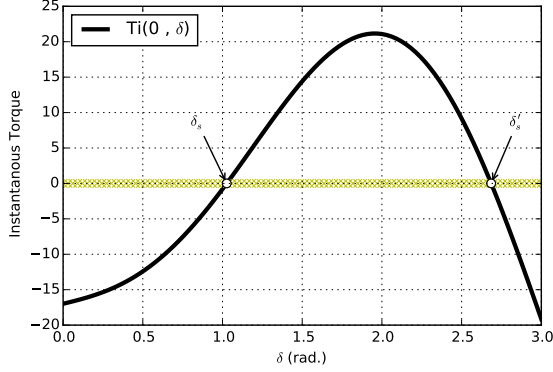


Figure 10: Instantaneous Torque at $s = 0$, as a function of the load angle.

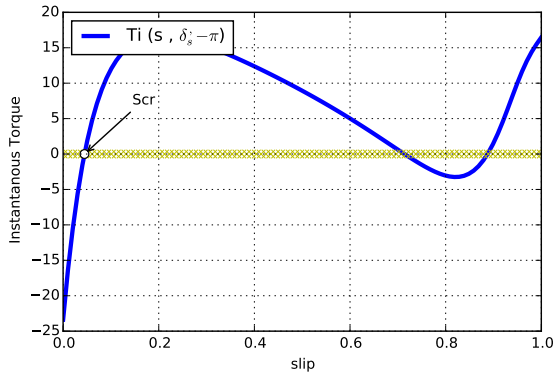


Figure 11: Local maximum s_{cr} , of the instantaneous torque.

3. VALIDATION OF SYNCHRONIZATION MODEL

In this section the synchronization criteria formulated in section 2 is verified using a number of different LS-PMSM designs. The basic specifications for all the designs are given in Table 1. In addition, the machines' rotor diameter, stack length and stator slot are all identical. The differences among these candidate designs are mainly in PM array topologies and rotor slot shapes. Figure 12 illustrates 4 of a total of 13 candidate designs.

For verification, ANSYS' Maxwell software suite that contains both a 2D FEM simulator and an analytical machine model solver (RMXprt) is used. A load equation emulating a fan load is defined for the simulation, which provides a rated load torque at synchronous speed with the inertia as in Table 1.

3.1 Analytical comparison

To accurately calculate the critical slip of a LS-PMSM, the analytical torque curves for the machine is required. RMXprt can produce the required torque curves for each of

Table 1: Machine and load specifications

Specification	Value
Rated output power, kW	2.2
Rated voltage (line-to-line), V	525
Rated speed, rpm	1500
Rated torque, Nm	14
Frame size	100L
Load type	Fan
Load inertia, kg.m ²	0.15
Steady state performance	IE4

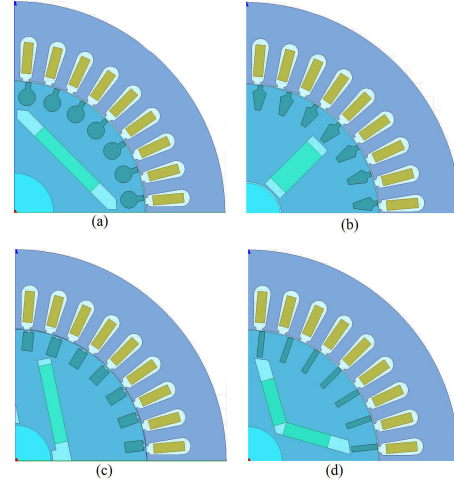


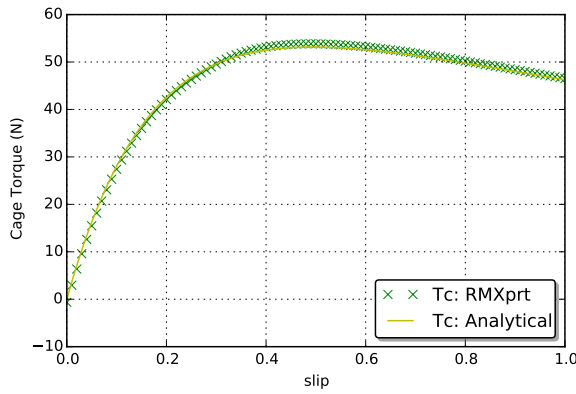
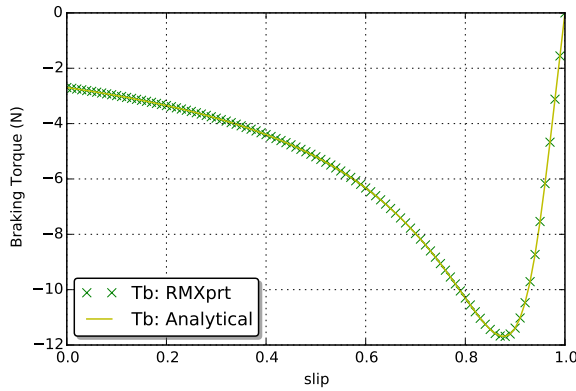
Figure 12: Rotor topology used for verification designs: a) Radial Flux, b) Spoke-type, c) Asymmetric Flux, d) V-type

the candidate designs as well as the key equivalent circuit parameters. However, the exact equations employed by RMXprt torque calculations are unknown. To validate the torque equations (A.7) to (A.9) used in the study, the parameters obtained from RMXprt are used as inputs to reproduce the torque curves from RMXprt. The required RMXprt parameters for a total of 13 designs are listed in Table 2 (See the Appendix for detailed definition of each parameter in the table).

For each machine $T_c(s)$, $T_b(s)$, $T_a(s)$ and $T_s(\delta)$ were created and compared with those from RMXprt. Figures 13 to 16 compare the torque plots for the candidate design 6. Clearly there is a good correlation between the

Table 2: RMXprt output parameters

	E_0	X_d	X_q	R_1	R'_2	X_1	X_2
1	171.20	33.25	99.53	6.63	3.99	3.07	1.80
2	171.20	33.25	99.53	6.63	2.1	3.07	1.80
3	232.40	50.08	107.21	6.64	4.11	4.29	1.52
4	218.36	51.03	107.55	9.91	4.11	4.63	1.52
5	247.86	51.53	159.32	9.92	2.35	4.22	1.45
6	241.26	55.22	153.49	7.61	3.22	4.19	2.43
7	224.94	37.11	99.72	3.69	2.45	3.06	1.98
8	189.60	37.70	101.37	8.42	2.74	3.96	1.85
9	227.41	39.07	106.88	8.42	2.85	3.95	2.64
10	233.03	35.99	172.59	9.66	1.97	6.06	0.832
11	166.92	37.14	164.94	9.30	3.35	5.61	1.56
12	187.65	33.63	99.75	8.42	2.89	3.92	2.06
13	181.16	28.32	101.37	8.43	2.47	3.92	1.63


Figure 13: Torque curve comparison of T_c

Figure 14: Torque curve comparison of T_b

results from equations (A.7) to (A.9) and RMXprt. The same was found to be true for the remaining 12 candidate designs, which means that these torque equations of LS-PMSMs can be used to solve eqn. (2b).

3.2 Synchronization comparison

In this section the synchronization capabilities of all 13 candidate designs are inspected with the proposed fan load. The analytical synchronization criteria model is applied to each candidate design and the results are verified by using ANSYS' Maxwell 2D transient FEM solver.

In 2D FEM, a load equation can be include in the transient time-step simulation set-up. This was done by defining the

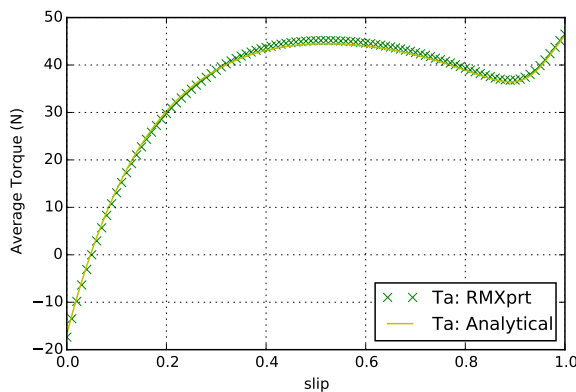
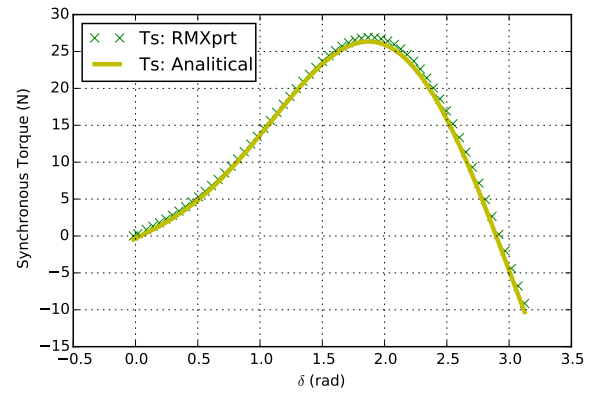
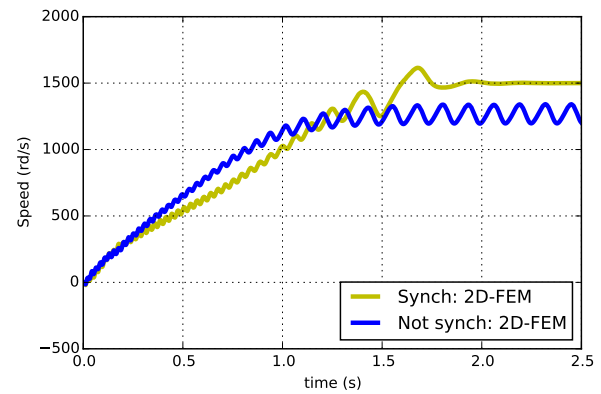

Figure 15: Torque curve comparison of T_a

Figure 16: Torque curve comparison of T_s


Figure 17: Synchronized vs non-synchronized FEM simulation representations, where design 1 in blue, design 2 in yellow.

load equation as $T_l = 14(1 - (157.08 - \omega_r)/157.08)^2$ with ω_r referring to the rotors angular velocity in rad/s. The system inertia (J_l) was set at 0.15 kg.m^2 and a time-step of 1 ms was used in the analyses. Using the results from the simulations both speed vs. time and instantaneous torque vs. speed graphs are compiled for each candidate design. Figure 17 represents two cases (designs 1 and 2) obtained from the simulation results. The simulation results are interpreted as follows:

- A machine is seen as synchronized once the rotational speed settles at 1500 rpm (yellow line);
- A machine is seen as not synchronized when the rotational speed oscillates at a point below 1500 rpm (blue line).

Figures 18 and 19 are the instantaneous torque vs. speed plots for the two cases. It can be seen that it closely resembles that of Figures 6 and 7 in Section 2 that was obtained using the proposed analytical approach.

The comparison for all the candidate designs is presented in Table 3. The synchronization state of a design is indicated under the method used. The first coulomb from the right states if the result of the proposed method matches that of ANSYS Maxwell 2D FEM. From the table it is clear that a 100% match was achieved.

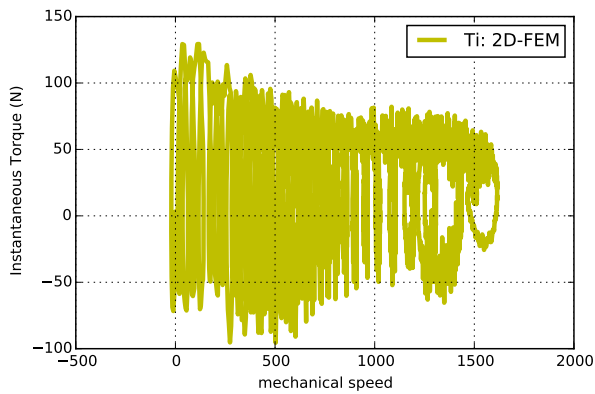


Figure 18: Torque vs speed characteristics obtained from FEM

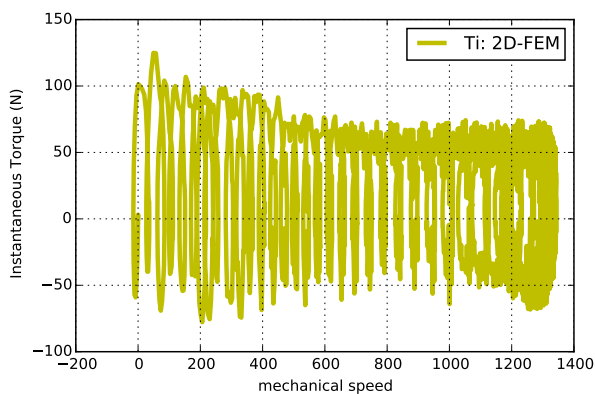


Figure 19: Torque vs speed characteristics obtained from FEM (design 1).

4. CONCLUSION

This paper revisits the energy based synchronization criteria as presented in past literature. An improved and more consistent approach for the study of synchronization by using an energy based synchronization criteria model has been presented. Using an implicit non-linear solver, we have shown how to determine the $s - \delta$ plane function, which can then be used to evaluate the state of synchronization. Despite the simplicity of the algorithm it provides highly accurate result with a large order of convergence. Indeed even the most popular numerical solvers such as the finite element method rarely can provide a second order of convergence, whereas the algorithm used in our case has five order of convergence.

The new approach was verified by means of comparison against 2D FEM transient time-step simulation and an alternative analytical LS-PMSM machine simulation tool. Results proved to compare well and as a result the proposed method can be deemed valid for the use of synchronization estimation during the design of LS-PMSMs. It does however still require experimental validation. This can be done by implementing the proposed method during the design of LS-PMSM in future work and as a result also limit the use of time-step simulations and decreasing design optimization time.

Table 3: Verification results

ID	Synchronize?	2D FEM	Analytical	Match
1	Synchronize?	no	no	✓
2	Synchronize?	yes	yes	✓
3	Synchronize?	yes	yes	✓
4	Synchronize?	no	no	✓
5	Synchronize?	no	no	✓
6	Synchronize?	yes	yes	✓
7	Synchronize?	yes	yes	✓
8	Synchronize?	yes	yes	✓
9	Synchronize?	no	no	✓
10	Synchronize?	no	no	✓
11	Synchronize?	no	no	✓
12	Synchronize?	no	no	✓
13	Synchronize?	no	no	✓

REFERENCES

- [1] Honsinger, V.B., "Permanent magnet machines: asynchronous operation," *IEEE Trans on Power Apparatus and Systems*, PAS-99(4): 1503-1509, July 1980.
- [2] Miller, T.J.E., "Synchronization of line-start permanent magnet AC motors," *IEEE Trans on Power Apparatus and Systems*, PAS-103(7): 1822-1828, July 1984.
- [3] Rahman, M.A., Osheiba, A.M., Radwan, T.S., "Synchronization process of line-start permanent magnet synchronous motors", *Electric Machines and Power Systems*, 24(6):77-592, 1997.
- [4] Isfahani, A.H., Vaez-Zadeh, S., Rahman, M.A., "Evaluation of synchronization capability in line start permanent magnet synchronous motors," *IEEE International Electric Machines and Drives Conference (IEMDC)*, pp.1346-1350, 15-18 May 2011.
- [5] Rabbi, S.F., Rahman, M.A., "Critical criteria for successful synchronization of line-start IPM motors", *IEEE Journal of Emerging and Selected Topics in Power Electronics*, 2(2):348-358, June 2014.
- [6] Soulard, J., Nee, H.P., "Study of the synchronization of line-start permanent magnet synchronous motors," *Conference Record of the 2000 IEEE Industry Applications Conference*, 1:424-431, 2000.
- [7] Tang, R.Y. *Modern Permanent Magnet Machines: Theory and Design*, China Machine Press, Beijing, December 1997.

APPENDIX

List of Symbols

Symbol	definition	unit
c_1	T_c correction factor	
E_o	Back-EMF	V
E_k	Kinetic energy	J
E_{syn}	Synchronization energy	J
E_{scr}	Critical synchronization energy	J
f	Frequency	Hz
J	Inertia	kgm ²
J_l/J_s	Load/system inertia	kgm ²
l	Load	
m	Stator phases	
p	Pole pairs	
R_1	Stator resistance	Ω
R'_2	Rotor resistance referred	Ω
r	Rotor	
s	Slip	
s_{scr}	Critical slip	
T_a	Average torque	Nm
T_b	Magnetic braking torque	Nm
T_c	Cage torque	Nm
T_i	Instantaneous torque	Nm
T_s	Synchronous torque	Nm
X_1	Stator leakage reactance	Ω
X'_2	Rotor leakage reactance	Ω
X_d/X_q	d-q reactances	Ω
V_{ph}	rms phase voltage	V
δ	Load angle	rad
δ_s	Synchronous load angle	rad
δ'_{scr}	Critical load angle	rad
ω_r	Rotating angular velocity	rad/s
ω_s	Angular frequency	rad/s

Subscripts

scr	Critical
l	Load
r	Rotor

List of Torque Equations

$$X_d = X_1 + X_r d \quad (A.1)$$

$$X_q = X_1 + X_r q \quad (A.2)$$

$$\omega_s = \pi f \quad (A.3)$$

$$X'_2 = \frac{X'_{2d} + X'_{2q}}{2} \quad (A.4)$$

$$X_m = \frac{2 \cdot X_d X_q}{X_d + X_q} \quad (A.5)$$

$$c_1 = \frac{1 + X_1}{X_m} \quad (A.6)$$

$$T_b(s) = \frac{mpE_0^2 R_1}{\omega_s} \cdot \frac{[R_1^2 + (1-s)^2 X_q^2] (1-s)}{[R_1^2 + (1-s)^2 X_q X_d]^2} \quad (A.7)$$

$$T_c(s) = \frac{mp}{\omega_s} \cdot \frac{s R'_2 V_{ph}}{(s R_1 + c_1 R_2)^2 + (s X_1 + c_1 X_2)^2} \quad (A.8)$$

$$T_s(\delta) = T_{s0} + T_{s1} \sin \delta + T_{s2} \sin 2\delta + T_{s3} \cos \delta + T_{s4} \cos 2\delta \quad (A.9)$$

$$T_{s0} = \frac{mp R_1 X_q}{w_s (R_1^2 + X_d X_q)^2} \left[\begin{aligned} &(X_d - X_q) \left(\frac{V_{ph}^2}{2} - 1 + E_0^2 \right) \\ &- E_0^2 \left(\frac{R_1^2}{X_q} + X_d \right) \end{aligned} \right]; \quad (A.10a)$$

$$T_{s1} = \frac{mp E_0 V_{ph}}{w_s (R_1^2 + X_d X_q)^2} \left[\begin{aligned} &(X_d - X_q) (R_1^2 - X_d X_q) + \\ &(R_1^2 + X_d X_q) X_d \end{aligned} \right]; \quad (A.10b)$$

$$T_{s2} = \frac{mp V_{ph}^2}{2 w_s (R_1^2 + X_d X_q)^2} [(X_d - X_q) (X_q X_d - R_1^2)]; \quad (A.10c)$$

$$T_{s3} = \frac{mp E_0 V_{ph} R_1}{w_s (R_1^2 + X_d X_q)^2} [(R_1^2 + X_d X_q) - 2 X_q (X_d - X_q)]; \quad (A.10d)$$

$$T_{s4} = \frac{mp V_{ph}^2 R_1}{2 w_s (R_1^2 + X_d X_q)^2} [(X_d - X_q) (X_d + X_q)]; \quad (A.10e)$$

COMPARISON OF OPERATING MODES FOR THE ROTOR-TIED DOUBLY FED INDUCTION GENERATOR

O.I. Olubamiwa^{*}, N.L. Zietsman[†] and N. Gule[‡]

^{*} *Electrical Machines Laboratory, Department of Electrical & Electronic Engineering, Stellenbosch University, Private Bag X1, Matieland 7602 South Africa. E-mail: 19469462@sun.ac.za*

[†] *E-mail: 15714403@sun.ac.za*

[‡] *Email: nathie@sun.ac.za*

Abstract: In this paper, two modes of operation for rotor-tied doubly fed induction generator systems are discussed. The modes are described in terms of the rotational speed and direction of the stator and rotor fluxes alongside the rotor mechanical rotation. 2D-FEA is carried out on DFIG models to analyse the characteristics of these modes. Their performances are highlighted and compared.

Key words: Rotor-tied doubly fed induction generators, finite element analysis

1. INTRODUCTION

The push to reduce adverse environmental effects caused by the use of fossil fuels as energy sources has seen increased interests in green energy. In view of this, wind energy has emerged as one of the favourite alternatives.

With the rise in support for wind energy conversion systems, a leap in the rated output power of production-type wind turbine units has been observed [1]. The size of generators used in these systems increases with system rated power, and at times at rates higher than the increase in power. These increases in size tell greatly as material costs take a sizeable chunk of the overall machine cost [2]. Consequently, studies geared towards reducing the weight and size of these systems are finding more relevance. Other factors like cost and efficiency are also being considered.

Doubly fed induction generators (DFIGs) are the most widely used generators in wind energy conversion systems (WECs) given their wide operating speed range, low power converters (compared to synchronous and squirrel cage induction generators), and cheaper power factor control implementation [1,3,4].

In line with increasing the competitiveness of WECs as compared to the use of fossil fuels and other generation alternatives, reducing generator sizes help lower the generating costs significantly. In [4, 5], a novel system of designing DFIGs was proposed such that the rotors of these machines are first designed and dimensioned for direct connection to the grid, and a suitable and smaller stator is then fitted over the rotors to which converters are connected to. This method with an ensuing new configuration was observed to significantly reduce the overall machine size with converter power ratings unchanged.

In [4,5], two 5 kW machines designed for the conventional and Rotor-tied DFIG configurations were tested as motors. The efficiency of the Rotor-tied type was observed to be 92.98% with a 0.5% increase over the stator tied variant.

In [6], the Rotor-tied type was analyzed as a generator. Given the increased difficulty a coupled control circuit adds to running a DFIG model, and the further lengthening of simulation time, the simulations were based on DC generation. As such, there is a lack of details as to how the machine will actually be implemented as a grid connected DFIG.

David [7] proposes a mode detailing the operations of the machine with regards to the rotor speed and the stator/converter field frequencies and directions. In this paper, this mode is described with some details and modifications for better interpretation alongside a novel alternative mode. For convenience the mode proposed in [7] will be termed the reverse rotation mode and the alternative, the forward rotation mode. The performances of both modes are also highlighted.

2. THE ROTOR-TIED DFIG

Although in certain cases, DFIGs generate power exclusively on the rotor-side for rectifier loads [8], they are conventionally operated by connecting the stator side to the power grid while the rotor side is connected to an adjustable converter as shown in Figure 1. The rotor-tied operated DFIGs, where the rotor by virtue of being connected to the grid bears the machine rated power while the stator is connected to a fractionally rated converter, was proposed in [5] as illustrated in Figure 2.

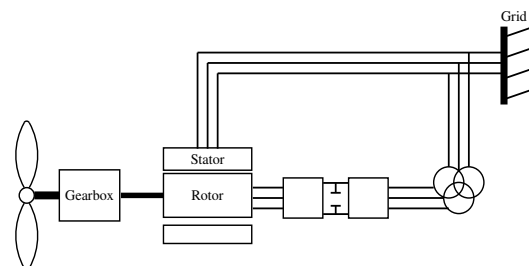


Figure 1: A conventional DFIG setup

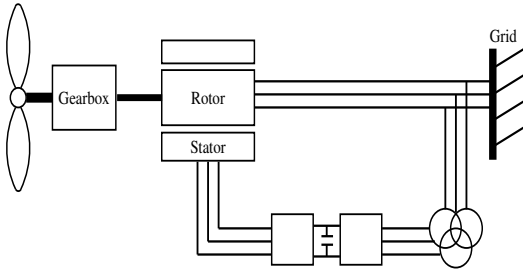


Figure 2: A rotor-tied DFIG setup

It is argued that the traditional methods of designing DFIGs seek to maximise torque production by the stator thereby compromising the effectiveness of the rotor. This is so because, by designing the stator first, an automatic outer diameter for the rotor is decided. It was proposed that connecting the rotor windings to the grid ensures that the rotor core is designed for maximum usage and a suitable minimally sized stator core is fitted.

3. MACHINE OPERATING MODES

3.1 Reverse Rotation mode

In this mode proposed by David [7], the mechanical rotor rotation is in an opposite direction to the rotation of the magnetic fields on the rotor and the stator. The frequency of the induced voltage on an induction machine rotor is dependent on the stator flux rotational speed and the rotor rotational speed. The relationship is given as:

$$\omega_r = \omega_s - \omega_m \quad (1)$$

where:

ω_r = the angular frequency of rotor flux which is invariably $2\pi 50$ (rad/s) for a 50 Hz system

ω_s = the stator flux frequency (rad/s)

ω_m = the angular frequency of the rotor (rad/s)

With

$$\omega_m = p_1 \Omega_m \quad (2)$$

Where:

Ω_m = mechanical rotational speed of the rotor (rad/s)

p_1 = number of pole pairs of the machine [8, 9]. Using the classical definition of induction machine slip, s ,

$$s = \frac{\omega_s - \omega_m}{\omega_s} \quad (3)$$

With the connection of the rotor windings to the grid, for a 50 Hz grid, the slip equation becomes

$$s = \frac{\omega_s - \omega_m}{\omega_s} = \frac{2\pi 50}{\omega_m + 2\pi 50} \quad (4)$$

Figure 3 illustrates the reverse rotation mode showing the direction of the rotor rotation with respect to the magnetic fields on the stator and rotor. Converters in DFIGs are usually sized to handle only a percentage of the rated

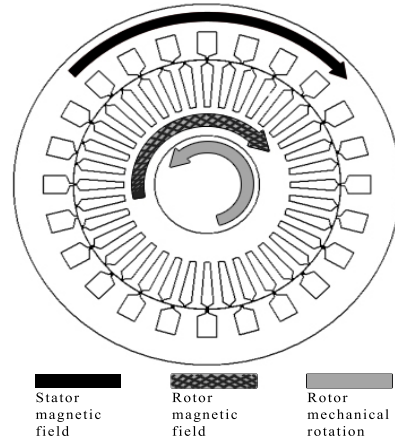


Figure 3: The Reverse rotation mode

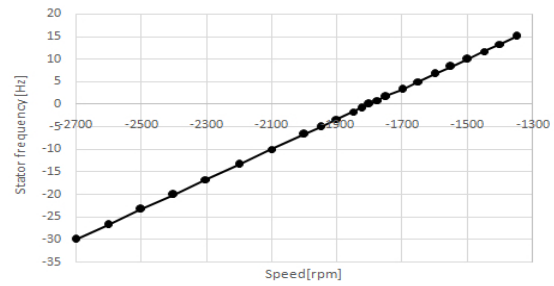


Figure 4: Stator flux frequency with respect to rotor speed for Reverse rotation mode

machine power. At a fixed turbine speed for a lossless DFIG system in a steady state, the mechanical power applied to the generator shaft from the turbine is

$$P_m = P_s + P_r \quad (5)$$

Where:

P_m = the input mechanical power into the generator

P_s = the electrical power input or output at the converter side/stator

P_r = the electrical power output at the rotor.

It follows that

$$P_r = P_m - P_s = T_m \omega_m - T_{em} \omega_s \quad (6)$$

Where:

T_m = the mechanical torque input acting on the generator

T_{em} = the electromagnetic torque produced by the machine [3]

For a lossless DFIG system:

$$T_m = T_{em} \quad (7)$$

Therefore:

$$P_r = T_m (\omega_m - \omega_s) = -T_m (s \omega_s) = -s P_s \quad (8)$$

Substituting (8) into (5),

$$P_m = P_s - s P_s = P_s (1 - s) \quad (9)$$

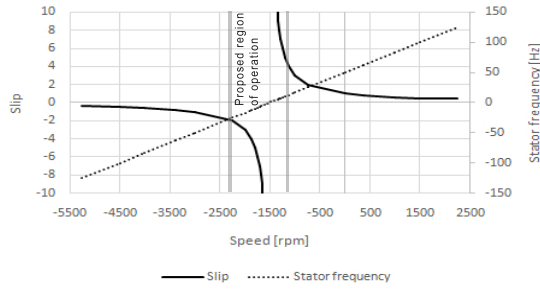


Figure 5: Operating regions for the Reverse rotation mode

Giving

$$P_s = \frac{P_m}{1-s} \quad (10)$$

Noting the bidirectional nature of the converters used in DFIGs, the stator power can thus be termed input or output depending on the rotor speed. Assuming the converters are sized to handle about a third of the turbine rated output, setting P_s to $\frac{-P_m}{3}$ (at the lowest subsynchronous speed) or $\frac{P_m}{3}$ (at the highest supersynchronous speed), we obtain slip limits of 4 and -2 respectively. Considering these limits for a 4 pole 50 Hz machine, the operating mechanical rotor speed range is between 1125 rpm to 2250 rpm. A slip limit of 2 to -2 was given in [7] which translates to a range between 750 rpm to 2250 rpm for a similar machine. If the positive slip limit is set at 2, $P_s = -P_m$ considering (10), therefore requiring a fully rated converter. Figure 5 highlights the proposed regions of operations given these conditions.

3.2 Forward Rotation mode

This is a different mode in which the rotor rotates mechanically in the same direction as the magnetic fields on the stator and the rotor. Figure 6 illustrates the forward rotation mode showing the direction of the rotor rotation with respect to the magnetic fields on the stator and rotor in contrast to the reverse rotation mode. Here the slip can be calculated as,

$$s = \frac{\omega_{syn} + \omega_m}{\omega_{syn}} \quad (11)$$

Where:

$\omega_{syn} \equiv \omega_r$ = the grid or synchronous frequency,*with the other parameters retaining their identities as described in the Reverse rotation mode.

The numerator of (11) represents the frequency of the field on the stator or converter side.

$$\omega_m = s\omega_{syn} - \omega_{syn} = \omega_{syn}(s-1) \quad (12)$$

From (5) (also assuming a lossless system), it can be

*Should not be confused with the stator frequency

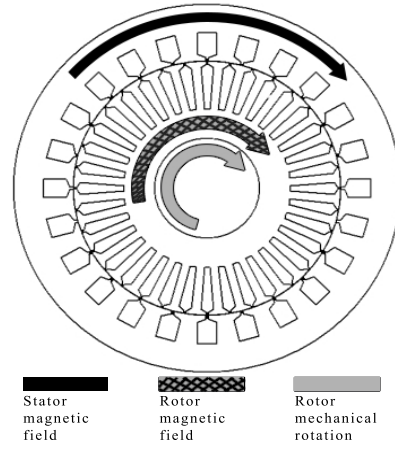


Figure 6: The Forward rotation mode

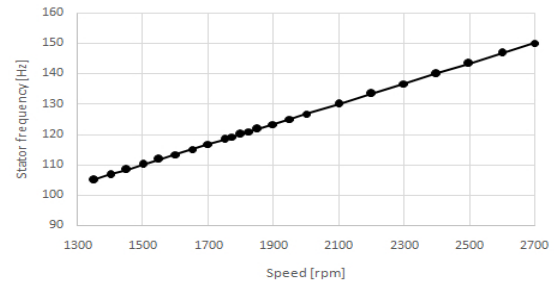


Figure 7: Stator flux frequency with respect to rotor speed for Forward rotation mode

deduced that:

$$T_m \omega_m = P_s + T_{em} \omega_{syn} \quad (13)$$

$$P_s = T_m \omega_m - T_{em} \omega_{syn} = T_m (\omega_m - \omega_{syn}) \quad (14)$$

combining (12) and (14)

$$\begin{aligned} P_s &= T_m (s\omega_{syn} - \omega_{syn} - \omega_{syn}) \\ &= T_m (s\omega_{syn} - 2\omega_{syn}) = T_m \omega_{syn} (s-2) \\ &= P_r (s-2) \end{aligned} \quad (15)$$

Using

$$P_m = P_r (s-2) + P_r = P_r (s-1) \quad (16)$$

The rotor power (power supplied directly to the grid) is thus calculated as:

$$P_r = \frac{P_m}{s-1} \quad (17)$$

Applying the same converter power limits of a third of the mechanical power, a slip range of $\frac{7}{4} \leq s \leq \frac{5}{2}$ is obtained. A similar mechanical speed range is obtained as the reverse rotation mode as shown in Figure 8.

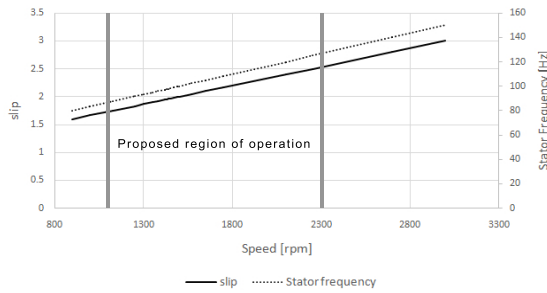


Figure 8: Operating regions for the Forward rotation mode

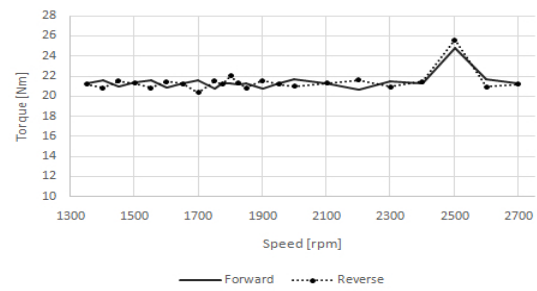


Figure 9: The machine torque production in both modes

Table 1: Different DFIG setups machine design results

Items		Unit	Stator-tied DFIG	Rotor-tied DFIG
Power		kW	5	
Rated line to line voltage		V	220	
Poles			4	
Stator	Outer diameter	mm	222	197
	Inner diameter	mm	136	136.6
	Coil Area	mm ²	3.46	16
	Turns per slot	turns	14	4
Rotor	Outer diameter	mm	135.4	136
	Inner diameter	mm	75	54
	Coil Area	mm ²	16	3.46
	Turns per slot	turns	4	14
Air gap		mm	0.3	
Stack length		mm	116	

4. FINITE ELEMENT ANALYSIS

2D-FEA DFIG models of the Rotor-tied machine detailed in Table 1 were simulated in the Ansys Maxwell environment. Other necessary unspecified parameters such as slot opening widths, rotor slot bottom width, and equivalent circuit parameters were calculated using equations given in [10]. For both modes, 24 different rotor speed instances within the range of 1350 *rpm* and 2700 *rpm* (representative of the speed range at which the stator converter is rated at a third of the turbine output power for a 60 Hz system) were simulated. This was done using a parametric analysis in Maxwell. The frequency of currents fed into the stator windings were calculated according to the denominator of (4) and the numerator of (11) for the Reverse and Forward rotation modes respectively. Figures 4 and 7 illustrate the stator flux frequency variations with the simulated rotor speeds for the modes.

4.1 Analysis conditions

The FEA models were created by first designing the machine in RMxprt then converting to a 2D Maxwell model and run as Rotor-tied DFIGs. The Grid/Rotor windings were set as voltage windings with the calculated equivalent circuit parameters (Leakage inductance and

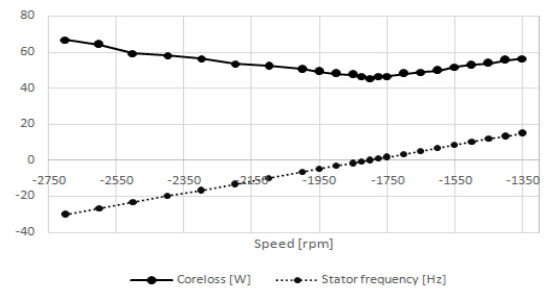


Figure 10: Reverse rotation mode Core losses

resistance). The windings had phase voltages of 127 V_{rms} . The frequency of the voltages were set at 60 Hz (because the machine model used was designed for 60 Hz). The Stator/Converter windings were set as current windings with a current value used was set at 73.8 A_{rms} (the rated converter side current) as given in [5]. The frequency of the currents in these windings were calculated and set according to the mode used and speed at which the machine was being tested at. The material used for the rotor and stator laminations was the M19_24G steel.

For simulations in the Reverse rotation mode, the speeds were run at negative values to indicate the direction of rotation in Maxwell.

5. DISCUSSION

Torque Characteristics: The torque produced by the machine for both modes was basically similar and near constant for all speeds. As seen in Figure 9, it is difficult to draw any conclusions on the slight variances observed for different speeds as there was no noticeable pattern.

Losses: The Stranded losses were more or less constant for both modes and all speeds. The core losses varied, as expected with the frequencies at the stator windings. Figures 10 and 11 show that the core losses for both modes were dependent on the frequency of the stator flux. The higher the frequency, the more the core loss. The core losses were significantly higher for the forward rotation mode.

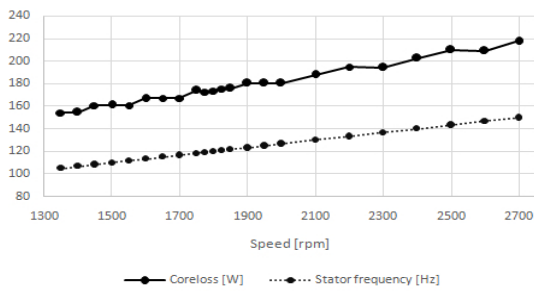


Figure 11: Forward rotation mode Core losses

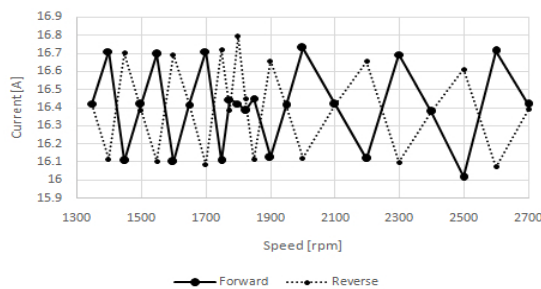


Figure 12: Grid side current

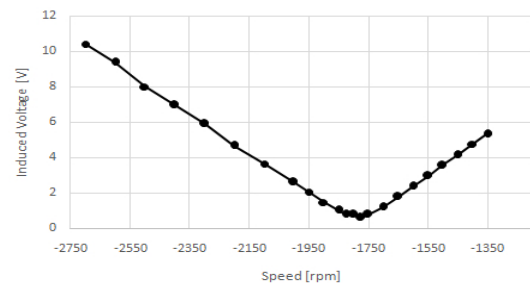


Figure 13: Reverse rotation mode Stator induced voltages

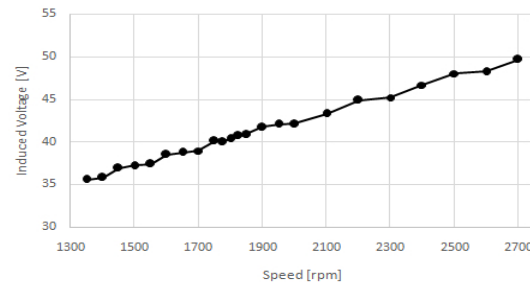


Figure 14: Forward rotation mode Stator induced voltages

Currents and Induced Voltages: The currents on the grid side windings are shown in Figure 12. For the reverse rotation mode, the induced voltages at the stator windings varied with the stator field frequency (similar to the pattern of the core losses) at relatively low values, the highest being $10.4 V_{rms}$ when the machine speed was 2700 rpm as illustrated in Figure 13. Figure 14 shows the induced voltages at the stator windings for the forward rotation mode which were significantly higher, the highest being $49.6 V_{rms}$ also at 2700 rpm .

6. CONCLUSION

In this paper, two possible modes of operation for the rotor-tied DFIG are examined. The modes were expressly described with operating regions identified. 2D-FEA models of a 5 kW rotor-tied DFIG were analyzed running in both modes. With regards to the results, the reverse rotation mode is the preferable operating mode, due to its lower core losses and reconcilable induced stator voltages.

REFERENCES

- [1] S. Müller, M. Deicke, and D. W., & Rik Doncker, "Doubly fed induction generator systems for wind turbines," *Industry Applications Magazine, IEEE*, vol. 8, no. 3, pp. 26–33, 2002.
- [2] G. Shrestha, D. J. Bang, H. Polinder, and J. a. Ferreira, "Structural flexibility: a solution for weight reduction of large direct-drive wind-turbine generators," *IEEE Transactions on Energy Conversion IF - 2.489*, vol. 25, no. 3, pp. 732–740, 2010.
- [3] J. Fletcher and J. Yang, "Introduction to Doubly-Fed Induction Generator for Wind Power Applications," *Paths to Sustainable Energy*, pp. 259–278, 2010.
- [4] Y.-M. You, T. a. Lipo, and B.-I. Kwon, "A Novel Grid-connected to Rotor Type Doubly Fed Induction Generator for Wind Turbine Systems," in *8th International Conference on Power Electronics - ECCE Asia*, The Shilla Jeju, 2011, pp. 646–653.
- [5] —, "Design and Analysis of a Novel Grid-Connected to Rotor Type Doubly Fed Induction Machine," *IEEE Transactions on Magnetics*, vol. 48, no. 2, pp. 919–922, 2012.
- [6] —, "Optimal Design of a Grid-Connected-to-Rotor Type Doubly Fed Induction Generator for Wind Turbine Systems," *IEEE Transactions on Magnetics*, vol. 48, no. 11, pp. 3124–3127, 2012.
- [7] N. David and D. C. Aliprantis, "DFIG with grid-connected rotor for wind energy conversion system," *Proceedings of the 2013 IEEE International Electric Machines and Drives Conference, IEMDC 2013*, pp. 125–130, 2013.
- [8] I. Boldea, *Variable Speed Generators*, 2005.
- [9] G. Abad, *Doubly fed induction machine : modeling and control for wind energy generation applications*, 2011.
- [10] I. Boldea and S. A. Nasar, *The induction machines design handbook*, 2009.

ROTOR POSITION MEASUREMENT WITH MAGNETIC STRAY FIELDS

A. Treurnicht¹ and P. J. Randewijk²

^{1,2}Department of Electrical and Electromechanical Engineering, Stellenbosch University, Banghoek road, Stellenbosch, 7600, South Africa

¹e-mail: 13951874@sun.ac.za

²e-mail: pjrandew@sun.ac.za

Abstract: Vector control of synchronous motors require accurate rotor position measurements. Rotor position is generally measured with rotary position sensors mounted directly on the rotor shaft. Due to the mechanical construction of some motors, sensors cannot always be mounted on the rotor shafts. This paper introduces an alternative technique that uses the magnetic stray field behind the Halbach permanent magnet array of an ironless permanent magnet synchronous motor to measure rotor electrical angle. This study shows that the magnetic stray field angle can be used for rotor position identification since it changes linearly with rotor position. It is further observed that the measurement accuracy is strongly influenced by the magnetic field strength tolerance of the magnets.

Key words: Ironless permanent magnet synchronous motor, Halbach permanent magnet array, magnetic stray field, rotor position sensor

1. NOMENCLATURE

BLDC	Brushless DC
PMSM	Permanent magnet synchronous motor
IDRFPM	Ironless double-rotor radial flux permanent magnet synchronous machine
PWM	Pulse width modulation
MSFRP	Magnetic stray field rotor position

2. INTRODUCTION

Permanent magnet synchronous motors became very popular due to their high efficiency, high torque to inertia ratio, high speed etc. [1]. Vector control requires accurate rotor angular position measurement [2]. Rotor angular position is generally measured with shaft mounted rotary position sensors. The mechanical construction of some of these motors prevents commercially available sensors to be mounted on the shaft. An alternative method is therefore developed that measures the rotor angle by analysing the magnetic stray field surrounding the permanent magnet rotor.

Adam et al. [3] conducted a study that analysed the magnetic stray fields surrounding PMSM motors. The study shed some light on magnetic stray field strength around motors and the sources that contribute to the motors' magnetic stray fields. The author found that the magnetic stray fields are comprised of a permanent magnet rotor component and stator winding current component.

Kim et al. [2] used two linear Hall sensors to measure the rotor permanent magnet edge field of a 10 kW 4-pole commercial PMSM (containing iron). These edge-field

measurements are used to estimate the rotor position. In this study the author found non-linearities in the estimated rotor angle. Further investigation showed that higher harmonics, especially the third harmonic, is the cause of this non-linearity.

Sergeant et al. [4] used magnetic stray fields on the outside of an outer rotor brushless DC motor to detect rotor position. The motor stray field was analysed with a FEM simulation to determine the optimal sensor position. Fig. 1 shows a simulation of the magnetic field density around the brushless DC motor (BLDC) [4]. It is apparent that the magnetic field density and direction patterns can be used to identify rotor position.

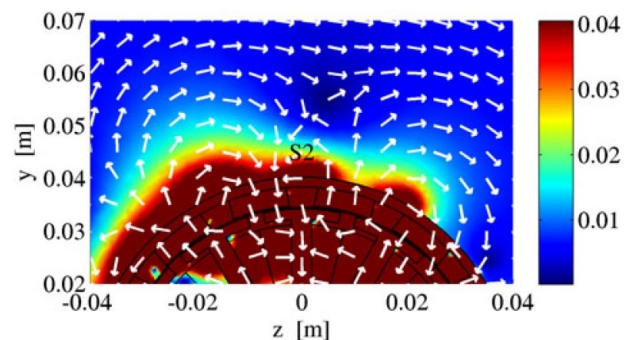


Figure 1: Magnetic field density of BLDC motor [4]

Three SS411A digital hall sensors were positioned at electrical angles of -120° , 0° and 120° respectively as shown in Fig.2. The sensor outputs latches low when exposed to a magnetic field exceeding 7 mT in the normal direction and high when exposed to a magnetic field

exceeding 7 mT in the opposite direction.

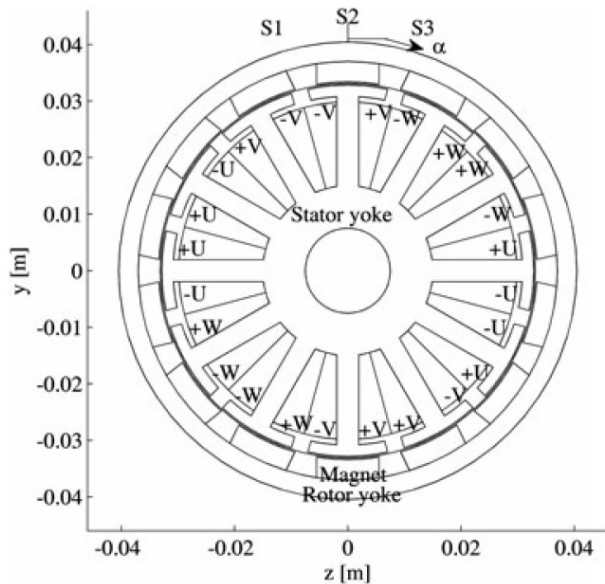


Figure 2: Hall effect sensor placement on BLDC motor [4]

Sensors were placed at a distance of 3 mm from the rotor's outer shell. The author claimed that good results were recorded but did not specify the measurement accuracy. It was noted that the stator current causes a measured phase shift that is directly proportional to the current magnitude, the larger the stator current, the larger the phase shift.

3. METHOD OF IMPLEMENTING MSFRP MEASUREMENT FOR IRONLESS PMSM

In 2015 an ironless double-rotor radial flux permanent magnet synchronous machine (IDRFPM) with carbon fibre body were developed by the University of Stellenbosch. Fig. 3 shows a photo of this IDRFPM. The mechanical construction of this motor prevents a commercial absolute-position sensor from being mounted on the shaft. A custom sensor is therefore developed to measure rotor position. This motor has no iron structure, a Halbach permanent magnet array rather manipulates the magnetic flux path. Since the carbon fibre is non-magnetic, the magnetic stray fields behind the Halbach permanent magnet array is unaffected by the motor body. It is therefore possible to use the magnetic stray field on the outside the PM rotor to determine rotor position.



Figure 3: IDRFPM synchronous machine

The technique presented in [4] focuses specifically on rotor position measurement used for BLDC motor control. In [4] the author constructed a three-element Hall effect rotor position sensor by positioning three digital hall sensors at 120° electrical-angles around the outside rotor facing the radial axis. This method provides a sixty electrical-degree resolution, which is sufficient for BLDC motor control, but not accurate enough for vector control. The implementation investigated in this paper is initial rotor position measurement for an IDRFPM from rotor magnetic stray fields. Fig. 4 shows the magnetic field density pattern of a single rotor Halbach permanent magnet array. Even though the magnetic field density pattern of the Halbach rotor shown in Fig. 4 looks significantly different from that of the BLDC machine shown in Fig. 1, there is still a pattern that can be exploited to measure rotor position. Sensors are mounted on the outside of the rotor as show in Fig. 4. The aim is to identify rotor position by analysing the magnetic field density and direction measured at three key points. The sensors was positioned at a number of different positions. It was decided to position the sensors sixty electrical degree apart, which would allow enough magnetic field change between sensors for accurate rotor measurement, but still keeping the sensor PCB small.

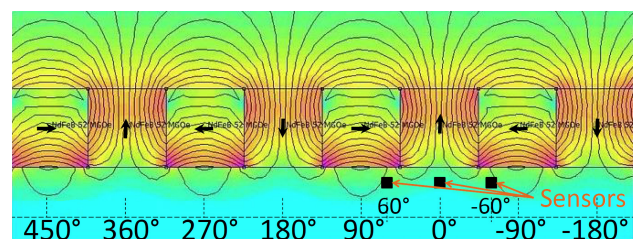


Figure 4: Magnetic field density of a Halbach single rotor [5]

Two types of magnetic sensors were considered. The first is a magnetoresistive sensor, the AFF755B manufactured by Sensitec. This magnetoresistive sensor measures magnetic field density and direction. At first glance this sensor looked like the ideal option. After further investigation it came to light that the nature of the magnetoresistive phenomenon and construction of this sensor prevents it from distinguishing between a change in magnetic field density and direction. Since both the magnetic field density and direction is unknown, this sensor will not be ideal. The second sensor considered is a linear unidirectional Hall sensor the SS496A1 manufactured by Honeywell. This sensor measures the magnetic field density on a single axis with the Hall-effect phenomenon as described by,

$$V_H = I \times B . \quad (1)$$

It was therefore decided to rather measure the magnetic field density on two separate axes with two orthogonally positioned sensors and calculate the field vector magnitude and angle from these measurements.

4. SIMULATED MAGNETIC FIELD LINES AND FLUX DENSITY OF IDRFPM

Fig. 5 shows a Maxwell simulation result of the IDRFPM that need be controlled in this project. In Fig. 5 the magnetic field lines and flux density is clearly shown. The magnetic stray field on the outside of the Halbach rotor is used to identify the rotor electrical angle. The SS496A1 magnetic sensors are placed at a distance of 5.5 mm behind the magnets. At this distance a maximum magnetic flux density of ± 75 mT is expected, which is within the sensor's range of ± 85 mT.

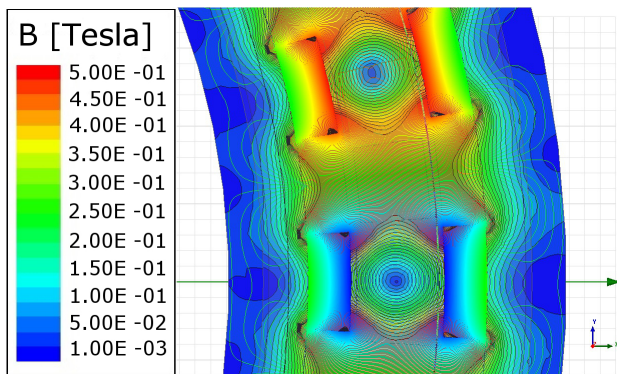


Figure 5: Simulated magnetic field lines and flux density of the IDRFPM for one electrical rotation

Fig. 6 shows the magnetic stray field vector on the magnetic sensor path for one electrical rotation. For every electrical rotation the magnetic stray field vector completes three rotations.

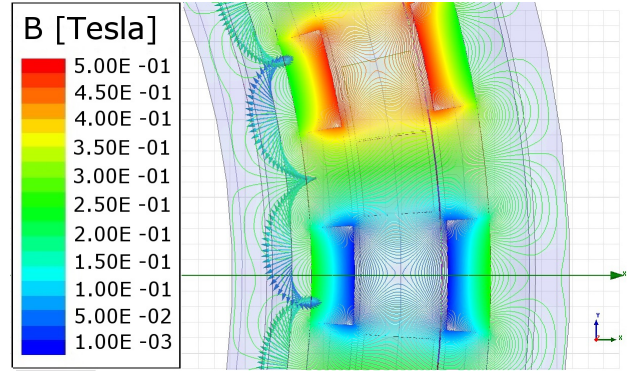


Figure 6: Simulated magnetic field vector on the sensor track for one electrical rotation

The electrical rotor angle is calculated directly from the magnetic stray field vector angle as,

$$\theta_{Electrical} = \frac{\theta_{StrayField}}{3} + \theta_{Initial-region} . \quad (2)$$

The initial magnetic stray field angle-region is however unknown at sensor power-on. The magnitude of the stray field vectors at carefully selected sensor locations can be used to identify the starting region.

Fig. 7 shows the simulated radial (red) and azimuthal (green) stray field magnitude on the sensor track for one electrical rotation. The stray-field vector magnitude (purple) and angle (blue) are calculated from the radial and azimuthal components.

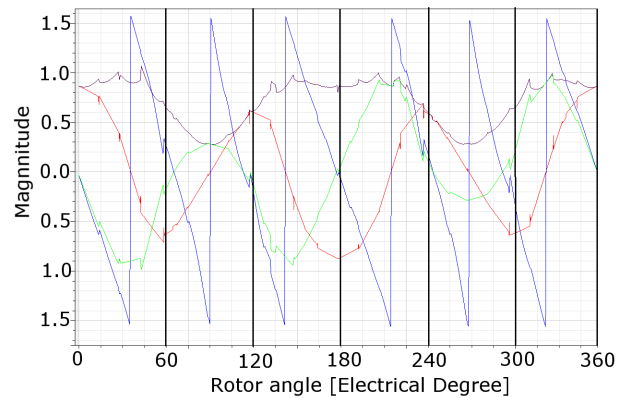


Figure 7: Simulated radial and azimuthal components on the sensor track for one electrical rotation

5. MSFRP-SENSOR PCB

A sensor-PCB containing a microcontroller and Hall sensors was developed. The microcontroller calculates the magnetic stray field vectors from the radial and azimuthal sensor components. These vectors in turn, are used to calculate the rotor electrical angle. The MSFRP-sensor

output is delivered as a varying duty cycle on a PWM signal. The SS496A Hall effect sensor requires a supply rail of 5V. The SS496A sensor output-pin voltage level change between 0.5V and 4.5V for a flux density of between $\pm 85\text{mT}$. The PIC24FV32KA304 microcontroller is chosen since it can operate from a 5V supply rail. Figure 8 shows the MSFRP-sensor block diagram.

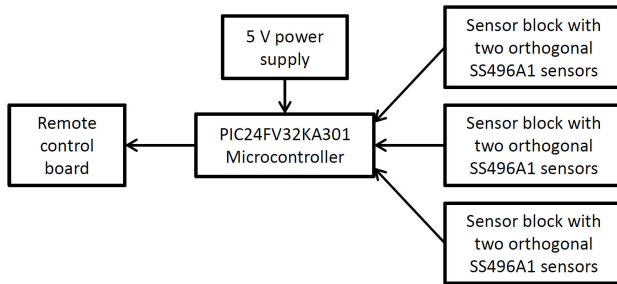


Figure 8: MSFRP-sensor schematic diagram

Figure 9 shows a photo of the populated PCB.

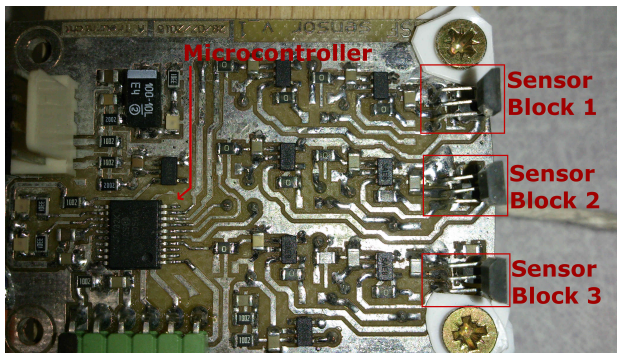


Figure 9: Populated MSFRP-sensor PCB

6. TEST BENCH MEASUREMENTS OF MAGNETIC STRAY FIELDS

Figure 10 shows the angle and magnitude of the magnetic stray field vectors measured at the three sensor locations for two electrical revolutions. The blue, green and turquoise curves show the angle and the red, purple and orange curves show the magnitude of the magnetic stray field vectors at sensor blocks one to three respectively. The simulated magnetic stray field vector shown in Fig. 7 can now be compared with the measured data in Fig. 10. There is a strong correspondence between the measured and simulated stray field angle, the stray field angle changes linearly with rotor position and can therefore be used to measure the rotor electrical angle. Each electrical angle revolution results in three stray field angle revolutions. The vector magnitude is however different from one electrical rotation to the next. This is due to magnet strength and motor manufacturing tolerances. The stray field vector magnitudes can therefore not be used to identify the angle

region as proposed earlier in Ch4. The angle region identification will be performed by a controller probing technique discussed in a future publication.

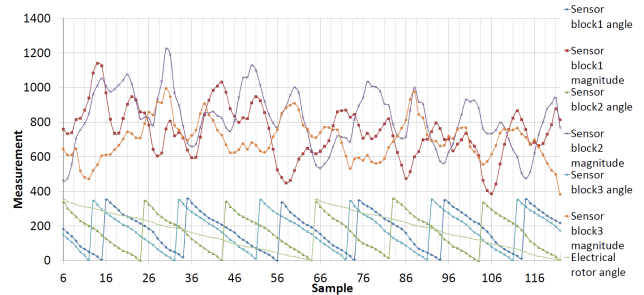


Figure 10: Test bench measurement of magnetic stray field vector for two electrical rotations at three sensor locations

7. MSFRP-SENSOR MEASUREMENT RESULT

Figure 11 shows the measurement result for one electrical rotation with the MSFRP-sensor. The solid line shows the measured electrical angle and the dashed line shows the actual electrical angle.

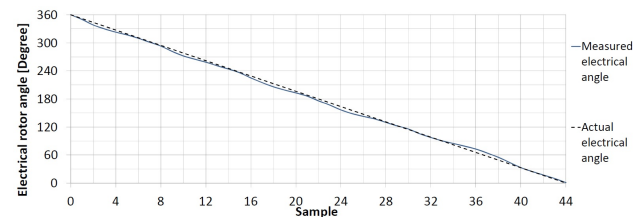


Figure 11: MSFRP-sensor measurement result

Figure 12 shows a graph of the total measurement error for one electrical rotation. This graph is unique to a specific Halbach magnet array. This is due to different magnet strength and motor manufacture tolerances in different areas. A maximum electric angle error of 7.3° is recorded. This translates to a mechanical rotor angle error of 0.56° .

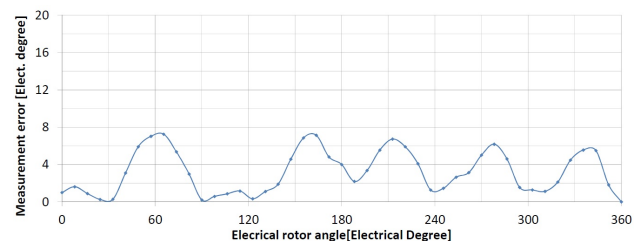


Figure 12: MSFRP-sensor measurement error

8. CONCLUSION

The MSFRP-sensor is a reliable non-contact relative sensor that uses the stray magnetic field behind the

Halbach magnet structure to calculate rotor electrical angle. A similar approach to that presented in [4] is implemented. The magnetic stray field angle behind the Halbach rotor is analysed instead of the magnitude as was done in [4]. This alternative presents better measurement resolution. The magnetic stray field completes three revolutions for every electrical revolution. A relative sensor is constructed using the magnetic stray field angle at one sensor block. An absolute sensor which identifies the region of operation by comparing the relative magnetic stray field magnitudes at three key points was investigated. Different magnet strength tolerances in different Halbach magnet arrays led to unexpected measurements in some areas. The magnetic stray field vector magnitude will therefore not be used. The magnetic stray field angle measurement is also affected by these magnet strength tolerances, but to a lesser degree.

The sensor developed for this study is specifically designed for an IDRFPM, but the technique introduced here can also be applied to different outside-rotor motor topologies. A maximum measurement error of 7.3 electrical degrees was recorder in a practical implementation. The measurement error is caused by magnet strength and motor manufacture tolerances. For the same reason the error curve for each Halbach magnet array is unique to that array.

REFERENCES

- [1] Jaganathan, B., Venkatesh, S., Bhardwaj, Y. and Prakash, C.A.: Kohonen's Self Organizing Map method of estimation of optimal parameters of a Permanent Magnet Synchronous Motor drive. In: *India International Conference on Power Electronics 2010 (IICPE2010)*, pp. 1–6. IEEE, January 2011. ISBN 978-1-4244-7883-5.
- [2] Kim, J.-U., Jung, S.-Y. and Nam, K.-H.: PMSM Angle Detection Based on the Edge Field Measurements by Hall Sensors. *Journal of Power Electronics*, vol. 10, no. 3, pp. 300–305, May 2010. ISSN 1598-2092.
- [3] Adam, A.A., Gülez, K. and Köroğlu, S.: Stray magnetic field distributed around a PMSM. *Turkish Journal of Electrical Engineering and Computer Sciences*, vol. 19, no. 1, pp. 119–131, 2011. ISSN 13000632.
- [4] Sergeant, P., Hofman, I. and Van den Bossche, A.: Magnetic stray field based position detection in BLDC outer rotor permanent magnet synchronous machines. *International Journal of Numerical Modelling*, vol. 27, no. August 2013, pp. 544–554, 2013. ISSN 08943370.
- [5] Wikimedia-Commons: Halbach array field. 2011. Field lines of a single rotor halbach magnet array.
Available at: <https://commons.wikimedia.org>

Enhancing the Dynamic Performance of a Direct-Drive PMSG Wind Turbine Using Damping Controllers

A. N. Legesse^{1*}, A. K. Saha¹ and R. Pillay Carpanen¹

¹ School of Engineering,
University of KwaZulu-Natal,
Durban 4041, South Africa

^{1*}Email: 214584668@stu.ukzn.ac.za, ²e-mail: saha@ukzn.ac.za, ³e-mail: PillayR21@ukzn.ac.za

Abstract: Enhancing the dynamic performance of a permanent magnet synchronous generator wind turbine is vital in its operation as well as integration into a power grid. Currently, proportional-integral controllers are widely employed to control and enhance the dynamic performance of wind turbines. This paper proposes the use of damping controllers, with proportional-integral controllers, to improve oscillation damping. In the proposed scheme, the d -axis damping controller is a supplementary controller based on the d -axis current, whereas the q -axis controller is a supplementary controller based on rotor speed deviation. Both controllers are implemented in the generator-side controller and their influences on the dynamic performance of the wind turbine are investigated. MATLAB/Simulink simulations on a wind turbine connected to a grid show their effectiveness in damping local oscillations. In the presence of the damping controllers, the rise and settling times of the rotor speed, electromagnetic torque, active power and reactive power are further reduced and the corresponding damping ratios are increased. Overall, supplementary damping controllers are capable of smoothing the rotor speed and power of a wind turbine.

1 INTRODUCTION

The world's demand for energy is rapidly growing due to population increase, modernization and technological advancements. Currently, we heavily rely on fossil fuels for our energy requirements. However, our fuel dependent economy is challenged by depletion of reserves, global warming, security concerns and rising cost [1]. In response to these factors, governments have revised their energy policies in favour of renewable energy resources, of which wind energy is the cheapest in the industry [2], [3].

Wind energy technologies, such as squirrel-cage induction generator (SCIG), doubly-fed induction generator (DFIG) and permanent magnet synchronous generator (PMSG) wind turbines, are prevalent in the market. In comparison with SCIG, the DFIG and PMSG are famous for two reasons [4]. Firstly, they can be operated at maximum power for ranging wind speeds.

Secondly, they have less stress on their shafts. Most large-scale wind farms use DFIG wind turbines [5]. Nonetheless, recently, direct drive PMSG wind turbines are gaining momentum among researchers, engineers and turbine manufacturers due to their high efficiency, low power loss and smaller size [6] – [11].

The level of penetration of wind power in power grids is growing fast. In some European countries, it has reached as high as 21% [12]. As a result, there are concerns such as generation reserve, system stability and reliability, related to the intermittent nature of the wind and its high presence [13]. Hence, the stability of wind turbines has started challenging transmission system operators. In large grids, damping capabilities of local and system-wide oscillations are imperative [14].

Local oscillations of a PMSG wind turbine can be damped through active power control [14] – [21] or reactive power control [4], [21] – [25]. In [16], springs and dampers are employed to give the PMSG wind turbine a damping capability, whereas [19] investigates an active damping strategy using DC-link current estimation for torsional oscillations. Most researchers focus on improving the dynamic performance of the wind turbine through the converters using proportional-integral (PI) controllers [14]. However, the performances of supplementary d -axis damping controller, which is based on d -axis current, and q -axis damping controller, which depends on rotor speed deviation, have not yet been investigated.

This paper, therefore, proposes the use of supplementary damping controllers, along with proportional-integral controllers, to improve the dynamic performance of a PMSG wind turbine. And the controllers are implemented in the generator-side converter controller.

In the paper, Section 2 presents the modeling of the supplementary controllers and the different components of a PMSG wind turbine, whereas Section 3 focuses on the model of the power grid. Subsequently, simulations are presented and discussed in 4. Finally, a conclusion is drawn in Section 5.

2 MODELING OF A PMSG WIND TURBINE

Fig. 1 shows the configuration of a wind turbine, employing a PMSG, where the generator is directly driven by a wind rotor. The back-to-back converters, the filter and the transformer connect the wind turbine to the power grid. The converters convert the low-frequency (10 – 15 Hz) voltage of the generator into a 50 or 60 Hz voltage, whereas the filter is responsible for filtering the harmonics created by the power electronic converters out. The transformer steps up the output voltage to the grid voltage level [26] – [29].

The next sub-sections discuss the models of the proposed controllers and the major components of the PMSG wind turbine.

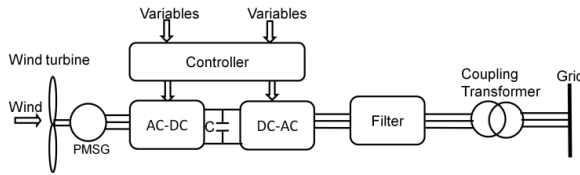


Fig. 1: A PMSG wind turbine connected to a grid

2.1. Wind Speed

Wind speed is a random variable and relies on the climate and geographic location of the wind farm. It consists of a base speed, gust, ramp and background noise components. Such behaviours of the wind can be represented by a Fourier series [5]. Equation (1) gives the wind speed model considered in this work.

$$v_w(t) = v_0 + \sum_{k=1}^N a_k \sin(\omega_k t) + \sum_{k=1}^N b_k \cos(\omega_k t) \quad (1)$$

v_w is the wind speed, v_0 refers to the base component of the wind speed, a_k and b_k are sine and cosine coefficients respectively, ω_k is the angular frequency of the k^{th} harmonics, and N is the number of harmonics. Appropriate selection of the harmonics can approximate the gust, ramp and background noise components. Particularly, the harmonics are important to study the small-signal performance of the PMSG wind turbine in relation to wind speed disturbances.

2.2. Drive Train

In Fig. 1, the power electronic converters decouple the wind turbine from the power grid. As a result, the disturbances in the grid could not be seen in the wind turbine [30]. Thus, the drive train is given by a one mass model as shown in (2).

$$\frac{d\omega_m}{dt} = \frac{1}{J} (T_e - T_m) \quad (2)$$

$$J = J_t + J_g \quad (3)$$

In (2) and (3), J , J_t and J_g are the moments of inertia of the whole drive train, the wind turbine, and the PMSG respectively. ω_m is the rotor speed, and T_m refers to the mechanical torque and is given as,

$$T_m = \frac{P_w}{\omega_m} \quad (4)$$

The density of air, ρ , tip to wind speed ratio, λ , pitch angle, θ_p , area swept by the blades, A_r , and the wind speed determine the power, P_w , of the wind turbine (5).

$$P_w = \frac{1}{2} \rho C_p(\lambda, \theta_p) A_r v_w^3 \quad (5)$$

C_p is the power coefficient of the turbine which depends on λ and θ_p , and it can be given as in (6) [26].

$$C_p = 0.5 \left(\frac{116}{\lambda_i} - 0.4\theta_p - 5 \right) e^{\frac{-21}{\lambda_i}} \quad (6)$$

$$\frac{1}{\lambda_i} = \frac{1}{\lambda + 0.08\theta_p} - \frac{0.035}{\theta_p^3 + 1} \quad (7)$$

2.3. Pitch Angle and Speed Regulators

The pitch angle controller tries to keep the PMSG at its rated power for wind speeds exceeding the nominal value. In this paper, a proportional controller, as shown in (8), is used. Besides, the controller contains rate, upper and lower limiters. In (8), K_p is a proportional constant, and ω_{mref} is a reference rotor speed. For speeds less than the nominal value, K_p is zero.

$$\theta_p = K_p(\omega_m - \omega_{mref}) \quad (8)$$

The wind turbine power depends on the wind speed and the pitch angle as shown in (5) and (6). For a particular wind speed and pitch angle, there is an optimum rotor speed at which the output power is also optimum. The controller tries to keep the generator at this optimum power. The speed regulator is governed by (9) [31].

$$P_{ref} = \begin{cases} P_{max} & \text{for } \omega_m > \omega_{m \text{ nominal}} \\ K_{opt} \omega_m^3 & \text{for } \omega_m \leq \omega_{m \text{ nominal}} \end{cases} \quad (9)$$

P_{ref} is the reference wind turbine power, whereas P_{max} is the maximum power. K_{opt} refers to the power constant of the corresponding wind turbine.

2.4. PMSG Model

Fig. 2 shows the equivalent circuit of the PMSG of a wind turbine [30]. Applying Kirchhoff's voltage law to the circuits in Figs. 2(a) and (b), we can write the corresponding d - and q -axis voltages as given in (10) and (11).

$$v_d = R_s i_d + L_d \frac{di_d}{dt} - \omega L_q i_q \quad (10)$$

$$v_q = R_s i_q + L_q \frac{di_q}{dt} + \omega (L_d i_d + \phi_p) \quad (11)$$

L_d and L_q refer to the d - and q -axis inductances, ω is the rotor speed in electrical radian, i_d and i_q are the d -

and q -axis currents, and ϕ_p is the permanent magnet flux.

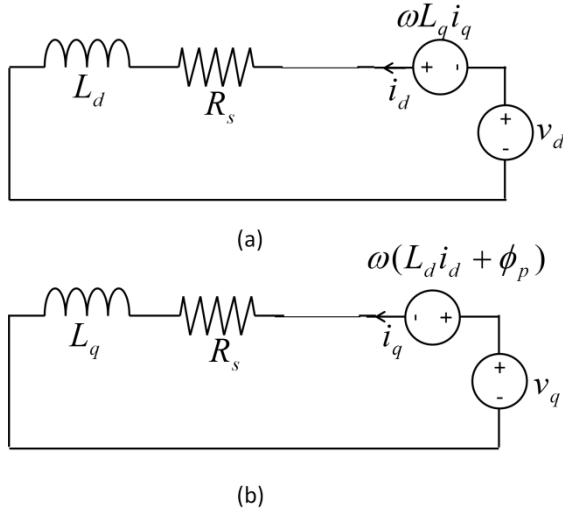


Fig. 2: (a) d -axis and (b) q -axis equivalent circuits of a PMSG

The electromagnetic torque developed in the PMSG is given as [5],

$$T_e = \frac{3}{4}n(\phi_p i_q + (L_d - L_q)i_d i_q) \quad (12)$$

where n is the number of poles of the PMSG.

2.5. Generator-Side Converter Controller

This controller controls the real power of the PMSG through the q -axis voltage, v_q , aiming at minimizing power loss. The d -axis current is maintained at zero to decrease the nonlinearity of (12) and minimize current coupling, and it is achieved through the d -axis voltage, v_d [31].

The proposed damping controllers are implemented in this controller. Fig. 3 shows the main and supplementary controllers in the generator-side controller, and $H(s)$ is the corresponding transfer function. The transfer function may have different forms. However, for this work, proportional-integral controllers have performed well in enhancing the dynamic performance of the wind turbine. In the main control structure, a proportional and two proportional-integral (PI) controllers are used. K_{p1} , K_{p2} , K_{p3} , K_{i1} and K_{i3} are the corresponding gains, and the superscript * shows that the variable is a reference. The main controllers in Figs 3(a) and (b) control i_d and i_q respectively.

The d -axis supplementary controller modifies the corresponding reference voltage by taking the direct axis current as its input, whereas the q -axis supplementary controller totally depends on the rotor speed deviation. In general, the damping controllers act as negative forward loops.

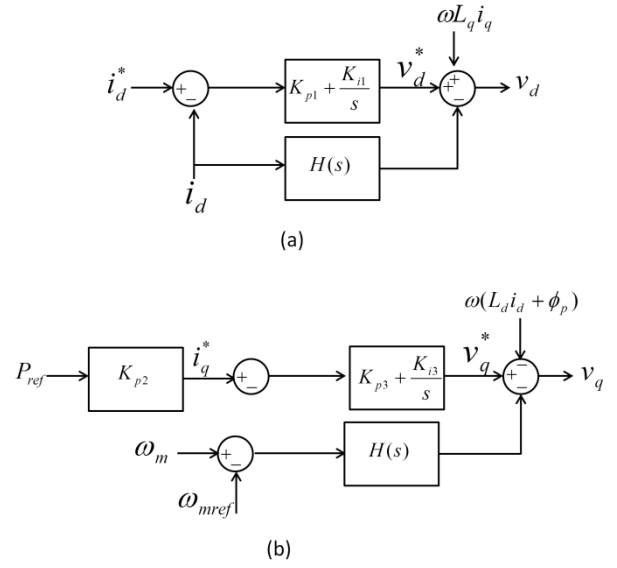


Fig. 3: Generator-side controller with damping controllers

2.6. DC-Link Model

In Fig. 1, as the active power flow through the back-to-back converters and the DC-link is balanced, the net power is nil as shown in (13).

$$P_s + P_{DC} + P_g = 0 \quad (13)$$

In (13), P_{DC} , P_g and P_s are the DC-link power, the real power supplied to the grid and the output power of the PMSG respectively. These powers are given in (14), (15) and (16).

$$P_{DC} = v_{DC} i_{DC} = -C v_{DC} \frac{dv_{DC}}{dt} \quad (14)$$

$$P_s = v_d i_d + v_q i_q \quad (15)$$

$$P_g = v_{Dg} i_{Dg} + v_{Qg} i_{Qg} \quad (16)$$

v_{DC} is the voltage across the capacitor, i_{DC} is the current through the capacitor, v_{Dg} and v_{Qg} refer to the D - and Q -axis voltages at the grid-side converter terminal. As the wind turbine and the grid are decoupled, they operate at different frequencies and the d - and q -axes are not necessarily the same as the D - and Q -axes. i_{Dg} and i_{Qg} are grid currents. Finally, the model of the DC-link is given as,

$$C v_{DC} \frac{dv_{DC}}{dt} = v_{Dg} i_{Dg} + v_{Qg} i_{Qg} + v_d i_d + v_q i_q \quad (17)$$

2.7. Grid-Side Converter Controller

In Fig. 1, the D -axis and Q -axis voltages at the terminal of the grid-side converter are expressed as in (18) and (19) respectively [31].

$$v_{Dg} = v_{Ds} + R_f i_{Dg} + L_f \frac{di_{Dg}}{dt} - \omega_f L_f i_{Qg} \quad (18)$$

$$v_{Qg} = v_{Qs} + R_f i_{Qg} + L_f \frac{di_{Qg}}{dt} + \omega_f L_f i_{Dg} \quad (19)$$

v_{Ds} and v_{Qs} refer to the D -axis and Q -axis voltages at the right end of the filter. R_f and L_f are the filter resistance and inductance, and ω_f is the filter frequency.

In Fig. 4, the grid-side controller has four PI controllers, which control the DC voltage, the D - and Q -axis currents, and the reactive power [31]. All quantities with the superscript * are reference inputs.

Q is reactive power. $K_{p4}, K_{p5}, K_{p6}, K_{p7}, K_{i4}, K_{i5}, K_{i6}$, and K_{i7} are the gains of the controllers. For unity power factor, the reference reactive power is kept at zero.

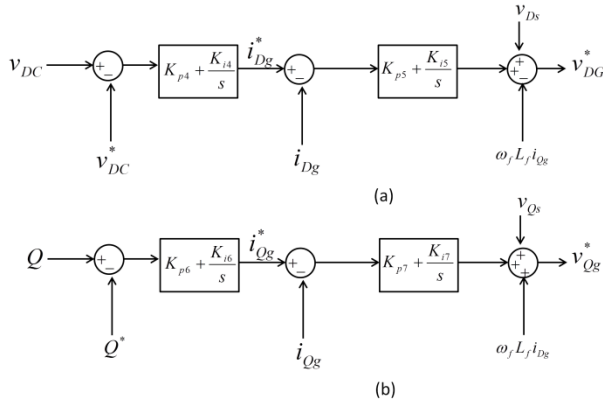


Fig. 4: Grid-side controller structure

3 POWER GRID MODEL

Part of the configuration in Fig. 1 is shown again in Fig. 5 in the form of a one-line diagram. In the diagram, x_T and x_L are the transformer and transmission line impedances respectively, where the respective resistances are neglected, and v_{DQi} is the grid voltage, which leads the terminal voltage of the filter, v_{DQs} , by δ .

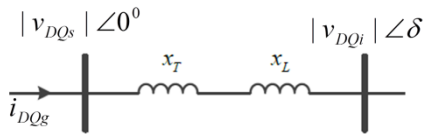


Fig. 5: One-line diagram of the grid, transmission line and transformer

The current, i_{DQg} , which flows from the wind turbine to the grid, is given as,

$$i_{DQg} = \frac{|v_{DQs}| \sin 0 - |v_{DQi}| \sin \delta}{x_T + x_L} + j \frac{-|v_{DQs}| \cos 0 + |v_{DQi}| \cos \delta}{x_T + x_L} \quad (20)$$

For unity power factor, as i_{DQg} is in phase with v_{DQs} , its real and imaginary parts can be expressed as,

$$i_{Dg} = \frac{-|v_{DQi}| \sin \delta}{x_T + x_L} \quad (21)$$

$$i_{Qg} = \frac{-v_{DQs} + |v_{DQi}| \cos \delta}{x_T + x_L} \quad (22)$$

4 SIMULATION RESULTS AND DISCUSSION

In this section, the validity of the proposed method is verified by implementing the models in sections 2 and 3 in MATLAB\Simulink. The dynamic performance of the wind turbine relies on the system characteristics, the intermittent nature of the wind and the load disturbances in the power system. Particularly, the nature of the wind makes the evaluation of this performance challenging, and in this work, large wind speed disturbances are considered.

In general, the performance indices employed in this paper are rise time for assessing the speed of response, settling time for measuring the stability and speed of response, and maximum percent overshoot for determining the relative stability of the wind turbine. Moreover, the degree of oscillation damping is assessed through maximum percent overshoot and damping ratio, which are related as [32],

$$M_p = 100e^{-(\zeta/(1-\zeta^2))\pi} \quad (23)$$

where M_p is the maximum percent overshoot, and ζ is the damping ratio.

In the simulation, the higher order harmonics in (1) were neglected, and a step increase of 12 m/s in the wind speed at the beginning was applied to the wind turbine. Thereafter, the effects of the supplementary controllers on the dynamic performance of the wind turbine were observed.

Fig. 6 indicates the speed response of the PMSG wind turbine when the supplementary controllers are employed in the generator-side controller. In the figure, speed oscillations are successfully damped. Besides, the maximum percent undershoot is significantly reduced, illustrating the system being more stable with the damping controllers.

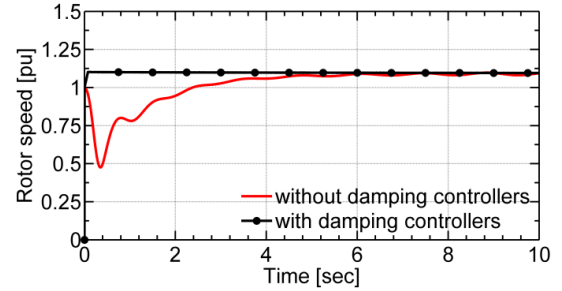


Fig. 6: Effect of the damping controllers on rotor speed

The rise time of the rotor speed is reduced from 3.5 to 0.4 seconds, and the settling time is reduced from 4.8 to 0.6 seconds. Thus, the damping controllers are imperative in damping rotor speed oscillations for large disturbances.

The simulation results in Figs 7, 8 and 9 show that the oscillations in real power, reactive power, electromagnetic torque, and DC-link voltage are effectively damped. Therefore, for large disturbances, the dynamic performance of the wind turbine can be enhanced by employing damping controllers, which depend on direct axis current and rotor speed deviation, for the d - and q -axis voltages of the generator.

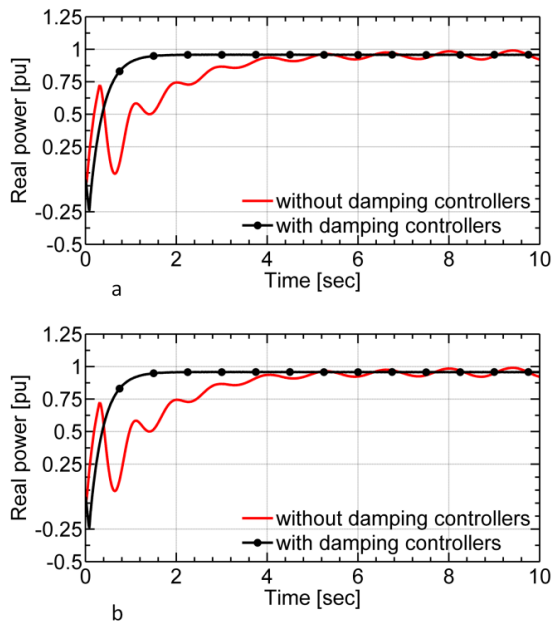


Fig. 7: Effect of damping controller on (a) real power (b) reactive power

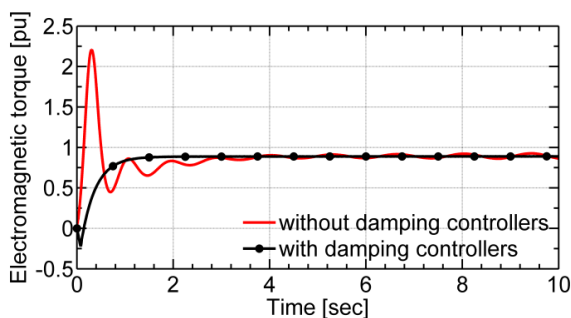


Fig 8: Effect of damping controller on electromagnetic torque

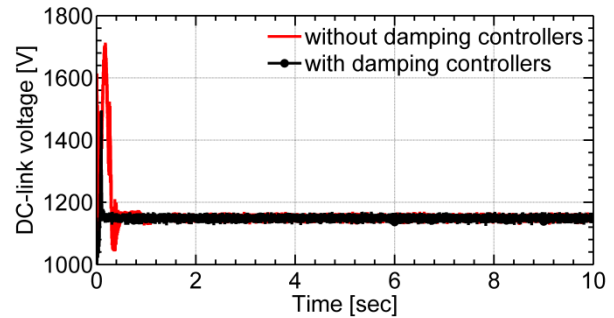


Fig 9: Effect of damping controller on DC-link voltage

In general, implementing supplementary controllers in the generator-side controller significantly enhances the dynamic performance of a PMSG wind turbine.

5 CONCLUSION

This paper proposes the use of supplementary damping controllers in conjunction with PI controllers to enhance the dynamic performance of a PMSG wind turbine. The proposed controllers and the different components of the wind turbine are modelled. Thereafter, all the models have been implemented in MATLAB/Simulink.

Time-domain simulation results have shown that the proposed scheme efficiently enhances the performance of the wind turbine by damping local oscillations. Speed, power, and electromagnetic torque oscillations, caused by wind disturbances, are well damped with supplementary controllers. Moreover, the controllers significantly improve the DC-link response. The technique proposed in this work is applicable in smoothing the rotor speed and the output power of a PMSG wind turbine.

6 REFERENCES

- [1] M. Asif and T. Muneer, "Energy supply, its demand and security issues for developed and emerging economies," *Renewable and Sustainable Energy Reviews*, vol. 11, pp. 1388-1413, 2007.
- [2] REN21, "Renewables global status report [2009 Update]," Renewable Energy Policy Network for the 21st Century, 2009.
- [3] G. Joselin Herberta, S. Iniyan, E. Sreevalsan and S. Rajapandian, "A review of wind energy technologies," *Renewable and Sustainable Energy Reviews*, vol. 11, pp. 1117-1145, 2007.
- [4] Z. Miao, L. Fan, D. Osborn and S. Yuvarajan, "Control of DFIG-based wind generation to improve interarea oscillation damping," *IEEE Transactions on Energy Conversion*, vol. 24, no. 2, pp. 415-422, 2009.
- [5] A. Rolan, A. Luna, G. Vazquez, A. Daniel and G. Azevedo, "Modeling of a variable speed wind turbine with a permanent magnet synchronous generator," in *IEEE International Symposium on Industrial Electronics*, Seoul, Korea, July 5-8, 2009.
- [6] L. B. Shi, L. Kang, L. Z. Yao, S. Y. Qin, R. M. Wang and J. P. Zhang, "Effects of wind generation uncertainty and volatility

- on power system small-signals Stability,” *Journal of Electrical Engineering Technology*, vol. 9, no. 1, pp. 60-70, 2014.
- [7] H. Espen, I. Norheim and K. Uhlen, “Large-scale wind power integration in Norway and impact on damping in the Nordic grid,” *Wind Energy*, vol. 8, no. 3, pp. 375-384, 2005.
- [8] M. A. Mahmud, M. J. Hossain, H. R. Pota and C. Zhang, “Investigation of critical factors affecting dynamic stability of wind generation systems with permanent magnet synchronous generators,” in *The International Federation of Automatic Control*, Cape Town, South Africa, August 24-29, 2014.
- [9] E. Mahersi, A. Khedher and M. Mimouni, “The wind energy conversion system using PMSG controlled by vector control and SMC strategies,” *International journal of renewable energy research*, vol. 3, no. 1, pp. 41-50, 2013.
- [10] K. Zhao, G. Li, B. Wang and M. Zhou, “Grid-connected topology of PMSG wind power system based on VSC-HVDC,” in *Electric Utility Deregulation and Restructuring and Power Technologies (DRPT)*, Weihai, Shandong, 2011.
- [11] N. Abdolghani, J. Milimonfared and G. B. Gharehpetian, “A direct torque control method for CSC based PMSG wind energy conversion systems,” in *International Conference on Renewable Energies and Power Quality*, Santiago de Compostela, Spain, 28-30 March 2012.
- [12] WWEA, “World wind energy report,” 2010;2011.
- [13] H. Ahmadi and H. Ghasemi, “Maximum penetration level of wind generation considering power system security limits,” *IET Generation, Transmission & Distribution*, vol. 6, no. 11, pp. 1164-1170, 2012.
- [14] J. L. Domínguez-García, O. G. Bellmunt, F. D. Bianchi and A. Sumper, “Power oscillation damping supported by wind power: a review,” *Renewable and Sustainable Energy Reviews*, vol. 16, pp. 4994-5006, 2012.
- [15] A. Sanchez, M. Molina and A. Lede, “Dynamic model of wind energy conversion systems with PMSG-based variable-speed wind turbines for power system studies,” *International Journal of Hydrogen Energy*, vol. 37, pp. 10064-10069, 2012.
- [16] A. Westlake, J. Bumby and E. Spooner, “Damping the power-angle oscillations of a permanent-magnet synchronous generator with particular reference to wind turbine applications,” *IEE Proceedings Electric Power Applications*, vol. 143, no. 3, pp. 269 - 280, 1996.
- [17] C. Jauch, S. M. Islam, P. Sørensen and B. B. Jensen, “Design of a wind turbine pitch angle controller for power system stabilisation,” *Renewable Energy*, vol. 32, pp. 2334-2349, 2007.
- [18] C. Jauch, T. Cronin, P. Sørensen and B. Jensen, “A fuzzy logic pitch angle controller for power system stabilization,” *Wind Energy*, vol. 10, pp. 19-30, 2007.
- [19] H. Geng, D. Xu, B. Wu and G. Yang, “Active damping for PMSG-based WECS with DC-Link current estimation,” *IEEE Transactions on Industrial Electronics*, vol. 58, no. 4, pp. 1110-1119, 2011.
- [20] Xu, H. Geng and Dewei, “Stability analysis and improvements for variable-speed multipole PMSG-based wind energy conversion system,” *IEEE Transactions on Sustainable Energy*, vol. 2, no. 4, pp. 459-466, 2011.
- [21] B. Han, Y. Wang, H. Li and X. Zhang, “Supplementary power control of PMSG-based wind farms for system dynamic stability,” in *IEEE international conference on electrical machines and systems*, Busan, Korea, 2013.
- [22] S. Rodrigues, R. T. Pinto, P. Bauer and J. Pierik, “Multi-objective optimization of a PMSG control system through small-signal analysis,” in *IEEE ECCE Asia Downunder (ECCE Asia)*, Melbourne, VIC, 3-6 June 2013.
- [23] A. Adamczyk, R. Teodorescu and P. Rodriguez, “Control of full-scale converter based wind power plants for damping of low frequency system oscillations,” in *IEEE PowerTech*, Trondheim, 2011.
- [24] X. Zhang, Y. Wang and H. Li, “Control of PMSG-based wind turbines to damp the power system oscillations,” in *IEEE PEDS 2011*, Singapore, December 2011.
- [25] L. Fan, H. Yin and Z. Miao, “Active/reactive power modulation of DFIG-based wind generation for inter area oscillation damping,” *IEEE Transactions on Energy Conversion*, vol. 26, pp. 513-521, 2011.
- [26] T. Ackermann, *Wind power in power systems*, Stockholm, Sweden: John Wiley and Sons, Ltd, 2005.
- [27] J. F. McGowan and G. J. Manwell, *Wind energy explained: design and application*, Washington DC: John Wiley & Sons Ltd, 2009.
- [28] I. Al-Bahadly, *Wind turbines*, Rijek, Croatia: InTech, 2011.
- [29] B. Fox, D. Flynn, L. Bryans, N. Jenkins, D. Milborrow, M. O'Malley, R. Watson and O. Anaya-Lara, *Wind power integration connection and system operational aspects*, London, United Kingdom: The Institution of Engineering and Technology, 2007.
- [30] F. Wu, X.-P. Zhang and a. P. Ju, “Small signal stability analysis and control of the wind turbine with the direct-drive permanent magnet generator integrated to the grid,” *Electric Power Systems Research*, vol. 79, pp. 1661-1667, 2009.
- [31] S. K. Yun, Y. C. Il and I. M. Seung, “Tuning of the PI controller parameters of a PMSG wind turbine to improve control performance under various wind speeds,” *Energies*, vol. 8, pp. 1406-1425, 2015.
- [32] K. Ogata, *Modern Control Engineering*, New Jersey: Prentice Hall, 2002.